Paola F. Antonietti
Lourenço Beirão da Veiga
Gianmarco Manzini   *Editors*

The Virtual Element Method and its Applications

SēMA

SIMAI
SOCIETÀ ITALIANA DI MATEMATICA
APPLICATA E INDUSTRIALE

Springer

SEMA SIMAI Springer Series

Volume 31

Editors-in-Chief

José M. Arrieta, Departamento de Análisis Matemático y Matemática Aplicada, Facultad de Matemáticas, Universidad Complutense de Madrid, Madrid, Spain

Luca Formaggia ⓘ, MOX–Department of Mathematics, Politecnico di Milano, Milano, Italy

Series Editors

Mats G. Larson, Department of Mathematics, Umeå University, Umeå, Sweden

Tere Martínez-Seara Alonso, Departament de Matemàtiques, Universitat Politècnica de Catalunya, Barcelona, Spain

Carlos Parés, Facultad de Ciencias, Universidad de Málaga, Málaga, Spain

Lorenzo Pareschi, Dipartimento di Matematica e Informatica, Università degli Studi di Ferrara, Ferrara, Italy

Andrea Tosin, Dipartimento di Scienze Matematiche "G. L. Lagrange", Politecnico di Torino, Torino, Italy

Elena Vázquez-Cendón, Departamento de Matemática Aplicada, Universidade de Santiago de Compostela, A Coruña, Spain

Paolo Zunino, Dipartimento di Matematica, Politecnico di Milano, Milano, Italy

As of 2013, the SIMAI Springer Series opens to SEMA in order to publish a joint series aiming to publish advanced textbooks, research-level monographs and collected works that focus on applications of mathematics to social and industrial problems, including biology, medicine, engineering, environment and finance. Mathematical and numerical modeling is playing a crucial role in the solution of the complex and interrelated problems faced nowadays not only by researchers operating in the field of basic sciences, but also in more directly applied and industrial sectors. This series is meant to host selected contributions focusing on the relevance of mathematics in real life applications and to provide useful reference material to students, academic and industrial researchers at an international level. Interdisciplinary contributions, showing a fruitful collaboration of mathematicians with researchers of other fields to address complex applications, are welcomed in this series.

THE SERIES IS INDEXED IN SCOPUS

Paola F. Antonietti • Lourenço Beirão da Veiga •
Gianmarco Manzini
Editors

The Virtual Element Method and its Applications

Springer

Editors

Paola F. Antonietti
Dipartimento di Matematica
MOX - Politecnico di Milano
Milano, Italy

Lourenço Beirão da Veiga
Dipartimento di Matematica e Applicazioni
Università di Milano Bicocca
Milano, Italy

Gianmarco Manzini
Istituto di Matematica Applicata e
Tecnologie Informatiche
Consiglio Nazionale delle Ricerche
Pavia, Italy

Next above these come the Nobility, of whom there are several degrees, beginning at Six-Sided Figures, or Hexagons, and from thence rising in the number of their sides till they receive the honourable title of Polygonal, or many-sided (from "Flatland Project - The cultural experience by K. Sadanand")

Preface

The possibility of making use of arbitrarily shaped polygonal/polyhedral meshes in a Galerkin framework like that of the Finite Element Method (FEM) has aroused a large wave of interest among mathematicians and engineers during the last two decades. Handling such kind of meshes is indeed an edge when treating computational domains with a complex geometry, and the number of potential benefits that are worth mentioning is quite long. Efficient algorithms can easily be devised for grid refinement and de-refinement by conveniently adding/removing nodes and edges and through agglomeration techniques. Very simple but effective mesh cutting techniques can also be implemented to deal with cracks in materials. In this setting, moving domains and mesh gluing techniques make it possible to deal with hybrid-dimensional problems, layer approximation, independent sub-domain mesh combination, etc.

Robust and accurate numerical schemes, sometimes logically and conveniently regrouped in "families", have thus been proposed to the numerical community and widely investigated in the last two decades such as the Virtual Element Method (VEM), the Polygonal/Polyhedral Finite Element Method (PFEM), the Mimetic Finite Difference (MFD) method, the weak Galerkin (wG) method, the Polygonal Discontinuous Galerkin (PDG) methods, the Hybrid High-Order (HHO) method, and their many variants.

The VEM was first proposed in 2013 by Beirao da Veiga, Brezzi, Cangiani, Manzini, Marini, and Russo, and since then has rapidly set itself as one of the leading technologies in this field. Unique to the VEM among the methods previously mentioned is the interpretation of the functional approximation spaces as provided by the solutions of elementwise Partial Differential Equation (PDE) problems. Ancestors of the VEM can be drawn back to the compatible and mimetic discretization proposed since the mid-1960s by Samarski's school in Moscow. Limiting the historical range to this century, it is worth mentioning the Mimetic Finite Difference method, which, in 2005, stemmed out of the collaboration of Prof. F. Brezzi, from the University of Pavia and IMATI-CNR, and Drs. M. Shashkov and K. Lipnikov, from Los Alamos National Laboratory in Los Alamos, NM.

Effectively, the MFD approach is somehow in between finite differences and finite elements, since the discrete solution can be represented by a collection of degree of freedom–like nodal values as in finite differences rather than a function, but the discrete scheme is built according to a sort of variational formulation where grid functions are used as test and trial functions. L^2 and H^1 inner products used in the variational formulations are approximated by discrete scalar products mimicking their continuous counterparts and aiming at consistency and stability in accordance with the Lax principle that states that stability and convergence are equivalent for a consistent scheme. Elementwise constructions of related stiffness and mass matrices make the implementation structurally similar to that of the FEM. MFD schemes have been applied to a wide range of problems, and the flexibility in using polygonal and polyhedral meshes without the need to integrate complex shape functions, as it happens in polygonal FEM, has made them very successful. Eventually, limitations of the MFD method came out and had to be addressed by numerical mathematicians. Nonetheless, a wide literature of MFD schemes for different applications is currently available, and MFD schemes are still employed in production codes.

The limitations of the MFD method are basically two: the first one is of practical character and related to the extension to nonlinear PDEs, and the second one is of theoretical nature with some "psychological" aspects, which are not less important. Mathematical models involving nonlinear PDEs can hardly be handled in an iterative way without an explicit knowledge of the intermediate approximate solutions. Even the most elementary approach, based, for example, on Picard Iterations, requires the evaluation of nonlinear functionals and/or multilinear forms that may nonlinearly depend on the solution, and in MFD, this solution is not available numerically unless pursuing some "ad hoc" reconstruction or post-processing from the degrees of freedom. The most theoretical issue was conversely related to the absence of the shape functions (or of an equivalent definition of them), which makes the convergence analysis and the derivation of error estimates quite cumbersome. Hermetic language and notation made it also somehow difficult to appreciate the interesting novelties of the MFD approach.

Objectively speaking, the Virtual Element Method was very successful in addressing these two key points, and providing a solid Galerkin background and a formal finite element backbone to mimetic discretization. Despite being born as a bridge between the FEM and the MFD method, the VEM has soon turned out into a new original paradigm for the numerical resolution of PDEs due to the significant advantages it offers in a broad and somehow initially unexpected range of directions. Indeed, the possibility of building approximation spaces, with the associated set of degrees of freedom but without the need of explicitly specifying the construction of the corresponding basis functions, provides a strong tool that simplifies and drives its application to new and more complex problems. Specifically, the novel idea of using projectors in order to build the discrete bilinear forms made the construction of the approximate weak formulations more systematic. The use of projectors allowed, indeed, the extension to a whole new range of nonlinear problems that were out of reach for MFD.

Herein, the few fundamental concepts are the following, briefly mentioned in this paragraph as a sort of a *VEM in a nutshell*. Element by element, the local finite element space is *virtual* in the sense that it is defined implicitly by all the solutions of a suitable local partial differential equation problem. Based on such principle, all associated shape functions are also virtual, and they never need to be explicitly computed in any practical implementation of the method. Elemental degrees of freedom are carefully chosen to have some special polynomial projections of the virtual element functions directly computable and guarantee certain conformity conditions when glued together to form the global virtual element spaces. Such projectors are used to build the discrete forms needed in the variational formulation of the problem according to the classical Galerkin paradigm. To avoid the ensuing non-physical kernel that stems out of the presence of the projections, an ad-hoc stabilization term is finally added to the discrete formulation.

A major advantage in the VEM approach is the possibility to construct discrete spaces featuring higher-order continuity properties, for example, C^1 and C^2 or even higher global regularity. Novel competitive elements/schemes also on classical triangular/quadrilateral and tetrahedral/hexahedral grids can thus be designed to preserve important physical features/constraints, such as the divergence-free nature of the magnetic field in Maxwell equations and the velocity in incompressible Navier-Stokes equations, or the symmetry of a tensor field in the Hellinger-Reissner formulation of elasticity. Doubtlessly, the number of degrees of freedom in a VEM formulation can be bigger when compared to FEM on quadrilaterals and hexahedra, but serendipity makes it possible to reduce such number and obtain more computationally efficient schemes with less degrees of freedom than standard FEM.

The Virtual Element Method has enjoyed a large success in these years, and many articles were published from researchers all over the world to address theoretical challenges that are peculiar to this methodology, such as, for instance, the development of interpolation estimates on general polygonal/polyhedral meshes under different mesh assumptions, and the design and analysis of stabilization strategies that are robust with respect to the mesh geometry. Highest priority in the design of the method has also been given to applications from fluid mechanics, solid mechanics, and geophysics and, specifically, to phase transition problems, time-dependent parabolic and hyperbolic problems, problems in electro-magnetism, and topology optimization, just to mention a few. Examples of open-source codes that illustrate the most practical and technical aspects of the implementation are also available and publicly accessible from open software repositories.

Generally speaking, the large interest on the VEM triggered the launch of this volume, which presents snapshots of state-of-the-art advances in some of the fields mentioned above. Ranging through challenging problems in the field of computational mechanics, fluid dynamics, wave propagations phenomena, and magneto-hydrodynamics, the various chapters of this volume review a number of modern topics of the VEM for the numerical approximation of linear and non-linear PDEs. Each invited paper has been authored by some of the most active scientists within the VEM research community. Additionally, it is worth mentioning that most

of the authors of different chapters have also jointly collaborated to the development of the virtual element method in other scientific areas.

The chapters in this volume can be roughly classified into three groups, starting from three chapters that discuss more technical and theoretical aspects such as the generality of the meshes suitable to the VEM, the implementation of the VEM for linear and nonlinear PDEs, and the construction of discrete hessian complexes in three dimensions in the VEM framework:

– Chapter 1, "VEM and the Mesh", by Tommaso Sorgente, Daniele Prada, Daniela Cabiddu, Silvia Biasotti,Giuseppe Patanè, Micol Pennacchio, Silvia Bertoluzza, Gianmarco Manzini, and Michela Spagnuolo
– Chapter 2, "On the Implementation of Virtual Element Method for Non-linear Problems over Polygonal Meshes", by Dibyendu Adak, M Arrutselvi, E Natarajan, and S Natarajan
– Chapter 3, "Discrete Hessian Complexes in Three Dimensions", by Long Chen and Xuehai Huang

Effective VEMs for applied mathematical modeling are presented in the second group, which comprises the following seven chapters focusing on the numerical discretization of paradigmatic linear and non-linear partial differential problems from computational mechanics, fluid dynamics, and wave propagation phenomena:

– Chapter 4, "Some Virtual Element Methods for Infinitesimal Elasticity Problems", by Edoardo Artioli, Stefano de Miranda, Carlo Lovadina, Luca Patruno, and Michele Visinoni
– Chapter 5, "An Introduction to Second-Order Divergence-Free VEM for Fluidodynamics", by Lourenço Beirão da Veiga and Giuseppe Vacca
– Chapter 6, "Virtual Marriage à la Mode: Some Recent Results on the Coupling of VEM and BEM", by Gabriel N. Gatica, Antonio Márquez, and Salim Meddahi
– Chapter 7, "Virtual Element Approximation of Eigenvalue Problems", by Daniele Boffi, Francesca Gardini, and Lucia Gastaldi
– Chapter 8, "Virtual Element Methods for a Stream-Function Formulation of the Oseen Equations", by David Mora and Alberth Silgado
– Chapter 9, "The Non-conforming Trefftz Virtual Element Method: General Setting, Applications, and Dispersion Analysis for the Helmholtz Equation", by Lorenzo Mascotto, Ilaria Perugia, and Alexander Pichler
– Chapter 10, "The Conforming Virtual Element Method for Polyharmonic and Elastodynamics Problems: A Review", by Paola F. Antonietti, Gianmarco Manzini, Ilario Mazzieri, Simone Scacchi, and Marco Verani

Solid mechanics modeling of materials with fractures, magneto-hydrodynamics phenomena, and contact solid mechanics using the VEM are addressed in the last three chapters:

– Chapter 11, "The Virtual Element Method in Nonlinear and Fracture Solid Mechanics", by Edoardo Artioli, Sonia Marfia, and Elio Sacco

– Chapter 12, "The Virtual Element Method for the Coupled System of Magneto-hydrodynamics", by Sebastián Naranjo Álvarez, Vrushali Bokil, Vitaliy Gyrya, and Gianmarco Manzini
– Chapter 13, "Virtual Element Methods for Engineering Applications", by Peter Wriggers, Fadi Aldakheel, and Blaž Hudobivnik

The ultimate goal of this work, and our greatest hope and willingness on serving as the editors of this volume, is to make the fascinating world of virtual elements known and interesting to as many scientists as possible so to attract other research communities to the development of the VEM beyond that of the numerical mathematicians.

Milano, Italy   Paola F. Antonietti
Milano, Italy   Lourenço Beirão da Veiga
Pavia, Italy   Gianmarco Manzini
September 2022

Contents

Editors and Contributors

About the Editors

Paola F. Antonietti is Full Professor of Numerical Analysis at Politecnico di Milano, Italy. Her research interests concern the development and analysis of numerical methods for partial differential equations with applications to computational geosciences. She is particularly interested in nonstandard high-order finite element methods, including virtual elements and discontinuous Galerkin methods on polygonal and polyhedral grids.

Lourenço Beirão da Veiga is Full Professor of Numerical Analysis at the University of Milano-Bicocca, Italy. His research mainly concerns the development and theoretical analysis of numerical methods for partial differential equations, with a particular focus on solid and fluid mechanics. His more recent interests are on novel and nonstandard methodologies such as isogeometric analysis, mimetic finite differences, and virtual element methods.

Gianmarco Manzini is a Research Director of the Consiglio Nazionale delle Ricerche in Pavia, Italy, and a senior scientist at the Los Alamos National Laboratory in Los Alamos, New Mexico. His research interests mainly concern the design and implementation of numerical methods for partial differential equations, with a special focus on numerical methods for polygonal and polyhedral meshes such as finite volumes, mimetic finite differences, and virtual element methods.

Contributors

Dibyendu Adak GIMNAP, Departamento de Matemática, Universidad del Bío-Bío, Concepción, Chile

Fadi Aldakheel Institute of Continuum Mechanics, Department of Mechanical Engineering, Leibniz University Hannover, An der Universität 1, Garbsen, Germany

Sebastián Naranjo Álvarez Dipartimento di Matematica, Università degli Studi di Milano-Bicocca, Milano, Italia

Paola F. Antonietti MOX, Dipartimento di Matematica, Politecnico di Milano, Milan, Italy

M. Arrutselvi Department of Mathematics, Indian Institute of Space Science and Technology, Thiruvananthapuram, Kerala, India

Edoardo Artioli Department of Civil Engineering and Computer Science, University of Rome Tor Vergata, Rome, Italy
Department of Civil Engineering and Computer Science, University of Rome Tor Vergata, Via del, Rome, Italy

Silvia Bertoluzza IMATI-CNR, Pavia, Italy

Silvia Biasotti IMATI-CNR, Genova, Italy

Daniele Boffi King Abdullah University of Science and Technology (KAUST), Thuwal, Saudi Arabia
Dipartimento di Matematica "F. Casorati", Università degli Studi di Pavia, Pavia, Italy

Vrushali A. Bokil Department of Mathematics, Oregon State University, Corvallis, OR, USA

Daniela Cabiddu IMATI-CNR, Genova, Italy

Long Chen Department of Mathematics, University of California at Irvine, Irvine, CA, USA

Lourenço Beirão da Veiga Dipartimento di Matematica e Applicazioni, Università degli Studi di Milano Bicocca, Milano, Italy

Stefano de Miranda DICAM, University of Bologna, Bologna, Italy

Francesca Gardini Dipartimento di Matematica "F. Casorati", Università degli Studi di Pavia, Pavia, Italy

Lucia Gastaldi DICATAM, Università degli Studi di Brescia, Brescia, Italy

Gabriel N. Gatica CI^{2}MA and Departamento de Ingeniería Matemática, Universidad de Concepción, Concepción, Chile

Vitaliy Gyrya Group T-5, Theoretical Division, Los Alamos National Laboratory, Los Alamos, NM, USA

Xuehai Huang School of Mathematics, Shanghai University of Finance and Economics, Shanghai, China

Blaž Hudobivnik Institute of Continuum Mechanics, Department of Mechanical Engineering, Leibniz University Hannover, An der Universität 1, Garbsen, Germany

Carlo Lovadina Department of Mathematics, University of Milan, Milan, Italy

Gianmarco Manzini IMATI-CNR, Pavia, Italy
Group T-5, Theoretical Division, Los Alamos National Laboratory, Los Alamos, NM, USA

Sonia Marfia Department of Engineering, University of Roma Tre, Roma, Italy

Antonio Márquez Departamento de Construcción e Ingeniería de Fabricación, Universidad de Oviedo, Oviedo, España

Lorenzo Mascotto Department of Mathematics and Applications, University of Milano-Bicocca, Milan, Italy
Faculty of Mathematics, University of Vienna, Vienna, Austria
IMATI-CNR, Pavia, Italy

Ilario Mazzieri MOX, Dipartimento di Matematica, Politecnico di Milano, Milan, Italy

Salim Meddahi Departamento de Matemáticas, Facultad de Ciencias, Universidad de Oviedo, Oviedo, España

David Mora GIMNAP, Departamento de Matemática, Universidad del Bío-Bío, Concepción, Chile
CI2MA, Universidad de Concepción, Concepción, Chile

E. Natarajan Department of Mathematics, Indian Institute of Space Science and Technology, Thiruvananthapuram, Kerala, India

S. Natarajan Department of Mechanical Engineering, Indian Institute of Technology Madras, Chennai, Tamil Nadu, India

Giuseppe Patanè IMATI-CNR, Genova, Italy

Luca Patruno DICAM, University of Bologna, Bologna, Italy

Micol Pennacchio IMATI-CNR, Pavia, Italy

Ilaria Perugia Faculty of Mathematics, University of Vienna, Vienna, Austria

Alexander Pichler Faculty of Mathematics, University of Vienna, Vienna, Austria

Daniele Prada IMATI-CNR, Pavia, Italy

Elio Sacco Department of Structures for Engineering and Architecture, University of Naples Federico II, Naples, Italy

Simone Scacchi Dipartimento di Matematica, Università di Milano, Milan, Italy

Alberth Silgado GIMNAP, Departamento de Matemática, Universidad del Bío-Bío, Concepción, Chile

Tommaso Sorgente IMATI-CNR, Genova, Italy

Michela Spagnuolo IMATI-CNR, Genova, Italy

Giuseppe Vacca Dipartimento di Matematica, Università degli Studi di Bari, Bari, Italy

Marco Verani MOX, Dipartimento di Matematica, Politecnico di Milano, Milan, Italy

Michele Visinoni Department of Mathematics and Applications, University of Milano Bicocca, Milan, Italy

Peter Wriggers Institute of Continuum Mechanics, Department of Mechanical Engineering, Leibniz University Hannover, An der Universität 1, Garbsen, Germany

Chapter 1
VEM and the Mesh

**Tommaso Sorgente, Daniele Prada, Daniela Cabiddu, Silvia Biasotti,
Giuseppe Patanè, Micol Pennacchio, Silvia Bertoluzza, Gianmarco Manzini,
and Michela Spagnuolo**

Abstract In this work we report some results, obtained within the framework of the
ERC Project CHANGE, on the impact on the performance of the virtual element
method of the shape of the polygonal elements of the underlying mesh. More in
detail, after reviewing the state of the art, we present (a) an experimental analysis of
the convergence of the VEM under condition violating the standard shape regularity
assumptions, (b) an analysis of the correlation between some mesh quality metrics
and a set of different performance indexes, and (c) a suitably designed mesh quality
indicator, aimed at predicting the quality of the performance of the VEM on a given
mesh.

1.1   Introduction

Geometrically complex domains are frequently encountered in mathematical mod-
els of real engineering applications. Their representation in some discrete form
is a key aspect in the numerical approximation of the solutions of the partial
differential equations (PDEs) describing such models and can be extremely difficult.
The finite element method has been proved to be very successful as it allows
the computational domains to be discretized by using triangular and quadrilateral
meshes in 2D and tetrahedral and hexahedral meshes in 3D. Meshes with more
complex elements, even admitting curved edges and faces, can be considered in
the finite element formulation through reference elements and suitable remappings
onto the problem space. To obtain accurate solutions, stringent constraints must be
imposed, for example on the internal angles of the triangles and tetrahedra, thus
requiring in extreme situations meshes with very small sized elements. To alleviate

T. Sorgente (✉) · D. Cabiddu · S. Biasotti · G. Patanè · M. Spagnuolo
IMATI-CNR, Genova, Italy
e-mail: tommaso.sorgente@ge.imati.cnr.it

D. Prada · M. Pennacchio · S. Bertoluzza · G. Manzini
IMATI-CNR, Pavia, Italy

meshing issues, we can resort to numerical methods that are designed from the very beginning to provide arbitrary order of accuracy on more generally shaped elements. A class of methods with these features is the class of the so called polytopal element method, or PEM for short, that make it possible to numerically solve PDEs using polygonal and polyhedral grids.

The PEMs allow the user to incorporate complex geometric features at different scales without triggering mesh refinement, thus achieving high flexibility in the treatment of complex geometries. Moreover, nonconformal meshes can be treated in a straightforward way, by automatically including hanging nodes (i.e., T-junctions), and the design of refinement and coarsening algorithms is greatly simplified.

Such polytopal methods normally rely on a special design, as a straightforward generalization of the FEM is not possible because the finite element variational formulation requires an explicit knowledge of the basis functions. This requirement typically implies that such basis functions are elements of a subset of scalar and vector polynomials, and, as a consequence, the FEM is mostly restricted to meshes with elements having a simple geometrical shape, such as triangles or quadrilaterals.

The virtual element method (VEM) is a very successful example of PEM. The VEM formulation and implementation are based on suitable polynomial projections that we can always compute from the degrees of freedom of the basis functions. Since the explicit knowledge of the basis functions for the approximation space is not required, the method is dubbed as *virtual*. This fundamental property allows the virtual element to be formulated on meshes with elements having a very general geometric shapes.

The VEM was originally formulated in [11] as a conforming FEM for the Poisson problem by rewriting in a variational setting the *nodal* mimetic finite difference (MFD) method [10, 14, 32, 33, 51, 55] for solving diffusion problems on unstructured polygonal meshes. A survey on the MFD method can be found in the review paper [52] and the research monograph [13]. The VEM scheme inherits the flexibility of the MFD method with respect to the admissible meshes and this feature is well reflected in the many significant applications that have been developed so far, see, for example, [2, 4–8, 15–17, 20–25, 38, 40, 41, 45, 47, 57, 59, 62, 63, 72]. Since the VEM is a reformulation of the MFD method that generalizes the FEM to polytopal meshes as the other PEMs, it is clearly related with many other polytopal schemes. The connection between the VEM and finite elements on polygonal/polyhedral meshes is thoroughly investigated in [37, 46, 54], between VEM and discontinuous skeletal gradient discretizations in [46], and between the VEM and the BEM-based FEM method in [39]. The VEM has been extended to convection-reaction-diffusion problems with variable coefficients in [16]. The issue of preconditioning the VEM has been considered in [3, 26, 27, 36].

If on one hand, the VEM makes it possible to discretize a PDE on computational domains partitioned by a polytopal mesh, on the other hand this flexibility poses the fundamental question of what is a "good" polytopal mesh. All available theoretical and numerical results in the literature strongly support the fact that the quality of the mesh is crucial to determine the accuracy of the method and its effectiveness in solving problems on difficult geometries. This fact is not surprising as such

dependence of the behavior of the numerical approximation in terms of accuracy, stability, and overall computational cost on the quality of the underlying mesh has been a very well known fact for decades in the finite element framework and has been formalized in concepts like mesh regularity, shape regularity, etc. However, the concept of shape regularity of triangular/tetrahedral and quadrangular/hexahedral meshes is well understood [29, 44, 66], but the characterization of a good polytopal mesh is still subject to ongoing research. Optimal convergence rates for the virtual element approximations of the Poisson equation were proved in H^1 and L^2 norms, see for instance [1, 9, 11, 18, 30, 31, 43]. These theoretical results involve an estimate of the approximation error, which is due to both analytical assumptions (interpolation and polynomial projections of the virtual element functions) and geometrical assumptions (the geometrical shape of the mesh elements).

A major point here is that the polytopal framework provides an enormous freedom to the possible geometric shapes of the mesh elements. This freedom makes it difficult to identify which geometric features may have a negative effect on the performance of the VEM. Various geometrical (or *regularity*) assumptions have been proposed to ensure that all elements of any mesh of a given mesh family in the refinement process are sufficiently regular. Many papers prove the convergence of the VEM and derive optimal error estimates under the assumption that the polygonal elements are star-shaped with respect to all the points in a disc whose diameter is comparable with the diameter of the elements itself. This assumption is combined with a second scaling assumption on the mesh elements in the sequence of refined meshes that is used in the numerical approximation. For example, we can assume that either the length of all the edges or the distance between any two vertices of a polygonal element scale comparably with the element diameter, or even weaker conditions. These assumptions guarantee the VEM convergence and optimal estimates of the approximation error with respect to different norms. However, as already observed from the very first papers, cf. [1], the VEM seems to maintain its optimal convergence rates also when we use mesh families that do not satisfy the usual geometrical assumptions. Since the VEM was proposed in 2013, many more examples have accumulate in the literature (some also reviewed in this chapter) that show that a virtual element solver on a simple model problem as the Poisson equation may still provide a very good behavior, even if all the theoretical conditions of the analysis are violated. Good behavior means that the VEM is convergent and the loss of accuracy is significant only when the degeneracy of the meshes becomes really extreme. This suggests that more permissive shape-regularity criteria should be devised so that the VEM can be considered as effective, and a lot of work still has to be carried out to identify the specific issues that may negatively affect its accuracy. Clearly, these points are also crucial to support the design of better polygonal meshing algorithm for the tessellation of computational domains.

Understanding the influence of the geometrical characteristics of the elements on the performance of the VEM and, more generally, of the PEM, is one of the goals that the unit based at the *Istituto di Matematica Applicata e Tecnologie Informatiche del CNR* is pursuing within the Advanced Grant Project *New CHallenges in (adaptive) PDE solvers: the interplay of ANalysis and GEometry* (CHANGE),

whose final goal is the design of tools embracing geometry and analysis within a multi-level, multi-resolution paradigm. Indeed, a deeper understanding of such an interrelation can provide, on the one hand, the geometry processing community with information on the requirements to be incorporated into the meshing tools in order to generate "good" polytopal meshes, and, on the other hand, the mathematical community with possible new directions to pursue in the theoretical analysis of the VEM.

In Sect. 1.5 we review the main results of a recent work aimed at identifying the correlation between the performance of the virtual element method and a set of polygonal quality metrics. To this end, a systematic exploration was carried out to correlate the performance of the VEM and the geometric properties of the polygonal elements forming the mesh. In such study, the performance of the VEM is characterized by different "performance indexes", including (but not limited to) the accuracy of the solution and the conditioning of the associated linear system. The quality "metrics" measuring the "goodness" of a mesh are built by considering several geometric properties of polygons (see Sect. 1.5.1) from the simplest ones such as areas, angles, and edge length, to most complex ones as kernels, inscribed and circumscribed circles. The individual quality metrics of the polygonal elements of a mesh are combined in a single quality metric for the mesh itself by different aggregation strategies, such as minima, maxima, averages, worst case scenario and Euclidean norm. The numerical experiments to collect the results are performed on a family of parametric elements, which is designed to progressively stress one or more of the proposed geometric metrics, enriched with random polygons in order to avoid a bias in the study.

A second critical point developed in Sect. 1.6, is the connection between the performance of the method and how the regularity of the mesh refinements impacts on the approximation process. Note indeed that the way the geometric objects forming a mesh as edges and polygons (and faces and polytopal elements in 3D) scale is crucial in all possible geometric assumptions. It is a remarkable example shown in Sect. 1.4.1 that even the star-shaped assumption can be violated on a sequence of rectangular meshes (rectangular elements are star-shaped!) if the element aspect ratio scales badly when the mesh is refined. See also [68] for more details. To study how the geometrical conditions that are found in the literature may really impact on the convergence and accuracy of the VEM, we gradually introduce several pathologies in the mesh datasets used in the numerical experiments. These datasets systematically violate all the geometrical assumptions, and enhance a correlation analysis between such assumptions and the VEM performance. As expected from other works in the literature, these numerical experiments confirm the remarkable robustness of the VEM as it fails only in very few and extreme situations and a good convergence rate is still visible in most examples. To quantify this correlation, we build an indicator that measure the violation of the geometrical assumptions. This indicator depends uniquely on the geometry of the mesh elements. A correspondence is visible between this indicator and the performance of the VEM on a given mesh, or mesh family, in terms of approximation error and convergence rate. This correspondence and such an indicator can be used to devise a

strategy to evaluate if a given sequence of meshes is suited to the VEM, and possibly to predict the behaviour of the numerical discretization *before* applying the method.

The chapter is organized as follows. In Sect. 1.2, we present the VEM and the convergence results for the Poisson equation with Dirichlet boundary conditions. In Sect. 1.3.1, we detail the geometrical assumptions on the mesh elements that are used in the literature to guarantee the convergence of the VEM. In Sect. 1.3.2 we review the major theoretical results on the error analysis that are available in the virtual element literature, reporting the geometrical conditions assumed in each result. In Sect. 1.4.1, we present a number of datasets which do not satisfy these assumptions, and experimentally investigate the convergence of the VEM over them. In Sect. 1.5 we present the statistical analysis of the correlation between some notable mesh quality metrics and a selection of quantities measuring different aspects of the performance of the VEM. In Sect. 1.6, we propose a mesh quality indicator to predict the behaviour of the VEM over a given dataset. In Sect. 1.7 we present the open source benchmarking software tools PEMesh [35], developed at IMATI.

1.2   Model Problem

The elliptic model problem that we focus on in this paper is the Poisson equation with Dirichlet boundary conditions. In this section, we briefly review the strong and weak forms of the model equations and recall the formulation of its virtual element discretization.

The Poisson Equation and Its Virtual Element Discretization   Let Ω be an open, bounded, connected subset of $\mathbb{R}^2$ with polygonal boundary Γ. We consider the Poisson equation with homogeneous Dirichlet boundary conditions, whose strong form is:

$$-\Delta u = f \qquad \text{in } \Omega, \tag{1.1}$$

$$u = 0 \qquad \text{on } \Gamma. \tag{1.2}$$

Remark that, while, for the sake of simplicity, we consider here homogeneous Dirichlet boundary conditions, the method that we are going to present also applies to the non homogeneous case, the extension being straightforward. The variational formulation of problem (1.1)–(1.2) takes the form: *Find $u \in H_0^1(\Omega)$ such that*

$$a(u, v) = F(v) \qquad \forall v \in H_0^1(\Omega), \tag{1.3}$$

with the bilinear form $a(\cdot, \cdot) : H^1(\Omega) \times H^1(\Omega) \to \mathbb{R}$ and the right-hand side linear functional $F : L^2(\Omega) \to \mathbb{R}$ respectively defined as

$$a(u, v) = \int_\Omega \nabla u \cdot \nabla v \, d\mathbf{x} \tag{1.4}$$

and

$$F(v) = \int_\Omega f v \, d\mathbf{x}, \tag{1.5}$$

where we implicitly assumed that $f \in L^2(\Omega)$. The well-posedness of the weak formulation (1.3) can be proven by applying the Lax-Milgram theorem [64, Section 2.7], thanks to the coercivity and continuity of the bilinear form $a(\cdot, \cdot)$, and to the continuity the linear functional $F(v)$.

We consider here the virtual element approximation of Eq. (1.3), mainly based on [1, 11], which provides an optimal approximation on polygonal meshes when the diffusion coefficient is variable in space.

The discrete equation will take the form: *Find $u_h \in V_k^h$ such that*

$$a_h(u_h, v_h) = F_h(v_h) \qquad v_h \in V_k^h, \tag{1.6}$$

where u_h, V_k^h, $a_h(\cdot, \cdot)$, $F_h(\cdot)$ are the virtual element approximations of u, $H_0^1(\Omega)$, $a(\cdot, \cdot)$, and $F(\cdot)$. In the rest of this section we recall the construction of these mathematical objects.

Mesh Notation Let $\mathcal{T} = \{\Omega_h\}_{h \in \mathcal{H}}$ be a family of decompositions Ω_h of the computational domain Ω into a finite set of nonoverlapping polygonal elements E. Each of the members Ω_h of the family $\mathcal{T}$ will be referred to as the *mesh*. The *mesh size h*, which also serves as subindex, is the maximum of the diameters of the mesh elements, which is defined by $h_E = \sup_{\mathbf{x}, \mathbf{y} \in E} |\mathbf{x} - \mathbf{y}|$. We assume that the mesh sizes of the mesh family $\mathcal{T}$ are in a countable subset $\mathcal{H}$ of the real line $(0, +\infty)$ having 0 as its unique accumulation point. We let ∂E denote the polygonal boundary of E, which we assume to be nonintersecting and formed by straight edges e. The center of gravity of E will be denoted by $\mathbf{x}_E = (x_E, y_E)$ and its area by $|E|$. We denote the edge mid-point $\mathbf{x}_e = (x_e, y_e)$ and its length $|e|$, and, with a small abuse of notation, we write $e \in \partial E$ to indicate that edge e is running throughout the set of edges forming the elemental boundary ∂E. In the next section we will discuss in detail the different assumptions on the mesh family $\mathcal{T}$, under which he convergence analysis of the VEM and the derivation of the error estimates in the L^2 and H^1 are carried out in the literature.

The Virtual Element Spaces Let $k \geq 1$ integer and $E \in \Omega_h$ a generic mesh element. We define the local virtual element space $V_k^h(E)$, following to the *enhancement strategy* proposed in [1]:

$$V_k^h(E) = \left\{ v_h \in H^1(E) : v_{h|\partial E} \in C^0(\partial E), \ v_{h|e} \in \mathbb{P}_k(e) \ \forall e \in \partial E, \right.$$

$$\Delta v_h \in \mathbb{P}_k(E), \text{ and}$$

$$\left. \int_E (v_h - \Pi_k^{\nabla, E} v_h) \, q \, dV = 0 \ \forall q \in \mathbb{P}_k(E) \backslash \mathbb{P}_{k-2}(E) \right\}. \qquad (1.7)$$

Here, $\Pi_k^{\nabla, E}$ is the elliptic projection that will be discussed in the next section; $\mathbb{P}_k(E)$ and $\mathbb{P}_k(e)$ are the linear spaces of the polynomials of degree at most k, which are respectively defined over an element E or an edge e according to our notation; and $\mathbb{P}_k(E) \backslash \mathbb{P}_{k-2}(E)$ is the space of polynomials of degree equal to $k-1$ and k. By definition, the space $V_k^h(E)$ contains $\mathbb{P}_k(E)$ and the global space V_k^h is a conforming subspace of $H^1(\Omega)$. The global *conforming virtual element space* V_k^h of order k *built on mesh* Ω_h is obtained by gluing together the elemental approximation spaces, that is

$$V_k^h := \left\{ v_h \in H_0^1(\Omega) : v_{h|E} \in V_k^h(E) \ \forall E \in \Omega_h \right\}. \qquad (1.8)$$

On every mesh Ω_h, given an integer $k \geq 0$, we also define the space of discontinuous piecewise polynomials of degree at most k, $\mathbb{P}_k(\Omega_h)$, whose elements are the functions q such that $q_{|E} \in \mathbb{P}_k(E)$ for every $E \in \Omega_h$.

The Degrees of Freedom For each element E and each virtual element function $v_h \in V_k^h(E)$, we consider the following set of degrees of freedom [11]:

(D1) for $k \geq 1$, the values of v_h at the vertices of E;
(D2) for $k \geq 2$, the values of v_h at the $k-1$ internal points of the $(k+1)$-point Gauss-Lobatto quadrature rule on every edge $e \in \partial E$.
(D3) for $k \geq 2$, the cell moments of v_h of order up to $k-2$ on element E:

$$\frac{1}{|E|} \int_E v_h \, q \, dV \quad \forall q \in \mathbb{P}_{k-2}(E). \qquad (1.9)$$

It is possible to prove that this set of values is unisolvent in $V_k^h(E)$, cf. [11]; hence, every virtual element function is uniquely identified by it. The global degrees of freedom of a virtual element function in the space V_k^h are given by collecting the elemental degrees of freedom **(D1)**-**(D3)** for all vertices, edges and elements. Their unisolvence in V_k^h is an immediate consequence of their unisolvence in every elemental space $V_k^h(E)$.

The Elliptic Projection Operators The *elliptic projection operator* $\Pi_k^{\nabla,E}$: $H^1(E) \rightarrow \mathbb{P}_k(E)$, whose definition is required in (1.7) and which will be instrumental in the definition of the bilinear form a_h in the following, is given, for any $v_h \in V_k^h(E)$, by:

$$\int_E \nabla \Pi_k^{\nabla,E} v_h \cdot \nabla q \, dV = \int_E \nabla v_h \cdot \nabla q \, dV \quad \forall q \in \mathbb{P}_k(E), \tag{1.10}$$

$$\int_{\partial E} \left(\Pi_k^{\nabla,E} v_h - v_h \right) dS = 0. \tag{1.11}$$

Equation (1.11) allows us to remove the kernel of the gradient operator from the definition of $\Pi_k^{\nabla,E}$, so that the k-degree polynomial $\Pi_k^{\nabla,E} v_h$ is uniquely defined for every virtual element function $v_h \in V_k^h(E)$. Furthermore, projector $\Pi_k^{\nabla,E}$ is a polynomial-preserving operator, i.e., $\Pi_k^{\nabla,E} q = q$ for every $q \in \mathbb{P}_k(E)$. By assembling elementwise contributions we define a global projection operator $\Pi_k^{\nabla} : H^1(\Omega) \rightarrow \mathbb{P}_k(\Omega_h)$, which is such that $\Pi_k^{\nabla} v_{h|E} = \Pi_k^{\nabla,E}(v_{h|E}) \, \forall E \in \Omega_h$. A key property of the elliptic projection operator is that the projection $\Pi_k^{\nabla,E} v_h$ of any virtual element function $v_h \in V_k^h(E)$ is computable from the degrees of freedom (**D1**)–(**D3**) of v_h associated with element E.

Orthogonal Projections From the degrees of freedom of a virtual element function $v_h \in V_k^h(E)$ we can also compute the $L^2(E)$ orthogonal projections $\Pi_k^{0,E} v_h \in \mathbb{P}_k(E)$, cf. [1]. In fact, $\Pi_k^{0,E} v_h$ of a function $v_h \in V_k^h(E)$ is, by definition, the solution of the variational problem:

$$\int_E \Pi_k^0 v_h \, q \, dV = \int_E v_h \, q \, dV \qquad \forall q \in \mathbb{P}_k(E). \tag{1.12}$$

The right-hand side is the integral of v_h against the polynomial q, and, when q is a polynomial of degree up to $k - 2$, it is computable from the degrees of freedom (**D3**) of v_h. When q is a polynomial of degree $k - 1$ or k, it is computable from the moments of $\Pi_k^{\nabla,E} v_h$, cf. (1.7). Clearly, the orthogonal projection $\Pi_{k-1}^{0,E} v_h$ is also computable. Also here we can define a global projection operator $\Pi_k^0 : L^2(\Omega) \rightarrow \mathbb{P}(\Omega_h)$, which projects the virtual element functions on the space of discontinuous polynomials of degree at most k built on mesh Ω_h. This operator is obtained by assembling the elemental L^2-orthogonal projections $\Pi_k^{0,E} v_h$ for all mesh elements E, that is $\left(\Pi_k^0 v_h \right)_{|E} = \Pi_k^{0,E}(v_{h|E})$.

The Virtual Element Bilinear Forms Taking advantage of the elliptic and orthogonal projectors we can now define the virtual element bilinear form $a_h(\cdot, \cdot)$: $V_k^h \times V_k^h \to \mathbb{R}$. We start by splitting the discrete bilinear form $a_h(\cdot, \cdot)$ as the sum of elemental contributions

$$a_h(u_h, v_h) = \sum_{E \in \Omega_h} a_h^E(u_h, v_h), \tag{1.13}$$

where the contribution of every element is a bilinear form $a_h^E(\cdot, \cdot)$: $V_k^h(E) \times V_k^h(E) \to \mathbb{R}$, approximating the corresponding elemental bilinear form $a^E(\cdot, \cdot)$: $H^1(E) \times H^1(E) \to \mathbb{R}$,

$$a^E(v, w) = \int_E \nabla v \cdot \nabla w \, dV, \quad \forall v, w \in H^1(E).$$

The bilinear form $a_h^E(\cdot, \cdot)$ on each element E is itself split as the sum of two contributions: by

$$a_h^E(u_h, v_h) = \int_E \nabla \Pi_k^{\nabla, E} u_h \cdot \nabla \Pi_k^{\nabla, E} v_h \, dV + \tag{1.14}$$

$$S_h^E\left(\left(I - \Pi_k^{\nabla, E}\right)u_h, \left(I - \Pi_k^{\nabla, E}\right)v_h \right).$$

The *stabilization term* $S_h^E(\cdot, \cdot)$ in (1.14) can be any computable, symmetric, positive definite bilinear form defined on $V_k^h(E)$ such that

$$c_* a^E(v_h, v_h) \leq S_h^E(v_h, v_h) \leq c^* a^E(v_h, v_h) \quad \forall v_h \in V_k^h(E) \cap \ker\left(\Pi_k^{\nabla, E}\right), \tag{1.15}$$

for two positive constants c_* and c^*. Property (1.15) states that that $S_h^E(\cdot, \cdot)$ scales like $a^E(\cdot, \cdot)$ with respect to h_E. As $\Pi_k^{\nabla, E}$ is a polynomial preserving operator, the contribution of the stabilization term in the definition of $a_h^E(\cdot, \cdot)$ is zero one (or both) of the two entries is a polynomial of degree less than or equals to k.

Condition (1.15), is designed so that $a_h^E(\cdot, \cdot)$ satisfies the two following fundamental properties:

– *k-consistency*: for all $v_h \in V_k^h(E)$ and for all $q \in \mathbb{P}_k(E)$ it holds that

$$a_h^E(v_h, q) = a^E(v_h, q); \tag{1.16}$$

– *stability*: there exist two positive constants α_*, α^*, independent of h and E, such that

$$\alpha_* a^E(v_h, v_h) \leq a_h^E(v_h, v_h) \leq \alpha^* a^E(v_h, v_h) \quad \forall v_h \in V_k^h(E). \tag{1.17}$$

In our implementation of the VEM, we consider the stabilization proposed in [56], that is we set:

$$S_h^E(v_h, w_h) = \sum_{i=1}^{N^{\text{dofs}}} \mathscr{A}_{ii}^E \text{DOF}_i(v_h) \text{DOF}_i(w_h), \quad\quad (1.18)$$

where $\mathscr{A}^E = (\mathscr{A}_{ij}^E)$ is the matrix stemming from the implementation of the first term in the bilinear form $a_h^E(\cdot, \cdot)$. More precisely, let ϕ_i be the i-th "canonical" basis functions generating the virtual element space, which is the function in $V_k^h(E)$ whose i-th degree of freedom for $i = 1, \ldots, N^{\text{dofs}}$ (according to a suitable renumbering of the degrees of freedom in **(D1)**, **(D2)**, and **(D3)**), has value equal to 1 and all other degrees of freedom are zero. The i, j-th entry of matrix $\mathscr{A}^E$ is given by

$$\mathscr{A}_{ij}^E := a^E(\Pi_k^{\nabla, E} \phi_i, \Pi_k^{\nabla, E} \phi_j). \quad\quad (1.19)$$

The stabilization in (1.18) is sometimes called the "*D-recipe stabilization*" in the virtual element literature. Observe that, if we instead replace $\mathscr{A}^P$ with the identity matrix, we get the the so called "*dofi-dofi (dd) stabilization*" originally proposed in [11]:

$$S_h^{E,\text{dd}}(v_h, w_h) = \sum_{i=1}^{N^{\text{dofs}}} \text{DOF}_i(v_h) \text{DOF}_i(w_h). \quad\quad (1.20)$$

The stabilization (1.20) underlies many of the convergence results available from the literature, which we briefly review in Sect. 1.3.2.

The Virtual Element Forcing Term We approximate the right-hand side of (1.6), by splitting it into the sum of elemental contributions and approximating every local linear functional by replacing v_h with $\Pi_k^{0,E} v_h$:

$$F(v_h) = \sum_{E \in \Omega_h} (f, \Pi_k^{0,E} v_h)_E. \text{ where } (f, \Pi_k^{0,E} v_h)_E = \int_E f \, \Pi_k^{0,E} v_h \, dV.$$
$$\quad\quad (1.21)$$

Approximation Properties in the Virtual Element Space Under a suitable regularity assumption on the mesh family $\mathscr{T}$ (see assumption **G1** in the next section), we can prove the following estimates on the projection and interpolation operators:

1. for every s with $1 \le s \le k + 1$ and for every $w \in H^s(E)$ there exists a $w_\pi \in \mathbb{P}_k(E)$ such that

$$|w - w_\pi|_{0,E} + h_E |w - w_\pi|_{1,E} \le C h_E^s |w|_{s,E} ; \quad\quad (1.22)$$

2. for every s with $2 \leq s \leq k + 1$, for every h, for all $E \in \Omega_h$ and for every $w \in H^s(E)$ there exists a $w_I \in V_k^h(E)$ such that

$$|w - w_I|_{0,E} + h_E |w - w_I|_{1,E} \leq Ch_E^s |w|_{s,E}. \tag{1.23}$$

Here, C is a positive constant depending only on the polynomial degree k and on some mesh regularity constants that we will present and discuss in the next section.

Main Convergence Properties Thanks to the coercivity and continuity of the bilinear form $a_h(\cdot, \cdot)$, and to the continuity of the right-hand side linear functional $(f, \Pi_k^0 \cdot)$, by applying the Lax-Milgram theorem [64, Section 2.7], we obtain the well-posedness of the discrete formulation (1.6).

Let then $u \in H^{k+1}(\Omega)$ be the solution to the variational problem (1.3) on a convex domain Ω with $f \in H^k(\Omega)$. Let $u_h \in V_k^h$ be the solution of the virtual element method (1.6) on every mesh of a mesh family $\mathscr{T} = \{\Omega_h\}$ satisfying a suitable set of mesh geometrical assumptions. Under suitable assumptions on the mesh family $\mathscr{T}$, it is possible to prove that the following error estimates hold:

- the H^1-error estimate holds:

$$\|u - u_h\|_{1,\Omega} \leq Ch^k \left(\|u\|_{k+1,\Omega} + |f|_{k,\Omega}\right); \tag{1.24}$$

- the L^2-error estimate holds:

$$\|u - u_h\|_{0,\Omega} \leq Ch^{k+1} \left(\|u\|_{k+1,\Omega} + |f|_{k,\Omega}\right). \tag{1.25}$$

Constant C in (1.24) and in (1.25) may depend on the stability constants α_* and α^*, on mesh regularity constants which we will introduce in the next section, on the size of the computational domain $|\Omega|$, and on the approximation degree k. Constant C is normally independent of h, but for the most extreme meshes it may depend on the ratio between the longest and shortest edge lengths, cf. Sect. 1.3.2.

Finally, we note that the approximate solution u_h is not explicitly known inside the elements. Consequently, in the numerical experiments of Sect. 1.4.2, we approximate the error in the L^2-norm as follows:

$$\|u - u_h\|_{0,\Omega} \approx \|u - \Pi_k^0 u_h\|_{0,\Omega},$$

where $\Pi_k^0 u_h$ is the global L^2-orthogonal projection of the virtual element approximation u_h to u. On its turn, we approximate the error in the energy norm as follows:

$$|u - u_h|_{1,\Omega} \approx a_h(u_I - u_h, u_I - u_h)$$

where u_I is the virtual element interpolant of the exact solution u.

In this work, we are interested in checking whether optimal convergence rates put forward by these estimates are maintained on different mesh families that may

display some pathological situations. From a theoretical viewpoint, the convergence estimates hold under some constraints on the shapes of the elements forming the mesh, called *mesh geometrical (or regularity) assumptions*. We summarize the major findings from the literature in Sect. 1.3.2 and in the next sections we will investigate how breaking such constraints may affect these results.

1.3 State of the Art

Various geometrical (or *regularity*) assumptions have been proposed in the literature to ensure that all elements of all meshes in a given mesh family in the refinement process are sufficiently regular. These assumptions guarantee the convergence of the VEM and optimal estimates of the approximation error with respect to different norms.

In this section, we overview the geometrical assumptions introduced in the VEM literature to guarantee the convergence of the method, and we provide a list of the main convergence results based on such assumptions.

1.3.1 Geometrical Assumptions

We start by reviewing the geometrical assumptions appeared in the VEM literature since their definition in [11]. Note that these assumptions are defined for a single mesh Ω_h, but the conditions contained in them are required to hold independently of the mesh size h. As a consequence, when an assumption is imposed to a mesh family $\mathcal{T} = \{\Omega_h\}_h$, it has to be verified simultaneously by every $\Omega_h \in \mathcal{T}$.

It is well-known from the FEM literature that the approximation properties of a method depend on specific assumptions on the geometry of the mesh elements. Classical examples of geometrical assumptions for a family of triangulations $\{\Omega_h\}_{h \to 0}$, are the ones introduced in [44] and [73], respectively:

(a) *Shape regularity condition:* there exists a real number $\gamma \in (0, 1)$, independent of h, such that for any triangle $E \in \Omega_h$ we have

$$r_E \geq \gamma h_E, \tag{1.26}$$

being h_E the longest edge in E and r_E its inradius;

(b) *Minimum angle condition:* there exists an angle $\alpha_0 > 0$, independent of h, such that for any triangle $E \in \Omega_h$ we have

$$\alpha_E \geq \alpha_0, \tag{1.27}$$

being α_E the minimal angle of E.

When we turn our focus on polygonal meshes, a preliminar consideration is needed on the definition of the polygonal elements. It is commonly accepted, even if not always explicitly specified, that a mesh Ω_h has to be made of a finite number of *simple polygons*, i.e. open simply connected sets whose boundary is a non-intersecting line made of a finite number of straight line segments.

The other regularity assumptions proposed in the VEM literature to ensure approximation properties have been deduced in analogy to the similar conditions developed for the FEMs. The main assumption, which systematically recurs in every VEM paper, is the so-called *star-shapedness* of the mesh elements.

Assumption G1 *There exists a real number $\rho \in (0, 1)$, independent of h, such that every polygon $E \in \Omega_h$ is star-shaped with respect to a disc with radius*

$$r_E \geq \rho h_E.$$

We denote r_E the radius of the greatest possible inscribed disk in E and *star center* the center of such disk, where it exists. We stress the fact that **G1** does not accept polygons star-shaped with respect to a single point, as both ρ and h_E are greater than zero, and we conventionally say that $r_E = 0$ if E is not star-shaped (Fig. 1.1). Assumption **G1** is nothing but the polygonal extension of the classical *shape regularity condition* for triangular meshes. In fact, any triangular element E is star-shaped with respect to its maximum inscribed disk (the one with radius r_E) and the diameter h_E coincides with its longest edge. Moreover, **G1** can also be stated in the following weak form, as specified in [11] and more accurately in [30]:

Assumption G1-Weak *There exists a real number $\rho \in (0, 1)$, independent of h, such that every polygon $E \in \Omega_h$ can be split into a finite number N of disjoint polygonal subcells $E_1, \ldots, E_N$ where, for $j = 1, \ldots, N$,*

(a) *element E_j is star-shaped with respect to a disc with radius $r_{E_j} \geq \rho h_{E_j}$;*
(b) *elements E_j and E_{j+1} share a common edge.*

From a practical point of view, Assumptions **G1** and **G1-weak** are almost equivalent, and they are treated equivalently in all papers reviewed in Sect. 1.3.2. Assumption **G1** plays a key role in most of the theoretical results regarding polygonal methods. It is needed by the Bramble-Hilbert lemma [64], an important

Fig. 1.1 The element in (**a**) is star-shaped with respect to the disk $\mathscr{B}$ but not with respect to the disk $\mathscr{B}'$, while the element in (**b**) is not star-shaped with respect to any disk
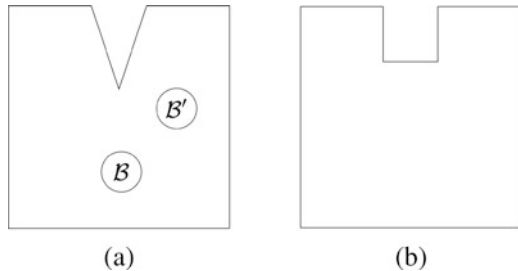
result on polynomial approximation that is often used for building approximation estimates, and also by the following lemma.

Lemma 1.1 *If a mesh Ω_h satisfies Assumption **G1** then for all polygons $E \in \Omega_h$ there exists a mapping $F : \mathscr{B}_1 \to E$, with the Jacobian J of F satisfying*

$$\|J\|_2 \lesssim h, \qquad |\det(J)| \lesssim h^2 \qquad and \qquad \|J^{-1}\|_2 \lesssim h^{-1}, \tag{1.28}$$

and, for a sufficiently regular u, the following relations hold

$$\|u\|_{0,E} \simeq h_E \|u \circ F\|_{0,\mathscr{B}_1}, \qquad\qquad \|u\|_{0,\partial E} \simeq h_E^{1/2} \|u \circ F\|_{0,\partial\mathscr{B}_1},$$

$$|u|_{1,E} \simeq |u \circ F|_{1,\mathscr{B}_1}, \qquad\qquad |u|_{1/2,\partial E} \simeq |u \circ F|_{1/2,\partial\mathscr{B}_1},$$

*where all the implicit constants only depend on the constant ρ from **G1**.*

Thanks to the relations in Lemma 1.1, inequalities that we have on the unit circle $\mathscr{B}_1$, such as the Poincaré inequality or the trace inequalities, may be transferred to the polygon E by a "scaling" argument.

In the very first VEM paper [11], where the method was introduced, Assumption **G1** was followed by another condition on the maximum point-to-point distance.

Assumption G2-Strong *There exists a real number $\rho \in (0, 1)$, independent of h, such that for every polygon $E \in \Omega_h$, the the distance $d_{i,j}$ between any two vertices v_i, v_j of E satisfies*

$$d_{i,j} \geq \rho h_E.$$

In fact, Assumption **G2-strong** was soon replaced in the following works [1, 18] and [30] by a weaker condition on the length of the elemental edges. This new version allows, for example, the existence of four-sided polygons with equal edges but one diagonal much smaller than the other.

Assumption G2 *There exists a real number $\rho \in (0, 1)$, independent of h, such that for every polygon $E \in \Omega_h$, the length $|e|$ of every edge $e \in \partial E$ satisfies*

$$|e| \geq \rho h_E.$$

The Authors consider a single constant ρ for both Assumption **G1** and **G2** and refer to it as the *mesh regularity constant* or *parameter*.

Under Assumption **G1-weak** and **G2**, it can be proved [30] that the simplicial triangulation of E determined by the star-centers of $E_1, \ldots, E_N$ satisfies the *shape regularity* and the *minimum angle* conditions. The same holds under Assumptions **G1** and **G2**, as a special case of the previous statement. Moreover, Assumption **G2** implies that for $1 \leq j, k \leq N$ it holds $h_{E_j}/h_{E_k} \leq \rho^{-|j-k|}$.

As already mentioned in the very first papers, these assumptions are more restrictive than necessary, but at the same time they allow the VEM to work on very general meshes. For example, Ahmad et al. in [1] state that:

> Actually, we could get away with even more general assumptions, but then it would be long and boring to make precise (among many possible crazy decompositions that nobody will ever use) the ones that are allowed and the ones that are not.

In the subsequent papers [18] and [31] Assumption **G1** is preserved, but Assumption **G2** is substituted by the alternative version:

Assumption G3 *There exists a positive integer N, independent of h, such that the number of edges of every polygon $E \in \Omega_h$ is (uniformly) bounded by N.*

The Authors show how Assumption **G2** implies Assumption **G3**, but Assumption **G3** is weaker than Assumption **G2**, as it allows for edges arbitrarily small with respect to h_E. Both combinations **G1**+**G2** and **G1**+**G3** imply that the number of vertices of E and the minimum angle of the simplicial triangulation of E obtained by connecting all the vertices of E to its star-center, are controlled by the constant ρ.

Another step forward in the refinement of the geometrical assumptions was made by Beirão Da Veiga et al. in [9]. Besides assuming **G1**, the Authors imagine to "unwrap" the boundary ∂E of each element $E \in \Omega_h$ onto an interval of the real line, obtaining a one-dimensional mesh $\mathscr{I}_E$. The mesh $\mathscr{I}_E$ can be subdivided into a number of disjoint sub-meshes $\mathscr{I}_E^1, \dots, \mathscr{I}_E^N$, corresponding to the edges of E. Then, the following condition is assumed.

Assumption G4 *There exists a real number $\delta > 0$, independent of h, such that for every polygon $E \in \Omega_h$:*

(a) *the one-dimensional mesh $\mathscr{I}_E$ can be subdivided into a finite number N of disjoint sub-meshes $\mathscr{I}_E^1, \dots, \mathscr{I}_E^N$;*
(b) *for each sub-mesh $\mathscr{I}_E^i$, $i = 1, \dots, N$, it holds that*

$$\frac{\max_{e \in \mathscr{I}_E^i} |e|}{\min_{e \in \mathscr{I}_E^i} |e|} \leq \delta.$$

Each polygon E corresponds to a one-dimensional mesh $\mathscr{I}_E$, but a sub-mesh $\mathscr{I}_E^i \subset \mathscr{I}_E$ might contain more than one edge of E, cf. Fig. 1.2. Therefore Assumption **G4** does not require a uniform bound on the number of edges in each element and does not exclude the presence of small edges. Mesh families created by agglomeration, cracking, gluing, etc. of existing meshes are admissible according to **G4**.

As we will see in the next section, possible assumption pairs requested in the literature to guarantee the convergence of the VEM are given by combining **G1** (or, equivalently, **G1-weak**) with either **G2-strong**, **G2**, **G3** or **G4**.
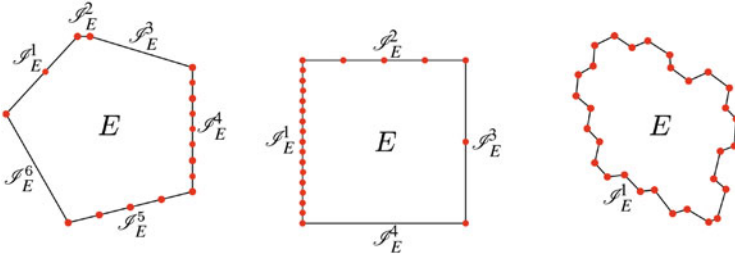
Fig. 1.2 Examples of admissible elements according to Assumption **G4**. Red dots indicate the vertices of the element

Last, we report a condition (together with its weaker version) that appears in the literature related to the *non-conforming* version of the VEM, which we do not cover in this work. It is defined for instance in [28], but it can also be found under the name of *local quasi-uniformity*.

Assumption G5 *There exists a real number* $\gamma \in (0, 1)$, *independent of h, such that for every polygon* $E \in \Omega_h$, *for all* e, e' *adjacent edges of E it holds that*

$$\frac{1}{\gamma} \leq \frac{|e|}{|e'|} \leq \gamma.$$

In this case, the polygonal elements of the mesh are allowed to have a very large number of very small edges, provided that every two consecutive edges scale proportionally. This assumption also has a weak version, in which we essentially ask that, for every $E \in \Omega_h$, a part of ∂E satisfies **G5** and the remaining part satisfies **G3**.

Assumption G5-Weak *There exist a real number* $\gamma \in (0, 1)$ *and a positive integer N, both independent of h, such that for every polygon* $E \in \Omega_h$, *the set* $\mathscr{E}_E$ *of the edges of E can be split as* $\mathscr{E}_E = \mathscr{E}_E^1 \cup \mathscr{E}_E^2$, *where* $\mathscr{E}_E^1$ *and* $\mathscr{E}_E^2$ *are such that*

– *for any pair of adjacent edges* e, $e' \in \mathscr{E}_E$ *with* $e \in \mathscr{E}_E^1$, *the inequality holds*

$$\frac{1}{\gamma} \leq \frac{|e|}{|e'|} \leq \gamma;$$

– $\mathscr{E}_E^2$ *contains at most N edges.*

Assumption **G5-weak** allows for situations where a large number of small edges coexists with some large edges. We can think of families of meshes for which such an assumption is not satisfied, but they would be extremely pathological. Assumptions **G5** and **G5-weak** are here reported for the sake of completeness but are not considered in the analysis of the following sections, as they refer to a different context.

1.3.2 Convergence Results in the VEM Literature

In this section, we briefly overview the literature on the main results of the convergence analysis of the VEM method. For each article, we explicitly report (if available) the theoretical results and highlight the geometric assumptions used, reporting the abstract energy error, the H^1 error estimate, and the L^2 error. For a greater uniformity of the presentation with the rest of the chapter, we have slightly modified some notations and introduced minimal variations to some statements of the theorems.

Basic Principles of Virtual Elements Methods [11]
This is the paper in which the VEM method was introduced and defined. In the original formulation, the paper introduced the regular conforming virtual element space. For simplicity and with a small abuse of notation, the regular conforming virtual element space is denoted by V_k^h as in (1.8) and (1.7):

$$V_k^h := \{v_h \in H^1(\Omega) : v_{h|E} \in V_k^h(E) \; \forall E \in \Omega_h\}, \tag{1.29a}$$

where

$$V_k^h(E) := \{v_h \in H^1(E) : v_{h|\partial E} \in C^0(\partial E), \; v_{h|e} \in \mathbb{P}_k(e) \; \forall e \in \partial E, \tag{1.29b}$$

$$\text{and } \Delta v_h \in \mathbb{P}_{k-2}(E)\},$$

and the *dofi-dofi* formulation $S_h^{E,\text{dd}}$ defined in (1.20) is used for the stabilization bilinear form.

There, the authors introduced the concept of *simple polygon* and the geometric regularity assumptions **G1** and **G2-strong**. The following statement on the convergence of VEM in the energy norm is general and largely used in the VEM literature, even if not explicitly stated in [11]. To this purpose, for functions $v \in H^1(\Omega_h)$ the broken H^1-seminorm is defined as follows:

$$|v|_{h,1} := \left(\sum_{E \in \Omega_h} |\nabla v|_{0,E}^2 \right)^{1/2}. \tag{1.30}$$

Theorem 1.3.1 (Abstract Energy Error) *Under the k-consistency and stability assumptions defined in Sect. 1.2, cf. (1.16) and (1.17), the discrete problem has a unique solution u_h. Moreover, for every approximation $u_I \in V_k^h$ of u and every approximation u_π of u that is piecewise in $\mathbb{P}_k(\Omega_h)$, we have*

$$|u - u_h|_{1,\Omega} \le C(|u - u_I|_{1,\Omega} + |u - u_\pi|_{h,1} + \mathfrak{F}_h), \tag{1.31}$$

where C is a constant depending only on α_* and α^* (the constants in (1.17)), and, for any h, $\mathfrak{F}_h = |f - f_h|_{V_k^{h'}}$ is the smallest constant such that

$$(f, v) - \langle f_h - f, v \rangle \le \mathfrak{F}_h |f|_1 \qquad \forall v \in V_k^h.$$

In [11] it was claimed that it is possible to estimate the convergence rate in terms of the L^2 error using duality argument techniques.

Equivalent Projectors for Virtual Element Methods [1]
In [1], the enhanced VEM space (1.7) adopted in this chapter replaces $V_k^h(E)$ (in [1] the enhanced VEM space is named "modified VEM space"). This paper uses the *dofi-dofi* stabilization. Under the geometrical assumptions **G1** and **G2**, the paper provides an explicit estimation of H^1 and L^2 errors and introduces the Theorem 1.3.1 for the abstract energy error.

Theorem 1.3.2 (H^1 **Error Estimate**) *Assuming **G1**, **G2**, let the right-hand side f belong to $H^{k-1}(\Omega)$, and that the exact solution u belong to $H^{k+1}(\Omega)$. Then*

$$\|u - u_h\|_{1,\Omega} \le C|h|^k |u|_{k+1,\Omega} \tag{1.32}$$

with C a positive constant independent of h.

Theorem 1.3.3 (L^2 **Error Estimate**) *Assuming **G1**, **G2** and with Ω convex, let the right-hand side f belong to $H^k(\Omega)$, and that the exact solution u belong to $H^{k+1}(\Omega)$. Then*

$$\|u - u_h\|_{0,\Omega} + |h| \|u - u_h\|_{1,\Omega} \le C|h|^{k+1} |u|_{k+1,\Omega}, \tag{1.33}$$

with C a constant independent of h.

Stability Analysis for the Virtual Element Method [18]
This contribution deals with the regular conforming VEM space (1.29) defined in [11]. The paper [18] provides a new estimation of the abstract energy error and analyses the H^1 error with respect to two different stabilization techniques. Moreover, new analytical assumptions on the bilinear form $a_h(\cdot, \cdot)$ to replace (1.17) are introduced:

$$a_h^E(v_h, v_h) \le C_1(E) \|\|v_h\|\|_E^2, \text{ for all } v_h \in V_k^h(E); \tag{1.34a}$$

$$\|\|q\|\|_E^2 \le C_2(E) a_h^E(q, q), \text{ for all } q \in \mathbb{P}_k(E), \tag{1.34b}$$

being $\|\| \cdot \|\|_E$ a discrete semi-norm induced by the stability term and $C_1(E)$, $C_2(E)$ positive constants which depend on the shape and possibly on the size of E. In this paper, the estimate is necessary for the polynomials $q \in \mathbb{P}_k(E)$ only, while in the standard analysis in [11] a kind of bound (1.34a)(b) was required for every

$v_h \in V_k^h(E)$. Thus, even when $C_1(E)$ and $C_2(E)$ can be chosen independent of E, on $V_k^h(E)$ the semi-norm induced by the stabilization term may be stronger than the energy $a_h^E(\cdot, \cdot)^{1/2}$.

Theorem 1.3.4 (Abstract Energy Error) *Under the stability assumptions* (1.34a), *let the continuous solution u of the problem satisfy $u_{|E} \in \mathcal{V}_E$ for all $E \in \Omega_h$, where $\mathcal{V}_E \subseteq V_k^h(E)$ is a subspace of sufficiently regular functions. Then, for every $u_I \in V_k^h$ and for every u_π such that $u_{\pi|E} \in \mathbb{P}_k(E)$, the discrete solution u_h satisfies*

$$|u - u_h|_{1,\Omega} \lesssim C_{err}(h) \left(\mathfrak{F}\mathfrak{s}_h + \|\!|u - u_I\|\! | + \|\!|u - u_\pi\|\! | + |u - u_I|_{1,\Omega} + |u - u_\pi|_{h,1} \right), \tag{1.35}$$

where the constant $C_{err}(h)$ is given by

$$C_{err}(h) = \max \left\{ 1, \, \tilde{C}(h)C_1(h), \, \tilde{C}(h)^{3/2}\sqrt{C^*(h)C_1(h)} \right\}.$$

From the previous theorem, the following quantities are derived from the constants in (1.34a):

$$\tilde{C}(h) = \max_{E \in \Omega_h}\{1, \, C_2(E)\}, \quad C_1(h) = \max_{E \in \Omega_h}\{C_1(E)\},$$

$$C^*(h) = \frac{1}{2} \max_{E \in \Omega_h} \{\min\{1, \, C_2(E)^{-1}\}\}.$$

In [18] the stability term $S_h^E(\cdot, \cdot)$ is considered as the combination of two contributions: the first, $S_h^{\partial E}$, related to the boundary degrees of freedom; the second, S_h^{oE}, related to the internal degrees of freedom. In the following statements, we restrict the analysis to $S_h^{\partial E}$ without losing generality. In this case, $S_h^{\partial E}$ is expressed in the *dofi-dofi* form $S_h^{\partial E,\mathrm{dd}}$ defined in (1.20), or in the *trace* form introduced in [72]:

$$S_h^{\partial E,\mathrm{tr}}(v_h, w_h) = h_E \int_{\partial E} \partial_s v_h \partial_s w_h ds, \tag{1.36}$$

where $\partial_s v_h$ denotes the tangential derivative of v_h along ∂E.

Theorem 1.3.5 (H^1 Error Estimate with *dofi-dofi* Stabilization) *Assuming **G1, G3**, let $u \in H^s(\Omega)$, $s > 1$, be the solution of the problem with $S_h^E = S_h^{\partial E,\mathrm{dd}}$. Let u_h be the solution of the discrete problem, then it holds*

$$\|u - u_h\|_{1,\Omega} \lesssim C(h)h^{s-1}|u|_{s,\Omega} \quad 1 < s \le k+1, \tag{1.37}$$

with

$$C(h) = \max_{E \in \Omega_h} (\log(1 + h_E/h_m(E))),$$

where $h_m(E)$ denotes the length of the smallest edge of E.

Corollary 1.1 *Assuming **G1** and **G2** instead, then $c(h) \lesssim 1$ and therefore*

$$\|u - u_h\|_{1,\Omega} \lesssim h^{s-1}|u|_{s,\Omega} \qquad 1 < s \le k+1.$$

Theorem 1.3.6 (H^1 Error Estimate with *trace* Stabilization) *Under Assumption **G1**, let $u \in H^s(\Omega)$, $s > 3/2$ be the solution of the problem with $S_h^E = S_h^{\partial E,\mathrm{tr}}$. Let u_h be the solution of the discrete problem, then it holds*

$$\|u - u_h\|_{1,\Omega} \lesssim h^{s-1}|u|_{s,\Omega} \quad 3/2 < s \le k+1. \tag{1.38}$$

Some Estimates for Virtual Element Methods [30]

In [30], the enhanced VEM space is defined as in the following:

$$
\begin{aligned}
V_k^h(E) := \big\{ v_h \in H^1(E) : & v_{h|\partial E} \in \mathbb{P}_k(\partial E), \\
& \exists q_{v_h}(= -\Delta v_h) \in \mathbb{P}_k(E) \text{ such that} \\
& \int_E \nabla v_h \cdot \nabla w_h \, d\mathbf{x} = \int_E q_{v_h} w_h \, d\mathbf{x} \quad \forall w_h \in H_0^1(E), \\
& \text{and } \Pi_k^{0,E} v_h - \Pi_k^{\nabla,E} v_h \in \mathbb{P}_{k-2}(E) \big\}.
\end{aligned}
\tag{1.39}
$$

i.e., in a slightly different but equivalent way than (1.7). In this work, the Authors consider different types of stabilization, but the convergence results are independent of S_h^E. The geometrical assumptions used in [30] are **G1** and **G2**.

Theorem 1.3.7 (Abstract Energy Error) *Assuming **G1**, **G2**, if $f \in H^{s-1}(\Omega)$ for $1 \le s \le k$, then there exists a positive constant C depending only on k and ρ from **G1** such that*

$$|u - u_h|_{1,\Omega} \le C(\inf_{v \in V_k^h} |u - v|_{1,\Omega} + \inf_{w \in \mathbb{P}_k(\Omega_h)} |u - w|_{h,1} + h^s|f|_{s-1,\Omega}). \tag{1.40}$$

Theorem 1.3.8 (H^1 Error Estimate) *Assuming **G1**, **G2**, if $u \in H^{s+1}(\Omega)$ for $1 \le s \le k$, then there exists positive constants C_1, C_2 depending only on k and ρ from **G1** such that*

$$|u - u_h|_{1,\Omega} + |u - \Pi_k^\nabla u_h|_{h,1} \le C_1 h^s|u|_{s+1,\Omega}. \tag{1.41}$$

Theorem 1.3.9 (L^2 **Error Estimate**) *Assuming **G1**, **G2**, with Ω convex, if $u \in H^{s+1}(\Omega)$ for for $1 \leq s \leq k$, then there exists a positive constant C depending only on Ω, k and ρ from **G1** such that*

$$\|u - u_h\|_{0,\Omega} \leq Ch^{s+1}|u|_{s+1,\Omega}. \tag{1.42}$$

Virtual Element Methods on Meshes with Small Edges or Faces [31]
In this paper, error estimates of the VEM are yield for polygonal or polyhedral meshes possibly equipped with small edges ($d = 2$) or faces ($d = 3$). In this case, the VEM space is formulated as (1.39) (i.e., the so-called enhanced space). The local stabilizing bilinear form is considered in both the *dofi-dofi* ($S_h^{E,\mathrm{dd}}$) and in the *trace* ($S_h^{E,\mathrm{tr}}$ of (1.36)) formulations. The Authors introduce also the constants:

$$\mathscr{H} := \sup_{E \in \Omega_h} \left(\frac{\max_{e \in \partial E} h_e}{\min_{e \in \partial E} h_e} \right), \qquad \alpha_h := \begin{cases} \ln(1 + \mathscr{H}) & \text{with } S_h^{E,\mathrm{dd}} \\ 1 & \text{with } S_h^{E,\mathrm{tr}} \end{cases} \tag{1.43}$$

The geometrical assumptions considered in this work are **G1** and **G3**. In particular, a mesh-dependent energy norm $\|\cdot\|_h := \sqrt{a_h(\cdot,\cdot)}$ and a functional $\Xi_h : V_k^h \to \mathbb{P}_k(\Omega_h)$ are introduced. The function Ξ_h is defined as:

$$\Xi_h = \begin{cases} \Pi_1^0 & \text{if } k = 1, 2 \\ \Pi_{k-1}^0 & \text{if } k \geq 3. \end{cases} \tag{1.44}$$

Theorem 1.3.10 (Abstract Energy Error) *Assuming **G1**, **G3**, let u and u_h be the solutions of the continuous and discrete problems. We have:*

$$\|u - u_h\|_h \lesssim \inf_{w \in V_k^h} \|u - w\|_h + \|u - \Pi_k^\nabla u\|_h + \tag{1.45}$$

$$\sqrt{\alpha_h} \left(\|u - \Pi_k^\nabla u\|_{h,1} + \sup_{w \in V_k^h} \frac{(f, w - \Xi_h w)}{|w|_{1,\Omega}} \right). \tag{1.46}$$

Theorem 1.3.11 (H^1 **Error Estimate**) *Assuming **G1**, **G3**, if the solution u belongs to $H^{s+1}(\Omega)$ for some $1 \leq s \leq k$, we have:*

$$\|u - u_h\|_h \lesssim \sqrt{\alpha_h} h^s |u|_{s+1,\Omega}, \text{ and} \tag{1.47}$$

$$|u - u_h|_{1,\Omega} + \sqrt{\alpha_h} \left[|u - \Pi_k^\nabla u_h|_{h,1} + |u - \Pi_k^0 u|_{h,1} \right] \lesssim \alpha_h h^s |u|_{s+1,\Omega}. \tag{1.48}$$

Theorem 1.3.12 (L^2 **Error Estimate**) *Assuming **G1**, **G3**, if the solution u belongs to $H^{s+1}(\Omega)$ for some $1 \le s \le k$, we have:*

$$\|u - u_h\|_{0,\Omega} \le C \, \alpha_h h^{s+1} |u|_{s+1,\Omega}. \tag{1.49}$$

The notation $A \lesssim B$ denotes that $A \le CB$, with a positive constant C depending on: (i) the mesh regularity parameter ρ of **G1**, (ii) the degree k in the case of $S_h^{E,\text{tr}}$, and (iii) the maximum number of edges N of **G3** in the case of $S_h^{E,\text{dd}}$.

Sharper Error Estimates for Virtual Elements and a Bubble-Enriched Version [9]

This paper shows that the H^1 interpolation error $|u - u_I|_{1,E}$ on each element E can be split into two parts: a boundary and a bulk contribution. The intuition behind this work is that it is possible to decouple the polynomial order on the boundary and in the bulk of the element. Let k_o and k_∂ be two positive integers with $k_o \ge k_\partial$ and let $\mathbf{k} = (k_o, k_\partial)$. For any $E \in \Omega_h$, the *generalized virtual element space* is defined as follows:

$$V_{\mathbf{k}}^h := \{v_h \in H_0^1(\Omega) : v_{h|E} \in) V_{\mathbf{k}}^h(E), \ \forall E \in \Omega_h\}, \tag{1.50a}$$

where

$$V_{\mathbf{k}}^h(E) := \{v_h \in H_0^1(E) : v_{h|\partial E} \in C^0(\partial E), \ v_{h|e} \in \mathbb{P}_{k_\partial}(e) \ \forall e \in \partial E, \tag{1.50b}$$

$$\text{and } \Delta v_h \in \mathbb{P}_{k_o-2}(E)\}.$$

For $k_o = k_\partial$, the space $V_{\mathbf{k}}^h(E)$ coincides with the regular virtual element space in (1.29). In addition, given a function $v \in H_0^1 \cap H^s(\Omega_h)$, on each element $E \in \Omega_h$ the interpolant function $\mathscr{I}_h v$ is defined as the solution of an elliptic problem as follows:

$$\begin{cases} \Delta \mathscr{I}_h v = \Pi_{k_o-2}^{0,E} \Delta v & \text{in } E \\ \mathscr{I}_h v = v_b & \text{on } \partial E, \end{cases}$$

where v_b is the standard 1D piecewise polynomial interpolation of $v|_{\partial E}$.

Theorem 1.3.13 (**Abstract Energy Error**) *Under Assumption **G1**, let $u \in H_0^1(\Omega_h) \cap H^s(\Omega_h)$ with $s > 1$ be the solution of the continuous problem and $u_h \in V_{\mathbf{k}}^h$ be the solution of the discrete problem. Consider the functions*

$$e_h = u_h - \mathscr{I}_h u, \ e_{\mathscr{I}} = u - \mathscr{I}_h u, \ e_\pi = u - u_\pi, \ e_u = u_\pi - \mathscr{I}_h u,$$

where $u_\pi \in \mathbb{P}_{k_o}(\Omega_h)$ is the piecewise polynomial approximation of u defined in Bramble-Hilbert Lemma. Then it holds that

$$|u - u_h|^2_{1,\Omega} + \alpha \, a_h(e_h, e_h) \lesssim \alpha^2 \sum_{E \in \Omega_h} h_E^2 \|f - f_h\|^2_{0,E} + \alpha^2 |e_\pi|^2_{1,\Omega_h} + \qquad (1.51)$$

$$\alpha |e_\mathscr{I}|^2_{1,\Omega} + \alpha \sum_{E \in \Omega_h} \sigma^E \qquad (1.52)$$

where α is the coercivity constant and $\sigma^E := S_h^E((I - \Pi_{k_0}^{\nabla,E})e_u, (I - \Pi_{k_0}^{\nabla,E})e_u)$.

Theorem 1.3.14 (H^1 **Error Estimate with** *dofi-dofi* **Stabilization**) *Assuming **G1, G4**, let $u \in H_0^1(\Omega_h)$ be the solution of the continuous problem and $u_h \in V_\mathbf{k}^h$ be the solution of the discrete problem obtained with the dofi-dofi stabilization. Assume moreover that $u \in H^{\bar{k}}(\Omega_h)$ with $\bar{k} = \max\{k_o + 1, k_\partial + 2\}$ and $f \in H^{k_o-1}$. Then it holds that*

$$|u - u_h|^2_{1,\Omega} \lesssim \alpha \sum_{E \in \Omega_h} \left((\alpha + \mathscr{N}_E)^{1/2} h_E^{k_o} + h_{\partial E}^{k_\partial}\right)^2, \qquad (1.53)$$

where $h_{\partial E}$ denotes the maximum edge length, α is the constant defined in (1.43), and $\mathscr{N}_E$ is the number of edges in E.

Theorem 1.3.15 (H^1 **Error Estimate with** *trace* **Stabilization**) *Under Assumption **G1**, let $u \in H_0^1(\Omega_h)$ be the solution of the continuous problem and $u_h \in V_\mathbf{k}^h$ be the solution of the discrete problem obtained with the trace stabilization. Assume moreover that $u \in H^{\bar{k}}(\Omega_h)$ with $\bar{k} = \max\{k_o + 1, k_\partial + 2\}$ and $f \in H^{k_o-1}$. Then it holds that*

$$|u - u_h|^2_{1,\Omega} \lesssim \sum_{E \in \Omega_h} \left(h_E^{k_o} + h_{\partial E}^{k_\partial}\right)^2. \qquad (1.54)$$

1.4 Violating the Geometrical Assumptions

We are here interested in testing the behaviour of the VEM on a number of mesh "datasets" which systematically stress or violate the geometrical assumptions from Sect. 1.3.1. This enhances a correlation analysis between such assumptions and the VEM performance, and we experimentally show how the VEM presents a good convergence rate on most examples and only fails in very few situations.

1.4.1 Datasets Definition

We start with defining the concept of dataset over a domain Ω, that for us will be the unit square $[0, 1]^2$.

Definition 1.1 We call a *dataset* a collection $\mathscr{D} := \{\Omega_n\}_{n=0,\dots,N}$ of discretizations of the domain Ω such that

(i) the mesh size of Ω_{n+1} is smaller than the mesh size of Ω_n for every $n = 0, \dots, N - 1$;

(ii) meshes from the same dataset follow a common refinement pattern, so that they contain similar polygons organized in similar configurations.

Each mesh Ω_n can be uniquely identified via its size as Ω_h, therefore every dataset $\mathscr{D}$ can be considered as a subset of a mesh family: $\mathscr{D} = \{\Omega_h\}_{h \in \mathscr{H}'} \subset \mathscr{T}$, being $\mathscr{H}'$ a finite subset of $\mathscr{H}$.

Together with the violation of the geometrical assumptions, we are also interested in measuring the behaviour of the VEM when the sizes of mesh elements and edges scale in a nonuniform way during the refinement process. To this purpose, for each mesh $\Omega_n \in \mathscr{D}$ we define the following *scaling indicators* and study their trend for $n \to N$:

$$A_n = \frac{\max_{E \in \Omega_n} |E|}{\min_{E \in \Omega_n} |E|} \quad \text{and} \quad e_n = \frac{\max_{e \in \Omega_n} |e|}{\min_{e \in \Omega_n} |e|}. \tag{1.55}$$

We designed six particular datasets in order to cover a wide range of combinations of geometrical assumptions and scaling indicators, as shown in Table 1.1. For each of them we describe how it is built, how A_n and e_n scale in the limit for $n \to N$ and which assumptions it fulfills or violates.

Note that none of the considered datasets (exception made for the reference dataset $\mathscr{D}_{\text{Triangle}}$) fulfills any of the sets of assumptions required by the convergence analysis found in the literature, cf. Sect. 1.3.2.

Each dataset is built around (and often takes its name from) a particular polygonal element, or elements configurations, contained in it, which is meant to stress one or more assumptions or indicators. The detailed construction algorithms, together with the explicit computations of A_n and e_n for all datasets, can be found in [68, Appendix B], while the complete collection of the dataset can be downloaded at https://github.com/TommasoSorgente/vem-quality-dataset.

Reference Dataset The first dataset, $\mathscr{D}_{\text{Triangle}}$, serves as a reference to evaluate the other datasets by comparing the respective performance of the VEM over each one. It contains only triangular meshes, built by inserting a number of vertices in the domain through the *Poisson Disk Sampling* algorithm [34], and connecting these vertices in a Delaunay triangulation through the *Triangle* library [65]. The refinement is obtained by increasing the number of vertices generated by the Poisson algorithm and computing a new Delaunay triangulation. The meshes in this dataset

perfectly satisfy all the geometrical assumptions and the indicators A_n and e_n are almost constant.

Hybrid Datasets Next, we define some *hybrid* datasets, which owe their name to the presence of both triangular and polygonal elements (meaning elements with more than three edges). A number of identical polygonal elements (called the *initial polygons*) is inserted in Ω, and the rest of the domain is tessellated by triangles with area smaller than the one of the initial polygons. These triangles are created through the *Triangle* library, with the possibility to add Steiner points [65] and to split the edges of the initial polygons, when necessary, with the insertion of new vertices. The refinement process is iterative, with parameters regulating the size, the shape and the number of initial polygons.

We defined two hybrid datasets, $\mathscr{D}_{\text{Maze}}$ and $\mathscr{D}_{\text{Star}}$ shown in Fig. 1.3, as they violate different sets of geometrical assumptions. Other choices for the initial polygons are possible, for instance considering the ones in Sect. 1.5.3.

Dataset $\mathscr{D}_{\text{Maze}}$ is named after a 10-sided polygonal element E, called "maze", spiralling around an external point. Progressively, as $n \to N$, each mesh Ω_n in $\mathscr{D}_{\text{Maze}}$ contains an increasing number of mazes E with decreasing thickness. Concerning the scaling indicators, we have $A_n \sim a^n$ for a constant $e < a < 3$ and $e_n \sim n \log(n)$, and the geometrical assumptions violated by this dataset are:

G1   because every E is obviously *not* star-shaped;
G1-weak   because of the decreasing thickness of the mazes. Indeed, it would be trivial to split E into a collection of star-shaped elements E_i (rectangles, for instance), but as $n \to N$ each radius r_{E_i} would decrease faster than the respective diameter h_{E_i}, unless considering an infinite number of them. Therefore, it
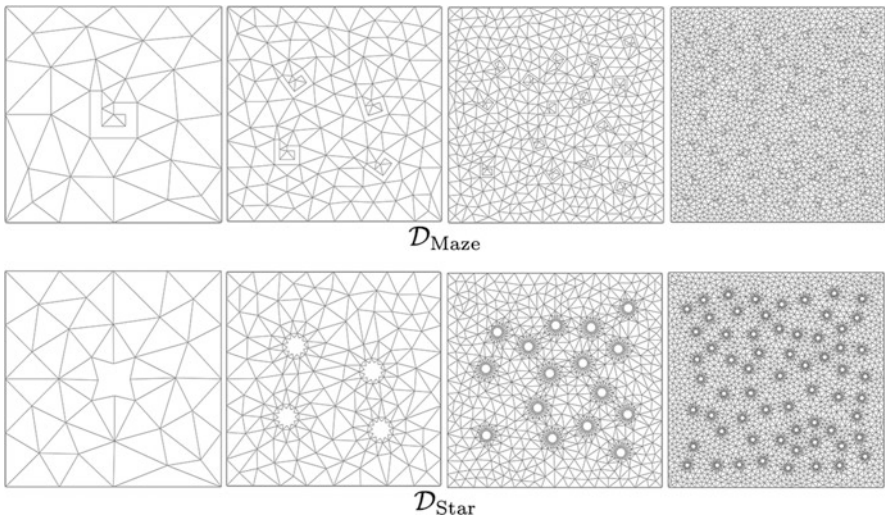
$\mathscr{D}_{\text{Maze}}$

$\mathscr{D}_{\text{Star}}$

Fig. 1.3 Meshes $\Omega_0, \Omega_2, \Omega_4, \Omega_6$ from datasets $\mathscr{D}_{\text{Maze}}$ and $\mathscr{D}_{\text{Star}}$
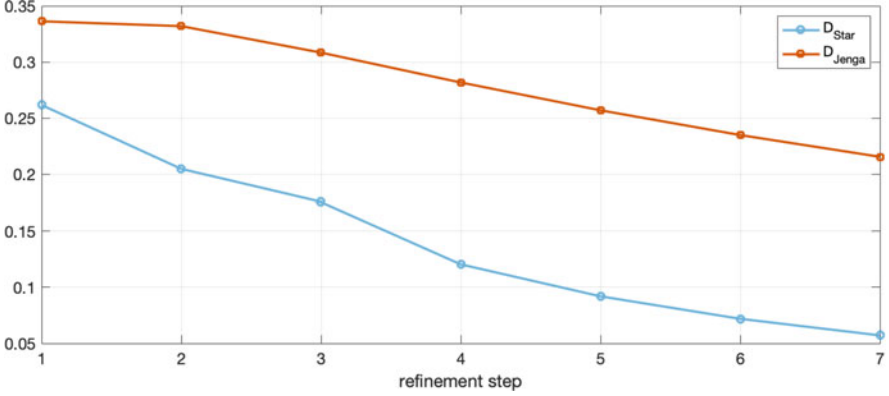
Fig. 1.4 Evolution of the ratio r_E / h_E for the meshes in datasets $\mathscr{D}_{Star}$ and $\mathscr{D}_{Jenga}$

would not be possible to bound the ratio r_{E_i} / h_{E_i} from below with a global ρ independent of h;

G2, G2-strong   because the length of the shortest edge e of E decreases faster than the diameter h_E.

Dataset $\mathscr{D}_{Star}$ is built by inserting star-like polygonal elements, still denoted by E. As $n \rightarrow N$, the number of spikes in each E increases and the inner vertices are moved towards the barycenter of the element. Both indicators A_n and e_n scale linearly, and the dataset violates the assumptions:

G1   each star E is star-shaped with respect to the maximum circle inscribed in it, but as shown in Fig. 1.4, the radius r_E of such circle decreases faster than the elemental diameter h_E, therefore it is not possible uniformly bound from below the quantity r_E / h_E with a global ρ;

G1-weak   in order to satisfy it, we should split each E into a number of sub-polygons, each of them fulfilling **G1**. Independently of the way we partition E, the number of sub-polygons would always be bigger than or equal to the number of spikes in E, which is constantly increasing, hence the number of sub-polygons would tend to infinity;

G2-strong   because the distance between the inner vertices of E decreases faster than h_E (but **G2** holds, because the edges scale proportionally to h_E);

G3   because the number of spikes in each E increases from mesh to mesh, therefore the total number of vertices and edges in a single element cannot be bounded uniformly.

Mirroring Datasets As an alternative strategy to build a sequence of meshes whose elements are progressively smaller, we adopt an iterative *mirroring* technique: given a mesh $\mathscr{M}$ defined on Ω, we generate a new mesh $\mathscr{M}'$ containing four adjacent copies of $\mathscr{M}$, opportunely scaled to fit Ω.

$\mathcal{D}_{\text{Jenga}}$

$\mathcal{D}_{\text{Slices}}$
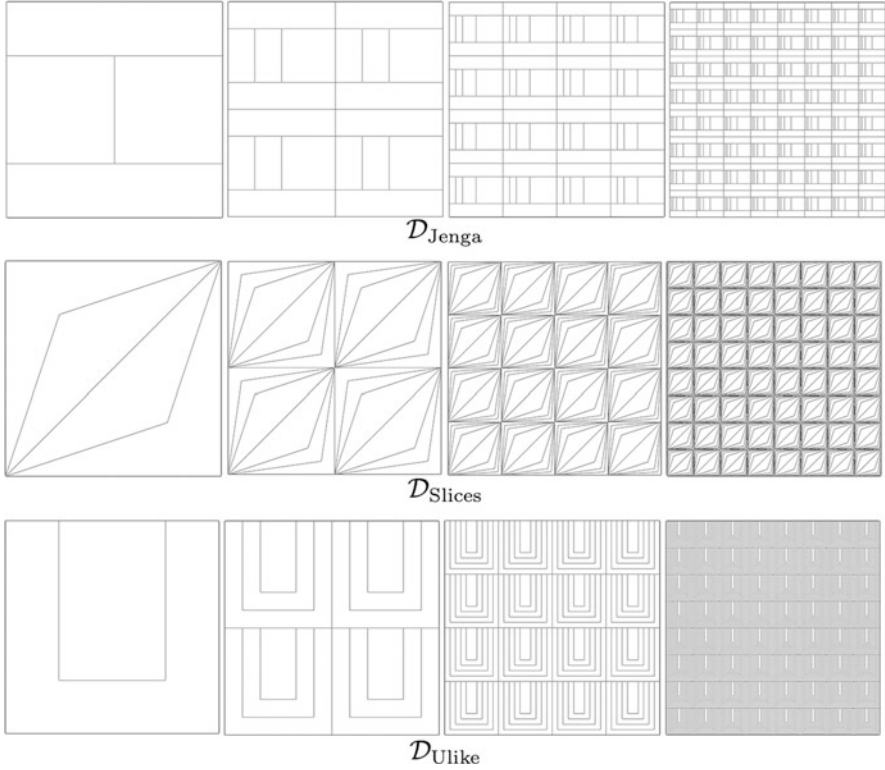
$\mathcal{D}_{\text{Ulike}}$

Fig. 1.5 Meshes Ω_0, Ω_1, Ω_2, Ω_3 from datasets $\mathcal{D}_{\text{Jenga}}$, $\mathcal{D}_{\text{Slices}}$ and $\mathcal{D}_{\text{Ulike}}$

The starting point for the construction of a dataset is the first base mesh $\widehat{\Omega}_0$, which coincides with the first computational mesh Ω_0. At every step $1 \leq n \leq N$, a new base mesh $\widehat{\Omega}_n$ is built from the previous base mesh $\widehat{\Omega}_{n-1}$. The computational mesh Ω_n is then obtained by applying the mirroring technique 4^n times to the base mesh $\widehat{\Omega}_n$. This construction allows us to obtain a number of vertices and degrees of freedom in each mesh that is comparable to that of the meshes at the same refinement level in datasets $\mathcal{D}_{\text{Maze}}$ and $\mathcal{D}_{\text{Star}}$.

The n-th base mesh $\widehat{\Omega}_n$ of dataset $\mathcal{D}_{\text{Jenga}}$ (Fig. 1.5, top) is built as follows. We start by subdividing the domain $(0, 1)^2$ into three horizontal rectangles with area equal to $1/4$, $1/2$ and $1/4$ respectively. Then, we split the rectangle with area $1/2$ vertically, into two identical rectangles with area $1/4$. This concludes the construction of the base mesh $\widehat{\Omega}_0$, which coincides with mesh Ω_0. At each next refinement step $n \geq 1$, we split the left-most rectangle in the middle of the base mesh $\widehat{\Omega}_{n-1}$ by adding a new vertical edge, and apply the mirroring technique to obtain Ω_n. Despite being made entirely by simple rectangular elements, this mesh family is the most complex one: both A_n and e_n scale like 2^n and it breaks all the assumptions.

G2, G2-strong   because the ratio $|e|/h_E$ decreases unboundedly in the left rectangle E, as shown in Fig. 1.4. This implies that a lower bound with a uniform constant ρ independent of h cannot exist;

G1, G1-weak   since the length of the radius r_E of the maximum disc inscribed into a rectangle is equal to $1/2$ of its shortest edge e, the ratio r_E/h_E also decreases;

G3   because the number of edges of the top (or the bottom) rectangular element grows unboundedly;

G4   because the one-dimensional mesh built on the boundary of the top rectangular element cannot be subdivided into a finite number of quasi uniform sub-meshes. In fact, either we have infinite sub-meshes or an infinite edge ratio.

For the dataset $\mathscr{D}_{\text{Slices}}$ (Fig. 1.5, middle), the n-th base mesh $\widehat{\Omega}_n$ is built as follows. First, we sample a set of points along the diagonal (the one connecting the vertices $(0, 1)$ and $(1, 0)$) of the reference square $[0, 1]^2$, and connect them to the vertices $(0, 0)$ and $(1, 1)$. In particular, at each step $n \geq 0$, the base mesh $\widehat{\Omega}_n$ contains the vertices $(0, 0)$ and $(1, 1)$, plus the vertices with coordinates $(2^{-i}, 1 - 2^{-i})$ and $(1 - 2^{-i}, 2^{-i})$ for $i = 1, \ldots, n + 2$. Then, we apply the mirroring technique. Since no edge is ever split, we find that $e_n \sim c$, while $A_n \sim 2^n$. The dataset $\mathscr{D}_{\text{Slices}}$ violates assumptions

G1, G1-weak   because, up to a multiplicative scaling factor depending on h, the radius r_E is decreasing faster than the diameter h_E, which is constantly equal to $\sqrt{2}$ times the same scaling factor. Moreover, any finite subdivisions of the mesh elements would suffer the same issue;

G2-strong   the vertices sampled along the diagonal have accumulation points at $(0, 1)$ and $(1, 0)$, therefore the distance between two vertices decreases progressively.

In $\mathscr{D}_{\text{Ulike}}$ (Fig. 1.5, bottom), we build the mesh $\widehat{\Omega}_n$ at each step $n \geq 0$ by inserting 2^n equispaced U-shaped continuous polylines inside the domain, creating as many U-like polygons. Then, we apply the mirroring technique as usual. Edge lengths scale exponentially and areas scale uniformly, i.e., $e_n \sim 2^n$, $A_n \sim c$, and the violated assumptions are:

G1, G1-weak, G2, G2-strong   for arguments similar to the ones seen for $\mathscr{D}_{\text{Maze}}$;

G3   in order to preserve the connectivity, the lower edge of the more external U-shaped polygon in every base mesh must be split into smaller edges before applying the mirroring technique. Hence the number of edges of such elements cannot be bounded from above.

Multiple Mirroring Datasets   As a final test, we modified datasets $\mathscr{D}_{\text{Jenga}}$, $\mathscr{D}_{\text{Slices}}$ and $\mathscr{D}_{\text{Ulike}}$ in order to particularly stress the scaling indicators A_n and e_n.
We obtained this by simply inserting four new elements at each step instead of one. The resulting datasets, $\mathscr{D}_{\text{Jenga4}}$, $\mathscr{D}_{\text{Slices4}}$ and $\mathscr{D}_{\text{Ulike4}}$, are qualitatively similar to the correspondent mirroring datasets above. Each of these datasets respects the same assumptions of its original version, but the number of elements at each refinement step now increases four times faster. Consequently, the indicators A_n and e_n change

from 2^n to 2^{4n}, but A_n remains constant for $\mathscr{D}_{\text{Ulike4}}$, and e_n remains constant for $\mathscr{D}_{\text{Slices4}}$.

1.4.2 VEM Performance over the Datasets

We solved the discrete Poisson problem (1.3) with the VEM (1.6) described in Sect. 1.2 for $k = 1, 2, 3$ over each mesh of each of the datasets defined in Sect. 1.4.1, using as groundtruth the function

$$u(x, y) = \frac{\sin(\pi x) \sin(\pi y)}{2\pi^2}, \quad (x, y) \in \Omega = (0, 1)^2. \tag{1.56}$$

This function has homogeneous Dirichlet boundary conditions, and this choice was appositely made to prevent the boundary treatment from having an influence on the approximation error.

Performance Indicators After computing the solution of the problem on a particular dataset, we want to measure the performance of the method over that dataset, that is, the accuracy and the convergence rate. We selected, among many possible alternatives, some quantities which can indicate if the error between the continuous solution u and the computed solution u_h is small and if the VEM worked properly in the computation of u_h. A more complete and accurate analysis of the possible performance indicators can be found in Sect. 1.5.2.

The approximation error might be measured in different norms: the most widely used in our framework are the relative H^1-seminorm and the relative L^2-norm (in the following we use the generic term *norms* to indicate both of them):

$$\frac{|u - u_h|_{1,\Omega}}{|u|_{1,\Omega}} \quad \text{and} \quad \frac{\|u - u_h\|_{0,\Omega}}{\|u\|_{0,\Omega}}.$$

In Figs. 1.6 and 1.7 we plot the two norms of the error generated by the VEM on each dataset as the number of DOFs increases (that is, as $n \to N$).

Another quantity, not directly related to the error, which can be of interest is the condition number of the matrices $\mathbf{G}$ and $\mathbf{H}$ (with the notation adopted in [12]):

$$\text{cond}(\mathbf{G}) = \|\mathbf{G}\| \|\mathbf{G}^{-1}\|, \qquad \text{cond}(\mathbf{H}) = \|\mathbf{H}\| \|\mathbf{H}^{-1}\|$$

Matrix $\mathbf{G}$ is involved in the computation of the *local stiffness matrix* and the projector Π_k^{∇}, while matrix $\mathbf{H}$ is involved in the computation of the *local mass matrix* and the projector Π_k^0.
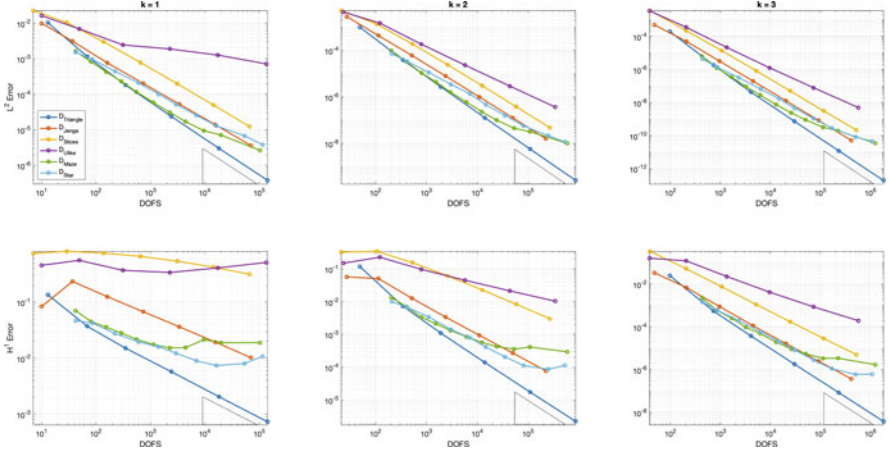
Fig. 1.6 L^2-norm and H^1-seminorm of the approximation errors of the reference, hybrid and mirroring datasets for $k = 1, 2, 3$
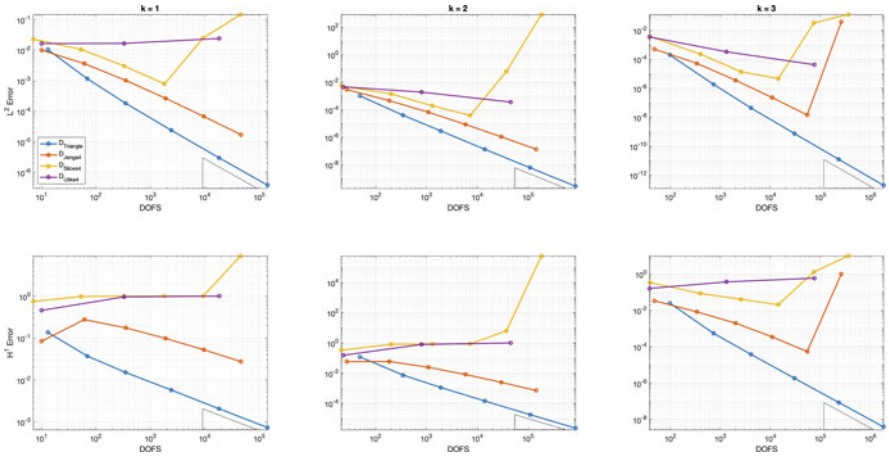
Fig. 1.7 L^2-norm and H^1-seminorm of the approximation errors of the reference and multiple mirroring datasets for $k = 1, 2, 3$

Last, as an estimate of the error produced by projectors Π_k^∇ and Π_k^0, represented by matrices $\mathbf{\Pi}_k^\nabla$ and $\mathbf{\Pi}_k^0$, we check the identities

$$|\mathbf{\Pi}_k^\nabla \mathbf{D} - \mathbf{I}| = 0 \quad \text{and} \quad |\mathbf{\Pi}_k^0 \mathbf{D} - \mathbf{I}| = 0, \tag{1.57}$$

where for $k < 3$ we have $\mathbf{\Pi}_k^0 := \mathbf{\Pi}_k^\nabla$. The computation of the projectors is obviously affected by the condition numbers of $\mathbf{G}$ and $\mathbf{H}$, but the two indicators are not necessarily related.

Condition numbers and identity values for $k = 1, 2, 3$ are reported in Table 1.2. All of these quantities are computed element-wise and the maximum value among all elements of the mesh is selected.

Performance The VEM performs perfectly over the reference dataset $\mathscr{D}_{\text{Triangle}}$, and this guarantees for the correctness of the method. The approximation error evolves in accordance to the theoretical results (the slopes being indicated by the triangles) both in L^2 and in H^1 norms for all k values, and condition numbers and optimal errors on the projectors Π_k^0 and Π_k^∇ remain optimal.

For the hybrid datasets $\mathscr{D}_{\text{Star}}$ and $\mathscr{D}_{\text{Maze}}$, errors decrease at the correct rate for most of the meshes, and only start deflecting for very complicated meshes with very high numbers of DOFs. These deflections are probably due to the extreme geometry of the star and maze polygons and not to numerical problems, as in both datasets we have $\text{cond}(\mathbf{G}) < 10^6$ and $\text{cond}(\mathbf{H}) < 10^9$, which are still reasonable values. Projectors seem to work properly: $|\mathbf{\Pi}_k^\nabla \mathbf{D} - \mathbf{I}|$ remains below 10^{-8} and $|\mathbf{\Pi}_k^0 \mathbf{D} - \mathbf{I}|$ below 10^{-7}. In a preliminary stage of this work, we obtained similar plots (not reported here) using other hybrid datasets built in the same way, with polygons surrounded by triangles. In particular, we did not notice big differences when constructing hybrid datasets as in Sect. 1.4.1 with any of the initial polygons of Sect. 1.5.3.

On the meshes from mirroring datasets A_n or e_n may scale exponentially instead of uniformly, as reported in Table 1.1. This reflects to $\text{cond}(\mathbf{G})$ and $\text{cond}(\mathbf{H})$, which grow up to, respectively, 10^{10} and 10^{14} for $\mathscr{D}_{\text{Jenga}}$ in the case $k = 3$. Nonetheless, the discrepancy of the projectors identities (1.57) remains below 10^{-5}, which is not far from the results obtained with datasets $\mathscr{D}_{\text{Maze}}$ and $\mathscr{D}_{\text{Star}}$. The method exhibits an almost perfect convergence rate on dataset $\mathscr{D}_{\text{Jenga}}$, even though L^2 and H^1 errors are bigger in magnitude than the ones measured for hybrid datasets. $\mathscr{D}_{\text{Slices}}$ produces even bigger errors and a non-optimal convergence rate, and $\mathscr{D}_{\text{Ulike}}$ is the dataset with the poorest performance, but the VEM still converges at a decent rate for $k > 1$. This may be due to the fact that for $k = 1$ the DOFs correspond to the vertices of the mesh, which are disposed in a particular configuration that generates horizontal bands in the domain completely free of vertices, and therefore of data. For $k > 1$

Table 1.1 Summary of the geometrical conditions violated and the asymptotic trend of the indicators A_n and e_n for all datasets. **G1w** and **G2s** stand for **G1-weak** and **G2-strong**, respectively, and a is a constant such that $e < a < 3$

Dataset	$\mathscr{D}_{\text{Triangle}}$	$\mathscr{D}_{\text{Maze}}$	$\mathscr{D}_{\text{Star}}$	$\mathscr{D}_{\text{Jenga}}$	$\mathscr{D}_{\text{Slices}}$	$\mathscr{D}_{\text{Ulike}}$
G1, G1w, G2s		×	×	×	×	×
G2		×		×		×
G3			×	×		×
G4				×		
A_n	c	a^n	n	2^n	2^n	c
e_n	c	$n \log(n)$	n	2^n	c	2^n

instead, we have DOFs also on the edges and inside the elements, hence the information is more uniformly distributed.

In the case of multiple mirroring datasets the method diverges badly on all datasets (see Fig. 1.7), and this is principally due to the very poor condition numbers of the matrices involved in the calculations (see Table 1.2). The plots relative to datasets $\mathscr{D}_{\text{Jenga4}}$ and $\mathscr{D}_{\text{Slices4}}$ maintain a similar trend to those of $\mathscr{D}_{\text{Jenga}}$ and $\mathscr{D}_{\text{Slices}}$ in Fig. 1.6, until numerical problems cause cond($\mathbf{G}$) and cond($\mathbf{H}$) to explode up to over 10^{30} for $\mathscr{D}_{\text{Jenga4}}$ and 10^{18} for $\mathscr{D}_{\text{Slices4}}$. In such conditions, the projection matrices $\mathbf{\Pi}_k^{\nabla}$ and $\mathbf{\Pi}_k^0$ become meaningless and the method diverges. The situation slightly improves for $\mathscr{D}_{\text{Ulike4}}$: cond($\mathbf{H}$) is still 10^{16}, but the discrepancy of $\mathbf{\Pi}_k^{\nabla}$ and $\mathbf{\Pi}_k^0$ remain acceptable. As a result, the method on $\mathscr{D}_{\text{Ulike4}}$ does not properly explode, but the approximation error and the convergence rate are much worse than those seen for $\mathscr{D}_{\text{Ulike}}$ in Fig. 1.6.

As a preliminary conclusion, by simply looking at the previous plots we observe that the relationship between the geometrical assumptions respected by a certain dataset and the performance of the VEM on it is not particularly strong. In fact, we obtained reasonable errors and convergence results on datasets violating several assumptions (all of them, in the case of $\mathscr{D}_{\text{Jenga}}$).

1.5   Mesh Quality Metrics

The aim of this section is to introduce some geometrical parameters, that we will refer to as *quality metrics*, which are potentially well suited to measure the shape regularity of a polygon, and study, statistically, the behavior of a VEM solver, as such measures degrade. In the following we present a list of polygon quality metrics and different strategies to combine them to form a quality metric for a polygonal tessellation. We will also introduce a list of parameters providing us with different ways of measuring the performance of the VEM solver at hand.

1.5.1   Polygon Quality Metrics

Different parameters provide us with some information on how much an element is far from being "nice", and the different assumptions presented in Sect. 1.3.1 give us a first list of possibilities. In the following we present the list of polygon quality metrics that we singled out for our study.

– *Circumscribed circle radius (CC)*: this is defined as the radius of the smallest circle fully containing P. The parameter CC is computed by treating the vertices of P as a point cloud and running the Welzl's algorithm to solve the minimum covering circle problem [71]. We point out that this choice does not yield the classical definition of circumscribed circle, requiring that all the vertices of

Table 1.2 Summary of numerical performance for all datasets. We report the $\log_{10}$ of the original values for the condition number of $\mathbf{G}$ and $\mathbf{H}$ and the discrepancy of projection matrices $\mathbf{\Pi}_k^\nabla$ and $\mathbf{\Pi}_k^0$. Note that for $k < 3$ we have $\mathbf{\Pi}_k^0 := \mathbf{\Pi}_k^\nabla$

Dataset	$\mathscr{D}_{\text{Triangle}}$			$\mathscr{D}_{\text{Maze}}$			$\mathscr{D}_{\text{Star}}$			$\mathscr{D}_{\text{Jenga}}$			$\mathscr{D}_{\text{Slices}}$			$\mathscr{D}_{\text{Ulike}}$			$\mathscr{D}_{\text{Jenga4}}$			$\mathscr{D}_{\text{Slices4}}$			$\mathscr{D}_{\text{Ulike4}}$		
k	1	2	3	1	2	3	1	2	3	1	2	3	1	2	3	1	2	3	1	2	3	1	2	3	1	2	3
cond(**G**)	0	2	5	2	3	6	1	3	6	1	5	10	2	4	6	1	4	7	6	18	31	6	8	10	2	6	11
cond(**H**)	2	5	7	3	5	8	3	6	9	4	9	14	2	8	10	3	7	10	13	26	39	2	15	18	5	10	16
$|\mathbf{\Pi}_k^\nabla \mathbf{D} - \mathbf{I}|$	−13	−11	−9	−12	−10	−8	−12	−10	−8	−12	−8	−5	−12	−10	−9	−13	−10	−8	−9	3	13	−8	−6	−5	−13	−8	−5
$|\mathbf{\Pi}_k^0 \mathbf{D} - \mathbf{I}|$			−10			−8			−7			−5			−5			−7			20			8			−4

Fig. 1.8 To be able to scale on general polygons, we define the radius of the circumscribed circle (CC) as the radius of the smallest circle containing the polygon itself. (Left) For a skinny triangle, CC is the radius of the smallest circle that passes through the endpoints of its longest edge (green), and not of the circle passing through all its three vertices (red). (Right) A general polygon and its CC

the polygon lie on the circle, that does not necessarily exist for all polygons (Fig. 1.8).

– *Inscribed circle radius (IC)*: this is defined as the radius of the biggest circle fully contained in P. For the computation of IC, starting from a Voronoi diagram of the edges of P, we select the corner in the diagram that is furthest from all edges as center of the circle. The radius of the IC is the minimum distance between such point and any of the edges of P. For the computation of the diagram of the set of edges, which, differently from the point case, has curved boundaries between cells, we apply the Boost Polygon Library [67].

– *Circle ratio (CR)*: the ratio between IC and CC. Differently from the previous two, this measure does not depend on the scale of the polygon, and is always defined in the range (0, 1].

– *Area (AR)*: the area of the polygon P.

– *Kernel area (KE)*: the area of the kernel of the polygon, defined as the set of points $p \in P$ from which the whole polygon is visible. If the polygon is convex, then the area of the polygon and the area of the kernel are equal. If the polygon is star-shaped, then the area of the kernel is a positive number. If the kernel is not star-shaped, then the kernel of the polygon is empty and KE will be zero.

– *Kernel-area/area ratio (KAR)*: the ratio between the area of the kernel of P and its whole area. For convex polygons, this ratio is always 1. For concave star-shaped polygons, KAR is strictly defined in between 0 and 1. For non star-shaped polygons, KAR is always zero.

– *Area/perimeter ratio (APR)*, or *compactness*: defined as $\frac{2\pi * \text{area}(P)}{\text{perimeter}(P)^2}$. This measure reaches its maximum for the most compact 2D shape (the circle), and becomes smaller for less compact polygons.

– *Shortest edge (SE)*: the length of the shortest edge of P.

– *Edge ratio (ER)*: the ratio between the length of the shortest and the longest edge of P.

Fig. 1.9 Polygon shape
regularity expressed in terms
of the ratio between the radius
maximal ball inscribed in the
kernel of the polygon (d), and
the radius of the maximal ball
inscribing the element (D)
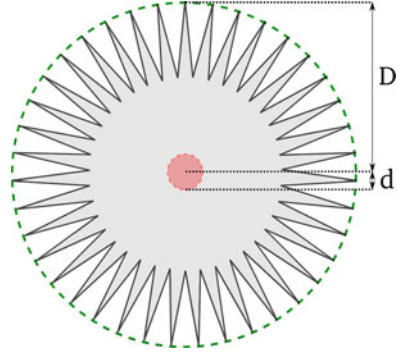
- *Minimum vertex to vertex distance (MPD)*, which is the minimum distance between any two vertexes in P. MPD is always less then or equal to SE. In case the two vertexes realizing the minimum distance are also extrema of a common edge, MPD and SE are equals.
- *Minimum angle (MA)*: the minimum inner angle of the polygon P.
- *Maximum angle (MXA)*: the maximum inner angle of the polygon P.
- *Number of edges ($N^{\mathscr{S}}$)*: the number of edges of the polygon.
- *Shape regularity (SR)*: the ratio between the radius of the circle inscribed in the kernel of the element and the radius CC of the circumscribed circle (Fig. 1.9). This assumes the value 0 for polygons which are not star shaped.

Remark that, while in triangular elements all the previous metrics are strictly bound to each other, for general polygons this is not the case, and, given a couple of such metrics, it is in general possible to find sequences of polygons for which one of the two degenerates, while the other stays constant. Remark also that some of the metrics, namely CR, KAR, APR, ER, MA, MXA, $N^{\mathscr{S}}$ and SR, are scale invariant, and only depend on the shape of the polygon and not on its size.

Aggregating Polygon Quality Metrics into Mesh Quality Metrics Let now consider a tessellation $\Omega_h = \{P_i, i = 1, \cdots, N\}$ with N elements. For $\mathfrak{m}$ being any of the above polygon quality metrics we can consider the vector

$$\mathfrak{m}(\Omega_h) = (\mathfrak{m}(P_1), \cdots, \mathfrak{m}(P_N)).$$

Starting from such a vector we can define a measure of the quality of the whole mesh, by following different strategies. More precisely, we considered the following possibilities.

- *Average*

$$\mathfrak{m}_{\mathrm{av}}(\Omega_h) = \mathrm{average}(\mathfrak{m}(\Omega_h)) = \frac{1}{N} \sum_{i=1}^{N} \mathfrak{m}(P_i).$$

– *Euclidean norm*

$$m_{l_2}(\Omega_h) = \|m(\Omega_h)\|_2 = \left(\sum_{i=1}^{N} m(P_i)^2\right)^{1/2}$$

– *Maximum*

$$m_{\max}(\Omega_h) = \max\{m(P_i), i = 1, \cdot, N\}$$

– *Minimum*

$$m_{\min}(\Omega_h) = \min\{m(P_i), i = 1, \cdot, N\}$$

To these four strategies, we add a fifth strategy, namely we define m_{worst} as the one, between $m_{\min}$ and $m_{\max}$, that singles out the worst polygon. More precisely, for $m \in \{IC, CR, KE, KAR, APR, SE, ER, MPD, MA, SR\}$ we set

$$m_{\text{worst}}(\Omega_h) = m_{\min}(\Omega_h),$$

while for $m \in \{CC, MXA, N^{\mathscr{S}}\}$ we set

$$m_{\text{worst}}(\Omega_h) = m_{\max}(\Omega_h).$$

1.5.2 Performance Indicators

Let us now consider how we can measure the performance of a PDE solver. Depending on the context, saying that a solver is "good" can have different meanings. Typically, the first thing that comes to mind, is that a solver is good when the error between the computed and the true solution is small. However the error might be measured in different norms: for instance, while the most natural norm in our framework is the H^1 norm (which is spectrally equivalent to the energy norm), if one is interested in the point value of the solution, the right information on the accuracy of the method is provided by the L^∞ norm of the error. The L^2 norm of the error is also frequently used to measure the accuracy. On the other hand, other quantities, not directly related to the error, can be of interest. For instance, if the problem considered involves inexact data, in order to limit the effect on the computed solution of the error on the data, the condition number of the stiffness matrix in the linear system of equations stemming from the discrete problem (1.6)

should be kept as small as possible, compatibly with the known fact that such a quantity increases as the mesh size decreases. The condition number of the stiffness matrix is also of interested if one aims at solving a large number of different problems, therefore needing a good computational performance of the numerical method. Here we introduce the different *performance indicators* that we chose to consider in our statistical analysis of the the Virtual Element Method.

Energy Norm Error The first indicator that we consider is the error between the computed solution u_h and the continuous solution u, measured in the energy norm. We recall that the quantity on the left hand side of inequality (1.24) is not computable. What is then usually done is to evaluate instead some computable quantity, such as the energy norm relative to the discrete equation, or the broken $H^1(\Omega_h)$ norm of $u - \Pi^\nabla u_h$. For our statistical analysis we chose, as first performance indicator

$$\mathbf{p}_1 = \frac{\sqrt{a_h(u_h - u_I, u_h - u_I)}}{\sqrt{a_h(u_I, u_I)}}.$$

Observe that this indicator depends on the data f and g of the model problem considered, so that for different values of such data we have different values of the indicator.

L^∞ *Error* In the finite element framework, under a shape regularity condition for the underlying triangular/quadrangular mesh, it is possible to bound, a priori, the maximum pointwise error. More precisely, under suitable assumptions on the discretization space which are satisfied by the most commonly used finite elements, if u_h is the finite element solution to Problem (1.1)–(1.2) defined on a quasi uniform triangular/quadrangular grid of mesh size h, it is possible to prove (see [64]) that

$$\|u - u_h\|_{0,\infty,\Omega} \le C h_{\max}^k \|u\|_{k,\infty,\Omega}.$$

While to our knowledge the problem of giving an L^∞ a priori bound on the error for the virtual element method has not yet been addressed in the literature, measuring the error in such a norm is relevant to many applications. It is then interesting to measure such an error and see how it is affected by the shape of the elements of the tessellation. However, also in this case, as we do not have access to the point values of the discrete function u_h, we will instead compute, as a performance indicator, the quantity

$$\mathbf{p}_2 = \frac{\max_i |\mathrm{dof}_i(u_h - u)|}{\max_i |\mathrm{dof}_i(u)|}.$$

Also this indicator depends on the data f and g of the model problem considered.

L^2 *Error* The third quantity that we consider, is the L^2 norm of the error. As usual, the proof of an inequality of the form (1.25) involves a duality argument and relies on the same a priori interpolation estimates used for proving (1.24). It requires, therefore, the same shape regularity assumption on the tessellation. As for the H^1 and the L^∞ norm errors, the L^2 norm of the error is not computable, and we replace it, in our experiments with the quantity

$$\mathbf{p}_3 = \frac{\|u_h - \Pi_k^0 u\|_{0,\Omega}}{\|\Pi_k^0 u\|_{0,\Omega}},$$

Also this indicator depends on the data f and g of the model problem considered.

Condition Number The condition number of the global stiffness matrix has a twofold effect:

- it provides reliable information on the efficiency of iterative solvers for the linear system arising from the discretization, ad on the need (or lack thereof) of resorting to some kind of preconditioning;
- more importantly, it provides a bound on how errors are propagated and, possibly, amplified, in the solution process. We recall, in fact, that the condition number is defined as

$$\kappa(\mathbf{R}) = \|\mathbf{R}\| \, \|\mathbf{R}^{-1}\|,$$

where $\mathbf{R}$ is the stiffness matrix stemming from Eq. (1.6). A large condition number for $\mathbf{R}$ might signify that the norm of $\mathbf{R}^{-1}$ is large. In turn, this implies that possible errors on the evaluation of right hand side of (1.6), which might derive not only from round off, but also from error on the data, are amplified by the solver resulting in a possibly much larger error in the computed discrete solution.

Estimating, a priori, the condition number of the stiffness matrix $\mathbf{R}$ is not difficult and relies on the use of an inverse inequality of the form

$$\|v_h\|_{1,\Omega} \le C_{\text{inv}} h_{\text{min}}^{-1} \|v_h\|_{0,\Omega}. \tag{1.58}$$

Under Assumptions **G1** and **G2**, such an inequality can be proven to hold with a constant C_{inv} independent of the polygon. If (1.58) holds, and if the chosen scaling for degrees of freedom is such that, letting $v_h \in V_h$ and $\mathbf{v}$ the vector of its degrees of freedom, we have

$$\|v_h\|_{0,\Omega}^2 \simeq \mathbf{v}^T \mathbf{v} \tag{1.59}$$

(if Assumptions **G1** and **G2** hold, this is always possible [27, 42]), then, for λ eigenvalue of **R** and **v** corresponding eigenvector, with v_h denoting the corresponding function in V_h, we can write

$$\mathbf{v}^T\mathbf{v} \lesssim \|v_h\|_{0,\Omega}^2 \le \|v_h\|_{1,\Omega}^2 \lesssim a_h(v_h, v_h) = \mathbf{v}^T\mathbf{R}\mathbf{v} = \lambda\mathbf{v}^T\mathbf{v},$$

as well as

$$\lambda\mathbf{v}^T\mathbf{v} = \mathbf{v}^T\mathbf{R}\mathbf{v} = a_h(v_h, v_h) \lesssim \|v_h\|_{1,\Omega}^2 \le C_{\text{inv}}h_{\min}^{-2}\|v_h\|_{0,\Omega} \lesssim C_{\text{inv}}h^{-2}\mathbf{v}^T\mathbf{v}$$

finally yielding

$$\mathbf{v}^T\mathbf{v} \lesssim \lambda\mathbf{v}^T\mathbf{v} \lesssim C_{\text{inv}}h_{\min}^{-2}\mathbf{v}^T\mathbf{v},$$

which implies

$$\kappa_2(\mathbf{R}) \lesssim C_{\text{inv}}h_{\min}^{-2}.$$

While the geometry of the elements also affects the implicit constant in the above inequality in different way (in particular through the continuity and coercivity constants and through the constants implicit in the equivalence relation (1.59)), we underlined here the effect of the constant appearing in the inverse inequality (1.58). Observe that if Assumption **G2** is violated, then C_{inv} is known to explode as the ratio between the diameter and the length of the smaller edge.

As computing the condition number exactly can be, for large matrices, extremely expensive, we used, as the performance indicator $\mathbf{p}_4$, a lower estimate of the 1-norm condition number, computed by the Lanczos method, according to [49, 50].

Condition Number After Preconditioning As already observed, for ill conditioned stiffness matrices, it is customary to resort to some form of preconditioning, and, consequently, a fairer estimation of the efficiency attained by a given solver requires taking into account the effect of preconditioning. Several approaches are available to precondition the stiffness matrix arising from the VEM discretization. We recall, among others, preconditioners based on domain decomposition, such as Schwarz [36], and FETI-DP and BDDC [26, 27], and multigrid [3]. Here we rather consider a simpler algebraic preconditioner, namely, the Incomplete Choleski factorization preconditioner [48]. Also here we use, as the preformance indicator $\mathbf{p}_5$, the lower estimate of the 1-norm condition number of the preconditioned stiffenss marix, computed according to [49, 50].

Constant in the Error Estimate While the theoretical error bound (1.24) puts forward the dependence of the error, measured in the $H^1(\Omega)$ norm, on the diameter of the largest element in the tessellation, the correlation analysis which, we will present in Sect. 1.5.3, shows a higher correlation of the error with the average

diameter size, suggesting that, in practice, an estimate such as

$$\|u - u_h\|_{1,\Omega} \leq C(u) h_{\mathrm{av}}^k \tag{1.60}$$

might hold. Of course, for fixed tessellation Ω_h and solution u an equality will hold in (1.60), for a suitable constant $C(u)$ depending on the tessellation Ω_h. We then use such a constant as a performance indicator $\mathbf{p}_6$:

$$\mathbf{p}_6 = \frac{\mathbf{p}_1}{h_{\mathrm{av}}^k}.$$

Aubin-Nitsche Trick Constant In the finite element framework, the Aubin-Nitsche duality trick allows to bound the L^2-norm of the error as

$$\|u - u_h\|_{0,\Omega} \leq C_{\mathrm{AN}} h_{\max} \|u - u_h\|_{1,\Omega},$$

from which a bound of the form (1.25) immediately results. While an analogous estimate cannot be proven for the VEM method, for which (1.25) is proven directly, as, once again, the two quantities $\|u - u_h\|_{0,\Omega}$ and $h_{\max}\|u - u_h\|_{1,\Omega}$ are both positive and finite, the above inequality can be replaced by an equality for a given constant C_{AN}, depending on the data and on the tessellation. Also in this case our correlation suggests to replace, in an estimate of this kind, the diameter $h_{\max}$ of the largest element with the average diameter, and we propose, as a performance indicator, the quantity

$$\mathbf{p}_7 = \frac{\mathbf{p}_2}{h_{\mathrm{av}} \mathbf{p}_1}.$$

Effectiveness of the Preconditioner The last performance indicator aims at evaluating if and how the geometry of the tessellation affects the effectiveness of the preconditioner by comparing the condition number of the preconditioned stiffness matrix with the one of the same matrix without any preconditioning. More precisely, the last performance indicator is defined as

$$\mathbf{p}_8 = \frac{\mathbf{p}_5}{\mathbf{p}_4}.$$

Remark that we expect $\mathbf{p}_8$ to be less than 1. $\mathbf{p}_8$ close to 1 indicates an ineffective preconditioner, while $\mathbf{p}_8 \ll 1$ indicates that the preconditioner is performing its role, while $\mathbf{p}_8 \geq 1$ indicates the failure of the preconditioning algorithm.

1.5.3   Results

We considered two different test problem corresponding to two different solutions to the Poisson equation (1.1)–(1.2), both with $\Omega = (0, 1)^2$.

Test 1   For the first test problem, the groundtruth is, once again,

$$u_1(x, y) = \frac{\sin(\pi x)\sin(\pi y)}{2\pi^2}.$$

Test 2   For the second test problem the groundtruth is the Franke function, namely

$$u_2(x, y) := \frac{3}{4}e^{-((9x-2)^2+(9y-2)^2)/4} + \frac{3}{4}e^{-((9x+1)^2/49+(9y+1)/10)}$$

$$+ \frac{1}{2}e^{-((9x-7)^2+(9y-3)^2)/4} + \frac{1}{5}e^{-((9x-4)^2+(9y-7)^2)}.$$

We solved each problem with the VEM solver of order $k = 1, 2, 3$ on 260 hybrid tessellations explicitly designed to progressively stress the polygon quality metrics described in Sect. 1.5.1. Specifically, a family of parametric polygons have been designed: the baseline configuration of each polygon (P(0)) does not present critical geometric features, and 20 versions of the same polygon are generated by progressively deforming the baseline by a parameter t. Each polygon (its baseline version and its deformations) is placed at the center of a canvas representing the squared domain $[0, 1]^2$. the space of the domain complementary to the polygon is filled with triangles [53, 65]. Figure 1.10 shows the list of our parametric polygons and how they have been used to generate the dataset. Note that the parametric polygons "maze" and "star" are similar to the initial polygons of the hybrid datasets defined in Sect. 1.4.1, meaning that they contain the same pathologies even if edges and areas scale differently. The resulting meshes, however, have little in common, as meshes from $\mathscr{D}_{\text{Maze}}$ and $\mathscr{D}_{\text{Star}}$ contain several of such polygons with different sizes.

For each test case we compute the 5 performance indexes $\mathbf{p}_1$, $\mathbf{p}_2$, $\mathbf{p}_3$, $\mathbf{p}_6$, $\mathbf{p}_7$ corresponding to each tessellation. Moreover, for each tessellation, we computed the three performance indexes $\mathbf{p}_4$, $\mathbf{p}_5$ and $\mathbf{p}_8$, for a grand total of 13 performance indexes for each tessellation. We then computed the Spearman correlation index [58, 69] between the 14 quality metrics, with the five aggregation methods, and the 13 performance indexes. The results are displayed in Fig. 1.11. As the Euclidean norm aggregation method gives results that are substantially similar to the average aggregation method and as the worst aggregation method summarized the most significant of the minimum and maximum aggregation methods, we only show the results for average and worst aggregation method.

We next consider the cases that result in the overall lowest and highest correlation index. For such cases, we present the related scatterplots (displayed either in semi-logarithmic or in logarithmic scale). More precisely the scatterplot corresponding to low correlation are shown in Fig. 1.12, while in Fig. 1.13 we can look at the
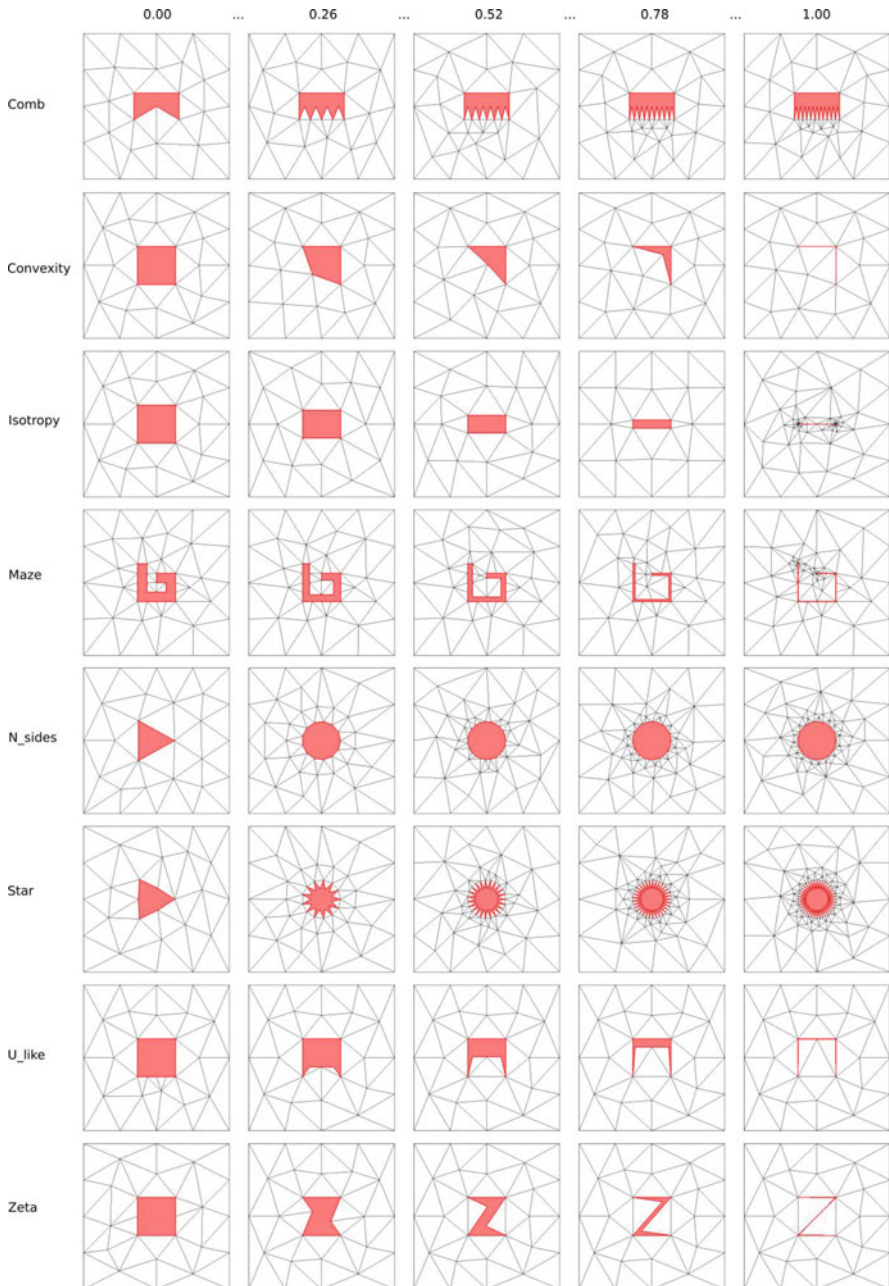
Fig. 1.10 A subset of meshes in our dataset. On the left column, the list of names associated to parametric polygons (in red). On the top row, the values of the deformation parameter
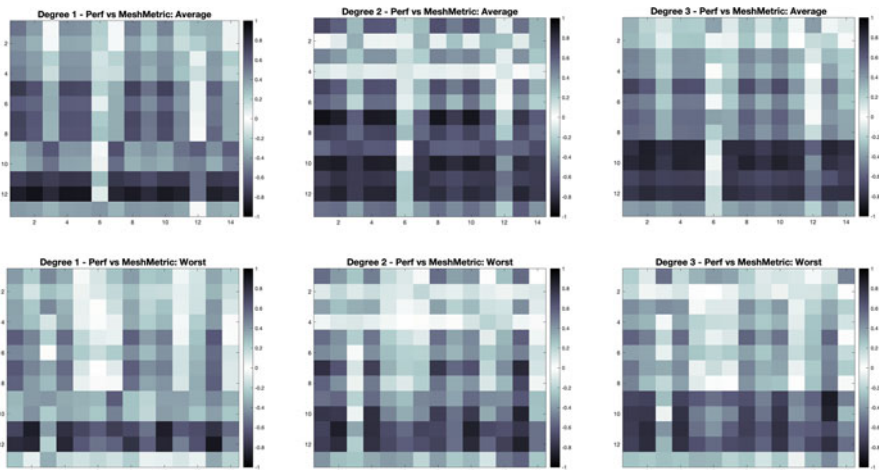
Fig. 1.11 Mesh metrics (average agglomeration method, top and worst agglomeration method, bottom) vs Performance metrics for k equals 1 through 3
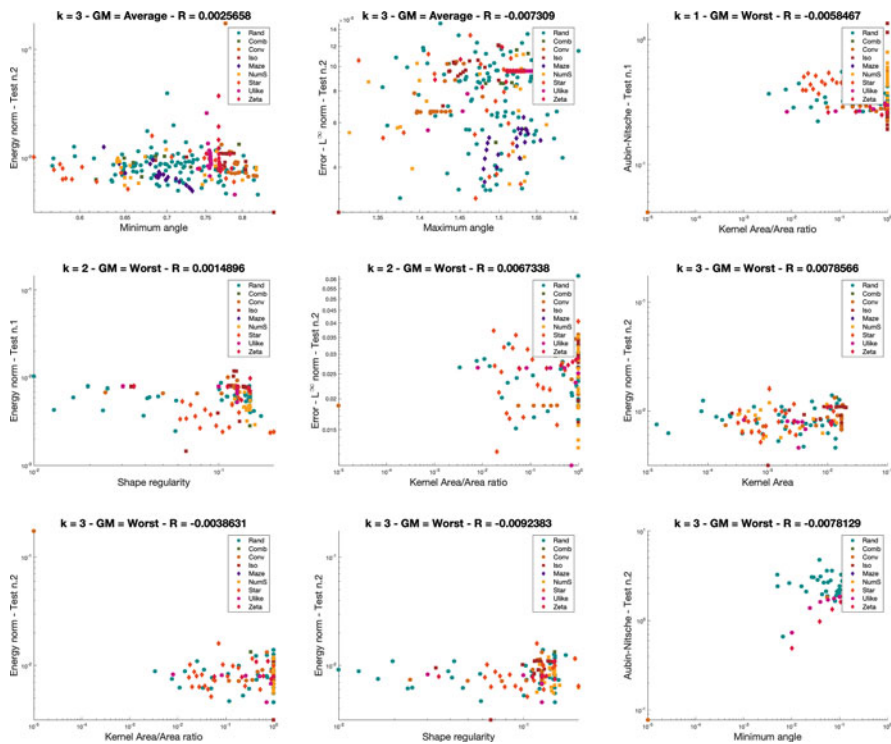
Fig. 1.12 Scatterplots corresponding to an absolute value of the Spearman correlation lower than .03. On the x-axis the geometric metric, on the y-axis the performance metric
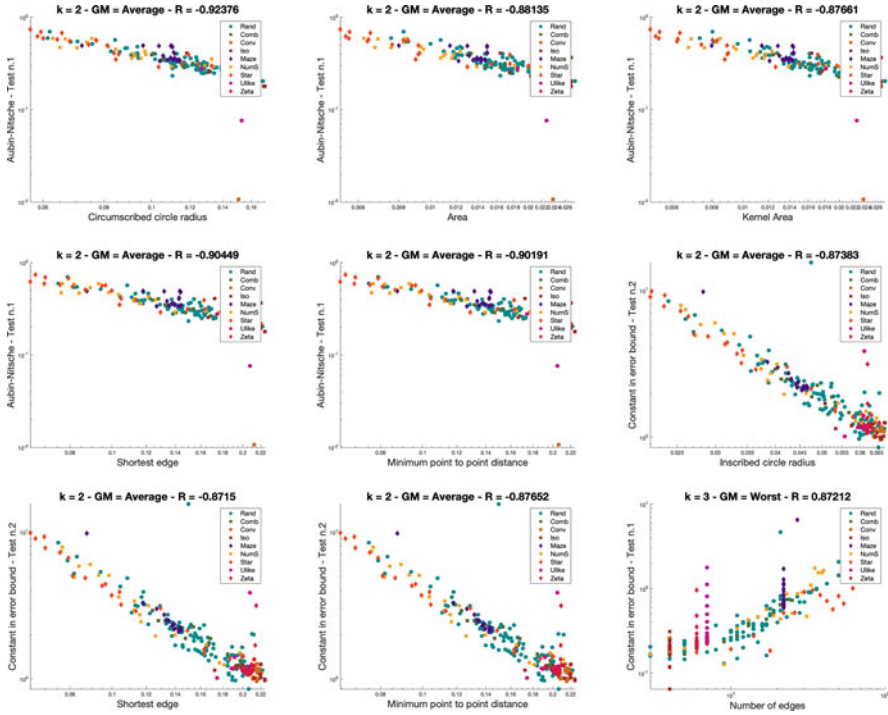
Fig. 1.13 Scatterplots corresponding to an absolute value of the Spearman correlation greater than .9. On the x-axis the geometric metric, on the *y*-axis the performance metric

scatterplots corresponding to the high correlation cases. The first thing that jumps to the eye is that all high correlation case except one correspond to the average aggregation method, while the converse holds for the low correlation (all cases but two correspond to the worst aggregation method). Looking at Fig. 1.12 we also see that the SR metric has low correlation with the error in the energy norm. This confirms the experimental observations, already pointed out in the literature, and is particularly interesting, as it shows that violating Assumption **G1**, which is the commonly used assumption in the analysis of VEM methods, does not necessarily result in a deterioration of the accuracy of the method. This suggests to try to carry out the convergence analysis in the absence of such a bound (and, in particular, for meshes of non star shaped polygons). The minimum and maximum angle also seem to have little correlation with the error. Conversely, two quantities that are clearly highly correlated with several of the metrics are the constants in the error estimate $\mathbf{p}_6^{(1)}$ and $\mathbf{p}_6^{(2)}$ and the Aubin Nitsche trick constants $\mathbf{p}_7^{(1)}$ and $\mathbf{p}_7^{(2)}$. We also observe that the constant in the error bound is highly correlated with the highest number of edges. This is also very interesting, as it suggests that even a single polygon with a high number of edges can affect the performance of the method. It is then

worth devoting some effort to the design of variants of the VEM, aimed at attaining robustness with respect to the number of edges.

Comparison Between Methods of Different Orders The previously presented set of tests is also aimed at gaining some insight on the combined influence of geometry and order of the method on the performance of the method itself. Theoretical results on the performance of the VEM rarely track the dependence of the constant in the inequality on the order k of the method. Notable exceptions are [17, 19], that however, in order to give an a priori error bound bound, require the polygonal meshes to satisfy the very restrictive assumptions **G1** and **G2**. Focusing on three of the performance indexes, which we expect to be scale independent, and on the six scale independent geometric quality measures, we present the superposed scatter plots for $k = 1, 2$ and 3. The resulting comparison yields some interesting observations. In Fig. 1.14, we see that the Aubin-Nitsche constant for $k = 2$ and 3 is lower and less spread out than for $k = 1$. The opposite happens for the constant in the classical error bound of the form (1.24). Such constant increases as k increases (as it is to be expected), but it also appear that higher values of k amplify the negative influence of the bad quality of the mesh (Fig. 1.15). Figure 1.16
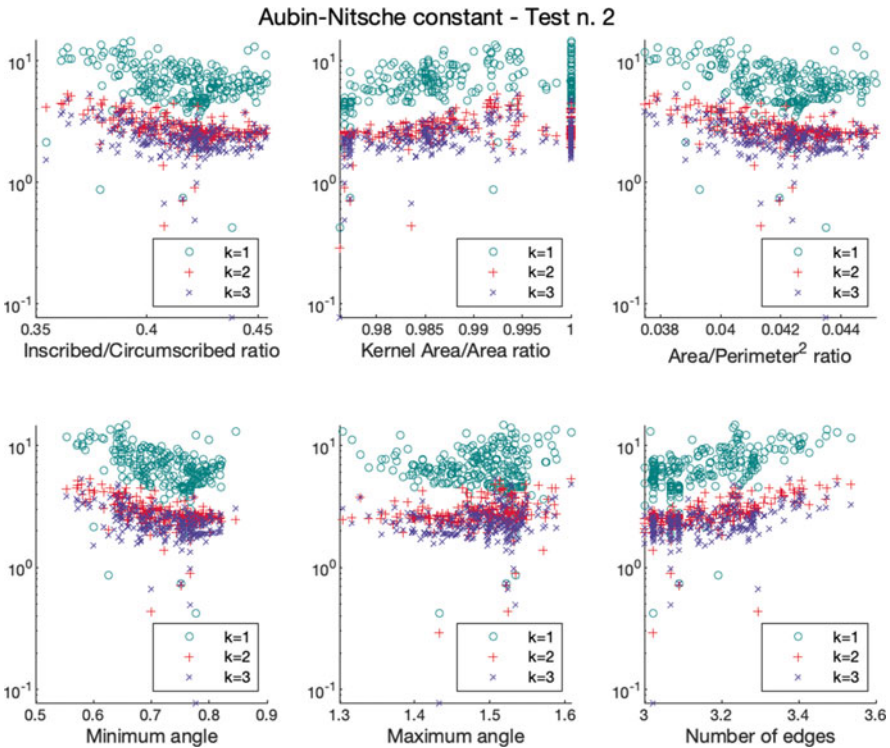
Fig. 1.14 Relation between Aubin-Nitsche constant and the scale invariant metrics for $k = 1, 2$ and 3

Constant in energy error bound - Test n. 2
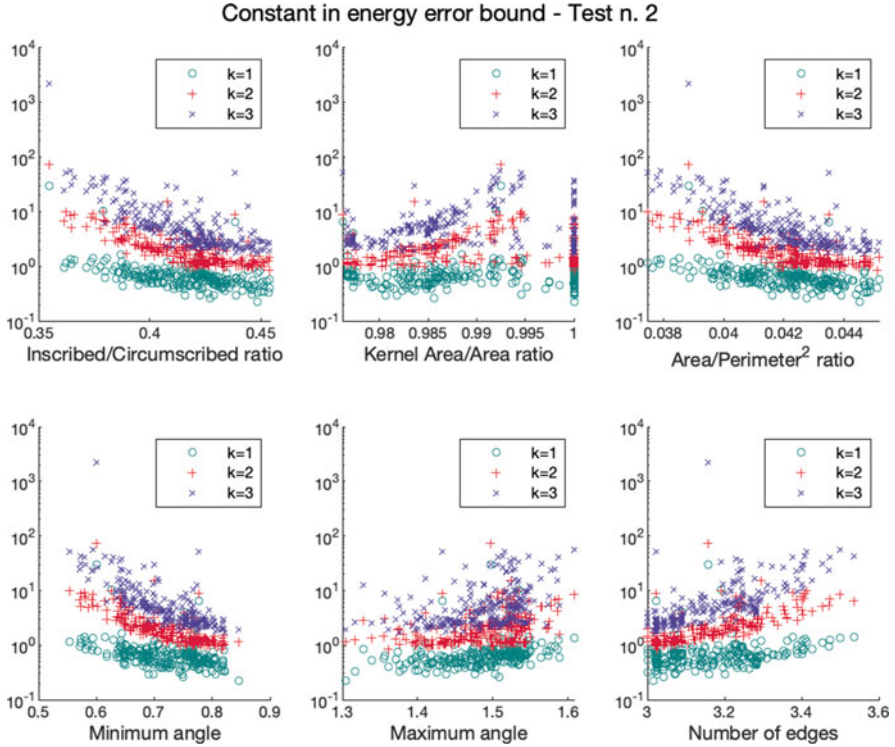
Fig. 1.15 Relation between the constant in the classical a priori error bound and the scale invariant metrics for $k = 1$, 2 and 3

is particularly interesting: for $k = 2$, the incomplete Choleski preconditioner is less effective than it is for $k = 1$ and 3, and it even appears to be failing in a number of cases, giving an effectiveness index > 1. This might be the consequence of a difference between odd and even order method, that is sometimes encountered in non conforming discretizations.

1.6 Mesh Quality Indicators

In this section we define a *mesh quality indicator*, that is, a scalar function capable of providing insights on the behaviour of the VEM over a particular mesh Ω_h, before actually computing the approximated solution u_h. This indicator depends uniquely on the geometry of the mesh elements, but has interesting correspondences with the performance of the VEM, in terms of approximation error and convergence rate.
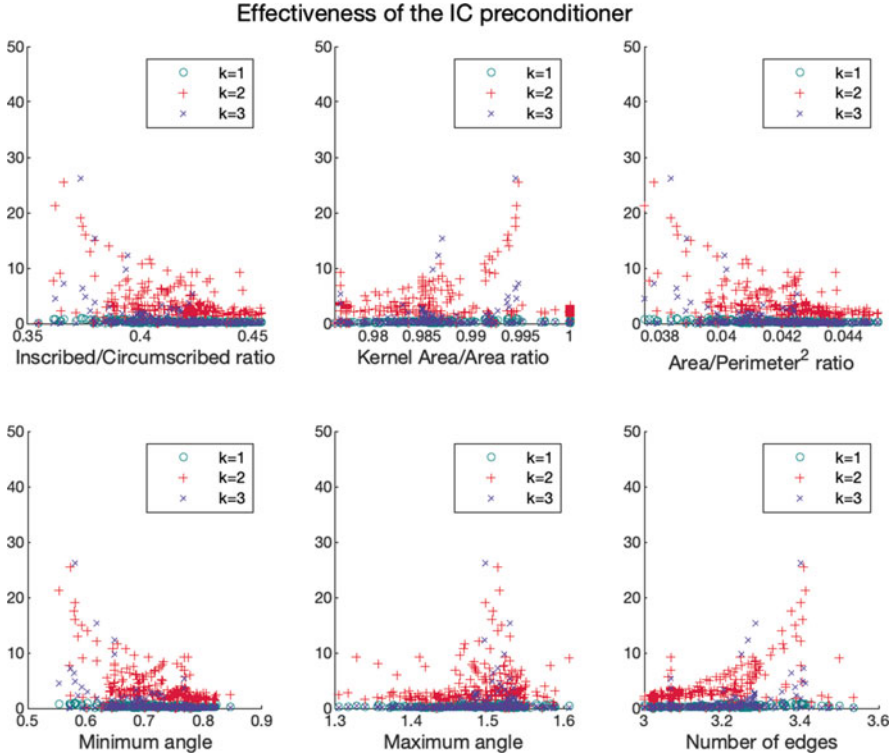
Fig. 1.16 Relation between the effectiveness of the incomplete Choleski preconditioner and the scale invariant metrics for $k = 1, 2$ and 3

1.6.1 Definition

We start from the geometrical assumptions defined in Sect. 1.3.1. The driving idea is that instead of imposing an absolute condition that a mesh can only satisfy or violate, we want to measure *how much* the mesh satisfies or violate that condition. This approach is more accurate, as it captures small quality differences between meshes, and it does not exclude a priori all the particular cases of meshes only slightly outside the geometrical assumptions.

From each geometrical assumption **Gi**, **i** $= 1, \ldots, 4$, we derive a scalar function $\varrho_i : \{E \subset \Omega_h\} \rightarrow [0, 1]$ defined element-wise, which measures how well the element $E \in \Omega_h$ meets the requirements of **Gi** from 0 (E does not respect **Gi**) to 1 (E fully respects **Gi**).

From assumption **G1** we derive the indicator ϱ_1, which can be interpreted as an estimate of the value of the constant ρ from **G1** on the polygon E:

$$\varrho_1(E) = \frac{k(E)}{|E|},$$

being $k(E)$ the area of the *kernel* of a polygon E, defined as the set of points in E from which the whole polygon is visible (cf. *(KE)* of Sect. 1.5.1). Therefore, $\varrho_1(E) = 1$ if E is convex, $\varrho_1(E) = 0$ if E is not star-shaped and $\varrho_1(E) \in (0, 1)$ if E is concave but star-shaped.

Similarly, the function ϱ_2 returns an estimate of the constant ρ introduced in **G2**, expressed trough the ratio $|e|/h_E$:

$$\varrho_2(E) = \frac{\min(\sqrt{|E|}, \ \min_{e \in \partial E} |e|)}{\max(\sqrt{|E|}, \ h_E)}.$$

The insertion of the quantity $\sqrt{|E|}$ is needed in order to scale the indicator in the range [0, 1] and to avoid pathological situations.

Function ϱ_3 is a simple counter of the number of edges of the polygon, which penalizes elements with numerous edges as required by **G3**:

$$\varrho_3(E) = \frac{3}{\#\{e \in \partial E\}}.$$

It returns 1 if E is a triangle, and it decreases as the number of edges increases.

Last, we recall from Sect. 1.3.1 that the boundary of a polygon E can be considered as a 1-dimensional mesh $\mathscr{I}_E$, which can be subdivided into disjoint sub-meshes $\mathscr{I}_E^1, \ldots, \mathscr{I}_E^N$, each one containing possibly more than one edge of E. In practice, we consider as a sub-mesh the collection of all edges whose vertices lie on the same line. An example is shown in Fig. 1.17, where the boundary of the top bar element E in the base mesh of $\mathscr{D}_{\mathrm{Jenga}}$ is represented by a mesh

Fig. 1.17 One-dimensional mesh $\mathscr{I}_E = \{\mathscr{I}_E^1, \mathscr{I}_E^2, \mathscr{I}_E^3, \mathscr{I}_E^4\}$ for the top bar element E of a $\mathscr{D}_{\mathrm{Jenga}}$ base mesh
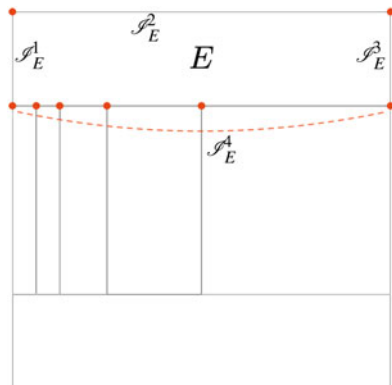
$\mathscr{I}_E = \{\mathscr{I}_E^1, \mathscr{I}_E^2, \mathscr{I}_E^3, \mathscr{I}_E^4\}$. The sub-meshes $\mathscr{I}_E^1$, $\mathscr{I}_E^2$ and $\mathscr{I}_E^3$ contain, respectively, the left, top and right edge of E, while $\mathscr{I}_E^4$ contains all the aligned edges in the bottom of E.

The indicator ϱ_4 returns the minimum ratio between the smallest and the largest element in every $\mathscr{I}_E$, that is a measure of the quasi-uniformity of $\mathscr{I}_E$ imposed by **G4**:

$$\varrho_4(E) = \min_i \frac{\min_{e \in \mathscr{I}_E^i} |e|}{\max_{e \in \mathscr{I}_E^i} |e|}.$$

Combining together ϱ_1, ϱ_2, ϱ_3 and ϱ_4, we define a global function $\varrho : \{\Omega_h\}_h \to [0, 1]$ which measures the overall quality of a mesh Ω_h. Given a dataset $\mathscr{D}$, we can study the behaviour of $\varrho(\Omega_h)$ for $h \to 0$ and determine the quality of the meshes through the refinement process. In particular, we combine the indicators with the formula $\varrho_1\varrho_2 + \varrho_1\varrho_3 + \varrho_1\varrho_4$ as it reflects the way in which these assumptions are typically imposed: **G1** and **G2**, **G1** and **G3** or **G1** and **G4** (but not, for instance, **G2** and **G3** simultaneously):

$$\varrho(\Omega_h) = \sqrt{\frac{1}{\#\{E \in \Omega_h\}} \sum_{E \in \Omega} \frac{\varrho_1(E)\varrho_2(E) + \varrho_1(E)\varrho_3(E) + \varrho_1(E)\varrho_4(E)}{3}}.$$

$$(1.61)$$

We list some observations on the newly defined mesh quality indicator ϱ:

- we have $\varrho(\Omega_h) = 1$ if and only if Ω_h contains only equilateral triangles, $\varrho(\Omega_h) = 0$ if and only if Ω_h contains only non star-shaped polygons, and $0 < \varrho(\Omega_h) < 1$ otherwise;
- the indicator ϱ only depends on the geometrical properties of the mesh elements (because the same holds for ϱ_1, ϱ_2, ϱ_3 and ϱ_4), therefore it can be computed before applying the numerical scheme;
- the construction of ϱ is easily upgradeable to future developments: whenever new assumptions on the features of a mesh should come up, one simply needs to introduce a new function ϱ_i that measures the violation of the new assumption and opportunely insert it into Eq. (1.61);
- similarly, this indicator is easily extendable to other numerical schemes by substituting the assumptions designed for the VEM with the assumptions on the new scheme, and defining the relative indicators ϱ_i.

1.6.2 Results

We evaluated the indicator ϱ over the datasets defined in Sect. 1.4.1; results are shown in Fig. 1.18. We want to investigate if the ϱ values of the meshes of a certain
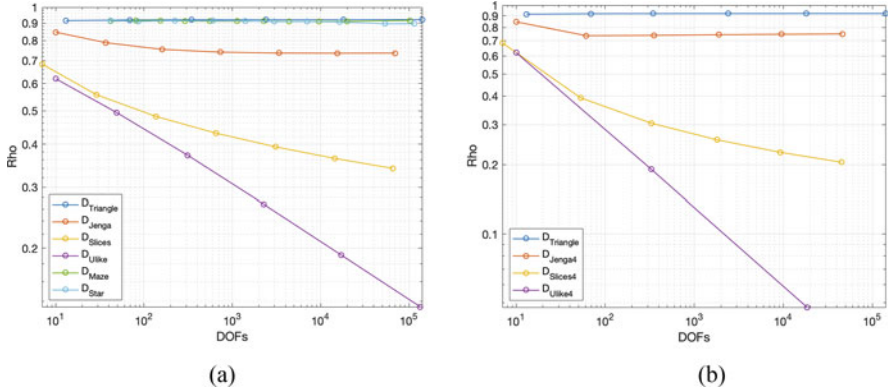
Fig. 1.18 Indicator ϱ for all datasets from Sect. 1.4.1

dataset in Fig. 1.18, computed before solving the problem, are somehow related to the performance of the VEM over the meshes of the same dataset, shown in Figs. 1.6 and 1.7, in terms of error approximation and convergence rate.

Since ϱ does not depend on the polynomial degree k nor on the type of norm used, we have to consider an hypothetical average of the plots for the different k values and for the different norms (L^2 and H^1) from Figs. 1.6 and 1.7.

As already seen, for an ideal dataset made by meshes containing only equilateral triangles, ϱ would be constantly equal to 1. We assume this value as a reference for the other datasets: the closer ϱ is on a dataset to the line $y = 1$, the smaller is the approximation error that we expect that dataset to produce. Similarly, the more negative is the ϱ slope, the worse is the convergence rate that we expect the method to obtain over that dataset.

For meshes belonging to $\mathscr{D}_{\text{Triangle}}$, ϱ is almost constant and very close to 1, thus foreseeing the excellent convergence rates and the low errors relative to $\mathscr{D}_{\text{Triangle}}$ in every sub-figure of Fig. 1.6.

The plots for $\mathscr{D}_{\text{Maze}}$ and $\mathscr{D}_{\text{Star}}$ in Fig. 1.18a are close to the $\mathscr{D}_{\text{Triangle}}$ one, hence we expect the method to perform similarly over the three of them. This is confirmed by Fig. 1.6: $\mathscr{D}_{\text{Maze}}$ and $\mathscr{D}_{\text{Star}}$ are almost coincident and very close to $\mathscr{D}_{\text{Triangle}}$ until the very last meshes, especially in the L^2 plots.

The $\mathscr{D}_{\text{Jenga}}$ plot in Fig. 1.18a suggests a perfect convergence rate but greater error values with respect to the previous three, and again this behaviour is respected in Fig. 1.6.

The curve relative to $\mathscr{D}_{\text{Slices}}$ in Fig. 1.18a is quite distant from the ideal value of 1. Moreover, the curve keeps decreasing from mesh to mesh, even if we may assume that it would flatten within few more meshes. Looking at Fig. 1.6, we notice that $\mathscr{D}_{\text{Slices}}$ produces an error significantly higher than the previous ones ($\mathscr{D}_{\text{Triangle}}, \mathscr{D}_{\text{Maze}}, \mathscr{D}_{\text{Star}}, \mathscr{D}_{\text{Jenga}}$), and in some cases the H^1 error convergence rate is significantly lower than the theoretical estimate, thus confirming the prediction.

Last, the ϱ values in Fig. 1.18a predict huge errors and a completely wrong convergence rate for $\mathscr{D}_{\text{Ulike}}$. In fact, this dataset is the one with the worst performance in Fig. 1.6, where the VEM does not even always converge (for example in the case $k = 1$ with the H^1 seminorm).

As far as multiply refined datasets are concerned, we note that, since ϱ only depends on the geometry of the elements, it is not affected by numerical errors. The ϱ plot for $\mathscr{D}_{\text{Jenga4}}$ in Fig. 1.18b is very similar to the one relative to $\mathscr{D}_{\text{Jenga}}$ in Fig. 1.18a, therefore we should expect $\mathscr{D}_{\text{Jenga4}}$ in Fig. 1.7 to perform similarly to $\mathscr{D}_{\text{Jenga}}$ in Fig. 1.6. This is actually the case, at least until the finest mesh for $k = 3$ where numerical problems appear which ϱ is not able to predict. Also $\mathscr{D}_{\text{Slices4}}$ and $\mathscr{D}_{\text{Slices}}$ are similar in Fig. 1.18, but ϱ decreases faster on the first than on the second one, reaching a ϱ value of ~ 0.2 instead of ~ 0.34 within a smaller number of meshes. Again, this information is correct because the method performs similarly over $\mathscr{D}_{\text{Slices4}}$ and $\mathscr{D}_{\text{Slices}}$ until condition numbers explode, in the last two meshes for every value of k. Last, the ϱ plot of $\mathscr{D}_{\text{Ulike4}}$ is significantly worse than any other (including the one of $\mathscr{D}_{\text{Ulike}}$), both in terms of distance from $y = 1$ and slope. In Fig. 1.7 we can observe how, even if $\mathscr{D}_{\text{Ulike4}}$ does not properly explode (as it suffers less from numerical problems, cf. Table 1.2), the approximation error and the convergence rate are the worst among all the considered datasets.

Summing up these results, we conclude that the indicator ϱ is able, up to a certain accuracy, to predict the behaviour of the VEM over the considered datasets, both in terms of error magnitude and convergence rate. Looking at the ϱ values it is possible to estimate in advance if a mesh or a dataset is going to be more or less critical for the VEM, and it is possible to compare the values relatives to different meshes and datasets to understand which one is going to perform better. The prediction may be less accurate in presence of very similar performance (e.g. the case of $\mathscr{D}_{\text{Maze}}$ and $\mathscr{D}_{\text{Star}}$) or in extremely pathological situations, where numerical problems become so significant to overcome any influence that the geometrical features of the mesh may have on the performance (e.g. the last meshes of $\mathscr{D}_{\text{Jenga4}}$ and $\mathscr{D}_{\text{Slices4}}$).

1.7 `PEMesh` Benchmarking Tool

Main existing tools for the numerical solution of PDEs include *VEMLab* [61], which is an open source MATLAB library for the virtual element method and *Veamy*, which is a free and open source C++ library that implements the virtual element method (C++ version of [61]). This library allows the user to solve 2D linear elasto-static problems and the 2D Poisson problem [60]. Additional tools include the 50-lines MATLAB implementation of the lowest order virtual element method for the two-dimensional Poisson problem on general polygonal meshes [70] and the MATLAB implementation of the lowest order Virtual Element Method (VEM) [56].

In this context, `PEMesh` [35] (Fig. 1.19) is an open-source software tool for experiments on the analysis and design of polytopal meshes for PEM solvers.
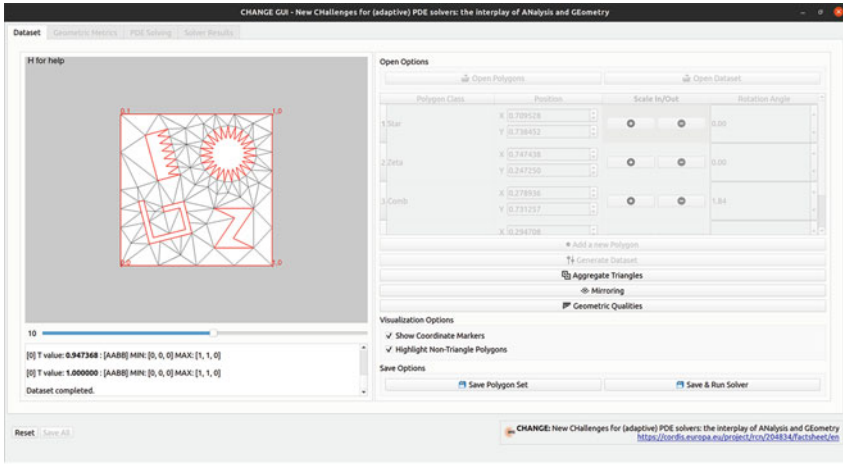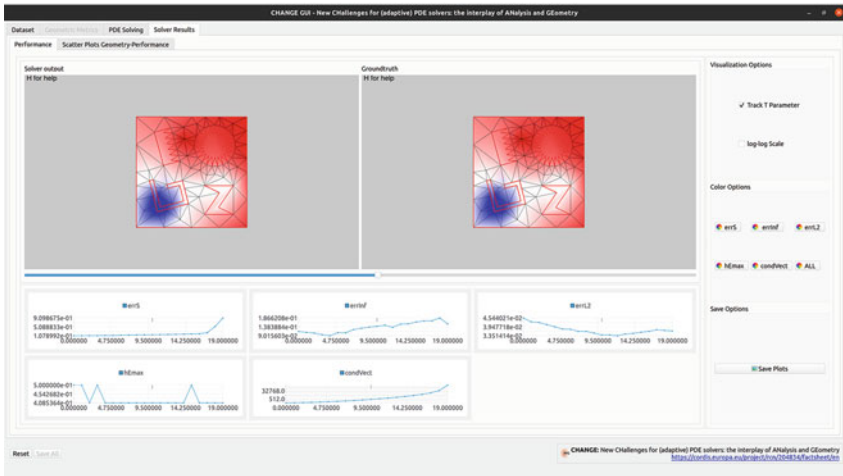
Fig. 1.19 (**a**) Main window of `PEMesh` and (**b**) examples of PEM solver results. On the top, both solver output and ground truth are color-mapped on the input polygon meshes, while on the bottom a set of linear plots show how solver performances vary in the data set

`PEMesh` is an advanced graphical tool that seamless integrates the geometric design of 2D domains and PEM simulations. It supports the design and generation of complex input polygonal meshes by stressing geometric properties and provides the possibility to solve PEMs on the generated meshes. Furthermore, `PEMesh` allows us to correlate several geometric properties of the input polytopal mesh with the performances of PEM solvers, and to visualise the results though customisable and interactive plots. `PEMesh` also supports to evaluate the dependence of the performances of a PEM solver on geometrical properties of the input polygonal mesh. `PEMesh` includes four main modules, which are briefly described in the following.

Polygon mesh generation & *loading* allow us to load one or more existing meshes or to generate new ones from scratch by either exploiting a set of polytopal elements available in the module or providing an external polytopal element. In this way, the user can easily generate a large set of options and parameters.

We used this module for the generation of most of the datasets considered in this work: $\mathscr{D}_{\text{Triangle}}$, $\mathscr{D}_{\text{Star}}$, $\mathscr{D}_{\text{Maze}}$ and all datasets from Sect. 1.5.3. The mirroring and multiple mirroring datasets defined in Sect. 1.4.1 have been generated separately and then loaded into the software to be used in the subsequent modules.

Geometric analysis allows the user to perform a deep analysis of geometric properties of the input polygonal meshes, to correlate each of them with the others, and to visualise the results of this analysis though scatter plots (see Fig. 1.20).

PEM solver allows the user to run a PEM solver and to analyse its performances on input polygonal meshes. Any PEM solver, which is run from command line, can be integrated in the software together with its output. The PEM and ground-through (if any) solutions of the PEM are shown directly on the meshes, while the performances of the solver are visualized through linear plots.

This module has been used for solving the problem and analyzing the performance of the VEM over all datasets in this work.

Correlation visualization allows the user to analyse the correlation between geometric properties of the polygonal meshes and numerical performances of the PEM solver. Then, the results are visualised as customizable scatter plots, as shown in Fig. 1.21.
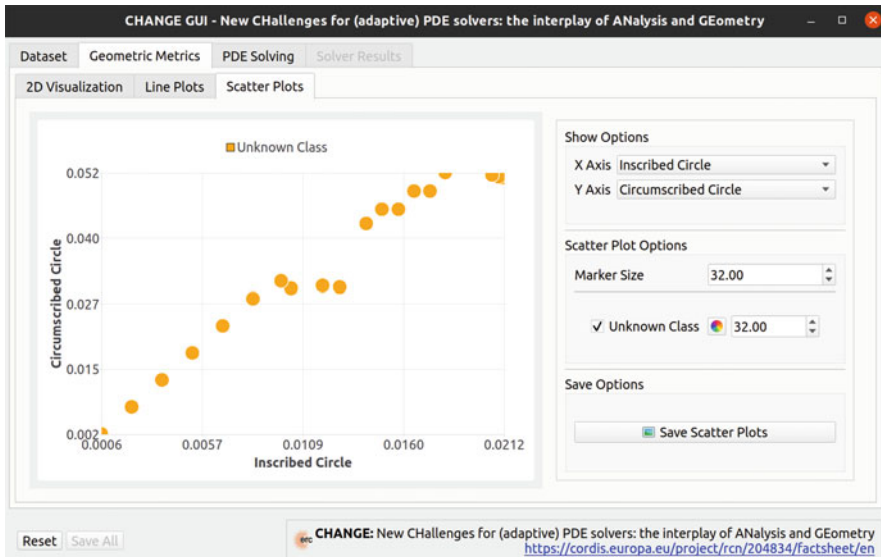
Fig. 1.20 PEMesh window specialized on the visualization of the correlation between geometric metrics. The right side of the window provides some visualization options to enable the possibility to select which metrics to be visualized and how (i.e. size, color, ...)
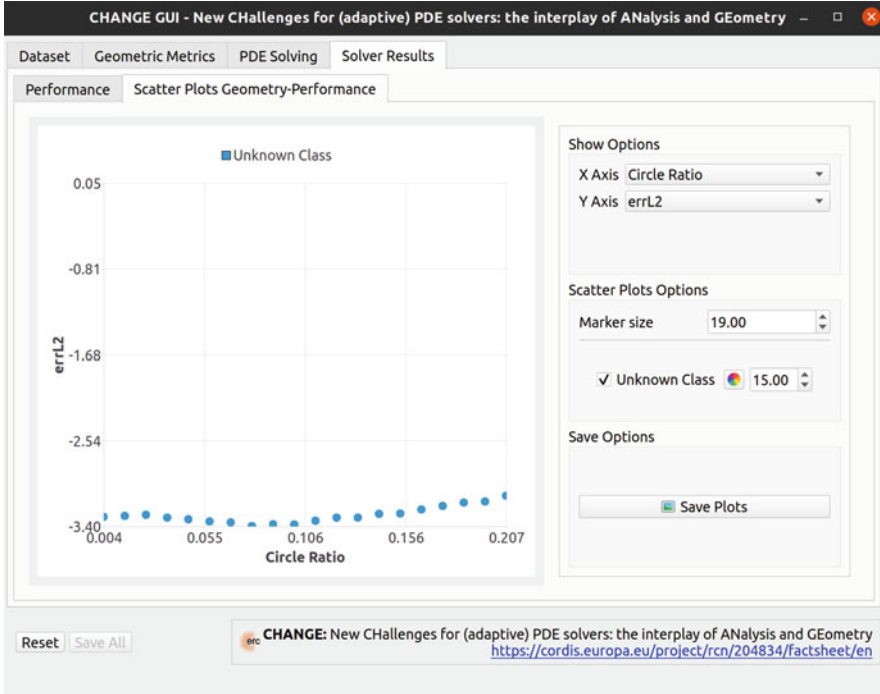
Fig. 1.21 PEMesh window specialized on the visualization of the correlation of geometric metrics and PEM performances. The right side of the window provides some visualization options to enable the possibility to select which metrics to be visualized and how (i.e. size, color, ...)

PEMesh provides the possibility to solve PEMs on a polygonal mesh and to visualize the performances of any PEM solver. To this end, the PEM solver is not part of the tool, but is handled as an external resource that is called by PEMesh graphical interface. Through a general approach, PEMesh assumes that the selected PEM solver takes an input mesh and returns both the solution and the ground-truth (if any) of a PDE, together with statistics (e.g., approximation accuracy, condition number of the mass and stiffness matrices) of the PEM solver. Then, the results of the PEM solver are visualised in a specialized window, and the numerical and geometric metrics are shown as linear plots (Fig. 1.19b). Finally, a set of visualization options are available for the customisation of color-maps and linear plots. Through a modular and customisable system, PEMesh allows us to run any PEM solver, thus providing an easy way to generate complex discrete polytopal meshes and to study the correlation between geometric properties of the input mesh and numerical PEMs solvers.

References

1. B. Ahmad, A. Alsaedi, F. Brezzi, L.D. Marini, A. Russo, Equivalent projectors for virtual element methods. Comput. Math. Appl. **66**, 376–391 (2013)
2. P.F. Antonietti, L. Beirão da Veiga, S. Scacchi, M. Verani, A C^1 virtual element method for the Cahn-Hilliard equation with polygonal meshes. SIAM J. Numer. Anal. **54**(1), 34–56 (2016)
3. P.F. Antonietti, L. Mascotto, M. Verani, A multigrid algorithm for the p-version of the virtual element method. ESAIM: Math. Model. Numer. Anal. **52**(1), 337–364 (2018)
4. P.F. Antonietti, G. Manzini, M. Verani, The conforming virtual element method for polyharmonic problems. Comput. Math. Appl. **79**(7), 2021–2034 (2020)
5. P.F. Antonietti, G. Manzini, I. Mazzieri, H.M. Mourad, M. Verani, The arbitrary-order virtual element method for linear elastodynamics models. convergence, stability and dispersion-dissipation analysis. Int. J. Numer. Methods Eng. **122**(4), 934–971 (2021)
6. P.F. Antonietti, G. Manzini, S. Scacchi, M. Verani, A review on arbitrarily regular conforming virtual element methods for second- and higher-order elliptic partial differential equations. Math. Models Methods Appl. Sci. **31**(14), 2825–2853 (2021)
7. L. Beirão da Veiga, G. Manzini, A virtual element method with arbitrary regularity. IMA J. Numer. Anal. **34**(2), 782–799 (2014)
8. L. Beirão da Veiga, G. Manzini, Residual a posteriori error estimation for the virtual element method for elliptic problems. ESAIM: Math. Modell. Numer. Anal. **49**, 577–599 (2015)
9. L. Beirão da Veiga, G. Vacca, Sharper error estimates for virtual elements and a bubble-enriched version. Preprint (2020). arXiv:2005.12009
10. L. Beirão da Veiga, K. Lipnikov, G. Manzini, Arbitrary order nodal mimetic discretizations of elliptic problems on polygonal meshes. SIAM J. Numer. Anal. **49**(5), 1737–1760 (2011)
11. L. Beirão da Veiga, F. Brezzi, A. Cangiani, G. Manzini, L.D. Marini, A. Russo, Basic principles of virtual element methods. Math. Models Methods Appl. Sci. **23**, 119–214 (2013)
12. L. Beirão da Veiga, F. Brezzi, L.D. Marini, A. Russo, The Hitchhiker's guide to the virtual element method. Math. Models Methods Appl. Sci. **24**(8), 1541–1573 (2014)
13. L. Beirão da Veiga, K. Lipnikov, G. Manzini, *The Mimetic Finite Difference Method*, vol. 11 of *MS&A. Modeling, Simulations and Applications*, I edn. (Springer, 2014)
14. L. Beirão da Veiga, G. Manzini, M. Putti, Post-processing of solution and flux for the nodal mimetic finite difference method. Numer. Methods Partial Differ. Equ. **31**(1), 336–363 (2015)
15. L. Beirão da Veiga, F. Brezzi, L.D. Marini, A. Russo, H(div) and H(curl)-conforming VEM. Numerische Mathematik **133**(2), 303–332 (2016)
16. L. Beirão da Veiga, F. Brezzi, L.D. Marini, A. Russo, Virtual element methods for general second order elliptic problems on polygonal meshes. Math. Models Methods Appl. Sci. **26**(4), 729–750 (2016)
17. L. Beirão da Veiga, A. Chernov, L. Mascotto, A. Russo, Basic principles of hp virtual elements on quasiuniform meshes. Math. Models Methods Appl. Sci. **26**(8), 1567–1598 (2016)
18. L. Beirão da Veiga, C. Lovadina, A. Russo, Stability analysis for the virtual element method. Math. Models Methods Appl. Sci. **27**(13), 2557–2594 (2017)
19. L. Beirão da Veiga, A. Chernov, L. Mascotto, A. Russo, Exponential convergence of the hp virtual element method in presence of corner singularities. Numerische Mathematik **138**(3), 581–613 (2018)
20. L. Beirão da Veiga, F. Dassi, G. Manzini, L. Mascotto, Virtual elements for Maxwell's equations. Comput. Math. Appl. (2021)
21. M.F. Benedetto, S. Berrone, S. Pieraccini, S. Scialò, The virtual element method for discrete fracture network simulations. Comput. Methods Appl. Mech. Eng. **280**(0), 135–156 (2014)
22. E. Benvenuti, A. Chiozzi, G. Manzini, N. Sukumar, Extended virtual element method for the Laplace problem with singularities and discontinuities. Comput. Methods Appl. Mech. Eng. **356**, 571–597 (2019)
23. E. Benvenuti, A. Chiozzi, G. Manzini, N. Sukumar, Extended virtual element method for two-dimensional linear elastic fracture. Comput. Methods Appl. Mech. Eng. **390**, 114352 (2022)

24. S. Berrone, S. Pieraccini, S. Scialò, F. Vicini, A parallel solver for large scale DFN flow simulations. SIAM J. Sci. Comput. **37**(3), C285–C306 (2015)
25. S. Berrone, A. Borio, G. Manzini, SUPG stabilization for the nonconforming virtual element method for advection–diffusion–reaction equations. Comput. Methods Appl. Mech. Eng. **340**, 500–529 (2018)
26. S. Bertoluzza, M. Pennacchio, D. Prada, BDDC and FETI-DP for the virtual element method. Calcolo **54**(4), 1565–1593 (2017)
27. S. Bertoluzza, M. Pennacchio, D. Prada, FETI-DP for the three dimensional virtual element method. SIAM J. Numer. Anal. 58 (2020)
28. S. Bertoluzza, G. Manzini, M. Pennacchio, D. Prada, Stabilization of the nonconforming virtual element method. Comput. Math. Appl. (2021)
29. J. Brandts, S. Korotov, M. Krizek, On the equivalence of regularity criteria for triangular and tetrahedral finite element partitions. Comput. Math. Appl. 55 (2008)
30. S.C. Brenner, Q. Guan, L.-Y. Sung, Some estimates for virtual element methods. Comput. Methods Appl. Math. **17**(4), 553–574 (2017)
31. S.C. Brenner, L.-Y. Sung, Virtual element methods on meshes with small edges or faces. Math. Models Methods Appl. Sci. **28**(07), 1291–1336 (2018)
32. F. Brezzi, A. Buffa, K. Lipnikov, Mimetic finite differences for elliptic problems. M2AN Math. Model. Numer. Anal. **43**, 277–295 (2009)
33. F. Brezzi, A. Buffa, G. Manzini, Mimetic inner products for discrete differential forms. J. Comput. Phys. **257**(Part B), 1228–1259 (2014)
34. R. Bridson, Fast Poisson disk sampling in arbitrary dimensions. SIGGRAPH Sketches **10**, 1 (2007)
35. D. Cabiddu, G. Patanè, M. Spagnuolo, PEMesh: Graphical framework for the analysis of the interplay between geometry and PEM solvers (2021). https://arxiv.org/abs/2102.11578
36. J.G. Calvo, An overlapping Schwarz method for virtual element discretizations in two dimensions. Comput. Math. Appl. **77**(4), 1163–1177 (2019)
37. A. Cangiani, G. Manzini, A. Russo, N. Sukumar, Hourglass stabilization of the virtual element method. Int. J. Numer. Methods Eng. **102**(3–4), 404–436 (2015)
38. A. Cangiani, E.H. Georgoulis, T. Pryer, O.J. Sutton, A posteriori error estimates for the virtual element method. Numerische Mathematik 1–37 (2017)
39. A. Cangiani, V. Gyya, G. Manzini, O. Sutton, Chapter 14: Virtual element methods for elliptic problems on polygonal meshes, in *Generalized Barycentric Coordinates in Computer Graphics and Computational Mechanics*, ed. by K. Hormann, N. Sukumar (CRC Press, Taylor & Francis Group, 2017), pp. 1–20
40. O. Certik, F. Gardini, G. Manzini, G. Vacca, The virtual element method for eigenvalue problems with potential terms on polytopic meshes. Appl. Math. **63**(3), 333–365 (2018)
41. O. Certik, F. Gardini, G. Manzini, L. Mascotto, G. Vacca, The p- and hp-versions of the virtual element method for elliptic eigenvalue problems. Comput. Math. Appl. **79**(7), 2035–2056 (2020)
42. L. Chen, J. Huang, Some error analysis on virtual element methods. Calcolo 55 (2018)
43. C. Chinosi, L.D. Marini, Virtual element method for fourth order problems: L2-estimates. Comput. Math. Appl. **72**(8), 1959–1967 (2016). Finite Elements in Flow Problems 2015
44. P.G. Ciarlet, *The Finite Element Method for Elliptic Problems* (SIAM, 2002)
45. F. Dassi, L. Mascotto, Exploring high-order three dimensional virtual elements: bases and stabilizations. Comput. Math. Appl. **75**(9), 3379–3401 (2018)
46. D.A. Di Pietro, J. Droniou, G. Manzini, Discontinuous skeletal gradient discretisation methods on polytopal meshes. J. Comput. Phys. **355**, 397–425 (2018)
47. F. Gardini, G. Manzini, G. Vacca, The nonconforming virtual element method for eigenvalue problems. ESAIM Math. Modell. Numer. Anal. **53**, 749–774 (2019). Accepted for publication: 29 November 2018. https://doi.org/10.1051/m2an/2018074
48. G.H. Golub, C.F. Van Loan, *Matrix Computations (3rd ed.)* (Johns Hopkins, 1996)
49. W.W. Hager, Condition estimates. SIAM J. Sci. Stat. Comput. 5 (1984)

50. N.J. Higham, F. Tisseur, A block algorithm for matrix 1-norm estimation with an application to 1-norm pseudospectra. SIAM J. Matrix Anal. Appl. 21 (2000)
51. K. Lipnikov, G. Manzini, F. Brezzi, A. Buffa, The mimetic finite difference method for 3D magnetostatics fields problems. J. Comput. Phys. **230**(2), 305–328 (2011)
52. K. Lipnikov, G. Manzini, M. Shashkov, Mimetic finite difference method. J. Comput. Phys. **257**(Part B), 1163–1227 (2014). Review paper
53. M. Livesu, cinolib: a generic programming header only C++ library for processing polygonal and polyhedral meshes, in *Transactions on Computational Science XXXIV* (Springer, 2019), pp. 64–76
54. G. Manzini, A. Russo, N. Sukumar, New perspectives on polygonal and polyhedral finite element methods. Math. Models Methods Appl. Sci. **24**(8), 1621–1663 (2014)
55. G. Manzini, K. Lipnikov, J.D. Moulton, M. Shashkov, Convergence analysis of the mimetic finite difference method for elliptic problems with staggered discretizations of diffusion coefficients. SIAM J. Numer. Anal. **55**(6), 2956–2981 (2017)
56. L. Mascotto, Ill-conditioning in the virtual element method: stabilizations and bases. Numer. Methods Partial Differ. Equ. **34**(4), 1258–1281 (2018)
57. D. Mora, G. Rivera, R. Rodríguez, A virtual element method for the Steklov eigenvalue problem. Math. Models Methods Appl. Sci. **25**(08), 1421–1445 (2015)
58. J.L. Myers, A.D. Well, *Research Design and Statistical Analysis (2nd ed.)* (Lawrence Erlbaum., 2003)
59. S. Naranjo-Alvarez, V. Bokil, V. Gyrya, G. Manzini, The virtual element method for resistive magnetohydrodynamics. Comput. Methods Appl. Mech. Eng. **381**, 113815 (2021)
60. A. Ortiz-Bernardin, C. Alvarez, N. Hitschfeld-Kahler, A. Russo, R. Silva-Valenzuela, E. Olate-Sanzana, Veamy: an extensible object-oriented C++ library for the virtual element method. Numerical Algorithms **82**(4), 1189–1220 (2019)
61. A. Ortiz-Bernardin, C. Alvarez, N. Hitschfeld-Kahler, A. Russo, R. Silva-Valenzuela, E. Olate-Sanzana, VEMLab: A MATLAB library for the virtual element method (2020). https://github.com/cemcen/vemlab
62. G.H. Paulino, A.L. Gain, Bridging art and engineering using Escher-based virtual elements. Struct. Multidiscip. Optim. **51**(4), 867–883 (2015)
63. I. Perugia, P. Pietra, A. Russo, A plane wave virtual element method for the Helmholtz problem. ESAIM: Math. Modell. Numer. Anal. **50**(3), 783–808 (2016)
64. L. Ridgway Scott, S.C. Brenner, *The Mathematical Theory of Finite Element Methods*. Texts in Aapplied Mathematics, vol. 15, 3rd edn. (Springer, New York, 2008)
65. J.R. Shewchuk, Triangle: Engineering a 2d quality mesh generator and delaunay triangulator, in *Selected Papers from the Workshop on Applied Computational Geormetry, Towards Geometric Engineering*, FCRC '96/WACG '96 (Springer, Berlin, Heidelberg, 1996), pp. 203–222
66. J.R. Shewchuk, What is a good linear finite element? - interpolation, conditioning, anisotropy, and quality measures. Technical report, in *Proc. of the 11th International Meshing Roundtable* (2002)
67. L. Simonson, G. Suto, Geometry template library for stl-like 2d operations. Colorado: GTL Boostcon (2009)
68. T. Sorgente, S. Biasotti, G. Manzini, M. Spagnuolo, The role of mesh quality and mesh quality indicators in the virtual element method. Adv. Comput. Math. **48**(3) (2022)
69. C. Spearman, The proof and measurement of association between two things. J. Psychol. 15 (1904)
70. O.J. Sutton, The Virtual Element Method in 50 lines of MATLAB. Numer. Algorithms **75**(4), 1141–1159 (2017)
71. E. Welzl, Smallest enclosing disks (balls and ellipsoids), in *New Results and New Trends in Computer Science* (Springer, 1991), pp. 359–370
72. P. Wriggers, W.T. Rust, B.D. Reddy, A virtual element method for contact. Computational Mechanics **58**(6), 1039–1050 (2016)
73. M. Zlámal, On the finite element method. Numerische Mathematik **12**(5), 394–409 (1968)

Chapter 2
On the Implementation of Virtual Element Method for Nonlinear Problems over Polygonal Meshes

Dibyendu Adak, M. Arrutselvi, E. Natarajan, and S. Natarajan

Abstract We present the details of the implementation of the Virtual Element Method (VEM) for nonlinear elliptic and parabolic problems, over polygonal meshes. The VEM implementation of a nonlinear problem does not follow the traditional way of implementation of the nonlinear problems as done in finite element/finite volume or finite difference methods. To facilitate this, suitable projection operators are used for the nonlinear terms that are rewritten in terms of the degrees of freedom associated with the virtual element space and thus are computable. We explicitly present the discretization and include sample codes that will help readers with the basic implementation of the nonlinear problems.

2.1 Introduction

Although, the traditional Galerkin methods such as the finite elements are very appealing, they have two major drawbacks: (a) they require an explicit form of the basis functions and (b) the domain discretization is restricted to simplex elements, thus increasing the meshing burden. Further, the unknown field variables over the simplex elements are approximated with polynomials, hence, a very fine mesh is required to capture steep gradients in the solution. In the last decade, there has been a growing interest in numerical methods that can accommodate elements with more general shapes and sizes. This has led to the development of a variety of numerical

D. Adak
GIMNAP, Departamento de Matemática, Universidad del Bío-Bío, Concepción, Chile
e-mail: dadak@ubiobio.cl

M. Arrutselvi · E. Natarajan (✉)
Department of Mathematics, Indian Institute of Space Science and Technology, Thiruvananthapuram, Kerala, India

S. Natarajan
Department of Mechanical Engineering, Indian Institute of Technology Madras, Chennai, Tamil Nadu, India
e-mail: snatarajan@iitm.ac.in

techniques, such as, the Mimetic Finite Difference Methods [8, 9, 13], Weak Galerkin Methods [40, 50], Polygonal Finite Element Method (PFEM) [21, 44, 46], Scaled boundary finite element methods [41, 42] and the Virtual Element Method (VEM) [12, 23, 47, 48]. These methods are very similar to each other because they require suitable discrete formulation of the model problem avoiding traditional approach. Both the polygonal finite element and the virtual element method can work with polygonal meshes, but a VEM when compared to the PFEM is that the latter requires an explicit form of the basis functions to compute the bilinear and the linear forms. The basis functions over polytopes are rational polynomials, and thus require high order numerical quadrature rules. To the best of author's knowledge, conventional polygonal finite elements are restricted to quadratic elements [34, 43]. In the case of the VEM, no such explicit form of the basis functions is required and higher order elements even in higher dimensions can be constructed.

The virtual element method, originally introduced in [12], is a generalization of Galerkin's finite element method over polygonal meshes. The greatest development of Mimetic Finite Difference Method is the VEM satisfying the Galerkin orthogonality property on polygonal meshes. In contrast with the FEM, the virtual element space consists of non-polynomial basis functions that are implicitly defined on the VEM space. To avoid this issue, suitable projection operators are introduced, which are computable from the degrees of freedom (DoFs) associated with the virtual element space. These projection operators approximate the basis functions optimally and make the discrete scheme computable from the DoFs. The VEM is designed to approximate the model problem over polygonal elements irrespective of their shape and size. Further, the construction of the VEM space in three dimension is also feasible and the matrices corresponding to the discrete bilinear forms can be computed using matrix multiplication avoiding numerical integration. The virtual element method can be treated as numerical technique on polygonal meshes. The primary difference with other numerical methods on polygonal meshes, however, is that the computation of nonpolynomial part from the DoFs. In practice, the nonpolynomial part is approximated ensuring same scaling as polynomial consistency part.

Since its inception, the VEM has been used to approximate several model problems. Some of them include Stokes equations [5, 17, 26], elasticity problem [10, 14], plate bending problems [23, 30, 52], parabolic and hyperbolic equations [47, 48], stationary convection diffusion equation [19] and elliptic equation [11, 16], eigenvalue problem [28, 35, 38, 39], mixed virtual element [15, 24, 25, 36], contact problem [51], obstacle problem [32, 49]. The nonconforming counterpart of VEM has been proposed by Ayuso *et al.* in [22], later extended to general elliptic equation,plate bending problem and Stokes equation in [26, 27, 52]. An open source C++ library has been developed by Ortiz-Bernardin et al. [20]. Sutton [45] developed a 50-line MATLAB implementation for the lowest order VEM for the two-dimensional Poisson's problem. Dhanush and Natarajan implemented the VEM into the commercial finite element software Abaqus [33] based on the user defined subroutines for thermo-elasticity.

However, most of the highlighted works deal with linear model problems. To the best of the authors' knowledge, limited research has been focused on employing the VEM for nonlinear problems. By employing the standard linearization technique, Antonietti et al. [6] introduced the $\mathscr{C}^1$ VEM for the Cahn-Hilliard problem. Beirão da Veiga et al. designed a new projection operator to approximate the trilinear term in the Navier-Stokes equation [18]. Adak et al. [2, 3], extended the VEM to semilinear parabolic and hyperbolic equations. The nonlinear term was approximated by employing the L^2 projection operator. Motivated by the work of Sutton [45] and Ortiz-Bernardin et al. [20], the main objective of this chapter is to present the details of the implementation of the VEM for nonlinear elliptic and parabolic problems over polygonal meshes.

2.1.1 Structure of the Chapter

In this chapter, we introduce the quasilinear parabolic equation in Sect. 2.2. In Sect. 2.3, we discuss the virtual element approximation of the resulting nonlinear problem. Section 2.4 presents the details of the computation of the projection operators and the corresponding discrete bilinear form. The fully discrete scheme is presented in Sect. 2.5. The Newtwon-Raphson iterative scheme and fixed point scheme are briefly discussed in the same section to solve the nonlinear system of equations. Further, we also discuss the VEM for quasilinear elliptic equation as a special case. In Sect. 2.6, we present a simple MATLAB implementation of the VEM for nonlinear equations. The section also presents the fundamental matrices and the Jacobian matrix for a quadrilateral and a polygonal element for the lowest order VEM. In Sect. 2.7, a few test cases are presented to show the convergence properties and the accuracy of the virtual element formulation over polygonal meshes, followed by conclusions in the final section.

2.1.2 Basic Notation

Before we discuss the virtual element framework for the nonlinear problems, we first present the notation that are followed in this chapter. Let $\{\Sigma_h\}_h$ be a family of decompositions of Ω into polygonal elements. Let K be an element with diameter h_K and N_K^{dof} be the total number of vertices of a polygon K. Let us define the mesh diameter as $h := \max_{K \in \mathscr{T}_h}(h_K)$. For a Banach space H with norm $\|\cdot\|_H$, and a function $\omega : [0, T] \to H$, which is Lebesgue measurable, the following norms are defined:

$$\|\omega\|_{L^2(0,T;H)} := \left(\int_0^T \|\omega\|_H^2 \, ds \right)^{1/2} \quad \text{and} \quad \|\omega\|_{L^\infty(0,T;H)} := \operatorname*{ess\,sup}_{0 \le t \le T} \|\omega(\cdot, t)\|_H.$$
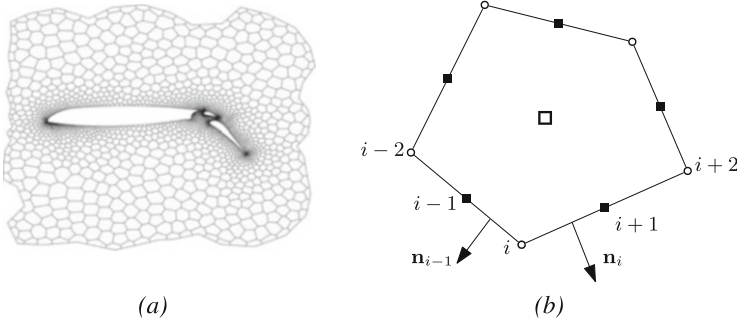
Fig. 2.1 (**a**) Domain discretized with polygons; (**b**) representative polygonal element, 'open' circles denote the vertex nodes, 'filled' squares are the edge nodes and 'open' square represents the centroid of the element. Vector $\mathbf{n}_i$ is the outward unit normal to the edge e_i connecting the vertex nodes V_i and V_{i+2}

We define,

$$L^2(0, T; H) = \{\omega : (0, T] \to H : \|\omega\|_{L^2(0,T;H)} < \infty\}.$$

Also, we assume that ∂K denotes the boundary of a polygonal element K, which is subdivided into $n(K)$ edges. Figure 2.1 shows a schematic of one of such decompositions of a domain Ω. Further, the following assumptions on the mesh regularity [7] are considered:

Assumption 2.1 (Mesh Regularity)

- *Every polygon is star-shaped with respect to a ball of radius greater than $\gamma\, h_K$, where γ denotes a real positive constant.*
- *For all $K \in \Sigma_h$, each side e of K is such that the length of e is greater than $c\, h_K$, where c denotes a positive constant.*
- *There exists a positive constant $\Lambda \in \mathbb{N}$ such that $n(K) \leq \Lambda$, for all elements $K \in \Sigma_h$.*

For a given polygon $K \subset \mathbb{R}^2$, and for a given integer $k \geq 2$, we denote the linear space of polynomials of degree k by $\mathbb{P}_k(K)$. This space is a subspace of local virtual element space that will be defined in the next section. The dimension of $\mathbb{P}_k(K)$ is:

$$N_k = \dim \mathbb{P}_k(K) = \frac{(k + 1)(k + 2)}{2}.$$

2.2 Governing Equations

Consider the following quasilinear parabolic equation

$$\begin{cases} D_t\, u - \nabla \cdot (\kappa(u)\nabla u) + \mathbf{b}(\mathbf{x}) \cdot \nabla u + c(\mathbf{x})\, u = f(u,t) & \text{in} \quad \Omega, \quad t \in (0,T) \\ u = 0 & \text{on} \quad \Gamma = \partial\Omega, \quad t \in (0,T) \\ u(0,\mathbf{x}) = u_0(\mathbf{x}) & \text{in} \quad \Omega \end{cases}$$

$$(2.2.1)$$

$\kappa(u)$ is a 2×2 diffusivity tensor with $\kappa(u)_{ij} = \kappa_{ij}(\mathbf{x}, t; u)$ and $\mathbf{b}(\mathbf{x})$ is a 1×2 convective coefficient with entries $b_i(\mathbf{x})$. As demanded by the analysis, we make the following reasonable assumptions:

- $\kappa_{ij}(\mathbf{x}, t; u)$, $b_i(\mathbf{x})$, $c(\mathbf{x})$ are $L^\infty(\Omega)$.
- $B_0^K = \sup\limits_{\mathbf{x}} \|\mathbf{b}(\mathbf{x})\|_{(L^2(K))^2} < \infty$.
- $C_0^K = \sup\limits_{\mathbf{x} \in K} c(\mathbf{x}) < \infty$
- $f(u, \mathbf{x}) \in L^2(\Omega)\ \forall \Omega \in \mathbb{R}$

Now by multiplying the first equation in (2.2.1) by the test function v and employing the Gauss divergence theorem, the weak formulation of the problem (2.2.1) reads as: Find $u \in H_0^1(\Omega)$ such that:

$$\begin{cases} (D_t u, v) + (\kappa(u)\nabla u, \nabla v) + \\ (\mathbf{b} \cdot \nabla u, v) + (c\, u, v) = (f(u), v) \quad \forall v \in H_0^1(\Omega) \text{ for a.e. } t \in [0, T] \quad (2.2.2) \\ u(0) = u_0, \end{cases}$$

where,

$$\begin{cases} (D_t u, v) = \displaystyle\int_\Omega D_t u\, v, \quad (\kappa(u)\nabla u, \nabla v) = \displaystyle\int_\Omega \kappa(u)\nabla u \cdot \nabla v \\[2mm] (\mathbf{b} \cdot \nabla u, v) = \displaystyle\int_\Omega \mathbf{b} \cdot \nabla u\, v, \quad (c\, u, v) = \displaystyle\int_\Omega c\, u\, v, \quad (f(u), v) = \displaystyle\int_\Omega f(u)\, v \end{cases}$$

Further, we would like to assume the following assumption on the coefficients for the existence and uniqueness of solution of (2.2.2) [31, Theorem 12.1] and [37].

Assumption 2.2

- $\kappa_{ij}(\mathbf{x}, t; u)$ *be Carathéodory function satisfying*

$$u \longmapsto \kappa_{ij}(\mathbf{x}, t; u) \text{ is continuous a.e. } (\mathbf{x}, t) \in \Omega \times \mathbb{R}^+.$$

Moreover, we assume that for some constants $\hat{K}, K_0$

$$0 < \hat{K} \leq |\kappa_{ij}(\mathbf{x}, t; u)| \leq K_0 \quad a.e.\ (\mathbf{x}, t) \in \Omega \times \mathbb{R}^+, \quad \forall u \in \mathbb{R}.$$

- $f : (\Omega \times \mathbb{R}) \to \mathbb{R}$ *is a Carathéodory function and satisfies for some constant* $F_0 > 0$,

$$|f(\mathbf{x}, u) - f(\mathbf{x}, \omega)| \leq F_0 |u - \omega| \quad \forall \mathbf{x} \in \Omega, \forall u, v \in \mathbb{R}.$$

- $\mu(\mathbf{x}) := c(\mathbf{x}) - \frac{1}{2}\nabla \cdot \mathbf{b}(\mathbf{x}) \geq \mu_0 > 0$ *for a.e.* $\mathbf{x} \in \Omega$ *and assume that* $\nabla \cdot \mathbf{b}(\mathbf{x}) \in L^\infty(\Omega)$.

Theorem 2.3 *Under the above Assumptions 2.2, there exists a solution*

$$\begin{cases} u \in L^2(0, T; H_0^1(\Omega)), D_t u \in L^2(0, T; H_0^1(\Omega)'), \\ u(0) = u_0, \\ (D_t u, v) + (\kappa(u)\nabla u, \nabla v) + (\mathbf{b} \cdot \nabla u, v) + (c\, u, v) = \\ (f(u), v) \quad \text{for a.e.t} \in (0, T], \forall v \in H_0^1(\Omega). \end{cases}$$

Proof Splitting the convective term $(\mathbf{b} \cdot \nabla u, v)$ into symmetric and non-symmetric part and then using Assumption 2.2 and Brouwer fixed point theorem, we can prove the existence and uniqueness of the weak solution of (2.2.2) □

2.3 Virtual Element Framework

In this section, we discuss the construction of the two and three dimensional virtual element spaces that were originally introduced in [11]. Unlike the finite element space, the virtual element space consists of polynomial functions and unknown functions that can be approximated using polynomial projection operators. These projection operators are computable from the information available from the degrees of freedom (DoFs) of the discrete space.

For each element K, we define:

- the standard L^2 projection operator $\Pi_{k,K}^0 : L^2(K) \to \mathbb{P}_k(K)$;
- the elliptic projection operator $\Pi_{k,K}^\nabla : H^1(K) \to \mathbb{P}_k(K)$ such that

$$\begin{aligned} &(\nabla \Pi_{k,K}^\nabla u, \nabla q) = (\nabla u, \nabla q) \quad \forall q \in \mathbb{P}_k(K) \setminus \mathbb{P}_0(K), \\ &P^0(\Pi_{k,K}^\nabla u) = P^0(u), \end{aligned} \tag{2.3.1}$$

where the operator P^0 is defined as

$$P^0(\phi) := \frac{1}{|\partial K|} \int_{\partial K} \phi \quad \text{if } k \geq 1,$$

and $\mathbb{P}_0(K)$ is set of constant polynomial on K. Further, we can discretize the operator ∇ using the vector valued L^2 projection operator $\mathbf{\Pi}^0_{k-1,K} : (L^2(K))^2 \rightarrow (\mathbb{P}_{k-1}(K))^2$.

The global projection operators Π^0_k, and Π^∇_k, and $\mathbf{\Pi}^0_{k-1,K}$ are defined as $\Pi^0_k|_K = \Pi^0_{k,K}$ and $\Pi^\nabla_k|_K = \Pi^\nabla_{k,K}$, and $\mathbf{\Pi}^0_{k-1}|_K = \mathbf{\Pi}^0_{k-1,K}$. Upon utilizing the projection operators, for the polygonal element $K \in \Sigma_h$, we introduce the local virtual element space in two dimensions. Let

$$\mathscr{H}^k(K) := \{v \in H^1(K), v|_{\partial K} \in \mathscr{C}^o(\partial K) : v|_e \in \mathbb{P}_k(e) \; \forall \, e \in \partial K, \; \Delta v \in \mathbb{P}_k(K)$$

$$\text{and} \int_K (\Pi^\nabla_{k,K} v - v)q = 0 \forall \, q \in \mathbb{P}_k \setminus \mathbb{P}_{k-2}(K)\},$$

$$(2.3.2)$$

where $\mathbb{P}_k \setminus \mathbb{P}_{k-2}(K)$ denotes the set of scaled monomials of degrees k and $k - 1$, i.e.

$$\mathbb{P}_k \setminus \mathbb{P}_{k-2}(K) := \left\{ \left(\frac{\mathbf{x} - \mathbf{x}_K}{h_K} \right)^{\boldsymbol{\alpha}}, |\boldsymbol{\alpha}| = k \right\} \cup \left\{ \left(\frac{\mathbf{x} - \mathbf{x}_K}{h_K} \right)^{\boldsymbol{\alpha}}, |\boldsymbol{\alpha}| = k - 1 \right\},$$

where, α signifies multi-index and defined as $\boldsymbol{\alpha} := (\alpha_1, \alpha_2, \cdots, \alpha_d)$, and the element $\mathbf{x}^\alpha := x_1^{\alpha_1} x_2^{\alpha_2}, \cdots, x_d^{\alpha_d}$. $\mathbf{x}_K$ denotes the centroid of K. The global space is defined as follows

$$\mathscr{H}^k_h := \{v \in H^1_0(\Omega)| \; v|_K \in \mathscr{H}^k(K), \forall K \in \Sigma_h\}. \quad (2.3.3)$$

For a typical function $\omega \in H^1_0(K)$, we introduce the set of functionals:

- (d_1) The values of ω at each vertex of the element K.
- (d_2) On each edge $s \subset \partial K$, the moments of ω of order $k - 2$ i.e.,

$$\frac{1}{|s|} \int_s \omega m_\alpha \quad \forall \, m_\alpha \in \mathbb{P}_{k-2}(s).$$

- (d_3) The cell moment up to order $k - 2$,

$$\int_K \omega \, m_\alpha, \qquad \forall m_\alpha \in \mathbb{P}_{k-2}(K)$$

The set of functional $(d_1) - (d_3)$ forms the degrees of freedom (DoFs) for the local space $\mathscr{H}^k(K)$. Using the projection operators $\Pi_{k,K}^0$ and $\mathbf{\Pi}_{k-1}^0$, we discretize the bilinear form locally on each polygon K as:

$$\mathscr{M}_h^K(u_h, v_h) := \int_K \Pi_{k,K}^0 u_h \, \Pi_{k,K}^0 v_h + S_K^c((I - \Pi_k^0)u_h, (I - \Pi_k^0)v_h)$$

$$(2.3.4)$$

$$\mathscr{A}_h^K(u_h; u_h, v_h) := \int_K \kappa(\Pi_{k,K}^0 u_h) \, \mathbf{\Pi}_{k-1,K}^0(\nabla u_h) \cdot \mathbf{\Pi}_{k-1,K}^0(\nabla v_h)$$

$$+ S_K(u_h; (I - \Pi_{k,K}^0)u_h, (I - \Pi_{k,K}^0)v_h) \qquad (2.3.5)$$

$$\mathscr{B}_h^K(u_h, v_h) := \int_K \mathbf{b} \cdot \mathbf{\Pi}_{k-1,K}^0(\nabla u_h) \, \Pi_{k,K}^0 v_h \qquad (2.3.6)$$

$$\mathscr{C}_h^K(u_h, v_h) := \int_K c(\mathbf{x}) \Pi_{k,K}^0 u_h \Pi_{k,K}^0 v_h$$

$$+ \sup_{\mathbf{x} \in K} c(\mathbf{x}) S_K^c((I - \Pi_k^0)u_h, (I - \Pi_k^0)v_h) \qquad (2.3.7)$$

$$F_{u_h}^K(v_h) := \int_K f(\Pi_{k,K}^0 u_h) \, \Pi_{k,K}^0 v_h \qquad (2.3.8)$$

The stabilizers $S_K(z_h; u_h, v_h)$ and $S_K^c(u_h, v_h)$ in (2.3.5) and (2.3.7) are defined as:

$$S_K(z_h; u_h, v_h) := \kappa(\Pi_{k,K}^0 z_h) \sum_{j=1}^{N_K^{\text{dof}}} \text{dof}_j(u_h)\text{dof}_j(v_h), \qquad (2.3.9)$$

$$S_K^c(u_h, v_h) := h_K^2 \sum_{j=1}^{N_K^{\text{dof}}} \text{dof}_j(u_h)\text{dof}_j(v_h). \qquad (2.3.10)$$

The polynomial parts of $\mathscr{A}_h(\cdot; \cdot, \cdot)$ and $\mathscr{M}_h$ scale as 1 and h_K^2 respectively. The nonpolynomial parts of the discrete bilinear forms $S_K(z_h; u_h, v_h)$ and $S_K^c(u_h, v_h)$ scale as the polynomial parts. For the non-symmetric convection part, we consider only the polynomial part of the discrete function. Although, only polynomial part is considered, it has been shown that this choice does not affect the efficiency and/or

the accuracy of the numerical scheme [27]. The global discrete forms are defined as sum of local contributions as:

$$\mathscr{M}_h(u_h, v_h) = \sum_{K \in \Sigma_h} \mathscr{M}_h^K(u_h, v_h) \quad \mathscr{A}_h(u_h; u_h, v_h) = \sum_{K \in \Sigma_h} \mathscr{A}_h^K(u_h; u_h, v_h)$$

(2.3.11)

$$\mathscr{B}_h(u_h, v_h) = \sum_{K \in \Sigma_h} \mathscr{B}_h^K(u_h, v_h) \quad \mathscr{C}_h(u_h, v_h) = \sum_{K \in \Sigma_h} \mathscr{C}_h^K(u_h, v_h) \qquad (2.3.12)$$

$$F_{u_h}(v_h) = \sum_{K \in \Sigma_h} F_{u_h}^K(v_h). \qquad (2.3.13)$$

2.4 Computation of the Projection Operators and Discrete Bilinear Forms

Once the bilinear forms are defined, the next step is to compute the bilinear forms given in Eqs. (2.3.4)–(2.3.8). To be able to compute them, let the set $\widetilde{\beta} = \{\phi_1, \cdots, \phi_{N_K^{\mathrm{dof}}}\}$ form a basis of the finite dimensional space $\mathscr{H}^k(K)$. Using the matrix representation of the projection operators, we will compute the discrete bilinear forms. From the degrees of freedom associated with $\mathscr{H}^k(K)$, we can compute the projection operators $\Pi_{k,K}^0, \Pi_{k,K}^\nabla$, and $\mathbf{\Pi}_{k-1,K}^0$. In continuation, we would like to highlight that the projection operator $\Pi_{k,K}^0$ is not computable on the virtual element space of order k defined in [3, 4, 48]. To avoid this issue, Ahmad et al. [4] has modified the virtual element space by imposing the condition

$$\int_K (\Pi_{k,K}^\nabla \phi_i - \Pi_{k,K}^0 \phi_i)\, q = 0 \quad \forall q \in \mathbb{P}_k \setminus \mathbb{P}_{k-2}(K) \text{ and } \phi_i \in \widetilde{\beta}. \qquad (2.4.1)$$

For any basis function ϕ_i, $\Pi_{k,K}^\nabla \phi_i \in \mathscr{H}^k(K)$. Therefore, $\Pi_k^\nabla \phi_i$ can be written as linear combination of the basis functions such as

$$\Pi_k^\nabla \phi_i = \sum_{j=1}^{N_K^{\mathrm{dof}}} \phi_j (\mathbf{\Pi}^\nabla)_{ji}, \qquad (2.4.2)$$

where $\mathbf{\Pi}^\nabla$ is the matrix representation of the projection operator $\Pi_{k,K}^\nabla$ in terms of basis function $\widetilde{\beta}$. Following [12, Equation 3.18], we can express this matrix as:

$$\mathbf{\Pi}^\nabla = \mathbf{D}\mathbf{G}^{-1}\mathbf{B}, \qquad (2.4.3)$$

where

$$
\mathbf{D} = \begin{bmatrix}
\mathrm{dof}_1(m_1) & \mathrm{dof}_1(m_2) & \dots & \mathrm{dof}_1(m_{N_K}) \\
\mathrm{dof}_2(m_1) & \mathrm{dof}_2(m_2) & \dots & \mathrm{dof}_2(m_{N_K}) \\
\vdots & \vdots & \ddots & \vdots \\
\mathrm{dof}_{N_K^{\mathrm{dof}}}(m_1) & \mathrm{dof}_{N_K^{\mathrm{dof}}}(m_2) & \dots & \mathrm{dof}_{N_K^{\mathrm{dof}}}(m_{N_K})
\end{bmatrix}_{N_K^{\mathrm{dof}} \times N_k}
$$

$$
\mathbf{G} = \begin{bmatrix}
P_0 m_1 & P_0 m_2 & \dots & P_0 m_{N_k} \\
0 & (\nabla m_2, \nabla m_2)_{0,K} & \dots & (\nabla m_2, \nabla m_{N_k})_{0,K} \\
\vdots & \vdots & \ddots & \vdots \\
0 & (\nabla m_{N_k}, \nabla m_2)_{0,K} & \dots & (\nabla m_{N_k}, \nabla m_{N_k})_{0,K}
\end{bmatrix}_{N_k \times N_k}
$$

$$
\mathbf{B} = \begin{bmatrix}
P_0 \phi_1 & P_0 \phi_2 & \dots & P_0 \phi_{N_K^{\mathrm{dof}}} \\
(\nabla m_2, \nabla \phi_1) & (\nabla m_2, \nabla \phi_2) & \dots & (\nabla m_2, \nabla \phi_{N_K^{\mathrm{dof}}}) \\
\vdots & \vdots & \ddots & \vdots \\
(\nabla m_{N_k}, \nabla \phi_1) & (\nabla m_{N_k}, \nabla \phi_2) & \dots & (\nabla m_{N_k}, \nabla \phi_{N_K^{\mathrm{dof}}})
\end{bmatrix}.
$$

where $N_K^{\mathrm{dof}} = \dim(\mathbb{H}^k(K))$, $N_k = \dim(\mathbb{P}_k(K))$ and $\mathrm{dof}_1(\cdot)$ is the ith degree of freedom of v_h. By using the DoFs associated with the virtual element space, we can easily compute matrix $\mathbf{D}$. The computation of $\mathbf{G}$ requires the integration of the polynomials m_α on the polygonal element K. Further, the computation of matrix $\mathbf{B}$ follows from the integration by parts:

$$
(\nabla m_\alpha, \nabla \phi_i)_K = -\int_K \phi_i \, \Delta m_\alpha + \int_{\partial K} \nabla m_\alpha \cdot \boldsymbol{v} \, \phi_i, \tag{2.4.4}
$$

where $\boldsymbol{v}$ is outward unit normal vector to the element boundary ∂K. The right hand side of (2.4.4) can be computed by using DoFs $(d_1) - (d_3)$. Since $\mathrm{dof}_j(\phi_i) = \delta_{ij}$, it holds that $\int_K \phi_i \, \Delta m_\alpha = 1$ if ϕ_i is the basis function corresponding to this cell moment and 0 for the other cases. The term $\int_{\partial K} \nabla m_\alpha \cdot \boldsymbol{v} \, \phi_i$ can be computed from the DoFs (d_1)-(d_2). Further, $\Pi_{k,K}^\nabla \phi_i \in \mathbb{P}_k(K)$ for all basis function ϕ_i. Therefore, we can write $\Pi_{k,K}^\nabla \phi_i$ in terms of monomials m_α, i.e.,

$$
\Pi_{k,K}^\nabla \phi_i = \sum_{\alpha=1}^{N_k} (\mathbf{\Pi}_*^\nabla)_{\alpha i} m_\alpha,
$$

where $\mathbf{\Pi}_*^\nabla$ denotes the matrix representation of $\Pi_{k,K}^\nabla$ when the projection is expanded on the monomial basis functions. It can be computed as

$$\mathbf{\Pi}_*^\nabla = \mathbf{G}^{-1}\mathbf{B}.$$

Using the DoFs $(d_1) - (d_3)$ and the condition (2.4.1), the orthogonal L^2 projection operator $\Pi_{k,K}^0$ can be evaluated. By using the monomial basis of $\mathbb{P}_k(K)$, we can explicitly write

$$\Pi_{k,K}^0 \phi_i = \sum_{\alpha=1}^{N_k} (\mathbf{\Pi}_*^0)_{\alpha i} m_\alpha,$$

where $\mathbf{\Pi}_*^0$ is the matrix representation of $\Pi_{k,K}^0$ in terms of the monomial basis functions, which can be computed as

$$\mathbf{\Pi}_*^0 = \mathbf{H}^{-1}\mathbf{C}, \qquad (2.4.5)$$

where, $\mathbf{H}$ is defined as

$$(\mathbf{H})_{\alpha,\beta} := (m_\alpha, m_\beta)_K. \qquad (2.4.6)$$

In (2.4.1), we define $\mathbf{C}$ as

$$\mathbf{C}_{\alpha,i} := (m_\alpha, \phi_i)_K. \qquad (2.4.7)$$

which is the right hand side of the orthogonal projection problem. At the implementation level of condition (2.4.1) for $N_{k-2} + 1 \leq \alpha \leq N_k$,

$$\mathbf{C}_{\alpha,i} := (m_\alpha, \Pi_{k,K}^\nabla \phi_i) = (\mathbf{H}\mathbf{G}^{-1}\mathbf{B})_{\alpha,i}.$$

Further, $\Pi_{k,K}^0 \phi_i$ can be expressed in terms of the basis function of $\mathscr{H}^k(K)$ as

$$\Pi_{k,K}^0 \phi_i = \sum_{j=1}^{N_K^{\text{dof}}} (\mathbf{\Pi}^0)_{\alpha j} \phi_j.$$

The coefficient matrix $\mathbf{\Pi}^0$ can be computed by using matrices $\mathbf{D}$, $\mathbf{H}$ and $\mathbf{C}$ as

$$\mathbf{\Pi}^0 = \mathbf{D}\mathbf{H}^{-1}\mathbf{C}.$$

Next, we present the computable forms of the bilinear forms given in Eqs. (2.3.4)–(2.3.8). Of these, the quasi-linear diffusion term requires special

attention. This is due to the presence of the nonlinear term. The quasilinear diffusion term is written as:

$$\mathscr{A}_h(u_h; u_h, v_h) = \int_K \kappa(\Pi_{k,K}^0 u_h) \mathbf{\Pi}_{K-1,k}^0 \nabla u_h \cdot \mathbf{\Pi}_{K-1,k}^0 \nabla v_h$$

$$+ \kappa(\Pi_{k,K}^0 u_h) \sum_{i=1}^{N^{\text{dof}}} \text{dof}_i((I - \Pi_k^0)u_h)\text{dof}_i((I - \Pi_k^0)v_h).$$

$$(2.4.8)$$

By using $u_h = \sum_{j=1}^{N_K^{\text{dof}}} \text{dof}_j(u_h)\phi_j$, and choosing $v_h = \phi_i$ in (2.4.8), we write Eq. (2.4.8) in discrete form as:

$$\mathscr{A}_h(\sum_{j=1}^{N_K^{\text{dof}}} \text{dof}_j(u_h)\phi_j; \sum_{j=1}^{N_K^{\text{dof}}} \text{dof}_j(u_h)\phi_j, \phi_i) =$$

$$\int_K \kappa(\sum_{j=1}^{N_K^{\text{dof}}} \text{dof}_j(u_h)\Pi_{k,K}^0\phi_j) \sum_{j=1}^{N_K^{\text{dof}}} \text{dof}_j(u_h)\mathbf{\Pi}_{k-1,K}^0 \nabla\phi_j \cdot \mathbf{\Pi}_{k-1,K}^0 \nabla\phi_i$$

$$+ \kappa(\sum_{j=1}^{N_K^{\text{dof}}} \text{dof}_j(u_h)\Pi_{k,K}^0\phi_j) \sum_{j=1}^{N_K^{\text{dof}}} \text{dof}_j(u_h)S_K((I - \Pi_{k,K}^0)\phi_j, (I - \Pi_{k,K}^0)\phi_i).$$

$$(2.4.9)$$

Following [27], we would like to discuss the computation of the vector valued L^2 projection operator $\mathbf{\Pi}_{k-1,K}^0$. Using orthogonality property of $\mathbf{\Pi}_{k-1,K}^0$, we can write

$$(\mathbf{\Pi}_{k-1,K}^0 \nabla\phi_i, \mathbf{m}_\alpha)_K = (\nabla\phi_i, \mathbf{m}_\alpha)_K = \int_{\partial K} \mathbf{m}_\alpha \cdot \mathbf{\nu}\phi_i \, ds -$$

$$\int_K \phi_i \nabla \cdot \mathbf{m}_\alpha \, dK. \quad \forall \mathbf{m}_\alpha \in \mathbb{P}_{k-1}(K) \times \mathbb{P}_{k-1}(K).$$

$$(2.4.10)$$

$\mathbf{\nu}$ is outward unit normal vector. We define the vector containing polynomial entries as

$$\mathbf{\Pi}_{k-1}^0 \nabla\phi_i = [\Pi_{k-1}^0 \frac{\partial\phi_i}{\partial x} \quad \Pi_{k-1}^0 \frac{\partial\phi_i}{\partial y}], \qquad (2.4.11)$$

and expand in term of monomials as:

$$\Pi^0_{k-1,K} \frac{\partial \phi_i}{\partial x} = \sum_{\alpha=1}^{N_{k-1}} m_\alpha (\Pi^{0,x}_{k-1,K})_{\alpha i}. \qquad (2.4.12)$$

$\Pi^{0,x}_{k-1,K}$ is the coefficient matrix defined by:

$$\mathbf{H}_{k-1,K} \Pi^{0,x}_{k-1,K} = \mathbf{R}^x_K, \qquad (2.4.13)$$

where, the matrix $\mathbf{H}_{k-1,K}$ is defined in (2.4.6) for monomials $m_\alpha \in \mathbb{P}_{k-1}(K)$. The right hand side matrix is defined as

$$(\mathbf{R}^x_K)_{\alpha i} = \underbrace{\sum_{e \subset \partial K} \int_e m_\alpha \mathbf{v}_x \phi_i ds}_{\sigma_1} - \underbrace{(\phi_i, \frac{\partial m_\alpha}{\partial x})_K}_{\sigma_2} \quad m_\alpha \in \mathbb{P}_{k-1}(K). \qquad (2.4.14)$$

The term σ_1 can be computed from edge and vertex degrees of freedom (d_1)-(d_2) and the term σ_2 can be computed form the cell momentum (d_3). The term corresponding to the bilinear form (2.4.8) can be written as

$$\left(\kappa(\Pi^0_{k,K} u_h) \Pi^0_{k-1,K} \nabla\phi_i, \Pi^0_{k-1,K} \nabla\phi_j \right) = \left(\kappa(\Pi^0_{k,K} u_h) \Pi^0_{k-1,K} \frac{\partial \phi_i}{\partial x}, \right.$$
$$\left. \Pi^0_{k-1,K} \frac{\partial \phi_j}{\partial x} \right) + \left(\kappa(\Pi^0_{k,K} u_h) \Pi^0_{k-1,K} \frac{\partial \phi_i}{\partial y}, \Pi^0_{k-1,K} \frac{\partial \phi_j}{\partial y} \right). \qquad (2.4.15)$$

In the above equation, the term $\left(\kappa(\Pi^0_{k,K} u_h) \Pi^0_{k-1,K} \frac{\partial \phi_i}{\partial x}, \Pi^0_{k-1,K} \frac{\partial \phi_j}{\partial x} \right)$ can be written in terms of the monomials as

$$\left(\kappa(\Pi^0_{k,K} u_h) \Pi^0_{k-1,K} \frac{\partial \phi_i}{\partial x}, \Pi^0_{k-1,K} \frac{\partial \phi_j}{\partial x} \right)$$

$$= \sum_{\alpha,\beta=1}^{N_{k-1}} \left(\kappa(\Pi^0_{k,K} u_h) m_\alpha, m_\beta \right)_K (\Pi^{0,x}_{k-1})_{\alpha i} (\Pi^{0,x}_{k-1})_{\beta j}$$

$$= \sum_{\alpha,\beta=1}^{N_{k-1}} \left(\kappa(\sum_{j=1}^{N^{\mathrm{dof}}_K} \mathrm{dof}_j(u_h) \Pi^0_{k,K} \phi_j) m_\alpha, m_\beta \right)_K (\Pi^{0,x}_{k-1})_{\alpha i} (\Pi^{0,x}_{k-1})_{\beta j}$$

$$= \sum_{\alpha,\beta=1}^{N_{k-1}} \left(\kappa(\sum_{j=1}^{N^{\mathrm{dof}}_K} \mathrm{dof}_j(u_h) \sum_{z=1}^{N_k} (\Pi^0_*)_{zj} m_z) m_\alpha, m_\beta \right)_K (\Pi^{0,x}_{k-1})_{\alpha i} (\Pi^{0,x}_{k-1})_{\beta j}.$$
$$(2.4.16)$$

By choosing $v_h = \phi_i$ in $\mathscr{B}_h^K(\cdot, \cdot)$ (defined in (2.3.6)), the convective term can be written as

$$\mathscr{B}_h^K(u_h, \phi_i) = \int_K \sum_{j=1}^{N^{\text{dof}}} \text{dof}_j(u_h)(\mathbf{b} \cdot \mathbf{\Pi}_{k-1,K}^0 \nabla \phi_j) \Pi_{k,K}^0 \phi_i. \tag{2.4.17}$$

Further, we can write the scalar product explicitly as

$$\mathbf{b} \cdot \mathbf{\Pi}_{k-1,K}^0(\nabla \phi_j) = b_1 \Pi_{k-1,K}^0 \frac{\partial \phi_j}{\partial x} + b_2 \Pi_{k-1,K}^0 \frac{\partial \phi_j}{\partial y}. \tag{2.4.18}$$

Using (2.4.18), we can write the convective term as

$$\int_K \mathbf{b} \cdot \mathbf{\Pi}_{k-1,K}^0 \nabla \phi_j \Pi_{k,K}^0 \phi_i = \sum_{\alpha=1}^{N_k} \sum_{\beta=1}^{N_{k-1}} (b_1 m_\alpha, m_\beta)_K (\mathbf{\Pi}_{k,K}^0)_{\alpha i} (\mathbf{\Pi}_{k-1,K}^{0,x})_{\beta j}$$
$$+ \sum_{\alpha=1}^{N_k} \sum_{\beta=1}^{N_{k-1}} (b_2 m_\alpha, m_\beta)_K (\mathbf{\Pi}_{k,K}^0)_{\alpha i} (\mathbf{\Pi}_{k-1,K}^{0,y})_{\beta j}. \tag{2.4.19}$$

By choosing $v_h = \phi_i$ in (2.3.7) and explicit expression of discrete function u_h, the reaction term can be written as:

$$\mathscr{C}_h^K(u_h, \phi_i) = \int_K \sum_{j=1}^{N_K^{\text{dof}}} \text{dof}_j(u_h) \Pi_{k,K}^0 \phi_j \Pi_{k,K}^0 \phi_i +$$
$$\sum_{j=1}^{N_K^{\text{dof}}} \text{dof}_j(u_h) S_K((I - \Pi_{k,K}^0)\phi_j, (I - \Pi_{k,K}^0)\phi_i). \tag{2.4.20}$$

With the polynomial consistency part of (2.3.7), given by:

$$\int_K \Pi_{k,K}^0 \phi_i \Pi_{k,K}^0 \phi_j = \sum_{\alpha,\beta=1}^{N_k} \int_K m_\alpha m_\beta \, dK \, (\mathbf{\Pi}_*^0)_{\alpha i}(\mathbf{\Pi}_*^0)_{\beta j}, \tag{2.4.21}$$

where $\mathbf{\Pi}_*^0$ is the coefficient matrix corresponding to the operator $\Pi_{k,K}^0$ defined in (2.4.5).

Remark 2.1 In (2.2.1), the convection and the reaction terms are linear which can be updated easily in Newton-Raphson method. In this work, we will primarily focus

on the implementation technique of the nonlinear terms such as nonlinear diffusion and load terms.

By choosing $v_h = \phi_i$ in (2.3.10), the nonlinear force term can be written as:

$$(f_h(u_h), \phi_i) = \sum_{K \in \Sigma_h} f\Big(\sum_{j=1}^{N_K^{\text{dof}}} \text{dof}_j(u_h) \Pi_k^0 \phi_j \Big) \Pi_k^0 \phi_i. \qquad (2.4.22)$$

Further, by using the L^2 projection operator on K, the nonlinear force function $f(u)$ is discretized as follows

$$(f_h(u_h), \phi_i) := (f(\Pi_k^0 u_h), \phi_i)$$

$$= \sum_{K \in \Sigma_h} \int_K \Pi_{k,K}^0 f\big(\sum_{j=1}^{N_K^{\text{dof}}} \text{dof}_j(u_h) \Pi_{k,K}^0 \phi_j \big) \phi_i$$

$$= \sum_{K \in \Sigma_h} \int_K f\big(\sum_{j=1}^{N_K^{\text{dof}}} \text{dof}_j(u_h) \Pi_{k,K}^0 \phi_j \big) \Pi_{k,K}^0 \phi_i$$

$$= \sum_{K \in \Sigma_h} \int_K f\big(\sum_{j=1}^{N_K^{\text{dof}}} \text{dof}_j(u_h) \Pi_{k,K}^0 \phi_j \big) \Pi_{k,K}^0 \phi_i.$$

$$= \sum_{K \in \Sigma_h} \int_K f\big(\sum_{j=1}^{N_K^{\text{dof}}} \text{dof}_j(u_h) \sum_{\alpha=1}^{N_K^{\text{dof}}} (\mathbf{\Pi}_*^0)_{\alpha j} m_\alpha \big) \sum_{\alpha=1}^{N_K^{\text{dof}}} (\mathbf{\Pi}_*^0)_{\alpha i} m_\alpha.$$
$$(2.4.23)$$

Remark 2.2 The nonlinear load term $(f_h(u_h), \phi_i)$ can be computed using the projection operator $\Pi_{k,K}^0$ which is described in (2.4.23). This procedure demands computation of the polynomial integration over polygon K which is numerically expensive. In case of time dependent problem, this numerical integration has to be computed at each iteration which is numerically expensive. Following [1], we could define the nonlinear load term as $(f_h(u_h), \phi_i) := (I_h(f(u_h)), \Pi_{k,K}^0 \phi_i)$ for linear VEM space. Using the properties of the interpolation operator I_h [1, Section 3.2], we rewrite the discrete load term as

$$(f_h(u_h), \phi_i) := \widetilde{\mathbf{M}} \widetilde{\mathbf{F}}, \qquad (2.4.24)$$

where $\widetilde{\mathbf{M}}$ is the matrix corresponding to the polynomial consistency part of $\mathcal{M}_h^K(\cdot, \cdot)$ and the $(\widetilde{\mathbf{F}})_i := f(\text{dof}_i(u_h))$. Equation (2.4.24) reduces the computational cost effectively since we need just multiplication of matrices.

The stabilizers S_K and S_K^c can be approximated using the matrix representation of the projection operator Π_k^0. Now, we would like to discuss the approximation. Recalling the definition of **D** matrix, we have the matrix relation

$$\mathbf{\Pi}^0 = \mathbf{D}\mathbf{\Pi}_*^0, \qquad (2.4.25)$$

where the coefficient matrices $\mathbf{\Pi}^0$ and $\mathbf{\Pi}_*^0$ are defined in beginning of this section. With the choice of the basis functions and (2.4.25), the stabilizing term can be approximated as follows:

$$S^K ((I - \Pi_k^0)\phi_i, (I - \Pi_k^0)\phi_j) \approx C(h_K) \left((\mathbf{I} - \mathbf{\Pi}^0)^T (\mathbf{I} - \mathbf{\Pi}^0) \right)_{ij}, \qquad (2.4.26)$$

since $\mathrm{dof}_r((I - \Pi_k^0)\phi_i) = (\mathbf{I} - \mathbf{\Pi}^0)_{ir}$, where $C(h_K)$ is the scaling factor ensuring same scaling as the polynomial part of the polynomial consistency part of the discrete bilinear forms.

2.5 Fully Discrete Scheme

We employ the virtual element method and the Crank-Nicolson scheme for discretizing the space variable and the time variable, respectively [29]. Let $(U^n)_{n\in\mathbb{N}}$ be a sequence of approximations of (u_h) at time $t = t_n$. The fully discrete scheme is obtained by a partition of non-overlapping sub interval $[t_{n-1}, t_n]$ of $[0, T]$, where $n = 1, 2, \cdots, N_T$ with time-step $\Delta t^n := t_n - t_{n-1}$ such that $T = \sum_{n=1}^{N_T} \Delta t^n$. To reduce the computational complexity, we split $[0, T]$ into equal time-step, i.e. $\Delta t^n = \Delta t$ for all n. The fully discrete scheme for the Eq. (2.2.1) reads: Find $U^n \in \mathscr{H}_h^k$ such that:

$$\mathscr{M}_h\Big(\frac{U^n - U^{n-1}}{\Delta t}, v_h\Big) + \mathscr{A}_h\Big(\frac{U^n + U^{n-1}}{2}; \frac{U^n + U^{n-1}}{2}, v_h\Big) + \mathscr{B}_h\Big(\frac{U^n + U^{n-1}}{2}, v_h\Big)$$

$$+ \mathscr{C}_h\Big(\frac{U^n + U^{n-1}}{2}, v_h\Big) = \Big\langle f_h\Big(\frac{U^n + U^{n-1}}{2}\Big), v_h \Big\rangle \quad \forall v_h \in \mathscr{H}_h^k.$$

$$(2.5.1)$$

Equation (2.5.1) is nonlinear due to the presence of the nonlinear diffusion coefficient. The first step is to linearize the system, which is done by adopting the Taylor series expansion of the unknown solution. The resulting linear system is then solved by using the Newton-Raphson method.

Let $\mathscr{U}^n$ be the initial guess and $U^n := \mathscr{U}^n + \delta u^n$, where δu^n is the increment in the solution vector. We rewrite (2.5.1) as

$$\mathscr{M}_h\left(\mathscr{U}^n + \delta u^n - U^{n-1}, v_h\right) + \Delta t\, \mathscr{A}_h\left(\frac{\mathscr{U}^n + \delta u^n + U^{n-1}}{2}; \frac{\mathscr{U}^n + \delta u^n + U^{n-1}}{2}, v_h\right)$$

$$+ \Delta t\, \mathscr{B}_h\left(\frac{\mathscr{U}^n + \delta u^n + U^{n-1}}{2}, v_h\right) + \Delta t\, \mathscr{C}_h\left(\frac{\mathscr{U}^n + \delta u^n + U^{n-1}}{2}, v_h\right) =$$

$$\Delta t\left\langle f_h\left(\frac{\mathscr{U}^n + \delta u^n + U^{n-1}}{2}\right), v_h\right\rangle.$$

Using Taylor's expansion and neglecting the terms $O(\delta u^{nd})$, $d \geq 2$, the following linear system of equations is obtained:

$$\mathbf{Jac}\,\delta u^n = \mathbf{R}, \tag{2.5.2}$$

where, $\mathbf{R}$ and $\mathbf{Jac}$ are the residual force vector and the Jacobian matrix, respectively, given by:

$$(\mathbf{R})_i := \Delta t\left\langle f_h\left(\frac{\mathscr{U}^n + U^{n-1}}{2}\right), \phi_i\right\rangle - \mathscr{M}_h\left(\mathscr{U}^n - U^{n-1}, \phi_i\right) -$$

$$\Delta t\, \mathscr{A}_h\left(\frac{\mathscr{U}^n + U^{n-1}}{2}; \frac{\mathscr{U}^n + U^{n-1}}{2}, \phi_i\right) \tag{2.5.3}$$

$$- \Delta t\, \mathscr{B}_h\left(\frac{\mathscr{U}^n + U^{n-1}}{2}, \phi_i\right) - \Delta t\, \mathscr{C}_h\left(\frac{\mathscr{U}^n + U^{n-1}}{2}, \phi_i\right).$$

and the Jacobian matrix is given

$$(\mathbf{Jac})_{ij} = \mathscr{M}_h\left(\phi_j, \phi_i\right) + \Delta t\, \mathscr{A}_h\left(\frac{\mathscr{U}^n + U^{n-1}}{2}; \frac{\phi_j}{2}, \phi_i\right) + \Delta t\, b_h\left(\frac{\mathscr{U}^n + U^{n-1}}{2}; \frac{\phi_j}{2}, \phi_i\right)$$

$$+ \Delta t\, \mathscr{B}_h\left(\frac{\phi_j}{2}, \phi_i\right) + \Delta t\, \mathscr{C}_h\left(\frac{\phi_j}{2}, \phi_i\right) -$$

$$\Delta t\left\langle D_u f\left(\Pi_k^0 \frac{\mathscr{U}^n + U^{n-1}}{2}\right)\frac{\Pi_k^0 \phi_j}{2}, \Pi_k^0 \phi_i\right\rangle.$$

$$\tag{2.5.4}$$

The discrete form $b_h(;,)$ is locally defined as

$$b_h(z_h; u_h, v_h)|_K = b_h^K(z_h; u_h, v_h) := \int_K \boldsymbol{\kappa}_u (\Pi_k^0 z_h) \Pi_k^0 u_h \boldsymbol{\Pi}_{k-1,K}^0 \nabla z_h \cdot \boldsymbol{\Pi}_{k-1,K}^0 \nabla v_h$$

$$+ \boldsymbol{\kappa}_u (\Pi_{0,K}^0 z_h) \Pi_{0,K}^0 u_h \sum_{j=1}^{N_K^{\text{dof}}} \text{dof}_j(z_h - \Pi_{k,K}^0 z_h) \text{dof}_j(v_h - \Pi_{k,K}^0 v_h).$$

$$(2.5.5)$$

and we write $\delta u^n = \sum_{j=1}^{N^{\text{dof}}} \text{dof}_j(\delta u^n) \phi_j$. Clearly, $\Pi_{0,K}^0$ denotes constant L^2 projection operator on polygon K and we introduce the column vector $(\boldsymbol{\delta u^n})_j = \text{dof}_j(\delta u^n)$. Equation (2.5.2) can be written in matrix form as

$$\left(\mathbf{M} + \Delta t \, \mathbf{J}_1 + \Delta t \, \mathbf{J}_2 + \frac{\Delta t}{2} \mathscr{B} + \frac{\Delta t}{2} \mathscr{C} - \frac{\Delta t}{2} \mathbf{F}_{\mathscr{U}^n + U^{n-1}} \right) \boldsymbol{\delta u^n}$$

$$= \Delta t \, \mathbf{F} - \mathbf{M}(\mathscr{U}^n - \mathbf{U}^{n-1}) - \Delta t \, \mathbf{A} - \Delta t \, (\mathscr{B} + \mathscr{C})(\mathscr{U}^n + \mathbf{U}^{n-1}),$$

$$(2.5.6)$$

where

$$(\mathbf{J}_1)_{ij} := \mathscr{A}_h \left(\frac{\mathscr{U}^n + U^{n-1}}{2}; \phi_j, \phi_i \right), \tag{2.5.7}$$

$$(\mathbf{J}_2)_{ij} := b_h \left(\frac{\mathscr{U}^n + U^{n-1}}{2}; \phi_j, \phi_i \right). \tag{2.5.8}$$

$$(\mathscr{B})_{ij} := \int_K (\mathbf{b} \cdot \boldsymbol{\Pi}_{k-1,K}^0 \nabla \phi_j) \Pi_{k,K}^0 \phi_i \tag{2.5.9}$$

$$(\mathscr{C})_{ij} := \int_K \Pi_{k,K}^0 \phi_j \Pi_{k,K}^0 \phi_i + S_K((I - \Pi_{k,K}^0)\phi_j, (I - \Pi_{k,K}^0)\phi_i) \tag{2.5.10}$$

$$(\mathbf{F}_{\mathscr{U}^n + U^{n-1}})_{ij} := \sum_{K \in \Sigma_h} \int_K f_u \left(\sum_{j=1}^{N_K^{\text{dof}}} \left(\frac{\text{dof}_j(\mathscr{U}^n) + \text{dof}_j(U^{n-1})}{2} \right) \Pi_{k,K}^0 \phi_j \right) \Pi_{k,K}^0 \phi_j \Pi_{k,K}^0 \phi_i$$

$$(2.5.11)$$

$$(\mathbf{A})_i := \mathscr{A}_h \left(\frac{\mathscr{U}^n + U^{n-1}}{2}; \frac{\mathscr{U}^n + U^{n-1}}{2}, \phi_i \right) \tag{2.5.12}$$

$$(\mathbf{F})_i := \left\langle f_h \left(\frac{\mathscr{U}^n + U^{n-1}}{2} \right), \phi_i \right\rangle \tag{2.5.13}$$

and $\mathbf{M}$ denotes the matrix representation corresponding to the discrete bilinear form $\mathscr{M}_h(\phi_i, \phi_j)$.

For stationary case, the discrete scheme (c.f. (2.5.1)) is rewritten after ignoring the transient term as: Find $u_h \in \mathscr{H}_h^k$ such that

$$\mathscr{A}_h(u_h; u_h, v_h) + \mathscr{B}_h(u_h, v_h) + \mathscr{C}_h(u_h, v_h) = F_{u_h}(v_h) \quad \forall v_h \in \mathscr{H}_h^k. \quad (2.5.14)$$

The nonlinear system of equation (2.5.14) can be solved using Newton-Raphson method. Let $\widetilde{u_h}$ be the initial guess and the solution of the discrete scheme is $u_h = \widetilde{u_h} + \delta u$. The increment in the solution vector, δu is computed by solving a linear system of equations in a iterative process: Find $\delta u \in \mathscr{H}_h^k$ such that

$$
\begin{aligned}
&\mathscr{A}_h(\widetilde{u_h}; \delta u, v_h) + b_h(\widetilde{u_h}; \delta u, v_h) + \mathscr{B}_h(\delta u, v_h) + \mathscr{C}_h(\delta u, v_h) \\
&\quad - \langle D_u f(\Pi_k^0 \widetilde{u_h}) \Pi_k^0 \delta u, \Pi_k^0 v_h \rangle = \langle f(\Pi_k^0 \widetilde{u_h}), \Pi_k^0 v_h \rangle - \mathscr{A}_h(\widetilde{u_h}; \widetilde{u_h}, v_h) \\
&\quad - \mathscr{B}_h(\widetilde{u_h}, v_h) - \mathscr{C}_h(\widetilde{u_h}, v_h) \quad \forall v_h \in \mathscr{H}_h^k.
\end{aligned}
$$
$$(2.5.15)$$

In matrix form, (2.5.15) can be written as:

$$\mathbf{Jac}\, \delta u = \mathbf{R}, \quad (2.5.16)$$

where, $\mathbf{Jac} = [\mathbf{J_1} + \mathbf{J_2} + \mathscr{B} + \mathscr{C} - \mathbf{F_u}]$ and $\mathbf{R}$ denotes the matrix representation of the discrete bilinear form $\langle f(\Pi_k^0 \widetilde{u_h}), \Pi_k^0 v_h \rangle - \mathscr{A}_h(\widetilde{u_h}; \widetilde{u_h}, v_h) - \mathscr{B}_h(\widetilde{u_h}, v_h) - \mathscr{C}_h(\widetilde{u_h}, v_h)$.

2.6 Implementation

In this section, we discuss the implementation of the VEM fundamental matrices and the computation of different terms in the model problem (see (2.5.1)). In particular, we focus on the lowest order implementation of the VEM for the nonlinear system considered in this paper. With appropriate changes, the presented code can be extended to higher order VEM and also to treat other types of non-linearities that may arise. For the computation of the VEM fundamental matrices, viz., **B**, **D** and **G**, we refer the reader to [12] for the theoretical explanation and to [45] for the Matlab® code. In this section, we present a code to compute the Jacobian matrix (c.f. (2.5.7)) and the right hand side force vector (c.f. (2.5.13)) in Listings (2.1)–(2.2), respectively.

Listing 2.1 Computation of the Jacobian matrix
```
function [J1,J2]=getJacobian(coord,a0,D,G,B,phistr,$\ldots$
pix,piy)
% purpose:
%    to compute the jacobian matrix for the quasilinear
```

```matlab
% diffusion  term ,
%    -\nabla ( k(u) \nabla u )
% inputs :
%   coord    - coordinates  of  the  current  element
%   D,G,B,   - fundamental  VEM  matrices
%   a0       - solution  vector
%   pix , piy - gradient  of  the  basis  function
% outputs :
%   J1 ,  J2 - Jacobian  matrices .
%———————————————————————————————————
% number  of  vertices  of  the  current  element
numVert = size (coord , 1);

% get  the  area  of  the  current  element
area_com = coord (: ,1).* coord ([2: end ,1] ,2) ...
- coord ([2: end ,1] ,1).* coord (: ,2);
Areap = 0.5 * abs(sum(area_com ));
% get  the  geometric  centroid  of  the  element
centroid = sum(( coord + coord ([2: end ,1] ,:)).*...
 repmat (area_com ,1 ,2))/(6* AreaP );
% Compute  the  diameter  by  looking  at
% every  pair  of  vertices
h_d = 0;
for  i = 1:(numVer -1)
     for  j = (i+1):numVer
          h_d = max(h_d , norm(coord (i ,:) - coord (j ,:)));
     end
end

% get  quadrature  points  over  the  triangle
xw=TriGaussPoints (8);

% initialize  the  matrices ...
NP=length (xw (: ,1));
Nw=zeros (numVert , numVert );
N=zeros (numVert , numVert ) ;

% the  stabilization  term
phidg=D*inv (G)*B;
I = eye(numVert , numVert ) ;
str2 =(I-phidg ) '*(I-phidg );

for  i =1:numVert
     if  i ~=numVert
          xv=[x(i)  x(i+1)  x_d ];
          yv=[y(i)  y(i+1)  y_d ];
     else
```

```
        xv=[x(n)  x(1)  x_d];
        yv=[y(n)  y(1)  y_d];
    end
    xn=xv(1)*(ones(NP,1)-xw(:,1)-xw(:,2))+...
                xv(2)*xw(:,1)+xv(3)*xw(:,2);
    yn=yv(1)*(ones(NP,1)-xw(:,1)-xw(:,2))+...
                yv(2)*xw(:,1)+yv(3)*xw(:,2);

    % get the scaled monomials
    M=[ones(NP,1)  (xn-x_d*ones(NP,1))/h_d,...
                    (yn-y_d*ones(NP,1))/h_d];
    ZZ=M*phistr*a0;

    % the nonlinear diffusion coefficient
    a11=(1./((1+ZZ).*(1+ZZ)));
    a12=1+ZZ;a21=a12;
    a22=1+(1./(1+ZZ.*ZZ));

    mx=M(:,1)*pix; my=M(:,1)*piy;
    Xw11=repmat((xw(:,3).*a11),1,numVert);
    Xw12=repmat((xw(:,3).*a12),1,numVert);
    Xw22=repmat((xw(:,3).*a22),1,numVert);
    N2=mx'*(Xw11.*mx)+my'*(Xw22.*my)+...
        mx'*(Xw12.*my)+my'*(Xw12.*mx);
    Nw = Nw + Areap*N2;

    % the gradient of the nonlienar
    % diffusion coefficient
    a11u=-2.*(1+ZZ).*a11.*a11;
    a12u=ones(NP,1); a21u=a12u;
    a22u=-2.*ZZ.*(1./(1+ZZ.*ZZ)).*(1./(1+ZZ.*ZZ));

    npx=mx*a0; npy=my*a0;
    Xwx11=repmat((xw(:,3).*a11u.*npx),1,numVert);
    Xwx22=repmat((xw(:,3).*a22u.*npy),1,numVert);
    Xwx12=repmat((xw(:,3).*a12u.*npx),1,numVert);
    Xwx21=repmat((xw(:,3).*a21u.*npy),1,numVert);

    Mp=M*phistr;
    N3=mx'*(Xwx11.*Mp)+my'*(Xwx22.*Mp)+...
                my'*(Xwx21.*Mp)+my'*(Xwx12.*Mp);
    N = N + Areap*N3;
end
ml=(sum(a0)/numVert);
ml1=1/(1+ml); ml2=ml1*ml1; ml3=1+1/(1+ml*ml);
dup0pro=(-2*(1+ml)/((1+ml)^4))+(-2)*ml/((1+ml*ml)^2);
A0=a0'*(I-phidg); xx=(1/numVert)*ones(size(a0'));
```

```
A1=xx*(I-phidg );

% the jacobian for the quasilinear diffusion term
J1 = Nw+(ml2+ml3)*str2 ;
J2 = N+dup0pro*(A1'*A0) ;
end
```

Listing 2.2 Computation of the right hand side force vector

```
function [F]=getRHS(coord, alphak)
% inputs:
%    coord   - coordinates of the current element
%    alphak  - vectex value (DoF)
% outputs:
%    F        - rhs vector
%────────────────────────────────────────────────────────
x = coord(:,1); y = coord(:,2);
numVert=size(coord,1);

% get the fundamental matrices...
[D,B,G,H] = getVEM_matrices(coord) ;

C=H*inv(G)*B;
phistar=inv(H)*C;

% get the diameter, area of the element and the centroid
[h_d,AreaP,x_d,y_d] = getDiam_area(coord) ;

xw=TriGaussPoints(8); % get the integration points

% initialize the force matrix
F=zeros(numVert,numVert);

for r=1:numVert
    for s=1:numVert
        ff1=0;
        for i=1:numVert
            if i~=numVert
                xv=[x(i) x(i+1) x_d];
                yv=[y(i) y(i+1) y_d];
            else
                xv=[x(numVert) x(1) x_d];
                yv=[y(numVert) y(1) y_d];
            end
            z1=0;
```

```
% loop over gauss points
for j=1: size (xw,1)
    xn=xv(1)*(1-xw(j,1)-xw(j,2))+...
        xv(2)*xw(j,1)+xv(3)*xw(j,2);
    yn=yv(1)*(1-xw(j,1)-xw(j,2))+...
        yv(2)*xw(j,1)+yv(3)*xw(j,2);
    xvl=(xn-x_d)/h_d; yvl=(yn-y_d)/h_d;
    prdd1=phistar(1,r)*1+phistar(2,r)*xvl;
    prdd2=phistar(3,r)*yvl;

    prd1=prdd1+prdd2;
    prde1=phistar(1,s)*1+phistar(2,s)*xvl;
    prde2=phistar(3,s)*yvl;

    % fvec -
    z1 = z1 + fvec*prd1*prd2*xw(j,3);
end
ff1 = ff1 + AreaP*z1;
end
F(r,s)=ff1;
end
end
```

Next, we will present two worked examples in which we compute the VEM fundamental matrices **B**, **D** and **G** for a 4-noded quadrilateral element and a pentagon. The coordinates of the elements are given in Fig. 2.2. Further, we have chosen scalar valued convection coefficients as $\mathbf{b} = [2\ 3]_{1 \times 2}$ and the reaction coefficient $c = 1$ and the Jacobian is computed at the first step, with an initial guess $U^0 = [0]_{N_K^{\text{dof}} \times 1}$.

Fig. 2.2 A quadrilateral and a pentagon, where Vi are the coordinates of the element
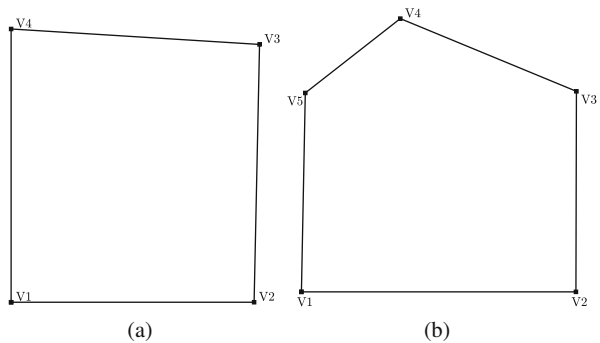
Square For a square consider the following coordinates: $V1(0, 0)$, $V2(0.1039, 0)$, $V3(0.1062, 0.1102)$, $V4(0, 0.1169)$. The VEM fundamental matrices for a square are given by:

$$\mathbf{B} = \begin{bmatrix} 0.2500 & 0.2500 & 0.2500 & 0.2500 \\ -0.3700 & 0.3490 & 0.3700 & -0.3490 \\ -0.3290 & -0.3363 & 0.3290 & 0.3363 \end{bmatrix} \qquad \mathbf{G} = \begin{bmatrix} 1.0000 & 0.0032 & -0.0015 \\ 0 & 0.4785 & 0 \\ 0 & 0 & 0.4785 \end{bmatrix}$$

$$\mathbf{D} = \begin{bmatrix} 1.0000 & -0.3295 & -0.3610 \\ 1.0000 & 0.3285 & -0.3610 \\ 1.0000 & 0.3432 & 0.3371 \\ 1.0000 & -0.3295 & 0.3790 \end{bmatrix}$$

The quasi-linear, reaction and convection term is given by:

$$\mathbf{J}_1 = \begin{bmatrix} 1.9710 & -0.5537 & -0.4979 & -0.9195 \\ -0.5537 & 1.0485 & -1.0070 & 0.5121 \\ -0.4979 & -1.0070 & 2.0247 & -0.5199 \\ -0.9195 & 0.5121 & -0.5199 & 0.9272 \end{bmatrix}$$

$$\mathscr{B} = \begin{bmatrix} -0.0686 & -0.0123 & 0.0686 & 0.0123 \\ -0.0673 & -0.0121 & 0.0673 & 0.0121 \\ -0.0678 & -0.0122 & 0.0678 & 0.0122 \\ -0.0691 & -0.0124 & 0.0691 & 0.0124 \end{bmatrix}$$

$$\mathscr{C} = \begin{bmatrix} 0.0041 & -0.0023 & 0.0032 & -0.0021 \\ -0.0023 & 0.0045 & -0.0024 & 0.0032 \\ 0.0032 & -0.0024 & 0.0043 & -0.0022 \\ -0.0021 & 0.0032 & -0.0022 & 0.0040 \end{bmatrix} \qquad \mathbf{J}_2 = \begin{bmatrix} 0 \end{bmatrix}_{4 \times 4}$$

Pentagon For the pentagon shown in Fig. 2.2b, the coordinates are: $V1(0.2163, 0)$, $V2(0.3373, 0)$, $V3(0.3375, 0.0884)$, $V4(0.2599, 0.1205)$ and $V5(0.2180, 0.0877)$. The VEM fundamental matrices are given by:

$$\mathbf{B} = \begin{bmatrix} 0.2000 & 0.2000 & 0.2000 & 0.2000 & 0.2000 \\ -0.2565 & 0.2586 & 0.3524 & -0.0021 & -0.3524 \\ -0.3490 & -0.3547 & 0.2265 & 0.3497 & 0.1275 \end{bmatrix}$$

$$\mathbf{G} = \begin{bmatrix} 1.0000 & -0.0158 & 0.0401 \\ 0 & 0.4291 & 0 \\ 0 & 0 & 0.4291 \end{bmatrix}$$

$$
\mathbf{D} = \begin{bmatrix}
1.0000 & -0.3523 & -0.3069 \\
1.0000 & 0.3558 & -0.3069 \\
1.0000 & 0.3571 & 0.2104 \\
1.0000 & -0.0972 & 0.3980 \\
1.0000 & -0.3423 & 0.2062
\end{bmatrix}
$$

The quasi-linear, reaction and convection term is given by:

$$
\mathbf{J}_1 = \begin{bmatrix}
1.9287 & -0.2951 & -0.3340 & -0.5991 & -0.7005 \\
-0.2951 & 1.1663 & -1.3093 & 0.0099 & 0.4282 \\
-0.3340 & -1.3093 & 2.2161 & -0.2445 & -0.3283 \\
-0.5991 & 0.0099 & -0.2445 & 2.0625 & -1.2288 \\
-0.7005 & 0.4282 & -0.3283 & -1.2288 & 1.8295
\end{bmatrix}
\qquad
\mathbf{J}_2 = \begin{bmatrix} 0 \end{bmatrix}_{5 \times 5}
$$

$$
\mathscr{B} = \begin{bmatrix}
-0.0595 & -0.0209 & 0.0528 & 0.0399 & -0.0123 \\
-0.0647 & -0.0227 & 0.0574 & 0.0433 & -0.0134 \\
-0.0511 & -0.0179 & 0.0454 & 0.0342 & -0.0106 \\
-0.0446 & -0.0156 & 0.0396 & 0.0299 & -0.0092 \\
-0.0467 & -0.0164 & 0.0414 & 0.0313 & -0.0096
\end{bmatrix}
$$

$$
\mathscr{C} = \begin{bmatrix}
0.0044 & -0.0022 & 0.0029 & 0.0009 & -0.0032 \\
-0.0022 & 0.0048 & -0.0035 & 0.0018 & 0.0022 \\
0.0029 & -0.0035 & 0.0064 & -0.0032 & -0.0002 \\
0.0009 & 0.0018 & -0.0032 & 0.0069 & -0.0043 \\
-0.0032 & 0.0022 & -0.0002 & -0.0043 & 0.0077
\end{bmatrix}
$$

Remark 2.3 We have computed the Jacobian with the initial guess as column vector containing zeros. Initially, $\mathbf{J}_2$ contains zeros but after few iterations, $\mathbf{J}_2$ matrix contains significant digits. Therefore, neglecting $\mathbf{J}_2$ could severely affect the convergence of the scheme and consequently, numerical solution. We would also like to highlight that $\mathbf{J}_2$ depends on initial guess of the solution U_0^n.

2.7   Numerical Examples

This section is dedicated to demonstrate the robustness of the VEM to handle polygonal meshes and to discuss the convergence properties in spatial and temporal variables. The optimal order of convergence of the numerical solution in the L^2 and H^1 norms are demonstrated. First, we examine quasilinear elliptic problem and later we extend the discussion for quasi linear parabolic problem.

For the numerical studies, four different types of meshes are employed, viz., distorted square, non-convex polygons, regular polygons and smoothed Voronoi, see Fig. 2.3 for a representative mesh for each category. Since u_h is defined implicitly,

(a)   (b)

(c)   (d)
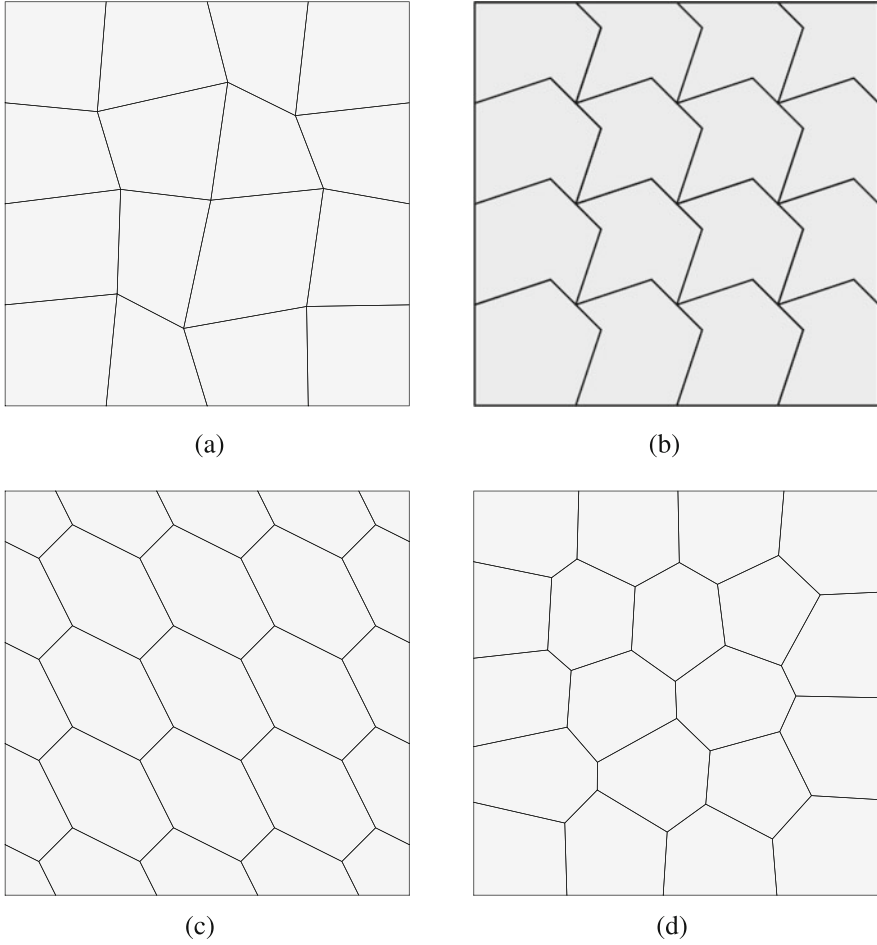
Fig. 2.3 Domain discretized with different discretizations. (**a**) Distorted square. (**b**) Non-convex polygons. (**c**) Regular polygons. (**d**) Smoothed voronoï

in order to evaluate error numerically, we borrow the idea form [19]. The errors $e_{h,0}$ and $e_{h,1}$ are defined as

- L^2-norm error : $e_{h,0} = \sqrt{\sum_{K \in \mathscr{T}_h} \|u - \Pi^0_{k,K} u_h\|^2_{L^2(K)}}$,
- H^1-norm error : $e_{h,1} = \sqrt{\sum_{K \in \mathscr{T}_h} \|\nabla(u - \Pi^\nabla_{k,K} u_h)\|^2_{L^2(K)}}$.

Furthermore, $r_{h,0}$ and $r_{h,1}$ denote rate of convergence in L^2-norm and H^1 semi-norm.

Table 2.1 Mesh parameters with degrees of freedom (Dof) and number of elements (N_E)

h	Distorted squares		Regular polygons		Smoothed voronoi		Non-convex	
	Dof	N_E	Dof	N_E	Dof	N_E	Dof	N_E
1/5	64	49	862	430	162	80	1201	400
1/10	225	196	3322	1660	601	300	4801	1600
1/20	841	784	13042	6520	2599	1300	19201	6400
1/40	3249	3136	51682	25840	9998	5000	76801	25600
1/80	11236	11025	205762	102800	47959	24000	307201	102400

The virtual element approximation of orders $k = 1,2$ and 3 are performed on four different types of meshes; Fig. 2.3 shows a schematic of different types of meshes employed in this study, viz., namely distorted squares, regular hexagons, random polygons and non-convex polygons. The Newton method with tolerance 10^{-12} was employed to solve the resulting nonlinear system. The size of the element is kept the same for all the meshes, this leads to different number of elements (N_E) and degrees of freedom (Dof) for the meshes considered in this study. Table 2.1, presents the mesh size (h) and the corresponding Dof for distorted square, hexagons, non-convex and Smoothed voronoi meshes.

Example 1

Consider the quasi-linear elliptic problem, (2.2.1), but without the convection term and the reaction term. In this problem, we choose the polynomial exact solution as $u(x, y) = x (x - 1)^2 y (y - 1)^2$ and a non-constant coefficient as:

$$\kappa(u) := \begin{bmatrix} \dfrac{1}{(1 + u)^2} & 1 + u \\ 1 + u & 1 + \dfrac{1}{(1 + u^2)} \end{bmatrix}.$$

The convergence of the error in the L^2 norm and H^1 seminorm is shown in Figs. 2.4, 2.5 for distorted squares, regular polygons and smoothed Voronoi and non-convex meshes, respectively. The results are presented for different orders, viz., $k = 1$, 2 and 3. It can be inferred that the results from the present framework based on the VEM yields accurate results and converges with optimal convergence rates as the mesh is refined. Further, we would like to highlight that one can use backward Euler scheme for the time discretization, which converges in first order. Therefore, very small values of Δt will be demanded to achieve optimal order of convergence in spatial direction.

Example 2

Next, we consider the model problem with the transient term. The exact solution was chosen as $u(x, y, t) = \exp(t) x (x - 1)^2 y (y - 1)^2$. The coefficient parameters and computational domain are same as previous example,i.e. unit square and the time interval is chosen as $t \in (0, 1]$ with $T = 1$. In this case, the domain is discretized with distorted square and non-convex elements. For spatial discretization, we

(a) roc L^2 errors

(b) roc H^1 errors

(c) roc L^2 errors

(d) roc H^1 errors
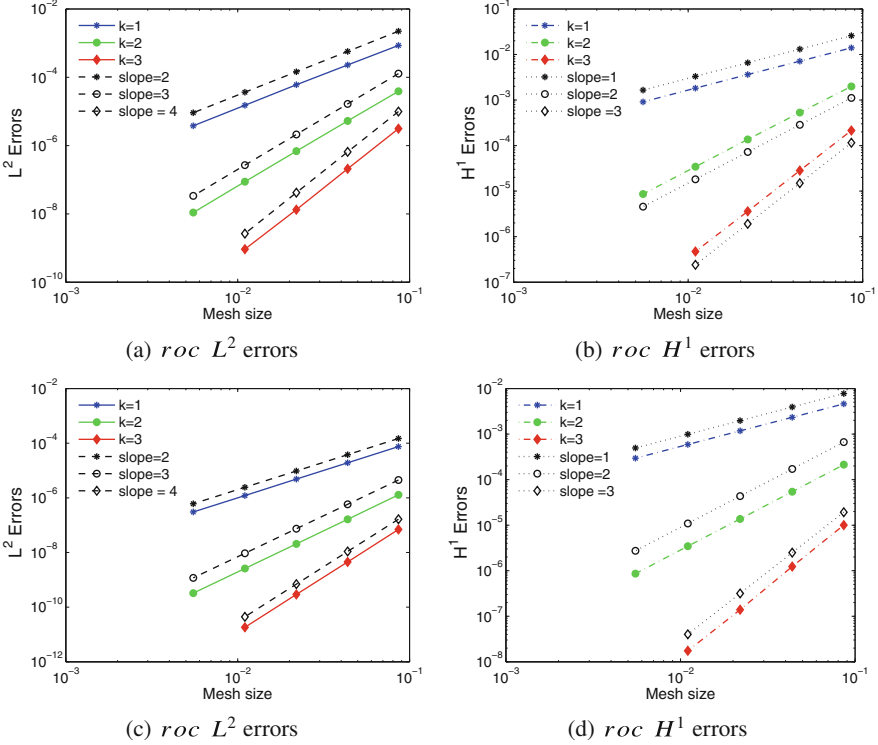
Fig. 2.4 Convergence of the error in the L^2 and H^1 for (**a,b**) Distorted squares and (**c,d**) Regular polygons for $k = 1$, 2 and 3

employ the VEM orders $k = 1$, 2 and 3 and for the temporal, we adopt the Crank-Nicholson scheme, which is unconditionally stable, with $\Delta t = \mathcal{O}(h^{k+1})$. The Crank-Nicolson scheme is second order convergence hence the solution converges faster than backward Euler scheme. The nonlinear equations were solved using the Newton's method with a tolerance 10^{-12}. The convergence of the error in L^2 and H^1 norm with mesh size for two different type of discretization is depicted in Tables 2.2, 2.3, 2.4 at final time $T = 1$. The rate of convergence (roc) is also shown in the table. It can be inferred that the present framework yields accurate results and converges with an optimal rate in both L^2 and H^1 norms for both the meshes.

Example 3

In this example, we consider the following semilinear problem:

$$\frac{\partial u}{\partial t} - \Delta u = (u - u^2) + g(\mathbf{x}, t) \qquad \text{on} \quad \Omega \times T \qquad (2.7.1)$$

(a) $roc\ L^2$ errors

(b) $roc\ H^1$ errors

(c) $roc\ L^2$ errors

(d) $roc\ H^1$ errors
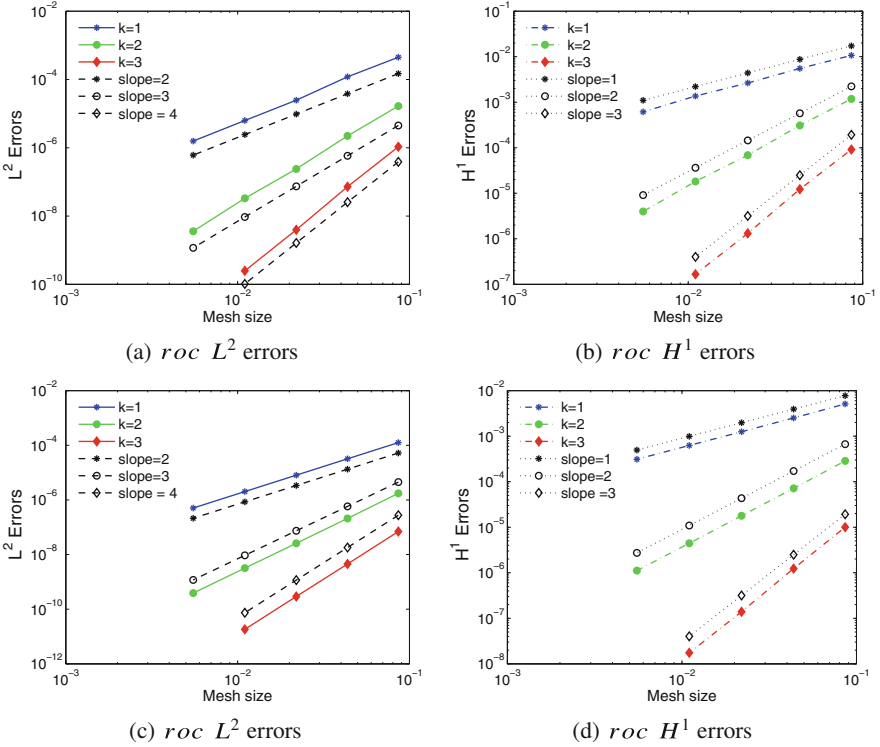
Fig. 2.5 Convergence of the error in the L^2 and H^1 for (**a,b**) Smoothed Voronoi and (**c,d**) Non-convex poylgons for $k = 1, 2$ and 3

Table 2.2 k=1: Convergence of the errors in L^2 and H^1 norm for the transient problem. The rate of convergence (*roc*) is also given

h	Distorted square				Non-convex mesh			
	L^2 error	roc	H^1 error	roc	L^2 error	roc	H^1 error	roc
1/4	2.1596×10^{-3}	–	3.7899×10^{-2}	–	2.2615×10^{-3}	–	4.0376×10^{-2}	–
1/8	5.7290×10^{-4}	1.91	1.9323×10^{-2}	0.97	6.0861×10^{-4}	1.89	1.9914×10^{-2}	1.01
1/16	1.5056×10^{-4}	1.92	9.8291×10^{-3}	0.97	1.5639×10^{-4}	1.96	9.8289×10^{-3}	1.01
1/32	3.7716×10^{-5}	1.99	4.9410×10^{-3}	0.99	3.9537×10^{-5}	1.98	4.8746×10^{-3}	1.01

over a square domain $\Omega = [0, 1]^2$ and time, $T = (0, 1]$ and $g(\mathbf{x}, t)$ is chosen such that $u(\mathbf{x}, t) = e^t \sin(\pi x) \sin(\pi y)$ is the exact solution to the problem. In this case, the nonlinearity is only on the right hand size forcing term and for the numerical study the domain is discretized only with polygonal meshes. Tables 2.5, 2.6, 2.7 shows the convergence of the error in the L^2 and H^1 norm with mesh refinement. It is inferred that the present framework yields optimal rate of convergence in the respective norms.

Table 2.3 k=2: Convergence of the errors in L^2 norm and H^1 semi-norm for the transient problem. The rate of convergence (roc) is also given

	Distorted square				Non-convex mesh			
h	L^2 error	roc	H^1 error	roc	L^2 error	roc	H^1 error	roc
1/4	1.0350×10^{-4}	–	5.3891×10^{-3}	–	1.1662×10^{-4}	–	6.1972×10^{-3}	–
1/8	1.4096×10^{-5}	2.87	1.4347×10^{-3}	1.90	1.4073×10^{-5}	3.05	1.5782×10^{-03}	1.97
1/16	1.8461×10^{-6}	2.93	3.6961×10^{-4}	1.95	1.6931×10^{-6}	3.05	3.9464×10^{-4}	1.99
1/32	2.3377×10^{-7}	2.99	9.3103×10^{-5}	1.99	2.1153×10^{-7}	3.01	9.8760×10^{-5}	1.99

Table 2.4 k=3: Convergence of the errors in L^2 norm and H^1 semi-norm for the transient problem. The rate of convergence (roc) is also given

	Distorted square				Non-convex mesh			
h	L^2 error	roc	H^1 error	roc	L^2 error	roc	H^1 error	roc
1/4	8.412×10^{-6}	–	5.8018×10^{-4}	–	1.3841×10^{-5}	–	6.6240×10^{-4}	–
1/8	5.6470×10^{-7}	3.89	7.6407×10^{-5}	2.92	8.0998×10^{-7}	4.09	7.9991×10^{-5}	3.04
1/16	3.5387×10^{-8}	3.99	9.5650×10^{-6}	2.99	5.0149×10^{-8}	4.02	9.7130×10^{-6}	3.04

Table 2.5 k=1: Convergence of the errors in L^2 norm and H^1 semi-norm for Eq. (2.7.1). The rate of convergence (roc) is also given

h	L^2 error	roc	H^1 error	roc
1/5	2.5421×10^{-3}	–	1.1388×10^{-2}	–
1/10	5.9296×10^{-4}	2.10	5.5768×10^{-3}	1.03
1/20	1.4319×10^{-4}	2.05	2.8667×10^{-3}	0.96
1/40	3.6046×10^{-5}	1.99	1.4234×10^{-3}	1.01
1/80	8.9492×10^{-6}	2.01	7.0190×10^{-4}	1.02

Table 2.6 k=2: Convergence of the errors in L^2 norm and H^1 semi-norm for Eq. (2.7.1). The rate of convergence (roc) is also given

h	L^2 error	roc	H^1 error	roc
1/5	9.6422×10^{-4}	–	6.4534×10^{-2}	–
1/10	1.3072×10^{-4}	2.88	1.6937×10^{-2}	1.92
1/20	1.4279×10^{-5}	3.19	3.8228×10^{-3}	2.14
1/40	1.7742×10^{-6}	3.01	9.4151×10^{-4}	2.01
1/80	2.1375×10^{-7}	3.04	2.3145×10^{-4}	2.02

Table 2.7 k=3: Convergence of the errors in L^2 norm and H^1 semi-norm for Eq. (2.7.1). The rate of convergence (roc) is also given

h	L^2 error	roc	H^1 error	roc
1/5	4.1565×10^{-5}	–	3.3546×10^{-3}	–
1/10	2.6784×10^{-6}	3.95	4.3964×10^{-4}	2.93
1/20	1.6547×10^{-7}	4.02	5.3857×10^{-5}	3.03

Example 4

In this example, we would like to show the rate of convergence in time variable. The nonlinear coefficient $\kappa(u)$ is chosen as $1/(1+u)^2$ and reaction and convection coefficient chosen as zero. The right hand side force function f is computed by

Table 2.8 Results are computed on smoothed Voronoi mesh for linear VEM space with mesh size, $h = 1/80$

Δt	L^2 error	roc
1/2	1.501×10^{-02}	-
1/4	3.762×10^{-03}	1.99
1/8	9.431×10^{-04}	1.87
1/16	2.311×10^{-04}	1.97

considering $u = \exp(t)\,(x - x^2)(y - y^2)$ as exact solution of (2.2.2). The errors are computed using the formula

$$
e_{0,T,h,0} := \left(\Delta t \sum_{n=1}^{N_T} \left(\sum_{K \in \Sigma_h} \| u(t_n) - \Pi_{k,K}^0 U^n \|^2 \right) \right)^{1/2}, \tag{2.7.2}
$$

for time step $\Delta t = 1/2, 1/4, 1/8, 1/16$ with fixed mesh size $h = 1/80$. The posted rate of convergence is ≈ 2 that is optimal rate of convergence for Crank-Nicolson scheme (Table 2.8).

2.8 Conclusion

In this chapter, we have presented the details of the implementation the virtual element method for nonlinear elliptic and parabolic equations over polytopes. The chapter also includes Matlab® codes to compute the VEM fundamental matrices and the Jacobian matrix that results from the linearization of the model problem. To the best of authors' knowledge, this is the first open source implementation of the VEM for nonlinear problems. Although, the code given in this chapter is for the lowest order (i.e., $k = 1$) VEM, the code can be generalized for higher order VEM. Interested readers can download the codes from https://github.com/nsundar/vem.

References

1. D. Adak, S. Natarajan, Virtual element method for semilinear sine-Gordon equation over polygonal mesh using product approximation technique. Math. Comput. Simul. **172**, 224–243 (2020)
2. D. Adak, E. Natarajan, S. Kumar, Virtual element method for semilinear hyperbolic problems on polygonal meshes. Int. J. Comput. Math., **96**, 971–991 (2018)
3. D. Adak, E. Natarajan, S. Kumar, Convergence analysis of virtual element methods for semilinear parabolic problems on polygonal meshes. Numer. Methods Partial Differ. Equ. **35**(1), 222–245 (2019)
4. B. Ahmad, A. Alsaedi, F. Brezzi, L.D. Marini, A. Russo, Equivalent projectors for virtual element methods. Comput. Math. Appl. **66**(3), 376–391 (2013)

5. P.F. Antonietti, L. Beirão da Veiga, D. Mora, M. Verani, A stream virtual element formulation of the Stokes problem on polygonal meshes. SIAM J. Numer. Anal. **52**(1), 386–404 (2014)
6. P.F. Antonietti, L. Beirão da Veiga, S. Scacchi, M. Verani, A C^1 virtual element method for the Cahn-Hilliard equation with polygonal meshes. SIAM J. Numer. Anal. **54**(1), 34–56 (2016)
7. L. Beirão da Veiga, G. Manzini, Residual a posteriori error estimation for the virtual element method for elliptic problems. ESAIM Math. Model. Numer. Anal. **49**(2), 577–599 (2015)
8. L. Beirão da Veiga, K. Lipnikov, G. Manzini, Convergence analysis of the high-order mimetic finite difference method. Numer. Math. **113**(3), 325–356 (2009)
9. L. Beirão da Veiga, K. Lipnikov, G. Manzini, Error analysis for a mimetic discretization of the steady Stokes problem on polyhedral meshes. SIAM J. Numer. Anal. **48**(4), 1419–1443 (2010)
10. L. Beirão da Veiga, F. Brezzi, L.D. Marini, Virtual elements for linear elasticity problems. SIAM J. Numer. Anal. **51**(2), 794–812 (2013)
11. L. Beirão da Veiga, F. Brezzi, A. Cangiani, G. Manzini, L.D. Marini, A. Russo, Basic principles of virtual element methods. Math. Models Methods Appl. Sci. **23**(01), 199–214 (2013)
12. L. Beirão da Veiga, F. Brezzi, L.D. Marini, A. Russo, The hitchhiker's guide to the virtual element method. Math. Models Methods Appl. Sci. **24**(08), 1541–1573 (2014)
13. L. Beirão da Veiga, K. Lipnikov, G. Manzini, *The Mimetic Finite Difference Method for Elliptic Problems*, vol. 11 (Springer, 2014)
14. L. Beirão da Veiga, C. Lovadina, D. Mora, A virtual element method for elastic and inelastic problems on polytope meshes. Comput. Methods Appl. Mech. Eng. **295**, 327–346 (2015)
15. L. Beirão da Veiga, F. Brezzi, L.D. Marini, A. Russo, Mixed virtual element methods for general second order elliptic problems on polygonal meshes. ESAIM Math. Model. Numer. Anal. **50**(3), 727–747 (2016)
16. L. Beirão da Veiga, F. Brezzi, L.D. Marini, A. Russo, Virtual element method for general second-order elliptic problems on polygonal meshes. Math. Models Methods Appl. Sci. **26**(04), 729–750 (2016)
17. L. Beirão da Veiga, C. Lovadina, G. Vacca, Divergence free virtual elements for the Stokes problem on polygonal meshes. ESAIM Math. Model. Numer. Anal. **51**(2), 509–535 (2017)
18. L. Beirão da Veiga, C. Lovadina, G. Vacca, Virtual elements for the Navier-Stokes problem on polygonal meshes. SIAM J. Numer. Anal. **56**(3), 1210–1242 (2018)
19. M.F. Benedetto, S. Berrone, A. Borio, S. Pieraccini, S. Scialò, Order preserving SUPG stabilization for the virtual element formulation of advection-diffusion problems. Comput. Methods Appl. Mech. Eng. **311**, 18–40 (2016)
20. A.O. Bernardin, C. Alvarez, N.H. Kahler, A. Russo, R.S. Valenzuela, E.O. Sanzana, Veamy: an extensible object-oriented c++ library for the virtual element method. Numer. Algorithms, 1–32 (2017)
21. J.E. Bishop, A displacement based finite element formulation for general polyhedra using harmonic shape functions. Int. J. Numer. Meth. Eng. **97**, 1–31 (2014)
22. A.D. Blanca, K. Lipnikov, G. Manzini, The nonconforming virtual element method. ESAIM Math. Model. Numer. Anal. **50**(3), 879–904 (2016)
23. F. Brezzi, L.D. Marini, Virtual Element Methods for plate bending problems. Comput. Methods Appl. Mech. Eng. **253**, 455–462 (2013)
24. F. Brezzi, R.S. Falk, L.D. Marini, Basic principles of mixed virtual element methods. ESAIM: Math. Modell. Numer. Anal., **48**(4), 1227–1240 (2014)
25. E. Cáceres, G. Gatica, A mixed virtual element method for the pseudostress-velocity formulation of the Stokes problem. IMA J. Numer. Anal. **37**(1), 296–331 (2017)
26. A. Cangiani, V. Gyrya, G. Manzini, The nonconforming virtual element method for the Stokes equations. SIAM J. Numer. Anal. **54**(6), 3411–3435 (2016)
27. A. Cangiani, G. Manzini, O.J. Sutton, Conforming and nonconforming virtual element methods for elliptic problems. IMA J. Numer. Anal. **37**(3), 1317–1354 (2016)
28. O. Čertík, F. Gardini, G. Manzini, G. Vacca, The virtual element method for eigenvalue problems with potential terms on polytopic meshes. Appl. Math. **63**(3), 333–365 (2018)
29. C. Chen, K. Li, Y. Chen, Y. Huang, Two-grid finite element methods combined with Crank-Nicolson scheme for nonlinear Sobolev equations. Adv. Comput. Math. **45**(2), 611–630 (2019)

30. C. Chinosi, Virtual elements for the reissner-mindlin plate problem. Numer. Methods Partial Differ. Equ. **34**(4), 1117–1144 (2018)
31. M. Chipot, *Elements of Nonlinear Analysis* (Springer Science & Business Media, 2000)
32. Y. Deng, F. Wang, H. Wei, A posteriori error estimates of virtual element method for a simplified friction problem. J. Sci. Comput. **83**, 52 (2020)
33. V. Dhanush, S. Natarajan, Implementation of the virtual element method for coupled thermo-elasticity in Abaqus. Numer. Algorithms **80**(3), 1037–1058 (2019)
34. M.S. Floater, M.J. Lai, Polygonal spline spaces and the numerical solution of the Poisson equation. SIAM J Numer. Anal. **54**, 794–827 (2016)
35. F. Gardini, G. Vacca, Virtual element method for second-order elliptic eigenvalue problems. IMA J. Numer. Anal. **38**(4), 2026–2054 (2018)
36. G. Gatica, M. Munar, F. Sequeira, A mixed virtual element method for the Navier-Stokes equations. Math. Models Methods Appl. Sci. **28**(14), 2719–2762 (2018)
37. O.A. Ladyzhenskaia, V.A. Solonnikov, N.N. Ural'tseva, *Linear and Quasi-Linear Equations of Parabolic Type*, vol. 23 (American Mathematical Soc., 1988)
38. D. Mora, G. Rivera, R. Rodríguez, A virtual element method for the Steklov eigenvalue problem. Math. Model Methods Appl. Sci. **25**(08), 1421–1445 (2015)
39. D. Mora, G. Rivera, R. Rodríguez, A posteriori error estimates for a virtual element method for the Steklov eigenvalue problem. Comput. Math. Appl. **74**(9), 2172–2190 (2017)
40. L. Mu, J. Wang, G. Wei, X. Ye, S. Zhao, Weak Galerkin methods for second order elliptic interface problems. J. Comput. Phys. **250**, 106–125 (2013)
41. S. Natarajan, E.T. Ooi, I. Chiong, C. Song, Convergence and accuracy of displacement based finite element formulation over arbitrary polygons: Laplace interpolants, strain smoothing and scaled boundary polygon formulation. Finite Elem. Anal. Des. **85**, 101–122 (2014)
42. E.T. Ooi, A.A. Aaputra, S. Natarajan, E.H. Ooi, C. Song, A dual scaled boundary finite element formulation over arbitrary faceted star convex polyhedra. Computational Mechanics **66**, 27–47 (2020)
43. A. Sinu, S. Natarajan, S. Krishnapillai, Quadratic serendipity finite elements over convex polyhedra. Int. J. Numer. Meth. Eng. **113**, 109–129 (2018)
44. N. Sukumar, E.A. Malsch, Recent advances in the construction of polygonal finite element interpolants. Arch. Comput. Methods Eng. **13**(1), 129 (2006)
45. O.J. Sutton, The virtual element method in 50 lines of matlab. Numer. Algorithms **75**(4), 1141–1159 (2017)
46. K.Y. Sze, N. Sheng, Polygonal finite element method for nonlinear constitutive modeling of polycrystalline ferroelectrics. Finite Elem. Anal. Des. **42**(2), 107–129 (2005)
47. G. Vacca, Virtual element methods for hyperbolic problems on polygonal meshes. Comput. Math. Appl. **74**, 882–898 (2017)
48. G. Vacca, L. Beirão da Veiga, Virtual element methods for parabolic problems on polygonal meshes. Numer. Methods Partial Differ. Equ. **31**(6), 2110–2134 (2015)
49. F. Wang, H. Wei, Virtual element methods for the obstacle problem. IMA J. Numer. Anal. **40**(1), 708–728 (2020)
50. J. Wang, X. Ye, A weak Galerkin finite element method for second-order elliptic problems. J. Comput. Appl. Math. **241**, 103–115 (2013)
51. P. Wriggers, W.T. Rust, B.D. Reddy, A virtual element method for contact. Computational Mechanics **58**(6), 1039–1050 (2016)
52. J. Zhao, S. Chen, B. Zhang, The nonconforming virtual element method for plate bending problems. Math. Models Methods Appl. Sci. **26**(09), 1671–1687 (2016)

Chapter 3
Discrete Hessian Complexes in Three Dimensions

Long Chen and Xuehai Huang

Abstract A family of conforming virtual element Hessian complexes on tetrahedral meshes are constructed based on decompositions of polynomial tensor spaces. They are applied to discretize the linearized time-independent Einstein-Bianchi system with optimal order convergence.

3.1 Introduction

Let Ω be a bounded Lipschitz domain in $\mathbb{R}^3$. The Hessian complex, also known as grad-grad complex, in three dimensions reads as [6, 41]

$$\mathbb{P}_1(\Omega) \xrightarrow{\subseteq} H^2(\Omega) \xrightarrow{\text{hess}} \boldsymbol{H}(\text{curl}, \Omega; \mathbb{S}) \xrightarrow{\text{curl}} \boldsymbol{H}(\text{div}, \Omega; \mathbb{T}) \xrightarrow{\text{div}} \boldsymbol{L}^2(\Omega; \mathbb{R}^3) \to \boldsymbol{0},$$

where $\mathbb{P}_1(\Omega)$ is the linear polynomial space, $H^2(\Omega)$ and $\boldsymbol{L}^2(\Omega; \mathbb{R}^3)$ are standard Sobolev spaces, $\boldsymbol{H}(\text{curl}, \Omega; \mathbb{S})$ is the space of symmetric matrices whose curl is in $\boldsymbol{L}^2(\Omega; \mathbb{T})$, and $\boldsymbol{H}(\text{div}, \Omega; \mathbb{T})$ is the space of trace-free matrices whose div is in $\boldsymbol{L}^2(\Omega; \mathbb{R}^3)$. Here both curl and div are applied to matrices row-wisely. Given a tetrahedral mesh of domain Ω, we shall construct discrete Hessian complexes with conforming virtual element spaces and apply to solve the linearized Einstein-Bianchi (EB) system [42].

Finding finite elements with continuous derivatives (the so-called C^1 element), symmetry, or trace-free leads to higher number of degrees of freedom. To avoid this issue, Arnold and Quenneville-Belair [42] use multipliers to impose the weak H^2-conforming and weak symmetry and obtain an optimal order discretization of the EB

L. Chen
Department of Mathematics, University of California at Irvine, Irvine, CA, USA
e-mail: chenlong@math.uci.edu

X. Huang (✉)
School of Mathematics, Shanghai University of Finance and Economics, Shanghai, China
e-mail: huang.xuehai@sufe.edu.cn

system. In [32] Hu and Liang construct the first finite element Hessian complexes in three dimensions. The lowest order complex starts with the $\mathbb{P}_9$ $\mathscr{C}^1$-element constructed in [46] and consists of $\mathbb{P}_7$ for $\boldsymbol{H}(\text{curl}, \Omega; \mathbb{S})$ and $\mathbb{P}_6$ for $\boldsymbol{H}(\text{div}, \Omega; \mathbb{T})$, where $\mathbb{P}_k$ stands for the polynomail space of degree k. Although the practical significance may be limited due to the high polynomial degree of the elements, the work [32] is the first construction of conforming discrete Hessian complexes consisting of finite element spaces in $\mathbb{R}^3$, and it motivates us to the development of simpler methods.

We shall use ideas of virtual element methods (VEMs) to construct discrete Hessian complexes with fewer degrees of freedom. The virtual element developed in [9, 10] is a generalization of the finite element on tensorial/simplicial meshes to a general polyhedral mesh and can be also thought of as a variational framework for the mimetic finite difference methods [18, 36]. Compared with the standard finite element methods mainly working on tensorial/simplicial meshes, VEMs have a variety of distinct advantages. The VEMs are, foremost, highly adaptable to the polygonal/polyhedral, and even anisotropic quadrilateral/hexahedral meshes. For problems with complex geometries, this leads to great convenience in the mesh generation, e.g., discrete fracture network simulations [15], and the elliptic interface problems in three dimensions [26]. Another trait of VEMs is its astoundingly painless construction of smooth elements for high-order elliptic problems. For instance, H^2-conforming VEMs have been constructed in [3, 13, 17] which shows a simple and elegant construction readily to be implemented. A uniform construction of the H^m-nonconforming virtual elements of any order k and m on any shape of polytopes in $\mathbb{R}^n$ with constraint $k \geq m$ has been developed in [24, 33]. One more merit is that the virtual element space can be devised to be structure preserving, such as the harmonic VEM [27, 37] and the divergence-free Stokes VEMs [12, 45]. VEMs for de Rham complex [11] and Stokes complexes [14] have been also constructed recently.

In the construction of the VEM spaces, the subtlest and a key component is the well-posedness of a local problem with non-zero Dirichlet boundary conditions. Take an H^2-conforming VEM space as an example. Given data (f, g_1, g_2), consider the biharmonic equation with Dirichlet boundary condition on a polyhedron K

$$\Delta^2 v = f \text{ in } K, \quad v = g_1, \partial_n v = g_2 \text{ on } \partial K. \tag{3.1.1}$$

When $g_1 = g_2 = 0$, the existence and uniqueness is a consequence of the Lax-Milligram lemma on $H_0^2(K)$. The classical way to deal with the non-zero Dirichlet boundary condition (g_1, g_2) is to find a lifting $v^b \in H^2(K)$ with $v^b = g_1$, $\partial_n v^b = g_2$ and change (3.1.1) to the homogenous boundary condition with modified source $f - \Delta^2 v^b$. Such lifting is guaranteed by trace theorems of Sobolev spaces which is usually established for smooth domains. For polyhedral domains, however, compatible conditions [20] are needed. Although the traces g_1 and g_2 are defined piece-wisely on each face F of K, for H^2-functions, $(g_2|_F \boldsymbol{n}_F + \nabla_F(g_1|_F))|_e$ should be single-valued across each edge e of the polyhedron K, for F containing edge e. That is g_1 and g_2 cannot be chosen independently.

For vector function spaces, characterization of the trace spaces and corresponding compatible conditions is harder as tangential and normal components of the trace should be treated differently. We refer to [14, Appendix A] for the discussion of the well-posedness of the biharmonic problem of vector functions with a non-homogeneous boundary conditions, and refer to [19] and references therein for the trace of $H(\mathrm{curl}, \Omega)$, where variants of space $H^{1/2}(\partial\Omega)$ are introduced. Specifically a lifting for the trace of a function in $H(\mathrm{curl}, \Omega)$ on a Lipschitz domain is explicitly constructed in [44] which is highly non-trivial.

We are not able to characterize the trace space of $\boldsymbol{H}(\mathrm{curl}, \Omega; \mathbb{S})$ and thus cannot follow the classical approach of VEM to define the shape function space using local problems. Instead we still consider tetrahedron element K and combine finite element and virtual element spaces. We first establish a polynomial Hessian complex and corresponding Koszul complex, which leads to the decomposition

$$\mathbb{P}_k(K; \mathbb{S}) = \nabla^2 \mathbb{P}_{k+2}(K) \oplus \mathrm{sym}(\mathbb{P}_{k-1}(K; \mathbb{T}) \times \boldsymbol{x}) \quad k \geq 1.$$

Based on this decomposition, we can construct a virtual element space

$$\boldsymbol{\Sigma}(K) = \nabla^2 W(K) \oplus \mathrm{sym}(\boldsymbol{V}(K) \times \boldsymbol{x}),$$

where $W(K)$ is an H^2-conforming VEM space and $\boldsymbol{V}(K) = \mathbb{P}_{k-1}(K; \mathbb{T})$ is an $H(\mathrm{div})$-conforming finite element space. Degrees of freedom for $\boldsymbol{\Sigma}(K)$ are carefully chosen so that the resulting global space $\boldsymbol{\Sigma}_h$ is $H(\mathrm{curl})$-conforming and its L^2-projection to $\mathbb{P}_k(\mathbb{S})$ is computable. Our construction is different from the approach in [32] for constructing a finite element Hessian complex, where characterization of polynomial bubble functions is crucial.

Our H^2-conforming virtual element $W(K)$ is slightly different from those constructed in [3, 13, 17]. Again we take the advantage of K being a tetrahedron to construct an element so that when restricted to each face, $v|_F \in \mathbb{P}_{k+2}(F)$ is an Argyris element [4, 16] and $(\partial_n v)|_F \in \mathbb{P}_{k+1}(F)$ is a Hermite element [28].

The $\boldsymbol{H}(\mathrm{div}, \Omega; \mathbb{T})$ finite element $\boldsymbol{V}(K) = \mathbb{P}_{k-1}(K; \mathbb{T})$ is a variant of finite element spaces constructed in [32] for $k \geq 3$. The space $\mathscr{Q}(K) = \mathbb{P}_{k-2}(K; \mathbb{R}^3)$.

The four local spaces $(W(K), \boldsymbol{\Sigma}(K), \boldsymbol{V}(K), \mathscr{Q}(K))$ will contain polynomial spaces $(\mathbb{P}_{k+2}, \mathbb{P}_k, \mathbb{P}_{k-1}, \mathbb{P}_{k-2})$ with $2k(k-1)$ non-polynomial shape functions added in $W(K)$ and $\Sigma(K)$ with $k \geq 3$. For the lowest order case, i.e., $k = 3$, the dimensions are (68, 132, 80, 12) which are more tractable for implementation.

We show the constructed discrete spaces form a discrete Hessian complex

$$\mathbb{P}_1(\Omega) \xrightarrow{\subset} W_h \xrightarrow{\nabla^2} \boldsymbol{\Sigma}_h \xrightarrow{\mathrm{curl}} \boldsymbol{V}_h \xrightarrow{\mathrm{div}} \mathscr{Q}_h \to \boldsymbol{0}.$$

Optimal order discretization of the linearized EB system is obtained consequently.

During the construction, integration by parts is indispensable and therefore the dual complex: div-div complex as well as its polynomial versions are also presented. Finite elements for div-div complex are recently constructed in [22, 23].

The rest of this paper is organized as follows. Some matrix and vector operations are shown in Sect. 3.2. In Sect. 3.3 Hessian complex and divdiv complex are presented. Several polynomial complexes are explored in Sect. 3.4. A family of conforming virtual element Hessian complexes are constructed in Sect. 3.5. In Sect. 3.6, the conforming virtual element Hessian complexes are adopted to discretize the linearized EB system.

3.2 Matrix and Vector Operations

In this section, we shall survey the notation system for operations for vectors and tensors used in the solid mechanic [34]. In particular, we shall distinguish operators applied to columns and rows of a matrix. The presentation here follows our recent work [23, 25].

3.2.1 Matrix-Vector Products

The matrix-vector product Ab can be interpreted as the inner product of b with the row vectors of A. We thus define the dot operator $A \cdot b := Ab$. Similarly we can define the row-wise cross product from the right $A \times b$. Here rigorously speaking when a column vector b is treated as a row vector, notation b^T should be used. In most places, however, we will sacrifice this precision for the ease of notation. When the vector is on the left of the matrix, the operation is defined column-wise. For example, $b \cdot A := b^\mathsf{T} A$. For dot products, we will still mainly use the conventional notation, e.g. $b \cdot A \cdot c = b^\mathsf{T} A c$. But for the cross products, we emphasize again the cross product of a vector from the left is column-wise and from the right is row-wise. The transpose rule still works, i.e. $b \times A = -(A^\mathsf{T} \times b)^\mathsf{T}$. Here again, we mix the usage of column vector b and row vector b^T.

The ordering of performing the row and column products does not matter which leads to the associative rule of the triple products

$$b \times A \times c := (b \times A) \times c = b \times (A \times c).$$

Similar rules hold for $b \cdot A \cdot c$ and $b \cdot A \times c$ and thus parentheses can be safely skipped when no differentiation is involved.

For two column vectors $\boldsymbol{u}$, $\boldsymbol{v}$, the tensor product $\boldsymbol{u} \otimes \boldsymbol{v} := \boldsymbol{u}\boldsymbol{v}^\mathsf{T}$ is a matrix which is also known as the dyadic product $\boldsymbol{u}\boldsymbol{v} := \boldsymbol{u}\boldsymbol{v}^\mathsf{T}$ with more clean notation (one $^\mathsf{T}$ is skipped). The row-wise product and column-wise product with another vector will be applied to the neighboring vector:

$$\boldsymbol{x} \cdot (\boldsymbol{u}\boldsymbol{v}) = (\boldsymbol{x} \cdot \boldsymbol{u})\boldsymbol{v}^\mathsf{T}, \quad (\boldsymbol{u}\boldsymbol{v}) \cdot \boldsymbol{x} = \boldsymbol{u}(\boldsymbol{v} \cdot \boldsymbol{x}),$$

$$\boldsymbol{x} \times (\boldsymbol{u}\boldsymbol{v}) = (\boldsymbol{x} \times \boldsymbol{u})\boldsymbol{v}, \quad (\boldsymbol{u}\boldsymbol{v}) \times \boldsymbol{x} = \boldsymbol{u}(\boldsymbol{v} \times \boldsymbol{x}).$$

3.2.2   Differentiation

We treat Hamilton operator $\nabla = (\partial_1, \partial_2, \partial_3)^\mathsf{T}$ as a column vector. For a vector function $\boldsymbol{u} = (u_1, u_2, u_3)^\mathsf{T}$, $\operatorname{curl} \boldsymbol{u} = \nabla \times \boldsymbol{u}$, and $\operatorname{div} \boldsymbol{u} = \nabla \cdot \boldsymbol{u}$ are standard differential operations. Define $\nabla \boldsymbol{u} := \nabla \boldsymbol{u}^\mathsf{T} = (\partial_i u_j)$, which can be understood as the dyadic product of Hamilton operator ∇ and column vector $\boldsymbol{u}$.

Apply these matrix-vector operations to the Hamilton operator ∇, we get column-wise differentiation $\nabla \cdot \boldsymbol{A}$, $\nabla \times \boldsymbol{A}$, and row-wise differentiation $\boldsymbol{A} \cdot \nabla$, $\boldsymbol{A} \times \nabla$. Conventionally, the differentiation is applied to the function after the ∇ symbol. So a more conventional notation is

$$\boldsymbol{A} \cdot \nabla := (\nabla \cdot \boldsymbol{A}^\mathsf{T})^\mathsf{T}, \quad \boldsymbol{A} \times \nabla := -(\nabla \times \boldsymbol{A}^\mathsf{T})^\mathsf{T}.$$

By moving the differential operator to the right, the notation is simplified and the transpose rule for matrix-vector products can be formally used. Again the right most column vector ∇ is treated as a row vector ∇^T to make the notation cleaner.

In the literature, differential operators are usually applied row-wisely to tensors. To distinguish with ∇ notation, we define operators in letters which are applied row-wisely

$$\operatorname{grad} \boldsymbol{u} := \boldsymbol{u}\nabla^\mathsf{T} = (\partial_j u_i) = (\nabla \boldsymbol{u})^\mathsf{T},$$

$$\operatorname{curl} \boldsymbol{A} := -\boldsymbol{A} \times \nabla = (\nabla \times \boldsymbol{A}^\mathsf{T})^\mathsf{T},$$

$$\operatorname{div} \boldsymbol{A} := \boldsymbol{A} \cdot \nabla = (\nabla \cdot \boldsymbol{A}^\mathsf{T})^\mathsf{T}.$$

3.2.3   Matrix Decompositions

Denote the space of all 3×3 matrices by $\mathbb{M}$, all symmetric 3×3 matrices by $\mathbb{S}$, all skew-symmetric 3×3 matrices by $\mathbb{K}$, and all trace-free 3×3 matrices by $\mathbb{T}$. For any matrix $\boldsymbol{B} \in \mathbb{M}$, we can decompose it into symmetric and skew-symmetric parts as

$$\boldsymbol{B} = \operatorname{sym}(\boldsymbol{B}) + \operatorname{skw}(\boldsymbol{B}) := \frac{1}{2}(\boldsymbol{B} + \boldsymbol{B}^\mathsf{T}) + \frac{1}{2}(\boldsymbol{B} - \boldsymbol{B}^\mathsf{T}).$$

We can also decompose it into a direct sum of a trace free matrix and a diagonal matrix as

$$\boldsymbol{B} = \operatorname{dev}\boldsymbol{B} + \frac{1}{3}\operatorname{tr}(\boldsymbol{B})\boldsymbol{I} := (\boldsymbol{B} - \frac{1}{3}\operatorname{tr}(\boldsymbol{B})\boldsymbol{I}) + \frac{1}{3}\operatorname{tr}(\boldsymbol{B})\boldsymbol{I}.$$

Define the sym curl operator for a matrix $\boldsymbol{A}$

$$\operatorname{sym}\operatorname{curl}\boldsymbol{A} := \frac{1}{2}(\nabla \times \boldsymbol{A}^{\mathsf{T}} + (\nabla \times \boldsymbol{A}^{\mathsf{T}})^{\mathsf{T}}) = \frac{1}{2}(\nabla \times \boldsymbol{A}^{\mathsf{T}} - \boldsymbol{A} \times \nabla).$$

We define an isomorphism of $\mathbb{R}^3$ and the space of skew-symmetric matrices $\mathbb{K}$ as follows: for a vector $\boldsymbol{\omega} = (\omega_1, \omega_2, \omega_3)^{\mathsf{T}} \in \mathbb{R}^3$,

$$\operatorname{mskw}\boldsymbol{\omega} := \begin{pmatrix} 0 & -\omega_3 & \omega_2 \\ \omega_3 & 0 & -\omega_1 \\ -\omega_2 & \omega_1 & 0 \end{pmatrix}.$$

Obviously $\operatorname{mskw} : \mathbb{R}^3 \to \mathbb{K}$ is a bijection. We define $\operatorname{vskw} : \mathbb{M} \to \mathbb{R}^3$ by $\operatorname{vskw} := \operatorname{mskw}^{-1} \circ \operatorname{skw}$.

We will use the following identities which can be verified by direct calculation.

$$\operatorname{skw}(\operatorname{grad}\boldsymbol{u}) = \frac{1}{2}\operatorname{mskw}(\operatorname{curl}\boldsymbol{u}), \tag{3.2.1}$$

$$\operatorname{skw}(\operatorname{curl}\boldsymbol{A}) = \frac{1}{2}\operatorname{mskw}\left[\operatorname{div}(\boldsymbol{A}^{\mathsf{T}}) - \operatorname{grad}(\operatorname{tr}(\boldsymbol{A}))\right],$$

$$\operatorname{div}\operatorname{mskw}\boldsymbol{u} = -\operatorname{curl}\boldsymbol{u},$$

$$2\operatorname{div}\operatorname{vskw}\boldsymbol{A} = \operatorname{tr}\operatorname{curl}\boldsymbol{A}, \tag{3.2.2}$$

$$\operatorname{curl}(u\boldsymbol{I}) = -\operatorname{mskw}\operatorname{grad}(u).$$

More identities involving the matrix operation and differentiation are summarized in [6]; see also [23, 25].

3.2.4 Projections to a Plane

Given a plane F with normal vector $\boldsymbol{n}$, for a vector $\boldsymbol{v} \in \mathbb{R}^3$, we have the orthogonal decomposition

$$\boldsymbol{v} = \Pi_n \boldsymbol{v} + \Pi_F \boldsymbol{v} := (\boldsymbol{v} \cdot \boldsymbol{n})\boldsymbol{n} + (\boldsymbol{n} \times \boldsymbol{v}) \times \boldsymbol{n}.$$

The matrix representation of Π_n is $\boldsymbol{n}\boldsymbol{n}^{\mathsf{T}}$ and $\Pi_F = \boldsymbol{I} - \boldsymbol{n}\boldsymbol{n}^{\mathsf{T}}$. The vector $\Pi_F^{\perp}\boldsymbol{v} := \boldsymbol{n} \times \boldsymbol{v}$ is also on the plane F and is a rotation of $\Pi_F \boldsymbol{v}$ by $90°$ counter-clockwise with

respect to $\boldsymbol{n}$. We treat Hamilton operator $\nabla = (\partial_1, \partial_2, \partial_3)^{\mathsf{T}}$ as a column vector and define

$$\nabla_F^{\perp} := \boldsymbol{n} \times \nabla, \quad \nabla_F := \Pi_F \nabla = -\boldsymbol{n} \times (\boldsymbol{n} \times \nabla).$$

For a scalar function v,

$$\text{grad}_F \, v := \nabla_F v = \Pi_F(\nabla v),$$

$$\text{curl}_F \, v := \nabla_F^{\perp} v = \boldsymbol{n} \times \nabla v,$$

are the surface gradient and surface curl of v, respectively. For a vector function $\boldsymbol{v}$, $\nabla_F \cdot \boldsymbol{v}$ is the surface divergence

$$\text{div}_F \, \boldsymbol{v} := \nabla_F \cdot \boldsymbol{v} = \nabla_F \cdot (\Pi_F \boldsymbol{v}).$$

By the cyclic invariance of the mix product and the fact $\boldsymbol{n}$ is constant, the surface rot operator is

$$\text{rot}_F \boldsymbol{v} := \nabla_F^{\perp} \cdot \boldsymbol{v} = (\boldsymbol{n} \times \nabla) \cdot \boldsymbol{v} = \boldsymbol{n} \cdot (\nabla \times \boldsymbol{v}),$$

which is the normal component of $\nabla \times \boldsymbol{v}$. The tangential trace of $\nabla \times \boldsymbol{v}$ is

$$\boldsymbol{n} \times (\nabla \times \boldsymbol{v}) = \nabla(\boldsymbol{n} \cdot \boldsymbol{v}) - \partial_n \boldsymbol{v}.$$

By definition,

$$\text{rot}_F \boldsymbol{v} = -\text{div}_F(\boldsymbol{n} \times \boldsymbol{v}), \quad \text{div}_F \, \boldsymbol{v} = \text{rot}_F(\boldsymbol{n} \times \boldsymbol{v}).$$

Note that the three dimensional curl operator restricted to a two dimensional plane F results in two operators: curl_F maps a scalar to a vector, which is a rotation of grad_F, and rot_F maps a vector to a scalar which can be thought as a rotated version of div_F. The surface differentiations satisfy the property $\text{div}_F \, \text{curl}_F = 0$ and $\text{rot}_F \, \text{grad}_F = 0$ and when F is simply connected, $\ker(\text{div}_F) = \text{img}(\text{curl}_F)$ and $\ker(\text{rot}_F) = \text{img}(\text{grad}_F)$.

Differentiation for two dimensional tensors on face F can be defined similarly.

3.3 Two Hilbert Complexes for Tensors

In this section we shall present two Hilbert complexes for tensors: the Hessian complex and the divdiv complex. They are dual to each other. The Hessian complex will be used for the construction of shape function spaces and the divdiv complex for the degrees of freedom.

Recall that a Hilbert complex is a sequence of Hilbert spaces $\{\mathscr{V}_i\}$ connected by a sequence of closed densely defined linear operators $\{d_i\}$

$$0 \longrightarrow \mathscr{V}_1 \xrightarrow{d_1} \mathscr{V}_2 \xrightarrow{d_2} \cdots \xrightarrow{d_{n-2}} \mathscr{V}_{n-1} \xrightarrow{d_{n-1}} \mathscr{V}_n \longrightarrow 0,$$

satisfying the property $\mathrm{img}(d_i) \subseteq \ker(d_{i+1})$, i.e., $d_{i+1} \circ d_i = 0$. In this paper, we shall consider domain complexes only, i.e., $\mathrm{dom}(d_i) = \mathscr{V}_i$. The complex is called an exact sequence if $\mathrm{img}(d_i) = \ker(d_{i+1})$ for $i = 1, \ldots, n$. We usually skip the first 0 in the complex and use the embedding operator to indicate d_1 is injective. We refer to [5] for background on Hilbert complexes.

3.3.1 Hessian Complexes

The Hessian complex in three dimensions reads as [6, 41]

$$\mathbb{P}_1(\Omega) \xrightarrow{\subseteq} H^2(\Omega) \xrightarrow{\mathrm{hess}} \boldsymbol{H}(\mathrm{curl}, \Omega; \mathbb{S}) \xrightarrow{\mathrm{curl}} \boldsymbol{H}(\mathrm{div}, \Omega; \mathbb{T}) \xrightarrow{\mathrm{div}} \boldsymbol{L}^2(\Omega; \mathbb{R}^3) \rightarrow \boldsymbol{0}. \tag{3.3.1}$$

For the completeness we shall prove the exactness following [41] and refer to [6] for a systematical way of deriving complexes from complexes.

Lemma 3.1 *Assume Ω is a bounded Lipschitz domain in $\mathbb{R}^3$. It holds*

$$\mathrm{div}\,\boldsymbol{H}^1(\Omega; \mathbb{T}) = \boldsymbol{L}^2(\Omega; \mathbb{R}^3). \tag{3.3.2}$$

Proof First consider $\boldsymbol{v} = \nabla w \in \boldsymbol{L}^2(\Omega; \mathbb{R}^3)$ with $w \in H^1(\Omega)$. There exists $\boldsymbol{\phi} \in \boldsymbol{H}^2(\Omega; \mathbb{R}^3)$ satisfying $2\,\mathrm{div}\,\boldsymbol{\phi} = -3w$. Take $\boldsymbol{\tau} = w\boldsymbol{I} + \mathrm{curl}\,\mathrm{mskw}\,\boldsymbol{\phi} \in \boldsymbol{H}^1(\Omega; \mathbb{M})$. It is obvious that $\mathrm{div}\,\boldsymbol{\tau} = \mathrm{div}(w\boldsymbol{I}) = \boldsymbol{v}$. It follows from (3.2.2) that

$$\mathrm{tr}\,\boldsymbol{\tau} = 3w + \mathrm{tr}\,\mathrm{curl}\,\mathrm{mskw}\,\boldsymbol{\phi} = 3w + 2\,\mathrm{div}\,\mathrm{vskw}\,\mathrm{mskw}\,\boldsymbol{\phi} = 3w + 2\,\mathrm{div}\,\boldsymbol{\phi} = 0.$$

Next consider general $\boldsymbol{v} \in \boldsymbol{L}^2(\Omega; \mathbb{R}^3)$. There exists $\boldsymbol{\tau}_1 \in \boldsymbol{H}^1(\Omega; \mathbb{M})$ satisfying $\mathrm{div}\,\boldsymbol{\tau}_1 = \boldsymbol{v}$. Then there exists $\boldsymbol{\tau}_2 \in \boldsymbol{H}^1(\Omega; \mathbb{T})$ satisfying $\mathrm{div}\,\boldsymbol{\tau}_2 = \frac{1}{3}\nabla(\mathrm{tr}\,\boldsymbol{\tau}_1)$. Now take $\boldsymbol{\tau} = \mathrm{dev}\,\boldsymbol{\tau}_1 + \boldsymbol{\tau}_2 \in \boldsymbol{H}^1(\Omega; \mathbb{T})$. We have

$$\mathrm{div}\,\boldsymbol{\tau} = \mathrm{div}(\mathrm{dev}\,\boldsymbol{\tau}_1) + \mathrm{div}\,\boldsymbol{\tau}_2 = \mathrm{div}(\mathrm{dev}\,\boldsymbol{\tau}_1) + \frac{1}{3}\nabla(\mathrm{tr}\,\boldsymbol{\tau}_1) = \mathrm{div}\,\boldsymbol{\tau}_1 = \boldsymbol{v}.$$

Thus (3.3.2) follows. $\qquad\qquad\qquad\qquad\qquad\qquad\qquad\qquad\qquad\qquad\qquad\qquad\qquad\qquad\square$

Lemma 3.2 *Assume Ω is a bounded and topologically trivial Lipschitz domain in $\mathbb{R}^3$. It holds*

$$\operatorname{curl} \boldsymbol{H}^1(\Omega; \mathbb{S}) = \boldsymbol{H}(\operatorname{div}, \Omega; \mathbb{T}) \cap \ker(\operatorname{div}). \qquad (3.3.3)$$

Proof By [29, Theorem1.1], for any $\boldsymbol{\tau} \in \boldsymbol{H}(\operatorname{div}, \Omega; \mathbb{T}) \cap \ker(\operatorname{div})$, there exists $\boldsymbol{\sigma}_1 \in \boldsymbol{H}^1(\Omega; \mathbb{M})$ such that

$$\boldsymbol{\tau} = \operatorname{curl} \boldsymbol{\sigma}_1.$$

Thanks to (3.2.2), we have

$$2 \operatorname{div} \operatorname{vskw} \boldsymbol{\sigma}_1 = \operatorname{tr} \operatorname{curl} \boldsymbol{\sigma}_1 = \operatorname{tr} \boldsymbol{\tau} = 0.$$

Hence there exists $\boldsymbol{v} \in \boldsymbol{H}^2(\Omega; \mathbb{R}^3)$ such that $\operatorname{vskw} \boldsymbol{\sigma}_1 = \frac{1}{2} \operatorname{curl} \boldsymbol{v}$. Then apply mskw and use (3.2.1) to get

$$\operatorname{skw} \boldsymbol{\sigma}_1 = \frac{1}{2} \operatorname{mskw} \operatorname{curl} \boldsymbol{v} = \operatorname{skw}(\operatorname{grad} \boldsymbol{v}).$$

Taking $\boldsymbol{\sigma} = \boldsymbol{\sigma}_1 - \operatorname{grad} \boldsymbol{v}$, we have $\boldsymbol{\sigma} \in \boldsymbol{H}^1(\Omega; \mathbb{S})$ and $\operatorname{curl} \boldsymbol{\sigma} = \boldsymbol{\tau}$. □

Theorem 3.1 *Assume Ω is a bounded and topologically trivial Lipschitz domain in $\mathbb{R}^3$. Then (3.3.1) is a Hilbert complex and exact sequence.*

Proof It is obvious that (3.3.1) is a complex and $H^2(\Omega) \cap \ker(\operatorname{hess}) = \mathbb{P}_1(\Omega)$. As results of (3.3.2) and (3.3.3), we have

$$\operatorname{div} \boldsymbol{H}(\operatorname{div}, \Omega; \mathbb{T}) = \boldsymbol{L}^2(\Omega; \mathbb{R}^3), \quad \operatorname{curl} \boldsymbol{H}(\operatorname{curl}, \Omega; \mathbb{S}) = \boldsymbol{H}(\operatorname{div}, \Omega; \mathbb{T}) \cap \ker(\operatorname{div}).$$

We only need to prove $\boldsymbol{H}(\operatorname{curl}, \Omega; \mathbb{S}) \cap \ker(\operatorname{curl}) = \operatorname{hess} H^2(\Omega)$. For any $\boldsymbol{\sigma} \in \boldsymbol{H}(\operatorname{curl}, \Omega; \mathbb{S}) \cap \ker(\operatorname{curl})$, there exists $\boldsymbol{v} \in \boldsymbol{H}^1(\Omega; \mathbb{R}^3)$ such that

$$\boldsymbol{\sigma} = \operatorname{grad} \boldsymbol{v}.$$

Since $\boldsymbol{\sigma}$ is symmetric, by (3.2.1), we have

$$\operatorname{mskw}(\operatorname{curl} \boldsymbol{v}) = 2 \operatorname{skw}(\operatorname{grad} \boldsymbol{v}) = 2 \operatorname{skw}(\boldsymbol{\sigma}) = \boldsymbol{0},$$

which means $\operatorname{curl} \boldsymbol{v} = \boldsymbol{0}$. Hence there exists $w \in H^2(\Omega)$ that $\boldsymbol{v} = \nabla w$ and consequently $\boldsymbol{\sigma} = \operatorname{hess} w \in \operatorname{hess} H^2(\Omega)$. □

As a result of the Hessian complex (3.3.1), we have the Poincaré inequality [6, the inequality above (14)]

$$\|\boldsymbol{\tau}\|_0 \lesssim \|\operatorname{curl} \boldsymbol{\tau}\|_0 \tag{3.3.4}$$

for any $\boldsymbol{\tau} \in \boldsymbol{H}(\operatorname{curl}, \Omega; \mathbb{S})$ satisfying

$$(\boldsymbol{\tau}, \nabla^2 w) = 0 \quad \forall\, w \in H^2(\Omega).$$

When $\Omega \subset \mathbb{R}^2$, the Hessian complex in two dimensions becomes

$$\mathbb{P}_1(\Omega) \xrightarrow{\subseteq} H^2(\Omega) \xrightarrow{\text{hess}} \boldsymbol{H}(\operatorname{rot}, \Omega; \mathbb{S}) \xrightarrow{\text{rot}} \boldsymbol{L}^2(\Omega; \mathbb{R}^2) \to \boldsymbol{0},$$

which is a rotation of the elasticity complex [7, 30].

3.3.2 divdiv Complexes

The div div complex in three dimensions reads as [6, 41]

$$\boldsymbol{RT} \xrightarrow{\subseteq} \boldsymbol{H}^1(\Omega; \mathbb{R}^3) \xrightarrow{\text{dev grad}} \boldsymbol{H}(\operatorname{sym} \operatorname{curl}, \Omega; \mathbb{T}) \xrightarrow{\text{sym} \operatorname{curl}} \boldsymbol{H}(\operatorname{div} \operatorname{div}, \Omega; \mathbb{S}) \xrightarrow{\text{div div}} L^2(\Omega) \to 0, \tag{3.3.5}$$

where $\boldsymbol{RT} := \{a\boldsymbol{x} + \boldsymbol{b} : a \in \mathbb{R}, \boldsymbol{b} \in \mathbb{R}^3\}$ is the lowest order Raviart-Thomas space.

A proof of the following theorem can be found in [6, 23, 41].

Theorem 3.2 *Assume Ω is a bounded and topologically trivial Lipschitz domain in $\mathbb{R}^3$. Then (3.3.5) is a Hilbert complex and exact sequence.*

When $\Omega \subset \mathbb{R}^2$, the div div complex in two dimensions becomes (cf. [21])

$$\boldsymbol{RT} \xrightarrow{\subseteq} \boldsymbol{H}^1(\Omega; \mathbb{R}^2) \xrightarrow{\text{sym} \operatorname{curl}} \boldsymbol{H}(\operatorname{div} \operatorname{div}, \Omega; \mathbb{S}) \xrightarrow{\text{div div}} L^2(\Omega) \to 0.$$

3.4 Polynomial Complexes for Tensors

In this section we consider Hessian and divdiv polynomial complexes on a bounded and topologically trivial domain $D \subset \mathbb{R}^3$. Without loss of generality, we assume $(0, 0, 0) \in D$.

Given a non-negative integer k, let $\mathbb{P}_k(D)$ stand for the set of all polynomials in D with the total degree no more than k, and $\mathbb{P}_k(D; \mathbb{X})$ denote the tensor or vector version. Let $\mathbb{H}_k(D) := \mathbb{P}_k(D)/\mathbb{P}_{k-1}(D)$ be the space of functions spanned by the

homogenous polynomials of degree k. Denote by Q_k^D the L^2-orthogonal projector onto $\mathbb{P}_k(D)$, and $\boldsymbol{Q}_k^D$ the tensor or vector version.

3.4.1 De Rham and Koszul Polynomial Complexes

First we recall the polynomial de Rham complex

$$\mathbb{R} \xrightarrow{\subseteq} \mathbb{P}_{k+1}(D) \xrightarrow{\nabla} \mathbb{P}_k(D; \mathbb{R}^3) \xrightarrow{\nabla \times} \mathbb{P}_{k-1}(D; \mathbb{R}^3) \xrightarrow{\nabla \cdot} \mathbb{P}_{k-2}(D) \to 0, \qquad (3.4.1)$$

and the Koszul complex going backwards

$$\mathbb{P}_{k+1}(D) \xleftarrow{\boldsymbol{x} \cdot} \mathbb{P}_k(D; \mathbb{R}^3) \xleftarrow{\boldsymbol{x} \times} \mathbb{P}_{k-1}(D; \mathbb{R}^3) \xleftarrow{\boldsymbol{x}} \mathbb{P}_{k-2}(D) \leftarrow 0. \qquad (3.4.2)$$

Those two complexes can be combined into one

$$\mathbb{R} \xrightarrow{\subseteq} \mathbb{P}_{k+1}(D) \underset{\boldsymbol{x} \cdot}{\overset{\nabla}{\rightleftarrows}} \mathbb{P}_k(D; \mathbb{R}^3) \underset{\boldsymbol{x} \times}{\overset{\nabla \times}{\rightleftarrows}} \mathbb{P}_{k-1}(D; \mathbb{R}^3) \underset{\boldsymbol{x}}{\overset{\nabla \cdot}{\rightleftarrows}} \mathbb{P}_{k-2}(D) \underset{\supset}{\longleftarrow} 0 \, . \qquad (3.4.3)$$

We refer to [8] for a systematical derivation of (3.4.1)–(3.4.2) and focus on two decompositions of vector polynomial spaces $\mathbb{P}_k(D; \mathbb{R}^3)$ based on (3.4.3). One subspace is the range space of a differential operator in the de Rham complex from left to right and another is the range space of the Koszul operator.

The first one is, for an integer $k \geq 1$,

$$\mathbb{P}_k(D; \mathbb{R}^3) = \nabla \mathbb{P}_{k+1}(D) \oplus \boldsymbol{x} \times \mathbb{P}_{k-1}(D; \mathbb{R}^3),$$

which leads to

$$\mathbb{P}_k(D; \mathbb{R}^3) = \nabla \mathbb{H}_{k+1}(D) \oplus \mathscr{N}\mathscr{D}_{k-1},$$

where

$$\mathscr{N}\mathscr{D}_{k-1} := \mathbb{P}_{k-1}(D; \mathbb{R}^3) \oplus \boldsymbol{x} \times \mathbb{H}_{k-1}(D; \mathbb{R}^3) = \mathbb{P}_{k-1}(D; \mathbb{R}^3) + \boldsymbol{x} \times \mathbb{P}_{k-1}(D; \mathbb{R}^3)$$

is the first family of Nédélec element [39]. Note that the component $\boldsymbol{x} \times \mathbb{H}_{k-1}(D; \mathbb{R}^3)$ can be also written as $\ker(\boldsymbol{x} \cdot) \cap \mathbb{H}_k(D; \mathbb{R}^3)$ by the exactness of the Koszul complex (3.4.2), which unifies the notation in both two and three dimensions.

The second decomposition is, for an integer $k \geq 1$,

$$\mathbb{P}_k(D; \mathbb{R}^3) = \nabla \times \mathbb{P}_{k+1}(D; \mathbb{R}^3) \oplus \boldsymbol{x}\mathbb{P}_{k-1}(D), \qquad (3.4.4)$$

which leads to

$$\mathbb{P}_k(D; \mathbb{R}^3) = \nabla \times \mathbb{H}_{k+1}(D; \mathbb{R}^3) \oplus \mathscr{R}\mathscr{T}_{k-1},$$

where

$$\mathscr{R}\mathscr{T}_{k-1} := \mathbb{P}_{k-1}(D; \mathbb{R}^3) \oplus \boldsymbol{x}\mathbb{H}_{k-1}(D) = \mathbb{P}_{k-1}(D; \mathbb{R}^3) + \boldsymbol{x}\mathbb{P}_{k-1}(D)$$

is the Raviart-Thomas face element in three dimensions [40, 43].

3.4.2   Hessian Polynomial Complexes

By the Euler's formula, for an integer $k \geq 0$,

$$\boldsymbol{x} \cdot \nabla q = kq \quad \forall\, q \in \mathbb{H}_k(D). \tag{3.4.5}$$

Due to (3.4.5), for any $q \in \mathbb{P}_k(D)$ satisfying $\boldsymbol{x} \cdot \nabla q + q = 0$, we have $q = 0$. And

$$\mathbb{P}_k(D) \cap \ker(\boldsymbol{x} \cdot \nabla) = \mathbb{P}_0(D), \tag{3.4.6}$$

$$\mathbb{P}_k(D) \cap \ker(\boldsymbol{x} \cdot \nabla + \ell) = 0 \tag{3.4.7}$$

for any positive number ℓ.

Lemma 3.3 *The operator* $\mathrm{div} : \mathrm{dev}(\mathbb{P}_k(D; \mathbb{R}^3)\boldsymbol{x}^\mathsf{T}) \to \mathbb{P}_k(D; \mathbb{R}^3)$ *is bijective.*

Proof Since $\mathrm{div}\, \mathrm{dev}(\mathbb{P}_k(D; \mathbb{R}^3)\boldsymbol{x}^\mathsf{T}) \subseteq \mathbb{P}_k(D; \mathbb{R}^3)$ and

$$\dim \mathrm{dev}(\mathbb{P}_k(D; \mathbb{R}^3)\boldsymbol{x}^\mathsf{T}) = \dim \mathbb{P}_k(D; \mathbb{R}^3),$$

it suffices to show that $\mathrm{div} : \mathrm{dev}(\mathbb{P}_k(D; \mathbb{R}^3)\boldsymbol{x}^\mathsf{T}) \to \mathbb{P}_k(D; \mathbb{R}^3)$ is injective.

For any $\boldsymbol{q} \in \mathbb{P}_k(D; \mathbb{R}^3)$ satisfying $\mathrm{div}\, \mathrm{dev}(\boldsymbol{q}\boldsymbol{x}^\mathsf{T}) = 0$, we have

$$\mathrm{div}(\boldsymbol{q}\boldsymbol{x}^\mathsf{T}) - \frac{1}{3}\nabla(\boldsymbol{x}^\mathsf{T}\boldsymbol{q}) = \mathrm{div}(\mathrm{dev}(\boldsymbol{q}\boldsymbol{x}^\mathsf{T})) = \boldsymbol{0}. \tag{3.4.8}$$

Since $\boldsymbol{x}^\mathsf{T}\,\mathrm{div}(\boldsymbol{q}\boldsymbol{x}^\mathsf{T}) = (\boldsymbol{x} \cdot \nabla)(\boldsymbol{x}^\mathsf{T}\boldsymbol{q}) + 2\boldsymbol{x}^\mathsf{T}\boldsymbol{q}$, we obtain

$$\left(\boldsymbol{x} \cdot \nabla + \frac{5}{3}\right)(\boldsymbol{x}^\mathsf{T}\boldsymbol{q}) = \boldsymbol{x}^\mathsf{T}\left(\mathrm{div}(\boldsymbol{q}\boldsymbol{x}^\mathsf{T}) - \frac{1}{3}\nabla(\boldsymbol{x}^\mathsf{T}\boldsymbol{q})\right) = 0.$$

By (3.4.7), we have $\boldsymbol{x}^\mathsf{T}\boldsymbol{q} = 0$. In turn, it follows from (3.4.8) that $(\boldsymbol{x} \cdot \nabla + 3)\boldsymbol{q} = \mathrm{div}(\boldsymbol{q}\boldsymbol{x}^\mathsf{T}) = \boldsymbol{0}$, which together with (3.4.7) gives $\boldsymbol{q} = \boldsymbol{0}$.   □

Lemma 3.4 *For $k \in \mathbb{N}$, $k \geq 2$, the polynomial Hessian complex*

$$\mathbb{P}_1(D) \overset{\subseteq}{\rightarrow} \mathbb{P}_{k+2}(D) \xrightarrow{\text{hess}} \mathbb{P}_k(D; \mathbb{S}) \xrightarrow{\text{curl}} \mathbb{P}_{k-1}(D; \mathbb{T}) \xrightarrow{\text{div}} \mathbb{P}_{k-2}(D; \mathbb{R}^3) \rightarrow \mathbf{0}$$

$$(3.4.9)$$

is exact.

Proof It is obvious $\nabla^2(\mathbb{P}_{k+2}(D)) \subseteq \mathbb{P}_k(D; \mathbb{S}) \cap \ker(\text{curl})$. By identity (3.2.2),

$$\text{tr}(\text{curl } \boldsymbol{\tau}) = 2 \text{ div}(\text{vskw } \boldsymbol{\tau}) \quad \forall \, \boldsymbol{\tau} \in \boldsymbol{H}^1(D; \mathbb{M}).$$

Hence we have $\text{curl}(\mathbb{P}_k(D; \mathbb{S})) \subseteq \mathbb{P}_{k-1}(D; \mathbb{T}) \cap \ker(\text{div})$. Therefore (3.4.9) is a complex.

We then verify this complex is exact. By the polynomial version of de Rham complex (3.4.1), we have $\text{hess } \mathbb{P}_{k+2}(D) = \mathbb{P}_k(D; \mathbb{S}) \cap \ker(\text{curl})$, and

$$\dim \text{curl} \, \mathbb{P}_k(D; \mathbb{S}) = \dim \mathbb{P}_k(D; \mathbb{S}) - \dim \text{hess } \mathbb{P}_{k+2}(D) = \frac{1}{6}k(k+1)(5k+19).$$

Thanks to Lemma 3.3, we get $\text{div} \, \mathbb{P}_{k-1}(D; \mathbb{T}) = \mathbb{P}_{k-2}(D; \mathbb{R}^3)$. And then

$$\dim(\mathbb{P}_{k-1}(D; \mathbb{T}) \cap \ker(\text{div})) = \dim \mathbb{P}_{k-1}(D; \mathbb{T}) - \dim \mathbb{P}_{k-2}(D; \mathbb{R}^3) = \dim \text{curl} \, \mathbb{P}_k(D; \mathbb{S}),$$

which means $\mathbb{P}_{k-1}(D; \mathbb{T}) \cap \ker(\text{div}) = \text{curl} \, \mathbb{P}_k(D; \mathbb{S})$. Therefore the complex (3.4.9) is exact. $\square$

Define operator $\pi_1 : \mathscr{C}^1(D) \rightarrow \mathbb{P}_1(D)$ as

$$\pi_1 v := v(0, 0, 0) + \boldsymbol{x}^{\mathsf{T}}(\nabla v)(0, 0, 0).$$

It is exactly the first order Taylor polynomial of v at $(0, 0, 0)$. Obviously

$$\pi_1 v = v \quad \forall \, v \in \mathbb{P}_1(D). \tag{3.4.10}$$

We present the following Koszul-type complex associated to the Hessian complex.

Lemma 3.5 *For $k \in \mathbb{N}$, $k \geq 2$, the polynomial complex*

$$0 \overset{\subseteq}{\rightarrow} \mathbb{P}_{k-2}(D; \mathbb{R}^3) \xrightarrow{\text{dev}(\boldsymbol{v}\boldsymbol{x}^{\mathsf{T}})} \mathbb{P}_{k-1}(D; \mathbb{T}) \xrightarrow{\text{sym}(\boldsymbol{\tau} \times \boldsymbol{x})} \mathbb{P}_k(D; \mathbb{S}) \xrightarrow{\boldsymbol{x}^{\mathsf{T}}\boldsymbol{\tau}\boldsymbol{x}} \mathbb{P}_{k+2}(D) \xrightarrow{\pi_1} \mathbb{P}_1(D)$$

$$(3.4.11)$$

is exact.

Proof For any $\boldsymbol{v} \in \mathbb{P}_{k-2}(D; \mathbb{R}^3)$, it follows

$$\mathrm{sym}((\mathrm{dev}(\boldsymbol{v}\boldsymbol{x}^\mathsf{T})) \times \boldsymbol{x}) = \mathrm{sym}((\boldsymbol{v}\boldsymbol{x}^\mathsf{T}) \times \boldsymbol{x}) - \frac{1}{3}(\boldsymbol{x}^\mathsf{T}\boldsymbol{v})\,\mathrm{sym}(\boldsymbol{I} \times \boldsymbol{x}) = \boldsymbol{0}.$$

For any $\boldsymbol{\tau} \in \mathbb{P}_{k-1}(D; \mathbb{T})$, we have

$$\boldsymbol{x}^\mathsf{T}(\mathrm{sym}(\boldsymbol{\tau} \times \boldsymbol{x}))\boldsymbol{x} = \boldsymbol{x}^\mathsf{T}(\boldsymbol{\tau} \times \boldsymbol{x})\boldsymbol{x} = 0.$$

It is trivial that $\pi_1(\boldsymbol{x}^\mathsf{T}\boldsymbol{\tau}\boldsymbol{x}) = 0$ for any $\boldsymbol{\tau} \in \mathbb{P}_k(D; \mathbb{S})$. Thus (3.4.11) is a complex.

Next we prove that the complex (3.4.11) is exact. By the Taylor's theorem, we get $\mathbb{P}_{k+2}(D) \cap \ker(\pi_1) = \boldsymbol{x}^\mathsf{T}\mathbb{P}_k(D; \mathbb{S})\boldsymbol{x}$, and

$$\dim \boldsymbol{x}^\mathsf{T}\mathbb{P}_k(D; \mathbb{S})\boldsymbol{x} = \dim \mathbb{P}_{k+2}(D) - 4 = \frac{1}{6}(k+5)(k+4)(k+3) - 4.$$

For any $\boldsymbol{\tau} \in \mathbb{P}_k(D; \mathbb{S})$ satisfying $\boldsymbol{x}^\mathsf{T}\boldsymbol{\tau}\boldsymbol{x} = 0$, there exists $\boldsymbol{q} \in \mathbb{P}_{k-1}(D; \mathbb{R}^3)$ such that $\boldsymbol{\tau}\boldsymbol{x} = \boldsymbol{q} \times \boldsymbol{x} = (\mathrm{mskw}\,\boldsymbol{q})\boldsymbol{x}$, that is $(\boldsymbol{\tau} - \mathrm{mskw}\,\boldsymbol{q})\boldsymbol{x} = \boldsymbol{0}$. As a result, there exists $\boldsymbol{\varsigma} \in \mathbb{P}_k(D; \mathbb{M})$ such that

$$\boldsymbol{\tau} = \mathrm{mskw}\,\boldsymbol{q} + \boldsymbol{\varsigma} \times \boldsymbol{x}.$$

From the symmetry of $\boldsymbol{\tau}$, we obtain

$$\boldsymbol{\tau} = \mathrm{sym}(\mathrm{mskw}\,\boldsymbol{q} + \boldsymbol{\varsigma}\times\boldsymbol{x}) = \mathrm{sym}(\boldsymbol{\varsigma}\times\boldsymbol{x}) = \mathrm{sym}(\mathrm{dev}\,\boldsymbol{\varsigma}\times\boldsymbol{x}) \in \mathrm{sym}(\mathbb{P}_{k-1}(D; \mathbb{T})\times\boldsymbol{x}).$$

Hence

$$\dim \mathrm{sym}(\mathbb{P}_{k-1}(D; \mathbb{T}) \times \boldsymbol{x}) = \mathbb{P}_k(D; \mathbb{S}) - \dim \boldsymbol{x}^\mathsf{T}\mathbb{P}_k(D; \mathbb{S})\boldsymbol{x} = \frac{1}{6}k(k+1)(5k+19).$$

Since $\dim \mathrm{dev}(\mathbb{P}_{k-2}(D; \mathbb{R}^3)\boldsymbol{x}^\mathsf{T}) = \dim \mathbb{P}_{k-2}(D; \mathbb{R}^3)$, we have

$$\dim \mathbb{P}_{k-1}(D; \mathbb{T}) = \dim \mathrm{dev}(\mathbb{P}_{k-2}(D; \mathbb{R}^3)\boldsymbol{x}^\mathsf{T}) + \dim \mathrm{sym}(\mathbb{P}_{k-1}(D; \mathbb{T}) \times \boldsymbol{x}).$$

Thus the complex (3.4.11) is exact.   □

Combining the two complexes (3.4.9) and (3.4.11) yields

$$\mathbb{P}_1(D) \underset{\pi_1}{\overset{\subset}{\rightleftarrows}} \mathbb{P}_{k+2}(D) \underset{\boldsymbol{x}^\mathsf{T}\boldsymbol{\tau}\boldsymbol{x}}{\overset{\mathrm{hess}}{\rightleftarrows}} \mathbb{P}_k(D; \mathbb{S}) \underset{\mathrm{sym}(\boldsymbol{\tau}\times\boldsymbol{x})}{\overset{\mathrm{curl}}{\rightleftarrows}} \mathbb{P}_{k-1}(D; \mathbb{T}) \underset{\mathrm{dev}(\boldsymbol{v}\boldsymbol{x}^\mathsf{T})}{\overset{\mathrm{div}}{\rightleftarrows}} \mathbb{P}_{k-2}(D; \mathbb{R}^3) \underset{\supset}{\rightleftarrows} \boldsymbol{0} .$$

Unlike the Koszul complex for vector functions, we do not have the identity property applied to homogenous polynomials. Fortunately decomposition of polynomial spaces using Koszul and differential operators still holds.

It follows from (3.4.10) and the complex (3.4.11) that

$$\mathbb{P}_{k+2}(D) = \boldsymbol{x}^{\mathsf{T}} \mathbb{P}_k(D; \mathbb{S}) \boldsymbol{x} \oplus \mathbb{P}_1(D), \quad k \geq 0.$$

Then we give the following decompositions for the polynomial tensor spaces $\mathbb{P}_k(D; \mathbb{S})$ and $\mathbb{P}_{k-1}(D; \mathbb{T})$. Again one subspace is the range space of a differential operator in the Hessian complex from left-to-right and another is the range space in the Koszul type complex from right-to-left.

Lemma 3.6 *For $k \in \mathbb{N}$, we have the decompositions*

$$\mathbb{P}_k(D; \mathbb{S}) = \text{hess } \mathbb{P}_{k+2}(D) \oplus \text{sym}(\mathbb{P}_{k-1}(D; \mathbb{T}) \times \boldsymbol{x}) \quad k \geq 1, \qquad (3.4.12)$$

$$\mathbb{P}_{k-1}(D; \mathbb{T}) = \text{curl } \mathbb{P}_k(D; \mathbb{S}) \oplus \text{dev}(\mathbb{P}_{k-2}(D; \mathbb{R}^3) \boldsymbol{x}^{\mathsf{T}}) \quad k \geq 2. \qquad (3.4.13)$$

Proof Noting that the dimension of space in the left hand side is the summation of the dimension of two subspaces in the right hand side in (3.4.12) and (3.4.13), we only need to prove the sum is direct. The direct sum of (3.4.13) follows from Lemma 3.3. We then focus on (3.4.12).

For any $\boldsymbol{\tau} = \nabla^2 q$ with $q \in \mathbb{P}_{k+2}(D)$ satisfying $\boldsymbol{\tau} \in \text{sym}(\mathbb{P}_{k-1}(D; \mathbb{T}) \times \boldsymbol{x})$, it follows from the fact $(\boldsymbol{x} \cdot \nabla)\boldsymbol{x} = \boldsymbol{x}$ that

$$(\boldsymbol{x} \cdot \nabla)(\boldsymbol{x} \cdot \nabla q - q) = (\boldsymbol{x} \cdot \nabla)(\boldsymbol{x} \cdot \nabla q) - \boldsymbol{x} \cdot \nabla q = \boldsymbol{x}^{\mathsf{T}}((\boldsymbol{x} \cdot \nabla)\nabla q) = \boldsymbol{x}^{\mathsf{T}}(\nabla^2 q)\boldsymbol{x} = 0.$$

Apply (3.4.6) to get $\boldsymbol{x} \cdot \nabla q - q \in \mathbb{P}_0(K)$, which together with (3.4.5) gives $q \in \mathbb{P}_1(D)$. Thus the decomposition (3.4.12) holds. $\qquad \square$

When $D \subset \mathbb{R}^2$, the Hessian polynomial complex in two dimensions

$$\mathbb{P}_1(D) \overset{\subseteq}{\to} \mathbb{P}_{k+2}(D) \xrightarrow{\text{hess}} \mathbb{P}_k(D; \mathbb{S}) \xrightarrow{\text{rot}} \mathbb{P}_{k-1}(D; \mathbb{R}^2) \to 0 \qquad (3.4.14)$$

has been proved in [22], which is a rotation of the elasticity polynomial complex [7].

3.4.3 Divdiv Polynomial Complexes

In this subsection we present divdiv polynomial complexes derived in [22, 23] and refer to [23] for proofs.

Lemma 3.7 *For $k \in \mathbb{N}, k \geq 2$, the polynomial complex*

$$\boldsymbol{RT} \overset{\subseteq}{\to} \mathbb{P}_{k+2}(D; \mathbb{R}^3) \xrightarrow{\text{dev grad}} \mathbb{P}_{k+1}(D; \mathbb{T}) \xrightarrow{\text{sym curl}} \mathbb{P}_k(D; \mathbb{S}) \xrightarrow{\text{div div}} \mathbb{P}_{k-2}(D) \to 0 \qquad (3.4.15)$$

is exact.

Define operator $\boldsymbol{\pi}_{RT} : \mathscr{C}^1(D; \mathbb{R}^3) \to \boldsymbol{RT}$ as

$$\boldsymbol{\pi}_{RT}\boldsymbol{v} := \boldsymbol{v}(0,0,0) + \frac{1}{3}(\operatorname{div}\boldsymbol{v})(0,0,0)\boldsymbol{x}.$$

Apparently

$$\boldsymbol{\pi}_{RT}\boldsymbol{v} = \boldsymbol{v} \quad \forall\, \boldsymbol{v} \in \boldsymbol{RT}. \tag{3.4.16}$$

We have the following Koszul-type complex.

Lemma 3.8 *For $k \in \mathbb{N}, k \geq 2$, the polynomial complex*

$$0 \xrightarrow{\subset} \mathbb{P}_{k-2}(D) \xrightarrow{\boldsymbol{x}\boldsymbol{x}^\mathsf{T}} \mathbb{P}_k(D; \mathbb{S}) \xrightarrow{\times \boldsymbol{x}} \mathbb{P}_{k+1}(D; \mathbb{T}) \xrightarrow{\cdot \boldsymbol{x}} \mathbb{P}_{k+2}(D; \mathbb{R}^3) \xrightarrow{\boldsymbol{\pi}_{RT}} \boldsymbol{RT} \to \boldsymbol{0} \tag{3.4.17}$$

is exact.

Those two complexes (3.4.15) and (3.4.17) are connected as

$$\boldsymbol{RT} \underset{\boldsymbol{\pi}_{RT}}{\overset{\subset}{\rightleftarrows}} \mathbb{P}_{k+2}(D; \mathbb{R}^3) \underset{\cdot \boldsymbol{x}}{\overset{\operatorname{dev\,grad}}{\rightleftarrows}} \mathbb{P}_{k+1}(D; \mathbb{T}) \underset{\times \boldsymbol{x}}{\overset{\operatorname{sym\,curl}}{\rightleftarrows}} \mathbb{P}_k(D; \mathbb{S}) \underset{\boldsymbol{x}\boldsymbol{x}^\mathsf{T}}{\overset{\operatorname{div\,div}}{\rightleftarrows}} \mathbb{P}_{k-2}(D) \underset{\supset}{\rightleftarrows} 0 .$$

It follows from (3.4.16) and the complex (3.4.17) that

$$\mathbb{P}_k(D; \mathbb{R}^3) = (\mathbb{P}_{k-1}(D; \mathbb{T}) \cdot \boldsymbol{x}) \oplus \boldsymbol{RT} \quad k \geq 1.$$

We then move to the space $\mathbb{P}_{k+1}(D; \mathbb{T})$ and $\mathbb{P}_k(D; \mathbb{S})$.

Lemma 3.9 *We have the decompositions*

$$\mathbb{P}_k(D; \mathbb{T}) = (\mathbb{P}_{k-1}(D; \mathbb{S}) \times \boldsymbol{x}) \oplus \operatorname{dev\,grad} \mathbb{P}_{k+1}(D; \mathbb{R}^3) \quad k \geq 1,$$

and

$$\mathbb{P}_k(D; \mathbb{S}) = \operatorname{sym\,curl} \mathbb{P}_{k+1}(D; \mathbb{T}) \oplus \boldsymbol{x}\boldsymbol{x}^\mathsf{T}\mathbb{P}_{k-2}(D) \quad k \geq 2.$$

When $D \subset \mathbb{R}^2$, the divdiv polynomial complex in two dimensions

$$\boldsymbol{RT} \xrightarrow{\subset} \mathbb{P}_{k+1}(D; \mathbb{R}^2) \xrightarrow{\operatorname{sym\,curl}} \mathbb{P}_k(D; \mathbb{S}) \xrightarrow{\operatorname{div\,div}} \mathbb{P}_{k-2}(D) \to 0 \tag{3.4.18}$$

has been proved in [22] and used to construct a finite element divdiv complex in two dimensions.

3.5   A Conforming Virtual Element Hessian Complex

In this section we shall construct virtual element and finite element spaces and obtain a discrete Hessian complex ($k \geq 3$):

$$\mathbb{P}_1(\Omega) \overset{\subset}{\rightarrow} W_h \overset{\nabla^2}{\longrightarrow} \mathbf{\Sigma}_h \overset{\text{curl}}{\longrightarrow} \mathbf{V}_h \overset{\text{div}}{\longrightarrow} \mathscr{Q}_h \rightarrow 0, \qquad (3.5.1)$$

where

- W_h is an $H^2(\Omega)$-conforming virtual element space containing piecewise $\mathbb{P}_{k+2}$ polynomials;
- $\mathbf{\Sigma}_h$ is an $\boldsymbol{H}(\text{curl}, \Omega; \mathbb{S})$-conforming virtual element space containing piecewise $\mathbb{P}_k$ polynomials;
- $\boldsymbol{V}_h$ is an $\boldsymbol{H}(\text{div}, \Omega; \mathbb{T})$-conforming finite element space containing piecewise $\mathbb{P}_{k-1}$ polynomials;
- $\mathscr{Q}_h$ is piecewise $\mathbb{P}_{k-2}(\mathbb{R}^3)$ polynomial which is obviously conforming to $L^2(\Omega)$.

The domain Ω is decomposed into a triangulation $\mathscr{T}_h$ consisting of tetrahedrons. That is each element $K \in \mathscr{T}_h$ is a tetrahedron. Extension to general polyhedral meshes will be explored in a future work.

In [32], a finite element Hessian complex has been constructed and the lowest polynomial degree for $(W_h, \mathbf{\Sigma}_h, \boldsymbol{V}_h, \mathscr{Q}_h)$ is $(9, 7, 6, 5)$ and ours is $(5, 3, 2, 1)$ but with a few additional virtual shape functions in W_h and $\mathbf{\Sigma}_h$.

For each element $K \in \mathscr{T}_h$, denote by $\boldsymbol{n}_K$ the unit outward normal vector to ∂K, which will be abbreviated as $\boldsymbol{n}$. Let $\mathscr{F}_h$, $\mathscr{E}_h$ and $\mathscr{V}_h$ be the union of all faces, edges and vertices of the partition $\mathscr{T}_h$, respectively. For any $F \in \mathscr{F}_h$, fix a unit normal vector $\boldsymbol{n}_F$. For any $e \in \mathscr{E}_h$, fix a unit tangent vector $\boldsymbol{t}_e$ and two unit normal vectors $\boldsymbol{n}_{e,1}$ and $\boldsymbol{n}_{e,2}$, which will be abbreviated as $\boldsymbol{n}_1$ and $\boldsymbol{n}_2$ without causing any confusions. For K being a polyhedron, denote by $\mathscr{F}(K)$, $\mathscr{E}(K)$ and $\mathscr{V}(K)$ the set of all faces, edges and vertices of K, respectively. For any $F \in \mathscr{F}_h$, let $\mathscr{E}(F)$ and $\mathscr{V}(F)$ be the set of all edges and vertices of F, respectively. For each $e \in \mathscr{E}(F)$, denote by $\boldsymbol{n}_{F,e}$ the unit vector being parallel to F and outward normal to ∂F.

3.5.1 $H(\text{div})$-Conforming Element for Trace-Free Tensors

For an integer $k \geq 3$, we choose $\mathbb{P}_{k-1}(K; \mathbb{T})$ as the shape function space. Its trace $\boldsymbol{vn}$ on each face F is in $\mathbb{P}_{k-1}(F; \mathbb{R}^3)$. In the classic $H(\text{div})$ element for vector functions, such trace can be determined by the face moments $\int_F (\boldsymbol{vn}) \cdot \boldsymbol{q}$ for $\boldsymbol{q} \in \mathbb{P}_{k-1}(F; \mathbb{R}^3)$. For the tensor polynomial with additional structure, e.g., here is the trace-free, face moments cannot reflect to this property. One fix is to introduce the nodal continuity of each component of the tensor so that the structure of the tensor is utilized.

For any $F \in \mathscr{F}(K)$, let $\mathbb{P}_{k-1,2}^{\perp}(F) \subseteq \mathbb{P}_{k-1}(F)$ be the L^2-orthogonal complement space of $\mathbb{P}_2(F)$ in $\mathbb{P}_{k-1}(F)$ with respect to the L^2-inner product $(\cdot, \cdot)_F$ on face F. Denote by $\mathbb{P}_{k-1,2}^{\perp}(F; \mathbb{R}^d)$ the vector version of $\mathbb{P}_{k-1,2}^{\perp}(F)$ with $d = 2, 3$. Let $\mathbb{P}_{k-2,\mathrm{RT}}^{\perp}(K; \mathbb{R}^3) \subseteq \mathbb{P}_{k-2}(K; \mathbb{R}^3)$ be the L^2-orthogonal complement space of $\boldsymbol{RT}$ in $\mathbb{P}_{k-2}(K; \mathbb{R}^3)$ with respect to the inner product $(\cdot, \cdot)_K$.

Lemma 3.10 *Let $F \in \mathscr{F}(K)$ be a triangular face and $v \in \mathbb{P}_{k-1}(F)$. If*

$$v(a_1) = v(a_2) = v(a_3) = 0, \quad (v, q)_F = 0 \quad \forall\, q \in \mathbb{P}_1(F) \oplus \mathbb{P}_{k-1,2}^{\perp}(F)$$

with a_1, a_2 and a_3 being the vertices of triangle F, then $v = 0$.

Proof Since $v \in \mathbb{P}_{k-1}(F)$ and $(v, q)_F = 0$ for all $q \in \mathbb{P}_{k-1,2}^{\perp}(F)$, we get $v \in \mathbb{P}_2(F)$. Let $(\lambda_1, \lambda_2, \lambda_3)$ be the barycentric coordinate of point $\boldsymbol{x}$ with respect to F. Since $v(a_1) = v(a_2) = v(a_3) = 0$, we have $v = c_1 \lambda_2 \lambda_3 + c_2 \lambda_3 \lambda_1 + c_3 \lambda_1 \lambda_2$, where c_1, c_2 and c_3 are constants. Now taking $q = \lambda_i$ with $i = 1, 2, 3$, we obtain

$$\frac{1}{60} |F| \begin{pmatrix} 1 & 2 & 2 \\ 2 & 1 & 2 \\ 2 & 2 & 1 \end{pmatrix} \begin{pmatrix} c_1 \\ c_2 \\ c_3 \end{pmatrix} = \begin{pmatrix} 0 \\ 0 \\ 0 \end{pmatrix}.$$

Noting that the coefficient matrix is invertible, it follows $c_1 = c_2 = c_3 = 0$. $\square$

Next we use the $H(\mathrm{div}; \mathbb{T})$ polynomial bubble function space introduced in [32] to characterize the interior part. Denote by

$$\mathbb{B}_{k-1}(K; \mathbb{T}) := \mathbb{P}_{k-1}(K; \mathbb{T}) \cap \boldsymbol{H}_0(\mathrm{div}, K; \mathbb{T}),$$

where $\boldsymbol{H}_0(\mathrm{div}, K; \mathbb{T}) := \{\boldsymbol{\tau} \in \boldsymbol{H}(\mathrm{div}, K; \mathbb{T}) : \boldsymbol{\tau n}|_{\partial K} = \boldsymbol{0}\}$. In [32], a constructive characterization of $\mathbb{B}_{k-1}(K; \mathbb{T})$ is given by

$$\mathbb{B}_{k-1}(K; \mathbb{T}) = \sum_{i=1}^{4} \sum_{\substack{1 \leq j < l \leq 4 \\ j,l \neq i}} \lambda_j \lambda_l \mathbb{P}_{k-3}(K) \boldsymbol{n}_i \boldsymbol{t}_{j,l}^{\mathsf{T}}, \tag{3.5.2}$$

where $(\lambda_1, \lambda_2, \lambda_3, \lambda_4)$ is the barycentric coordinate of point $\boldsymbol{x}$ with respect to K, and $\boldsymbol{t}_{j,l} := \boldsymbol{x}_l - \boldsymbol{x}_j$ with the set of vertices $\mathscr{V}(K) := \{\boldsymbol{x}_1, \boldsymbol{x}_2, \boldsymbol{x}_3, \boldsymbol{x}_4\}$. That is on each face use the normal vector and an edge vector to form a traceless matrix and extend to the whole element by the scalar edge bubble function. It was proved in [32] that

$$\mathrm{div}\, \mathbb{B}_{k-1}(K; \mathbb{T}) = \mathbb{P}_{k-2,\mathrm{RT}}^{\perp}(K; \mathbb{R}^3). \tag{3.5.3}$$

The sum in (3.5.2), however, is not a direct sum. We present a refined characterization of the bubble function below.

Lemma 3.11 *We have*

$$
\mathbb{B}_{k-1}(K; \mathbb{T}) = \sum_{i=1}^{4} \bigoplus_{\substack{1 \leq j < l \leq 4 \\ j,l \neq i}} \lambda_j \lambda_l \mathbb{P}_{k-3}^{F_{ijl}}(K) \boldsymbol{n}_i \boldsymbol{t}_{j,l}^{\mathsf{T}} \oplus \sum_{i=1}^{4} \sum_{\substack{1 \leq j < l \leq 4 \\ j,l \neq i}} b_{F_i} \mathbb{P}_{k-4}(K) \boldsymbol{n}_i \boldsymbol{t}_{j,l}^{\mathsf{T}},
$$

(3.5.4)

where b_{F_i} is the cubic face bubble function corresponding to face F_i and

$$
\mathbb{P}_{k-3}^{F_{ijl}}(K) := span\{\lambda_i^{\alpha_1} \lambda_j^{\alpha_2} \lambda_l^{\alpha_3} : \alpha_1, \alpha_2, \alpha_3 \in \mathbb{N}, \alpha_1 + \alpha_2 + \alpha_3 = k - 3\}.
$$

Proof By $\lambda_j \lambda_l \mathbb{P}_{k-3}(K) = \lambda_j \lambda_l \mathbb{P}_{k-3}^{F_{ijl}}(K) + b_{F_i} \mathbb{P}_{k-4}(K)$, it follows from (3.5.2) that

$$
\mathbb{B}_{k-1}(K; \mathbb{T}) = \sum_{i=1}^{4} \sum_{\substack{1 \leq j < l \leq 4 \\ j,l \neq i}} \lambda_j \lambda_l \mathbb{P}_{k-3}^{F_{ijl}}(K) \boldsymbol{n}_i \boldsymbol{t}_{j,l}^{\mathsf{T}} + \sum_{i=1}^{4} \sum_{\substack{1 \leq j < l \leq 4 \\ j,l \neq i}} b_{F_i} \mathbb{P}_{k-4}(K) \boldsymbol{n}_i \boldsymbol{t}_{j,l}^{\mathsf{T}}.
$$

Next we prove

$$
\sum_{\substack{1 \leq j < l \leq 4 \\ j,l \neq i}} \lambda_j \lambda_l \mathbb{P}_{k-3}^{F_{ijl}}(K) \boldsymbol{t}_{j,l} + \sum_{\substack{1 \leq j < l \leq 4 \\ j,l \neq i}} b_{F_i} \mathbb{P}_{k-4}(K) \boldsymbol{t}_{j,l}
$$

$$
= \bigoplus_{\substack{1 \leq j < l \leq 4 \\ j,l \neq i}} \lambda_j \lambda_l \mathbb{P}_{k-3}^{F_{ijl}}(K) \boldsymbol{t}_{j,l} \oplus \sum_{\substack{1 \leq j < l \leq 4 \\ j,l \neq i}} b_{F_i} \mathbb{P}_{k-4}(K) \boldsymbol{t}_{j,l}.
$$

Consider $i = 4$. Assume there exist $q_{jl} \in \mathbb{P}_{k-3}^{F_{4jl}}(K)$ and $p_{jl} \in \mathbb{P}_{k-4}(K)$ for $1 \leq j < l \leq 3$ such that

$$
\lambda_1 \lambda_2 q_{12} \boldsymbol{t}_{1,2} + \lambda_1 \lambda_3 q_{13} \boldsymbol{t}_{1,3} + \lambda_2 \lambda_3 q_{23} \boldsymbol{t}_{2,3} + b_{F_4} p_{12} \boldsymbol{t}_{1,2} + b_{F_4} p_{13} \boldsymbol{t}_{1,3} + b_{F_4} p_{23} \boldsymbol{t}_{2,3} = \boldsymbol{0}.
$$

Hence

$$
(\lambda_1 \lambda_2 q_{12} + \lambda_1 \lambda_3 q_{13} + b_{F_4}(p_{12} + p_{13})) \boldsymbol{t}_{1,2} + (\lambda_2 \lambda_3 q_{23} + \lambda_1 \lambda_3 q_{13} + b_{F_4}(p_{23} + p_{13})) \boldsymbol{t}_{2,3} = \boldsymbol{0},
$$

which implies

$$
\lambda_2 q_{12} + \lambda_3 q_{13} + \lambda_2 \lambda_3 (p_{12} + p_{13}) = 0, \quad \lambda_2 q_{23} + \lambda_1 q_{13} + \lambda_1 \lambda_2 (p_{23} + p_{13}) = 0.
$$

Therefore $q_{12} = q_{13} = q_{23} = 0$, as required. $\square$

By (3.5.4), we have

$$\dim \mathbb{B}_{k-1}(K; \mathbb{T}) = 12 \binom{k-1}{2} + 8 \binom{k-1}{3} = \frac{2}{3}(k-1)(k-2)(2k+3)$$

$$= \frac{2}{3}(2k^3 - 3k^2 - 5k + 6),$$

$$\dim(\mathbb{B}_{k-1}(K; \mathbb{T}) \cap \ker(\mathrm{div})) = \frac{1}{6}k(k+1)(5k-17) + 8 = \frac{1}{6}(5k^3 - 12k^2 - 17k) + 8.$$

Now we define an $H(\mathrm{div})$-conforming finite element for trace-free tensors with $k \geq 3$. Take $\mathbb{P}_{k-1}(K; \mathbb{T})$ as the space of shape functions. The degrees of freedom are given by

$$\boldsymbol{v}(\delta) \quad \forall \, \delta \in \mathscr{V}(K), \tag{3.5.5}$$

$$(\boldsymbol{v}\boldsymbol{n}, \boldsymbol{q})_F \quad \forall \, \boldsymbol{q} \in \mathbb{P}_1(F; \mathbb{R}^3) \oplus \mathbb{P}_{k-1,2}^{\perp}(F; \mathbb{R}^3), \, F \in \mathscr{F}(K), \tag{3.5.6}$$

$$(\boldsymbol{v}, \boldsymbol{q})_K \quad \forall \, \boldsymbol{q} \in \mathrm{dev\,grad}\,\mathbb{P}_{k-2}(K; \mathbb{R}^3) \oplus (\mathbb{B}_{k-1}(K; \mathbb{T}) \cap \ker(\mathrm{div})). \tag{3.5.7}$$

We can also replace the degree of freedom (3.5.7) by

$$(\boldsymbol{v}, \boldsymbol{q})_K \quad \forall \, \boldsymbol{q} \in \mathbb{B}_{k-1}(K; \mathbb{T}). \tag{3.5.8}$$

Thanks to the explicit formulation of bubble functions (3.5.2), the implementation using (3.5.8) will be easier. On the other hand, (3.5.7) will be helpful when defining discrete spaces for $\boldsymbol{H}(\mathrm{curl}, K; \mathbb{S})$.

Lemma 3.12 *The degrees of freedom* (3.5.5)–(3.5.7) *are unisolvent for* $\mathbb{P}_{k-1}(K; \mathbb{T})$.

Proof First of all the number of the degrees of freedom (3.5.5)–(3.5.7) is

$$32 + 36 + [6k(k+1) - 72] + \left[\frac{1}{2}(k^3 - k) - 4\right] + \frac{1}{6}(5k^3 - 12k^2 - 17k) + 8 = \frac{4}{3}k(k+1)(k+2),$$

which equals to $\dim \mathbb{P}_{k-1}(K; \mathbb{T})$.

Take any $\boldsymbol{v} \in \mathbb{P}_{k-1}(K; \mathbb{T})$ and suppose all the degrees of freedom (3.5.5)–(3.5.7) vanish. Applying Lemma 3.10 to each component of $\boldsymbol{v}\boldsymbol{n}$, we get $\boldsymbol{v} \in \mathbb{B}_{k-1}(K; \mathbb{T})$. It follows from the integration by parts and the first part of the degrees of freedom (3.5.7) that $\mathrm{div}\,\boldsymbol{v} = \boldsymbol{0}$, i.e., $\boldsymbol{v} \in \mathbb{B}_{k-1}(K; \mathbb{T}) \cap \ker(\mathrm{div})$. Finally we arrive at $\boldsymbol{v} = \boldsymbol{0}$ by using the second part of the degrees of freedom (3.5.7). $\qquad\square$

The global finite element space is

$$\boldsymbol{V}_h := \{\boldsymbol{v}_h \in \boldsymbol{H}(\mathrm{div}, \Omega; \mathbb{T}) : \boldsymbol{v}_h|_K \in \mathbb{P}_{k-1}(K; \mathbb{T}) \ \forall \ K \in \mathscr{T}_h, \text{ all degrees of}$$

$$\text{freedom } (3.5.5)\text{--}(3.5.7) \text{ are single-valued}\},$$

For $\boldsymbol{v} \in \boldsymbol{V}_h$, by Lemma 3.10, the trace $\boldsymbol{vn}|_F \in \mathbb{P}_{k-1}(F; \mathbb{R}^3)$ is determined uniquely by the degree of freedom (3.5.5)–(3.5.6). Therefore $\boldsymbol{V}_h \subset \boldsymbol{H}(\mathrm{div}, \Omega; \mathbb{T})$ is a conforming finite element space.

3.5.2 H^2-Conforming Virtual Element

To define an H^2-conforming virtual element in three dimensions, we shall adapt two dimensional H^2-conforming virtual elements constructed in [3, 17] and three dimensional C^1 virtual element in [13].

Define an H^2-conforming virtual element space on tetrahedron K

$$\widetilde{W}(K) := \{v \in H^2(K) : \Delta^2 v \in \mathbb{P}_{k-2}(K), \text{ both } v|_{\partial K} \text{ and } \nabla v|_{\partial K} \text{ are continuous},$$

$$v|_F \in \mathbb{P}_{k+2}(F), \partial_n v|_F \in \mathbb{P}_{k+1}(F) \text{ for each } F \in \mathscr{F}(K)\}.$$

The space of degrees of freedom $\mathscr{N}(K)$ consists of

$$v(\delta), \nabla v(\delta), \nabla^2 v(\delta) \quad \forall \, \delta \in \mathscr{V}(K), \tag{3.5.9}$$

$$(v, q)_e \quad \forall \, q \in \mathbb{P}_{k-4}(e), e \in \mathscr{E}(K), \tag{3.5.10}$$

$$(\partial_{n_i} v, q)_e \quad \forall \, q \in \mathbb{P}_{k-3}(e), e \in \mathscr{E}(K), i = 1, 2, \tag{3.5.11}$$

$$(v, q)_F \quad \forall \, q \in \mathbb{P}_{k-4}(F), F \in \mathscr{F}(K), \tag{3.5.12}$$

$$(\partial_n v, q)_F \quad \forall \, q \in \mathbb{P}_{k-2}(F), F \in \mathscr{F}(K), \tag{3.5.13}$$

$$(v, q)_K \quad \forall \, q \in \mathbb{P}_{k-2}(K). \tag{3.5.14}$$

The space $\widetilde{W}(K)$ is not empty as $\mathbb{P}_{k+2}(K) \subset \widetilde{W}(K)$. Its dimension is, however, not so clear from the definition. There is a compatible condition given implicitly in the definition of the local space $\widetilde{W}(K)$. As the trace of a function in $H^2(K)$, the boundary value $v|_{\partial K}$ and $\partial_n v|_{\partial K}$ are compatible in the sense that $\nabla v|_F = \nabla_F v + (\partial_n v)|_F \boldsymbol{n}_F$ should be continuous on edges [20, Theorem 5]. The degree of freedom $\nabla^2 v(\delta)$ is also questionable for a function $v \in H^2(K)$ only. In the classic finite element space, this is not an issue as shape functions are polynomials.

For a more rigorous verification of unisolvence, we introduce data space

$$\mathscr{D}(K) = \{(f, v_0, \boldsymbol{v}_1, \boldsymbol{v}_2, u_0^e, \boldsymbol{u}_1^e, u_0^F, u_1^F) : f \in \mathbb{P}_{k-2}(K), v_0 \in \mathbb{P}_0(\mathscr{V}(K)),$$

$$\boldsymbol{v}_1 \in \mathbb{P}_0(\mathscr{V}(K), \mathbb{R}^3), \boldsymbol{v}_2 \in \mathbb{P}_0(\mathscr{V}(K), \mathbb{S}), u_0^e \in \mathbb{P}_{k-4}(\mathscr{E}(K)),$$

$$\boldsymbol{u}_1^e \in \mathbb{P}_{k-3}(\mathscr{E}(K), \mathbb{R}^2), u_0^F \in \mathbb{P}_{k-4}(\mathscr{F}(K)), u_1^F \in \mathbb{P}_{k-2}(\mathscr{F}(K))\}.$$

Obviously $\dim \mathscr{D}(K) = \dim \mathscr{N}(K)$. For function $v \in \widetilde{W}(K) \cap C^2(K)$, the mapping

$$(\Delta^2 v, v(\delta), \nabla v(\delta), \nabla^2 v(\delta), Q_{k-4}^e v, Q_{k-3}^e (\partial_{n_i} v), Q_{k-4}^F v, Q_{k-2}^F (\partial_n v)),$$

for all $\delta \in \mathscr{V}(K)$, $e \in \mathscr{E}(K)$ and $F \in \mathscr{F}(K)$, is from $\widetilde{W}(K) \cap C^2(K) \to \mathscr{D}(K)$.

Let $\mathbb{P}_k(\partial K)$ be the function space which is continuous on the boundary ∂K and its restriction to each face is a polynomial of degree at most k. Given a data $(f, v_0, \boldsymbol{v}_1, \boldsymbol{v}_2, u_0^e, \boldsymbol{u}_1^e, u_0^F, u_1^F) \in \mathscr{D}(K)$, using $(v_0, \boldsymbol{v}_1, \boldsymbol{v}_2, u_0^e, \boldsymbol{u}_1^e, u_0^F)$, we can determine a $\mathbb{P}_{k+2}(F)$ Argyris element [4, 16] and consequently define a function $g_1 \in \mathbb{P}_{k+2}(\partial K)$. Similarly using $(\boldsymbol{v}_1, \boldsymbol{v}_2, \boldsymbol{u}_1^e, u_1^F)$, we can determine a $\mathbb{P}_{k+1}(F)$ Hermite element [28] and consequently a function $g_2 \in \mathbb{P}_{k+1}(\partial K)$. By the unisolvence of the Argyris element and Hermite element in two dimensions, we know (g_1, g_2) is uniquely determined by $(v_0, \boldsymbol{v}_1, \boldsymbol{v}_2, u_0^e, \boldsymbol{u}_1^e, u_0^F, u_1^F)$ and $(g_2|_F \boldsymbol{n}_F + \nabla_F (g_1|_F))|_e$ is single-valued across each edge $e \in \mathscr{E}(K)$.

Given data (f, g_1, g_2), we consider the biharmonic equation with Dirichlet boundary condition

$$\Delta^2 v = f \text{ in } K, \quad v = g_1, \partial_n v = g_2 \text{ on } \partial K. \tag{3.5.15}$$

As g_1, g_2 are compatible in the sense $g_2 \boldsymbol{n} + \nabla_{\partial K}(g_1) \in \mathbb{P}_{k+1}(\partial K; \mathbb{R}^3)$ with $\mathbb{P}_{k+1}(\partial K; \mathbb{R}^3)$ being the vector version of $\mathbb{P}_{k+1}(\partial K)$, by the trace theorem of $H^2(K)$ on polyhedral domains [20, Theorem 5], there exists $v^b \in H^2(K)$ such that

$$v^b|_{\partial K} = g_1, \quad \partial_n v^b|_{\partial K} = g_2.$$

Indeed v^b can be chosen as a polynomial in $\mathbb{P}_{\max\{k+1, 9\}}(K)$ using the $\mathscr{C}^1$ finite element constructed in [46]. Then consider the biharmonic equation with the homogenous boundary condition

$$\Delta^2 v^0 = f - \Delta^2 v^b \text{ in } K, \quad v^0 = 0, \partial v^0 = 0 \text{ on } \partial K.$$

The existence and uniqueness of v^0 is guaranteed by the Lax-Milligram lemma. Setting $v = v^b + v^0$ gives a solution to (3.5.15). The uniqueness of the solution to (3.5.15) is trivial.

Therefore we have constructed an embedding operator $\mathscr{L} : \mathscr{D}(K) \to \widetilde{W}(K)$ and $\mathscr{L}$ is injective. We shall choose

$$W(K) = \mathscr{L}(\mathscr{D}(K))$$

and by construction $\mathscr{L} : \mathscr{D}(K) \to W(K)$ is a bijection. Functions in $W(K)$ are defined as solutions to (3.5.15) which may still not be smooth enough to take nodal values of the Hessian.

To be consistent with finite element notation, we still use the form $\nabla^2 v(\delta)$ but understand it with the help of $\mathscr{L}$. For $v \in W(K)$, $\mathscr{L}^{-1} v = (f, v_0, \boldsymbol{v}_1, \boldsymbol{v}_2, u_0^e, \boldsymbol{u}_1^e, u_0^F, u_1^F) \in \mathscr{D}(K)$. We define $\nabla^2 v(\delta) \in W'(K)$ by

$$\nabla^2 v(\delta) := \boldsymbol{v}_2. \tag{3.5.16}$$

That is we understand $\nabla^2 v$ as a functional defined on $W(K)$ which will match the vertex value of the hessian if v is smooth enough. Other degrees of freedom (3.5.9)–(3.5.13) can be understood in a similar fashion. The interior moment (3.5.14) keeps unchanged and the relation of (3.5.14) and $f \in \mathscr{L}^{-1} v$ is discussed below.

Lemma 3.13 *The degrees of freedom* (3.5.9)–(3.5.14) *are unisolvent for* $W(K)$.

Proof First of all $\dim W(K) = \dim \mathcal{N}(K) = \frac{1}{6}(k^3 + 24k^2 + 35k + 60)$. Take any $v \in W(K)$ and suppose all the degrees of freedom (3.5.9)–(3.5.14) vanish. By the unisolvence of the Argyris element and Hermite element in two dimensions, we have $v \in H_0^2(K)$. It follows from the integration by parts that

$$\|\nabla^2 v\|_{0,K}^2 = (\Delta^2 v, v)_{0,K} = 0,$$

as $\Delta^2 v \in \mathbb{P}_{k-2}(K)$ and the vanishing degree of freedom (3.5.14). Thus $v = 0$. $\quad\square$

As $\dim \mathbb{P}_{k+2}(K) = \frac{1}{6}(k^3 + 12k^2 + 47k + 60)$, there are $2k(k-1)$ shape functions in $W(K)$ are non-polynomials and thus are treated as virtual. The L^2-projection of $\nabla^2 v$ to $\mathbb{P}_k(K, \mathbb{S})$ can be computed by degrees of freedom using the following Green's identity [23]: for $\boldsymbol{\tau} \in \mathbb{P}_k(K, \mathbb{S})$ and $v \in W(K)$,

$$(\nabla^2 v, \boldsymbol{\tau})_K = (\operatorname{div} \operatorname{div} \boldsymbol{\tau}, v)_K + \sum_{F \in \mathscr{F}(K)} \sum_{e \in \mathscr{E}(F)} (\boldsymbol{n}_{F,e}^\mathsf{T} \boldsymbol{\tau} \boldsymbol{n}, v)_e$$

$$+ \sum_{F \in \mathscr{F}(K)} \left[(\boldsymbol{n}^\mathsf{T} \boldsymbol{\tau} \boldsymbol{n}, \partial_n v)_F - (2 \operatorname{div}_F (\boldsymbol{\tau} \boldsymbol{n}) + \partial_n (\boldsymbol{n}^\mathsf{T} \boldsymbol{\tau} \boldsymbol{n}), v)_F \right].$$

As $\operatorname{div} \operatorname{div} \boldsymbol{\tau} \in \mathbb{P}_{k-2}(K)$, the first term can be computed by (3.5.14). On the boundary, $v|_F$ is a $\mathbb{P}_{k+2}(F)$ Argyris element, and $\partial_n v|_F$ is a $\mathbb{P}_{k+1}(F)$ Hermite element and thus all boundary terms are computable. In particular by choosing $\boldsymbol{\tau} \in \nabla^2 \mathbb{P}_{k+2}(K)$, we can compute an H^2-projection of v to $\mathbb{P}_{k+2}(K)$, that is

$\Pi^K v \in \mathbb{P}_{k+2}(K)$ is determined by

$$(\nabla^2 \Pi^K v, \nabla^2 q)_K = (\nabla^2 v, \nabla^2 q)_K \quad \forall\, q \in \mathbb{P}_{k+2}(K), \qquad (3.5.17)$$

$$(\Pi^K v, q)_K = (v, q)_K \qquad \forall\, q \in \mathbb{P}_1(K). \qquad (3.5.18)$$

We have the following properties of Π^K. Obviously Π^K is a projector, i.e.,

$$\Pi^K q = q \quad \forall\, q \in \mathbb{P}_{k+2}(K).$$

By the standard Bramlbe-Hilbert lemma, we have

$$h_K^i |v - \Pi^K v|_{i,K} \lesssim h_K^2 \inf_{q \in \mathbb{P}_{k+2}(K)} |v - q|_{2,K} \quad \forall\, v \in H^2(K), i = 0, 1, 2. \tag{3.5.19}$$

Remark 3.1 The C^1 macro-element on the Alfeld split in [1, 31, 35] has the same degrees of freedom on boundary as (3.5.9)–(3.5.13). We can construct a conforming macro-element Hessian complex on the Alfeld split following the approach in this paper. Here we present the lowest order C^1 macro-element, i.e. $k = 3$. For any tetrahedron K, let Alfeld split $\mathcal{T}_A(K)$ be the set of the four subtetrahedra obtained by connecting $\mathbf{x}_K$ to each of the vertices of K, where $\mathbf{x}_K$ is the barycenter of K. The shape function space of the lowest order C^1 macro-element on the Alfeld split in [1, 31, 35] is given by

$$W_A(K) := \{v \in H^2(K) : v|_{K'} \in \mathbb{P}_5(K') \text{ for each } K' \in \mathcal{T}_A(K)\}.$$

And the degrees of freedom are

$$v(\delta), \nabla v(\delta), \nabla^2 v(\delta) \quad \forall\, \delta \in \mathcal{V}(K), \qquad (3.5.20)$$

$$\int_e \partial_{n_i} v \, \mathrm{d}s \quad \forall\, e \in \mathcal{E}(K), i = 1, 2, \qquad (3.5.21)$$

$$(\partial_n v, q)_F \quad \forall\, q \in \mathbb{P}_1(F), F \in \mathcal{F}(K), \qquad (3.5.22)$$

$$(\nabla v, \nabla q)_K \quad \forall\, q \in \mathring{W}_A(K), \qquad (3.5.23)$$

where $\mathring{W}_A(K) := \{v \in W_A(K) : \text{ all the degrees of freedom (3.5.20)–(3.5.22)}$ vanish$\}$. $\qquad\qquad\qquad\qquad\qquad\qquad\qquad\qquad\qquad\qquad\qquad\qquad\quad\square$

For any $F \in \mathscr{F}(K)$, both $v|_F$ and $\partial_{n_F} v|_F$ are determined by the degrees of freedom (3.5.9)–(3.5.13) on the face F. Thus we can define the H^2-conforming virtual element space

$$W_h := \{v_h \in H^2(\Omega) : v_h|_K \in W(K) \text{ for each } K \in \mathscr{T}_h, \text{ all degrees of}$$

$$\text{freedom (3.5.9)–(3.5.14) are single-valued}\}.$$

Let $I_h^\Delta : H^4(\Omega) \to W_h$ be the nodal interpolation operator with respect to the degrees of freedom (3.5.9)–(3.5.14). For each tetrahedron K, by the scaling argument and the norm equivalence on the finite dimensional spaces (cf. [28, Section 3.1]), it holds

$$h_K^i |v - I_h^\Delta v|_{i,K} \lesssim h_K^{k+2} |v|_{k+2,K} \quad \forall\, v \in H^{k+2}(\Omega), i = 0, 1, 2. \qquad (3.5.24)$$

Here we take the advantage that the element is a tetrahedron and by transferring back to the reference element, one can show the constant in (3.5.24) depends only on the shape regularity of the element.

3.5.3   Trace Complexes

We have the following trace complexes

$$
\begin{array}{ccccccccc}
\boldsymbol{a} \cdot \boldsymbol{x} + b & \xrightarrow{\subset} & v & \xrightarrow{\text{hess}} & \boldsymbol{\tau} & \xrightarrow{\text{curl}} & \boldsymbol{\sigma} & \xrightarrow{\text{div}} & \boldsymbol{p} \\
\downarrow & & \downarrow & & \downarrow & & \downarrow & & \\
\boldsymbol{a}_F \cdot \boldsymbol{x}_F + b_F & \xrightarrow{\subset} & v|_F & \xrightarrow{\nabla_F^2} & \Pi_F \boldsymbol{\tau} \Pi_F & \xrightarrow{\text{rot}_F} & \boldsymbol{n}^\mathsf{T} \boldsymbol{\sigma} \Pi_F & \longrightarrow & 0
\end{array}
$$
(3.5.25)

where $b_F := \boldsymbol{a} \cdot \boldsymbol{n}(\boldsymbol{x} \cdot \boldsymbol{n})|_F + b$, and

$$
\begin{array}{ccccccccc}
\boldsymbol{a} \cdot \boldsymbol{x} + b & \xrightarrow{\subset} & v & \xrightarrow{\text{hess}} & \boldsymbol{\tau} & \xrightarrow{\text{curl}} & \boldsymbol{\sigma} & \xrightarrow{\text{div}} & \boldsymbol{p} \\
\downarrow & & \downarrow & & \downarrow & & \downarrow & & \\
\boldsymbol{a} \cdot \boldsymbol{n} & \xrightarrow{\subset} & \partial_n v|_F & \xrightarrow{\text{grad}_F} & \boldsymbol{n}^\mathsf{T} \boldsymbol{\tau} \Pi_F & \xrightarrow{\text{rot}_F} & \boldsymbol{n}^\mathsf{T} \boldsymbol{\sigma} \boldsymbol{n} & \longrightarrow & 0
\end{array}
$$
(3.5.26)

In (3.5.25) and (3.5.26), on the bottom of the diagram, all functions are evaluated on one face F. We present the concrete form instead of trace operators of Sobolev spaces as we will work mostly on polynomial functions when restricting to faces.

The trace complexes will motivate the correct continuity and degrees of freedom on edges and faces. For example, the 2×2 symmetric matrix $\Pi_F \boldsymbol{\tau} \Pi_F \in H(\text{rot}_F, F, \mathbb{S})$ and the vector $\boldsymbol{n}^\mathsf{T} \boldsymbol{\tau} \Pi_F \in H(\text{rot}_F, F, \mathbb{R}^2)$ imply the tangential continuity of $\boldsymbol{\tau} t$ on edges. The face moments for $\boldsymbol{n}^\mathsf{T} \boldsymbol{\tau} \Pi_F$ will come from that of the Nédélec element. The face moments for $\Pi_F \boldsymbol{\tau} \Pi_F$ will be based on the decomposition build-in the polynomial complex (3.4.18).

One important relation is the commutative diagram build-in the trace complex. For example, the third block of (3.5.25) and (3.5.26) implies $\text{rot}_F(\boldsymbol{\tau} \Pi_F) = (\text{curl } \boldsymbol{\tau})\boldsymbol{n}|_F$ which can be verified easily by definition.

As $\text{div}_F(\boldsymbol{\tau} \times \boldsymbol{n}) = \text{rot}_F(\boldsymbol{\tau} \Pi_F)$, i.e., div_F is a rotation of rot_F, the trace $\boldsymbol{\tau} \times \boldsymbol{n} \in H(\text{div}_F, F)$ and conclusion for $\boldsymbol{\tau} \times \boldsymbol{n}$ can be transfer to $\boldsymbol{\tau} \Pi_F$ and vice verse.

3.5.4 $H(\textbf{curl})$-*Conforming Element for Symmetric Tensors*

Motivated by the decomposition (3.4.12), we take the space of shape functions

$$\boldsymbol{\Sigma}(K) := \nabla^2 W(K) \oplus \text{sym}(\mathbb{P}_{k-1}(K; \mathbb{T}) \times \boldsymbol{x}).$$

The degrees of freedom are given by

$$\text{curl } \boldsymbol{\tau}(\delta) \quad \forall \, \delta \in \mathscr{V}(K), \tag{3.5.27}$$

$$\boldsymbol{\tau}(\delta) \quad \forall \, \delta \in \mathscr{V}(K), \tag{3.5.28}$$

$$(\boldsymbol{\tau} t, \boldsymbol{q})_e \quad \forall \, \boldsymbol{q} \in \mathbb{P}_{k-2}(e; \mathbb{R}^3), e \in \mathscr{E}(K), \tag{3.5.29}$$

$$(\Pi_F \boldsymbol{\tau} \Pi_F, \boldsymbol{q})_F \quad \forall \, \boldsymbol{q} \in \mathbb{P}_0(F, \mathbb{S}) \oplus \text{sym} \nabla_F^\perp \mathbb{P}_{k-1,2}^\perp(F; \mathbb{R}^2) \oplus \boldsymbol{x}\boldsymbol{x}^\mathsf{T} \mathbb{P}_{k-4}(F),$$
$$F \in \mathscr{F}(K), \tag{3.5.30}$$

$$(\boldsymbol{n}^\mathsf{T} \boldsymbol{\tau} \Pi_F, \boldsymbol{q})_F \quad \forall \, \boldsymbol{q} \in \mathbb{P}_0(F, \mathbb{R}^2) \oplus \nabla_F^\perp \mathbb{P}_{k-1,2}^\perp(F) \oplus \mathbb{P}_{k-2}(F)\boldsymbol{x}, F \in \mathscr{F}(K),$$
$$\tag{3.5.31}$$

$$(\text{curl } \boldsymbol{\tau}, \boldsymbol{q})_K \quad \forall \, \boldsymbol{q} \in \mathbb{B}_{k-1}(K; \mathbb{T}) \cap \ker(\text{div}), \tag{3.5.32}$$

$$(\boldsymbol{\tau}, \boldsymbol{x}\boldsymbol{x}^\mathsf{T} q)_K \quad \forall \, q \in \mathbb{P}_{k-2}(K). \tag{3.5.33}$$

From the decomposition (3.4.12), we know that $\mathbb{P}_k(K; \mathbb{S}) \subset \boldsymbol{\Sigma}(K)$. The dimension of the space is

$$\dim \boldsymbol{\Sigma}(K) = \dim W(K) - 4 + \dim \text{sym}(\mathbb{P}_{k-1}(K; \mathbb{T}) \times \boldsymbol{x}) = k^3 + 8k^2 + 9k + 6.$$

The number of the degrees of freedom (3.5.27)–(3.5.33) is

$$32 + 24 + 18(k-1) + (6k^2 - 6k - 24) + (4k^2 - 16)$$

$$+\frac{1}{6}(5k^3 - 12k^2 - 17k + 48) + \frac{1}{6}(k^3 - k) = k^3 + 8k^2 + 9k + 6,$$

which agrees with dim $\boldsymbol{\Sigma}(K)$. In (3.5.30)–(3.5.31) we separate the trace $\boldsymbol{\tau}\Pi_F$ into the tangential-tangential part $\Pi_F\boldsymbol{\tau}\Pi_F$ and the tangential-normal part $\boldsymbol{n}^{\mathsf{T}}\boldsymbol{\tau}\Pi_F$. Most of the shape functions in $\boldsymbol{\Sigma}(K)$ are polynomials except $2k(k-1)$ non-polynomial ones in the form $\nabla^2 v$ for some $v \in W(K)$ and $\nabla^2 v(\delta)$ should be understood in the sense of (3.5.16).

Although there are non-polynomial shape functions, the trace $\boldsymbol{\tau} \times \boldsymbol{n}$ on each face is always polynomial and determined by (3.5.27)–(3.5.31).

Lemma 3.14 *For each $F \in \mathscr{F}(K)$ and any $\boldsymbol{\tau} \in \boldsymbol{\Sigma}(K)$, $\boldsymbol{\tau} \times \boldsymbol{n}|_F \in \mathbb{P}_k(F; \mathbb{M})$ is determined by the degrees of freedom* (3.5.27)–(3.5.31) *on face F.*

Proof First of all, we show although $\boldsymbol{\tau} \in \boldsymbol{\Sigma}(K)$ may be from a virtual element space, its trace $\boldsymbol{\tau} \times \boldsymbol{n}|_F \in \mathbb{P}_k(F; \mathbb{M})$. To see this, it suffices to check $(\nabla^2 v)\Pi_F$ for $v \in W(K)$. Using notation in Sect. 3.2, it is straightforward to verify that

$$\Pi_F \nabla^2 v \Pi_F = \nabla_F^2(v|_F), \quad \boldsymbol{n} \cdot \nabla^2 v \Pi_F = \nabla_F(\partial_n v|_F).$$

As $v|_F \in \mathbb{P}_{k+2}(F)$ and $\partial_n v|_F \in \mathbb{P}_{k+1}(F)$ are polynomials, $\boldsymbol{\tau} \times \boldsymbol{n}|_F$ is a polynomial of degree k.

Assume all the degrees of freedom (3.5.27)–(3.5.31) on face F are zeros. We are going to prove this polynomial is vanished. The vanishing degrees of freedom (3.5.28)–(3.5.29) imply $\boldsymbol{\tau}\boldsymbol{t}|_e = \boldsymbol{0}$ for every $e \in \partial F$ as $\boldsymbol{\tau}\boldsymbol{t}|_e \in \mathbb{P}_k(e; \mathbb{R}^3)$. Then $\boldsymbol{\tau} \times \boldsymbol{n}|_F \in \boldsymbol{H}_0(\mathrm{div}_F, F)$. Using the integration by parts and the vanishing degrees of freedom (3.5.30)–(3.5.31), we obtain

$$(\mathrm{div}_F(\boldsymbol{\tau} \times \boldsymbol{n}), \boldsymbol{q})_F = (\boldsymbol{\tau} \times \boldsymbol{n}, \mathrm{grad}_F \, \boldsymbol{q})_F = 0 \quad \forall \, \boldsymbol{q} \in \mathbb{P}_1(F; \mathbb{R}^3) \oplus \mathbb{P}_{k-1,2}^{\perp}(F; \mathbb{R}^3).$$

Using the relation $-\mathrm{div}_F(\boldsymbol{\tau} \times \boldsymbol{n}) = (\mathrm{curl} \, \boldsymbol{\tau})\boldsymbol{n}|_F \in \mathbb{P}_{k-1}(F; \mathbb{R}^3)$ and the vanishing degree of freedom (3.5.27), we know $\mathrm{div}_F(\boldsymbol{\tau} \times \boldsymbol{n})(\delta) = 0$ for all $\delta \in \mathscr{V}(F)$. Applying Lemma 3.10, we acquire $\mathrm{div}_F(\boldsymbol{\tau} \times \boldsymbol{n}) = \boldsymbol{0}$ which is equivalent to $\mathrm{rot}_F(\boldsymbol{\tau}\Pi_F) = 0$.

The tangential component $\boldsymbol{\tau}\Pi_F$ can be further decomposed into two components: the tangential-tangential part $\Pi_F\boldsymbol{\tau}\Pi_F$ and the tangential-normal part $\boldsymbol{n}^{\mathsf{T}}\boldsymbol{\tau}\Pi_F$. Noting that $\boldsymbol{n}^{\mathsf{T}}\boldsymbol{\tau}\Pi_F \in \boldsymbol{H}_0(\mathrm{rot}_F, F) \cap \mathbb{P}_k(F; \mathbb{R}^2)$ and $\mathrm{rot}_F(\boldsymbol{n}^{\mathsf{T}}\boldsymbol{\tau}\Pi_F) = 0$, which implies $\boldsymbol{n}^{\mathsf{T}}\boldsymbol{\tau}\Pi_F \perp \nabla_F^{\perp} H^1(F)$. We get from the vanishing degrees of freedom (3.5.31) that

$$(\boldsymbol{n}^{\mathsf{T}}\boldsymbol{\tau}\Pi_F, \boldsymbol{q})_F = 0 \quad \forall \, \boldsymbol{q} \in \mathbb{P}_{k-1}(F; \mathbb{R}^2),$$

where we use the decomposition $\mathbb{P}_{k-1}(F; \mathbb{R}^2) = \nabla_F^\perp \mathbb{P}_k(F) \oplus \boldsymbol{x} \mathbb{P}_{k-2}(F)$ which is a two dimensional version of (3.4.4). Due to the unisolvence of the second-type Nédélec element [40], we get $\boldsymbol{n}^\mathsf{T} \boldsymbol{\tau} \Pi_F = \boldsymbol{0}$.

For the tangential-tangential part, as $\Pi_F \boldsymbol{\tau} \Pi_F \in \mathbb{P}_k(F; \mathbb{S})$, by the Hessian complex (3.4.14) in two dimensions, there exists $w_F \in \mathbb{P}_{k+2}(F)$ such that $\Pi_F \boldsymbol{\tau} \Pi_F = \nabla_F^2 w_F$ and $w_F(\delta) = 0$ for each $\delta \in \mathscr{V}(F)$. Then we get from the vanishing degrees of freedom (3.5.28)–(3.5.29) that

$$\nabla_F^2 w_F(\delta) = \boldsymbol{0} \quad \forall \, \delta \in \mathscr{V}(F),$$

$$(\partial_t(\nabla_F w_F), \boldsymbol{q})_e = 0 \quad \forall \boldsymbol{q} \in \mathbb{P}_{k-2}(e; \mathbb{R}^3), e \in \mathscr{E}(F),$$

which indicate $\partial_t(\nabla_F w_F)|_e = \boldsymbol{0}$ for each $e \in \mathscr{E}(F)$. As a result $w_F \in H_0^2(F)$. Due to the vanishing degrees of freedom (3.5.30),

$$(w_F, \operatorname{div}_F \operatorname{div}_F(\boldsymbol{x} \boldsymbol{x}^\mathsf{T} q))_F = (\nabla_F^2 w_F, \boldsymbol{x} \boldsymbol{x}^\mathsf{T} q)_F = 0 \quad \forall \, q \in \mathbb{P}_{k-4}(F).$$

Therefore by $\operatorname{div}_F \operatorname{div}_F(\boldsymbol{x} \boldsymbol{x}^\mathsf{T} \mathbb{P}_{k-4}(F)) = \mathbb{P}_{k-4}(F)$, cf. (3.4.18), and the unisolvence of the Argyris element, it follows that $w_F = 0$. $\qquad\square$

To show the unisolvence, we adapt the unisolvence proof of three dimensional $H(\text{curl})$-conforming virtual element in [11]. We take the advantage of the fact that K is a tetrahedron and $\operatorname{curl} \boldsymbol{\Sigma}(K)$ is polynomial. The approach of using local problems is troublesome as for symmetric matrices, the well-posedness of $\operatorname{curl} - \operatorname{div}$ system with non-homogenous Dirichlet boundary condition is unclear. A crucial and missing part is the characterization of the trace space of $\boldsymbol{H}(\text{curl}, \Omega; \mathbb{S})$.

Lemma 3.15 *The degrees of freedom* (3.5.27)–(3.5.33) *are unisolvent for* $\boldsymbol{\Sigma}(K)$.

Proof Take any $\boldsymbol{\tau} \in \boldsymbol{\Sigma}(K)$ and suppose all the degrees of freedom (3.5.27)–(3.5.33) vanish. We are going to prove $\boldsymbol{\tau} = \boldsymbol{0}$.

With vanishing degrees of freedom (3.5.27)–(3.5.31), we have proved that $\boldsymbol{\tau} \in \boldsymbol{H}_0(\text{curl}, K; \mathbb{S})$. Then $\operatorname{curl} \boldsymbol{\tau} \in \mathbb{B}_{k-1}(K, \mathbb{T}) \cap \ker(\operatorname{div})$, together with the vanishing degree of freedom (3.5.32) implies $\operatorname{curl} \boldsymbol{\tau} = \boldsymbol{0}$.

Using integration by parts, with $\boldsymbol{\tau} \times \boldsymbol{n}|_{\partial K} = \boldsymbol{0}$ and $\operatorname{curl} \boldsymbol{\tau} = \boldsymbol{0}$,

$$(\boldsymbol{\tau}, \operatorname{sym} \operatorname{curl} \boldsymbol{\sigma})_K = (\operatorname{curl} \boldsymbol{\tau}, \boldsymbol{\sigma})_K + (\boldsymbol{\tau} \times \boldsymbol{n}, \boldsymbol{\sigma})_{\partial K}, \tag{3.5.34}$$

we conclude that $\boldsymbol{\tau} \perp \operatorname{sym} \operatorname{curl} \boldsymbol{\sigma}$ for any $\boldsymbol{\sigma} \in \boldsymbol{H}(\text{sym} \operatorname{curl}; \mathbb{M})$.

Use the fact $\operatorname{div} \operatorname{div} \boldsymbol{\tau} \in \mathbb{P}_{k-2}(K)$ and $\operatorname{div} \operatorname{div} : \boldsymbol{x} \boldsymbol{x}^\mathsf{T} \mathbb{P}_{k-2}(K) \to \mathbb{P}_{k-2}(K)$ is a bijection, cf. Lemma 3.9, we can find a polynomial $\boldsymbol{x} \boldsymbol{x}^\mathsf{T} q$ with $q \in \mathbb{P}_{k-2}(K)$ such that $\operatorname{div} \operatorname{div}(\boldsymbol{\tau} - \boldsymbol{x} \boldsymbol{x}^\mathsf{T} q) = 0$ and thus $\boldsymbol{\tau} = \boldsymbol{x} \boldsymbol{x}^\mathsf{T} q + \operatorname{sym} \operatorname{curl} \boldsymbol{\sigma}$ for some $\boldsymbol{\sigma} \in \boldsymbol{H}(\text{sym} \operatorname{curl}; \mathbb{M})$.

Then by the vanishing degree of freedom (3.5.33),

$$(\boldsymbol{\tau}, \boldsymbol{\tau})_K = (\boldsymbol{\tau}, \boldsymbol{x}\boldsymbol{x}^\mathsf{T}q + \operatorname{sym} \operatorname{curl} \boldsymbol{\sigma})_K = 0,$$

which implies $\boldsymbol{\tau} = \mathbf{0}$. $\qquad\qquad\qquad\qquad\qquad\qquad\qquad\qquad\qquad\qquad\qquad\qquad$ □

We now discuss how to compute the L^2-projection of an element $\boldsymbol{\tau} \in \boldsymbol{\Sigma}(K)$ to $\mathbb{P}_k(K; \mathbb{S})$. By Lemma 3.14, we can determine the piecewise polynomial $\boldsymbol{\tau} \times \boldsymbol{n}$ on the boundary and $(\operatorname{curl} \boldsymbol{\tau})\boldsymbol{n}|_F$. Together with (3.5.32), $\operatorname{curl} \boldsymbol{\tau} \in \mathbb{P}_{k-1}(K; \mathbb{T})$ is determined. Then, using (3.5.34), we can compute the L^2-projection to the subspace $\operatorname{sym} \operatorname{curl} \mathbb{P}_{k+1}(K; \mathbb{T})$. Use the degree of freedom (3.5.33), we can compute the L^2-projection to the subspace $\boldsymbol{x}\boldsymbol{x}^\mathsf{T}\mathbb{P}_{k-2}(K)$. Finally, recalling that $\mathbb{P}_k(K; \mathbb{S}) = \boldsymbol{x}\boldsymbol{x}^\mathsf{T}\mathbb{P}_{k-2}(K) \oplus \operatorname{sym} \operatorname{curl} \mathbb{P}_{k+1}(K; \mathbb{S})$, the L^2-projection to $\mathbb{P}_k(K; \mathbb{S})$ will be obtained by combining the projection to each subspace and an orthogonalization step.

Define the global finite element space

$$\boldsymbol{\Sigma}_h := \{\boldsymbol{\tau}_h \in \boldsymbol{L}^2(\Omega; \mathbb{S}) : \boldsymbol{\tau}_h|_K \in \boldsymbol{\Sigma}(K) \quad \forall\, K \in \mathscr{T}_h, \text{ all degrees of}$$

$$\text{freedom (3.5.27)–(3.5.33) are single-valued}\}.$$

It follows from Lemma 3.14 that $\boldsymbol{\Sigma}_h \subset \boldsymbol{H}(\operatorname{curl}, \Omega; \mathbb{S})$.

For any sufficiently smooth and symmetric tensor $\boldsymbol{\tau}$ defined on tetrahedron K, let $\boldsymbol{I}_K^c \boldsymbol{\tau} \in \boldsymbol{\Sigma}(K)$ be the nodal interpolation of $\boldsymbol{\tau}$ based on the degrees of freedom (3.5.27)–(3.5.33). We have

$$\boldsymbol{I}_K^c \boldsymbol{\tau} = \boldsymbol{\tau} \quad \forall\, \boldsymbol{\tau} \in \boldsymbol{\Sigma}(K),$$

and by the scaling argument and the norm equivalence on the finite dimensional spaces (cf. [28, Section 3.1])

$$\|\boldsymbol{\tau} - \boldsymbol{I}_K^c \boldsymbol{\tau}\|_{0,K} + h_K \|\operatorname{curl}(\boldsymbol{\tau} - \boldsymbol{I}_K^c \boldsymbol{\tau})\|_{0,K} \lesssim h_K^{k+1} |\boldsymbol{\tau}|_{k+1,K} \quad \forall\, \boldsymbol{\tau} \in \boldsymbol{H}^{k+1}(K; \mathbb{S}). \tag{3.5.35}$$

Again by transferring back to the reference tetrahedron, one can show the constant in (3.5.35) depends only on the shape regularity of the tetrahedron. For any sufficiently smooth and symmetric tensor $\boldsymbol{\tau}$ defined on Ω, let $\boldsymbol{I}_h^c \boldsymbol{\tau} \in \boldsymbol{\Sigma}_h$ be defined by $(\boldsymbol{I}_h^c \boldsymbol{\tau})|_K := \boldsymbol{I}_K^c(\boldsymbol{\tau}|_K)$ for each $K \in \mathscr{T}_h$.

If $\boldsymbol{\tau} \in \boldsymbol{H}^1(K; \mathbb{S})$ satisfying $\operatorname{curl} \boldsymbol{\tau} \in \mathbb{P}_{k-1}(K; \mathbb{T})$, due to Lemma 5.38 in [38] and Lemma 4.7 in [2], the interpolation $\boldsymbol{I}_K^c \boldsymbol{\tau}$ is well-defined, and it follows from the integration by parts and Lemma 3.12 that

$$\operatorname{curl}(\boldsymbol{I}_K^c \boldsymbol{\tau}) = \operatorname{curl} \boldsymbol{\tau}. \tag{3.5.36}$$

Moreover, by the scaling argument we have

$$\|\boldsymbol{\tau} - \boldsymbol{I}_K^c \boldsymbol{\tau}\|_{0,K} \lesssim h_K |\boldsymbol{\tau}|_{1,K}. \tag{3.5.37}$$

Remark 3.2 We can define an $H(\mathrm{curl})$-conforming macro-element for symmetric tensors. Let $W_A(K)$ be the H^2-conforming macro-element defined in Remark 3.1. Take the space of shape functions

$$\boldsymbol{\Sigma}_A(K) := \nabla^2 W_A(K) \oplus \mathrm{sym}(\mathbb{P}_2(K; \mathbb{T}) \times \boldsymbol{x}).$$

And the degrees of freedom are given by

$$\mathrm{curl}\,\boldsymbol{\tau}(\delta) \quad \forall\, \delta \in \mathscr{V}(K), \tag{3.5.38}$$

$$\boldsymbol{\tau}(\delta) \quad \forall\, \delta \in \mathscr{V}(K), \tag{3.5.39}$$

$$(\boldsymbol{\tau}\boldsymbol{t}, \boldsymbol{q})_e \quad \forall\, \boldsymbol{q} \in \mathbb{P}_1(e; \mathbb{R}^3), e \in \mathscr{E}(K), \tag{3.5.40}$$

$$(\boldsymbol{n} \times \boldsymbol{\tau} \times \boldsymbol{n}, \boldsymbol{q})_F \quad \forall\, \boldsymbol{q} \in \mathbb{P}_0(F, \mathbb{S}), F \in \mathscr{F}(K), \tag{3.5.41}$$

$$(\boldsymbol{n}^\mathsf{T} \boldsymbol{\tau} \Pi_F, \boldsymbol{q})_F \quad \forall\, \boldsymbol{q} \in \mathbb{P}_0(F, \mathbb{R}^2) \oplus \mathbb{P}_1(F)\boldsymbol{x}, F \in \mathscr{F}(K), \tag{3.5.42}$$

$$(\mathrm{curl}\,\boldsymbol{\tau}, \boldsymbol{q})_K \quad \forall\, \boldsymbol{q} \in \mathbb{B}_2(K; \mathbb{T}) \cap \ker(\mathrm{div}), \tag{3.5.43}$$

$$(\boldsymbol{\tau}, q\boldsymbol{I})_K \quad \forall\, q \in \mathring{W}_A(K). \tag{3.5.44}$$

The degrees of freedom (3.5.38)–(3.5.44) are the same as (3.5.27)–(3.5.33) except (3.5.44), which is inspired by (3.5.23) when defining W_A. One advantage of using the macro-element is that the shape functions are piecewise polynomial and thus no need to compute the L^2-projection. □

3.5.5 Discrete Conforming Hessian Complex

In this subsection we will prove the sequence (3.5.1) forms a discrete Hessian complex in three dimensions.

The polynomial space for $L^2(\Omega)$ is simply discontinuous $\mathbb{P}_{k-2}$ space

$$\mathscr{Q}_h := \{\boldsymbol{q}_h \in \boldsymbol{L}^2(\Omega; \mathbb{R}^3) : \boldsymbol{q}_h|_K \in \mathbb{P}_{k-2}(K; \mathbb{R}^3) \quad \forall\, K \in \mathscr{T}_h\}.$$

Lemma 3.16 *It holds*

$$\mathrm{div}\,\boldsymbol{V}_h = \mathscr{Q}_h. \tag{3.5.45}$$

Proof It is apparent that $\mathrm{div}\, \boldsymbol{V}_h \subseteq \mathcal{Q}_h$. Conversely taking any $\boldsymbol{p}_h \in \mathcal{Q}_h$, by (3.3.2) there exists $\boldsymbol{v} \in \boldsymbol{H}^1(\Omega; \mathbb{T})$ such that $\mathrm{div}\,\boldsymbol{v} = \boldsymbol{p}_h$. Choose $\boldsymbol{v}_1 \in \boldsymbol{V}_h$ determined by

$$\boldsymbol{v}_1(\delta) = \boldsymbol{0},$$

$$(\boldsymbol{v}_1\boldsymbol{n}, \boldsymbol{q})_F = (\boldsymbol{v}\boldsymbol{n}, \boldsymbol{q})_F \quad \forall\, \boldsymbol{q} \in \mathbb{P}_1(F; \mathbb{R}^3) \oplus \mathbb{P}^{\perp}_{k-1,2}(F; \mathbb{R}^3),$$

$$(\boldsymbol{v}_1, \boldsymbol{q})_K = (\boldsymbol{v}, \boldsymbol{q})_K \quad \forall\, \boldsymbol{q} \in \mathrm{dev\, grad}\,\mathbb{P}_{k-2}(K; \mathbb{R}^3) \oplus (\mathbb{B}_{k-1}(K; \mathbb{T}) \cap \mathrm{ker(div)})$$

for each $\delta \in \mathcal{V}_h$, $F \in \mathcal{F}_h$ and $K \in \mathcal{T}_h$. It follows from the integration by parts that

$$(\mathrm{div}(\boldsymbol{v} - \boldsymbol{v}_1), \boldsymbol{q})_K = 0 \quad \forall\, \boldsymbol{q} \in \mathbb{P}_1(K; \mathbb{R}^3), K \in \mathcal{T}_h,$$

which means $\mathrm{div}(\boldsymbol{v} - \boldsymbol{v}_1)|_K \in \mathbb{P}^{\perp}_{k-2,\mathrm{RT}}(K; \mathbb{R}^3)$. Employing (3.5.3), there exists $\boldsymbol{v}_2 \in \boldsymbol{V}_h$ such that $\mathrm{div}(\boldsymbol{v} - \boldsymbol{v}_1) = \mathrm{div}\,\boldsymbol{v}_2$. Therefore $\mathrm{div}\,\boldsymbol{v}_h = \mathrm{div}\,\boldsymbol{v} = \boldsymbol{q}_h$ by setting $\boldsymbol{v}_h = \boldsymbol{v}_1 + \boldsymbol{v}_2$. $\qquad\square$

Lemma 3.17 *Assume Ω is a topologically trivial domain. Then we have the discrete Hessian complex*

$$\mathbb{P}_1(\Omega) \xrightarrow{\subseteq} W_h \xrightarrow{\nabla^2} \boldsymbol{\Sigma}_h \xrightarrow{\mathrm{curl}} \boldsymbol{V}_h \xrightarrow{\mathrm{div}} \mathcal{Q}_h \to \boldsymbol{0}. \tag{3.5.46}$$

Proof It is easy to see that (3.5.46) is a complex as all discrete spaces are conforming. We check the exactness of this complex. First of all, $W_h \cap \mathrm{ker}(\nabla^2) = \mathbb{P}_1(\Omega)$. Then

$$\dim \nabla^2 W_h = \dim W_h - 4 = 10\#\mathcal{V}_h + (3k-7)\#\mathcal{E}_h + (k^2-3k+3)\#\mathcal{F}_h + \frac{1}{6}(k^3-k)\#\mathcal{T}_h - 4.$$

For any $\boldsymbol{\tau}_h \in \boldsymbol{\Sigma}_h \cap \mathrm{ker}(\mathrm{curl})$, there exists $w \in H^2(\Omega)$ satisfying $\boldsymbol{\tau}_h = \nabla^2 w$. On each element K, we have $\nabla^2(w|_K) \in \nabla^2 W(K)$, which means $w|_K \in W(K)$. Noting that $\nabla^2 w$ is single-valued at each vertex in $\mathcal{V}_h$. Then $w \in W_h$. This indicates $\boldsymbol{\Sigma}_h \cap \mathrm{ker}(\mathrm{curl}) = \nabla^2 W_h$, and

$$\dim \mathrm{curl}\, \boldsymbol{\Sigma}_h = \dim \boldsymbol{\Sigma}_h - \dim \nabla^2 W_h$$

$$= 14\#\mathcal{V}_h + (3k-3)\#\mathcal{E}_h + \frac{1}{2}(5k^2 - 3k - 20)\#\mathcal{F}_h$$

$$+ (k^3 - 2k^2 - 3k + 8)\#\mathcal{T}_h - \dim \nabla^2 W_h$$

$$= 4\#\mathcal{V}_h + 4\#\mathcal{E}_h + \frac{1}{2}(3k^2 + 3k - 26)\#\mathcal{F}_h + \frac{1}{6}(5k^3 - 12k^2 - 17k + 48)\#\mathcal{T}_h + 4.$$

On the other side, it holds from (3.5.45) that

$$\dim V_h \cap \ker(\mathrm{div}) = \dim V_h - \dim \mathscr{Q}_h$$

$$=8\#\mathscr{V}_h + \frac{1}{2}(3k^2 + 3k - 18)\#\mathscr{F}_h + \frac{2}{3}(2k^3 - 3k^2 - 5k + 6)\#\mathscr{T}_h - \frac{1}{2}(k^3 - k)\#\mathscr{T}_h$$

$$=8\#\mathscr{V}_h + \frac{1}{2}(3k^2 + 3k - 18)\#\mathscr{F}_h + \frac{1}{6}(5k^3 - 12k^2 - 17k + 24)\#\mathscr{T}_h.$$

Hence we acquire from the Euler's formula that

$$\dim V_h \cap \ker(\mathrm{div}) - \dim \mathrm{curl}\,\boldsymbol{\Sigma}_h = 4(-\#\mathscr{T}_h + \#\mathscr{F}_h - \#\mathscr{E}_h + \#\mathscr{V}_h - 1) = 0,$$

which yields $V_h \cap \ker(\mathrm{div}) = \mathrm{curl}\,\boldsymbol{\Sigma}_h$. $\qquad\square$

Remark 3.3 When the topology of Ω is non-trivial, it is assumed to be captured by the triangulation $\mathscr{T}_h$. As all discrete spaces are conforming, the co-homology groups defined by the Hessian complex is preserved in the discrete Hessian complex. $\qquad\square$

Remark 3.4 When Ω is a topologically trivial domain, the following macro-element Hessian complex based on the Alfeld split

$$\mathbb{P}_1(\Omega) \overset{\subset}{\to} W_h^A \overset{\nabla^2}{\longrightarrow} \boldsymbol{\Sigma}_h^A \overset{\mathrm{curl}}{\longrightarrow} V_h \overset{\mathrm{div}}{\longrightarrow} \mathscr{Q}_h \to \mathbf{0}$$

is also exact, where

$$W_h^A := \{v_h \in H^2(\Omega) : v_h|_K \in W_A(K) \text{ for each } K \in \mathscr{T}_h, \text{ all degrees of}$$
$$\text{freedom (3.5.20)–(3.5.23) are single-valued}\},$$

$$\boldsymbol{\Sigma}_h^A := \{\boldsymbol{\tau}_h \in \boldsymbol{L}^2(\Omega; \mathbb{S}) : \boldsymbol{\tau}_h|_K \in \boldsymbol{\Sigma}_A(K) \quad \forall\, K \in \mathscr{T}_h, \text{ all degrees of}$$
$$\text{freedom (3.5.38)–(3.5.44) are single-valued}\}. \qquad\square$$

3.5.6 Discrete Poincaré Inequality

Due to the exactness of the discrete Hessian complex, we have the following discrete Poincaré inequality.

Lemma 3.18 *Assume Ω is a topologically trivial domain. For any $\boldsymbol{\tau}_h \in \boldsymbol{\Sigma}_h$ satisfying*

$$(\boldsymbol{\tau}_h, \nabla^2 w_h) = 0 \quad \forall\, w_h \in W_h,$$

it holds the discrete Poincaré inequality

$$\|\boldsymbol{\tau}_h\|_0 \lesssim \|\operatorname{curl} \boldsymbol{\tau}_h\|_0. \tag{3.5.47}$$

In general,

$$\|\boldsymbol{\tau}_h\|_0 \le \|\operatorname{curl} \boldsymbol{\tau}_h\|_0 + \sup_{w_h \in W_h} \frac{(\boldsymbol{\tau}_h, \nabla^2 w_h)}{\|w_h\|_2} \qquad \forall \, \boldsymbol{\tau}_h \in \boldsymbol{\Sigma}_h.$$

Proof Since $\operatorname{curl} \boldsymbol{\tau}_h \in \boldsymbol{H}(\operatorname{div}, \Omega; \mathbb{T})$, by (3.3.3) there exists $\boldsymbol{\tau} \in \boldsymbol{H}^1(\Omega; \mathbb{S})$ such that

$$\operatorname{curl} \boldsymbol{\tau} = \operatorname{curl} \boldsymbol{\tau}_h, \quad \|\boldsymbol{\tau}\|_1 \lesssim \|\operatorname{curl} \boldsymbol{\tau}_h\|_0. \tag{3.5.48}$$

By (3.5.36), we have

$$\operatorname{curl}(\boldsymbol{I}_h^c \boldsymbol{\tau}) = \operatorname{curl} \boldsymbol{\tau} = \operatorname{curl} \boldsymbol{\tau}_h.$$

It follows from the complex (3.5.46) that $\boldsymbol{\tau}_h - \boldsymbol{I}_h^c \boldsymbol{\tau} \in \nabla^2 W_h$. Hence we obtain from (3.5.37) and (3.5.48) that

$$\|\boldsymbol{\tau}_h\|_0^2 = (\boldsymbol{\tau}_h, \boldsymbol{\tau}_h) = (\boldsymbol{\tau}_h, \boldsymbol{I}_h^c \boldsymbol{\tau}) \le \|\boldsymbol{\tau}_h\|_0 \|\boldsymbol{I}_h^c \boldsymbol{\tau}\|_0 \lesssim \|\boldsymbol{\tau}_h\|_0 \|\boldsymbol{\tau}\|_1,$$

which means (3.5.47).

For a general $\boldsymbol{\tau}_h \in \boldsymbol{\Sigma}_h$, by the exact sequence (3.5.46), we have the L^2-orthogonal Helmholtz decomposition

$$\boldsymbol{\tau}_h = \nabla^2 v_h + \boldsymbol{\tau}_h^0,$$

and $\boldsymbol{\tau}_h^0 \perp \nabla^2 W_h$ whose L^2-norm can be controlled by (3.5.47) $\|\boldsymbol{\tau}_h^0\|_0 \lesssim \|\operatorname{curl} \boldsymbol{\tau}_h^0\|_0 = \|\operatorname{curl} \boldsymbol{\tau}_h\|_0$. The first part $\nabla^2 v_h$ is the L^2-projection of $\boldsymbol{\tau}_h$ to $\nabla^2 W_h$ and thus

$$\|\nabla^2 v_h\|_0 = \sup_{w_h \in W_h/\mathbb{P}_1(\Omega)} \frac{(\nabla^2 v_h, \nabla^2 w_h)}{\|\nabla^2 w_h\|_0} = \sup_{w_h \in W_h/\mathbb{P}_1(\Omega)} \frac{(\boldsymbol{\tau}_h, \nabla^2 w_h)}{\|\nabla^2 w_h\|_0}.$$

Then we use Poincaré inequality

$$\|w_h\|_0 \lesssim \|\nabla^2 w_h\|_0 \quad \forall w_h \in W_h/\mathbb{P}_1(\Omega)$$

to finish the proof. $\qquad \square$

The discrete Poincaré inequality (3.5.47) is the discrete version of Poincaré inequality (3.3.4). The L^2-inner product $(\cdot, \cdot)$ and norm $\|\cdot\|_0$ can be changed to an equivalent one and similar results still hold.

3.6   Discretization for the Linearized Einstein-Bianchi System

In this section we will apply the constructed conforming virtual element Hessian complex to discretize the time-independent linearized Einstein-Bianchi system.

3.6.1   Linearized Einstein-Bianchi System

Consider the time-independent linearized Einstein-Bianchi system [42]: find $\sigma \in H^2(\Omega)$, $\boldsymbol{E} \in \boldsymbol{H}(\text{curl}, \Omega; \mathbb{S})$ and $\boldsymbol{B} \in \boldsymbol{L}^2(\Omega; \mathbb{T})$ such that

$$(\sigma, \tau) - (\boldsymbol{E}, \nabla^2 \tau) = 0 \qquad \forall \, \tau \in H^2(\Omega), \tag{3.6.1}$$

$$(\nabla^2 \sigma, \boldsymbol{v}) + (\boldsymbol{B}, \text{curl}\,\boldsymbol{v}) = (\boldsymbol{f}, \boldsymbol{v}) \qquad \forall \, \boldsymbol{v} \in \boldsymbol{H}(\text{curl}, \Omega; \mathbb{S}), \tag{3.6.2}$$

$$(\boldsymbol{B}, \boldsymbol{\psi}) - (\text{curl}\,\boldsymbol{E}, \boldsymbol{\psi}) = 0 \qquad \forall \, \boldsymbol{\psi} \in \boldsymbol{L}^2(\Omega; \mathbb{T}), \tag{3.6.3}$$

where $\boldsymbol{f} \in \boldsymbol{L}^2(\Omega; \mathbb{S})$. Here following [32, 42] we switch the notation and use σ, τ for functions in H^2 and $\boldsymbol{E}, \boldsymbol{v}$ for functions in $\boldsymbol{H}(\text{curl}, \Omega; \mathbb{S})$.

To show the well-posedness of the linearized Einstein-Bianchi system (3.6.1)–(3.6.3), we introduce the product space

$$\mathscr{X} = H^2(\Omega) \times \boldsymbol{H}(\text{curl}, \Omega; \mathbb{S}) \times \boldsymbol{L}^2(\Omega; \mathbb{T})$$

and the bilinear form $A(\cdot, \cdot) : \mathscr{X} \times \mathscr{X} \to \mathbb{R}$ as

$$A(\sigma, \boldsymbol{E}, \boldsymbol{B}; \tau, \boldsymbol{v}, \boldsymbol{\psi}) := (\sigma, \tau) - (\boldsymbol{E}, \nabla^2 \tau) - (\nabla^2 \sigma, \boldsymbol{v}) - (\boldsymbol{B}, \text{curl}\,\boldsymbol{v}) + (\boldsymbol{B}, \boldsymbol{\psi}) - (\text{curl}\,\boldsymbol{E}, \boldsymbol{\psi}).$$

It is easy to prove the continuity

$$A(\sigma, \boldsymbol{E}, \boldsymbol{B}; \tau, \boldsymbol{v}, \boldsymbol{\psi}) \lesssim (\|\sigma\|_2 + \|\boldsymbol{E}\|_{H(\text{curl})} + \|\boldsymbol{B}\|_0)(\|\tau\|_2 + \|\boldsymbol{v}\|_{H(\text{curl})} + \|\boldsymbol{\psi}\|_0) \tag{3.6.4}$$

for any $\sigma, \tau \in H^2(\Omega)$, $\boldsymbol{E}, \boldsymbol{v} \in \boldsymbol{H}(\text{curl}, \Omega; \mathbb{S})$ and $\boldsymbol{B}, \boldsymbol{\psi} \in \boldsymbol{L}^2(\Omega; \mathbb{T})$. The well-posedness of (3.6.1)–(3.6.3) is then derived from the following inf-sup condition.

Lemma 3.19 *For any $\sigma \in H^2(\Omega)$, $\boldsymbol{E} \in \boldsymbol{H}(\text{curl}, \Omega; \mathbb{S})$ and $\boldsymbol{B} \in \boldsymbol{L}^2(\Omega; \mathbb{T})$, it holds*

$$\|\sigma\|_2 + \|\boldsymbol{E}\|_{H(\text{curl})} + \|\boldsymbol{B}\|_0 \lesssim \sup_{(\tau, \boldsymbol{v}, \boldsymbol{\psi}) \in \mathscr{X}} \frac{A(\sigma, \boldsymbol{E}, \boldsymbol{B}; \tau, \boldsymbol{v}, \boldsymbol{\psi})}{\|\tau\|_2 + \|\boldsymbol{v}\|_{H(\text{curl})} + \|\boldsymbol{\psi}\|_0}. \tag{3.6.5}$$

Proof For ease of presentation, let

$$\alpha = \sup_{(\tau, \boldsymbol{v}, \boldsymbol{\psi}) \in \mathscr{X}} \frac{A(\sigma, \boldsymbol{E}, \boldsymbol{B}; \tau, \boldsymbol{v}, \boldsymbol{\psi})}{\|\tau\|_2 + \|\boldsymbol{v}\|_{H(\text{curl})} + \|\boldsymbol{\psi}\|_0}.$$

Then it follows from the Poincaré inequality that

$$\|E\|_0 \lesssim \|\operatorname{curl} E\|_0 + \sup_{\tau \in H^2(\Omega)} \frac{(E, \nabla^2 \tau)}{\|\tau\|_2}$$

$$\leq \|\operatorname{curl} E\|_0 + \|\sigma\|_0 + \sup_{\tau \in H^2(\Omega)} \frac{(E, \nabla^2 \tau) - (\sigma, \tau)}{\|\tau\|_2}$$

$$\leq \|\operatorname{curl} E\|_0 + \|\sigma\|_0 + \alpha. \tag{3.6.6}$$

On the other side, we have

$$A\left(\sigma, E, B; \sigma, -E - \nabla^2 \sigma, \frac{1}{2}(B - \operatorname{curl} E)\right) = \|\sigma\|_0^2 + |\sigma|_2^2 + \frac{1}{2}\|B\|_0^2 + \frac{1}{2}\|\operatorname{curl} E\|_0^2.$$

Hence we get from the definition of α and (3.6.6) that

$$\|\sigma\|_0^2 + |\sigma|_2^2 + \frac{1}{2}\|B\|_0^2 + \frac{1}{2}\|\operatorname{curl} E\|_0^2$$

$$\leq \alpha(\|\sigma\|_2 + \|E + \nabla^2 \sigma\|_{H(\operatorname{curl})} + \frac{1}{2}\|B - \operatorname{curl} E\|_0)$$

$$\lesssim \alpha(\|\sigma\|_2 + \|E\|_0 + \|\operatorname{curl} E\|_0 + \|B\|_0)$$

$$\lesssim \alpha(\|\sigma\|_2 + \|\operatorname{curl} E\|_0 + \|B\|_0) + \alpha^2,$$

which yields

$$\|\sigma\|_2 + \|\operatorname{curl} E\|_0 + \|B\|_0 \lesssim \alpha.$$

Finally the inf-sup condition (3.6.5) follows from the last inequality and (3.6.6).

□

As a result of (3.6.4) and the inf-sup condition (3.6.5), the variational formulation (3.6.1)–(3.6.3) of the linearized Einstein-Bianchi system is well-posed, and

$$\|\sigma\|_2 + \|E\|_{H(\operatorname{curl})} + \|B\|_0 \lesssim \|f\|_{(H(\operatorname{curl},\Omega;\mathbb{S}))'}.$$

It follows from (3.6.3) that $B = \operatorname{curl} E$, which can be eliminated from the system, so the linearized Einstein-Bianchi system (3.6.1)–(3.6.3) is equivalent to find $E \in H(\operatorname{curl}, \Omega; \mathbb{S})$ and $\sigma \in H^2(\Omega)$ such that

$$a(E, v) + b(v, \nabla^2 \sigma) = (f, v) \quad \forall v \in H(\operatorname{curl}, \Omega; \mathbb{S}), \tag{3.6.7}$$

$$b(E, \nabla^2 \tau) - c(\sigma, \tau) = 0 \quad \forall \tau \in H^2(\Omega), \tag{3.6.8}$$

where

$$a(\boldsymbol{E}, \boldsymbol{v}) = (\operatorname{curl} \boldsymbol{E}, \operatorname{curl} \boldsymbol{v}), \quad b(\boldsymbol{E}, \nabla^2 \tau) = (\boldsymbol{E}, \nabla^2 \tau), \quad c(\sigma, \tau) = (\sigma, \tau).$$

Then the inf-sup condition (3.6.5) is equivalent to

$$\|\sigma\|_2 + \|\boldsymbol{E}\|_{H(\operatorname{curl})} \lesssim \sup_{\substack{\tau \in H^2(\Omega) \\ \boldsymbol{v} \in \boldsymbol{H}(\operatorname{curl}, \Omega; \mathbb{S})}} \frac{a(\boldsymbol{E}, \boldsymbol{v}) + b(\boldsymbol{v}, \nabla^2 \sigma) + b(\boldsymbol{E}, \nabla^2 \tau) - c(\sigma, \tau)}{\|\tau\|_2 + \|\boldsymbol{v}\|_{H(\operatorname{curl})}}$$

for any $\sigma \in H^2(\Omega)$ and $\boldsymbol{E} \in \boldsymbol{H}(\operatorname{curl}, \Omega; \mathbb{S})$.

In summary, the simplified EB system (3.6.7)–(3.6.8) can be thought of as a generalization of Maxwell equations for $\boldsymbol{E} \in H(\operatorname{curl}, \Omega; \mathbb{R}^3)$ to the tensor version $\boldsymbol{E} \in H(\operatorname{curl}, \Omega; \mathbb{S})$. The scalar potential σ is also changed from $H^1(\Omega)$ to $H^2(\Omega)$ as the underline complex is changed from the de Rham complex to the Hessian complex.

3.6.2 Conforming Discretization

With conforming subspaces W_h and Σ_h, we could directly consider the Galerkin approximation of (3.6.7)–(3.6.8). However, as pointwise information of functions in virtual element spaces are not available, the L^2-inner product $(\cdot, \cdot)$ involved in $b(\cdot, \cdot)$ and $c(\cdot, \cdot)$ are not computable.

Remark 3.5 If we use the macro-elements W_A and Σ_A defined on the Alfeld split, cf. Remarks 3.1 and 3.2, the shape functions are piecewise polynomials and thus $b(\cdot, \cdot)$ and $c(\cdot, \cdot)$ are computable. $\qquad\square$

We will replace them by equivalent and accurate approximations which can be thought of as numerical quadrature. First introduce two stabilizations

$$S_K^0(\sigma, \tau) := h_K(\sigma, \tau)_{\partial K} + h_K^3(\partial_n \sigma, \partial_n \tau)_{\partial K},$$
$$S_K^1(\boldsymbol{E}, \boldsymbol{v}) := h_K^2(\operatorname{curl} \boldsymbol{E}, \operatorname{curl} \boldsymbol{v})_K + h_K(\boldsymbol{E} \times \boldsymbol{n}, \boldsymbol{v} \times \boldsymbol{n})_{\partial K},$$

which are computable as all integrands are polynomials.

Lemma 3.20 *For each tetrahedron $K \in \mathscr{T}_h$, we have*

$$S_K^0(\tau, \tau) \eqsim \|\tau\|_{0,K}^2 \quad \forall \, \tau \in W(K) \cap \ker(Q_{k-2}^K), \tag{3.6.9}$$

$$S_K^1(\boldsymbol{v}, \boldsymbol{v}) \eqsim \|\boldsymbol{v}\|_{0,K}^2 \quad \forall \, \boldsymbol{v} \in \boldsymbol{\Sigma}(K) \cap \ker(\boldsymbol{Q}_k^K). \tag{3.6.10}$$

Proof By the norm equivalence on the finite dimensional spaces and the scaling argument, it is sufficient to prove $S_K^0(\cdot, \cdot)$ and $S_K^1(\cdot, \cdot)$ are squared norms for the spaces $W(K) \cap \ker(Q_{k-2}^K)$ and $\Sigma(K) \cap \ker(\boldsymbol{Q}_k^K)$, respectively. Again as the element is a tetrahedron, by transferring back to the reference element, one can show the constants in (3.6.9) and (3.6.10) depends only on the shape regularity of the element.

Assume $\tau \in W(K) \cap \ker(Q_{k-2}^K)$ and $S_K^0(\tau, \tau) = 0$. Then $\tau \in H_0^2(K)$. By the integration by parts and the definition of $W(K)$, it follows

$$\|\nabla^2 \tau\|_{0,K}^2 = (\Delta^2 \tau, \tau)_K = (\Delta^2 \tau, Q_{k-2}^K \tau)_K = 0,$$

which results in $\tau = 0$. Hence $S_K^0(\cdot, \cdot)$ is a squared norm for the space $W(K) \cap \ker(Q_{k-2}^K)$.

Assume $\boldsymbol{v} \in \Sigma(K) \cap \ker(\boldsymbol{Q}_k^K)$ and $S_K^1(\boldsymbol{v}, \boldsymbol{v}) = 0$. Apparently $\boldsymbol{v} \in \boldsymbol{H}_0(\mathrm{curl}, \Omega; \mathbb{S}) \cap \ker(\mathrm{curl})$. Then there exists $w \in W(K) \cap H_0^2(K)$ satisfying $\boldsymbol{v} = \nabla^2 w$. Since $\boldsymbol{v} \in \ker(\boldsymbol{Q}_k^K)$, we get

$$(w, \mathrm{div\,div}\,\boldsymbol{q})_K = (\nabla^2 w, \boldsymbol{q})_K = 0 \quad \forall \boldsymbol{q} \in \mathbb{P}_k(K; \mathbb{S}),$$

which together with complex (3.4.15) implies

$$(w, q)_K = 0 \quad \forall q \in \mathbb{P}_{k-2}(K).$$

Therefore $w = 0$ and $\boldsymbol{v} = 0$. □

With these two stabilizations, define local bilinear forms

$$b_K(\boldsymbol{E}, \boldsymbol{v}) := (\boldsymbol{Q}_k^K \boldsymbol{E}, \boldsymbol{Q}_k^K \boldsymbol{v})_K + S_K^1(\boldsymbol{E} - \boldsymbol{Q}_k^K \boldsymbol{E}, \boldsymbol{v} - \boldsymbol{Q}_k^K \boldsymbol{v}),$$

$$c_K(\sigma, \tau) := (\widetilde{Q}_{k+2}^K \sigma, \widetilde{Q}_{k+2}^K \tau)_K + S_K^0(\sigma - \widetilde{Q}_{k+2}^K \sigma, \tau - \widetilde{Q}_{k+2}^K \tau),$$

where $\widetilde{Q}_{k+2}^K \sigma := Q_{k-2}^K \sigma + (I - Q_{k-2}^K)\Pi^K \sigma$. Recall that Π^K is the H^2-projection to $\mathbb{P}_{k+2}(K)$ defined by (3.5.17)–(3.5.18). The L^2-projection $Q_{k+2}^K \sigma$ is not computable but $Q_{k-2}^K \sigma$ is using the interior moments. Then $\widetilde{Q}_{k+2}^K \sigma$ is to augment $Q_{k-2}^K \sigma$ by the higher degree part from $\Pi^K \sigma$. It is obvious that

$$b_K(\boldsymbol{E}, \boldsymbol{q}) = (\boldsymbol{E}, \boldsymbol{q})_K \quad \forall \boldsymbol{E} \in \boldsymbol{H}^1(K; \mathbb{S}) \cup \Sigma(K), \boldsymbol{q} \in \mathbb{P}_k(K; \mathbb{S}), \quad (3.6.11)$$

$$c_K(\sigma, q) = (\widetilde{Q}_{k+2}^K \sigma, q)_K \quad \forall \sigma \in H^2(K) \cap W(K), q \in \mathbb{P}_{k+2}(K). \quad (3.6.12)$$

And we obtain from (3.6.9) and (3.6.10) that

$$b_K(\boldsymbol{v}, \boldsymbol{v}) \eqsim \|\boldsymbol{v}\|_{0,K}^2 \quad \forall \boldsymbol{v} \in \Sigma(K), \quad (3.6.13)$$

$$c_K(\tau, \tau) \eqsim \|\tau\|_{0,K}^2 \quad \forall \tau \in W(K). \quad (3.6.14)$$

Then we have from the Cauchy-Schwarz inequality that

$$b_K(\boldsymbol{E}, \boldsymbol{v}) \lesssim \|\boldsymbol{E}\|_{0,K} \|\boldsymbol{v}\|_{0,K} \quad \forall \, \boldsymbol{E}, \boldsymbol{v} \in \boldsymbol{\Sigma}(K), \tag{3.6.15}$$

$$c_K(\sigma, \tau) \lesssim \|\sigma\|_{0,K} \|\tau\|_{0,K} \quad \forall \, \sigma, \tau \in W(K). \tag{3.6.16}$$

We propose the following conforming mixed virtual element method for the variational formulation (3.6.7)–(3.6.8): find $\boldsymbol{E}_h \in \boldsymbol{\Sigma}_h$ and $\sigma_h \in W_h$ such that

$$a(\boldsymbol{E}_h, \boldsymbol{v}_h) + b_h(\boldsymbol{v}_h, \nabla^2 \sigma_h) = (\boldsymbol{f}, \boldsymbol{Q}_h \boldsymbol{v}_h) \quad \forall \, \boldsymbol{v}_h \in \boldsymbol{\Sigma}_h, \tag{3.6.17}$$

$$b_h(\boldsymbol{E}_h, \nabla^2 \tau_h) - c_h(\sigma_h, \tau_h) = 0 \quad\quad\quad \forall \, \tau_h \in W_h, \tag{3.6.18}$$

where $\boldsymbol{Q}_h \boldsymbol{v}_h \in \boldsymbol{L}^2(\Omega; \mathbb{S})$ is given by $(\boldsymbol{Q}_h \boldsymbol{v}_h)|_K := \boldsymbol{Q}_k^K (\boldsymbol{v}_h|_K)$ for each $K \in \mathscr{T}_h$ and

$$b_h(\boldsymbol{E}_h, \nabla^2 \tau_h) := \sum_{K \in \mathscr{T}_h} b_K(\boldsymbol{E}_h|_K, \nabla^2 \tau_h|_K), \quad c_h(\sigma_h, \tau_h) := \sum_{K \in \mathscr{T}_h} c_K(\sigma_h|_K, \tau_h|_K).$$

For any $\boldsymbol{E}_h, \boldsymbol{v}_h \in \boldsymbol{\Sigma}_h$ and $\sigma_h, \tau_h \in W_h$, it follows from (3.6.15)–(3.6.16) that

$$A_h(\boldsymbol{E}_h, \sigma_h; \boldsymbol{v}_h, \tau_h) \leq (\|\boldsymbol{E}_h\|_{H(\mathrm{curl})} + \|\sigma_h\|_2)(\|\boldsymbol{v}_h\|_{H(\mathrm{curl})} + \|\tau_h\|_2),$$

where

$$A_h(\boldsymbol{E}_h, \sigma_h; \boldsymbol{v}_h, \tau_h) := a(\boldsymbol{E}_h, \boldsymbol{v}_h) + b_h(\boldsymbol{v}_h, \nabla^2 \sigma_h) + b_h(\boldsymbol{E}_h, \nabla^2 \tau_h) - c_h(\sigma_h, \tau_h).$$

Following the proof of Lemma 3.18, we will have

$$\|\boldsymbol{v}_h\|_0 \lesssim \|\operatorname{curl} \boldsymbol{v}_h\|_0 + \sup_{\tau_h \in W_h} \frac{b_h(\boldsymbol{v}_h, \nabla^2 \tau_h)}{\|\tau_h\|_2}. \tag{3.6.19}$$

We then prove the discrete inf-sup condition.

Lemma 3.21 *For any $\boldsymbol{E}_h \in \boldsymbol{\Sigma}_h$ and $\sigma_h \in W_h$, it holds*

$$\|\boldsymbol{E}_h\|_{H(\mathrm{curl})} + \|\sigma_h\|_2 \lesssim \sup_{\substack{\boldsymbol{v}_h \in \boldsymbol{\Sigma}_h \\ \tau_h \in W_h}} \frac{A_h(\boldsymbol{E}_h, \sigma_h; \boldsymbol{v}_h, \tau_h)}{\|\boldsymbol{v}_h\|_{H(\mathrm{curl})} + \|\tau_h\|_2}. \tag{3.6.20}$$

Proof For ease of presentation, let

$$\alpha = \sup_{\substack{\boldsymbol{v}_h \in \boldsymbol{\Sigma}_h \\ \tau_h \in W_h}} \frac{A_h(\boldsymbol{E}_h, \sigma_h; \boldsymbol{v}_h, \tau_h)}{\|\boldsymbol{v}_h\|_{H(\mathrm{curl})} + \|\tau_h\|_2}.$$

Since

$$\sup_{\tau_h \in W_h} \frac{b_h(\boldsymbol{E}_h, \nabla^2 \tau_h)}{\|\tau_h\|_2} = \sup_{\tau_h \in W_h} \frac{b_h(\boldsymbol{E}_h, \nabla^2 \tau_h) - c_h(\sigma_h, \tau_h) + c_h(\sigma_h, \tau_h)}{\|\tau_h\|_2}$$

$$\lesssim \|\sigma_h\|_0 + \alpha,$$

we get from the discrete Poincaré inequality (3.6.19) that

$$\|\boldsymbol{E}_h\|_0 \lesssim \|\operatorname{curl} \boldsymbol{E}_h\|_0 + \|\sigma_h\|_0 + \alpha. \tag{3.6.21}$$

On the other side, by the fact $a(\boldsymbol{E}_h, \nabla^2 \sigma_h) = 0$ we have

$$A_h(\boldsymbol{E}_h, \sigma_h; \boldsymbol{E}_h + \nabla^2 \sigma_h, -\sigma_h) = a(\boldsymbol{E}_h, \boldsymbol{E}_h) + b_h(\nabla^2 \sigma_h, \nabla^2 \sigma_h) + c_h(\sigma_h, \sigma_h),$$

which combined with (3.6.13)–(3.6.14) implies

$$\|\sigma_h\|_2^2 + \|\operatorname{curl} \boldsymbol{E}_h\|_0^2 \lesssim \alpha(\|\sigma_h\|_2 + \|\boldsymbol{E}_h + \nabla^2 \sigma_h\|_{H(\operatorname{curl})}) \lesssim \alpha(\|\sigma_h\|_2 + \|\boldsymbol{E}_h\|_{H(\operatorname{curl})}).$$

Hence

$$\|\sigma_h\|_2^2 + \|\operatorname{curl} \boldsymbol{E}_h\|_0^2 \lesssim \alpha^2 + \alpha \|\boldsymbol{E}_h\|_0.$$

Finally combining the last inequality and (3.6.21) gives (3.6.20).   □

From now on we always denote by $\boldsymbol{E}_h \in \boldsymbol{\Sigma}_h$ and $\sigma_h \in W_h$ the solution of the mixed method (3.6.17)–(3.6.18).

Lemma 3.22 *Assume* $\boldsymbol{E} \in \boldsymbol{H}^{k+1}(\Omega; \mathbb{S})$ *and* $\sigma \in \boldsymbol{H}^{k+2}(\Omega)$. *Then*

$$b_h(\boldsymbol{v}_h, \nabla^2 I_h^\Delta \sigma) - b(\boldsymbol{v}_h, \nabla^2 \sigma) \lesssim h^k \|\boldsymbol{v}_h\|_0 |\sigma|_{k+2}, \tag{3.6.22}$$

$$b_h(\boldsymbol{I}_h^c \boldsymbol{E}, \nabla^2 \tau_h) - b(\boldsymbol{E}, \nabla^2 \tau_h) \lesssim h^{k+1} |\boldsymbol{E}|_{k+1} |\tau_h|_2, \tag{3.6.23}$$

$$(\sigma, \tau_h) - c_h(I_h^\Delta \sigma, \tau_h) \lesssim h_K^{k+1} \|\sigma\|_{k+1,K} \|\tau_h\|_{2,K}. \tag{3.6.24}$$

Proof For each $K \in \mathcal{T}_h$, we acquire from (3.6.11), (3.6.15) and (3.5.24) that

$$b_K(\boldsymbol{v}_h, \nabla^2 I_h^\Delta \sigma) - (\boldsymbol{v}_h, \nabla^2 \sigma)_K$$

$$= b_K(\boldsymbol{v}_h, \nabla^2 I_h^\Delta \sigma - \boldsymbol{Q}_k^K(\nabla^2 \sigma)) - (\boldsymbol{v}_h, \nabla^2 \sigma - \boldsymbol{Q}_k^K(\nabla^2 \sigma))_K$$

$$\lesssim \|\boldsymbol{v}_h\|_{0,K} \|\nabla^2 I_h^\Delta \sigma - \boldsymbol{Q}_k^K(\nabla^2 \sigma)\|_{0,K} + \|\boldsymbol{v}_h\|_{0,K} \|\nabla^2 \sigma - \boldsymbol{Q}_k^K(\nabla^2 \sigma)\|_{0,K}$$

$$\lesssim \|\boldsymbol{v}_h\|_{0,K} (|\sigma - I_h^\Delta \sigma|_{2,K} + \|\nabla^2 \sigma - \boldsymbol{Q}_k^K(\nabla^2 \sigma)\|_{0,K}) \lesssim h_K^k \|\boldsymbol{v}_h\|_{0,K} |\sigma|_{k+2,K}.$$

Thus

$$b_h(\boldsymbol{v}_h, \nabla^2 I_h^\Delta \sigma_h) - b(\boldsymbol{v}_h, \nabla^2 \sigma) = \sum_{K \in \mathscr{T}_h} \left(b_K(\boldsymbol{v}_h, \nabla^2 I_h^\Delta \sigma_h) - (\boldsymbol{v}_h, \nabla^2 \sigma)_K \right)$$

$$\lesssim h^k \|\boldsymbol{v}_h\|_0 |\sigma|_{k+2},$$

i.e. (3.6.22).

Similarly it holds from (3.6.11), (3.6.15) and (3.5.35) that

$$b_K(I_h^c \boldsymbol{E}, \nabla^2 \tau_h) - (\boldsymbol{E}, \nabla^2 \tau_h)_K = b_K(I_h^c \boldsymbol{E} - \boldsymbol{Q}_k^K \boldsymbol{E}, \nabla^2 \tau_h) - (\boldsymbol{E} - \boldsymbol{Q}_k^K \boldsymbol{E}, \nabla^2 \tau_h)_K$$

$$\lesssim (\|I_h^c \boldsymbol{E} - \boldsymbol{Q}_k^K \boldsymbol{E}\|_{0,K} + \|\boldsymbol{E} - \boldsymbol{Q}_k^K \boldsymbol{E}\|_{0,K}) |\tau_h|_{2,K}$$

$$\lesssim h_K^{k+1} |\boldsymbol{E}|_{k+1,K} |\tau_h|_{2,K},$$

which yields (3.6.23).

Employing (3.6.12), (3.6.16), (3.5.19) and (3.5.24), we get

$$(\sigma, \tau_h)_K - c_K(I_h^\Delta \sigma, \tau_h)$$

$$= (\sigma - \widetilde{Q}_{k+2}^K \sigma, \tau_h)_K - c_K(I_h^\Delta \sigma - \widetilde{Q}_{k+2}^K \sigma, \tau_h) + (\widetilde{Q}_{k+2}^K \sigma, \tau_h - \widetilde{Q}_{k+2}^K \tau_h)_K$$

$$= (\sigma - \widetilde{Q}_{k+2}^K \sigma, \tau_h)_K - c_K(I_h^\Delta \sigma - \widetilde{Q}_{k+2}^K \sigma, \tau_h) + (\Pi^K \sigma - Q_{k-2}^K \Pi^K \sigma, \tau_h - \widetilde{Q}_{k+2}^K \tau_h)_K$$

$$\lesssim \left(\|\sigma - \widetilde{Q}_{k+2}^K \sigma\|_{0,K} + \|I_h^\Delta \sigma - \widetilde{Q}_{k+2}^K \sigma\|_{0,K} \right) \|\tau_h\|_{0,K}$$

$$\quad + \|\Pi^K \sigma - Q_{k-2}^K \Pi^K \sigma\|_{0,K} \|\tau_h - \widetilde{Q}_{k+2}^K \tau_h\|_{0,K}$$

$$\lesssim \left(\|\sigma - \Pi^K \sigma\|_{0,K} + \|\sigma - I_h^\Delta \sigma\|_{0,K} \right) \|\tau_h\|_{0,K} + h_K^2 \|\Pi^K \sigma - Q_{k-2}^K \Pi^K \sigma\|_{0,K} |\tau_h|_{2,K}$$

$$\lesssim h_K^{k+1} \|\sigma\|_{k+1,K} \|\tau_h\|_{2,K}.$$

Therefore (3.6.24) is true.   □

Theorem 3.3 *Let $\boldsymbol{E}_h \in \boldsymbol{\Sigma}_h$ and $\sigma_h \in W_h$ be the solution of the mixed method* (3.6.17)–(3.6.18) *and let $\boldsymbol{E}$ and σ be the solution of* (3.6.7)–(3.6.8). *Assume $\boldsymbol{E} \in \boldsymbol{H}^{k+1}(\Omega; \mathbb{S})$, $\sigma \in H^{k+2}(\Omega)$ and $\boldsymbol{f} \in \boldsymbol{H}^k(\Omega; \mathbb{S})$. We have*

$$\|\boldsymbol{E} - \boldsymbol{E}_h\|_{H(\mathrm{curl})} + \|\sigma - \sigma_h\|_2 \lesssim h^k \left(|\boldsymbol{E}|_{k+1} + \|\sigma\|_{k+2} + |\boldsymbol{f}|_k \right).$$

Proof Take any $\boldsymbol{v}_h \in \boldsymbol{\Sigma}_h$ and $\tau_h \in W_h$. We get from the variational formulation (3.6.7)–(3.6.8), (3.5.35) and estimates (3.6.22)–(3.6.24) that

$$A_h(I_h^c \boldsymbol{E}, I_h^\Delta \sigma; \boldsymbol{v}_h, \tau_h) - (\boldsymbol{f}, \boldsymbol{v}_h)$$

$$= a(I_h^c \boldsymbol{E} - \boldsymbol{E}, \boldsymbol{v}_h) + b_h(\boldsymbol{v}_h, \nabla^2 I_h^\Delta \sigma) - b(\boldsymbol{v}_h, \nabla^2 \sigma)$$

$$+ b_h(I_h^c E, \nabla^2 \tau_h) - b(E, \nabla^2 \tau_h) + (\sigma, \tau_h) - c_h(I_h^\Delta \sigma, \tau_h)$$

$$\lesssim h^k |E|_{k+1} \|\operatorname{curl} v_h\|_0 + h^k \|v_h\|_0 |\sigma|_{k+2} + h^{k+1} |E|_{k+1} |\tau_h|_2 + h^{k+1} \|\sigma\|_{k+1} \|\tau_h\|_2.$$

Since

$$(f, v_h - Q_h v_h) = (f - Q_h f, v_h) \le \|f - Q_h f\|_0 \|v_h\|_0 \lesssim h^k |f|_k \|v_h\|_0,$$

we achieve from the mixed method (3.6.17)–(3.6.18) that

$$A_h(I_h^c E - E_h, I_h^\Delta \sigma - \sigma_h; v_h, \tau_h)$$

$$= A_h(I_h^c E, I_h^\Delta \sigma; v_h, \tau_h) - (f, Q_h v_h)$$

$$= A_h(I_h^c E, I_h^\Delta \sigma; v_h, \tau_h) - (f, v_h) + (f, v_h - Q_h v_h)$$

$$\lesssim h^k |E|_{k+1} \|\operatorname{curl} v_h\|_0 + h^k (|\sigma|_{k+2} + |f|_k) \|v_h\|_0 + h^{k+1} |E|_{k+1} |\tau_h|_2$$

$$+ h^{k+1} \|\sigma\|_{k+1} \|\tau_h\|_2.$$

Now it follows from the inf-sup condition (3.6.20) that

$$\|I_h^c E - E_h\|_{H(\operatorname{curl})} + \|I_h^\Delta \sigma - \sigma_h\|_2 \lesssim \sup_{\substack{v_h \in \Sigma_h \\ \tau_h \in W_h}} \frac{A_h(I_h^c E - E_h, I_h^\Delta \sigma - \sigma_h; v_h, \tau_h)}{\|v_h\|_{H(\operatorname{curl})} + \|\tau_h\|_2}$$

$$\lesssim h^k (|E|_{k+1} + \|\sigma\|_{k+2} + |f|_k).$$

Thus we acquire from (3.5.35) and (3.5.24) that

$$\|E - E_h\|_{H(\operatorname{curl})} + \|\sigma - \sigma_h\|_2$$

$$\le \|E - I_h^c E\|_{H(\operatorname{curl})} + \|\sigma - I_h^\Delta \sigma\|_2 + \|I_h^c E - E_h\|_{H(\operatorname{curl})} + \|I_h^\Delta \sigma - \sigma_h\|_2$$

$$\lesssim h^k (|E|_{k+1} + \|\sigma\|_{k+2} + |f|_k),$$

as required.   □

References

1. P. Alfeld, A trivariate Clough—Tocher scheme for tetrahedral data. Comput. Aided Geom. Design **1**(2), 169–181 (1984)
2. C. Amrouche, C. Bernardi, M. Dauge, V. Girault, Vector potentials in three-dimensional nonsmooth domains. Math. Methods Appl. Sci. **21**(9), 823–864 (1998)
3. P.F. Antonietti, L. Beirão da Veiga, S. Scacchi, M. Verani, A C^1 virtual element method for the Cahn-Hilliard equation with polygonal meshes. SIAM J. Numer. Anal. **54**(1), 34–56 (2016)
4. J. Argyris, I. Fried, D. Scharpf, The TUBA family of plate elements for the matrix displacement method. Aero. J. Roy. Aero. Soc. **72**, 701–709 (1968)
5. D.N. Arnold, *Finite Element Exterior Calculus* (Society for Industrial and Applied Mathematics (SIAM), Philadelphia, PA, 2018)
6. D.N. Arnold, K. Hu, Complexes from complexes. Found. Comput. Math. **21**(6), 1739–1774 (2021)
7. D.N. Arnold, R. Winther, Mixed finite elements for elasticity. Numer. Math. **92**(3), 401–419 (2002)
8. D.N. Arnold, R.S. Falk, R. Winther, Finite element exterior calculus, homological techniques, and applications. Acta Numer. **15**, 1–155 (2006)
9. L. Beirão da Veiga, F. Brezzi, A. Cangiani, G. Manzini, L.D. Marini, A. Russo, Basic principles of virtual element methods. Math. Models Methods Appl. Sci. **23**(1), 199–214 (2013)
10. L. Beirão da Veiga, F. Brezzi, L.D. Marini, A. Russo, The hitchhiker's guide to the virtual element method. Math. Models Methods Appl. Sci. **24**(8), 1541–1573 (2014)
11. L. Beirão da Veiga, F. Brezzi, L.D. Marini, A. Russo, $H(\mathrm{div})$ and $H(\mathbf{curl})$-conforming virtual element methods. Numer. Math. **133**(2), 303–332 (2016)
12. L. Beirão da Veiga, C. Lovadina, G. Vacca, Divergence free virtual elements for the Stokes problem on polygonal meshes. ESAIM Math. Model. Numer. Anal. **51**(2), 509–535 (2017)
13. L. Beirão da Veiga, F. Dassi, A. Russo, A C^1 virtual element method on polyhedral meshes. Comput. Math. Appl. **79**(7), 1936–1955 (2020)
14. L. Beirão da Veiga, F. Dassi, G. Vacca, The Stokes complex for virtual elements in three dimensions. Math. Models Methods Appl. Sci. **30**(3), 477–512 (2020)
15. M.F. Benedetto, S. Berrone, S. Pieraccini, S. Scialò, The virtual element method for discrete fracture network simulations. Comput. Methods Appl. Mech. Eng. **280**, 135–156 (2014)
16. S.C. Brenner, L.Y. Sung, C^0 interior penalty methods for fourth order elliptic boundary value problems on polygonal domains. J. Sci. Comput. **22/23**, 83–118 (2005)
17. F. Brezzi, L.D. Marini, Virtual element methods for plate bending problems. Comput. Methods Appl. Mech. Eng. **253**, 455–462 (2013)
18. F. Brezzi, K. Lipnikov, V. Simoncini, A family of mimetic finite difference methods on polygonal and polyhedral meshes. Math. Models Methods Appl. Sci. **15**(10), 1533–1551 (2005)
19. A. Buffa, Trace theorems on non-smooth boundaries for functional spaces related to Maxwell equations: An overview, in *Computational Electromagnetics* (Springer, Berlin, 2003), pp. 23–34
20. A. Buffa, G. Geymonat, On traces of functions in $W^{2,p}(\Omega)$ for Lipschitz domains in $\mathbb{R}^3$. C. R. Acad. Sci. Paris Sér. I Math. **332**(8), 699–704 (2001)
21. L. Chen, X. Huang, Decoupling of mixed methods based on generalized Helmholtz decompositions. SIAM J. Numer. Anal. **56**(5), 2796–2825 (2018)
22. L. Chen, X. Huang, Finite elements for divdiv-conforming symmetric tensors. Preprint (2020). arXiv:2005.01271
23. L. Chen, X. Huang, Finite elements for div div conforming symmetric tensors in three dimensions. Math. Comput. **91**(335), 1107–1142 (2022)
24. L. Chen, X. Huang, Nonconforming virtual element method for $2m$th order partial differential equations in $\mathbb{R}^n$. Math. Comput. **89**(324), 1711–1744 (2020)

25. L. Chen, X. Huang, A finite element elasticity complex in three dimensions. Math. Comput. (accepted) (2022). arXiv:2106.12786
26. L. Chen, H. Wei, M. Wen, An interface-fitted mesh generator and virtual element methods for elliptic interface problems. J. Comput. Phys. **334**, 327–348 (2017)
27. A. Chernov, L. Mascotto, The harmonic virtual element method: stabilization and exponential convergence for the Laplace problem on polygonal domains. IMA J. Numer. Anal. **39**(4), 1787–1817 (2019)
28. P.G. Ciarlet, *The Finite Element Method for Elliptic Problems* (North-Holland Publishing, Amsterdam, 1978)
29. M. Costabel, A. McIntosh, On Bogovskiĭ and regularized Poincaré integral operators for de Rham complexes on Lipschitz domains. Math. Z. **265**(2), 297–320 (2010)
30. M. Eastwood, A complex from linear elasticity, in *The Proceedings of the 19th Winter School "Geometry and Physics"* (Srní, 1999), 63, pp. 23–29 (2000)
31. G. Fu, J. Guzmán, M. Neilan, Exact smooth piecewise polynomial sequences on Alfeld splits. Math. Comput. **89**(323), 1059–1091 (2020)
32. J. Hu, Y. Liang, Conforming discrete Gradgrad-complexes in three dimensions. Math. Comput. **90**(330), 1637–1662 (2021)
33. X. Huang, Nonconforming virtual element method for $2m$th order partial differential equations in $\mathbb{R}^n$ with $m > n$. Calcolo **57**(4), Paper No. 42, 38 (2020)
34. P. Kelly, Mechanics lecture notes: An introduction to solid mechanics. Available from http://homepages.engineering.auckland.ac.nz/~pkel015/SolidMechanicsBooks/index.html
35. M.J. Lai, L.L. Schumaker, *Spline Functions on Triangulations* (Cambridge University Press, Cambridge, 2007)
36. K. Lipnikov, G. Manzini, M. Shashkov, Mimetic finite difference method. J. Comput. Phys. **257**(part B), 1163–1227 (2014)
37. L. Mascotto, I. Perugia, A. Pichler, Non-conforming harmonic virtual element method: h- and p-versions. J. Sci. Comput. **77**(3), 1874–1908 (2018)
38. P. Monk, *Finite Element Methods for Maxwell's Equations* (Oxford University Press, New York, 2003)
39. J.C. Nédélec, Mixed finite elements in $\mathbf{R}^3$. Numer. Math. **35**(3), 315–341 (1980)
40. J.C. Nédélec, A new family of mixed finite elements in $\mathbf{R}^3$. Numer. Math. **50**(1), 57–81 (1986)
41. D. Pauly, W. Zulehner, The divDiv-complex and applications to biharmonic equations. Appl. Anal. **99**(9), 1579–1630 (2020)
42. V. Quenneville-Belair, A new approach to finite element simulations of general relativity. Ph.D. thesis, University of Minnesota (2015)
43. P.A. Raviart, J.M. Thomas, A mixed finite element method for 2nd order elliptic problems, in *Mathematical Aspects of Finite Element Methods (Proc. Conf., Consiglio Naz. delle Ricerche (C.N.R.), Rome, 1975)*. Lecture Notes in Math., Vol. 606. (Springer, Berlin, 1977), pp. 292–315
44. L. Tartar, On the characterization of traces of a Sobolev space used for Maxwell's equation, in *Proceedings of a Meeting*, Bordeaux, France (1997)
45. H. Wei, X. Huang, A. Li, Piecewise divergence-free nonconforming virtual elements for Stokes problem in any dimensions. SIAM J. Numer. Anal. **59**(3), 1835–1856 (2021)
46. S. Zhang, A family of 3D continuously differentiable finite elements on tetrahedral grids. Appl. Numer. Math. **59**(1), 219–233 (2009)

Chapter 4
Some Virtual Element Methods
for Infinitesimal Elasticity Problems

Edoardo Artioli, Stefano de Miranda, Carlo Lovadina, Luca Patruno, and Michele Visinoni

Abstract The chapter presents Virtual Element Methods for linear elasticity. In particular, displacement based methods stemming from the principle of virtual works for 2D problems, and mixed methods based on the Hellinger-Reissner variational principle for 2D and 3D problems are discussed and detailed. A series of numerical examples for each set of methods are given in order to show the characteristic features of the newly developed methods and to assess their accuracy and convergence properties.

4.1 Introduction

This chapter presents a review of two families of Virtual Element Methods that have been recently studied by the authors in the framework of small strain small displacement linear elasticity problems (see [6, 8, 9, 44]).

The Virtual Element Method (VEM) is a recently introduced numerical method [18, 20] for the approximation of general PDEs, and can be seen as generalization of the classical Finite Element Method (e.g. [15, 49, 60]) and as evolution of modern mimetic schemes (see for instance [21, 34, 35]). Differing from standard

E. Artioli (✉)
Department of Civil Engineering and Computer Science, University of Rome Tor Vergata, Rome, Italy
e-mail: artioli@ing.uniroma2.it

S. de Miranda · L. Patruno
DICAM, University of Bologna, Bologna, Italy
e-mail: stefano.demiranda@unibo.it; luca.patruno@unibo.it

C. Lovadina
Department of Mathematics, University of Milan, Milan, Italy
e-mail: carlo.lovadina@unimi.it

M. Visinoni
Department of Mathematics and Applications, University of Milano Bicocca, Milan, Italy
e-mail: michele.visinoni@unimib.it

Finite Element methods, the VEM structure allows using very general polygonal or polyhedral meshes, which entails the capability of hanging vertices, highly distorted irregular polygonal element shapes, as well as curvilinear polygons [12, 13, 27]. As more recent works testify, mesh generation and adaptivity (local refinement/de-refinement) can be exploited in a very versatile form to give highly powerful and accurate schemes for applied physics and engineering problems requiring such complex features, which, for some selected applications, may result in methods quite more robust than established ones [16, 17, 25, 28, 36, 38].

The basic idea underneath the VEM is to use approximating functions which are solution to suitable local partial differential equations (hence the possibility to easily implement highly regular discrete spaces, see for instance [33]) departing from the standard local polynomial approximation approach. Price to pay is that these discrete non-polynomial shape functions are not explicitly known pointwise but only over the element boundary. Such limited information (the actual degrees of freedom of a VEM method) is indeed sufficient to derive suitable projection operators that enable computation of all the relevant element arrays and lead to a stiffness matrix and the right-hand side vector. A key ingredient of the method is represented by suitable quadrature rules for general convex/concave/curvilinear polygons/polyhaedra avoiding the explicit construction of the local basis functions [14, 57–59].

The interest in VEM has largely grown over recent years not only in the numerical analysis community (see for instance [19, 22, 24, 29, 31–33, 37, 42, 43, 51]) but in the applied mathematics and engineering ones as well, as confirmed by the many recent contributions among which we here mention a representative list in the framework of elasticity and, more in general, of computational mechanics [1–3, 6–11, 19, 22–27, 37, 40, 47, 48, 55, 61–64].

In the aforementioned setting, the present chapter represents a review of some recently proposed virtual element methods for two and three-dimensional linear elasticity. The methods are grouped as primal or displacement based methods, and mixed (i.e. stress/displacement) formulations, respectively. The former are based on the principle of virtual works, the latter on the classical Hellinger-Reissner variational principle. While the first family represents the typical VEM counterpart of standard Lagrangian finite elements and are based on a projection operator mapping local displacements of any chosen order to approximated polynomial strains, the second family is an innovative mixed VEM capable of naturally representing Cauchy stress symmetry and preserve inter-element traction continuity, notably non-trivial tasks in mixed finite element formulations [5, 30]. This issue can be efficiently solved in the VEM framework which enables the design of accurate and computationally light methods. Furthermore, the particular structure of the approximation spaces involved in the Hellinger-Reissner VEM schemes, easily allows to perform the so-called hybridization procedure to efficiently solve the resulting linear system and to design a suitable higher-order post-processing of the displacement field (see [45], where the ideas of [4] are developed in the elasticity problem framework). It is also worth remarking that hybridization is instead hardly applicable for the available conforming FEM schemes.

The outline of the paper is the following. In Sect. 4.2 we review the weak forms for linear elasticity, in primal and mixed form, respectively, in the realm of infinitesimal strain and small displacements. In Sect. 4.3 we explore the relevant Virtual Element Methods for the previously recalled boundary value problems: primal methods based on the principle of virtual works refer to two-dimensional domains, while, in the case of mixed methods cast in the framework of the Hellinger-Reissner variational formulation, discussion tackles both 2D and 3D numerical schemes. Last, in Sect. 4.4 a selection of numerical results, aiming at confirming numerical features and theoretical predictions on the examined methods, is presented.

4.2 Elasticity Formulation with Infinitesimal Strain

In this section we briefly present the elasticity problem in its simplest framework, i.e. within the infinitesimal strain theory and for a linear constitutive law (for a comprehensive description of the elasticity theory, one may look at classical monographs, such as [39, 50, 54], for instance). We thus consider the following first-order differential system.

$$
\begin{cases}
\text{Find } (\boldsymbol{\sigma}, \mathbf{u}) \text{ such that} \\
-\,\mathbf{div}\,\boldsymbol{\sigma} = \mathbf{f} & \text{in } \Omega \\
\boldsymbol{\sigma} = \mathbb{C}\boldsymbol{\varepsilon}(\mathbf{u}) & \text{in } \Omega \\
\mathbf{u}_{|\partial\Omega} = \mathbf{0}
\end{cases}
\tag{4.2.1}
$$

Above, $\boldsymbol{\sigma}$ is the *symmetric* stress field and $\mathbf{u}$ is the displacement field. Moreover, Ω is a sufficiently regular domain of $\mathbb{R}^d$, with $d = 2, 3$, while $\mathbf{f}$ represents the applied loads. Finally, $\boldsymbol{\varepsilon}(\cdot)$ is the symmetric gradient operator, i.e.

$$
\boldsymbol{\varepsilon}(\cdot) = \frac{1}{2}\left(\nabla(\cdot) + \nabla(\cdot)^T\right),
$$

div is the usual vectorial divergence operator acting on second-order tensors (thus, **div** $\boldsymbol{\tau}$ is, in Cartesian components: $\frac{\partial \tau_{ij}}{\partial x_j}$; Einstein's summation convention is here adopted), and $\mathbb{C}$ is the fourth-order symmetric and uniformly positive-definite elasticity tensor. Here we only consider homogeneous boundary conditions, but other cases can be treated using exactly the same techniques employed in the more classical Finite Element Method.

4.2.1   Primal Form

The easiest formulation of the elasticity problem (4.2.1) is the so-called *primal formulation*. It simply consists of the elimination of the stress field, by substituting the second equation of (4.2.1) into the first one. Thus, the differential problem now becomes

$$
\begin{cases}
\text{Find } \mathbf{u} \text{ such that} \\
-\operatorname{\mathbf{div}}(\mathbb{C}\boldsymbol{\varepsilon}(\mathbf{u})) = \mathbf{f} \qquad \text{in } \Omega \\
\mathbf{u}_{|\partial\Omega} = \mathbf{0}
\end{cases}
\tag{4.2.2}
$$

Since we are going to deal with a Galerkin method to approximate the solution to problem (4.2.2), we introduce the following (standard) variational formulation.

$$
\begin{cases}
\text{Find } \mathbf{u} \in V \text{ such that} \\
d(\mathbf{u}, \mathbf{v}) = (\mathbf{f}, \mathbf{v}) \qquad \forall \mathbf{v} \in V,
\end{cases}
\tag{4.2.3}
$$

where $V = H_0^1(\Omega)^d$ with $d = 2$ or $d = 3$, $(\cdot, \cdot)$ represents the usual L^2 inner product, and the bilinear form $d(\cdot, \cdot) : V \times V \to \mathbb{R}$ is defined by

$$
d(\mathbf{u}, \mathbf{v}) = (\mathbb{C}\boldsymbol{\varepsilon}(\mathbf{u}), \mathbf{v}) = \int_\Omega \mathbb{C}\boldsymbol{\varepsilon}(\mathbf{u}) : \mathbf{v}.
\tag{4.2.4}
$$

It is well-known that problem (4.2.3) is a continuous and elliptic problem, so well-posed. In particular, it holds:

$$
\|\mathbf{u}\|_V \le C \|\mathbf{f}\|_0,
\tag{4.2.5}
$$

where C is a constant depending on Ω and on the material tensor $\mathbb{C}$.

4.2.2   Mixed Form

We now introduce the so called Hellinger-Reissner mixed formulation of problem (4.2.1). Defining $\mathbb{D} = \mathbb{C}^{-1}$, and $a(\boldsymbol{\sigma}, \boldsymbol{\tau}) = (\mathbb{D}\boldsymbol{\sigma}, \boldsymbol{\tau})$, the variational formulation of problem (4.2.1) reads:

$$
\begin{cases}
\text{Find } (\boldsymbol{\sigma}, \mathbf{u}) \in \Sigma \times U \text{ such that} \\
a(\boldsymbol{\sigma}, \boldsymbol{\tau}) + (\operatorname{\mathbf{div}}\boldsymbol{\tau}, \mathbf{u}) = 0 \quad \forall \boldsymbol{\tau} \in \Sigma \\
(\operatorname{\mathbf{div}}\boldsymbol{\sigma}, \mathbf{v}) = -(\mathbf{f}, \mathbf{v}) \quad \forall \mathbf{v} \in U
\end{cases}
\tag{4.2.6}
$$

where $U = L^2(\Omega)^d$, the loading $\mathbf{f} \in L^2(\Omega)^d$ and

$$\Sigma = \{\boldsymbol{\tau} \in H(\mathbf{div}; \Omega) \ : \ \boldsymbol{\tau} \text{ is symmetric}\}.$$

Above, $H(\mathbf{div}; \Omega)$ denotes the space of tensor in $L^2(\Omega)^{d \times d}$, whose divergence is in $L^2(\Omega)^d$. Furthermore, given a functional space X, $X_s^{d \times d}$ denotes the $d \times d$ symmetric tensors whose components belong to X. It is well known that Problem (4.2.6) is well-posed (see [30], for instance). in particular, it holds:

$$||\boldsymbol{\sigma}||_\Sigma + ||\mathbf{u}||_U \le C ||\mathbf{f}||_0, \tag{4.2.7}$$

where C is a constant depending on Ω and on the material tensor $\mathbb{C}$.

Remark 4.1 As discussed in [30], estimate (4.2.7) does not break down for nearly incompressible materials. More precisely, considering the constitutive law:

$$\mathbb{C}\boldsymbol{\varepsilon} = 2\mu\boldsymbol{\varepsilon} + \lambda \text{tr}(\boldsymbol{\varepsilon}) Id \qquad \forall \text{symmetric tensor } \boldsymbol{\varepsilon}, \tag{4.2.8}$$

with $\lambda, \mu > 0$ Lame's parameters, Id the identity matrix and $tr(\cdot)$ the trace operator, the constant C in (4.2.7) can be chosen independent of λ.

4.3 Virtual Element Methods for Elasticity

Similarly to the Finite Element procedure, the starting point for the design of a Virtual Element scheme is the introduction of the computational domain mesh. Accordingly, let $\{\mathcal{T}_h\}_h$ be a sequence of decompositions of Ω into general polygonal (for $d = 2$) or polyhedral (for $d = 3$) elements E with

$$h_E : \text{diameter}(E), \quad h = \sup_{E \in \mathcal{T}_h} h_E.$$

In what follows, $|E|$ and $|e| = h_e$ will denote the d-volume of E and the length of the side $e \in \partial E$, respectively; for $d = 3$, $|f|$ and h_f denote the area and the diameter of the face $f \in \partial E$, respectively.

We suppose that for all h, each element E in $\mathcal{T}_h$ fulfils the following assumptions:

- (**A1**) E is star-shaped with respect to a ball of radius greater or equal to γh_E,
- (**A2**) for every edge $e \in \partial f$, we have $|e| \ge \gamma h_f \ge \gamma^2 h_E$,
- (**A3**) (only for $d = 3$) for every face $f \in \partial E$ we have $h_f \ge \gamma h_E$ and f is star-shaped with respect to a disk of radius greater or equal to γh_f,

where γ is a positive constant. We remark that the hypotheses above, though not too restrictive in many practical cases, can be further relaxed, as noted in [18].

Moreover, in what follows we suppose that $\mathbb{C}$ is constant inside each element E.

4.3.1 Primal Methods Based on Virtual Work Principle

A virtual element method (VEM) for problem (4.2.2) is constructed following a procedure that closely resembles the Finite Element approach, i.e. by restricting the original variational formulation (4.2.3) to the discrete space V_h and approximating the ensuing terms:

$$\begin{cases} \text{find } \mathbf{u}_h \in V_h \text{ such that} \\ d_h(\mathbf{u}_h, \mathbf{v}_h) = (\mathbf{f}, \mathbf{v}_h)_h \qquad \forall\, \mathbf{v}_h \in V_h, \end{cases} \tag{4.3.1}$$

where

- $V_h \subset V$ is the approximation virtual space;
- $d_h(\cdot, \cdot) : V_h \times V_h \to \mathbb{R}$ is a discrete bilinear form approximating the continuous form $d(\cdot, \cdot)$;
- $(\mathbf{f}, \mathbf{v}_h)_h$ is the term approximating the virtual work of the external load.

Furthermore, the method above is constructed by defining local (elemental) quantities and then by suitably glueing together the local contributions. For this primal formulation we focus on the 2D case; the 3D extension may be done using the ideas of [18] for the laplacian operator.

4.3.1.1 The Local Space

Let k be a positive integer, representing the "degree of accuracy" of the method. Then, given an element $E \in \mathcal{T}_h$, we define:

$$V_h(E) = \big\{ \mathbf{v}_h \in (H^1(E) \cap C^0(E))^2 \ : \ \Delta \mathbf{v}_h \in \mathbb{P}_{k-2}(E)^2,$$
$$\mathbf{v}_h|_e \in \mathbb{P}_k(e)^2 \quad \forall e \in \partial E \big\}, \tag{4.3.2}$$

where $\mathbb{P}_k(E)$ denotes the space of polynomials of degree (up to) k defined on E, with the agreement that $\mathbb{P}_{-1}(E) = \{0\}$.

The following important observations hold:

- the functions $\mathbf{v}_h \in V_h(E)$ are explicitly known on ∂E;
- the functions $\mathbf{v}_h \in V_h(E)$ are not explicitly known inside the element E;
- it holds $\mathbb{P}_k(E)^2 \subseteq V_h(E)$ (that is important for approximation).

In what follows, the integer $m_E = m$ will denote the number of edges in the polygon E (we will drop the subscript E if there is no risk of confusion). A sample polygon with $m = 5$ edges is represented in Fig. 4.1 with indication of vertexes and edges.

Fig. 4.1 A sample polygon with $m = 5$. (From: E. Artioli, L. Beirão da Veiga, C. Lovadina, and E. Sacco, Arbitrary order 2D virtual elements for polygonal meshes: Part I, elastic problem, Comput. Mech. 60 (2017), 355–377. Reproduced with permission)
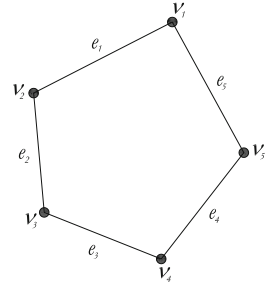
Taking into account that the unknown vector $\mathbf{v}_h \in V_h(E)$ has two components, for any $E \in \mathcal{T}_h$, the degrees of freedom for $V_h(E)$ will be:

– $2m$ pointwise values

$$\mathbf{v}_h \rightarrow \mathbf{v}_h(\mathbf{v}_i)$$

at corners $\mathbf{v}_i$ of E, $i = 1, 2, .., m$,
– $2m(k-1)$ pointwise values

$$\mathbf{v}_h \rightarrow \mathbf{v}_h(\mathbf{x}_j^e)$$

at edge internal nodes $\{\mathbf{x}_j^e\}$ (i.e. not comprising extrema of edge e), $j = 1, \ldots, k-1$, being m the number of edges of a polygon;
– $2\frac{k(k-1)}{2}$ moments of the unknown field over the element, not associated with a specific location over E:

$$\mathbf{v}_h \rightarrow \frac{1}{|E|} \int_E \mathbf{v}_h \cdot \mathrm{p}_{k-2} \qquad \forall \mathrm{p}_{k-2} \in \mathbb{P}_{k-2}(E)^2.$$

Sample figures for the degrees of freedom are shown in Fig. 4.2.

The dimension of the space $V_h(E)$ results

$$n = \dim(V_h(E)) = 2mk + k(k-1) , \qquad (4.3.3)$$

where $2m$ degrees of freedom are associated with the m corners of ∂E, $2m(k-1)$ degrees of freedom are associated with the m edges (with $(k-1)$ internal nodal points per edge), and $k(k-1)$ degrees of freedom are the moments. A local "Lagrange-type" basis for the space $V_h(E)$ can be chosen as follows: the i-th function of the local basis is given by the unique function in $V_h(E)$ that has unit value on the i-th degree of freedom and vanishes for the remaining ones.
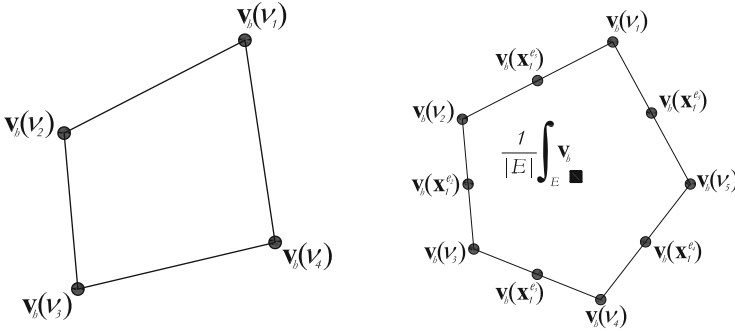
Fig. 4.2 Sample degrees of freedom for $k = 1$ (left), and for $k = 2$ (right). (From: E. Artioli, L. Beirão da Veiga, C. Lovadina, and E. Sacco, Arbitrary order 2D virtual elements for polygonal meshes: Part I, elastic problem, Comput. Mech. 60 (2017), 355–377. Reproduced with permission)

4.3.1.2 The Local Bilinear Form

As already mentioned, the discrete bilinear form is built element by element, assuming:

$$d_h(\mathbf{u}_h, \mathbf{v}_h) = \sum_{E \in \mathscr{T}_h} d_E^h(\mathbf{u}_h, \mathbf{v}_h) \quad \forall \mathbf{u}_h, \mathbf{v}_h \in V_h. \tag{4.3.4}$$

On the other hand, since the functions of the space V_h are not know explicitly inside the elements, the bilinear forms $d_E^h(\cdot, \cdot)$ cannot be evaluated by standard Gauss integration. The construction of the local discrete form $d_E^h(\cdot, \cdot)$, a key point in the VEM, is performed following the procedure described in the following.

Since neither the function $\mathbf{v}_h$ nor its gradient are explicitly computable in the element interior points, the method proceeds by introducing a projection operator G_E, representing the approximated strain associated with the virtual displacement, defined as:

$$G_E : \quad V_h(E) \longrightarrow \mathbb{P}_{k-1}(E)_s^{2 \times 2} \tag{4.3.5}$$

$$\mathbf{v}_h \quad \mapsto \quad G_E(\mathbf{v}_h),$$

where we recall that $\mathbb{P}_{k-1}(E)_s^{2 \times 2}$ denotes the space of 2×2 symmetry tensors whose components are in $\mathbb{P}_{k-1}(E)$. It is noted that $\dim(\mathbb{P}_{k-1}(E)_s^{2 \times 2}) = 2\frac{k(k+1)}{2}$.

Given $\mathbf{v}_h \in V_h(E)$, such an operator G_E is defined as the unique function $G_E(\mathbf{v}_h) \in \mathbb{P}_{k-1}(E)_s^{2 \times 2}$ that satisfies the condition:

$$\int_E G_E(\mathbf{v}_h) : \boldsymbol{\varepsilon} = \int_E \boldsymbol{\varepsilon}(\mathbf{v}_h) : \boldsymbol{\varepsilon}, \quad \forall \boldsymbol{\varepsilon} \in \mathbb{P}_{k-1}(E)_s^{2 \times 2}. \tag{4.3.6}$$

This operator represents the best approximation of the strains (in the square integral norm) in the space of piecewise polynomials of degree $(k - 1)$. Although the functions in $V_h(E)$ are virtual, the right hand side in (4.3.6) (and thus the operator G_E) turns out to be computable with simple calculations, see [6].

Once computed, the G_E operator approximates the internal work part associated to the equilibrium weak formulation as follows:

$$d_E^h(\mathbf{u}_h, \mathbf{v}_h) = \int_E \mathbb{C} G_E(\mathbf{u}_h) : G_E(\mathbf{v}_h) + s_E(\mathbf{u}_h, \mathbf{v}_h) \tag{4.3.7}$$

with $s_E(\cdot, \cdot)$ a stabilizing term, needed to preserve the coercivity of the system. For instance, one may consider the following structure, now standard in the Virtual Element community:

$$s_E(\mathbf{u}_h, \mathbf{v}_h) = \mathrm{tr}(\mathbb{C}) \sum_{i=1}^{n} \Xi_i(\mathbf{u}_h - P_k\mathbf{u}_h)\, \Xi_i(\mathbf{v}_h - P_k\mathbf{v}_h), \tag{4.3.8}$$

where $P_k : V_h(E) \to \mathbb{P}_k(E)^2$ is a suitable projection and $\Xi_i(\mathbf{w}_h)$ represents the i-th degree of freedom evaluation of $\mathbf{w}_h \in V_h(E)$. We refer to [6] for details.

4.3.1.3 The Local Loading Term

Also the loading term $(\mathbf{f}, \mathbf{v}_h)_h$, see (4.3.1), is constructed by summing local contributions. Accordingly, it holds

$$(\mathbf{f}, \mathbf{v}_h)_h = \sum_{E \in \mathscr{T}_h} (\mathbf{f}, \mathbf{v}_h)_{E,h},$$

where, for each $E \in \mathscr{T}_h$, $(\mathbf{f}, \mathbf{v}_h)_{E,h}$ is an approximation of the term:

$$\int_E \mathbf{f} \cdot \mathbf{v}_h. \tag{4.3.9}$$

Introducing $P_{k-2}^0 \mathbf{f}$ as the L^2-projection of $\mathbf{f}$, we thus set

$$(\mathbf{f}, \mathbf{v}_h)_{E,h} = \int_E (P_{k-2}^0\mathbf{f}) \cdot \mathbf{v}_h = \int_E \mathbf{f} \cdot (P_{k-2}^0\mathbf{v}_h). \tag{4.3.10}$$

which is a computable quantity, see for instance [18].

4.3.1.4 The Discrete Scheme

As in standard FE methods, the global space $V_h \subseteq V$ is built by assembling the local spaces $V_h(E)$ as usual:

$$V_h = \{\mathbf{v}_h \in V : \mathbf{v}_h|_E \in V_h(E) \ \forall E \in \mathscr{T}_h\}. \tag{4.3.11}$$

The discrete scheme now reads, cf. (4.3.1):

$$\begin{cases} \text{Find } \mathbf{u}_h \in V_h \text{ such that} \\ d_h(\mathbf{u}_h, \mathbf{v}_h) = (\mathbf{f}, \mathbf{v}_h)_h \qquad \forall \mathbf{v}_h \in V_h. \end{cases} \tag{4.3.12}$$

4.3.1.5 Mixed Methods Based on Hellinger Reissner Principle: 2D Case

As for the primal VEM formulation of Sect. 4.3.1, all the contributions to the bilinear and linear forms are locally defined, and then suitably glued together to form the global discrete problem.

4.3.1.6 The Local Spaces

Given a polygon $E \in \mathscr{T}_h$ with $m_E = m$ edges, we first introduce the space of local infinitesimal rigid body motions:

$$RM(E) = \left\{ \mathbf{r}(\mathbf{x}) = \mathbf{a} + b(\mathbf{x} - \mathbf{x}_C)^\perp \quad \mathbf{a} \in \mathbb{R}^2, \ b \in \mathbb{R} \right\}. \tag{4.3.13}$$

Here above, given $\mathbf{c} = (c_1, c_2)^T \in \mathbb{R}^2$, $\mathbf{c}^\perp$ is the clock-wise rotated vector $\mathbf{c}^\perp = (c_2, -c_1)^T$, and $\mathbf{x}_C$ is the barycenter of E. We remark that for a non-convex E the centroid $\mathbf{x}_C$ may lie outside the element; however, this does not cause any trouble, neither in the design nor in the analysis of the methods.

The description of the local spaces is divided into two different instances: a low-order case and a general high-order case.

The Lowest-Order Case
For each edge e of ∂E, we introduce the space

$$R(e) = \left\{ \mathbf{t}(s) = \mathbf{c} + c_3\, s\, \mathbf{n} \quad \mathbf{c} = (c_1, c_2)^T \in \mathbb{R}^2, \ c_3 \in \mathbb{R}, \ s \in [-1/2, 1/2] \right\}. \tag{4.3.14}$$

Here above, s is a local linear coordinate on e, such that $s = 0$ corresponds to the edge midpoint. Furthermore, $\mathbf{n}$ is the outward normal to the edge e. Hence, $R(e)$ consists of vectorial functions which have the edge tangential component constant, and the edge normal component linear along the edge. Therefore, the local stresses

are the stress solutions of suitable elastic problems where tractions are imposed on the whole element boundary. Of course, this is a virtual space, in that those solutions are not analytically available.

Our local approximation space for the stress field is then defined by

$$\Sigma_h(E) = \left\{ \boldsymbol{\tau}_h \in H(\mathbf{div}; E) \; : \; \exists \mathbf{w}^* \in H^1(E)^2 \text{ such that } \boldsymbol{\tau}_h = \mathbb{C}\boldsymbol{\varepsilon}(\mathbf{w}^*); \right.$$

$$\left. (\boldsymbol{\tau}_h \, \mathbf{n})_{|e} \in R(e) \quad \forall e \in \partial E; \quad \mathbf{div} \, \boldsymbol{\tau}_h \in RM(E) \right\}. \tag{4.3.15}$$

The definition above suggest to take the following functionals as degrees of freedom in $\Sigma_h(E)$.

– For each edge $e \in \partial E$, given $\boldsymbol{\tau}_h \in \Sigma_h(E)$:

$$\boldsymbol{\tau}_h \longrightarrow \int_e \boldsymbol{\tau}_h \mathbf{n} \,, \qquad \boldsymbol{\tau}_h \longrightarrow \int_e s \, \boldsymbol{\tau}_h \mathbf{n} \cdot \mathbf{n}. \tag{4.3.16}$$

We remark that, once $(\boldsymbol{\tau}_h \, \mathbf{n})_{|e} = \mathbf{c}_e + c_{3,e} s \, \mathbf{n}$ is given for all $e \in \partial E$, cf. (4.3.14), the quantity $\mathbf{div} \, \boldsymbol{\tau}_h \in RM(E)$ is determined. Indeed, denoting with $\boldsymbol{\varphi} : \partial E \to \mathbb{R}^2$ the function such that $\boldsymbol{\varphi}_{|e} = \mathbf{c}_e + c_{3,e} s \, \mathbf{n}$, integration by parts gives

$$\int_E \mathbf{div} \, \boldsymbol{\tau}_h \cdot \mathbf{r} = \int_{\partial E} \boldsymbol{\varphi} \cdot \mathbf{r} \qquad \forall \mathbf{r} \in RM(E), \tag{4.3.17}$$

allows to compute $\mathbf{div} \, \boldsymbol{\tau}_h$ using the $\mathbf{c}_e$'s and the $c_{3,e}$'s. More precisely, setting (cf. (4.3.13))

$$\mathbf{div} \, \boldsymbol{\tau}_h = \boldsymbol{\alpha}_E + \beta_E (\mathbf{x} - \mathbf{x}_C)^{\perp}, \tag{4.3.18}$$

from (4.3.17) we infer

$$\begin{cases} \boldsymbol{\alpha}_E = \dfrac{1}{|E|} \int_{\partial E} \boldsymbol{\varphi} = \dfrac{1}{|E|} \sum_{e \in \partial E} \int_e \mathbf{c}_e \\[2ex] \beta_E = \dfrac{1}{\int_E |\mathbf{x} - \mathbf{x}_C|^2} \int_{\partial E} \boldsymbol{\varphi} \cdot (\mathbf{x} - \mathbf{x}_C)^{\perp} \\[2ex] \qquad = \dfrac{1}{\int_E |\mathbf{x} - \mathbf{x}_C|^2} \sum_{e \in \partial E} \int_e (\mathbf{c}_e + c_{3,e} s \, \mathbf{n}) \cdot (\mathbf{x} - \mathbf{x}_C)^{\perp}. \end{cases} \tag{4.3.19}$$

Fig. 4.3 Schematic
description of the local
degrees of freedom for the
low-order method
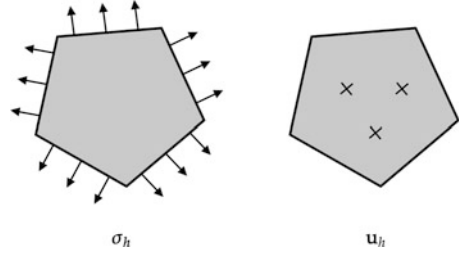
$$\sigma_h \qquad\qquad \mathbf{u}_h$$

The local approximation space for the displacement field is simply defined by,
see (4.3.13):

$$U_h(E) = \Big\{ \mathbf{v}_h \in L^2(E)^2 \; : \; \mathbf{v}_h \in RM(E) \Big\}. \qquad (4.3.20)$$

We notice that $\dim(\Sigma_h(E)) = 3\,m$, while $\dim(U_h(E)) = 3$.

In Fig. 4.3 the local degrees of freedom for stresses and displacements are
schematically depicted: arrows represent traction degrees of freedom (cf. (4.3.16)),
and crosses represent the displacement degrees of freedom (cf. (4.3.20)).

Remark 4.2 We notice that the degrees of freedom (4.3.16), which are defined edge
by edge, allow to easily glue the elemental stress contributions, complying the
$H(\mathbf{div}; \Omega)$ regularity requirement. In addition, Eq. (4.3.17) highlights that the L^2-
projection of $\mathbf{div}\ \boldsymbol{\tau}_h$ onto $RM(E)$ is determined by the boundary tractions $(\boldsymbol{\tau}_h\mathbf{n})_{|\partial E}$.
Therefore, if we use (4.3.16), we cannot restrict the condition $\mathbf{div}\ \boldsymbol{\tau}_h \in RM(E)$ in
(4.3.15). For instance, we cannot require $\mathbf{div}\ \boldsymbol{\tau}_h \in \mathbb{P}_0(E)^2$ because the boundary
traction $(\boldsymbol{\tau}_h\mathbf{n})_{|\partial E}$ typically leads to a $\mathbf{div}\ \boldsymbol{\tau}_h$ for which

$$\int_E \mathbf{div}\ \boldsymbol{\tau}_h \cdot (\mathbf{x} - \mathbf{x}_C)^\perp \neq 0.$$

Indeed, for a $\boldsymbol{\tau}_h$ such that $(\boldsymbol{\tau}_h\,\mathbf{n})_{|e} \in R(e)$ (cf. (4.3.15)), in general it holds

$$\int_{\partial E} \boldsymbol{\tau}_h\mathbf{n} \cdot (\mathbf{x} - \mathbf{x}_C)^\perp \neq 0.$$

We also remark that selecting piecewise constant tractions on ∂E does not alleviate
the trouble.

The Case of General $k \geq 1$
For any integer $k \geq 1$, we first need to introduce the space

$$RM_k^\perp(E) = \Big\{ \mathbf{p}_k(\mathbf{x}) \in \mathbb{P}_k(E)^2 \; : \; \int_E \mathbf{p}_k \cdot \mathbf{r} = 0 \quad \forall \mathbf{r} \in RM(E) \Big\}. \qquad (4.3.21)$$

Hence, the following L^2-orthogonal decomposition holds:

$$\mathbb{P}_k(E)^2 = RM(E) \bigoplus RM_k^\perp(E). \qquad (4.3.22)$$

Our local approximation space for the stress field is then defined by

$$\Sigma_h(E) = \Big\{ \boldsymbol{\tau}_h \in H(\mathbf{div}; E) \; : \; \exists \mathbf{w}^* \in H^1(E)^2 \text{ such that } \boldsymbol{\tau}_h = \mathbb{C}\boldsymbol{\varepsilon}(\mathbf{w}^*);$$

$$(\boldsymbol{\tau}_h \, \mathbf{n})_{|e} \in \mathbb{P}_k(e)^2 \quad \forall e \in \partial E; \quad \mathbf{div} \, \boldsymbol{\tau}_h \in \mathbb{P}_k(E)^2 \Big\}.$$
$$(4.3.23)$$

We remark that, due to the decomposition (4.3.22), we may write $\mathbf{div} \, \boldsymbol{\tau}_h = \mathbf{r}_\tau + \mathbf{p}_\tau$ for a unique couple $(\mathbf{r}_\tau, \mathbf{p}_\tau) \in RM(E) \times RM_k^\perp(E)$.

We now notice that the $RM(E)$-component $\mathbf{r}_\tau$ of $\mathbf{div} \, \boldsymbol{\tau}_h$ is completely determined once $(\boldsymbol{\tau}_h \, \mathbf{n})_{|e} = \mathbf{p}_{k,e} \in \mathbb{P}_k(e)^2$ is given for all $e \in \partial E$. Indeed, let us denote with $\boldsymbol{\varphi} : \partial E \to \mathbb{R}^2$ the function such that $\boldsymbol{\varphi}_{|e} = \mathbf{p}_{k,e}$. Using an integration by parts and the orthogonal decomposition (4.3.22), we have:

$$\int_E \mathbf{r}_\tau \cdot \mathbf{r} = \int_E \mathbf{div} \, \boldsymbol{\tau}_h \cdot \mathbf{r} = \int_{\partial E} \boldsymbol{\tau}_h \mathbf{n} \cdot \mathbf{r} = \int_{\partial E} \boldsymbol{\varphi} \cdot \mathbf{r} \qquad \forall \mathbf{r} \in RM(E), \quad (4.3.24)$$

which allows to compute $\mathbf{r}_\tau$ using the $\mathbf{p}_{k,e}$'s. More precisely, setting (cf (4.3.13))

$$\mathbf{r}_\tau = \boldsymbol{\alpha}_E + \beta_E (\mathbf{x} - \mathbf{x}_C)^\perp, \qquad (4.3.25)$$

from (4.3.24) we infer

$$\begin{cases} \boldsymbol{\alpha}_E = \dfrac{1}{|E|} \int_{\partial E} \boldsymbol{\varphi} = \dfrac{1}{|E|} \sum_{e \in \partial E} \int_e \mathbf{p}_{k,e} \\[2ex] \beta_E = \dfrac{1}{\int_E |\mathbf{x} - \mathbf{x}_C|^2} \int_{\partial E} \boldsymbol{\varphi} \cdot (\mathbf{x} - \mathbf{x}_C)^\perp \\[2ex] \qquad = \dfrac{1}{\int_E |\mathbf{x} - \mathbf{x}_C|^2} \sum_{e \in \partial E} \int_e \mathbf{p}_{k,e} \cdot (\mathbf{x} - \mathbf{x}_C)^\perp. \end{cases} \qquad (4.3.26)$$

The equations above suggest to take the following functionals as degrees of freedom in $\Sigma_h(E)$.

– For each edge $e \in \partial E$, given $\boldsymbol{\tau}_h \in \Sigma_h(E)$:

$$\boldsymbol{\tau}_h \longrightarrow \int_e \boldsymbol{\tau}_h \mathbf{n} \cdot \mathbf{p}_k \qquad \forall \mathbf{p}_k \in \mathbb{P}_k(e)^2. \qquad (4.3.27)$$

– In the polygon E, given $\boldsymbol{\tau}_h \in \Sigma_h(E)$:

$$\boldsymbol{\tau}_h \longrightarrow \int_E \mathbf{div}\, \boldsymbol{\tau}_h \cdot \boldsymbol{\psi}_k \qquad \forall \boldsymbol{\psi}_k \in RM_k^\perp(E). \tag{4.3.28}$$

Indeed, the following Lemma holds, cf. [9].

Lemma 4.1 *If $\boldsymbol{\tau}_h \in \Sigma_h(E)$, then*

$$\begin{cases} \displaystyle\int_e \boldsymbol{\tau}_h \mathbf{n} \cdot \mathbf{p}_k = 0 & \forall \mathbf{p}_k \in \mathbb{P}_k(e)^2, \quad \forall e \in \partial E; \\[2mm] \displaystyle\int_E \mathbf{div}\, \boldsymbol{\tau}_h \cdot \boldsymbol{\psi}_k = 0 & \forall \boldsymbol{\psi}_k \in RM_k^\perp(E), \end{cases} \tag{4.3.29}$$

imply $\boldsymbol{\tau}_h = \mathbf{0}$.

Alternatively, one may consider the following degrees of freedom (useful for the implementation purposes).

– For each edge $e \in \partial E$, given $\boldsymbol{\tau}_h \in \Sigma_h(E)$, the first subset of degrees of freedom is the set of values of $\boldsymbol{\tau}_h \mathbf{n}$ at $k+1$ distinct points in e (for instance, the $k+1$ Gauss-Lobatto nodes). Another possible choice, which has been used in our numerical tests of Sect. 4.4.1.2 is the following: for each e, we introduce a local linear coordinate $s \in [-1, 1]$; for both components of $\boldsymbol{\tau}_h \in \Sigma_h(E)$, the degrees of freedom are the $k + 1$ coefficients of their expansion with respect to the basis $\{1, s, s^2, \ldots, s^k\}$.

These $2(k+1)$ values account for the degrees of freedom described in (4.3.27).
– In the polygon E, let us choose a basis $\{\boldsymbol{\varphi}_i\}$ $(i = 1, \ldots, (k + 1)(k + 2) - 3)$ for $RM_k^\perp$, see (4.3.22). Then, for each $\boldsymbol{\tau}_h \in \Sigma_h(E)$, we may write

$$\mathbf{div}\, \boldsymbol{\tau}_h = \boldsymbol{\alpha} + \beta(\mathbf{x} - \mathbf{x}_C)^\perp + \sum_{i=1}^{m_k} \gamma_i \boldsymbol{\varphi}_i(\mathbf{x}), \tag{4.3.30}$$

where $n_k = (k + 1)(k + 2) - 3$.

The values $\{\gamma_1, \ldots, \gamma_{n_k}\}$ can be taken as the second subset of degrees of freedom. They account for the degrees of freedom described in (4.3.28), while $\{\boldsymbol{\alpha}, \beta\}$ are computed according with (4.3.19).

The construction of the basis $\{\boldsymbol{\varphi}_i\}$ can be done starting from the usual polynomial basis (or from the scaled one (see [20], for instance) and performing an L^2-orthogonalization procedure with respect to the space $RM(E)$. This approach has been followed for the numerical results presented in Sect. 4.4.1.2.

Fig. 4.4 Schematic
description of the local
degrees of freedom for $k = 1$
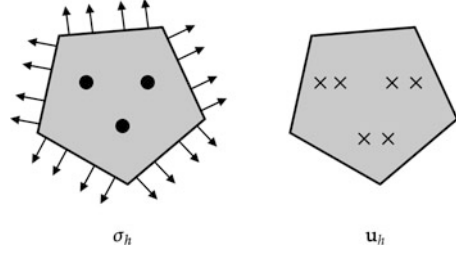
$$\sigma_h \qquad\qquad \mathbf{u}_h$$

The local approximation space for the displacement field is simply defined by, see (4.3.13):

$$U_h(E) = \left\{ \mathbf{v}_h \in L^2(E)^2 \ : \ \mathbf{v}_h \in \mathbb{P}_k(E)^2 \right\}, \tag{4.3.31}$$

and a set of degrees of freedom can be defined in a standard way.

We notice that $\dim(\Sigma_h(E)) = 2(k+1)\,m + n_k$, while $\dim(U_h(E)) = (k+1)(k+2)$. In Fig. 4.4 the local degrees of freedom for stresses and displacements are schematically depicted for $k = 1$: again, arrows represent traction degrees of freedom (cf. (4.3.27)), bullets represent the divergence degrees of freedom (cf. (4.3.28)), crosses represent the displacement degrees of freedom (cf. (4.3.31)).

4.3.1.7   The Local Bilinear Forms

Given $E \in \mathscr{T}_h$, we first notice that, for every $\boldsymbol{\tau}_h \in \Sigma_h(E)$ and $\mathbf{v}_h \in U_h(E)$, the term

$$\int_E \mathbf{div}\,\boldsymbol{\tau}_h \cdot \mathbf{v}_h \tag{4.3.32}$$

is computable from the knowledge of the degrees of freedom, since both factors are polynomials, whatever the low-order or the general case is considered (see (4.3.15), (4.3.20), (4.3.23) and (4.3.31)). Therefore, there is no need to introduce any approximation. Instead, the term

$$a_E(\boldsymbol{\sigma}_h, \boldsymbol{\tau}_h) = \int_E \mathbb{D}\boldsymbol{\sigma}_h : \boldsymbol{\tau}_h \tag{4.3.33}$$

is not computable for a general couple $(\boldsymbol{\sigma}_h, \boldsymbol{\tau}_h) \in \Sigma_h(E) \times \Sigma_h(E)$. We then must introduce a suitable approximation $a_E^h(\cdot, \cdot)$ of $a_E(\cdot, \cdot)$. To this end, for every non-negative integer k we need to define the projection operator Π_E (we use the convention that for the low-order scheme $k = 0$).

Given $E \in \mathscr{T}_h$, following [8, 9], we first need to introduce the space:

$$\widetilde{\Sigma}(E) = \left\{ \boldsymbol{\tau} \in H(\mathbf{div}; E) \ : \ \exists \mathbf{w} \in H^1(E)^2 \text{such that } \boldsymbol{\tau} = \mathbb{C}\boldsymbol{\varepsilon}(\mathbf{w}) \right\}. \qquad (4.3.34)$$

The projection operator Π_E onto the space

$$S_k(E) = \mathbb{C}\,\boldsymbol{\varepsilon}(\mathbb{P}_{k+1}(E)^2) = \left\{ \mathbb{C}\,\boldsymbol{\varepsilon}(\mathbf{p}_{k+1}) \ : \ \mathbf{p}_{k+1} \in \mathbb{P}_{k+1}(E)^2 \right\} \qquad (4.3.35)$$

is thus defined by:

$$\begin{cases} \Pi_E \ : \ \widetilde{\Sigma}(E) \rightarrow S_k(E) \\ \boldsymbol{\tau} \mapsto \Pi_E \boldsymbol{\tau} \\ a_E(\Pi_E \boldsymbol{\tau}, \boldsymbol{\pi}_k) = a_E(\boldsymbol{\tau}, \boldsymbol{\pi}_k) \qquad \forall \boldsymbol{\pi}_k \in S_k(E). \end{cases} \qquad (4.3.36)$$

We remark that (4.3.36) is equivalent to find $\mathbf{p}_{k+1} \in \mathbb{P}_{k+1}(E)^2$ such that

$$\int_E \mathbb{C}\,\boldsymbol{\varepsilon}(\mathbf{p}_{k+1}) \ : \ \boldsymbol{\varepsilon}(\mathbf{q}_{k+1}) = \int_E \boldsymbol{\tau} \ : \ \boldsymbol{\varepsilon}(\mathbf{q}_{k+1}) \qquad \forall \mathbf{q}_{k+1} \in \mathbb{P}_{k+1}(E)^2. \qquad (4.3.37)$$

Remark 4.3 Obviously, $\mathbf{p}_{k+1}$ is defined up to a term in $RM(E)$. In addition, we observe that since $\mathbb{C}$ constant in E, it holds $S_r(E) = \mathbb{P}_r(E)_s^{2 \times 2}$ if $r = 0, 1$; however, if $\mathbb{C}$ varies in E, the construction above can still be performed, though $S_k(E)$ is not even a polynomial space.

We now set

$$a_E^h(\boldsymbol{\sigma}_h, \boldsymbol{\tau}_h) = a_E(\Pi_E \boldsymbol{\sigma}_h, \Pi_E \boldsymbol{\tau}_h) + s_E \left((Id - \Pi_E)\boldsymbol{\sigma}_h, (Id - \Pi_E)\boldsymbol{\tau}_h\right)$$

$$= \int_E \mathbb{D}(\Pi_E \boldsymbol{\sigma}_h) : (\Pi_E \boldsymbol{\tau}_h) + s_E \left((Id - \Pi_E)\boldsymbol{\sigma}_h, (Id - \Pi_E)\boldsymbol{\tau}_h\right),$$
$$(4.3.38)$$

where $s_E(\cdot, \cdot)$ is a suitable stabilization term. We propose the following choice:

$$s_E(\boldsymbol{\sigma}_h, \boldsymbol{\tau}_h) = \kappa_E \, h_E \int_{\partial E} \boldsymbol{\sigma}_h \mathbf{n} \cdot \boldsymbol{\tau}_h \mathbf{n}, \qquad (4.3.39)$$

where κ_E is a positive constant to be chosen. For instance, in the numerical examples of Sect. 4.4.1.2, κ_E is set equal to $\frac{1}{2}\mathrm{tr}(\mathbb{D}_{|E})$; however, any norm of $\mathbb{D}_{|E}$ can be used. A possible variant of (4.3.39) is provided by

$$s_E(\boldsymbol{\sigma}_h, \boldsymbol{\tau}_h) = \kappa_E \sum_{e \in \partial E} h_e \int_e \boldsymbol{\sigma}_h \mathbf{n} \cdot \boldsymbol{\tau}_h \mathbf{n}. \qquad (4.3.40)$$

4.3.1.8   The Local Loading Term

We need to consider the term, see (4.2.6):

$$(\mathbf{f}, \mathbf{v}_h) = \int_\Omega \mathbf{f} \cdot \mathbf{v}_h = \sum_{E \in \mathcal{T}_h} \int_E \mathbf{f} \cdot \mathbf{v}_h. \tag{4.3.41}$$

We remark that, since $\mathbf{v}_h \in RM(E)$, computing (4.3.41) is possible once a suitable quadrature rule is available for polygonal domains. For such an issue, see for instance [52, 53, 57].

4.3.1.9   The Discrete Scheme

We are now ready to introduce the discrete scheme. We introduce a global approximation space for the stress field, by glueing the local approximation spaces (see (4.3.15) for the low-order scheme, (4.3.23) for the general case):

$$\Sigma_h = \left\{ \boldsymbol{\tau}_h \in H(\mathbf{div}; \Omega) \ : \ \boldsymbol{\tau}_{h|E} \in \Sigma_h(E) \quad \forall E \in \mathcal{T}_h \right\}. \tag{4.3.42}$$

For the global approximation of the displacement field, we take (see (4.3.20) for the low-order scheme, (4.3.31) for the general case):

$$U_h = \left\{ \mathbf{v}_h \in L^2(\Omega)^2 \ : \ \mathbf{v}_{h|E} \in U_h(E) \quad \forall E \in \mathcal{T}_h \right\}. \tag{4.3.43}$$

Furthermore, given a local approximation of $a_E(\cdot, \cdot)$, see (4.3.38), we set

$$a_h(\boldsymbol{\sigma}_h, \boldsymbol{\tau}_h) = \sum_{E \in \mathcal{T}_h} a_E^h(\boldsymbol{\sigma}_h, \boldsymbol{\tau}_h). \tag{4.3.44}$$

The method we consider is then defined by

$$\begin{cases} \text{Find } (\boldsymbol{\sigma}_h, \mathbf{u}_h) \in \Sigma_h \times U_h \text{ such that} \\ a_h(\boldsymbol{\sigma}_h, \boldsymbol{\tau}_h) + (\mathbf{div}\,\boldsymbol{\tau}_h, \mathbf{u}_h) = 0 \quad \forall \boldsymbol{\tau}_h \in \Sigma_h \\ (\mathbf{div}\,\boldsymbol{\sigma}_h, \mathbf{v}_h) = -(\mathbf{f}, \mathbf{v}_h) \quad \forall \mathbf{v}_h \in U_h. \end{cases} \tag{4.3.45}$$

For this problem the following error estimate holds true, see [8, 9].

$$||\boldsymbol{\sigma} - \boldsymbol{\sigma}_h||_\Sigma + ||\mathbf{u} - \mathbf{u}_h||_U \lesssim C\,h^k, \tag{4.3.46}$$

where $C = C(\Omega, \boldsymbol{\sigma}, \mathbf{u})$ is independent of h but depends on the domain Ω and on the Sobolev regularity of $\boldsymbol{\sigma}$ and $\mathbf{u}$.

4.3.2 Mixed Methods Based on Hellinger Reissner Principle: 3D Case

We now present a scheme, detailed in [44], which can be seen as the 3D extension of the 2D method introduced in [8]. Again, the bilinear and linear forms are locally defined, then are suitably glued together to form the global quantities which give rise to the final discrete problem.

4.3.2.1 The Local Spaces

To describe the local spaces involved in the VEM discretization, we first need to introduce the local space $RM(E)$ of infinitesimal rigid body motions in an element E. In the 3D case, we set

$$RM(E) = \left\{ \mathbf{r}(\mathbf{x}) = \boldsymbol{\alpha} + \boldsymbol{\omega} \wedge \left(\mathbf{x} - \mathbf{x}_E \right) \text{ s.t. } \boldsymbol{\alpha}, \ \boldsymbol{\omega} \in \mathbb{R}^3 \right\}, \qquad (4.3.47)$$

whose dimension is 6. Furthermore, for a given face $f \in \partial E$, we introduce:

$$T_h(f) = \left\{ \boldsymbol{\psi}(\tilde{\mathbf{x}}) = \mathbf{t}_f + a \left[\mathbf{n}_f \wedge (\mathbf{x}(\tilde{\mathbf{x}}) - \mathbf{x}_f) \right] + p_1(\tilde{\mathbf{x}})\mathbf{n}_f, \right.$$
$$\left. \text{s.t. } a \in \mathbb{R}, \ p_1(\tilde{\mathbf{x}}) \in \mathbb{P}_1(f) \right\}, \qquad (4.3.48)$$

where $\mathbf{n}_f$ the outward normal to the face f, and $\mathbf{t}_f$ is an arbitrary vector tangent to the face f. Above, $\mathbf{x}(\tilde{\mathbf{x}})$ is the three dimensional position vector of a point on f, determined by the two local coordinates $\tilde{\mathbf{x}}$. The dimension of such a space is 6, indeed:

– The three dimensional tangent vector $\mathbf{t}$ is determined by a linear combination of two given linearly independent tangential vectors $\mathbf{t}_1$ and $\mathbf{t}_2$, i.e.

$$\mathbf{t} = b_1 \mathbf{t}_1 + b_2 \mathbf{t}_2.$$

– The rotational term $a \left[\mathbf{n}_f \wedge (\mathbf{x}(\tilde{\mathbf{x}}) - \mathbf{x}_f) \right]$ is determined by a single scalar value $a \in \mathbb{R}$.
– The polynomial $p_1(\tilde{\mathbf{x}}) \in \mathbb{P}_1(f)$ is a two variable polynomial with respect to the local face coordinate system so it is determined by three parameters, and here we use:

$$p_1(\tilde{\mathbf{x}}) = c_1 + c_2(\tilde{x} - \tilde{x}_f) + c_3(\tilde{y} - \tilde{y}_f).$$

Therefore, this space consists of vector functions whose tangential component is a 2D face rigid body motion (the first two terms of (4.3.48)), while the normal component is a linear two-variable polynomial (the last term of (4.3.48)).

We are now ready to introduce our local approximation space for the stress field:

$$\Sigma_h(E) = \Big\{ \boldsymbol{\tau}_h \in H(\mathbf{div}; E) \; : \; \exists\, \mathbf{w}^* \in H^1(E)^3 \text{ such that } \boldsymbol{\tau}_h = \mathbb{C}\boldsymbol{\varepsilon}(\mathbf{w}^*);$$

$$(\boldsymbol{\tau}_h\,\mathbf{n})_{|f} \in T_h(f) \quad \forall f \in \partial E; \quad \mathbf{div}\,\boldsymbol{\tau}_h \in RM(E) \Big\}. \tag{4.3.49}$$

Accordingly, for the local space $\Sigma_h(E)$ the following degrees of freedom can be taken, see also (4.3.48).

- For each face f of the element E, the three degrees of freedom which determine the tangential component of the tractions:

$$\boldsymbol{\tau}_h \longrightarrow \int_f (\boldsymbol{\tau}_h\,\mathbf{n})_{|f} \cdot \Big[\boldsymbol{\theta}_f + \alpha\big[\mathbf{n}_f \wedge (\mathbf{x}(\tilde{\mathbf{x}}) - \mathbf{x}_f)\big] \Big]. \tag{4.3.50}$$

  Above, $\alpha \in \mathbb{R}$ and $\boldsymbol{\theta}_f$ is an arbitrary vector tangential to the face f.
- For each face f of the element E, the three degrees of freedom which determine the normal component of the tractions:

$$\boldsymbol{\tau}_h \longrightarrow \int_f (\boldsymbol{\tau}_h\,\mathbf{n})_{|f} \cdot \Big[q_1(\tilde{\mathbf{x}})\mathbf{n}_f \Big] \qquad \forall\, q_1(\tilde{\mathbf{x}}) \in \mathbb{P}_1(f). \tag{4.3.51}$$

Therefore, we infer that the dimension of the space (4.3.15) is

$$\dim(\Sigma_h(E)) = 6\,n_f^E,$$

n_f^E being the number of element faces.

For the space $\Sigma_h(E)$, the divergence of any element is determined by the values of its normal component on the boundary ∂E. In fact, in [44] the following result has been proved.

Proposition 4.1 *Let* $\boldsymbol{\tau}_h \in \Sigma_h(E)$, *then* $\mathbf{div}\,\boldsymbol{\tau}_h$ *is completely determined by* $(\boldsymbol{\tau}_h\,\mathbf{n})_{|f}$, *with* $f \in \partial E$ *face of* E. *More precisely, setting (cf* (4.3.47))

$$\mathbf{div}\,\boldsymbol{\tau}_h = \boldsymbol{\alpha}_E + \boldsymbol{\omega}_E \wedge (\mathbf{x} - \mathbf{x}_E), \tag{4.3.52}$$

it holds

$$\boldsymbol{\alpha}_E = \frac{1}{|E|} \left(\sum_{f \in \partial E} \int_f (\boldsymbol{\tau}_h\,\mathbf{n}) \right),$$
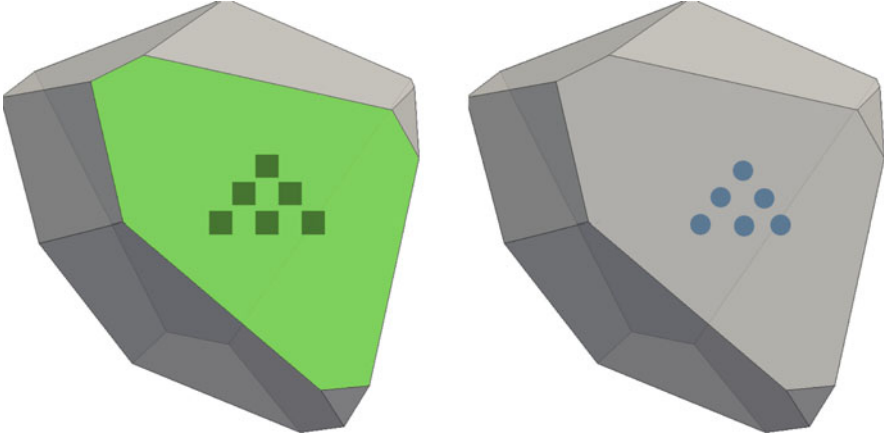
Fig. 4.5 Schematic description of the local degrees of freedom for the 3D method: stresses (left); displacements (right)

and $\boldsymbol{\omega}_E$ is the unique solution of the 3×3 linear system

$$\int_E (\mathbf{x} - \mathbf{x}_E) \wedge [\boldsymbol{\omega}_E \wedge (\mathbf{x} - \mathbf{x}_E)] = \sum_{f \in \partial E} \int_f (\mathbf{x} - \mathbf{x}_E) \wedge (\boldsymbol{\tau}_h \mathbf{n}). \qquad (4.3.53)$$

The local approximation space for the displacement field is defined by, see (4.3.47):

$$U_h(E) = \left\{ \mathbf{v}_h \in L^2(E)^3 \; : \; \mathbf{v}_h \in RM(E) \right\}. \qquad (4.3.54)$$

Accordingly, for the local space $U_h(E)$ the following degrees of freedom can be taken:

$$\mathbf{v}_h \longrightarrow \int_E \mathbf{v}_h \cdot \mathbf{r} \qquad \forall \, \mathbf{r} \in RM(E). \qquad (4.3.55)$$

It follows that $\dim(U_h(E)) = 6$.

In Fig. 4.5 the local degrees of freedom for stresses and displacements are schematically depicted.

4.3.2.2   The Local Forms

As for the 2D case, given $E \in \mathcal{T}_h$, the term

$$(\mathbf{div}\, \boldsymbol{\tau}_h, \mathbf{v}_h)_E = \int_E \mathbf{div}\, \boldsymbol{\tau}_h \cdot \mathbf{v}_h$$

is computable for every $\boldsymbol{\tau}_h \in \Sigma_h(E)$ and $\mathbf{v}_h \in U_h(E)$ via degrees of freedom. For this reason, we do not need to introduce any approximation of the terms $(\mathbf{div}\,\boldsymbol{\tau}, \mathbf{u})$ and $(\mathbf{div}\,\boldsymbol{\sigma}, \mathbf{v})$ in problem (4.2.6).

The local bilinear form

$$a_E(\boldsymbol{\sigma}_h, \boldsymbol{\tau}_h) = \int_E \mathbb{D}\boldsymbol{\sigma}_h : \boldsymbol{\tau}_h$$

is instead not computable for a general couple $(\boldsymbol{\sigma}_h, \boldsymbol{\tau}_h) \in \Sigma_h(E) \times \Sigma_h(E)$ and needs to be approximated. Similarly to the low-order 2D case, we introduce $\Pi_E : \Sigma_h(E) \to \mathbb{P}_0(E)_s^{3\times3}$ (see also Remark 4.3), by requiring

$$\int_E \Pi_E\,\boldsymbol{\tau}_h : \boldsymbol{\pi}_0 = \int_E \boldsymbol{\tau}_h : \boldsymbol{\pi}_0 \qquad \forall \boldsymbol{\pi}_0 \in \mathbb{P}_0(E)_s^{3\times3}. \qquad (4.3.56)$$

This is a projection operator onto the constant symmetric tensor functions and it is computable. $\mathbb{D}_{|E}$ is constant. Indeed, we notice that each $\boldsymbol{\pi}_0 \in \mathbb{P}_0(E)_s^{3\times3}$ can be written as the symmetric gradient of a linear vectorial function, i.e. $\boldsymbol{\pi}_0 = \boldsymbol{\varepsilon}(\mathbf{p}_1)$, with $\mathbf{p}_1 \in \mathbb{P}_1(E)^3$. Hence, using the divergence theorem, the right-hand side of (4.3.56) becomes

$$\int_E \boldsymbol{\tau}_h : \boldsymbol{\pi}_0 = \int_E \boldsymbol{\tau}_h : \boldsymbol{\varepsilon}(\mathbf{p}_1) = -\int_E \mathbf{div}\,\boldsymbol{\tau}_h \cdot \mathbf{p}_1 + \int_{\partial E} (\boldsymbol{\tau}_h\mathbf{n}) \cdot \mathbf{p}_1$$

which is clearly computable (see also Proposition 4.1). Then, the approximation of $a_E(\cdot, \cdot)$ reads:

$$a_E^h(\boldsymbol{\sigma}_h, \boldsymbol{\tau}_h) = a_E(\Pi_E\,\boldsymbol{\sigma}_h, \Pi_E\boldsymbol{\tau}_h) + s_E\left((I - \Pi_E)\boldsymbol{\sigma}_h, (I - \Pi_E)\boldsymbol{\tau}_h\right)$$

$$= \int_E \mathbb{D}(\Pi_E\boldsymbol{\sigma}_h) : (\Pi_E\boldsymbol{\tau}_h)\,\mathrm{d}E + s_E\left((I - \Pi_E)\boldsymbol{\sigma}_h, (I - \Pi_E)\boldsymbol{\tau}_h\right),$$

$$(4.3.57)$$

where $s_E(\cdot, \cdot)$ can be chosen, for instance (cf. (4.3.39) in the 2D setting), as:

$$s_E(\boldsymbol{\sigma}_h, \boldsymbol{\tau}_h) = \kappa_E\,h_E \int_{\partial E} (\boldsymbol{\sigma}_h\mathbf{n}) \cdot \boldsymbol{\tau}_h\mathbf{n}, \qquad (4.3.58)$$

Above, κ_E is a positive constant to be chosen according to $\mathbb{D}$.

4.3.2.3 The Local Loading Term

Finally, the local load term

$$(\mathbf{f}, \mathbf{v}_h)_E = \int_E \mathbf{f} \cdot \mathbf{v}_h.$$

does not need to be approximated, since it is computable via quadrature rules for polyhedral domains, because $\mathbf{v}_h \in RM(E)$.

4.3.2.4   The Discrete Scheme

Once we have defined all the local forms, the discrete scheme construction follows exactly the same lines of the 2D case, see Sect. 4.3.1.9. Hence the method reads

$$
\begin{cases}
\text{Find } (\boldsymbol{\sigma}_h, \mathbf{u}_h) \in \Sigma_h \times U_h \text{ such that} \\
a_h(\boldsymbol{\sigma}_h, \boldsymbol{\tau}_h) + (\mathbf{div}\,\boldsymbol{\tau}_h, \mathbf{u}_h) = 0 \quad \forall \boldsymbol{\tau}_h \in \Sigma_h \\
(\mathbf{div}\,\boldsymbol{\sigma}_h, \mathbf{v}_h) = -(\mathbf{f}, \mathbf{v}_h) \quad \forall \mathbf{v}_h \in U_h.
\end{cases}
\tag{4.3.59}
$$

For this problem the following error estimate holds true, see [44].

$$
||\boldsymbol{\sigma} - \boldsymbol{\sigma}_h||_\Sigma + ||\mathbf{u} - \mathbf{u}_h||_U \lesssim C\,h.
\tag{4.3.60}
$$

4.4   Numerical Results

In all the numerical campaigns, both 2D and 3D, the mesh size parameter is chosen to be the average edge length, still denoted with h, with an abuse of notation. We remark that, under mesh assumptions (**A1**)–(**A3**) and for a quasi-uniform family of meshes, such a parameter is indeed equivalent to both h_E and $\max\{h_E : E \in \mathscr{T}_h\}$.

Furthermore, the stabilization parameter is set $\kappa_E = 1$, see (4.3.39) and (4.3.58). We remark that this is essentially compatible with the choice $\kappa = \frac{1}{2}\mathrm{tr}(\mathbb{D})$. In fact, if the strain an stress tensors are described using the Voigt notation, the matrix $\mathbb{D}$ is given by (here below the 2D case is displayed, but an analogous situation occurs in 3D):

$$
\mathbb{D} = \begin{bmatrix}
\dfrac{2\mu + \lambda}{4\mu(\mu + \lambda)} & -\dfrac{\lambda}{4\mu(\mu + \lambda)} & 0 \\[3mm]
-\dfrac{\lambda}{4\mu(\mu + \lambda)} & \dfrac{2\mu + \lambda}{4\mu(\mu + \lambda)} & 0 \\[3mm]
0 & 0 & \dfrac{1}{\mu}
\end{bmatrix}.
$$

Hence, for our choice of the parameters (but also for the nearly incompressible case) the trace $\mathrm{tr}(\mathbb{D})$ is of the order of the unity.

4.4.1   2D Numerical Tests

For the 2D case we report our numerical results selecting the following three problems.

The first two tests are defined on the unit square domain $\Omega = [0, 1]^2$, with a given analytical solution and a corresponding body force density **f**, indicated in the following:

- Test *a*

$$\begin{cases} u_1 = x^3 - 3xy^2 \\ u_2 = y^3 - 3x^2y \\ \mathbf{f} = \mathbf{0} \end{cases} \tag{4.4.1}$$

- Test *b*

$$\begin{cases} u_1 = u_2 = \sin(\pi x) \sin(\pi y) \\ f_1 = f_2 = -\pi^2\big[-(3\mu + \lambda)\sin(\pi x)\sin(\pi y) \\ \qquad\qquad +(\mu + \lambda)\cos(\pi x)\cos(\pi y)\big] \end{cases} \tag{4.4.2}$$

A homogeneous and isotropic elastic body is considered. Material parameters are assigned in terms of Lamé constants $\lambda = 1$, $\mu = 1$. Plain strain regime is invoked.

Test *a* presents Dirichlet non-homogeneous boundary conditions, zero loading and polynomial displacements; whereas Test *b* has Dirichlet homogeneous boundary conditions, a trigonometric unit-area load function **f** and trigonometric displacements.

- Cook's membrane

    The third numerical test applies to classical 2D Cook's membrane problem [65]. Geometry of the domain Ω is reported in Fig. 4.6, where $H_1 = 44$, $H_2 = 16$, $L = 48$. Material parameters are Young modulus $E = 70$, and Poisson ratio $\nu = 1/3$. The left edge is clamped, while a constant tangential traction $q = 6.25 \cdot 10^{-3}$ is assigned on the right edge of the domain.

As far as the mesh adopted are concerned, for Test *a* quadrilaterals are used, as represented in Fig. 4.7. More precisely, they respectively are: squares (a), rhombic and concave quadrilaterals (b).

Sample meshes adopted in Test *b* are instead portrayed in Fig. 4.8. They comprise non-uniform quadrilaterals (a), uniform convex hexagons (b), and centroid-based Voronoi polygons (c), respectively.

Regarding the Cook's membrane, the problem is solved using two types of meshes: a structured quadrilateral mesh with equal number of subdivisions along each side of the membrane (see Fig. 4.9a), and centroid based [resp. random-based] Voronoi unstructured tessellations (see Fig. 4.9b).
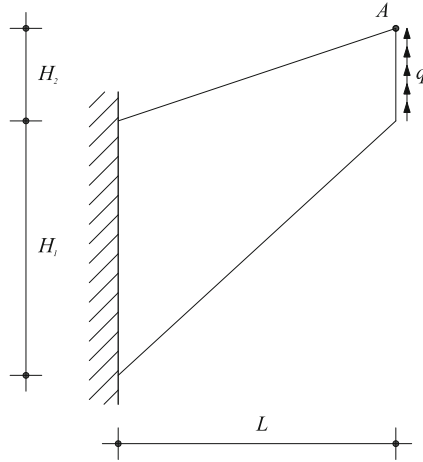
Fig. 4.6 Cook's membrane. Geometry, loading and boundary conditions. (From: E. Artioli, L. Beirão da Veiga, C. Lovadina, and E. Sacco, Arbitrary order 2D virtual elements for polygonal meshes: Part I, elastic problem, Comput. Mech. 60 (2017), 355–377. Reproduced with permission)
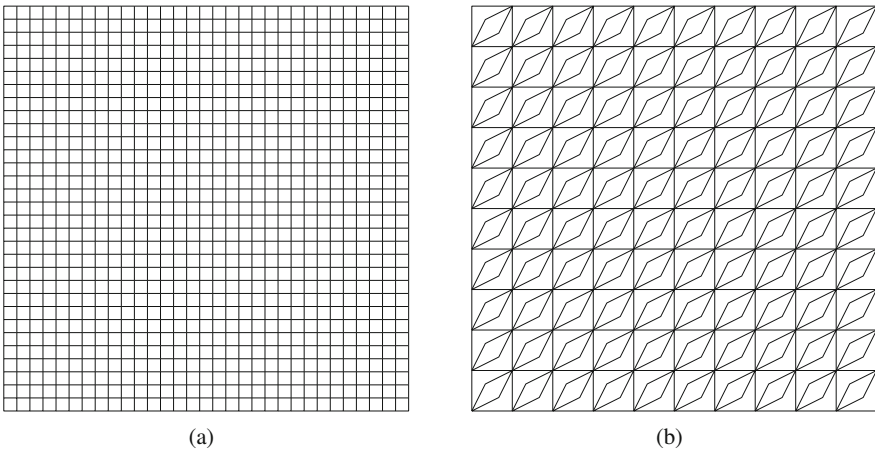
Fig. 4.7 Test a sample meshes. Uniform mesh of squares (**a**); Distorted concave rhombic quadrilaterals (**b**). (From: E. Artioli, L. Beirão da Veiga, C. Lovadina, and E. Sacco, Arbitrary order 2D virtual elements for polygonal meshes: Part I, elastic problem, Comput. Mech. 60 (2017), 355–377. Reproduced with permission)

4.4.1.1 Primal Formulation

Test a is used to compare accuracy level and convergence rate of the proposed primal VEM to standard displacement based FEM, using meshes with only quadrilaterals: linear and quadratic VEMs are compared to Lagrangian linear and quadratic
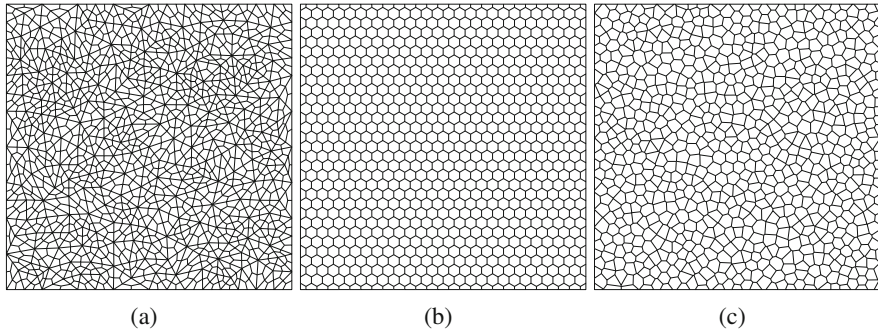
Fig. 4.8 Test *b* sample meshes. Non-uniform mesh of convex quadrilaterals (**a**); Uniform mesh of hexagons (**b**); Voronoi tessellation (**c**). (From: E. Artioli, L. Beirão da Veiga, C. Lovadina, and E. Sacco, Arbitrary order 2D virtual elements for polygonal meshes: Part I, elastic problem, Comput. Mech. 60 (2017), 355–377. Reproduced with permission)
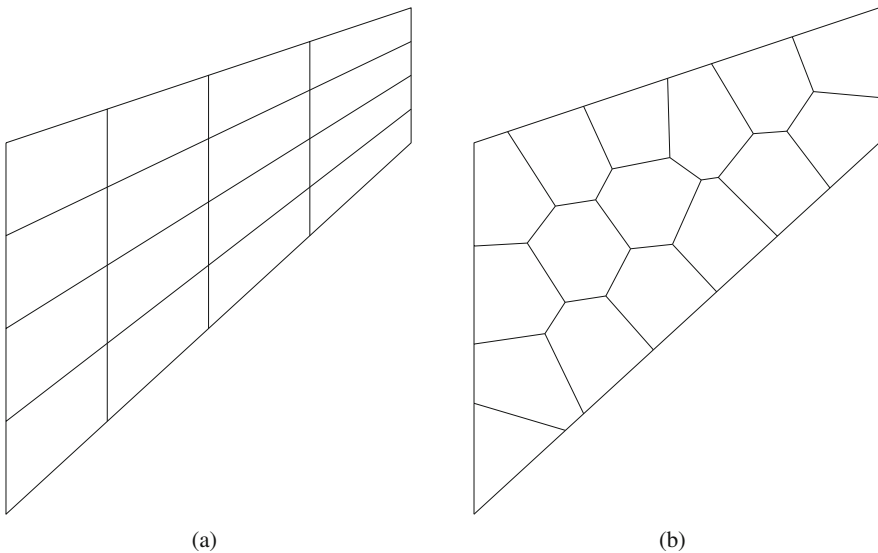
Fig. 4.9 Cook's membrane. Sample meshes: quad mesh (**a**); centroid-based Voronoi tessellation (**b**). (From: E. Artioli, L. Beirão da Veiga, C. Lovadina, and E. Sacco, Arbitrary order 2D virtual elements for polygonal meshes: Part I, elastic problem, Comput. Mech. 60 (2017), 355–377. Reproduced with permission)

quadrilateral finite elements, respectively indicated in the following as $Q4$ and $Q9$ [65]. Test *b* is instead analyzed with general polygonal meshes only testing VEM solutions of order $k = 1, 2, 3$, respectively.

In this test, accuracy and convergence levels are evaluated resorting to the following:

- Energy error norm:

$$D_1 = |||\mathbf{u}_h - \mathbf{u}|||_{\boldsymbol{\varepsilon}} = \left(\sum_{E \in \mathscr{T}_h} \int_E \|\boldsymbol{\varepsilon}(\mathbf{u}_h) - \boldsymbol{\varepsilon}(\mathbf{u})\|^2 \right)^{1/2} \qquad (4.4.3)$$

where $\boldsymbol{\varepsilon}(\mathbf{u})$ is the exact strain field, and $\boldsymbol{\varepsilon}(\mathbf{u}_h)$ here denotes (with a little abuse of notation) the strain field according to either a FEM or a VEM solution. In particular, for the FEM solution, $\boldsymbol{\varepsilon}(\mathbf{u}_h)$ is exactly computed, while for the VEM solution, such a strain field is obtained by means of (4.3.5).

- Discrete H^1 error norm:

$$D_2 = |||\mathbf{u}_h - \mathbf{u}|||_{1,h} = \left(\sum_{e \in \mathscr{E}_h} h_e \int_e \left\| \frac{\partial \mathbf{u}_h}{\partial \mathbf{t}_e} - \frac{\partial \mathbf{u}}{\partial \mathbf{t}_e} \right\|^2 \right)^{1/2} \qquad (4.4.4)$$

where $\mathbf{t}_e$ denotes the uniquely defined unit tangent vector to any edge e.

Figure 4.10a–d shows the h-convergence plots in terms of error D_1 and D_2 for the $Q4$, $Q9$ FEM, and $k = 1$, $k = 2$ VEM solutions, confirming the expected linear and quadratic convergence for linear and quadratic elements, respectively, and that the VEM method slightly outperforms the FEM of same order in terms of error D_1 and D_2.

D_2 error plots indicate that, for distorted meshes, the VEM solution on the mesh skeleton is more accurate than the FEM solution. Instead, D_1 error levels seem to indicate that the VEM suffers from a slight lack of accuracy in terms of strain if compared to the corresponding FEM. This may be justified by the fact that VEM strains are indeed computed by a suitable projection and not explicitly from the local displacements. More sophisticated strain post-processing procedures could be devised to overcome this issue and yield comparably or even more accurate results than FEM.

It is nonetheless quite remarkable that all the errors shown in Fig. 4.10 are actually comparable; showing that even for conforming quadrilaterals (i.e. a case where FEM are very accurate) the VEM grants equally accurate results.

Figures 4.11a–c show the h-convergence plots in terms of error D_1 for the $k = 1$, $k = 2$, and $k = 3$ VEM solutions. Clearly, these plots show the expected convergence rates, which, as seen in the previous campaign Test a, result quite robust regardless of mesh distortion.

The D_2-error patterns deployed by the h-convergence plots in Fig. 4.12 induce similar comments to the previous results.
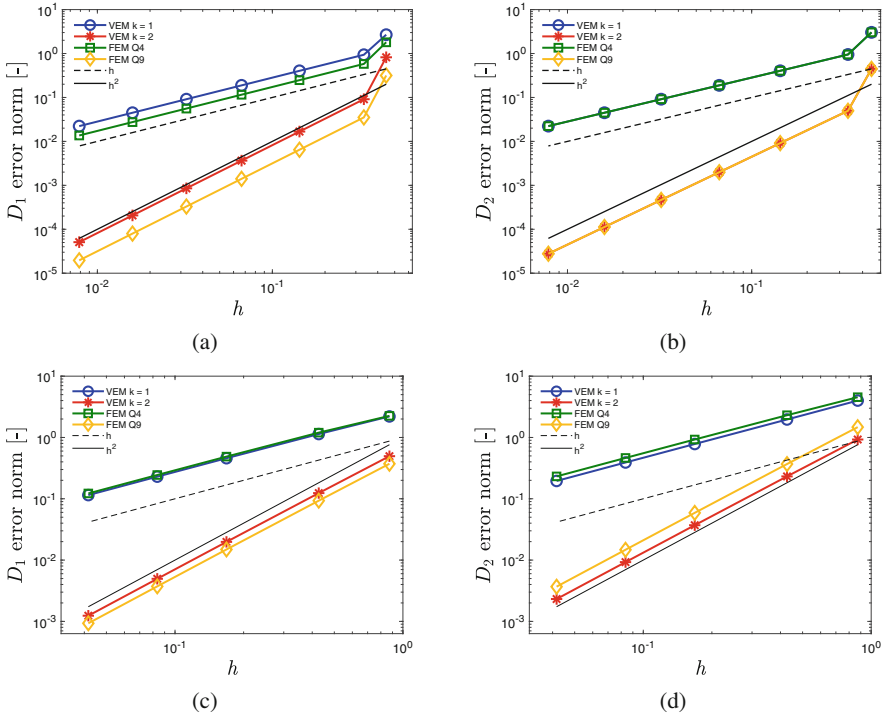
Fig. 4.10 VEM in primal form. Test *a* convergence plot. Error norms D_1-D_2 *vs* element size h. FEM $Q4$ and $Q9$; VEM $k = 1$ and $k = 2$, $m = 4$. Uniform meshes of squares (**a**),(**b**); Distorted concave rhombic quadrilaterals (**c**),(**d**)

For the Cook's membrane problem, the first mesh type (see Fig. 4.9a) is adopted for linear and quadratic VEMs in comparison with the same $Q4$ and $Q9$ FEM discretization; the second mesh type (see Fig. 4.9b) is adopted for VEM solutions only. Convergence results are reported in terms of mesh refinement monitoring $u_2(A)$, the vertical displacement of point A (see Fig. 4.6), as can be appreciated in Fig. 4.13a,b, where a reference solution corresponding to an overkilling solution, obtained with the hybrid-mixed CPE4I element [41], is indicated with a black dotted line. It is observed that quadrilateral VEMs have a slight edge in terms of accuracy with respect to Lagrangian finite elements of the corresponding order, while the polygonal VEMs from the centroid-based Voronoi tessellation slightly outperform the random-based VEMs.

4.4.1.2 Hellinger-Reissner Mixed Formulation

The accuracy and the convergence rate assessment is carried out for the 2D mixed formulation, using the following error norms:
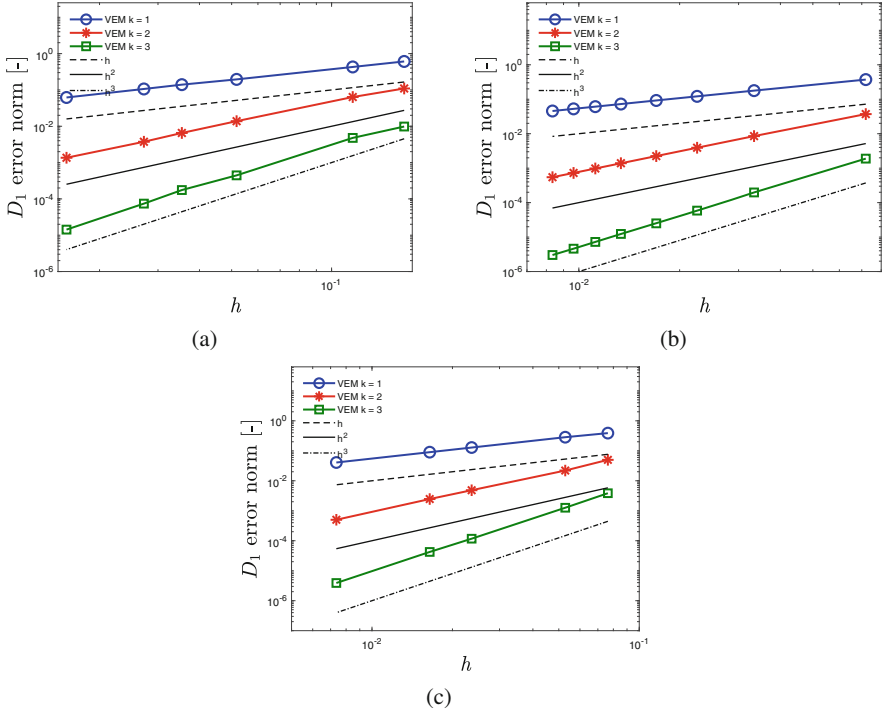
Fig. 4.11 VEM in primal form. Test b convergence plot. Error D_1 vs element size h. VEM $k = 1$, 2, 3. Non-uniform meshes of convex quadrilaterals (**a**) uniform meshes of hexagons (**b**); Voronoi tessellations (**c**)

- Discrete error norms for the stress field:

$$E_{\boldsymbol{\sigma}} = \left(\sum_{e \in \mathcal{E}_h} \kappa_e \, h_e \int_e |(\boldsymbol{\sigma} - \boldsymbol{\sigma}_h)\mathbf{n}|^2 \right)^{1/2}, \qquad (4.4.5)$$

where $\kappa_e = \kappa = \frac{1}{2}\mathrm{tr}(\mathbb{D})$ (the material is here homogeneous). We remark that the quantity above scales like the internal elastic energy, with respect to the size of the domain and of the elastic coefficients.

We make also use of the L^2 error on the divergence:

$$E_{\boldsymbol{\sigma},\mathbf{div}} = \left(\sum_{E \in \mathcal{T}_h} \int_E |\mathbf{div}(\boldsymbol{\sigma} - \boldsymbol{\sigma}_h)|^2 \right)^{1/2}. \qquad (4.4.6)$$
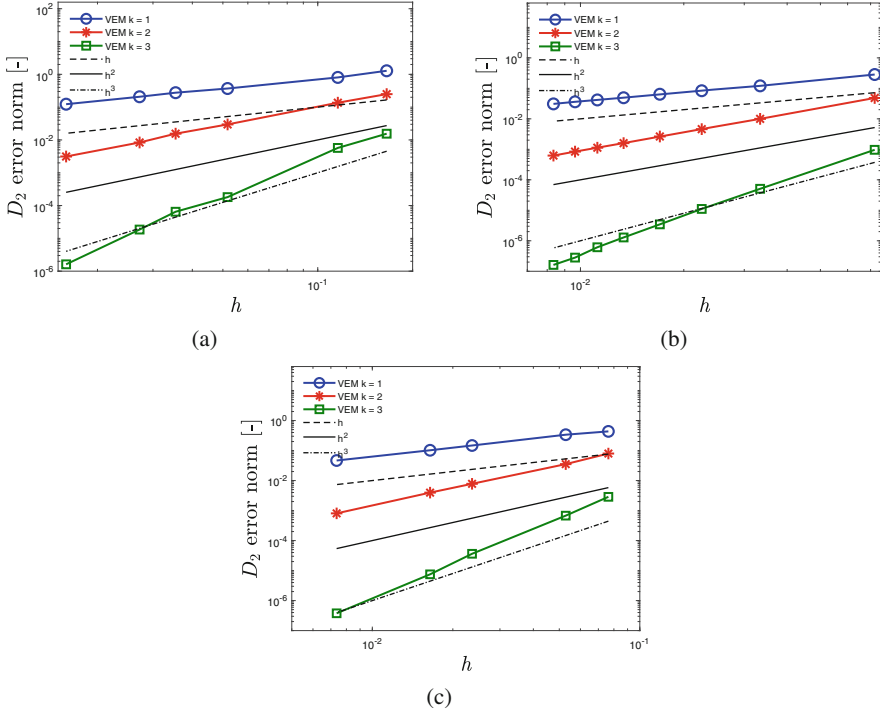
Fig. 4.12 VEM in primal form. Test *b* convergence plot. Error D_2 *vs* element size *h*. VEM $k = 1$, 2, 3. Non-uniform meshes of convex quadrilaterals (**a**); uniform meshes of hexagons (**c**); Voronoi tessellations (**d**)

- L^2 error norm for the displacement field:

$$E_{\mathbf{u}} = \left(\sum_{E \in \mathscr{T}_h} \int_E |\mathbf{u} - \mathbf{u}_h|^2 \right)^{1/2} = ||\mathbf{u} - \mathbf{u}_h||_0. \tag{4.4.7}$$

Low-Order Scheme

We now present the numerical results obtained with the scheme based on the choices (4.3.15) and (4.3.20).

Figure 4.14 reports the *h*-convergence of the proposed method for Test *a*. As expected, the asymptotic convergence rate is approximately equal to 1 for all the considered error norms and meshes. It is noted that, in this case, the $E_{\sigma,\mathbf{div}}$ plots are not reported because such a quantity is captured up to machine precision for all the considered computational grids.

(a)   (b)
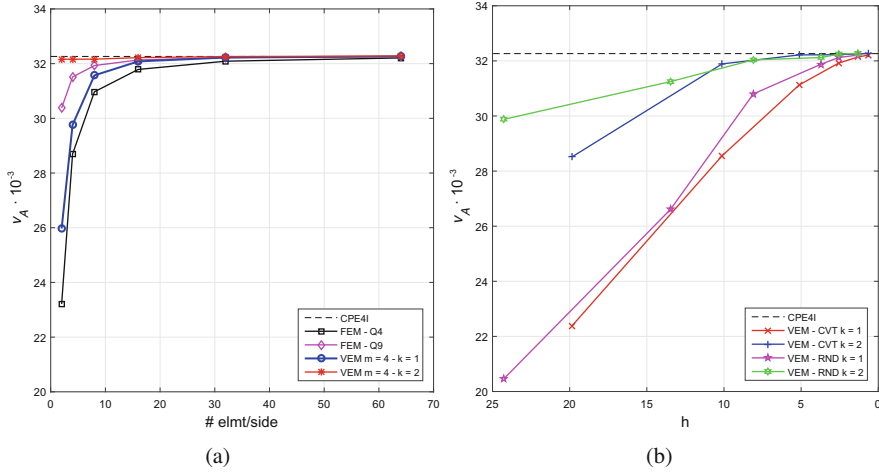
Fig. 4.13 VEM in primal form. Cook's membrane. Convergence results for vertical displacement of point A. Quad mesh with FEM $Q4$ and $Q9$; VEM $k = 1$ and $k = 2$ (**a**); Centroid-based and random-based Voronoi tessellations with VEM $k = 1$ and $k = 2$ (**b**). Reference solution based on overkilling size mesh of quadrilateral CPE4I hybrid-mixed finite elements. (From: E. Artioli, L. Beirão da Veiga, C. Lovadina, and E. Sacco, Arbitrary order 2D virtual elements for polygonal meshes: Part I, elastic problem, Comput. Mech. 60 (2017), 355–377. Reproduced with permission)

Figure 4.15 reports h-convergence for Test b. Asymptotic converge rate is approximately equal to 1 for all investigated mesh types and error measures, including $E_{\sigma,\mathbf{div}}$. These results highlight the expected optimal performance of the proposed VEM approach and its robustness with respect to the adopted computational grid.

Regarding the Cook's membrane problem, convergence results are reported in Fig. 4.16 in terms of mesh refinement monitoring $u_2(A)$, the vertical displacement of point A (see Fig. 4.6), approximated as the vertical displacement at the centroid of the closest polygon. The reference solution is indicated with a dotted red line corresponding to an overkilling accurate solution obtained with the hybrid-mixed CPE4I element [41].

Finally, contours representing the von Mises equivalent stress distributions are reported in Fig. 4.17. We remark that, inside the polygons, the stress distribution σ_h is not known, but its projection $\Pi_E\sigma_h$ onto the constant tensors is (cf. (4.3.56)). Thus, we have used this latter quantity to compute the von Mises equivalent stress displayed in Fig. 4.17. Finally, the results refer to the case $\nu = 1/3$, being the nearly incompressible case extremely similar.

Nearly Incompressibility Regime
A problem on the unit square domain $\Omega = [0, 1]^2$, with known analytical solution, is considered. A nearly incompressible material is chosen by selecting Lamé constants as $\lambda = 10^5$, $\mu = 0.5$. The test is designed by choosing a required solution for the

(a)

(b)

(c)

(d)
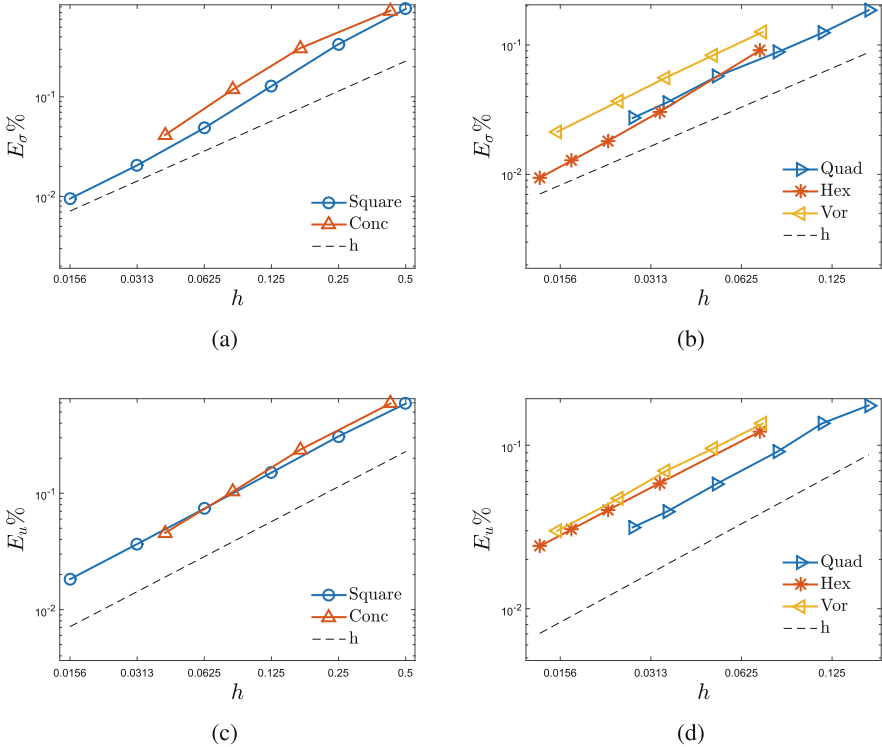
Fig. 4.14 h-convergence results for Test a on structured and unstructured meshes: (**a**) and (**b**) E_σ error norm plots, (**c**) and (**d**) $E_{\mathbf{u}}$ error norm plots

displacement field and deriving the load $\mathbf{f}$ accordingly. The displacement solution is as follows:

$$\begin{cases} u_1 = 0.5(\sin(2\pi x))^2 \sin(2\pi y)\cos(2\pi y) \\ u_2 = -0.5(\sin(2\pi y))^2 \sin(2\pi x)\cos(2\pi x). \end{cases} \tag{4.4.8}$$

Figure 4.18 reports the results obtained for both structured and unstructured meshes. In can be clearly seen that the proposed method shows the expected asymptotic rate of convergence also in this case.

Higher-Order Schemes
We now present the numerical results for Test a and Test b, obtained with the scheme based on the choices (4.3.23) and (4.3.31), for $k = 1, 2, 3$.

Results for $k = 1$ Figure 4.19 reports the h-convergence of the proposed method for Test a when k is equal to 1. The asymptotic convergence rate is approximately equal to 2 for all the considered error norms and meshes, as expected. The $E_{\sigma,\mathbf{div}}$
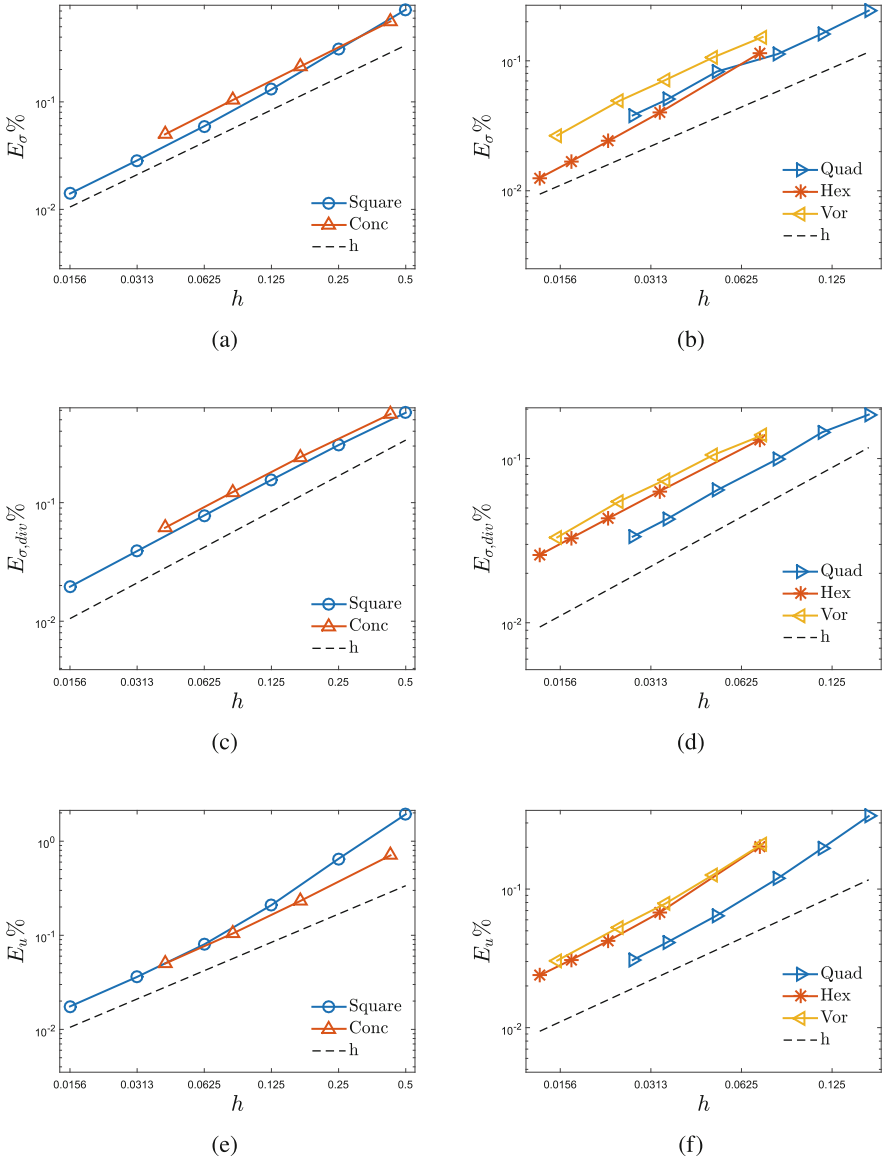
Fig. 4.15 *h*-convergence results for Test *b* on structured and unstructured meshes: (**a**) and (**b**) E_{σ} error norm plots, (**c**) and (**d**) $E_{\sigma,\mathbf{div}}$ error norm plots, (**e**) and (**f**) $E_{\mathbf{u}}$ error norm plots

plots are not reported for this case because such a quantity is captured up to machine precision for all the considered computational grids.

Figure 4.20 reports *h*-convergence for Test *b*. Asymptotic converge rate is approximately equal to 2 for all investigated mesh types and error measures. These
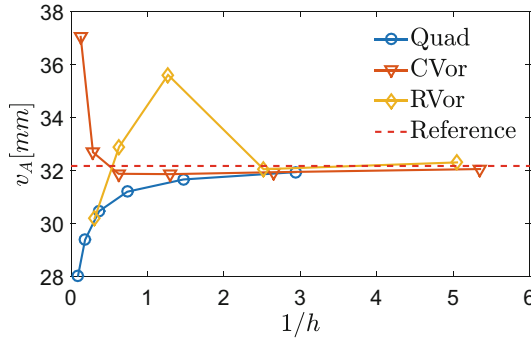
Fig. 4.16 Convergence of the tip vertical displacement $v_A = u_2(A)$
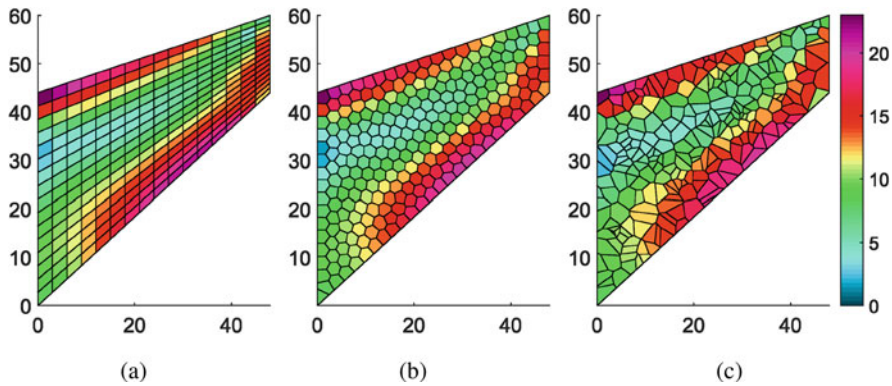
Fig. 4.17 Contours representing the von Mises equivalent stress distributions for $\nu = 1/3$: (**a**) Quad, (**b**) CVor, (**c**) RVor

results highlight the expected optimal performance of the proposed VEM approach and its robustness with respect to the adopted computational grid.

Results for $k = 2$ Figure 4.21 reports the h-convergence of the proposed method for Test a when k is equal to 2. The asymptotic convergence rate is approximately equal to 3 for all the considered error norms and meshes, as expected. In this case the E_σ and $E_{\sigma,\mathbf{div}}$ plots are not reported because such quantities are captured up to machine precision for all the considered computational grids.

Figure 4.22 reports h-convergence for Test b. Also in this case results confirm the soundness of the proposed approach.

Results for $k = 3$ Results in terms of h-convergence obtained for $k = 3$ are shown. In this case only Test b is reported, being Test a captured exactly up to machine precision by the proposed numerical scheme. In particular, Fig. 4.23 reports h-convergence graphs for Test b. The convergence rate is approximately equal to 4 for all the considered error norms and meshes, as expected.
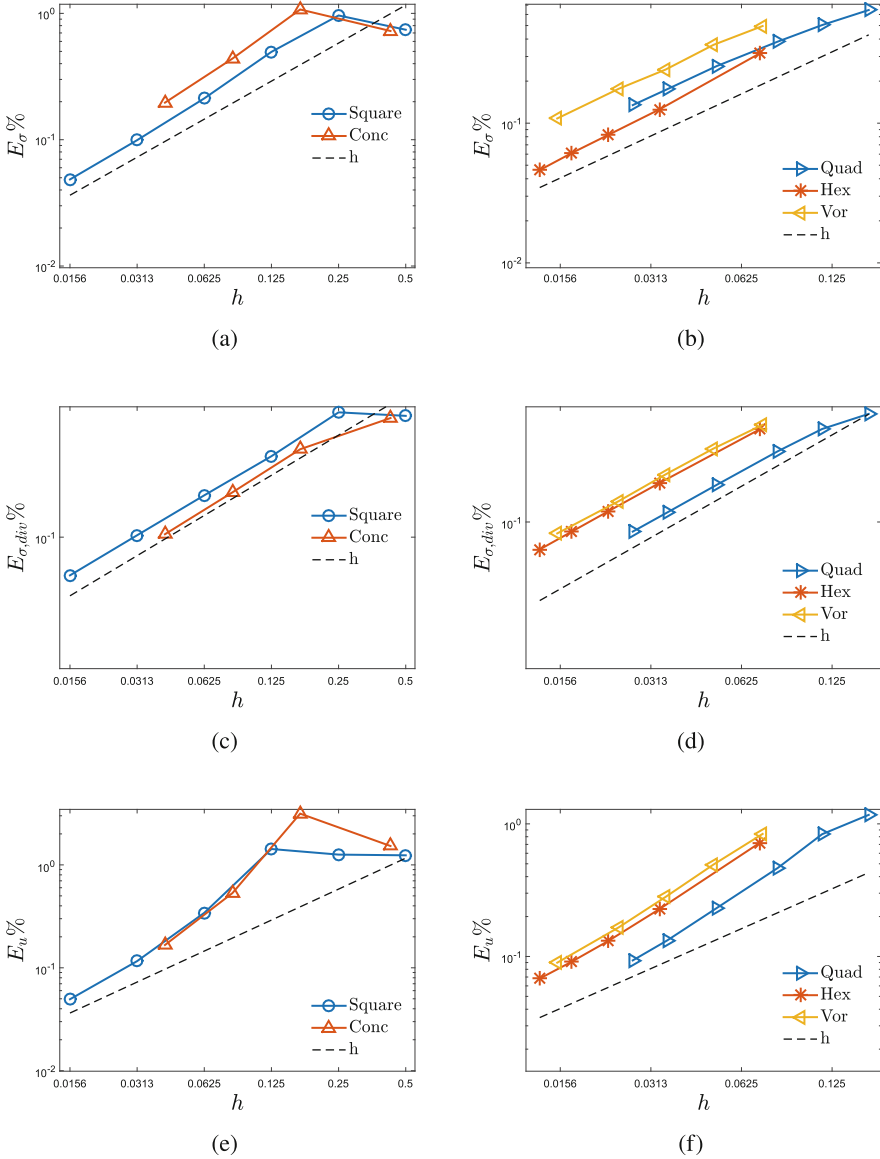
Fig. 4.18 Results for the nearly incompressible test on structured and unstructured meshes: (**a**) and (**b**) convergence of E_{σ}, (**c**) and (**d**) convergence of $E_{\sigma,\text{div}}$, (**e**) and (**f**) convergence for $E_{\mathbf{u}}$

4.4.2   3D Numerical Results

We here present the numerical results of the 3D Virtual Element Method based on the spaces detailed in (4.3.49) and (4.3.54).
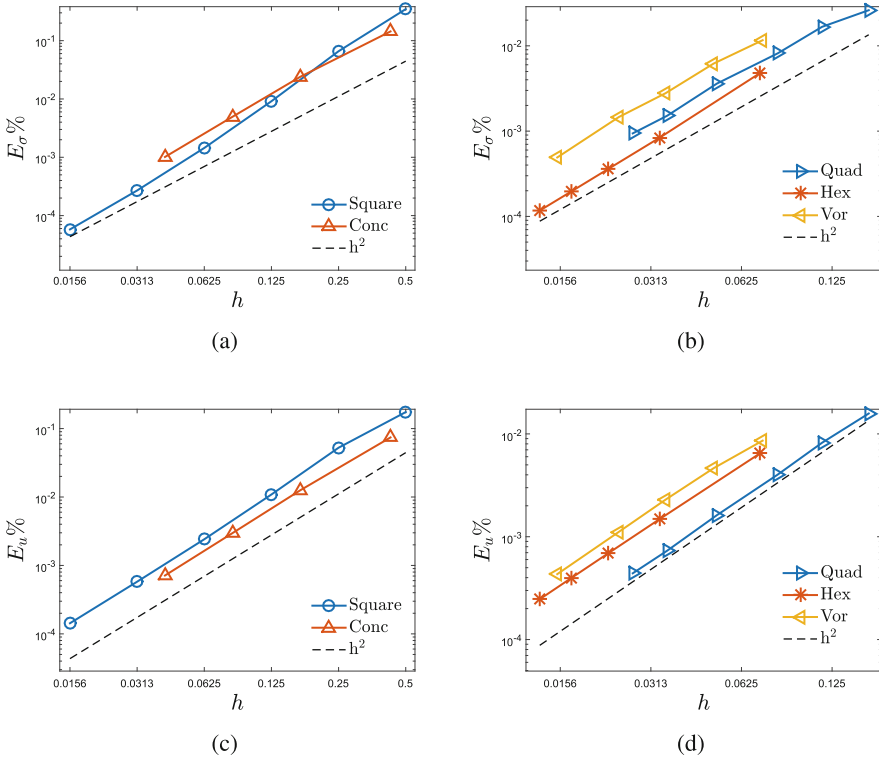
Fig. 4.19 *h*-convergence results for Test *a* on structured and unstructured meshes for $k = 1$: (**a**) and (**b**) E_σ error norm plots, (**c**) and (**d**) E_u error norm plots

Accuracy Assessment on a Cubic Domain

We consider the standard unit cube $\Omega = [0, 1]^3$ as computational domain and we take the following four mesh types, see Fig. 4.24:

- **Cube,** a mesh composed by standard structured cubes;
- **Tetra,** a Delaunay tetrahedralization of the domain Ω;
- **CVT,** a Voronoi tassellation obtained by the Lloyd algorithm [46];
- **Random,** a Voronoi tassellation achieved with random control points.

Meshes **CVT** and **Random** have some elements with small faces and edges, in such a way that at least one of the assumptions (**A1**), (**A2**) and (**A3**) is not satisfied. However, the numerical results show that the scheme is fairly robust with respect to this geometric situation. These two types of meshes are build via the `voro++` library [56]. Moreover, the whole numerical scheme is developed inside the `vem++` library, a `c++` code realized at the University Milano–Bicocca during the CAVE project (https://sites.google.com/view/vembic/home).

(a)

(b)

(c)

(d)

(e)

(f)
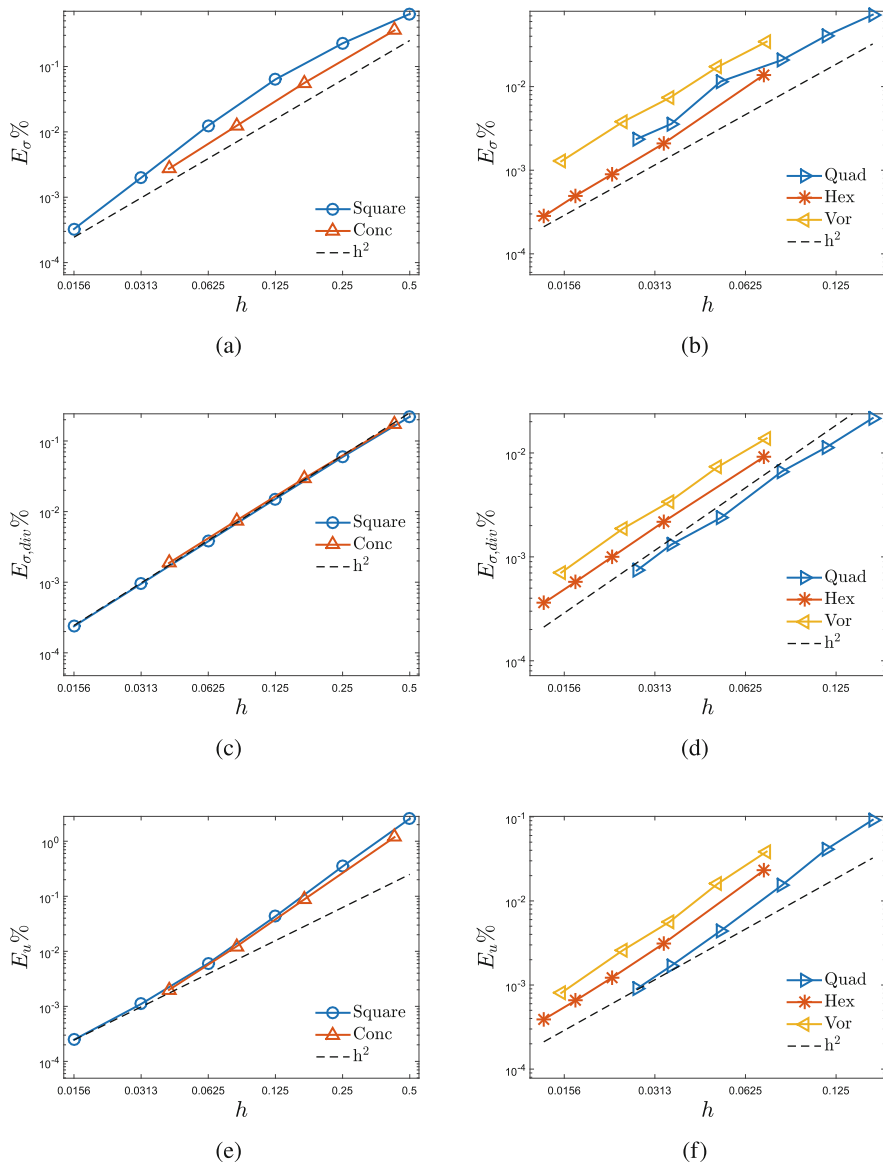
Fig. 4.20 h-convergence results for Test b on structured and unstructured meshes for $k = 1$: (**a**) and (**b**) $E_{\boldsymbol{\sigma}}$ error norm plots, (**c**) and (**d**) $E_{\boldsymbol{\sigma},\mathbf{div}}$ error norm plots, (**e**) and (**f**) $E_{\mathbf{u}}$ error norm plots

Fig. 4.21 h-convergence results for Test a on structured and unstructured meshes for $k = 2$: (**a**) and (**b**) $E_{\mathbf{u}}$ error norm plots

The accuracy and the convergence rate assessment is carried out using the obvious 3D versions of the error quantities E_σ, $E_{\sigma,\mathbf{div}}$ and $E_{\mathbf{u}}$ defined in (4.4.5), (4.4.6) and (4.4.7).

- Test a.

We consider an elastic problem where a trigonometric solution is a-priori selected. Accordingly, the applied loads are determined. Moreover, homogeneous Dirichlet boundary conditions are imposed on three faces of the cube ($x = 0$, $y = 0$, $z = 0$), as well as homogeneous Neumann boundary conditions on the remaining faces. The material is homogeneous and isotropic; the displacement solution and the loads are as follows:

$$\begin{cases} u_1 = u_2 = u_3 = 10\, S(x, y, z) \\ f_1 = -10\pi^2((\lambda + \mu)\cos(\pi x)\sin(\pi y + \pi z) - (\lambda + 4\mu)S(x, y, z)) \\ f_2 = -10\pi^2((\lambda + \mu)\cos(\pi y)\sin(\pi x + \pi z) - (\lambda + 4\mu)S(x, y, z)) \\ f_3 = -10\pi^2((\lambda + \mu)\cos(\pi z)\sin(\pi x + \pi y) - (\lambda + 4\mu)S(x, y, z)), \end{cases}$$

where $S(x, y, z) = \sin(\pi x)\sin(\pi y)\sin(\pi z)$. The Lamé constants are here set as $\lambda = 1$ and $\mu = 1$.

Figure 4.25 reports h-convergence of the proposed method for Test a. As expected, for the considered method, the asymptotic convergence rate is approximately equal to 1 for all error norms and meshes. In addition, the convergence graphs of each type of mesh are close to each others and this fact confirms the robustness of the proposed method with respect to the element shape.

- Test b.

We consider a problem with polynomial solution, non-homogeneous Dirichlet boundary conditions and zero loading. Again, the Lamé constants are $\lambda = 1$ and $\mu = 1$. As in the previous examples, the test is defined by choosing a required
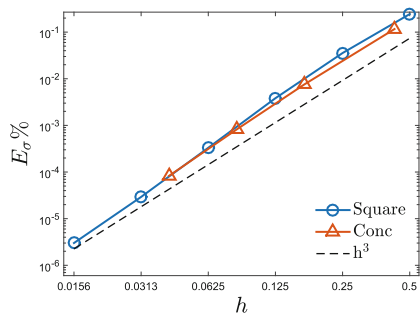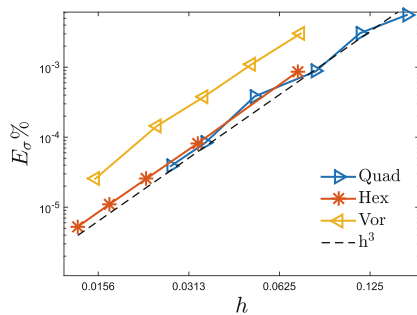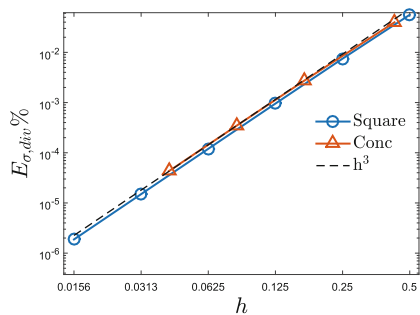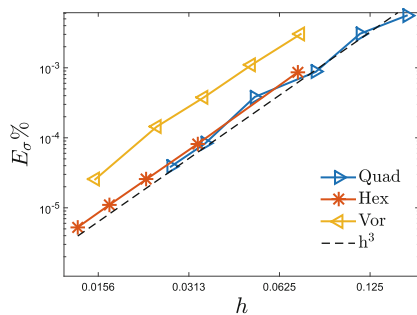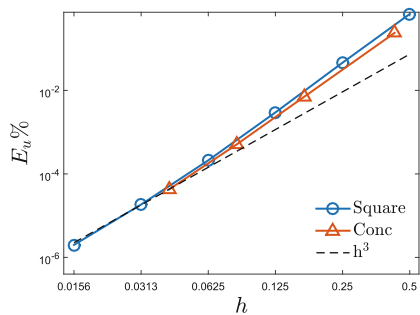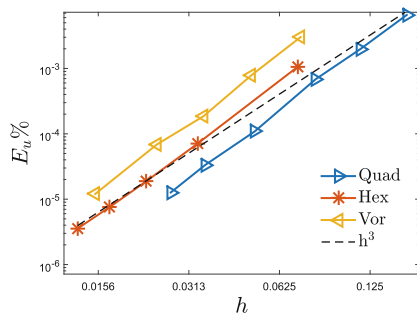
Fig. 4.22 h-convergence results for Test b on structured and unstructured meshes for $k = 2$: (**a**) and (**b**) E_σ error norm plots, (**c**) and (**d**) $E_{\sigma,\mathbf{div}}$ error norm plots, (**e**) and (**f**) $E_\mathbf{u}$ error norm plots
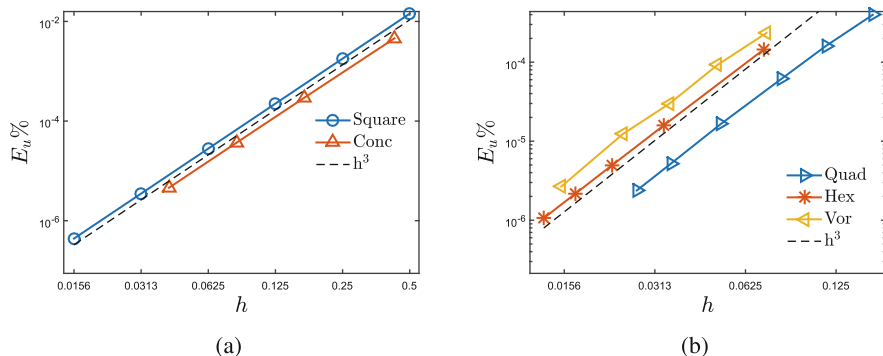
Fig. 4.23 h-convergence results for Test b on structured and unstructured meshes for $k = 3$: (**a**) and (**b**) E_{σ} error norm plots, (**c**) and (**d**) $E_{\sigma, \mathbf{div}}$ error norm plots, (**e**) and (**f**) $E_{\mathbf{u}}$ error norm plots

Cube   Tetra

CVT   Random
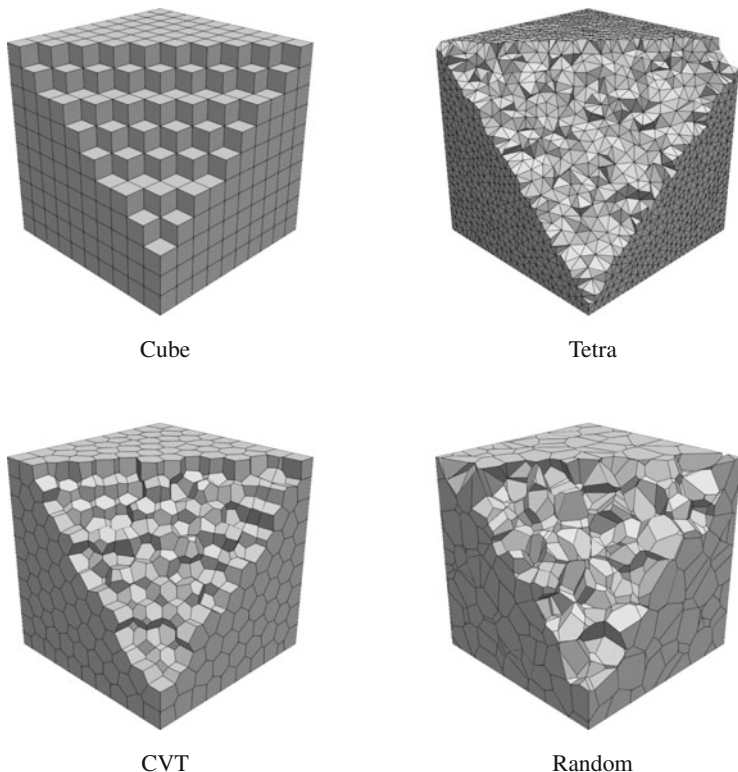
Fig. 4.24 Overview of adopted meshes for convergence assessment numerical tests

solution and deriving the corresponding body load ($\mathbf{f} = \mathbf{0}$):

$$\begin{cases} u_1 = 2x^3 - 3xy^2 - 3xz^2 \\ u_2 = 2y^3 - 3yx^2 - 3yz^2 \\ u_3 = 2z^3 - 3zy^2 - 3zx^2 \\ \mathbf{f} = \mathbf{0} \end{cases}$$

We remark that this is a typical example where the displacement field is nontrivial, while stresses are divergence-free. As expected, this latter feature is numerically satisfied by the proposed VEM scheme, as shown by Fig. 4.26, where also the other errors are displayed.

- L-shaped domain test.

In this subsection, we consider a problem for which we do not know the analytical solution. First of all, we take the 3D L-shaped domain $\Omega = A \setminus B$, where

(a)

(b)

(c)
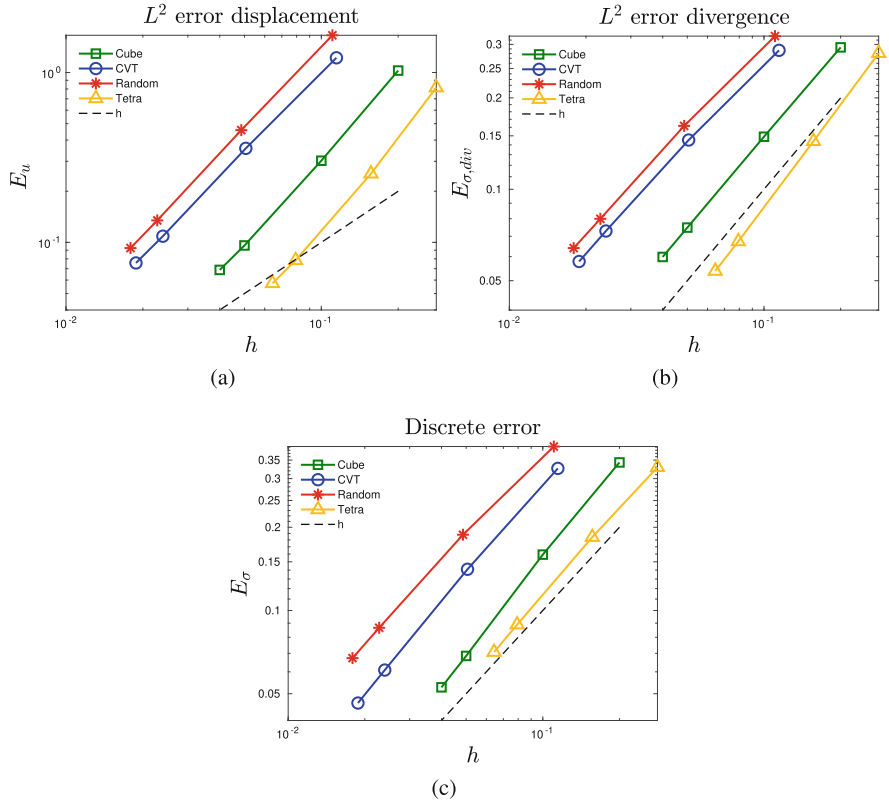
Fig. 4.25 Test a. h-convergence results for all meshes

$A = [0, 2] \times [0, 1] \times [0, 2]$ while $B = (1, 2) \times [0, 1] \times (1, 2)$. The problem we study is:

$$
\begin{cases}
\text{Find } (\boldsymbol{\sigma}, \mathbf{u}) \text{ such that} \\[4pt]
-\, \mathbf{div}\, \boldsymbol{\sigma} = \mathbf{f} & \text{in } \Omega \\[4pt]
\boldsymbol{\sigma} = \mathbb{C}\boldsymbol{\varepsilon}(\mathbf{u}) & \text{in } \Omega \\[4pt]
\mathbf{u} = \mathbf{0} & \text{in } \partial\Omega_D \\[4pt]
\boldsymbol{\sigma}\mathbf{n} = \mathbf{0} & \text{in } \partial\Omega_{N_0} \\[4pt]
\boldsymbol{\sigma}\mathbf{n} = \boldsymbol{\psi} & \text{in } \partial\Omega_{N_1},
\end{cases}
$$
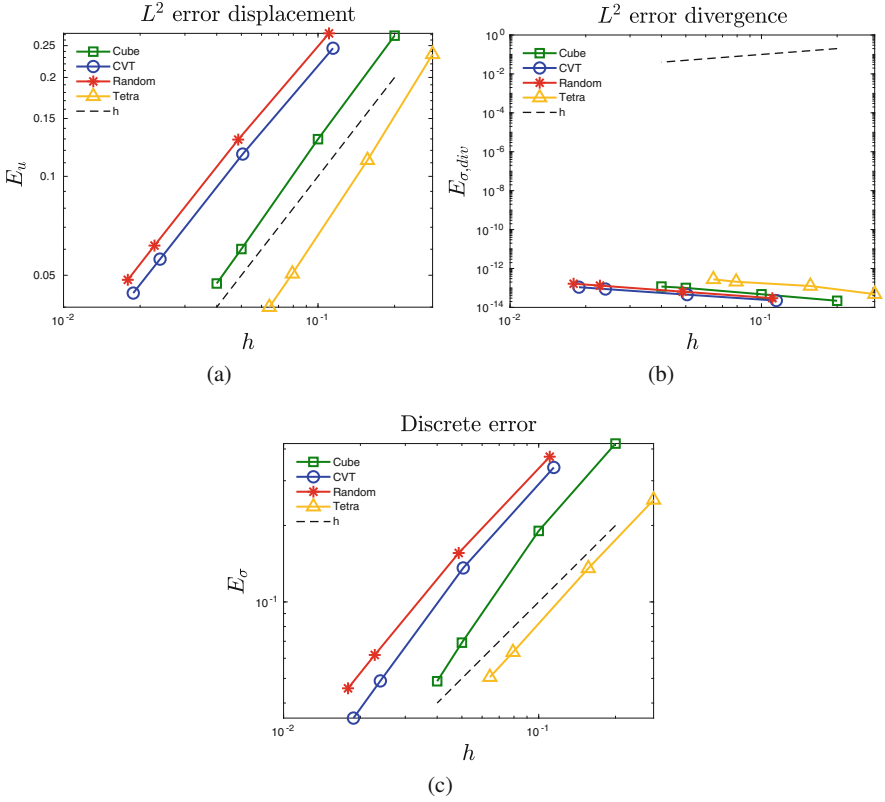
Fig. 4.26 Test *b*. *h*-convergence results for all meshes

where the boundary $\partial\Omega$ is divided into three regular disjoint parts:

$$\partial\Omega_D = \{(x, y, z) \in \partial\Omega \ : \ z = 2\}$$

$$\partial\Omega_{N_1} = \{(x, y, z) \in \partial\Omega \ : \ x = 2\}$$

$$\partial\Omega_{N_0} = \partial\Omega \setminus (\partial\Omega_D \cup \partial\Omega_{N_1}).$$

Furthermore, we take the loading term $\mathbf{f} = (0, 0, -0.001)^T$ and boundary traction $\boldsymbol{\psi} = (0, 0, -0.008)^T$. The material is again homogeneous and isotropic with Lamé coefficients $\lambda = 1$ and $\mu = 1$. For this simulation we only use a **Tetra** mesh.

In Fig. 4.27 we report both the mesh of our domain, and the deformed body. We also overlap the two images to better appreciate the load effects. Finally, contours representing the von Mises equivalent stress distribution are reported in Fig. 4.28. The discrete stress distribution $\boldsymbol{\sigma}_h$ is not known inside the polyhedrons, but its projection $\Pi_E \boldsymbol{\sigma}_h$ onto the constant tensors is computable. Thus, in Fig. 4.28 we have used this latter quantity to approximate and display the von Mises equivalent
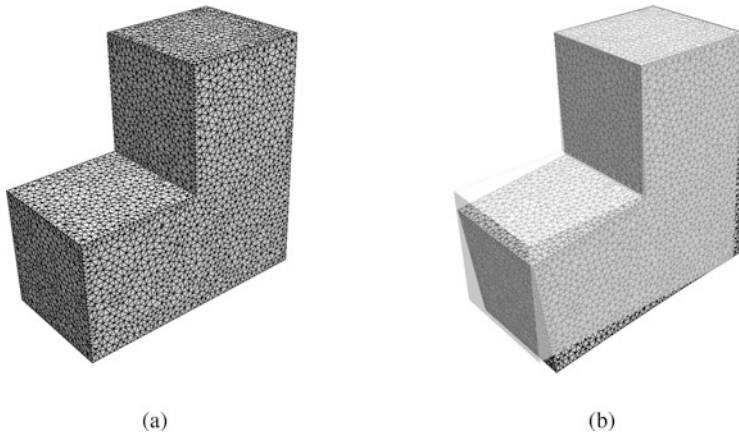
Fig. 4.27 L-shaped domain test. Contours representing the problem: (**a**) unloaded body and (**b**) deformed body
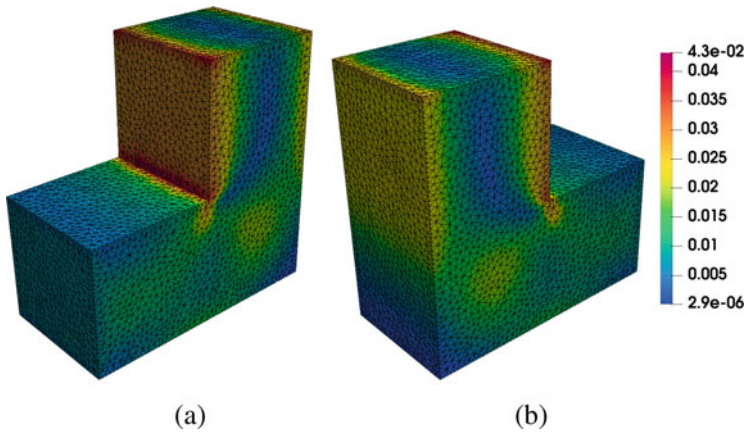
Fig. 4.28 L-shaped domain test. Contours representing the von Mises equivalent distribution: (**a**) front view and (**b**) rear view

stress. As already mentioned, the analytical solution to this problem is not available. However, Fig. 4.28 shows that both the computed deformed shape, and the von Mises equivalent stress distribution are qualitatively realistic.

4.5 Conclusions

We have discussed the application of the Virtual Element Method for linear elastostatic problems. In particular, both displacement based schemes and mixed methods based on the Hellinger-Reissner variational principle have been considered.

For the more standard primal (i.e. displacement based) schemes, only the 2D case has been detailed, but the usual techniques (see [20], for instance) can be used for the extension to 3D problems. On the contrary, for the mixed (Hellinger-Reissner) methods both 2D and 3D cases have been considered. More precisely, a whole family of 2D schemes has been presented, while in 3D only a low-order method has been extensively detailed. However, we remark that also in the 3D case it is possible to design high-order schemes, inspired by the 2D framework. This will be the topic of future communications. All the presented schemes has been supported by numerical results which show the actual performance of our VEMs.

We may conclude that the Virtual Element Method for elasticity problems definitely deserves to be considered as a valid alternative to other more standard approaches, such as the Finite Element Methods.

References

1. F. Aldakheel, B. Hudobivnik, E. Artioli, L. Beirão da Veiga, P. Wriggers, Curvilinear virtual elements for contact mechanics. Comput. Methods Appl. Mech. Eng. **372**, 113394 (2020)
2. O. Andersen, H.M. Nilsen, X. Raynaud, Virtual element method for geomechanical simulations of reservoir models. Comput. Geosci. **21**(5), 877–893 (2017)
3. P.F. Antonietti, G. Manzini, I. Mazzieri, H.M. Mourad, M. Verani, The arbitrary-order virtual element method for linear elastodynamics models: convergence, stability and dispersion-dissipation analysis. Int. J. Numer. Meth. Eng. **122**, 934–971 (2021)
4. D.N. Arnold, F. Brezzi, Mixed and nonconforming finite element methods: implementation, postprocessing and error estimates. ESAIM Math. Model. Numer. Anal. **19**, 7–32 (1985)
5. D.N. Arnold, R. Winther, Mixed finite elements for elasticity. Numer. Math. **92**, 401–419 (2002)
6. E. Artioli, L. Beirão da Veiga, C. Lovadina, E. Sacco, Arbitrary order 2D virtual elements for polygonal meshes: Part I, elastic problem. Comput. Mech. **60**, 355–377 (2017)
7. E. Artioli, L. Beirão da Veiga, C. Lovadina, E. Sacco, Arbitrary order 2D virtual elements for polygonal meshes: Part II, inelastic problem. Comput. Mech. **60**, 643–657 (2017)
8. E. Artioli, S. de Miranda, C. Lovadina, L. Patruno, A stress/displacement virtual element method for plane elasticity problems. Comput. Methods Appl. Mech. Eng. **325**, 155–174 (2017)
9. E. Artioli, S. de Miranda, C. Lovadina, L. Patruno, A family of virtual element methods for plane elasticity problems based on the hellinger-reissner principle. Comput. Methods Appl. Mech. Eng. **340**, 978–999 (2018)
10. E. Artioli, S. Marfia, E. Sacco, High-order virtual element method for the homogenization of long fiber nonlinear composites. Comput. Methods Appl. Mech. Eng. **341**, 571–585 (2018)

11. E. Artioli, S. de Miranda, C. Lovadina, L. Patruno, An equilibrium-based stress recovery procedure for the VEM. Int. J. Numer. Methods Eng. **117**, 885–900 (2019)
12. E. Artioli, L. Beirão da Veiga, F. Dassi, Curvilinear virtual elements for 2d solid mechanics applications. Comput. Methods Appl. Mech. Eng. **359**, 112667 (2020)
13. E. Artioli, L. Beirão da Veiga, M. Verani, An adaptive curved virtual element method for the statistical homogenization of random fibre-reinforced composites. Finite Elem. Anal. Des. **177**, 103418 (2020)
14. E. Artioli, A. Sommariva, M. Vianello, Algebraic cubature on polygonal elements with a circular edge. Comput. Math. Appl. **79**, 2057–2066 (2020)
15. K.J. Bathe, *Finite Element Procedures* (Prentice Hall, Upper Saddle River, New Jersey, 1996)
16. L. Beirão da Veiga, G. Manzini, A virtual element method with arbitrary regularity. IMA J. Numer. Anal. **34**(2), 759–781 (2014)
17. L. Beirão da Veiga, G. Manzini, Residual a posteriori error estimation for the virtual element method for elliptic problems. ESAIM: Math. Mod. Numer. Anal. **49**(2), 577–599 (2015)
18. L. Beirão da Veiga, F. Brezzi, A. Cangiani, G. Manzini, L.D. Marini, A. Russo, Basic principles of Virtual Element Methods. Math. Models Methods Appl. Sci. **23**, 119–214 (2013)
19. L. Beirão da Veiga, F. Brezzi, L.D. Marini, Virtual elements for linear elasticity problems. SIAM J. Numer. Anal. **51**(2), 794–812 (2013)
20. L. Beirão da Veiga, F. Brezzi, L.D. Marini, A. Russo, The Hitchhikers guide to the Virtual Element Method. Math. Models Methods Appl. Sci. **24**(8), 1541–1573 (2014)
21. L. Beirão da Veiga, K. Lipnikov, G. Manzini, *The Mimetic Finite Difference Method for Elliptic Problems,* series MS&A (vol. 11) (Springer, 2014)
22. L. Beirão da Veiga, C. Lovadina, D. Mora, A virtual element method for elastic and inelastic problems on polytope meshes. Comput. Methods Appl. Mech. Eng. **295**, 327–346 (2015)
23. L. Beirão da Veiga, F. Dassi, A. Russo, High-order virtual element method on polyhedral meshes. Comput. Math. Appl. **74**(5), 1110–1122 (2017)
24. L. Beirão da Veiga, C. Lovadina, A. Russo, Stability analysis for the virtual element method. Math. Models Methods Appl. Sci. **27**(13), 2557–2594 (2017)
25. L. Beirão da Veiga, C. Lovadina, G. Vacca, Divergence free virtual elements for the stokes problem on polygonal meshes. ESAIM: Math. Mod. Numer. Anal. **51**(2), 509–535 (2017)
26. L. Beirão da Veiga, F. Brezzi, F. Dassi, L.D. Marini, A. Russo, A family of three-dimensional virtual elements with applications to magnetostatics. SIAM J. Numer. Anal. **56**(5), 2940–2962 (2018)
27. L. Beirão da Veiga, A. Russo, G. Vacca, The virtual element method with curved edges. ESAIM: Math. Mod. Numer. Anal. **53**(2), 375–404 (2019)
28. S. Berrone, A. Borio, A residual *a posteriori* error estimate for the Virtual Element Method. Math. Models Methods Appl. Sci. **27**(8), 1423–1458 (2017)
29. S. Bertoluzza, M. Pennacchio, D. Prada, BDDC and FETI-DP for the virtual element method. Calcolo **54**(4), 1565–1593 (2017)
30. D. Boffi, F. Brezzi, M. Fortin, *Mixed Finite Element Methods and Aapplications*. Springer Series in Computational Mathematics, vol. 44 (Springer, Heidelberg, 2013). MR 3097958
31. S.C. Brenner, Li.-Y. Sung, Virtual element methods on meshes with small edges or faces. Math. Models Methods Appl. Sci. (2017)
32. S.C. Brenner, Q. Guan, Li.-Y. Sung, Some estimates for virtual element methods. Comput. Methods Appl. Math. **17** (2017)
33. F. Brezzi, L.D. Marini, Virtual element methods for plate bending problems. Comput. Methods Appl. Mech. Eng. **253**, 455–462 (2013)
34. F. Brezzi, K. Lipnikov, M Shashkov, V. Simoncini, A new discretization methodology for diffusion problems on generalized polyhedral meshes. Comput. Methods Appl. Mech. Eng. **196**, 3682–3692 (2007)
35. F. Brezzi, A. Buffa, K. Lipnikov, Mimetic finite differences for elliptic problems. Math. Mod. Numer. Anal. **43**, 277–295 (2009)
36. A. Cangiani, E.H. Georgoulis, T. Pryer, O.J. Sutton, A posteriori error estimates for the virtual element method. Numer. Math. **137**(4), 857–893 (2017). MR 3719046

37. H. Chi, L. Beirão da Veiga, G.H. Paulino, Some basic formulations of the virtual element method (VEM) for finite deformations. Comput. Methods Appl. Mech. Eng. **318**, 148–192 (2017)
38. H. Chi, L. Beirão da Veiga, G.H. Paulino, A simple and effective gradient recovery scheme and a posteriori error estimator for the Virtual Element Method (VEM). Comput. Methods Appl. Mech. Eng. **347**, 21–58 (2019)
39. P.G. Ciarlet, *Mathematical Elasticity volume I: Three Dimensional Elasticity* (Elsevier Science Publishers B. V., 1988)
40. M. Cihan, F. Aldakheel, B. Hudobivnik, P. Wriggers, 3d virtual elements for elastodynamic problems. PAMM **20**, e202000175 (2021)
41. Dassault Systèmes, *Abaqus Documentation,* Providence, RI, 2011
42. F. Dassi, L. Mascotto, Exploring high-order three dimensional virtual elements: bases and stabilizations. Comput. Math. Appl. **75**(9), 3379–3401 (2018)
43. F. Dassi, G. Vacca, Bricks for the mixed high-order virtual element method: Projectors and differential operators. Appl. Numer. Math. (2019)
44. F. Dassi, C. Lovadina, M. Visinoni, A three-dimensional Hellinger-Reissner virtual element method for linear elasticity problems. Comput. Methods Appl. Mech. Eng. **364**, 112910 (2020)
45. F. Dassi, C. Lovadina, M. Visinoni, Hybridization of a virtual element method for linear elasticity problems. Preprint. arXiv:2103.01164. Submitted for publication
46. Q. Du, V. Faber, M. Gunzburger, Centroidal voronoi tessellations: Applications and algorithms. SIAM Rev. **41**(4), 637–676 (1999)
47. A.M. D'Altri, S. de Miranda, L. Patruno, E. Sacco, An enhanced vem formulation for plane elasticity. Comput. Methods Appl. Mech. Eng. **376**, 113663 (2021)
48. A.L. Gain, C. Talischi, G.H. Paulino, On the virtual element method for three-dimensional linear elasticity problems on arbitrary polyhedral meshes. Comput. Methods Appl. Mech. Eng. **282**, 132–160 (2014). MR 3269894
49. T.J.R. Hughes, *The Finite Element Method: Linear Static and Dynamic Finite Element Analysis*, 2nd edn. (Dover, 2000)
50. J.E. Marsden, T.J.R. Hughes, *Mathematical Foundations of Elasticity* (Dover Publications, New York, 1994)
51. L. Mascotto, I. Perugia, A. Pichler, Non-conforming harmonic virtual element method: h- and p-versions. J. Sci. Comput. **77**(3), 1874–1908 (2018)
52. S.E. Mousavi, N. Sukumar, Numerical integration of polynomials and discontinuous functions on irregular convex polygons and polyhedrons. Comput. Mech. **47**(5), 535–554 (2011)
53. S.E. Mousavi, H. Xiao, N. Sukumar, Generalized Gaussian quadrature rules on arbitrary polygons. Int. J. Numer. Meth. Eng. **82**(1), 99–113 (2010)
54. R. Ogden, *Non-linear Elastic Deformations* (Dover Publications, Mineola, New York, 1997)
55. K. Park, H. Chi, G.H. Paulino, On nonconvex meshes for elastodynamics using virtual element methods with explicit time integration. Comput. Methods Appl. Mech. Eng. **356**, 669–684 (2019)
56. C.H. Rycroft, Voro++: A three-dimensional voronoi cell library in c++. Chaos (Woodbury, N.Y.) **19**, 041111 (2009)
57. A. Sommariva, M. Vianello, Product Gauss cubature over polygons based on Green's integration formula. BIT Numer. Math. **47**(2), 441–453 (2007)
58. A. Sommariva, M. Vianello, Gauss-green cubature and moment computation over arbitrary geometries. J. Comput. App. Math. **231**, 886–896 (2009)
59. A. Sommariva, M. Vianello, Compression of multivariate discrete measures and applications. Numer. Funct. Anal. Optim. **36**(9), 1198–1223 (2015)
60. P. Wriggers, *Nonlinear Finite Element Methods* (Springer, Berlin, Heidelberg, 2008)
61. P. Wriggers, B.D. Reddy, W. Rust, B. Hudobivnik, Efficient virtual element formulations for compressible and incompressible finite deformations. Comput. Mech., 253–268 (2017)
62. P. Wriggers, W. Rust, B.D. Reddy, A virtual element method for contact. Comput. Mech. **58**, 1039–1050 (2016)

63. B. Zhang, M. Feng, Virtual element method for two-dimensional linear elasticity problem in mixed weakly symmetric formulation. Appl. Math. Comput. **328**, 1–25 (2018)
64. B. Zhang, Y. Yang, M. Feng, Mixed virtual element methods for elastodynamics with weak symmetry. J. Comput. Appl. Math. **353**, 49–71 (2019)
65. O.C. Zienckiewicz, R.L. Taylor, *The Finite Element Method* (Butterworth Heinemann, 2000)

Chapter 5
An Introduction to Second Order Divergence-Free VEM for Fluidodynamics

Check for updates

Lourenço Beirão da Veiga and Giuseppe Vacca

Abstract The present contribution constitutes an introduction and a survey of the "divergence-free" Virtual Element Method (VEM) for the Stokes and Navier-Stokes equations. It is a survey since it reviews all the main concepts regarding this kind of Virtual Elements and it is an introduction since it is written, both in terms of presentation and details, in order to be easily readable for newcomers. In particular we show the construction of the divergence-free virtual element velocity space for the Stokes equation and its enhanced version for the Navier-Stokes equation, and the explicit computation of the projection operators. We exhibit both the 2D (straight and curved polygons) and the 3D case. Furthermore we explore the main features and the advantages of the "divergence-free" construction. We believe the present paper constitutes a good reading for researchers that have some minimal knowledge of virtual elements and want to understand the "divergence-free" VEM approach for fluid mechanics.

5.1 Introduction

The Virtual Element Method is a recent technology for the discretization of partial differential equations; after its introduction in [8, 9], it soon enjoyed a wide success in the Numerical Analysis and Engineering communities. It can be considered as a generalization of the Finite Element Method (FEM) that incorporates ideas from Mimetic Finite Differences [10, 54] and is able to handle general polytopal meshes, also including hanging nodes and non-convex elements. Although the main and initial motivation of VEM is to use more general grids, it was soon recognized

L. Beirão da Veiga

Dipartimento di Matematica e Applicazioni, Università degli Studi di Milano Bicocca, Milano, Italy

e-mail: lourenco.beirao@unimib.it

G. Vacca (✉)

Dipartimento di Matematica, Università degli Studi di Bari, Bari, Italy
e-mail: giuseppe.vacca@uniba.it

that the flexibility of Virtual Elements may also lead to other advantages. One such example is the construction introduced in [13] (see also [4]) for the discretization of the Stokes problem.

In the above paper the authors propose a family of VEM velocity spaces of general order k, with k positive integer, that is conforming in H^1 but has a divergence that is piecewise polynomial of degree $k - 1$. As a consequence, when coupled with a simple piecewise polynomial pressure space of degree $k - 1$, it leads to a scheme that, in addition to being inf-sup stable, guarantees a truly divergence-free velocity solution (as opposed to a relaxed divergence-free condition as it happens in standard FEM). There are many advantages of divergence-free schemes when compared to standard inf-sup stable ones, an example being that the discrete velocity error is not polluted by the pressure. Although the above VEM scheme is not pressure-robust (in the sense of [50]) it still retains many advantages when compared with standard FEM [22], in addition to the possibility of using general meshes.

Later, in [16, 64], the authors developed a more advanced velocity space that allowed to extend the method also to the Navier-Stokes and Brinkman equations. In [15, 18], the discrete Stokes complex structure laying behind the above discrete spaces (in 2D and 3D) was unveiled, leading also to alternative schemes such as those based on potentials (for a glimpse at the related FEM literature we refer to [7, 40]). Computational and implementation aspects, also related to linear algebra solvers, where further detailed and investigated in [37, 38], while in [35] the authors studied the method from the standpoint of hp analysis. In [41, 59] some right-hand side modifications are proposed in order to build a VEM scheme that is also pressure robust for the Stokes problem. In [20] a model fluid interaction problem is analyzed using mesh cutting techniques in combination with the above VEM approach. It must also be noted that the specific Finite Element literature on divergence-free and pressure robust methods is very wide, see for instance [47–49] and [44, 50, 52, 53]. Outside the divergence-free framework, there have been also other developments on Virtual Element Methods for fluid mechanics problems, such as non-conforming methods [32, 56–58, 66], non-standard mixed formulations [29–31, 42, 43, 60] and further derivations [34, 65]. Finally, a few references about the application of other polytopal technologies (such as polygonal FEM, polygonal DG, HHO, HDG) to fluid mechanic problems are [2, 5, 6, 23, 33, 36, 39, 55, 61].

The present contribution is somehow in between a survey and an introduction of the "divergence-free" Virtual Element Method for the Stokes and Navier-Stokes problems. It is a survey since it reviews all the fundamental concepts on "divergence-free" Virtual Elements and it is an introduction since it is written, both in terms of presentation and details, in order to be easily readable for newcomers. In particular, in order to reduce the technical aspects and highlight the main points in the construction, we make the choice of presenting the method only for the second-order case ($k = 2$). Moreover, we show in detail the proofs that are fundamental for the construction and the comprehension of the method, but we refer to previous literature for the (more technical) proofs involved in the stability and convergence of the scheme. We believe the present paper constitutes a good reading for researchers that have some minimal knowledge of virtual elements (such as that given in the

foundational paper [8]) and want to understand "divergence-free" virtual elements for fluid mechanics.

The paper is organized as follows. After briefly reviewing the Navier-Stokes equations in Sect. 5.2, in Sect. 5.3 we present some notation and preliminaries. Virtual Elements in two space dimensions are presented in Sect. 5.4, while in Sect. 5.5 we present a variant that allows also for curved edges. Virtual Elements in three space dimensions are presented in Sect. 5.6. The discretization of the problem is presented in Sect. 5.7, in a unified way that encompasses both dimension two and three. In Sect. 5.8 the analysis of the scheme and of the divergence-free properties are presented; this section included important aspects such as the reduced formulation and a quick survey of the underlying discrete complex structure. Finally, we present some basic numerical test in Sect. 5.9.

We close this introduction with some standard notation. Let $\Omega \subset \mathbb{R}^d$ with $d = 2, 3$ be the computational domain, we denote with $\boldsymbol{x} = (x_1, \ldots, x_d)$ the independent variable. With a usual notation the symbols ∇ and Δ denote the gradient and the Laplacian for scalar functions, while $\boldsymbol{\Delta}$, $\boldsymbol{\nabla}$, $\boldsymbol{\varepsilon}$, div and **curl** denote the vector Laplacian, the gradient and the symmetric gradient operator, the divergence operator and (in three space dimensions) the curl operator for vector fields, whereas **div** denotes the vector value divergence operator for tensor fields. In two space dimensions, with a small abuse of notation, we denote by **curl** the "rotated" gradient operator. Throughout the paper, we will follow the usual notation for Sobolev spaces and norms [1]. Hence, for an open bounded domain ω, the norms in the spaces $W_p^s(\omega)$ and $L^p(\omega)$ are denoted by $\|\cdot\|_{W_p^s(\omega)}$ and $\|\cdot\|_{L^p(\omega)}$ respectively. Norm and seminorm in $H^s(\omega)$ are denoted respectively by $\|\cdot\|_{s,\omega}$ and $|\cdot|_{s,\omega}$, while $(\cdot, \cdot)_\omega$ and $\|\cdot\|_\omega$ denote the L^2-inner product and the L^2-norm (the subscript ω may be omitted when ω is the whole computational domain Ω).

5.2 The Navier-Stokes Equation

We consider the steady Navier–Stokes equation on a polygonal simply connected domain $\Omega \subseteq \mathbb{R}^d$ with $d = 2, 3$ (for more details, see for instance [46])

$$
\begin{cases}
\text{find } (\boldsymbol{u}, p) \text{ such that} \\
-\nu \operatorname{div}(\boldsymbol{\varepsilon}(\boldsymbol{u})) + (\boldsymbol{\nabla} \boldsymbol{u})\, \boldsymbol{u} - \nabla p = \boldsymbol{f} & \text{in } \Omega, \\
\operatorname{div} \boldsymbol{u} = 0 & \text{in } \Omega, \\
\boldsymbol{u} = 0 & \text{on } \partial\Omega,
\end{cases}
\tag{5.1}
$$

where $\boldsymbol{u}$, p are the velocity and the pressure fields respectively, $\nu \in \mathbb{R}$, $\nu > 0$ is the viscosity of the fluid and $\boldsymbol{f} \in [L^2(\Omega)]^d$ represents the volume source term. For sake of simplicity we here consider Dirichlet homogeneous boundary conditions, different boundary conditions can be treated as well. Let us define the continuous

spaces

$$V := \left[H_0^1(\Omega) \right]^d, \qquad Q := L_0^2(\Omega) = \left\{ q \in L^2(\Omega) \quad \text{s.t.} \quad \int_\Omega q \, d\Omega = 0 \right\}$$

endowed with natural norms, and the continuous forms

$$a(\cdot, \cdot) \colon V \times V \to \mathbb{R}, \qquad a(\boldsymbol{u}, \boldsymbol{v}) := \int_\Omega \boldsymbol{\varepsilon}(\boldsymbol{u}) : \boldsymbol{\varepsilon}(\boldsymbol{v}) \, d\Omega, \qquad (5.2)$$

$$b(\cdot, \cdot) \colon V \times Q \to \mathbb{R}, \qquad b(\boldsymbol{v}, q) := \int_\Omega q \, \operatorname{div} \boldsymbol{v} \, d\Omega, \qquad (5.3)$$

$$c(\cdot; \cdot, \cdot) \colon V \times V \times V \to \mathbb{R}, \qquad c(\boldsymbol{w}; \boldsymbol{u}, \boldsymbol{v}) := \int_\Omega (\boldsymbol{\nabla} \boldsymbol{u}) \, \boldsymbol{w} \cdot \boldsymbol{v} \, d\Omega, \qquad (5.4)$$

for all $\boldsymbol{u}, \boldsymbol{v}, \boldsymbol{w} \in V$ and $q \in Q$. Then the variational formulation of Problem (5.1) reads as follows:

$$\begin{cases} \text{find } (\boldsymbol{u}, p) \in V \times Q, \text{ such that} \\ \nu \, a(\boldsymbol{u}, \boldsymbol{v}) + c(\boldsymbol{w}; \boldsymbol{u}, \boldsymbol{v}) + b(\boldsymbol{v}, p) = (\boldsymbol{f}, \boldsymbol{v}) & \text{for all } \boldsymbol{v} \in V, \qquad (5.5) \\ b(\boldsymbol{u}, q) = 0 & \text{for all } q \in Q. \end{cases}$$

It is well known that (see for instance [22, 46]) the problem (5.5) is well posed assuming suitable bounds on the external load $\boldsymbol{f}$ and the viscosity ν. To this end, in the context of the analysis of incompressible flows, it is useful to introduce the concept of Helmholtz–Hodge projector (see for instance [50, Lemma 2.6] and [44, Theorem 3.3]). For every $\boldsymbol{w} \in [L^2(\Omega)]^2$ there exist $\boldsymbol{w}_0 \in H(\operatorname{div}; \Omega)$ and $\zeta \in H^1(\Omega)/\mathbb{R}$ such that

$$\boldsymbol{w} = \boldsymbol{w}_0 + \nabla \zeta, \qquad (5.6)$$

where $\boldsymbol{w}_0$ is L^2-orthogonal to the gradients, that is $(\boldsymbol{w}_0, \nabla \varphi) = 0$ for all $\varphi \in H^1(\Omega)$ (which implies, in particular, that $\boldsymbol{w}_0$ is solenoidal, i.e. $\operatorname{div} \boldsymbol{w}_0 = 0$). The orthogonal decomposition (5.6) is unique and is called Helmholtz–Hodge decomposition, and $\mathscr{P}(\boldsymbol{w}) := \boldsymbol{w}_0$ is the Helmholtz–Hodge projector of $\boldsymbol{w}$.

Let C denote the continuity constant of $c(\cdot; \cdot, \cdot)$ with respect to the H^1-norm. Combining the argument in [46, Theorem IV.2.2] and the definition of Helmholtz–Hodge projector, it can be shown than under the assumption

(A0) Diffusion Dominated Assumption $\gamma := \dfrac{C \, \|\mathscr{P}(\boldsymbol{f})\|_{H^{-1}}}{\nu^2} < 1$
Problem (5.5) is well-posed and the unique solution $(\boldsymbol{u}, p) \in V \times Q$ is such that

$$|\boldsymbol{u}|_{[H^1(\Omega)]^2} \le \frac{\|\mathscr{P}(\boldsymbol{f})\|_{H^{-1}}}{\nu}. \qquad (5.7)$$

Let us introduce the kernel of the bilinear form $b(\cdot, \cdot)$ that corresponds to the functions in V with vanishing divergence

$$Z := \{v \in V \quad \text{s.t.} \quad \text{div } v = 0\}. \tag{5.8}$$

Then, Problem (5.5) can be formulated in the equivalent kernel form:

$$\begin{cases} \text{find } u \in Z, \text{ such that} \\ \nu\, a(u, v) + c(u; u, v) = (f, v) = (\mathscr{P}(f), v) \qquad \text{for all } v \in Z. \end{cases} \tag{5.9}$$

We can observe by a direct computation, that, for a fixed $w \in Z$, the bilinear form $c(w; \cdot, \cdot)$ is skew symmetric, i.e.

$$c(w; u, v) = -c(w; v, u) \qquad \text{for all } u, v \in V.$$

Therefore, the trilinear form $c(\cdot; \cdot, \cdot)$, for $w \in Z$, is equal to its skew-symmetric part, defined as:

$$c^{\text{skew}}(w; u, v) := \frac{1}{2}\big(c(w; u, v) - c(w; v, u)\big) \qquad \text{for all } u, v, w \in V. \tag{5.10}$$

However, at the discrete level $c(\cdot; \cdot, \cdot)$ and $c^{\text{skew}}(\cdot; \cdot, \cdot)$ will lead to different bilinear forms, in general.

Clearly if we neglect the nonlinear convective term in (5.1) we recover the linear Stokes equation. We finally remark that the proposed approach can be trivially extended to more general situations such as non-constant viscosity coefficients and different boundary conditions. Moreover different definitions of the trilinear form (5.4) can be also taken into account as explored in [18].

5.3   Notations and Preliminaries

We now introduce some basic tools and notations useful in the construction and the theoretical analysis of Virtual Element Methods.

Let $\{\Omega_h\}_h$ be a sequence of decompositions of the domain $\Omega \subset \mathbb{R}^d$ into general polytopal elements E where $h := \sup_{E \in \Omega_h} h_E$. We suppose that $\{\Omega_h\}_h$ fulfils the following assumption: there exists a positive constant ϱ such that for any $E \in \{\Omega_h\}_h$

(A1²ᴰ) Mesh Assumption in 2D

– E is star-shaped with respect to a ball B_E of radius $\geq \varrho\, h_E$;
– any edge e of E has length $\geq \varrho\, h_E$.

(A1$^{\text{3D}}$) Mesh Assumption in 3D

– E is star-shaped with respect to a ball B_E of radius $\geq \varrho \, h_E$;
– every face f of E is star-shaped with respect to a disk B_f of radius $\geq \varrho \, h_E$;
– any edge e of E has length $\geq \varrho \, h_E$.

We remark that the hypotheses above, though not too restrictive in many practical cases, could possibly be further relaxed, combining the present analysis with the studies in [14, 24, 25].

Using standard VEM notations, for $n \in \mathbb{N}$ and $m \in \mathbb{R}^+$ let us introduce the spaces:

– $\mathbb{P}_n(\omega)$: the set of polynomials on $\omega \subset \Omega$ of degree $\leq n$ (with $\mathbb{P}_{-1}(\omega) = \{0\}$),
– $\mathbb{P}_n(\Omega_h) := \{q \in L^2(\Omega) \quad \text{s.t} \quad q|_E \in \mathbb{P}_n(E) \quad \text{for all } E \in \Omega_h\}$,
– $H^m(\Omega_h) := \{v \in L^2(\Omega) \quad \text{s.t} \quad v|_E \in H^m(E) \quad \text{for all } E \in \Omega_h\}$

equipped with the broken norm and seminorm

$$\|v\|^2_{H^m(\Omega_h)} := \sum_{E \in \Omega_h} \|v\|^2_{H^m(E)}, \qquad |v|^2_{H^m(\Omega_h)} := \sum_{E \in \Omega_h} |v|^2_{H^m(E)}.$$

In the following $\mathscr{O}$ will denote a general geometrical entity (polyhedron or polygon) having diameter $h_\mathscr{O}$, measure $|\mathscr{O}|$, centroid $\boldsymbol{x}_\mathscr{O} = (x_{\mathscr{O},1}, \ldots, x_{\mathscr{O},d})$. A natural basis associated with the space $\mathbb{P}_n(\mathscr{O})$ is the set of normalized monomials

$$\mathbb{M}_n(\mathscr{O}) := \{m_{\boldsymbol{\alpha}}, \ \text{with } |\boldsymbol{\alpha}| \leq n\} \tag{5.11}$$

where, for any multi-index $\boldsymbol{\alpha} = (\alpha_1, \ldots, \alpha_d) \in \mathbb{N}^d$

$$m_{\boldsymbol{\alpha}} := \prod_{i=1}^d \left(\frac{x_i - x_{\mathscr{O},i}}{h_\mathscr{O}}\right)^{\alpha_i} \qquad \text{and} \qquad |\boldsymbol{\alpha}| := \sum_{i=1}^d \alpha_i.$$

Moreover for any $m \leq n$ we denote with

$$\widehat{\mathbb{P}}_{n\backslash m}(\mathscr{O}) = \text{span}\{m_{\boldsymbol{\alpha}}, \ \text{with } m+1 \leq |\boldsymbol{\alpha}| \leq n\}.$$

Note that the following useful polynomial decompositions hold [11, 37, 38]:

$$\begin{aligned}
[\mathbb{P}_n(\mathscr{O})]^2 &= \nabla\mathbb{P}_{n+1}(\mathscr{O}) \oplus \left(\boldsymbol{x}^\perp \mathbb{P}_{n-1}(\mathscr{O})\right) & \text{if } \dim(\mathscr{O}) = 2, \\
[\mathbb{P}_n(\mathscr{O})]^3 &= \nabla\mathbb{P}_{n+1}(\mathscr{O}) \oplus \left(\boldsymbol{x} \wedge [\mathbb{P}_{n-1}(\mathscr{O})]^3\right) & \text{if } \dim(\mathscr{O}) = 3,
\end{aligned} \tag{5.12}$$

where $\boldsymbol{x}^\perp = (x_2, -x_1)$.

For any $\mathcal{O}$, let us introduce the following polynomial projections:

– the **L^2-projection** $\Pi_n^{0,\mathcal{O}} : L^2(\mathcal{O}) \to \mathbb{P}_n(\mathcal{O})$, given by

$$\int_{\mathcal{O}} q_n(v - \Pi_n^{0,\mathcal{O}} v)\,d\mathcal{O} = 0 \qquad \text{for all } v \in L^2(\mathcal{O}) \text{ and } q_n \in \mathbb{P}_n(\mathcal{O}), \qquad (5.13)$$

with obvious extension for vector functions $\Pi_n^{0,\mathcal{O}} : [L^2(\mathcal{O})]^d \to [\mathbb{P}_n(\mathcal{O})]^d$ and tensor functions $\mathbf{\Pi}_n^{0,\mathcal{O}} : [L^2(\mathcal{O})]^{d\times d} \to [\mathbb{P}_n(\mathcal{O})]^{d\times d}$;

– the **H^1-seminorm projection** $\Pi_n^{\nabla,\mathcal{O}} : H^1(\mathcal{O}) \to \mathbb{P}_n(\mathcal{O})$, defined by

$$\begin{cases} \displaystyle\int_{\mathcal{O}} \nabla q_n \cdot \nabla(v - \Pi_n^{\nabla,\mathcal{O}} v)\,d\mathcal{O} = 0 & \text{for all } v \in H^1(\mathcal{O}) \text{ and } q_n \in \mathbb{P}_n(\mathcal{O}), \\[2ex] \displaystyle\int_{\partial\mathcal{O}} (v - \Pi_n^{\nabla,\mathcal{O}} v)\,ds = 0\,, \end{cases}$$

$$(5.14)$$

with extension for vector fields $\Pi_n^{\nabla,\mathcal{O}} : [H^1(\mathcal{O})]^d \to [\mathbb{P}_n(\mathcal{O})]^d$.

Finally, recalling that the virtual element functions, in general, are not known in explicit form, we conclude the section with the following definition.

Definition 5.1 A quantity (depending on a function living in a discrete space with given degrees of freedom operators) is said to be **computable** if it can be computed using, as unique information, the degree of freedom values.

5.4 Virtual Element Spaces in 2D

In the present section we outline an overview of the *second order* Virtual Element discretization of the Stokes and Navier–Stokes equation in the 2D case. In [13] the authors introduced a Virtual Element space associated to a Stokes-like problem, such that the discrete kernel of the bilinear form $b(\cdot, \cdot)$ is exactly divergence-free. Taking the inspiration from [3], in [16, 64] the authors presented an enhanced Virtual space that allows the explicit knowledge of the L^2-projection onto the polynomial space of corresponding degree.

Below we will give some basic tools and a brief overview of such spaces; we restrict our attention to the second order case which allows for an easier presentation for newcomers. First in Sect. 5.4.1 we review the Virtual Elements for Stokes flow and later in Sect. 5.4.2 we examine the enhanced Virtual Elements for the Navier-Stokes equation.

In the following we will denote by E a general polygon having ℓ_e edges e, while $\mathbf{n}_E^e$ (resp. $\mathbf{n}_E$) will denote the unit vector that is normal to the edge e (resp. to ∂E) and outward with respect to E.

5.4.1 Virtual Elements for Stokes

We consider on each polygonal element $E \in \Omega_h$ the finite dimensional virtual space

$$V_h^S(E) := \left\{ \boldsymbol{v} \in [H^1(E)]^2 \text{ s.t. } (i)\, \boldsymbol{\Delta v} + \nabla s = 0, \quad \text{for some } s \in L_0^2(E), \right.$$

$$(ii)\, \text{div}\, \boldsymbol{v} \in \mathbb{P}_1(E)\,,$$

$$\left. (iii)\, \boldsymbol{v}_{|\partial E} \in [C^0(\partial E)]^2, \quad \boldsymbol{v}_{|e} \in [\mathbb{P}_2(e)]^2 \ \forall e \in \partial E \right\}$$

$$(5.15)$$

where all the operators and equations above are to be interpreted in the distributional sense. We note that, in standard VEM fashion, the definition of $V_h^S(E)$ is associated to a PDE within the element, in this case a Stokes-like variational problem on E and the virtual element functions are implicitly defined and not known in a closed form.

We here summarize the main properties of the virtual space $V_h^S(E)$ (we refer [13] for a deeper analysis and the general order case).

Property 5.1 (Polynomial Inclusion) $[\mathbb{P}_2(E)]^2 \subseteq V_h^S(E)$.

Proof For any $\boldsymbol{p}_2 \in [\mathbb{P}_2(E)]^2$ we have

(i) $\boldsymbol{\Delta p}_2 \in [\mathbb{P}_0(E)]^2$, then by (5.12), there exists $s \in \mathbb{P}_1(E) \cap L_0^2(E)$ s.t. $\boldsymbol{\Delta p}_2 = -\nabla s$;
(ii) $\text{div}\, \boldsymbol{p}_2 \in \mathbb{P}_1(E)$;
(iii) $\boldsymbol{p}_{2|\partial E} \in [C^0(\partial E)]^2$ and $\boldsymbol{p}_{2|e} \in [\mathbb{P}_2(e)]^2$ for all edge $e \in \partial E$.   □

Property 5.2 (Dimension and Degrees of Freedom) The dimension of $V_h^S(E)$ is given by

$$\dim(V_h^S(E)) = 4\,\ell_E + 2\,. \tag{5.16}$$

Moreover, the following linear operators $\mathbf{D_V}$, split into three subsets (see Fig. 5.1) constitute a set of DoFs for $V_h^S(E)$:

– $\mathbf{D_V}1$: the values of $\boldsymbol{v}$ at the vertexes of the polygon E,
– $\mathbf{D_V}2$: the values of $\boldsymbol{v}$ at the midpoint of every edge $e \in \partial E$,
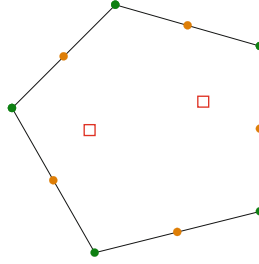
Fig. 5.1 DoFs for $V_h^S(E)$. We denote $\mathbf{D_V}1$ with the green dots, $\mathbf{D_V}2$ with the orange dots and $\mathbf{D_V}3$ with the red squares [18]

– $\mathbf{D_V}3$: the scaled moments of div $\boldsymbol{v}$

$$\frac{1}{h_E} \int_E \operatorname{div} \boldsymbol{v} \left(\frac{x_1 - x_{E,1}}{h_E} \right) \mathrm{d}E \qquad \frac{1}{h_E} \int_E \operatorname{div} \boldsymbol{v} \left(\frac{x_2 - x_{E,2}}{h_E} \right) \mathrm{d}E \, .$$

Proof It is well-known (see for instance [11]) that given

$$p_1 \in \mathbb{P}_1(E), \quad \text{and} \quad \boldsymbol{g}_2 \in [C^0(\partial E)]^2, \quad \boldsymbol{g}_{2|e} \in [\mathbb{P}_2(e)]^2 \quad \text{for all } e \in \partial E,$$

satisfying the compatibility condition

$$\int_E p_1 \, \mathrm{d}E = \int_{\partial E} \boldsymbol{g}_2 \cdot \boldsymbol{n}_E \, \mathrm{d}e \tag{5.17}$$

there exists a unique $\boldsymbol{v} \in [H^1(E)]^2$ such that

$$\boldsymbol{\Delta v} + \nabla s = 0 \quad \text{and} \quad \operatorname{div} \boldsymbol{v} = p_1 \quad \text{in } E, \qquad \boldsymbol{v}_{|e} = \boldsymbol{g}_{2|e} \quad \text{for all } e \in \partial E,$$

for some $s \in L_0^2(E)$. It follows that the dimension of $V_h^S(E)$ is given by the dimension of the data set that is

$$\dim(V_h^S(E)) = \dim([C^0(\partial E)]^2 \bigcap_{e \in \partial E} [\mathbb{P}_2(e)]^2) + \dim(\mathbb{P}_1(E)) - 1$$

where the term -1 ensues from the compatibility condition (5.17), that corresponds to (5.16).

We now prove that the linear operators $\mathbf{D_V}$ are a unisolvent set of degrees of freedom for the virtual space $V_h^S(E)$. We start noting that the dimension of $V_h^S(E)$ equals the number of functionals in $\mathbf{D_V}$ and thus we only need to show that if all the values $\mathbf{D_V}(\boldsymbol{v})$ vanish for a given $\boldsymbol{v} \in V_h^S(E)$, then $\boldsymbol{v} \equiv 0$.

It is clear that $\mathbf{D_V}1(v) = \mathbf{D_V}2(v) = 0$ implies $v_{|\partial E} \equiv 0$. Being div $v \in \mathbb{P}_1(E)$, by the definition of basis $\mathbb{M}_1(E)$ (cf. (5.11)) there exist $c_0, c_1, c_2 \in \mathbb{R}$ such that

$$\text{div } v = c_0 + c_1 \frac{x_1 - x_{E,1}}{h_E} + c_2 \frac{x_2 - x_{E,2}}{h_E}. \tag{5.18}$$

Then, recalling that $\mathbf{D_V}3(v) = 0$,

$$\int_E (\text{div } v)^2 \, dE = c_0 \int_E \text{div } v \, dE + \int_E \text{div } v \left(c_1 \frac{x_1 - x_{E,1}}{h_E} + c_2 \frac{x_2 - x_{E,2}}{h_E} \right) dE$$

$$c_0 \int_{\partial E} v \cdot n_E \, ds + c_1 \int_E \text{div } v \left(\frac{x_1 - x_{E,1}}{h_E} \right) dE + c_2 \int_E \text{div } v \left(\frac{x_2 - x_{E,2}}{h_E} \right) dE = 0 \,.$$

Therefore div $v \equiv 0$. Finally, employing the definition of $V_h^S(E)$, we infer

$$\|\nabla v\|_{0,E}^2 = \int_E \nabla v : \nabla v \, dE = -\int_E \Delta v \cdot v \, dE = \int_E \nabla s \cdot v \, dE = -\int_E s \, \text{div } v \, dE = 0 \,.$$

Then $\mathbf{D_V}(v) = 0$ implies $v \equiv 0$, and the proof is complete. $\qquad\qquad\square$

Remark 5.1 We observe that for any $v \in V_h^S(E)$, the DoFs $\mathbf{D_V}$ uniquely determine $v_{|\partial E}$ and allow us to compute exactly (cf. Definition 5.1) div v, i.e. to determine the coefficients c_0, c_1, c_2 in (5.18). Indeed simple computations yield

- $|E|c_0 = \displaystyle\sum_{e \in \partial E} \int_e v \cdot n_E^e \, de$

- $\displaystyle\sum_{i=1}^{2} c_i \int_E \left(\frac{x_i - x_{E,i}}{h_E} \right) \left(\frac{x_j - x_{E,j}}{h_E} \right) dE = \int_E \text{div } v \left(\frac{x_j - x_{E,j}}{h_E} \right) dE \quad j = 1, 2,$

and notice that the left-hand side matrix is computable, whereas the right-hand side employs only the DoFs $\mathbf{D_V}3$.

More generally, let v a sufficiently regular function defined on E that satisfies (ii) and (iii) in (5.15), then the linear operators $\mathbf{D_V}$ uniquely determine $v_{|\partial E}$ and div v.

Property 5.3 (Polynomial Projections) The DoFs $\mathbf{D_V}$ allow us to compute exactly (cf. (5.14) and (5.13) and Definition 5.1)

$$\Pi_2^{\nabla,E} : V_h^S(E) \to [\mathbb{P}_2(E)]^2 \,,$$

$$\Pi_0^{0,E} : V_h^S(E) \to [\mathbb{P}_0(E)]^2 \,,$$

$$\mathbf{\Pi}_1^{0,E} : \nabla V_h^S(E) \to [\mathbb{P}_1(E)]^{2\times 2} \,.$$

Proof We here limit to prove the first item, the last two follow by analogous techniques. By definition of H^1-projection (5.14), in order to determine, for any

$v \in V_h^S(E)$, the polynomial $\Pi_2^{\nabla,E} v$ we need to compute

$$\int_E \nabla v : \nabla p_2 \, dE \qquad \text{for all } p_2 \in [\mathbb{P}_2(E)]^2.$$

Integrating by parts and employing the polynomial decomposition (5.12), we infer

$$
\begin{aligned}
\int_E \nabla v : \nabla p_2 \, dE &= \int_{\partial E} v \cdot (\nabla p_2 n_E) \, de - \int_E v \cdot q_0 \, dE \quad (q_0 := \Delta \, p_2 \in [\mathbb{P}_0(E)]^2) \\
&= \int_{\partial E} v \cdot (\nabla p_2 n_E) \, de - \int_E v \cdot \nabla q_1 \, dE \quad (q_1 \in \mathbb{P}_1(E), \nabla q_1 := q_0) \\
&= \int_{\partial E} v \cdot (\nabla p_2 - q_1 I) n_E \, de + \int_E \operatorname{div} v \, q_1 \, dE
\end{aligned}
$$

(5.19)

that, recalling Remark 5.1, is a computable expression. $\qquad \square$

We stress that the property above shows that the degrees of freedom $\mathbf{D_V}$ allow us to compute exactly the L^2-projection $\Pi_0^{0,E}$. On the other hand we are not able to compute exactly from the DoFs the L^2-projection onto the space of polynomials of degree ≤ 2.

5.4.2 Enhanced Virtual Elements for Navier-Stokes

The goal of this section is to introduce, taking the inspiration from [3], a different virtual space $V_h^E(E)$ to be used in place of the space $V_h^S(E)$ in such a way that:

- Properties 5.1, 5.2, 5.3 are sill valid for $V_h^E(E)$,
- the full projection $\Pi_2^{0,E} : V_h^E(E) \rightarrow [\mathbb{P}_2(E)]^2$ is computable by the DoFs $\mathbf{D_V}$.

We preliminary observe that in order to compute $\Pi_2^{0,E} v$ we need to compute

$$\int_E v \cdot p_2 \, dE \qquad \text{for any } p_2 \in [\mathbb{P}_2(E)]^2.$$

Referring to (5.12), let $q_3 \in \mathbb{P}_3(E)$ and $q_1 \in \mathbb{P}_1(E)$, s.t. $p_2 = \nabla q_3 + x^\perp q_1$. Then, using the same argument in the proof of Property 5.3, we infer

$$
\begin{aligned}
\int_E v \cdot p_2 \, dE &= \int_E v \cdot (\nabla q_3 + x^\perp q_1) \, dE \\
&= \int_{\partial E} v \cdot n_E q_3 \, de - \int_E \operatorname{div} v \, q_3 \, dE + \int_E v \cdot x^\perp q_1 \, dE ,
\end{aligned}
$$

(5.20)

that is actually not computable since we have no way to compute $\int_E v \cdot x^\perp q_1 \, dE$.

To construct $V_h^E(E)$ we proceed as in [3]: we enlarge the space in order to have the computability of the missing moments $\int_E \mathbf{v} \cdot \mathbf{x}^\perp q_1 \, dE$, and then we put the so-called "enhanced constraints" to recover the right dimension of the space.

We consider on each element $E \in \Omega_h$ the finite dimensional virtual space

$$V_h^E(E) := \left\{ \mathbf{v} \in [H^1(E)]^2 \text{ s.t. } (i) \, \mathbf{\Delta v} + \nabla s \in \mathbf{x}^\perp \mathbb{P}_1(E), \quad \text{for some } s \in L_0^2(E), \right.$$

$$(ii) \, \text{div } \mathbf{v} \in \mathbb{P}_1(E),$$

$$(iii) \, \mathbf{v}_{|\partial E} \in [C^0(\partial E)]^2, \quad \mathbf{v}_{|e} \in [\mathbb{P}_2(e)]^2 \; \forall e \in \partial E$$

$$\left. (iv) \, \left(\mathbf{v} - \Pi_2^{\nabla,E} \mathbf{v}, \, \mathbf{x}^\perp p_1 \right)_E = 0 \; \forall p_1 \in \mathbb{P}_1(E) \right\}$$

$$(5.21)$$

In the following we prove the main properties for the enhanced space $V_h^E(E)$ (we refer to [64] for a deeper analysis and the general order case).

Property 5.4 (Polynomial Inclusion) $[\mathbb{P}_2(E)]^2 \subseteq V_h^E(E)$.

Proof The items (i), (ii) and (iii) follow by Property 5.1. The item (iv) is satisfied being $\Pi_2^{\nabla,E} \mathbf{p}_2 = \mathbf{p}_2$ for all $\mathbf{p}_2 \in [\mathbb{P}_2(E)]^2$. □

Property 5.5 (Dimension and Degrees of Freedom) The dimension of $V_h^E(E)$ is equal to that in (5.16). As DoFs in $V_h^E(E)$ we can take $\mathbf{D_V}$.

Proof We preliminary define an augmented virtual local space $\mathbf{W}_h(E)$ by taking

$$\mathbf{W}_h(E) := \left\{ \mathbf{v} \in [H^1(E)]^2 \text{ s.t. } (i) \, \mathbf{\Delta v} + \nabla s = \mathbf{x}^\perp \mathbb{P}_1(E), \quad \text{for some } s \in L_0^2(E), \right.$$

$$(ii) \, \text{div } \mathbf{v} \in \mathbb{P}_1(E),$$

$$\left. (iii) \, \mathbf{v}_{|\partial E} \in [C^0(\partial E)]^2, \quad \mathbf{v}_{|e} \in [\mathbb{P}_2(e)]^2 \; \forall e \in \partial E \right\}$$

$$(5.22)$$

Now we prove that the dimension of $\mathbf{W}_h(E)$ is

$$\dim(\mathbf{W}_h(E)) = 4\,\ell_E + 5 \tag{5.23}$$

and as DoFs for $\mathbf{W}_h(E)$ we can take the linear operators $\mathbf{D_V}$ plus

– $\mathbf{D_W}$: the moments

$$\int_E \mathbf{v} \cdot \mathbf{x}^\perp \, dE, \qquad \int_E \mathbf{v} \cdot \mathbf{x}^\perp x_1 \, dE, \qquad \int_E \mathbf{v} \cdot \mathbf{x}^\perp x_2 \, dE.$$

The proof is virtually identical to that given in Property 5.2 for $V_h^{\mathrm{E}}(E)$. For any data set $(x^{\perp}q_1, p_1, g_2)$ that satisfies the compatibility condition (5.17) there exists a unique couple $(v, s) \in W_h(E) \times L_0^2(E)$ s.t.

$$\Delta v + \nabla s = x^{\perp}q_1 \quad \text{and} \quad \mathrm{div}\, v = p_1 \quad \text{in } E, \qquad v_{|e} = g_{2|e} \quad \text{for all } e \in \partial E. \tag{5.24}$$

Moreover, let us assume that there exist two different data sets $(x^{\perp}q_1, p_1, g_2)$ and $(x^{\perp}\tilde{q}_1, \tilde{p}_1, \tilde{g}_2)$ satisfying the compatibility condition (5.17), which correspond respectively to the couples $(v, s), (v, \tilde{s}) \in W_h(E) \times L_0^2(E)$ (i.e. same velocity and different pressures). Then it is straightforward to see that

$$p_1 = \tilde{p}_1, \qquad g_2 = \tilde{g}_2, \qquad \text{and} \qquad \nabla(s - \tilde{s}) = x^{\perp}(q_1 - \tilde{q}_1).$$

Therefore, we get $\mathrm{rot}(x^{\perp}(q_1 - \tilde{q}_1)) = 0$. Employing (5.12), $\mathrm{rot}\colon x^{\perp}\mathbb{P}_1(E) \to \mathbb{P}_1(E)$ is an isomorphism, then we conclude that $q_1 = \tilde{q}_1$. Thus, there is an injective map $(x^{\perp}q_1, p_1, g_2) \mapsto v$ that associates a given compatible data set $(x^{\perp}q_1, p_1, g_2)$ to the velocity field v that solves (5.24). It follows that the dimension of $W_h(E)$ is

$$\dim(W_h(E)) = \dim([C^0(\partial E)]^2 \bigcap_{e \in \partial E} [\mathbb{P}_2(e)]^2) + \dim(\mathbb{P}_1(E)) + \dim(\mathbb{P}_1(E)) - 1$$

where the term -1 ensues from the compatibility condition (5.17), that corresponds to (5.23). We now prove that the linear operators $\mathbf{D_V} + \mathbf{D_W}$ are a unisolvent set of DoFs for the virtual space $W_h(E)$. The dimension of $W_h(E)$ corresponds to the number of operators in $\mathbf{D_V} + \mathbf{D_W}$ and thus we need to show that $\mathbf{D_V}(v) = 0$ and $\mathbf{D_W}(v) = 0$ implies $v \equiv 0$. Using the same arguments of Property 5.2, $\mathbf{D_V}(v) = 0$ imply $v_{|\partial E} \equiv 0$ and $\mathrm{div}\, v \equiv 0$. Furthermore, employing the definition of $W_h(E)$ we infer

$$\|\nabla v\|_{0,E}^2 = \int_E \nabla v : \nabla v \, \mathrm{d}E = - \int_E \Delta v \cdot v \, \mathrm{d}E$$

$$= \int_E \nabla s \cdot v \, \mathrm{d}E - \int_E x^{\perp} p_1 \cdot v \, \mathrm{d}E \qquad (\Delta v + \nabla s = x^{\perp} p_1, \, p_1 \in \mathbb{P}_1(E))$$

$$= - \int_E s \, \mathrm{div}\, v \, \mathrm{d}E - \int_E x^{\perp} p_1 \cdot v \, \mathrm{d}E = 0$$

where in the last identity we used $\mathbf{D_W}(v) = 0$. Therefore $v \equiv 0$.

Now neglecting the independence of the additional 3 conditions in $V_h^{\mathrm{E}}(E)$ with respect to $W_h(E)$ (i.e. item (iv) in (5.21)) it holds that

$$\dim(V_h^{\mathrm{E}}(E)) \geq \dim(W_h(E)) - 3 = 4\,\ell_E + 2. \tag{5.25}$$

We now prove that a function $\boldsymbol{v} \in V_h^E(E)$ such that $\mathbf{D_V}(\boldsymbol{v}) = 0$ is identically zero. Indeed, same computations in (5.19), show that $\mathbf{D_V}(\boldsymbol{v}) = 0$ implies that $\Pi_2^{\nabla,E} \boldsymbol{v}$ would be zero, implying that all its moments are zero, in particular, since $\boldsymbol{v} \in V_h^E(E)$, all the moments $\mathbf{D_W}$ of $\boldsymbol{v}$ are also zero. Then we conclude that $\boldsymbol{v}$ is zero. Therefore, from (5.25), we obtain that the dimension of $V_h^E(E)$ is actually $4\ell_E + 2$, and that the DoFs $\mathbf{D_V}$ are unisolvent for $V_h^E(E)$. $\qquad\square$

Property 5.6 (Polynomial Projection) The DoFs $\mathbf{D_V}$ allow us to compute exactly (cf. (5.14) and (5.13) and Definition 5.1)

$$\Pi_2^{\nabla,E} : V_h^E(E) \to [\mathbb{P}_2(E)]^2 \,,$$

$$\Pi_2^{0,E} : V_h^E(E) \to [\mathbb{P}_2(E)]^2 \,,$$

$$\boldsymbol{\Pi}_1^{0,E} : \nabla V_h^E(E) \to [\mathbb{P}_1(E)]^{2\times 2} \,.$$

Proof Our focus is to prove the second item. According to (5.20) and employing the definition of $V_h^E(E)$ we infer

$$\int_E \boldsymbol{v} \cdot \boldsymbol{p}_2 \, \mathrm{d}E = \int_{\partial E} \boldsymbol{v} \cdot \boldsymbol{n}_E \, q_3 \, \mathrm{d}e - \int_E \mathrm{div}\, \boldsymbol{v}\, q_3 \, \mathrm{d}E + \int_E \Pi_2^{\nabla,E} \boldsymbol{v} \cdot \boldsymbol{x}^\perp q_1 \, \mathrm{d}E$$

that, recalling also Remark 5.1, is a computable expression. $\qquad\square$

5.5   Virtual Elements on Curved Polygons

In the present section we introduce the second order Virtual Elements for the Stokes/Navier-Stokes equation on polygonal meshes with curved edges. We follow the approach detailed in the reference [17], other possible ways dealing with VEM on curved polygons can be found in [19, 21].

We consider that problem (5.1) is posed on a bounded Lipschitz domain $\Omega \subset \mathbb{R}^2$ whose boundary $\partial\Omega$ is made up of a finite number of smooth curves $\{\Gamma_i\}_{i=1,\dots,N}$. We assume that each curve Γ_i of $\partial\Omega$ is sufficiently smooth, for instance we require that Γ_i is of class C^2, i.e. there exists a given regular and invertible C^2-parametrization $\gamma_i \colon I_i \to \Gamma_i$ for $i = 1, \dots, N$, where $I_i \subset \mathbb{R}$ is a closed interval. In the following we will drop the index i from all the involved maps in order to obtain a lighter notation. It is important to note that the proposed approach is also valid for internal curved interfaces. However, to keep the presentation simple we assume only curved elements on the boundary, being its extension straightforward.

Let Ω_h be a decomposition of Ω into general polygons E completed along $\partial\Omega$ by curved elements whose boundary contains an arc $\subset \partial\Omega$ (see [17]). With a slight

abuse of notation, we define the following maps to deal with both straight and curved edges:

– for any curved mesh edge e, we call $\gamma : I_e := \gamma^{-1}(e) \subset I \to e$ the restriction of $\gamma : I \to \partial\Omega$ having image e,
– for any straight mesh edge e with endpoints $\boldsymbol{x}_{e_1}$ and $\boldsymbol{x}_{e_2}$, we denote by $\gamma : I_e := [0, h_e] \to e$ the standard affine map $\gamma(t) = \frac{t}{h_e}(\boldsymbol{x}_{e_2} - \boldsymbol{x}_{e_1}) + \boldsymbol{x}_{e_1}$.

Now for each mesh edge e we consider the following mapped polynomial space

$$\widetilde{\mathbb{P}}_n(e) := \{\widetilde{q} = q \circ \gamma^{-1} : q \in \mathbb{P}_n(I_e)\}$$

i.e. $\widetilde{\mathbb{P}}_n(e)$ is made of all functions that are polynomials with respect to the parametrization γ. It is important to note that for any edge mesh e it holds that

– $\mathbb{P}_n(E)|_e = \widetilde{\mathbb{P}}_n(e)$ if e is straight,
– $\mathbb{P}_0(E)|_e \subset \widetilde{\mathbb{P}}_n(e)$ and in general $\mathbb{P}_k(E)|_e \not\subset \widetilde{\mathbb{P}}_n(e)$, for $0 < k \le n$, if e is curved.

On each possibly curved polygonal element $E \in \Omega_h$ we define the local space

$$
V_h^{\mathrm{S}}(E) := \Big\{ \boldsymbol{v} \in [H^1(E)]^2 \ \text{s.t.} \ (i)\, \boldsymbol{\Delta v} + \nabla s = 0, \quad \text{for some } s \in L_0^2(E),
$$

$$
(ii)\, \operatorname{div} \boldsymbol{v} \in \mathbb{P}_1(E) ,
$$

$$
(iii)\, \boldsymbol{v}_{|\partial E} \in [C^0(\partial E)]^2, \quad \boldsymbol{v}_{|e} \in [\widetilde{\mathbb{P}}_2(e)]^2 \ \forall e \in \partial E \Big\}
$$

(5.26)

that is the "curved" counterpart of the space (5.15). Using analogous technique to that in Sect. 5.4.2 it is possible to define its enhanced version $V_h^{\mathrm{E}}(E)$.

We briefly list the main properties of the spaces $V_h^{\mathrm{S}}(E)$ and $V_h^{\mathrm{E}}(E)$.

Property 5.7 (Approximation) Differently to the standard case with straight edges, $[\mathbb{P}_2(E)]^2 \not\subset V_h^{\mathrm{S}}(E)$ but it holds $[\mathbb{P}_0(E)]^2 \subset V_h^{\mathrm{S}}(E)$. The same applies to $V_h^{\mathrm{E}}(E)$. Nevertheless, the spaces $V_h^{\mathrm{S}}(E)$ and $V_h^{\mathrm{E}}(E)$ enjoy optimal approximation properties [17].

Property 5.8 (Dimension and Degrees of Freedom) The dimension of $V_h^{\mathrm{S}}(E)$ is equal to that in Property 5.2. As DoFs in $V_h^{\mathrm{S}}(E)$ we can take $\mathbf{D_V}$ (see Fig. 5.2) with the following definition of $\mathbf{D_V}2$

– $\mathbf{D_V}2$: the values of $\boldsymbol{v}$ at the image through γ of the midpoint of I_e for every $e \in \partial E$.

The same applies to $V_h^{\mathrm{E}}(E)$.
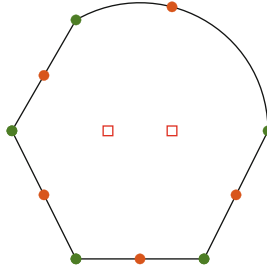
Fig. 5.2 DoFs for $V_h^S(E)$. We denote $\mathbf{D_V}1$ with the green dots, $\mathbf{D_V}2$ with the orange dots and $\mathbf{D_V}3$ with the red squares

Property 5.9 (Polynomial Projections) The spaces $V_h^S(E)$ and $V_h^E(E)$ satisfy Property 5.3 and Property 5.6 respectively. However we observe that, in the light of Property 5.7, the polynomial projectors in general fall outside to the spaces.

5.6 Virtual Element Spaces in 3D

The aim of this section is to develop the second order divergence-free Virtual Elements in three dimensions. This is the natural extension of the 2D VEM of Sect. 5.4, combined with the construction in [3]. We refer to [15] for a deeper analysis of the 3D VEM for the general order case.

We will denote with $E \in \Omega_h$ a general polyhedron having ℓ_V vertexes $\boldsymbol{x}_V$, ℓ_e edges e and ℓ_f faces f, while $\boldsymbol{n}_E^f$ (resp. $\boldsymbol{n}_E$) will denote the unit vector that is normal to the face f (resp. to ∂E) and outward with respect to E. Moreover for any face f of E, $\boldsymbol{\tau}_1^f$ and $\boldsymbol{\tau}_2^f$ are two orthogonal unit vectors lying on f and such that $\boldsymbol{\tau}_1^f \wedge \boldsymbol{\tau}_2^f = \boldsymbol{n}_P^f$. We denote with $\boldsymbol{x}_f := (x_{f_1}, x_{f_2})$ the independent variable (i.e. a local coordinate system on f associated with the axes $\boldsymbol{\tau}_1^f$ and $\boldsymbol{\tau}_2^f$). The tangential differential operators are denoted by a subscript f. Therefore the symbols ∇_f and Δ_f denote the gradient and Laplacian for scalar functions. For instance if f lies on the plane $x_3 = 0$ and $\boldsymbol{\tau}_1^f$ and $\boldsymbol{\tau}_2^f$ are associated with the coordinate system in $\boldsymbol{x}_f := (x_1, x_2)$ then $\nabla_f \varphi = \left(\frac{\partial \varphi}{\partial x_1}, \frac{\partial \varphi}{\partial x_2} \right)$ and $\Delta_f \varphi = \frac{\partial^2 \varphi}{\partial x_1^2} + \frac{\partial^2 \varphi}{\partial x_2^2}$, while $\nabla \varphi = \left(\frac{\partial \varphi}{\partial x_1}, \frac{\partial \varphi}{\partial x_2}, \frac{\partial \varphi}{\partial x_3} \right)$ and $\Delta \varphi = \frac{\partial^2 \varphi}{\partial x_1^2} + \frac{\partial^2 \varphi}{\partial x_2^2} + \frac{\partial^2 \varphi}{\partial x_3^2}$.

Inspired by Ahmad et al. [3], in order to define the VEM space in 3D we proceed in two steps: we first introduce suitable VEM spaces related to the faces of the element, then we define the local spaces defined on the polyhedron. The faces spaces have to be careful chosen in order to accommodate the computability of the projection operators.

5.6.1 Face Spaces

Let $n \geq 0$, we define on each face f of an element $E \in \Omega_h$ the face space

$$
\mathbb{B}^n(f) := \Big\{ v \in H^1(f) \text{ s.t. } (i)\, \Delta_f v \in \mathbb{P}_n(f),
$$

$$
(ii)\, v_{|\partial f} \in C^0(\partial f), \quad v_{|e} \in \mathbb{P}_2(e) \ \ \forall e \in \partial f
$$

$$
(iii)\, \left(v - \Pi_2^{\nabla, f} v, \, \widehat{p}_n \right)_E = 0 \ \ \forall \widehat{p}_n \in \widehat{\mathbb{P}}_{n \setminus 0} \Big\}
$$

$$(5.27)$$

For $n = 0$ we obtain the standard (second order) 2D VEM space from [8] while for higher values of n we obtain progressively more "enhanced" versions (for instance the case $n = 2$ recovers the second order space from [3]).

We here limit to sketch the main properties of the spaces $\mathbb{B}^n(f)$ (we refer to [3]).

Property 5.10 (Polynomial Inclusion) $\mathbb{P}_2(f) \subseteq \mathbb{B}^n(f)$.

Property 5.11 (Dimension and Degrees of Freedom) The dimension of $\mathbb{B}^n(f)$ is given by

$$
\dim(\mathbb{B}^n(f)) = 2\, \ell_{e,f} + 1 \,,
\tag{5.28}
$$

where $\ell_{e,f}$ is the number of edges of the face f. Moreover, the following linear operators $\mathbf{D_B}$, split into three subsets constitute a set of DoFs for $\mathbb{B}^n(f)$:

– $\mathbf{D_B}1$: the values of v at the vertexes of the polygon f,
– $\mathbf{D_B}2$: the values of v at the midpoint of every edge $e \in \partial f$,
– $\mathbf{D_B}3$: the scaled moment of v

$$
\frac{1}{h_f} \int_f v \, \mathrm{d}f \,.
$$

Property 5.12 (Polynomial Projections) The DoFs $\mathbf{D_B}$ allow us to compute exactly (cf. (5.14) and (5.13) and Definition 5.1)

$$
\Pi_2^{\nabla, f} : \mathbb{B}^n(f) \to \mathbb{P}_2(f), \qquad \Pi_n^{0,f} : \mathbb{B}^n(f) \to \mathbb{P}_n(f)\,.
$$

Finally, let us set

$$
\mathbb{B}^S(f) := \mathbb{B}^1(f), \qquad \mathbb{B}^E(f) := \mathbb{B}^3(f)\,.
\tag{5.29}
$$

The former is the face space associated with the VEM for the Stokes equation, the latter is suited to compute the full L^2-projection onto $\mathbb{P}_2$ (see Property 5.18 below).

5.6.2 Virtual Elements for Stokes

Referring to (5.29), we consider on each polyhedral element $E \in \Omega_h$ the finite dimensional virtual space

$$V_h^{3,S}(E) := \left\{ v \in [H^1(E)]^3 \text{ s.t. } (i) \, \boldsymbol{\Delta} v + \nabla s = 0, \quad \text{for some } s \in L_0^2(E), \right.$$

$$(ii) \operatorname{div} v \in \mathbb{P}_1(E),$$

$$\left. (iii) \, v_{|\partial E} \in [C^0(\partial E)]^3, \quad v_{|f} \in [\mathbb{B}^S(f)]^3 \; \forall f \in \partial E \right\}$$

(5.30)

We explore the usual properties for the space $V_h^{3,S}(E)$.

Property 5.13 (Polynomial Inclusion) $[\mathbb{P}_2(E)]^3 \subseteq V_h^{3,S}(E)$.

Proof For any $\boldsymbol{p}_2 \in [\mathbb{P}_2(E)]^3$ we have

(i) $\boldsymbol{\Delta} \boldsymbol{p}_2 \in [\mathbb{P}_0(E)]^3$, then by (5.12), there exists $s \in \mathbb{P}_1(E) \cap L_0^2(E)$ s.t. $\boldsymbol{\Delta} \boldsymbol{p}_2 = -\nabla s$;

(ii) $\operatorname{div} \boldsymbol{p}_2 \in \mathbb{P}_1(E)$;

(iii) $\boldsymbol{p}_{2|\partial E} \in [C^0(\partial E)]^2$ and by Property 5.10, $\boldsymbol{p}_{2|e} \in [\mathbb{P}_2(f)]^3 \subseteq [\mathbb{B}^S(f)]^3$ for all face $f \in \partial E$.

$\square$

Property 5.14 (Dimension and Degrees of Freedom) The dimension of $V_h^{3,S}(E)$ is given by

$$\dim(V_h^{3,S}(E)) = 3 \, \ell_V + 3 \, \ell_e + 3 \, \ell_f + 3 \,.$$

(5.31)

Moreover, the following linear operators $\mathbf{D_V}$, split into three subsets (see Fig. 5.3) constitute a set of DoFs for $V_h^{3,S}(E)$:

– $\mathbf{D_V}1$: the values of v at the vertexes of E and at the midpoint of every edge of E,
– $\mathbf{D_V}2$: the face moments of v (split into normal and tangential components) for every face $f \in \partial E$

$$\frac{1}{h_f} \int_f v \cdot \boldsymbol{n}_E^f \, \mathrm{d}f \qquad \frac{1}{h_f} \int_f v \cdot \boldsymbol{\tau}_i^f \, \mathrm{d}f \qquad \text{for } i = 1, 2,$$

– $\mathbf{D_V}3$: the scaled moments of $\operatorname{div} v$

$$\frac{1}{h_E} \int_E \operatorname{div} v \left(\frac{x_i - x_{E,i}}{h_E} \right) \mathrm{d}E \qquad \text{for } i = 1, 2, 3.$$
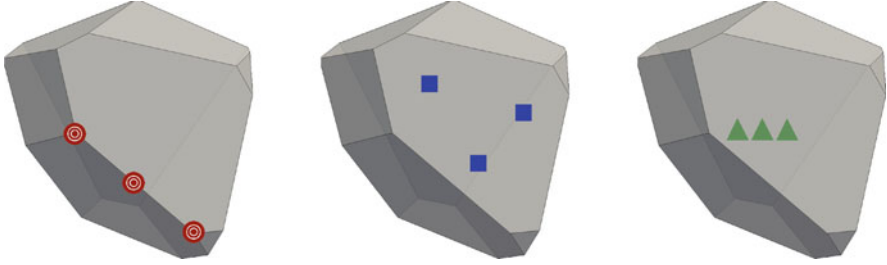
Fig. 5.3 DoFs for $V_h^{3,S}(E)$. We denote $\mathbf{D_V}1$ with the red dots, $\mathbf{D_V}2$ with the blue squares and $\mathbf{D_V}3$ with the green triangles

Proof We only sketch the proof since it follows the guidelines of Property 5.2. Employing Property 5.11, the DoFs $\mathbf{D_V}1$ and $\mathbf{D_V}2$ are unisolvent to determine the boundary space, then it holds that

$$\dim([C^0(\partial E) \bigcap_{f \in \partial E} [\mathbb{B}^S(f)]^3) = 3\,\ell_V + 3\,\ell_e + 3\,\ell_f\,. \tag{5.32}$$

Using the same argument in Property 5.2 it holds that

$$\dim(V_h^{3,S}(E)) = \dim([C^0(\partial E) \bigcap_{f \in \partial E} [\mathbb{B}^S(f)]^3) + \dim(\mathbb{P}_1(E)) - 1$$

where -1 ensues from the compatibility condition (5.17), that, combined with (5.32) corresponds to (5.31). Now the result follows by proving that $\mathbf{D_V}(\boldsymbol{v}) = 0$ implies that $\boldsymbol{v}$ is identically zero, which can be easily shown first working on ∂E and then inside E using respectively Property 5.11 and the same computations in Property 5.2. $\qquad\square$

Remark 5.2 Employing Property 5.11 and extending to the 3D case the observation in Remark 5.1, we have that for any sufficiently regular $\boldsymbol{v}$ defined on E that satisfies (ii) and (iii) in (5.30), the linear operators $\mathbf{D_V}$ allow to compute (cf. Definition 5.1) $\Pi_1^{0,f}(\boldsymbol{v}_{|f})$ for all $f \in \partial E$ and div $\boldsymbol{v}$.

Property 5.15 (Polynomial Projections) The DoFs $\mathbf{D_V}$ allow us to compute exactly (cf. (5.14) and (5.13) and Definition 5.1)

$$\Pi_2^{\nabla,E} : V_h^{3,S}(E) \rightarrow [\mathbb{P}_2(E)]^3\,,$$

$$\Pi_0^{0,E} : V_h^{3,S}(E) \rightarrow [\mathbb{P}_0(E)]^3\,,$$

$$\mathbf{\Pi}_1^{0,E} : \nabla V_h^{3,S}(E) \rightarrow [\mathbb{P}_1(E)]^{3\times 3}\,.$$

Proof We prove the first item, the last two follow analogous techniques. By definition of H^1-projection (5.14), in order to determine, for any $\boldsymbol{v} \in V_h^{3,S}(E)$, the polynomial $\Pi_2^{\nabla,E}\boldsymbol{v}$ we need to compute

$$\int_E \nabla \boldsymbol{v} : \nabla \boldsymbol{p}_2 \, \mathrm{d}E \qquad \text{for all } \boldsymbol{p}_2 \in [\mathbb{P}_2(E)]^3.$$

Using the same computations in (5.19) and definition (5.13), we infer

$$\int_E \nabla \boldsymbol{v} : \nabla \boldsymbol{p}_2 \, \mathrm{d}E = \int_{\partial E} \boldsymbol{v} \cdot (\nabla \boldsymbol{p}_2 - q_1 I)\boldsymbol{n}_E \, \mathrm{d}f + \int_E \mathrm{div}\, \boldsymbol{v}\, q_1 \, \mathrm{d}E$$

$$= \sum_{f \in \partial E} \int_f \Pi_1^{0,f}\boldsymbol{v} \cdot (\nabla \boldsymbol{p}_2 - q_1 I)\boldsymbol{n}_E^f \, \mathrm{d}f + \int_E \mathrm{div}\, \boldsymbol{v}\, q_1 \, \mathrm{d}E$$

that, recalling Remark 5.2, is a computable expression.   □

As for the bi-dimensional case, we stress that actually we are not able to compute the L^2-projection onto the space of polynomials of degree ≤ 2.

5.6.3 Enhanced Virtual Elements for Navier-Stokes

In analogy with Sect. 5.4.2, in the present subsection we introduce a virtual space $V_h^{3,E}(E)$ to be used in place of the space $V_h^{3,S}(E)$ in such a way that:

– Properties 5.13, 5.14, 5.15 are sill valid for $V_h^{3,E}(E)$,
– the full projection $\Pi_2^{0,E}: V_h^{3,E}(E) \rightarrow [\mathbb{P}_2(E)]^3$ is computable by the DoFs $\mathbf{D_V}$.

We preliminary observe that in order to compute $\Pi_2^{0,E}\boldsymbol{v}$ we need to compute

$$\int_E \boldsymbol{v} \cdot \boldsymbol{p}_2 \, \mathrm{d}E \qquad \text{for any } \boldsymbol{p}_2 \in [\mathbb{P}_2(E)]^3.$$

Referring to (5.12), let $q_3 \in \mathbb{P}_3(E)$ and $\boldsymbol{q}_1 \in [\mathbb{P}_1(E)]^3$, s.t. $\boldsymbol{p}_2 = \nabla q_3 + \boldsymbol{x} \wedge \boldsymbol{q}_1$. Then, using the same argument in (5.20), we infer

$$\int_E \boldsymbol{v} \cdot \boldsymbol{p}_2 \, \mathrm{d}E = \int_E \boldsymbol{v} \cdot (\nabla q_3 + \boldsymbol{x} \wedge \boldsymbol{q}_1) \, \mathrm{d}E$$

$$= \int_{\partial E} \boldsymbol{v} \cdot n_E \, q_3 \, \mathrm{d}f - \int_E \mathrm{div}\, \boldsymbol{v}\, q_3 \, \mathrm{d}E + \int_E \boldsymbol{v} \cdot (\boldsymbol{x} \wedge q_1) \, \mathrm{d}E \,,$$

$$\tag{5.33}$$

that is actually not computable since we have no way to compute the boundary integral $\int_{\partial E} \mathbf{v} \cdot \mathbf{n}_E \, q_3 \, \mathrm{d}f$ and the bulk integral $\int_E \mathbf{v} \cdot (\mathbf{x} \wedge \mathbf{q}_1) \, \mathrm{d}E$. Therefore to construct $V_h^{3,\mathrm{E}}(E)$, proceeding as in [3], we enlarge the space in order to have the computability of the missing moments $\int_{\partial E} \mathbf{v} \cdot \mathbf{n}_E \, q_3 \, \mathrm{d}f$ and $\int_E \mathbf{v} \cdot \mathbf{x}^\perp q_1 \, \mathrm{d}E$, and then we put the so-called "enhanced constraints" to keep the right dimension of the space.

We thus consider on each polyhedral element $E \in \Omega_h$ the "enhanced" virtual space

$$V_h^{3,\mathrm{E}}(E) := \left\{ \mathbf{v} \in [H^1(E)]^3 \text{ s.t. } (i) \, \mathbf{\Delta v} + \nabla s \in \mathbf{x} \wedge [\mathbb{P}_1(E)]^3, \text{ for some } s \in L_0^2(E), \right.$$

$$(ii) \, \mathrm{div}\, \mathbf{v} \in \mathbb{P}_1(E),$$

$$(iii) \, \mathbf{v}_{|\partial E} \in [C^0(\partial E)]^3, \quad \mathbf{v}_{|f} \in [\mathbb{B}^\mathrm{E}(f)]^3 \ \forall f \in \partial E$$

$$\left. (iv) \, \left(\mathbf{v} - \Pi_2^{\nabla,E} \mathbf{v}, \, \mathbf{x} \wedge \mathbf{p}_1\right)_E = 0 \ \forall \mathbf{p}_1 \in [\mathbb{P}_1(E)]^3 \right\}$$
$$(5.34)$$

We here summarize the usual properties for the space $V^{3,\mathrm{E}}$. Property 5.16 is a direct consequence of Property 5.13 (with the same argument of Property 5.4), whereas Property 5.17 follows by Properties 5.5 and 5.14.

Property 5.16 (Polynomial Inclusion) $[\mathbb{P}_2(E)]^3 \subseteq V_h^{3,\mathrm{E}}(E)$.

Property 5.17 (Dimension and Degrees of Freedom) The dimension of $V_h^{3,\mathrm{E}}(E)$ is equal to that in Proposition 5.14. As DoFs in $V_h^{3,\mathrm{E}}(E)$ we can take $\mathbf{D_V}$.

Property 5.18 (Polynomial Projection) The DoFs $\mathbf{D_V}$ allow us to compute exactly (cf. (5.14) and (5.13) and Definition 5.1)

$$\Pi_2^{\nabla,E} : V_h^{3,\mathrm{E}}(E) \to [\mathbb{P}_2(E)]^3,$$

$$\Pi_2^{0,E} : V_h^{3,\mathrm{E}}(E) \to [\mathbb{P}_2(E)]^3,$$

$$\mathbf{\Pi}_1^{0,E} : \nabla V_h^{3,\mathrm{E}}(E) \to [\mathbb{P}_1(E)]^{3\times 3}.$$

Proof Our focus is to prove the second item. According to (5.33) and employing the definition of $V_h^{3,\mathrm{E}}(E)$ and Property 5.11 we infer

$$\int_E \mathbf{v} \cdot \mathbf{p}_2 \, \mathrm{d}E = \int_{\partial E} \mathbf{v} \cdot \mathbf{n}_E \, q_3 \, \mathrm{d}f - \int_E \mathrm{div}\, \mathbf{v} \, q_3 \, \mathrm{d}E + \int_E \mathbf{v} \cdot (\mathbf{x} \wedge \mathbf{q}_1) \, \mathrm{d}E$$

$$= \sum_{f \in \partial E} \int_f \Pi_3^{0,f} \mathbf{v} \cdot \mathbf{n}_E \, q_3 \, \mathrm{d}f - \int_E \mathrm{div}\, \mathbf{v} \, q_3 \, \mathrm{d}E + \int_E \Pi_2^{\nabla,E} \mathbf{v} \cdot (\mathbf{x} \wedge \mathbf{q}_1) \, \mathrm{d}E$$

that is a computable expression.   □

5.7 Virtual Element Problem

5.7.1 Global Spaces

Let Ω_h be a decomposition of the domain $\Omega \subset \mathbb{R}^d$ with $d = 2, 3$ into general polytopal elements E. The total number of internal vertexes, internal edges, internal faces (if $d = 3$) and elements in the mesh Ω_h are denoted respectively with L_V, L_e, L_f, L_E.

For any $E \in \Omega_h$, let $V_h(E)$ denote one of the enhanced virtual element spaces introduced in Sects. 5.4.2, 5.5 and 5.6.3. The global virtual element space is defined by

$$V_h := \{v \in V \text{ s.t. } v_{|E} \in V_h(E) \text{ for all } E \in \Omega_h\}. \tag{5.35}$$

By Properties 5.5, 5.8 and 5.17 we infer that the dimension of V_h is

$$\begin{aligned}
\dim(V_h) &= 2\,L_V + 2\,L_e + 2\,L_E\,, & \text{if } d = 2, \\
\dim(V_h) &= 3\,L_V + 3\,L_e + 3\,L_f + 3\,L_E\,, & \text{if } d = 3.
\end{aligned} \tag{5.36}$$

The discrete pressure space is given by the piecewise polynomial functions of degree one, i.e. $Q_h(E)$ is simply defined by

$$Q_h(E) := \mathbb{P}_1(E)\,, \tag{5.37}$$

having dimension $\dim(Q_h(E)) = d + 1$. The corresponding DoFs are chosen, defining for each $q \in Q_h(E)$

– $\mathbf{D}_Q$: the scaled moments

$$\frac{1}{|E|} \int_E q \, \mathrm{d}E\,, \qquad \frac{1}{|E|} \int_E q \left(\frac{x_i - x_{E,i}}{h_E} \right) \mathrm{d}E \qquad \text{for } i = 1, \ldots, d.$$

The global space is given by

$$Q_h := \{q \in Q \text{ s.t. } q_{|E} \in Q_h(E) \text{ for all } E \in \Omega_h\}\,, \tag{5.38}$$

and the dimension of Q_h is

$$\dim(Q_h) = (d + 1)\,L_P - 1\,. \tag{5.39}$$

We finally mention the following results: the former states that the space V_h has an optimal interpolation order of accuracy (see Proposition 4.2. in [13] and Theorem 4.1 in [16]), the latter concerns the inf-sup stability of the couple of spaces (V_h, Q_h) (see Proposition 4.3 in [13]).

Proposition 5.1 *Under the mesh assumption (A1), let $v \in [H^s(\Omega_h)]^d$ with $1 < s \leq 3$. Then there exists $v_h \in V_h$ such that*

$$\|v - v_h\|_{0,\Omega} + h\|\nabla v - \nabla v_h\|_{0,\Omega} \lesssim h^s |v|_{H^s(\Omega_h)}$$

where the hidden constant depends only on the shape regularity constant ϱ in assumption (A1).

Proposition 5.2 *Given the discrete spaces V_h and Q_h defined in (5.35) and (5.38) respectively, there exists a positive constant $\widehat{\beta}$, independent of h, such that*

$$\sup_{v_h \in V_h,\ v_h \neq 0} \frac{b(v_h, q_h)}{\|\nabla v_h\|_{0,\Omega}} \geq \widehat{\beta} \, \|q_h\|_{0,\Omega} \qquad \text{for all } q_h \in Q_h.$$

Remark 5.3 In principle it might make sense to consider on each polygonal element $E \in \Omega_h$ the "degree one version" of the virtual element space (5.15), i.e.

$$V_h^S(E) := \left\{ v \in [H^1(E)]^2 \text{ s.t. } (i)\ \Delta v + \nabla s = 0, \quad \text{for some } s \in L_0^2(E), \right.$$

$$(ii)\ \text{div}\, v \in \mathbb{P}_0(E),$$

$$\left. (iii)\ v_{|\partial E} \in [C^0(\partial E)]^2, \quad v_{|e} \in [\mathbb{P}_1(e)]^2 \ \forall e \in \partial E \right\}$$

coupled with the pressures space $Q_h(E) := \mathbb{P}_0(E)$. However in general the couple of spaces (V_h^S, Q_h) is not inf-sup stable. For example on triangular meshes this choice leads to the couple $([\mathbb{P}_1(E)]^2, \mathbb{P}_0(E))$ that is not inf-sup stable (see for instance [22]).

The "degree one version" of the method has been introduced in [4]. The idea is that, as for standard FEM, adding an edge-based DoF representing the normal component of the velocities will grant an inf-sup stable couple. Therefore we define the space

$$V_h^S(E) := \left\{ v \in [H^1(E)]^2 \text{ s.t. } (i)\ \Delta v + \nabla s = 0, \quad \text{for some } s \in L_0^2(E), \right.$$

$$(ii)\ \text{div}\, v \in \mathbb{P}_0(E),$$

$$(iii_A)\ v_{|\partial E} \in [C^0(\partial E)]^2,$$

$$\left. (iii_B)\ v_{|e} \cdot \tau_E^e \in \mathbb{P}_1(e), \quad v_{|e} \cdot n_E^e \in \mathbb{P}_2(e) \ \forall e \in \partial E \right\}$$

where τ_E^e will denote the unit vector that is tangent to the edge e. The resulting couple (V_h^S, Q_h) is inf-sup stable. Notice that this couple can be seen as the extension of the so-called reduced $([\mathbb{P}_2(E)]^2, \mathbb{P}_0(E))$ to general polygonal meshes.

5.7.2 Discrete Forms

On the basis of Properties 5.6, 5.9 and 5.18, following a standard procedure in the VEM framework, we define the computable (in the sense of Definition 5.1) discrete local forms

$$a_h^E(\boldsymbol{u},\,\boldsymbol{v}) := \int_E \left(\boldsymbol{\Pi}_1^{0,E} \boldsymbol{\varepsilon}(\boldsymbol{u}) \right) : \left(\boldsymbol{\Pi}_1^{0,E} \boldsymbol{\varepsilon}(\boldsymbol{v}) \right) \mathrm{d}E + \mathscr{S}^E \left((I - \Pi_2^{0,E})\boldsymbol{u},\, (I - \Pi_2^{0,E})\boldsymbol{v} \right),$$
(5.40)

$$c_h^{o,E}(\boldsymbol{w};\,\boldsymbol{u},\,\boldsymbol{v}) := \int_E \left[\left(\boldsymbol{\Pi}_1^{0,E} \boldsymbol{\nabla}\,\boldsymbol{u} \right) \Pi_2^{0,P} \boldsymbol{w} \right] \cdot \Pi_2^{0,E} \boldsymbol{v} \,\mathrm{d}E,$$
(5.41)

$$c_h^{\mathrm{skew},E}(\boldsymbol{w};\,\boldsymbol{u},\,\boldsymbol{v}) := \frac{1}{2}\left(c_h^{o,E}(\boldsymbol{w};\,\boldsymbol{u},\,\boldsymbol{v}) - c_h^{o,E}(\boldsymbol{w};\,\boldsymbol{v},\,\boldsymbol{u}) \right),$$
(5.42)

for all $\boldsymbol{w},\boldsymbol{u},\boldsymbol{v} \in \boldsymbol{V}_h(E)$, where clearly

$$\boldsymbol{\Pi}_1^{0,E} \boldsymbol{\varepsilon}(\boldsymbol{v}) = \frac{\boldsymbol{\Pi}_1^{0,E} \boldsymbol{\nabla}\,\boldsymbol{v} + (\boldsymbol{\Pi}_1^{0,E} \boldsymbol{\nabla}\,\boldsymbol{v})^{\mathrm{T}}}{2}$$

and the symmetric stabilizing form $\mathscr{S}^E \colon \boldsymbol{V}_h(E) \times \boldsymbol{V}_h(E) \to \mathbb{R}$ satisfies

$$\|\boldsymbol{\nabla}\boldsymbol{v}\|_{0,E}^2 \lesssim \mathscr{S}^E(\boldsymbol{v},\,\boldsymbol{v}) \lesssim \|\boldsymbol{\nabla}\boldsymbol{v}\|_{0,E}^2 \qquad \text{for all } \boldsymbol{v} \in \boldsymbol{V}_h(E) \cap \mathrm{Ker}(\Pi_2^{0,E}).$$
(5.43)

The condition above essentially requires the stabilizing term $\mathscr{S}^E(\boldsymbol{v},\,\boldsymbol{v})$ to scale as $\|\boldsymbol{\nabla}\boldsymbol{v}\|_{0,E}^2$ that is h^{d-2}. For instance, a standard choice for the stabilization is the D-recipe stabilization introduced in [12].

Remark 5.4 Recalling Property 5.7, if E is a curved polygon the stabilizing form has to be defined onto the sum space $(\boldsymbol{V}_h(E) + [\mathbb{P}_2(E)]^2)$, i.e.

$$\mathscr{S}^E \colon (\boldsymbol{V}_h(E) + [\mathbb{P}_2(E)]^2) \times (\boldsymbol{V}_h(E) + [\mathbb{P}_2(E)]^2) \to \mathbb{R}.$$

The global virtual forms are defined by simply summing the local contributions:

$$a_h(\boldsymbol{u},\,\boldsymbol{v}) := \sum_{E \in \Omega_h} a_h^E(\boldsymbol{u},\,\boldsymbol{v}),$$

$$c_h(\boldsymbol{w};\,\boldsymbol{u},\,\boldsymbol{v}) := \sum_{E \in \Omega_h} c_h^{\mathrm{skew},E}(\boldsymbol{w};\,\boldsymbol{u},\,\boldsymbol{v}),$$
(5.44)

for all $\boldsymbol{w},\boldsymbol{u},\boldsymbol{v} \in \boldsymbol{V}_h$. We point out that

- the symmetry of $a_h(\cdot,\cdot)$ together with (5.43) easily implies that $a_h(\cdot,\cdot)$ is continuous and coercive with respect to the H^1-norm, i.e. there exist two positive

constants $\widehat{\alpha}$ and α s.t

$$\widehat{\alpha}\|\nabla\boldsymbol{v}\|_{0,\Omega}^2 \le a_h(\boldsymbol{v},\boldsymbol{v}) \le \alpha\|\nabla\boldsymbol{v}\|_{0,\Omega}^2 \quad \text{for all } \boldsymbol{v} \in \boldsymbol{V}_h; \tag{5.45}$$

– the discrete trilinear form $c_h(\cdot;\,\cdot,\,\cdot)$ is skew-symmetric and is continuous with respect to the H^1-norm, i.e. there exists a positive constant $\widehat{C}$ s.t.

$$|c_h(\boldsymbol{w};\,\boldsymbol{u},\boldsymbol{v})| \le \widehat{C}\|\nabla\boldsymbol{w}\|_{0,\Omega}\|\nabla\boldsymbol{u}\|_{0,\Omega}\|\nabla\boldsymbol{v}\|_{0,\Omega} \quad \text{for all } \boldsymbol{w},\boldsymbol{u},\boldsymbol{v} \in \boldsymbol{V}_h. \tag{5.46}$$

Finally the approximated load $\boldsymbol{f}_h \in [\mathbb{P}_2(\Omega_h)]^d$ is given by

$$\boldsymbol{f}_{h|E} := \Pi_2^{0,E}\boldsymbol{f} \qquad \text{for all } E \in \Omega_h \tag{5.47}$$

therefore the discrete right hand side

$$(\boldsymbol{f}_h,\,\boldsymbol{v}) := \sum_{E\in\Omega_h} \int_E \Pi_2^{0,E}\boldsymbol{f} \cdot \boldsymbol{v}\,\mathrm{d}E \qquad \text{for all } \boldsymbol{v} \in \boldsymbol{V}_h \tag{5.48}$$

is computable (cf. Properties 5.6, 5.9 and 5.18 and Definition 5.1).

5.7.3   Divergence-Free Velocity Solution

Referring to the discrete spaces (5.35), (5.38), the discrete forms (5.44), the div form (5.3) and the approximated load term (5.47) the virtual element approximation of the Navier-Stokes equation is given by

$$\begin{cases} \text{find } (\boldsymbol{u}_h,\,p_h) \in \boldsymbol{V}_h \times Q_h, \text{ such that} \\ \nu\,a_h(\boldsymbol{u}_h,\,\boldsymbol{v}_h) + c_h(\boldsymbol{u}_h;\,\boldsymbol{u}_h,\boldsymbol{v}_h) + b(\boldsymbol{v}_h,\,p_h) = (\boldsymbol{f}_h,\,\boldsymbol{v}_h) \qquad \text{for all } \boldsymbol{v}_h \in \boldsymbol{V}_h, \\ b(\boldsymbol{u}_h,\,q_h) = 0 \hspace{6.5cm} \text{for all } q_h \in Q_h. \end{cases} \tag{5.49}$$

The crucial observation is that, definitions (5.35) and (5.38) along with Proposition 5.2 implies that

$$\operatorname{div}\boldsymbol{V}_h = Q_h. \tag{5.50}$$

Therefore the second equation of (5.49), along with property (5.50), implies that the discrete velocity $\boldsymbol{u}_h \in \boldsymbol{V}_h$ is **exactly divergence-free**. More generally the discrete kernel

$$\boldsymbol{Z}_h := \{\boldsymbol{v}_h \in \boldsymbol{V}_h \text{ s.t. } b(\boldsymbol{v}_h, q_h) = 0 \text{ for all } q_h \in Q_h\} \tag{5.51}$$

is a subspace of the continuous kernel $\mathbf{Z}$ (cf. (5.8)), i.e.

$$\mathbf{Z}_h \subseteq \mathbf{Z}. \tag{5.52}$$

Then, Problem (5.49) can be formulated in the equivalent kernel form:

$$\begin{cases} \text{find } \boldsymbol{u}_h \in \mathbf{Z}_h, \text{ such that} \\ \nu\, a_h(\boldsymbol{u}_h, \boldsymbol{v}_h) + c_h(\boldsymbol{u}_h; \boldsymbol{u}_h, \boldsymbol{v}_h) = (\boldsymbol{f}_h, \boldsymbol{v}_h) = (\mathscr{P}(\boldsymbol{f}_h).\boldsymbol{v}_h) \qquad \text{for all } \boldsymbol{v}_h \in \mathbf{Z}_h. \end{cases} \tag{5.53}$$

The well-posedness of the discrete problems is stated in the following theorem. Note that an analogous result could be stated making use of a discrete Helmholtz–Hodge projector (cf. Assumption **A0**), but the result below is more suitable to the current presentation.

Theorem 5.1 *Referring to (5.45), (5.46) and (5.47) under the assumption*

$$(\widehat{\mathbf{A0}}) \qquad \widehat{\gamma} := \frac{\widehat{C}\,\|\boldsymbol{f}_h\|_{\mathbf{Z}_h^*}}{\widehat{\alpha}^2 \nu^2} < 1$$

with the usual definition of dual norm, Problem (5.49) is well-posed and the unique solution $(\boldsymbol{u}_h, p_h) \in \mathbf{V}_h \times Q_h$ is such that

$$|\boldsymbol{u}_h|_{[H^1(\Omega)]^2} \le \frac{\|\boldsymbol{f}_h\|_{\mathbf{Z}_h^*}}{\widehat{\alpha}\nu}. \tag{5.54}$$

5.8 Convergence Results and Exploring the Divergence-Free Property

The goal of the present section is to describe the main benefits of the proposed VEM scheme, in addition to the capability (shared by any VEM scheme) of using general polytopal meshes. The divergence-free property and the kernel inclusion (5.52) entail a range of advantages explored in the following subsections

- Section 5.8.1: the error components partly decouple, namely the influence of the pressure in the velocity error is weaker with respect to standard inf-sup stable elements (see [16]);
- Section 5.8.2: the scheme in (5.49) is equivalent to a suitable reduced problem, observing the internal DoFs $\mathbf{D_V}3$ (and the associated pressures DoFs) can be automatically ignored in the final linear system (see [13]);
- Section 5.8.3: the proposed Virtual Element enjoys an underlying discrete Stokes complex structure (see [15, 18]);
- Section 5.8.4: the space $\mathbf{V}_h$ is uniformly stable for the Darcy equation (see [64]).

5.8.1 Convergence Results

We here state the optimal convergence result for the proposed Virtual Element scheme (5.49). We refer to Theorem 4.6 in [16] for the proof.

Proposition 5.3 *Under the assumptions* (**A0**), $(\widehat{\mathbf{A0}})$ *and* (**A1**), *let* $(\boldsymbol{u}, p) \in V \times Q$ *be the solution of Problem* (5.5) *and* $(\boldsymbol{u}_h, p_h) \in V_h \times Q_h$ *be the solution of Problem* (5.49). *Assuming moreover* $\boldsymbol{u}, \boldsymbol{f} \in [H^3(\Omega_h)]^d$ *and* $p \in H^2(\Omega_h)$ *then*

$$|\boldsymbol{u} - \boldsymbol{u}_h|_1 \leq h^2 \, \mathscr{F}(\boldsymbol{u}; \nu, \gamma) + h^4 \, \mathscr{H}(\boldsymbol{f}; \nu), \qquad (5.55)$$

$$\|p - p_h\|_0 \leq h^2 \, |p|_{H^2(\Omega_h)} + h^2 \, \mathscr{K}(\boldsymbol{u}; \nu, \gamma) + h^4 \, |\boldsymbol{f}|_{[H^3(\Omega_h)]^d} \qquad (5.56)$$

for suitable functions $\mathscr{F}$, $\mathscr{H}$, $\mathscr{K}$ *independent of h.*

Note that the error components partly decouple: notably, the velocity error does not depend directly on the discrete pressures, but only indirectly through the approximation of the loading and convection terms and such dependence on the full load is much weaker with respect to standard mixed schemes. In some situations the partial decoupling of the errors induces a positive effect on the velocity approximation.

In particular, assume that the load in (5.5) is a gradient field, i.e. $\boldsymbol{f} = \nabla\zeta$, then $\mathscr{P}(\nabla\zeta) = \boldsymbol{0}$ and thus the solution of (5.1) satisfies $\boldsymbol{u} = \boldsymbol{0}$ (cf. (5.7)). From (5.55) and since $(\nabla\zeta, z_h) = 0$ for all $z_h \in Z_h$, and assuming $\boldsymbol{f} \in [H^3(\Omega_h)]^d$ one can easily derive

$$\|\boldsymbol{u}_h^{\mathrm{VEM}}\|_V \leq \frac{\|\boldsymbol{f}_h\|_{Z_h^\star}}{\widehat{\alpha} \, \nu} = \frac{\|\boldsymbol{f}_h - \boldsymbol{f}\|_{Z_h^\star}}{\widehat{\alpha} \, \nu} \lesssim \frac{h^4}{\nu} \, |\boldsymbol{f}|_{[H^3(\Omega_h)]^d} \, .$$

Notice that in the same situation the velocity solution of classical mixed finite element methods would have the form

$$\|\boldsymbol{u}_h^{\mathrm{FEM}}\|_V \lesssim \frac{h^2}{\nu} \, |\boldsymbol{f}|_{[H^1(\Omega_h)]^d} \, .$$

Remark 5.5 In the context of the approximation of the Navier–Stokes equation, a numerical method is said to be pressure-robust (see e.g. [50]) if the discrete velocity solution depends only on the Helmholtz–Hodge projector $\mathscr{P}(\boldsymbol{f})$ of the load $\boldsymbol{f}$ (as it happens for the exact velocity field). For instance, in the situation aforementioned, if the load is a gradient field, the discrete velocity solution $\boldsymbol{u}_h^{\mathrm{PR}}$ computed by means of a pressure-robust method satisfies $\boldsymbol{u}_h^{\mathrm{PR}} = \boldsymbol{0}$. Hence method (5.49) is not pressure-robust; on the other hand the dependence on the full load is much weaker with respect to standard mixed schemes. Suitable modifications of the right-hand side (5.48) have been proposed in [41, 59] in order to get a real pressure-robust VEM scheme. These approaches are based on a Raviart-Thomas interpolation of the test functions with respect to a subtriangulation of the mesh Ω_h.

5.8.2 Reduced Virtual Elements

In this section we show that Problem (5.49) is equivalent to a suitable reduced problem, involving significantly fewer degrees of freedom. Recalling that the discrete solution satisfies div $\boldsymbol{u}_h = 0$, by definition of DoFs $\mathbf{D_V}3$ (cf. Properties 5.2, 5.5, 5.14 and 5.17), one can immediately set to zero all $\mathbf{D_V}3$ degrees of freedom, and correspondingly eliminate also the associated discrete pressures. Hence referring to (5.21) and (5.34), on each polytopal element E, let us define the reduced space:

$$V_h^R(E) := \{\boldsymbol{v} \in V_h(E) \ s.t. \ \mathrm{div} \, \boldsymbol{v} \in \mathbb{P}_0(E)\} \tag{5.57}$$

i.e. we replace the item (ii) in (5.21) and (5.34) taking $\mathbb{P}_0(E)$ in the place of $\mathbb{P}_1(E)$. We briefly list the main properties of the space $V_h^R(E)$.

Property 5.19 (Polynomial Inclusion) Let $\mathbb{P}_2^R(E) \subset [\mathbb{P}_2(E)]^d$ denote the set of vector valued polynomials of degree 2 having constant divergence. Then $\mathbb{P}_2^R(E) \subseteq V_h^R(E)$.

Property 5.20 (Dimension and Degrees of Freedom) The dimension of $V_h^R(E)$ is given by

$$
\begin{aligned}
\dim(V_h^R(E)) &= 4\,\ell_E && \text{if } d = 2, \\
\dim(V_h^R(E)) &= 3\,\ell_V + 3\,\ell_e + 3\,\ell_f && \text{if } d = 3.
\end{aligned}
\tag{5.58}
$$

As DoFs in $V_h^R(E)$ we can take $\mathbf{D_V}1$ and $\mathbf{D_V}2$ defined in Property 5.2 and Property 5.14 for the 2D and the 3D case respectively (see Fig. 5.4 for the 2D case).

Property 5.21 (Polynomial Projections) The space $V_h^R(E)$ satisfies Property 5.6 and Property 5.18 for $d = 2, 3$ respectively. However we observe that, in the light of Property 5.19, the polynomial projectors in general fall outside to the spaces.

The global space V_h^R is obtained in the standard fashion by gluing the local spaces:
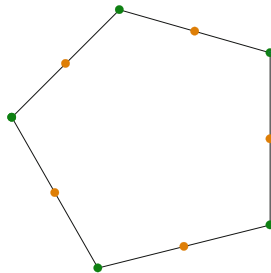
Fig. 5.4 DoFs for $V_h(E)$. We denote $\mathbf{D_V}1$ with the green dots and $\mathbf{D_V}2$ with the orange dots [18]

$$V_h^R := \{v \in V \text{ s.t. } v_{|E} \in V_h^R(E) \text{ for all } E \in \Omega_h\}. \tag{5.59}$$

Concerning the reduced space for the pressures we simply take

$$Q_h^R := \{q \in Q \text{ s.t. } q_{|E} \in \mathbb{P}_0(E) \text{ for all } E \in \Omega_h\}. \tag{5.60}$$

Referring to the discrete spaces (5.59), (5.60), the discrete forms (5.44), the div form (5.3) and the approximated load term (5.47), we consider the reduced problem given by

$$\begin{cases} \text{find } (u_h^R, \, p_h^R) \in V_h^R \times Q_h^R, \text{ such that} \\ v\, a_h(u_h^R, \, v_h) + c_h(u_h^R; \, u_h^R, \, v_h) + b(v_h, \, p_h^R) = (f_h, \, v_h) & \text{for all } v_h \in V_h^R, \\ b(u_h^R, \, q_h) = 0 & \text{for all } q_h \in Q_h^R. \end{cases} \tag{5.61}$$

It can be shown that, under the assumption $(\widehat{\mathbf{A0}})$, Problem (5.61) is well posed. Moreover the discrete reduced kernel

$$Z_h^R := \{v_h \in V_h^R \text{ s.t. } b(v_h, q_h) = 0 \text{ for all } q_h \in Q_h^R\}$$

satisfies $Z_h^R = Z_h \subset Z$. The following proposition is easy to check and states the relation between problem (5.49) and the reduced Problem (5.61).
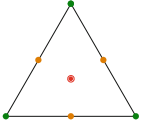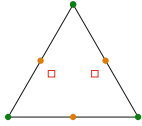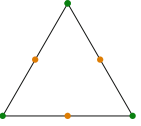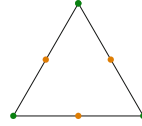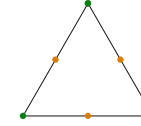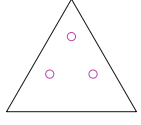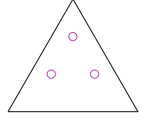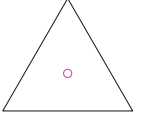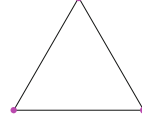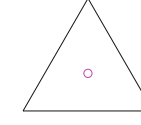
Proposition 5.4 *Under the assumption* $(\widehat{\mathbf{A0}})$, *let* $(u_h, p_h) \in V_h \times Q_h$ *and* $(u_h^R, p_h^R) \in V_h^R \times Q_h^R$ *be the solution of Problem (5.49) and Problem (5.61), respectively. Then*

$$u_h^R = u_h, \qquad and \qquad p_h^R = \Pi_0^{0,E} p_h \quad on\ every\ E \in \Omega_h.$$

It is trivial to check that the reduced scheme (5.61) has $2dL_E$ DoFs less when compared with the original one (5.49).

Remark 5.6 (Virtual Elements and FEM) The proposed Virtual Elements is different even on standard triangular/quadrilateral meshes or tetrahedral/hexahedral meshes from already-known inf-sup stable finite elements. Focusing on the bi-dimensional case and triangular meshes (see Table 5.1), we now briefly compare our VEM approach with the Crouzeix-Raviart element ($[\mathbb{P}_2(E) + \mathbb{B}_3(E)]^2$, $\mathbb{P}_1(E)$), where $\mathbb{B}_3(E)$ denotes the cubic bubble on E. We notice that $\dim(V_h(E)) = \dim([\mathbb{P}_2(E) + \mathbb{B}_3(E)]^2)$ and both spaces contain the polynomial space $[\mathbb{P}_2(E)]^2$. However the two methods do not coincide: for the VEM scheme it holds div $V_h(E) = \mathbb{P}_1(E)$ (cf. (5.50)), while for the FEM scheme it holds $\text{div}(([\mathbb{P}_2(E) + \mathbb{B}_3(E)]^2)) \not\subset \mathbb{P}_1(E)$, because the divergence of a cubic bubble function is not a linear polynomial. This argument shows that the two approaches are indeed different, and in particular the Crouzeix-Raviart element does not deliver

Table 5.1 Finite elements and virtual elements: velocities and pressures spaces

Crouzeix–Raviart	VEM-2	P2–P0	Taylor–Hood	VEM-2R
velocities				
$[\mathbb{P}_2(E) + \mathbb{B}_3(E)]^2$	$V_h(E)$	$[\mathbb{P}_2(E)]^2$	$[\mathbb{P}_2(E)]^2$	$V_h^{\mathrm{R}}(E)$
pressures				
$\mathbb{P}_1(E)$	$\mathbb{P}_1(E)$	$\mathbb{P}_0(E)$	$\mathbb{P}_1^{\mathrm{cont}}(E)$	$\mathbb{P}_0(E)$

a divergence-free velocity solution. Similar arguments apply for the P2-P0 element ($[\mathbb{P}_2(E)]^2, \mathbb{P}_0(E)$) and the Taylor-Hood element ($[\mathbb{P}_2(E)]^2, \mathbb{P}_1^{\mathrm{cont}}(E)$) compared with the reduced VEM $V_h^{\mathrm{R}}(E)$. Other interesting comments about the comparison with FEM can be found in [26].

5.8.3 *Stokes Complex and* **curl** *Formulation*

In the present subsection we investigate the underlying Stokes complex structure of the Virtual Element Method for Stokes and Navier–Stokes. For simplicity we here describe the 2D Stokes complex [18], the extension to the three-dimensional case is more technical and requires a more careful analysis (we refer the interested reader to [15], see also [7, 46]).

Assume that $\Omega \in \mathbb{R}^2$ is a simply connected domain. Let us consider the space

$$\Phi := H_0^2(\Omega) = \left\{ \varphi \in H^2(\Omega) \quad \text{s.t.} \quad \varphi = 0, \quad \frac{\partial \varphi}{\partial n} = 0 \quad \text{on } \partial\Omega \right\}. \tag{5.62}$$

The 2D de Rham complex is provided by [47]:

$$0 \xrightarrow{\;\;i\;\;} \Phi \xrightarrow{\;\;\textbf{curl}\;\;} V \xrightarrow{\;\;\text{div}\;\;} Q \xrightarrow{\;\;0\;\;} 0, \tag{5.63}$$

where i denotes the mapping that to every real number r associates the constant function identically equal to r and we recall that a sequence is exact if the range of each operator coincides with the kernel of the following one.

As a consequence of (5.63) we have the following characterization of the kernel Z (cf. (5.8))

$$\mathbf{curl}(\Phi) = Z.\tag{5.64}$$

Then, Problem (5.9) can be formulated in the following **curl** *formulation*:

$$\begin{cases} \text{find } \psi \in \Phi, \text{ such that} \\ \nu\, a(\mathbf{curl}\psi,\ \mathbf{curl}\varphi) + c(\mathbf{curl}\psi;\ \mathbf{curl}\psi, \mathbf{curl}\varphi) = (\boldsymbol{f}, \mathbf{curl}\varphi) \qquad \text{for all } \varphi \in \Phi. \end{cases}\tag{5.65}$$

Since the formulation (5.65) is equivalent to Problem (5.9) (in turn equivalent to Problem (5.5)), the well-posedness of **curl** formulation follows from assumption **(A0)**.

Referring to (5.35) and (5.38), our goal is to construct a conforming virtual element space $\Phi_h \subset \Phi$ such that

$$0 \xrightarrow{\ \ i\ \ } \Phi_h \xrightarrow{\ \ \mathbf{curl}\ \ } V_h \xrightarrow{\ \ \mathrm{div}\ \ } Q_h \xrightarrow{\ \ 0\ \ } 0,\tag{5.66}$$

is an exact sub-complex of (5.63). To this end we consider on each polygonal element $E \in \Omega_h$ the finite dimensional virtual space [27]

$$\Phi_h(E) := \left\{ \varphi \in H^2(E) \text{ s.t. } (i)\,\Delta^2\varphi = \mathbb{P}_1(E), \right.$$

$$(ii)\,\varphi_{|\partial E} \in C^0(\partial E),\quad \varphi_{|e} \in \mathbb{P}_3(e)\ \forall e \in \partial E,$$

$$(iii)\,\nabla\varphi_{|\partial E} \in [C^0(\partial E)]^2,\quad \nabla\varphi_{|e} \in [\mathbb{P}_2(e)]^2\ \forall e \in \partial E,$$

$$(iv)\,\left.\left(\mathbf{curl}\varphi - \Pi_2^{\nabla,E}\mathbf{curl}\varphi,\ \boldsymbol{x}^\perp p_1\right)_E = 0\ \forall p_1 \in \mathbb{P}_1(E)\right\}\tag{5.67}$$

We here summarize the main properties of the virtual space $\Phi_h(E)$ we refer to [18, 27] for the various proofs.

Property 5.22 (Polynomial Inclusion) $\mathbb{P}_3(E) \subseteq \Phi_h(E)$.

Property 5.23 (Dimension and Degrees of Freedom) The dimension of $\Phi_h(E)$ is given by

$$\dim(\Phi_h(E)) = 4\,\ell_E.\tag{5.68}$$
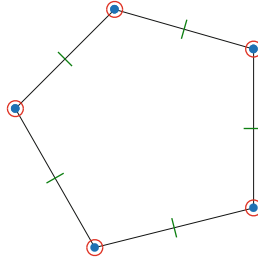
Fig. 5.5 DoFs for $\Phi_h(E)$. We denote $\mathbf{D_\Phi}1$ with the blue dots, $\mathbf{D_\Phi}2$ with the red circles and $\mathbf{D_\Phi}3$ with the green lines [18]

Moreover, the following linear operators $\mathbf{D_\Phi}$, split into three subsets (see Fig. 5.5) constitute a set of DoFs for $\Phi_h(E)$:

- $\mathbf{D_\Phi}1$: the values of φ at the vertexes of the polygon E,
- $\mathbf{D_\Phi}2$: the values of $h_e \nabla \varphi$ at the vertexes of the polygon E,
- $\mathbf{D_\Phi}3$: the values of $h_e \frac{\partial \varphi}{\partial \boldsymbol{n}}$ at the midpoint of every edge $e \in \partial E$.

Property 5.24 (Polynomial Projection) The DoFs $\mathbf{D_\Phi}$ allow us to compute exactly (cf. (5.14) and (5.13)and Definition 5.1)

$$\Pi_2^{\nabla,E} : \mathbf{curl}(\Phi_h(E)) \to [\mathbb{P}_2(E)]^2 ,$$

$$\Pi_2^{0,E} : \mathbf{curl}(\Phi_h(E)) \to [\mathbb{P}_2(E)]^2 ,$$

$$\mathbf{\Pi}_1^{0,E} : \nabla\mathbf{curl}(\Phi_h(E)) \to [\mathbb{P}_1(E)]^{2\times 2} .$$

The global virtual element space is defined by

$$\Phi_h := \{\varphi \in \Phi_h(E) \text{ s.t. } \varphi_{|E} \in \Phi_h(E) \text{ for all } E \in \Omega_h\}. \tag{5.69}$$

By Property 5.23 we infer that the dimension of Φ_h is

$$\dim(\Phi_h) = 3 L_V + L_e . \tag{5.70}$$

We now prove that the triad $\{\Phi_h, V_h, Q_h\}$ (cf. (5.69), (5.35), (5.38)) realizes the exact sequence (5.66).

Proposition 5.5 *The sequence* (5.66) *constitutes an exact complex.*

Proof We need to verify that the image of each operator in (5.66) coincides with the kernel of the next one. Recalling (5.50), we only need to prove that

$$(\boldsymbol{i}\mathbf{1}) \ \mathbf{curl}(\Phi_h) \subseteq \boldsymbol{Z}_h , \qquad (\boldsymbol{i}\mathbf{2}) \ \boldsymbol{Z}_h \subseteq \mathbf{curl}(\Phi_h) . \tag{5.71}$$

Let us analyse the inclusion $(\boldsymbol{i}\mathbf{1})$. Let $\varphi \in \Phi_h$, clearly $\mathbf{curl}\varphi \in \boldsymbol{Z}$. Therefore, we need to verify that $(\mathbf{curl}\varphi)_{|E} \in \boldsymbol{V}_h(E)$ for all $E \in \Omega_h$. It is evident that

the constraints (i.e. the item (iv)) in definition (5.67) are the curl version of the constraints in definition (5.21). Concerning the condition on the skeleton ∂E, we observe that items (ii) and (iii) in (5.67) easily imply that

$$\boldsymbol{v}_{|\partial E} = (\textbf{curl}\,\varphi)_{|\partial E} \in [C^0(\partial E)]^2 \quad \text{and} \quad \boldsymbol{v}_{|e} = (\textbf{curl}\,\varphi)_{|e} \in [\mathbb{P}_2(e)]^2. \quad (5.72)$$

Inside the element, by simple calculations and by item (i) in (5.67), we infer $\mathrm{rot}\,\boldsymbol{\Delta v} = \mathrm{rot}\,\boldsymbol{\Delta}(\textbf{curl}\,\varphi) = \Delta^2\varphi \in \mathbb{P}_1(E)$. In the light of (5.12), $\mathrm{rot}\colon \boldsymbol{x}^\perp\mathbb{P}_1(E) \to \mathbb{P}_1(E)$ is an isomorphism, then there exists $p_1 \in \mathbb{P}_1(E)$ such that $\mathrm{rot}\,\boldsymbol{\Delta v} = \mathrm{rot}\,\boldsymbol{x}^\perp p_1$. Since E is simply connected, there exists s such that $\boldsymbol{\Delta v} + \nabla s = \boldsymbol{x}^\perp p_1$, i.e. (i) in (5.21). That concludes the proof for $\textbf{(i1)}$.

The inclusion $\textbf{(i2)}$ follows by a dimensional argument. In fact, from (5.70) and (5.36) combined with (5.51), easily follows that

$$\dim(\textbf{curl}(\Phi_h)) - \dim(\boldsymbol{Z}_h) = \dim(\Phi_h) - \dim(\boldsymbol{Z}_h) - 1$$
$$= (3\,L_V + L_e) - (2\,L_V + 2\,L_e - N_E) - 1 = 0$$

by Euler formula. Therefore we can conclude that $\textbf{curl}(\Phi_h) = \boldsymbol{Z}_h$. $\qquad\qquad\square$

In the light of Proposition 5.5 we can characterize the divergence-free discrete kernel $\boldsymbol{Z}_h$ as $\textbf{curl}(\Phi_h)$. Therefore referring to (5.69), (5.44) and (5.47) we can set the virtual element approximation of the Navier–Stokes equation in the **curl** formulation:

$$\begin{cases} \text{find } \psi_h \in \Phi_h, \text{ such that} \\ \nu\,a_h(\textbf{curl}\psi_h,\ \textbf{curl}\varphi_h) + c_h(\textbf{curl}\psi_h;\ \textbf{curl}\psi_h, \textbf{curl}\varphi_h) = (\boldsymbol{f}_h, \textbf{curl}\varphi_h)\ \forall\varphi_h \in \Phi_h. \end{cases}$$
$$(5.73)$$

We stress that the linear system associated to Problem (5.73) has $2(L_E - 1)$ less DoFs even if considering the reduced Problem (5.61).

5.8.4 Stability in the Darcy Limit and Brinkman Equation

The focus of this subsection is on describing the VEM for the Brinkman problem. The Brinkman equation describes fluid flow in complex porous media with a viscosity coefficient highly varying so that the flow is dominated by the Darcy equation in some regions of the domain and by the Stokes equation in others. We consider the Brinkman equation on a polytopal simply connected domain $\Omega \subseteq \mathbb{R}^d$ with $d = 2, 3$ (see for instance [28])

$$\begin{cases} \text{find } (\boldsymbol{u},\, p) \text{ such that} \\ -\nu\,\mathrm{div}(\boldsymbol{\varepsilon}(\boldsymbol{u})) + \mathbb{K}^{-1}\boldsymbol{u} - \nabla p = \boldsymbol{f} & \text{in } \Omega, \\ \mathrm{div}\,\boldsymbol{u} = 0 & \text{in } \Omega, \\ \boldsymbol{u} = 0 & \text{on } \partial\Omega, \end{cases} \quad (5.74)$$

where $\boldsymbol{u}$, p are the velocity and the pressure fields, respectively, $\nu \in \mathbb{R}$, $\nu > 0$ is the viscosity of the fluid, $\mathbb{K}$ is a uniformly symmetric positive definite tensor and denotes the permeability tensor of the porous media and $\boldsymbol{f} \in [L^2(\Omega)]^d$ represents the volume source term. Notice that if ν approaches zero (5.74) becomes a singular perturbation of the classic Darcy equation.

We assume that ν and $\mathbb{K}$ are piecewise constants with respect to $E \in \Omega_h$ and let ν_E, κ_E and κ_E^i denote the L^∞-norm of ν, $\mathbb{K}$ and $\mathbb{K}^{-1}$ respectively on the element E. Then recalling Properties 5.6 and 5.18 let us define for all $\boldsymbol{u}$, $\boldsymbol{v} \in \boldsymbol{V}_h(E)$ the computable bilinear form

$$m_h^E(\boldsymbol{u},\, \boldsymbol{v}) := \int_E \mathbb{K}^{-1} \Pi_2^{0,E} \boldsymbol{u} \cdot \Pi_2^{0,E} \boldsymbol{v} \, \mathrm{d}E + \kappa_E^i \mathscr{R}^E \left((I - \Pi_2^{0,E}) \boldsymbol{u},\, (I - \Pi_2^{0,E}) \boldsymbol{v} \right),$$
(5.75)

where the symmetric stabilizing form $\mathscr{R}^E \colon \boldsymbol{V}_h(E) \times \boldsymbol{V}_h(E) \to \mathbb{R}$ satisfies

$$\|\boldsymbol{v}\|_{0,E}^2 \lesssim \mathscr{R}^E(\boldsymbol{v},\, \boldsymbol{v}) \lesssim \|\boldsymbol{v}\|_{0,E}^2 \qquad \text{for all } \boldsymbol{v} \in \boldsymbol{V}_h(E) \cap \mathrm{Ker}(\Pi_2^{0,E}).$$
(5.76)

The global approximated bilinear form $m_h(\cdot, \cdot) \colon \boldsymbol{V}_h \times \boldsymbol{V}_h \to \mathbb{R}$ is thus defined by summing the local contributions, i.e.

$$m_h(\boldsymbol{u},\, \boldsymbol{v}) := \sum_{E \in \Omega_h} m_h^E(\boldsymbol{u},\, \boldsymbol{v}) \qquad \text{for all } \boldsymbol{u}, \boldsymbol{v} \in \boldsymbol{V}_h.$$
(5.77)

Referring to the discrete spaces (5.35), (5.38), the discrete form in (5.77) and (5.44) and the div form (5.3) and the approximated load term (5.47), the virtual element approximation of the Brinkman equation is given by [64]

$$\begin{cases} \text{find } (\boldsymbol{u}_h,\, p_h) \in \boldsymbol{V}_h \times Q_h, \text{ such that} \\ \nu\, a_h(\boldsymbol{u}_h,\, \boldsymbol{v}_h) + m_h(\boldsymbol{u}_h,\, \boldsymbol{v}_h) + b(\boldsymbol{v}_h,\, p_h) = (\boldsymbol{f}_h,\, \boldsymbol{v}_h) & \text{for all } \boldsymbol{v}_h \in \boldsymbol{V}_h, \\ b(\boldsymbol{u}_h,\, q_h) = 0 & \text{for all } q_h \in Q_h. \end{cases}$$
(5.78)

Mathematically, the Brinkman equations can be viewed as a combination of the Stokes and the Darcy equations, that can change from place-to-place in the computational domain. Therefore, numerical schemes for Brinkman equations have to be carefully designed to accommodate both Stokes and Darcy simultaneously. Let us define the norm

$$|||\boldsymbol{v}|||^2 := \nu \|\boldsymbol{\nabla} \boldsymbol{v}\|_{0,\Omega}^2 + \|\mathbb{K}^{-1/2} \boldsymbol{v}\|_{0,\Omega}^2 + \|\mathrm{div}\, \boldsymbol{v}\|_{0,\Omega}^2.$$

Employing the kernel inclusion (5.52), the stability bounds in (5.43) and (5.76), it holds that

$$\nu\, a_h(\boldsymbol{v},\, \boldsymbol{v}) + m_h(\boldsymbol{v},\, \boldsymbol{v}) \gtrsim |||\boldsymbol{v}|||^2 \qquad \text{for all } \boldsymbol{v} \in \boldsymbol{Z}_h,$$
(5.79)

i.e. the discrete form $a_h(\cdot, \ \cdot) + m_h(\cdot, \ \cdot)$ is uniformly stable (w.r.t. ν, $\mathbb{K}$ and h) on the discrete kernel. Notice that for classical inf-sup stable Stokes finite elements one has

$$\nu \, a(\boldsymbol{v}, \ \boldsymbol{v}) + \int_{\Omega} \mathbb{K}^{-1} \boldsymbol{v} \cdot \boldsymbol{v} \, \mathrm{d}\Omega \gtrsim \min_{E \in \Omega_h} \max\{h_E^2, \nu_E\} |||\boldsymbol{v}|||^2 \qquad \text{for all } \boldsymbol{v} \in \boldsymbol{Z}_h^{\text{FEM}},$$

i.e. the bilinear form associated with the Brinkman equation is not uniformly coercive on the discrete kernel (being in general $\boldsymbol{Z}_h^{\text{FEM}} \not\subset \boldsymbol{Z}$).

On the basis of (5.79) we have the following results (we refer to [64] for the proof).

Theorem 5.2 *Problem* (5.78) *is well-posed and the unique solution* $(\boldsymbol{u}_h, p_h) \in \boldsymbol{V}_h \times Q_h$ *is such that*

$$|||\boldsymbol{u}_h||| \lesssim |||\boldsymbol{f}_h|||_{\boldsymbol{Z}_h^*} \, .$$

Proposition 5.6 *Under the assumption* (A1), *let* $(\boldsymbol{u}, \ p) \in \boldsymbol{V} \times Q$ *be the solution of Problem* (5.74) *and* $(\boldsymbol{u}_h, p_h) \in \boldsymbol{V}_h \times Q_h$ *be the solution of Problem* (5.78). *Assuming moreover* $\boldsymbol{u}, \boldsymbol{f} \in [H^3(\Omega_h)]^d$ *and* $p \in H^2(\Omega_h)$ *then*

$$|||\boldsymbol{u} - \boldsymbol{u}_h|||^2 \lesssim \sum_{E \in \Omega_h} \min\left\{\nu_E, h_E^2 \kappa_E^i\right\} h^4 \, |\boldsymbol{u}|_{3,E}^2 + \sum_{E \in \Omega_h} \min\left\{\frac{h_E^2}{\nu_E}, \kappa_E\right\} h^6 \, |\boldsymbol{f}|_{3,E}^2 \, ,$$

$$\|p - p_h\|_0 \lesssim |||\boldsymbol{u} - \boldsymbol{u}_h||| + h^2 \, |p|_{H^2(\Omega_h)} \, .$$

5.9 Numerical Tests

In this section we present two numerical experiments (in two space dimensions) to test the practical performances of the proposed VEM scheme (5.49). In the first academic test we numerically verify the theoretical convergence rate of Proposition 5.3. The second test assesses the method for the driven cavity problem. More numerical tests can be found, for instance, in [13, 15, 16, 18, 64]. Advices and details regarding coding can be found in [38], see also [9]. We here limit such discussion in showing the Newton linearization strategy (see for instance [62]) adopted to solve the non non linear equation (5.49). The Newton method applied to the (5.49) reads

$$\begin{cases} \text{until convergence find } (\boldsymbol{u}_h^{n+1}, \ p_h^{n+1}) \in \boldsymbol{V}_h \times Q_h, \text{ such that} \\ \nu \, a_h(\boldsymbol{u}_h^{n+1}, \ \boldsymbol{v}_h) + c_h(\boldsymbol{u}_h^{n+1}; \ \boldsymbol{u}_h^n, \boldsymbol{v}_h) + c_h(\boldsymbol{u}_h^n; \ \boldsymbol{u}_h^{n+1}, \boldsymbol{v}_h) + \\ \qquad + b(\boldsymbol{v}_h, \ p_h^{n+1}) = (\boldsymbol{f}_h, \ \boldsymbol{v}_h) + c_h(\boldsymbol{u}_h^n; \ \boldsymbol{u}_h^n, \boldsymbol{v}_h) \qquad \text{for all } \boldsymbol{v}_h \in \boldsymbol{V}_h, \\ b(\boldsymbol{u}_h^{n+1}, q_h) = 0 \qquad\qquad\qquad\qquad\qquad\qquad \text{for all } q_h \in Q_h. \end{cases}$$

starting from $(\boldsymbol{u}_h^0, \ p_h^0) = (\boldsymbol{0}, 0)$. Notice that at each step of the Newton iteration the solution $\boldsymbol{u}_h^{n+1}$ is still divergence-free, therefore the linearization procedure does non affect the divergence-free property of the final discrete solution.

Test 1. Error Convergence
In this test we examine the convergence properties of the proposed scheme (5.49) in the light of Proposition 5.3. In order to compute the VEM error between the exact solution $\boldsymbol{u}_{\text{ex}}$ and the VEM solution $\boldsymbol{u}_h$, we consider the computable error quantities

$$
\text{err}(\boldsymbol{u}_h, H^1) := \left(\sum_{E \in \Omega_h} \| \nabla \boldsymbol{u}_{\text{ex}} - \Pi_1^{0,E} \nabla \boldsymbol{u}_h \|_{L^2(E)}^2 \right)^{1/2} ,
$$

$$
\text{err}(\boldsymbol{u}_h, L^2) := \left(\sum_{E \in \Omega_h} \| \boldsymbol{u}_{\text{ex}} - \Pi_2^{0,E} \boldsymbol{u}_h \|_{L^2(E)}^2 \right)^{1/2} .
$$

For the pressure error we simply take $\text{err}(p_h, L^2) := \| p - p_h \|_{0,\Omega}$.

We consider the Navier-Stokes equation on the unit square $\Omega = [0, 1]^2$, the viscosity is $\nu = 1$, the load term and the Dirichlet boundary conditions are chosen in accordance with the analytical solution

$$
\boldsymbol{u}_{\text{ex}}(x, y) = e^x \begin{pmatrix} \sin y + y \cos y - x \sin y \\ -x \cos y - y \sin y - \cos y \end{pmatrix} \qquad p_{\text{ex}}(x, y) = \sin(\pi x) \cos(4\pi y) .
$$

The domain Ω is partitioned with the following sequences of polygonal meshes: QUADRILATERAL distorted meshes, TRIANGULAR meshes, CVT (Centroidal Voronoi Tessellations) meshes, RANDOM Voronoi meshes (see Fig. 5.6). For the generation of the Voronoi meshes we used the code Polymesher [63]. For each family of meshes we take the sequence with diameter $h = 2^{-2}, 2^{-3}, 2^{-4}, 2^{-5}, 2^{-6}$.

In Fig. 5.7 we display the errors $\text{err}(\boldsymbol{u}_h, H^1)$, $\text{err}(\boldsymbol{u}_h, L^2)$ and $\text{err}(p_h, L^2)$ for the the sequences of meshes aforementioned. We notice that the theoretical predictions of Proposition 5.3 are confirmed, moreover we observe that the method is robust with respect to the mesh distortion.

QUADRILATERAL   TRIANGULAR   VORONOI   RANDOM
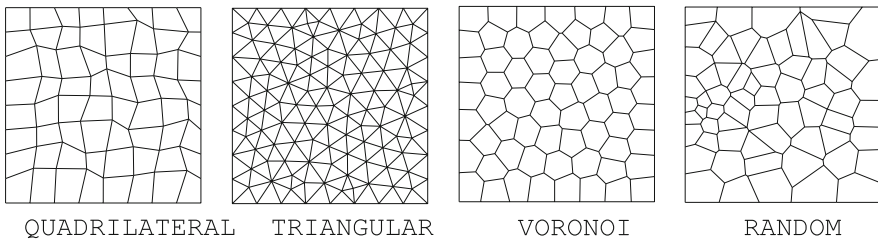
Fig. 5.6 Test 1. Example of the adopted polygonal meshes
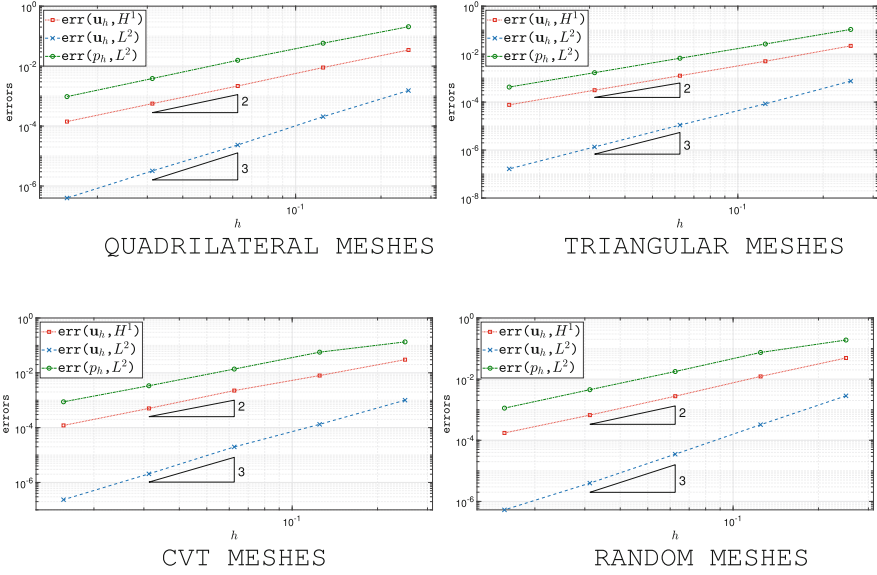
Fig. 5.7 Test 1. Convergence lines for the VEM (5.49)

Test 2. Driven Cavity

In the present test we consider the driven cavity problem on the domain $\Omega = [0, 1]^2$. We take viscosity $\nu = 100$, $\boldsymbol{f} = \boldsymbol{0}$ and Dirichlet boundary conditions

$$\boldsymbol{u}_{|\Gamma} = (1, 0)^{\mathrm{T}}, \qquad \text{and} \qquad \boldsymbol{u}_{|\partial\Omega\backslash\Gamma} = \boldsymbol{0},$$

where $\Gamma := [0, 1] \times \{1\}$. For this problem an exact solution is not available. The domain is partitioned with a sequence of Cartesian meshes with diameter $h = 2^{-2}, 2^{-3}, 2^{-4}, 2^{-5}, 2^{-6}$. In Fig. 5.8 we show the quiver of the numerical velocity $\boldsymbol{u}_h$ (left) and the contour plot of $|\boldsymbol{u}_h|$ (right) obtained with the mesh with $h = 2^{-5}$. The plots appear similar to the results obtained by several authors (see for instance [45, 51]).

Moreover the approximated L^2-norm of the numerical solution, i.e.

$$\texttt{norm}(\boldsymbol{u}_h, L^2) := \left(\sum_{E \in \Omega_h} \|\Pi_2^{0,E} \boldsymbol{u}_h\|_{L^2(E)}^2 \right)^{1/2}$$

converges to the value obtained with a finite volume solver $\approx 2.62\mathrm{e}{-01}$. The results are exhibited in Table 5.2.
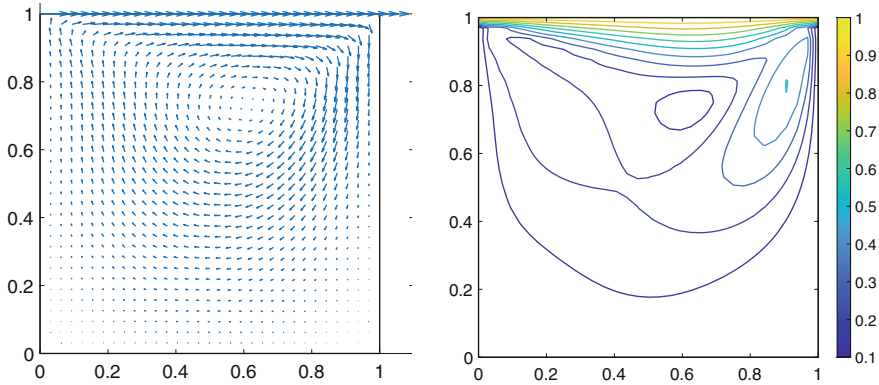
Fig. 5.8 Test 2. Quiver of the numerical velocity $\boldsymbol{u}_h$ (left), contour plot of $|\boldsymbol{u}_h|$ (right)

Table 5.2 Test 2. Approximated L^2-norm of the numerical solution

1/h	4	8	16	32	64
norm($\boldsymbol{u}_h, L^2$)	2.3576e−01	2.4293e−01	2.5169e−01	2.5679e−01	2.5955e−01

5.10 Conclusions

In the present contribution we gave an overview of the so-called divergence-free virtual elements for the Navier-Stokes equation. In particular we showed how to explore the flexibility of virtual elements construction in order to design a virtual element space for the velocities such that the discrete velocity solution is pointwise divergence-free. We stress that this feature is not shared by most of the standard mixed FEMs, where the divergence-free constraint is imposed only in a weak (relaxed) sense. In addition to the important flexibility of dealing with general (possibly curved) polygonal meshes and polyhedral meshes, we showed that the divergence-free construction of the proposed virtual element entails the following advantages:

1. the error components partly decouple, namely the influence of the pressure in the velocity error is weaker with respect to standard inf-sup stable elements;
2. the resulting scheme is equivalent to a suitable reduced problem, observing the internal DoFs can be automatically ignored in the final linear system;
3. it enjoys an underlying discrete Stokes complex structure;
4. the discrete velocity space is uniformly stable for the Darcy equation.

References

1. R.A. Adams, *Sobolev Spaces*, vol. 65. Pure and Applied Mathematics (Academic Press, New York, 1975)
2. J. Aghili, D.A. Di Pietro, An Advection-Robust hybrid high-order method for the oseen problem. J. Sci. Comput. **77**(3), 1310–1338 (2018)
3. B. Ahmad, A. Alsaedi, F. Brezzi, L.D. Marini, A. Russo, Equivalent projectors for virtual element methods. Comput. Math. Appl. **66**(3), 376–391 (2013)
4. P.F. Antonietti, L. Beirão da Veiga, D. Mora, M. Verani, A stream virtual element formulation of the Stokes problem on polygonal meshes. SIAM J. Numer. Anal. **52**(1), 386–404 (2014)
5. P. Antonietti, M. Verani, C. Vergara, S. Zonca, Numerical solution of fluid-structure interaction problems by means of a high order Discontinuous Galerkin method on polygonal grids. Finite Elem. Anal. Des. **159**, 1–14 (2019)
6. P. Antonietti, L. Mascotto, M. Verani, S. Zonca, Stability analysis of polytopic Discontinuous Galerkin approximations of the Stokes problem with applications to fluid-structure interaction problems. J. Sci. Comput., **90**(1), 23 (2022)
7. D.N. Arnold, R.S. Falk, R. Winther, Differential complexes and stability of finite element methods. I. The de Rham complex, in *Compatible Spatial Discretizations*, vol. 142. The IMA Volumes in Mathematics and its Applications (Springer, New York, 2006), pp. 24–46
8. L. Beirão da Veiga, F. Brezzi, A. Cangiani, G. Manzini, L.D. Marini, A. Russo, Basic principles of virtual element methods. Math. Models Methods Appl. Sci. **23**(1), 199–214 (2013)
9. L. Beirão da Veiga, F. Brezzi, L.D. Marini, A. Russo, The Hitchhiker's Guide to the virtual element method. Math. Models Methods Appl. Sci. **24**(8), 1541–1573 (2014)
10. L. Beirão da Veiga, K. Lipnikov, G. Manzini, *The Mimetic Finite Difference Method for Elliptic Problems*, vol. 11. MS & A (Springer, Berlin, 2014)
11. L. Beirão da Veiga, F. Brezzi, L.D. Marini, A. Russo, H(div) and H(**curl**)-conforming virtual element methods. Numer. Math. **133**(2), 303–332 (2016)
12. L. Beirão da Veiga, F. Dassi, A. Russo, High-order virtual element method on polyhedral meshes. Comput. Math. Appl. **74**(5), 1110–1122 (2017)
13. L. Beirão da Veiga, C. Lovadina, G. Vacca, Divergence free virtual elements for the Stokes problem on polygonal meshes. ESAIM Math. Model. Numer. Anal. **51**(2), 509–535 (2017)
14. L. Beirão da Veiga, C. Lovadina, A. Russo, Stability analysis for the virtual element method. Math. Mod. Meth. Appl. Sci. **27**(13), 2557–2594 (2017)
15. L. Beirão da Veiga, F. Dassi, G. Vacca, The Stokes complex for Virtual Elements in three dimensions. Math. Models Methods Appl. Sci. **30**(3), 477–512 (2018)
16. L. Beirão da Veiga, C. Lovadina, G. Vacca, Virtual elements for the Navier-Stokes problem on polygonal meshes. SIAM J. Numer. Anal. **56**(3), 1210–1242 (2018)
17. L. Beirão da Veiga, A. Russo, G. Vacca, The Virtual Element Method with curved edges. ESAIM Math. Model. Numer. Anal. **53**(2), 375–404 (2019)
18. L. Beirão da Veiga, D. Mora, G. Vacca, The Stokes complex for virtual elements with application to Navier–Stokes flows. J. Sci. Comput. **81**(2), 990–1018 (2019)
19. L. Beirão da Veiga, F. Brezzi, L.D. Marini, A. Russo, Polynomial preserving virtual elements with curved edges. Math. Models Methods Appl. Sci. **30**(8), 1555–1590 (2020)
20. L. Beirão da Veiga, C. Canuto, R.H. Nochetto, G. Vacca, Equilibrium analysis of an immersed rigid leaflet by the virtual element method. Math. Models Methods Appl. Sci. **31**(7), 1323–1372 (2021)
21. S. Bertoluzza, M. Pennacchio, D. Prada, High order VEM on curved domains. Atti Accad. Naz. Lincei Rend. Lincei Mat. Appl. **30**(2), 391–412 (2019)
22. D. Boffi, F. Brezzi, M. Fortin, *Mixed Finite Element Methods and Applications*, vol. 44. Springer Series in Computational Mathematics (Springer, Heidelberg, 2013)
23. L. Botti, D.A. Di Pietro, J. Droniou, A Hybrid High-Order discretisation of the Brinkman problem robust in the Darcy and Stokes limits. Comput. Methods Appl. Mech. Eng. **341**, 278–310 (2018)

24. S.C. Brenner, Q. Guan, L.Y. Sung, Some estimates for virtual element methods. Comput. Methods Appl. Math. **17**(4), 553–574 (2017)
25. S.C. Brenner, L.Y. Sung, Virtual element methods on meshes with small edges or faces. Math. Models Methods Appl. Sci. **28**(7), 1291–1336 (2018)
26. F. Brezzi, L. D. Marini, Finite elements and virtual elements on classical meshes. Vietnam J. Math. **49**, 871–899 (2021)
27. F. Brezzi, L.D. Marini, Virtual element method for plate bending problems. Comput. Methods Appl. Mech. Eng. **253**, 455–462 (2013)
28. H.C. Brinkman, A calculation of the viscous force exerted by a flowing fluid on a dense swarm of particles. Appl. Sci. Res. **1**(1), 27–34 (1949)
29. E. Caceres, G.N. Gatica, A mixed virtual element method for the pseudostress–velocity formulation of the Stokes problem. IMA J. Numer. Anal. **37**(1), 296–331 (2016)
30. E. Caceres, G.N. Gatica, F.A. Sequeira, A mixed virtual element method for the Brinkman problem. Math. Mod. Meth. Appl. Sci. **27**(04), 707–743 (2017)
31. E. Cáceres, G.N. Gatica, F.A. Sequeira, A mixed virtual element method for quasi-Newtonian Stokes flows. SIAM J. Numer. Anal. **56**(1), 317–343 (2018)
32. A. Cangiani, V. Gyrya, G. Manzini, The nonconforming virtual element method for the Stokes equations. SIAM J. Numer. Anal. **54**(6), 3411–3435 (2016)
33. D. Castañón Quiroz, D.A. Di Pietro, A Hybrid High-Order method for the incompressible Navier–Stokes problem robust for large irrotational body forces. Comput. Math. Appl. **79**(9), 2655–2677 (2020)
34. L. Chen, F. Wang, A divergence free weak virtual element method for the Stokes Problem on polytopal meshes. J. Sci. Comput. **78**(2), 864–886 (2019)
35. A. Chernov, C. Marcati, L. Mascotto, p- and hp- virtual elements for the Stokes problem. Adv. Comput. Math. **47**(2) (2021). Article number: 24
36. B. Cockburn, G. Fu, W. Qiu, A note on the devising of superconvergent HDG methods for Stokes flow by M-decompositions. IMA J. Numer. Anal. **37**(2), 730–749 (2017)
37. F. Dassi, S. Scacchi, Parallel block preconditioners for three-dimensional virtual element discretizations of saddle-point problems. Comput. Methods Appl. Mech. Eng. **372** (2020). Article number: 113424
38. F. Dassi, G. Vacca, Bricks for mixed high-order virtual element method: projectors and differential operators. Appl. Numer. Math. **155**, 140–159 (2020)
39. D.A. Di Pietro, S. Krell, A hybrid high-order method for the steady incompressible Navier-Stokes problem. J. Sci. Comput. **74**(3), 1677–1705 (2018)
40. R.S. Falk, M. Neilan, Stokes complexes and the construction of stable finite elements with pointwise mass conservation. SIAM J. Numer. Anal. **51**(2), 1308–1326 (2013)
41. D. Frerichs, C. Merdon, Divergence-preserving reconstructions on polygons and a really pressure-robust virtual element method for the Stokes problem. IMA J. Numer. Anal. **42**(1), 597–619 (2020)
42. G.N. Gatica, M. Munar, F.A. Sequeira, A mixed virtual element method for a nonlinear Brinkman model of porous media flow. Calcolo **55**(2) (2018). Art. 21, 36
43. G.N. Gatica, M. Munar, F.A. Sequeira, A mixed virtual element method for the Navier–Stokes equations. Math. Mod. Meth. Appl. Sci. **28**(14), 2719–2762 (2018)
44. N. Gauger, A. Linke, P. Schroeder, On high-order pressure-robust space discretisations, their advantages for incompressible high Reynolds number generalised Beltrami flows and beyond. SMAI J. Comput. Math. **5**, 88–129 (2019)
45. U. Ghia, K.N. Ghia, C.T. Shin, High-Re solutions for incompressible flow using the Navier-Stokes equations and a multigrid method. J. Comput. Phys. **48**(3), 387–411 (1982)
46. V. Girault, P.-A. Raviart, *Finite Element Approximation of the Navier-Stokes Equations*, vol. 749. Lecture Notes in Mathematics (Springer, Berlin, 1979)
47. J. Guzmán, M. Neilan, Conforming and divergence-free Stokes elements on general triangular meshes. Math. Comp. **83**(285), 15–36 (2014)

48. J. Guzmán, M. Neilan, Inf-sup stable finite elements on barycentric refinements producing divergence–free approximations in arbitrary dimensions. SIAM J. Numer. Anal. **56**(5), 2826–2844 (2018)
49. J. Guzmán, L.R. Scott, The Scott-Vogelius finite elements revisited. Math. Comp. **88**(316), 515–529 (2019)
50. V. John, A. Linke, C. Merdon, M. Neilan, L.G. Rebholz, On the divergence constraint in mixed finite element methods for incompressible flows. SIAM Rev. **59**(3), 492–544 (2017)
51. A. Linke, On the role of the Helmholtz decomposition in mixed methods for incompressible flows and a new variational crime. Comput. Methods Appl. Mech. Eng. **268**, 782–800 (2014)
52. A. Linke, C. Merdon, On velocity errors due to irrotational forces in the Navier-Stokes momentum balance. J. Comput. Phys. **313**, 654–661 (2016)
53. A. Linke, C. Merdon, Pressure-robustness and discrete Helmholtz projectors in mixed finite element methods for the incompressible Navier-Stokes equations. Comput. Methods Appl. Mech. Eng. **311**, 304–326 (2016)
54. K. Lipnikov, G. Manzini, M. Shashkov, Mimetic finite difference method. J. Comput. Phys. **257**, 1163–1227 (2014)
55. K. Lipnikov, D. Vassilev, I. Yotov, Discontinuous Galerkin and mimetic finite difference methods for coupled Stokes-Darcy flows on polygonal and polyhedral grids. Numer. Math. **126**(2), 321–360 (2014)
56. X. Liu, Z. Chen, The nonconforming virtual element method for the Navier-Stokes equations. Adv. Comput. Math. **45**(1), 51–74 (2019)
57. X. Liu, J. Li, Z. Chen, A nonconforming virtual element method for the Stokes problem on general meshes. Comput. Methods Appl. Mech. Eng. **320**, 694–711 (2017)
58. X. Liu, R. Li, Z. Chen, A virtual element method for the coupled Stokes–Darcy problem with the Beaver–Joseph–Saffman interface condition. Calcolo **56**(4) (2019). Article number: 48
59. X. Liu, R. Li, Y. Nie, A divergence-free reconstruction of the nonconforming virtual element method for the Stokes problem. Comput. Methods Appl. Mech. Eng. **372** (2020). Article number: 113351
60. M. Munar, F.A. Sequeira, A posteriori error analysis of a mixed virtual element method for a nonlinear Brinkman model of porous media flow. Comput. Math. Appl. **80**(5), 1240–1259 (2020)
61. S. Natarajan, On the application of polygonal finite element method for Stokes flow – a comparison between equal order and different order approximation. Comput. Aided Geom. Design **77** (2020). Article number: 101813
62. A. Quarteroni, A. Valli, *Numerical Approximation of Partial Differential Equations*, vol. 23. Springer Series in Computational Mathematics (Springer, Berlin, 1994)
63. C. Talischi, G.H. Paulino, A. Pereira, I.F.M. Menezes, Polymesher: a general-purpose mesh generator for polygonal elements written in matlab. Struct. Multidisc Optimiz. **45**(3), 309–328 (2012)
64. G. Vacca, An H^1-conforming virtual element for Darcy and Brinkman equations. Math. Models Methods Appl. Sci. **28**(1), 159–194 (2018)
65. G. Wang, Y. Wang, Y. He, A posteriori error estimates for the virtual element method for the stokes problem. J. Sci. Comput. **84**(2) (2020). Article number: 37
66. J. Zhao, B. Zhang, S. Mao, S. Chen, The nonconforming virtual element method for the Darcy–Stokes problem. Comput. Methods Appl. Mech. Eng. **370** (2020). Article number: 113251

Chapter 6
A Virtual Marriage à la Mode: Some Recent Results on the Coupling of VEM and BEM

Gabriel N. Gatica, Antonio Márquez, and Salim Meddahi

Abstract The aim of this chapter is to present in a unified way some recent results on the combined use of the virtual element method (VEM) and the boundary element method (BEM) to numerically solve linear transmission problems in 2D and 3D. As models we consider an elliptic equation in divergence form holding in an annular domain coupled with the Laplace equation in the corresponding unbounded exterior region, and an acoustic scattering problem determined by a bounded obstacle and a time harmonic incident wave, so that the scattered field, and hence the total wave as well, satisfies the homogeneous Helmholtz equation. Both sets of corresponding equations are complemented with proper transmission conditions at the respective interfaces, and suitable radiation conditions at infinity. We employ the usual primal formulation and the associated VEM approach in the respective bounded regions, and combine it, by means of either the Costabel & Han approach or a recent modification of it, with the boundary integral equation method in the exterior domain, thus yielding two possible VEM/BEM schemes. The first method is valid only in 2D and considers the main variable and its normal derivative as unknowns, whereas the second one, which includes additionally the trace of the former as a third unknown, is applicable in both dimensions. The well-posedness of the continuous and discrete formulations is established and a priori error estimates together with corresponding rates of convergence are derived. Finally, several

G. N. Gatica (✉)
CI^{2}MA and Departamento de Ingegnerìa Matemática, Universidad de Concepción, Concepción, Chile
e-mail: ggatica@ci2ma.udec.cl

A. Márquez
Departamento de Construcción e Ingeniería de Fabricación, Universidad de Oviedo, Oviedo, Spain
e-mail: amarquez@uniovi.es

S. Meddahi
Departamento de Matemáticas, Facultad de Ciencias, Universidad de Oviedo, Oviedo, Spain
e-mail: salim@uniovi.es

numerical examples in 2D illustrating the performance of the proposed discrete schemes are reported.

6.1 Introduction

The concept "marriage à la mode" was originally employed in [36], one of the seminal papers on the subject back in the 70', to refer to the combined use (also named coupling) of the finite element (FEM) and boundary element (BEM) methods and the advantages of performing this "marriage". The mathematical fundamentals of this novel idea was provided either around the same time or short after in [10, 35] and [26], and the first resulting method, which uses a single boundary integral equation arising from the Green representation formula of the solution, is known nowadays as the Johnson & Nédélec approach. Until a couple of decades after, the applicability of this technique, being based on the compactness of a boundary integral operator involved and the Fredholm theory, was restricted mainly to transmission problems involving the Laplace operator. For other problems of interest, such as the Lamé system, the compactness property does not hold and hence the method could not be employed to this model.

The aforementioned limitation motivated the coupling procedures by Costabel and Han in [17] and [24], respectively, which were both based on the incorporation of a second boundary integral equation, namely the one that is obtained after applying the normal derivative (or traction in the case of elasticity) to the Green formula. In this way, the former technique yielded a symmetric and non-positive definite scheme, whereas the latter, on the contrary, gave rise to a non-symmetric but elliptic system. However, one simply refers to either one of them as the Costabel & Han method since they only differ in the sign of a common integral identity. In turn, the historical drawback of the Johnson & Nédélec coupling method, was surprisingly solved in [31] (see also [32] and [33]), where it was shown that actually all Galerkin schemes for this approach are stable, thus extending its use to other elliptic equations and to arbitrary polygonal/polyhedral domains.

On the other hand, the virtual element method (VEM) has become during the last decade a very promising technique to numerically solve diverse linear and nonlinear boundary value problems in continuum mechanics. Among its many applications, we can mention linear elasticity, plate bending problems, the Steklov eigenvalue problem, acoustic vibration, and diverse models in fluid mechanics. In particular, the latter includes stream function-based, divergence free, and non-conforming virtual element methods for the classical velocity-pressure formulation of the Stokes equation, primal virtual element approaches for the Darcy, Brinkman, and Navier-Stokes models, and dual-mixed variational formulations yielding mixed virtual element schemes for the Stokes equation, the linear and nonlinear Brinkman problems, the nonlinear Stokes equation arising from quasi-Newtonian Stokes flows, and the Navier-Stokes equations, as well. A representative, though not exhaustive, list of works concerning theoretical and applied aspects of VEM, besides

certainly the other chapters of the present proceedings, includes [2–4], [5, 7–9, 11–14, 23, 29, 34] and the references therein.

In the same direction as above, and aiming to continue extending the applicability of VEM, we have recently introduced and analyzed in [21] and [22], up to our knowledge for the first time, the combined use of VEM and BEM for solving transmission problems in 2D and 3D. The own advantages of each method, properly discussed in those references, are certainly transferred to the combined use of them. The main purpose of this chapter is precisely to present a unified treatment of the main tools and results from [21] and [22]. While specific models are considered there, the main motivation of these works and hence of the present one, is to settle the main basis allowing to analyze later on any other particular model of interest that is solved via the coupling of VEM and BEM. In particular, this might be the case for unbounded domains with a bounded complex heterogeneous region for which the corresponding partitions are constructed in a much easier way by using nonconvex elements. Other recent contributions on the coupling of VEM and BEM, mainly referring to computational and applied aspects of it, are presented in [1] and [18].

Our models from [21] and [22] are described in what follows. To this end, we let Ω_0 and $\mathscr{O}$ be two simply connected and bounded polygonal/polyhedral domains in $\mathbb{R}^d$, $d = 2, 3$, with boundaries $\Gamma_0 := \partial\Omega_0$ and $\Gamma := \partial\mathscr{O}$, respectively, such that $\Omega_0 \subseteq \mathscr{O}$. In addition, we introduce the annular region $\Omega := \mathscr{O} \setminus \overline{\Omega}_0$ and the exterior domain $\mathscr{O}_e := \mathbb{R}^d \setminus \overline{\mathscr{O}}$ (see Fig. 6.1 below), and denote by $\boldsymbol{n}$ the unit outward normal to Γ pointing towards $\mathscr{O}_e$.

The first model consists of an elliptic equation in divergence form holding in Ω coupled with the Laplace equation in the unbounded exterior region $\mathscr{O}_e$, together with transmission conditions on the interface Γ and a suitable radiation condition at infinity, that is we look for $u : \Omega \to \mathbb{R}$ and $u_e : \mathscr{O}_e \to \mathbb{R}$ such that

$$
\begin{aligned}
-\operatorname{div}(\kappa\nabla u) &= f \quad \text{in} \quad \Omega, \quad u = 0 \quad \text{on} \quad \Gamma_0, \\
u &= u_e \quad \text{on} \quad \Gamma, \quad \kappa\frac{\partial u}{\partial\boldsymbol{n}} = \frac{\partial u_e}{\partial\boldsymbol{n}} \quad \text{on} \quad \Gamma, \\
\Delta u_e &= 0 \quad \text{in} \quad \mathscr{O}_e, \quad u_e(x) = O\big(|x|^{-1}\big) \quad \text{as} \quad |x| \to \infty,
\end{aligned}
\tag{6.1}
$$

Fig. 6.1 2D geometry of the model problems
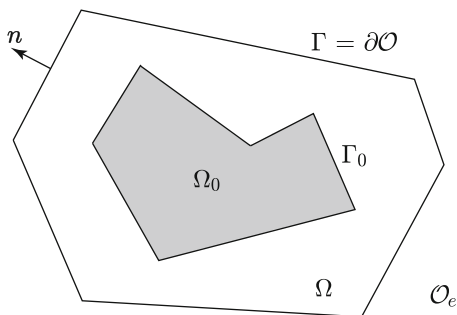
where $f \in L^2(\Omega)$ and $\kappa \in L^\infty(\Omega)$ are given functions. Additionally, we assume that there exists a constant $\underline{\kappa} > 0$ such that

$$\underline{\kappa} \leq \kappa(x) \leq \overline{\kappa} := \|\kappa\|_{L^\infty(\Omega)} \qquad \text{for almost all } x \in \Omega \,.$$

Throughout the rest of the paper we call (6.1) the Poisson model.

In turn, in order to define the second model we let $\vartheta : \mathbb{R}^d \to \mathbb{C}$ be a complex-valued piecewise constant function satisfying $\text{Re}(\vartheta(x)) > 0$ and $\text{Im}(\vartheta(x)) \geq 0$ for all $x \in \mathbb{R}^d$, and such that $1 - \vartheta(x)$ has a compact support contained in $\mathscr{O}$. Also, we let $\kappa > 0$ be a given constant, and let w be a function satisfying the Helmholtz equation $\Delta w + \kappa^2 w = 0$ in $\mathbb{R}^d$. Then, we consider an obstacle occupying $\mathscr{O}$ with refractive index given by ϑ, and assume that w acts as a time harmonic incident wave, so that the scattered field u^s, and hence the total wave $u := w + u^s$ as well, satisfy the homogeneous Helmholtz equation in $\mathscr{O}_e$. In this way, the resulting coupled problem, which is complemented with suitable transmission conditions on Γ and the Sommerfeld radiation condition at infinity, reduces to find $u : \mathscr{O} \to \mathbb{C}$ and $u^s : \mathscr{O}_e \to \mathbb{C}$ such that

$$\Delta u + \kappa^2 \vartheta(x)\, u = 0 \quad \text{in} \quad \mathscr{O} \,,$$
$$u = u^s + w \quad \text{on} \quad \Gamma \,, \quad \frac{\partial u}{\partial n} = \frac{\partial u^s}{\partial n} + \frac{\partial w}{\partial n} \quad \text{on} \quad \Gamma \,, \tag{6.2}$$
$$\Delta u^s + \kappa^2\, u^s = 0 \quad \text{in} \quad \mathscr{O}_e \,,$$
$$\frac{\partial u^s}{\partial r} - \iota \kappa u^s = o(r^{\frac{1-d}{2}}) \quad \text{when} \quad r := |x| \to \infty \,.$$

The above is named from now on the Helmholtz model.

The rest of the chapter is organized as follows. In Sect. 6.2 we first describe the basic aspects of the boundary integral equation method (BIEM), and then introduce and analyze the Costabel & Han and modified Costabel & Han coupling methods. The discrete VEM/BEM schemes for the Costabel & Han approach as applied to both models from Sect. 6.1 are studied in Sect. 6.3 for the 2D case. Next, in Sect. 6.4 we explain the necessity of introducing the modified Costabel & Han coupling procedure in the 3D case and introduce and analyze its applicability to the VEM/BEM scheme for the Poisson model. Finally, in Sect. 6.5 we illustrate the performance of our discrete methods with several numerical results in 2D.

We end this section with some notations to be employed throughout the rest of the paper. In particular, given a real number $r \geq 0$ and a polyhedron $\mathscr{G} \subseteq \mathbb{R}^d$, $d \in \{2, 3\}$, we denote by $\|\cdot\|_{r,\mathscr{G}}$ and $|\cdot|_{r,\mathscr{G}}$, respectively, the norm and seminorm of the usual Sobolev space $H^r(\mathscr{G})$ (cf. [27]). Also, we use the convention $L^2(\mathscr{G}) := H^0(\mathscr{G})$, and for all $t \in (0, 1]$ we let $H^{-t}(\partial \mathscr{G})$ be the dual of $H^t(\partial \mathscr{G})$ with respect to the pivot space $L^2(\partial \mathscr{G})$. In addition, we set $\mathscr{P}_{-1} = \{0\}$, and for a nonnegative integer m, $\mathscr{P}_m$ is the space of polynomials of degree $\leq m$. Then, given a set $D \subseteq \mathbb{R}^d$, $d \in \{2, 3\}$, $\mathscr{P}_m(D)$ stands for the restriction of $\mathscr{P}_m$ to D.

6.2   The Coupling Procedures

Here we introduce and analyze the continuous formulations of the two coupling procedures that we utilize for the combination of VEM and BEM. Both approaches require the basic aspects of the boundary integral equation method (BIEM) as applied to the Laplace and Helmholtz equations, which is addressed in the following section.

6.2.1   BIEM for Laplace and Helmholtz

We begin by letting γ and $\gamma_{\boldsymbol{n}}$ be the trace and normal trace operators, respectively, on Γ, acting either from $\mathscr{O}$ (equivalently from Ω) or from $\mathscr{O}_e$. Then, the harmonic solution u_e in the exterior domain $\mathscr{O}_e$ (cf. third row of (6.1)) can be represented by the Green formula

$$u_e(\boldsymbol{x}) \; = \; \int_{\Gamma} \frac{\partial \mathbf{E}(|\boldsymbol{x} - \boldsymbol{y}|)}{\partial \boldsymbol{n}_y} \gamma u(\boldsymbol{y}) \, \mathrm{d}s_y \; - \; \int_{\Gamma} \mathbf{E}(|\boldsymbol{x} - \boldsymbol{y}|)\lambda(\boldsymbol{y}) \, \mathrm{d}s_y \qquad \forall \, \boldsymbol{x} \in \mathscr{O}_e \, ,$$

(6.3)

where

$$\mathbf{E}(|\boldsymbol{x} - \boldsymbol{y}|) := \begin{cases} \dfrac{1}{4\pi} \dfrac{1}{|\boldsymbol{x} - \boldsymbol{y}|} & \text{if } d = 3 \, , \\[2mm] -\dfrac{1}{2\pi} \log |\boldsymbol{x} - \boldsymbol{y}| & \text{if } d = 2 \, , \end{cases}$$

is the fundamental solution of the Laplace operator, and, according to the transmission conditions at the second row of (6.1), $\gamma u = \gamma u_e$ and $\lambda := \gamma_{\boldsymbol{n}}(\kappa \nabla u) = \gamma_{\boldsymbol{n}}(\nabla u_e)$ are the Cauchy data on the interface Γ. Then, applying γ and $\gamma_{\boldsymbol{n}}$ from $\mathscr{O}_e$ to (6.3) and its gradient, respectively, and employing the jump conditions on Γ of the two potentials in the right hand side of (6.3), we arrive at (cf. [25, 30])

$$\gamma u_e \; = \; \left(\frac{\mathrm{id}}{2} + K \right) \gamma u \; - \; V\lambda \quad \text{on} \quad \Gamma \, ,$$

(6.4)

and

$$\gamma_{\boldsymbol{n}}(\nabla u_e) \; = \; -\, W\gamma u \; + \; \left(\frac{\mathrm{id}}{2} - K^{\mathsf{t}} \right)\lambda \quad \text{on} \quad \Gamma \, ,$$

(6.5)

where V, K, K^{t} are the boundary integral operators representing the single, double and adjoint of the double layer, respectively, id is a generic identity operator, and W is the hypersingular operator. In this way, replacing γu_e and $\gamma_{\boldsymbol{n}}(\nabla u_e)$ by γu and λ,

respectively, (6.4) and (6.5) become

$$0 = \left(\frac{\mathrm{id}}{2} - K\right)\gamma u + V\lambda \quad \text{on} \quad \Gamma\,, \tag{6.6}$$

and

$$\lambda = -W\gamma u + \left(\frac{\mathrm{id}}{2} - K^{\mathsf{t}}\right)\lambda \quad \text{on} \quad \Gamma\,. \tag{6.7}$$

In turn, denoting by $H_0^{(1)}$ the Hankel function of order 0 and first type, it can be proved that the solution u^s of the homogeneous Helmholtz equation in $\mathcal{O}_e$ (cf. third row of (6.2)) admits the integral representation

$$u^s(\boldsymbol{x}) = \int_\Gamma \frac{\partial \mathbf{E}_\kappa(|\boldsymbol{x}-\boldsymbol{y}|)}{\partial \boldsymbol{n}_{\boldsymbol{y}}}\gamma u^s(\boldsymbol{y})\,\mathrm{d}s_{\boldsymbol{y}} - \int_\Gamma \mathbf{E}_\kappa(|\boldsymbol{x}-\boldsymbol{y}|)\lambda(\boldsymbol{y})\,\mathrm{d}s_{\boldsymbol{y}} \qquad \forall \boldsymbol{x} \in \mathcal{O}_e\,, \tag{6.8}$$

where

$$\mathbf{E}_\kappa(|\boldsymbol{x}-\boldsymbol{y}|) := \begin{cases} \dfrac{\imath}{4}H_0^{(1)}(\kappa|\boldsymbol{x}-\boldsymbol{y}|) & \text{if } d=2\,, \\[2mm] \dfrac{e^{\imath\kappa|\boldsymbol{x}-\boldsymbol{y}|}}{4\pi|\boldsymbol{x}-\boldsymbol{y}|} & \text{if } d=3\,, \end{cases}$$

is the fundamental solution of the Helmholtz equation with wave number κ, and $\lambda := \gamma_{\boldsymbol{n}}(\nabla u^s) = \dfrac{\partial u^s}{\partial \boldsymbol{n}}$. Next, proceeding similarly to the derivation of (6.6) and (6.7), which means now applying γ and $\gamma_{\boldsymbol{n}}$ to (6.8), and taking into account the corresponding jump properties of the potentials involved (see again [25, 30]), we arrive at

$$0 = \left(\frac{\mathrm{id}}{2} - K_\kappa\right)\gamma u^s + V_\kappa\lambda\,, \tag{6.9}$$

and

$$\lambda = -W_\kappa\gamma u^s + \left(\frac{\mathrm{id}}{2} - K_\kappa^{\mathsf{t}}\right)\lambda\,, \tag{6.10}$$

where V_κ, K_κ, K_κ^{t}, and W_κ are the boundary integral operators representing the single, double, adjoint of the double, and hypersingular layer potentials, respectively.

We end this section with some useful properties of the boundary integral operators involved in (6.6)–(6.7) and (6.9)–(6.10). Indeed, V, K, K^{t}, and W are

formally defined at almost every point $\boldsymbol{x} \in \Gamma$ by

$$
\begin{aligned}
V\lambda(\boldsymbol{x}) &:= \int_{\Gamma} \mathbf{E}(|\boldsymbol{x} - \boldsymbol{y}|)\lambda(\boldsymbol{y}) \, ds_{\boldsymbol{y}}, \\
K\varphi(\boldsymbol{x}) &:= \int_{\Gamma} \frac{\partial \mathbf{E}(|\boldsymbol{x} - \boldsymbol{y}|)}{\partial \boldsymbol{n}_{\boldsymbol{y}}} \, \varphi(\boldsymbol{y}) \, ds_{\boldsymbol{y}}, \\
K^{\mathbf{t}}\lambda(\boldsymbol{x}) &:= \int_{\Gamma} \frac{\partial \mathbf{E}(|\boldsymbol{x} - \boldsymbol{y}|)}{\partial \boldsymbol{n}_{\boldsymbol{x}}} \, \lambda(\boldsymbol{y}) \, ds_{\boldsymbol{y}}, \\
W\varphi(\boldsymbol{x}) &:= -\frac{\partial}{\partial \boldsymbol{n}_{\boldsymbol{x}}} \int_{\Gamma} \frac{\partial \mathbf{E}(|\boldsymbol{x} - \boldsymbol{y}|)}{\partial \boldsymbol{n}_{\boldsymbol{y}}} \, \varphi(\boldsymbol{y}) \, ds_{\boldsymbol{y}},
\end{aligned} \tag{6.11}
$$

for suitable functions λ and φ, whereas V_{κ}, K_{κ}, $K_{\kappa}^{\mathbf{t}}$, and W_{κ} are defined analogously to (6.11) by replacing $\mathbf{E}$ by $\mathbf{E}_{\kappa}$. Moreover, the main mapping properties of these operators are collected in the following lemma (cf. [30]).

Lemma 6.1 *The operators*

$$
V, V_{\kappa} : H^{-1/2+\sigma}(\Gamma) \to H^{1/2+\sigma}(\Gamma), \qquad K, K_{\kappa} : H^{1/2+\sigma}(\Gamma) \to H^{1/2+\sigma}(\Gamma)
$$

$$
K^{\mathbf{t}}, K_{\kappa}^{\mathbf{t}} : H^{-1/2+\sigma}(\Gamma) \to H^{-1/2+\sigma}(\Gamma), \qquad W, W_{\kappa} : H^{1/2+\sigma}(\Gamma) \to H^{-1/2+\sigma}(\Gamma),
$$

are continuous for all $\sigma \in [-1/2, \, 1/2]$.

Furthermore, we now let $\langle \cdot, \cdot \rangle$ be both the inner product in $L^2(\Gamma)$ and the duality pairing between $H^{-1/2}(\Gamma)$ and $H^{1/2}(\Gamma)$ with respect to the pivot space $L^2(\Gamma)$, and introduce the subspaces

$$
H_0^{1/2}(\Gamma) := \{\varphi \in H^{1/2}(\Gamma) : \quad \langle 1, \varphi \rangle = 0\}
$$

and

$$
H_0^{-1/2}(\Gamma) := \{\mu \in H^{-1/2}(\Gamma) : \quad \langle \mu, 1 \rangle = 0\}.
$$

Then, we have the following lemma providing ellipticity-type properties of the operators V and W (cf. [27, 30]).

Lemma 6.2 *There exist positive constants* α_V, C_V, *and* α_W *such that*

$$
\langle \bar{\mu}, \, V\mu \rangle \geq \alpha_V \, \|\mu\|_{-1/2,\Gamma}^2 \quad
\begin{cases}
\forall \mu \in H_0^{-1/2}(\Gamma), & \text{if } d = 2, \\
\forall \mu \in H^{-1/2}(\Gamma), & \text{if } d = 3,
\end{cases} \tag{6.12}
$$

$$
\langle \bar{\mu}, \, V\mu \rangle_{\Gamma} + |\langle \bar{\mu}, 1 \rangle|^2 \geq C_V \, \|\mu\|_{-1/2,\Gamma}^2 \quad \forall \mu \in H^{-1/2}(\Gamma) \quad \text{if } d = 2, \tag{6.13}
$$

and

$$\langle W\varphi,\ \bar{\varphi}\rangle\ \geq\ \alpha_W\ \|\varphi\|^2_{1/2,\Gamma}\quad\forall\,\varphi\in \mathrm{H}^{1/2}_0(\Gamma)\,. \tag{6.14}$$

We end this section by stressing that the operators associated to the Helmholtz equation, that is V_κ, K_κ, K^{t}_κ, and W_κ, may be regarded as compact perturbations of those corresponding to the Laplacian, that is V, K, K^{t}, and W. In fact, we have the following lemma (cf. [30]).

Lemma 6.3 *The operators*

$$V_\kappa - V:\ H^{-1/2}(\Gamma)\to H^{1/2}(\Gamma),\qquad K_\kappa - K:\ H^{1/2}(\Gamma)\to H^{1/2}(\Gamma)$$

$$K^{\mathsf{t}}_\kappa - K^{\mathsf{t}}:\ H^{-1/2}(\Gamma)\to H^{-1/2}(\Gamma),\qquad W_\kappa - W:\ H^{1/2}(\Gamma)\to H^{-1/2}(\Gamma),$$

are compact.

6.2.2 The Costabel & Han Coupling

Our first coupling method, which makes use of the pairs of boundary integral equations (6.6)–(6.7) and (6.9)–(6.10) to reformulate problems (6.1) and (6.2) in the bounded domains Ω and $\mathcal{O}$, respectively, is due to Costabel and Han (cf. [17] and [24]). More precisely, the reformulation of (6.1) reads: Find $u:\ \Omega\to\mathbb{R}$ and $\lambda:\Gamma\to\mathbb{R}$ such that

$$\begin{aligned}
-\operatorname{div}(\kappa\nabla u)\ &=\ f\quad\text{in}\quad\Omega\,,\quad u=0\quad\text{on}\quad\Gamma_0\,,\\
\kappa\frac{\partial u}{\partial\boldsymbol{n}}\ &=\ \lambda\quad\text{on}\quad\Gamma\,,\\
0\ &=\ \Big(\frac{\mathrm{id}}{2}-K\Big)\gamma u + V\lambda\quad\text{on}\quad\Gamma\,,\\
\lambda\ &=\ -W\gamma u + \Big(\frac{\mathrm{id}}{2}-K^{\mathsf{t}}\Big)\lambda\quad\text{on}\quad\Gamma\,,
\end{aligned} \tag{6.15}$$

whereas the one of (6.2) becomes: Find $u:\ \mathcal{O}\to\mathbb{C}$ and $\lambda:\Gamma\to\mathbb{C}$ such that

$$\begin{aligned}
\Delta u + \kappa^2\vartheta(\boldsymbol{x})\,u\ &=\ 0\quad\text{in}\quad\mathcal{O}\,,\\
\gamma u = \gamma u^s + \gamma w\quad\text{on}\quad\Gamma\,,\quad \frac{\partial u}{\partial\boldsymbol{n}}\ &=\ \lambda + \frac{\partial w}{\partial\boldsymbol{n}}\quad\text{on}\quad\Gamma\,,\\
0\ &=\ \Big(\frac{\mathrm{id}}{2}-K_\kappa\Big)\gamma u^s + V_\kappa\lambda\quad\text{on}\quad\Gamma\,,\\
\lambda\ &=\ -W_\kappa\gamma u^s + \Big(\frac{\mathrm{id}}{2}-K^{\mathsf{t}}_\kappa\Big)\lambda\quad\text{on}\quad\Gamma\,.
\end{aligned} \tag{6.16}$$

Then, introducing the spaces

$$X := \{v \in H^1(\Omega) : v|_{\Gamma_0} = 0\} \quad \text{and} \quad \mathbf{X} := X \times H_0^{-1/2}(\Gamma),$$

multiplying the first equation of the first row of (6.15) by $v \in X$, integrating the resulting expression by parts, replacing $\lambda = \kappa \dfrac{\partial u}{\partial \boldsymbol{n}}$ on Γ by the right hand side of the fourth row of (6.15), and finally testing the third row of (6.15) against $\mu \in H_0^{-1/2}(\Gamma)$, we arrive at the variational formulation: Find $(u, \lambda) \in \mathbf{X}$ such that

$$\int_{\Omega} \kappa \nabla u \cdot \nabla v + \langle W \gamma u, \gamma v \rangle - \langle \lambda, \left(\frac{\text{id}}{2} - K \right) \gamma v \rangle = \int_{\Omega} f v \quad \forall v \in X,$$

$$\langle \mu, V \lambda \rangle + \langle \mu, \left(\frac{\text{id}}{2} - K \right) \gamma u \rangle = 0 \qquad \forall \mu \in H_0^{-1/2}(\Gamma).$$

$$(6.17)$$

Equivalently, (6.17) can be rewritten as: Find $(u, \lambda) \in \mathbf{X}$ such that

$$\mathbf{A}\big((u, \lambda), (v, \mu)\big) = \mathbf{F}(v, \mu) \qquad \forall (v, \mu) \in \mathbf{X}, \qquad (6.18)$$

where

$$\mathbf{A}\big((z, \xi), (v, \mu)\big) := a(z, v) + \langle W \gamma z, \gamma v \rangle + \langle \mu, V \xi \rangle$$
$$+ \langle \mu, \left(\frac{\text{id}}{2} - K \right) \gamma z \rangle - \langle \xi, \left(\frac{\text{id}}{2} - K \right) \gamma v \rangle,$$

$$(6.19)$$

with

$$a(z, v) := \int_{\Omega} \kappa \nabla z \cdot \nabla v, \qquad (6.20)$$

and

$$\mathbf{F}(v, \mu) := \int_{\Omega} f v, \qquad (6.21)$$

for all $(z, \xi), (v, \mu) \in \mathbf{X}$.

Proceeding similarly to the derivation of (6.17), we readily find that the variational formulation of (6.16) reads: Find $(u, \lambda) \in \mathbb{X} := H^1(\mathcal{O}) \times H^{-1/2}(\Gamma)$ such that

$$\mathbb{A}_\kappa\big((u, \lambda), (v, \mu)\big) = \mathbb{F}(v, \mu) \qquad \forall (v, \mu) \in \mathbb{X}, \qquad (6.22)$$

where

$$
\mathbb{A}_\kappa\big((z, \xi), (v, \mu)\big) := a_\kappa(z, v) + \big\langle W_\kappa \gamma z, \gamma v\big\rangle + \big\langle \mu, V_\kappa \xi\big\rangle
$$
$$
+ \Big\langle \mu, \Big(\frac{\mathrm{id}}{2} - K_\kappa\Big)\gamma z\Big\rangle - \Big\langle \xi, \Big(\frac{\mathrm{id}}{2} - K_\kappa\Big)\gamma v\Big\rangle, \tag{6.23}
$$

with

$$
a_\kappa(z, v) := \int_{\mathcal{O}} \nabla z \cdot \nabla v - \kappa^2 \int_{\mathcal{O}} \vartheta z v, \tag{6.24}
$$

and

$$
\mathbb{F}(v, \mu) := \Big\langle \frac{\partial w}{\partial \boldsymbol{n}} + W_\kappa \gamma w, \gamma v\Big\rangle + \Big\langle \mu, \Big(\frac{\mathrm{id}}{2} - K_\kappa\Big)\gamma w\Big\rangle,
$$

for all (z, ξ), $(v, \mu) \in X$.

6.2.3 The Modified Costabel & Han Coupling

We now consider the modified Costabel & Han coupling method that was introduced for the first time in [21, Section 4.2]. More precisely, in addition to $\lambda = \kappa \frac{\partial u}{\partial \boldsymbol{n}}$ (cf. (6.15)) or $\lambda = \gamma_{\boldsymbol{n}}(\nabla u^s)$ (cf. (6.16)), this approach introduces the trace $\psi := \gamma u$ or $\psi := \gamma u^s$ as a boundary unknown as well of the formulation. As a consequence, instead of (6.3) and (6.8), the harmonic function u_e and the scattered field u^s are computed as

$$
u_e(\boldsymbol{x}) = \int_\Gamma \frac{\partial \mathbf{E}(|\boldsymbol{x} - \boldsymbol{y}|)}{\partial \boldsymbol{n}_{\boldsymbol{y}}} \psi(\boldsymbol{y})\,\mathrm{d}s_{\boldsymbol{y}} - \int_\Gamma \mathbf{E}(|\boldsymbol{x} - \boldsymbol{y}|)\lambda(\boldsymbol{y})\,\mathrm{d}s_{\boldsymbol{y}} \qquad \forall\,\boldsymbol{x} \in \mathcal{O}_e,
$$

and

$$
u^s(\boldsymbol{x}) = \int_\Gamma \frac{\partial E_\kappa(|\boldsymbol{x} - \boldsymbol{y}|)}{\partial \boldsymbol{n}_{\boldsymbol{y}}} \psi(\boldsymbol{y})\,\mathrm{d}s_{\boldsymbol{y}} - \int_\Gamma E_\kappa(|\boldsymbol{x} - \boldsymbol{y}|)\lambda(\boldsymbol{y})\,\mathrm{d}s_{\boldsymbol{y}} \qquad \forall\,\boldsymbol{x} \in \mathcal{O}_e,
$$

respectively, whence the corresponding pairs of identities (6.6)–(6.7) and (6.9)–(6.10) become

$$
0 = \Big(\frac{\mathrm{id}}{2} - K\Big)\psi + V\lambda \quad \text{on} \quad \Gamma,
$$
$$
\lambda = -W\psi + \Big(\frac{\mathrm{id}}{2} - K^{\mathsf{t}}\Big)\lambda \quad \text{on} \quad \Gamma,
$$

and

$$0 = \left(\frac{\mathrm{id}}{2} - K_\kappa\right)\psi + V_\kappa\lambda \quad \text{on} \quad \Gamma,$$

$$\lambda = -W_\kappa\psi + \left(\frac{\mathrm{id}}{2} - K_\kappa^{\mathsf{t}}\right)\lambda \quad \text{on} \quad \Gamma.$$

Then, proceeding as for the derivation of (6.18), but additionally adding and subtracting the expression $\langle\lambda, \varphi\rangle$ with arbitrary $\varphi \in \mathrm{H}_0^{1/2}(\Gamma)$, and imposing weakly the relation $\psi = \gamma u$ in $\mathrm{H}^{1/2}(\Gamma)$, the modified Costabel & Han formulation of (6.1) reduces to: Find $(u, \psi, \lambda) \in \widetilde{\mathbf{X}} := X \times \mathrm{H}_0^{1/2}(\Gamma) \times \mathrm{H}^{-1/2}(\Gamma)$ such that

$$\widetilde{\mathbf{A}}\big((u, \psi, \lambda), (v, \varphi, \mu)\big) = \widetilde{\mathbf{F}}(v, \varphi, \mu) \qquad \forall\, (v, \varphi, \mu) \in \widetilde{\mathbf{X}}, \tag{6.25}$$

where

$$\widetilde{\mathbf{A}}\big((z, \phi, \xi), (v, \varphi, \mu)\big) = \mathbf{a}\big((z, \phi, \xi), (v, \varphi, \mu)\big) + \langle W\phi, \varphi\rangle$$
$$+ \langle \mu, V\xi\rangle - \Big\langle \xi, \Big(\frac{\mathrm{id}}{2} - K\Big)\varphi\Big\rangle + \Big\langle \mu, \Big(\frac{\mathrm{id}}{2} - K\Big)\phi\Big\rangle, \tag{6.26}$$

with

$$\mathbf{a}\big((z, \phi, \xi), (v, \varphi, \mu)\big) = a(z, v) - \langle \xi, \gamma v - \varphi\rangle + \langle \mu, \gamma z - \phi\rangle, \tag{6.27}$$

a being defined by (6.20), and

$$\widetilde{\mathbf{F}}(v, \varphi, \mu) := \int_\Omega f v, \tag{6.28}$$

for all $(z, \phi, \xi), (v, \varphi, \mu) \in \widetilde{\mathbf{X}}$.

Analogously, proceeding similarly to the derivation of (6.25), but now imposing weakly the relation $\psi = \gamma u^s$ in $\mathrm{H}^{1/2}(\Gamma)$, the modified Costabel & Han formulation of (6.2) reads: Find $(u, \psi, \lambda) \in \widetilde{\mathbb{X}} := \mathrm{H}^1(\mathscr{O}) \times \mathrm{H}_0^{1/2}(\Gamma) \times \mathrm{H}^{-1/2}(\Gamma)$ such that

$$\widetilde{\mathbb{A}}_\kappa\big((u, \psi, \lambda), (v, \varphi, \mu)\big) = \widetilde{\mathbb{F}}(v, \varphi, \mu) \qquad \forall\, (v, \varphi, \mu) \in \widetilde{\mathbb{X}}, \tag{6.29}$$

where

$$\widetilde{\mathbb{A}}_\kappa\big((z, \phi, \xi), (v, \varphi, \mu)\big) := \mathbf{a}_\kappa\big((z, \phi, \xi), (v, \varphi, \mu)\big) + \langle W_\kappa\phi, \varphi\rangle$$
$$+ \langle \mu, V_\kappa\xi\rangle + \Big\langle \mu, \Big(\frac{\mathrm{id}}{2} - K_\kappa\Big)\phi\Big\rangle - \Big\langle \xi, \Big(\frac{\mathrm{id}}{2} - K_\kappa\Big)\varphi\Big\rangle \tag{6.30}$$

with

$$\mathbf{a}_\kappa\big((z, \phi, \xi), (v, \varphi, \mu)\big) := a_\kappa(z, v) - \langle \xi, \gamma v - \varphi \rangle + \langle \mu, \gamma z - \phi \rangle,$$

a_κ given by (6.24), and

$$\widetilde{\mathbb{F}}(v, \varphi, \mu) := \langle \frac{\partial w}{\partial \boldsymbol{n}}, \gamma v \rangle + \langle \mu, \gamma w \rangle,$$

for all $(z, \phi, \xi),\ (v, \varphi, \mu) \in \widetilde{\mathbb{X}}$.

6.2.4 Solvability Analysis

In this section we address the solvability of the Costabel & Han and modified Costabel & Han coupling procedures as applied to the Poisson (cf. (6.18), (6.25)) and Helmholtz (cf. (6.22), (6.29)) models.

We begin the analysis with the formulations (6.18) and (6.25). Indeed, bearing in mind the definitions of the bilinear forms $\mathbf{A}$ (cf. (6.19)) and $\widetilde{\mathbf{A}}$ (cf. (6.26)), we easily deduce from Lemmas 6.1 and 6.2 that there exist positive constants $\|\mathbf{A}\|$, $\|\widetilde{\mathbf{A}}\|$, α, and $\widetilde{\alpha}$, such that

$$\mathbf{A}(z, \xi), (v, \mu) \leq \|\mathbf{A}\|\, \|(z, \xi)\|\, \|(v, \mu)\| \quad \forall\, (z, \xi),\ (v, \mu) \in X\,,$$

$$\widetilde{\mathbf{A}}(z, \phi, \xi), (v, \varphi, \mu) \leq \|\widetilde{\mathbf{A}}\|\, \|(z, \phi, \xi)\|\, \|(v, \varphi\mu)\| \quad \forall\, (z, \phi, \xi),\ (v, \varphi, \mu) \in \widetilde{X}\,,$$

$$\mathbf{A}(v, \mu), (v, \mu) \geq \alpha\, \|(v, \mu)\|^2 \quad \forall\, (v, \mu) \in X\,,$$

and

$$\widetilde{\mathbf{A}}(v, \varphi, \mu), (v, \mu) \geq \alpha\, \|(v, \varphi, \mu)\|^2 \quad \forall\, (v, \varphi, \mu) \in \widetilde{X}\,,$$

where

$$\|(v, \mu)\|^2 := \|v\|_{1,\Omega}^2 + \|\mu\|_{-1/2,\Gamma}^2$$

and

$$\|(v, \varphi, \mu)\|^2 := \|v\|_{1,\Omega}^2 + \|\varphi\|_{1/2,\Gamma}^2 + \|\mu\|_{-1/2,\Gamma}^2\,.$$

In this way, since the boundedness of the linear functionals $\mathbf{F}$ (cf. (6.21)) and $\widetilde{\mathbf{F}}$ (cf. (6.28)) follow from a simple application of the Cauchy-Schwarz inequality, we conclude the well-posedness of problems (6.18) and (6.25) as a straightforward consequence of the foregoing estimates and the Lax-Milgram lemma.

Next, we deal with the solvability analysis of (6.22) and (6.29). To this end, we now introduce the compact perturbations (fact to be confirmed later on) of the bilinear forms $\mathbb{A}$ and $\widetilde{\mathbb{A}}$ that are obtained from (6.23) and (6.30), respectively, by taking $\kappa = 0$, by replacing V_κ, K_κ, K_κ^{t}, and W_κ by V, K, K^{t}, and W, respectively, and by adding suitable one-dimensional terms, that is

$$
\mathbb{A}_0\big((z,\xi),(v,\mu)\big) := a(z,v) + \Big(\int_\Gamma z\Big)\Big(\int_\Gamma v\Big) + \langle W\gamma z, \gamma v\rangle + \langle \mu, V\xi\rangle
$$
$$
+ \langle \xi, 1\rangle\langle \mu, 1\rangle + \langle \mu, \Big(\frac{\mathrm{id}}{2} - K\Big)\gamma z\rangle - \langle \xi, (\frac{\mathrm{id}}{2} - K)\gamma v\rangle
$$
$$(6.31)$$

for all (z,ξ), $(v,\mu) \in \mathbb{X}$, and

$$
\widetilde{\mathbb{A}}_0\big((z,\phi,\xi),(v,\varphi,\mu)\big) = \mathbf{a}\big((z,\phi,\xi),(v,\varphi,\mu)\big) + \Big(\int_\Gamma z\Big)\Big(\int_\Gamma v\Big) + \langle W\phi, \varphi\rangle
$$
$$
+ \langle \mu, V\xi\rangle + \langle \xi, 1\rangle\langle \mu, 1\rangle + \langle \mu, \Big(\frac{\mathrm{id}}{2} - K\Big)\phi\rangle - \langle \xi, (\frac{\mathrm{id}}{2} - K)\varphi\rangle
$$
$$(6.32)$$

for all (z,ϕ,ξ), $(v,\varphi,\mu) \in \widetilde{\mathbb{X}}$. Then, bearing in mind now (6.31), (6.32), and the definitions of $\mathbb{A}_\kappa$ (cf. (6.23)) and $\widetilde{\mathbb{A}}_\kappa$ (cf. (6.30)), we easily deduce thanks to Lemma 6.1 that all these bilinear forms are bounded. Equivalently, there exist positive constants denoted $\|\mathbb{A}_\kappa\|$, $\|\mathbb{A}_0\|$, $\|\widetilde{\mathbb{A}}_\kappa\|$, and $\|\widetilde{\mathbb{A}}_0\| > 0$, such that for each $* \in \{\kappa, 0\}$ there hold

$$
\big|\mathbb{A}_*\big((z,\xi),(v,\mu)\big)\big| \leq \|\mathbb{A}_*\|\ \|(z,\xi)\|\ \|(v,\mu)\|
$$
$$(6.33)$$

for all (z,ξ), $(v,\mu) \in X$, and

$$
\big|\widetilde{\mathbb{A}}_*\big((z,\phi,\xi),(v,\varphi,\mu)\big)\big| \leq \|\widetilde{\mathbb{A}}_*\|\ \|(z,\phi,\xi)\|\ \|(v,\varphi,\mu)\|
$$
$$(6.34)$$

for all (z,ϕ,ξ), $(v,\varphi,\mu) \in \widetilde{X}$. In addition, if follows from Lemma 6.2 that $\mathbb{A}_0$ and $\widetilde{\mathbb{A}}_0$ are both elliptic, which means that there exist positive constants α_0, $\widetilde{\alpha}_0$, such that

$$
\mathrm{Re}\Big(\mathbb{A}_0\big((v,\mu),(\bar{v},\bar{\mu})\big)\Big) \geq \alpha_0\ \|(v,\mu)\|^2 \qquad \forall (v,\mu) \in X,
$$
$$(6.35)$$

and

$$
\mathrm{Re}\Big(\widetilde{\mathbb{A}}_0\big((v,\varphi,\mu),(\bar{v},\bar{\varphi},\bar{\mu})\big)\Big) \geq \widetilde{\alpha}_0\ \|(v,\varphi,\mu)\|^2 \qquad \forall (v,\varphi,\mu) \in \widetilde{X}.
$$
$$(6.36)$$

Regarding the ellipticity of $\widetilde{\mathbb{A}}_0$ given by the foregoing equation, we stress here that, due to the inequalities (6.12) and (6.13), the expression $\langle \xi, 1\rangle\langle \mu, 1\rangle$ is needed in the

definition of $\widetilde{\mathbb{A}}_0$ (cf. (6.32)) only for the 2D analysis, and hence it is omitted for the 3D one.

Next, we let $\mathbb{X}'$ and $\widetilde{\mathbb{X}}'$ be the duals of $\mathbb{X}$ and $\widetilde{\mathbb{X}}$ pivotal to $L^2(\mathcal{O}) \times L^2(\Gamma)$ and $L^2(\mathcal{O}) \times L^2(\Gamma) \times L^2(\Gamma)$, respectively, which yields $\mathbb{X} \subset L^2(\mathcal{O}) \times L^2(\Gamma) \subset \mathbb{X}'$ and $\widetilde{\mathbb{X}} \subset L^2(\mathcal{O}) \times L^2(\Gamma) \times L^2(\Gamma) \subset \widetilde{\mathbb{X}}'$ with dense inclusions. Thus, we denote by $[\,\cdot\,,\,\cdot\,]$ the corresponding duality pairings, and let $\mathscr{A}_\kappa : \, X \to X'$, $\mathscr{A}_0 : \, X \to X'$, $\widetilde{\mathscr{A}}_\kappa : \, \widetilde{X} \to \widetilde{X}'$, and $\widetilde{\mathscr{A}}_0 : \, \widetilde{X} \to \widetilde{X}'$ be the linear operators induced by $\mathbb{A}_\kappa$, $\mathbb{A}_0$, $\widetilde{\mathbb{A}}_\kappa$, and $\widetilde{\mathbb{A}}_0$, respectively, that is, for each $* \in \{\kappa, 0\}$

$$\left[\mathscr{A}_*(z, \xi), (v, \mu) \right] := \mathbb{A}_*\big((z, \xi), (v, \mu) \big)$$

for all $(z, \xi), \, (v, \mu) \in X$, and

$$\left[\widetilde{\mathscr{A}}_*(z, \phi, \xi), (v, \varphi, \mu) \right] := \widetilde{\mathbb{A}}_*\big((z, \phi, \xi), (v, \varphi, \mu) \big)$$

for all $(z, \phi, \xi), \, (v, \varphi, \mu) \in \widetilde{X}$. It is clear from (6.33) and (6.34) that $\mathscr{A}_\kappa$, $\mathscr{A}_0$, $\widetilde{\mathscr{A}}_\kappa$, and $\widetilde{\mathscr{A}}_0$ are all bounded. In addition, (6.35) and (6.36) guarantee that $\mathscr{A}_0$ and $\widetilde{\mathscr{A}}_0$ are isomorphisms. Furthermore, we easily deduce from Lemma 6.3 and the compactness of the canonical injection from $H^1(\mathcal{O})$ into $L^2(\mathcal{O})$, that $\mathscr{A}_\kappa - \mathscr{A}_0 : \mathbb{X} \to \mathbb{X}'$ and $\widetilde{\mathscr{A}}_\kappa - \widetilde{\mathscr{A}}_0 : \widetilde{\mathbb{X}} \to \widetilde{\mathbb{X}}'$ are compact, whence $\mathscr{A}_\kappa$ and $\widetilde{\mathscr{A}}_\kappa$ are Fredholm operators of index zero.

Furthermore, we recall from [22, Theorem 2.1] the following result.

Theorem 6.1 *A function* $u \in H^1_{\mathrm{loc}}(\mathbb{R}^d)$ *satisfying* (6.2) *with* $w = 0$ *vanishes identically everywhere.*

We are now in position to establish the conditions under which problems (6.18) and (6.29) are uniquely solvable.

Theorem 6.2 *Assume that* κ^2 *is not an eigenvalue of the Laplacian in* $\mathcal{O}$ *with a Dirichlet boundary condition on* Γ. *Then, problems* (6.18) *and* (6.29) *are well posed.*

Proof The proof is adapted from [28, Theorem 3.2]. According to our previous analysis, the Fredholm alternative is applicable and therefore the proof reduces to show uniqueness of solution for (6.18) and (6.29). In what follows we restrict ourselves to (6.18), the proof for (6.29) being analogous. To this end, given a solution $(u_0, \lambda_0) \in H^1(\mathcal{O}) \times H^{-1/2}(\Gamma)$ of (6.18) with $w = 0$, we introduce the function

$$\widetilde{u}(x) := \begin{cases} u_0(x) & \forall \, x \in \mathcal{O}, \\ \displaystyle\int_\Gamma \frac{\partial E_\kappa(|x - y|)}{\partial n_y} u^s(y) \, \mathrm{d}\sigma_y - \int_\Gamma E_\kappa(|x - y|) \lambda_0 \, \mathrm{d}\sigma_y & \forall \, x \in \mathcal{O}_e \,. \end{cases}$$

It is easy to verify that u_0 solves the equation

$$\Delta u_0 + \kappa^2 \vartheta(x) \, u_0 = 0 \quad \text{in} \quad \mathcal{O} \,, \tag{6.37}$$

and that $q := \widetilde{u}|_{\mathcal{O}_e}$ is a radiating solution of the Helmholtz equation with wave number κ, that is

$$\Delta q + \kappa^2 q = 0 \quad \text{in} \quad \mathcal{O}_e, \quad \frac{\partial q}{\partial r} - \imath \kappa q = o(r^{\frac{1-d}{2}}) \quad r := |\mathbf{x}| \to \infty. \qquad (6.38)$$

Furthermore, using the jump relations of the acoustic potential layers we obtain

$$\gamma q = \left(\frac{\mathrm{id}}{2} + K_\kappa\right)\gamma u_0 - V_\kappa \lambda_0 \quad \text{on} \quad \Gamma, \qquad (6.39)$$

$$\lambda_0 = -W_\kappa \gamma u_0 + \left(\frac{\mathrm{id}}{2} - K_\kappa^{\mathrm{t}}\right)\lambda_0 \quad \text{on} \quad \Gamma, \qquad (6.40)$$

from which, comparing in particular (6.4) and (6.39), we deduce that

$$\gamma q = \gamma u_0. \qquad (6.41)$$

In turn, subtracting equations (6.5) and (6.40) yields

$$\left(\frac{\mathrm{id}}{2} - K_\kappa^{\mathrm{t}}\right)\left(\frac{\partial u_0}{\partial \mathbf{n}} - \lambda_0\right) = 0, \qquad (6.42)$$

and using that, under our hypothesis on k, operator $\frac{\mathrm{id}}{2} - K_\kappa^{\mathrm{t}}$ is injective (cf. [16]), we deduce from (6.42) the identity

$$\frac{\partial q}{\partial \mathbf{n}} = \frac{\partial u_0}{\partial \mathbf{n}} \quad \text{on} \quad \Gamma. \qquad (6.43)$$

Finally, equations (6.37), (6.38), (6.41) and (6.43) show that $\widetilde{u} \in \mathrm{H}^1_{\mathrm{loc}}(\mathbb{R}^d)$ is a solution of (6.2) with $w = 0$, and therefore Theorem 6.1 ensures that such a function $\widetilde{u}$ should vanish identically in $\mathbb{R}^d$, which ends the proof. $\qquad\qquad \square$

Finally, as a consequence of Theorem 6.2 and the Fredholm alternative we conclude that the operators $\mathscr{A}_\kappa : \mathbb{X} \to \mathbb{X}'$ and $\widetilde{\mathscr{A}}_\kappa : \widetilde{\mathbb{X}} \to \widetilde{\mathbb{X}}'$ are bijective.

6.3 The Costabel & Han VEM/BEM Schemes in 2D

In this section we introduce and analyze the discrete VEM/BEM schemes for the Costabel & Han coupling procedure as applied to the Poisson and Helmholtz models in the 2D case. Similar analyses hold for the modified Costabel & Han approach, and hence they are omitted. We begin with some fundamental notations and results on VEM in 2D.

6.3.1 Preliminaries

From now on we assume that there exist polygonal partitions $\cup_{i=1}^{I} \overline{\Omega}_i = \overline{\Omega}$ and $\cup_{i=1}^{I} \overline{\mathcal{O}}_i = \overline{\mathcal{O}}$, and an integer $k \geq 1$, such that $f|_{\Omega_i} \in H^k(\Omega_i)$, $\kappa|_{\Omega_i} \in W^{k+1,\infty}(\Omega_i)$, and $\vartheta|_{\mathcal{O}_i} \in \mathbb{C}$ for all $i \in \{1, \ldots, I\}$. Then we let $\{\mathscr{F}_h\}_h$ be a family of partitions of $\overline{\Omega}$ (resp. of $\overline{\mathcal{O}}$), constituted of connected polygons $F \in \mathscr{F}_h$ of diameter $h_F \leq h$, and assume that the meshes $\{\mathscr{F}_h\}_h$ are aligned with each Ω_i (resp. $\mathcal{O}_i$), $i \in \{1, \ldots, I\}$. For each $F \in \mathscr{F}_h$ the boundary ∂F is subdivided into straight segments e, which are referred to in what follows as edges. In particular, we introduce the set

$$\mathscr{E}_h := \Big\{ \text{edges of } \mathscr{F}_h : \quad e \subseteq \Gamma \Big\}.$$

In addition, we assume that the family $\{\mathscr{F}_h\}_h$ of meshes satisfy the following conditions: There exists $\rho \in (0, 1)$ such that

(A1) each F of $\{\mathscr{F}_h\}_h$ is star-shaped with respect to a disk D_F of radius ρh_F,
(A2) for each F of $\{\mathscr{F}_h\}_h$ and for all edges $e \subseteq \partial F$ it holds $|e| \geq \rho h_F$.

Then, for each F of $\{\mathscr{F}_h\}_h$, we introduce the projection operator $\Pi_k^{\nabla, F}$: $H^1(F) \rightarrow \mathscr{P}_k(F)$, which, given $v \in H^1(F)$, is uniquely characterized by (see [6])

$$\int_F \nabla(\Pi_k^{\nabla,F} v) \cdot \nabla p + \Big(\int_{\partial F} \Pi_k^{\nabla,F} v \Big) \Big(\int_{\partial F} p \Big) = \int_F \nabla v \cdot \nabla p + \Big(\int_{\partial F} v \Big) \Big(\int_{\partial F} p \Big)$$
(6.44)

for all $p \in \mathscr{P}_k(F)$. Moreover, we let Π_k^F be the $L^2(F)$–orthogonal projection onto $\mathscr{P}_k(F)$ with vectorial counterpart $\boldsymbol{\Pi}_k^F : L^2(F)^2 \rightarrow \mathscr{P}_k(F)^2$, and following [2] we introduce, for $k \geq 1$, the local virtual element space

$$X_h^k(F) := \Big\{ v \in H^1(F) : \quad v|_e \in \mathscr{P}_k(e), \quad \forall e \subseteq \partial F,$$
$$\Delta v \in \mathscr{P}_k(F), \quad \Pi_k^F v - \Pi_k^{\nabla,F} v \in \mathscr{P}_{k-2}(F) \Big\}.$$
(6.45)

It can be shown (cf. [2]) that the degrees of freedom of $X_h^k(F)$ consist of:

 (i) the values at the vertices of F, and additionally for $k \geq 2$
 (ii) the moments of order $\leq k - 2$ on the edges of F, and
(iii) the moments of order $\leq k - 2$ on F.

We are then allowed to introduce the global virtual element space as

$$X_h^k := \Big\{ v \in X(\text{resp. } H^1(\Omega)) : \quad v|_F \in X_h^k(F) \quad \forall F \in \mathscr{F}_h \Big\}.$$
(6.46)

On the other hand, for any integer $k \geq 0$, we denote by $\mathscr{P}_k(\mathscr{F}_h)$ the space of piecewise polynomials of degree $\leq k$ with respect to $\mathscr{F}_h$, and let $\Pi_k^{\mathscr{F}}$ be the global $L^2(\Omega)$-orthogonal (resp. $L^2(\mathscr{O})$-orthogonal) projection onto $\mathscr{P}_k(\mathscr{F}_h)$, which is assembled cellwise, i.e.

$$(\Pi_k^{\mathscr{F}} v)|_F := \Pi_k^F(v|_F) \quad \forall F \in \mathscr{F}_h, \quad \forall v \in L^2(\Omega) \ (\text{resp. } v \in L^2(\mathscr{O})). \tag{6.47}$$

Similarly, for any $\boldsymbol{q} \in L^2(\Omega)^2$ (resp. $\boldsymbol{q} \in L^2(\mathscr{O})^2$), $\boldsymbol{\Pi}_k^{\mathscr{F}} \boldsymbol{q}$ is defined by $(\boldsymbol{\Pi}_k^{\mathscr{F}} \boldsymbol{q})|_F = \boldsymbol{\Pi}_k^F(\boldsymbol{q}|_F)$ for all $F \in \mathscr{F}_h$. It is important to notice that $\mathscr{P}_k(F) \subseteq X_h^k(F)$ and that the projectors $\Pi_k^{\nabla, F} v$ and $\Pi_k^F v$ are computable for all $v \in X_h^k(F)$. Furthermore, it is also easy to check that $\boldsymbol{\Pi}_{k-1}^F \nabla v$ is explicitly known for all $v \in X_h^k(F)$ (cf. [6]).

Hereafter, given any positive functions A_h and B_h of the mesh parameter h, the notation $A_h \lesssim B_h$ means that $A_h \leq C B_h$ with $C > 0$ independent of h, whereas $A_h \simeq B_h$ means that $A_h \lesssim B_h$ and $B_h \lesssim A_h$. Then, under the conditions on $\mathscr{F}_h$, the technique of averaged Taylor polynomials introduced in [20] permits to prove the following error estimates,

$$\|v - \Pi_k^F v\|_{0,F} + h_F |v - \Pi_k^F v|_{1,F} \lesssim h_F^{\ell+1} |v|_{\ell+1,F} \quad \forall \ell \in \{0, 1, \ldots, k\}, \tag{6.48}$$

$$\|v - \Pi_k^{\nabla, F} v\|_{0,F} + h_F \|v - \Pi_k^{\nabla, F} v\|_{1,F} \lesssim h_F^{\ell+1} |v|_{\ell+1,F} \quad \forall \ell \in \{1, 2, \ldots, k\} \tag{6.49}$$

for all $v \in H^{\ell+1}(F)$. In turn, the local interpolation operator $I_k^F : H^2(F) \to X_h^k(F)$ is defined for each $v \in H^2(F)$ by imposing that $v - I_k^F v$ has vanishing degrees of freedom, which satisfies (cf. [9, Lemma 2.23])

$$\|v - I_k^F v\|_{0,F} + h_F \left|v - I_k^F v\right|_{1,F} \lesssim h_F^{\ell+1} |v|_{\ell+1,F} \quad \forall \ell \in \{1, 2, \ldots, k\} \tag{6.50}$$

for all $v \in H^{\ell+1}(F)$. In addition, we denote by $I_k^{\mathscr{F}}$ the global virtual element interpolation operator, i.e., for each $v \in \mathscr{C}^0(\overline{\Omega})$ (resp. $v \in \mathscr{C}^0(\overline{\mathscr{O}})$), we set locally

$$(I_k^{\mathscr{F}} v)|_F = I_k^F(v|_F) \qquad \forall F \in \mathscr{F}_h. \tag{6.51}$$

On the other hand, in order to approximate the unknown $\lambda \in H_0^{-1/2}(\Gamma)$, we introduce the non-virtual (but explicit) subspace

$$\Lambda_h^{k-1} := \left\{ \mu \in L^2(\Gamma) : \quad \mu|_e \in P_{k-1}(e), \quad \forall e \in \mathscr{E}_h, \quad \int_\Gamma \mu = 0 \right\}, \tag{6.52}$$

and let $\Pi^{\mathscr{E}}_{k-1} : L^2(\Gamma) \to \Lambda^{k-1}_h$ be the $L^2(\Gamma)$-orthogonal projection. In addition, we let $\{\Gamma_1, \ldots, \Gamma_J\}$ be the set of segments constituting Γ, and for any $t \geq 0$ we consider the broken Sobolev space $H^t_b(\Gamma) := \prod^J_{j=1} H^t(\Gamma_j)$ endowed with the graph norm

$$\|\varphi\|^2_{t,b,\Gamma} := \sum_{j=1}^{J} \|\varphi\|^2_{t,\Gamma_j} \quad \forall\, \varphi \in H^t_b(\Gamma)\,.$$

Next, we recall from [30] the approximation property of the operator $\Pi^{\mathscr{E}}_{k-1}$.

Lemma 6.4 *Assume that $\mu \in H^{-1/2}(\Gamma) \cap H^r_b(\Gamma)$ for some $r \geq 0$. Then,*

$$\left\|\mu - \Pi^{\mathscr{E}}_{k-1}\mu\right\|_{-t,\Gamma} \lesssim h^{\min\{r,k\}+t}\, \|\mu\|_{r,b,\Gamma} \qquad \forall\, t \in \{0, 1/2\}.$$

6.3.2 The Costabel & Han VEM/BEM Scheme for Poisson

In this section we introduce and analyze the VEM/BEM scheme for the continuous formulation (6.18) in the 2D case.

6.3.2.1 The Discrete Setting

For all $F \in \mathscr{F}_h$ we let S^F_h be the symmetric bilinear form defined on $H^1(F) \times H^1(F)$ by

$$S^F_h(v, w) := h^{-1}_F \sum_{e \subseteq \partial F} \int_e \pi^e_k v\, \pi^e_k w \qquad \forall\, v,\, w \in H^1(F)\,, \tag{6.53}$$

where π^e_k is the $L^2(e)$-projection onto $\mathscr{P}_k(e)$. It is shown in [9, Lemma 3.2] that

$$S^F_h(v, v) \simeq a^F(v, v) \qquad \forall\, v \in X^k_h(F) \quad \text{such that} \quad \Pi^{\nabla, F}_k v = 0\,, \tag{6.54}$$

where a^F is the local version of a, that is

$$a^F(v, w) := \int_F \kappa\, \nabla v \cdot \nabla w \qquad \forall\, v,\, w \in H^1(F)\,. \tag{6.55}$$

It is important to notice that S_h^F is computable on $X_h^k(F) \times X_h^k(F)$ since $\pi_k^e v = v \in \mathscr{P}_k(e)$ for all $v \in X_h^k(F)$, and that, by symmetry, there holds

$$S_h^F(v, w) \leq S_h^F(v, v)^{1/2} S_h^F(w, w)^{1/2} \lesssim a^F(v, v)^{1/2} a^F(w, w)^{1/2}$$

for all $v, w \in X_h^k(F)$ satisfying $\Pi_k^{\nabla, F} v = \Pi_k^{\nabla, F} w = 0$. Next, for each $F \in \mathscr{F}_h$ we introduce

$$a_h^F(v, w) := \int_F \kappa \, \mathbf{\Pi}_{k-1}^F \nabla v \cdot \mathbf{\Pi}_{k-1}^F \nabla w + S_h^F(v - \Pi_k^{\nabla, F} v, w - \Pi_k^{\nabla, F} w), \quad (6.56)$$

and let a_h be the global extension of it, that is

$$a_h(v, w) = \sum_{F \in \mathscr{F}_h} a_h^F(v, w) \qquad \forall v, w \in X_h^k. \quad (6.57)$$

We now stress, as shown in [6], that the first term defining a_h^F is also computable on $X_h^k(F) \times X_h^k(F)$ even if κ is not a polynomial function. Indeed, using the fact that $\mathbf{\Pi}_{k-1}^F$ is self-adjoint and integrating by parts, we find that there holds

$$\int_F \kappa \, \mathbf{\Pi}_{k-1}^F \nabla v \cdot \mathbf{\Pi}_{k-1}^F \nabla w = \int_F \mathbf{\Pi}_{k-1}^F (\kappa \, \mathbf{\Pi}_{k-1}^F \nabla v) \cdot \nabla w$$

$$= -\int_F \mathrm{div}\left(\mathbf{\Pi}_{k-1}^F(\kappa \, \mathbf{\Pi}_{k-1}^F \nabla v)\right) w + \int_{\partial F} \mathbf{\Pi}_{k-1}^F(\kappa \, \mathbf{\Pi}_{k-1}^F \nabla v) \cdot \boldsymbol{n}_{\partial F} \, w$$

for all $v, w \in X_h^k(F)$. Then, we notice that the first term on the right hand side of the foregoing identity is computable thanks to the moments of w on F of order $\leq k - 2$, whereas the second one is computable as well since each factor of it is a known polynomial.

We now let $\mathbf{X}_h := X_h^k \times \Lambda_h^{k-1}$ and introduce the discrete version of problem (6.18): Find $(u_h, \lambda_h) \in \mathbf{X}_h$ such that

$$\mathbf{A}_h\big((u_h, \lambda_h), (v_h, \mu_h)\big) = \mathbf{F}_h(v_h, \mu_h) \qquad \forall (v_h, \mu_h) \in \mathbf{X}_h, \quad (6.58)$$

where

$$\mathbf{A}_h\big((z_h, \xi_h), (v_h, \mu_h)\big) := a_h(z_h, v_h) + \langle W \gamma z_h, \gamma v_h \rangle + \langle \mu_h, V \xi_h \rangle$$
$$+ \left\langle \mu_h, \left(\frac{\mathrm{id}}{2} - K\right) \gamma z_h \right\rangle - \left\langle \xi_h, \left(\frac{\mathrm{id}}{2} - K\right) \gamma v_h \right\rangle, \quad (6.59)$$

for all $(z_h, \xi_h), (v_h, \mu_h) \in \mathbf{X}_h$, and

$$\mathbf{F}_h(v_h, \mu_h) := \int_\Omega (\Pi_{k-1}^{\mathscr{F}} f) \, v_h \qquad \forall (v_h, \mu_h) \in \mathbf{X}_h. \quad (6.60)$$

We stress that, due to the degrees of freedom of the virtual element subspace X_h^k (cf. (6.46)), and thanks to the non-virtual character of the finite element subspace Λ_h^{k-1} (cf. (6.52)), all the terms in (6.59) involving the boundary integral operators are computable

6.3.2.2 Solvability and a Priori Error Analyses

We begin with the boundedness property of $\mathbf{A}_h$.

Lemma 6.5 *There hold*

$$|a_h^F(z, v)| \lesssim \|z\|_{1,F} \|v\|_{1,F} \qquad \forall\, F \in \mathscr{F}_h, \quad \forall\, z, v \in \mathrm{H}^1(F), \qquad (6.61)$$

and

$$|\mathbf{A}_h\big((z, \eta), (v, \mu)\big)| \lesssim \|(z, \eta)\|\, \|(v, \mu)\| \qquad \forall\, (z, \eta), (v, \mu) \in \mathbf{X}_h. \qquad (6.62)$$

Proof The local estimate (6.61) is basically a consequence of the Cauchy-Schwarz inequality and the fact that (see [6])

$$S_h^F(z - \Pi_k^{\nabla,F} z, v - \Pi_k^{\nabla,F} v) \lesssim |z - \Pi_k^{\nabla,F} z|_{1,F}\, |v - \Pi_k^{\nabla,F} v|_{1,F} \lesssim |z|_{1,F}\, |v|_{1,F}, \qquad (6.63)$$

whereas (6.62) follows from (6.61) and the mapping properties provided by Lemma 6.1. $\qquad\square$

The following lemma recalls from [6] some useful estimates between a^F and a_h^F, which involve the local operators Π_k^F and I_k^F.

Lemma 6.6 *For each $F \in \mathscr{F}_h$ there hold*

$$|a^F(\Pi_k^F z, v_h) - a_h^F(\Pi_k^F z, v_h)| \lesssim h_F^k\, \|z\|_{k+1,F}\, \|v_h\|_{1,F} \qquad (6.64)$$

for all $(z, v_h) \in \mathrm{H}^{k+1}(F) \times X_h^k(F)$,

$$|a^F(v_h, I_k^F z) - a_h^F(v_h, I_k^F z)| \lesssim h_F\, \|v_h\|_{1,F}\, \|z\|_{2,F} \qquad (6.65)$$

for all $(z, v_h) \in \mathrm{H}^2(F) \times X_h^k(F)$, and

$$|a^F(\Pi_k^F z, I_k^F v) - a_h^F(\Pi_k^F z, I_k^F v)| \lesssim h_F^{k+1}\, \|z\|_{k+1,F}\, \|v\|_{2,F} \qquad (6.66)$$

for all $(z, v) \in \mathrm{H}^{k+1}(F) \times \mathrm{H}^2(F)$.

Proof For the proof of (6.64) we refer to [6, Lemma 5.5], whereas (6.65) can be proved as explained in [6, Remark 5.1]. In turn, (6.66) follows by combining the proofs of (6.64) and (6.65). □

The $\mathbf{X}_h$-ellipticity of the bilinear form $\mathbf{A}_h$ is established next.

Lemma 6.7 *There holds*

$$\mathbf{A}_h\big((v, \mu), (v, \mu)\big) \gtrsim \|(v, \mu)\|^2 \qquad \forall (v, \mu) \in \mathbf{X}_h. \tag{6.67}$$

Proof We begin by observing, thanks to (6.13) and (6.14), that for all $(v, \mu) \in \mathbf{X}_h$ we obtain

$$\mathbf{A}_h\big((v, \mu), (v, \mu)\big) = a_h(v, v) + \langle W\gamma v, \gamma v \rangle + \langle \mu, V\mu \rangle \geq a_h(v, v) + \alpha_V \|\mu\|^2_{-1/2, \Gamma}. \tag{6.68}$$

On the other hand, according to the definition of a_h^F (cf. (6.56)), noting that certainly there holds $\Pi_k^{\nabla, F}\big(v - \Pi_k^{\nabla, F} v\big) = 0$, and then employing (6.54) and the fact that

$$|v - \Pi_k^{\nabla, F} v|_{1, F} = \|\nabla v - \nabla\Pi_k^{\nabla, F} v\|_{0, F} \geq \|\nabla v - \mathbf{\Pi}_{k-1}^F \nabla v\|_{0, F},$$

we deduce that

$$
\begin{aligned}
a_h^F(v, v) &\gtrsim \left\|\mathbf{\Pi}_{k-1}^F \nabla v\right\|_{0, F}^2 + a^F(v - \Pi_k^{\nabla, F} v, v - \Pi_k^{\nabla, F} v) \\
&\gtrsim \left\{ \left\|\mathbf{\Pi}_{k-1}^F \nabla v\right\|_{0, F}^2 + |v - \Pi_k^{\nabla, F} v|_{1, F}^2 \right\} \\
&\gtrsim \left\{ \left\|\mathbf{\Pi}_{k-1}^F \nabla v\right\|_{0, F}^2 + \left\|\nabla v - \mathbf{\Pi}_{k-1}^F \nabla v\right\|_{0, F}^2 \right\} \gtrsim |v|_{1, F}^2.
\end{aligned} \tag{6.69}
$$

In this way, the proof follows from the definition of a_h (cf. (6.57)), (6.68), and (6.69). □

As a consequence of Lemmas 6.5 and 6.7, a straightforward application again of the Lax-Milgram lemma shows that (6.58) admits a unique solution $(u_h, \lambda_h) \in \mathbf{X}_h$. Moreover, we have the following a priori error estimate.

Theorem 6.3 *Under the assumption that $u \in X \cap \prod_{i=1}^I H^2(\Omega_i)$, there holds*

$$
\begin{aligned}
\|(u, \lambda) - (u_h, \lambda_h)\| &\lesssim \left\|(u, \lambda) - (I_k^{\mathscr{F}} u, \Pi_{k-1}^{\mathscr{E}} \lambda)\right\| \\
&+ \sup_{w_h \in X_h^k} \frac{|a(u, w_h) - a_h(I_k^{\mathscr{F}} u, w_h)|}{\|w_h\|_{1, \Omega}} + \left\|f - \Pi_{k-1}^{\mathscr{F}} f\right\|_{0, \Omega}.
\end{aligned} \tag{6.70}
$$

Proof From the definitions of $\mathbf{F}$ and $\mathbf{F}_h$ (cf. (6.18) and (6.60)) we have that

$$\sup_{\substack{(v_h,\mu_h)\in\mathbf{X}_h \\ (v_h,\mu_h)\neq\mathbf{0}}} \frac{\left|\mathbf{F}(v_h,\mu_h) - \mathbf{F}_h(v_h,\mu_h)\right|}{\|(v_h,\mu_h)\|} \leq \left\|f - \Pi_{k-1}^{\mathscr{F}}f\right\|_{0,\Omega} .$$

In turn, according to the definitions of $\mathbf{A}$ and $\mathbf{A}_h$ (cf. (6.19) and (6.59)) it readily follows that

$$\mathbf{A}((v_h,\mu_h),(w_h,\xi_h)) - \mathbf{A}_h((v_h,\mu_h),(w_h,\xi_h)) = a(v_h,w_h) - a_h(v_h,w_h)$$

for all $(v_h,\mu_h),(w_h,\xi_h) \in \mathbf{X}_h$. In addition, adding and subtracting u to the first component of a, and using the boundedness of this bilinear form, we obtain

$$\left|a(v_h,w_h) - a_h(v_h,w_h)\right| \lesssim \left\{\|u - v_h\|\,\|w_h\|_{1,\Omega} + \left|a(u,w_h) - a_h(v_h,w_h)\right|\right\}$$

for all $v_h,\, w_h \in X_h^k$. Hence, bearing in mind the foregoing estimates, a straightforward application of the first Strang Lemma (cf. [15, Theorem 4.1.1]) to the context given by (6.18) and (6.58) gives

$$\|(u,\lambda) - (u_h,\lambda_h)\| \lesssim \inf_{(v_h,\mu_h)\in\mathbf{X}_h} \left\{ \|(u,\lambda) - (v_h,\mu_h)\| \right.$$

$$+ \sup_{\substack{w_h\in X_h^k \\ w_h\neq\mathbf{0}}} \frac{\left|a(u,w_h) - a_h(v_h,w_h)\right|}{\|w_h\|_{1,\Omega}} \right\} + \left\|f - \Pi_{k-1}^{\mathscr{F}}f\right\|_{0,\Omega} . \tag{6.71}$$

Next, since $X \cap \prod_{i=1}^I \mathrm{H}^2(\Omega_i) \subseteq \mathscr{C}^0(\overline{\Omega})$ and $\mathrm{H}_b^{1/2}(\Gamma) \subseteq \mathrm{L}^2(\Gamma)$, we deduce by hypotheses that $u \in \mathscr{C}^0(\overline{\Omega})$ and $\lambda = \kappa\nabla u \cdot \boldsymbol{n} \in \mathrm{L}^2(\Gamma)$, which implies that $I_k^{\mathscr{F}}u$ and $\Pi_{k-1}^{\mathscr{E}}\lambda$ are meaningful. In this way, taking in particular $(v_h,\mu_h) = (I_k^{\mathscr{F}}u, \Pi_{k-1}^{\mathscr{E}}\lambda) \in \mathbf{X}_h$ in (6.71) we arrive at (6.70) and conclude the proof. $\qquad\square$

It remains to bound the supremum in (6.70), for which we begin by noticing that for each $w_h \in X_h^k$ there holds

$$a(u,w_h) - a_h(I_k^{\mathscr{F}}u,w_h) = \sum_{F\in\mathscr{F}_h} \left\{a^F(u,w_h) - a_h^F(I_k^F u,w_h)\right\}, \tag{6.72}$$

where each term of the sum in (6.72) can be decomposed as

$$a^F(u,w_h) - a_h^F(I_k^F u,w_h) = a^F(u - \Pi_k^F u,w_h)$$

$$+ a^F(\Pi_k^F u,w_h) - a_h^F(\Pi_k^F u,w_h) + a_h^F(\Pi_k^F u - I_k^F u,w_h) . \tag{6.73}$$

Then, employing the boundedness of a^F (cf. (6.55)) and a_h^F (cf. (6.61)), we obtain

$$|a^F(u - \Pi_k^F u, w_h)| \lesssim \left\| u - \Pi_k^F u \right\|_{1,F} \| w_h \|_{1,F}$$

and

$$|a_h^F(\Pi_k^F u - I_k^F u, w_h)| \lesssim \left\{ \left\| u - I_k^F u \right\|_{1,F} + \left\| u - \Pi_k^F u \right\|_{1,F} \right\} \| w_h \|_{1,F} \, ,$$

respectively, which, replaced back in (6.73) and then in (6.72), yields

$$\sup_{w_h \in X_h^k} \frac{|a(u, w_h) - a_h(I_k^{\mathscr{F}} u, w_h)|}{\| w_h \|_{1,\Omega}} \lesssim \left\| u - I_k^{\mathscr{F}} u \right\|_{1,\Omega} + \left(\sum_{F \in \mathscr{F}_h} \left\| u - \Pi_k^F u \right\|_{1,F}^2 \right)^{1/2}$$

$$+ \sup_{w_h \in X_h^k} \frac{\displaystyle\sum_{F \in \mathscr{F}_h} \left| a^F(\Pi_k^F u, w_h) - a_h^F(\Pi_k^F u, w_h) \right|}{\| w_h \|_{1,\Omega}} \, .$$

$$(6.74)$$

Note that we used here that $\left\| u - I_k^{\mathscr{F}} u \right\|_{1,\Omega}^2 = \displaystyle\sum_{F \in \mathscr{F}_h} \left\| u - I_k^F u \right\|_{1,F}^2$. Hence, employing (6.74) in (6.70), we find that

$$\| (u, \lambda) - (u_h, \lambda_h) \| \lesssim \left\{ \left\| (u, \lambda) - (I_k^{\mathscr{F}} u, \Pi_{k-1}^{\mathscr{E}} \lambda) \right\| + \left(\sum_{F \in \mathscr{F}_h} \left\| u - \Pi_k^F u \right\|_{1,F}^2 \right)^{1/2} \right.$$

$$\left. + \sup_{w_h \in X_h^k} \frac{\displaystyle\sum_{F \in \mathscr{F}_h} \left| a^F(\Pi_k^F u, w_h) - a_h^F(\Pi_k^F u, w_h) \right|}{\| w_h \|_{1,\Omega}} + \left\| f - \Pi_{k-1}^{\mathscr{F}} f \right\|_{0,\Omega} \right\} .$$

$$(6.75)$$

The foregoing a priori error estimate together with the regularity assumptions on u and f, and the approximation properties of the projection and interpolation operators involved, allow us to establish the rates of convergence of our VEM/BEM scheme (6.58). More precisely, we have the following result.

Theorem 6.4 *Assuming that* $u \in X \cap \prod_{i=1}^I H^{k+1}(\Omega_i)$ *and* $f \in \prod_{i=1}^I H^k(\Omega_i)$, *there holds*

$$\| (u, \lambda) - (u_h, \lambda_h) \| := \| u - u_h \|_{1,\Omega} + \| \lambda - \lambda_h \|_{-1/2,\Gamma}$$

$$\lesssim h^k \sum_{i=1}^I \left\{ \| u \|_{k+1,\Omega_i} + \| f \|_{k,\Omega_i} \right\} .$$

$$(6.76)$$

Proof We first notice from (6.64) (cf. Lemma 6.6) that

$$\left| a^F(\Pi_k^F u, w_h) - a_h^F(\Pi_k^F u, w_h) \right| \lesssim h_F^k \, \|u\|_{k+1,F} \, \|w_h\|_{1,F} \qquad \forall \, F \in \mathscr{F}_h \,,$$

which implies

$$\sup_{w_h \in X_h^k} \frac{\displaystyle\sum_{F \in \mathscr{F}_h} \left| a^F(\Pi_k^F u, w_h) - a_h^F(\Pi_k^F u, w_h) \right|}{\|w_h\|_{1,\Omega}} \lesssim h^k \sum_{i=1}^I \|u\|_{k+1,\Omega_i} \,. \qquad (6.77)$$

Then, by applying (6.48) and (6.50), we readily deduce that

$$\begin{aligned}
\left\| u - I_k^{\mathscr{F}} u \right\|_{1,\Omega} + \left(\sum_{F \in \mathscr{F}_h} \left\| u - \Pi_k^F u \right\|_{1,F}^2 \right)^{1/2} + \left\| f - \Pi_{k-1}^{\mathscr{F}} f \right\|_{0,\Omega} \\
\lesssim h^k \sum_{i=1}^I \Big\{ \|u\|_{k+1,\Omega_i} + \|f\|_{k,\Omega_i} \Big\} \,.
\end{aligned} \qquad (6.78)$$

In turn, by hypothesis $\lambda = \kappa \nabla u \cdot \boldsymbol{n}$ satisfies $\lambda|_{\Gamma_j} \in \mathrm{H}^{k-1/2}(\Gamma_j)$ on each straight segment Γ_j, $j \in \{1, \dots, J\}$, constituting Γ, and therefore Lemma 6.4 and the trace theorem yield

$$\left\| \lambda - \Pi_{k-1}^{\mathscr{E}} \lambda \right\|_{-1/2,\Gamma} \lesssim h^k \sum_{j=1}^J \|\lambda\|_{k-1/2,\Gamma_j} \lesssim h^k \sum_{i=1}^I \|u\|_{k+1,\Omega_i} \,. \qquad (6.79)$$

Finally, replacing (6.77), (6.78), and (6.79) in (6.75) we obtain (6.76) and conclude the proof. $\qquad\qquad\qquad\qquad\qquad\qquad\qquad\qquad\qquad\qquad\qquad\qquad\qquad\qquad\qquad \square$

We end this section by stressing that rates of convergence for u in the $\mathrm{L}^2(\Omega)$-norm, and for a computable approximation $\widehat{u}$ of u in a broken $\mathrm{H}^1(\Omega)$-norm, can also be derived. In fact, under a suitable regularity hypothesis on the solution of the dual problem to (6.18), and assuming that $u \in X \cap \prod_{i=1}^I \mathrm{H}^{k+1}(\Omega_i)$ and $f \in \prod_{i=1}^I \mathrm{H}^k(\Omega_i)$, there holds (cf. [21, Theorem 3.7])

$$\|u - u_h\|_{0,\Omega} \lesssim h^{k+1} \sum_{i=1}^I \Big\{ \|u\|_{k+1,\Omega_i} + \|f\|_{k,\Omega_i} \Big\} \,.$$

In turn, introducing the fully computable approximation of u given by $\widehat{u} := \Pi_k^{\mathscr{F}} u_h$, defining the broken $\mathrm{H}^1(\Omega)$-seminorm

$$|u - \widehat{u}|_{1,b,\Omega} := \left\{ \sum_{F \in \mathscr{F}_h} |u - \widehat{u}_h|_{1,F}^2 \right\}^{1/2} \,,$$

and assuming that $u \in X \cap \prod_{i=1}^{I} H^{k+1}(\Omega_i)$ and $f \in \prod_{i=1}^{I} H^k(\Omega_i)$, there holds (cf. [21, Theorem 3.8])

$$\|u - \widehat{u}_h\|_{0,\Omega} + h \, |u - \widehat{u}|_{1,b,\Omega} \lesssim h^{k+1} \sum_{i=1}^{I} \left\{ \|u\|_{k+1,\Omega_i} + \|f\|_{k,\Omega_i} \right\}.$$

6.3.3 The Costabel & Han VEM/BEM Scheme for Helmholtz

In what follows we introduce and analyze the VEM/BEM scheme for the continuous formulation (6.22) in the 2D case.

6.3.3.1 The Discrete Setting

We also make use of the symmetric bilinear form S_h^F (cf. (6.53)) for each $F \in \mathscr{F}_h$, and notice now from [9, Lemma 3.2] that

$$S_h^F(v, \bar{v}) \simeq a_0^F(v, \bar{v}) \quad \forall v \in X_h^k(F) \quad \text{such that } \Pi_k^{\nabla,F} v = 0,$$

where a_0^F is the local version of a_0, that is

$$a_0^F(z, v) := \int_F \nabla z \cdot \nabla v \qquad \forall z, v \in H^1(F). \tag{6.80}$$

In addition, by symmetry there holds

$$S_h^F(z, v) \le S_h^F(z, z)^{1/2} S_h^F(v, v)^{1/2} \lesssim a_0^F(z, z)^{1/2} a_0^F(v, v)^{1/2} \tag{6.81}$$

for all $z, v \in X_h^k(F)$. Next, for each $F \in \mathscr{F}_h$ we introduce

$$a_{0,h}^F(z, v) := a_0^F(\Pi_k^{\nabla,F} z, \Pi_k^{\nabla,F} v) + S_h^F(z - \Pi_k^{\nabla,F} z, v - \Pi_k^{\nabla,F} v) \quad \forall z, v \in X_h^k(F), \tag{6.82}$$

and

$$a_{\kappa,h}^F(z, v) := a_{0,h}^F(z, v) - \kappa^2 \vartheta_F \int_F (\Pi_{k-1}^F z)(\Pi_{k-1}^F v) \quad \forall z, v \in X_h^k(F), \tag{6.83}$$

where $\vartheta_F = \vartheta|_F \in \mathbb{C}$. We also let $a_{0,h}$ and $a_{\kappa,h}$ be the corresponding global extensions of $a_{0,h}^F$ and $a_{\kappa,h}^F$, respectively, that is

$$a_{0,h}(z, v) := \sum_{F \in \mathscr{F}_h} a_{0,h}^F(z, v)$$

and

$$a_{\kappa,h}(z, v) := \sum_{F \in \mathscr{F}_h} a_{\kappa,h}^F(z, v) \quad \forall z, \, v \in X_h^k. \tag{6.84}$$

Then, denoting $\boldsymbol{X}_h^k := X_h^k \times \Lambda_h^{k-1}$, the discrete version of problem (6.22) reduces to: Find $(u_h, \lambda_h) \in \boldsymbol{X}_h^k$ such that

$$\mathbb{A}_{\kappa,h}\big((u_h, \lambda_h), (v_h, \mu_h)\big) = \mathbb{F}(v_h, \mu_h) \qquad \forall (v_h, \mu_h) \in \boldsymbol{X}_h^k, \tag{6.85}$$

where

$$\mathbb{A}_{\kappa,h}\big((z_h, \xi_h), (v_h, \mu_h)\big) := a_{\kappa,h}(z_h, v_h) + \big\langle W_\kappa \gamma z_h, \gamma v_h \big\rangle + \big\langle \mu_h, V_\kappa \xi_h \big\rangle$$

$$+ \big\langle \mu_h, \big(\tfrac{\mathrm{id}}{2} - K_\kappa\big) \gamma z_h \big\rangle - \big\langle \xi_h, \big(\tfrac{\mathrm{id}}{2} - K_\kappa\big) \gamma v_h \big\rangle$$

for all $(z_h, \xi_h), (v_h, \mu_h) \in \boldsymbol{X}_h^k$.

6.3.3.2 Solvability and a Priori Error Analyses

For the solvability of (6.85), we now introduce the perturbation of the bilinear form $\mathbb{A}_{\kappa,h}$ given by

$$\mathbb{A}_{0,h}\big((z_h, \xi_h), (v_h, \mu_h)\big) := a_{0,h}(z_h, v_h) + \left\{ \int_\Gamma z_h \right\} \left\{ \int_\Gamma v_h \right\} + \big\langle W \gamma z_h, \gamma v_h \big\rangle$$

$$+ \big\langle \mu_h, V \xi_h \big\rangle + \big\langle \xi_h, 1 \big\rangle \big\langle \mu_h, 1 \big\rangle + \big\langle \mu_h, \big(\tfrac{\mathrm{id}}{2} - K\big) \gamma z_h \big\rangle - \big\langle \xi_h, \big(\tfrac{\mathrm{id}}{2} - K\big) \gamma v_h \big\rangle \tag{6.86}$$

for all $(z_h, \xi_h), (v_h, \mu_h) \in \boldsymbol{X}_h^k$. Next, the boundedness of $\mathbb{A}_{\kappa,h}$ and $\mathbb{A}_{0,h}$, and the ellipticity of $\mathbb{A}_{0,h}$, are provided by the following two lemmas.

Lemma 6.8 *There exist positive constants M_κ and M_0, independent of h, such that for each $* \in \{\kappa, 0\}$ there hold*

$$\big| \mathbb{A}_{*,h}\big((z_h, \xi_h), (v_h, \mu_h)\big) \big| \; \leq \; M_* \, \|(z_h, \xi_h)\| \, \|(v_h, \mu_h)\|$$

for all $(z_h, \xi_h), (v_h, \mu_h) \in \boldsymbol{X}_h^k$.

Proof Starting from the corresponding definitions (cf. (6.59) and (6.86)), it suffices to employ the mapping properties of the boundary integral operators (cf. Lemma 6.1), and then notice from (6.80), (6.81) and [6], that for each $F \in \mathscr{F}_h$

there holds

$$S_h^F(z_h - \Pi_k^{\nabla,F} z_h, v_h - \Pi_k^{\nabla,F} v_h)$$

$$\lesssim |z_h - \Pi_k^{\nabla,F} z_h|_{1,F} |v_h - \Pi_k^{\nabla,F} v_h|_{1,F} \lesssim |z_h|_{1,F} |v_h|_{1,F}$$

for all $z_h,\, v_h \in X_h^k(F)$. $\square$

Lemma 6.9 *There exist a positive constant β_0, independent of h, such that*

$$Re\Big\{ \mathbb{A}_{0,h}\big((v_h, \mu_h), (\bar{v}_h, \bar{\mu}_h)\big) \Big\} \geq \beta_0 \, \|(v_h, \mu_h)\|^2 \qquad \forall\, (v_h, \mu_h) \in X_h^k.$$

Proof Bearing in mind the definition (6.86), and proceeding as in the deduction of (6.35), we first apply the positivity properties of the boundary integral operators (cf. Lemma 6.2). In this way, noticing from (6.82), (6.80) and (6.54) that for each $F \in \mathscr{F}_h$ there holds

$$a_{0,h}^F(v, \bar{v}) = |\Pi_k^{\nabla,F} v|_{1,F}^2 + S_h^F(v - \Pi_k^{\nabla,F} v, \bar{v} - \Pi_k^{\nabla,F} \bar{v})$$

$$\gtrsim |\Pi_k^{\nabla,F} v|_{1,F}^2 + |v - \Pi_k^{\nabla,F} v|_{1,F}^2 \gtrsim |v|_{1,F}^2 \qquad \forall\, v \in X_h^k(F),$$

we arrive at the required inequality and conclude the proof. $\square$

Furthermore, thanks to Lemmas 6.8 and 6.9, and the boundedness estimate (6.33), we can apply the Lax-Milgram lemma to introduce the Galerkin projection-type operator $\mathscr{R}_h : X \rightarrow X_h^k$, which, given $(z, \xi) \in X$, is uniquely characterized by

$$\mathbb{A}_{0,h}\big(\mathscr{R}_h(z, \xi), (v_h, \mu_h)\big) = \mathbb{A}_0\big((z, \xi), (v_h, \mu_h)\big) \qquad \forall\, (v_h, \mu_h) \in X_h^k. \tag{6.87}$$

Moreover, it readily follows from the aforementioned classical lemma that $\mathscr{R}_h$ is uniformly bounded in h with $\|\mathscr{R}_h\| \leq \|\mathbb{A}_0\|/\beta_0$. The approximation property of this operator is established next. As usual, given a finite dimensional subspace X_h of a normed space X, we set for each $x \in X$, $\text{dist}(x, X_h) := \inf_{x_h \in X_h} \|x - x_h\|$.

Theorem 6.5 *There exists a positive constant C, independent of h, such that*

$$\|\mathscr{R}_h(z, \xi) - (z, \xi)\| \leq C \left\{ \text{dist}\big((z, \xi), X_h^k\big) + \left(\sum_{F \in \mathscr{F}_h} |z - \Pi_k^{\nabla,F} z|_{1,F}^2 \right)^{1/2} \right\} \tag{6.88}$$

for all $(z, \xi) \in X$.

Proof Given $(z, \xi) \in X$ and $(z_h, \xi_h) \in X_h^k$, we first observe by triangle inequality that

$$\|\mathscr{R}_h(z, \xi) - (z, \xi)\| \leq \|(v_h, \mu_h)\| + \|(z, \xi) - (z_h, \xi_h)\|, \tag{6.89}$$

with $(v_h, \mu_h) := \mathscr{R}_h(z, \xi) - (z_h, \xi_h) \in X_h^k$, so that in what follows we focus on estimating $\|(v_h, \mu_h)\|$. In fact, applying the ellipticity property (6.67), the identity (6.87), the boundedness of $\mathbb{A}_0$ (cf. (6.33)), and the fact that the difference between $\mathbb{A}_0$ and $\mathbb{A}_{0,h}$ (cf. (6.31), (6.86)) reduces to $a_0 - a_{0,h}$, we obtain

$$
\begin{aligned}
\beta_0 \|(v_h, \mu_h)\|^2 &\leq \mathrm{Re}\Big\{\mathbb{A}_{0,h}\big((v_h, \mu_h), (\bar{v}_h, \bar{\mu}_h)\big)\Big\} \\
&= \mathrm{Re}\Big\{\mathbb{A}_0\big((z, \xi), (\bar{v}_h, \bar{\mu}_h)\big) - \mathbb{A}_{0,h}\big((z_h, \xi_h), (\bar{v}_h, \bar{\mu}_h)\big)\Big\} \\
&\leq \big|\mathbb{A}_0\big((z, \xi) - (z_h, \xi_h), (\bar{v}_h, \bar{\mu}_h)\big)\big| \\
&\quad + \big|\mathbb{A}_0\big((z_h, \xi_h), (\bar{v}_h, \bar{\mu}_h)\big) - \mathbb{A}_{0,h}\big((z_h, \xi_h), (\bar{v}_h, \bar{\mu}_h)\big)\big| \\
&\leq \|\mathbb{A}_0\| \, \|(z, \xi) - (z_h, \xi_h)\| \, \|(v_h, \mu_h)\| \\
&\quad + \sum_{F \in \mathscr{F}_h} \Big|a_0^F(z_h, \bar{v}_h) - a_{0,h}^F(z_h, \bar{v}_h)\Big|.
\end{aligned}
\tag{6.90}
$$

Then, subtracting and adding $\Pi_k^{\nabla, F} z$ in the first component of the expression $a_{0,h}^F(z_h, \bar{v}_h)$, using that $a_{0,h}^F(\Pi_k^{\nabla, F} z, v_h) = a_0^F(\Pi_k^{\nabla, F} z, \Pi_k^{\nabla, F} v_h) = a_0^F(\Pi_k^{\nabla, F} z, v_h)$ (which follows from (6.82) and after taking $(v, p) = (v_h, 1)$ and $(v, p) = (v_h, \Pi_k^{\nabla, F} z)$ in (6.44)), and employing the triangle inequality and the boundedness of a_0^F and $a_{0,h}^F$, the latter being consequence of (6.81), we find that

$$
\begin{aligned}
\big|a_0^F(z_h, \bar{v}_h) - a_{0,h}^F(z_h, \bar{v}_h)\big| &\leq \big|a_0^F(z_h - \Pi_k^{\nabla, F} z, \bar{v}_h)\big| + \big|a_{0,h}^F(z_h - \Pi_k^{\nabla, F} z, \bar{v}_h)\big| \\
&\lesssim |z_h - \Pi_k^{\nabla, F} z|_{1,F} \, |v_h|_{1,F} \lesssim \Big\{|z_h - z|_{1,F} + |z - \Pi_k^{\nabla, F} z|_{1,F}\Big\} |v_h|_{1,F}.
\end{aligned}
$$

In this way, summing up over $F \in \mathscr{F}_h$, it follows that

$$
\begin{aligned}
\sum_{F \in \mathscr{F}_h} &\big|a_0^F(z_h, \bar{v}_h) - a_{0,h}^F(z_h, \bar{v}_h)\big| \\
&\lesssim \Big\{|z_h - z|_{1,\mathscr{O}} + \Big(\sum_{F \in \mathscr{F}_h} |z - \Pi_k^{\nabla, F} z|_{1,F}^2\Big)^{1/2}\Big\} |v_h|_{1,\mathscr{O}} \\
&\lesssim \Big\{\|(z, \xi) - (z_h, \xi_h)\| + \Big(\sum_{F \in \mathscr{F}_h} |z - \Pi_k^{\nabla, F} z|_{1,F}^2\Big)^{1/2}\Big\} \|(v_h, \mu_h)\|,
\end{aligned}
$$

which, combined with (6.90), yields

$$\|(v_h, \mu_h)\| \lesssim \|(z, \xi) - (z_h, \xi_h)\| + \left(\sum_{F \in \mathcal{T}_h} |z - \Pi_k^{\nabla, F} z|_{1,F}^2 \right)^{1/2} .$$

Finally, replacing the foregoing inequality back into (6.89) and taking infimum with respect to $(z_h, \xi_h) \in X_h^k$, we arrive at (6.88) and finish the proof. $\square$

Having proved Theorem 6.5, we now employ classical density arguments, the approximation properties provided by (6.49), (6.50), and Lemma 6.4, and the uniform boundedness of $\mathcal{R}_h$, to deduce that

$$\lim_{h \to 0} \|\mathcal{R}_h(z, \xi) - (z, \xi)\| = 0 \qquad \forall (z, \xi) \in X , \tag{6.91}$$

or, equivalently, that $\mathcal{R}_h$ converges pointwise to the identity operator in X.

The unique solvability and associated stability estimate of the VEM/BEM scheme (6.85) follows from the discrete inf-sup condition for $\mathbb{A}_{\kappa,h}$, which is established next. For later use, we now let $\langle \cdot, \cdot \rangle_X$ be the inner product of X.

Theorem 6.6 *Assume that κ^2 is not an eigenvalue of the Laplacian in $\mathcal{O}$ with a Dirichlet boundary condition on Γ. Then, there exist positive constants h_0 and α_κ, independent of h, such that for each $h \leq h_0$ there holds*

$$\sup_{\substack{(z_h, \xi_h) \in X_h^k \\ (z_h, \xi_h) \neq \mathbf{0}}} \frac{\left| \mathbb{A}_{\kappa,h}\big((z_h, \xi_h), (v_h, \mu_h)\big) \right|}{\|(z_h, \xi_h)\|} \geq \alpha_\kappa \|(v_h, \mu_h)\| \qquad \forall (v_h, \mu_h) \in X_h^k .$$

$$\tag{6.92}$$

Proof We first employ the bijectivity of $\mathscr{A}_\kappa : X \to X'$ to deduce the existence of a bounded operator $\Theta : X \to X$ such that, given $(z, \xi) \in X$, $\Theta(z, \xi) \in X$ is uniquely characterized by the identity

$$\mathbb{A}_\kappa\big(\Theta(z, \xi), (v, \mu)\big) = \langle (z, \xi), (v, \mu) \rangle_X \qquad \forall (v, \mu) \in X ,$$

which implies, in particular, that

$$\mathbb{A}_\kappa\big(\Theta(z, \xi), (z, \xi)\big) = \|(z, \xi)\|^2 \qquad \forall (z, \xi) \in X . \tag{6.93}$$

Then, given $(v_h, \mu_h) \in X_h^k$, we set $(z_h^+, \xi_h^+) := \mathscr{R}_h \Theta(v_h, \mu_h) \in X_h^k$, and observe that certainly

$$\sup_{\substack{(z_h, \xi_h) \in X_h^k \\ (z_h, \xi_h) \neq \mathbf{0}}} \frac{\left| \mathbb{A}_{\kappa,h}\big((z_h, \xi_h), (v_h, \mu_h)\big) \right|}{\|(z_h, \xi_h)\|} \geq \frac{\left| \mathbb{A}_{\kappa,h}\big((z_h^+, \xi_h^+), (v_h, \mu_h)\big) \right|}{\|(z_h^+, \xi_h^+)\|} . \tag{6.94}$$

In turn, adding and subtracting the bilinear forms $\mathbb{A}_\kappa$, $\mathbb{A}_0$, and $\mathbb{A}_{0,h}$, so that

$$\mathbb{A}_{\kappa,h} = \mathbb{A}_{0,h} + (\mathbb{A}_\kappa - \mathbb{A}_0) + (\mathbb{A}_0 - \mathbb{A}_{0,h}) + (\mathbb{A}_{\kappa,h} - \mathbb{A}_\kappa),$$

and noticing from the definitions of $\mathbb{A}_\kappa$, $\mathbb{A}_0$, $\mathbb{A}_{\kappa,h}$, and $\mathbb{A}_{0,h}$ (cf. (6.19), (6.31), (6.59), and (6.86)), that

$$\big(\mathbb{A}_0 - \mathbb{A}_{0,h}\big)\big((z_h^+, \xi_h^+), (v_h, \mu_h)\big) = \int_{\mathcal{O}} \nabla z_h^+ \cdot \nabla v_h - a_{0,h}(z_h^+, v_h)$$

and

$$\big(\mathbb{A}_{\kappa,h} - \mathbb{A}_\kappa\big)\big((z_h^+, \xi_h^+), (v_h, \mu_h)\big) = a_{\kappa,h}(z_h^+, v_h) - a_\kappa(z_h^+, v_h)$$

$$= a_{0,h}(z_h^+, v_h) - \int_{\mathcal{O}} \nabla z_h^+ \cdot \nabla v_h \tag{6.95}$$

$$+ \kappa^2 \sum_{F \in \mathscr{F}_h} \vartheta_F \int_F \left\{ z_h^+ v_h - \big(\Pi_{k-1}^F z_h^+\big) \big(\Pi_{k-1}^F v_h\big) \right\},$$

we readily arrive at

$$\mathbb{A}_{\kappa,h}\big((z_h^+, \xi_h^+), (v_h, \mu_h)\big) = \mathbb{A}_{0,h}\big(\mathscr{R}_h \Theta(v_h, \mu_h), (v_h, \mu_h)\big)$$

$$+ \big[\mathscr{C} \mathscr{R}_h \Theta(v_h, \mu_h), (v_h, \mu_h)\big] \tag{6.96}$$

$$+ \kappa^2 \sum_{F \in \mathscr{F}_h} \vartheta_F \int_E \left\{ z_h^+ v_h - \big(\Pi_{k-1}^F z_h^+\big) \big(\Pi_{k-1}^F v_h\big) \right\},$$

where $\mathscr{C} := \mathscr{A}_\kappa - \mathscr{A}_0 : X \to X'$ is a compact operator. Hence, starting from (6.96), denoting by I the identity operator from X into itself, letting ϑ_M be the maximum value of $|\vartheta_F|$, $F \in \mathscr{F}_h$, and employing the characterization of $\mathscr{R}_h$ (cf. (6.87)), the orthogonality condition satisfied by Π_{k-1}^F, the identity (6.93), the approximation properties of Π_{k-1}^F (cf. (6.48)), and the fact that $\mathscr{R}_h$ is uniformly bounded, we find that

$$\mathbb{A}_{\kappa,h}\big((z_h^+, \xi_h^+), (v_h, \mu_h)\big) = \mathbb{A}_0\big(\Theta(v_h, \mu_h), (v_h, \mu_h)\big) + \big[\mathscr{C} \mathscr{R}_h \Theta(v_h, \mu_h), (v_h, \mu_h)\big]$$

$$+ \kappa^2 \sum_{F \in \mathscr{F}_h} \vartheta_F \int_F \left\{ z_h^+ v_h - \big(\Pi_{k-1}^F z_h^+\big) \big(\Pi_{k-1}^F v_h\big) \right\}$$

$$= \mathbb{A}_\kappa\big(\Theta(v_h, \mu_h), (v_h, \mu_h)\big) + \big[\mathscr{C}\big(\mathscr{R}_h - I\big)\Theta(v_h, \mu_h), (v_h, \mu_h)\big]$$

$$+ \kappa^2 \sum_{F \in \mathscr{F}_h} \vartheta_F \int_F \left\{ z_h^+ - \Pi_{k-1}^F z_h^+ \right\} \left\{ v_h - \Pi_{k-1}^F v_h \right\}$$

$$\geq \left\{ 1 - \|\mathscr{C}\big(\mathscr{R}_h - I\big)\| \|\Theta\| \right\} \|(v_h, \mu_h)\|^2$$

$$- \kappa^2 \vartheta_M \sum_{F \in \mathscr{F}_h} \left\| z_h^+ - \Pi_{k-1}^F z_h^+ \right\|_{0,F} \left\| v_h - \Pi_{k-1}^F v_h \right\|_{0,F}$$

$$\geq \left\{ 1 - \|\mathscr{C}(\mathscr{R}_h - \mathrm{I})\| \|\Theta\| \right\} \|(v_h, \mu_h)\|^2 - C h^2 \|(z_h^+, \xi_h^+)\| \|(v_h, \mu_h)\|$$

$$\geq \left\{ 1 - \|\mathscr{C}(\mathscr{R}_h - \mathrm{I})\| \|\Theta\| - C h^2 \right\} \|(z_h^+, \xi_h^+)\| \|(v_h, \mu_h)\|,$$

where C is a positive constant depending on κ and ϑ_M, but independent of h, and the last inequality uses that $\|(v_h, \mu_h)\| \gtrsim \|(z_h^+, \xi_h^+)\|$. Finally, the compactness of $\mathscr{C}$ and the pointwise convergence of $\mathscr{R}_h - \mathrm{I}$ to zero (cf. (6.91)) guarantee that $\lim_{h \to 0} \|\mathscr{C}(\mathscr{R}_h - \mathrm{I})\| = 0$, which, together with the foregoing estimate and (6.94), yield (6.92) for a sufficiently small h_0. $\qquad \square$

Under the same assumptions of Theorem 6.6, and as a straightforward consequence of (6.92), we conclude that, given $\mathbb{F} \in X'$ and $h \leq h_0$, the VEM/BEM scheme (6.85) has a unique solution $(u_h, \lambda_h) \in X_h^k$.

We now turn to provide a priori error bounds and associated rates of convergence for the solution of the VEM/BEM scheme (6.85). For this purpose, we first define the discrete analogue of Θ (though with respect to the second component of the bilinear form involved), namely the operator $\Theta_h : X_h^k \to X_h^k$ that, given $(v_h, \mu_h) \in X_h^k$, is uniquely characterized by the equation

$$\mathbb{A}_{\kappa,h}\big((z_h, \xi_h), \Theta_h(v_h, \mu_h)\big) = \langle (z_h, \xi_h), (v_h, \mu_h) \rangle_X \qquad \forall (z_h, \xi_h) \in X_h^k,$$

so that, in particular,

$$\mathbb{A}_{\kappa,h}\big((v_h, \mu_h), \Theta_h(v_h, \mu_h)\big) = \|(v_h, \mu_h)\|^2 \qquad \forall (v_h, \mu_h) \in X_h^k. \tag{6.97}$$

Note that the above identity and the discrete inf-sup condition (6.92) yield

$$\|\Theta_h\| \leq \frac{1}{\alpha_\kappa}. \tag{6.98}$$

Hence, we have the following Cea-type estimate, which makes use of $\Pi_{k-1}^{\mathscr{F}}$ (cf. (6.47)), the global $L^2(\mathscr{O})$-orthogonal projection onto $\mathscr{P}_{k-1}(\mathscr{F}_h)$.

Theorem 6.7 *Assume that κ^2 is not an eigenvalue of the Laplacian in $\mathscr{O}$ with a Dirichlet boundary condition on Γ, and let $h_0 > 0$ be the constant whose existence is guaranteed by Theorem 6.6. Then, there exists a constant $C > 0$, independent of h, such that for each $h \leq h_0$ there holds*

$$\|(u, \lambda) - (u_h, \lambda_h)\|$$

$$\leq C \left\{ \mathrm{dist}\big((u, \lambda), X_h^k\big) + \Big(\sum_{F \in \mathscr{F}_h} \big\| u - \Pi_k^{\nabla, F} u \big\|_{1,F}^2 \Big)^{1/2} + \big\| u - \Pi_{k-1}^{\mathscr{F}} u \big\|_{0,\mathscr{O}} \right\}. \tag{6.99}$$

Proof We begin by observing, thanks to the triangle inequality, that

$$\|(u, \lambda) - (u_h, \lambda_h)\| \leq \|(u, \lambda) - (v_h, \mu_h)\| + \|(z_h, \xi_h)\| \qquad \forall\, (v_h, \mu_h) \in X_h^k, \tag{6.100}$$

where $(z_h, \xi_h) := (u_h, \lambda_h) - (v_h, \mu_h)$. Then, setting $(z_h^+, \xi_h^+) := \Theta_h(z_h, \xi_h) \in X_h^k$, employing the identity (6.97) and the fact that $\mathbb{A}_\kappa\big((u, \lambda), \cdot\big)$ and $\mathbb{A}_{\kappa,h}\big((u_h, \lambda_h), \cdot\big)$ coincide on X_h^k (which follows from (6.18) and (6.58)), adding and subtracting (v_h, μ_h) in the first component of $\mathbb{A}_\kappa$, using the uniform boundedness of Θ_h (cf. (6.98)) and the identity provided by the first row of (6.95), and then adding and subtracting u in the first component of a_κ, we obtain

$$\begin{aligned}
\|(z_h, \xi_h)\|^2 &= \mathbb{A}_{\kappa,h}\big((u_h, \lambda_h), \Theta_h(z_h, \xi_h)\big) - \mathbb{A}_{\kappa,h}\big((v_h, \mu_h), \Theta_h(z_h, \xi_h)\big) \\
&= \mathbb{A}_\kappa\big((u, \lambda) - (v_h, \mu_h), \Theta_h(z_h, \xi_h)\big) + \big(\mathbb{A}_\kappa - \mathbb{A}_{\kappa,h}\big)\big((v_h, \mu_h), (z_h^+, \xi_h^+)\big) \\
&\leq \|\mathbb{A}_\kappa\|\, \alpha_\kappa^{-1}\, \|(u, \lambda) - (v_h, \mu_h)\|\, \|(z_h, \xi_h)\| + \big| a_\kappa(v_h, z_h^+) - a_{\kappa,h}(v_h, z_h^+) \big| \\
&\leq \big(\|\mathbb{A}_\kappa\| + \|a_\kappa\| \big)\, \alpha_\kappa^{-1}\, \|(u, \lambda) - (v_h, \mu_h)\|\, \|(z_h, \xi_h)\| \\
&\quad + \big| a_\kappa(u, z_h^+) - a_{\kappa,h}(v_h, z_h^+) \big|.
\end{aligned} \tag{6.101}$$

In this way, we now focus on estimating the last term on the right hand side of the foregoing equation. Indeed, according to the definitions of a_κ and $a_{\kappa,h}$ (cf. (6.24) and (6.83)–(6.84)), we first obtain

$$\begin{aligned}
\big| a_\kappa(u, z_h^+) - a_{\kappa,h}(v_h, z_h^+) \big| &\leq \sum_{F \in \mathscr{F}_h} \big| a_\kappa^F(u, z_h^+) - a_{\kappa,h}^F(v_h, z_h^+) \big| \\
&\leq \sum_{F \in \mathscr{F}_h} \big| a_0^F(u, z_h^+) - a_{0,h}^F(v_h, z_h^+) \big| \\
&\quad + \kappa^2 \sum_{F \in \mathscr{F}_h} |\vartheta_F| \left| \int_F \left\{ u z_h^+ - \big(\Pi_{k-1}^F v_h\big)\big(\Pi_{k-1}^F z_h^+\big) \right\} \right|.
\end{aligned} \tag{6.102}$$

Next, adding and subtracting $\Pi_k^{\nabla,F} u$ in the first component of $a_0^F(u, z_h^+)$, recalling that there holds $a_0^F(\Pi_k^{\nabla,F} u, z_h^+) = a_{0,h}^F(\Pi_k^{\nabla,F} u, z_h^+)$ (cf. proof of Theorem 6.5),

and thanks to the uniform boundedness of $a_{0,h}^F$, we find that

$$
\begin{aligned}
\left| a_0^F(u, z_h^+) - a_{0,h}^F(v_h, z_h^+) \right| &= \left| a_0^F(u - \Pi_k^{\nabla,F} u, z_h^+) + a_0^F(\Pi_k^{\nabla,F} u, z_h^+) - a_{0,h}^F(v_h, z_h^+) \right| \\
&= \left| a_0^F(u - \Pi_k^{\nabla,F} u, z_h^+) + a_{0,h}^F(\Pi_k^{\nabla,F} u - v_h, z_h^+) \right| \\
&\lesssim \left\{ \left\| u - \Pi_k^{\nabla,F} u \right\|_{1,F} + \left\| \Pi_k^{\nabla,F} u - v_h \right\|_{1,F} \right\} \| z_h^+ \|_{1,F} \\
&\lesssim \left\{ \left\| u - \Pi_k^{\nabla,F} u \right\|_{1,F} + \| u - v_h \|_{1,F} \right\} \| z_h^+ \|_{1,F} .
\end{aligned}
\tag{6.103}
$$

In turn, the orthogonality condition satisfied by Π_{k-1}^F and the triangle inequality yield

$$
\begin{aligned}
\left| \int_F \left\{ u z_h^+ - (\Pi_{k-1}^F v_h)(\Pi_{k-1}^F z_h^+) \right\} \right| &= \left| \int_F \left\{ u - (\Pi_{k-1}^F v_h) \right\} z_h^+ \right| \\
&\leq \left\{ \| u - v_h \|_{0,F} + \| u - \Pi_{k-1}^F u \|_{0,F} \right\} \| z_h^+ \|_{0,F} .
\end{aligned}
\tag{6.104}
$$

Hence, plugging (6.103) and (6.104) in (6.102), and applying the Cauchy-Schwarz inequality, we deduce the existence of a positive constant C_1, depending on κ and ϑ_M, but independent of h, such that

$$
\begin{aligned}
\left| a_\kappa(u, z_h^+) - a_{\kappa,h}(v_h, z_h^+) \right| &\leq C_1 \left\{ \left(\sum_{F \in \mathscr{F}_h} \| u - \Pi_k^{\nabla,F} u \|_{1,F}^2 \right)^{1/2} \right. \\
&\quad \left. + \| u - v_h \|_{1,\mathscr{O}} + \| u - \Pi_{k-1}^{\mathscr{F}} u \|_{0,\mathscr{O}} \right\} \| z_h^+ \|_{1,\mathscr{O}} .
\end{aligned}
\tag{6.105}
$$

Thus, replacing (6.105) back into (6.101), and bounding $\| z_h^+ \|_{1,\mathscr{O}}$ by $\alpha_\kappa^{-1} \| (z_h, \xi_h) \|$, we conclude that

$$
\begin{aligned}
\| (z_h, \xi_h) \| &\leq C_2 \left\{ \left\| (u, \lambda) - (v_h, \mu_h) \right\| \right. \\
&\quad \left. + \left(\sum_{F \in \mathscr{F}_h} \| u - \Pi_k^{\nabla,F} u \|_{1,F}^2 \right)^{1/2} + \| u - \Pi_{k-1}^{\mathscr{F}} u \|_{0,\mathscr{O}} \right\},
\end{aligned}
\tag{6.106}
$$

where C_2 is a positive constant depending on $\| \mathbb{A}_\kappa \|$, $\| a_\kappa \|$, α_κ, and C_1, but independent of h. Finally, combining (6.100) and (6.106), and then taking infimum over $(v_h, \mu_h) \in X_h^k$, we arrive at (6.99). $\qquad\square$

The rates of convergence of our discrete scheme are provided next. To this end, we recall from (6.51) that $I_k^{\mathscr{F}}$ stands for the global virtual element interpolation operator. Then, we have the following result.

Theorem 6.8 *Assume that κ^2 is not an eigenvalue of the Laplacian in $\mathcal{O}$ with a Dirichlet boundary condition on Γ, and that both u and the datum w belong to $H^1(\mathcal{O}) \cap \prod_{i=1}^{I} H^{k+1}(\mathcal{O}_i)$. In addition, let $h_0 > 0$ be the constant whose existence is guaranteed by Theorem 6.6. Then, there exists a constant $C_0 > 0$, independent of h, such that for each $h \leq h_0$ there holds*

$$\|(u, \lambda) - (u_h, \lambda_h)\| \leq C_0 \, h^k \sum_{i=1}^{I} \|u\|_{k+1, \mathcal{O}_i} . \tag{6.107}$$

Proof We begin by observing that $H^1(\mathcal{O}) \cap \prod_{i=1}^{I} H^{k+1}(\mathcal{O}_i) \subseteq \mathscr{C}^0(\overline{\mathcal{O}})$, which implies that $I_k^{\mathscr{F}} u$ is meaningful. Furthermore, we have that $\lambda = \gamma_n\big(\nabla(u - w)\big) \in H^{-1/2}(\Gamma) \cap H_b^{k-1/2}(\Gamma) \subseteq L^2(\Gamma)$, whence $\Pi_{k-1}^{\mathscr{E}} \lambda$ is meaningful as well, and hence

$$\text{dist}\big((u, \lambda), X_h^k\big) \leq \|u - I_k^{\mathscr{F}} u\|_{1,\Omega} + \|\lambda - \Pi_{k-1}^{\mathscr{E}} \lambda\|_{-1/2,\Gamma} .$$

In this way, replacing the foregoing estimate back into (6.99), applying the approximation properties of $I_k^{\mathscr{F}}$ (cf. (6.50)), $\Pi_{k-1}^{\mathscr{E}}$ (cf. Lemma 6.4), $\Pi_k^{\nabla, F}$ (cf. (6.49)), and $\Pi_{k-1}^{\mathscr{F}}$ (cf. (6.48)), and employing the trace inequality

$$\|\lambda\|_{k-1/2, b, \Gamma} \lesssim \sum_{i=1}^{I} \|u\|_{k+1, \Omega_i} ,$$

we are led to (6.107), thus concluding the proof.   □

6.4 The Modified Costabel & Han VEM/BEM Schemes in 3D

In spite of the plural sense of its title, in this section we introduce and analyze the discrete VEM/BEM scheme for the modified Costabel & Han coupling procedure as applied to the Poisson model only, in the 3D case. The corresponding analysis for the Helmholtz model arises from a suitable combination of the tools to be employed in what follows with those utilized in Sect. 6.3.3. We refer to [22, Section 6] for details.

We begin by stressing that the Costabel & Han coupling procedure, that is the variational formulation (6.18), is not applicable to a VEM/BEM coupling in three dimensions. In fact, as it will become clear below from definitions (6.108) and (6.109), the restriction of a VEM function v_h to the boundary of a given element in 3D is not a polynomial function but a virtual function as well. As a consequence, the term $\big\langle \mu_h, (\frac{\text{id}}{2} - K)\gamma v_h\big\rangle$ of the bilinear form $\mathbf{A}_h$ (cf. (6.59)) defining (6.58), is not computable. Moreover, it is easy to show that, replacing this term by $\big\langle \mu_h, (\frac{\text{id}}{2} - K)\Pi_k^{\mathscr{F}} \gamma v_h\big\rangle$, implies a dramatic loss of accuracy because, as

Γ is a polyhedral Lipschitz boundary, the boundary integral operator K does not yield any further regularity. Summarizing, the fact that the original Costabel & Han coupling method is only applicable to a VEM/BEM scheme in 2D has motivated the introduction of the modified version that we employ in this section.

Similarly as in Sect. 6.3.1, we previously need to collect some fundamental notations and results on VEM in 3D.

6.4.1   Preliminaries

We let $\{\mathscr{T}_h\}_h$ be a family of decompositions of $\overline{\Omega}$ into polyhedral elements E of diameter $h_E \leq h$, and assume again that the meshes $\{\mathscr{T}_h\}_h$ are aligned with each of the subdomaines Ω_i, $i = 1, \ldots, I$ mentioned at the beginning of Sect. 6.3.1. In turn, the boundary ∂E of each $E \in \mathscr{T}_h$ is subdivided into planar faces denoted by F, and we let $\mathscr{F}_h$ be the set of faces of $\mathscr{T}_h$ that are contained in Γ. In addition, we assume that the family $\{\mathscr{T}_h\}_h$ of meshes satisfy the following conditions: There exists $\rho \in (0, 1)$ such that

(B1) each E of $\{\mathscr{T}_h\}_h$ is star-shaped with respect to a ball B_E of radius ρh_E,
(B2) for each E of $\{\mathscr{T}_h\}_h$, the diameters h_F of all its faces $F \subseteq \partial E$ satisfy $h_F \geq \rho h_E$,
(B3) the faces of each $E \in \{\mathscr{T}_h\}_h$, viewed as two-dimensional elements, satisfy the properties **(A1)** and **(A2)** (cf. Sect. 6.3.1) with the same ρ.

Next, given an integer $k \geq 1$ and $E \in \mathscr{T}_h$, and bearing in mind the definition (6.45), we set

$$X_h^k(\partial E) := \left\{ v \in \mathscr{C}^0(\partial E) : \quad v|_F \in X_h^k(F) \quad \forall F \subseteq \partial E \right\}, \qquad (6.108)$$

and introduce the local virtual element space

$$W_h^k(E) := \Big\{ v \in H^1(E) : \ v|_{\partial E} \in X_h^k(\partial E), \ \Delta v \in \mathscr{P}_k(E),$$
$$\Pi_k^E v - \Pi_k^{\nabla, E} v \ \in \ \mathscr{P}_{k-2}(E) \Big\}, \qquad (6.109)$$

where, analogously to the 2D case (cf. Sect. 6.3.1), Π_k^E is now the $L^2(E)$–orthogonal projection onto $\mathscr{P}_k(E)$, and the projection operator $\Pi_k^{\nabla, E} : H^1(E) \to \mathscr{P}_k(E)$ is defined as in (6.44) after replacing F with E. In addition, the degrees of freedom of $W_h^k(E)$ consist of:

(i) the values at the vertices of E,
(ii) the moments of order $\leq k - 2$ on the edges of E,

(iii) the moments of order $\leq k-2$ on the faces of E, and
(iv) the moments of order $\leq k-2$ on E.

We can then define the global virtual element space as

$$W_h^k := \left\{ v \in X : \quad v|_E \in W_h^k(E) \quad \forall E \in \mathcal{T}_h \right\}. \tag{6.110}$$

In addition, and coherently with the notations of Sect. 6.3.1, given any integer $k \geq 0$, we let Π_k^E and $\Pi_k^{\mathcal{T}}$ be the L^2–orthogonal projections onto $\mathscr{P}_k(E)$ and $\mathscr{P}_k(\mathcal{T}_h)$, respectively, and denote by $\boldsymbol{\Pi}_k^E$ and $\boldsymbol{\Pi}_k^{\mathcal{T}}$ their corresponding vectorial counterparts. Here again, we stress that $\mathscr{P}_k(E) \subseteq X_h^k(E)$ and that $\Pi_k^{\nabla,E}v$, $\Pi_k^E v$ and $\boldsymbol{\Pi}_{k-1}^E \nabla v$ are all computable for each $v \in X_h^k(E)$ (cf. [2]). In turn, we let $I_k^E : \text{H}^2(E) \rightarrow W_h^k(E)$ be the local interpolation operator, which is uniquely determined by the degrees of freedom of $W_h^k(E)$, and whose corresponding global operator is denoted $I_k^{\mathcal{T}} : \text{H}^2(\Omega) \rightarrow W_h^k$. The error estimates satisfied by the operators Π_k^E, $\Pi_k^{\nabla,E}$ and I_k^E are given by analogue versions of (6.48), (6.49) and (6.50), respectively, in which F is replaced with E.

Furthermore, we also introduce the simplicial submesh $\mathfrak{F}_h$ of Γ obtained by subdividing each face $F \in \mathscr{F}_h$ into the set of triangles that arise after joining each vertex of F with the midpoint of the disc with respect to which F is star-shaped. Since we are assuming that the meshes satisfy conditions **(A1)** and **(A2)** (cf. Sect. 6.3.1), the triangles $T \in \mathfrak{F}_h$ have a shape ratio that is uniformly bounded with respect to h. According to the above, and in order to approximate the non-virtual boundary unknowns of our scheme (cf. Sect. 6.4.2 below), we now introduce the piecewise polynomial spaces

$$\Lambda_h^{k-1} := \left\{ \mu_h \in \text{L}^2(\Gamma) : \quad \mu_h|_T \in P_{k-1}(T) \quad \forall T \in \mathfrak{F}_h \right\} \tag{6.111}$$

and

$$\Psi_h^k := \left\{ \varphi_h \in \mathscr{C}^0(\Gamma) : \quad \varphi_h|_T \in \mathscr{P}_k(T) \quad \forall T \in \mathfrak{F}_h \right\} \cap \text{H}_0^{1/2}(\Gamma). \tag{6.112}$$

Thus, we let $\Pi_{k-1}^{\mathfrak{F}}$ be the L$^2(\Gamma)$-orthogonal projection onto Λ_h^{k-1}, and let $\mathscr{L}_k^{\mathfrak{F}} : \mathscr{C}^0(\Gamma) \rightarrow \Psi_h^k$ be the corresponding global Lagrange interpolation operator of order k. Then, denoting by $\{\Gamma_1, \ldots, \Gamma_J\}$ the open polygons, contained in different hyperplanes of $\mathbb{R}^3$, such that $\Gamma = \cup_{j=1}^J \overline{\Gamma}_j$, we now recall from [30] the following approximation properties of $\Pi_{k-1}^{\mathfrak{F}}$ and $\mathscr{L}_k^{\mathfrak{F}}$.

Lemma 6.10 *Assume that $\mu \in H_0^{-1/2}(\Gamma) \cap H_b^r(\Gamma)$ for some $r \geq 0$. Then*

$$\left\| \mu - \Pi_{k-1}^{\mathfrak{F}} \mu \right\|_{-t,\Gamma} \lesssim h^{\min\{r,k\}+t} \, \|\mu\|_{r,b,\Gamma} \qquad \forall t \in \{0, 1/2\}.$$

Proof See [30, Theorem 4.3.20].   □

Lemma 6.11 *Assume that $\varphi \in H_b^{r+1/2}(\Gamma) \cap H^1(\Gamma)$ for some $r > 1/2$. Then*

$$\left\| \varphi - \mathscr{L}_k^{\widetilde{\mathfrak{F}}} \varphi \right\|_{t,\Gamma} \lesssim h^{\min\{r+1/2,k+1\}-t} \, \|\varphi\|_{r+1/2,b,\Gamma} \qquad \forall \, t \in \{0, 1/2, 1\} \, .$$

Proof See [30, Proposition 4.1.50].   □

6.4.2   The Discrete Setting

According to the finite dimensional subspaces defined in (6.110), (6.111), and (6.112), we now propose the following discrete formulation for (6.25): Find $(u_h, \psi_h, \lambda_h) \in \widetilde{\mathbf{X}}_h := W_h^k \times \Psi_h^k \times \Lambda_h^{k-1}$ such that

$$\widetilde{\mathbf{A}}_h\big((u_h, \psi_h, \lambda_h), (v_h, \varphi_h, \mu_h)\big) = \widetilde{\mathbf{F}}_h(v_h, \varphi_h, \mu_h) \quad \forall \, (v_h, \varphi_h, \mu_h) \in \widetilde{\mathbf{X}}_h \, , \tag{6.113}$$

where

$$\widetilde{\mathbf{A}}_h\big((z_h, \phi_h, \xi_h), (v_h, \varphi_h, \mu_h)\big) = \mathbf{a}_h\big((z_h, \phi_h, \xi_h), (v_h, \varphi_h, \mu_h)\big) + \big\langle W\phi_h, \varphi_h \big\rangle$$

$$+ \big\langle \mu_h, V\xi_h \big\rangle - \big\langle \xi_h, \big(\tfrac{\mathrm{id}}{2} - K\big)\varphi_h \big\rangle + \big\langle \mu_h, \big(\tfrac{\mathrm{id}}{2} - K\big)\phi_h \big\rangle, \tag{6.114}$$

$$\mathbf{a}_h\big((z_h, \phi_h, \xi_h), (v_h, \varphi_h, \mu_h)\big) = a_h(z_h, v_h) - \sum_{F \in \mathscr{F}_h} \int_F \xi_h \, \Pi_{k-1}^F(\gamma v_h - \varphi_h)$$

$$+ \sum_{F \in \mathscr{F}_h} \int_F \mu_h \, \Pi_{k-1}^F(\gamma z_h - \phi_h) \, , \tag{6.115}$$

and

$$\widetilde{\mathbf{F}}_h(v_h, \varphi_h, \mu_h) := \int_\Omega \Pi_{k-1}^{\mathscr{T}} f \, v_h \tag{6.116}$$

for all $(z_h, \phi_h, \xi_h), (v_h, \varphi_h, \mu_h) \in \widetilde{\mathbf{X}}_h$. We notice here that the bilinear form a_h forming part of the definition of $\mathbf{a}_h$ (cf. (6.115)) is defined as in Sect. 6.3. Namely, denoting by $\mathscr{E}(E)$ and $\mathscr{F}(E)$ the sets of edges and faces, respectively, of a given

$E \in \mathscr{T}_h$, we introduce

$$S_h^E(v, z) := \sum_{e \in \mathscr{E}(E)} \int_e \Pi_k^e v \, \Pi_k^e z \; + \; h_E^{-1} \sum_{F \in \mathscr{F}(E)} \int_F \Pi_{k-2}^F v \, \Pi_{k-2}^F z$$

for all $v, z \in W_h^k(E)$, set

$$a_h^E(v, z) := \int_E \kappa \, \mathbf{\Pi}_{k-1}^E \nabla v \cdot \mathbf{\Pi}_{k-1}^E \nabla z \; + \; S_h^E(v - \Pi_k^{\nabla, E} v, z - \Pi_k^{\nabla, E} z) \quad (6.117)$$

for all $v, z \in \mathrm{H}^1(E)$, and define

$$a_h(v, z) := \sum_{E \in \mathscr{T}_h} a_h^E(v, z)$$

for all $v, z \in W_h^k$. Furthermore, we stress that the boundary terms in (6.115) are certainly induced by the corresponding boundary terms in (6.26). More precisely, the fact that the discrete version of the second term on the right hand side of (6.26), that is $\langle \xi_h, \gamma v_h - \varphi_h \rangle$, is not computable since the virtual trace γv_h is not known, suggests to replace $\gamma v_h - \varphi_h$ by a suitable projection such as $\Pi_{k-1}^{\widetilde{\mathfrak{F}}}(\gamma v_h - \varphi_h)$, thus yielding the new term $\sum_{F \in \mathscr{F}_h} \int_F \xi_h \, \Pi_{k-1}^F(\gamma v_h - \varphi_h)$. An analogue reason explains the replacement of $\langle \mu_h, \gamma z_h - \phi_h \rangle$ by $\sum_{F \in \mathscr{F}_h} \int_F \mu_h \, \Pi_{k-1}^F(\gamma z_h - \phi_h)$. In turn, the use here of the global orthogonal projector $\Pi_{k-1}^{\widetilde{\mathfrak{F}}} : \mathrm{L}^2(\Gamma) \to \Lambda_h^{k-1}$, equivalently the local projections Π_{k-1}^F on each face F of $\mathscr{F}_h$, is strongly motivated by the fact that λ_h and μ_h live in the subspace Λ_h^{k-1}, which allows to apply later on the corresponding orthogonality condition, a key property for the derivation of the a priori error estimate and the associated rates of convergence (see below Theorem 6.9, estimate (6.124), and Theorem 6.10, all in Sect. 6.4.3).

Finally, we highlight that the discrete problem (6.113) is meaningful since $S_h^E(\cdot, \cdot)$ is computable on $W_h^k(E) \times W_h^k(E)$. Moreover, it can be shown that $S_h^E(v, z)$ scales like $a^E(v, z) := \int_E \kappa \nabla v \cdot \nabla z$ on the kernel of $\Pi_k^{\nabla, E}$ in $W_h^k(E)$. In other words, the three-dimensional counterpart of (6.54) holds true (cf. [9, Section 5.5]), which implies, in particular, that we have the corresponding 3D versions of (6.63) and (6.69) as well.

6.4.3   Solvability and a Priori Error Analyses

We begin by introducing further notations to be employed later on. In fact, for any $s \geq 0$ we define the broken Sobolev spaces

$$\mathrm{H}^s(\mathscr{T}_h) := \prod_{E \in \mathscr{T}_h} \mathrm{H}^s(K), \qquad \mathrm{H}^s(\mathscr{F}_h) := \prod_{F \in \mathscr{F}_h} \mathrm{H}^s(F),$$

which are endowed with the Hilbertian norms and corresponding seminorms, given respectively, by

$$\|v\|_{s,\mathscr{T}_h}^2 := \sum_{E \in \mathscr{T}_h} \|v\|_{s,E}^2, \qquad \|\varphi\|_{s,\mathscr{F}_h}^2 := \sum_{F \in \mathscr{F}_h} \|\varphi\|_{s,F}^2.$$

and

$$|v|_{s,\mathscr{T}_h}^2 := \sum_{E \in \mathscr{T}_h} |v|_{s,E}^2, \qquad |\varphi|_{s,\mathscr{F}_h}^2 := \sum_{F \in \mathscr{F}_h} |\varphi|_{s,F}^2,$$

for all $v \in \mathrm{H}^s(\mathscr{T}_h)$ and for all $\varphi \in \mathrm{H}^s(\mathscr{F}_h)$. In addition, we set as usual $\mathrm{H}^0(\mathscr{T}_h) = \mathrm{L}^2(\mathscr{T}_h)$ and $\mathrm{H}^0(\mathscr{F}_h) = \mathrm{L}^2(\mathscr{F}_h)$.

Now, concerning the solvability of (6.113), we first notice that the boundedness of $\widetilde{\mathbf{A}}_h$ follows exactly as proved for the 2D case (cf. Sect. 6.3.3). Thus, we continue the analysis with the $\widetilde{\mathbf{X}}_h$-ellipticity of $\widetilde{\mathbf{A}}_h$ with respect to the usual product norm of $\widetilde{\mathbf{X}}$.

Lemma 6.12 *There holds*

$$\widetilde{\mathbf{A}}_h\big(v_h, \varphi_h, \mu_h\big), \big(v_h, \varphi_h, \mu_h\big) \gtrsim \|(v_h, \varphi_h, \mu_h)\|^2$$

for all $\big(v_h, \varphi_h, \mu_h\big) \in \widetilde{\mathbf{X}}_h$.

Proof Given $(v_h, \varphi_h, \mu_h) \in \widetilde{\mathbf{X}}_h$, it follows from (6.114) and (6.115) that

$$\widetilde{\mathbf{A}}_h\big(v_h, \varphi_h, \mu_h\big), \big(v_h, \varphi_h, \mu_h\big) = a_h(v_h, v_h) + \big\langle W\varphi_h, \varphi_h \big\rangle + \big\langle \mu_h, V\mu_h \big\rangle,$$

and hence the 3D version of (6.69) and Lemma 6.1 finish the proof.   □

As a consequence of the previous analysis and the Lax-Milgram lemma, we conclude that (6.113) has a unique solution $(u_h, \psi_h, \lambda_h) \in \mathbb{X}_h$. Next, in order to establish the corresponding a priori error estimate, we follow the same notations from Sect. 6.3.1 and for each planar face $F \in \mathscr{F}_h$ we let Π_k^F be the $\mathrm{L}^2(F)$-orthogonal projection onto $\mathscr{P}_k(F)$ with vectorial counterpart $\mathbf{\Pi}_k^F$. In addition, $\Pi_k^{\mathscr{F}}$ and $\mathbf{\Pi}_k^{\mathscr{F}}$ stand for their global extensions to $\mathrm{L}^2(\Gamma)$ and $\mathrm{L}^2(\Gamma)^2$, respectively, which

are assembled cellwise. The approximation properties of Π_k^F (and hence of $\mathbf{\Pi}_k^F$, $\Pi_k^{\mathscr{F}}$ and $\mathbf{\Pi}_k^{\mathscr{F}}$) are exactly those given by (or derived from) (6.48).

The 3D analogue of Theorem 6.3 is given by the following result.

Theorem 6.9 *Under the assumption that $u \in X \cap \prod_{i=1}^{I} \mathrm{H}^2(\Omega_i)$, there holds*

$$\|(u, \psi, \lambda) - (u_h, \psi_h, \lambda_h)\|$$

$$\lesssim \left\| f - \Pi_{k-1}^{\mathscr{T}} f \right\|_{0,\Omega} + \|(u, \psi, \lambda) - (I_k^{\mathscr{T}} u, \mathscr{L}_k^{\mathfrak{F}} \psi, \Pi_{k-1}^{\mathfrak{F}} \lambda)\|$$

$$+ \sup_{\substack{(w_h, \phi_h, \xi_h) \in \widetilde{\mathbf{X}}_h \\ (w_h, \phi_h, \xi_h) \neq \mathbf{0}}} \frac{\left| \mathbf{a}\big((u, \psi, \lambda), (w_h, \phi_h, \xi_h)\big) - \mathbf{a}_h\big((I_k^{\mathscr{T}} u, \mathscr{L}_k^{\mathfrak{F}} \psi, \Pi_{k-1}^{\mathfrak{F}} \lambda), (w_h, \phi_h, \xi_h)\big) \right|}{\|(w_h, \phi_h, \xi_h)\|}.$$

$$(6.118)$$

Proof We follow basically the same sequence of arguments provided in the proof of Theorem 6.3. Indeed, according to the definitions of $\widetilde{\mathbf{F}}$ (cf. (6.28)), $\widetilde{\mathbf{F}}_h$ (cf. (6.116)), $\widetilde{\mathbf{A}}$ (cf. (6.26)–(6.27)) and $\widetilde{\mathbf{A}}_h$ (cf. (6.114)–(6.115)), which yields, in particular

$$\big(\widetilde{\mathbf{A}} - \widetilde{\mathbf{A}}_h\big)\big((v_h, \varphi_h, \mu_h), (w_h, \phi_h, \xi_h)\big) = \big(\mathbf{a} - \mathbf{a}_h\big)\big((v_h, \varphi_h, \mu_h), (w_h, \phi_h, \xi_h)\big)$$

for all $(v_h, \varphi_h, \mu_h), (w_h, \phi_h, \xi_h) \in \widetilde{\mathbf{X}}_h$, and using the boundedness of $\mathbf{a}$, we find that a direct application of the first Strang Lemma (cf. [15, Theorem 4.1.1]) to the context given now by (6.25) and (6.113), gives

$$\|(u, \psi, \lambda) - (u_h, \psi_h, \lambda_h)\|$$

$$\lesssim \left\| f - \Pi_{k-1}^{\mathscr{T}} f \right\|_{0,\Omega} + \inf_{(v_h, \varphi_h, \mu_h) \in \widetilde{\mathbf{X}}_h} \Bigg\{ \|(u, \psi, \lambda) - (v_h, \varphi_h, \mu_h)\|$$

$$+ \sup_{\substack{(w_h, \phi_h, \xi_h) \in \widetilde{\mathbf{X}}_h \\ (w_h, \phi_h, \xi_h) \neq \mathbf{0}}} \frac{\left| \mathbf{a}\big((u, \psi, \lambda), (w_h, \phi_h, \xi_h)\big) - \mathbf{a}_h\big((v_h, \varphi_h, \mu_h), (w_h, \phi_h, \xi_h)\big) \right|}{\|(w_h, \phi_h, \xi_h)\|} \Bigg\}.$$

$$(6.119)$$

Thanks to the hypothesis we have that both u and $\psi = \gamma u$ are continuous, and hence $I_k^{\mathscr{T}} u$ and $\mathscr{L}_k^{\mathfrak{F}} \psi$ are meaningful. In addition, the fact that $u \in \prod_{i=1}^{I} \mathrm{H}^2(\Omega_i)$ implies that $\lambda = \kappa \nabla u \cdot \mathbf{n} \in \mathrm{H}_b^{1/2}(\Gamma) \subseteq \mathrm{L}^2(\Gamma)$, and hence $\Pi_{k-1}^{\mathfrak{F}} \lambda$ is meaningful as well. In this way, taking in particular $(v_h, \varphi_h, \mu_h) = (I_k^{\mathscr{T}} u, \mathscr{L}_k^{\mathfrak{F}} \psi, \Pi_{k-1}^{\mathfrak{F}} \lambda) \in \widetilde{\mathbf{X}}_h$ in (6.119) we arrive at (6.118) and conclude the proof. $\square$

Analogously to the analysis for the 2D case, we now aim to estimate the supremum in (6.118), for which we first notice from the definitions of $\mathbf{a}$ (cf. (6.27))

and $\mathbf{a}_h$ (cf. (6.115)), and using that $\psi = \gamma u$, that

$$
\mathbf{a}\big((u, \psi, \lambda), (w_h, \phi_h, \xi_h)\big) - \mathbf{a}_h\big((I_k^{\mathscr{T}} u, \mathscr{L}_k^{\widetilde{\mathfrak{F}}} \psi, \Pi_{k-1}^{\widetilde{\mathfrak{F}}} \lambda), (w_h, \phi_h, \xi_h)\big)
$$

$$
= a(u, w_h) - a_h(I_k^{\mathscr{T}} u, w_h) - \langle \lambda, \gamma w_h - \phi_h \rangle \tag{6.120}
$$

$$
+ \int_{\Gamma} \Pi_{k-1}^{\widetilde{\mathfrak{F}}} \lambda \, \Pi_{k-1}^{\mathscr{F}} (\gamma w_h - \phi_h) - \int_{\Gamma} \xi_h \, \Pi_{k-1}^{\mathscr{F}} (\gamma I_k^{\mathscr{T}} u - \mathscr{L}_k^{\widetilde{\mathfrak{F}}} \psi)
$$

for all $(w_h, \phi_h, \xi_h) \in \mathbb{X}_h$. Then, in what follows we proceed to estimate the right hand side of (6.120) by splitting it into the three expressions determined by the first and second terms, the third and fourth terms, and the fifth term, respectively.

Firstly, recalling that κ has been assumed to be piecewise constant, and noting that certainly $\nabla \Pi_k^E u \in \mathscr{P}_{k-1}(E)^3$, we deduce, according to the definition of a_h^E (cf. (6.117)), that

$$
a_h^E(\Pi_k^E u, w_h) = a^E(\Pi_k^E u, w_h) \qquad \forall E \in \mathscr{T}_h, \quad \forall w_h \in W_h^k(E),
$$

and therefore, adding and subtracting $\Pi_k^E u$ in the first components of a^E and a_h^E, we readily find that

$$
a(u, w_h) - a_h(I_k^{\mathscr{T}} u, w_h) = \sum_{E \in \mathscr{T}_h} \left\{ a^E(u - \Pi_k^E u, w_h) + a_h^E(\Pi_k^E u - I_k^E u, w_h) \right\}
$$

for all $w_h \in W_h^k$. In this way, thanks to the foregoing identity and the boundedness of a^E and a_h^E, the latter being proved similarly to the proof of Lemma 6.5, and then adding and subtracting u in the expression resulting from bounding a_h^E, we arrive at

$$
|a(u, w_h) - a_h(I_k^{\mathscr{T}} u, w_h)| \lesssim \left\{ |u - I_k^{\mathscr{T}} u|_{1,\Omega} + |u - \Pi_k^{\mathscr{T}} u|_{1, \mathscr{T}_h} \right\} |w_h|_{1,\Omega}. \tag{6.121}
$$

Secondly, noting that $\Pi_{k-1}^{\mathscr{F}} (\gamma w_h - \phi_h) \in \Lambda_h^{k-1}$ (cf. (6.111)), and employing the orthogonality condition satisfied by $\Pi_{k-1}^{\widetilde{\mathfrak{F}}}$, as well as the symmetry of $\Pi_{k-1}^{\mathscr{F}}$, we obtain

$$
\int_{\Gamma} \Pi_{k-1}^{\widetilde{\mathfrak{F}}} \lambda \, \Pi_{k-1}^{\mathscr{F}} (\gamma w_h - \phi_h) = \int_{\Gamma} \lambda \, \Pi_{k-1}^{\mathscr{F}} (\gamma w_h - \phi_h) = \int_{\Gamma} \Pi_{k-1}^{\mathscr{F}} \lambda \, (\gamma w_h - \phi_h),
$$

which yields

$$
- \langle \lambda, \gamma w_h - \phi_h \rangle + \int_{\Gamma} \Pi_{k-1}^{\widetilde{\mathfrak{F}}} \lambda \, \Pi_{k-1}^{\mathscr{F}} (\gamma w_h - \phi_h) = \langle \Pi_{k-1}^{\mathscr{F}} \lambda - \lambda, \gamma w_h - \phi_h \rangle,
$$

and hence, according to the duality pairing between $H^{-1/2}(\Gamma)$ and $H^{1/2}(\Gamma)$, and using the trace theorem, we obtain

$$
\begin{aligned}
\Big| \int_\Gamma \Pi_{k-1}^{\mathfrak{F}} \lambda \, \Pi_{k-1}^{\mathscr{F}}(\gamma w_h - \phi_h) \; - \; \langle \lambda, \gamma w_h - \phi_h \rangle \Big| \\
\lesssim \|\lambda - \Pi_{k-1}^{\mathscr{F}} \lambda\|_{-1/2,\Gamma} \left\{ \|w_h\|_{1,\Omega} + \|\phi_h\|_{1/2,\Gamma} \right\} .
\end{aligned}
\tag{6.122}
$$

Finally, adding and subtracting $\gamma u = \psi$, we readily get

$$
-\int_\Gamma \xi_h \, \Pi_{k-1}^{\mathscr{F}}(\gamma I_k^{\mathscr{T}} u - \mathscr{L}_k^{\mathfrak{F}} \psi) = \int_\Gamma \xi_h \, \Pi_{k-1}^{\mathscr{F}} \big(\gamma(u - I_k^{\mathscr{T}} u) - (\psi - \mathscr{L}_k^{\mathfrak{F}} \psi) \big),
$$

from which, applying the Cauchy-Schwarz inequality in $L^2(\Gamma)$ and the inverse inequality satisfied by Λ_h^{k-1} (cf. (6.111)), we find that

$$
\begin{aligned}
\Big| \int_\Gamma \xi_h \, \Pi_{k-1}^{\mathscr{F}}(\gamma I_k^{\mathscr{T}} u - \mathscr{L}_k^{\mathfrak{F}} \psi) \Big| \\
\lesssim h^{-1/2} \left\{ \|\gamma(u - I_k^{\mathscr{T}} u)\|_{0,\Gamma} + \|\psi - \mathscr{L}_k^{\mathfrak{F}} \psi\|_{0,\Gamma} \right\} \|\xi_h\|_{-1/2,\Gamma} .
\end{aligned}
\tag{6.123}
$$

Consequently, using (6.121), (6.122), and (6.123) to bound (6.120), and then replacing the resulting estimate into (6.118), we arrive at the a priori error estimate

$$
\begin{aligned}
\|(u, \psi, \lambda) - (u_h, \psi_h, \lambda_h)\| \lesssim \; & \left\| f - \Pi_{k-1}^{\mathscr{T}} f \right\|_{0,\Omega} + |u - I_k^{\mathscr{T}} u|_{1,\Omega} + \|\psi - \mathscr{L}_k^{\mathfrak{F}} \psi\|_{1/2,\Gamma} \\
& + \|\lambda - \Pi_{k-1}^{\mathfrak{F}} \lambda\|_{-1/2,\Gamma} + |u - \Pi_k^{\mathscr{T}} u|_{1,\mathscr{T}_h} + \|\lambda - \Pi_{k-1}^{\mathscr{F}} \lambda\|_{-1/2,\Gamma} \\
& + h^{-1/2} \left\{ \|\gamma(u - I_k^{\mathscr{T}} u)\|_{0,\Gamma} + \|\psi - \mathscr{L}_k^{\mathfrak{F}} \psi\|_{0,\Gamma} \right\} .
\end{aligned}
\tag{6.124}
$$

The foregoing inequality constitutes the key estimate to derive the rates of convergence of the present 3D VEM/BEM scheme. In this regard, and in order to bound one of the terms involved, we also need the scaled trace inequality (cf. [19, Lemma 1.49]), which says that for each $E \in \mathscr{T}_h$ there holds

$$
\|v\|_{0,\partial E}^2 \lesssim \left\{ h_E^{-1} \|v\|_{0,E}^2 + h_E |v|_{1,E}^2 \right\} \qquad \forall v \in H^1(E) .
\tag{6.125}
$$

Indeed, we end this section with the following main result.

Theorem 6.10 *Assuming that* $u \in X \cap \prod_{i=1}^I H^{k+1}(\Omega_i)$ *and* $f \in \prod_{i=1}^I H^k(\Omega_i)$, *there holds*

$$
\|(u, \psi, \lambda) - (u_h, \psi_h, \lambda_h)\| \lesssim h^k \sum_{i=1}^I \left\{ \|u\|_{k+1,\Omega_i} + \|f\|_{k,\Omega_i} \right\} .
\tag{6.126}
$$

Proof We first observe, thanks to the regularity assumption on u, that $\psi = \gamma u \in \mathrm{H}_b^{k+1/2}(\Gamma)$ and $\lambda = \kappa \nabla u \cdot \boldsymbol{n} \in \mathrm{H}_b^{k-1/2}(\Gamma)$. Throughout the rest of the proof we identify the terms on the right hand side of (6.124) according to the order they have been written there, from left to right and from up to down. Thus, applying the 3D versions of (6.48) (to the first and fifth terms), (6.50) (to the second term), and Lemma 6.4 (to the sixth term), and using by the trace inequality that $\|\lambda\|_{k-1/2,b,\Gamma} \leq c \sum_{i=1}^{I} \|u\|_{k+1,\Omega_i}$, we obtain

$$
\|f - \Pi_{k-1}^{\mathcal{T}} f\|_{0,\Omega} + |u - I_k^{\mathcal{T}} u|_{1,\Omega} + |u - \Pi_k^{\mathcal{T}} u|_{1,\mathcal{T}_h} + \|\lambda - \Pi_{k-1}^{\mathcal{F}} \lambda\|_{-1/2,\Gamma}
$$

$$
\lesssim h^k \sum_{i=1}^{I} \left\{ \|f\|_{k,\Omega_i} + \|u\|_{k+1,\Omega_i} \right\}.
$$

(6.127)

In turn, invoking Lemmas 6.11 and 6.10 to bound the third and fourth terms, respectively, and employing also by trace theorem that $\|\psi\|_{k+1/2,b,\Gamma} \leq c \sum_{i=1}^{I} \|u\|_{k+1,\Omega_i}$, we find that

$$
\|\psi - \mathcal{L}_k^{\widetilde{\mathfrak{F}}} \psi\|_{1/2,\Gamma} + \|\lambda - \Pi_{k-1}^{\widetilde{\mathfrak{F}}} \lambda\|_{-1/2,\Gamma}
$$

(6.128)

$$
\lesssim h^k \left\{ \|\psi\|_{k+1/2,b,\Gamma} + \|\lambda\|_{k-1/2,b,\Gamma} \right\} \lesssim h^k \sum_{i=1}^{I} \|u\|_{k+1,\Omega_i}.
$$

Furthermore, a straightforward application of Lemma 6.11 to the eighth term, gives

$$
\|\psi - \mathcal{L}_k^{\widetilde{\mathfrak{F}}} \psi\|_{0,\Gamma} \lesssim h^{k+1/2} \|\psi\|_{k+1/2,b,\Gamma},
$$

and hence

$$
h^{-1/2} \|\psi - \mathcal{L}_k^{\widetilde{\mathfrak{F}}} \psi\|_{0,\Gamma} \lesssim h^k \sum_{i=1}^{I} \|u\|_{k+1,\Omega_i}.
$$

(6.129)

Next, employing the scaled trace inequality (6.125) and the 3D version of (6.50), we obtain that for each face F of an element $E \in \mathcal{T}_h$ there holds

$$
h_F^{-1} \|\gamma (u - I_k^E u)\|_{0,F}^2 \leq h_F^{-1} \|\gamma (u - I_k^E u)\|_{0,\partial E}^2
$$

$$
\lesssim h_E^{-2} \|u - I_k^E u\|_{0,E}^2 + |u - I_k^E u|_{1,E}^2 \lesssim h_E^{2k} \|u\|_{k+1,E}^2,
$$

from which we arrive at

$$h^{-1/2} \left\| \gamma \left(u - I_k^{\mathscr{T}} u \right) \right\|_{0,\Gamma} \lesssim h^k \sum_{i=1}^{I} \|u\|_{k+1,\Omega_i} \ . \tag{6.130}$$

Finally, utilizing (6.127), (6.128), (6.129), and (6.130) in (6.124), we get (6.126) and conclude the proof. $\qquad\qquad\qquad\qquad\qquad\qquad\qquad\qquad\qquad\qquad\qquad\square$

6.5 Numerical Results

In this section we show that the numerical rates of convergence delivered by the VEM/BEM schemes (6.58), (6.85), and the 2D version of (6.113) are in accordance with the theoretical ones. For simplicity, we restrict our tests to two-dimensional model problems and to the lowest polynomial degree $k = 1$.

In what follows h and N stand for the meshsize and the total number of degrees of freedom, respectively, of each partition of $\overline{\Omega}$. In addition, the individual and global errors are defined by

$$\mathrm{e}(u) := \|u - \widehat{u}\|_{0,\Omega} + |u - \widehat{u}|_{1,b,\Omega}, \ \ \mathrm{e}(\lambda) := \|\lambda - \lambda_h\|_{-1/2,\Gamma}, \ \ \mathrm{e}(\psi) := \|\psi - \psi_h\|_{1/2,\Gamma},$$

with corresponding rates of convergence

$$\mathrm{r}(\star) := \frac{\log(\mathrm{e}(\star)/\mathrm{e}'(\star))}{\log(h/h')} \quad \forall \star \in \left\{ u, \lambda, \psi \right\},$$

where h and h' denote two consecutive meshsizes with errors e and e'. Note here that the exact error for u, that is $\|u - u_h\|_{1,\Omega}$, is not computable since u_h, being virtual, is not known explicitly in Ω. This is the reason why $\mathrm{e}(u)$ is defined above with $\widehat{u}$ (cf. the end of Sect. 6.3.2) instead of u_h.

6.5.1 Convergence Tests for the Poisson Model

We first investigate the performance of the discrete schemes (6.58) and (6.113) when applied to problem (6.1). We point out that the VEM/BEM discretization method (6.113) has been introduced and analyzed in the 3D case only. However, it is not difficult to see that it is also applicable to two-dimensional problems.

We choose $\kappa = 1$ so that the harmonic function $u(\boldsymbol{x}) = \dfrac{x_1 + x_2}{|\boldsymbol{x}|^2}$, $\boldsymbol{x} := (x_1, x_2)$, is a solution of problem (6.1) with a nonhomogeneous Dirichlet boundary condition on Γ_0. We consider two different geometry settings. In the first example, we take $\Omega_0 = (-0.25, 0.25)^2$ and $\mathscr{O} = (-0.5, 0.5)^2$, and use a sequence of meshes

Table 6.1 Convergence history of the VEM/BEM schemes (6.58) and (6.113) for Poisson, Example 1

h	N	$\mathrm{e}(u)$	$\mathrm{r}(u)$	$\mathrm{e}(\lambda)$	$\mathrm{r}(\lambda)$
1/64	3521	2.914E−01	–	1.066E−01	–
1/128	13,185	1.458E−01	0.999	5.327E−02	1.001
1/256	50,945	7.292E−02	1.000	2.663E−02	1.000
1/512	200,193	3.646E−02	1.000	1.332E−02	1.000

h	N	$\mathrm{e}(u)$	$\mathrm{r}(u)$	$\mathrm{e}(\psi)$	$\mathrm{r}(\psi)$	$\mathrm{e}(\lambda)$	$\mathrm{r}(\lambda)$
1/64	3777	2.914E−01	–	7.522E−03	–	1.068E−1	–
1/128	13,697	1.458E−01	0.999	2.659E−03	1.500	5.338E−02	1.001
1/256	51,969	7.292E−02	1.000	9.454E−04	1.492	2.669E−02	1.000
1/512	202,241	3.646E−02	1.000	3.387E−04	1.481	1.335E−02	1.000

Table 6.2 Convergence history of the VEM/BEM schemes (6.58) and (6.113) for Poisson, Example 2

h	N	$\mathrm{e}(u)$	$\mathrm{r}(u)$	$\mathrm{e}(\lambda)$	$\mathrm{r}(\lambda)$
1/64	7197	3.488E−01	–	1.053E−01	–
1/128	27,529	1.749E−01	0.997	5.294E−02	0.993
1/256	107,683	8.743E−02	1.001	2.656E−02	0.996
1/384	240,512	5.825E−02	1.002	1.774E−02	0.996

h	N	$\mathrm{e}(u)$	$\mathrm{r}(u)$	$\mathrm{e}(\psi)$	$\mathrm{r}(\psi)$	$\mathrm{e}(\lambda)$	$\mathrm{r}(\lambda)$
1/64	7459	3.488E−01	–	1.744E−02	–	1.053E−01	–
1/128	28,047	1.749E−01	0.997	6.559E−03	1.539	5.295E−02	0.994
1/256	108,713	8.743E−02	1.001	2.472E−03	1.402	2.655E−02	0.997
1/384	242,054	5.825E−02	1.002	1.349E−03	1.493	1.772E−02	0.997

constructed out of square elements. In turn, in the second example, we select $\Omega_0 = \left\{ \boldsymbol{x} \in \mathbb{R}^2 : x_1^2 + x_2^2 < 0.25^2 \right\}$ and $\mathcal{O} = (-0.5, 0.5)^2$, and employ a sequence of Voronoi meshes initially generated from random seeds and subsequently smoothed using Lloyd's relaxation algorithm.

The convergence history of both schemes are reported in Tables 6.1 and 6.2 for Examples 1 and 2, respectively. There we can see that the rates of convergence predicted by Theorems 6.4 and 6.10, that is $O(h)$ for $k = 1$, are confirmed for each one of the unknowns in both examples. The higher rate provided by the unknown ψ for the scheme (6.113) must be simply understood as a proper super convergence behavior of this particular exact solution u. In addition, we observe that, except for the additional direct approximation ψ_h of the trace of u provided by (6.113), both VEM/BEM schemes behave very similarly since, at each partition, they yield basically the same errors for each common unknown. Certainly, the advantage of (6.113) with respect to (6.58) is that the former is applicable in 2D and 3D, whereas the latter is restricted to 2D. In turn, the advantage of (6.58) with respect to (6.113), which is obviously valid only in 2D, is that the former, having one less boundary unknown, is a bit cheaper than (6.113) in terms of the total number

Table 6.3 Convergence history of the VEM/BEM scheme (6.85) for Helmholtz with $\kappa = 2$

h	N	$\mathtt{e}(u)$	$\mathtt{r}(u)$	$\mathtt{e}(\lambda)$	$\mathtt{r}(\lambda)$
1/64	3951	2.920E−01	–	7.550E−01	–
1/128	15,336	1.464E−01	0.966	3.584E−01	1.021
1/192	34,133	9.715E−02	1.050	2.394E−01	1.035
1/256	60,430	7.259E−02	0.962	1.757E−01	1.020

Table 6.4 Convergence history of the VEM/BEM scheme (6.113) adapted for Helmholtz with $\kappa = 1$

h	N	$\mathtt{e}(u)$	$\mathtt{r}(u)$	$\mathtt{e}(\lambda)$	$\mathtt{r}(\lambda)$	$\mathtt{e}(\psi)$	$\mathtt{r}(\psi)$
1/64	4113	2.882E−01	–	1.280E−01	–	5.682E−03	–
1/128	15,666	1.447E−01	0.965	6.467E−02	0.962	2.735E−03	0.997
1/192	34,620	9.602E−02	1.051	4.345E−02	1.019	1.800E−03	1.072
1/256	61,089	7.178E−02	0.960	3.240E−02	0.969	1.352E−03	0.945

of degrees of freedom. This is illustrated in the present examples by the second columns of Tables 6.1 and 6.2.

6.5.2 Convergence Tests for the Helmholtz Model

We finally report numerical results carried out with the method based on the scheme (6.85) (cf. Sect. 6.3.3) and with an adaptation of scheme (6.113) for problem (6.2).

We consider problem (6.2) with $\vartheta = 1$, $\Omega_0 = \left\{ \boldsymbol{x} \in \mathbb{R}^2 : \frac{x_1^2}{0.5^2} + \frac{x_2^2}{0.7^2} < 1 \right\}$, $\mathscr{O} = \left\{ \boldsymbol{x} \in \mathbb{R}^2 : \frac{x_1^2}{1.1^2} + \frac{x_2^2}{1.5^2} < 1 \right\}$, and use a sequence of successively refined Voronoi meshes of the domain $\Omega = \mathscr{O} \setminus \Omega_0$. We select the incident wave w in such a way that the exact solution is given in the following closed form

$$u(\boldsymbol{x}) = \begin{cases} (1 + \iota) \dfrac{x_1 + x_2}{|\boldsymbol{x}|^2} & \text{in } \Omega \\ H_0^{(1)}(\kappa |\boldsymbol{x}|) & \text{in } \mathscr{O}_e. \end{cases}$$

We observe from Tables 6.3 and 6.4 that the expected linear convergence rate of the error is attained in each variable for both schemes.

References

1. D. Adak, A.L.N. Pramod, E.T. Ooi, S. Natarajan, A combined virtual element method and the scaled boundary finite element method for linear elastic fracture mechanics.Eng. Anal. Bound. Elem. **113**, 9–16 (2020)
2. B. Ahmad, A. Alsaedi, F. Brezzi, L.D. Marini, A. Russo, Equivalent projectors for virtual element methods. Comput. Math. Appl. **66**(3), 376–391 (2013)
3. P.F. Antonietti, L. Beirão da Veiga, D. Mora, M. Verani, A stream virtual element formulation of the Stokes problem on polygonal meshes. SIAM J. Numer. Anal. **52**(1), 386–404 (2014)
4. L. Beirão da Veiga, F. Brezzi, A. Cangiani, G. Manzini, L.D. Marini, A. Russo, Basic principles of virtual element methods. Math. Models Methods Appl. Sci. **23**(1), 199–214 (2013)
5. L. Beirão da Veiga, F. Brezzi, L.D. Marini, Virtual elements for linear elasticity problems. SIAM J. Numer. Anal. **51**(2), 794–812 (2013)
6. L. Beirão da Veiga, F. Brezzi, L.D. Marini, A. Russo, Virtual element method for general second-order elliptic problems on polygonal meshes. Math. Models Methods Appl. Sci. **26**(4), 729–750 (2016)
7. L. Beirão da Veiga, C. Lovadina, G. Vacca, Divergence free virtual elements for the Stokes problem on polygonal meshes. ESAIM Math. Model. Numer. Anal. **51**(2), 509–535 (2017)
8. L. Beirão da Veiga, C. Lovadina, G. Vacca, Virtual elements for the Navier-Stokes problem on polygonal meshes. SIAM J. Numer. Anal. **56**(3), 1210–1242 (2018)
9. S.C. Brenner, Q. Guan, L.-Y. Sung, Some estimates for virtual element methods. Comput. Methods Appl. Math. **17**(4), 553–574 (2017)
10. F. Brezzi, C. Johnson, On the coupling of boundary integral and finite element methods. Calcolo **16**(2), 189–201 (1979)
11. F. Brezzi, R.S. Falk, L.D. Marini, Basic principles of mixed virtual element methods. ESAIM Math. Model. Numer. Anal. **48**(4), 1227–1240 (2014)
12. E. Cáceres, G.N. Gatica, A mixed virtual element method for the pseudostress-velocity formulation of the Stokes problem. IMA J. Numer. Anal. **37**(1), 296–331 (2017)
13. E. Cáceres, G.N. Gatica, F.A. Sequeira, A mixed virtual element method for the Brinkman problem. Math. Models Methods Appl. Sci. **27**(4), 707–743 (2017)
14. E. Cáceres, G.N. Gatica, F.A. Sequeira, A mixed virtual element method for quasi-Newtonian Stokes flows. SIAM J. Numer. Anal. **56**(1), 317–343 (2018)
15. P.G. Ciarlet, *The Finite Element Method for Elliptic Problems*, vol. 4. Studies in Mathematics and Its Applications (North-Holland Publishing Co., Amsterdam, 1978)
16. D. Colton, R. Kress, *Inverse Acoustic and Electromagnetic Scattering Theory*, vol. 93, 2nd edn. Applied Mathematical Sciences (Springer, Berlin, 1998)
17. M. Costabel, Symmetric methods for the coupling of finite elements and boundary elements, in *Mathematical and Computational Aspects. Boundary Elements* ed. by C.A. Brebbia, W.L. Wendland, G. Kuhn (Springer, Berlin, 1987), pp. 411–420. https://doi.org/10.1007/978-3-662-21908-9. Invited contribution
18. L. Desiderio, S. Falletta, L. Scuderi, A virtual element method coupled with a boundary integral non reflecting condition for 2D exterior Helmholtz problems. Comput. Math. Appl. **84**, 296–313 (2021)
19. D.A. Di Pietro, A. Ern, *Mathematical Aspects of Discontinuous Galerkin Methods*, vol. 69. Mathématiques & Applications (Berlin) [Mathematics & Applications] (Springer, Heidelberg, 2012)
20. T. Dupont, R. Scott, Polynomial approximation of functions in Sobolev spaces. Math. Comp. **34**(150), 441–463 (1980)
21. G.N. Gatica, S. Meddahi, On the coupling of VEM and BEM in two and three dimensions. SIAM J. Numer. Anal. **57**(6), 2493–2518 (2019)
22. G.N. Gatica, S. Meddahi, Coupling of virtual element and boundary element methods for the solution of acoustic scattering problems. J. Numer. Math. **28**(4), 223–245 (2020)

23. G.N. Gatica, M. Munar, F.A. Sequeira, A mixed virtual element method for the Navier-Stokes equations. Math. Models Methods Appl. Sci. **28**(14), 2719–2762 (2018)
24. H.D. Han, A new class of variational formulations for the coupling of finite and boundary element methods. J. Comput. Math. **8**(3), 223–232 (1990)
25. G.C. Hsiao, W.L. Wendland, *Boundary Integral Equations*, vol. 164. Applied Mathematical Sciences (Springer, Berlin, 2008)
26. C. Johnson, J.-C. Nédélec, On the coupling of boundary integral and finite element methods. Math. Comp. **35**(152), 1063–1079 (1980)
27. W. McLean, *Strongly Elliptic Systems and Boundary Integral Equations* (Cambridge University Press, Cambridge, 2000)
28. S. Meddahi, A. Márquez, V. Selgas, Computing acoustic waves in an inhomogeneous medium of the plane by a coupling of spectral and finite elements.SIAM J. Numer. Anal. **41**(5), 1729–1750 (2003)
29. D. Mora, G. Rivera, R. Rodríguez, A virtual element method for the Steklov eigenvalue problem. Math. Models Methods Appl. Sci. **25**(8), 1421–1445 (2015)
30. S.A. Sauter, C. Schwab, *Boundary Element Methods*, vol. 39. Springer Series in Computational Mathematics (Springer, Berlin, 2011). Translated and expanded from the 2004 German original
31. F.-J. Sayas, The validity of Johnson-Nédélec's BEM-FEM coupling on polygonal interfaces. SIAM J. Numer. Anal. **47**(5), 3451–3463 (2009)
32. F.-J. Sayas, The validity of Johnson-Nédélec's BEM-FEM coupling on polygonal interfaces [reprint of mr2551202]. SIAM Rev. **55**(1), 131–146 (2013)
33. O. Steinbach, A note on the stable one-equation coupling of finite and boundary elements. SIAM J. Numer. Anal. **49**(4), 1521–1531 (2011)
34. G. Vacca, An H^1-conforming virtual element for Darcy and Brinkman equations. Math. Models Methods Appl. Sci. **28**(1), 159–194 (2018)
35. O.C. Zienkiewicz, D.W. Kelly, P. Bettess, The coupling of the finite element method and boundary solution procedures. Int. J. Numer. Methods Eng. **11**(2), 355–375 (1977)
36. O.C. Zienkiewicz, D.W. Kelly, P. Bettess, Marriage à la mode—the best of both worlds (finite elements and boundary integrals), in *Energy Methods in Finite Element Analysis* (Wiley, Chichester, 1979), pp. 81–107

Chapter 7
Virtual Element Approximation of Eigenvalue Problems

Daniele Boffi, Francesca Gardini, and Lucia Gastaldi

Abstract We discuss the approximation of eigenvalue problems associated with elliptic partial differential equations using the virtual element method. After recalling the abstract theory, we present a model problem, describing in detail the features of the scheme, and highlighting the effects of the stabilizing parameters. We conclude the discussion with a survey of several application examples.

7.1 Introduction

In this chapter we discuss the use of the Virtual Element Method (VEM) for the approximation of eigenvalue problems associated with partial differential equations. Eigenvalue problems are present in several applications and are the object of an appealing and vast research area. It is known that the analysis of numerical schemes for the approximation of eigenmodes is based on suitable a priori estimates and appropriate compactness assumptions (see, for instance [4, 10, 29]).

Moreover, a good knowledge of the spectral properties of a discretization scheme is essential for the stability analysis of transient problems. It is well known, for instance, that the solution of parabolic and hyperbolic linear evolution problems (heat/wave equation) can be presented as a Fourier series in terms of eigenfunctions and eigenvalues of the corresponding elliptic eigenproblem (Laplace eigenproblem).

D. Boffi
King Abdullah University of Science and Technology (KAUST), Thuwal, Saudi Arabia

Università degli Studi di Pavia, Pavia, Italy
e-mail: daniele.boffi@kaust.edu.sa

F. Gardini (✉)
Dipartimento di Matematica "F. Casorati", Università degli Studi di Pavia, Pavia, Italy
e-mail: francesca.gardini@unipv.it

L. Gastaldi
DICATAM, Università degli Studi di Brescia, Brescia, Italy
e-mail: lucia.gastaldi@unibs.it

We refer the interested reader to [36] for more information and to [13, 14] for an example of how things can go wrong if the eigenvalue problem is not correctly approximated.

The virtual element method has been successfully used for the approximation of several eigenvalue problems. Starting from the pioneering works [26, 32], where the analysis of the Steklov and the Laplace eigenproblems was developed, other applications of VEM to eigenvalue problems include an acoustic vibration problem [8], plates models [34, 35], linear elasticity [31], and a transmission problem [33]. Moreover, nonconforming, p, and hp VEM have been considered in [21, 27] for the Laplace eigenvalue problem.

The above mentioned references make use of classical tools for the spectral analysis, such as the Babuška–Osborn theory [4] for compact operators or the Descloux–Nassif–Rappaz theory [24] for non-compact operators, typically adopted in connection with a shift procedure. In the case of the mixed formulation for the Laplace eigenproblem [30], the conditions introduced in [11, 12] are considered.

An important feature of VEM, as compared to standard FEM, is that suitable stabilizing forms, depending on appropriate parameters, have to be introduced in order to guarantee consistency and stability of the approximation. Indeed, as it is well known, the matrices assembled for the discretization are computed by the use of suitable projection operators. This is due to the *virtual* nature of the basis functions corresponding to the degrees of freedom at the interior of the elements. The lack of knowledge of such basis functions is compensated by adding appropriately chosen stabilization terms. Typical theoretical results state that, for given choices of the stabilization parameters, the discrete solution converges to the continuous one with optimal order asymptotically in h or p. In the case of eigenvalue problems, the presence of the stabilizing forms may introduce artificially additional eigenmodes and we have to make sure that they will not pollute the portion of the spectrum we are interested in. Some of the above mentioned references address this issue even if they are not conclusive in this respect. In [15] we presented a systematic study of the eigenvalue dependence on the parameters. If the discrete eigenvalue problem can be written in the form $\mathsf{A}\mathsf{u} = \lambda\mathsf{M}\mathsf{u}$, with A and M depending linearly on the stabilizing parameters α and β, respectively, then the *quick and easy recipe* is to pick a sufficiently large α and a small (possibly zero) β. Such discussion is summarized in Sect. 7.5.

After describing the general setting of a variationally posed eigenvalue problem in Sect. 7.2, we recall the basic theory for the VEM approximation of the Laplace eigenproblem in Sect. 7.3. The case of nonconforming, p, and hp VEM is treated in Sect. 7.4. As already mentioned, Sect. 7.5 deals with the choice of the stabilizing parameters. Finally, Sect. 7.6 presents a survey of applications of VEM to the discretization of eigenproblems of interest.

In this chapter, we adopt the usual notation $|| \cdot ||_{s,D}$ and $| \cdot |_{s,D}$ for norm and seminorm in the Sobolev space $H^s(D)$. When $D = \Omega$ we omit the subindex Ω.

Later on we shall use also the broken Sobolev space: let $\mathscr{T}_h$ be a decomposition of Ω into a finite number of subdomains, we set

$$H_h^s = \left\{ v \in L^2(\Omega) : v|_P \in H^s(P) \ \forall P \in \mathscr{T}_h \right\}$$

endowed with the corresponding broken norm

$$||v||_{s,h} = \left(\sum_{P \in \mathscr{T}_h} ||v||_{s,P}^2 \right)^{\frac{1}{2}}.$$

7.2   Abstract Setting

Let V and H be two Hilbert spaces such that $V \subset H$ with dense and compact embedding, and $a(\cdot, \cdot)$ and $b(\cdot, \cdot)$ be two continuous and symmetric bilinear forms defined on $V \times V$ and $H \times H$, respectively. We consider the following eigenvalue problem in variational form: find $(\lambda, u) \in \mathbb{R} \times V$ with $u \neq 0$ such that

$$a(u, v) = \lambda b(u, v) \quad \forall v \in V. \tag{7.1}$$

The source problem associated with problem (7.1) reads: given $f \in H$, find $u \in V$ such that

$$a(u, v) = b(f, v) \quad \forall v \in V. \tag{7.2}$$

We assume that $a(\cdot, \cdot)$ is coercive on V, that is there exists $\alpha > 0$ such that

$$a(v, v) \geq \alpha ||v||_V^2 \quad \forall v \in V.$$

Under these assumptions, there exists a unique solution $u \in V$ of problem (7.2) satisfying the following stability estimate

$$||u||_V \leq C||f||_H. \tag{7.3}$$

We then consider the solution operator $T : H \to V \subset H$ defined as follows:

$$Tf = u, \ u \in V,$$

with u the unique solution of the source problem (7.2). Since problem (7.2) is well posed, T is a well defined, self-adjoint linear bounded operator. Thanks to the compact embedding of V in H, it turns out that T is also compact. The same conclusions apply to the situation when V is not compact in H, by assuming

directly the compactness of the operator T. We observe that (λ, u) is an eigenpair of problem (7.1) if and only if $\left(\frac{1}{\lambda}, u\right)$ is an eigenpair of T. Thanks to the spectral theory of compact operators, we have that the eigenvalues of problem (7.1) are real and positive and form a divergent sequence

$$0 < \lambda_1 \leq \lambda_2 \leq \cdots \leq \lambda_i \leq \ldots; \tag{7.4}$$

conventionally, we repeat them according to their multiplicities. The corresponding eigenfunctions u_i are chosen with the following properties

$$||u_i||_H = 1, \quad a(u_i, u_i) = \lambda_i,$$

and so that they form an orthonormal basis both in V and in H.

We introduce a Galerkin type discretization of problems (7.1) and (7.2). To this end, let $V_h \subset V$ be a finite dimensional subspace of V, and $a_h : V_h \times V_h \to \mathbb{R}$ and $b_h : H \times H \to \mathbb{R}$ two discrete symmetric continuous bilinear forms. Then, the discrete eigenvalue problem and the discrete source problems are given by: find $(\lambda_h, u_h) \in \mathbb{R} \times V_h$ with $u_h \neq 0$ such that

$$a_h(u_h, v_h) = \lambda_h b_h(u_h, v_h) \quad \forall v_h \in V_h, \tag{7.5}$$

and, given $f \in H$, find $u_h \in V_h$ such that

$$a_h(u_h, v_h) = b_h(f, v_h) \quad \forall v_h \in V_h. \tag{7.6}$$

In order to guarantee existence, uniqueness, and stability of the solution to the discrete source problem (7.6), we assume that the discrete bilinear form a_h is coercive.

Similarly to the continuous case, we introduce the discrete solution operator $T_h : H \to V_h \subset H$ defined by

$$T_h f = u_h,$$

with $u_h \in V_h$ the unique solution to the discrete source problem (7.6). T_h is a self-adjoint operator with finite range, hence it is compact and has N_h positive discrete eigenvalues

$$0 < \lambda_{h,1} \leq \lambda_{h,2} \leq \cdots \leq \lambda_{h,N_h},$$

where N_h denotes the dimension of V_h. Moreover, the discrete eigenfunctions $u_{h,i}$ span V_h and can be chosen as an orthogonal basis satisfying

$$||u_{h,i}||_H = 1, \quad a(u_{h,i}, u_{h,i}) = \lambda_{h,i} \quad \forall i = 1, \ldots N_h.$$

We recall some results of the spectral approximation theory for compact operators [4, 10, 29]. In the following we denote by $\delta(E, F)$ the gap between the spaces E and F, that is

$$\delta(E, F) = \max(\hat{\delta}(E, F), \hat{\delta}(F, E)) \quad \text{with } \hat{\delta}(E, F) = \sup_{\substack{u \in E \\ ||u||_H=1}} \inf_{v \in F} ||u - v||_H.$$

Theorem 7.1 *Let us assume that*

$$||T - T_h||_{\mathscr{L}(H,H)} \to 0 \text{ as } h \to 0. \tag{7.7}$$

Let λ_i be an eigenvalue of problem (7.1) with multiplicity equal to m, namely $\lambda_i = \lambda_{i+1} = \cdots = \lambda_{i+m-1}$. Then, for h small enough such that $N_h \geq i + m - 1$, exactly m discrete eigenvalues $\lambda_{h,i} = \lambda_{h,i+1} = \cdots = \lambda_{h,i+m-1}$ converge to λ_i.

Moreover, let $\mathscr{E}_i$ be the eigenspace of dimension m associated with λ_i and $\mathscr{E}_{h,i} = \bigoplus_{j=i}^{i+m-1} \operatorname{span}(u_{h,j})$ be the direct sum of the eigenspaces associated with the discrete eigenvalues. Then

$$\delta(\mathscr{E}_i, \mathscr{E}_{h,i}) \to 0 \quad \text{as } h \to 0, \tag{7.8}$$

where $\delta(E, F)$ denotes the gap between the spaces E and F.

Theorem 7.2 *Using the same notation as in Theorem 7.1, then there exists a positive constant C independent of h such that*

$$\delta(\mathscr{E}_i, \mathscr{E}_{h,i}) \leq C ||(T - T_h)|_{\mathscr{E}_i}||_{\mathscr{L}(H,H)}. \tag{7.9}$$

Let $\varphi_1, \ldots, \varphi_m$ be a basis of the eigenspace $\mathscr{E}_i$ corresponding to the eigenvalue λ_i. Then, for $= j = i, \ldots, i + m - 1$

$$|\lambda_j - \lambda_{j,h}| \leq C \Big(\sum_{l,k=1}^{m} |((T - T_h)\varphi_k, \varphi_l)_H| + ||(T - T_h)|_{\mathscr{E}_i}||_{\mathscr{L}(H,H)} \Big), \tag{7.10}$$

where $(\cdot, \cdot)_H$ stands for the scalar product in H.

Remark 7.1 The solution operator could also be defined as $T_V : V \to V$ such that for all $f \in V$, $T_V f$ is the solution to problem (7.2). If T_V is compact, then one can obtain results similar to those presented above with due modifications.

7.2.1 Model Problem

Let $\Omega \subset \mathbb{R}^d$ $(d = 2, 3)$ be an open bounded Lipschitz domain. As a model problem, we consider the Laplace eigenvalue equation with homogeneous Dirichlet boundary

conditions:

$$-\Delta u = \lambda u \quad \text{in } \Omega$$
$$u = 0 \qquad \text{on } \partial\Omega.$$

$$(7.11)$$

Setting

$$V = H_0^1(\Omega) \quad H = L^2(\Omega)$$
$$a(u, v) = \int_\Omega \nabla u \cdot \nabla v \, dx \quad b(u, v) = \int_\Omega uv \, dx$$

$$(7.12)$$

the weak formulation of (7.11) fits the above abstract setting. Here and in what follows, we set $a^D(u, v) = \int_D \nabla u \cdot \nabla v \, dx$ and $b^D(u, v) = \int_D uv \, dx$.

Later on we will use the following additional regularity result [1, 28]: if $f \in L^2(\Omega)$ there exists $r \in \left(\frac{1}{2}, 1\right]$ such that $u \in H^{1+r}(\Omega)$, with

$$||u||_{1+r} \le C||f||_0.$$

$$(7.13)$$

The regularity index r depends on the maximum interior wedge angle of Ω. In particular, if the domain is convex r can be taken equal to 1.

7.3 Virtual Element Approximation of the Laplace Eigenvalue Problem

In this section, we consider the Laplace eigenproblem and, after recalling the definition and the approximation properties of VEM, we present the discretization of the eigenvalue problem (7.1) and the relative convergence analysis. We treat in detail only the two dimensional case; for the three dimensional one, which can be analyzed with the same arguments, we refer to [26, 27].

7.3.1 Virtual Element Method

We denote by $\mathcal{T}_h$ a family of polygonal decomposition of Ω, by h_P the diameter of the element $P \in \mathcal{T}_h$, by h the maximum of such diameters, and by $\mathcal{E}_h$ the set of the edges of the mesh. Moreover, $\mathcal{E}_h^0$ and $\mathcal{E}_h^\partial$ stand for the subset of internal and boundary edges, respectively.

We suppose that for all h, there exists a constant ϱ such that each element $P \in \mathcal{T}_h$ is star-shaped with respect to a disk with radius greater than ϱh_P, and for every edge $e \in \partial P$ it holds that $h_e \geq \varrho h_P$ (see [5]). We observe that the scaling assumption implies that the number of edges in the boundary of each element is uniformly bounded over the whole mesh family $\mathcal{T}_h$. However, there is no restriction on the interior angles of the polygons which can be convex, flat, or concave.

Let $k \geq 1$ be a given integer, we denote by $\mathbb{P}_k(P)$ the space of polynomials of degree at most equal to k. We introduce the *enhanced* virtual element space V_h of order k (see [2]). We consider the local space

$$V_h^k(P) = \left\{ v \in \widetilde{V}_h^k(P) : \int_P (v - \Pi_k^\nabla v) p \, dx = 0 \quad \forall p \in (\mathbb{P}_k \setminus \mathbb{P}_{k-2})(P) \right\},$$
(7.14)

with the following definitions:

$$\widetilde{V}_h^k(P) = \left\{ v \in H^1(P) : v|_{\partial P} \in C^0(\partial P), v|_e \in \mathbb{P}_k(e) \, \forall e \in \partial P, \Delta v \in \mathbb{P}_k(P) \right\}$$

$\Pi_k^\nabla : \widetilde{V}_h^k(P) \to \mathbb{P}_k(P)$ is a projection operator defined by

$$a^P(\Pi_k^\nabla v - v, p) = 0 \quad \forall p \in \mathbb{P}_k(P)$$

$$\int_{\partial P} (\Pi_k^\nabla v - v) \, ds = 0.$$
(7.15)

In (7.14), $(\mathbb{P}_k \setminus \mathbb{P}_{k-2})(P)$ stands for the space of polynomials in $\mathbb{P}_k(P)$ L^2-othogonal to $\mathbb{P}_{k-2}(P)$.

As shown in [2], it is possible to compute $\Pi_k^\nabla v_h$ for all $v_h \in V_h^k(P)$ using the following degrees of freedom: the values $v(V_i)$ at the vertices V_i of P, the scaled moments up to order $k-2$ on each edge $e \subset \partial P$, and on the element P.

The global virtual element space is obtained by gluing together the local spaces, that is

$$V_h^k = \left\{ v \in H_0^1(\Omega) : v|_P \in V_h^k(P) \, \forall P \in \mathcal{T}_h \right\}.$$

From now on, we denote by N_h the dimension of V_h^k.

We highlight that, differently from finite elements, we do not have at hand the explicit knowledge of the basis functions of V_h^k; in this sense the basis functions are *virtual*. On the other hand, polynomials of degree at most k are in the VEM space; this will guarantee the optimal order of accuracy. Actually, the following approximation results hold true, see [5, 17, 20].

Proposition 7.1 *There exists a positive constant C, depending only on the polyno-mial degree k and the shape regularity ϱ, such that for every s with $1 \leq s \leq k + 1$ and for every $v \in H^s(\Omega)$ there exists $v_\pi \in \mathbb{P}_k(P)$ such that*

$$\|v - v_\pi\|_{0,P} + h_P|v - v_\pi|_{1,P} \leq Ch_P^s|v|_{s,P}. \tag{7.16}$$

Moreover, there exists a constant C, depending only on the polynomial degree k and the shape regularity ϱ, such that for every s with $1 \leq s \leq k + 1$, for every h, and for every $v \in H^s(\Omega)$ there exists $v_I \in V_h^k$ such that

$$\|v - v_I\|_0 + h_P|v - v_I|_1 \leq Ch_P^s|v|_s. \tag{7.17}$$

Notice that v_π is defined element by element, and does not belong to the space $H^1(\Omega)$. We shall denote its broken H^1-seminorm by $|v_\pi|_{1,h}$.

7.3.2 The VEM Discretization of the Laplace Eigenproblem

In the VEM context, the discrete bilinear forms $a_h(\cdot, \cdot)$ and $b_h(\cdot, \cdot)$ are written as sum over the elements $P \in \mathscr{T}_h$ of local contributions $a_h^P(\cdot, \cdot)$ and $b_h^P(\cdot, \cdot)$ for all $P \in \mathscr{T}_h$, that is

$$a_h(\cdot, \cdot) = \sum_{P \in \mathscr{T}_h} a_h^P(\cdot, \cdot), \quad b_h(\cdot, \cdot) = \sum_{P \in \mathscr{T}_h} b_h^P(\cdot, \cdot).$$

For the readers' convenience, we recall here the discrete source problem (7.6): given $f \in L^2(\Omega)$, find $u_h \in V_h^k$ such that

$$a_h(u_h, v_h) = b_h(f, v_h) \quad \forall v_h \in V_h^k. \tag{7.18}$$

It is well known that solving this problem is equivalent to solve a linear system of equations $\mathsf{A}u = \mathsf{f}$, where A is the $N_h \times N_h$ matrix corresponding to the form a_h and f is the vector with components $b_h(f, \varphi_h)$ with φ_h the basis functions of V_h^k.

We now address the issue of the construction of the discrete bilinear forms along the lines of [5]. First of all, they are required to be similar to the continuous ones

$$a_h^P(v_h, v_h) \approx a^P(v_h, v_h), \quad b_h^P(v_h, v_h) \approx b^P(v_h, v_h),$$

where by $m \approx n$ we denote as usual that $(1/C)m \leq n \leq Cm$ with C independent of h.

We underline that the continuous forms $a(\cdot, \cdot)$ and $b(\cdot, \cdot)$ in general are not computable on the basis functions, except for those which are polynomials. Hence we need to project the elements of $V_h^k(P)$ onto $\mathbb{P}_k(P)$. This could be done locally

as follows:

$$a_h^P(u_h, v_h) = a^P(\Pi_k^\nabla u_h, \Pi_k^\nabla v_h) \quad \forall u_h, v_h \in \mathcal{T}_h, \tag{7.19}$$

but it might happen that a non vanishing element $u_h \in V_h^k(P)$ is such that $\Pi_k^\nabla u_h = 0$, and so the form $a_h^P(u_h, v_h) = 0$ for all $v_h \in V_h^k(P)$. In this case the local contribution to the matrix A_h results to be singular and the global matrix might lack control on some components of V_h^k. To avoid this eventuality, we add a stability term as follows:

$$a_h^P(u_h, v_h) = a^P(\Pi_k^\nabla u_h, \Pi_k^\nabla v_h) + S_a^P((I - \Pi_k^\nabla)u_h, (I - \Pi_k^\nabla)v_h), \tag{7.20}$$

where $S_a^P(\cdot, \cdot)$ is a symmetric positive definite bilinear form defined on $V_h^k(P) \times V_h^k(P)$ scaling like $a^P(\cdot, \cdot)$.

For proper choices of S_a^P, it turns out that $a_h^P(\cdot, \cdot)$ fulfils the following local *stability* and *consistency* properties for all $P \in \mathcal{T}_h$.

Stability: there exists two positive constants a_* and a^* such that for all $v_h \in V_h^k(P)$

$$a_* a^P(v_h, v_h) \le a_h^P(v_h, v_h) \le a^* a^P(v_h, v_h). \tag{7.21}$$

Consistency: for all $v_h \in V_h^k(P)$ and for all $p_k \in \mathbb{P}_k(P)$ it holds

$$a_h^P(v_h, p_k) = a^P(v_h, p_k). \tag{7.22}$$

In order to deal with the right hand side in (7.18), we define another projection operator Π_k^0 from $L^2(P)$ onto $\mathbb{P}_k(P)$ as

$$b^P(\Pi_k^0 f, p_k) = b^P(f, p_k) \quad \forall p_k \in \mathbb{P}_k(P), \ \forall P \in \mathcal{T}_h.$$

This projection operator is computable starting from the degrees of freedom as well. Thus the local contribution to the right hand side is given by

$$b_h^P(f, v_h) = b^P(\Pi_k^0 f, v_h) \quad \forall v_h \in V_h^k(P), \ \forall P \in \mathcal{T}_h. \tag{7.23}$$

With the above definitions, the discrete source problem is well-posed and its solution converges to the continuous one with optimal order, (see [2, 5]): there exists a positive constant C, independent of h such that

$$||u - u_h||_1 \le C \left(|u - u_I|_1 + |u - u_\pi|_{1,h} + \sup_{v_h \in V_h^k} \frac{|b(f, v_h) - b_h(f, v_h)|}{|v_h|_1} \right), \tag{7.24}$$

where $u_I \in V_h^k$ and u_π are defined in Proposition 7.1. We observe that the last term in (7.24) is a consistency term in the spirit of the *first Strang Lemma* [22, Th. 4.1.1]. Indeed, the VEM discretization provides a conforming discrete subspace of V, but the bilinear forms a_h and b_h differ from the continuous ones. The consistency error generated by the difference between a and a_h is already incorporated in the first two terms on the right hand side of (7.24), while the one related to b depends on the properties of the source term f. In particular, if $f \in L^2(\Omega)$ we obtain that the error converges to zero with optimal order depending on the regularity of the solution u:

$$||u - u_h||_1 \le C \left(h^r |u|_{1+r} + h ||f||_0 \right).$$

We now turn to the virtual element discretization of the eigenvalue problem (7.1). Let us recall the discrete formulation: find $(\lambda_h, u_h) \in \mathbb{R} \times V_h^k$ with $u_h \ne 0$ such that

$$a_h(u_h, v_h) = \lambda_h b_h(u_h, v_h) \quad \forall v_h \in V_h^k, \tag{7.25}$$

where, using definition (7.23)

$$b_h^P(u_h, v_h) = b^P(\Pi_k^0 u_h, v_h) = b^P(\Pi_k^0 u_h, \Pi_k^0 v_h). \tag{7.26}$$

The following generalized algebraic eigenvalue problem corresponds to the discrete eigenvalue problem:

$$\mathsf{A}u = \lambda_h \mathsf{M}u, \tag{7.27}$$

where A and M are the $N_h \times N_h$ matrices associated with the bilinear forms a_h and b_h, respectively.

As observed for the form a_h^P, it might happen that $\Pi_k^0 u_h = 0$ for a non vanishing u_h and thus $b_h^P(u_h, v_h) = 0$ for all $v_h \in V_h^k$. This means that the local contribution to the matrix M has a non trivial kernel similarly to what we have observed for the form a_h^P and some components of V_h^k may not be controlled by the global mass matrix. It is then natural to add a stabilization term as follows:

$$b_h^P(u_h, v_h) = b^P(\Pi_k^0 u_h, \Pi_k^0 v_h) + S_b^P((I - \Pi_k^0)u_h, (I - \Pi_k^0)v_h), \tag{7.28}$$

where S_b^P is a symmetric positive definite bilinear form defined on $V_h^k(P) \times V_h^k(P)$ scaling as $b^P(\cdot, \cdot)$, that is there exist two positive constants β_* and β^* such that for all $P \in \mathcal{T}_h$ it holds

$$\beta_* b^P(v_h, v_h) \le S_b^P(v_h, v_h) \le \beta^* b^P(v_h, v_h) \quad \forall v_h \in V_h^k(P), \text{ with } \Pi_k^0 v_h = 0. \tag{7.29}$$

Remark 7.2 It is out of the aims of this paper to discuss the choice of algorithms for the solution of the algebraic eigenvalue problem $\mathsf{A}u = \lambda \mathsf{M}u$. Nevertheless, the presence of the stabilizing parameters may influence such choice. For instance, if the

matrix M is singular and A is not, then it might be convenient to solve the reciprocal system $\mathsf{M}\mathsf{u} = \lambda^{-1}\mathsf{A}\mathsf{u}$. The definition itself of solution for problems like this can be difficult to give, in particular, when both A and M are singular and their kernels have a non trivial intersection. On the other hand if u belongs to the kernel of M and not to that of A, we may conventionally say that it is an eigenfunction corresponding to the eigenvalue $\lambda = \infty$.

From now on, unless explicitly stated, we shall consider the discrete eigenvalue problem (7.25) with the local form b_h^P defined as in (7.28).

7.3.3 Convergence Analysis

In this section we show the convergence of the discrete eigenpairs to the continuous ones by applying Theorem 7.1 and prove a priori error estimates.

In order to apply Theorem 7.1 we need to prove L^2-error estimates for the source problems (7.2) and (7.6). For the sake of completeness, we report here the proof, (see [2, Theorem 3]).

Theorem 7.3 *Given $f \in L^2(\Omega)$, let $u \in H_0^1(\Omega)$ and $u_h \in V_h^k$ denote the solutions to (7.2) and to (7.6), respectively. Then there exists a constant C independent of h such that*

$$||u - u_h||_0 \leq Ch^t \left(|u - u_I|_1 + |u - u_\pi|_{1,h} + ||f - \Pi_k^0 f||_0 \right), \qquad (7.30)$$

where $t = \min(r, 1)$, being r the regularity index of the solution u, see (7.13) and u_I and u_π are defined in Proposition 7.1.

Proof We use a duality argument and denote by $\psi \in H_0^1(\Omega)$ the solution to

$$a(\psi, v) = b(u - u_h, v) \quad \forall v \in H_0^1(\Omega). \qquad (7.31)$$

Since $u - u_h \in L^2(\Omega)$, then $\psi \in H^{1+r}(\Omega)$ with $||\psi||_{1+r} \leq C||u - u_h||_0$. Let $\psi_I \in V_h^k$ be the interpolant of ψ given by Proposition 7.1, then for $t = \min(r, 1)$ it holds

$$||\psi - \psi_I||_0 + h|\psi - \psi_I|_1 \leq Ch^{1+t}||u - u_h||_0. \qquad (7.32)$$

We have that

$$\begin{aligned} ||u - u_h||_0^2 &= b(u - u_h, u - u_h) = a(u - u_h, \psi) \\ &= a(u - u_h, \psi - \psi_I) + a(u - u_h, \psi_I) = I + II. \end{aligned} \qquad (7.33)$$

We first estimate the term I as follows

$$I = a(u - u_h, \psi - \psi_I) \leq C\big(|u - u_h|_1 h^t \|u - u_h\|_0\big). \tag{7.34}$$

Then

$$\begin{aligned} II = a(u - u_h, \psi_I) &= b(f, \psi_I) - a_h(u_h, \psi_I) + a_h(u_h, \psi_I) - a(u_h, \psi_I) \\ &= [b(f, \psi_I) - b_h(f, \psi_I)] + [a_h(u_h, \psi_I) - a(u_h, \psi_I)] \\ &= III + IV. \end{aligned}$$

We have that

$$III = \sum_P \Big(b^P(f, \psi_I) - b^P(\Pi_k^0 f, \Pi_k^0 \psi_I) - S_b^P((I - \Pi_k^0)f, (I - \Pi_k^0)\psi_I) \Big). \tag{7.35}$$

It holds

$$\begin{aligned} b^P(f, \psi_I) - b^P(\Pi_k^0 f, \Pi_k^0 \psi_I) &= b^P(f - \Pi_k^0 f, \psi_I - \Pi_k^0 \psi_I) \\ &\leq C h^t \|f - \Pi_k^0 f\|_0 \|u - u_h\|_0 \end{aligned} \tag{7.36}$$

and

$$\begin{aligned} S_b^P\big((I - \Pi_k^0)f, (I - \Pi_k^0)\psi_I)\big) &\leq \beta^* \|(I - \Pi_k^0)f\|_0 \|(I - \Pi_k^0)\psi_I\|_0 \\ &\leq C h^t \|(I - \Pi_k^0)f\|_0 \|u - u_h\|_0. \end{aligned} \tag{7.37}$$

Finally, estimating the term IV with standard VEM argument, we obtain

$$IV \leq C\Big(\|u - u_h\|_1 + \|u - \Pi_k^0 u\|_{1,h} \Big) h^t \|u - u_h\|_0.$$

Putting together all the estimates, we conclude the proof. $\qquad\qquad\square$

The L^2-error estimate proved above implies the uniform convergence stated in Theorem 7.1 (see [26, Theorem 6.1]).

Theorem 7.4 *Let T_h and T be the families of operators associated with problems (7.6) and (7.2), respectively. Then the following uniform convergence holds true:*

$$\|T - T_h\|_{\mathscr{L}(L^2(\Omega), L^2(\Omega))} \to 0 \quad for \quad h \to 0.$$

Proof Given $f \in L^2(\Omega)$, let Tf and $T_h f$ be the solutions to problems (7.2) and (7.6), respectively. Then, using the L^2-estimate of Theorem 7.3, the interpolation and approximation results in Proposition 7.1, and the stability condition (7.13),

we obtain

$$||Tf - T_h f||_0 \leq Ch^t ||f||_0,$$

where $t = \min(k, r)$, $k \geq 1$ is the order of the method, r the regularity exponent in (7.13), and C a constant independent of f and h. From this inequality it follows that

$$||T - T_h||_{\mathscr{L}(L^2(\Omega), L^2(\Omega))} = \sup_{f \in L^2(\Omega)} \frac{||Tf - T_h f||_0}{||f||_0} \leq Ch^t,$$

which implies the uniform convergence.   □

We now turn to error estimates for the approximation of the eigenvalues and the eigenfunctions. First of all we state a result on the rate of convergence for the solutions to the source problems when f is smooth.

Proposition 7.2 *Assume that $f \in H^{1+s_1}(\Omega)$ and that the solution u of problem (7.2) belongs to $H^{1+s_2}(\Omega)$ for some s_1 and s_2 greater than 0, then the estimate (7.30) implies*

$$||u - u_h||_0 \leq Ch^t \left(h^{\min(k, s_2)} |u|_{1+s_2} + h^{1+\min(k, s_1)} |f|_{1+s_1} \right) \tag{7.38}$$

where $t = \min(1, r)$.

Remark 7.3 We point out that an eigenfunction u can be seen as the solution of a source problem with right hand side equal to λu, which belongs at least to $H_0^1(\Omega)$. Hence the second term in the right side of (7.38) is at least of first order. In general, if the domain is non convex, the solution u to (7.2) belongs at least to $H^{1+r}(\Omega)$ with $r \in (\frac{1}{2}, 1]$, even if the right hand side is more regular, see (7.13). However, it might happen that u is more regular, for example that it belongs to the space $H^{1+s}(\Omega)$ with $s \geq r$, then estimate (7.38) reduces to

$$||u - u_h||_0 \leq Ch^{t+\min(k, s)} |u|_{1+s}. \tag{7.39}$$

Taking into account the above L^2-estimates and using the abstract Theorem 7.2, we obtain the optimal rate of convergence for the approximation of the eigenpairs (see [26, Theorem 6.1]).

Theorem 7.5 *Let λ_i be an eigenvalue of problem (7.1), with multiplicity m (that is $\lambda_i = \cdots = \lambda_{i+m-1}$) and let $\mathscr{E}_i$ be the corresponding eigenspace. We assume that all the elements in $\mathscr{E}_i$ belong to $H^{1+s}(\Omega)$ for some $s \geq r$ (see (7.13)). Moreover, let $\mathscr{E}_{i,h} = \bigoplus_{j=i}^{i+m-1} \text{span}(u_{h,j})$, where $u_{h,j}$ is the discrete eigenfunction associated*

with $\lambda_{h,j}$. Then, for h small enough, there exists a constant C independent of h such that

$$\delta(\mathcal{E}_i, \mathcal{E}_{i,h}) \leq Ch^{t+\min(k,s)} \tag{7.40}$$

with $t = \min(1, r)$.

Proof The result directly stems from (7.9). Indeed,

$$\delta(\mathcal{E}_i, \mathcal{E}_{i,h}) \leq C||(T - T_h)|_{\mathcal{E}_i}||_{\mathcal{L}(L^2(\Omega), L^2(\Omega))} = C \sup_{\substack{u \in \mathcal{E}_i \\ ||u||_0 = 1}} ||(T - T_h)u||_0. \tag{7.41}$$

Since $u \in \mathcal{E}_i$, it holds that $u \in H^{1+s}(\Omega)$ with $||u||_{1+s} \leq C||u||_0$ (see (7.13)). Hence the result follows from estimate (7.39). $\qquad\square$

Now we state the *a priori* error estimates for the eigenvalues (see [26, Theorem 6.1]).

Theorem 7.6 *Using the notation of Theorem 7.5, there exists a constant C independent of h, but depending on λ_i such that the following error estimate for the eigenvalues holds true:*

$$|\lambda_j - \lambda_{j,h}| \leq Ch^{2\min(k,s)} \quad for \ j = i, \ldots, i + m - 1.$$

Proof We apply Theorem 7.2. Thanks to (7.41), it remains to bound the first term in (7.10). This is equivalent to estimate $b((T - T_h)w, z)$ for all w and z in $\mathcal{E}_i$. After some computations we get

$$\begin{aligned}
b((T - T_h)w, z) &= a(Tz, (T - T_h)w) \\
&= a((T - T_h)z, (T - T_h)w) + b(T_h z, w) - b_h(T_h z, w) \\
&\quad - a(T_h z, T_h w) + a_h(T_h z, T_h w) \\
&= I' + II' + III'.
\end{aligned}$$

We estimate separately the three terms. It is straightforward to obtain

$$I' \leq ||(T - T_h)z||_1 ||(T - T_h)w||_1 \leq Ch^{2\min(k,s)}. \tag{7.42}$$

In order to estimate the second term, we proceed as in (7.35) by writing it as a sum over the elements $P \in \mathcal{T}_h$,

$$II' = \sum_P \left(b^P(T_h z - \Pi_k^0(T_h z), w - \Pi_k^0 w) - S_b^P((I - \Pi_k^0)T_h z, (I - \Pi_k^0)w) \right)$$

$$\leq C \sum_P ||(I - \Pi_k^0)T_h z||_{0,P} ||I - \Pi_k^0)w||_{0,P} \leq Ch^{2\min(k,s)}.$$

$$\tag{7.43}$$

Finally,

$$
\begin{aligned}
III' &= \sum_P \left(a_h^P (T_h z - \Pi_k^0 T z, T_h w - \Pi_k^0 T w) - a^P (T_h z - \Pi_k^0 T z, T_h w - \Pi_k^0 T w) \right) \\
&\le C \sum_P \left(|T_h z - T z|_{1,P} + |(I - \Pi_k^0) T z|_{1,P} \right) \\
&\qquad \left(|T_h w - T w|_{1,P} + |(I - \Pi_k^0) T w|_{1,P} \right) \le C h^{2 \min(k,s)}.
\end{aligned}
\tag{7.44}
$$

Collecting estimates (7.42)–(7.44) yields the required estimate. $\qquad\square$

Bearing in mind Remark 7.1, we state the rate of convergence for the error in the approximation of the eigensolutions with respect to the H^1-norm. To this aim we denote by $\delta_1(E, F)$ the gap between the spaces E and F measured in the H^1-norm.

Theorem 7.7 *Using the same notation as in Theorem 7.5, and assuming that all the elements in $\mathscr{E}_i$ belong to $H^{1+s}(\Omega)$ for some $s \ge r$, then for h small enough, there exists a constant C independent of h such that*

$$
\delta_1(\mathscr{E}_i, \mathscr{E}_{i,h}) \le C h^{\min(k,s)}.
$$

Remark 7.4 The above analysis has been carried on considering the stabilized discrete bilinear form b_h, whose local counterpart is given in (7.28). However, in [26] it has been shown that the results stated in Theorems 7.5–7.7 hold true also when b_h is defined using the *non-stabilized* local version in (7.26).

7.3.4 Numerical Results

Here and in the following sections devoted to the numerical experiments, we focus on the solution to problem (7.11) on a square and an *L-shaped* domain. It is well known that in the first test case the eigenfunctions are analytic, while in the latter they can be singular due to the presence of a reentrant corner in the domain. All the results that we are going to present are not new, including the figures which have been already published in [21, 26, 27].

The implementation of the method requires a precise definition for the stabilization terms. Here we are going to consider one possible choice, other possibilities are reported in [26]. For v_h and w_h in $V_h^k(P)$, the stabilizing bilinear forms $S_a^P(v_h, w_h)$ and $S_b^P(v_h, w_h)$ (see (7.20) and (7.28)) are defined using the local degrees of freedom associated to $V_h^k(P)$. Let N_P be the dimension of $V_h^k(P)$, then v and w stand for the vectors in $\mathbb{R}^{N_P}$ with components the local degrees of freedom

associated to v_h and w_h. More precisely, we set

$$S_a^P(v_h, w_h) = \alpha_P \mathbf{v}^\top \mathbf{w} \qquad \text{and} \qquad S_b^P(v_h, w_h) = \beta_P h_P^2 \mathbf{v}^\top \mathbf{w}, \qquad (7.45)$$

where α_P and β_P are constants independent of h. The numerical results we report here are obtained choosing α_P as the mean value of the eigenvalues of the local matrix associated to the consistency term $a^P(\Pi_k^\nabla v_h, \Pi_k^\nabla w_h)$. The parameter β_P is given by the mean value of the eigenvalues of the local mass matrix associated to $\frac{1}{h_P^2} b^P(\Pi_k^0 v_h, \Pi_k^0 w_h)$. With this definition α_P and β_P depend only on the shape of P.

Square Domain Let Ω be the square $(0, \pi)^2$, then the eigensolutions of (7.11) are given by

$$\begin{aligned} \lambda_{i,j} &= (i^2 + j^2) \quad \text{for } i, j \in \mathbb{N}, \text{ with } i, j \neq 0 \\ u_{i,j}(x, y) &= \sin(ix)\sin(jy) \quad \text{for } (x, y) \in \Omega. \end{aligned} \qquad (7.46)$$

We consider different refinements of a *Voronoi* mesh, an example of them is shown in Fig. 7.1 left. Figure 7.2 reports the error for the first six eigenvalues obtained with different polynomial degrees $k = 1, 2, 3, 4$ on meshes with size $h = \frac{\pi}{8}, \frac{\pi}{16}, \frac{\pi}{32}, \frac{\pi}{64}$. The slopes of the lines corresponding to the error for each eigenvalue clearly reflects the theoretical rate of convergence stated in Theorem 7.6. For $k = 4$ the error is close to the machine precision for the two last refinements, therefore the effect of propagation of rounding error prevents further decreasing. Remark 7.4 points out that the stabilization on the right hand side is not necessary at the theoretical level. In order to understand if it might impact the numerical results, we report in Table 7.1 a comparison between the errors obtained using the stabilized or non-stabilized bilinear form b_h, corresponding to the first four distinct eigenvalues for
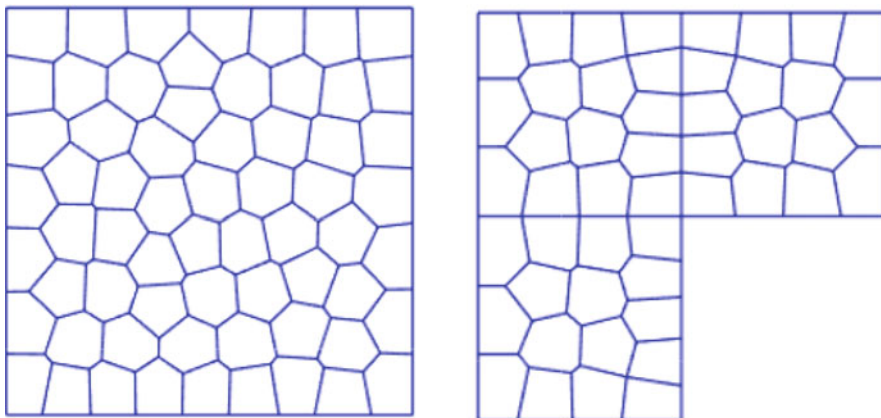

Fig. 7.1 Examples of Voronoi mesh of the unit square and the L-shaped domain
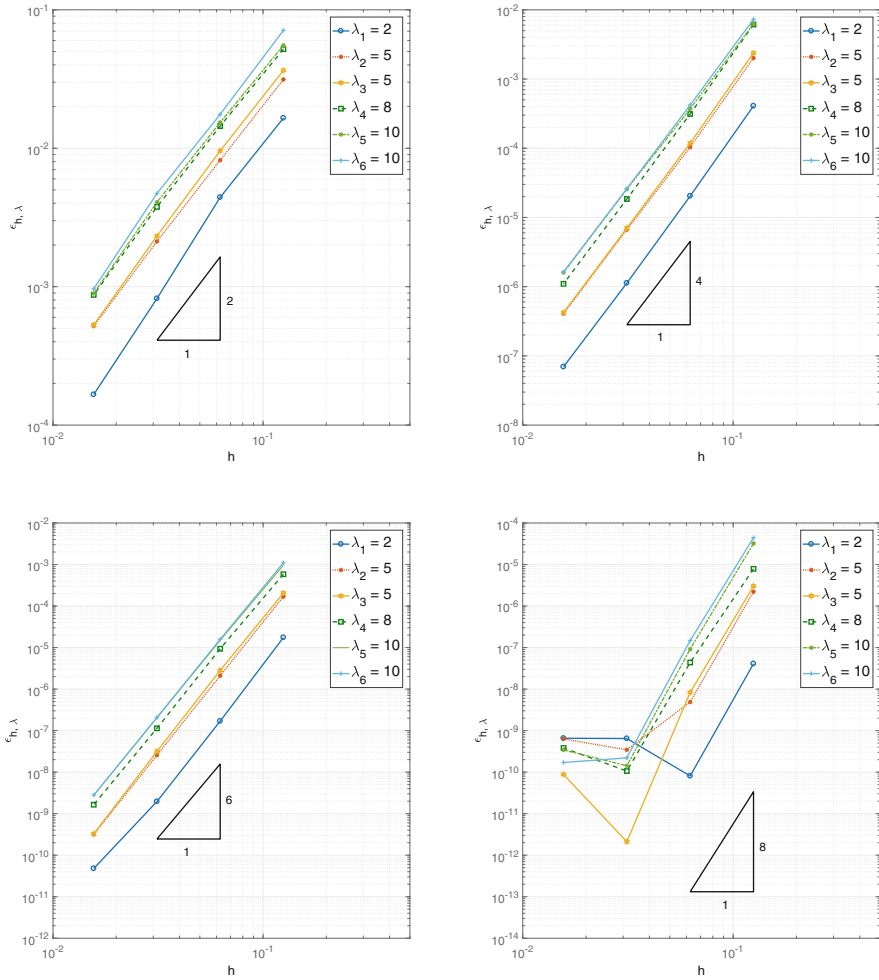
Fig. 7.2 Rate of convergence for the first six eigenvalues on the square domain. Top left: $k = 1$, top right: $k = 2$, bottom left: $k = 3$, bottom right: $k = 4$. (From: F. Gardini and G. Vacca. Virtual element method for second-order elliptic eigenvalue problems. IMA J. Numer. Anal., 38(4):2026–2054, 2018. Oxford University Press. Reproduced with permission)

$k = 1$ and $k = 4$. It might be appreciated that the magnitude of the error is actually the same. A more detailed discussion on the role of the stabilizing parameters will performed in Sect. 7.5.

L-Shaped Domain The Laplace eigenvalue problem with Neumann boundary conditions on the non convex L-shaped domain $\Omega = (-1, 1)^2 \setminus (0, 1) \times (-1, 0)$ (displayed in Fig. 7.1 right with an example of the used Voronoi mesh) is a well-known benchmark test to check the capability of the numerical scheme to

Table 7.1 Comparison of the errors for the first eigenvalues between stabilized and non stabilized bilinear form b_h

| h	$\lambda_1 = 2$		$\lambda_2 = 5$		$\lambda_4 = 8$		$\lambda_5 = 10$	
	Stab	Non stab	Stab	Non stab	Stab	Non stab	Stab	Non stab
$k = 1$								
$\pi/8$	1.654e−2	1.766e−2	3.650e−2	4.098e−2	5.196e−2	6.384e−2	7.107e−2	8.488e−2
$\pi/16$	4.418e−3	4.611e−3	9.578e−3	1.026e−2	1.446e−2	1.558e−2	1.758e−2	1.926e−2
$\pi/32$	8.206e−4	8.784e−4	2.320e−3	2.465e−3	3.768e−3	4.003e−3	4.715e−3	5.038e−3
$\pi/64$	1.662e−4	1.808e−4	5.289e−4	5.663e−4	8.722e−4	9.340e−4	9.643e−4	1.042e−3
$k = 4$								
$\pi/8$	4.087e−08	4.094e−08	3.033e−06	3.046e−06	7.856e−06	7.915e−06	4.428e−05	4.470e−05
$\pi/16$	8.101e−11	8.098e−11	8.329e−09	8.340e−09	4.364e−08	4.373e−08	1.475e−07	1.475e−07
$\pi/32$	6.451e−10	6.449e−10	2.109e−12	1.283e−12	1.062e−10	1.060e−10	2.211e−10	2.223e−10
$\pi/64$	6.54e−10	6.542e−10	8.818e−11	8.829e−11	3.815e−10	3.817e−10	1.706e−10	1.707e−10
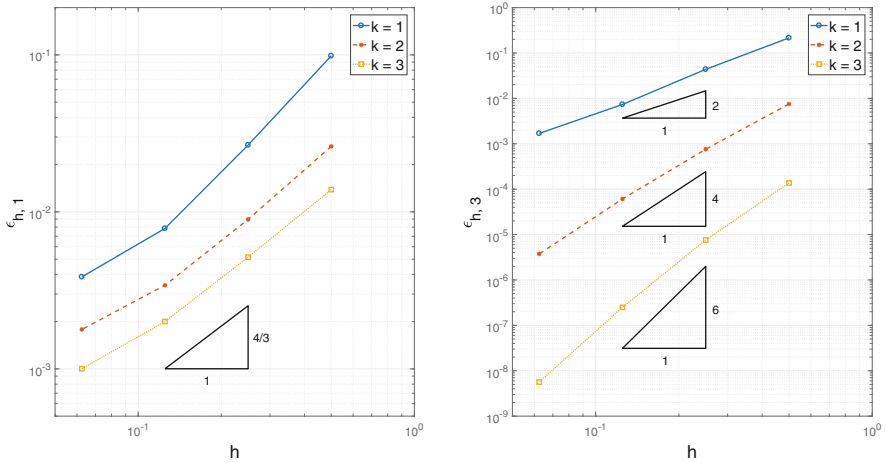
Fig. 7.3 Rate of convergence for the first eigenvalue (left) and the third one (right) on the L-shaped domain (From: F. Gardini and G. Vacca. Virtual element method for second-order elliptic eigenvalue problems. IMA J. Numer. Anal., 38(4):2026–2054, 2018. Oxford University Press. Reproduced with permission)

approximate singular eigensolutions. The analysis presented above for the Dirichlet eigenvalue problem extends analogously to this situation. In Fig. 7.3, we show the convergence history for the first and the third eigenvalues computed with $k = 1, 2, 3$ and the stabilization parameter chosen as in (7.45). The reference value for the eigenvalues has been taken form the benchmark solution set [23]. Due to the presence of the reentrant corner, the first eigensolution is singular belonging to $H^{1+r}(\Omega)$ with $r = 2/3 - \varepsilon$, hence the rate of convergence for the first eigenvalue results to be 4/3. On the other hand, the third eigenfunction is analytic and the scheme provides the correct $O(h^{2k})$ rate of convergence.

7.4 Extension to Nonconforming and *hp* Version of VEM

This section is devoted to the presentation of the nonconforming, p and hp versions of the discrete virtual space and reports the main results relative to the approximation of the eigenvalue problem. In particular, we are going to report on the results of [21, 27].

7.4.1 Nonconforming VEM

We start by treating the nonconforming case following [27]. With the aim of constructing the nonconforming space, we need some definitions. Let P^+ and P^- be two elements sharing the edge e and $\mathbf{n}_e^{\pm}$ the outward unit normal vector to $\partial P^{\pm}$. The jump of v across any internal edge e is $[\![v]\!] = v^+ \mathbf{n}_e^+ + v^- \mathbf{n}_e^-$, where $v^{\pm}$ is the restriction of v to $P^{\pm}$. If $e \in \mathscr{E}_h^{\partial}$ we set $[\![v]\!] = v_e \mathbf{n}_e$.

The construction of the nonconforming virtual element space is based on a different definition of the local space $V_h^k(P)$. More precisely, instead of imposing that the functions have a continuous trace along the element boundary, we prescribe the normal derivative on each edge of P to be a polynomial of degree $k - 1$, that is $V_h^k(P)$ is given by (7.14) and (7.15) with

$$\widetilde{V}_h^k(P) = \left\{ v_h \in H^1(P) : \ \frac{\partial v_h}{\partial \mathbf{n}} \in \mathbb{P}_{k-1}(P) \ \forall e \subset \partial P, \ \Delta v_h \in \mathbb{P}_k(P) \right\}. \qquad (7.47)$$

The degrees of freedom are given by the moments of v_h of order up to $k - 1$ on each edge e of P and the moments up to order $k - 2$ on P. As in the conforming case, $\Pi_k^{\nabla} v_h$ can be exactly evaluated by means of these degrees of freedom.

The *global nonconforming virtual element space* is then defined for, $k \geq 1$, as

$$V_h^{k,nc} = \left\{ v_h \in H^{1,nc}(\mathscr{T}_h; k) : v_h|_P \in V_h^k(P) \ \forall P \in \mathscr{T}_h \right\}, \qquad (7.48)$$

where as in the finite element framework,

$$H^{1,nc}(\mathscr{T}_h; k) = \left\{ v \in H_h^1 : \int_e [\![v]\!] \cdot \mathbf{n}_e \, p \, ds = 0 \ \forall p \in \mathbb{P}_{k-1}(e), \ \forall e \in \mathscr{E}_h \right\}, \qquad (7.49)$$

being $\mathbf{n}_e$ the outward normal unit vector to e with orientation fixed once and for all. It is clear that $V_h^{k,nc}$ is not a subspace of $H_0^1(\Omega)$, this will imply that in the error analysis we have to take into account a *consistency error*.

Proposition 7.1 still holds true with v_I being the interpolant of v constructed using the above degrees of freedom, see for example [20].

The discrete eigenvalue problem reads: find $(\lambda_h, u_h) \in \mathbb{R} \times V_h^{k,nc}$ with $u_h \neq 0$ such that

$$a_h(u_h, v_h) = \lambda_h b_h(u_h, v_h) \quad \forall v_h \in V_h^{k,nc}, \qquad (7.50)$$

where the bilinear forms a_h and b_h are defined in (7.20) and in (7.28). We recall also the discrete source problem: given $f \in L^2(\Omega)$ find $u_h \in V_h^{k,nc}$ such that

$$a_h(u_h, v_h) = b_h(f, v_h) \quad \forall v_h \in V_h^{k,nc}. \qquad (7.51)$$

We define, as usual, the resolvent operator $T_h : L^2(\Omega) \to L^2(\Omega)$ with $T_h f = u_h \in V_h^{k,nc}$ solution to (7.51). We notice that in this case T_h cannot be defined with range in $H_0^1(\Omega)$, therefore we shall obtain a result similar to Theorem 7.7 with the gap measured in the broken H^1-norm.

The analysis of the nonconforming case can be carried on with the same arguments used in the conforming case, stemming from the broken H^1-norm estimate for the error of the solution of the source problem. We start with the following result proved in [3]: there exists a positive constant C independent of h such that

$$
\|u - u_h\|_{1,h} \leq C\Big(|u - u_I|_{1,h} + |u - u_\pi|_{1,h}
$$
$$
+ \sup_{v_h \in V_h^{k,nc}} \frac{|b(f, v_h) - b_h(f, v_h)|}{|v_h|_{1,h}} + \sup_{v_h \in V_h^{k,nc}} \frac{\mathscr{R}_h(u, v_h)}{|v_h|_{1,h}} \Big), \tag{7.52}
$$

where

$$
\mathscr{R}_h(u, v_h) = \sum_{P \in \mathscr{T}_h} a^P(u, v_h) - b(f, v_h) = \sum_{e \in \mathscr{E}_h^0} \int_e \nabla u \cdot [\![v_h]\!] \, ds. \tag{7.53}
$$

The term $\mathscr{R}_h(u, v_h)$ represents an additional *consistency error* which, in the spirit of the *second Strang Lemma* [22, Th. 4.2.2], is due to the fact that the discrete functions are not continuous across inter-element edges. With standard arguments using the degrees of freedom of the nonconforming virtual elements on the element boundary and a Poincaré inequality (see [16]), one can prove that for $u \in H^{1+r}(\Omega)$, with $r > 1/2$, (see [3, Lemma 4.1])

$$
\mathscr{R}_h(u, v_h) \leq Ch^r \|u\|_{1+r} |v_h|_{1,h} \quad \forall v_h \in V_h^{k,nc}. \tag{7.54}
$$

In order to obtain the uniform convergence of T_h to T, we first show the L^2-error estimate for the solution to the source problem. In the case of a convex domain, a similar result can be found in [3, Theorem 4.5].

Theorem 7.8 *Let $f \in L^2(\Omega)$, $u \in H_0^1(\Omega)$ and $u_h \in V_h^{k,nc}$ be the solutions to (7.2) and (7.51), respectively. Then there exists a constant C, independent of h, such that for $t = \min(1, r)$*

$$
\|u - u_h\|_0 \leq Ch^t \Big(|u - u_h|_{1,h} + |u - u_\pi|_{1,h}
$$
$$
+ \|f - \Pi_k^0 f\|_0 + \sup_{v_h \in V_h^{k,nc}} \frac{\mathscr{R}_h(u, v_h)}{|v_h|_{1,h}} \Big). \tag{7.55}
$$

Proof The proof follows the same lines as that of Theorem 7.3. We have to take into account the consistency error. Let $\psi \in H_0^1(\Omega)$ be the solution to (7.31), then we have

$$\|u - u_h\|_0^2 = \sum_P \left(a^P(u - u_h, \psi - \psi_I) + a^P(u - u_h, \psi_I) \right) + \mathscr{R}_h(\psi, u_h).$$

Thanks to (7.34) and (7.54), it remains to estimate the second term in the sum, which can be split as follows:

$$\sum_P a^P(u, \psi_I) = b(f, \psi_I) + \mathscr{R}_h(u, \psi_I)$$

$$\sum_P a^P(u_h, \psi_I) = b_h(f, \psi_I) + \sum_P \left(a^P(u_h, \psi_I) - a_h^P(u_h, \psi_I) \right).$$

We use again (7.54) and observe that the other terms can be estimated as the terms III and IV in the proof of Theorem 7.3. Putting together all the estimates yields the required bound. □

Assuming that $f \in H^{1+s_1}(\Omega)$ and that the solution u to problem (7.2) belongs to $H^{1+s_2}(\Omega)$ for some $s_1 > 0$ and $s_2 > \frac{1}{2}$, then we obtain again the bound (7.38). This optimal rate of convergence yields the rate convergence for the gap between the eigenspaces and for the eigenvalue error as in Theorems 7.5 and 7.6. The analogous result as the one in Theorem 7.7 can be obtained if the gap is measured using the broken H^1-norm.

Numerical results confirming the theory are presented in [27] where the domain is a square or L-shaped. The nonconforming VEM has been tested on four different types of meshes including also non convex elements providing always optimal rate of convergence in the case of analytic eigenfunctions. In particular, in [27] a comparison of the rate of convergence between conforming and nonconforming approximation has been presented showing very close behavior. The benchmark with the L-shaped domain has been also considered and again the results agree with those presented in Fig. 7.3.

7.4.2 hp *Version of VEM*

Let us now recall briefly the p and hp version of the virtual element method and show how these methods can be applied to the discretization of the eigenvalue problem. We refer, in particular, to [21] although we are considering the simpler model problem (7.11), and to [7] for the basic principles of hp virtual elements.

In this case the spaces we are considering, are labeled with a subindex $n \in \mathbb{N}$ and refer to conforming polygonal decompositions of Ω denoted by $\mathscr{T}_n$. Given an element $P \in \mathscr{T}_n$ and the polynomial degree $p \in \mathbb{N}$, $V_n^p(P)$ is the local virtual space

and coincides with the space $V_h^k(P)$, with the due changes in the notation. Hence the global space V_n^p is the subspace of $H_0^1(\Omega)$ defined as $V_n^p = \{v_n \in H_0^1(\Omega) : v_n|_P \in V_n^p(P) \ \forall P \in \mathcal{T}_n\}$. Analogously, we shall use the subindex n instead of h in all the definitions involving discrete quantities.

The results of approximation in the space V_n^p are similar to those in Proposition 7.1, but trace the dependence on the degree p, so that the exponential convergence of the error can be deduced (see [21, Theorem 2.1, and Corollary 2.3]).

Proposition 7.3 *Given $P \in \mathcal{T}_n$ and $u \in H^{1+s}(P)$, $s > 0$, for all $p \in \mathbb{N}$, there exists $u_\pi \in \mathbb{P}_p(P)$ and a constant C independent of p, such that*

$$|u - u_\pi|_{\ell, P} \le C \frac{h_P^{1+\min(p,s)-\ell}}{p^{1+s-\ell}} ||u||_{1+s, P} \quad for \ 0 \le \ell \le s.$$

Moreover, given $u \in H_0^1(\Omega)$ with $u|_P \in H^{1+s}(P)$ for all $P \in \mathcal{T}_n$ and for some $s \ge 1$, there exists $u_I \in V_n^p$ such that

$$|u - u_I|_1 \le C \frac{h^{\min(p,s)}}{p^{s-1}} \left(\sum_{P \in \mathcal{T}_n} ||u||_{1+s, P}^2 \right)^{\frac{1}{2}}.$$

We point out that the use of high degree p is convenient in the approximation of smooth (piecewise smooth) functions.

The approximation of the eigenvalue problem (7.11) can be written introducing the local discrete bilinear forms already used in the h-conforming case (7.20) and (7.28). Then the discrete eigenvalue problem reads: find $(\lambda_n, u_n) \in \mathbb{R} \times V_n^p$ with $u_n \ne 0$ such that

$$a_n(u_n, v_n) = \lambda_n b_n(u_n, v_n) \quad \forall v_n \in V_n^p. \tag{7.56}$$

As it is standard for eigenvalue problems, we associate the discrete source problem: given $f \in L^2(\Omega)$ find $u_n \in V_n^p$ such that

$$a_n(u_n, v_n) = b_n(f, v_n) \quad \forall v_n \in V_n^p. \tag{7.57}$$

In order to take advantage of the approximation properties listed in Proposition 7.3, we define the resolvent operator T on $H^1(\Omega)$ in the spirit of Remark 7.1. Hence for $f \in H^1(\Omega)$, $Tf = u$ is the solution to the continuous source problem (7.2), while in the discrete case, $T_n f = u_n \in V_n^p$ stands for the solution to (7.57).

The convergence of eigensolutions derives from the uniform convergence of T_n to T, which in turn is a consequence of the error estimates for the source problem (see [21, Theorem 3.2]).

Theorem 7.9 *Given $f \in H^1(\Omega)$, let $u \in H_0^1(\Omega)$ and $u_n \in V_n^p$ be the solutions to (7.2) and (7.57), respectively. Assume that the restrictions of f and u to every*

element $P \in \mathcal{T}_n$ belong to $H^{1+s}(P)$ for some $s \geq 0$, then there exists a constant C independent of h and p such that

$$|u - u_n|_1 \leq C \frac{h^{\min(p,s)}}{p^{s-1}} \left(h^2 ||f||_{1+s,n} + ||u||_{1+s,n} \right).$$

For the proof it is enough to combine Proposition 7.3 with standard VEM arguments. In [21], a precise dependence of C on the ellipticity constant of the form a and the constants in (7.21), and (7.29) is obtained. In particular, it is shown that the constants in (7.21) and (7.29) might depend on p, as we shall see later.

The result in Theorem 7.9, together with the arguments of [7, Section 5], yields the following exponential convergence (see [21, Theorem 3.3]):

Theorem 7.10 *Let u and u_n be as in Theorem 7.9, and assume that u is the restriction on Ω of an analytic function defined on an extension of Ω. Then there exist two positive constants C and c independent of the discretization parameters such that*

$$|u - u_n|_1 \leq C \exp(-cp).$$

Theorem 7.9 implies the uniform convergence of $||T - T_n||_{\mathscr{L}(H^1(\Omega), H^1(\Omega))}$ to zero, more precisely one can show that under the same assumptions as in Theorem 7.10 it holds true:

$$||T - T_n||_{\mathscr{L}(H^1(\Omega), H^1(\Omega))} \leq C \exp(-cp).$$

Then, applying Theorems 7.6 and 7.7, we obtain the spectral convergence both for the error in the approximation of the eigenvalues, and the gap between the continuous and the discrete eigenspaces, provided the eigenfunctions are analytic. For the details, we refer to [21]. Figure 7.4 shows the convergence of the p-version of VEM in comparison with the h-version with fixed $p = 1, 2, 3$ for the test case on the square $(0, \pi)^2$ with exact values given by (7.46). The domain is partitioned into a family of Voronoi meshes, and for the p-version the coarsest one employed for the h version has been used. These results has been obtained using the so called *diagonal* recipe for the stabilization of a defined as

$$\widetilde{S}_a^P(\varphi_i, \varphi_j) = \max(1, a^P(\Pi_k^\nabla \varphi_i, \Pi_k^\nabla \varphi_j))\delta_{ij}$$

where φ_i is the canonical basis in $V_n(P)$ and δ_{ij} is the Kroenecker index, and the following choice for the stabilization of b

$$S_b^P(u_n, v_n) = \frac{h_P}{p^2} \int_{\partial P} u_n v_n \, ds,$$

which satisfies (7.29) with $\beta_*(p) \gtrsim p^{-6}$ and $\beta^*(p) \lesssim 1$.
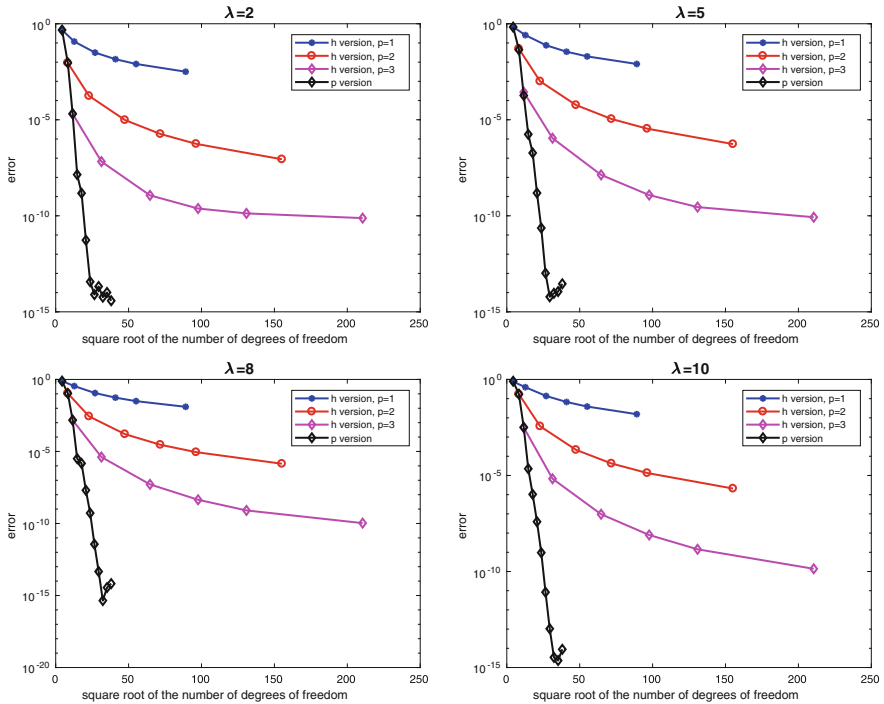
Fig. 7.4 Convergence of the error for the first four distinct Dirichlet eigenvalues of the Laplace operator on the unit square domain. On the *x*-axis, the square root of the number of degrees of freedom is reported (From: Čertík, F. Gardini, G. Manzini, L. Mascotto, and G. Vacca. The *p*- and *hp*-versions of the virtual element method for elliptic eigenvalue problems. Comput. Math. Appl., 79(7):2035–2056, 2020. Elsevier. Reproduced with permission)

Although these values inserted in the estimates reported in Theorem 7.9 might seem pessimistic, in reality the numerical results seem to be not affected by the behavior of the stability constants.

If the eigenfunctions are not smooth enough, the spectral convergence of *p* version of VEM cannot be achieved. However, as in the finite element method, one can resort to the *hp* approach which combines the *p* and the *h* versions using locally geometrical refined meshes where the solution is singualar. For the source problem, the analysis of the exponential convergence of the *hp* VEM in presence of corner singularities has been tackled in [7]. The paper [21] merely investigates numerically the convergence of the *hp* approximation of the eigenvalues, showing the exponential decay in terms of the cubic root of the number of degrees of freedom, in the case of eigenfunctions with finite Sobolev regularity. We report in Fig. 7.5 the convergence of the error for the first four distinct eigenvalues of the Laplace eigenproblem with Neumann boundary condition on the L-shaped domain obtained in [21]. It is well-known that the first eigenfunction is singular. In order to recover the spectral convergence the *hp*-version of VEM has been applied on a graded mesh
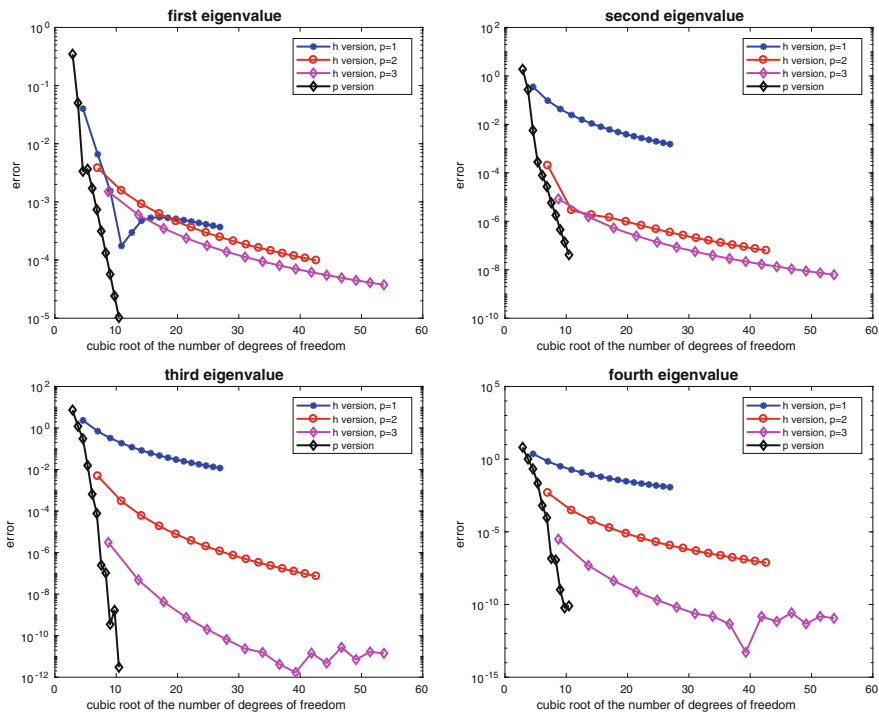
Fig. 7.5 Convergence of the error for the first four distinct Neumann eigenvalues of the Laplace operator on the L-shaped domain. Comparison of the *hp*-version with the *h*-version with $p = 1, 2, 3$. On the x-axis, we report the cubic root of the number of degrees of freedom. (From: Čertík, F. Gardini, G. Manzini, L. Mascotto, and G. Vacca. The p- and hp-versions of the virtual element method for elliptic eigenvalue problems. Comput. Math. Appl., 79(7):2035–2056, 2020. Elsevier. Reproduced with permission)

with a non uniform distribution of p. The domain has been divided into layers around the reentrant corner and the local polynomial degree of $V_n(P)$ increases as the layer is farer from the singularity. The results show spectral convergence with respect to the cubic root of the number of degrees of freedom for the *hp*-version.

7.5 The Choice of the Stabilization Parameters

In Sect. 7.3 we have seen that an effective VEM approximation of eigenvalue problems requires the introduction of appropriate stabilization parameters. In practice, the discrete problem has the form of the following algebraic generalized eigenvalue problem

$$\mathsf{A}u = \lambda \mathsf{M}u \tag{7.58}$$

where both the involved matrices A and M depend on the stabilization parameters introduced for the VEM discretization.

The results of the previous sections assume that such parameters have been fixed and show the convergence of the method when the meshsize goes to zero and/or p goes to ∞. By doing so, it is implicitly understood that the convergence behavior depends on the choice of the parameters. In this section we want to discuss this dependence and see how the discrete solution is influenced by such choice. We would like to make it clear from the very beginning that the optimal strategy for the choice of the parameters is still the object of ongoing research and that the aim of our presentation is more related to the description of the phenomenon than to an ultimate answer to the open questions. Nevertheless, the *easy and quick recipe* will be that the parameter related to A should be large enough, while the parameter related to M should be small enough and possibly equal to zero.

The results presented in this section are a condensed version of what is published in [15]. The interested reader will find there a more general theory and more specific numerical tests.

Although the general picture of VEM approximation of eigenvalue problems is more complicated, the following simplified setting proves useful in order to understand its main features.

7.5.1 A Simplified Setting

We assume that all matrices are symmetric and that $\mathsf{A} = \mathsf{A}_1 + \alpha \mathsf{A}_2$ and $\mathsf{M} = \mathsf{M}_1 + \beta \mathsf{M}_2$, where $\alpha \geq 0$ and $\beta \geq 0$ play the role of the stabilization parameters. More precisely, we assume that

  (i) A_1 and M_1 are positive semidefinite;
 (ii) A_2 and M_2 are positive semidefinite and positive definite on the kernel of A_1 and M_1, respectively;
(iii) A_2 and M_2 vanish on the orthogonal complement of the kernel of A_1 and M_1, respectively.

In [15] we have studied several examples and described the spectrum of the generalized eigenvalue problem (7.58) as a function of α and β. The main features are easily understood with a simple example when α or β are constant.

When $\beta > 0$ is constant, then M is positive definite and the eigenvalues of (7.58) are all positive, possibly vanishing for $\alpha = 0$ (see assumption (i) above), and are formed by two families: the first one is independent on α and corresponds to eigenvectors v orthogonal to the kernel of A_1 and to the eigenvalues λ that satisfy
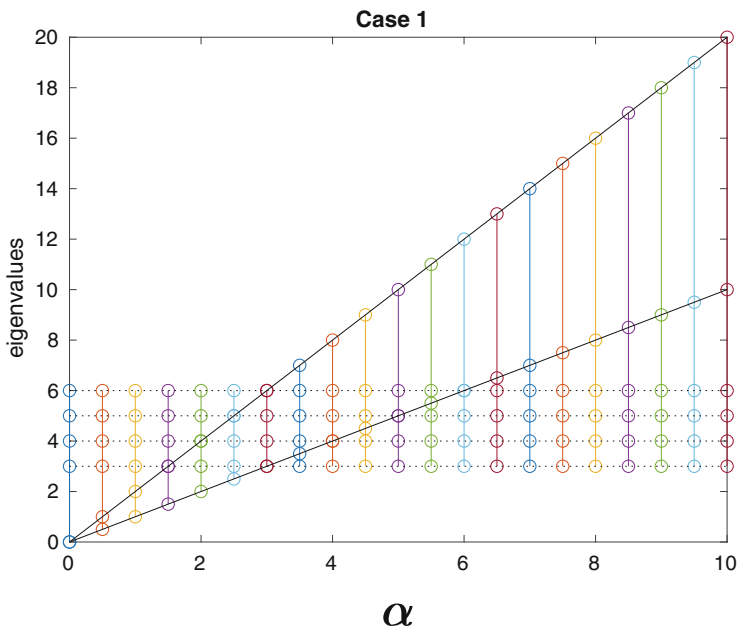
$$\mathsf{A}_1 \mathsf{v} = \lambda \mathsf{M} \mathsf{v}$$

Fig. 7.6 Eigenvalues of (7.58) for $\beta > 0$ fixed [15]

(see assumption (iii) above), while the second family contains eigenvectors w in the kernel of A_1 and the eigenvalues $\lambda = \alpha\mu$ where (μ, w) satisfies

$$\mathsf{A}_2\mathsf{w} = \mu\mathsf{M}\mathsf{w}$$

(see assumption (ii) above). In particular the second family contains eigenvalues growing linearly with α and includes, for $\alpha = 0$, the eigenvalue $\lambda = 0$ with eigenspace equal to the kernel of A_1.

Figure 7.6 gives a graphical indication of the eigenvalues of (7.58) as a function of α when $\beta > 0$ is fixed: the horizontal lines correspond to the eigenvalues of the first family, while the linearly increasing curves starting at the origin correspond to the eigenvalues of the second family.

The second case that is useful to discuss is when $\alpha > 0$ is fixed and β is varying. This case is analogous to the previous one with the roles of A and M exchanged. This means that A is positive definite and the behavior of the solutions (ω, u) to the following eigenvalue problem

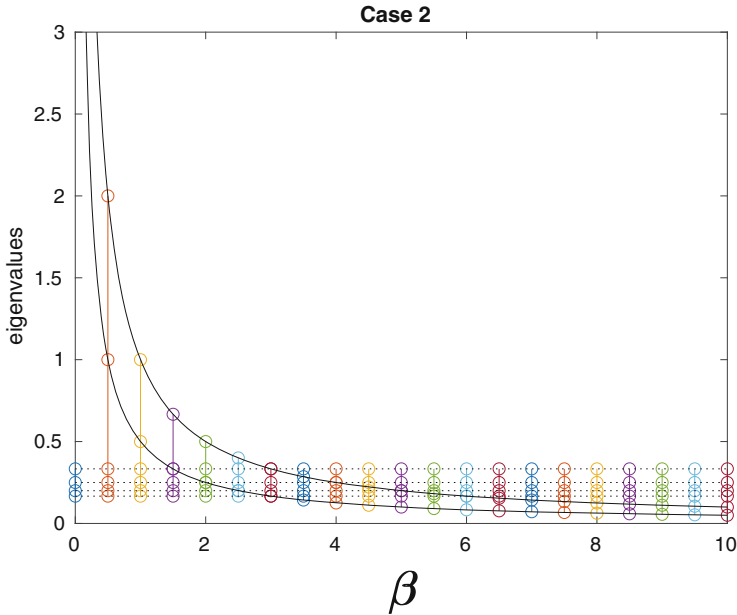$$\mathsf{M}\mathsf{u} = \omega\mathsf{A}\mathsf{u}$$

Fig. 7.7 Eigenvalues of (7.58) for $\alpha > 0$ fixed [15]

is analogous to the one depicted in Fig. 7.6 with α replaced by β. Since the original eigenmodes of problem (7.58) are given by $(\lambda, \mathsf{u}) = (1/\omega, \mathsf{u})$ for $\omega \neq 0$ and (∞, u) for $\omega = 0$, it turns out that the eigenvalues in this case are split again into two families: the first one is independent of β and corresponds to eigenvectors v orthogonal to the kernel of M_1 and to the eigenvalues $\lambda = 1/\omega$ that satisfy

$$\mathsf{M}_1\mathsf{v} = \omega\mathsf{A}\mathsf{v}$$

while the second family contains eigenvectors w in the kernel of M_1 and eigenvalues $\lambda = 1/(\beta\omega)$ where (ω, w) satisfies

$$\mathsf{M}_2\mathsf{w} = \omega\mathsf{A}\mathsf{w}.$$

In particular, the second family contains eigenvalues that behave like decreasing hyperbolas tending to zero as β goes to infinity. For $\beta = 0$ the eigenvalues of the second family degenerate to $\lambda = \infty$ with eigenspace equal to the kernel of M_1.

Figure 7.7 shows the behavior of the eigensolution of (7.58) for fixed $\alpha > 0$ and varying β: the horizontal lines correspond to the eigenvalues of the first family while the hyperbolas represent those of the second one.

7.5.2 The Role of the VEM Stabilization Parameters

The general setting of the problems we have discussed in Sect. 7.3 does not fit exactly the simplified framework presented in the previous subsection. In particular, the matrices A and M do not satisfy the assumptions made above. Nevertheless, a similar splitting into a matrix that is singular due to the presence of the projection operator and a stabilizing matrix that takes care of the kernel of the singular part is present both in A and M. Actually, the numerical experiments reveal a dependence on the parameters that resembles pretty much the one presented in Figs. 7.6 and 7.7.

Redirecting the interested reader to [15] for more details, we report here only some results related to the properties of the matrices A and M, together with some numerical experiments corresponding to the simplified situations of Figs. 7.6 and 7.7. All the presented results are taken from [15].

We consider Ω as the square of side π and introduce a sequence of five Voronoi meshes of polygons with increasing number of elements from $N = 50$ to $N = 800$. Table 7.2 reports the dimension of the kernels of the two matrices A_1 and M_1 as a function of the meshsize and of the degree of approximation k. As it is known, both matrices are non singular in the lowest order case for $k = 1$; the matrix M_2 is non singular for $k = 2$ as well for the considered meshes.

For completeness, we also computed the lowest eigenvalue of the generalized problem

$$A_1 u = \lambda M_1 u$$

that is reported in Table 7.3. The fact that the value of the eigenvalue is decreasing as the number of elements increases, confirms the need for a stabilization.

In the rest of this section we show and comment some results of our computations of the eigenvalues of the Dirichlet problem for the Laplace operator in the case of the mesh $N = 200$.

Table 7.2 Dimension of the kernels of A_1 and M_1 with respect to the degree k and the number of elements N in the mesh

k	$N = 50$	$N = 100$	$N = 200$	$N = 400$	$N = 800$
Kernel of A_1					
1	0	0	0	0	0
2	3	30	99	258	565
3	27	94	246	588	1312
Kernel of M_1					
1	0	0	0	0	0
2	0	0	0	0	0
3	0	1	43	182	504

Table 7.3 First eigenvalues of $A_1 x = \lambda B_1 x$ for different meshes

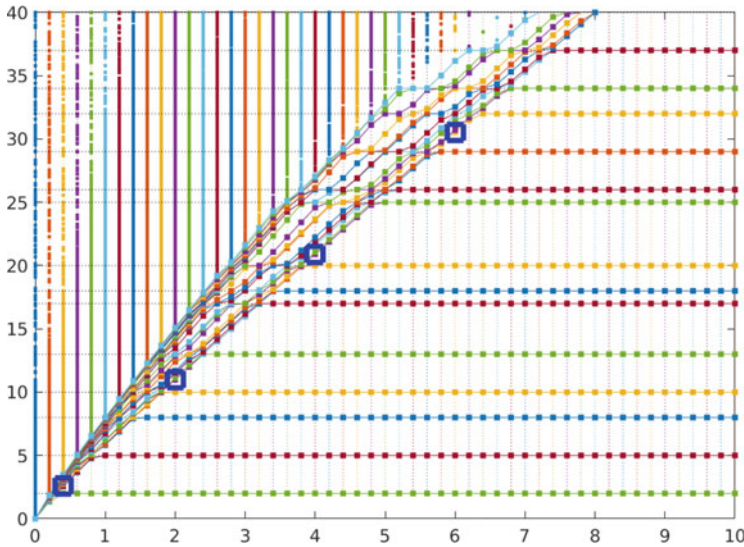| $N = 50$	$N = 100$	$N = 200$	$N = 400$	$N = 800$
1.92654e+00	1.74193e+00	1.06691e+00	6.81927e−01	5.54346e−01

Fig. 7.8 Eigenvalues computed for $\beta = 1$ and $\alpha \in [0, 10]$ with $k = 3$ [15]

Figure 7.8 reports the computed eigenvalues in the range $[0, 40]$, for $\beta = 1$ and $\alpha \in [0, 10]$ with elements of degree $k = 3$. Comparing these results with Fig. 7.6 it is easy to recognize the horizontal lines corresponding to the *good* eigenvalues we are interested in. At the same time it is apparent the presence of some oblique lines that correspond to *spurious* modes introduced by the stabilization of A.

Figure 7.9 shows the eigenfunctions corresponding to the marked values of Fig. 7.8 that belong to the same oblique line. It can be seen that the eigenfunctions look similar to each other, which confirms the analogy with the situation presented in Fig. 7.6.

Several other cases when $\beta \geq 0$ is fixed and α is varying are reported in Fig. 7.10 for different values of k.

The last computations of this section involve the situation when $\alpha > 0$ is fixed and β is varying.

Figure 7.11 shows the behavior of the eigenvalues for different values of α and k and with β varying in the interval $[0, 5]$; the analogies with the simplified case shown in Fig. 7.7 are evident.

In conclusion, the reader might wonder what is our suggestion for the choice of the parameters. The answer is not immediate and is not definitive. One clear message is that the dependence on β may have more dangerous effects than the one on α. As a rule of thumb, our numerical tests indicate that α should be chosen large enough, possibly using the same criteria adopted for the source problem, while small values of β (or even $\beta = 0$) are preferable. Clearly, a small value of β leads to an ill-conditioned problem: the limit case $\beta = 0$ may corresponds to a degenerate eigenvalue problem where the matrix M is singular. As it is typical for eigenvalue
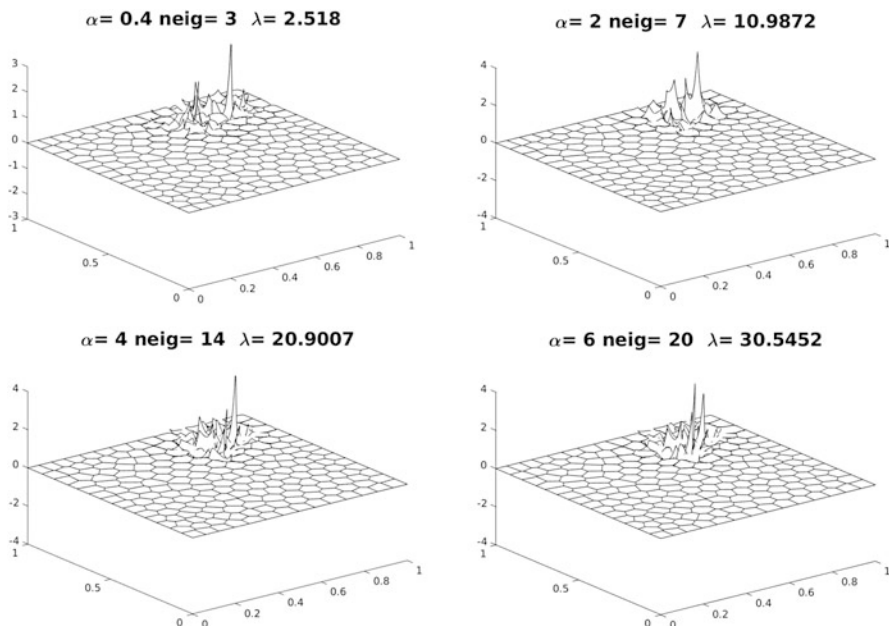
Fig. 7.9 Eigenfunctions associated with the marked eigenvalues of Fig. 7.8 [15]

problems, if h is not small enough the eigenvalues are not yet well resolved and the dependence on the parameters might be more complicated to analyze and may lead to useless results. In order to better illustrate how large values of β can produce wrong results, in Fig. 7.12 we show the computation of the first four eigenvalues with $\alpha = 10$, $k = 1$, and $\beta \in [0, 400]$. Each subplot represents one of the first four eigenvalues as function of β; different colors correspond to different meshes. These plots should be compared to Fig. 7.11. In particular, Fig. 7.11c shows computations for the same values of α and k on the mesh $N = 200$. We comment in detail the behavior of the approximation to the fourth eigenvalue shown in the bottom/right subplot of Fig. 7.12; similar considerations apply to the other eigenvalues. First of all, it is clear that if h is small enough then the solution is correct: when $N = 6400$ the fourth computed eigenvalue is independent on β and provides a good approximation of $\lambda = 8$. On the coarsest mesh, however, the results obtained are useless in order to predict the correct value of the fourth eigenvalue: for large values of β the computed eigenvalue is much smaller than 8 and tends to zero as β increases; for a value of β between 10 and 20 the computed eigenvalue crosses the line $\lambda = 8$ and it becomes much larger for smaller values of β reaching a value of approximately 12 for $\beta = 0$. The results for the next mesh for $N = 400$ are similar for large β but are significantly different after the red line crosses the value $\lambda = 8$. For values of β smaller than the crossing point, the computed eigenvalue remains closer to the correct value of the exact solution. Another interesting phenomenon related to this curve is that when it reaches $\lambda = 2$ and, more evidently, $\lambda = 5$, the
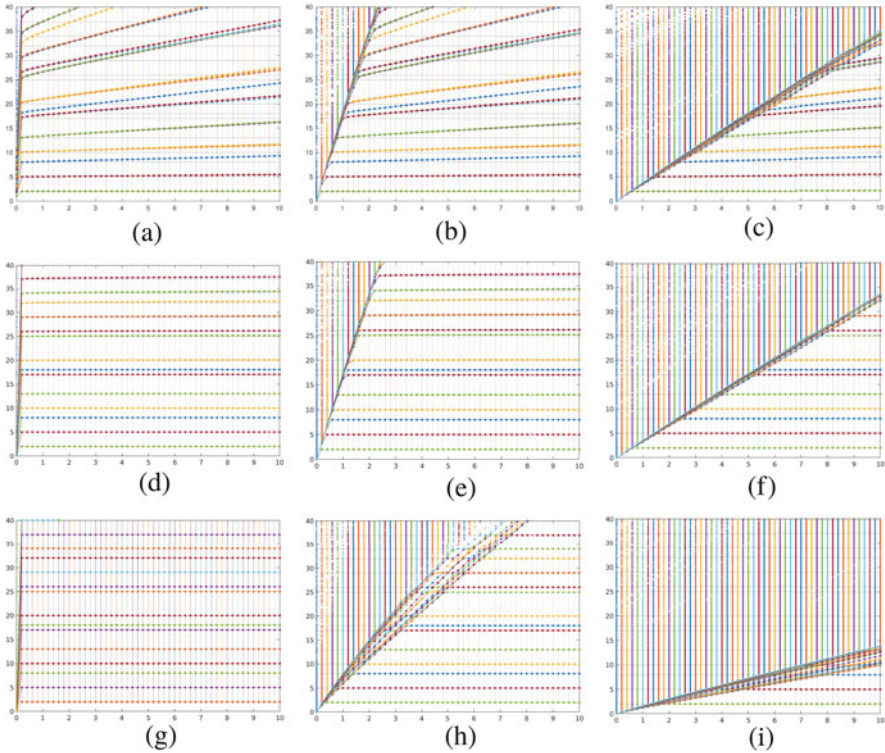
Fig. 7.10 Eigenvalues with fixed k and $\beta \geq 0$ and varying $\alpha \in [0, 10]$ [15]. (**a**) $k = 1$, $\beta = 0$, $\alpha \in [0, 10]$. (**b**) $k = 1$, $\beta = 1$, $\alpha \in [0, 10]$. (**c**) $k = 1$, $\beta = 5$, $\alpha \in [0, 10]$. (**d**) $k = 2$, $\beta = 0$, $\alpha = [0, 10]$. (**e**) $k = 2$, $\beta = 1$, $\alpha = [0, 10]$. (**f**) $k = 2$, $\beta = 5$, $\alpha = [0, 10]$. (**g**) $k = 3$, $\beta = 0$, $\alpha = [0, 10]$. (**h**) $k = 3$, $\beta = 1$, $\alpha = [0, 10]$. (**i**) $k = 3$, $\beta = 5$, $\alpha = [0, 10]$

curve seems to bend and to be attracted for a while by the first and second (double) eigenvalue. This behavior is due to the fact that the curve is crossing other computed eigenvalues which are not plotted in this figure and, after the crossing, it continues along another hyperbola.

7.6 Applications

We conclude this paper with a discussion on the application of VEM to eigenvalue problems arising from various models and formulations. We start with a presentation of the mixed formulation for our model problem and then we continue with other applications following the chronological order of the related publications.
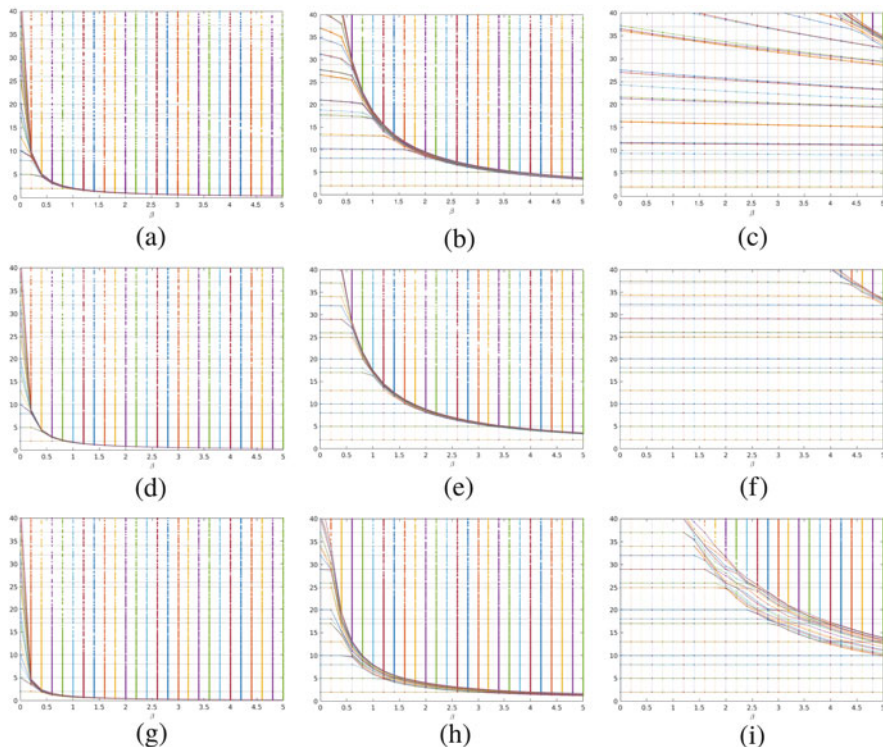
Fig. 7.11 Eigenvalues with fixed k and $\alpha > 0$ and varying $\beta \in [0, 5]$ [15]. (**a**) $k = 1, \alpha = 0.1$, $\beta \in [0, 5]$. (**b**) $k = 1, \alpha = 1, \beta \in [0, 5]$. (**c**) $k = 1, \alpha = 10, \beta \in [0, 5]$. (**d**) $k = 2, \alpha = 0.1$, $\beta = [0, 5]$. (**e**) $k = 2, \alpha = 1, \beta = [0, 5]$. (**f**) $k = 2, \alpha = 10, \beta = [0, 5]$. (**g**) $k = 3, \alpha = 0.1$, $\beta = [0, 5]$. (**h**) $k = 3, \alpha = 1, \beta = [0, 5]$. (**i**) $k = 3, \alpha = 10, \beta = [0, 5]$

7.6.1 The Mixed Laplace Eigenvalue Problem

In [30] the mixed formulation of the Laplace eigenvalue is considered. The following usual mixed formulation is consider: $\Sigma = \mathbf{H}(\mathrm{div}; \Omega), U = L^2(\Omega)$, so that we are seeking for $\lambda \in \mathbb{R}$ and a non vanishing $u \in U$ such that for $\boldsymbol{\sigma} \in \mathbf{H}(\mathrm{div}; \Omega)$ it holds

$$(\boldsymbol{\sigma}, \boldsymbol{\tau}) + (\mathrm{div}\,\boldsymbol{\tau}, u) = 0 \quad \forall \boldsymbol{\tau} \in \Sigma$$

$$(\mathrm{div}\,\boldsymbol{\sigma}, v) = -\lambda(u, v) \quad \forall v \in U.$$

It is well known that the analysis of the approximation of the Laplace eigenvalue in mixed form requires particular care because of the lack of compactness of the solution operator with respect to the component $\boldsymbol{\sigma}$. The analysis of [30] extends the theory of [11] to the virtual element method. The discrete spaces are constructed as
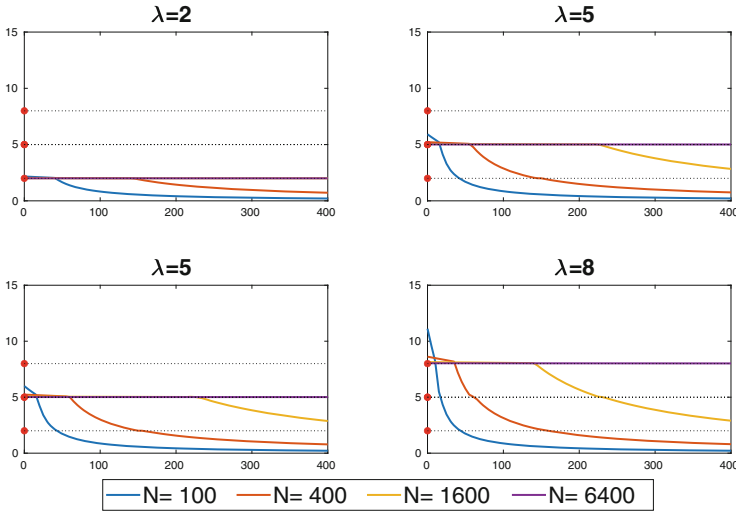
Fig. 7.12 First four eigenvalues depending on β for $\alpha = 10$ and $k = 1$ [15]

follows: the space Σ is approximated by the following space described in [19]

$$\Sigma_h = \{\boldsymbol{\tau}_h \in \Sigma : (\boldsymbol{\tau}_h \cdot \mathbf{n})|_e \in \mathbb{P}_k(e) \ \forall e \in \mathscr{E}_h, \ \mathrm{div}\,\boldsymbol{\tau}_h|_P \in \mathbb{P}_{k-1}(P),$$
$$\mathrm{rot}\,\boldsymbol{\tau}_h|_P \in \mathbb{P}_{k-1}(P) \ \forall P \in \mathscr{T}_h\}$$

while the space U is approximated by a standard piecewise discontinuous space

$$U_h = \{v_h \in U : v_h|_P \in \mathbb{P}_{k-1}(P) \ \forall P \in \mathscr{T}_h\}.$$

The matrix form of the approximate problem reads

$$\begin{pmatrix} \mathsf{A} & \mathsf{B}^\top \\ \mathsf{B} & 0 \end{pmatrix} \begin{pmatrix} \sigma \\ u \end{pmatrix} = -\lambda \begin{pmatrix} 0 & 0 \\ 0 & \mathsf{M} \end{pmatrix} \begin{pmatrix} \sigma \\ u \end{pmatrix}.$$

In this case, the matrix M does not contain any stabilization parameter since the space U_h is a standard mass matrix arising from discontinuous finite elements. The same applies to the matrix B that can be constructed directly by using the degrees of freedom of the spaces Σ_h and U_h. Hence, the only matrix that requires a stabilization is A.

The analysis of [30] shows, using the tools of [11] and the properties of the spaces Σ_h and U_h, the following uniform bound for the solution of the source problem with right hand side $f \in L^2(\Omega)$:

$$\|\sigma - \sigma_h\|_0 + \|u - u_h\|_0 \le Ch^t \|f\|_0$$

where $t = \min(k, r)$, r being such that $u \in H^{1+r}(\Omega)$ (see (7.13)). From this estimate the convergence of the eigenvalues and eigenfunctions follows by standard arguments and an appropriate definition of the solution operator (see Sect. 7.2 and [10]).

7.6.2 The Steklov Eigenvalue Problem

Another formulation where the stabilization parameter enters only the matrix on the left hand side of the discrete system, is given by the so called Steklov eigenvalue problem

$$\Delta u = 0 \quad \text{in } \Omega$$

$$\frac{\partial u}{\partial \mathbf{n}} = \lambda u \quad \text{on } \partial\Omega.$$

A more general setting could be actually considered by taking the second equation only on a subset Γ_0 of $\partial\Omega$ and homogeneous Neumann boundary conditions on the remaining part of the boundary. We refer to [32] for the analysis of its VEM discretization.

The variational formulation is obtained by considering $V = H^1(\Omega)$ and seeks for $\lambda \in \mathbb{R}$ and a non vanishing $u \in V$ such that

$$\int_\Omega \nabla u \cdot \nabla v \, dx = \lambda \int_{\partial\Omega} uv \, ds \qquad \forall v \in V.$$

Since the bilinear form on the left hand side is not $H^1(\Omega)$-elliptic, the analysis is based on the use of a shift argument by adding the boundary integral on both sides of the eigenvalue problem in weak form. Hence, the resolvent operator and its discrete counterpart are defined using the shifted problem. In this case, it is necessary to consider $T : V \to V$ in order to give sense to the datum of the source problem.

The approximation of the problem makes use of the standard VEM spaces described in Sect. 7.3. As we have seen before, the discrete problem requires to introduce a discretization of the bilinear form on the left hand side, with the addition of a stabilization term. Whereas, the integral on the right hand side can be computed using the degrees of freedom on the element boundaries.

For $f \in H^1(\Omega)$, the solution to the associated source problem belongs to $H^{1+r}(\Omega)$, with $r > \frac{1}{2}$. This implies that the resolvent operator is compact on V, so that the analysis in [32] relies on the standard theory for compact operators that we have recalled in Sect. 7.2. In particular, it is based on the following uniform convergence of T_h to T:

$$\|(T - T_h)f\|_1 \leq Ch^r \|f\|_1 \quad \forall f \in H^1(\Omega),$$

which in turn gives the same rate of convergence for the gap between eigenspaces and double rate of convergence for the eigenvalue error.

The matrix form of the discrete problem is

$$\mathsf{A}u = \lambda \mathsf{M}u,$$

where A depends on the stabilization parameter α_P. In [32] one can find an interesting test case which models the sloshing modes of a two dimensional fluid contained in a square. In this test case, Ω is the unit square and its boundary is divided into two parts: Γ_0 the top side of the square and Γ_1 the remaining three sides. On Γ_0 the Steklov condition is imposed, while on Γ_1 homogeneous Neumann condition is enforced. The convergence analysis with fixed parameter $\alpha_P = 1$ for all $P \in \mathcal{T}_h$ confirms the theoretical results. The paper contains, for the first time, the study of the effect of the stability on the computed eigenvalues on a fixed mesh. It has been observed that, when α_P is independent of the element P and varies from 4^{-3} to 4^3 spurious eigenvalues appear among the correct ones. In Fig. 7.13, we plot the first 16 eigenvalues reported in [32, Table 3]. These eigenvalues were been obtained using a triangular mesh, considering the middle point of each edge as a new vertex of the polygon. Each side of the square has been divided into 8 parts and virtual elements with $k = 1$ are applied. The plot on the right is a zoom of the one on the left. The dotted black horizontal lines represent the first 3 exact eigenvalues. One can see that for $\alpha_P > 1$ the spurious eigenvalues seems to be proportional to the stabilization parameter and this appears to be in agreement with the analysis reported in Sect. 7.5, while the approximation of the three correct ones is independent of α_P.
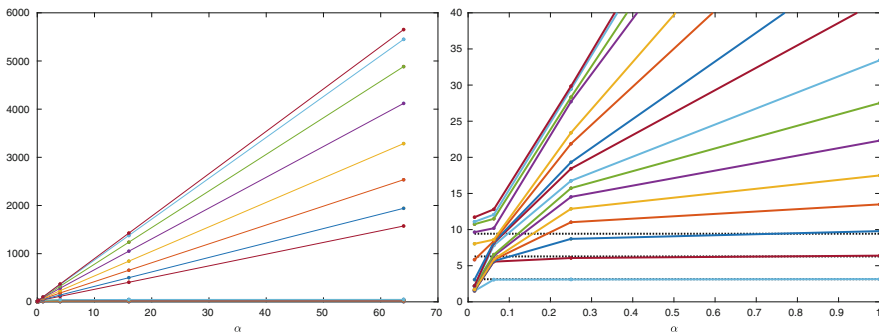

Fig. 7.13 First 16 eigenvalues for $4^{-3} \le \alpha_P \le 4^3$

7.6.3   An Acoustic Vibration Problem

The next application has been considered in [8] and is an example where only the matrix on the right hand side of the discrete algebraic system contains a parameter.

The model describes the free vibrations of an inviscid compressible fluid within a bounded rigid cavity Ω. The simplest model consists in finding eigenvalues $\lambda \in \mathbb{R}$ and non vanishing eigenfunctions $\mathbf{u} \in \mathbf{H}_0(\mathrm{div}; \Omega)$ such that

$$\int_\Omega \mathrm{div}\,\mathbf{u}\,\mathrm{div}\,\mathbf{v}\,dx = \lambda \int_\Omega \mathbf{u} \cdot \mathbf{v}\,dx \qquad \forall \mathbf{v} \in \mathbf{H}_0(\mathrm{div}; \Omega).$$

Here $\mathbf{H}_0(\mathrm{div}; \Omega)$ is the subspace of $\mathbf{H}(\mathrm{div}; \Omega)$ of functions with vanishing trace of the normal component on $\partial\Omega$.

The approximation is performed by the following VEM space that has been designed taking inspiration from [6, 19]:

$$V_h = \{\mathbf{v}_h \in \mathbf{H}_0(\mathrm{div}; \Omega) : (\mathbf{v}_h \cdot \mathbf{n})|_e \in \mathbb{P}_k(e)\ \forall e \in \mathscr{E}_h,\ \mathrm{div}\,\mathbf{v}_h|_P \in \mathbb{P}_k(P),$$

$$\mathrm{rot}\,\mathbf{v}_h|_P = 0\ \forall P \in \mathscr{T}_h\}.$$

The discretized problem has the classical form

$$\mathsf{A}\mathbf{u} = \lambda \mathsf{M}\mathbf{u}$$

and the matrix A can be formed directly using the degrees of freedom since the divergence of elements in V_h are piecewise polynomials. On the other hand, the mass matrix M should be constructed by using the typical VEM approach and requires a stabilization in order to control the non polynomial part of the space V_h.

The convergence analysis of [8] is performed as in case of standard finite elements [9] by shifting the solution operator in order to deal with the kernel of the divergence operator, and by exploiting the theory of [24] related to the analysis of non compact operators. More precisely, the continuous solution operator $T : \mathbf{H}_0(\mathrm{div}; \Omega) \to \mathbf{H}_0(\mathrm{div}; \Omega)$ is defined as the solution $T\mathbf{f} \in \mathbf{H}_0(\mathrm{div}; \Omega)$ of

$$\int_\Omega \mathrm{div}\,T\mathbf{f}\,\mathrm{div}\,\mathbf{v}\,dx + \int_\Omega T\mathbf{f} \cdot \mathbf{v}\,dx = \int_\Omega \mathbf{f} \cdot \mathbf{v}\,dx \qquad \forall \mathbf{v} \in \mathbf{H}_0(\mathrm{div}; \Omega)$$

and its discrete counterpart $T_h : V_h \to V_h$ is defined as the solution $T_h\mathbf{f}_h \in V_h$ of

$$\int_\Omega \mathrm{div}\,T_h\mathbf{f}_h\,\mathrm{div}\,\mathbf{v}_h\,dx + \int_\Omega T_h\mathbf{f}_h \cdot \mathbf{v}_h\,dx = \int_\Omega \mathbf{f}_h \cdot \mathbf{v}_h\,dx \qquad \forall \mathbf{v}_h \in V_h.$$

The theory of [24] consists in showing the following mesh dependent uniform convergence

$$\lim_{h \to 0} \sup_{\substack{\mathbf{f}_h \in V_h \\ \|\mathbf{f}_h\|_{\mathrm{div}} = 1}} \|(T - T_h)\mathbf{f}_h\|_{\mathrm{div}} = 0$$

together with the density of V_h in $\mathbf{H}_0(\mathrm{div}; \Omega)$. In particular, in [8] it is proved the following estimate

$$\sup_{\substack{\mathbf{f}_h \in V_h \\ \|\mathbf{f}_h\|_{\mathrm{div}} = 1}} \|(T - T_h)\mathbf{f}_h\|_{\mathrm{div}} \le Ch^s,$$

where $s \in]\frac{1}{2}, 1]$ is the regularity index of the solution to the associated source problem. This results implies that for h small enough the virtual element method does not introduce spurious eigenvalues interspersed among the physical ones we are interested in. Optimal error estimates depending on the regularity of the eigenfunctions follow by combining the technique of [25] with the first Strang lemma.

The above theoretical results were obtained when the stability parameter β_P is positive. The numerical experiments show that for $k = 0$ the optimal second order rate of convergence for the eigenvalues can be achieved for several choices of meshes. The effect of the stability constant has also been investigated. In Fig. 7.14, we plot the first eigenvalue for β_P ranging from 2^{-6} to 2^6 for different
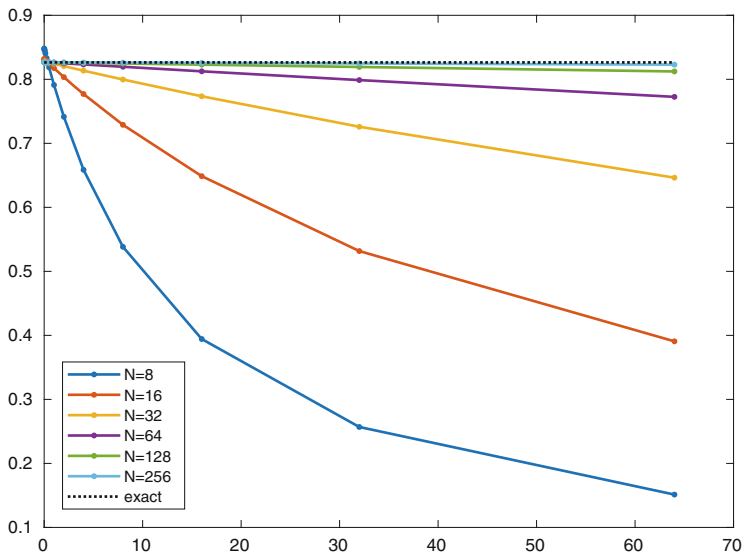

Fig. 7.14 First eigenvalue with $2^{-6} \le \beta \le 2^6$ and different meshes

square meshes as reported in [8, Table 4]. It can be seen that as the mesh gets finer the results are less sensible to the value of β_P, while for coarse meshes the behavior looks similar to that shown in Fig. 7.12 corresponding to Case 2 in Sect. 7.5. Moreover, although the choice $\beta_P = 0$ is not covered by the theory, the computational results appear to be very accurate in this case, and also this is in agreement with the observations reported in Sect. 7.5.

7.6.4   Eigenvalue Problems Related to Plate Models

The computation of vibration frequencies and modes of an elastic solid is a very important topic in engineering applications. This and the following sections are devoted to report on the results obtained in [31, 34, 35] concerning the use of VEM to approximate the eigenvalues of the Kirchhoff–Love model for plates and of linear elasticity equations.

We consider a plate whose mean surface, in its reference configuration, occupies a polygonal bounded domain $\Omega \subset \mathbb{R}^2$. The plate is clamped on its whole boundary. Let u denote the transverse displacement and λ the vibration frequency, then the plate vibration problem, modeled by Kirchhoff–Love equations reads: find $\lambda \in \mathbb{R}$ and a non vanishing u such that:

$$\Delta^2 u = \lambda u \qquad \text{in } \Omega$$

$$u = \frac{\partial u}{\partial \mathbf{n}} = 0 \qquad \text{on } \partial\Omega.$$

The corresponding weak form reads: find $(\lambda, u) \in \mathbb{R} \times H_0^2(\Omega)$ with $u \neq 0$ such that

$$\int_\Omega D^2 u : D^2 v \, dx = \lambda \int_\Omega uv \, dx \qquad \forall v \in H_0^2(\Omega), \tag{7.59}$$

where $D^2 v$ denotes the Hessian matrix of v. The associated resolvent operator T is defined for all $f \in H_0^2(\Omega)$ as the solution Tf of the corresponding source problem. It results to be self adjoint and compact thanks to the fact that Tf belongs to $H^{2+s}(\Omega)$ for some $s \in]\frac{1}{2}, 1]$ being the Sobolev regularity for the biharmonic equation with homogeneous Dirichlet boundary conditions.

We recall here the construction of the virtual elements space proposed in [35] which differs from those presented in the previous sections since C^1-regularity is required for approximating functions in $H_0^2(\Omega)$. Given a sequence $\{\mathscr{T}_h\}_h$ of decompositions of Ω into polygons P, we introduce first the following finite

dimensional space:

$$V_h(P) = \Big\{ v_h \in H^2(P) : \Delta^2 v_h \in \mathbb{P}_2(P), \ v_h|_{\partial P} \in C^0(\partial P),$$

$$\nabla v_h|_{\partial P} \in C^0(\partial P)^2, \ v_h|_e \in \mathbb{P}_3(e), \ \frac{\partial v_h}{\partial \mathbf{n}}\Big|_e \in \mathbb{P}_1(e) \ \forall e \in \partial P \Big\}.$$

The corresponding degrees of freedom are the values of v_h and ∇v_h at the vertices of P. Using these degrees of freedom it is possible to define a projection operator $\Pi_2^\Delta : V_h(P) \to \mathbb{P}_2(P) \subseteq V_h(P)$ by solving for each $v \in V_h(P)$ the following problem:

$$a_\Delta^P(\Pi_2^\Delta v, q) = a_\Delta^P(v, q) \qquad \forall q \in \mathbb{P}_2(P)$$

$$((\Pi_2^\Delta v, q))_P = ((v, q))_P \qquad \forall q \in \mathbb{P}_1(P),$$

where

$$a_\Delta^P(u, v) = \int_P D^2 u : D^2 v \, dx, \quad ((v, q))_P = \sum_{i=1}^{N_P} u(V_i) v(V_i) \qquad \forall u, v \in H^2(P),$$

and $V_i \ i = 1, \ldots, N_P$ are the vertices of P.

Then the local virtual space is:

$$W_h(P) = \Big\{ v_h \in V_h(P) : \int_P (\Pi_2^\Delta v_h - v_k) q \, dx = 0 \ \forall q \in \mathbb{P}_2(P) \Big\}.$$

Thanks to this characterization of $W_h(P)$, the $L^2(P)$-projection operator onto $\mathbb{P}_2(P)$ coincides with Π_2^Δ.

With the above definitions, the global virtual space is defined as:

$$W_h = \{ v_h \in H_0^2(\Omega) : v_h|_P \in W_h(P) \}$$

and the discrete bilinear forms are given for all $u_h, v_h \in W_h$ by

$$a_h(u_h, v_h) = \sum_{P \in \mathcal{T}_h} a_{\Delta,h}^P(u_h, v_h), \quad b_h(u_h, v_h) = \sum_{P \in \mathcal{T}_h} b_{\Delta,h}^P(u_h, v_h),$$

with

$$a_{\Delta,h}^P(u_h, v_h) = a_\Delta^P(\Pi_2^\Delta u_h, \Pi_2^\Delta v_h) + s_{\Delta,a}^P(u_h - \Pi_2^\Delta u_h, v_h - \Pi_2^\Delta v_h)$$

$$b_{\Delta,h}^P(u_h, v_h) = \int_P \Pi_2^\Delta u_h \Pi_2^\Delta v_h \, dx + s_{\Delta,b}^P(u_h - \Pi_2^\Delta u_h, v_h - \Pi_2^\Delta v_h).$$

As usual the stabilization terms $s_{\Delta,a}^P$ and $s_{\Delta,b}^P$ have been added in order to guarantee consistency and stability.

With the above definitions, the discrete counterpart of equation (7.59) reads: find $(\lambda_h, u_h) \in \mathbb{R} \times W_h$ with $u \neq 0$ such that

$$a_h(u_h, v_h) = \lambda_h b_h(u_h, v_h) \quad \forall v_h \in W_h.$$

After introducing the resolvent operator $T_h : W_h \to W_h$ as the mapping that associates to any $f_h \in W_h$ the solution $T_h f_h$ to the corresponding source problem, the convergence analysis follows from the theory developed in [24, 25] and gives optimal rate of convergence for the gap between continuous and discrete eigenspaces according to the regularity of the eigenfunctions and double rate of convergence for the eigenvalue error.

The numerical results require that the choice for the stabilization terms is made precise, therefore using the degrees of freedom of the local space one can set

$$s_{\Delta,a}^P(u_h, v_h) = \alpha_P \sum_{i=1}^{N_P} (u_h(V_i)v_h(V_i) + h_{V_i}^2 \nabla u_h(V_i) \cdot \nabla v_h(V_i))$$

$$s_{\Delta,b}^P(u_h, v_h) = \beta_P \sum_{i=1}^{N_P} (u_h(V_i)v_h(V_i) + h_{V_i}^2 \nabla u_h(V_i) \cdot \nabla v_h(V_i))$$

for all $u_h, v_h \in W_h(P)$. In the numerical experiments presented in [35], the stabilization parameters α_P and β_P are chosen as the mean value of the eigenvalues of the local matrices $a_\Delta^P(\Pi_2^\Delta u_h, \Pi_2^\Delta v_h)$ and $\int_P \Pi_2^\Delta u_h \Pi_2^\Delta v_h \, dx$, respectively. Hence, the matrices A and M of the associated algebraic eigenvalue problem $\mathsf{A}u = \lambda\mathsf{M}u$ depend on stabilization parameters and we shall discuss later on their choice.

The numerical results reported in [35] show that the first four eigenvalues converge to the exact or extrapolated values with quadratic rate in agreement with the theoretical results.

In order to analyze the effect of the parameters on the computed eigenvalues, in [35] it has been done the choice to multiply the stabilizing forms $s_{\Delta,a}^P$ and $s_{\Delta,b}^P$ by the same value of the parameter. This makes very difficult to compare the results with the behavior described in Sect. 7.5, since the better choice would be to take large values of α_P and small ones of β_P. Coherently, the conclusions of [35] is that the optimal choice is for value of the parameter in the middle.

We end this subsection with some consideration relative to the buckling problem of a clamped plate, which can be formulated as a spectral problem of fourth order as follows: given a plane stress tensor field $\boldsymbol{\eta} : \Omega \to \mathbb{R}^{2\times2}$, find the non vanishing

deflection of the plate u and the eigenvalue (the buckling coefficient) λ such that

$$\Delta^2 u = -\lambda \operatorname{div}(\boldsymbol{\eta} \nabla u) \qquad \text{in } \Omega$$

$$u = \frac{\partial u}{\partial \mathbf{n}} = 0 \qquad \text{on } \partial \Omega.$$

Setting $a_\Delta(u, v) = \int_\Omega D^2 u : D^2 v \, dx$ and $b_b(u, v) = \int_\Omega \boldsymbol{\eta} \nabla u \nabla v \, dx$ the weak problem can be written as (7.59) with $b_b(u, v)$ on the right hand side instead of the $L^2(\Omega)$-scalar product.

The virtual element discretization of this problem has been discussed in [34] using virtual element spaces of any degree $k \geq 2$ introduced in [18]:

$$V_h(P) = \left\{ v_h \in \widetilde{V}_h(P) : \int_P (v_h - \Pi_k^\Delta v_h) q \, dx = 0 \; \forall q \in \mathbb{P}_{k-3}^*(P) \cup \mathbb{P}_{k-2}^*(P) \right\}$$

where $\mathbb{P}_\ell^*(P)$ denotes homogeneous polynomials of degree ℓ with the convention that $\mathbb{P}_{-1}^*(P) = \{0\}$. In the definition above the following notation have been used: for $r = \max(3, k)$ and $s = k - 1$

$$\widetilde{V}_h(P) = \left\{ v_h \in H^2(P) : \Delta^2 v_h \in \mathbb{P}_{k-2}(P), \; v_h|_{\partial P} \in C^0(\partial P), \right.$$

$$\left. \nabla v_h|_{\partial P} \in C^0(\partial P)^2, \; v_h|_e \in \mathbb{P}_r(e), \; \frac{\partial v_h}{\partial \mathbf{n}}\bigg|_e \in \mathbb{P}_s(e) \; \forall e \in \partial P \right\}.$$

and $\Pi_k^\Delta : H^2(P) \to \mathbb{P}_k(P) \subseteq \widetilde{V}_h(P)$ is the computable projection operator solution of local problems:

$$a_\Delta^P(\Pi_k^\Delta v, q) = a_\Delta^P(v, q) \quad \forall q \in \mathbb{P}_k(P) \quad \forall v \in H^2(P)$$

$$\widehat{\Pi_k^\Delta v} = \widehat{v}, \quad \widehat{\nabla \Pi_k^\Delta v} = \widehat{\nabla v}$$

with $\widehat{v} = \frac{1}{N_P} \sum_{i=1}^{N_P} v(V_i)$, and V_i the N_P vertices of P. Then the discrete bilinear form a_h is the sum of local terms composed by a consistency and a stabilizing part

$$a_h^P(u_h, v_h) = a_\Delta^P(\Pi_k^\Delta u_h, \Pi_k^\Delta v_h) + s_{\Delta,a}^P(u_h - \Pi_k^\Delta u_h, v_h - \Pi_k^\Delta v_h).$$

On the other hand the discrete right hand side can be constructed using the degrees of freedom without the necessity of stabilizing

$$b_b^P(u_h, v_h) = \int_P \boldsymbol{\eta} \Pi_{k-1}^\Delta u_h \Pi_{k-1}^\Delta v_h \, dx.$$

The analysis of this problem follows the same lines as the one for the vibrating plate reported above. In [34] the theoretical results are confirmed by several numerical experiments showing that the method produces accurate solutions.

Another eigenvalue problem that involves a fourth order operator and whose approximation has been analyzed when VEM spaces are used, can be found in [33] where a transmission problem is considered.

7.6.5 Eigenvalue Problems Related to Linear Elasticity Models

In this section we report on the analysis presented in [31] about the VEM approximation of the linear elasticity eigenvalue problem in two space dimensions. We consider the functional space $V = H^1_{\Gamma_D}(\Omega)^2$, where Γ_D is the part of $\partial\Omega$ where homogeneous Dirichlet boundary condition are imposed, that is where the displacement of the structure is prescribed and equal to zero. The equation we are interested in is: find $\lambda \in \mathbb{R}$ and $\mathbf{u} \in V$ different from zero such that

$$\int_\Omega \mathscr{C}\,\underline{\varepsilon}(\mathbf{u}) : \underline{\varepsilon}(\mathbf{v})\,d\mathbf{x} = \lambda \int_\Omega \varrho\mathbf{u}\cdot\mathbf{v}\,d\mathbf{x},$$

where $\varrho > 0$ is the density of the material, $\underline{\varepsilon}$ is the symmetric gradient, and the compliance tensor $\mathscr{C}$ is defined as

$$\mathscr{C}\boldsymbol{\tau} = 2\mu\boldsymbol{\tau} + \lambda\mathrm{tr}(\boldsymbol{\tau})\underline{\mathbf{I}},$$

μ and λ being the Lamé constants.

It is well known that the problem under consideration is associated with a compact resolvent operator, so that the analysis of its approximation relies on the standard Babuška–Osborn theory.

The VEM discretization makes use of the natural vectorial generalization $V_h \subset V$ based on the local standard spaces (7.14) and of the projection operator defined as in (7.15) with the due modifications.

The discrete problem has the standard form of a generalized eigenvalue problem $\mathsf{A}u = \lambda\mathsf{M}u$, where both matrices A and M contain a stabilization parameter. The analysis, both a priori and a posteriori, is performed for a given choice of the stabilizing parameters, which is analogous to the one described in Sect. 7.3.4 As in [35], see also Sect. 7.6.4, in [31] a study on the dependence of the stabilizing parameters is performed when the parameters of A and M are chosen equal to each other. It turns out that when the parameter is not too large or not too small, the first eigenvalues of the considered example are not polluted by spurious modes. This is compatible with what we have found in Sect. 7.5, although a safer choice would imply to take a larger parameter for stabilizing the matrix A and a smaller one (or even zero) for M.

References

1. S. Agmon, *Lectures on Elliptic Boundary Value Problems*. Prepared for publication by B. Frank Jones, Jr. with the assistance of George W. Batten, Jr. Van Nostrand Mathematical Studies, No. 2 (D. Van Nostrand Co., Inc., Princeton, 1965)
2. B. Ahmad, A. Alsaedi, F. Brezzi, L.D. Marini, A. Russo, Equivalent projectors for virtual element methods. Comput. Math. Appl. **66**(3), 376–391 (2013)
3. B. Ayuso de Dios, K. Lipnikov, G. Manzini, The nonconforming virtual element method. ESAIM Math. Model. Numer. Anal. **50**(3), 879–904 (2016)
4. I. Babuška, J. Osborn, Eigenvalue problems, in *Handbook of Numerical Analysis*, vol. II. Handbook of Numerical Analysis, II (North-Holland, Amsterdam, 1991), pp. 641–787
5. L. Beirão da Veiga, F. Brezzi, A. Cangiani, G. Manzini, L.D. Marini, A. Russo, Basic principles of virtual element methods. Math. Models Methods Appl. Sci. **23**(1), 199–214 (2013)
6. L. Beirão da Veiga, F. Brezzi, L.D. Marini, A. Russo, Mixed virtual element methods for general second order elliptic problems on polygonal meshes. ESAIM Math. Model. Numer. Anal. **50**(3), 727–747 (2016)
7. L. Beirão da Veiga, A. Chernov, L. Mascotto, A. Russo, Basic principles of hp virtual elements on quasiuniform meshes. Math. Models Methods Appl. Sci. **26**(8), 1567–1598 (2016)
8. L. Beirão da Veiga, D. Mora, G. Rivera, R. Rodríguez, A virtual element method for the acoustic vibration problem. Numer. Math. **136**(3), 725–763 (2017)
9. A. Bermúdez, R. Durán, M.A. Muschietti, R. Rodríguez, J. Solomin, Finite element vibration analysis of fluid-solid systems without spurious modes. SIAM J. Numer. Anal. **32**(4), 1280–1295 (1995)
10. D. Boffi, Finite element approximation of eigenvalue problems. Acta Numer. **19**, 1–120 (2010)
11. D. Boffi, F. Brezzi, L. Gastaldi, On the convergence of eigenvalues for mixed formulations. Ann. Scuola Norm. Sup. Pisa Cl. Sci. (4) **25**(1–2), 131–154 (1998). 1997. Dedicated to Ennio De Giorgi.
12. D. Boffi, F. Brezzi, L. Gastaldi, On the problem of spurious eigenvalues in the approximation of linear elliptic problems in mixed form. Math. Comp. **69**(229), 121–140 (2000)
13. D. Boffi, L. Gastaldi, Analysis of finite element approximation of evolution problems in mixed form. SIAM J. Numer. Anal. **42**(4), 1502–1526 (2004)
14. D. Boffi, A. Buffa, L. Gastaldi, Convergence analysis for hyperbolic evolution problems in mixed form. Numer. Linear Algebra Appl. **20**(4), 541–556 (2013)
15. D. Boffi, F. Gardini, L. Gastaldi, Approximation of PDE eigenvalue problems involving parameter dependent matrices. Calcolo **57**(4), 41 (2020)
16. S.C. Brenner, Poincaré-Friedrichs inequalities for piecewise H^1 functions. SIAM J. Numer. Anal. **41**(1), 306–324 (2003)
17. S.C. Brenner, L.R. Scott, *The Mathematical Theory of Finite Element Methods*, vol. 15. Texts in Applied Mathematics, 3rd edn. (Springer, New York, 2008)
18. F. Brezzi, L.D. Marini, Virtual element methods for plate bending problems. Comput. Methods Appl. Mech. Eng. **253**, 455–462 (2013)
19. F. Brezzi, R.S. Falk, L.D. Marini, Basic principles of mixed virtual element methods. ESAIM Math. Model. Numer. Anal. **48**(4), 1227–1240 (2014)
20. A. Cangiani, E.H. Georgoulis, T. Pryer, O.J. Sutton, A posteriori error estimates for the virtual element method. Numer. Math. **137**(4), 857–893 (2017)
21. O. Čertík, F. Gardini, G. Manzini, L. Mascotto, G. Vacca, The p- and hp-versions of the virtual element method for elliptic eigenvalue problems. Comput. Math. Appl. **79**(7), 2035–2056 (2020)
22. P.G. Ciarlet, *The Finite Element Method for Elliptic Problems*, vol. 4 (North-Holland Publishing Co., Amsterdam, 1978). Studies in Mathematics and its Applications
23. M. Dauge, Benchmark computations for maxwell equations for the approximation of highly singular solutions (2004). http://perso.univ-rennes1.fr/monique.dauge/benchmax.html

24. J. Descloux, N. Nassif, J. Rappaz, On spectral approximation. I. The problem of convergence. RAIRO Anal. Numér., **12**(2), 97–112, iii (1978)
25. J. Descloux, N. Nassif, J. Rappaz, On spectral approximation. II. Error estimates for the Galerkin method. RAIRO Anal. Numér. **12**(2), 113–119, iii (1978)
26. F. Gardini, G. Vacca, Virtual element method for second-order elliptic eigenvalue problems. IMA J. Numer. Anal. **38**(4), 2026–2054 (2018)
27. F. Gardini, G. Manzini, G. Vacca, The nonconforming virtual element method for eigenvalue problems. ESAIM Math. Model. Numer. Anal. **53**(3), 749–774 (2019)
28. P. Grisvard, *Elliptic Problems in Nonsmooth Domains*, vol. 69. Classics in Applied Mathematics (Society for Industrial and Applied Mathematics (SIAM), Philadelphia, 2011)
29. T. Kato, *Perturbation Theory for Linear Operators*. Classics in Mathematics (Springer, Berlin, 1995). Reprint of the 1980 edition
30. J. Meng, Y. Zhang, L. Mei, A virtual element method for the Laplacian eigenvalue problem in mixed form. Appl. Numer. Math. **156**, 1–13 (2020)
31. D. Mora, G. Rivera, *A priori* and *a posteriori* error estimates for a virtual element spectral analysis for the elasticity equations. IMA J. Numer. Anal. **40**(1), 322–357 (2020)
32. D. Mora, G. Rivera, R. Rodríguez, A virtual element method for the Steklov eigenvalue problem. Math. Models Methods Appl. Sci. **25**(8), 1421–1445 (2015)
33. D. Mora, I. Velásquez, A virtual element method for the transmission eigenvalue problem. Math. Models Methods Appl. Sci. **28**(14), 2803–2831 (2018)
34. D. Mora, I. Velásquez, Virtual element for the buckling problem of Kirchhoff-Love plates. Comput. Methods Appl. Mech. Eng. **360**, 112687, 22 (2020)
35. D. Mora, G. Rivera, I. Velásquez, A virtual element method for the vibration problem of Kirchhoff plates. ESAIM Math. Model. Numer. Anal. **52**(4), 1437–1456 (2018)
36. P.-A. Raviart, J.-M. Thomas, *Introduction à l'analyse numérique des équations aux dérivées partielles*. Collection Mathématiques Appliquées pour la Maîtrise. [Collection of Applied Mathematics for the Master's Degree] (Masson, Paris, 1983)

Chapter 8
Virtual Element Methods for a Stream-Function Formulation of the Oseen Equations

David Mora and Alberth Silgado

Abstract The aim of this work is to analyze virtual element methods to solve the Oseen equations in terms of the stream-function on simply connected polygonal domains. The methods are based on a C^1-conforming discretization of arbitrary order $k \geq 2$. Under standard assumptions on the computational domain, we establish that the resulting schemes converge with an optimal order in $H^2(\Omega)$. The proposed methods have the advantages of using general polygonal meshes and the possibility to compute further variables of interest, such as the velocity, the vorticity and the pressure. Finally, we report some numerical test illustrating the behavior of the virtual schemes and supporting our theoretical results on different families of polygonal meshes.

8.1 Introduction

The numerical solution of the time-dependent Navier-Stokes equations is still a great challenge of computational fluid dynamics. Using time discretization and linearization, the generalized Oseen problem arises as an important subproblem. Different formulations and discretizations have been proposed and analyzed in the last years for the Oseen equations; see for instance [2, 6, 10–12, 21, 25, 28, 33, 34, 39] and the references therein.

The aim of the present work is to introduce and analyze conforming virtual element methods (VEM) to solve the Oseen equations on polygonal simply connected domains, formulated in terms of the stream-function of the velocity field. We

D. Mora (✉)
GIMNAP, Departamento de Matemática, Universidad del Bío-Bío, Concepción, Chile

CI2MA, Universidad de Concepción, Concepción, Chile
e-mail: dmora@ubiobio.cl

A. Silgado
GIMNAP, Departamento de Matemática, Universidad del Bío-Bío, Concepción, Chile
e-mail: alberth.silgado1701@alumnos.ubiobio.cl

observe that it corresponds to a fourth order PDE. Thus, a conforming discretization requires globally C^1 continuity. Among the important advantages of VEM, in this work, we will exploit the possibility of easily implement global discrete spaces of $H^2(\Omega)$ (see [24, 36]) to solve the Oseen problem.

The VEM introduced in [13] is a recent generalization of the finite element method that allows to use general polygonal/polyhedral meshes. The method has been applied successfully in a large range of problems in fluid mechanics; see for instance [8, 16, 17, 19, 26, 27, 29, 35, 37, 40, 42, 44, 45, 48, 49], where Stokes, Brinkman, Stokes–Darcy, Navier-Stokes and Boussinesq equations have been recently developed.

Recently in [47], it has been presented a C^1 VEM method for the Brinkman problem written in terms of the stream-function. In this work, we will extend these results to the generalized Oseen problem, where an additional term is presented in the momentum equation. There are several advantages of utilizing the stream-function formulation for fluid flow problems: there is only one scalar variable, the incompressible condition is satisfied automatically, the stream-function is one of the most useful tools in flow visualization. Moreover, further variables of interest, such as the velocity, the fluid vorticity and the pressure, can be easily obtained from the VEM discrete stream-function. In fact, we will show that we compute the velocity by a simple postprocess and we recover the fluid pressure by solving a primal formulation of a second order elliptic problem with right hand side coming from the discrete stream-function (see [43, 47]). We note that there are other procedures to recover fluid pressure. For instance, in [32] has been presented an algorithm for pressure recovery which is based on a mixed finite element discretization with inf-sup stable pairs. In addition, we will propose a novel strategy to recover the fluid vorticity, which is key in several applications [5, 20, 38], from the virtual element stream-function solution with the help of a proper polynomial projector.

This paper is concerned with a non-symmetric VEM discretization of arbitrary order $k \geq 2$ for the Oseen equations formulated in terms of the stream-function, which will be analysed using the Lax-Milgram Theorem and we will show well-posedness provided a CFL type condition is satisfied (cf. (8.33)). Under standard assumptions on the polygonal meshes, we establish optimal order error estimates in $H^2(\Omega)$. Moreover, we show that velocity, vorticity and pressure can be recovered (cf. Sect. 8.5). We also derive error estimates for these fields. In particular, under the assumptions that the family of polygonal meshes is quasi-uniform and that the continuous solutions are sufficiently smooth (pressure and stream-function), we write an error estimate in $H^1(\Omega)$ for the fluid pressure. In summary, the advantages of the proposed VEM methods are: the use of general polygonal meshes and the possibility to recover further variables of interest for fluid flow problems.

The rest of the paper is organized as follows: In Sect. 8.2, we introduce the variational formulation of the Oseen problem in terms of the stream-function. We prove existence and uniqueness of this formulation by using the Lax-Milgram Theorem. In Sect. 8.3, we present the virtual element discretization of arbitrary order $k \geq 2$. We also prove the existence and uniqueness of the discrete formulation. In Sect. 8.4, we obtain error estimates for the stream-function in $H^2(\Omega)$. In Sect. 8.5,

we recover other important variables for fluid flow problems from the discrete stream-function, such as the velocity $\mathbf{u}$, the fluid vorticity ω and the fluid pressure p. In Sect. 8.6, we report a set of numerical examples which allows us to assess the performance of the proposed method.

Throughout the paper, we will follow the usual notation for Sobolev spaces and norms [1]. We will denote a simply connected polygonal Lipschitz bounded domain of $\mathbb{R}^2$ by Ω and $\mathbf{n} = (n_i)_{1 \leq i \leq 2}$ is the outward unit normal vector to the boundary $\partial\Omega$. For $\mathscr{D}$ an open bounded domain, the $L^2(\mathscr{D})$ inner product will be denoted by $(\cdot, \cdot)_{0,\mathscr{D}}$. Moreover, c and C, with or without subscripts, tildes, or hats, will represent a generic constant independent of the mesh parameter h, assuming different values in different occurrences.

8.2 Model Problem

Let $\Omega \subset \mathbb{R}^2$ be a simply connected polygonal domain with boundary $\Gamma := \partial\Omega$. The incompressible Oseen equations are given by the following set of equations and boundary condition:

$$
\begin{aligned}
-\nu\Delta\mathbf{u} + (\nabla\mathbf{u})\boldsymbol{\beta} + \gamma\mathbf{u} + \nabla p &= \mathbf{f} &&\text{in}\quad \Omega, \\
\operatorname{div}\mathbf{u} &= 0 &&\text{in}\quad \Omega, \\
\mathbf{u} &= \mathbf{0} &&\text{on}\quad \Gamma, \\
(p, 1)_{0,\Omega} &= 0,
\end{aligned}
\tag{8.1}
$$

where $\mathbf{u} : \Omega \to \mathbb{R}^2$ is the velocity field, $p : \Omega \to \mathbb{R}$ is the pressure field, $\mathbf{f} : \Omega \to \mathbb{R}^2$ is the external body force, $\nu > 0$ the kinematic viscosity, $\boldsymbol{\beta} \in W^{1,\infty}(\Omega)^2$ with $\operatorname{div}\boldsymbol{\beta} = 0$ a given convective velocity field, and $\gamma \in L^{\infty}(\Omega)$ a given scalar function, respectively. We assume that there exists γ_0 such that $\gamma(\mathbf{x}) \geq \gamma_0 > 0$ for almost all $\mathbf{x} \in \Omega$.

The standard velocity-pressure variational formulation of the Oseen problem reads as follows: find $(\mathbf{u}, p) \in H_0^1(\Omega)^2 \times L_0^2(\Omega)$, such that

$$
\nu\int_{\Omega}\nabla\mathbf{u} : \nabla\mathbf{v} + \int_{\Omega}(\nabla\mathbf{u})\boldsymbol{\beta}\cdot\mathbf{v} + \int_{\Omega}\gamma\mathbf{u}\cdot\mathbf{v} - \int_{\Omega}p\operatorname{div}\mathbf{v} = \int_{\Omega}\mathbf{f}\cdot\mathbf{v} \quad \forall\mathbf{v}\in H_0^1(\Omega)^2,
$$

$$
\int_{\Omega}q\operatorname{div}\mathbf{u} = 0 \qquad \forall q \in L_0^2(\Omega),
$$

where $L_0^2(\Omega) := \left\{q \in L^2(\Omega) : (q, 1)_{0,\Omega} = 0\right\}$.

Let us introduce the space of divergence-free functions

$$
\mathbf{V} := \left\{\mathbf{v} \in H_0^1(\Omega)^2 : \operatorname{div}\mathbf{v} = 0\right\}.
$$

Since Ω is a simply connected domain, a well known result states that a vector function $\mathbf{v} \in \mathbf{V}$ if and only if there exists a scalar function $\varphi \in H^2(\Omega)$, which is called *stream-function*, such that

$$\mathbf{v} = \mathbf{curl}\,\varphi \in H_0^1(\Omega)^2.$$

The function φ is defined up to a constant (see [41]). Thus, we consider the following space

$$X := \left\{ \varphi \in H^2(\Omega) : \varphi = \partial_{\mathbf{n}}\varphi = 0 \quad \text{on} \quad \Gamma \right\},$$

where $\partial_{\mathbf{n}}$ denotes the normal derivative. We endow X with the norm

$$\|\varphi\|_X := |\varphi|_{2,\Omega} \qquad \forall \varphi \in X.$$

Then, choosing $\psi \in X$ the *stream-function* of the velocity field $\mathbf{u} \in \mathbf{V}$ (i.e. $\mathbf{u} = \mathbf{curl}\,\psi$), we write the following equivalent weak formulation of the Oseen problem: find $\psi \in X$ such that

$$\nu \int_\Omega \mathrm{D}^2\psi : \mathrm{D}^2\phi + \int_\Omega (\nabla\mathbf{curl}\,\psi)\boldsymbol{\beta}\cdot\mathbf{curl}\phi + \int_\Omega \gamma\,\mathbf{curl}\,\psi\cdot\mathbf{curl}\phi = \int_\Omega \mathbf{f}\cdot\mathbf{curl}\phi \quad \forall\phi \in X,$$

where ":" denotes the usual scalar product of 2×2-matrices and $\mathrm{D}^2\phi := (\partial_{ij}\phi)_{1\leq i,j\leq 2}$ denotes the Hessian matrix of ϕ. We rewrite this variational problem as follows: find $\psi \in X$ such that

$$\mathscr{O}(\psi,\phi) := \nu A(\psi,\phi) + B(\psi,\phi) + C(\psi,\phi) = F(\phi) \qquad \forall\phi \in X, \tag{8.2}$$

where $A : X \times X \to \mathbb{R}$, $B : X \times X \to \mathbb{R}$ and $C : X \times X \to \mathbb{R}$ are the bilinear forms and $F : X \to \mathbb{R}$ is a linear functional, defined as follows:

$$A(\psi,\phi) := \int_\Omega \mathrm{D}^2\psi : \mathrm{D}^2\phi, \quad \forall\psi,\phi \in X, \tag{8.3}$$

$$B(\psi,\phi) := \int_\Omega (\nabla\mathbf{curl}\,\psi)\boldsymbol{\beta}\cdot\mathbf{curl}\,\phi \quad \forall\psi,\phi \in X, \tag{8.4}$$

$$C(\psi,\phi) := \int_\Omega \gamma\,\mathbf{curl}\,\psi\cdot\mathbf{curl}\,\phi \quad \forall\psi,\phi \in X, \tag{8.5}$$

$$F(\phi) := \int_\Omega \mathbf{f}\cdot\mathbf{curl}\,\phi \quad \forall\phi \in X. \tag{8.6}$$

The following lemma establishes some properties for the bilinear forms and the linear functional previously defined.

Lemma 8.1 *There exist positive constants $C_{\boldsymbol{\beta}}$ and C_γ such that the forms defined in* (8.3)–(8.6) *satisfy the following properties:*

$$
\begin{aligned}
|A(\varphi, \phi)| &\leq \|\varphi\|_X \|\phi\|_X & \forall \varphi, \phi \in X, \\
A(\phi, \phi) &\geq \|\phi\|_X^2 & \forall \phi \in X, \\
|B(\varphi, \phi)| &\leq C_{\boldsymbol{\beta}} \|\varphi\|_X \|\phi\|_X & \forall \varphi, \phi \in X, \\
|C(\varphi, \phi)| &\leq C_\gamma \|\varphi\|_X \|\phi\|_X & \forall \varphi, \phi \in X, \\
C(\phi, \phi) &\geq \gamma_0 |\phi|_{1,\Omega}^2 & \forall \phi \in X, \\
|F(\phi)| &\leq \|F\|_{-2,\Omega} \|\phi\|_X & \forall \phi \in X.
\end{aligned}
$$

As a consequence of Lemma 8.1, the fact that div $\boldsymbol{\beta} = 0$, and the Lax-Milgram Theorem, we state the solvability of the continuous problem (8.2).

Theorem 8.1 *There exists a unique $\psi \in X$ solution to problem* (8.2)*, which satisfies the following continuous dependence on the data*

$$
\|\psi\|_X \leq C \|F\|_{-2,\Omega},
$$

where C is a positive constant.

Remark 8.1 In this work, we will require an additional regularity for the unique solution of problem (8.2). More precisely, in what follows we assume that there exists $s > 1/2$ such that $\psi \in H^{2+s}(\Omega)$. This additional regularity will play an important role in the error analysis (cf. Sects. 8.4 and 8.5).

The goal of this paper is to propose a conforming C^1-VEM of arbitrary order to solve problem (8.2) and to prove that the method is optimally convergent. In addition, we will propose simple post-processes from the discrete stream-function to recover the velocity, pressure and vorticity fields.

8.3   Virtual Element Methods

In this section, we will write C^1-virtual element discretizations for the numerical approximation of problem (8.2). We start by introducing some notations and assumptions to construct a discrete virtual subspace X_h^k, for arbitrary order $k \geq 2$ and to write the discrete bilinear forms and the discrete linear functional to propose the discrete scheme.

Let $\{\Omega_h\}_{h>0}$ be a sequence of decompositions of Ω into general polygonal elements K. Let h_K denote the diameter of the element K and h the maximum of the diameters of all the elements of the mesh, i.e., $h := \max_{K \in \Omega_h} h_K$. In what follows, we denote by N_K the number of vertices of K, by $\mathbf{v}_i$ a generic vertex of K,

with $i \in \{1, \ldots, N_K\}$ and by e a generic edge of Ω_h. In addition for all e, we denote by h_e the length of edge and we define a unit normal vector $\mathbf{n}_K^e$ that points outside of K. Moreover, we denote by x_e and $\mathbf{x}_K$ the midpoint of e and the baricenter of K, respectively.

For the theoretical analysis, we will consider the following assumptions: there exists a real number $C_{\Omega_h} > 0$ such that, for every h and every $K \in \Omega_h$,

A1 : the ratio between the shortest edge and the diameter h_K of K is larger than C_{Ω_h};

A2 : K is star-shaped with respect to every point of a ball of radius $C_{\Omega_h} h_K$.

8.3.1 Virtual Spaces and Polynomial Projections Operator

We will denote by $\mathbb{P}_\ell(\mathscr{D})$ the space of polynomial functions defined locally in $\mathscr{D}$ and being of total degree $\leq \ell$ and by $\mathbb{M}_\ell^*(K)$ the set of scaled monomials defined on each polygon K:

$$\mathbb{M}_\ell^*(K) := \left\{ \left(\frac{\mathbf{x} - \mathbf{x}_K}{h_K} \right)^{\boldsymbol{a}} : |\boldsymbol{a}| = \ell \right\}, \tag{8.7}$$

where for a non-negative multi-index $\boldsymbol{a} = (a_1, a_2)$, we set $|\boldsymbol{a}| := a_1 + a_2$ and $\mathbf{x}^{\boldsymbol{a}} = x_1^{a_1} x_2^{a_2}$, with $\mathbf{x} = (x_1, x_2)$. Now, we define $\mathbb{M}_k(K) := \bigcup_{\ell \leq k} \mathbb{M}_\ell^*(K) =: \{m_j\}_{j=1}^{d_k}$ as a basis of $\mathbb{P}_k(K)$, where $d_k = \dim(\mathbb{P}_k(K))$. Moreover we consider the set of the scaled monomials defined on each edge e:

$$\mathbb{M}_\ell(e) := \left\{ 1, \frac{x - x_e}{h_e}, \left(\frac{x - x_e}{h_e} \right)^2, \ldots, \left(\frac{x - x_e}{h_e} \right)^\ell \right\}.$$

Now, for any integer $k \geq 2$ and for every polygon $K \in \Omega_h$, we introduce the following preliminary local virtual space:

$$\widetilde{X}_h^k(K) := \Big\{ \phi_h \in H^2(K) : \Delta^2 \phi_h \in \mathbb{P}_{k-2}(K), \phi_h|_{\partial K} \in C^0(\partial K), \phi_h|_e \in \mathbb{P}_r(e) \; \forall e \in \partial K,$$

$$\nabla \phi_h|_{\partial K} \in C^0(\partial K)^2, \partial_{\mathbf{n}_K^e} \phi_h|_e \in \mathbb{P}_\alpha(e) \; \forall e \in \partial K \Big\},$$

where $r := \max\{3, k\}$ and $\alpha := k - 1$.

Next, for a given $\phi_h \in \widetilde{X}_h^k(K)$, we introduce the following sets of linear operators from the local virtual space $\widetilde{X}_h^k(K)$ into $\mathbb{R}$:

– **D$_1$** : contains linear operators evaluating ϕ_h at the N_K vertices of K;
– **D$_2$** : contains linear operators evaluating $h_{\mathbf{v}_i} \nabla \phi_h$ at the N_K vertices of K;
– **D$_3$** : for $r > 3$, the moments $\dfrac{1}{h_e} \displaystyle\int_e q(\zeta) \phi_h(\zeta) \, d\zeta \quad \forall q \in \mathbb{M}_{r-4}(e), \quad \forall \text{edge } e$;

- **D$_4$** : for $\alpha > 1$, the moments $\int_e q(\zeta) \partial_{\mathbf{n}_K^e} \phi_h(\zeta)\, d\zeta \quad \forall q \in \mathbb{M}_{\alpha-2}(e), \quad \forall$ edge e;

- **D$_5$** : for $k \geq 4$, the moments $\dfrac{1}{h_K^2} \int_K q(\mathbf{x}) \phi_h(\mathbf{x})\, d\mathbf{x} \quad \forall q \in \mathbb{M}_{k-4}(K), \quad \forall$ polygon K,

where $h_{\mathbf{v}_i}$ corresponds to the average of the diameters corresponding to the elements with $\mathbf{v}_i$ as a vertex.

Now, we decompose into local contributions the bilinear forms $A(\cdot, \cdot)$, $B(\cdot, \cdot)$ and $C(\cdot, \cdot)$:

$$A(\varphi, \phi) = \sum_{K \in \Omega_h} A^K(\varphi, \phi) := \sum_{K \in \Omega_h} \int_K \mathrm{D}^2 \varphi : \mathrm{D}^2 \phi \qquad \forall \varphi, \phi \in X,$$

$$B(\varphi, \phi) = \sum_{K \in \Omega_h} B^K(\varphi, \phi) := \sum_{K \in \Omega_h} \int_K (\nabla \mathbf{curl}\, \varphi) \boldsymbol{\beta} \cdot \mathbf{curl}\, \phi \qquad \forall \varphi, \phi \in X,$$

$$C(\varphi, \phi) = \sum_{K \in \Omega_h} C^K(\varphi, \phi) = \sum_{K \in \Omega_h} \int_K \gamma\, \mathbf{curl}\, \varphi \cdot \mathbf{curl}\, \phi, \qquad \forall \varphi, \phi \in X.$$

In what follows, we are going to build discrete version of the local bilinear forms. With this aim, for each polygon K, we define the following projector:

$$\Pi_K^{k,\mathrm{D}} : \widetilde{X}_h^k(K) \longrightarrow \mathbb{P}_k(K) \subseteq \widetilde{X}_h^k(K),$$

$$\phi_h \longmapsto \Pi_K^{k,\mathrm{D}} \phi_h,$$

where $\Pi_K^{k,\mathrm{D}} \phi_h$ is the solution of the local problems:

$$A^K(\Pi_K^{k,\mathrm{D}} \phi_h, q) = A^K(\phi_h, q) \quad \forall q \in \mathbb{P}_k(K),$$

$$\widehat{\Pi_K^{k,\mathrm{D}} \phi_h} = \widehat{\phi_h}, \quad \widehat{\nabla \Pi_K^{k,\mathrm{D}} \phi_h} = \widehat{\nabla \phi_h},$$

with $\widehat{(\cdot)}$ is defined as follows:

$$\widehat{\varphi_h} := \frac{1}{N_K} \sum_{i=1}^{N_K} \varphi_h(\mathbf{v}_i) \qquad \forall \varphi_h \in C^0(\partial K), \tag{8.8}$$

and $\mathbf{v}_i$, $1 \leq i \leq N_K$, are the vertices of K.

The following result establishes that the projector $\Pi_K^{k,\mathrm{D}}$ is fully computable using the sets **D$_1$** $-$ **D$_5$** (see [36]).

Lemma 8.2 *The operator* $\Pi_K^{k,\mathrm{D}} : \widetilde{X}_h^k(K) \to \mathbb{P}_k(K)$ *is explicitly computable for every* $\phi_h \in \widetilde{X}_h^k(K)$, *using only the information of the linear operators* $\mathbf{D_1} - \mathbf{D_5}$.

For each $K \in \Omega_h$ our local virtual space is given by:

$$X_h^k(K) := \left\{ \phi_h \in \widetilde{X}_h^k(K) : \int_K q^* \, \Pi_K^{k,\mathrm{D}}\phi_h = \int_K q^* \, \phi_h, \quad \forall q^* \in \mathbb{M}_{k-3}^*(K) \cup \mathbb{M}_{k-2}^*(K) \right\},$$

$$(8.9)$$

where $\mathbb{M}_{k-3}^*(K)$ and $\mathbb{M}_{k-2}^*(K)$ are scaled monomials of degree $k-3$ and $k-2$, respectively (see (8.7)), with the convention that $\mathbb{M}_{-1}^*(K) = \emptyset$ (for further details, see [36]).

It is easy to observe that $\mathbb{P}_k(K) \subseteq X_h^k(K) \subseteq \widetilde{X}_h^k(K)$. Moreover, the sets of linear operators $\mathbf{D_1} - \mathbf{D_5}$ constitutes a set of degrees of freedom for $X_h^k(K)$ (see [36]). Additionally, we note that the condition appearing in the definition of the local space $X_h^k(K)$ will be useful to construct an L^2-projection which will be employed to build the discrete bilinear forms. In fact, we consider the $L^2(K)$-projection onto $\mathbb{P}_{k-2}(K)$. For each $\phi \in L^2(K)$, $\Pi_K^{k-2}\phi \in \mathbb{P}_{k-2}(K)$ satisfies

$$\int_K q\phi = \int_K q(\Pi_K^{k-2}\phi) \qquad \forall q \in \mathbb{P}_{k-2}(K).$$

The following lemma establishes that Π_K^{k-2} is computable on $X_h^k(K)$. The proof follows from the definition of the local virtual space and the set of degrees of freedom.

Lemma 8.3 *The operator* $\Pi_K^{k-2} : X_h^k(K) \to \mathbb{P}_{k-2}(K)$ *is explicitly computable for each* $\phi_h \in X_h^k(K)$, *using only the information of the degrees of freedom* $\mathbf{D_1} - \mathbf{D_5}$.

Now, for $k \geq 2$, we will consider the following projection onto the polynomial space $\mathbb{P}_{k-1}(K)^2$: we define $\mathbf{\Pi}_K^{k-1} : L^2(K)^2 \to \mathbb{P}_{k-1}(K)^2$, for each $\mathbf{v} \in L^2(K)^2$ by

$$\int_K \mathbf{q} \cdot \mathbf{v} = \int_K \mathbf{q} \cdot \mathbf{\Pi}_K^{k-1}\mathbf{v} \quad \forall \mathbf{q} \in \mathbb{P}_{k-1}(K)^2. \tag{8.10}$$

Using integration by parts, it is easy to see that for any $\phi_h \in X_h^k(K)$, the vector function $\mathbf{\Pi}_K^{k-1}\mathbf{curl}\,\phi_h \in \mathbb{P}_{k-1}(K)^2$ can be explicitly computed from the degrees of freedom $\mathbf{D_1} - \mathbf{D_5}$ (see [47]).

Now, we will establish a stability property of the projector $\mathbf{\Pi}_K^{k-1}$. We will use the following inverse inequality for polynomials on polygons, which holds true under assumption **A2** (see [15, Remark 6.1]).

Lemma 8.4 *If the assumption* **A2** *is satisfied, then there exists* $\widetilde{C} > 0$, *independent of h, such that*

$$|q|_{1,K} \leq \widetilde{C} h_K^{-1} \|q\|_{0,K} \quad \forall q \in \mathbb{P}_\ell(K), \quad \ell \geq 0.$$

Thus, using Lemma 8.4 the projector $\mathbf{\Pi}_K^{k-1}$ satisfies the following stability property: let $K \in \Omega_h$, then for each $\phi_h \in X_h^k(K)$, there exists $C_N > 0$, independent of K and h, such that

$$|\mathbf{\Pi}_K^{k-1}\mathbf{curl}\,\phi_h|_{1,K} \leq C_N|\phi_h|_{2,K}. \tag{8.11}$$

Now, for $k \geq 2$, we introduce an additional projector which will be used to write the virtual scheme; we define $\Pi_K^{k,\nabla^\perp} : X_h^k(K) \longrightarrow \mathbb{P}_k(K) \subseteq X_h^k(K)$ for each $\phi_h \in X_h^k(K)$ as the solution of the following local problem:

$$\int_K \mathbf{curl}\,\Pi_K^{k,\nabla^\perp}\phi_h \cdot \mathbf{curl}\,q = \int_K \mathbf{curl}\,\phi_h \cdot \mathbf{curl}\,q \qquad \forall q \in \mathbb{P}_k(K),$$

$$\widehat{\Pi_K^{k,\nabla^\perp}\phi_h} = \widehat{\phi_h},$$

where $\widehat{(\cdot)}$ has been defined in (8.8). The following result states that this operator is fully computable using the sets $\mathbf{D_1} - \mathbf{D_5}$ (see [47, Lemma 3.4]).

Lemma 8.5 *The operator* $\Pi_K^{k,\nabla^\perp} : X_h^k(K) \to \mathbb{P}_k(K) \subseteq X_h^k(K)$ *is explicitly computable for each* $\phi_h \in X_h^k(K)$, *using only the information of the set of degrees of freedom* $\mathbf{D_1} - \mathbf{D_5}$.

Now, we introduce the global virtual space to approximate the solution of problem (8.2). For every decomposition Ω_h of Ω into polygons K, we define

$$X_h^k := \left\{\phi_h \in X : \phi_h|_K \in X_h^k(K)\right\}.$$

8.3.2 Construction of the Local and Global Discrete Forms

In this section, we will construct the discrete version of the continuous local bilinear forms and the right hand side, using the projection operators introduced in Sect. 8.3.1.

First, let $\mathscr{S}_D^K(\cdot, \cdot)$ and $\mathscr{S}_{\mathbf{curl}}^K(\cdot, \cdot)$ be any symmetric positive definite bilinear forms to be chosen as to satisfy:

$$c_0 A^K(\phi_h, \phi_h) \leq \mathscr{S}_D^K(\phi_h, \phi_h) \leq c_1 A^K(\phi_h, \phi_h) \quad \forall \phi_h \in X_h^k(K),\ \text{with}\ \ \Pi_K^{k,D}\phi_h = 0,$$

$$c_2 C^K(\phi_h, \phi_h) \leq \mathscr{S}_{\mathbf{curl}}^K(\phi_h, \phi_h) \leq c_3 C^K(\phi_h, \phi_h)\ \ \forall \phi_h \in X_h^k(K),\ \text{with}\ \Pi_K^{k,\nabla^\perp}\phi_h = 0,$$

$$\tag{8.12}$$

with c_0, c_1, c_2 and c_3 positive constants independent of h and K. We will introduce bilinear forms $\mathscr{S}_D^K(\cdot, \cdot)$ and $\mathscr{S}_{\mathbf{curl}}^K(\cdot, \cdot)$ satisfying (8.12) in Sect. 8.6.

For all $\psi_h, \phi_h \in X_h^k(K)$ we now define the local discrete bilinear forms

$$A^{h,K}(\psi_h, \phi_h) := A^K\left(\Pi_K^{k,D}\psi_h, \Pi_K^{k,D}\phi_h\right) + \mathscr{S}_D^K\left(\psi_h - \Pi_K^{k,D}\psi_h, \phi_h - \Pi_K^{k,D}\phi_h\right),$$

(8.13)

$$B^{h,K}(\psi_h, \phi_h) := \int_K \left(\nabla\Pi_K^{k-1}\mathbf{curl}\,\psi_h\right)\boldsymbol{\beta}\cdot\Pi_K^{k-1}\mathbf{curl}\,\phi_h,$$

(8.14)

$$C^{h,K}(\psi_h, \phi_h) := \int_K \gamma\,\Pi_K^{k-1}\mathbf{curl}\,\psi_h\cdot\Pi_K^{k-1}\mathbf{curl}\,\phi_h$$

(8.15)

$$+ \mathscr{S}_{\mathbf{curl}}^K\left(\psi_h - \Pi_K^{k,\nabla^\perp}\psi_h, \phi_h - \Pi_K^{k,\nabla^\perp}\phi_h\right).$$

Next, for all $\psi_h, \phi_h \in X_h^k$, we define the global discrete bilinear form as follows:

$$A^h : X_h^k \times X_h^k \to \mathbb{R}, \quad A^h(\psi_h, \phi_h) := \sum_{K\in\Omega_h} A^{h,K}(\psi_h, \phi_h),$$

(8.16)

$$B^h : X_h^k \times X_h^k \to \mathbb{R}, \quad B^h(\psi_h, \phi_h) := \sum_{K\in\Omega_h} B^{h,K}(\psi_h, \phi_h),$$

(8.17)

$$C^h : X_h^k \times X_h^k \to \mathbb{R}, \quad C^h(\psi_h, \phi_h) := \sum_{K\in\Omega_h} C^{h,K}(\psi_h, \phi_h).$$

(8.18)

We note that the bilinear form $B^h(\cdot, \cdot)$ is immediately extendable to the continuous space X.

The following result establishes the usual consistency and stability properties for the discrete local forms $A^{h,K}(\cdot, \cdot)$ and $C^{h,K}(\cdot, \cdot)$. The proof follows standard arguments in the VEM literature (see [9, 13, 14]). We omit further details.

Proposition 8.1 *The local bilinear form $A^{h,K}(\cdot, \cdot)$, $C^{h,K}(\cdot, \cdot)$ defined in* (8.13) *and* (8.15) *respectively, on each element K satisfy*

– *Consistency: for all $h > 0$ and for all $K \in \Omega_h$, we have that*

$$A^{h,K}(q, \phi_h) = A^K(q, \phi_h) \qquad \forall q \in \mathbb{P}_k(K), \qquad \forall\phi_h \in X_h^k(K).$$ (8.19)

– *Stability and boundedness: There exist positive constants $\alpha_i, i = 0, 1, 2, 3$ independent of K, such that:*

$$\alpha_0 A^K(\phi_h, \phi_h) \le A^{h,K}(\phi_h, \phi_h) \le \alpha_1 A^K(\phi_h, \phi_h) \qquad \forall\phi_h \in X_h^k(K),$$ (8.20)

$$\alpha_2 C^K(\phi_h, \phi_h) \le C^{h,K}(\phi_h, \phi_h) \le \alpha_3 C^K(\phi_h, \phi_h) \qquad \forall\phi_h \in X_h^k(K).$$ (8.21)

The next step consists in constructing a computable approximation of the linear functional defined in (8.6). With this aim, we define, for each element K, the

following computable term:

$$F^{h,K}(\phi_h) := \int_K \mathbf{\Pi}_K^{k-1}\mathbf{f} \cdot \mathbf{curl}\,\phi_h \equiv \int_K \mathbf{f} \cdot \mathbf{\Pi}_K^{k-1}\mathbf{curl}\,\phi_h \qquad \forall \phi_h \in X_h^k(K).$$

Thus, we consider the following approximation of the functional defined in (8.6):

$$F^h(\phi_h) := \sum_{K \in \Omega_h} F^{h,K}(\phi_h) \qquad \forall \phi_h \in X_h^k. \tag{8.22}$$

The following lemma establishes some properties for the discrete forms defined in (8.16), (8.17), (8.18), and (8.22).

Lemma 8.6 *There exist positive constants C_{A^h}, C_{B^h}, C_2 and C_{F^h}, independent of h, such that the forms defined in (8.16)–(8.22) satisfy the following properties:*

$$|A^h(\psi_h, \phi_h)| \le C_{A^h} \|\psi_h\|_X \|\phi_h\|_X \qquad \forall \psi_h, \phi_h \in X_h^k, \tag{8.23}$$

$$A^h(\phi_h, \phi_h) \ge \alpha_0 \|\phi_h\|_X^2 \qquad \forall \phi_h \in X_h^k, \tag{8.24}$$

$$|B^h(\psi_h, \phi_h)| \le C_{B^h} \|\psi_h\|_X \|\phi_h\|_X \qquad \forall \psi_h, \phi_h \in X_h^k, \tag{8.25}$$

$$|C^h(\psi_h, \phi_h)| \le C_2 \|\psi_h\|_X \|\phi_h\|_X \qquad \forall \psi_h, \phi_h \in X_h^k, \tag{8.26}$$

$$C^h(\phi_h, \phi_h) \ge \alpha_2 \gamma_0 |\phi_h|_{1,\Omega}^2 \qquad \forall \psi_h, \phi_h \in X_h^k, \tag{8.27}$$

$$|F^h(\phi_h)| \le C_{F^h} \|\mathbf{f}\|_{0,\Omega} \|\phi_h\|_X \qquad \forall \phi_h \in X_h^k. \tag{8.28}$$

Proof The proof of these properties follow standard arguments in the VEM literature (see [9, 13, 14]). Nevertheless, we will prove the property (8.25). Indeed, let $\psi_h, \phi_h \in X_h^k$, then using the definition of the bilinear form $B^h(\cdot, \cdot)$ and the Cauchy-Schwarz inequality, we have that

$$
\begin{aligned}
|B^h(\psi_h, \phi_h)| &\le \sum_{K \in \Omega_h} \left| \int_K \left(\nabla \mathbf{\Pi}_K^{k-1}\mathbf{curl}\,\psi_h \right) \boldsymbol{\beta} \cdot \mathbf{\Pi}_K^{k-1}\mathbf{curl}\,\phi_h \right| \\
&\le \sum_{K \in \Omega_h} \|\boldsymbol{\beta}\|_{L^\infty(K)} \|\nabla \mathbf{\Pi}_K^{k-1}\mathbf{curl}\,\psi_h\|_{0,K} \|\mathbf{\Pi}_K^{k-1}\mathbf{curl}\,\phi_h\|_{0,K} \\
&\le \|\boldsymbol{\beta}\|_{L^\infty(\Omega)} \sum_{K \in \Omega_h} |\mathbf{\Pi}_K^{k-1}\mathbf{curl}\,\psi_h|_{1,K} \|\mathbf{curl}\,\phi_h\|_{0,K} \\
&\le C_N \|\boldsymbol{\beta}\|_{L^\infty(\Omega)} \sum_{K \in \Omega_h} |\psi_h|_{2,K} |\phi_h|_{1,K} \\
&\le C_N \|\boldsymbol{\beta}\|_{L^\infty(\Omega)} \|\psi_h\|_X |\phi_h|_{1,\Omega} \\
&\le C_N C_p \|\boldsymbol{\beta}\|_{L^\infty(\Omega)} \|\psi_h\|_X \|\phi_h\|_X,
\end{aligned}
\tag{8.29}
$$

where we have used the inequality (8.11) and $C_p > 0$ is the constant such that

$$|\phi_h|_{1,\Omega} \le C_p \|\phi_h\|_X,$$

which is independent of h and K, for all $K \in \Omega_h$. Then, taking $C_{B^h} := C_N C_p \|\boldsymbol{\beta}\|_{L^\infty(\Omega)} > 0$, we conclude the proof. $\qquad\qquad\qquad\qquad\qquad\qquad\qquad\qquad\qquad\qquad\qquad\square$

Remark 8.2 We observe that using the projector $\Pi_K^{k,\nabla^\perp}$, it is possible to construct alternative discrete bilinear forms in (8.14) and (8.15). More precisely, we can consider the following computable discrete forms:

$$\widetilde{B}^{h,K}(\psi_h, \phi_h) := \int_K \left(\nabla \mathbf{curl}\, \Pi_K^{k,\nabla^\perp} \psi_h \right) \boldsymbol{\beta} \cdot \mathbf{curl}\, \Pi_K^{k,\nabla^\perp} \phi_h, \qquad (8.30)$$

$$\widetilde{C}^{h,K}(\psi_h, \phi_h) := \int_K \gamma\, \mathbf{curl}\, \Pi_K^{k,\nabla^\perp} \psi_h \cdot \mathbf{curl}\, \Pi_K^{k,\nabla^\perp} \psi_h \qquad (8.31)$$

$$+ \mathscr{S}_{\mathbf{curl}}^K \left(\psi_h - \Pi_K^{k,\nabla^\perp} \psi_h, \phi_h - \Pi_K^{k,\nabla^\perp} \phi_h \right).$$

With these new forms, it is possible to write a different discrete formulation to solve the Oseen problem. We will test the discrete method derived with these forms in the numerical result section (see Sect. 8.6.3).

8.3.3 Discrete Formulation

Now we write the discrete formulation by using the discrete forms and employing the results of the previous sections we establish existence and uniqueness for our discrete scheme.

The virtual element discretization reads as follows: find $\psi_h \in X_h^k$ such that

$$\mathscr{O}^h(\psi_h, \phi_h) := \nu A^h(\psi_h, \phi_h) + B^h(\psi_h, \phi_h) + C^h(\psi_h, \phi_h) = F^h(\phi_h) \quad \forall \phi_h \in X_h^k. \tag{8.32}$$

The following result establishes that the bilinear form $\mathscr{O}^h(\cdot, \cdot)$ is elliptic.

Lemma 8.7 *Let C_N be the constant such that* (8.11) *holds true. Suppose that*

$$\frac{C_N^2 \|\boldsymbol{\beta}\|_{L^\infty(\Omega)}^2}{2\nu\gamma_0\alpha_0\alpha_2} < 1, \tag{8.33}$$

then there exists $\widehat{\alpha} > 0$, independent of h, such that

$$\mathscr{O}^h(\phi_h, \phi_h) \geq \widehat{\alpha} \|\phi_h\|_X^2 \qquad \forall \phi_h \in X_h^k.$$

Proof Let $\phi_h \in X_h^k$. Then, using (8.24), (8.27), and (8.29) we get

$$
\begin{aligned}
\mathscr{O}^h(\phi_h, \phi_h) &= \nu A^h(\phi_h, \phi_h) + B^h(\phi_h, \phi_h) + C^h(\phi_h, \phi_h) \\
&\geq \nu \alpha_0 \|\phi_h\|_X^2 - C_N \|\boldsymbol{\beta}\|_{L^\infty(\Omega)} \|\phi_h\|_X |\phi_h|_{1,\Omega} + \alpha_2 \gamma_0 |\phi_h|_{1,\Omega}^2 \\
&\geq \nu \alpha_0 \|\phi_h\|_X^2 - \frac{C_N^2 \|\boldsymbol{\beta}\|_{L^\infty(\Omega)}^2}{2\alpha_2 \gamma_0} \|\phi_h\|_X^2 - \frac{\alpha_2 \gamma_0}{2} |\phi_h|_{1,\Omega}^2 + \alpha_2 \gamma_0 |\phi_h|_{1,\Omega}^2 \\
&= \left(\nu \alpha_0 - \frac{C_N^2 \|\boldsymbol{\beta}\|_{L^\infty(\Omega)}^2}{2\alpha_2 \gamma_0} \right) \|\phi_h\|_X^2 + \frac{\alpha_2 \gamma_0}{2} |\phi_h|_{1,\Omega}^2 \\
&\geq \left(\nu \alpha_0 - \frac{C_N^2 \|\boldsymbol{\beta}\|_{L^\infty(\Omega)}^2}{2\alpha_2 \gamma_0} \right) \|\phi_h\|_X^2,
\end{aligned}
$$

where we have used the Young inequality. Then, taking $\widehat{\alpha} := \nu \alpha_0 - \dfrac{C_N^2 \|\boldsymbol{\beta}\|_{L^\infty(\Omega)}^2}{2\alpha_2 \gamma_0} > 0$, the proof is complete. $\qquad\square$

As a consequence of the previous lemma, we have the following result.

Theorem 8.2 *Suppose that (8.33) holds true. Then, there exists a unique $\psi_h \in X_h^k$ solution to problem (8.32) satisfying the following estimate*

$$\|\psi_h\|_X \leq C \|\mathbf{f}\|_{0,\Omega},$$

where C is a positive constant independent of h.

Remark 8.3 Assumption (8.33) holds provided one selects γ appropriately. For instance, when the Oseen system is derived as a time discretisation of Navier-Stokes equations, this parameter represents the inverse of the timestep. Thus, the aforementioned relation can be regarded as a CFL-type condition at a discrete level.

8.4 Error Analysis

In the present section, we develop an error analysis for the discrete virtual element scheme presented in Sect. 8.3. We start with some preliminary results.

8.4.1 Preliminary Results

We will use the following broken H^ℓ-seminorm, for each integer $\ell > 0$:

$$|\phi|_{\ell,h} := \left(\sum_{K \in \Omega_h} |\phi|_{\ell,K}^2 \right)^{1/2},$$

which is well defined for every $\phi \in L^2(\Omega)$ such that $\phi|_K \in H^\ell(K)$ for all $K \in \Omega_h$.

Next, we recall the estimate for the interpolant $\phi_I \in X_h^k$ of ϕ (see [9, 18]).

Proposition 8.2 *Assume that* **A1** *and* **A2** *are satisfied. Then, for each* $\phi \in H^\delta(\Omega)$, *there exist* $\phi_I \in X_h^k$ *and* $C > 0$, *independent of h, such that*

$$\|\phi - \phi_I\|_{m,\Omega} \le Ch^{\delta-m}|\phi|_{\delta,\Omega}, \quad m = 0, 1, 2, \quad 2 \le \delta \le k + 1, \quad k \ge 2.$$

Now, invoking the Scott-Dupont Theory (see [22]) for the polynomial approximation, we have

Proposition 8.3 *If the assumption* **A2** *is satisfied, then there exists a constant* $C > 0$, *such that for every* $\phi \in H^\delta(K)$, *there exists* $\phi_\pi \in \mathbb{P}_k(K)$, $k \ge 0$, *such that*

$$\|\phi - \phi_\pi\|_{m,K} \le Ch_K^{\delta-m}|\phi|_{\delta,K}, \quad 0 \le m \le \delta \le k + 1, \, \ell = 0, 1, \dots, [\delta],$$

where $[\delta]$ *denoting largest integer equal or smaller than* $\delta \in \mathbb{R}$.

We are going to use the following standard approximation property (see [22, 26]):

Lemma 8.8 *There exists a constant* $C > 0$, *independent of* h_K, *such that for all* $\mathbf{v} \in H^\delta(K)^2$

$$\|\mathbf{v} - \mathbf{\Pi}_K^{k-1}\mathbf{v}\|_{m,K} \le Ch_K^{\delta-m}|\mathbf{v}|_{\delta,K} \quad 0 \le m \le \delta \le k, \quad k \ge 1.$$

Now, we continue with the following bound for the continuous and discrete linear functionals.

Proposition 8.4 *Let* $k \ge 2$. *Assume that* $\mathbf{f} \in L^2(\Omega)^2$ *such that* $\mathbf{f}|_K \in H^{k-2}(K)^2$ *for each* $K \in \Omega_h$. *Let* $F(\cdot)$ *and* $F^h(\cdot)$ *be the functionals defined in* (8.6) *and* (8.22), *respectively. Then, we have the following estimate:*

$$\|F - F^h\| := \sup_{\substack{\phi_h \in X_h^k \\ \phi_h \neq 0}} \frac{|F(\phi_h) - F^h(\phi_h)|}{\|\phi_h\|_X} \le Ch^{k-1}|\mathbf{f}|_{k-2,h}.$$

Since γ is a scalar function, the bilinear form $C^{h,K}(\cdot,\cdot)$ does not satisfy the consistency property. Nevertheless, we have the following auxiliary results which will be useful to prove the error estimates.

Lemma 8.9 *Let $K \in \Omega_h$ and let γ be a smooth scalar field defined on K. For any* **p**, **q** *smooth enough vector fields defined on K, we have*

$$
\begin{aligned}
(\gamma\,\mathbf{p},\mathbf{q})_{0,K} - (\gamma\,\mathbf{\Pi}_K^{k-1}\mathbf{p},\mathbf{\Pi}_K^{k-1}\mathbf{q})_{0,K} \le &\|\gamma\,\mathbf{p} - \mathbf{\Pi}_K^{k-1}(\gamma\,\mathbf{p})\|_{0,K}\|\mathbf{q} - \mathbf{\Pi}_K^{k-1}\mathbf{q}\|_{0,K} \\
&+ \|\mathbf{p} - \mathbf{\Pi}_K^{k-1}\mathbf{p}\|_{0,K}\|\gamma\,\mathbf{q} - \mathbf{\Pi}_K^{k-1}(\gamma\,\mathbf{q})\|_{0,K} \\
&+ \|\gamma\|_{L^\infty(K)}\|\mathbf{p} - \mathbf{\Pi}_K^{k-1}\mathbf{p}\|_{0,K}\|\mathbf{q} - \mathbf{\Pi}_K^{k-1}\mathbf{q}\|_{0,K}.
\end{aligned}
$$

Proof The proof follows adding and subtracting suitable terms and using the properties of the projection $\mathbf{\Pi}_K^{k-1}$. We omit further details. $\qquad\square$

As an immediate consequence of Lemma 8.9, we have the following result.

Lemma 8.10 *For all $K \in \Omega_h$ and for all $\varphi_h, \phi_h \in X_h^k(K)$, we have that*

$$
\begin{aligned}
C^K(\varphi_h,\phi_h) &- C^{h,K}(\varphi_h,\phi_h) \\
&\le \|\gamma\,\mathbf{curl}\,\varphi_h - \mathbf{\Pi}_K^{k-1}(\gamma\,\mathbf{curl}\,\varphi_h)\|_{0,K}\|\mathbf{curl}\,\phi_h - \mathbf{\Pi}_K^{k-1}\mathbf{curl}\,\phi_h\|_{0,K} \\
&\quad + \|\gamma\,\mathbf{curl}\,\phi_h - \mathbf{\Pi}_K^{k-1}(\gamma\,\mathbf{curl}\,\phi_h)\|_{0,K}\|\mathbf{curl}\,\varphi_h - \mathbf{\Pi}_K^{k-1}\mathbf{curl}\,\varphi_h\|_{0,K} \\
&\quad + C_\gamma\|\mathbf{curl}\,\phi_h - \mathbf{\Pi}_K^{k-1}\mathbf{curl}\,\phi_h\|_{0,K}\|\mathbf{curl}\,\varphi_h - \mathbf{\Pi}_K^{k-1}\mathbf{curl}\,\varphi_h\|_{0,K} \\
&\quad + s_{\mathbf{curl}}^K(\varphi_h - \Pi_K^{k,\nabla^\perp}\varphi_h, \phi_h - \Pi_K^{k,\nabla^\perp}\phi_h),
\end{aligned}
$$

where $C_\gamma > 0$ is a constant depending on the function γ.

For the bilinear forms $B^K(\cdot,\cdot)$ and $B^{h,K}(\cdot,\cdot)$, we have the following analogous result.

Lemma 8.11 *For all $K \in \Omega_h$ and for all $\varphi_h, \phi_h \in X_h^k(K)$, we have that*

$$
\begin{aligned}
B^K(\varphi_h,\phi_h) &- B^{h,K}(\varphi_h,\phi_h) \\
&\le \|(\nabla\mathbf{curl}\,\varphi_h)\boldsymbol{\beta} - \mathbf{\Pi}_{\phi_h}^{k-1}[(\nabla\mathbf{curl}\,\varphi_h)\boldsymbol{\beta}]\|_{0,K}\|\mathbf{curl}\,\phi_h - \mathbf{\Pi}_K^{k-1}\mathbf{curl}\,\phi_h\|_{0,K} \\
&\quad + \|\boldsymbol{\beta}\|_{L^\infty(K)}|\mathbf{curl}\,\varphi_h - \mathbf{\Pi}_K^{k-1}\mathbf{curl}\,\varphi_h|_{1,K}\|\mathbf{\Pi}_K^{k-1}\mathbf{curl}\,\phi_h\|_{0,K}.
\end{aligned}
$$

Proof Let $\varphi_h, \phi_h \in X_h^k(K)$. Then, by using the definition of the bilinear forms $B^K(\cdot,\cdot)$ and $B^{h,K}(\cdot,\cdot)$, adding and subtracting suitable terms and using the

properties of the projection $\mathbf{\Pi}_K^{k-1}$, we have

$$B^K(\varphi_h, \phi_h) - B^{h,K}(\varphi_h, \phi_h)$$

$$= \int_K (\nabla \mathbf{curl}\, \varphi_h)\boldsymbol{\beta} \cdot (\mathbf{curl}\, \phi_h - \mathbf{\Pi}_K^{k-1}\mathbf{curl}\, \phi_h)$$

$$+ \int_K (\nabla \mathbf{curl}\, \varphi_h - \nabla \mathbf{\Pi}_K^{k-1}\mathbf{curl}\, \varphi_h)\boldsymbol{\beta} \cdot \mathbf{\Pi}_K^{k-1}\mathbf{curl}\, \phi_h$$

$$= \int_K \left((\nabla \mathbf{curl}\, \varphi_h)\boldsymbol{\beta} - \mathbf{\Pi}_K^{k-1}[(\nabla \mathbf{curl}\, \varphi_h)\boldsymbol{\beta}] \right) \cdot (\mathbf{curl}\, \phi_h - \mathbf{\Pi}_K^{k-1}\mathbf{curl}\, \phi_h)$$

$$+ \int_K (\nabla \mathbf{curl}\, \varphi_h - \nabla \mathbf{\Pi}_K^{k-1}\mathbf{curl}\, \varphi_h)\boldsymbol{\beta} \cdot \mathbf{\Pi}_K^{k-1}\mathbf{curl}\, \phi_h$$

$$\leq \|(\nabla \mathbf{curl}\, \varphi_h)\boldsymbol{\beta} - \mathbf{\Pi}_K^{k-1}[(\nabla \mathbf{curl}\, \varphi_h)\boldsymbol{\beta}]\|_{0,K} \|\mathbf{curl}\, \phi_h - \mathbf{\Pi}_K^{k-1}\mathbf{curl}\, \phi_h\|_{0,K}$$

$$+ \|\boldsymbol{\beta}\|_{L^\infty(K)} |\mathbf{curl}\, \varphi_h - \mathbf{\Pi}_K^{k-1}\mathbf{curl}\, \varphi_h|_{1,K} \|\mathbf{\Pi}_K^{k-1}\mathbf{curl}\, \phi_h\|_{0,K},$$

where in the last step we have used the Cauchy-Schwarz inequality. $\square$

8.4.2 A Priori Error Estimates

We start with the following result.

Lemma 8.12 *Suppose that* (8.33) *holds true. Let* ψ *and* ψ_h *be the unique solutions of problem* (8.2) *and problem* (8.32), *respectively. Suppose that* $\psi \in H^{2+s}(\Omega)$, $\boldsymbol{\beta} \in W^{s-1,\infty}(\Omega)^2$ *and* $\gamma \in W^{1+s,\infty}(\Omega)$, *for* $1/2 < s \leq k-1$, *then there exists a constant* $C > 0$, *independent of* h, *such that*

$$\|\psi - \psi_h\|_X \leq C \left(\|F - F^h\| + \|\psi - \psi_I\|_X + |\psi - \psi_\pi|_{1,h} + |\psi - \psi_\pi|_{2,h} + h^s\|\psi\|_{2+s,\Omega} \right),$$

for all $\psi_I \in X_h^k$ *and for all* $\psi_\pi \in L^2(\Omega)$ *such that* $\psi_\pi|_K \in \mathbb{P}_k(K)$ *for all polygon* $K \in \Omega_h$.

Proof Let $\psi_I \in X_h^k$. We set $\delta_h := \psi_h - \psi_I$, then

$$\|\psi - \psi_h\|_X \leq \|\psi - \psi_I\|_X + \|\delta_h\|_X. \qquad (8.34)$$

We will bound the second term above, we begin by using Lemma 8.7, adding and subtracting the term $\mathcal{O}(\psi, \delta_h)$ and using the definition of the continuous and

discrete problems (8.2) and (8.32), respectively, we have

$$
\begin{aligned}
\widehat{\alpha}\|\delta_h\|_X^2 &\leq \mathscr{O}^h(\delta_h, \delta_h) \\
&= \mathscr{O}^h(\psi_h, \delta_h) - \mathscr{O}^h(\psi_I, \delta_h) \\
&= F^h(\delta_h) - \mathscr{O}^h(\psi_I, \delta_h) \\
&= F^h(\delta_h) - F(\delta_h) + \mathscr{O}(\psi, \delta_h) - \mathscr{O}^h(\psi_I, \delta_h) \\
&= (F^h(\delta_h) - F(\delta_h)) + \sum_{K \in \Omega_h} \left\{ \nu A^K(\psi, \delta_h) + B^K(\psi, \delta_h) + C^K(\psi, \delta_h) \right\} \\
&\quad - \sum_{K \in \Omega_h} \left\{ \nu A^{h,K}(\psi_I, \delta_h) + B^{h,K}(\psi_I, \delta_h) + C^{h,K}(\psi_I, \delta_h) \right\} \\
&= (F^h(\delta_h) - F(\delta_h)) + \sum_{K \in \Omega_h} \left\{ \nu A^K(\psi - \psi_\pi, \delta_h) - \nu A^{h,K}(\psi_I - \psi_\pi, \delta_h) \right\} \\
&\quad + \sum_{K \in \Omega_h} \left\{ B^K(\psi, \delta_h) - B^{h,K}(\psi_I, \delta_h) \right\} \\
&\quad + \sum_{K \in \Omega_h} \left\{ C^K(\psi, \delta_h) - C^{h,K}(\psi_I, \delta_h) \right\} \\
&=: T_F + \sum_{K \in \Omega_h} \{T_A\} + \sum_{K \in \Omega_h} \{T_B\} + \sum_{K \in \Omega_h} \{T_C\},
\end{aligned}
\tag{8.35}
$$

where we have added and subtracted $\psi_\pi \in \mathbb{P}_k(K)$ for all $K \in \Omega_h$ (recall $k \geq 2$) and we have used the consistency property (8.19). Next, we bound each term on the right hand side above.

For the term T_F, we have

$$
T_F \leq \|F - F^h\| \|\delta_h\|_X.
\tag{8.36}
$$

Now, for the term T_A, we use the continuity of the bilinear forms $A^K(\cdot, \cdot)$ and $A^{h,K}(\cdot, \cdot)$, together with the triangular inequality to obtain that

$$
\begin{aligned}
T_A &= \nu \left\{ A^K(\psi - \psi_\pi, \delta_h) + A^{h,K}(\psi_I - \psi_\pi, \delta_h) \right\} \\
&\leq C(|\psi - \psi_\pi|_{2,K} |\delta_h|_{2,K} + |\psi_I - \psi_\pi|_{2,K} |\delta_h|_{2,K}) \\
&\leq C \left(|\psi - \psi_\pi|_{2,K} + |\psi - \psi_I|_{2,K} \right) |\delta_h|_{2,K}.
\end{aligned}
\tag{8.37}
$$

For term T_B, we add and subtract $B^K(\psi_I, \delta_h)$,

$$
\begin{aligned}
T_B &= B^K(\psi, \delta_h) - B^{h,K}(\psi_I, \delta_h) \\
&= B^K(\psi, \delta_h) - B^K(\psi_I, \delta_h) + B^K(\psi_I, \delta_h) - B^{h,K}(\psi_I, \delta_h) \\
&= B^K(\psi - \psi_I, \delta_h) + \left(B^K(\psi_I, \delta_h) - B^{h,K}(\psi_I, \delta_h) \right) \\
&\leq C|\psi - \psi_I|_{2,K}|\delta_h|_{2,K} + \left(B^K(\psi_I, \delta_h) - B^{h,K}(\psi_I, \delta_h) \right),
\end{aligned}
\tag{8.38}
$$

where we have used the continuity of $B^K(\cdot, \cdot)$. To bound the second term on the right hand side above, we use Lemma 8.11 along with the stability and approximation properties of projector $\mathbf{\Pi}_K^{k-1}$. We have that

$$
\begin{aligned}
B^K(\psi_I, \delta_h) &- B^{h,K}(\psi_I, \delta_h) \\
&\leq \|(\nabla\mathbf{curl}\,\psi_I)\boldsymbol{\beta} - \mathbf{\Pi}_K^{k-1}[(\nabla\mathbf{curl}\,\psi_I)\boldsymbol{\beta}]\|_{0,K}\|\mathbf{curl}\,\delta_h - \mathbf{\Pi}_K^{k-1}\mathbf{curl}\,\delta_h\|_{0,K} \\
&\quad + \|\boldsymbol{\beta}\|_{L^\infty(K)}|\mathbf{curl}\,\psi_I - \mathbf{\Pi}_K^{k-1}\mathbf{curl}\,\psi_I|_{1,K}\|\mathbf{\Pi}_K^{k-1}\mathbf{curl}\,\delta_h\|_{0,K} \\
&\leq C\|(\nabla\mathbf{curl}\,\psi_I)\boldsymbol{\beta} - \mathbf{\Pi}_K^{k-1}[(\nabla\mathbf{curl}\,\psi_I)\boldsymbol{\beta}]\|_{0,K}\,h_K|\delta_h|_{2,K} \\
&\quad + C\|\boldsymbol{\beta}\|_{L^\infty(K)}|\mathbf{curl}\,\psi_I - \mathbf{\Pi}_K^{k-1}\mathbf{curl}\,\psi_I|_{1,K}|\delta_h|_{2,K} \\
&= Ch_K|\delta_h|_{2,K}E_1 + C|\delta_h|_{2,K}E_2.
\end{aligned}
\tag{8.39}
$$

In what follows, we bound the terms E_1 and E_2. For the term E_1, we have

$$
\begin{aligned}
E_1 :={}& \|(\nabla\mathbf{curl}\,\psi_I)\boldsymbol{\beta} - \mathbf{\Pi}_K^{k-1}[(\nabla(\mathbf{curl}\,\psi_I)\boldsymbol{\beta}]\|_{0,K} \\
\leq{}& \|(\nabla\mathbf{curl}\,\psi_I)\boldsymbol{\beta} - (\nabla\mathbf{curl}\,\psi)\boldsymbol{\beta}\|_{0,K} + \|(\nabla\mathbf{curl}\,\psi)\boldsymbol{\beta} - \mathbf{\Pi}_K^{k-1}[(\nabla\mathbf{curl}\,\psi)\boldsymbol{\beta}]\|_{0,K} \\
&+ \|\mathbf{\Pi}_K^{k-1}[(\nabla\mathbf{curl}\,\psi)\boldsymbol{\beta}] - \mathbf{\Pi}_K^{k-1}[(\nabla\mathbf{curl}\,\psi_I)\boldsymbol{\beta}]\|_{0,K} \\
\leq{}& \|(\nabla\mathbf{curl}\,(\psi_I - \psi))\boldsymbol{\beta}\|_{0,K} + \|(\nabla\mathbf{curl}\,\psi)\boldsymbol{\beta} - \mathbf{\Pi}_K^{k-1}[(\nabla\mathbf{curl}\,\psi)\boldsymbol{\beta}]\|_{0,K} \\
&+ \|(\nabla\mathbf{curl}\,(\psi - \psi_I))\boldsymbol{\beta}\|_{0,K} \\
\leq{}& 2\|\boldsymbol{\beta}\|_{L^\infty(K)}|\psi - \psi_I|_{2,K} + h_K^{s-1}|\nabla(\mathbf{curl}\,\psi)\boldsymbol{\beta}|_{s-1,K} \\
\leq{}& 2\|\boldsymbol{\beta}\|_{L^\infty(K)}|\psi - \psi_I|_{2,K} + h_K^{s-1}\|\boldsymbol{\beta}\|_{W^{s-1,\infty}(K)}\|\nabla(\mathbf{curl}\,\psi)\|_{s-1,K} \\
\leq{}& 2\|\boldsymbol{\beta}\|_{L^\infty(K)}|\psi - \psi_I|_{2,K} + h_K^{s-1}\|\boldsymbol{\beta}\|_{W^{s-1,\infty}(K)}\|\psi\|_{2+s,K},
\end{aligned}
\tag{8.40}
$$

where we have used the approximation and stability properties of projector $\mathbf{\Pi}_K^{k-1}$. Now, for the term E_2, we proceed as follows,

$$
\begin{aligned}
E_2 &:= |\mathbf{curl}\,\psi_I - \mathbf{\Pi}_K^{k-1}\mathbf{curl}\,\psi_I|_{1,K} \\
&\le |\mathbf{curl}\,\psi_I - \mathbf{curl}\,\psi|_{1,K} + |\mathbf{curl}\,\psi - \mathbf{\Pi}_K^{k-1}\mathbf{curl}\,\psi|_{1,K} \\
&\quad + |\mathbf{\Pi}_K^{k-1}\mathbf{curl}\,\psi - \mathbf{\Pi}_K^{k-1}\mathbf{curl}\,\psi_I|_{1,K} \\
&\le C\left(|\psi - \psi_I|_{2,K} + h^s|\mathbf{curl}\,\psi|_{1+s,K} + |\mathbf{\Pi}_K^{k-1}\mathbf{curl}\,(\psi - \psi_I)|_{1,K}\right) \\
&\le C(|\psi - \psi_I|_{2,K} + h^s|\mathbf{curl}\,\psi|_{1+s,K} + |\psi - \psi_I|_{2,K}) \\
&\le C(|\psi - \psi_I|_{2,K} + h^s|\psi|_{2+s,K}),
\end{aligned}
\tag{8.41}
$$

where, once again, we have used the approximation and stability properties of $\mathbf{\Pi}_K^{k-1}$.

Inserting (8.40) and (8.41) into (8.39), we obtain

$$
\begin{aligned}
B^K(\psi_I, \delta_h) &- B^{h,K}(\psi_I, \delta_h) \\
&\le C(\|\boldsymbol{\beta}\|_{L^\infty(K)}h_K|\psi - \psi_I|_{2,K} + h_K^s\|\boldsymbol{\beta}\|_{W^{s-1,\infty}(K)}\|\psi\|_{2+s,K})|\delta_h|_{2,K} \\
&\quad + C\|\boldsymbol{\beta}\|_{L^\infty(K)}(|\psi - \psi_I|_{2,K} + h^s\|\psi\|_{2+s,K})|\delta_h|_{2,K} \\
&\le C(|\psi - \psi_I|_{2,K} + h_K^s\|\psi\|_{2+s,K})|\delta_h|_{2,K}.
\end{aligned}
\tag{8.42}
$$

Now, using estimate (8.42), from (8.38), we obtain

$$
T_B \le C(|\psi - \psi_I|_{2,K} + h_K^s\|\psi\|_{2+s,K})|\delta_h|_{2,K}.
\tag{8.43}
$$

By using Lemma 8.10 and repeating analogous arguments as above, we can prove that

$$
T_C \le C\left(|\psi - \psi_I|_{2,K} + |\psi - \psi_\pi|_{1,K} + h_K^{s+1}\|\psi\|_{2+s,K}\right)|\delta_h|_{2,K}.
\tag{8.44}
$$

Then, inserting (8.36), (8.37), (8.43), and (8.44) into (8.35) and employing the Hölder inequality (for sequences), we obtain

$$
\widehat{\alpha}\|\delta_h\|_X \le C\left(\|F - F^h\| + \|\psi - \psi_I\|_X + |\psi - \psi_\pi|_{1,h} + |\psi - \psi_\pi|_{2,h} + h^s\|\psi\|_{2+s,\Omega}\right),
\tag{8.45}
$$

Therefore, the proof follows from (8.34) and (8.45). □

The following result establishes the convergence order of our discrete scheme.

Theorem 8.3 *Let $k \ge 2$ and $\mathbf{f} \in L^2(\Omega)^2$ such that $\mathbf{f}|_K \in H^{k-2}(K)^2$ for each $K \in \Omega_h$. Suppose that (8.33) holds true. Let ψ and ψ_h be the unique solutions*

of problem (8.2) *and problem* (8.32)*, respectively. We suppose that* $\psi \in H^{2+s}(\Omega)$*,* $\boldsymbol{\beta} \in W^{s-1,\infty}(\Omega)^2$ *and* $\gamma \in W^{1+s,\infty}(\Omega)$*, for* $1/2 < s \le k - 1$*, then there exists a constant* $C > 0$*, independent of h, such that*

$$\|\psi - \psi_h\|_X \le Ch^s \left(|\mathbf{f}|_{k-2,h} + \|\psi\|_{2+s,\Omega} \right).$$

Proof The result follows from Lemma 8.12 and Propositions 8.2, 8.3, and 8.4. □

8.5 Recovering the Velocity, Vorticity and Pressure Fields

The solution of the proposed virtual element method (8.32) delivers an approximation of the stream-function field. We remark that one of the advantages of solving fluid flow problems through a stream-function formulation is the possibility of computing further variables of interest, such as the velocity $\mathbf{u}$, the fluid pressure p and the fluid vorticity ω. In this section, we will present strategies to recover these three fields. We compute a discrete velocity and discrete vorticity as a simple postprocess of the computed stream-function using suitable projections, while to recover the pressure we will write a generalized Poisson problem with data coming from the computed stream-function and the load term $\mathbf{f}$, then we propose a discrete virtual scheme, based on the C^0 enhanced virtual element space from [3] to approximate the pressure. Besides, in this section we will establish error estimates in a broken H^1-norm for the velocity and in the L^2-norm for the vorticity. Moreover, under the assumptions that Ω is a convex domain and that the family of polygonal meshes Ω_h is quasi-uniform also we will establish an error estimate for the pressure in the H^1-norm.

8.5.1 Computing the Velocity Field

We start by noticing that if the stream-function $\psi \in X$ is the unique solution of (8.2), then we have that the velocity $\mathbf{u}$ satisfies:

$$\mathbf{u} = \mathbf{curl}\,\psi. \tag{8.46}$$

At the discrete level, we compute a discrete velocity as a post-processing of the computed stream-function $\psi_h \in X_h^k$ as follows: if ψ_h is the unique solution of problem (8.32), then the function

$$\mathbf{u}_h := \mathbf{\Pi}^{k-1}\mathbf{curl}\,\psi_h, \tag{8.47}$$

is an approximation of the velocity, where $\mathbf{\Pi}^{k-1}$ is defined in $L^2(\Omega)^2$ by

$$(\mathbf{\Pi}^{k-1}\mathbf{v})|_K = \mathbf{\Pi}_K^{k-1}(\mathbf{v}|_K) \qquad \forall K \in \Omega_h.$$

The following result establishes the accuracy of the discrete velocity.

Theorem 8.4 *Assume that the hypotheses of Theorem 8.3 holds true, then there exists a positive constant C, independent of h, such that*

$$|\mathbf{u} - \mathbf{u}_h|_{1,h} \leq Ch^s \left(|\mathbf{f}|_{k-2,h} + \|\psi\|_{2+s,\Omega}\right).$$

Proof From (8.46) and (8.47), triangular inequality and property (8.11), we have

$$|\mathbf{u} - \mathbf{u}_h|_{1,h}^2 = |\mathbf{curl}\,\psi - \mathbf{\Pi}^{k-1}\mathbf{curl}\,\psi_h|_{1,h}^2$$

$$= \sum_{K \in \Omega_h} |\mathbf{curl}\,\psi - \mathbf{\Pi}_K^{k-1}\mathbf{curl}\,\psi_h|_{1,K}^2$$

$$\leq C \sum_{K \in \Omega_h} \left(|\mathbf{curl}\,\psi - \mathbf{\Pi}_K^{k-1}\mathbf{curl}\,\psi|_{1,K}^2 + |\mathbf{\Pi}_K^{k-1}(\mathbf{curl}\,\psi - \mathbf{curl}\,\psi_h)|_{1,K}^2\right)$$

$$\leq C \left(\sum_{K \in \Omega_h} h_K^{2s}\|\mathbf{curl}\,\psi\|_{1+s,K}^2 + \sum_{K \in \Omega_h} |\mathbf{\Pi}_K^{k-1}\mathbf{curl}\,(\psi - \psi_h)|_{1,K}^2\right)$$

$$\leq Ch^{2s} \left(\sum_{K \in \Omega_h} \|\psi\|_{2+s,K}^2 + C_N \sum_{K \in \Omega_h} |\psi - \psi_h|_{2,K}^2\right)$$

$$\leq C(h^{2s}\|\psi\|_{2+s,\Omega}^2 + \|\psi - \psi_h\|_X^2)$$

$$\leq Ch^{2s} \left(|\mathbf{f}|_{k-2,h}^2 + \|\psi\|_{2+s,\Omega}^2\right),$$

where we have used the approximation properties of projector $\mathbf{\Pi}_K^{k-1}$ and Theorem 8.3. The proof is complete. □

8.5.2 Computing the Fluid Vorticity

Now, we will present an strategy to recover the fluid vorticity ω, which is key in several important applications in fluid mechanics (see [4, 7, 20, 38]). First, we remark that $\omega = \mathrm{rot}\,\mathbf{u}$, then using the identity $\mathbf{u} = \mathbf{curl}\,\psi$, we have that

$$\omega = \mathrm{rot}\,\mathbf{u} = \mathrm{rot}(\mathbf{curl}\,\psi) = -\Delta\psi. \tag{8.48}$$

We introduce an L^2-ortogonal projection which will be used to construct the discrete vorticity. For $k \geq 2$ and for each $K \in \Omega_h$, we consider the L^2-projection

onto $\mathbb{P}_{k-2}(K)$: for $v \in L^2(K)$, $\Pi_K^{k-2}v \in \mathbb{P}_{k-2}(K)$ is the unique function such that

$$(v - \Pi_K^{k-2}v, q)_{0,K} = 0 \quad \forall q \in \mathbb{P}_{k-2}(K). \tag{8.49}$$

We have the following approximation result (see [14, 22]).

Proposition 8.5 *Let Π_K^{k-2} be the projection defined in (8.49). Then, the following approximation property holds true: there exists a constant $\hat{C}$, independent of h_K, such that*

$$\|v - \Pi_K^{k-2}v\|_{m,K} \leq \hat{C}h_K^{\delta-m}|v|_{\delta,K} \quad \forall v \in H^\delta(K), \qquad 0 \leq m \leq \delta \leq k-1, \quad k \geq 2.$$

Now, we compute a discrete vorticity as follows: if $\psi_h \in X_h^k$ is the unique solution of (8.32), then the function

$$\omega_h := -\Pi^{k-2}(\Delta\psi_h), \tag{8.50}$$

is an approximation of the vorticity, where we have used the notation

$$(\Pi^{k-2}v)|_K = \Pi_K^{k-2}(v|_K) \qquad \forall v \in L^2(\Omega) \text{ and } \forall K \in \Omega_h.$$

Remark 8.4 We observe that for each $\phi_h \in X_h^k(K)$ the polynomial function $\Pi_K^{k-2}(\Delta\phi_h) \in \mathbb{P}_{k-2}(K)$, $k \geq 2$, is computable using the degrees of freedom $\mathbf{D_1} - \mathbf{D_5}$, where $X_h^k(K)$ is the local virtual space defined in (8.9). Indeed, for each $\phi_h \in X_h^k(K)$ and for all $q \in \mathbb{P}_{k-2}(K)$, we have

$$\int_K q \, \Pi_K^{k-2}(\Delta\phi_h) = \int_K q \, \Delta\phi_h$$

$$= \int_K \phi_h \Delta q - \int_{\partial K} \phi_h \, \partial_n q + \int_{\partial K} q \, \partial_n \phi_h,$$

since $\Delta q \in \mathbb{P}_{k-4}(K)$, the first integral on the right hand side above is computable using the output values of the set $\mathbf{D_5}$. Moreover, the boundary terms are fully computable using the information of $\mathbf{D_1} - \mathbf{D_4}$.

We are now ready to prove the following convergence result for the discrete vorticity.

Theorem 8.5 *Assume that the hypotheses of Theorem 8.3 holds true, then there exists a positive constant C, independent of h, such that*

$$\|\omega - \omega_h\|_{0,\Omega} \leq Ch^s \left(|\mathbf{f}|_{k-2,h} + \|\psi\|_{2+s,\Omega}\right).$$

Proof From (8.48) and (8.50), triangular inequality, we have

$$
\begin{aligned}
\|\omega - \omega_h\|_{0,\Omega}^2 &= \|\Delta\psi - \Pi^{k-2}(\Delta\psi_h)\|_{0,\Omega}^2 \\
&= \sum_{K \in \Omega_h} \|\Delta\psi - \Pi_K^{k-2}(\Delta\psi_h)\|_{0,K}^2 \\
&\leq C \sum_{K \in \Omega_h} \left(\|\Delta\psi - \Pi_K^{k-2}(\Delta\psi)\|_{0,K}^2 + \|\Pi_K^{k-2}(\Delta\psi - \Delta\psi_h)\|_{0,K}^2 \right) \\
&\leq C \left(\sum_{K \in \Omega_h} h_K^{2s} \|\Delta\psi\|_{s,K}^2 + \sum_{K \in \Omega_h} \|\Pi_K^{k-2}\Delta(\psi - \psi_h)\|_{0,K}^2 \right) \\
&\leq C h^{2s} \left(\sum_{K \in \Omega_h} \|\psi\|_{2+s,K}^2 + \sum_{K \in \Omega_h} \|\Delta(\psi - \psi_h)\|_{0,K}^2 \right) \\
&\leq C (h^{2s} \|\psi\|_{2+s,\Omega}^2 + \|\psi - \psi_h\|_X^2) \\
&\leq C h^{2s} \left(|\mathbf{f}|_{k-2,h}^2 + \|\psi\|_{2+s,\Omega}^2 \right),
\end{aligned}
$$

where we have used Proposition 8.5 and Theorem 8.3. The proof is complete. $\square$

8.5.3   Computing the Fluid Pressure

Now, we will present an strategy to recover the fluid pressure. We will follow recent results presented in [47] for the Brinkman equations.

We start by considering the following Hilbert space:

$$
\widetilde{H}^1(\Omega) := \left\{ q \in H^1(\Omega) : (q, 1)_{0,\Omega} = 0 \right\}.
$$

By using the identity $-\Delta\mathbf{u} = \mathbf{curl}\,(\mathrm{rot}\,\mathbf{u}) - \nabla(\mathrm{div}\,\mathbf{u})$ in the momentum equation of problem (8.1) and the fact that $\mathbf{u} = \mathbf{curl}\,\psi$, we have that

$$
\begin{aligned}
\mathbf{f} &= -\nu\,\Delta\mathbf{u} + (\nabla\mathbf{u})\boldsymbol{\beta} + \gamma\,\mathbf{u} + \nabla p \\
&= \nu\,(\mathbf{curl}\,(\mathrm{rot}\,\mathbf{u}) - \nabla(\mathrm{div}\,\mathbf{u})) + (\nabla\mathbf{u})\boldsymbol{\beta} + \gamma\,\mathbf{u} + \nabla p \\
&= \nu\,\mathbf{curl}\,(\mathrm{rot}(\mathbf{curl}\,\psi)) + (\nabla\mathbf{curl}\,\psi)\boldsymbol{\beta} + \gamma\,\mathbf{curl}\,\psi + \nabla p,
\end{aligned}
$$

where we have used that $\mathrm{div}\,\mathbf{u} = 0$ in Ω (cf. (8.1)). Now using the identity $\mathrm{rot}(\mathbf{curl}\,\psi) = -\Delta\psi$, the above equality can be rewritten as follows:

$$
\nabla p = \mathbf{f} - \gamma\,\mathbf{curl}\,\psi - (\nabla\mathbf{curl}\,\psi)\boldsymbol{\beta} + \nu\,\mathbf{curl}\,(\Delta\psi). \tag{8.51}
$$

Then, by testing (8.51) with ∇q for $q \in \widetilde{H}^1(\Omega)$, we get the following variational problem to calculate the fluid pressure: find $p \in \widetilde{H}^1(\Omega)$ such that

$$D_\nabla(p, q) = G^\psi(q) \quad \forall q \in \widetilde{H}^1(\Omega), \tag{8.52}$$

where $D_\nabla : \widetilde{H}^1(\Omega) \times \widetilde{H}^1(\Omega) \to \mathbb{R}$ is defined by

$$D_\nabla(p, q) := \int_\Omega \nabla p \cdot \nabla q \qquad \forall p, q \in \widetilde{H}^1(\Omega) \tag{8.53}$$

and $G^\psi : \widetilde{H}^1(\Omega) \to \mathbb{R}$ is the functional defined by:

$$G^\psi(q) := \int_\Omega \mathbf{f} \cdot \nabla q - \gamma \, \mathbf{curl} \, \psi \cdot \nabla q - (\nabla \mathbf{curl} \, \psi) \boldsymbol{\beta} \cdot \nabla q + \nu \, \mathbf{curl} \, (\Delta \psi) \cdot \nabla q \quad \forall q \in \widetilde{H}^1(\Omega). \tag{8.54}$$

From now on, we assume that Ω is a convex domain. As a consequence, we have an additional regularity for the unique solution of problem (8.2). More precisely, we have that $\psi \in H^3(\Omega)$ and that there exists a positive constant C such that

$$\|\psi\|_{3,\Omega} \le C\|\mathbf{f}\|_{0,\Omega}.$$

As an immediate consequence of the above regularity result, the generalized Poincaré inequality and the Lax-Milgram Theorem, we have the following result.

Theorem 8.6 *There exists a unique* $p \in \widetilde{H}^1(\Omega)$ *solution of problem* (8.52). *In addition, there exists* $C > 0$ *such that*

$$\|p\|_{1,\Omega} \le C\|\mathbf{f}\|_{0,\Omega}.$$

In what follows, we will propose a lowest order discrete virtual element scheme to approximate the fluid pressure over the same polygonal mesh Ω_h used to solve the stream-function discrete formulation (8.32). With this aim, we split the bilinear form $D_\nabla(\cdot, \cdot)$, as a contribution element by element as follows:

$$D_\nabla(p, q) := \sum_{K \in \Omega_h} D_\nabla^K(p, q) = \sum_{K \in \Omega_h} \int_K \nabla p \cdot \nabla q, \qquad \forall p, q \in \widetilde{H}^1(\Omega). \tag{8.55}$$

Now, for each polygon $K \in \Omega_h$, we consider the finite-dimensional space $\widetilde{W}_h(K)$, defined as

$$\widetilde{W}_h(K) := \left\{ q_h \in H^1(K) \cap C^0(\partial K) : q_h|_e \in \mathbb{P}_1(e) \quad \forall e \subset \partial K, \ \Delta q_h \in \mathbb{P}_0(K) \right\}.$$

The following set of linear operator is defined for all $q_h \in \widetilde{W}_h(K)$:

P$_1$: the values of q_h at the vertices of K.

We define the projector $\Pi_K^\nabla : \widetilde{W}_h(K) \to \mathbb{P}_1(K) \subseteq \widetilde{W}_h(K)$ for each $q_h \in \widetilde{W}_h(K)$ as the solution of

$$D_\nabla^K (\Pi_K^\nabla q_h, p_1) = D_\nabla^K (q_h, p_1) \qquad \forall p_1 \in \mathbb{P}_1(K),$$

$$\widehat{\Pi_K^\nabla q_h} = \widehat{q_h},$$

where $\widehat{(\cdot)}$ is defined in (8.8). We note that the operator Π_K^∇ is explicitly computable using the set **P$_1$** (see [14]). In addition, using this projection and the definition of $\widetilde{W}_h(K)$, we introduce our local virtual space:

$$W_h(K) := \left\{ q_h \in \widetilde{W}_h(K) : (q_h - \Pi_K^\nabla q_h, 1)_{0,K} = 0 \right\}.$$

It is easy to observe that $\mathbb{P}_1(K) \subseteq W_h(K) \subseteq \widetilde{W}_h(K)$. Moreover, we have that the set **P$_1$** constitutes a set of degrees of freedom for $W_h(K)$ and operator Π_K^∇ is also computable using only the set **P$_1$** (see [14]).

Now, we define the following global virtual space to approximate the discrete pressure

$$W_h := \left\{ q_h \in \widetilde{H}^1(\Omega) : q_h|_K \in W_h(K) \right\}.$$

Next, we will continue with the construction of the discrete version of the bilinear form and the linear functional introduced in (8.53) and (8.54), respectively. To do that, we consider an L^2-orthogonal projection. For each $K \in \Omega_h$, we define $\mathbf{\Pi}_K^0 : L^2(K)^2 \to \mathbb{P}_0(K)^2$ as the unique function such that

$$\int_K (\mathbf{v} - \mathbf{\Pi}_K^0 \mathbf{v}) \cdot \mathbf{q} = 0 \qquad \forall \mathbf{q} \in \mathbb{P}_0(K)^2.$$

It is easy to check that $\mathbf{\Pi}_K^0 \nabla q_h$ is fully computable, using the degrees of freedom **P$_1$**, for each $q_h \in W_h(K)$.

Let $\mathscr{S}_\nabla^K (\cdot, \cdot)$ be any symmetric positive definite bilinear form such that

$$c_4 D_\nabla^K (q_h, q_h) \leq \mathscr{S}_\nabla^K (q_h, q_h) \leq c_5 D_\nabla^K (q_h, q_h) \quad \forall q_h \in W_h(K), \text{ with } \Pi_K^\nabla q_h = 0, \tag{8.56}$$

for some positive constants c_4 and c_5 independent of K. We will make a choose for $\mathscr{S}_\nabla^K (\cdot, \cdot)$ satisfying (8.56) in Sect. 8.6.

Then, we set

$$D_\nabla^h(p_h, q_h) := \sum_{K \in \Omega_h} D_\nabla^{h,K}(p_h, q_h) \qquad \forall p_h, q_h \in W_h, \tag{8.57}$$

where

$$D_\nabla^{h,K}(p_h, q_h) := \int_K \mathbf{\Pi}_K^0 \nabla p_h \cdot \mathbf{\Pi}_K^0 \nabla q_h + \mathscr{S}_\nabla^K \left(p_h - \Pi_K^\nabla p_h, q_h - \Pi_K^\nabla q_h \right), \tag{8.58}$$

for all $p_h, q_h \in W_h(K)$.

The following result gives us consistency and stability properties of the local discrete bilinear form $D_\nabla^{h,K}(\cdot, \cdot)$.

Proposition 8.6 *The local bilinear forms $D_\nabla^K(\cdot, \cdot)$ and $D_\nabla^{h,K}(\cdot, \cdot)$ defined in* (8.55) *and* (8.58)*, respectively, satisfy the following properties:*

– *Consistency: for each $h > 0$ and each $K \in \Omega_h$, we have*

$$D_\nabla^{h,K}(q_h, p_1) = D_\nabla^K(q_h, p_1) \quad \forall p_1 \in \mathbb{P}_1(K), \quad \forall q_h \in W_h(K). \tag{8.59}$$

– *Stability: there exist positive constants α_4, α_5, independent of h_K and K, such that*

$$\alpha_4 D_\nabla^K(q_h, q_h) \le D_\nabla^{h,K}(q_h, q_h) \le \alpha_5 D_\nabla^K(q_h, q_h) \quad \forall q_h \in W_h(K). \tag{8.60}$$

The next step consists in constructing an approximation of the right hand side (8.54), which depends on the stream-function ψ and the source term $\mathbf{f}$. With this aim, from now on, we assume that the discrete problem (8.32) has been solved with $k = 3$. So, $\psi_h \in X_h^3$ is available and satisfies the error bound presented in Theorem 8.3.

Now, for each $K \in \Omega_h$ and each $q_h \in W_h(K)$, we define the following discrete linear functional:

$$G^{\psi_h,K}(q_h) := \int_K \mathbf{f} \cdot \mathbf{\Pi}_K^0 \nabla q_h - \int_K \left(\nabla \mathbf{\Pi}_K^2 \mathbf{curl}\, \psi_h \right) \boldsymbol{\beta} \cdot \mathbf{\Pi}_K^0 \nabla q_h$$

$$- \int_K \gamma \mathbf{\Pi}_K^2 \mathbf{curl}\, \psi_h \cdot \mathbf{\Pi}_K^0 \nabla q_h + \nu \int_K \mathbf{curl}\, (\Pi_K^1(\Delta \psi_h)) \cdot \mathbf{\Pi}_K^0 \nabla q_h,$$

where $\mathbf{\Pi}_K^2$ and Π_K^1 are the projections defined in (8.10) and (8.49), for $k = 3$, respectively. We have that $G^{\psi_h,K}(\cdot)$ is fully computable for each $K \in \Omega_h$ using the set degrees of freedom $\mathbf{P_1}$.

We define the following global computable linear functional:

$$G^{\psi_h}(q_h) := \sum_{K \in \Omega_h} G^{\psi_h,K}(q_h) \qquad \forall q_h \in W_h. \tag{8.61}$$

Therefore, we propose the following virtual element discretization of lowest order to recover the fluid pressure: Given $\psi_h \in X_h^3$, find $p_h \in W_h$ such that

$$D_\nabla^h(p_h, q_h) = G^{\psi_h}(q_h) \qquad \forall q_h \in W_h. \tag{8.62}$$

We observe that by virtue of (8.60) the bilinear form $D_\nabla^h(\cdot, \cdot)$ is bounded. Moreover, the following result states that it is also elliptic.

Lemma 8.13 *There exists a constant $\alpha_p > 0$, independent of h, such that*

$$D_\nabla^h(q_h, q_h) \geq \alpha_p \|q_h\|_{1,\Omega}^2 \qquad \forall q_h \in W_h.$$

Next, we will prove that the linear functional defined in (8.61) is bounded. To do that, we consider the following approximation result (see [22]).

Proposition 8.7 *If the assumption* **A2** *is satisfied, then there exists a constant $C > 0$, such that for every $v \in H^2(K)$, there exists $v_\pi \in \mathbb{P}_1(K)$ such that*

$$\|v - v_\pi\|_{0,K} + h_K |v - v_\pi|_{1,K} \leq Ch_K^2 |v|_{2,K}.$$

Now, we present an interpolation result in the virtual space W_h (see [30, 46]).

Proposition 8.8 *If the assumptions* **A1** *and* **A2** *are satisfied, then there exists a constant $C > 0$, independent of h, such that for each $v \in H^2(\Omega)$ there exists $v_I \in W_h$ such that*

$$\|v - v_I\|_{0,\Omega} + h|v - v_I|_{1,\Omega} \leq Ch^2 |v|_{2,\Omega}.$$

To prove that the functional $G^{\psi_h}(\cdot)$ defined in (8.61) is bounded we will assume that the family of polygonal meshes Ω_h is quasi-uniform. More precisely, from now on, we will assume the following:

A3: For each $h > 0$ and for each $K \in \Omega_h$, there exists a constant $\widehat{c} > 0$, independent of h, such that $h_K \geq \widehat{c}h$.

The following result establishes that the linear functional $G^{\psi_h}(\cdot)$ defined in (8.61) is bounded under assumptions **A1**, **A2** and **A3**.

Lemma 8.14 *Let $\psi \in H^3(\Omega)$ be the unique solution of problem (8.2) and let $\psi_h \in X_h^3$ be the unique solution of problem (8.32). We assume that* **A1** $-$ **A3** *are satisfied, then the functional $G^{\psi_h} : W_h \to \mathbb{R}$ defined in (8.61) is bounded.*

Proof The result follows repeating the arguments used in the proof of Proposition 4.20 of [47]. □

As a consequence of Lemmas 8.13, 8.14 and the Lax-Milgram Theorem, we have the following result.

Theorem 8.7 *The discrete virtual element scheme* (8.62) *admits a unique solution* $p_h \in W_h$ *and there exists* $C > 0$*, independent of h, such that*

$$\|p_h\|_{1,\Omega} \le C \left(\|\mathbf{f}\|_{0,\Omega} + |\mathbf{f}|_{1,h} \right).$$

In what follows, we will establish the order of convergence of the discrete scheme (8.62) under the assumptions **A1** − **A3** and the additional regularity results $p \in H^2(\Omega)$ and $\psi \in H^4(\Omega)$. This additional regularity for the stream-function can be attained, for instance, if $\mathbf{f} \in L^2(\Omega)^2$ and Ω is a rectangular domain (see [23]). We begin with the following result which proof follows standard arguments in the VEM literature (see [13, 31]).

Proposition 8.9 *Let* p *and* p_h *be the unique solutions of problems* (8.52) *and* (8.62)*, respectively. If the assumptions* **A1** − **A3** *are satisfied, then there exists* $C > 0$*, independent of h, such that*

$$\|p - p_h\|_{1,\Omega} \le C \left(\|G^\psi - G^{\psi_h}\| + \|p - p_I\|_{1,\Omega} + |p - p_\pi|_{1,h} \right),$$

for all $p_I \in H_h$ *and for each* $p_\pi \in L^2(\Omega)$ *such that* $p_\pi|_K \in \mathbb{P}_1(K)$ *for all* $K \in \Omega_h$*, where*

$$\|G^\psi - G^{\psi_h}\| := \sup_{\substack{q_h \in W_h \\ q_h \ne 0}} \frac{|G^\psi(q_h) - G^{\psi_h}(q_h)|}{\|q_h\|_{1,\Omega}}.$$

Now, we will bound the term $\|G^\psi - G^{\psi_h}\|$.

Proposition 8.10 *Let* $\mathbf{f} \in L^2(\Omega)^2$ *such that* $\mathbf{f}|_K \in H^1(K)^2$ *for all* $K \in \Omega_h$*. Let* $\psi \in H^4(\Omega)$ *and* $\psi_h \in X_h^3$ *be the unique solutions of problems* (8.2) *and* (8.32)*, respectively. Let* $G^\psi(\cdot)$ *and* $G^{\psi_h}(\cdot)$ *be the linear functionals defined in* (8.54) *and* (8.61)*, respectively. Then, there exists* $C > 0$*, independent of h, such that*

$$\left\| G^\psi - G^{\psi_h} \right\| \le Ch \left(\|\psi\|_{4,\Omega} + |\mathbf{f}|_{1,h} \right).$$

Proof Let $q_h \in W_h$, then using the definition of $G^\psi(\cdot)$ and $G^{\psi_h}(\cdot)$, and the Cauchy-Schwarz inequality, we have

$$|G^\psi(q_h) - G^{\psi_h}(q_h)| \leq \sum_{K \in \Omega_h} \left| \int_K \mathbf{f} \cdot \left(\nabla q_h - \mathbf{\Pi}_K^0 \nabla q_h \right) \right|$$

$$+ \sum_{K \in \Omega_h} \left| \int_K (\nabla \mathbf{curl}\, \psi) \boldsymbol{\beta} \cdot \nabla q_h - (\nabla \mathbf{\Pi}_K^2 \mathbf{curl}\, \psi_h) \boldsymbol{\beta} \cdot \mathbf{\Pi}_K^0 \nabla q_h \right|$$

$$+ \sum_{K \in \Omega_h} \left| \int_K \gamma \mathbf{curl}\, \psi \cdot \nabla q_h - \gamma \mathbf{\Pi}_K^2 \mathbf{curl}\, \psi_h \cdot \mathbf{\Pi}_K^0 \nabla q_h \right|$$

$$+ \sum_{K \in \Omega_h} \nu \left| \int_K \mathbf{curl}\,(\Delta \psi) \cdot \nabla q_h - \mathbf{curl}\,\left(\mathbf{\Pi}_K^1 (\Delta \psi_h) \right) \cdot \mathbf{\Pi}_K^0 \nabla q_h \right|$$

$$:= T_1 + T_2 + T_3 + T_4.$$

Now, repeating the arguments used in the proof of Proposition 4.23 of [47], we have that

$$T_1 \leq Ch |\mathbf{f}|_{1,h} \|q_h\|_{1,\Omega}, \tag{8.63}$$

$$T_3 \leq Ch(\|\psi_h\|_X + |\mathbf{f}|_{1,h} + \|\psi\|_{4,\Omega}) \|q_h\|_{1,\Omega}, \tag{8.64}$$

and

$$T_4 \leq Ch \left(\|\psi\|_{4,\Omega} + |\mathbf{f}|_{1,h} \right) \|q_h\|_{1,\Omega}. \tag{8.65}$$

Thus, in what follows, we are going to estimate the term T_2. We start by adding and subtracting suitable terms, and employing the triangular inequality, we have that

$$T_2 \leq \sum_{K \in \Omega_h} \left| \int_K (\nabla \mathbf{curl}\, \psi) \boldsymbol{\beta} \cdot (\nabla q_h - \mathbf{\Pi}_K^0 \nabla q_h) \right|$$

$$+ \sum_{K \in \Omega_h} \left| \int_K \left[\nabla(\mathbf{curl}\, \psi - \mathbf{\Pi}_K^2 \mathbf{curl}\, \psi_h) \right] \boldsymbol{\beta} \cdot \mathbf{\Pi}_K^0 \nabla q_h \right| \tag{8.66}$$

$$=: I + II.$$

In that follows, we will bound the terms I and II. We begin with the term I. By using the properties of the operator $\mathbf{\Pi}_K^0$, we get

$$
\begin{aligned}
I :&= \sum_{K \in \Omega_h} \left| \int_K \left[(\nabla \mathbf{curl}\, \psi) \boldsymbol{\beta} - \mathbf{\Pi}_K^0 \big((\nabla \mathbf{curl}\, \psi) \boldsymbol{\beta} \big) \right] \cdot (\nabla q_h - \mathbf{\Pi}_K^0 \nabla q_h) \right| \\
&\leq \sum_{K \in \Omega_h} \| (\nabla \mathbf{curl}\, \psi) \boldsymbol{\beta} - \mathbf{\Pi}_K^0 \big((\nabla \mathbf{curl}\, \psi) \boldsymbol{\beta} \big) \|_{0,K} \| \nabla q_h - \mathbf{\Pi}_K^0 \nabla q_h \|_{0,K} \\
&\leq C \sum_{K \in \Omega_h} h_K |(\nabla \mathbf{curl}\, \psi) \boldsymbol{\beta}|_{1,K} \| \nabla q_h \|_{0,K} \\
&\leq Ch \left(\sum_{K \in \Omega_h} |(\nabla \mathbf{curl}\, \psi) \boldsymbol{\beta}|_{1,K}^2 \right)^{1/2} \left(\sum_{K \in \Omega_h} \| \nabla q_h \|_{0,K}^2 \right)^{1/2} \\
&\leq Ch \| (\nabla \mathbf{curl}\, \psi) \boldsymbol{\beta} \|_{1,\Omega} |q_h|_{1,\Omega} \\
&\leq Ch \| \boldsymbol{\beta} \|_{W^{1,\infty}(\Omega)} \| \nabla (\mathbf{curl}\, \psi) \|_{1,\Omega} \| q_h \|_{1,\Omega} \\
&\leq Ch \| \psi \|_{3,\Omega} \| q_h \|_{1,\Omega}.
\end{aligned}
\tag{8.67}
$$

Now, we continue by estimating II (cf. (8.66)). By using the approximation properties of operator $\mathbf{\Pi}_K^2$, we obtain that

$$
\begin{aligned}
II :&= \sum_{K \in \Omega_h} \left| \int_K \left[\nabla (\mathbf{curl}\, \psi - \mathbf{\Pi}_K^2 \mathbf{curl}\, \psi_h) \right] \boldsymbol{\beta} \cdot \mathbf{\Pi}_K^0 \nabla q_h \right| \\
&\leq \sum_{K \in \Omega_h} \| \boldsymbol{\beta} \|_{L^\infty(K)} \| \nabla (\mathbf{curl}\, \psi - \mathbf{\Pi}_K^2 \mathbf{curl}\, \psi_h) \|_{0,K} \| \mathbf{\Pi}_K^0 \nabla q_h \|_{0,K} \\
&\leq C \| \boldsymbol{\beta} \|_{L^\infty(\Omega)} \sum_{K \in \Omega_h} |\mathbf{curl}\, \psi - \mathbf{\Pi}_K^2 \mathbf{curl}\, \psi_h|_{1,K} \| \nabla q_h \|_{0,K} \\
&\leq C \sum_{K \in \Omega_h} \left(|\mathbf{curl}\, \psi - \mathbf{\Pi}_K^2 \mathbf{curl}\, \psi|_{1,K} + |\mathbf{\Pi}_K^2 \mathbf{curl}\, (\psi - \psi_h)|_{1,K} \right) \| \nabla q_h \|_{0,K} \\
&\leq C \sum_{K \in \Omega_h} \left(h_K \| \mathbf{curl}\, \psi \|_{1,K} + C_N |\psi - \psi_h|_{2,K} \right) \| \nabla q_h \|_{0,K} \\
&\leq Ch (|\mathbf{f}|_{1,h} + \| \psi \|_{4,\Omega}) \| q_h \|_{1,\Omega},
\end{aligned}
\tag{8.68}
$$

where we have added and subtracted the term $\mathbf{\Pi}_K^2\,\mathbf{curl}\,\psi$, and used (8.11) together with the Hölder inequality. Then, inserting (8.67) and (8.68) into (8.66), we obtain

$$T_2 \le C h \left(\|\psi\|_{4,\Omega} + |\mathbf{f}|_{1,h}\right)\|q_h\|_{1,\Omega}. \tag{8.69}$$

Finally, the proof follows from the estimates (8.63)–(8.65) and (8.69).   □

The following theorem provides the rate of convergence of our virtual element scheme (8.62) to recover the fluid pressure. The proof follows from Propositions 8.9, 8.10, 8.7, and 8.8.

Theorem 8.8 *Let* $\mathbf{f} \in L^2(\Omega)^2$ *such that* $\mathbf{f}|_K \in H^1(K)^2$ *for all* $K \in \Omega_h$. *Let* ψ, ψ_h, p *and* p_h *be the unique solutions of problems* (8.2), (8.32), (8.52), *and* (8.62), *respectively. Suppose that* $\mathbf{A1} - \mathbf{A3}$ *are satisfied,* $p \in H^2(\Omega)$ *and* $\psi \in H^4(\Omega)$. *Then, there exists* $C > 0$, *independent of* h, *such that*

$$\|p - p_h\|_{1,\Omega} \le C h \left(\|\psi\|_{4,\Omega} + |\mathbf{f}|_{1,h}\right).$$

8.6 Numerical Results

In this section, we present three numerical experiments in order to illustrate the practical performance of the proposed virtual element methods (8.32) and (8.62) and to confirm the theoretical results established in previous sections. We will test the method for the cases $k = 2$ and $k = 3$ on different polygonal meshes.

Now, we introduce the bilinear forms $\mathscr{S}_{\mathrm{D}}^K(\cdot,\cdot)$ and $\mathscr{S}_{\mathbf{curl}}^K(\cdot,\cdot)$ (cf. (8.12)) to complete the virtual element discretization (8.32). We take (see [9, 24, 47]):

$$\mathscr{S}_{\mathrm{D}}^K(\psi_h,\phi_h) := \sigma^K \sum_{i=1}^{N_K^{\mathrm{dof}}} \mathrm{dof}_i(\psi_h)\mathrm{dof}_i(\phi_h) \qquad \forall \psi_h, \phi_h \in X_h^k(K),$$

$$\mathscr{S}_{\mathbf{curl}}^K(\psi_h,\phi_h) := \sigma_\gamma^K \sum_{i=1}^{N_K^{\mathrm{dof}}} \mathrm{dof}_i(\psi_h)\mathrm{dof}_i(\phi_h) \qquad \forall \psi_h, \phi_h \in X_h^k(K),$$

where for each polygon $K \in \Omega_h$, N_K^{dof} denote the number of degrees freedom of $X_h^k(K)$ and dof_i, with $1 \le i \le \dim(X_h^k(K))$, denote the operator that to each smooth enough function ϕ associates the ith local degree of freedom $\mathrm{dof}_i(\phi)$ and the parameters $\sigma^K, \sigma_\gamma^K > 0$ are multiplicative factors to take into account the physical magnitudes and the h-scaling. On the other hand, the bilinear form $\mathscr{S}_\nabla^K(\cdot,\cdot)$ (cf.
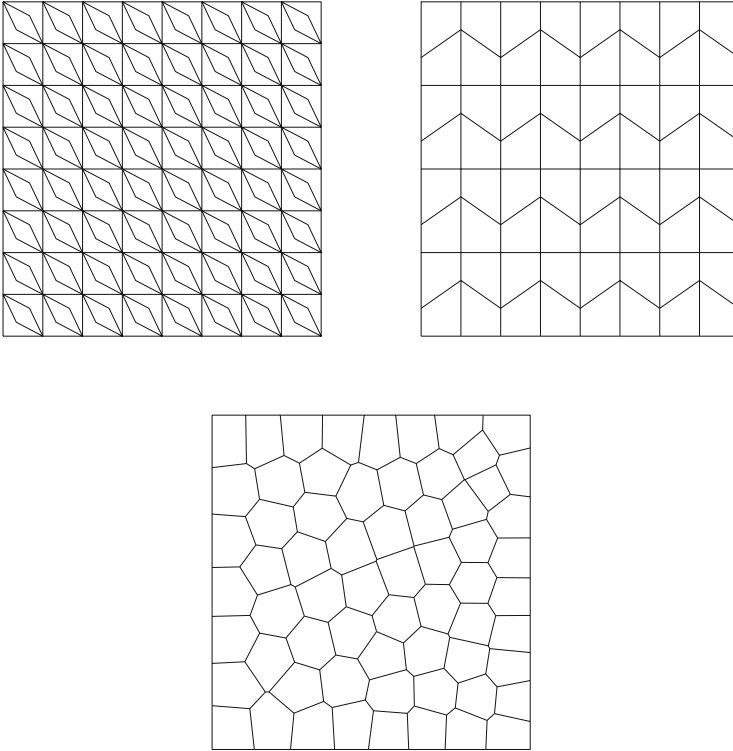
Fig. 8.1 Sample meshes. Ω_h^1, Ω_h^2 and Ω_h^3

(8.56)), is given by (see [13, 46]):

$$\mathscr{S}_\nabla^K(p_h, q_h) := \sum_{i=1}^{N_K} p_h(\mathbf{v}_i) q_h(\mathbf{v}_i) \quad \forall p_h, q_h \in W_h(K).$$

We have tested the method by using the following families of meshes (Fig. 8.1):

– Ω_h^1: Distorted concave rhombic quadrilaterals;
– Ω_h^2: Trapezoidal meshes;
– Ω_h^3: Sequence of CVT (Centroidal Voronoi Tessellation).

In order to compute the VEM errors, we consider the following computable error quantities.

$$\mathsf{e}_i(\psi) = \mathrm{error}(\psi, H^i) := \left(\sum_{K \in \Omega_h} |\psi - \Pi_K^{k,\mathrm{D}} \psi_h|_{i,K}^2 \right)^{1/2}, \quad i = 0, 1, 2.$$

$$\mathsf{e}_1(p) = \mathrm{error}(p, H^1) := \left(\sum_{K \in \Omega_h} \left| p - \Pi_K^\nabla p_h \right|_{1,K}^2 \right)^{1/2},$$

$$\mathsf{e}_0(\omega) = \mathrm{error}(\omega, L^2) := \left(\sum_{K \in \Omega_h} \left\| \omega - \Pi_K^{k-2}(\Delta \psi_h) \right\|_{0,K}^2 \right)^{1/2}.$$

Moreover, if h, h' denote two consecutive mesh sizes with their respective errors e_i and e_i', then we will compute experimental rates of convergence for each variable as follows:

$$\mathsf{r}_i(\cdot) := \frac{\log(\mathsf{e}_i(\cdot)/\mathsf{e}_i'(\cdot))}{\log(h/h')}, \quad i = 0, 1, 2.$$

8.6.1 Test 1: Smooth Solution

In this test we solve the Oseen equations (8.1) on the square domain $\Omega := (0, 1)^2$. We take $\nu = 1$, $\gamma = 100$, and the load term $\mathbf{f}$ and boundary conditions in such a way that the analytical solution is given by:

$$\mathbf{u}(x, y) = \begin{pmatrix} 2x^2(1-x)^2 y(y-1)(2y-1) \\ -2y^2(1-y)^2 x(x-1)(2x-1) \end{pmatrix}, \qquad \omega(x, y) = \mathrm{rot}\,\mathbf{u} = -\Delta \psi,$$

$$p(x, y) = x^3 + y^3 - \frac{1}{2} \quad \text{and} \quad \psi(x, y) = x^2(1-x)^2 y^2(1-y)^2.$$

Moreover, we consider the following convective velocity:

$$\boldsymbol{\beta}(x, y) = \begin{pmatrix} \sin(x)\sin(y) \\ \cos(x)\cos(y) \end{pmatrix}.$$

Table 8.1 shows the convergence history of the virtual element scheme (8.32) applied to our test problem for $k = 2$. In addition, Table 8.2 shows the convergence history of the virtual element schemes (8.32) and (8.62) for $k = 3$. In both cases, we have considered meshes Ω_h^1.

It can be seen from Tables 8.1 and 8.2 that the methods converge with an optimal order for all the variables.

Table 8.1 Test 1. Errors and experimental rates for the stream-function ψ_h and vorticity ω_h, using the meshes Ω_h^1, $k = 2$, $\nu = 1$ and $\gamma = 100$

h	$e_0(\psi)$	$r_0(\psi)$	$e_1(\psi)$	$r_1(\psi)$	$e_2(\psi)$	$r_2(\psi)$	$e_0(\omega)$	$r_0(\omega)$
1/4	7.473458e−4	–	3.931137e−3	–	3.515403e−2	–	2.579728e−2	–
1/8	1.219438e−4	2.61	8.002679e−4	2.29	1.606165e−2	1.13	8.728651e−3	1.56
1/16	1.750743e−5	2.80	1.633574e−4	2.29	7.852990e−3	1.03	3.750317e−3	1.21
1/32	3.151107e−6	2.47	3.947501e−5	2.04	3.894174e−3	1.01	1.738230e−3	1.10
1/64	6.698881e−7	2.23	9.958959e−6	1.98	1.942167e−3	1.00	8.414948e−4	1.04

Table 8.2 Test 1. Errors and experimental rates for the stream-function ψ_h, pressure p_h and vorticity ω_h using the meshes Ω_h^1, $k = 3$, $\nu = 1$ and $\gamma = 100$

h	$e_0(\psi)$	$r_0(\psi)$	$e_1(\psi)$	$r_1(\psi)$	$e_2(\psi)$	$r_2(\psi)$	$e_1(p)$	$r_1(p)$	$e_0(\omega)$	$r_0(\omega)$
1/4	1.852106e−4	–	1.106299e−3	–	1.949383e−2	–	3.158359e−1	–	1.970323e−2	–
1/8	1.405414e−5	3.72	1.110736e−4	3.31	5.057026e−3	1.94	1.622020e−1	0.96	5.128756e−3	1.94
1/16	1.027443e−6	3.77	1.160837e−5	3.25	1.285563e−3	1.97	8.253523e−2	0.97	1.303501e−3	1.97
1/32	7.173524e−8	3.84	1.230588e−6	3.23	3.062095e−4	2.06	4.055215e−2	1.02	3.103413e−4	2.07
1/64	4.450005e−9	4.01	1.352796e−7	3.18	7.017355e−5	2.12	1.986404e−2	1.02	7.098042e−5	2.12

Figure 8.2 shows plots of the exact (left) and computed (right) stream-function, pressure and vorticity, obtained with the virtual element methods analyzed in this paper, using the meshes Ω_h^1, with $h = 1/32$, $k = 3$ and $\nu = 1$.

In Fig. 8.3 we depict approximate velocity field obtained from the discrete stream-function using the meshes Ω_h^1, with $h = 1/32$, $k = 3$, $\nu = 1$ and $\gamma = 100$.

8.6.2   Test 2: Solution with Boundary Layer

In this numerical experiment, we solve the Oseen equations (8.1) on the square domain $\Omega := (0, 1)^2$. We take $\nu = 10^{-3}$, $\gamma = 50$ and the load term $\mathbf{f}$ and boundary conditions in such a way that the analytical solution is given by:

$$\mathbf{u}(x, y) = \frac{2}{\lambda^2}\begin{pmatrix} x^2 y(e^{\lambda(x-1)} - 1)^2(e^{\lambda(y-1)} - 1)(e^{\lambda(y-1)} + \lambda y e^{\lambda(y-1)} - 1) \\ -xy^2(e^{\lambda(y-1)} - 1)^2 e^{\lambda(x-1)} - 1)(e^{\lambda(x-1)} + \lambda x e^{\lambda(x-1)} - 1) \end{pmatrix},$$

$$\omega(x, y) = \mathrm{rot}\,\mathbf{u} = -\Delta\psi, \qquad p(x, y) = e^{x+y} - (e - 1)^2,$$

and

$$\psi(x, y) = \frac{1}{\lambda^2} x^2 y^2 (1 - e^{\lambda(x-1)})^2 (1 - e^{\lambda(y-1)})^2,$$

where $\lambda = 0.5/\sqrt{\nu}$, while the convective velocity is $\boldsymbol{\beta} = (1, 1)$. We observe that ψ has a boundary layer on the top-right corner of the domain for small values of ν.
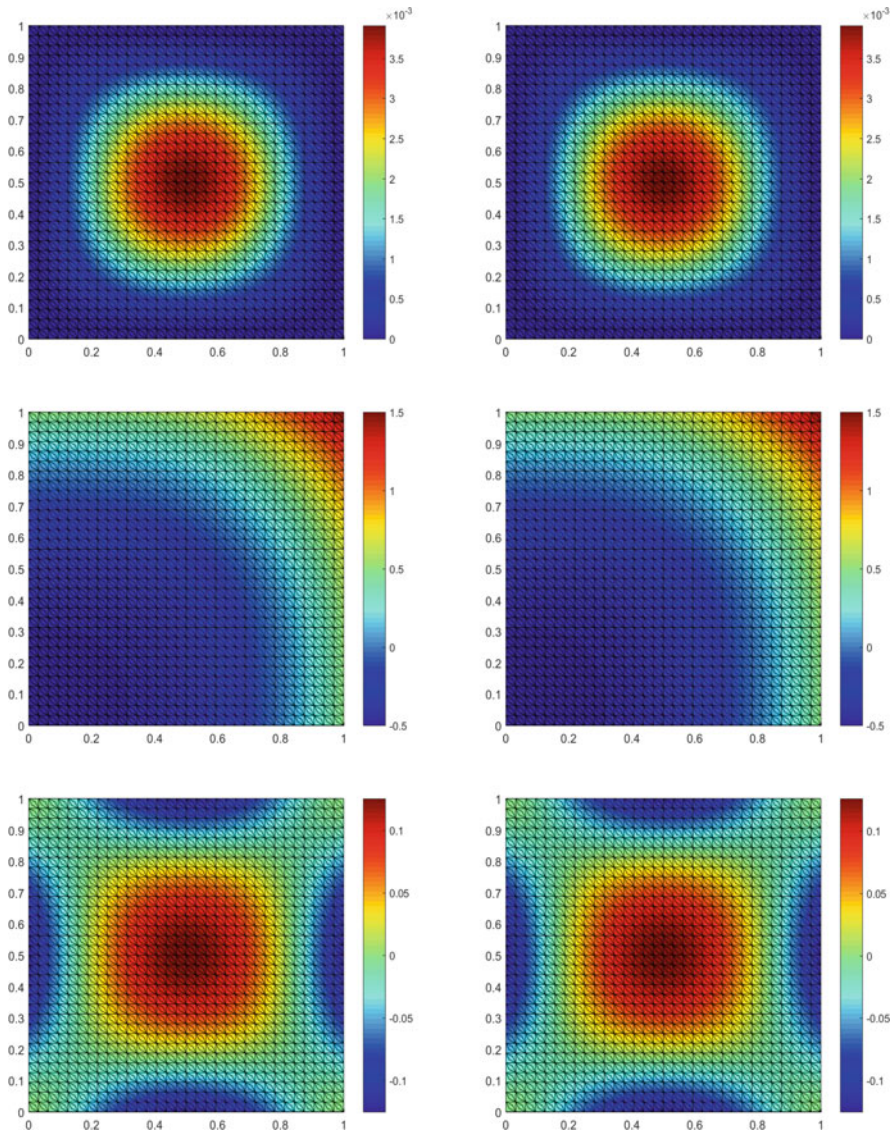
Fig. 8.2 Test 1. Exact (left) and computed (right) stream-function, pressure and vorticity, using the VEM methods (8.2) and (8.62) with Ω_h^1, $h = 1/32$, $k = 3$, $\nu = 1$ and $\gamma = 100$

Table 8.3 shows the convergence history of our virtual element scheme (8.32) applied to the present test for $k = 2$, while Table 8.4 shows the convergence history of the virtual element schemes (8.32) and (8.62) for $k = 3$. In both cases, the set of decompositions utilized is Ω_h^2.
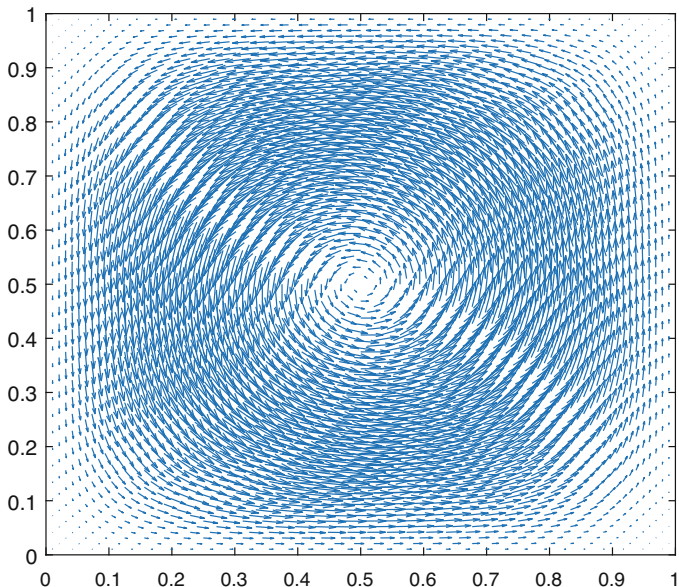
Fig. 8.3 Test 1. Velocity field obtained from the discrete stream-function with Ω_h^1, $h = 1/32$, $k = 3$, $\nu = 1$ and $\gamma = 100$

Table 8.3 Test 2. Errors and experimental rates for the stream-function ψ_h and vorticity ω_h, using the meshes Ω_h^2, $k = 2$, $\nu = 10^{-3}$ and $\gamma = 50$

h	$e_0(\psi)$	$r_0(\psi)$	$e_1(\psi)$	$r_1(\psi)$	$e_2(\psi)$	$r_2(\psi)$	$e_0(\omega)$	$r_0(\omega)$
1/8	2.784694e−4	–	2.973866e−3	–	9.076308e−2	–	5.838607e−2	–
1/16	1.030198e−4	1.43	1.690738e−3	0.81	7.965350e−2	0.18	4.042055e−2	0.53
1/32	1.926182e−5	2.14	6.324576e−4	1.41	5.785738e−2	0.46	3.638668e−2	0.15
1/64	1.992073e−6	3.27	1.607822e−4	1.97	3.321376e−2	0.88	2.211350e−2	0.71
1/128	3.418173e−7	2.54	3.208248e−5	2.32	1.593417e−2	1.05	9.492817e−3	1.22

Table 8.4 Test 2. Errors and experimental rates for the stream-function ψ_h, pressure p_h and vorticity ω_h using the meshes Ω_h^2, $k = 3$, $\nu = 10^{-3}$ and $\gamma = 50$

h	$e_0(\psi)$	$r_0(\psi)$	$e_1(\psi)$	$r_1(\psi)$	$e_2(\psi)$	$r_2(\psi)$	$e_1(p)$	$r_1(p)$	$e_0(\omega)$	$r_0(\omega)$
1/8	2.197659e−4	–	2.548761e−3	–	8.465258e−2	–	2.466608e−1	–	8.483406e−2	–
1/16	4.584130e−5	2.26	1.000595e−3	1.34	5.882760e−2	0.52	1.244517e−1	0.98	5.890052e−2	0.52
1/32	3.579805e−6	3.67	2.019404e−4	2.30	2.659083e−2	1.14	6.250501e−2	0.99	2.659606e−2	1.14
1/64	2.381437e−7	3.90	3.314490e−5	2.60	8.793503e−3	1.59	3.130231e−2	0.99	8.787307e−3	1.59
1/128	3.084086e−8	2.94	4.223090e−6	2.97	2.148259e−3	2.03	1.565467e−2	0.99	2.144776e−3	2.03

In this numerical example, we notice that the rate of convergence predicted by Theorems 8.3, 8.5, and 8.8 is attained by all the variables, in the corresponding norms. However, in Table 8.4 we observe a degeneracy of the optimal convergence rate for the stream-function in the L^2-norm, we attribute this to the existence of the boundary layer on the top-right corner of the domain.

Figure 8.4 shows plots of the exact (left) and computed (right) stream-function, pressure and vorticity, obtained with the virtual element methods analyzed in this paper, using the meshes Ω_h^2, with $h = 1/64$, $k = 3$, $\nu = 10^{-3}$ and $\gamma = 50$.

Figure 8.5 shows the approximate velocity field obtained from the discrete stream-function and the streamlines using the meshes Ω_h^2, with $h = 1/64$, $k = 3$, $\nu = 10^{-3}$ and $\gamma = 50$.

8.6.3   Test 3: Solution with Non Homogeneous Dirichlet Boundary Conditions

The aim of this numerical test is twofold: consider small values of viscosity and solve the Oseen equations (8.1) on the square domain $\Omega := (0, 1)^2$ with the proposed scheme (8.32) and with the scheme obtained by using the projection $\Pi_K^{k,\nabla^\perp}$ to discretize (8.17)–(8.18) (cf. Remark 8.2).

We take $\nu = 10^{-7}$, $\gamma = 100$, $\boldsymbol{\beta} = (1, 1)$ and the load term $\mathbf{f}$ and boundary conditions in such a way that the analytical solution is given by:

$$\mathbf{u}(x, y) = \frac{1}{4\pi^2} \begin{pmatrix} e^{x^2+y^2} \sin(2\pi x)(y \cos(2\pi y) - \pi \sin(2\pi y)) \\ -e^{x^2+y^2} \cos(2\pi y)(x \sin(2\pi x) + \pi \cos(2\pi x)) \end{pmatrix}, \quad \omega(x, y) = \operatorname{rot} \mathbf{u},$$

$$p(x, y) = \sin(x) - \sin(y) \quad \text{and} \quad \psi(x, y) = \frac{1}{8\pi^2} \sin(2\pi x) \cos(2\pi y) e^{x^2+y^2}.$$

Table 8.5 shows the convergence history of the scheme (8.32) and the scheme obtained by using the projection $\Pi_K^{k,\nabla^\perp}$ to discretize (8.17)–(8.18) for $k = 2$ with meshes Ω_h^3.

In this numerical example, we notice that the rate of convergence predicted by Theorems 8.3 and 8.5 is attained by all the variables for both methods. However, we have not proved any order of convergence for the second method (denoted by $\Pi_K^{k,\nabla^\perp}$).
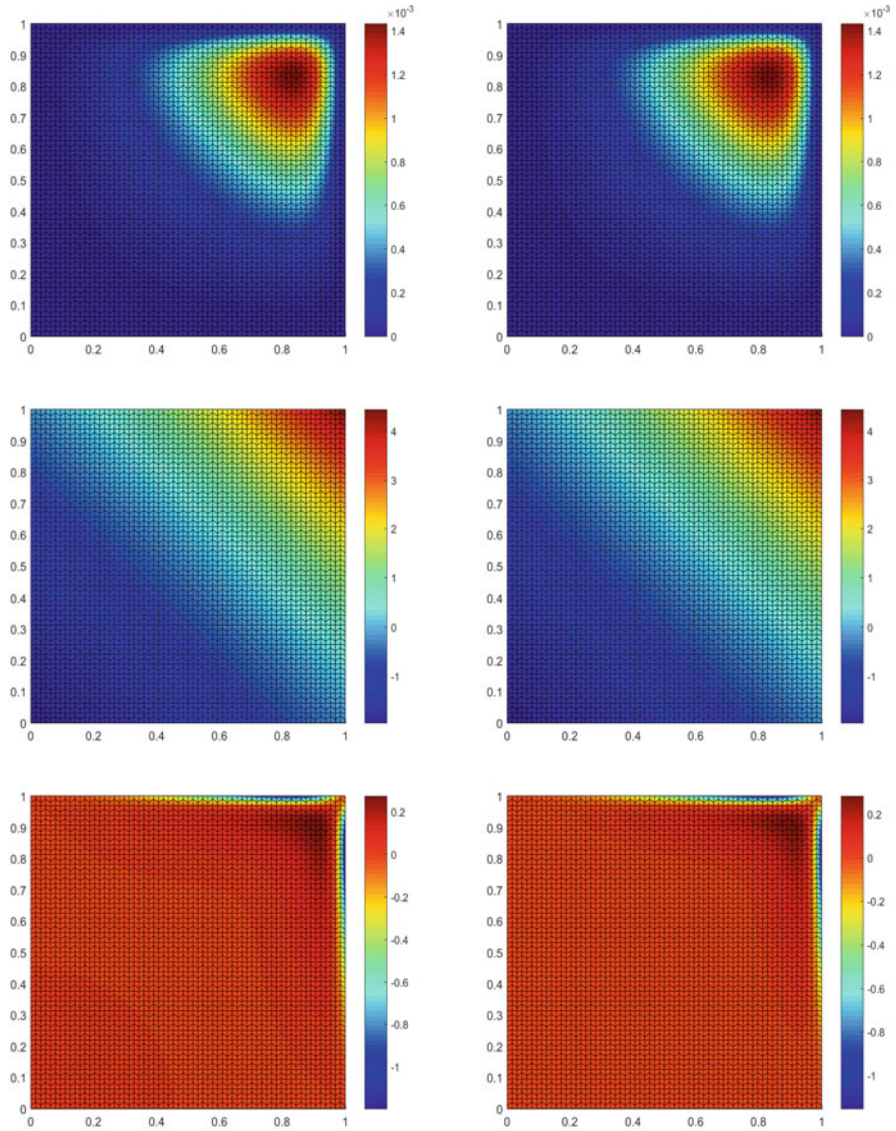
Fig. 8.4 Test 2. Exact (left) and computed (right) stream-function, pressure and vorticity, using the VEM methods (8.2) and (8.62) with Ω_h^2, $h = 1/64$, $k = 3$, $\nu = 10^{-3}$ and $\gamma = 50$
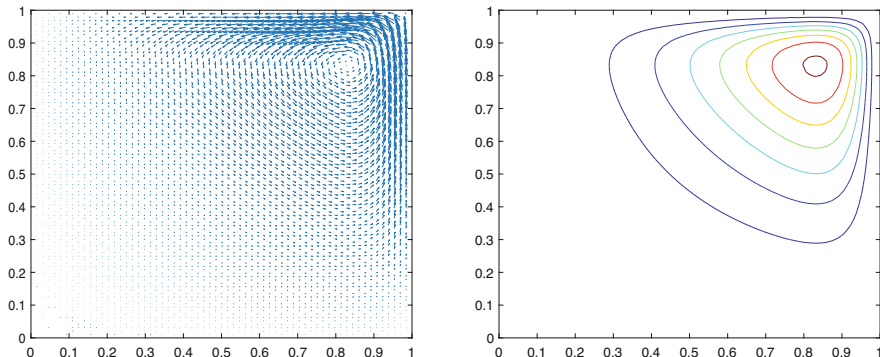
Fig. 8.5 Test 2. Velocity field and streamlines obtained from the discrete stream-function with Ω_h^2, $k = 3$, $\nu = 10^{-3}$ and $\gamma = 50$

Table 8.5 Test 3. Errors and experimental rates for the stream-function ψ_h and vorticity ω_h, using the meshes Ω_h^3, $k = 2$, $\nu = 10^{-7}$ and $\gamma = 100$

h	$e_2(\psi)$	$r_2(\psi)$	$e_0(\omega)$	$r_0(\omega)$	$e_2(\psi)$	$r_2(\psi)$	$e_0(\omega)$	$r_0(\omega)$
	$\Pi_K^{k-1}\mathbf{curl}$				$\Pi_K^{k,\nabla^\perp}$			
1/4	7.353181e−1	–	4.192605e−1	–	7.080137e−1	–	3.472549e−1	–
1/8	3.884964e−1	0.92	1.422766e−1	1.55	3.794077e−1	0.90	1.070817e−1	1.69
1/16	2.110175e−1	0.88	7.320291e−2	0.95	2.071037e−1	0.87	6.068313e−2	0.81
1/32	1.032265e−1	1.03	3.079478e−2	1.24	1.013613e−1	1.03	2.376248e−2	1.35
1/64	5.059447e−2	1.02	1.499318e−2	1.03	4.957692e−2	1.03	1.100301e−2	1.11
1/128	2.512584e−2	1.00	6.807878e−3	1.13	2.476607e−2	1.00	5.318140e−3	1.04

References

1. R.A. Adams, J.J.F. Fournier, Sobolev spaces, in *Pure and Applied Mathematics (Amsterdam)*, 2nd edn., vol. 140. Elsevier/Academic Press, Amsterdam (2003)
2. J. Aghili, D.A. Di Pietro, An advection-robust hybrid high-order method for the Oseen problem. J. Sci. Comput. **77**(3), 1310–1338 (2018)
3. B. Ahmad, A. Alsaedi, F. Brezzi, L.D. Marini, A. Russo, Equivalent projectors for virtual element methods. Comput. Math. Appl. **66**(3), 376–391 (2013)
4. V. Anaya, G.N. Gatica, D. Mora, R. Ruiz-Baier, An augmented velocity-vorticity-pressure formulation for the Brinkman equations. Internat. J. Numer. Methods Fluids **79**(3), 109–137 (2015)

5. V. Anaya, M. Bendahmane, D. Mora, R. Ruiz-Baier, On a vorticity-based formulation for reaction-diffusion-Brinkman systems. Netw. Heterog. Media **13**(1), 69–94 (2018)
6. V. Anaya, A. Bouharguane, D. Mora, C. Reales, R. Ruiz-Baier, N. Seloula, H. Torres, Analysis and approximation of a vorticity-velocity-pressure formulation for the Oseen equations. J. Sci. Comput. **80**(3), 1577–1606 (2019)
7. V. Anaya, D. Mora, C. Reales, R. Ruiz-Baier, Vorticity-pressure formulations for the Brinkman-Darcy coupled problem, Numer. Methods Partial Differ. Equations **35**(2), 528–544 (2019)
8. P.F. Antonietti, L. Beirão da Veiga, D. Mora, M. Verani, A stream virtual element formulation of the Stokes problem on polygonal meshes. SIAM J. Numer. Anal. **52**(1), 386–404 (2014)
9. P.F. Antonietti, L. Beirão da Veiga, S. Scacchi, M. Verani, A C^1 virtual element method for the Cahn-Hilliard equation with polygonal meshes. SIAM J. Numer. Anal. **54**(1), 34–56 (2016)
10. G.R. Barrenechea, A. Wachtel, Stabilised finite element methods for the Oseen problem on anisotropic quadrilateral meshes. ESAIM Math. Model. Numer. Anal. **52**(1), 99–122 (2018)
11. T.P. Barrios, J. M. Cascón, M. González, Augmented mixed finite element method for the Oseen problem: a priori and a posteriori error analyses. Comput. Methods Appl. Mech. Eng. **313**, 216–238 (2017)
12. T.P. Barrios, J. M. Cascón, M. González, On an adaptive stabilized mixed finite element method for the Oseen problem with mixed boundary conditions. Comput. Methods Appl. Mech. Eng. **365**, 113007 (2020)
13. L. Beirão da Veiga, F. Brezzi, A. Cangiani, G. Manzini, L.D. Marini, A. Russo, Basic principles of virtual element methods. Math. Models Methods Appl. Sci. **23**(1), 199–214 (2013)
14. L. Beirão da Veiga, F. Brezzi, L.D. Marini, A. Russo, Virtual element method for general second-order elliptic problems on polygonal meshes. Math. Models Methods Appl. Sci. **26**(4), 729–750 (2016)
15. L. Beirão da Veiga, C. Lovadina, A. Russo, Stability analysis for the virtual element method. Math. Models Methods Appl. Sci. **27**(13), 2557–2594 (2017)
16. L. Beirão da Veiga, C. Lovadina, G. Vacca, Divergence free virtual elements for the Stokes problem on polygonal meshes. ESAIM Math. Model. Numer. Anal. **51**(2), 509–535 (2017)
17. L. Beirão da Veiga, C. Lovadina, G. Vacca, Virtual elements for the Navier-Stokes problem on polygonal meshes. SIAM J. Numer. Anal. **56**(3), 1210–1242 (2018)
18. L. Beirão da Veiga, D. Mora, G. Rivera, Virtual elements for a shear-deflection formulation of Reissner-Mindlin plates. Math. Comp. **88**(315), 149–178 (2019)
19. L. Beirão da Veiga, D. Mora, G. Vacca, The Stokes complex for virtual elements with application to Navier-Stokes flows. J. Sci. Comput. **81**(2), 990–1018 (2019)
20. C. Bernardi, N. Chorfi, Spectral discretization of the vorticity, velocity, and pressure formulation of the Stokes problem. SIAM J. Numer. Anal. **44**(2), 826–850 (2006)
21. M. Braack, E. Burman, V. John, G. Lube, Stabilized finite element methods for the generalized Oseen problem. Comput. Methods Appl. Mech. Eng. **196**(4–6), 853–866 (2007)
22. S.C. Brenner, L.R. Scott, The mathematical theory of finite element methods, in *Texts in Applied Mathematics*, vol. 15, 3rd edn. (Springer, New York, 2008)
23. S.C. Brenner, P. Monk, J. Sun, C^0 interior penalty Galerkin method for biharmonic eigenvalue problems, in *Spectral and High Order Methods for Partial Differential Equations—ICOSAHOM 2014*. Lecture Notes in Computer Science Engineering , vol. 106, pp. 3–15 (Springer, Cham, 2015)
24. F. Brezzi, L.D. Marini, Virtual element methods for plate bending problems. Comput. Methods Appl. Mech. Eng. **253**, 455–462 (2013)
25. E. Burman, A. Ern, M.A. Fernández, Fractional-step methods and finite elements with symmetric stabilization for the transient Oseen problem. ESAIM Math. Model. Numer. Anal. **51**(2), 487–507 (2017)
26. E. Cáceres, G.N. Gatica, A mixed virtual element method for the pseudostress-velocity formulation of the Stokes problem. IMA J. Numer. Anal. **37**(1), 296–331 (2017)
27. E. Cáceres, G.N. Gatica, F.A. Sequeira, A mixed virtual element method for the Brinkman problem. Math. Models Methods Appl. Sci. **27**(4), 707–743 (2017)

28. Z. Cai, B. Chen, Least-squares method for the Oseen equation. Numer. Methods Partial Differ. Equations **32**(4), 1289–1303 (2016)
29. A. Cangiani, V. Gyrya, G. Manzini, The nonconforming virtual element method for the Stokes equations. SIAM J. Numer. Anal. **54**(6), 3411–3435 (2016)
30. A. Cangiani, E.H. Georgoulis, T. Pryer, O.J. Sutton, A posteriori error estimates for the virtual element method. Numer. Math. **137**(4), 857–893 (2017)
31. A. Cangiani, G. Manzini, O.J. Sutton, Conforming and nonconforming virtual element methods for elliptic problems. IMA J. Numer. Anal. **37**(3), 1317–1354 (2017)
32. M.E. Cayco, R.A. Nicolaides, Finite element technique for optimal pressure recovery from stream function formulation of viscous flows. Math. Comp. **46**(174), 371–377 (1986)
33. A. Cesmelioglu, B. Cockburn, N.C. Nguyen, J. Peraire, Analysis of HDG methods for Oseen equations. J. Sci. Comput. **55**(2), 392–431 (2013)
34. C.L. Chang, S.-Y. Yang, Analysis of the $[L^2, L^2, L^2]$ least-squares finite element method for incompressible Oseen-type problems. Int. J. Numer. Anal. Model. **4**(3–4), 402–424 (2007)
35. A. Chernov, C. Marcati, L. Mascotto, p- and hp- virtual elements for the Stokes problem. Adv. Comput. Math. **47**(2), 24 (2021)
36. C. Chinosi, L.D. Marini, Virtual element method for fourth order problems: L^2-estimates. Comput. Math. Appl. **72**(8), 1959–1967 (2016)
37. F. Dassi, G. Vacca, Bricks for the mixed high-order virtual element method: projectors and differential operators. Appl. Numer. Math. **155**, 140–159 (2020)
38. A. Ern, Vorticity-velocity formulation of the Stokes problem with variable density and viscosity. Math. Models Methods Appl. Sci. **8**(2), 203–218 (1998)
39. S. Franz, K. Höhne, G. Matthies, Grad-div stabilized discretizations on S-type meshes for the Oseen problem. IMA J. Numer. Anal. **38**(1), 299–329 (2018)
40. G.N. Gatica, M. Munar, F. Sequeira, A mixed virtual element method for the Boussinesq problem on polygonal meshes. J. Comput. Math. **39**(3), 392–427 (2021)
41. V. Girault, P.-A. Raviart, Finite element methods for Navier-Stokes equations, in *Springer Series in Computational Mathematics*, vol. 5. (Springer, Berlin, 1986). Theory and algorithms
42. D. Irisarri, G. Hauke, Stabilized virtual element methods for the unsteady incompressible Navier-Stokes equations. Calcolo **56**(4), Paper No. 38, 21 (2019)
43. M.-J. Lai, P. Wenston, Bivariate spline method for numerical solution of steady state Navier-Stokes equations over polygons in stream function formulation. Numer. Methods Partial Differ. Equations **16**(2), 147–183 (2000)
44. X. Liu, Z. Chen, The nonconforming virtual element method for the Navier-Stokes equations. Adv. Comput. Math. **45**(1), 51–74 (2019)
45. X. Liu, R. Li, Z. Chen, A virtual element method for the coupled Stokes-Darcy problem with the Beaver-Joseph-Saffman interface condition. Calcolo **56**(4), Paper No. 48, 28 (2019)
46. D. Mora, G. Rivera, R. Rodríguez, A virtual element method for the Steklov eigenvalue problem. Math. Models Methods Appl. Sci. **25**(8), 1421–1445 (2015)
47. D. Mora, C. Reales, A. Silgado, A C^1-virtual element method of high order for the Brinkman equations in stream function formulation with pressure recovery (2022, in press). https://doi.org/10.1093/imanum/drab078
48. G. Vacca, An H^1-conforming virtual element for Darcy and Brinkman equations. Math. Models Methods Appl. Sci. **28**(1), 159–194 (2018)
49. J. Zhao, B. Zhang, S. Mao, S. Chen, The divergence-free nonconforming virtual element for the Stokes problem. SIAM J. Numer. Anal. **57**(6), 2730–2759 (2019)

Chapter 9
The Nonconforming Trefftz Virtual Element Method: General Setting, Applications, and Dispersion Analysis for the Helmholtz Equation

Lorenzo Mascotto, Ilaria Perugia, and Alexander Pichler

Abstract We present a survey of the nonconforming Trefftz virtual element method for the Laplace and Helmholtz equations. As for the latter, we show a new abstract analysis, based on weaker assumptions on the stabilization, and numerical results on the dispersion analysis, including comparison with the plane wave discontinuous Galerkin method.

9.1 Introduction

In this chapter, we present a survey of a methodology, which dovetails the nonconforming virtual element setting with the Trefftz paradigm.

The *nonconforming virtual element method* is an extension of the nonconforming finite element method to polytopal meshes, which is based on the virtual element method (VEM) framework. Notably, the continuity constraint of functions in the approximation spaces are imposed in a weak sense only. Since its inception [6], the nonconforming VEM has received an increasing attention, and has been analysed and applied to several problems: general elliptic problems [14]; Stokes and Navier-Stokes equations [13, 35, 36, 51, 52]; eigenvalue problems [23]; the plate bending problem [50]; equations involving the biharmonic and $2m$-th operators [4, 17]; anisotropic error estimates [15]; the linear elasticity problem [49]; parabolic and

L. Mascotto (✉)
Department of Mathematics and Applications, University of Milano-Bicocca, Milan, Italy

Faculty of Mathematics, University of Vienna, Vienna, Austria

IMATI-CNR, Pavia, Italy
e-mail: lorenzo.mascotto@unimib.it

I. Perugia · A. Pichler
Faculty of Mathematics, University of Vienna, Vienna, Austria
e-mail: ilaria.perugia@univie.ac.at; alex.pichler@univie.ac.at

fractional-reaction subdiffusion problems [34, 53]; the VEM with a SUPG stabilization for advection-diffusion-reaction [11]; fourth order singular perturbation problems [48]; the Kirchhoff plate contact problem [46]; the medius error analysis for the Poisson and biharmonic problem [30]. Its comparison with other skeletal methods such as the hybridized discontinuous Galerkin method (HDG) and the hybrid high-order (HHO) method is investigated in [21].

Trefftz methods are Galerkin-type methods for the approximation of linear partial differential equations (PDEs) with piecewise constant coefficients, where the test and/or trial functions belong to the kernel of the differential operator defining the PDE to be approximated. Trefftz methods have been applied mainly to time-harmonic wave propagation problems, but also to advection-diffusion problems and to wave problems in the time-domain. Typically, Trefftz methods are obtained by combining these functions (*Trefftz function*) with the discontinuous Galerkin method (dG) or with the partition of unity method (PUM). Out of the former category, restricting ourselves to the Helmholtz problem, we recall several approaches, which trace back to the ultra weak variational formulation [16]: the wave based method [19]; discontinuous methods based on Lagrange multipliers [22] and on least square formulation [43]; the plane wave discontinuous Galerkin (PWDG) method [25, 28]; the variational theory of complex rays [45]; see [29] for an overview of such methods. We also mention the quasi-Trefftz dG method for the case of smoothly varying coefficients, where functions that "almost" belong to the kernel of the operator appearing in the PDE are employed [32, 33]. Instead, the latter category consists of methods based on approximation spaces of continuous functions given by the product of pure Trefftz functions with partition of unity, low order, hat functions. Amongst them, we highlight the classical PUM [7, 8] and its virtual element version [44].

More recently, the Trefftz gospel has been combined with the nonconforming VEM setting for the Laplace equation [37], and the Helmholtz equation with constant [38, 39] and piecewise constant wave number [40]. Albeit the nonconforming Trefftz VEM is not an H^1 conforming method, the interelement continuity is imposed weakly within the approximation spaces, unlike in the dG setting. Moreover, unlike in the PUM setting, its basis functions are exactly Trefftz.

In this contribution, we review the methods presented in [37–39], and elaborate a common framework for nonconforming Trefftz VEMs. We start by considering the simplest case of the Laplace equation in Sect. 9.3. Then, we extrapolate the core idea of the nonconforming Trefftz VEM approach and extend it to general linear differential operators of the second order; see Sect. 9.4. In Sect. 9.5, we recast the case of the Helmholtz equation studied in [38] into the setting of Sect. 9.4. Additionally, we present a new abstract analysis of the method, which is based on weaker assumptions on the stabilization than those in [38]. While we refer to [39] for the implementation details and an extended numerical testing of the nonconforming Trefftz VEM for the Helmholtz problem, we present in Sect. 9.6 unpublished work on its numerical dispersion analysis, where the performance of the nonconforming Trefftz VEM are compared to those of the PWDG method that have been studied in [24].

Notation

We employ standard notation for Sobolev spaces. Given $s \in \mathbb{N}$ and a domain Ω, we denote the Sobolev space of order s taking values in the complex field $\mathbb{C}$ by $H^s(\Omega)$. In the special case $s = 0$, $H^s(\Omega)$ reduces to the Lebesgue space $L^2(\Omega)$. We introduce the Sobolev sesquilinear forms, seminorms, and norms

$$(\cdot, \cdot)_{s,\Omega}, \qquad |\cdot|_{s,\Omega}, \qquad \|\cdot\|_{s,\Omega}.$$

We define Sobolev spaces of order $s \in \mathbb{R}$ by interpolation. Analogously, we denote the Sobolev spaces on $\partial\Omega$ by $H^s(\partial\Omega)$. If we consider Sobolev spaces of functions taking values only in $\mathbb{R}$, we employ the same notation $H^s(\Omega)$ thanks to the trivial embedding $\mathbb{R} \hookrightarrow \mathbb{C}$.

Assume that the domain Ω is Lipschitz. Then, we can define the standard Dirichlet trace operator $\mathrm{tr}_{\partial\Omega} : H^s(\Omega) \to H^{s-\frac{1}{2}}(\partial\Omega)$ for all $s \in (1/2, 3/2)$. Thanks to this operator, we are allowed to introduce affine Sobolev spaces with boundary conditions: given $g \in H^{\frac{1}{2}}(\partial\Omega)$,

$$H_g^1(\Omega) := \left\{ v \in H^1(\Omega) \mid \mathrm{tr}_{\partial\Omega}(v) = g \right\}.$$

Henceforth, as standard in the VEM literature, a quantity is said to be *computable* if it can be evaluated using the degrees of freedom of the trial and test spaces under consideration.

9.2 Polygonal Meshes and Broken Sobolev Spaces

We denote a family of polygonal meshes over a polygonal domain $\Omega \subset \mathbb{R}^2$ by $\{\mathscr{T}_h\}_{h>0}$, and the sets of edges and vertices of $\mathscr{T}_h$ by $\mathscr{E}_h$ and $\mathscr{V}_h$, respectively. In particular, we split $\mathscr{E}_h$ into the sets of boundary and internal edges $\mathscr{E}_h^B$ and $\mathscr{E}_h^I$, respectively. Given a polygon $K \in \mathscr{T}_h$, we denote its barycenter, size, set of edges, set of vertices, and outward normal to ∂K by $\mathbf{x}_K$, h_K, $\mathscr{E}^K$, $\mathscr{V}^K$, and $\mathbf{n}_K$, respectively, and given an edge $e \in \mathscr{E}_h$, we denote its size by h_e.

As customary in polygonal methods, we demand the following shape-regularity assumption on $\{\mathscr{T}_h\}_h$:

there exists a positive constant $\gamma > 0$ such that, for all $K \in \mathscr{T}_h$,

i) $K \in \mathscr{T}_h$ is star-shaped with respect to a ball of radius γh_K; $\qquad$ (9.1)

ii) every edge $e \in \mathscr{E}^K$ is such that $h_e \leq h_K \leq \gamma h_e$.

We introduce the broken Sobolev space associated with the mesh $\mathscr{T}_h$

$$H^1(\Omega, \mathscr{T}_h) := \{ v \in L^2(\Omega) \mid v \in H^1(K) \, \forall K \in \mathscr{T}_h \}, \qquad (9.2)$$

and endow it with the broken seminorm

$$|v|^2_{1,\mathscr{T}_h} := \sum_{K \in \mathscr{T}_h} |v_K|^2_{1,K} \qquad \forall v \in H^1(\Omega, \mathscr{T}_h). \tag{9.3}$$

Given $e \in \mathscr{E}_h^I$, we define the jump operator across e as follows:

$$[\![v]\!]_e = v^+{}_{|e}\, \mathbf{n}_{K^+} + v^-{}_{|e}\, \mathbf{n}_{K^-} \qquad \text{if } e \subset \partial K^+ \cap \partial K^- \tag{9.4}$$

for all v in $H^1(\Omega, \mathscr{T}_h)$, where $v^+ := v_{|K^+}$ and $v^- := v_{|K^-}$.

9.3 The Nonconforming Trefftz Virtual Element Method for the Laplace Problem

In this section, we focus on the approximation of a two dimensional Laplace problem by means of the nonconforming Trefftz virtual element method that was originally introduced in [37]; see also [18] for its conforming version.

The Continuous Problem
Let $\Omega \subset \mathbb{R}^2$ be a polygonal domain and $g \in H^{\frac{1}{2}}(\partial\Omega)$. Introduce the following notation:

$$V_g := H^1_g(\Omega), \qquad V_0 := H^1_0(\Omega), \qquad a(\cdot, \cdot) := (\nabla\cdot, \nabla\cdot)_{0,\Omega}.$$

We consider the following Laplace problem: find a sufficiently smooth $u : \Omega \to \mathbb{R}$ such that

$$\begin{cases} \Delta u = 0 & \text{in } \Omega \\ u = g & \text{on } \partial\Omega, \end{cases}$$

which in weak formulation reads

$$\begin{cases} \text{find } u \in V_g \text{ such that} \\ a(u, v) = 0 \qquad \forall v \in V_0. \end{cases} \tag{9.5}$$

An Explicit Discontinuous Space
Let $p \in \mathbb{N}$. Given a sequence $\{\mathscr{T}_h\}_h$ of polygonal decompositions over Ω as in Sect. 9.1, we define the corresponding sequence of discontinuous, piecewise harmonic polynomials over $\mathscr{T}_h$:

$$\mathscr{S}_p^{0,\Delta}(\Omega, \mathscr{T}_h) := \left\{ q_p^\Delta \in L^2(\Omega) \mid q_p^\Delta{}_{|K} \in \mathbb{H}_p(K) \; \forall K \in \mathscr{T}_h \right\},$$

where, for all $K \in \mathscr{T}_h$,

$$\mathbb{H}_p(K) := \left\{ q_p^\Delta \in \mathbb{P}_p(K) \mid \Delta q_p^\Delta = 0 \right\}.$$

We recall the following approximation property of discontinuous, piecewise harmonic polynomials for harmonic functions; see, e.g., [41, Theorem 2.9].

Proposition 9.1 *Under the shape regularity assumption* (9.1) *with constant γ, given a harmonic function $u \in H^{s+1}(\Omega)$, $s > 0$, there exists $q_p^\Delta \in \mathscr{S}_p^{0,\Delta}(\Omega, \mathscr{T}_h)$ such that*

$$|u - q_p^\Delta|_{1,h} \le ch^s \|u\|_{s+1,\Omega}.$$

The positive constant c depends on γ and on the polynomial degree p.

The importance of Proposition 9.1 resides in the fact that there exists a subset of the space of piecewise polynomials of degree at most p having optimal approximation properties for harmonic functions. This subset is the space of piecewise harmonic polynomials of degree at most p, whose local dimension in 2D is $2p + 1$, while the local dimension of the space of complete polynomials of degree at most p is $(p + 1)(p + 2)/2$.

Design of the VE Trefftz Space
Here, we recall from [37] the definition of local and global nonconforming Trefftz spaces for the Laplace problem. Given $K \in \mathscr{T}_h$, define

$$\begin{aligned}
V_h^\Delta(K) := \{ v_h^\Delta \in H^1(K) \mid \Delta v_h^\Delta = 0 \text{ in } K, \\
\forall e \in \mathscr{E}^K \; \exists q_p^\Delta \in \mathbb{H}_p^\Delta(K) \text{ s.t. } \mathbf{n}_e \cdot \nabla v_{h\,|e}^\Delta = \mathbf{n}_e \cdot \nabla q_{p\,|e}^\Delta \}.
\end{aligned} \tag{9.6}$$

Equivalently, we are requiring that the Neumann traces of functions in $V_h^\Delta(K)$ belong to $\mathbb{P}_{p-1}(e)$ for all $e \in \mathscr{E}^K$. It is more convenient to define $V_h^\Delta(K)$ as in (9.6) in view of the general setting presented in Sect. 9.4 below.

The idea behind the definition of $V_h^\Delta(K)$ is as follows. According to the Trefftz gospel, we consider a local space, which consists of Trefftz functions, i.e., harmonic functions in our case. A possible way to pick a finite dimensional subspace $V_h^\Delta(K)$ is to require that, on each $e \in \mathscr{E}^K$, a suitable trace of any element in $V_h^\Delta(K)$ belongs to a suitable explicit finite element space. In our case, we require that the Neumann traces belong to $\mathbb{P}_{p-1}(e)$, the space of polynomials of degree at most $p-1$ ($\dim(\mathbb{P}_{p-1}(e)) = p$). By doing this, harmonic polynomials are included in the space $V_h^\Delta(K)$, which yields good approximation properties; see Proposition 9.3 below.

For any edge $e \in \mathscr{E}^K$, let $\{m_\alpha^e\}_{\alpha=1}^p$ be a basis of $\mathbb{P}_{p-1}(e)$. Consider the following set of linear functionals on $V_h^\Delta(K)$:

$$v_h^\Delta \in V_h^\Delta(K) \mapsto \frac{1}{h_e} \int_e v_h^\Delta m_\alpha^e \qquad \forall \alpha = 1, \ldots, p, \; \forall e \in \mathscr{E}^K. \tag{9.7}$$

Proposition 9.2 *The set of functionals in* (9.7) *is a set of unisolvent degrees of freedom.*

Proof The proof is standard and can be found, e.g., in [37, Section 3.1]. For the sake of completeness, we recall it here. The number of the functionals in (9.7) is smaller than or equal to the dimension of $V_h^\Delta(K)$. Thus, it suffices to show the unisolvence of such a set of functionals.

Assume that $v_h^\Delta \in V_h^\Delta(K)$ has the moments in (9.7) all equal to zero. Then, we have

$$\int_{\partial K} v_h^\Delta = 0.$$

Consequently, in order to prove the unisolvence, i.e., that $v_h^\Delta = 0$, it is enough to show that v_h^Δ has zero gradient. This is a consequence of an integration by parts, and the fact that v_h^Δ is harmonic, that $\mathbf{n}_K \cdot \nabla v_h^\Delta{}_{|e}$ is a polynomial of degree at most $p-1$ on each edge $e \in \mathscr{E}^K$, and that the functionals in (9.7) are zero:

$$|v_h^\Delta|_{1,K}^2 = -\int_K \Delta v_h^\Delta \, v_h^\Delta + \int_{\partial K} \mathbf{n}_K \cdot \nabla v_h^\Delta \, v_h^\Delta = \sum_{e \in \mathscr{E}^K} \int_e \mathbf{n}_K \cdot \nabla v_h^\Delta \, v_h^\Delta = 0. \tag{9.8}$$

$\square$

In the proof of Proposition 9.2, the choice of the local polynomial traces in the definition of (9.6) is important. More precisely, we fixed polynomial Neumann traces, for they appear in the integration by Parts (9.8). At the same time, the choice of the "Dirichlet"-type degrees of freedom in (9.7) is relevant as well, and will play a role in the construction of the global space.

We define the infinite dimensional, nonconforming spaces

$$H_p^{nc,\Delta}(\Omega, \mathscr{T}_h) := \left\{ v \in H^1(\Omega, \mathscr{T}_h) \, | \, \int_e [\![v]\!]_e \cdot \mathbf{n}_e \, m_\alpha^e = 0 \; \forall \alpha = 1, \ldots, p, \; \forall e \in \mathscr{E}_h^I \right\},$$

where the broken Sobolev spaces $H^1(\Omega, \mathscr{T}_h)$ and the jump operator $[\![\cdot]\!]$ are defined in (9.2) and (9.4), respectively, and we introduce the global nonconforming Trefftz virtual element space for the Laplace problem:

$$V_h^\Delta := \left\{ v_h^\Delta \in H_p^{nc,\Delta}(\Omega, \mathscr{T}_h) \, | \, v_h^\Delta{}_{|K} \in V_h^\Delta(K) \; \forall K \in \mathscr{T}_h \right\}.$$

We obtain the set of global degrees of freedom of the space v_h^Δ by patching the local ones in (9.7). In particular, we use the Dirichlet edge moments of (9.7) in the definition of the infinite dimensional, nonconforming space $H_p^{nc,\Delta}(\Omega, \mathcal{T}_h)$ in order to weakly impose the interelement continuity.

We summarize the main features of the space v_h^Δ, highlighting a "duality" between Dirichlet moments and local Neumann traces, as follows.

Trefftz spaces	**Contain**	Harmonic functions
Nonconformity	**Imposed through**	Dirichlet moments
Unis. of DOFs in (9.7)	**Implied by**	Pol. Neumann traces in (9.6)

For the design of the method, we define spaces that incorporate Dirichlet boundary conditions. More precisely, given $g \in H^{\frac{1}{2}}(\partial\Omega)$, we define

$$V_{h,g}^\Delta := \left\{ v_h^\Delta \in V_h^\Delta \mid \int_e (v_h^\Delta - g) m_\alpha^e = 0 \quad \forall e \in \mathcal{E}_h^B, \ \forall \alpha = 1, \dots, p \right\}.$$

The seminorm $|\cdot|_{1,\mathcal{T}_h}$ defined in (9.3) is actually a norm in $V_{h,0}^\Delta$.

Interpolation Properties
An interesting property of the nonconforming Trefftz virtual element space for the Laplace problem is that, given a harmonic function $u \in H^1(\Omega)$, there exists $u_I^\Delta \in V_h^\Delta$, which approximates u better than any *discontinuous*, piecewise harmonic polynomial of degree at most p. This property was originally shown in [37, Proposition 3.1].

Proposition 9.3 *Given a harmonic function $u \in H^1(\Omega)$, there exists $u_I^\Delta \in V_h^\Delta$ such that*

$$|u - u_I^\Delta|_{1,\mathcal{T}_h} \le |u - q_p^\Delta|_{1,\mathcal{T}_h} \qquad \forall q_p^\Delta \in \mathcal{S}_p^{0,\Delta}(\Omega, \mathcal{T}_h),$$

where the broken Sobolev seminorm is defined in (9.3)*.*

Proof Define $u_I^\Delta \in V_h^\Delta$ as the interpolant of u, i.e.,

$$\int_e (u - u_I^\Delta) m_\alpha^e = 0 \qquad \forall e \in \mathcal{E}_h, \ \forall \alpha = 1, \dots, p, \tag{9.9}$$

and let q_p^Δ be any function in $\mathcal{S}_p^{0,\Delta}(\Omega, \mathcal{T}_h)$. For any $K \in \mathcal{T}_h$, since both $(\mathbf{n}_K \cdot \nabla u_I^\Delta)_{|e}$ and $(\mathbf{n}_K \cdot \nabla q_p^\Delta)_{|e}$ belong to $\mathbb{P}_{p-1}(e)$ for all $e \in \mathcal{E}^K$, Definition (9.9) implies

$$\int_e \mathbf{n}_K \cdot \nabla u_I^\Delta (u - u_I^\Delta) = \int_e \mathbf{n}_K \cdot \nabla q_p^\Delta (u - u_I^\Delta) = 0 \qquad \forall e \in \mathcal{E}^K. \tag{9.10}$$

Therefore, by integrating by parts twice and using (9.10), as well as $\Delta u = \Delta u_I^\Delta = \Delta q_p^\Delta = 0$, we deduce that

$$
|u - u_I^\Delta|_{1,K}^2 = - \int_K \underbrace{\Delta(u - u_I^\Delta)}_{=0} (u - u_I^\Delta) + \sum_{e \in \mathscr{E}^K} \int_e \mathbf{n}_K \cdot \nabla(u - u_I^\Delta) (u - u_I^\Delta)
$$

$$
\overset{(9.10)}{=} - \int_K \underbrace{\Delta(u - q_p^\Delta)}_{=0} (u - u_I^\Delta) + \sum_{e \in \mathscr{E}^K} \int_e \mathbf{n}_K \cdot \nabla(u - q_p^\Delta) (u - u_I^\Delta)
$$

$$
= (\nabla(u - q_p^\Delta), \nabla(u - u_I^\Delta))_{0,K} \le |u - q_p^\Delta|_{1,K} |u - u_I^\Delta|_{1,K},
$$

whence the assertion follows.   □

Projections and Stabilizations

For future convenience, split

$$
a(u, v) = \sum_{K \in \mathscr{T}_h} a^K(u_{|K}, v_{|K}) := \sum_{K \in \mathscr{T}_h} (\nabla(u_{|K}), \nabla(v_{|K}))_{0,K}.
$$

Since the functions in the virtual element space v_h^Δ are not known in closed form, we cannot compute the local bilinear forms $a^K(\cdot, \cdot)$ applied to functions in v_h^Δ. Rather, we introduce computable bilinear forms as in the standard virtual element approach of [10].

To this aim, we need two main ingredients. The first one is a local projection into harmonic polynomial spaces. Define $\Pi_p^{\nabla,\Delta} : V_h^\Delta(K) \to \mathbb{H}_p(K)$ as follows:

$$
\begin{cases} a^K(v_h^\Delta - \Pi_p^{\nabla,\Delta} v_h^\Delta, q_p^\Delta) = 0 \\ \int_{\partial K} (v_h^\Delta - \Pi_p^{\nabla,\Delta} v_h^\Delta) = 0 \end{cases} \qquad \forall q_p^\Delta \in \mathbb{H}_p(K), \ \forall v_h^\Delta \in V_h^\Delta(K). \qquad (9.11)
$$

This is a typical VEM projection. Here, we project into the subspace of harmonic polynomials of degree at most p whereas, in the standard setting [10], the projection is into the full space of polynomials of degree at most p.

The definition of the degrees of freedom in (9.7) allows us to compute the projector $\Pi_p^{\nabla,\Delta}$. This is clear for the second condition in (9.11). As for the first condition, we observe that

$$
a^K(\Pi_p^{\nabla,\Delta} v_h^\Delta, q_p^\Delta) = a^K(v_h^\Delta, q_p^\Delta) = - \int_K v_h^\Delta \underbrace{\Delta q_p^\Delta}_{=0} + \sum_{e \in \mathscr{E}^K} \int_e v_h^\Delta \underbrace{\mathbf{n}_K \cdot \nabla q_p^\Delta}_{\in \mathbb{P}_{p-1}(e)},
$$

where the right-hand side is computable using (9.7).

The second ingredient is a computable stabilization on each element, which is needed since the bilinear form $a^K(\cdot, \cdot)$ is not computable on $\ker(\Pi_p^{\nabla, \Delta}) \times \ker(\Pi_p^{\nabla, \Delta})$. More precisely, for all $K \in \mathcal{T}_h$, let $S^{K, \Delta} : \ker(\Pi_p^{\nabla, \Delta}) \times \ker(\Pi_p^{\nabla, \Delta}) \to \mathbb{R}$ be a bilinear form that is computable via the degrees of freedom in (9.7) and that satisfies the following property: there exist two positive constant α_* and α^* independent of the mesh size such that

$$\alpha_* |v_h^\Delta|_{1,K}^2 \leq S^{K, \Delta}(v_h^\Delta, v_h^\Delta) \leq \alpha^* |v_h^\Delta|_{1,K}^2 \qquad \forall v_h^\Delta \in \ker(\Pi_p^{\nabla, \Delta}). \qquad (9.12)$$

We allow α_* and α^* to depend on the shape regularity constant γ in (9.1).

Then, we define

$$\begin{aligned} a_h^\Delta(u_h^\Delta, v_h^\Delta) &:= \sum_{K \in \mathcal{T}_h} a_h^{K, \Delta}(u_{h|K}^\Delta, v_{h|K}^\Delta) \\ &:= \sum_{K \in \mathcal{T}_h} a^K(\Pi_p^{\nabla, \Delta} u_{h|K}^\Delta, \Pi_p^{\nabla, \Delta} v_{h|K}^\Delta) \\ &\quad + S^{K, \Delta}((I - \Pi_p^{\nabla, \Delta}) u_{h|K}^\Delta, (I - \Pi_p^{\nabla, \Delta}) v_{h|K}^\Delta). \end{aligned}$$

As in [10, 37], the discrete bilinear form $a_h^\Delta(\cdot, \cdot)$ is coercive and continuous with constants $\min(1, \alpha_*)$ and $\max(1, \alpha^*)$.

Remark 9.1 We refer to [37, Section 3.3] for an explicit stabilization satisfying (9.12). There, stability bounds are proven, which are explicit also in terms of the polynomial degree. ∎

The Method
We have introduced all the ingredients needed for the design of the nonconforming Trefftz VEM for the Laplace problem:

$$\begin{cases} \text{find } u_h^\Delta \in V_{h,g}^\Delta \text{ such that} \\ a_h^\Delta(u_h^\Delta, v_h^\Delta) = 0 \qquad \forall v_h^\Delta \in V_{h,0}^\Delta. \end{cases} \qquad (9.13)$$

The well-posedness of the method follows from the coercivity and the continuity of the discrete bilinear form $a_h^\Delta(\cdot, \cdot)$.

Convergence Analysis
The abstract error analysis of method (9.13) is carried out in [37, Theorem 3.3] and is based on the second Strang's lemma. The result is that the error of the method is controlled by the sum of two terms: the best approximation error in the space of *discontinuous*, piecewise polynomials and a term that measures the nonconformity

of the method. The latter is expressed in terms of the bilinear form $\mathcal{N}_h : H^1(\Omega) \times H_p^{nc,\Delta}(\Omega, \mathcal{T}_h) \to \mathbb{R}$ defined as

$$\mathcal{N}_h(u, v) = \sum_{e \in \mathcal{E}_h} \int_e \nabla u \cdot [\![v]\!]. \tag{9.14}$$

Theorem 9.1 *Let u and u_h^Δ be the solutions to* (9.5) *and* (9.13)*, respectively. Under the shape regularity assumption* (9.1)*, the following bound is valid:*

$$|u - u_h|_{1, \mathcal{T}_h} \le \frac{\alpha^*}{\alpha_*} \left\{ 6 \inf_{q_p^\Delta \in \mathcal{S}_p^{0,\Delta}(\Omega, \mathcal{T}_h)} |u - q_p^\Delta|_{1, \mathcal{T}_h} + \sup_{0 \ne v_h^\Delta \in V_{h,0}^\Delta} \frac{\mathcal{N}_h(u, v_h^\Delta)}{|v_h^\Delta|_{1, \mathcal{T}_h}} \right\}.$$

As a consequence of Theorem 9.1, Proposition 9.1, and estimates of $\mathcal{N}_h$ derived by standard computations that are typical in nonconforming Galerkin methods, the convergence of the method follows; see [37, Section 3.5] for more details.

Corollary 9.1 *Let u and u_h^Δ be the solutions to* (9.5) *and* (9.13)*, respectively, with $u \in H^{s+1}(\Omega)$. Under the shape regularity assumption* (9.1) *with constant γ, the following convergence result is valid:*

$$|u - u_h|_{1, \mathcal{T}_h} \le ch^s \|u\|_{s+1, \Omega}.$$

Here, c is a positive constant, which depends on γ and on the polynomial degree p.

Overall, the nonconforming Trefftz VEM for the Laplace problem is a modification of the standard nonconforming VEM, in the sense that it encodes certain properties of the solution to the problem within the definition of the VE spaces. The resulting method has significantly fewer degrees of freedom than a standard VEM based on complete polynomial spaces, yet keeping the same convergence properties.

9.4 General Structure of Nonconforming Trefftz Virtual Element Methods

In this section, we pinpoint the structure lying behind the nonconforming Trefftz VEM for the Laplace equation and extend it to a more general and abstract setting. In particular, given a homogeneous, linear partial differential equation, we highlight which ideas we can extend to the new setting and which not. For the sake of presentation, we assume that the solution to the involved partial differential equation has to be sought in H^1-type Sobolev spaces with values in the field of complex numbers $\mathbb{C}$, although generalizations to other problems are possible as well.

The Continuous Problem

Let $\Omega \subset \mathbb{R}^2$ be a polygonal domain and $g \in H^s(\partial\Omega)$, where $s \in \mathbb{R}$. In typical cases, we have $s \in \{-1/2, 1/2\}$. Let $\mathscr{L} : H^1(\Omega) \to H^{-1}(\Omega)$ be a linear differential operator of the second order and $\mathrm{tr}_{\partial\Omega} : H^1(\Omega) \to H^s(\partial\Omega)$, s as above, a trace operator.

Consider the following *abstract* problem: find $u : \Omega \to \mathbb{C}$ such that

$$\begin{cases} \mathscr{L}u = 0 & \text{in } \Omega \\ \mathrm{tr}_{\partial\Omega}(u) = g & \text{on } \partial\Omega, \end{cases}$$

which, in weak formulation, reads

$$\begin{cases} \text{find } u \in V \text{ such that} \\ a(u, v) + b(u, v) = G(v) & \forall v \in W. \end{cases} \tag{9.15}$$

Here, we have introduced an affine space $V \subseteq H^1(\Omega)$, a test space $W \subseteq H^1(\Omega)$, sesquilinear forms $a : V \times W \to \mathbb{C}$ and $b : V \times W \to \mathbb{C}$, and an antilinear functional $G : W \to \mathbb{C}$. The form $b(\cdot, \cdot)$ and the functional $G(\cdot)$ accommodate the treatment of several types of boundary conditions. In particular, they are defined only on $\partial\Omega$. In what follows, we assume that $a(\cdot, \cdot)$, $\mathscr{L}$, and $\mathrm{tr}_{\partial\Omega}$ are related by the following identity: for sufficiently smooth u and v,

$$a(u, v) = -(\mathscr{L}u, v)_{0,\Omega} + G(v) - b(u, v). \tag{9.16}$$

After splitting

$$a(u, v) = \sum_{K \in \mathscr{T}_h} a^K(u_{|K}, v_{|K}),$$

we demand that, for all $K \in \mathscr{T}_h$ and all sufficiently smooth u and v,

$$a^K(u_{|K}, v_{|K}) = -(\mathscr{L}u_{|K}, v_{|K})_{0,K} + \sum_{e \in \mathscr{E}^K} (\mathrm{tr}^e(u_{|K}), v_{|K})_{0,e} - b^K(u_{|K}, v_{|K}), \tag{9.17}$$

where tr^e denotes the restriction to an edge $e \in \mathscr{E}_h$ of a trace operator tr, which is not necessarily of the same type as $\mathrm{tr}_{\partial\Omega}$, and where $b^K(\cdot, \cdot)$ is a local sequilinear form.

For example, in Sect. 9.3, we fixed

$$V = H^1_g(\Omega), \qquad W = H^1_0(\Omega), \qquad \mathscr{L} = \Delta, \qquad \mathrm{tr} = \text{Dirichlet trace operator},$$

$$a(u, v) = (\nabla u, \nabla v)_{0,\Omega}, \qquad b(u, v) = 0, \qquad G(v) = 0.$$

In the abstract formulation (9.15), we can deal with the boundary datum g by tuning either the trial space V or the right-hand side $G(v)$.

An Explicit Discontinuous Space

The basic tool in the construction of a Trefftz VEM is the existence of finite dimensional space consisting of globally discontinuous, piecewise smooth functions, which lie in the kernel of the operator $\mathscr{L}$ and possess suitable approximation properties for solutions to problem (9.15). We denote such approximation space by $\mathscr{S}_p^{0,\mathscr{L}}(\Omega, \mathscr{T}_h)$ and its local counterpart on every element K by $\mathscr{S}_p^{\mathscr{L}}(K)$, where the index $p \in \mathbb{N}$ is related to the local space dimension.

For instance, in Sect. (9.3), we considered as $\mathscr{S}_p^{0,\mathscr{L}}(\Omega, \mathscr{T}_h)$ the space of *discontinuous*, piecewise harmonic polynomials of degree at most p, which has optimal approximation properties in terms of the mesh size; see Proposition 9.1.

Design of the VE Trefftz Space

Given $K \in \mathscr{T}_h$, we define the local Trefftz virtual element space on K as follows:

$$
\begin{aligned}
V_h^{\mathscr{L}}(K) := \{v_h^{\mathscr{L}} \in H^1(K) \mid \; &\mathscr{L}(v_h^{\mathscr{L}}) = 0 \text{ in } K, \\
&\forall e \in \mathscr{E}^K \; \exists s_p^{\mathscr{L}} \in \mathscr{S}_p^{\mathscr{L}}(K) \text{ s.t. } \mathsf{tr}^e(v_h^{\mathscr{L}}{}_{|e}) = \mathsf{tr}^e(s_p^{\mathscr{L}}{}_{|e})\}.
\end{aligned}
\tag{9.18}
$$

The idea behind the construction of $V_h^{\mathscr{L}}(K)$ hinges upon the existence of an infinite dimensional, local space, which consists of functions in the kernel of the operator $\mathscr{L}$ (Trefftz space). We define the finite dimensional subspace $V_h^{\mathscr{L}}(K)$ by requiring that, on each $e \in \mathscr{E}^K$, a suitable trace belongs to a suitable explicit finite element space having good approximation properties for functions in the kernel of $\mathscr{L}$. More precisely, we require that the trace tr^e on each edge $e \in \mathscr{E}^K$ of any function in $V_h^{\mathscr{L}}(K)$ belongs to $\mathsf{tr}^e(\mathscr{S}_p^{\mathscr{L}}(K))$. In this way, we include the functions in $\mathscr{S}_p^{\mathscr{L}}(K)$ within the space $V_h^{\mathscr{L}}(K)$. The hope is that this will yield good interpolation properties of the local virtual element space.

In the setting of Sect. 9.3, we obtained a local space of harmonic functions, whose Neumann trace tr^e belongs to the space of Neumann traces of harmonic polynomials on every edge e, namely to $\mathbb{P}_{p-1}(e)$.

As for the degrees of freedom, for all edges $e \in \mathscr{E}^K$, let $\{m_\alpha^e\}_{\alpha=1}^{p^{\mathscr{L}}}$ be a basis of $\mathsf{tr}(\mathscr{S}_p^{\mathscr{L}}(K))$. Consider the following set of antilinear functionals on $V_h^{\mathscr{L}}(K)$:

$$
v_h^{\mathscr{L}} \in V_h^{\mathscr{L}}(K) \; \mapsto \; c(h_e) \int_e v_h^{\mathscr{L}} \overline{m}_\alpha^e \qquad \forall \alpha = 1, \ldots, p^{\mathscr{L}}, \; \forall e \in \mathscr{E}^K,
\tag{9.19}
$$

where $c(h_e)$ is a constant depending only on h_e and providing a suitable scaling of the degrees of freedom.

We aim at getting the following result.

Proposition 9.4 *The set of functionals in* (9.19) *is a set of unisolvent degrees of freedom.*

The number of the functionals in (9.19) is smaller than or equal to the dimension of $V_h^{\mathscr{L}}(K)$. Thus, in order to prove Proposition 9.4, it suffices to show the unisolvence of such a set of functionals.

Using assumption (9.17), we get

$$
a^K(v_h^{\mathscr{L}}, v_h^{\mathscr{L}}) + b^K(v_h^{\mathscr{L}}, v_h^{\mathscr{L}}) = -(\underbrace{\mathscr{L} v_h^{\mathscr{L}}}_{=0}, v_h^{\mathscr{L}})_{0,K} + \sum_{e \in \mathscr{E}^K} (\underbrace{\text{tr}^e(v_h^{\mathscr{L}})}_{\in \text{tr}^e(\mathscr{S}_p^{\mathscr{L}}(K))}, v_h^{\mathscr{L}})_{0,e} = 0.
$$

In general, this is not enough to prove the unisolvence of the DOFs. In case of the Dirichlet-Laplace problem, this is indeed sufficient; see Proposition 9.2. Notwithstanding, in the case of the Helmholtz problem in Sect. 9.5 below, we also need assumptions on the size of the mesh elements; see Proposition 9.7.

Importantly, while the definition of the local spaces is problem-dependent, as it depends on the elliptic operator and suitable traces associated with the problem under consideration, the choice of the degrees of freedom is fixed, and always consists of (suitably scaled) Dirichlet moments; see (9.19).

Next, we construct global nonconforming VE Trefftz spaces for problem (9.15). We define the infinite dimensional, nonconforming spaces

$$
H_p^{nc,\mathscr{L}}(\Omega, \mathscr{T}_h) := \left\{ v \in H^1(\Omega, \mathscr{T}_h) \,|\, \int_e [\![v]\!]_e \cdot \mathbf{n}_e \, \overline{m}_\alpha^e = 0 \;\; \forall \alpha = 1, \dots, p^{\mathscr{L}}, \; \forall e \in \mathscr{E}_h^I \right\},
$$

where $H^1(\Omega, \mathscr{T}_h)$ and $[\![\cdot]\!]$ are defined in (9.2) and (9.4), respectively. Then, the global nonconforming Trefftz virtual element space for problem (9.15) is defined as

$$
V_h^{\mathscr{L}} := \left\{ v_h^{\mathscr{L}} \in H_p^{nc,\mathscr{L}}(\Omega, \mathscr{T}_h) \,|\, v_h^{\mathscr{L}}|_K \in V_h^{\mathscr{L}}(K) \;\; \forall K \in \mathscr{T}_h \right\}.
$$

We obtain the set of global degrees of freedom of the space $V_h^{\mathscr{L}}$ by patching the local ones in (9.19). In particular, we use the Dirichlet edge moments in the definition of the infinite dimensional, nonconforming space $H_p^{nc,\mathscr{L}}(\Omega, \mathscr{T}_h)$ in order to weakly impose the interelement continuity.

We can summarize the Trefftz feature of the space $V_h^{\mathscr{L}}$ and the "duality" between Dirichlet moments and the local tr^e-type trace as follows.

Trefftz spaces	**Contain**	Functions in $\ker(\mathscr{L})$
Nonconformity	**Imposed through**	Dirichlet moments
Unis. of DOFs in (9.19)	**Implied by**	Traces of the type tr^e in (9.18)

As already mentioned, we incorporate the boundary conditions within the method either by enforcing them in the trial space or by suitably tuning the functional $G(\cdot)$ on the right-hand side.

Interpolation Properties

A desirable property of the local space $V_h^{\Delta}(K)$ is that the following result is valid.

Proposition 9.5 *Given a function $u \in H^1(\Omega)$ in the kernel of $\mathscr{L}$, there exists $u_I^{\mathscr{L}} \in V_h^{\mathscr{L}}$ such that*

$$|u - u_I^{\mathscr{L}}|_{1,\mathscr{T}_h} \leq c|u - s_p^{\mathscr{L}}|_{1,\mathscr{T}_h} \qquad \forall s_p^{\mathscr{L}} \in \mathscr{S}_p^{0,\mathscr{L}}(\Omega, \mathscr{T}_h),$$

where the broken Sobolev seminorm is defined in (9.3) *and c is a positive constant independent of the mesh size.*

In particular, we wish that functions in the kernel of $\mathscr{L}$ can be approximated in $V_h^{\mathscr{L}}$ not worse than in the explicit space $\mathscr{S}_p^{0,\mathscr{L}}(\Omega, \mathscr{T}_h)$. For the Laplace problem the constant is 1; see Proposition 9.3. Moreover, we expect that u_I in Proposition 9.5 can be defined as the interpolant of u through the degrees of freedom in (9.19).

In what follows, we assume that the local sesquilinear forms $b^K(\cdot, \cdot)$ appearing in (9.17) satisfy

$$\begin{aligned} &\text{whenever } s_p^{\mathscr{L}} \in \mathscr{S}_p^{\mathscr{L}}(K), \; v_h^{\mathscr{L}} \in V_h^{\mathscr{L}}(K) \\ &\text{then} \quad b^K(s_p^{\mathscr{L}}, v_h^{\mathscr{L}}) \text{ and } b^K(v_h^{\mathscr{L}}, s_p^{\mathscr{L}}) \quad \text{are computable.} \end{aligned} \tag{9.20}$$

Projections and Stabilizations

Recall the splitting

$$a(u, v) = \sum_{K \in \mathscr{T}_h} a^K(u_{|K}, v_{|K}).$$

We consider the following discretizations of a and a^K:

$$\begin{aligned} a_h^{\mathscr{L}}(u_h^{\mathscr{L}}, v_h^{\mathscr{L}}) &:= \sum_{K \in \mathscr{T}_h} a_h^{K,\mathscr{L}}(u_{h\,|K}^{\mathscr{L}}, v_{h\,|K}^{\mathscr{L}}) \\ &:= \sum_{K \in \mathscr{T}_h} a^K(\Pi_p^{\nabla,\mathscr{L}} u_{h\,|K}^{\mathscr{L}}, \Pi_p^{\nabla,\mathscr{L}} v_{h\,|K}^{\mathscr{L}}) + S^{K,\mathscr{L}}((I - \Pi_p^{\nabla,\mathscr{L}})u_{h\,|K}^{\mathscr{L}}, (I - \Pi_p^{\nabla,\mathscr{L}})v_{h\,|K}^{\mathscr{L}}), \end{aligned}$$

where we have to define the projector $\Pi_p^{\nabla,\mathscr{L}}$ and the sequilinear form $S^{K,\mathscr{L}}(\cdot, \cdot)$.

The operator $\Pi_p^{\nabla,\mathscr{L}} : V_h^{\mathscr{L}}(K) \rightarrow \mathscr{S}_p^{\mathscr{L}}(K)$ is the projection operator with respect to the local sesquilinear form $a^K(\cdot,\cdot)$. More precisely, for all $K \in \mathscr{T}_h$, we set

$$\begin{cases} a^K(\Pi_p^{\nabla,\mathscr{L}} v_h^{\mathscr{L}} - v_h^{\mathscr{L}}, s_p^{\mathscr{L}}) = 0 & \forall v_h^{\mathscr{L}} \in V_h^{\mathscr{L}}(K), \forall s_p^{\mathscr{L}} \in \mathscr{S}_p^{\mathscr{L}}(K) \\ +\text{computable conditions for the uniqueness of } \Pi_p^{\nabla,\mathscr{L}} v_h^{\mathscr{L}}. \end{cases}$$

In the nonconforming Trefftz VEM for the Laplace equation, the computable condition for uniqueness was on the average on ∂K; see (9.11).

The computability of $\Pi_p^{\nabla,\mathscr{L}}$ follows from the definitions of the local spaces $V_h^{\mathscr{L}}(K)$ and the degrees of freedom in (9.19), and from the property (9.20):

$$a^K(s_p^{\mathscr{L}}, \Pi_p^{\nabla,\mathscr{L}} v_h^{\mathscr{L}}) = a^K(s_p^{\mathscr{L}}, v_h^{\mathscr{L}})$$

$$= -\underbrace{(\mathscr{L} s_p^{\mathscr{L}}, v_h^{\mathscr{L}})_{0,K}}_{=0} + \sum_{e \in \mathscr{E}^K} (\underbrace{\text{tr}^e(s_p^{\mathscr{L}})}_{\in \text{tr}^e(\mathscr{S}_p^{\mathscr{L}}(K))}, v_h^{\mathscr{L}})_{0,e} - \underbrace{b^K(s_p^{\mathscr{L}}, v_h^{\mathscr{L}})}_{\text{(9.20)}}.$$

The choice of the degrees of freedom in (9.19) allows us to compute the L^2-edge projector $\Pi_p^{e,\mathscr{L}} : V_h^{\mathscr{L}}(K)_{|e} \rightarrow \text{tr}^e(\mathscr{S}_p^{\mathscr{L}}(K)_{|e})$, which is defined as

$$(\Pi_p^{e,\mathscr{L}} v_h^{\mathscr{L}}{}_{|e} - v_h^{\mathscr{L}}{}_{|e}, \text{tr}^e(s_p^{\mathscr{L}}{}_{|e}))_{0,e} \qquad \forall e \in \mathscr{E}^K, \ \forall v_h^{\mathscr{L}} \in V_h^{\mathscr{L}}, \ \forall s_p^{\mathscr{L}} \in \mathscr{S}_p^{\mathscr{L}}(\Omega, \mathscr{T}_h).$$

We need this projector for the discretization of the boundary terms, i.e., the sesquilinear form $b(\cdot,\cdot)$ and the right-hand side $G(\cdot)$ appearing in (9.15). Such terms do not appear in the Dirichlet-Laplace setting of Sect. 9.3. They would appear in the case of the Laplace problem with inhomogenous Neumann boundary conditions.

For future convenience, we introduce the approximations

$$b_h^{\mathscr{L}}(u_h^{\mathscr{L}}, v_h^{\mathscr{L}}) \approx b(u_h^{\mathscr{L}}, v_h^{\mathscr{L}}) \qquad G_h^{\mathscr{L}}(v_h^{\mathscr{L}}) \approx G(v_h^{\mathscr{L}}).$$

As for the stabilization $S^{K,\mathscr{L}}$, we require it to satisfy two properties: it has to be computable via the DOFs and it must lead to a well-posed problem. For instance, in Sect. 9.3, we considered stabilizations leading to coercive and continuous discrete sesquilinear forms. This is not necessary in all situations. We will see in Sect. 9.5 below that, in the Helmholtz case, the coercivity is not required.

The Method
With $\hat{V}_h^{\mathscr{L}} \subseteq V_h^{\mathscr{L}}$ and $\hat{W}_h^{\mathscr{L}} \subseteq W_h^{\mathscr{L}}$, which may or not contain information about the boundary conditions depending on the choice of V, W, b, and G in (9.15), the nonconforming Trefftz VEM for problem (9.15) reads

$$
\begin{cases}
\text{find } u_h^{\mathscr{L}} \in \hat{V}_h^{\mathscr{L}} \text{ such that} \\
a_h^{\mathscr{L}}(u_h^{\mathscr{L}}, v_h^{\mathscr{L}}) + b_h^{\mathscr{L}}(u_h^{\mathscr{L}}, v_h^{\mathscr{L}}) = G_h^{\mathscr{L}}(v_h^{\mathscr{L}}) \qquad \forall v_h^{\mathscr{L}} \in \hat{W}_h^{\mathscr{L}}.
\end{cases}
\tag{9.21}
$$

The well-posedness of the method relies on suitable properties of the stabilization $S^{K,\mathscr{L}}(\cdot,\cdot)$.

Convergence Analysis
Here, we state the Strang-type result that would be the target of the error analysis for method (9.21).

Theorem 9.2 *Let u and $u_h^{\mathscr{L}}$ be the solutions to (9.15) and (9.21), respectively. Under the shape regularity assumption (9.1), the following bound is valid:*

$$
|u - u_h^{\mathscr{L}}|_{1,\mathscr{T}_h} \leq c(S^{K,\mathscr{L}}) \{A + B + C\},
$$

where

- *$c(S^{K,\mathscr{L}})$ is a constant possibly depending on the stabilization $S^{K,\mathscr{L}}$;*
- *A is the best approximation of u in the explicit space $\mathscr{S}_p^{0,\mathscr{L}}(\Omega, \mathscr{T}_h)$, i.e.,*

$$
\inf_{s_p^{\mathscr{L}} \in \mathscr{S}_p^{0,\mathscr{L}}(\Omega, \mathscr{T}_h)} \|u - s_p^{\mathscr{L}}\|_{NORM},
$$

  where $\|\cdot\|_{NORM}$ is a suitable norm;
- *B is a term addressing the nonconformity of the global space;*
- *C is a term involving the approximation of the boundary terms.*

In the light of Theorem 9.2, we could deduce an optimal convergence result from best approximation estimates in $\mathscr{S}_p^{0,\mathscr{L}}(\Omega, \mathscr{T}_h)$, and bounds on the nonconformity at interior and boundary edges.

In the setting of the nonconforming Trefftz VEM for the Laplace problem, we had $C = 0$ and

$$
c(S^{K,\mathscr{L}}) = \frac{\alpha^*}{\alpha_*}, \quad A = \inf_{q_p^{\Delta} \in \mathscr{S}_p^{0,\Delta}(\Omega, \mathscr{T}_h)} |u - q_p^{\Delta}|_{1,\mathscr{T}_h}, \quad B = \sup_{0 \neq v_h^{\Delta} \in V_{h,0}^{\Delta}} \frac{\mathscr{N}_h(u, v_h^{\Delta})}{|v_h^{\Delta}|_{1,\mathscr{T}_h}},
$$

where $\mathscr{N}_h(u, v)$ is defined in (9.14).

An important tool in the proof of Theorem 9.2 is Proposition 9.5, which allows us to absorb a best approximation term in $\mathscr{S}_p^{0,\Delta}(\Omega, \mathscr{T}_h)$ in the term A.

Common and Problem-Related Features

We conclude this section with a summary of the common features in nonconforming Trefftz VEM and the differences depending on the problem under consideration.

Common features:

– in the definition of the local spaces, the existence of an underlying finite dimensional Trefftz space and the characterization through a given edge trace;
– the definition of Dirichlet-type degrees of freedom;
– the fact that we can control best interpolation errors in VEM spaces by best approximation errors in explicit discontinuous spaces.

Problem-related features:

– in the definition of the local spaces, the kind of trace used in the characterization;
– how to prove the unisolvence of the DOFs (additional assumptions might be needed);
– required properties on the stabilization form;
– the definition and the well-posedness of the projections;
– the imposition of the boundary conditions.

9.5 The Nonconforming Trefftz Virtual Element Method for the Helmholtz Problem

In this section, according to the framework established in Sect. 9.4, we describe the construction and the main steps of the analysis of a nonconforming Trefftz VEM for the Helmholtz equation. We follow the framework of [38, 39]. However, we propose a slightly different analysis, based on milder assumptions on the stabilization form.

The Continuous Problem

Let $\Omega \subset \mathbb{R}^2$ be a polygonal domain, $g \in H^{-\frac{1}{2}}(\partial\Omega)$, and $k > 0$. Introduce the following space of complex-valued functions and the following sesquilinear forms:

$$V := H^1(\Omega), \qquad a(\cdot, \cdot) := (\nabla\cdot, \nabla\cdot)_{0,\Omega} - k^2(\cdot, \cdot)_{0,\Omega}, \qquad b(\cdot, \cdot) := ik(\cdot, \cdot)_{0,\partial\Omega}.$$

We consider the following Helmholtz problem endowed with impedance boundary conditions: find a sufficiently smooth $u : \Omega \to \mathbb{C}$ such that

$$\begin{cases} \Delta u + k^2 u = 0 & \text{in } \Omega \\ iku + \mathbf{n}_\Omega \cdot \nabla u = g & \text{on } \partial\Omega, \end{cases}$$

which in weak formulation reads

$$\begin{cases} \text{find } u \in V \text{ such that} \\ a(u, v) + b(u, v) = (g, v)_{0, \partial\Omega} \qquad \forall v \in V. \end{cases} \tag{9.22}$$

Observe that (9.22) falls in the broader abstract setting (9.15).

An Explicit Discontinuous Space

Let $p \in \mathbb{N}$. Given $\{\mathscr{T}_h\}_h$ a sequence of polygonal decompositions over Ω as in Sect. 9.1, we introduce the corresponding sequence of piecewise plane waves over $\mathscr{T}_h$:

$$\mathbb{PW}_p(\Omega, \mathscr{T}_h) := \left\{ w_p \in L^2(\Omega) \mid w_{p|K} \in \mathbb{PW}_p(K) \; \forall K \in \mathscr{T}_h \right\},$$

where, for all $K \in \mathscr{T}_h$, the local space of plane waves $\mathbb{PW}_p(K)$ is constructed as follows.

Introduce the set of indices $\mathscr{J} := \{1, \ldots, 2p + 1\}$ and the set of pairwise different and normalized directions $\{\mathbf{d}_\ell\}_{\ell \in \mathscr{J}}$. In each $K \in \mathscr{T}_h$, consider the set of plane waves

$$w_\ell(\mathbf{x}) := e^{ik\mathbf{d}_\ell \cdot (\mathbf{x} - \mathbf{x}_K)} \qquad \forall \ell \in \mathscr{J}, \; \forall \mathbf{x} \in K, \tag{9.23}$$

and define

$$\mathbb{PW}_p(K) := \text{span}\{w_\ell, \ell \in \mathscr{J}\}.$$

These plane waves belong to the kernel of the Helmholtz operator, i.e.,

$$\Delta w_p + k^2 w_p = 0 \qquad \forall w_p \in \mathbb{PW}_p(K), \; \forall K \in \mathscr{T}_h.$$

Introduce the weighted broken norms and seminorms

$$| \cdot |^2_{s, \mathscr{T}_h} := \sum_{K \in \mathscr{T}_h} | \cdot |^2_{s, K}, \qquad \| \cdot \|^2_{s, k, \mathscr{T}_h} := \sum_{K \in \mathscr{T}_h} \| \cdot \|^2_{s, k, K}$$

$$\text{with } \| \cdot \|^2_{s, k, K} := \sum_{j=0}^{s} k^{2(s-j)} | \cdot |^2_{j, K} \; \forall K \in \mathscr{T}_h.$$

For future convenience, we demand that the directions $\mathbf{d}_\ell$ are uniformly separated. More precisely, we ask that

there exists $\delta \in (0, 1]$ such that the angle between $\mathbf{d}_{\ell_1}$ and $\mathbf{d}_{\ell_2}$

is larger than or equal to $\delta(2\pi/p)$ for every $\ell_1, \ell_2 \in \mathscr{J}, \ell_1 \neq \ell_2$. $\qquad$ (9.24)

This assumption allows us to recall the following approximation property of discontinuous, piecewise plane waves for functions in the kernel of the Helmholtz operator; see, e.g., [42, Theorem 5.2].

Proposition 9.6 *Let $u \in H^{s+1}(\Omega)$, $s > 0$, belong to the kernel of the Helmholtz operator. Under the shape-regularity assumption* (9.1) *with constant γ and assumption* (9.24) *on the directions $\mathbf{d}_\ell$, for all $L \in \mathbb{R}$ with $1 \leq L \leq \min(p, s)$, there exists $w_p \in \mathbb{PW}_p(\Omega, \mathscr{T}_h)$ such that the following estimate is valid: for every $0 \leq j \leq L$,*

$$\|u - w_p\|_{j,k,\mathscr{T}_h} \leq c_{pw}(hk)h^{L+1-j}\|u\|_{L+1,k,\Omega},$$

where

$$c_{pw}(t) := Ce^{bt}(1 + t^{j+q+8}), \qquad b, C \in \mathbb{R}.$$

The constant $C > 0$ depends on p, j, L, γ, and the directions $\{\mathbf{d}_\ell\}$, but is independent of k, h, and u. On the other hand, the constant b depends on the geometric properties of the mesh only. Observe that $c_{pw}(hk)$ remains bounded as $h \to 0$.

The importance of Proposition 9.6 resides in the fact that there exists a finite dimensional space, whose dimension is lower than that of the piecewise polynomial space of degree at most p, locally $2p+1$ instead of $(p+1)(p+2)/2$ in 2D, but with the same approximation rates for functions in the kernel of the Helmholtz operator.

Design of the VE Trefftz Space
Here, we recall from [38] the definition of local and global nonconforming Trefftz spaces for the Helmholtz problem. Given $K \in \mathscr{T}_h$, for all $e \in \mathscr{E}^K$, introduce the space

$$\mathbb{PW}_p(e) := \{w_\ell^e \mid w_\ell^e = w_{p|e} \text{ for some } w_p \in \mathbb{PW}_p(K)\}.$$

We have that $\dim(\mathbb{PW}_p(e)) \leq \dim(\mathbb{PW}_p(K))$. More precisely, the dimension of $\mathbb{PW}_p(e)$ gets smaller whenever the restrictions to e of two basis functions of $\mathbb{PW}_p(K)$ coincide. Below, we use the notation $N_{\text{PW}}^e := \dim(\mathbb{PW}_p(e))$.

Given $K \in \mathscr{T}_h$ and $e \in \mathscr{E}^K$, introduce the local impedance trace operators

$$\text{tr}_I^K(v) := ikv + \mathbf{n}_K \cdot \nabla v, \quad \text{tr}_I^e(v) := ikv_{|e} + \mathbf{n}_e \cdot (\nabla v)_{|e} \qquad \forall v \in H^1(K),$$

and define the local space

$$
\begin{aligned}
V_h^H(K) := \{v_h^H \in H^1(K) \mid \Delta v_h^H + k^2 v_h^H = 0 \text{ in } K, \\
\forall e \in \mathscr{E}^K \exists w_p \in \mathbb{PW}_p(K) \text{ s.t. } \text{tr}_I^e(v_h^H) = \text{tr}_I^e(w_p)\}.
\end{aligned}
\tag{9.25}
$$

Equivalently, we are requiring that the impedance trace of functions in $V_h^H(K)$ belongs to $\mathbb{PW}_p(e)$ for all $e \in \mathscr{E}^K$.

The idea behind the definition of $V_h^H(K)$ is exactly the one described in Sect. 9.4 after formula (9.18), with $\mathsf{tr}^e = \mathsf{tr}_I^e$. The inclusion of $\mathbb{PW}_p(K)$ within $V_h^H(K)$ yields good interpolation properties of the space; see Proposition 9.8 below.

For all edges $e \in \mathscr{E}^K$, let $\{w_\alpha^e\}_{\alpha=1}^{N_{\mathrm{PW}}^e}$ be a basis of $\mathbb{PW}_p(e)$. Consider the following set of antilinear functionals on $V_h^H(K)$:

$$v_h^H \in V_h^H(K) \;\mapsto\; \frac{1}{h_e} \int_e v_h^H \overline{w_\alpha^e} \qquad \forall \alpha = 1, \ldots, N_{\mathrm{PW}}^e, \; \forall e \in \mathscr{E}^K. \qquad (9.26)$$

So far, the construction falls in the abstract setting detailed in Sect. 9.4. The first big difference with respect to the case of the Laplace problem in Sect. 9.3 is in the proof of the unisolvence of the degrees of freedom, which requires the following additional assumption: for all $K \in \mathscr{T}_h$,

$$k \text{ is such that } k^2 \text{ is not a Dirichlet-Laplace eigenvalue on } K. \qquad (9.27)$$

As discussed, e.g., in [38, Section 3.1], the condition (9.27) boils down to a threshold condition on the mesh size.

Proposition 9.7 *Under assumption* (9.27)*, the set of functionals* (9.26) *is a set of unisolvent degrees of freedom.*

Proof The proof can be found, e.g., in [38, Lemma 3.1]. For the sake of completeness, we recall it here. The number of the functionals in (9.26) is smaller than or equal to the dimension of $V_h^\Delta(K)$. Thus, it suffices to show the unisolvence of such a set of functionals.

Let $v_h^H \in V_h^H(K)$ be such that the functionals (9.26) are zero in v_h^H. An integration by parts and the properties of functions in $V_h^H(K)$ yield

$$|v_h^H|_{1,K}^2 - k^2 \|v_h^H\|_{0,K}^2 - \mathrm{i}k\|v_h^H\|_{0,\partial K}^2$$

$$= \underbrace{\int_K v_h^H \overline{(-\Delta v_h^H - k^2 v_h^H)}}_{=0} + \sum_{e \in \mathscr{E}^K} \int_e v_h^H \underbrace{\overline{\mathsf{tr}_I^K(v_h^H)}}_{\in \mathbb{PW}_p(e)} = 0.$$

By taking the imaginary part on both sides, we deduce that v_h^H has zero trace on ∂K. Since v_h^H also satisfies $\Delta v_h^H + k^2 v_h^H = 0$, assumption (9.27) implies that $v_h^H = 0$, whence the unisolvence follows. $\qquad\square$

In the present case, the local forms b^K in (9.17) of the abstract setting of Sect. 9.4 are given by

$$b^K(u_h^H, v_h^H) := \mathrm{i}k \int_{\partial K} u_h^H \overline{v_h^H}.$$

The forms $b^K(\cdot, \cdot)$ fulfil assumption (9.20) for all $K \in \mathscr{T}_h$.

Next, we construct global nonconforming Trefftz VE spaces for problem (9.22). Recalling the definition of the broken Sobolev spaces $H^1(\Omega, \mathscr{T}_h)$ and of the jump operator $[\![\cdot]\!]$ in (9.2) and (9.4), respectively, and that $\{w_\alpha^e\}_{\alpha=1}^{N_{\mathrm{PW}}^e}$ denotes a basis of $\mathbb{PW}_p(e)$, we set

$$H_p^{nc,H}(\Omega, \mathscr{T}_h) := \left\{ v \in H^1(\Omega, \mathscr{T}_h) \,|\, \int_e [\![v]\!]_e \cdot \mathbf{n}_e \, \overline{w_\alpha^e} = 0 \;\; \forall \alpha = 1, \ldots, N_{\mathrm{PW}}^e, \forall e \in \mathscr{E}_h^I \right\}.$$

Then, we define the global nonconforming Trefftz virtual element space for the problem (9.22) as

$$V_h^H := \left\{ v_h^H \in H_p^{nc,H}(\Omega, \mathscr{T}_h) \,|\, v_h^H{}_{|K} \in V_h^H(K) \;\forall K \in \mathscr{T}_h \right\}.$$

We obtain the set of global degrees of freedom of the space v_h^H by patching the local ones in (9.26). In particular, we use the Dirichlet edge moments in the definition of the infinite dimensional, nonconforming space $H_p^{nc,H}(\Omega, \mathscr{T}_h)$ in order to weakly impose the interelement continuity.

As in Sect. 9.4, we summarize the features of the space $V_h^H(K)$, including the "duality" between Dirichlet moments and the local impedance traces tr_I^K as follows.

Trefftz spaces	**Contain**	Functions in $\ker(\Delta + k^2)$
Nonconformity	**Imposed through**	Dirichlet moments
Unis. of DOFs in (9.19)	**Implied by**	Traces of the type tr_I^K in (9.25)

Differently from the Laplace case, the boundary conditions are incorporated within the weak formulation of the problem, and not in the trial and test spaces.

Interpolation Properties

Similarly to the Laplace case, we can approximate any target function $u \in H^1(\Omega)$ by functions in the space v_h^H better than by functions in the space of discontinuous, piecewise plane waves. This was shown in [38, Theorem 4.2].

Proposition 9.8 *Let assumptions* (9.1)*,* (9.24)*, and* (9.27) *be valid. Moreover, let hk be sufficiently small; see [38, equation (4.17)]. Given a function $u \in H^1(\Omega)$, there exists $u_I^H \in V_h^H$ such that*

$$\|u - u_I^H\|_{1,k,\mathscr{T}_h} \le c_{BA}(hk)\|u - w_p\|_{1,k,\mathscr{T}_h} \qquad \forall w_p \in \mathbb{PW}_p(\Omega, \mathscr{T}_h),$$

where

$$c_{BA}(t) := 2c_1(1 + c_2 t^2)(2 + c_3 t^2),$$

for three positive constants c_1, c_2, and c_3.

Proof The proof is rather technical. Therefore, we refer to [38, Theorem 4.2] for details. There, the constants c_1, c_2, and c_3 are provided explicitly. We can define the function u_I^H as the interpolant of u through the degrees of freedom (9.26).   □

The target function u in the statement of Proposition 9.8 does not need to belong to the kernel of the Helmholtz operator. We only require that it belongs to $H^1(\Omega)$. Clearly, we need to require that u belongs to the kernel of the Helmholtz operator if we want to combine Proposition 9.6 together with Proposition 9.8 in order to recover high-order approximation rates in virtual element spaces.

Projections and Stabilizations
Recall the splitting

$$a(u, v) = \sum_{K \in \mathscr{T}_h} a^K(u_{|K}, v_{|K}).$$

We consider the following discretizations of a and a^K:

$$\begin{aligned}
a_h^H(u_h^H, v_h^H) &:= \sum_{K \in \mathscr{T}_h} a_h^{K,H}(u_{h\,|K}^H, v_{h\,|K}^H) \\
&:= \sum_{K \in \mathscr{T}_h} a^K(\Pi_p^{\nabla,H} u_{h\,|K}^H, \Pi_p^{\nabla,H} v_{h\,|K}^H) \\
&\quad + S^{K,H}((I - \Pi_p^{\nabla,H})u_{h\,|K}^H, (I - \Pi_p^{\nabla,H})v_{h\,|K}^H),
\end{aligned} \tag{9.28}$$

where we still have to define the projector $\Pi_p^{\nabla,H}$ and the sesquilinear form $S^{K,H}(\cdot, \cdot)$. The operator $\Pi_p^{\nabla,H} : V_h^H(K) \to \mathbb{PW}_p(K)$ is the projection operator with respect to the local sesquilinear form $a^K(\cdot, \cdot)$. More precisely, for all $K \in \mathscr{T}_h$, we set

$$a^K(\Pi_p^{\nabla,H} v_h^H - v_h^H, w_p) = 0 \quad \forall v_h^H \in V_h^H(K), \forall w_p \in \mathbb{PW}_p(K).$$

The computability of such a projector follows from the definition of the local spaces $V_h^H(K)$ and of the degrees of freedom in (9.19):

$$
\begin{aligned}
a^K(\Pi_p^{\nabla,H} v_h^H, w_\ell) &= a^K(v_h^H, w_\ell) \\
&= -(v_h^H, \underbrace{(\Delta + k^2)w_\ell}_{=0})_{0,K} + \sum_{e \in \mathscr{E}^K} (v_h^H, \underbrace{\mathrm{tr}_I^e(w_\ell)}_{\in \mathrm{tr}_I^e(\mathbb{PW}_p(K))})_{0,e} - \mathrm{i}k \sum_{e \in \mathscr{E}^K} (v_h^H, \underbrace{w_\ell}_{\in \mathrm{tr}_I^e(\mathbb{PW}_p(K))})_{0,e}.
\end{aligned}
$$

In order to have the well-posedness of the projector $\Pi_p^{\nabla,H}$, we do not need to impose any additional computable condition. Rather, we need to require a threshold condition on the mesh size that, in addition to (9.27), also guarantees that k^2 is not a Neumann-Laplace eigenvalue. In particular, the following result is valid; see [38, Proposition 3.1] and [44, Propositions 2.1 and 2.3].

Proposition 9.9 *Let the assumptions* (9.1)*,* (9.24)*, and* (9.27) *be valid. Moreover, assume that h is sufficiently small, so that k^2 is smaller that the first Neumann-Laplace eigenvalue on each $K \in \mathscr{T}_h$. Then, the projector $\Pi_p^{\nabla,H}$ is well-defined and continuous. More precisely, there exists a positive constant $\beta(h_K k)$, uniformly bounded away from zero as $h_K k \to 0$, such that*

$$
\|\Pi_p^{\nabla,H} v_h^H\|_{1,k,K} \le \frac{1}{\beta(h_K k)} \|v_h^H\|_{1,k,K} \qquad \forall v_h^H \in V_h^H(K), \, \forall K \in \mathscr{T}_h. \tag{9.29}
$$

By defining

$$
\beta_{\min} := \min_{K \in \mathscr{T}_h} \beta(h_K k), \tag{9.30}
$$

inequality (9.29) implies

$$
\|\Pi_p^{\nabla,H} v_h^H\|_{1,k,K} \le \frac{1}{\beta_{\min}} \|v_h^H\|_{1,k,K} \qquad \forall v_h^H \in V_h^H(K), \, \forall K \in \mathscr{T}_h. \tag{9.31}
$$

We observe that the choice of the degrees of freedom (9.26) also allows us to compute the L^2-edge projector $\Pi_p^{e,H} : V_h^H(K)_{|e} \to \mathrm{tr}_I^e(\mathbb{PW}_p(K))_{|e}$ into traces of plane waves, which is defined as follows: for all $e \in \mathscr{E}^K$,

$$
(\Pi_p^{e,H} v_{h\,|e}^H - v_{h\,|e}^H, \mathrm{tr}_I^e(w_p))_{0,e} = 0 \quad \forall v_h^H \in V_h^H(K), \, \forall w_p \in \mathbb{PW}_p(K). \tag{9.32}
$$

This projector is needed for the discretization of the boundary terms, i.e., the sesquilinear form $b(\cdot, \cdot)$ and the right-hand side $(g, \cdot)_{0,\partial\Omega}$ appearing in (9.22). We introduce

$$
\begin{aligned}
b_h^H(u_h^H, v_h^H) &:= \mathrm{i}k \sum_{e \in \mathscr{E}_h^B} (\Pi_p^{e,H} u_{h|e}^H, \Pi_p^{e,H} v_{h|e}^H)_{0,e}, \\
(g, v_h^H)_{0,\partial\Omega} &\approx \sum_{e \in \mathscr{E}_h^B} (g, \Pi_p^{e,H} v_{h|e}^H)_{0,e}.
\end{aligned}
\tag{9.33}
$$

With respect to the abstract setting in Sect. 9.4, the form $G(\cdot)$ is here given by

$$
G(v_h^H) := \int_{\partial\Omega} g \overline{v_h^H}.
$$

The last ingredient we need is a stabilization $S^{K,H}(\cdot, \cdot)$ for all $K \in \mathscr{T}_h$, which is computable via the degrees of freedom (9.26) and satisfies certain properties. So far, we have recalled the setting of [38]. Here, we weaken the assumptions on the stabilization demanded there, and yet deduce the well-posedness and convergence for the method.

More precisely, for all $K \in \mathscr{T}_h$, we require that

$$
S^{K,H}(v_h^H, v_h^H) \geq |v_h^H|_{1,K}^2 - (1 + C_S)k^2 \|v_h^H\|_{0,K}^2 \qquad \forall v_h^H \in \ker(\Pi_p^{\nabla,H}) \tag{9.34}
$$

and the continuity

$$
|S^{K,H}(u_h^H, v_h^H)| \leq C_C \|u_h^H\|_{1,k,K} \|v_h^H\|_{1,k,K} \qquad \forall u_h^H, v_h^H \in \ker(\Pi_p^{\nabla,H}), \tag{9.35}
$$

where C_S and C_C are two positive constants independent of k, with C_S a sufficiently small, positive constant to be fixed below; see Eq. (9.41).

With these choices, we are in a position to prove the following "weak" version of the Gårding inequality.

Proposition 9.10 *For every $K \in \mathscr{T}_h$, let the stabilization $S^{K,H}(\cdot, \cdot)$ satisfy* (9.34). *Then, the following Gårding-type inequality is valid:*

$$
\begin{aligned}
\mathbb{RE}[a_h^H(v_h^H, v_h^H) + b_h^H(v_h^H, v_h^H)] &+ 2k^2 \|v_h^H\|_{0,\Omega}^2 \\
+ C_S k^2 \sum_{K \in \mathscr{T}_h} \|(I - \Pi_p^{\nabla,H})v_h^H\|_{0,K}^2 &\geq \|v_h^H\|_{1,k,\mathscr{T}_h}^2 \quad \forall v_h^H \in V_h^H,
\end{aligned}
\tag{9.36}
$$

where C_S is the same constant as in (9.34).

Proof The proof follows along the same lines as the one of [44, Proposition 4.2].
For the sake of completeness, we carry out the details here. From (9.33), (9.28), and
simple algebra, we get

$$\mathbb{RE}[a_h^H(v_h^H, v_h^H) + b_h^H(v_h^H, v_h^H)] + 2k^2\|v_h^H\|_{0,\Omega}^2 = a_h^H(v_h^H, v_h^H) + 2k^2\|v_h^H\|_{0,\Omega}^2$$

$$= \sum_{K\in\mathscr{T}_h} \left\{ a^K(\Pi_p^{\nabla,H}v_h^H, \Pi_p^{\nabla,H}v_h^H) + 2k^2\|\Pi_p^{\nabla,H}v_h^H\|_{0,K}^2 \right\}$$

$$+ \sum_{K\in\mathscr{T}_h} \left\{ S^{K,H}((I-\Pi_p^{\nabla,H})v_h^H, (I-\Pi_p^{\nabla,H})v_h^H) + 2k^2\|(I-\Pi_p^{\nabla,H})v_h^H\|_{0,K}^2 \right\}$$

$$+ \sum_{K\in\mathscr{T}_h} 4k^2\mathbb{RE}\left[\int_K \Pi_p^{\nabla,H}v_h^H \overline{(I-\Pi_p^{\nabla,H})v_h^H} \right].$$

Then, using (9.34) and simple calculations, we deduce

$$\mathbb{RE}[a_h^H(v_h^H, v_h^H) + b_h^H(v_h^H, v_h^H)] + 2k^2\|v_h^H\|_{0,\Omega}^2$$

$$\geq \sum_{K\in\mathscr{T}_h} \left\{ |\Pi_p^{\nabla,H}v_h^H|_{1,K}^2 + k^2\|\Pi_p^{\nabla,H}v_h^H\|_{0,K}^2 \right\}$$

$$+ \sum_{K\in\mathscr{T}_h} \left\{ |(I-\Pi_p^{\nabla,H})v_h^H|_{1,K}^2 + (1-C_S)k^2\|(I-\Pi_p^{\nabla,H})v_h^H\|_{0,K}^2 \right\}$$

$$+ \sum_{K\in\mathscr{T}_h} 2\,\mathbb{RE}\left[\int_K \nabla\Pi_p^{\nabla,H}v_h^H \overline{\nabla(I-\Pi_p^{\nabla,H})v_h^H} \right]$$

$$+ \sum_{K\in\mathscr{T}_h} 2k^2\mathbb{RE}\left[\int_K \Pi_p^{\nabla,H}v_h^H \overline{(I-\Pi_p^{\nabla,H})v_h^H} \right].$$

Thus, we have

$$\mathbb{RE}[a_h^H(v_h^H, v_h^H) + b_h^H(v_h^H, v_h^H)] + 2k^2\|v_h^H\|_{0,\Omega}^2 + C_S k^2 \sum_{K\in\mathscr{T}_h} \|(I-\Pi_p^{\nabla,H})v_h^H\|_{0,K}^2$$

$$\geq \sum_{K\in\mathscr{T}_h} \left\{ |\Pi_p^{\nabla,H}v_h^H|_{1,K}^2 + |(I-\Pi_p^{\nabla,H})v_h^H|_{1,K}^2 \right.$$

$$\left. +2\,\mathbb{RE}\left[\int_K \nabla\Pi_p^{\nabla,H}v_h^H \cdot \overline{\nabla(I-\Pi_p^{\nabla,H})v_h^H} \right] \right\}$$

$$+ \sum_{K\in\mathscr{T}_h} \left\{ k^2\|\Pi_p^{\nabla,H}v_h^H\|_{0,K}^2 + k^2\|(I-\Pi_p^{\nabla,H})v_h^H\|_{0,K}^2 \right.$$

$$+2k^2 \mathbb{RE}\left[\int_K \Pi_p^{\nabla,H} v_h^H \overline{(I - \Pi_p^{\nabla,H})v_h^H}\right]\Big\}$$

$$= \sum_{K \in \mathscr{T}_h} \left(|v_h^H|_{1,K}^2 + k^2 \|v_h^H\|_{0,K}^2\right) = \|v_h^H\|_{1,k,\mathscr{T}_h}^2,$$

whence the assertion follows. $\square$

Assuming (9.35), we also get the continuity of the discrete sesquilinear form $a_h^H(\cdot, \cdot)$ in (9.28).

Proposition 9.11 *Under assumption* (9.35)*, the discrete sesquilinear form* $a_h^H(\cdot, \cdot)$ *in* (9.28) *satisfies*

$$a_h^H(u_h^H, v_h^H) \le \frac{1 + C_C(1 + \beta_{\min})^2}{\beta_{\min}^2} \|u_h^H\|_{1,k,\mathscr{T}_h} \|v_h^H\|_{1,k,\mathscr{T}_h}, \tag{9.37}$$

where C_C is the constant in (9.35) *and $\beta_{\min}$ is defined in* (9.30)*.*

Proof We have

$$a_h^H(u_h^H, v_h^H) = \sum_{K \in \mathscr{T}_h} \Big\{ a^K(\Pi_p^{\nabla,H} u_h^H, \Pi_p^{\nabla,H} v_h^H)$$

$$+ S^{K,H}\left((I - \Pi_p^{\nabla,H})u_h^H, (I - \Pi_p^{\nabla,H})v_h^H\right)\Big\}$$

$$\overset{(9.35)}{\le} \sum_{K \in \mathscr{T}_h} \Big\{ \|\Pi_p^{\nabla,H} u_h^H\|_{1,k,K} \|\Pi_p^{\nabla,H} v_h^H\|_{1,k,K}$$

$$+ C_C \|(I - \Pi_p^{\nabla,H})u_h^H\|_{1,k,K} \|(I - \Pi_p^{\nabla,H})v_h^H\|_{1,k,K}\Big\}$$

$$\overset{(9.31)}{\le} \sum_{K \in \mathscr{T}_h} \frac{1 + C_C(1 + \beta_{\min})^2}{\beta_{\min}^2} \|u_h^H\|_{1,k,K} \|v_h^H\|_{1,k,K}$$

$$\le \frac{1 + C_C(1 + \beta_{\min})^2}{\beta_{\min}^2} \|u_h^H\|_{1,k,\mathscr{T}_h} \|v_h^H\|_{1,k,\mathscr{T}_h}.$$

$\square$

Remark 9.2 In [38], the assumption on the stabilization $S^{K,H}(\cdot, \cdot)$ was slightly stronger than (9.34), namely we required

$$S^{K,H}(v_h^H, v_h^H) \ge |v_h^H|_{1,K}^2 - k^2 \|v_h^H\|_{0,K}^2 \qquad \forall v_h^H \in \ker(\Pi_p^{\nabla,H}). \tag{9.38}$$

This assumption results in the following stronger version of the Gårding inequality:

$$\mathbb{RE}[a_h^H(v_h^H, v_h^H) + b_h^H(v_h^H, v_h^H)] + 2k^2\|v_h^H\|_{0,\Omega}^2 \geq \|v_h^H\|_{1,k,\mathcal{T}_h}^2 \quad \forall v_h^H \in V_h^H.$$

As we will see in Theorem 9.3 below, the present weaker setting still allows us to derive an abstract error analysis for the method (9.39) below. The advantage of the new setting is that the design of a computable stabilization $S^{K,H}(\cdot, \cdot)$ becomes easier.

For a stronger version of Theorem 9.3 below, relying on the assumption (9.38) instead of (9.36), we refer to [38, Theorem 4.3].

The Method
We have introduced all the ingredients needed for the design of the nonconforming Trefftz VEM for the Helmholtz problem:

$$\begin{cases} \text{find } u_h^H \in V_h^H \text{ such that} \\ a_h^H(u_h^H, v_h^H) + b_h^H(u_h^H, v_h^H) = (g, \Pi_p^{e,H} v_h^H) \quad \forall v_h^H \in V_h^H. \end{cases} \quad (9.39)$$

The well-posedness of the method follows by using a Schatz-type argument, as detailed in Theorem 9.3 below.

Convergence Analysis
In the following theorem, we prove well-posedness and abstract error estimates for method (9.39). In particular, the error of the method is controlled by two terms: a best approximation estimate in discontinuous, piecewise plane wave spaces and an estimate of the approximation of the boundary condition g. For simplicity, an additional term involving the nonconformity of the method, which is hidden in the proof, is not explicitly reported. Proposition 9.8 is used in order to absorb an interpolation error term within the best approximation in discontinuous, piecewise plane wave spaces.

Theorem 9.3 *Let the solution u to (9.5) be in $H^2(\Omega)$. Let the number of local plane wave directions in (9.23) be $2p + 1$, with $p \geq 2$. Let the assumptions (9.1) and (9.27) on the meshes, the assumption (9.24) on the local plane wave directions, and the assumptions (9.34) and (9.35) on the local stabilization forms be valid. Additionally, we require that hk^2 is sufficiently small; see [38, eqt. (4.65)]. Then, there exists a unique solution u_h^H to the method (9.39), and the following a priori estimate is valid:*

$$\|u - u_h^H\|_{1,k,\mathcal{T}_h} \lesssim c_1(h,k)\|u - w_p\|_{1,k,\mathcal{T}_h} + h\,c_2(h,k)|u - w_p|_{2,\mathcal{T}_h}$$

$$+ h^{\frac{1}{2}}c_2(h,k)\Big(\sum_{e \in \mathcal{E}_h^B} \|g - \Pi_p^{e,H}g\|_{0,e}^2\Big)^{1/2} \quad \forall w_p \in \mathbb{PW}_p(\Omega, \mathcal{T}_h).$$

Indeed, we can express c_1 and c_2 explicitly; see the statement of [38, Theorem 4.3]. Moreover, $hk \lesssim 1$ implies that

$$c_1(h, k) \lesssim (1 + C_C)(1 + k), \qquad c_2(h, k) \lesssim 1 + k.$$

Proof The proof follows along the same lines as that of [38, Theorem 4.3]. For this reason, we only present the modifications that are due to the validity of the weaker Gårding-type inequality (9.36); see Remark 9.2.

We first observe that, for all $u_I^H \in V_h^H$,

$$\|u - u_h^H\|_{1,k,\mathscr{T}_h} \le \|u - u_I^H\|_{1,k,\mathscr{T}_h} + \|u_I^H - u_h^H\|_{1,k,\mathscr{T}_h}.$$

We focus on the second term on the right-hand side. For the sake of simplicity, write $\delta_h := u_I^H - u_h^H$. By applying the Gårding-type inequality (9.36), we deduce

$$\|\delta_h\|_{1,k,\mathscr{T}_h}^2 \le \mathbb{RE}(a_h^H(\delta_h, \delta_h) + b_h^H(\delta_h, \delta_h)) + 2k^2\|\delta_h\|_{0,\Omega}^2 \\ + C_S k^2 \sum_{K \in \mathscr{T}_h} \|(I - \Pi_p^{\nabla,H})\delta_h\|_{0,K}^2 =: I + II + III. \tag{9.40}$$

The terms I and II are dealt with exactly as in [38]. As for the term III, we proceed as follows:

$$III = C_S k^2 \sum_{K \in \mathscr{T}_h} \|(I - \Pi_p^{\nabla,H})\delta_h\|_{0,K}^2 \le C_S \|(I - \Pi_p^{\nabla,H})\delta_h\|_{1,k,\mathscr{T}_h}^2$$

$$\le 2C_S(\|\delta_h\|_{1,k,\mathscr{T}_h}^2 + \|\Pi_p^{\nabla,H}\delta_h\|_{1,k,\mathscr{T}_h}^2) \overset{(9.29)}{\le} 2C_S\left(\frac{1}{\beta^2} + 1\right)\|\delta_h\|_{1,k,\mathscr{T}_h}^2.$$

Picking C_S in (9.34), e.g., such that

$$C_S \le \frac{1}{8}\frac{\beta_{\min}^2}{\beta_{\min}^2 + 1}, \tag{9.41}$$

with $\beta_{\min}$ as in (9.30), we get

$$III \le \frac{1}{4}\|\delta_h\|_{1,k,\mathscr{T}_h}^2.$$

Thus, we absorb the term III within the left-hand side of (9.40) yielding

$$\frac{3}{4}\|\delta_h\|_{1,k,\mathscr{T}_h}^2 \le I + II.$$

The proof follows then along the same lines as that of [38, Theorem 4.3] with $\alpha_h = 3/4$. Therefore, we omit further details.   □

Remark 9.3 In view of Theorem 9.3, the approximation properties in Proposition 9.6 and some algebra, we deduce that the optimal h-convergence is valid under suitable regularity assumptions on the solution u to problem (9.22) and on the boundary datum g. We refer to [38, Theorem 4.4] for a precise statement.

Overall, the nonconforming Trefftz VEM for the Helmholtz problem is a modification of the standard nonconforming VEM, in the sense that it encodes certain properties of the solution to the problem within the definition of the VE spaces. The resulting method has significantly fewer degrees of freedom than a standard VEM based on complete polynomial spaces, yet keeping the same convergence properties. Differently from the case of the Laplace problem, we need to resort to nonpolynomial underlying spaces (plane wave spaces, in our presentation).

9.6 Stability and Dispersion Analysis for the Nonconforming Trefftz VEM for the Helmholtz Equation

Here, we address the issue of the dispersion analysis for the nonconforming Trefftz VEM for the Helmholtz equation detailed in Sect. 9.5.

Amongst the difficulties in approximating time-harmonic wave propagation problems, we highlight the so-called *pollution effect* [9], which describes the widening discrepancy between the best approximation error and the discretization error for large values of the wave number k.

This effect is directly linked to *numerical dispersion*, representing the failure of the numerical method to reproduce the correct oscillating behaviour of the analytical solution. More precisely, for a given wave number k, a continuous problem with plane wave solution is considered. Its numerical approximation delivers an approximate solution, which can be interpreted as a wave with a deviated wave number k_n. We can measure this mismatch of the continuous and discrete wave numbers k and k_n separately in terms of the real part and the imaginary part with the following interpretation. The term $|\operatorname{Re}(k - k_n)|$ represents the deviation (shift) of the phase (*dispersion*), and the term $|\operatorname{Im}(k - k_n)| = |\operatorname{Im}(k_n)|$ refers to the damping of the amplitude (*dissipation*) of the computed discrete solution. Moreover, the difference $|k - k_n|$ measures the total amount of dispersion and dissipation and is sometimes referred to as *total dispersion* or *total error*.

We summarize the general strategy for a dispersion analysis in the following two steps:

1. Consider the discretization scheme of the numerical method applied to $-\Delta u - k^2 u = 0$ in $\mathbb{R}^2$ using infinite meshes which are invariant under a discrete group of translations. Due to translation invariance, it is then possible to reduce the infinite mesh to a finite one.

2. Given a plane wave with wave number k travelling in a fixed direction, seek a so-called discrete *Bloch wave solution*, which can be regarded as a generalization of the given continuous plane wave based on the underlying approximating spaces, and determine for which (discrete) wave number k_n this Bloch wave solution actually solves the discrete variational formulation. This procedure leads to small nonlinear eigenvalue problems, which need to be solved.

In the framework of standard conforming finite element methods (FEM) for the Helmholtz problem, a full dispersion analysis was done in [20] for dimensions one to three. Furthermore, in [9] it was shown that the pollution effect can be avoided in 1D, but not in higher dimensions, and a generalized pollution-free FEM in 1D was constructed. Moreover, we highlight the work in [31], where a link between the results of the dispersion analysis and the numerical analysis was established for finite elements, and the work in [1], where quantitative, fully explicit estimates for the behaviour and decay rates of the dispersion error were derived in dependence on the order of the method relative to the mesh size and the wave number. Also in the context of nonconforming methods, dispersion analyses have been performed for the discontinuous Galerkin (DG)-FEM [2, 3], the discontinuous Petrov-Galerkin (DPG) method [26], and the plane wave discontinuous Galerkin method (PWDG) [24]. Recently, a dispersion analysis for hybridized DG (HDG)-methods has been carried out in [27], including an explicit derivation of the wave number error for lowest order single face HDG methods.

Here, we numerically investigate the dispersion and dissipation properties of the nonconforming Trefftz VEM (ncTVEM), and compare the results to those obtained in [24] for PWDG, and to those for standard polynomial based FEM.

The remainder of the section is organized as follows. In Sect. 9.6.1, we describe the abstract setting for the dispersion analysis. Then, in Sect. 9.6.2, we specify the set of basis functions and the sesquilinear forms defining the numerical discretization schemes for the ncTVEM. Finally, in Sect. 9.6.3, we numerically study the dispersion and dissipation and we compare the results with those obtained with other methods.

9.6.1   Abstract Dispersion Analysis

In this section, we fix the abstract setting for the dispersion analysis employing the notation of [24].

To this purpose, in order to remove possible dependencies of the dispersion on the boundary conditions of the problem, we consider the Helmholtz problem (9.22) on the unbounded domain $\Omega = \mathbb{R}^2$. Let $\mathscr{T}_h := \{K\}$ be a translation-invariant partition of Ω into polygons with mesh size $h := \max_{K \in \mathscr{T}_h} h_K$, where $h_K := \text{diam}(K)$, i.e., there exists a set of elements $\widehat{K}_1, \ldots, \widehat{K}_r$, $r \in \mathbb{N}$, such that the whole infinite mesh can be covered in a nonoverlapping way by shifts of the "reference" patch $\widehat{K} := \bigcup_{j=1}^r \widehat{K}_j$. In other words, this assumption implies the existence of translation
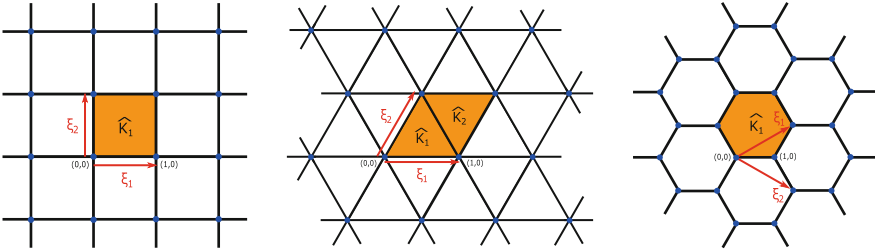
Fig. 9.1 Examples of translation-invariant meshes with the corresponding translation vectors $\boldsymbol{\xi}_1$ and $\boldsymbol{\xi}_2$: regular Cartesian mesh, triangular mesh, and hexagonal mesh, from *left* to *right*

vectors $\boldsymbol{\xi}_1, \boldsymbol{\xi}_2 \in \mathbb{R}^2$, such that every element $K \in \mathcal{T}_h$ can be written as a linear combination with coefficients in $\mathbb{N}_0$ of one of the reference polygons $\widehat{K}_\ell$, $\ell = 1, \ldots, r$. Some examples for translation-invariant meshes are shown in Fig. 9.1. Moreover, we denote by $\mathcal{E}^K$ the set of edges belonging to K.

Let $u(\mathbf{x}) = e^{ik\mathbf{d}\cdot\mathbf{x}}$, $\mathbf{d} \in \mathbb{R}^2$ with $|\mathbf{d}| = 1$ be a plane wave with wave number k and traveling in direction $\mathbf{d}$. We denote by $\mathcal{V}_n$ the global approximation space resulting from the discretization of (9.22) using a Galerkin based numerical method, and by $\widehat{\mathcal{V}}_n \subset \mathcal{V}_n$ a minimal subspace generating $\mathcal{V}_n$ by translations with

$$\boldsymbol{\xi}_{\mathbf{n}} := n_1 \boldsymbol{\xi}_1 + n_2 \boldsymbol{\xi}_2, \quad \mathbf{n} = (n_1, n_2) \in \mathbb{Z}^2. \tag{9.42}$$

More precisely, depending on the structure of the method, $\widehat{\mathcal{V}}_n$ is determined as follows.

1. *Vertex-related* basis functions: In this case, $\widehat{\mathcal{V}}_n$ is the span of all basis functions related to a minimal set of vertices $\{v_i\}_{i=1}^{\lambda^{(0)}}$, $\lambda^{(0)} \in \mathbb{N}$, such that all the other mesh vertices are obtained by translations with $\boldsymbol{\xi}_n$ of the form (9.42). An example is the FEM.
2. *Edge-related* basis functions: Similarly as above, the space $\widehat{\mathcal{V}}_n$ is in this case the span of all basis functions related to a minimal set of edges $\{\eta_i\}_{i=1}^{\lambda^{(1)}}$, $\lambda^{(1)} \in \mathbb{N}$, such that all the other edges of the mesh are obtained by translations with $\boldsymbol{\xi}_n$ of the form (9.42). This is, for instance, the case of the ncTVEM [38, 39].
3. *Element-related* basis functions: Here, the space $\widehat{\mathcal{V}}_n$ is simply given as the span of all basis functions related to a minimal set of elements $\{\sigma_i\}_{i=1}^{\lambda^{(2)}}$, $\lambda^{(2)} \in \mathbb{N}$, such that all other elements of the mesh are obtained by a translation with a vector $\boldsymbol{\xi}_n$ of the form (9.42). One representative of this category is the PWDG [25, 28].

In the following, we will refer to these minimal sets of vertices $\{v_i\}_{i=1}^{\lambda^{(0)}}$, edges $\{\eta_i\}_{i=1}^{\lambda^{(1)}}$, and elements $\{\sigma_i\}_{i=1}^{\lambda^{(2)}}$ as *fundamental sets* of vertices, edges, and elements, respectively.

As a direct consequence, every $v_n \in \mathscr{V}_n$ can be written as

$$v_n(\mathbf{x}) = \sum_{\mathbf{n} \in \mathbb{Z}^2} \widehat{v}_n(\mathbf{x} - \boldsymbol{\xi}_{\mathbf{n}}), \quad \widehat{v}_n \in \widehat{\mathscr{V}}_n.$$

Next, we define the discrete *Bloch wave* with wave number k_n and traveling in direction $\mathbf{d}$ by

$$u_n(\mathbf{x}) = \sum_{\mathbf{n} \in \mathbb{Z}^2} e^{\mathrm{i}k_n \mathbf{d} \cdot \boldsymbol{\xi}_{\mathbf{n}}} \widehat{u}_n(\mathbf{x} - \boldsymbol{\xi}_{\mathbf{n}}), \tag{9.43}$$

where $\widehat{u}_n \in \widehat{\mathscr{V}}_n$, and $k_n \in \mathbb{C}$ with $\mathrm{Re}(k_n) > 0$. Note that, since $\widehat{u}_n \in \widehat{\mathscr{V}}_n$, the infinite sum in (9.43) is in fact finite. Furthermore, given $\mathbf{d} \in \mathbb{R}^2$ with $|\mathbf{d}| = 1$, the Bloch wave u_n in (9.43) satisfies

$$u_n(\mathbf{x} + \boldsymbol{\xi}_{\boldsymbol{\ell}}) = e^{\mathrm{i}k_n \mathbf{d} \cdot \boldsymbol{\xi}_{\boldsymbol{\ell}}} u_n(\mathbf{x}),$$

for all $\boldsymbol{\ell} \in \mathbb{Z}^2$. This property follows directly by using the definition of the Bloch wave:

$$u_n(\mathbf{x} + \boldsymbol{\xi}_{\boldsymbol{\ell}}) = \sum_{\mathbf{n} \in \mathbb{Z}^2} e^{\mathrm{i}k_n \mathbf{d} \cdot \boldsymbol{\xi}_{\mathbf{n}}} \widehat{u}_n(\mathbf{x} + \boldsymbol{\xi}_{\boldsymbol{\ell}} - \boldsymbol{\xi}_{\mathbf{n}}) = \sum_{n \in \mathbb{Z}^2} e^{\mathrm{i}k_n \mathbf{d} \cdot \boldsymbol{\xi}_{\mathbf{n}}} \widehat{u}_n(\mathbf{x} - \boldsymbol{\xi}_{\mathbf{n}-\boldsymbol{\ell}})$$

$$= e^{\mathrm{i}k_n \mathbf{d} \cdot \boldsymbol{\xi}_{\boldsymbol{\ell}}} \sum_{\mathbf{m} \in \mathbb{Z}^2} e^{\mathrm{i}k_n \mathbf{d} \cdot \boldsymbol{\xi}_{\mathbf{m}}} \widehat{u}_n(\mathbf{x} - \boldsymbol{\xi}_{\mathbf{m}}) = e^{\mathrm{i}k_n \mathbf{d} \cdot \boldsymbol{\xi}_{\boldsymbol{\ell}}} u_n(\mathbf{x}).$$

Therefore, Bloch waves can be regarded as discrete counterparts, based on the approximation spaces, of continuous plane waves.

We introduce the global (continuous) sesquilinear form

$$a(u, v) := \sum_{K \in \mathscr{T}_h} a^K(u, v) := \sum_{K \in \mathscr{T}_h} \left[\int_K \nabla u \cdot \overline{\nabla v} - k^2 \int_K u \overline{v} \right] \quad \forall u, v \in H^1(\mathbb{R}^2), \tag{9.44}$$

and we denote by $a_n(\cdot, \cdot)$ the global discrete sesquilinear form defining the numerical method under consideration. In Sect. 9.6.2 below, we will specify $\widehat{\mathscr{V}}_n$ and $a_n(\cdot, \cdot)$ for the ncTVEM and the PWDG.

Next, we define the discrete wave number $k_n \in \mathbb{C}$ as follows.

Definition 9.1 Given $k > 0$ and $\mathbf{d} \in \mathbb{R}^2$ with $|\mathbf{d}| = 1$, the *discrete wave number* $k_n \in \mathbb{C}$ is the number with minimal $|k - k_n|$, for which a discrete Bloch wave u_n of the form (9.43) is a solution to the discrete problem

$$a_n(u_n, \widehat{v}_n) = 0 \quad \forall \widehat{v}_n \in \widehat{\mathscr{V}}_n. \tag{9.45}$$

Due to the scaling invariance of the mesh, we can assume that $h = 1$. The wave number k on a mesh with $h = 1$ corresponds to the wave number $k_0 = \frac{k}{h_0}$ on a mesh with mesh size h_0.

Having this, the general procedure in the dispersion analysis now consists in finding those discrete wave numbers $k_n \in \mathbb{C}$ and coefficients $\widehat{u}_n \in \widehat{\mathscr{V}}_n$, for which a Bloch wave solution of the form (9.43) satisfies (9.45), and to measure the deviation of k_n from k afterwards. This strategy results in solving small nonlinear eigenvalue problems. In fact, by plugging the Bloch wave ansatz (9.43) into (9.45) and using the sesquilinearity of $a_n(\cdot, \cdot)$, we obtain

$$\sum_{\mathbf{n} \in \mathbb{Z}^2} e^{ik_n \mathbf{d} \cdot \boldsymbol{\xi}_\mathbf{n}} a_n(\widehat{u}_n(\cdot - \boldsymbol{\xi}_\mathbf{n}), \widehat{v}_n) = 0 \quad \forall \widehat{v}_n \in \widehat{\mathscr{V}}_n. \tag{9.46}$$

Let $\{\widehat{\chi}_s\}_{s=1}^{\Xi} \subset \widehat{\mathscr{V}}_n$ be a set of basis functions for the space $\widehat{\mathscr{V}}_n$ that are related to fundamental elements, vertices, or edges, depending on the method. Then, we can expand $\widehat{u}_n$ in terms of this basis as

$$\widehat{u}_n = \sum_{t=1}^{\Xi} u_t \widehat{\chi}_t.$$

Plugging this ansatz into (9.46), testing with $\widehat{\chi}_s$, $s = 1, \ldots, \Xi$, and interchanging the sums (this can be done since the infinite sum over $\mathbf{n}$ is in fact finite) yields

$$\sum_{t=1}^{\Xi} u_t \left(\sum_{\mathbf{n} \in \mathbb{Z}^2} e^{ik_n \mathbf{d} \cdot \boldsymbol{\xi}_\mathbf{n}} a_n(\widehat{\chi}_t(\cdot - \boldsymbol{\xi}_\mathbf{n}), \widehat{\chi}_s) \right) = 0 \quad \forall s = 1, \ldots, \Xi, \tag{9.47}$$

which can be represented as

$$\sum_{t=1}^{\Xi} \boldsymbol{T}_{s,t}(k_n) u_t = 0 \quad \forall s = 1, \ldots, \Xi, \tag{9.48}$$

with

$$\boldsymbol{T}_{s,t}(k_n) := \sum_{\mathbf{n} \in \mathbb{Z}^2} e^{ik_n \mathbf{d} \cdot \boldsymbol{\xi}_\mathbf{n}} a_n(\widehat{\chi}_t(\cdot - \boldsymbol{\xi}_\mathbf{n}), \widehat{\chi}_s). \tag{9.49}$$

The matrix problem corresponding to (9.48) has the form

$$\boldsymbol{T}(k_n) \mathbf{u} = \mathbf{0}, \tag{9.50}$$

where $\boldsymbol{T} : \mathbb{C} \to \mathbb{C}^{\Xi \times \Xi}$ is defined via (9.49), and $\boldsymbol{u} = (u_1, \ldots, u_\Xi)^T \in \mathbb{C}^\Xi$. We highlight that $\boldsymbol{T}$ is a holomorphic map and (9.50) is a small nonlinear eigenvalue

problem, which can be solved using, e.g., an iterative method as done in [24], or a direct method based on a rational interpolation procedure [47] or on a contour integral approach [5, 12]. For the numerical experiments presented in Sect. 9.6.3, we will make use of the latter, which we will denote by *contour integral method* (CIM) in the sequel. Due to the use of plane wave related basis functions, deriving an exact analytical solution to (9.50) is not possible even for the lowest order case.

9.6.2 Minimal Generating Subspaces

In this section, we specify the minimal generating subspaces $\widehat{\mathscr{V}}_n$, the corresponding sets of basis functions $\{\widehat{\chi}_s\}_{s=1}^{\Xi}$, and the sequilinear forms $a_n(\cdot, \cdot)$ for the ncTVEM and the PWDG [25, 28]. The basis functions for these two methods are edge-related and element-related, respectively. In Figs. 9.2, 9.3, and 9.4, the stencils related to the fundamental sets of vertices, edges, and elements are depicted for these three methods and the meshes in Fig. 9.1.

Before doing that, we recall some notation from Sect. 9.5. Let $\{\mathbf{d}_j\}_{j=1}^p$, $p = 2q + 1$, $q \in \mathbb{N}$, be a set of equidistributed plane wave directions. We denote by

$$w_j(\mathbf{x}) := e^{\mathrm{i}k\mathbf{d}_j \cdot \mathbf{x}}, \quad j = 1, \ldots, p, \tag{9.51}$$

the plane wave with wave number k and traveling along the direction $\mathbf{d}_j$. Furthermore, for every $K \in \mathscr{T}_h$, we set $w_j^K := w_{j|_K}$, and we introduce the bulk place waves space

$$\mathbb{PW}_p(K) := \mathrm{span}\{w_j^K, \ j = 1, \ldots, p\}.$$

The Case of ncTVEM
Let now $\{\eta_i\}_{i=1}^{\lambda^{(1)}}$ be a fundamental set of edges. Then, the set of basis functions $\{\widehat{\chi}_s^{(1)}\}_{s=1}^{\Xi}$ spanning the minimal generating subspace $\widehat{\mathscr{V}}_n^{(1)}$ is given by the union of the canonical basis functions related to $\{\eta_i\}_{i=1}^{\lambda^{(1)}}$. More precisely, for $s \leftrightarrow (i, j)$, $i \in \{1, \ldots, \lambda^{(1)}\}$ and $j \in \mathscr{J}_{\eta_i}$, i.e. we identify s with the edge index i and the index j associated with the j-th plane wave basis function on this edge as above,

$$\widehat{\chi}_s^{(1)} = \widehat{\chi}_{(i,j)}^{(1)} := \Psi_{(\eta_i, j)},$$

where $\Psi_{(\eta_i, j)}$ is defined elementwise as follows. If $K \in \mathscr{T}_h$ is an element abutting the edge η_i, then $\Psi_{(\eta_i, j)|_{\eta_i}}$ coincides with the local canonical basis function associated with the (global) edge η_i and the j-th orthogonalized edge plane wave basis function; otherwise $\Psi_{(\eta_i, j)}$ is zero. Clearly, $\Xi = \sum_{i=1}^{\lambda^{(1)}} \widetilde{p}_{\eta_i}$.

As for the sesquilinear form $a_n^{(1)}(\cdot, \cdot)$, it coincides with that in (9.28), where the projector $\Pi_p^{e,H}$ is defined in (9.32).

The Case of PWDG

For PWDG, we refer to [24] for a full dispersion analysis. For the sake of completeness, we shortly recall here the definitions of the minimal generating subspace and the sesquilinear form adapted to our setting.

The global approximation space $\mathscr{V}_n^{(2)}$ is given by

$$\mathscr{V}_n^{(2)} := \{v_n \in L^2(\mathbb{R}^2) : \ v_{n|K} \in \mathbb{PW}_p(K) \quad \forall K \in \mathscr{T}_h\}.$$

Moreover, the global sesquilinear form $a_n^{(2)}(\cdot, \cdot)$ is defined by

$$
\begin{aligned}
a_n^{(2)}(u_n, v_n) := \ & \sum_{K \in \mathscr{T}_h} a^K(u_n, v_n) - \int_{\mathscr{E}_h} [\![u_n]\!] \cdot \{\overline{\nabla_n v_n}\} \\
& - \frac{\beta}{ik} \int_{\mathscr{E}_h} [\![\nabla_n u_n]\!] \, [\![\overline{\nabla_n v_n}]\!] - \int_{\mathscr{E}_h} \{\nabla_n u_n\} \cdot [\![\overline{v_n}]\!] \qquad (9.52) \\
& + ik\alpha \int_{\mathscr{E}_h} [\![u_n]\!] \cdot [\![\overline{v_n}]\!] \qquad\qquad \forall u_n, v_n \in \mathscr{V}_n^{(2)}.
\end{aligned}
$$

where $a^K(\cdot, \cdot)$ is given in (9.44), $\mathscr{E}_h$ is the mesh skeleton, $\alpha, \beta > 0$ are the flux parameters, and ∇_n is the broken gradient. For $v = u_n$ or v_n, $[\![v]\!]$ is the standard trace jump as defined in (9.4), and, on a given edge e, denoting by K^- and K^+ its adjacent elements,

$$\{\nabla_n v\} := \frac{1}{2}\left(\nabla v_{|_{K^+}} + \nabla v_{|_{K^-}}\right), \quad [\![\nabla_n v]\!] := \nabla v_{|_{K^+}} \cdot \mathbf{n}_{K^+} + \nabla v_{|_{K^-}} \cdot \mathbf{n}_{K^-}$$

are the trace average and normal jump, respectively, of $\nabla_n v$. Recall that $\mathscr{T}_h$ is a partition of $\Omega = \mathbb{R}^2$, thus all edges in $\mathscr{E}_h$ are shared by two elements.

Let now $\{\sigma_i\}_{i=1}^{\lambda^{(2)}}$ be a fundamental set of elements. Then, the basis functions $\{\widehat{\chi}_s^{(2)}\}_{s=1}^{\Xi}$ are given by $\{w_j^{\sigma_i}\}_{i=1,\dots,\lambda^{(2)}, j=1\dots,p}$, where $s \leftrightarrow (i, j)$, i.e. s is identified with the element index i and the plane wave direction index j, and $\Xi = \lambda^{(2)}p$. As mentioned above, the minimal generating subspace $\widehat{\mathscr{V}}_n^{(2)} \subset \mathscr{V}_n^{(2)}$ is simply the span of the basis functions $\{\widehat{\chi}_s^{(2)}\}_{s=1}^{\Xi}$, and the sesquilinear form $a_n^{(2)}(\cdot, \cdot)$ is given in (9.52).

Overview of the Stencils Generating the Minimal Subspaces

In Figs. 9.2, 9.3, and 9.4, we illustrate the stencils of the basis functions for the ncTVEM and the PWDG, employing the meshes made of squares, triangles, and hexagons, respectively, depicted in Fig. 9.1. The fundamental sets of vertices, edges, and elements are displayed in dark-blue, and the translation vectors $\boldsymbol{\xi}_1$ and $\boldsymbol{\xi}_2$ in red. Furthermore, the supports of the basis functions spanning the minimal generating subspaces are coloured in light-blue for the ncTVEM. Due to the locality of the basis functions, only those associated with the vertices, edges, and elements displayed in dark-blue and dark-yellow contribute to the sum (9.47). Integration only has to be performed over the elements K^ζ and the adjacent edges.
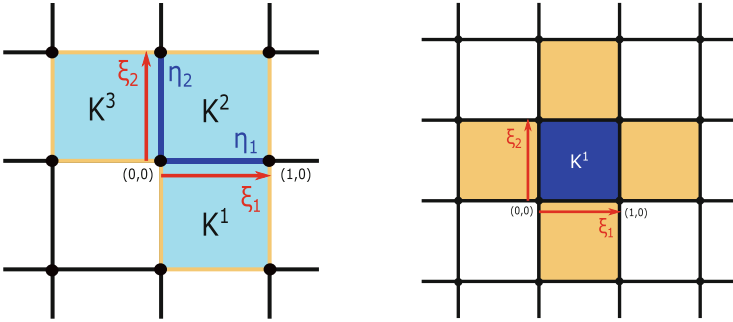
Fig. 9.2 Stencils of the basis functions related to the fundamental sets of edges (ncTVEM) and elements (PWDG), respectively, from *left* to *right*, when employing the meshes made of squares in Fig. 9.1
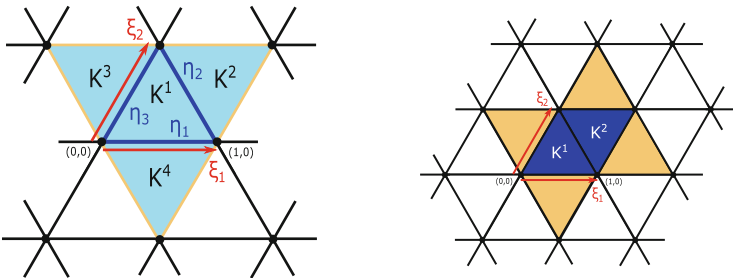

Fig. 9.3 Stencils of the basis functions related to the fundamental sets of edges (ncTVEM) and elements (PWDG), respectively, from *left* to *right*, when employing the meshes made of triangles in Fig. 9.1
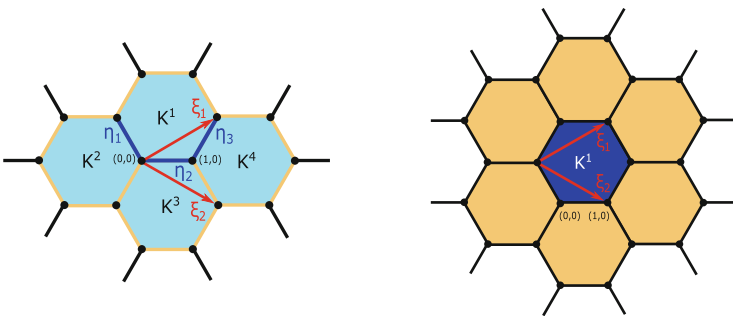

Fig. 9.4 Stencils of the basis functions related to the fundamental sets of edges (ncTVEM) and elements (PWDG), respectively, from *left* to *right*, when employing the meshes made of hexagons in Fig. 9.1

9.6.3 Numerical Results

In this section, after fixing some parameters for the different methods in Sect. 9.6 and specifying the quantities to be compared, we present a series of numerical tests using the meshes portrayed in Fig. 9.1. Firstly, in Sect. 9.6.3.1, we investigate the qualitative behaviour of dispersion and dissipation depending on the Bloch wave angle ϑ in Definition 9.43. Then, in Sect. 9.6.3.2, we compare the dispersion and dissipation errors against the effective plane wave degree q and against the dimensions of the minimal generating subspaces. Finally, in Sect. 9.6.3.3, the dependence of the errors on the wave number is studied.

Choice of the Parameters in PWDG and the Stabilizations in the ncTVEM
We use the choice of the flux parameters of the ultra weak variational formulation (UWVF), i.e. $\alpha = \beta = 1/2$, in PWDG, and we employ the stabilization terms suggested in [38, 39] for the ncTVEM.

As for the ncTVEM, we employ a modified D-recipe stabilization detailed in [39, Section 4]. More precisely, for all $K \in \mathcal{T}_h$, consider the set of local canonical basis function $\{\varphi_i^H\}$ of $V_h^H(K)$. For all φ_i^H and φ_j^H basis functions, we consider

$$S^{K,H}(\varphi_i^H, \varphi_j^H) = a^K(\Pi_p^{\nabla,H}\varphi_i^H, \Pi_p^{\nabla,H}\varphi_j^H).$$

An essential element in the implementation of the method is the orthogonalization-and-filtering process detailed in [39, Algorithm 2]. The basic idea is that the plane waves on each edge e used in the definition of the degrees of freedom are first orthogonalized in $L^2(e)$. Then, all combinations of plane waves that are close to be linearly dependent to others are eliminated. This is explained in Algorithm 1.

A consequence of this approach is that, after few steps of both the h- and p-versions of the method, the accuracy improves with an extremely slow growth of the number of degrees of freedom. This results in the so called *cliff-edge effect*, which was observed in [39, 40]; we shall exhibit such fast decay of the error notably for the p-version in Figs. 9.8, 9.9, 9.11, and 9.12.

Numerical Quantities
Given a wave number $k > 0$ and k_n the discrete wave number in Definition 9.1, we will study the following quantities:

- the *dispersion error* $|\operatorname{Re}(k - k_n)|$, which describes the difference of the propagation velocities of the continuous and discrete plane wave solutions;
- the *dissipation error* $|\operatorname{Im}(k_n)| = |\operatorname{Im}(k - k_n)|$, which represents the difference of the amplitudes (damping) of the continuous and discrete plane wave solution;
- the *total error* $|k - k_n|$, which measures the total deviation of the continuous and discrete wave numbers.

Algorithm 1

Let $\sigma > 0$ be a given threshold.

1. For all edges $e \in \mathscr{E}_h$:

   a. Assemble the matrix $\mathbf{G}^e$ associated with the $L^2(e)$ inner product:

   $$(\mathbf{G}^e)_{j,\ell} = (w_\ell^e, w_j^e)_{0,e} \quad \forall j, \ell = 1, \ldots, N_{\mathrm{PW}}^e,$$

   where we recall that $N_{\mathrm{PW}}^e := \dim(\mathbb{PW}_p(e))$, and $\{w_r^e\}_{r=1}^{N_{\mathrm{PW}}^e}$ denotes the original basis of $\mathbb{PW}_p(e)$.

   b. Compute the eigenvalue/eigenvector decomposition of $\mathbf{G}^e$:

   $$\mathbf{G}^e \mathbf{Q}^e = \mathbf{Q}^e \mathbf{\Lambda}^e,$$

   where $\mathbf{Q}^e$ is a matrix whose columns are right-eigenvectors of $\mathbf{G}^e$, and $\mathbf{\Lambda}^e$ is a diagonal matrix of the corresponding eigenvalues.

   c. Remove the columns of $\mathbf{Q}^e$ corresponding to the eigenvalues with absolute value smaller than σ. Denote by $\widehat{N}_{\mathrm{PW}}^e \leq N_{\mathrm{PW}}^e$ the number of remaining columns, and re-label them by $1, \ldots, \widehat{N}_{\mathrm{PW}}^e$.

   d. For $\ell = 1, \ldots, \widehat{N}_{\mathrm{PW}}^e$, set

   $$\widehat{w}_\ell^e := \sum_{r=1}^{N_{\mathrm{PW}}^e} \mathbf{Q}_{r,\ell}^e \, w_r^e.$$

   The new, *filtered basis* $\{\widehat{w}_\ell^e\}_{\ell=1}^{\widehat{N}_{\mathrm{PW}}^e}$ is $L^2(e)$ orthogonal.

2. For all $K \in \mathscr{T}_h$, the new basis of $V_h^H(K)$ is built by using the filtered basis $\{\widehat{w}_\ell^e\}_{\ell=1}^{\widehat{N}_{\mathrm{PW}}^e}$ instead of the original basis $\{w_r^e\}_{r=1}^{N_{\mathrm{PW}}^e}$ for each $e \in \mathscr{E}^K$.

9.6.3.1 Dependence of Dispersion and Dissipation on the Bloch Wave Angle

In this section, we study dispersion and dissipation of the different methods in dependence on the angle ϑ of the direction $\mathbf{d}$ in the definition of the Bloch wave in (9.43). Importantly, we are interested in a qualitative comparison of the methods. A quantitative comparison should be performed in terms of the dimensions of the minimal generating subspaces instead of the effective degrees, and is discussed in Sect. 9.6.3.2 below.

To this purpose, in Figs. 9.5, 9.6, and 9.7, the numerical quantities $|\operatorname{Re}(k - k_n)|$ and $|\operatorname{Im}(k_n)|$ are plotted against ϑ for the meshes made of squares, triangles, and hexagons, respectively, shown in Fig. 9.1. We took $k = 3$ and $q = 7$ for all those types of meshes (Figs. 9.5, 9.6, and 9.7, left). Moreover, for $k = 10$, we chose $q = 10$ for the squares (Fig. 9.5, right) and the triangles (Fig. 9.6, right), and $q = 13$
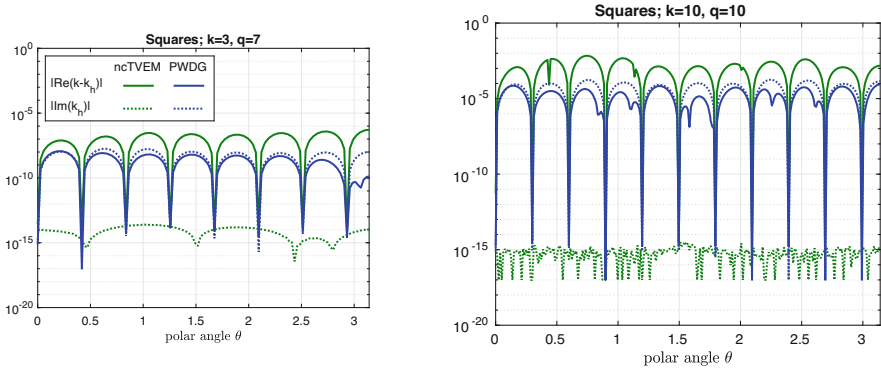
Fig. 9.5 Dispersive and dissipative behaviour of PWDG and ncTVEM in dependence on the polar angle ϑ of the Bloch wave direction $\mathbf{d}$ in (9.43) on the meshes made of squares in Fig. 9.1, with $k = 3$ and $q = 7$ (*left*), and $k = 10$ and $q = 10$ (*right*)
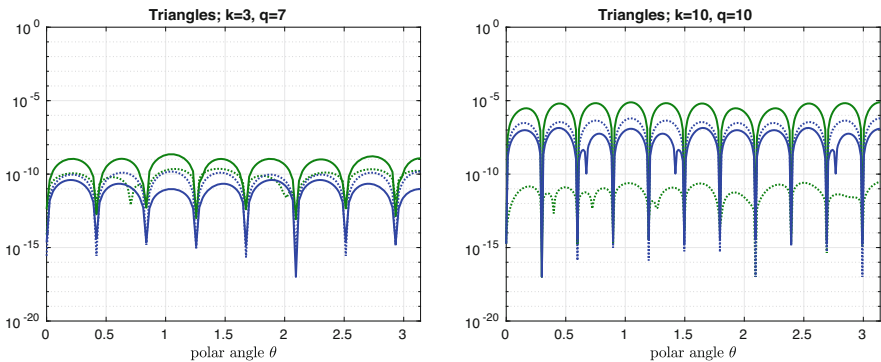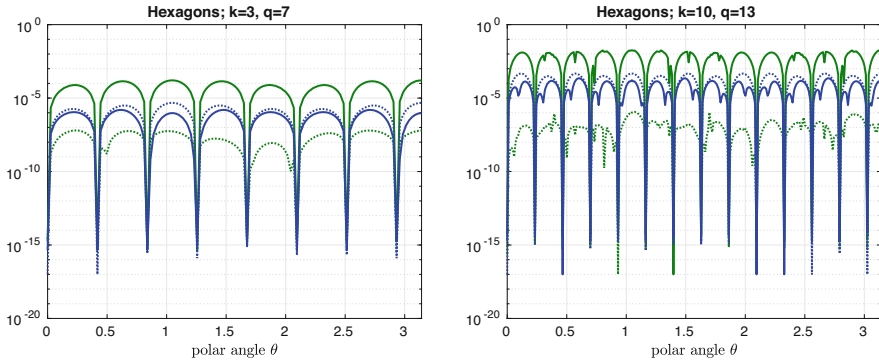

Fig. 9.6 Dispersive and dissipative behaviour of PWDG and ncTVEM in dependence on the polar angle ϑ of the Bloch wave direction $\mathbf{d}$ in (9.43) on the meshes made of triangles in Fig. 9.1, with $k = 3$ and $q = 7$ (*left*), and $k = 10$ and $q = 1$ (*right*). The colour legend is the same as in Fig. 9.5

for the hexagons (Fig. 9.7, right). We remark that the latter choice for q on the meshes made of hexagons is purely for demonstration purposes, in order to obtain a reasonable range for the errors, where one can see the behaviour more clearly. Moreover, the wave number k here (mesh size $h = 1$) corresponds to the wave number $k_0 = \frac{k}{h_0}$ on a mesh with mesh size h_0.

The dispersion and dissipation are zero, up to machine precision, for choices of the Bloch wave direction $\mathbf{d}$ in (9.43) coinciding with one of the plane wave directions $\{\mathbf{d}_j\}_{j=1}^{p}$ (here we always took equidistributed directions $\mathbf{d}_j$, where $\mathbf{d}_1 = (1, 0)$). This follows directly from the fact that, in this case, the Bloch wave satisfying (9.45) coincides with the corresponding plane wave traveling along the direction $\mathbf{d}$. Moreover, for the ncTVEM, the dispersion error dominates the dissipation error, whereas for PWDG the dissipation dominates the dispersion.

Fig. 9.7 Dispersive and dissipative behaviour of PWDG and ncTVEM in dependence on the polar angle ϑ of the Bloch wave direction **d** in (9.43) on the meshes made of hexagons in Fig. 9.1, with $k = 3$ and $q = 7$ (*left*), and $k = 10$ and $q = 13$ (*right*). The colour legend is the same as in Fig. 9.5

9.6.3.2 Exponential Convergence of the Dispersion Error Against the Effective Degree q

Here, we investigate the dependence of dispersion and dissipation on the effective plane wave degree q (namely, $p = 2q + 1$ bulk plane waves). For fixed wave number k, we will observe exponential convergence of the total error for increasing q, as already seen in [24] for PWDG. This result is not unexpected since also the p-versions for the discretization errors have exponential convergence, provided that the exact analytical solution is smooth; see [28] for PWDG, and the numerical experiments in [38] for the ncTVEM, respectively. Moreover, we will make a comparison of these methods in terms of the total error versus the dimensions of the minimal generating subspaces.

To this purpose, we consider the following range for the wave number: $k \in \{2, 3, 4, 5\}$. We recall again that k corresponds to $k_0 = \frac{k}{h_0}$ on a mesh with mesh size h_0.

Dispersion and Dissipation vs. Effective Degree q
In Figs. 9.8, 9.9, and 9.10, the relative dispersion error $|\operatorname{Re}(k - k_n)|/k$ and the relative damping error $|\operatorname{Im}(k_n)|/k$ are displayed against q, for the meshes made of squares, triangles, and hexagons, respectively. The maxima of the relative dispersion and the relative dissipation, respectively, are taken over a large set of Bloch wave directions **d**. After a preasymptotic regime, we observe exponential convergence of the dispersion error for all methods and the dissipation error for the PWDG. The dispersion error is consistently smaller for the PWDG than for the ncTVEM.

Dispersion and Dissipation vs. Dimensions of Minimal Generating Subspaces
From a computational point of view, it is also important to consider a comparison of the dispersion errors in terms of the dimensions of the minimal generating subspaces (density of the degrees of freedom). We directly compare the relative total dispersion
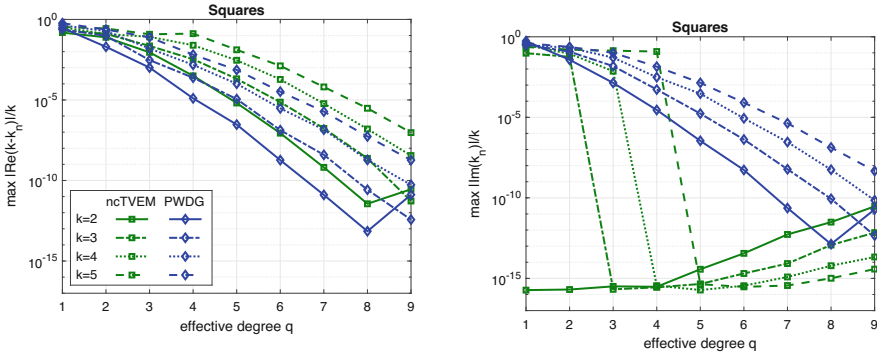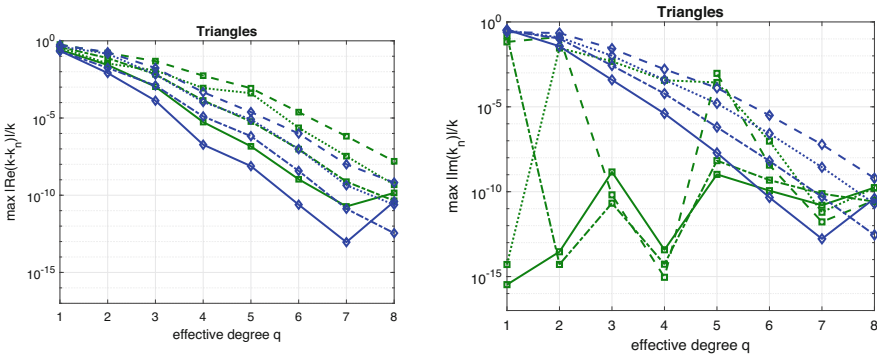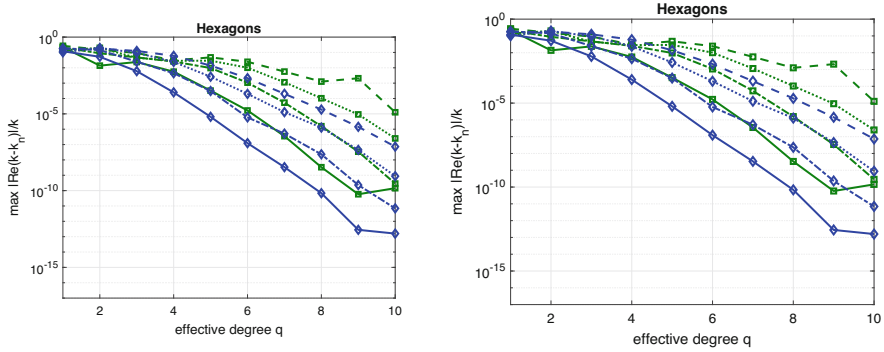
Fig. 9.8 Relative dispersion (*left*) and relative dissipation (*right*) for the different methods in dependence on the effective degree q and the wave numbers $k = 2, \ldots, 5$ on the meshes made of squares in Fig. 9.1. The maxima over a large set of Bloch wave directions **d** are taken

Fig. 9.9 Relative dispersion (*left*) and relative dissipation (*right*) for the different methods in dependence on the effective degree q and the wave numbers $k = 2, \ldots, 5$ on the meshes made of triangles in Fig. 9.1. The maxima over a large set of Bloch wave directions **d** are taken. The colour legend is the same as in Fig. 9.8

errors $|k_n - k|/k$, thus measuring the total deviation of the discrete wave number from the continuous one. As above, the maxima over a large set of Bloch wave directions are taken. In Fig. 9.11, those errors are displayed for the meshes in Fig. 9.1. For the ncTVEM, we can recognize the *cliff-edge effect*, meaning that, at some point, the dispersion error decreases without increase of the dimension of the minimal generating subspace. This effect has already been remarked in [39, 40] for the discretization error and is a peculiarity of the orthogonalization-and-filtering process mentioned in [39, Algorithm 1]. Moreover, we can observe a direct correlation between the density of the degrees of freedom, which depends on the shape of the meshes, see Figs. 9.2, 9.3, and 9.4, and the error plots (larger cardinalities of the fundamental sets lead to larger errors; as mentioned above, for ncTVEM, the filtering process leads to dimensionality reductions).

Fig. 9.10 Relative dispersion (*left*) and relative dissipation (*right*) for the different methods in dependence on the effective degree q and the wave numbers $k = 2, \ldots, 5$ on the meshes made of hexagons in Fig. 9.1. The maxima over a large set of Bloch wave directions **d** are taken. The colour legend is the same as in Fig. 9.8
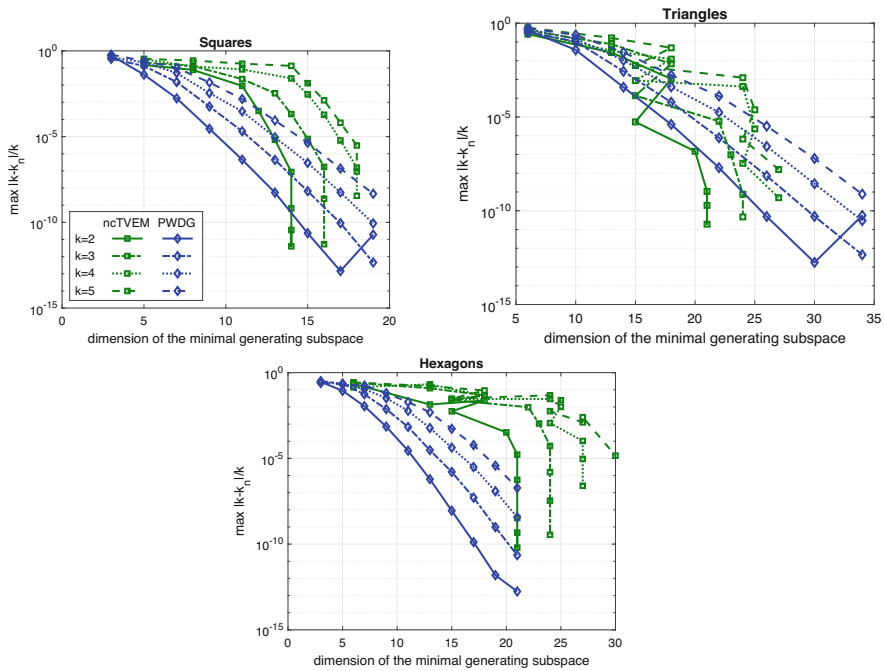
Fig. 9.11 Relative total dispersion error in dependence on the dimensions of the minimal generating subspaces for different values of k on the meshes in Fig. 9.1

Comparison with the Standard FEM

Here, we highlight the advantages of using full Trefftz methods (ncTVEM, PWDG) in comparison to standard polynomial based methods, such as the FEM, whose dispersion properties were studied in, e.g., [1, 9, 20, 31]. For simplicity, we focus on the meshes made of squares in Fig. 9.1, since, in this case, the basis functions in the FEM have a tensor product structure and an explicit dispersion relation can be derived [1, Theorem 3.1]:

$$\cos(k_n) = R_q(k), \qquad (9.53)$$

where, denoting by $[\cdot/\cdot]_{z\cot z}$ and $[\cdot/\cdot]_{z\tan z}$ the Padé approximants to the functions $z\cot z$ and $z\tan z$, respectively,

$$R_q(2z) := \frac{[2N_0/2N_0 - 2]_{z\cot z} - [2N_e + 2/2N_e]_{z\tan z}}{[2N_0/2N_0 - 2]_{z\cot z} + [2N_e + 2/2N_e]_{z\tan z}},$$

with $N_0 := \lfloor (q+1)/2 \rfloor$ and $N_e := \lfloor q/2 \rfloor$. From (9.53), one can see that only dispersion plays a role in the FEM. In Fig. 9.12, we display the relative total dispersion errors against the effective degree q (left) and against the dimensions of the minimal generating subspaces (right) for fixed $k = 3$. Similar results are obtained for other values of k and are not shown. One can clearly notice that the dispersion error for the FEM is lower than for the other methods, when comparing it in terms of q, but higher, when comparing it in terms of the dimensions of the minimal generating subspaces.
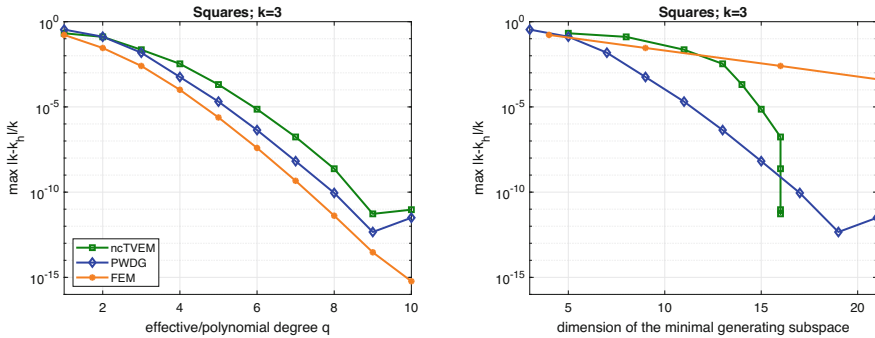
Fig. 9.12 Comparison of the relative total dispersion errors for ncTVEM, PWDG, and the standard polynomial based FEM on a mesh made of squares as in Fig. 9.1 for fixed wave number $k = 3$, in dependence on the effective/polynomial degree q (*left*) and the dimension of the minimal generating subspaces (*right*). The maxima over a large set of Bloch wave directions **d** are taken

9.6.3.3 Algebraic Convergence of the Dispersion Error Against the Wave Number k

We study the dispersion and dissipation properties of the three methods with respect to the wave number k. Due to the fact that $h = 1$, and k is related to the wave number k_0 on a mesh with mesh size h_0 by $k = kh = k_0h_0$, the limit $k \to 0$ corresponds in fact to an h-version with $h_0 \to 0$ for fixed k_0. We will observe algebraic convergence of the total dispersion error in terms of k. This resembles the algebraic convergence of the discretization error in the h-version, proved in [25, 39] for the ncTVEM and the PWDG, respectively.

For the numerical experiments, we fix the effective degrees $q = 3, 5, 7$. We employ once again the meshes made of squares and triangles in Fig. 9.1. Similar results have been obtained on the mesh made of hexagons. In Fig. 9.13, the relative total errors $|k - k_n|/k$ determined over a large set of Bloch wave directions **d** are depicted against k. Algebraic convergence can be observed. Furthermore, larger values of q lead to smaller errors. The peaks occurring in the convergence regions of the ncTVEM could be related to the presence of Neumann eigenvalues, and Dirichlet and Neumann eigenvalues, that have to be excluded in the construction of the ncTVEM, respectively, in order to have a well-posed variational formulation. Moreover, the oscillations for larger and smaller values of k are related to the pre-asymptotic regime and the instability regime, which are typical of wave based methods.

In Table 9.1, we list some relative total errors for different values of k. They indicate a convergence behaviour of

$$\max \frac{|k - k_n|}{|k|} \approx \mathcal{O}(k^\eta), \quad k \to 0, \tag{9.54}$$

where $\eta \in [2q - 1, 2q]$. This was already observed in [24] for PWDG.
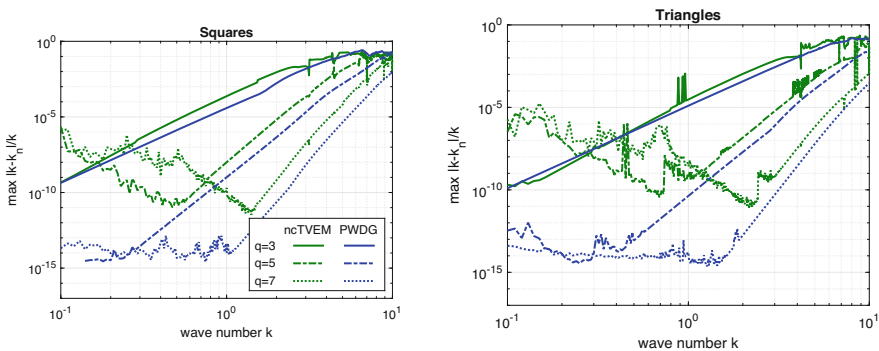

Fig. 9.13 Relative total dispersion in dependence on the wave number k for fixed effective degrees $q = 3, 5, 7$. The maxima over a large set of Bloch wave directions **d** are taken. As meshes, those made of squares (*left*) and triangles (*right*) in Fig. 9.1 are employed

Table 9.1 Rates of the relative total error for $k \to 0$

		Squares					Triangles				
	Method	k	$\frac{|k-k_n|}{k}$	k	$\frac{|k-k_n|}{k}$	Rate	k	$\frac{|k-k_n|}{k}$	k	$\frac{|k-k_n|}{k}$	Rate
$q=3$	PWVEM	2	1.50e−03	0.3	4.59e−08	5.48	2	2.71e−04	0.3	3.42e−09	5.95
	ncTVEM	2	9.04e−03	0.3	3.69e−07	5.33	2	1.07e−03	0.3	4.09e−08	5.36
	PWDG	2	1.71e−03	0.3	1.04e−07	5.11	2	3.87e−04	0.3	3.04e−08	4.98
$q=5$	PWVEM	2	3.68e−06	0.8	5.09e−10	9.70	3	2.17e−05	2	4.54e−07	9.53
	ncTVEM	2	6.48e−06	0.8	1.21e−09	9.37	3	5.91e−06	2	1.47e−07	9.11
	PWDG	2	4.56e−07	0.8	1.47e−10	8.77	3	7.75e−07	2	1.97e−08	9.06
$q=7$	PWVEM	4	1.55e−05	2	2.23e−09	12.76	6	7.79e−05	4	5.57e−07	12.19
	ncTVEM	4	5.93e−06	2	6.54e−10	13.15	6	6.01e−06	4	3.39e−08	12.77
	PWDG	4	2.92e−07	2	2.33e−11	13.62	6	7.10e−07	4	2.76e−09	13.69
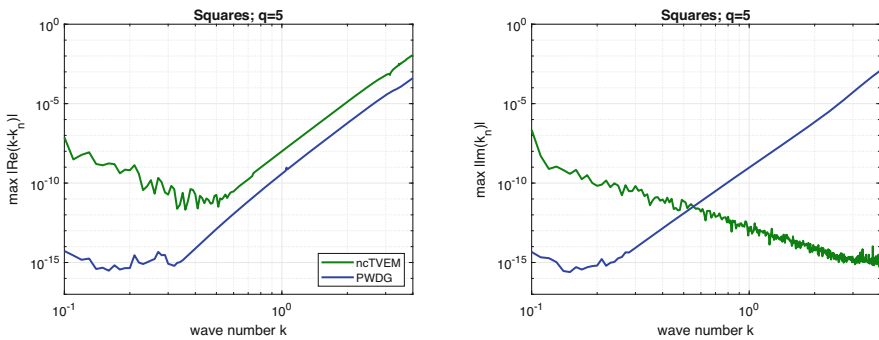
Fig. 9.14 Relative dispersion (*left*) and relative dissipation (*right*) in dependence on the wave number k for fixed $q = 5$ on the meshes made of squares in Fig. 9.1. The maxima over a large set of Bloch wave directions **d** are taken

Remark 9.4 Clearly, similarly as above, dispersion and dissipation can be investigated again separately from each other. Here, we only show the results, depicted in Fig. 9.14, for fixed $q = 5$ and varying k on the meshes made of squares. As already observed, one can deduce that the ncTVEM are dispersion dominated, whereas dissipation plays a major role for the PWDG.

References

1. M. Ainsworth, Discrete dispersion relation for hp-version finite element approximation at high wave number. SIAM J. Num. Anal. **42**, 553–575 (2004)
2. M. Ainsworth, Dispersive and dissipative behaviour of high order discontinuous Galerkin finite element methods. J. Comput. Phys. **198**(1), 106–130 (2004)
3. M. Ainsworth, P. Monk, W. Muniz, Dispersive and dissipative properties of discontinuous Galerkin finite element methods for the second-order wave equation. J. Sci. Comput. **27**(1–3), 5–40 (2006)
4. P.F. Antonietti, G. Manzini, M. Verani, The fully nonconforming virtual element method for biharmonic problems. Math. Models Methods Appl. Sci. **28**(02), 387–407 (2018)
5. J. Asakura, T. Sakurai, H. Tadano, T. Ikegami, K. Kimura, A numerical method for nonlinear eigenvalue problems using contour integrals. JSIAM Lett. **1**, 52–55 (2009)
6. B.P. Ayuso de Dios, K. Lipnikov, G. Manzini, The nonconforming virtual element method. ESAIM Math. Model. Numer. Anal. **50**(3), 879–904 (2016)
7. I. Babuška, J.M. Melenk, The partition of unity finite element method: basic theory and applications. Comput. Methods Appl. Mech. Eng. **139**(1–4), 289–314 (1996)
8. I. Babuška, J.M. Melenk, Approximation with harmonic and generalized harmonic polynomials in the partition of unity method. Comput. Assist. Methods Eng. Sci. **4**, 607–632 (1997)
9. I. Babuška, S. Sauter, Is the pollution effect of the FEM avoidable for the Helmholtz equation considering high wave numbers? SIAM J. Numer. Anal. **34**(6), 2392–2423 (1997)
10. L. Beirão da Veiga, F. Brezzi, A. Cangiani, G. Manzini, L.D. Marini, A. Russo, Basic principles of virtual element methods. Math. Models Methods Appl. Sci. **23**(01), 199–214 (2013)
11. S. Berrone, A. Borio, G. Manzini, SUPG stabilization for the nonconforming virtual element method for advection–diffusion–reaction equations. Comput. Meth. Appl. Mech. Eng. **340**, 500–529 (2018)
12. W.-J. Beyn, An integral method for solving nonlinear eigenvalue problems. Linear Algebra Appl. **436**(10), 3839–3863 (2012)
13. A. Cangiani, V. Gyrya, G. Manzini, The non-conforming virtual element method for the Stokes equations. SIAM J. Numer. Anal. **54**(6), 3411–3435 (2016)
14. A. Cangiani, G. Manzini, O.J. Sutton, Conforming and nonconforming virtual element methods for elliptic problems. IMA J. Numer. Anal. **37**(3), 1317–1354 (2016)
15. S. Cao, L. Chen, Anisotropic error estimates of the linear nonconforming virtual element methods. SIAM J. Numer. Anal. **57**(3), 1058–1081 (2019)
16. O. Cessenat, B. Despres, Application of an ultra weak variational formulation of elliptic PDEs to the two-dimensional Helmholtz problem. SIAM J. Numer. Anal. **35**(1), 255–299 (1998)
17. L. Chen, X. Huang, Nonconforming virtual element method for $2m$-th order partial differential equations in $\mathbb{R}^n$. Math. Comp. **89**, 1711–1744 (2020)
18. A. Chernov, L. Mascotto, The harmonic virtual element method: stabilization and exponential convergence for the Laplace problem on polygonal domains. IMA J. Numer. Anal. **39**, 1787–1817 (2019)
19. E. Deckers, O. Atak, L. Coox, R. D'Amico, H. Devriendt, S. Jonckheere, K. Koo, B. Pluymers, D. Vandepitte, W. Desmet, The wave based method: An overview of 15 years of research. Wave Motion **51**(4), 550–565 (2014)
20. A. Deraemaeker, I. Babuška, P. Bouillard, Dispersion and pollution of the FEM solution for the Helmholtz equation in one, two and three dimensions. Int. J. Numer. Meth. Eng. **46**, 471–499 (1999)
21. D.A. Di Pietro, J. Droniou, G. Manzini, Discontinuous skeletal gradient discretisation methods on polytopal meshes. J. Comput. Phys. **355**, 397–425 (2018)
22. C. Farhat, I. Harari, L.P. Franca, The discontinuous enrichment method. Comput. Methods Appl. Mech. Eng. **190**(48), 6455–6479 (2001)
23. F. Gardini, G. Manzini, G. Vacca, The nonconforming virtual element method for eigenvalue problems. ESAIM Math. Model. Numer. Anal. **53**(3), 749–774 (2019)

24. C.J. Gittelson, R. Hiptmair, Dispersion analysis of plane wave discontinuous Galerkin methods. Int. J. Numer. Meth. Eng. **98**(5), 313–323 (2014)
25. C.J. Gittelson, R. Hiptmair, I. Perugia, Plane wave discontinuous Galerkin methods: analysis of the *h*-version. ESAIM Math. Model. Numer. Anal. **43**(2), 297–331 (2009)
26. J. Gopalakrishnan, I. Muga, N. Olivares, Dispersive and dissipative errors in the DPG method with scaled norms for Helmholtz equation. SIAM J. Sci. Comput. **36**(1), A20–A39 (2014)
27. J. Gopalakrishnan, M. Solano, F. Vargas, Dispersion analysis of HDG methods. J. Sci. Comput. **77**(3), 1–33 (2018)
28. R. Hiptmair, A. Moiola, I. Perugia, Plane wave discontinuous Galerkin methods for the 2D Helmholtz equation: analysis of the *p*-version. SIAM J. Numer. Anal. **49**(1), 264–284 (2011)
29. R. Hiptmair, A. Moiola, I. Perugia, A survey of Trefftz methods for the Helmholtz equation, in *Building Bridges: Connections and Challenges in Modern Approaches to Numerical Partial Differential Equations*, pp. 237–279 (Springer, Berlin, 2016)
30. J. Huang, Y. Yu, A medius error analysis for nonconforming virtual element methods for Poisson and biharmonic equations. J. Comput. Appl. Math. **386**, 113229 (2021)
31. F. Ihlenburg, I. Babuška, Dispersion analysis and error estimation of Galerkin finite element methods for the Helmholtz equation. Int. J. Numer. Meth. Eng. **38**(22), 3745–3774 (1995)
32. L.-M. Imbert-Gérard, Interpolation properties of generalized plane waves. Numer. Math. **131**(4), 683–711 (2015)
33. L.-M. Imbert-Gérard, B. Després, A generalized plane-wave numerical method for smooth nonconstant coefficients. IMA J. Numer. Anal. **34**(3), 1072–1103 (2014)
34. M. Li, J. Zhao, C. Huang, S. Chen, Nonconforming virtual element method for the time fractional reaction–subdiffusion equation with non-smooth data. J. Sci. Comput. **81**(3), 1823–1859 (2019)
35. X. Liu, Z. Chen, The nonconforming virtual element method for the Navier-Stokes equations. Adv. Comput. Math. **45**(1), 51–74 (2019)
36. X. Liu, J. Li, Z. Chen, A nonconforming virtual element method for the Stokes problem on general meshes. Comp. Method Appl. Mech. Eng. **320**, 694–711 (2017)
37. L. Mascotto, I. Perugia, A. Pichler, Non-conforming harmonic virtual element method: *h*- and *p*-versions. J. Sci. Comput. **77**(3), 1874–1908 (2018)
38. L. Mascotto, I. Perugia, A. Pichler, A nonconforming Trefftz virtual element method for the Helmholtz problem. Math. Models Methods Appl. Sci. **29**, 1619–1656 (2019)
39. L. Mascotto, I. Perugia, A. Pichler, A nonconforming Trefftz virtual element method for the Helmholtz problem: numerical aspects. Comput. Methods Appl. Mech. Eng. **347**, 445–476 (2019)
40. L. Mascotto, A. Pichler, Extension of the nonconforming Trefftz virtual element method to the Helmholtz problem with piecewise constant wave number. Appl. Numer. Math. **155**, 160–180 (2020)
41. J.M. Melenk, Operator adapted spectral element methods I: harmonic and generalized harmonic polynomials. Numer. Math. **84**(1), 35–69 (1999)
42. A. Moiola, R. Hiptmair, I. Perugia, Plane wave approximation of homogeneous Helmholtz solutions. Zeitschrift für Z. Angew. Math. Phys. **62**(5), 809 (2011)
43. P. Monk, D.-Q. Wang, A least-squares method for the Helmholtz equation. Comput. Methods Appl. Mech. Eng. **175**(1–2), 121–136 (1999)
44. I. Perugia, P. Pietra, A. Russo, A plane wave virtual element method for the Helmholtz problem. ESAIM Math. Model. Numer. Anal. **50**(3), 783–808 (2016)
45. H. Riou, P. Ladeveze, B. Sourcis, The multiscale VTCR approach applied to acoustics problems. J. Comput. Acoust. **16**(04), 487–505 (2008)
46. F. Wang, J. Zhao, Conforming and nonconforming virtual element methods for a Kirchhoff plate contact problem. IMA J. Numer. Anal. **41**(2), 1496–1521 (2021)
47. J. Xiao, C. Zhang, T.-M. Huang, T. Sakurai, Solving large-scale nonlinear eigenvalue problems by rational interpolation and resolvent sampling based Rayleigh–Ritz method. Int. J. Numer. Meth. Eng. **110**(8), 776–800 (2017)

48. B. Zhang, J. Zhao, S. Chen, The nonconforming virtual element method for fourth-order singular perturbation problem. Adv. Comput. Math. **46**(2), 1–23 (2020)
49. B. Zhang, J. Zhao, Y. Yang, S. Chen, The nonconforming virtual element method for elasticity problems. J. Comput. Phys. **378**, 394–410 (2019)
50. J. Zhao, S. Chen, B. Zhang, The nonconforming virtual element method for plate bending problems. Math. Models Methods Appl. Sci. **26**(09), 1671–1687 (2016)
51. J. Zhao, B. Zhang, S. Mao, S. Chen, The divergence-free nonconforming virtual element for the Stokes problem. SIAM J. Numer. Anal. **57**(6), 2730–2759 (2019)
52. J. Zhao, B. Zhang, S. Mao, S. Chen, The nonconforming virtual element method for the Darcy–Stokes problem. Comput. Methods Appl. Mech. Eng. **370**, 113251 (2020)
53. J. Zhao, B. Zhang, X. Zhu, The nonconforming virtual element method for parabolic problems. Appl. Numer. Math. **143**, 97–111 (2019)

Chapter 10
The Conforming Virtual Element Method for Polyharmonic and Elastodynamics Problems: A Review

Paola F. Antonietti, Gianmarco Manzini, Ilario Mazzieri, Simone Scacchi, and Marco Verani

Abstract In this chapter we review recent results on the conforming virtual element approximation of polyharmonic and eleastodynamics problems. The structure and the content of this review is motivated by three paradigmatic examples of applications: classical and anisotropic Cahn-Hilliard equation and phase field models for brittle fracture, that are briefly discussed in the first part of the chapter. We present and discuss the mathematical details of the conforming virtual element approximation of linear polyharmonic problems, the classical Cahn-Hilliard equation and linear elastodynamics problems.

10.1 Introduction

In the recent years, there has been a tremendous interest to numerical methods that approximate partial differential equations (PDEs) on computational meshes with arbitrarily-shaped polytopal elements. One of the most successful method is the virtual element method (VEM), originally proposed in [16] for second-order elliptic problems and then extended to a wide range of applications.

The VEM was originally developed as a variational reformulation of the *nodal* mimetic finite difference (MFD) method [15, 37, 38, 73, 78] for solving partial differential equation problems on unstructured polygonal meshes. A survey on the MFD method can be found in the review paper [74] and the research mono-

P. F. Antonietti · I. Mazzieri · M. Verani (✉)
MOX, Dipartimento di Matematica, Politecnico di Milano, Milan, Italy
e-mail: paola.antonietti@polimi.it; ilario.mazzieri@polimi.it; marco.verani@polimi.it

G. Manzini
IMATI-CNR, Pavia, Italy
e-mail: marco.manzini@imati.cnr.it

S. Scacchi
Dipartimento di Matematica, Università di Milano, Milan, Italy
e-mail: simone.scacchi@unimi.it

graph [18]. The VEM inherits the flexibility of the MFD method with respect to the admissible meshes and this feature is well reflected in the many significant applications using polytopal meshes that have been developed so far, see, for example, [6, 19, 21, 23, 24, 27, 28, 30, 45, 48, 49, 54, 82, 84, 87, 88, 94, 99]. Meanwhile, the mixed VEM for elliptic problems were introduced in setting *a la'* Raviart-Thomas in [22] and in a BDM-like setting in [39]. The nonconforming formulation for diffusion problems was proposed in [13] as the finite element reformulation of [72] and later extended to general elliptic problems [32, 47], Stokes problem [44], eigenvalue problems [63], and the biharmonic equation [7, 100]. equation [7]. Moreover, the connection between the VEM and the finite elements on polygonal/polyhedral meshes is thoroughly investigated in [43, 77], between VEM and discontinuous skeletal gradient discretizations in [55], and between the VEM and the BEM-based FEM method in [46].

The virtual element method combines a great flexibility in using polytopal meshes with a great versatility and easiness in designing approximation spaces with high-order continuity properties on general polytopal meshes. These two features turn out to be essential in the numerical treatment of the classical plate bending problem, for which a C^1-regular conforming virtual element approximation has been introduced in [36, 53]. Virtual elements with C^1- regularity have been proposed to solve elliptic problems on polygonal meshes [19] and polyedral meshes in [26], the transmission eigenvalue problem in [80], the vibration problem of Kirchhoff plates in [83], the buckling problem of Kirchhoff-Love plates in [81]. The use of C^1-virtual elements has also been employed in the conforming approximation of the Cahn-Hilliard problem [6] and the von Kármán equations [76], and in the context of residual based a posteriori error estimators for second-order elliptic problems [21].

Higher-order of regularity of the numerical approximation is also required when addressing PDEs with differential operators of order higher than two as the already mentioned biharmonic problem and the more general case of the polyharmonic equations. An example of the latter is found in the work of Reference [9].

In this chapter we consider three paradigmatic examples of applications where the conforming discretization requires highly regular approximation spaces. The first two examples are the classical and the anisotropic Cahn-Hilliard equations, that are used in modelling a wide range of problems such as the tumor growth, the origin of the Saturn rings, the separation of di-block copolymers, population dynamics, crystal growth, image processing and even the clustering of mussels, see [6] and the references therein. The third example highlights the importance of coupling phase field equations with the elastodynamic equation in the context of modelling fracture propagation (see also [3] for a phase-field besed VEM and the references therein). These three examples motivate the structure of this review, where we consider the conforming virtual approximation of the polyharmonic equation, the classical Cahn-Hilliard equation and the time-dependent elastodynamics equation.

Historically, the numerical approximation of polyharmonic problems dates back to the eighties [34], and more recently, this problem has been addressed in the context of the finite element method by [14, 62, 67, 93, 97]. The conforming virtual element approximation of the biharmonic problem has been addressed in

[36, 53]. while a non-conforming approximation has been proposed in [7, 100, 101]. In Sect. 10.2, we review the conforming virtual element approximation of polyharmonic problems following [9, 12]. A nonconforming approximation is studied in [52].

The Cahn-Hilliard equation involves fourth-order spatial derivatives and the conforming finite element method is not really popular approach because primal variational formulations of fourth-order operators requires the use of finite element basis functions that are piecewise-smooth and globally C^1-continuous. Only a few finite element formulations exists with the C^1-continuity property, see for example [57, 58], but in general, these methods are not simple and easy to implement. This high-regularity issue has successfully been addressed in the framework of isogeometric analysis [65]. The virtual element method provides a very effective framework for the design and development of highly regular conforming approximation, and in Sect. 10.3 we review the method proposed in [6].

Alternative approaches are offered by nonconforming methods [59] or discontinuous methods [98]), but these methods do not provide C^1-regular approximations. Another common strategy employed *in practice* to solve the Cahn-Hilliard equation by finite elements resorts to mixed methods; see, e.g., [56, 60, 68] for the continuous and discontinuous setting, respectively. Recently, mixed based discretization schemes on polytopal meshes have been addressed in [50] in the context of the Hybrid High Order Method, and in [75] in the context of the mixed Virtual Element Method. However, mixed finite element methods requires a bigger number of degrees of freedom, which implies, as a drawback, an increased computational cost.

Very popular strategies for numerically solving the time-dependent elastodynamics equations in the *displacement formulation* are based on spectral elements [61, 69], discontinuous Galerkin and discontinuos Galerkin spectral elements [4, 5, 91]. High-order DG methods for elastic and elasto-acoustic wave propagation problems have been extended to arbitrarily-shaped polygonal/polyhedral grids [8, 10] to further enhance the geometrical flexibility of the discontinuous Galerkin approach while guaranteeing low dissipation and dispersion errors. Recently, the lowest-order Virtual Element Method has been applied for the solution of the elastodynamics equation on nonconvex polygonal meshes [85, 86]. See also [17] for the approximation of the linear elastic problem, [20] for elastic and inelastic problems on polytope meshes, [96] for virtual element approximation of hyperbolic problems. In Sect. 10.4, we review the conforming virtual element method of arbitrary order of accuracy proposed in [11].

10.1.1   Paradigmatic Examples

In this section, we briefly describe some relevant applications whose mathematical modelling involves partial differential equations with higher order spatial operators or the combination of the elastodynamics equation and higher-order spatial partial differential equations.

10.1.1.1 Cahn-Hilliard Equation

Phase field models, which date back to the works of Korteweg [70], Cahn and Hilliard [40–42], Landau and Ginzburg [71] and van der Waals [92], have been classicaly employed to describe phase separation in binary alloys.

Consider a bounded domain $\Omega \subset \mathbb{R}^d$, $d = 1, 2, 3$, filled with components A and B presenting different properties and let $c_A(x)$ and $c_B(x)$ be their relative nonuniform mass fraction for every $x \in \Omega$. We assume that $c_i(\cdot) : \Omega \to [0, 1]$ for $i \in \{A, B\}$ and $c_A(x) + c_B(x) = 1$. Choosing one of the two functions and renaming it as $c(x)$, Cahn and Hilliard, under the additional hypothesis that the mixture is isothermal and the molar volume is uniform and independent of the pressure, proposed a model minimizing the energy functional

$$E(c) = \int_{\Omega} \left(F(c) + \frac{\varepsilon^2}{2} |\nabla c|^2 \right) d\mathbf{x}, \qquad (10.1)$$

where $F(c)$ is the Helmholtz single-component free-energy density

$$F(c) = 2\kappa_B T_c c(1 - c) + \kappa_B T \big(c \ln(c) + (1 - c) \ln(1 - c) \big).$$

Here, κ_B is the Boltzmann constant, T the temperature and T_c the critical temperature threshold. If $T \geq T_c$ the behaviour is trivial since $F(c)$ presents a single global minimum at $c = 1/2$, and therefore the minimization of (10.1) returns a homogeneous distribution $c(x) = 1/2$ for all $x \in \Omega$. On the other hand, if $T \leq T_c$, a physically relevant double-well appears in the graph of the function.

Let us briefly comment on the structure of the energy functional (10.1). The first term takes into account the interfacial nature of the phenomenon: it increases the energy in those region of the space where both A and B are present (thus c exhibits a high gradient). The second term penalizes the measure of the interface separating the two phases. However, even if the interface separating the substances looks sharp from a macroscopic point of view, there is experimental evidence of an intermediate, diffusive, stripe; the term ε^2 is such that ε is proportional to the thickness of the stripe.

In the mathematical treatment of this problem, it is convenient to introduce the so-called *order parameter*, which we still denote by $c(x)$ and we define as $c(x) = c_A(x) - c_B(x)$ so that $c(\cdot) : \Omega \to [-1, 1]$.

Employing the order parameter, the energy functional (10.1) remains unmodified (up to a multiplicative constant), while $F(c)$ becomes

$$F(c) = -c_0 c^2 + c_1 \big((1 + c) \ln(1 + c) + (1 - c) \ln(1 - c) \big) \quad c_0 > c_1 > 0$$

as we fixed $T < T_c$. Recalling the assumption that the phenomenon mimimizes the energy (10.1) over time and denoting by $\dot{c}$ the time derivative of c, we get the

following differential description of the phenomenon

$$\dot{c} + \nabla \cdot J = 0 \quad \text{in } \Omega, \tag{10.2}$$

where the flux J is defined as

$$J = -M(c)\nabla\left(\frac{\delta E(c)}{\delta c}\right) = M(c)\nabla(F'(c) - \varepsilon^2 \Delta c).$$

The function $M(c)$ is the mobility of the substances and measures how much the molecules are free to move. The typical choices for the boundary conditions on the domain boundary Γ are:

$$n \cdot M(c)\nabla(F'(c) - \varepsilon^2 \Delta c) = 0 \quad \text{on } \Gamma, \tag{10.3}$$

$$\partial_n c = 0 \quad \text{on } \Gamma, \tag{10.4}$$

where n is the unit normal vector to Γ pointing out of Ω. The conservation of c follows from the integration of (10.2) and an application of the divergence theorem, which formally gives the relation $\partial_t \int_\Omega c \, d\mathbf{x} = 0$. In practice, the following choices for $M(c)$ and $F(c)$ are common

$$F(c) = \frac{1}{4}(c^2 - 1)^2,$$

$$M(c) = constant.$$

Setting for simplicity $M(c) = 1$, problem (10.2) takes the simpler form of the nonlinear fourth-order parabolic equation:

$$\dot{c} + \nabla \cdot \nabla(F'(c)) - \varepsilon^2 \Delta^2 c = 0 \quad \text{in } \Omega.$$

Note the presence of the fourth-order term $\Delta^2 c$, whose numerical treatment, as it will be clear in the sequel of the paper, requires special care.

10.1.1.2   Anisotropic Cahn-Hilliard Equation

We consider the following modified free energy density

$$E(c) = \int_\Omega \frac{\gamma(n)}{\varepsilon}\left(F(c) + \frac{\varepsilon^2}{2}|\nabla c|^2\right) d\mathbf{x}, \tag{10.5}$$

where function $\gamma(n)$ describes the anisotropic property and $n = \frac{\nabla c}{|\nabla c|}$ is the interface unit normal vector. When $\gamma(n) = 1$ the H^{-1}-gradient flow of (10.5) leads to the Cahn-Hilliard equation of the previous section. In the anisotropic case, function γ

depends on n in a non-trivial way. For instance, the so-called four-fold symmetric anisotropic function is defined as follows:

$$\gamma(n) = 1 + \alpha \cos(\vartheta) \tag{10.6}$$

where ϑ is the orientation angle of the normal vector to the interface and α is the intensity of the anisotropy. For sufficiently large values of α, the corresponding Cahn-Hilliard equation becomes ill-posed and needs to be regularized [95]. To this end, we consider an extra regularizing term $\mathscr{G}(c)$ in the energy functional (10.5), which takes the form

$$E(c) = \int_{\Omega} \frac{\gamma(n)}{\varepsilon} \left(F(c) + \frac{\varepsilon^2}{2} |\nabla c|^2 \right) + \frac{\beta}{2} \mathscr{G}(c) \tag{10.7}$$

where $\beta > 0$ is a regularization parameter. A possible choice for the extra term $\mathscr{G}$ is the following (see, e.g., [51] for other possible choices)

$$\mathscr{G}(c) = \varepsilon |\Delta c|^2 \tag{10.8}$$

for which the corresponding H^{-1}-gradient flow of the energy (10.7) gives rise to the following *anisotropic Cahn-Hilliard* equation

$$\dot{c} - \frac{1}{\varepsilon} \Delta \left(\frac{\gamma(n)}{\varepsilon} F'(c) - \varepsilon \nabla \cdot m + \beta \varepsilon \Delta^2 c \right) = 0 \tag{10.9}$$

with

$$m = \gamma(n) \nabla c + \mathbb{P} \nabla_n \gamma(n) \left(\frac{F(c)}{\varepsilon^2 |\nabla c|} + \frac{1}{2} |\nabla c| \right)$$

where $\mathbb{P} = \mathsf{I} - n \otimes n$, I being the identity matrix and $\nabla_n \gamma(n)$ is the gradient vector containing the partial derivatives of $\gamma(n)$ with respect to the components of the normal n.

In view of the subsequent discussion on the numerical approximation of higher-order spatial differential operators, it is important to highlight the presence of the sixth-order term $\Delta^3 c$ in (10.9).

10.1.1.3 A High Order Phase Field Model for Brittle Fracture

A popular approach for the numerical solutions of fracture models is based on introducing discontinuities into the displacement field by means of remeshing or by enriching the set of basis functions by inserting discontinuities using the partition of unity method. An alternative approach is the variational approach to brittle where the solution to the fracture problem is searched as the minimizer of an

energy functional. The corresponding numerical solution hinges upon the phase-field implementation and the fracture problem is reformulated as a system of partial differential equations completely determininig the evolution of the cracks. For a short overview of these two classes of methods see, e.g., [33] and the references therein.

Recently, in [33] the variational approach to brittle fracture has been extended by proposing a fourth-order model for the phase-field approximation. The presence of higher-order derivative terms in the phase-field equation leads to a greater regularity of the solution. In the sequel, we briefly summarize the resulting differential problem so to highlight the interplay between the elastodynamics equation (cf. Eq. (10.10a) below) and the fourth-order phase field equation (cf. Eq. (10.10b) below). The unknowns of the problem are the displacement field $\mathbf{u} : \Omega \to \mathbb{R}^d$ $d = 2, 3$ and the continuous phase field variable $c : \Omega \to [0, 1]$ describing the crack ($c = 1$ away from the crack and $c = 0$ at the crack). Let λ and μ denote the usual the Lamé constants and $\epsilon = \frac{1}{2}(\nabla \mathbf{u} + \nabla \mathbf{u}^T)$ the symmetric gradient. Since ϵ is a real symmetric matrix, there exists a real orthogonal matrix P and a real diagonal matrix $\mathbf{\Lambda}$ such that $\epsilon = \mathsf{P}\mathbf{\Lambda}\mathsf{P}^T$. We define the matrix $\mathbf{\Lambda}^+ = \mathrm{diag}(\langle\lambda_1\rangle, \langle\lambda_2\rangle, \langle\lambda_3\rangle)$ where $\langle x \rangle$ is the Heaviside function, the matrix $\mathbf{\Lambda}^- = \mathbf{\Lambda} - \mathbf{\Lambda}^+$, and the matrices $\epsilon^\pm = \mathsf{P}\mathbf{\Lambda}^\pm\mathsf{P}^T$. Using these matrices, we introduce the functions

$$\psi_e^+(\epsilon) = \frac{1}{2}\lambda\langle\mathrm{tr}\epsilon\rangle^2 + \mu\mathrm{tr}[(\epsilon^+)^2],$$

$$\psi_e^-(\epsilon) = \frac{1}{2}\lambda(\mathrm{tr}\epsilon - \langle\mathrm{tr}\epsilon\rangle)^2 + \mu\mathrm{tr}\big((\epsilon - \epsilon^+)^2\big),$$

and define the stress tensor as

$$\boldsymbol{\sigma}(\mathbf{u}) = c^2\frac{\partial\psi_e^+}{\partial\epsilon} + \frac{\partial\psi_e^-}{\partial\epsilon}.$$

Finally, the differential problem reads as:

$$\rho\ddot{\mathbf{u}} - \nabla\cdot\boldsymbol{\sigma}(\mathbf{u}) = \mathbf{f} \qquad \text{in } \Omega \times (0, T], \qquad (10.10\text{a})$$

$$\frac{4\ell_0 c}{g_c}\psi_e^+(\epsilon)c - 2\ell_0^2\Delta c + \ell_0^4\Delta^2 c = 1 \qquad \text{in } \Omega \times (0, T], \qquad (10.10\text{b})$$

$$\mathbf{u} = \mathbf{g}_D \qquad \text{on } \Gamma_D \times (0, T], \qquad (10.10\text{c})$$

$$\boldsymbol{\sigma}(\mathbf{u})\mathbf{n} = \mathbf{g}_N \qquad \text{on } \Gamma_N \times (0, T], \qquad (10.10\text{d})$$

$$\Delta c = 0 \qquad \text{in } \partial\Omega \times \times(0, T], \qquad (10.10\text{e})$$

$$\nabla(\ell_0^4\Delta c - 2\ell_0^2 c)\mathbf{n} = 0 \qquad \text{in } \partial\Omega \times \times(0, T], \qquad (10.10\text{f})$$

$$(\mathbf{u}, \dot{\mathbf{u}}) = (\mathbf{u}_0, \mathbf{u}_1) \quad \text{in } \Omega \times \{0\}, \qquad (10.10\text{g})$$

where we split $\partial\Omega = \Gamma_D \cup \Gamma_N$ for the Dirichlet and Neumann boundary conditions, and $\ell_0 > 0$ is suitable length scale parameter.

10.1.2 Notation and Technicalities

Throughout the paper, we consider the usual multi-index notation. In particular, if v is a sufficiently regular bivariate function and $\alpha = (\alpha_1, \alpha_2)$ a multi-index with α_1, α_2 nonnegative integer numbers, the function $D^\alpha v = \partial^{|\alpha|} v / \partial x_1^{\alpha_1} \partial x_2^{\alpha_2}$ is the partial derivative of v of order $|\alpha| = \alpha_1 + \alpha_2 > 0$. For $\alpha = (0,0)$, we adopt the convention that $D^\alpha v$ coincides with v. Also, for the sake of exposition, we may use the shortcut notation $\partial_x v, \partial_y v, \partial_{xx} v, \partial_{xy} v, \partial_{yy} v$, to denote the first- and second-order partial derivatives along the coordinate directions x and y; $\partial_n v, \partial_t v, \partial_{nn} v, \partial_{nt} v, \partial_{tt} v$ to denote the first- and second-order normal and tangential derivatives along a given mesh edge; and $\partial_n^m v$ and $\partial_t^m v$ to denote the normal and tangential derivative of v of order m along a given mesh edge. Finally, let $\mathbf{n} = (n_x, n_y)$ and $\boldsymbol{\tau} = (\tau_x, \tau_y)$ be the unit normal and tangential vectors to a given edge e of an arbitrary polygon P, respectively. We recall the following relations between the first derivatives of v:

$$\partial_n v = \nabla v^T \mathbf{n} = n_x \partial_x v + n_y \partial_y v, \quad \partial_\tau v = \nabla v^T \boldsymbol{\tau} = \tau_x \partial_x v + \tau_y \partial_y v, \qquad (10.11)$$

and the second derivatives of v:

$$\partial_{nn} v = \mathbf{n}^T \mathsf{H}(v)\mathbf{n}, \quad \partial_{n\tau} v = \mathbf{n}^T \mathsf{H}(v)\boldsymbol{\tau}, \quad \partial_{\tau\tau} v = \boldsymbol{\tau}^T \mathsf{H}(v)\boldsymbol{\tau}, \qquad (10.12)$$

respectively, where the matrix $\mathsf{H}(v)$ is the Hessian of v, i.e., $\mathsf{H}_{11}(v) = \partial_{xx} v$, $\mathsf{H}_{12}(v) = \mathsf{H}_{21}(v) = \partial_{xy} v$, $\mathsf{H}_{22}(v) = \partial_{yy} v$.

We use the standard definitions and notation of Sobolev spaces, norms and seminorms [1]. Let k be a nonnegative integer number. The Sobolev space $H^k(\omega)$ consists of all square integrable functions with all square integrable weak derivatives up to order k that are defined on the open bounded connected subset ω of $\mathbb{R}^2$. As usual, if $k = 0$, we prefer the notation $L^2(\omega)$. Norm and seminorm in $H^k(\omega)$ are denoted by $\| \cdot \|_{k,\omega}$ and $| \cdot |_{k,\omega}$, respectively, and $(\cdot, \cdot)_\omega$ denote the L^2-inner product. We omit the subscript ω when ω is the whole computational domain Ω.

Given the mesh partitioning $\Omega_h = \{\mathsf{P}\}$ of the domain Ω into elements P, we define the broken (scalar) Sobolev space for any integer $k > 0$

$$H^k(\Omega_h) = \prod_{\mathsf{P} \in \Omega_h} H^k(\mathsf{P}) = \left\{ v \in L^2(\Omega) : v_{|\mathsf{P}} \in H^k(\mathsf{P}) \right\},$$

which we endow with the broken H^k-norm

$$\|v\|_{k,h}^2 = \sum_{\mathsf{P} \in \Omega_h} \|v\|_{k,\mathsf{P}}^2 \qquad \forall v \in H^k(\Omega_h), \qquad (10.13)$$

and, for $k = 1$, with the broken H^1-seminorm

$$|v|_{1,h}^2 = \sum_{\mathsf{P} \in \Omega_h} \|\nabla v\|_{0,\mathsf{P}}^2 \qquad \forall\, v \in H^1(\Omega_h). \tag{10.14}$$

We denote the linear space of polynomials of degree up to ℓ defined on ω by $\mathbb{P}_\ell(\omega)$, with the useful conventional notation that $\mathbb{P}_{-1}(\omega) = \{0\}$. We denote the space of two-dimensional vector polynomials of degree up to ℓ on ω by $\left[\mathbb{P}_\ell(\omega)\right]^2$; the space of symmetric 2×2-sized tensor polynomials of degree up to ℓ on ω by $\mathbb{P}_{\ell,\mathrm{sym}}^{2\times 2}(\omega)$. Space $\mathbb{P}_\ell(\omega)$ is the span of the finite set of *scaled monomials of degree up to ℓ*, that are given by

$$\mathscr{M}_\ell(\omega) = \left\{ \left(\frac{\mathbf{x} - \mathbf{x}_\omega}{h_\omega} \right)^\alpha \text{ with } |\alpha| \leq \ell \right\},$$

where

– $\mathbf{x}_\omega$ denotes the center of gravity of ω and h_ω its characteristic length, as, for instance, the edge length or the cell diameter for $d = 1, 2$;
– $\alpha = (\alpha_1, \alpha_2)$ is the two-dimensional multi-index of nonnegative integers α_i with degree $|\alpha| = \alpha_1 + \alpha_2 \leq \ell$ and such that $\mathbf{x}^\alpha = x_1^{\alpha_1} x_2^{\alpha_2}$ for any $\mathbf{x} \in \mathbb{R}^2$.

We will also use the set of *scaled monomials of degree exactly equal to ℓ*, denoted by $\mathscr{M}_\ell^*(\omega)$ and obtained by setting $|\alpha| = \ell$ in the definition above.

Finally, we use the letter C in the estimates below to denote a strictly positive constant whose value can change at any instance but that is independent of the discretization parameters such as the mesh size h. Note that C may depend on the the polynomial order, on the constants of the model equations or the variational problem, like the coercivity and continuity constants, or even constants that are uniformly defined for the family of meshes of the approximation while $h \to 0$, such as the mesh regularity constant, the stability constants of the discrete bilinear forms, etc. Whenever it is convenient, we will simplify the notation by using expressions like $x \lesssim y$ and $x \gtrsim y$ to mean that $x \leq Cy$ and $x \geq Cy$, respectively, C being the generic constant in the sense defined above.

10.1.3 Mesh Assumptions

Throughout the paper we assume that $\mathscr{T} = \left\{\Omega_h\right\}_h$ is a family of decompositions of the computational domain Ω, where each mesh Ω_h is a collection of nonoverlapping polygonal elements P with boundary $\partial\mathsf{P}$, such that $\bar{\Omega} = \biguplus_{\mathsf{P} \in \Omega_h} \bar{\mathsf{P}}$. Each mesh is labeled by the *mesh size h*, the diameter of the mesh, defined as usual by $h = \max_{\mathsf{P} \in \Omega_h} h_\mathsf{P}$, where $h_\mathsf{P} = \sup_{\mathbf{x},\mathbf{y} \in \mathsf{P}} |\mathbf{x} - \mathbf{y}|$. We assume the mesh sizes of family $\mathscr{T}$ form a countable subset of $\mathscr{H} = (0, \infty)$ having zero as its unique accumulation

point. We denote the set of mesh vertices v by $\mathscr{V}_h$ and the set of mesh edges e by $\mathscr{E}_h$ Moreover, the symbol h_v is a characteristic lenght associated with each vertex; more precisely, h_v is the average of the diameters of the polygons sharing vertex v. We consider the following mesh regularity assumptions:

(M)   There exists a positive constant γ, *mesh regularity constant*, which is independent of h (and P) and such that for $K \in \Omega_h$ there hold:

   –   **(M1)** P is star-shaped with respect to every point of a ball of radius γh_P, where h_P is the diameter of P;
   –   **(M2)** for every edge e of the cell boundary ∂P of every cell P of Ω_h, it holds that $h_e \geq \gamma h_P$, where h_e denotes the length of e.

All the results contained in the rest of the paper are obtained under assumptions **(M1)–(M2)**.

10.2   The Virtual Element Method for the Polyharmonic Problem

10.2.1   The Continuous Problem

Let $\Omega \subset \mathbb{R}^2$ be a open, bounded, convex domain with polygonal boundary Γ. For any integer $p \geq 1$, we introduce the conforming virtual element method for the approximation of the following problem:

$$(-\Delta)^p u = f \qquad \text{in } \Omega, \tag{10.1a}$$

$$\partial_n^j u = 0 \qquad \text{for } j = 0, \ldots, p - 1 \text{ on } \Gamma, \tag{10.1b}$$

(recall the conventional notation $\partial_n^0 u = u$). Let

$$V \equiv H_0^p(\Omega) = \left\{ v \in H^p(\Omega) : \partial_n^j v = 0 \text{ on } \Gamma, \ j = 0, \ldots, p - 1 \right\}.$$

Denoting the duality pairing between V and its dual V' by $\langle \cdot, \cdot \rangle$, the variational formulation of the polyharmonic problem (10.1) reads as: *Find $u \in V$ such that*

$$a(u, v) = \langle f, v \rangle \qquad \forall v \in V, \tag{10.2}$$

where, for any nonnegative integer ℓ, the bilinear form is given by:

$$a(u, v) = \begin{cases} \int_\Omega \nabla \Delta^\ell u \cdot \nabla \Delta^\ell v \, d\mathbf{x} & \text{for } p = 2\ell + 1, \\[2ex] \int_\Omega \Delta^\ell u \, \Delta^\ell v \, d\mathbf{x} & \text{for } p = 2\ell. \end{cases} \tag{10.3}$$

Whenever $f \in L^2(\Omega)$ we have

$$\langle f, v \rangle = (f, v) = \int_\Omega f v \, dV \, d\mathbf{x}. \tag{10.4}$$

where $(\cdot, \cdot)$ denotes the L^2-inner product. The existence and uniqueness of the solution to (10.2) follows from the Lax-Milgram Theorem because of the continuity and coercivity of the bilinear form $a(\cdot, \cdot)$ with respect to $\| \cdot \|_V = | \cdot |_{p, \Omega}$ which is a norm on $H_0^p(\Omega)$. Moreover, since Ω is a convex polygon, from [64] we know that $u \in H^{2p-m}(\Omega) \cap H_0^p(\Omega)$ if $f \in H^{-m}(\Omega)$, $m \leq p$ and it holds that $\|u\|_{2p-m} \leq C\|f\|_{-m}$. In the following, we denote the coercivity and continuity constants of $a(\cdot, \cdot)$ by α and M, respectively.

Let P be a polygonal element and set

$$a_{\mathsf{P}}(u, v) = \begin{cases} \int_{\mathsf{P}} \nabla \Delta^\ell u \cdot \nabla \Delta^\ell v \, d\mathbf{x} & \text{for } p = 2\ell + 1, \\[2mm] \int_{\mathsf{P}} \Delta^\ell u \, \Delta^\ell v \, d\mathbf{x} & \text{for } p = 2\ell. \end{cases}$$

For an odd p, i.e., $p = 2\ell + 1$, a repeated application of the integration by parts formula yields

$$a_{\mathsf{P}}(u, v) = - \int_{\mathsf{P}} \Delta^p u \, v \, d\mathbf{x} + \int_{\partial \mathsf{P}} \partial_n(\Delta^\ell u) \, \Delta^\ell v \, ds$$

$$+ \sum_{i=1}^{\ell} \left(\int_{\partial \mathsf{P}} \partial_n(\Delta^{p-i} u) \, \Delta^{i-1} v \, ds - \int_{\partial \mathsf{P}} \Delta^{p-i} u \, \partial_n(\Delta^{i-1} v) \, ds \right), \tag{10.5}$$

while, for an even p, i.e., $p = 2\ell$, we have

$$a_{\mathsf{P}}(u, v) = \int_{\mathsf{P}} \Delta^p u \, v \, d\mathbf{x}$$

$$+ \sum_{i=1}^{\ell} \left(\int_{\partial \mathsf{P}} \partial_n(\Delta^{p-i} u) \, \Delta^{i-1} v \, ds - \int_{\partial \mathsf{P}} \Delta^{p-i} u \, \partial_n(\Delta^{i-1} v) \, ds \right). \tag{10.6}$$

10.2.2 The Conforming Virtual Element Approximation

The conforming virtual element discretization of problem (10.2) hinges upon three mathematical objects: (1) the finite dimensional conforming virtual element space

$V_{h,r}^p \subset V$; (2) the continuous and coercive discrete bilinear form $a_h(\cdot,\cdot)$; (3) the linear functional $\langle f_h,\cdot\rangle$.

Using such objects, we formulate the virtual element method as: *Find $u_h \in V_{h,r}^p$ such that*

$$a_h(u_h,v_h) = \langle f_h,v_h\rangle \quad \forall v_h \in V_{h,r}^p. \tag{10.7}$$

The existence and uniqueness of the solution u_h is again a consequence of the Lax-Milgram theorem [35, Theorem 2.7.7, page 62].

10.2.2.1 Virtual Element Spaces

For $p \geq 1$ and $r \geq 2p-1$, the local Virtual Element space on element P is defined by

$$V_{h,r}^p(\mathsf{P}) = \Big\{v_h \in H^p(\mathsf{P}) : \Delta^p v_h \in \mathbb{P}_{r-2p}(\mathsf{P}),\ v_h \in \mathbb{P}_r(\mathrm{e}),\ \partial_n^i v_h \in \mathbb{P}_{r-i}(\mathrm{e}),$$
$$i = 1,\ldots,p-1\ \forall \mathrm{e} \in \partial\mathsf{P}\Big\},$$

with the conventional notation that $\mathbb{P}_{-1}(\mathsf{P}) = \{0\}$. The virtual element space $V_{h,r}^p(\mathsf{P})$ contains the space of polynomials $\mathbb{P}_r(\mathsf{P})$, for $r \geq 2p-1$. Moreover, for $p = 1$, it coincides with the conforming virtual element space for the Poisson equation [16], and for $p = 2$, it coincides with the conforming virtual element space for the biharmonic equation [36]. The requirement $v_h \in H^p(\mathsf{P})$ implies that suitable compatibility conditions for v_h and its derivatives up to order $p-1$ must hold at the vertices of the polygon (see, e.g., [66, Theorems 1.5.2.4 and 1.5.7.8] and [29, Section 5]).

We characterize the functions in $V_{h,r}^p(\mathsf{P})$ through the following set of *degrees of freedom*:

(D1) $h_\mathsf{v}^{|v|} D^v v_h(\mathsf{v})$, $|v| \leq p-1$ for any vertex v of the polygonal boundary $\partial\mathsf{P}$;

(D2) $h_\mathrm{e}^{-1} \int_\mathrm{e} q v_h\, ds$ for any $q \in \mathbb{P}_{r-2p}(\mathrm{e})$ and any edge e of the polygonal boundary $\partial\mathsf{P}$;

(D3) $h_\mathrm{e}^{-1+j} \int_\mathrm{e} q \partial_n^j v_h\, ds$ for any $q \in \mathbb{P}_{r-2p+j}(\mathrm{e})$, $j = 1,\ldots,p-1$ and any edge e of $\partial\mathsf{P}$;

(D4) $h_\mathsf{P}^{-2} \int_\mathsf{P} q_h v_h\, d\mathbf{x}$ for any $q \in \mathbb{P}_{r-2p}(\mathsf{P})$.

Here, as usual, we assume that $\mathbb{P}_{-n}(\cdot) = \{0\}$ for $n \geq 1$. Figure 10.1 illustrates the degrees of freedom on a given edge e for $p = 1,2,3$ (Laplace, biharmonic, and triharmonic case) and $r = 2p-1, 2p$; the corresponding internal degrees of freedom (D4) are absent in the case $r = 2p-1$, while reduce to a single one in the
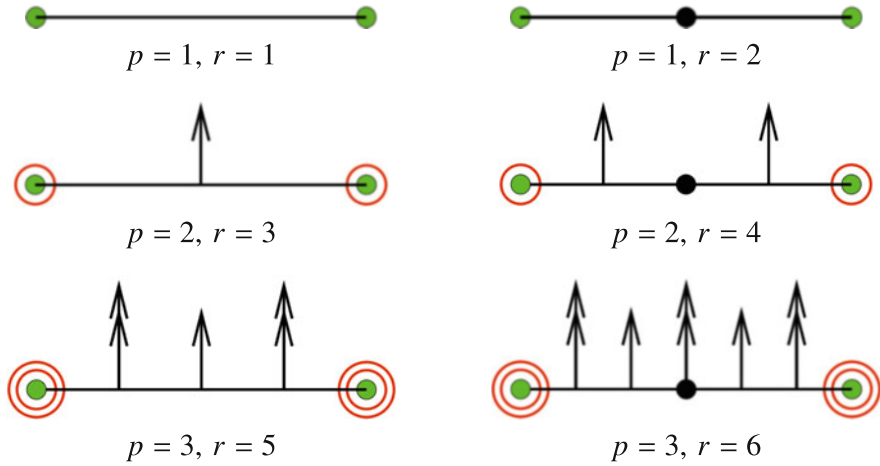
Fig. 10.1 Edge degrees of freedom of the Virtual Element space $V_{h,r}^p(\mathsf{P})$ for the polyharmonic problem with $p = 1$ (top panels, Laplace operator), $p = 2$ (middle panels, bi-harmonic operator), $p = 3$ (bottom panels, tri-harmonic operator). Here, p is the order of the partial differential operator; $r = 1, 2, \ldots, 6$ are the integer parameters that specify the degree of the polynomial subspace $\mathbb{P}_r(\mathsf{P})$ of the VEM space $V_{h,r}^3(\mathsf{P})$. The (green) dots at the vertices represent the vertex values and each (red) vertex circle represents an order of derivation. The (black) dot on the edge represents the moment of $v_{h|e}$; the arrows represent the moments of $\partial_n v_{h|e}$; the double arrows represent the moments of $\partial_{nn} v_{h|e}$. The corresponding internal degrees of freedom (D4) are absent in the case $r = 2p - 1$, while reduce to a single one in the case $r = 2p$

case $r = 2p$. Finally, we note that in general the internal degrees of freedom **(D4)** make it possible to define the L^2-orthogonal polynomial projection of v_h onto the space of polynomial of degree $r - 2p$.

The dimension of $V_{h,r}^p(\mathsf{P})$ is

$$d(V_{h,r}^p(\mathsf{P})) = \frac{p(p+1)}{2} N^{\mathscr{P}} + N^{\mathscr{P}} \sum_{j=0}^{p-1} (r - 2p + j + 1) + \frac{(r - 2p + 1)(r - 2p + 2)}{2},$$

where $N^{\mathscr{P}}$ is the number of vertices, which equals the number of edges, of P.

In [9], it is proved that the above choice of degrees of freedom is unisolvent in $V_{h,r}^p(\mathsf{P})$.

Building upon the local spaces $V_{h,r}^p(\mathsf{P})$ for all $\mathsf{P} \in \Omega_h$, the *global* conforming virtual element space $V_{h,r}^p$ is defined on Ω as

$$V_{h,r}^p = \left\{ v_h \in H_0^p(\Omega) \; : \; v_{h|\mathsf{P}} \in V_{h,r}^p(\mathsf{P}) \; \forall \mathsf{P} \in \Omega_h \right\}. \tag{10.8}$$

We remark that the associated global space is made of $H^p(\Omega)$ functions. Indeed, the restriction of a virtual element function v_h to each element P belongs to $H^p(\mathsf{P})$ and

glues with C^{p-1}-regularity across the internal mesh faces. The set of global degrees of freedom inherited by the local degrees of freedom are:

- $h_V^{|v|} D^v v_h(v)$, $|v| \leq p-1$ for every interior vertex v of Ω_h;
- $h_e^{-1} \int_e q v_h \, ds$ for any $q \in \mathbb{P}_{r-2p}(e)$ and every interior edge $e \in \mathcal{E}_h$;
- $h_e^{-1+j} \int_e q \partial_n^j v_h \, ds$ for any $q \in \mathbb{P}_{r-2p+j}(e)$ $j = 1, \ldots, p-1$ and every interior edge $e \in \mathcal{E}_h$;
- $h_P^{-2} \int_P q v_h \, d\mathbf{x}$ for any $q \in \mathbb{P}_{r-2p}(P)$ and every $P \in \Omega_h$.

10.2.2.2 Modified Lowest Order Virtual Element Spaces

In this section, we briefly discuss the possibility of introducing modified lowest order virtual element spaces with a reduced number of degrees of freedom with respect to the corresponding lowest order ones that were introduced previously. The price we pay is a reduced order of accuracy since the polynomial functions included in such modified spaces has a lower degree.

For the sake of presentation we start from the case $p = 3$, while we refer the reader to [36] for the case of $p = 2$ and Sect. 10.3.2.1 where the reduced virtual space is employed in the context of the approximation of the Cahn-Hilliard problem. Consider the modified local virtual element space:

$$\tilde{V}_{h,5}^3(P) = \left\{ v_h \in H^3(P) \; : \; \Delta^3 v_h = 0, \, v_h \in \mathbb{P}_5(e), \, \partial_n v_h \in \mathbb{P}_3(e), \right.$$

$$\left. \partial_{nn} v_h \in \mathbb{P}_2(e) \; \forall e \in \partial P \right\}$$

with associated degrees of freedom:

(D1') $\quad h_V^{|v|} D^v v_h(v)$, $|v| \leq 2$ for any vertex v of ∂P;

(D2') $\quad h_e \int_e \partial_{nn} v_h \, ds$ for any edge e of ∂P.

In Ref. [9], we proved that the degrees of freedom **(D1')** and **(D2')** are unisolvent in $\tilde{V}_{h,5}^3(P)$ and this space contains the linear subspace of polynomials of degree up to 4. Moreover, the associated global space obtained by gluing together all the elemental spaces $\tilde{V}_{h,5}^3(P)$ reads as:

$$\tilde{V}_{h,5}^3 = \left\{ v_h \in H_0^3(\Omega) \; : \; v_h|_P \in \tilde{V}_{h,5}^3(P) \; \forall P \in \Omega_h \right\}, \tag{10.9}$$

is made of $H^3(\Omega)$ functions.

Analogously, in the general case we can build the modified lowest order spaces containing the space of polynomials of degree up to $2p - 2$:

$$\tilde{V}_{h,2p-1}^{p}(\mathsf{P}) = \Big\{ v_h \in H^p(\mathsf{P}) : \Delta^p v_h = 0, \, v_h \in \mathbb{P}_{2p-1}(e), \, \partial_n^i v_h \in \mathbb{P}_{2p-2-i}(e),$$

$$i = 1, \dots, p - 1 \, \forall e \in \partial \mathsf{P} \Big\},$$

with associated degrees of freedom:

(D1') $h_{\mathsf{v}}^{|v|} D^v v_h(\mathsf{v}), \, |v| \leq p - 1$ for any vertex v of $\partial \mathsf{P}$;

(D2') $h_{\mathsf{e}}^{-1+j} \displaystyle\int_{\mathsf{e}} q \, \partial_n^i v_h \, ds$ for any $q \in \mathbb{P}_{j-2}(\mathsf{e})$ and edge e of $\partial \mathsf{P}$, $j = 1, \dots, p-1$.

10.2.2.3   Discrete Bilinear Form

To define the elliptic projection $\Pi_r^{\nabla, \mathsf{P}} : V_{h,r}^p(\mathsf{P}) \to \mathbb{P}_r(\mathsf{P})$, we first need to introduce the *vertex average projector* $\widehat{\Pi}^{\mathsf{P}} : V_{h,r}^p(\mathsf{P}) \to \mathbb{P}_0(\mathsf{P})$, which projects any smooth enough function defined on P onto the space of constant polynomials. To this end, consider the continuous function ψ defined on P. The *vertex average projection* of ψ onto the constant polynomial space is given by:

$$\widehat{\Pi}^{\mathsf{P}} \psi = \frac{1}{N^{\mathscr{P}}} \sum_{\mathsf{v} \in \partial \mathsf{P}} \psi(\mathsf{v}). \qquad (10.10)$$

Finally, we define the elliptic projection $\Pi_r^{\nabla, \mathsf{P}} : V_{h,r}^p(\mathsf{P}) \to \mathbb{P}_r(\mathsf{P})$ as the solution of the following finite dimensional variational problem

$$a_{\mathsf{P}}(\Pi_r^{\nabla, \mathsf{P}} v_h, q) = a_{\mathsf{P}}(v_h, q) \qquad \forall q \in \mathbb{P}_r(\mathsf{P}), \qquad (10.11)$$

$$\widehat{\Pi}^{\mathsf{P}} D^v \Pi_r^{\nabla, \mathsf{P}} v_h = \widehat{\Pi}^{\mathsf{P}} D^v v_h \qquad |v| \leq p - 1. \qquad (10.12)$$

According to Reference [9], such operator has two important properties:

(i) it is a polynomial-preserving operator in the sense that $\Pi_r^{\nabla, \mathsf{P}} q = q$ for every $q \in \mathbb{P}_r(\mathsf{P})$;

(ii) $\Pi_r^{\nabla, \mathsf{P}} v_h$ is *computable* using only the degrees of freedom of v_h.

We write the symmetric bilinear form $a_h : V_{h,r}^p \times V_{h,r}^p \to \mathbb{R}$ as the sum of local terms

$$a_h(u_h, v_h) = \sum_{\mathsf{P} \in \Omega_h} a_{h,\mathsf{P}}(u_h, v_h), \qquad (10.13)$$

where each local term $a_{h,\mathsf{P}} : V_{h,r}^p(\mathsf{P}) \times V_{h,r}^p(\mathsf{P}) \to \mathbb{R}$ is a symmetric bilinear form. We set

$$a_{h,\mathsf{P}}(u_h, v_h) = a_{\mathsf{P}}(\Pi_r^{\nabla,\mathsf{P}} u_h, \Pi_r^{\nabla,\mathsf{P}} v_h) + S^{\mathsf{P}}(u_h - \Pi_r^{\nabla,\mathsf{P}} u_h, v_h - \Pi_r^{\nabla,\mathsf{P}} v_h), \tag{10.14}$$

where $S^{\mathsf{P}} : V_{h,r}^p(\mathsf{P}) \times V_{h,r}^p(\mathsf{P}) \to \mathbb{R}$ is a symmetric positive definite bilinear form such that

$$\sigma_* a_{\mathsf{P}}(v_h, v_h) \le S^{\mathsf{P}}(v_h, v_h) \le \sigma^* a_{\mathsf{P}}(v_h, v_h) \qquad \forall v_h \in V_{h,r}^p(\mathsf{P}) \text{ with } \Pi_r^{\nabla,\mathsf{P}} v_h = 0, \tag{10.15}$$

for two some positive constants σ_*, σ^* independent of h and P. The bilinear form $a_{h,\mathsf{P}}(\cdot, \cdot)$ has the two fundamental properties of *r-consistency* and *stability* [9]:

(*i*) *r*-**Consistency**: for every polynomial $q \in \mathbb{P}_r(\mathsf{P})$ and function $V_{h,r}^p(\mathsf{P})$ we have:

$$a_{h,\mathsf{P}}(v_h, q) = a_{\mathsf{P}}(v_h, q); \tag{10.16}$$

(*ii*) **Stability**: there exist two positive constants α_*, α^* independent of h and P such that for every $v_h \in V_{h,r}^p(\mathsf{P})$ it holds:

$$\alpha_* a_{\mathsf{P}}(v_h, v_h) \le a_{h,\mathsf{P}}(v_h, v_h) \le \alpha^* a_{\mathsf{P}}(v_h, v_h). \tag{10.17}$$

10.2.2.4 Discrete Load Term

We denote by f_h the piecewise polynomial approximation of f on Ω_h given by

$$f_{h|\mathsf{P}} = \Pi_{r-p}^{0,\mathsf{P}} f, \tag{10.18}$$

for $r \ge 2p - 1$ and $\mathsf{P} \in \Omega_h$. Then, we set

$$\langle f_h, v_h \rangle = \sum_{\mathsf{P} \in \Omega_h} \int_{\mathsf{P}} f_h v_h \, d\mathbf{x} \tag{10.19}$$

which implies, using the L^2-orthogonal projection, that

$$\langle f_h, v_h \rangle = \sum_{\mathsf{P} \in \Omega_h} \int_{\mathsf{P}} \Pi_{r-p}^{0,\mathsf{P}} f \, \Pi_{r-p}^{0,\mathsf{P}} v_h \, d\mathbf{x} = \sum_{\mathsf{P} \in \Omega_h} \int_{\mathsf{P}} f \, \Pi_{r-p}^{0,\mathsf{P}} v_h \, d\mathbf{x}. \tag{10.20}$$

The right-hand side of (10.20) is computable by a combined use of the degrees of freedom **(D1)–(D4)** and the enhanced approach of Reference [2].

10.2.2.5 VEM Spaces with Arbitrary Degree of Continuity

In this section we briefly sketch the construction of global virtual element spaces with arbitrary high order of continuity. More precisely, we consider the local virtual element space defined as before, for $r \geq 2p - 1$:

$$V_{h,r}^p(\mathsf{P}) = \Big\{ v_h \in H^p(\mathsf{P}) : \; \Delta^p v_h \in \mathbb{P}_{r-2p}(\mathsf{P}), \; v_h \in \mathbb{P}_r(\mathsf{e}), \; \partial_n^j v_h \in \mathbb{P}_{r-j}(\mathsf{e}),$$

$$j = 1, \ldots, p - 1 \; \forall \mathsf{e} \in \partial \mathsf{P} \Big\}.$$

Differently from the previous section, we make the degrees of freedom depend on a given parameter t with $0 \leq t \leq p - 1$. For a given value of t we choose the *degrees of freedom* as follows

(D1) $\quad h_\mathsf{v}^{|\nu|} D^\nu v_h(\mathsf{v}), |\nu| \leq p - 1$ for any vertex v of P;

(D2) $\quad h_\mathsf{e}^{-1} \displaystyle\int_\mathsf{e} v_h q \, ds$ for any $q \in \mathbb{P}_{r-2p}(\mathsf{e})$, for any edge e of $\partial \mathsf{P}$;

(D3) $\quad h_\mathsf{e}^{-1+j} \displaystyle\int_\mathsf{e} \partial_n^j v_h q \, ds$ for any $q \in \mathbb{P}_{r-2p+j}(\mathsf{e})$ and edge $\mathsf{e} \in \partial \mathsf{P}$, $j = 1, \ldots, p - 1$;

(D4') $\quad h_\mathsf{P}^{-2} \displaystyle\int_\mathsf{P} q v_h \, d\mathbf{x}$ for any $q \in \mathbb{P}_{r-2(p-t)}(\mathsf{P})$;

where as usual we assume $\mathbb{P}_{-n}(\cdot) = \{0\}$ for $n = 1, 2, 3, \ldots$.

This set of degrees is still unisolvent, cf. [9]. Moreover, for $r \geq 2p - 1$ it holds that $\mathbb{P}_r(\mathsf{P}) \subset V_{h,r}^p(\mathsf{P})$. Finally, it is worth noting that the choice **(D4')**, if compared with **(D4)**, still guarantees that the associated global space is made of C^{p-1} functions.

However, in this latter case we can use the degrees of freedom **(D1)–(D4')** to solve a differential problem involving the Δ^{p-t} operator and $C^{p-1}(\Omega)$ basis functions. For the sake of exposition, let us consider the following two examples, in the context of the Laplacian and the Bilaplacian problem.

1. Choosing p and t such that $p - t = 1$ we obtain a C^{p-1}-conforming virtual element method for the solution of the Laplacian problem. For example, for $p = 3, t = 2$ and $r = 5$, the local space $V_{h,5}^3(\mathsf{P})$ endowed with the corresponding degrees of freedom **(D1)–(D4')** can be employed to build a global space made of C^2 functions. It is also worth mentioning that the new choice **(D4')**, differently from the original choice **(D4)**, is essential for the computability of the elliptic projection, see (10.11)–(10.12), with respect to the bilinear form $a_\mathsf{P}(\cdot, \cdot) = \int_\mathsf{P} \nabla(\cdot)\nabla(\cdot) \, d\mathbf{x}$.

P. F. Antonietti et al.

2. Choosing p and t such that $p - t = 2$ we have a C^{p-1}-conforming virtual element method for the solution of the Bilaplacian problem. For example, for $p = 3$, $t = 1$ and $r = 5$, similarly to the previous case, the space $V_{h,5}^3(\mathsf{P})$ together with (D1)–(D4') provides a global space of C^2 functions that can be employed for the solution of the biharmonic problem.

It is worth remembering that C^1-regular virtual element basis function has been employed, e.g., in [21] to study residual based a posteriori error estimators for the virtual element approximation of second order elliptic problems. Moreover, the solution of coupled elliptic problems of different order can take advantage from this flexibility of the degree of continuity of the basis functions. Indeed, for the sake of clarity consider the conforming virtual element approximation of the following simplified situation:

$$
\begin{aligned}
-\Delta u_1 &= f_1 & &\text{in } \Omega_1, \\
\Delta^2 u_2 &= f_2 & &\text{in } \Omega_2, \\
u_1 &= u_2 & &\text{on } \Gamma = \Omega_1 \cap \Omega_2, \\
\partial_n u_1 &= \partial_n u_2 & &\text{on } \Gamma, \\
u_1 &= 0 & &\text{on } \partial\Omega_1 \setminus \Gamma, \\
u_2 &= 0 & &\text{on } \partial\Omega_2 \setminus \Gamma, \\
\partial_n u_2 &= 0 & &\text{on } \partial\Omega_2 \setminus \Gamma.
\end{aligned}
$$

Handling the coupling conditions on Γ asks for the use of C^1-regular virtual basis functions not only in Ω_2 where the bilaplacian problem is defined, but also in Ω_1, where the second order elliptic problem is defined. Indeed, a simple use of C^0-basis functions in Ω_1, which would be natural given the second order of the problem, would not allow the imposition (or at least a simple imposition) of the gluing condition on the normal derivatives.

10.2.2.6 Convergence Results

The following convergence result in the energy norm holds (see [9] for the proof).

Theorem 10.1 *Let $f \in H^{r-p+1}(\Omega)$ be the forcing term at the right-hand side, u the solution of the variational problem* (10.2) *and $u_h \in V_{h,r}^p$ the solution of the virtual element method* (10.7). *Then, it holds that*

$$
\|u - u_h\|_V \leq C h^{r-(p-1)}\big(|u|_{r+1} + |f|_{r-p+1}\big). \tag{10.21}
$$

Moreover, the following convergence results in lower order norms can established [9].

Theorem 10.2 (Even p, Even Norms) *Let $f \in H^{r-p+1}(\Omega)$, u the solution of the variational problem (10.2) with $p = 2\ell$ and $v_h \in V_{h,r}^p$ the solution of the virtual element method (10.7). Then, there exists a positive constant C independent of h such that*

$$|u - u_h|_{2i} \le Ch^{r+1-2i}\Big(|u|_{r+1} + |f|_{r-(p-1)}\Big), \tag{10.22}$$

for every integer $i = 0, \dots, \ell - 1$.

Theorem 10.3 (Even p, Odd Norms) *Let $f \in H^{r-p+1}(\Omega)$, and u the solution of the variational problem (10.2) with $p = 2\ell$ and $u_h \in V_{h,r}^p$ the solution of the virtual element method (10.7). Then, there exists a positive constant C independent of h such that*

$$|u - u_h|_{2i+1} \le Ch^{(r+1)-(2i+1)}\Big(|u|_{r+1} + |f|_{r-(p-1)}\Big), \tag{10.23}$$

for every integer $i = 0, \dots, \ell - 1$.

Theorem 10.4 (Odd p, Even Norms) *Let u be the solution of the variational problem (10.2) and $u_h \in V_{h,r}^p$ the solution of the virtual element method (10.7). Then, there exists a positive constant C independent of h such that*

$$|u - u_h|_{2i} \le Ch^{(r+1)-2i}\Big(|u|_{r+1} + |f|_{r-(p-1)}\Big), \tag{10.24}$$

for every integer $i = 0, \dots, \ell - 1$.

Theorem 10.5 (Odd p, Odd Norms) *Let u be the solution of the variational problem (10.2) and $u_h \in V_{h,r}^p$ the solution of the virtual element method (10.7). Then, there exists a positive constant C independent of h such that*

$$|u - u_h|_{2i+1} \le Ch^{(r+1)-(2i+1)}\Big(|u|_{r+1} + |f|_{r-(p-1)}\Big), \tag{10.25}$$

for every integer $i = 0, \dots, \ell - 1$.

10.3   The Virtual Element Method for the Cahn-Hilliard Problem

10.3.1   The Continuous Problem

Let $\Omega \subset \mathbb{R}^2$ be an open, bounded domain with polygonal boundary Γ, $\psi : \mathbb{R} \to \mathbb{R}$ with $\psi(x) = (1 - x^2)^2/4$ and $\phi(x) = \psi'(x)$. We consider the Cahn-Hilliard

problem: *Find $u(x, t) : \Omega \times [0, T] \to \mathbb{R}$ such that:*

$$\dot{u} - \Delta\big(\phi(u) - \gamma^2 \Delta u\big) = 0 \qquad \text{in } \Omega \times [0, T], \tag{10.1a}$$

$$u(\cdot, 0) = u_0(\cdot) \quad \text{in } \Omega, \tag{10.1b}$$

$$\partial_n u = \partial_n\big(\phi(u) - \gamma^2 \Delta u\big) = 0 \qquad \text{on } \partial\Omega \times [0, T], \tag{10.1c}$$

where ∂_n denotes the (outward) normal derivative and $\gamma \in \mathbb{R}^+$, $0 < \gamma \ll 1$, represents the interface parameter. On the domain boundary we impose a no flux-type condition on u and the chemical potential $\phi(u) - \gamma^2 \Delta u$.

To define the variational formulation of problem (10.1a)–(10.1c) we introduce the three bilinear forms:

$$a^\Delta(v, w) = \int_\Omega (\nabla^2 v) : (\nabla^2 w)\, d\mathbf{x} \qquad \forall v, w \in H^2(\Omega),$$

$$a^\nabla(v, w) = \int_\Omega \nabla v \cdot \nabla w\, d\mathbf{x} \qquad \forall v, w \in H^1(\Omega),$$

$$a^0(v, w) = \int_\Omega v\, w\, d\mathbf{x} \qquad \forall v, w \in L^2(\Omega),$$

(∇^2 being the Hessian operator) and the semi-linear form

$$r(z; v, w) = \int_\Omega \phi'(z) \nabla v \cdot \nabla w\, d\mathbf{x} \quad \forall z, v, w \in H^2(\Omega).$$

Finally, introducing the functional space

$$V = \big\{ v \in H^1(\Omega) : \partial_n v = 0 \text{ on } \Gamma \big\}, \tag{10.2}$$

which is a subspace of $H^1(\Omega)$.

The weak formulation of problem (10.1a)–(10.1c) reads as: *Find $u(\cdot, t) \in V$ such that*

$$a^0(\dot{u}, v) + \gamma^2 a^\Delta(u, v) + r(u; u, v) = 0 \quad \forall v \in V, \tag{10.3a}$$

$$u(\cdot, 0) = u_0. \tag{10.3b}$$

10.3.2   The Conforming Virtual Element Approximation

In this section, we introduce the main building blocks for the conforming virtual discretization of the Cahn-Hilliard equation, report a convergence result and collect some numerical results assessing the theoretical properties of the proposed scheme.

10.3.2.1   A C^1 Virtual Element Space

We briefly recall the construction of the virtual element space $W_h \subset H^2(\Omega)$ that we use to discretize (10.3a)–(10.3b); see [6] for more details.

Given an element $\mathsf{P} \in \Omega_h$, the *augmented* local space $\widetilde{V}_{h|\mathsf{P}}$ is defined by

$$
\widetilde{V}_{h|\mathsf{P}} = \Big\{ v \in H^2(\mathsf{P}) : \Delta^2 v \in \mathbb{P}_2(\mathsf{P}),\, v_{|\partial\mathsf{P}} \in C^0(\partial\mathsf{P}),\, v_{|e} \in \mathbb{P}_3(e) \quad \forall e \in \partial\mathsf{P},
$$

$$
\nabla v_{|\partial\mathsf{P}} \in \big[C^0(\partial\mathsf{P})\big]^2,\, \partial_n v_{|e} \in \mathbb{P}_1(e) \quad \forall e \in \partial\mathsf{P} \Big\}, \qquad (10.4)
$$

with ∂_n denoting the (outward) normal derivative.

Remark 10.1 The space $\widetilde{V}_{h|\mathsf{P}}$ corresponds to the space $\widetilde{V}_{h,2p-1}^p(\mathsf{P})$ with $p = 2$ introduced in Sect. 10.2.2.2.

We consider the two sets of linear operators from $\widetilde{V}_{h|\mathsf{P}}$ into $\mathbb{R}$ denoted by **(D1)** and **(D2)** and defined as follows:

(D1)   contains linear operators evaluating v_h at the $n = n(\mathsf{P})$ vertices of P;
(D2)   contains linear operators evaluating ∇v_h at the $n = n(\mathsf{P})$ vertices of P.

The output values of the two sets of operators **(D1)** and **(D2)** are sufficient to uniquely determine v_h and ∇v_h on the boundary of P (cf. Sect. 10.2.2.2).

We use of the following local bilinear forms for all $\mathsf{P} \in \Omega_h$

$$
a_\mathsf{P}^\Delta(v, w) = \int_\mathsf{P} (\nabla^2 v) : (\nabla^2 w)\, d\mathbf{x} \quad \forall v, w \in H^2(\mathsf{P}), \qquad (10.5)
$$

$$
a_\mathsf{P}^\nabla(v, w) = \int_\mathsf{P} \nabla v \cdot \nabla w\, d\mathbf{x} \quad \forall v, w \in H^1(\mathsf{P}), \qquad (10.6)
$$

$$
a_\mathsf{P}^0(v, w) = \int_\mathsf{P} v\, w\, d\mathbf{x} \qquad\qquad \forall v, w \in L^2(\mathsf{P}). \qquad (10.7)
$$

Now, we introduce the elliptic projection operator $\Pi_2^{\Delta,\mathsf{P}} : \widetilde{V}_{h|\mathsf{P}} \rightarrow \mathbb{P}_2(\mathsf{P})$ defined by

$$
a_\mathsf{P}^\Delta(\Pi_2^{\Delta,\mathsf{P}} v_h, q) = a_\mathsf{P}^\Delta(v_h, q) \qquad\qquad \forall q \in \mathbb{P}_2(\mathsf{P}), \qquad (10.8)
$$

$$
(\!(\Pi_2^{\Delta,\mathsf{P}} v_h, q)\!)_\mathsf{P} = (\!(v_h, q)\!)_\mathsf{P} \qquad\qquad \forall q \in \mathbb{P}_1(\mathsf{P}), \qquad (10.9)
$$

for all $v_h \in \widetilde{V}_{h|\mathsf{P}}$ where $(\!(\cdot, \cdot)\!)_\mathsf{P}$ is the Euclidean scalar product acting on the vectors that collect the vertex function values, i.e.

$$
(\!(v_h, w_h)\!)_\mathsf{P} = \sum_{\mathsf{v} \in \mathscr{V}_\mathsf{P}} v_h(\mathsf{v})\, w_h(\mathsf{v}) \quad \forall v_h, w_h \in C^0(\mathsf{P}).
$$

As shown in [6], the operator $\Pi_2^{\Delta,\mathsf{P}} : \widetilde{V}_{h|\mathsf{P}} \to \mathbb{P}_2(\mathsf{P})$ is well defined and uniquely determined on the basis of the informations carried by the linear operators in **(D1)** and **(D2)**.

Hinging upon the augmented space $\widetilde{V}_{h|\mathsf{P}}$ and employing the projector $\Pi_2^{\Delta,\mathsf{P}}$ we define our virtual local space

$$W_{h|\mathsf{P}} = \big\{ v \in \widetilde{V}_{h|\mathsf{P}} \ : \ a_\mathsf{P}^0(\Pi_2^{\Delta,\mathsf{P}}(v), q) = a_\mathsf{P}^0(v, q) \quad \forall q \in \mathbb{P}_2(\mathsf{P}) \big\}. \qquad (10.10)$$

Since $W_{h|\mathsf{P}} \subset \widetilde{V}_{h|\mathsf{P}}$, operator $\Pi_2^{\Delta,\mathsf{P}}$ is well defined on $W_{h|\mathsf{P}}$ and computable by using the values provided by **(D1)** and **(D2)**. Moreover, the set of operators **(D1)** and **(D2)** constitutes a set of degrees of freedom for the space $W_{h|\mathsf{P}}$. Finally, there holds $\mathbb{P}_2(\mathsf{P}) \subseteq W_{h|\mathsf{P}}$.

We now introduce two further projectors on the local space $W_{h|\mathsf{P}}$, namely $\Pi_2^{0,\mathsf{P}}$ and $\Pi_2^{\nabla,\mathsf{P}}$, that will be employed together with the above projector $\Pi_2^{\Delta,\mathsf{P}}$ to build the discrete counterparts of the bilinear forms in (10.5). Operator $\Pi_2^{0,\mathsf{P}} : W_{h|\mathsf{P}} \to \mathbb{P}_2(\mathsf{P})$ is the standard L^2 projector on the space of quadratic polynomials in P. This is computable by means of the values of the degrees of freedom **(D1)** and **(D2)** (cf. [6]). To define $\Pi_2^{\nabla,\mathsf{P}} : W_{h|\mathsf{P}} \to \mathbb{P}_2(\mathsf{P})$ we need the additional bilinear form $a^\nabla(\cdot, \cdot) : W_{h|\mathsf{P}} \times W_{h|\mathsf{P}} \to \mathbb{R}$ that is given by

$$a^\nabla(v, w) = \int_\Omega \nabla v \cdot \nabla w \, d\mathbf{x} \quad \forall v, w \in H^1(\Omega).$$

Operator $\Pi_2^{\nabla,\mathsf{P}}$ is the elliptic projection defined with respect to $a^\nabla(\cdot, \cdot)$:

$$a_\mathsf{P}^\nabla(\Pi_2^{\nabla,\mathsf{P}} v_h, q) = a_\mathsf{P}^\nabla(v_h, q) \quad \forall q \in \mathbb{P}_2(\mathsf{P}), \qquad (10.11\text{a})$$

$$\int_\mathsf{P} \Pi_2^{\nabla,\mathsf{P}} v_h d\mathbf{x} = \int_\mathsf{P} v_h \, d\mathbf{x}. \qquad (10.11\text{b})$$

Such operator is well defined and uniquely determined by the values of **(D1)** and **(D2)** [6].

We are now ready to introduce the global virtual element space, which defined as follows

$$W_h = \big\{ v \in V \ : \ v_{|\mathsf{P}} \in W_{h|\mathsf{P}} \quad \forall \mathsf{P} \in \Omega_h \big\}.$$

The virtual element functions in W_h and their gradients are continuous fields on Ω, so this functional space is a conforming subspace of $H^2(\Omega)$. The *global degrees of freedom* of W_h are obtained by collecting the elemental degrees of freedom, so the

dimension of W_h is three times the number of the mesh vertices, and every virtual element function v_h defined on Ω is uniquely determined by

(*i*) its values at the mesh vertices;
(*ii*) its gradient values at the mesh vertices.

Finally, we recommended to scale the degrees of freedom **(D2)** by some local characteristic mesh size h_V in order to obtain a better condition number of the final system.

10.3.2.2 Virtual Element Bilinear Forms

We start by introducing the discrete versions of the elemental bilinear form forms in (10.5). Let $\mathsf{P} \in \Omega_h$ be a generic mesh element and $s_{\mathsf{P}}(\cdot, \cdot) : W_{h|\mathsf{P}} \times W_{h|\mathsf{P}} \to \mathbb{R}$ the positive definite bilinear form given by:

$$s_{\mathsf{P}}(v_h, w_h) = \sum_{\mathsf{V} \in \mathscr{V}_{\mathsf{P}}} \left(v_h(\mathsf{V}) \, w_h(\mathsf{V}) + h_{\mathsf{V}}^2 \, \nabla v_h(\mathsf{V}) \cdot \nabla w_h(\mathsf{V}) \right) \quad \forall v_h, w_h \in W_{h|\mathsf{P}},$$

where h_{V} is a characteristic mesh size lenght associated with node V, e.g., the maximum diameter among the elements having V as a vertex.

Recalling (10.5), we consider the virtual element bilinear forms:

$$a_{h,\mathsf{P}}^{\triangle}(v_h, w_h) = a_{\mathsf{P}}^{\triangle}(\Pi_2^{\triangle,\mathsf{P}} v_h, \Pi_2^{\triangle,\mathsf{P}} w_h) + h_{\mathsf{P}}^{-2} s_{\mathsf{P}}\left(v_h - \Pi_2^{\triangle,\mathsf{P}} v_h, w_h - \Pi_2^{\triangle,\mathsf{P}} w_h\right),$$
$$(10.12)$$

$$a_{h,\mathsf{P}}^{\nabla}(v_h, w_h) = a_{\mathsf{P}}^{\nabla}(\Pi_2^{\nabla,\mathsf{P}} v_h, \Pi_2^{\nabla,\mathsf{P}} w_h) + s_{\mathsf{P}}\left(v_h - \Pi_2^{\nabla,\mathsf{P}} v_h, w_h - \Pi_2^{\nabla,\mathsf{P}} w_h\right),$$
$$(10.13)$$

$$a_{h,\mathsf{P}}^{0}(v_h, w_h) = a_{\mathsf{P}}^{0}(\Pi_2^{0,\mathsf{P}} v_h, \Pi_2^{0,\mathsf{P}} w_h) + h_{\mathsf{P}}^2 s_{\mathsf{P}}\left(v_h - \Pi_2^{0,\mathsf{P}} v_h, w_h - \Pi_2^{0,\mathsf{P}} w_h\right)$$
$$(10.14)$$

for all $v_h, w_h \in W_{h|\mathsf{P}}$. Under the mesh regularity conditions of Sect. 10.1.3, we can prove the consistency and stability of the discrete bilinear forms. Let the symbol † stands for "$\triangle$", "∇" or "0". We have:

(A) (*polynomial consistency*) $a_{h,\mathsf{P}}^{\dagger}(p, v_h) = a_{\mathsf{P}}^{\dagger}(p, v_h) \quad \forall p \in \mathbb{P}_2(\mathsf{P}), \, v_h \in W_{h|\mathsf{P}}$;
(B) (*stability*) there exist two positive constants c_* and c^* independent of h and the element $\mathsf{P} \in \Omega_h$ such that

$$c_* a_{\mathsf{P}}^{\dagger}(v_h, v_h) \leq a_{h,\mathsf{P}}^{\dagger}(v_h, v_h) \leq c^* a_{\mathsf{P}}^{\dagger}(v_h, v_h) \quad \forall v_h \in W_{h|\mathsf{P}}.$$

A consequence of the above properties is that the bilinear form $a_{h,\mathsf{P}}^{\dagger}(\cdot,\cdot)$ is continuous with respect to the relevant norm, which is H^2 for (10.12), H^1 for (10.13), and L^2 for (10.14). For every choice of $\dagger$, the corresponding global bilinear form is

$$a_h^{\dagger}(v_h, w_h) = \sum_{\mathsf{P} \in \Omega_h} a_{h,\mathsf{P}}^{\dagger}(v_h, w_h) \quad \forall v_h, w_h \in W_h.$$

(10.1a)–(10.1c)

We now turn our attention to the semilinear form $r(\cdot; \cdot, \cdot)$, which we can also write as the sum of elemental contributions:

$$r(z; v, w) = \sum_{\mathsf{P} \in \Omega_h} r_{\mathsf{P}}(z; v, w) \quad \forall z, vw \in H^2(\Omega)$$

where

$$r_{\mathsf{P}}(z; v, w) = \int_{\mathsf{P}} (3z^2 - 1) \nabla v \cdot \nabla w d\mathbf{x} \quad \forall \mathsf{P} \in \Omega_h.$$

On each element P, we approximate the term $z(x)^2$ by means of its cell average, which we compute using the $L^2(\mathsf{P})$ bilinear form $a_{h,\mathsf{P}}^0(\cdot,\cdot)$:

$$z_{h|\mathsf{P}}^2 \approx |\mathsf{P}|^{-1} a_{h,\mathsf{P}}^0(z_h, z_h),$$

where we recall that $|\mathsf{P}|$ is the area of element P. This approach has the correct approximation properties and preserves the positivity of z^2.

We therefore propose the following approximation of the local nonlinear forms

$$r_{h,\mathsf{P}}(z_h; v_h, w_h) = \widehat{\phi'(z_h)}_{|\mathsf{P}} \, a_{h,\mathsf{P}}^{\nabla}(v_h, w_h) \quad \forall z_h, v_h, w_h \in W_{h|\mathsf{P}},$$

where $\widehat{\phi'(z_h)}_{|\mathsf{P}} = 3 |\mathsf{P}|^{-1} a_{h,\mathsf{P}}^0(z_h, z_h) - 1$. The global form is then assembled as

$$r_h(z_h; v_h, w_h) = \sum_{\mathsf{P} \in \Omega_h} r_{h,\mathsf{P}}(z_h; v_h, w_h) \quad \forall z_h, v_h w_h \in W_h.$$

10.3.2.3 The Discrete Problem

The virtual element discretization of problem (10.3a), (10.3b) follows a Galerkin approach in space combined with a backward Euler time-stepping scheme. Consider

the functional space

$$W_h^0 = W_h \cap V = \{v \in W_h : \partial_n v = 0 \text{ on } \partial\Omega\},$$

which includes the boundary conditions. Then, we introduce the semi-discrete approximation: *Find $u_h(\cdot, t)$ in W_h^0 such that*

$$a_h^0(\dot{u}_h, v_h) + \gamma^2 a_h^\Delta(u_h, v_h) + r_h(u_h; u_h, v_h) = 0 \quad \forall v_h \in W_h^0, \qquad (10.15)$$

$$u_h(0, \cdot) = u_{0,h}(\cdot), \qquad (10.16)$$

where $u_{0,h}$ is a suitable approximation of u_0 in W_h^0 and $a_h^0(\cdot, \cdot)$, a_h^Δ and r_h are the virtual element bilinear forms defined in the previous section.

To formulate the fully discrete scheme, we subdivide the time interval $[0, T]$ into N uniform sub-intervals of length $k = T/N$ by means of the time nodes $0 = {}_0 < {}_1 < \ldots < {}_{N-1} < {}_N = T$, and denote the virtual element approximation of the solution $u(\cdot,)$ at $u(\cdot, {}^i)$ in W_h^0 by $u_{h,k}^i$. The fully discrete problem reads as: *Given* $u_{hk}^0 = u_{0,h} \in W_h^0$, *find* $u_{hk}^i \in W_h^0$, $i = 1, \ldots, N$ *such that*

$$k^{-1} a_h^0(u_{hk}^i - u_{hk}^{i-1}, v_h) + \gamma^2 a_h^\Delta(u_{hk}^i, v_h) + r_h(u_{hk}^i, u_{hk}^i; v_h) = 0 \quad \forall v_h \in W_h^0. \qquad (10.17)$$

The semidiscrete Virtual Element formulation given in (10.15)–(10.16) converges to the exact solution of problem (10.3a)–(10.3b) according to the result stated in this theorem and proved in [6].

Theorem 10.6 *Let u be the solution of problem* (10.3a)–(10.3b). *Let u_h be the virtual element approximation provided by* (10.15)–(10.16) *and assume that*

$$\|u_h\|_{L^\infty(\Omega)} \leq C$$

for all $t \in (0, T]$ and some positive contant C independent of h. Then, it holds that

$$\|u - u_h\|_{L^2(\Omega)} \lesssim h^2$$

for every $\in [0, T]$.

10.3.3 Numerical Results

In this test, taken from [6] we study the convergence of our VEM discretization applied to the Cahn-Hilliard problem with a load term f obtained by enforcing as exact solution $u(x, y, t) = t \cos(2\pi x) \cos(2\pi y)$. The parameter γ is set to $1/10$ and the time step size Δ is $1e - 7$. The H^2, H^1 and L^2 errors are computed at $t = 0.1$

on four quadrilateral meshes discretizing the unit square. The time discretization is performed by the Backward Euler method. The resulting non-linear system (10.17) at each time step is solved by the Newton method, using the l^2 norm of the relative residual as a stopping criterion. The tolerance for convergence is $1e-6$.

The results reported in Table 10.1 show that the VEM method converges is convergent with a convergence rate close to 2 in the L^2 norm as expected from Theorem 10.6. In the H^2 and H^1 seminorms, the method converges with order 1 and 2 respectively, as we can expect from the FEM theory and the approximation properties of the virtual element space. Finally, in Fig. 10.2 we report the results of a spinoidal decomposition. For completeness, we recall that spinodal decomposition is a physical phenomenon consisting of the separation of a mixture of two or more components to bulk regions of each, which occurs when a high-temperature mixture of different components is rapidly cooled. We employ an initial datum u_0 chosen to be a uniformly distributed random perturbation between -1 and 1. Results are consistent with the literature, cf. [6].

Table 10.1 H^2, H^1 and L^2 errors and convergence rates α computed on four quadrilateral meshes discretizing the unit square [6]

h	$|u-u_h|_{H^2(\Omega)}$	α	$|u-u_h|_{H^1(\Omega)}$	α	$\|u-u_h\|_{L^2(\Omega)}$	α
1/16	1.35e−1	–	8.57e−2	–	8.65e−2	–
1/32	5.86e−2	1.20	2.20e−2	1.96	2.20e−2	1.97
1/64	2.79e−2	1.07	5.53e−3	1.99	5.52e−3	1.99
1/128	1.38e−2	1.02	1.37e−3	2.01	1.37e−3	2.01
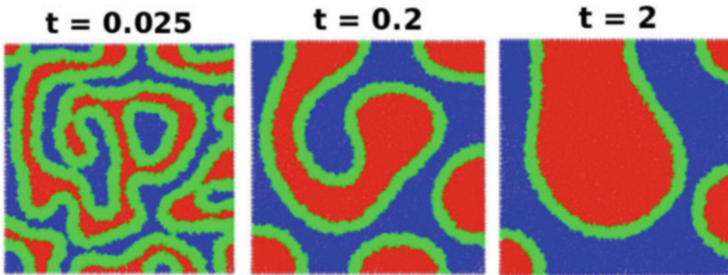
Fig. 10.2 Spinoidal decomposition on the unit square at three temporal frames for a Voronoi polygonal mesh of 4096 elements

10.4   The Virtual Element Method for the Elastodynamics Problem

10.4.1   The Continuous Problem

We consider an elastic body occupying the open, bounded polygonal domain $\Omega \subset \mathbb{R}^2$ with Lipschitz boundary Γ. We assume that boundary Γ can be split into the two disjoint subsets Γ_D and Γ_N, so that $\Gamma = \Gamma_D \cup \Gamma_N$ and with the one-dimensional Lebesgue measure (length) $|\Gamma_D \cap \Gamma_N| = 0$. For the well-posedness of the mathematical model, we further require length of Γ_D is nonzero, i.e., $|\Gamma_D| > 0$. Let $T > 0$ denote the final time. We consider the external load $\mathbf{f} \in L^2\big(0, T; [L^2(\Omega)]^2\big)$, the boundary function $\mathbf{g}_N \in C^1\big(0, T; [H^{1/2}_{0,\Gamma_N}]^2\big)$, and the initial functions $\mathbf{u}_0 \in [H^1_{0,\Gamma_D}(\Omega)]^2$, $\mathbf{u}_1 \in [L^2(\Omega)]^2$. For such time-dependent vector fields, we may indicate the dependence on time explicitly, e.g., $\mathbf{f}(t) := \mathbf{f}(\cdot, t) \in [L^2(\Omega)]^2$, or drop it out to ease the notation when it is obvious from the context.

The equations governing the two-dimensional initial/boundary-value problem of linear elastodynamics for the displacement vector $\mathbf{u} : \Omega \times [0, T] \to \mathbb{R}^2$ are:

$$\rho \ddot{\mathbf{u}} - \nabla \cdot \boldsymbol{\sigma}(\mathbf{u}) = \mathbf{f} \qquad \text{in } \Omega \times (0, T], \tag{10.1}$$

$$\mathbf{u} = \mathbf{0} \qquad \text{on } \Gamma_D \times (0, T], \tag{10.2}$$

$$\boldsymbol{\sigma}(\mathbf{u})\mathbf{n} = \mathbf{g}_N \qquad \text{on } \Gamma_N \times (0, T], \tag{10.3}$$

$$\mathbf{u} = \mathbf{u}_0 \qquad \text{in } \Omega \times \{0\}, \tag{10.4}$$

$$\dot{\mathbf{u}} = \mathbf{u}_1 \qquad \text{in } \Omega \times \{0\}. \tag{10.5}$$

Here, ρ is the mass density, which we suppose to be a strictly positive and uniformly bounded function and $\boldsymbol{\sigma}(\mathbf{u})$ is the stress tensor. In (10.2) we assume homogeneous Dirichlet boundary conditions on Γ_D. This assumption is made only to ease the exposition and the analysis, as our numerical method is easily extendable to nonhomogeneous Dirichlet boundary conditions.

We denote the space of the symmetric, 2×2-sized, real-valued tensors by $\mathbb{R}^{2\times 2}_{\text{sym}}$ and assume that the stress tensor $\boldsymbol{\sigma} : \Omega \times [0, T] \to \mathbb{R}^{2\times 2}_{\text{sym}}$ is expressed, according to Hooke's law, by $\boldsymbol{\sigma}(\mathbf{u}) = \mathscr{D}\boldsymbol{\varepsilon}(\mathbf{u})$, where, $\boldsymbol{\varepsilon}(\mathbf{u})$ denotes the symmetric gradient of $\mathbf{u}$, i.e., $\boldsymbol{\varepsilon}(\mathbf{u}) = \big(\nabla\mathbf{u} + (\nabla\mathbf{u})^T\big)/2$, and $\mathscr{D} = \mathscr{D}(\mathbf{x}) : \mathbb{R}^{2\times 2}_{\text{sym}} \longrightarrow \mathbb{R}^{2\times 2}_{\text{sym}}$ is the *stiffness tensor*

$$\mathscr{D}\boldsymbol{\tau} = 2\mu\boldsymbol{\tau} + \lambda\text{tr}(\boldsymbol{\tau})\mathsf{I} \tag{10.6}$$

for all $\boldsymbol{\tau} \in \mathbb{R}^{2\times 2}_{\text{sym}}$. In this definition, I and $\text{tr}(\cdot)$ are the identity matrix and the trace operator; λ and μ are the first and second Lamé coefficients, which we assume to

be in $L^\infty(\Omega)$ and nonnegative. The compressional (P) and shear (S) wave velocities of the medium are respectively obtained through the relations $c_P = \sqrt{(\lambda + 2\mu)/\rho}$ and $c_S = \sqrt{\mu/\rho}$.

Let $\mathbf{V} = \left[H^1_{\Gamma_D}(\Omega)\right]^2$ be the space of H^1 vector-valued functions with null trace on Γ_D. We consider the two bilinear forms $m(\cdot, \cdot)$, $a(\cdot, \cdot) : \mathbf{V} \times \mathbf{V} \to \mathbb{R}$ defined as

$$m(\mathbf{w}, \mathbf{v}) = \int_\Omega \rho \mathbf{w} \cdot \mathbf{v} \, d\mathbf{x} \quad \forall \mathbf{w}, \mathbf{v} \in \mathbf{V}, \tag{10.7}$$

$$a(\mathbf{w}, \mathbf{v}) = \int_\Omega \boldsymbol{\sigma}(\mathbf{w}) : \boldsymbol{\varepsilon}(\mathbf{v}) \, d\mathbf{x} \quad \forall \mathbf{w}, \mathbf{v} \in \mathbf{V}, \tag{10.8}$$

and the linear functional $F(\cdot) : \mathbf{V} \to \mathbb{R}$ defined as

$$F(\mathbf{v}) = \int_\Omega \mathbf{f} \cdot \mathbf{v} \, d\mathbf{x} + \int_{\Gamma_N} \mathbf{g}_N \cdot \mathbf{v} \, ds \quad \forall \mathbf{v} \in \mathbf{V}. \tag{10.9}$$

The variational formulation of the linear elastodynamics equations reads as: *For all $t \in (0, T]$ find $\mathbf{u}(t) \in \mathbf{V}$ such that for $t = 0$ it holds that $\mathbf{u}(0) = \mathbf{u}_0$ and $\dot{\mathbf{u}}(0) = \mathbf{u}_1$ and*

$$m(\ddot{\mathbf{u}}, \mathbf{v}) + a(\mathbf{u}, \mathbf{v}) = F(\mathbf{v}) \qquad \forall \mathbf{v} \in \mathbf{V}. \tag{10.10}$$

As shown, for example, by Raviart and Thomas (see Theorem 8–3.1 [90]) the variational problem (10.10) is well posed and its unique solution satisfies $\mathbf{u} \in C^0(0, T; \mathbf{V}) \cap C^1(0, T; [L^2(\Omega)]^2)$.

10.4.2 The Conforming Virtual Element Approximation

In this section we introduce the main building blocks for the conforming virtual element discretization of the elastodynamics equation, report stability and convergence results and collect some numerical results assessing the theoretical properties of the proposed scheme.

10.4.2.1 Virtual Element Spaces

Let $k \geq 1$ be an integer number. The global virtual element space is defined as

$$\mathbf{V}^h_k := \left\{ \mathbf{v} \in \mathbf{V} : \mathbf{v}_{|\mathsf{P}} \in \mathbf{V}^h_k(\mathsf{P}) \text{ for every } \mathsf{P} \in \Omega_h \right\} \tag{10.11}$$

where $\mathbf{V}_k^h(\mathsf{P}) = \left[V_k^h(\mathsf{P})\right]^2$, with

$$V_k^h(\mathsf{P}) := \left\{ v_h \in H^1(\mathsf{P}) : v_{h|_{\partial\mathsf{P}}} \in C(\partial\mathsf{P}),\ v_{h|_e} \in \mathbb{P}_k(e)\ \forall e \in \partial\mathsf{P},\ \Delta v_h \in \mathbb{P}_k(\mathsf{P}), \right.$$

$$\left. \left(v_h - \Pi_k^\nabla v_h, \mu_h\right)_{\mathsf{P}} = 0\ \forall \mu_h \in \mathbb{P}_k(\mathsf{P})\backslash\mathbb{P}_{k-2}(\mathsf{P}) \right\},$$

$$(10.12)$$

where $\Pi_k^\nabla : H^1(\mathsf{P}) \cap C^0(\overline{\mathsf{P}}) \to \mathbb{P}_k(\mathsf{P})$ is the usual elliptic projection of a function v_h on the space of polynomials of degree k, cf. (10.11)–(10.12).

Each virtual element function $v_h \in V_k^h(\mathsf{P})$ is uniquely characterized by

(C1) the values of v_h at the vertices of P;
(C2) the moments of v_h of order up to $k-2$ on each one-dimensional edge $e \in \partial\mathsf{P}$:

$$\frac{1}{|e|} \int_e v_h\, m\, ds,\ \ \forall m \in \mathcal{M}_{k-2}(e),\ \forall e \in \partial\mathsf{P};$$

$$(10.13)$$

(C3) the moments of v_h of order up to $k-2$ on P:

$$\frac{1}{|\mathsf{P}|} \int_{\mathsf{P}} v_h\, m\, d\mathbf{x},\ \ \forall m \in \mathcal{M}_{k-2}(\mathsf{P}).$$

$$(10.14)$$

As usual, the degrees of freedom of the global space $\mathbf{V}_k^h$ are provided by collecting all the local degrees of freedom (which allow the computation of the elliptic projection Π_k^∇), and their unisolvence is an immediate consequence of the unisolvence of the local degrees of freedom for the elemental spaces $V_k^h(\mathsf{P})$.

10.4.2.2 Discrete Bilinear Forms

In the virtual element setting, we define the bilinear forms $m_h(\cdot, \cdot)$ and $a_h(\cdot, \cdot)$ as the sum of elemental contributions, which are respectively denoted by $m_{h,\mathsf{P}}(\cdot, \cdot)$ and $a_{h,\mathsf{P}}(\cdot, \cdot)$:

$$m_h(\cdot, \cdot) : \mathbf{V}_k^h \times \mathbf{V}_k^h \to \mathbb{R}, \quad \text{with} \quad m_h(\mathbf{v}_h, \mathbf{w}_h) = \sum_{\mathsf{P} \in \Omega_h} m_{h,\mathsf{P}}(\mathbf{v}_h, \mathbf{w}_h),$$

$$a_h(\cdot, \cdot) : \mathbf{V}_k^h \times \mathbf{V}_k^h \to \mathbb{R}, \quad \text{with} \quad a_h(\mathbf{v}_h, \mathbf{w}_h) = \sum_{\mathsf{P} \in \Omega_h} a_{h,\mathsf{P}}(\mathbf{v}_h, \mathbf{w}_h).$$

The local bilinear form $m_{h,\mathsf{P}}(\cdot, \cdot)$ is given by

$$m_{h,\mathsf{P}}(\mathbf{v}_h, \mathbf{w}_h) = \int_{\mathsf{P}} \rho\, \Pi_k^0 \mathbf{v}_h \cdot \Pi_k^0 \mathbf{w}_h\, dV + S_m^{\mathsf{P}}(\mathbf{v}_h, \mathbf{w}_h),$$

$$(10.15)$$

where $S_m^{\mathsf{P}}(\cdot, \cdot)$ is the local stabilization term. The bilinear form $m_{h,\mathsf{P}}$ depends on the orthogonal projections $\Pi_k^0 \mathbf{v}_h$ and $\Pi_k^0 \mathbf{w}_h$, which are computable from the degrees of freedom of $\mathbf{v}_h$ and $\mathbf{w}_h$. The local form $S_m^{\mathsf{P}}(\cdot, \cdot) : \mathbf{V}_k^h \times \mathbf{V}_k^h \to \mathbb{R}$ can be *any* symmetric and coercive bilinear form that is computable from the degrees of freedom and for which there exist two strictly positive real constants σ_* and σ^* such that

$$\sigma_* m_{\mathsf{P}}(\mathbf{v}_h, \mathbf{v}_h) \leq S_m^{\mathsf{P}}(\mathbf{v}_h, \mathbf{v}_h) \leq \sigma^* m_{\mathsf{P}}(\mathbf{v}_h, \mathbf{v}_h) \quad \mathbf{v}_h \in \ker(\Pi_k^0) \cap \mathbf{V}_k^h(\mathsf{P}). \tag{10.16}$$

Computable stabilizations $S_m^{\mathsf{P}}(\cdot, \cdot)$ are provided by resorting to the two-dimensional stabilizations of the effective choices for the scalar case proposed in the literature [54, 79].

The local bilinear form $a_{h,\mathsf{P}}$ is given by

$$a_{h,\mathsf{P}}(\mathbf{v}_h, \mathbf{w}_h) = \int_{\mathsf{P}} \mathsf{D}\Pi_{k-1}^0(\boldsymbol{\varepsilon}(\mathbf{v}_h)) : \Pi_{k-1}^0(\boldsymbol{\varepsilon}(\mathbf{w}_h)) \, dV + S_a^{\mathsf{P}}(\mathbf{v}_h, \mathbf{w}_h), \tag{10.17}$$

where $S_a^{\mathsf{P}}(\cdot, \cdot)$ is the local stabilization term. The bilinear form $a_{h,\mathsf{P}}$ depends on the orthogonal projections $\Pi_{k-1}^0 \nabla \mathbf{v}_h$ and $\Pi_{k-1}^0 \nabla \mathbf{w}_h$, which are computable from the degrees of freedom of $\mathbf{v}_h$ and $\mathbf{w}_h$. On its turn, $S_a^{\mathsf{P}}(\cdot, \cdot) : \mathbf{V}_k^h \times \mathbf{V}_k^h \to \mathbb{R}$ can be *any* symmetric and coercive bilinear form that is computable from the degrees of freedom and for which there exist two strictly positive real constants $\overline{\sigma}_*$ and $\overline{\sigma}^*$ such that

$$\overline{\sigma}_* a_{\mathsf{P}}(\mathbf{v}_h, \mathbf{v}_h) \leq S_m^{\mathsf{P}}(\mathbf{v}_h, \mathbf{v}_h) \leq \overline{\sigma}^* a_{\mathsf{P}}(\mathbf{v}_h, \mathbf{v}_h) \quad \mathbf{v}_h \in \ker(\Pi_k^0) \cap \mathbf{V}_k^h(\mathsf{P}). \tag{10.18}$$

Moreover, the bilinear form $S_a^{\mathsf{P}}(\cdot, \cdot)$ must scale with respect to h like $a_{\mathsf{P}}(\cdot, \cdot)$, i.e., as $\mathcal{O}(1)$. As before, we can define computable stabilizations $S_a^{\mathsf{P}}(\cdot, \cdot)$ by resorting to the two-dimensional stabilizations for the scalar case proposed in the literature [54, 79]. As usual, the discrete bilinear forms $a_{h,\mathsf{P}}(\cdot, \cdot)$ and $m_{h,\mathsf{P}}(\cdot, \cdot)$ satisfy the *k-consistency* and *stability* properties. The stability constants may depend on physical parameters and the polynomial degree k [11, 24].

10.4.2.3 Discrete Load Term

We approximate the right-hand side (10.21) of the variational formulation by means of the linear functional $F_h(\cdot) : \mathbf{V}_k^h \to \mathbb{R}^2$ given by

$$F_h(\mathbf{v}_h) = \int_{\Omega} \mathbf{f} \cdot \Pi_{k-2}^0(\mathbf{v}_h) \, dV + \sum_{e \in \Gamma_N} \int_e \mathbf{g}_N \cdot \mathbf{v}_h \, ds \quad \forall \mathbf{v}_h \in \mathbf{V}_k^h. \tag{10.19}$$

The linear functional $F_h(\cdot)$ is clearly computable since the edge trace $\mathbf{v}_{h|e}$ is a known polynomial and $\Pi_k^0(\mathbf{v}_h)$ is computable from the degrees of freedom of $\mathbf{v}_h$. Moreover, $F_h(\cdot)$ is a bounded functional. In fact, when $\mathbf{g}_N = 0$ using the stability of the projection operator and the Cauchy-Schwarz inequality, we note that

$$|F_h(\mathbf{v}_h)| \leq \left| \int_\Omega \mathbf{f}(t) \cdot \Pi_{k-2}^0(\mathbf{v}_h) \, dV \right| \leq \|\mathbf{f}(t)\|_0 \left\| \Pi_{k-2}^0(\mathbf{v}_h) \right\|_0$$

$$\leq \|\mathbf{f}(t)\|_0 \|\mathbf{v}_h\|_0 \quad \forall t \in [0, T]. \tag{10.20}$$

This estimate is used in the proof of the stability of the semi-discrete virtual element approximation (see Theorem 10.7).

10.4.2.4   The Discrete Problem

The semi-discrete virtual element approximation of (10.10) reads as: *For all $t \in (0, T]$ find $\mathbf{u}_h(t) \in \mathbf{V}_k^h$ such that for $t = 0$ it holds that $\mathbf{u}_h(0) = (\mathbf{u}_0)_I$ and $\dot{\mathbf{u}}_h(0) = (\mathbf{u}_1)_I$ and*

$$m_h(\ddot{\mathbf{u}}_h, \mathbf{v}_h) + a_h(\mathbf{u}_h, \mathbf{v}_h) = F_h(\mathbf{v}_h) \quad \forall \mathbf{v}_h \in \mathbf{V}_k^h. \tag{10.21}$$

Here, $\mathbf{u}_h(t)$ is the virtual element approximation of $\mathbf{u}$ and $\mathbf{v}_h$ is the generic test function in $\mathbf{V}_k^h$, while $(\mathbf{u}_0)_I$ and $(\mathbf{u}_1)_I$ are the virtual element interpolants of the initial solution functions $\mathbf{u}(0)$ and $\dot{\mathbf{u}}(0)$.

We carry out the time integration by applying the leap-frog time marching scheme [89] to the second derivative in time $\ddot{\mathbf{u}}_h$. To this end, we subdivide the interval $(0, T]$ into N_T subintervals of amplitude $\Delta t = T/N_T$ and at every time level $t^n = n\Delta t$ we consider the variational problem for $n \geq 1$:

$$m_h(\mathbf{u}_h^{n+1}, \mathbf{v}_h) - 2m_h(\mathbf{u}_h^n, \mathbf{v}_h) + m_h(\mathbf{u}_h^{n-1}, \mathbf{v}_h) + \Delta t^2 a_h(\mathbf{u}_h^n, \mathbf{v}_h)$$

$$= \Delta t^2 F_h^n(\mathbf{v}_h) \quad \forall \mathbf{v}_h \in \mathbf{V}_k^h, \tag{10.22}$$

and initial step

$$m_h(\mathbf{u}_h^1, \mathbf{v}_h) - m_h(\mathbf{u}_0, \mathbf{v}_h) - \Delta t m_h(\mathbf{u}_1, \mathbf{v}_h) + \frac{\Delta t^2}{2} a_h(\mathbf{u}_0, \mathbf{v}_h)$$

$$= \frac{\Delta t^2}{2} F_h^0(\mathbf{v}_h) \quad \forall \mathbf{v}_h \in V_k^h.$$

The leap-frog scheme is second-order accurate, explicit and conditionally stable. [89] It is straightforward to show that these properties are inherited by the fully-discrete scheme (10.22).

10.4.2.5 Stability and Convergence Analysis for the Semi-Discrete Problem

We employ the *energy* norm

$$\||\mathbf{v}_h(t)\||^2 = \left\|\rho^{\frac{1}{2}}\dot{\mathbf{v}}_h(t)\right\|_0^2 + |\mathbf{v}_h(t)|_1^2, \qquad t \in [0, T], \tag{10.23}$$

which is defined for all $\mathbf{v}_h \in \mathbf{V}_k^h$. The local stability property of the bilinear forms $m_h(\cdot, \cdot)$ and $a_h(\cdot, \cdot)$ implies the equivalence relation

$$m_h(\dot{\mathbf{v}}_h, \dot{\mathbf{v}}_h) + a_h(\mathbf{v}_h, \mathbf{v}_h) \lesssim \||\mathbf{v}_h(t)\||^2 \lesssim m_h(\dot{\mathbf{v}}_h, \dot{\mathbf{v}}_h) + a_h(\mathbf{v}_h, \mathbf{v}_h) \tag{10.24}$$

for all time-dependent virtual element functions $\mathbf{v}_h(t)$ with square integrable derivative $\dot{\mathbf{v}}_h(t)$.

The hidden constants in (10.24) are independent of the mesh size parameter h [11]. However, they may depend on the stability parameters, the physical parameters and the polynomial degree k [25]. It is worth noting that the dependence on k does not seem to have a relevant impact on the optimality of the convergence rates in the numerical experiments of Sect. 10.4.3. The following stability result has been proved in [11].

Theorem 10.7 *Let* $\mathbf{f} \in L^2(0, T; [L^2(\Omega)]^2)$ *and let* $\mathbf{u}_h \in C^2(0, T; \mathbf{V}_k^h)$ *be the solution of* (10.21). *Then, it holds*

$$\||\mathbf{u}_h(t)\|| \lesssim \||(\mathbf{u}_0)_I\|| + \int_0^t \|\mathbf{f}(\tau)\|_{0,\Omega}\, d\tau. \tag{10.25}$$

The hidden constant in $\lesssim$ *is independent of h, but may depend on the model parameters and approximation constants and the polynomial degree k.*

We point out that in the case of $\mathbf{f}$ null external force, i.e. $\mathbf{f} = \mathbf{0}$, the above bound reduces to

$$\||\mathbf{u}_h(t)\|| \lesssim \||(\mathbf{u}_0)_I\||$$

that is the virtual element approximation is dissipative.

Now, we recall [11] the convergence of the semi-discrete virtual element approximation in the energy norm (10.23).

Theorem 10.8 *Let* $\mathbf{u} \in C^2(0, T; [H^{m+1}(\Omega)]^2)$, $m \in \mathbb{N}$, *be the exact solution of problem* (10.10). *Let* $\mathbf{u}_h \in \mathbf{V}_k^h$ *be the solution of the semi-discrete problem* (10.21).

For $\mathbf{f} \in L^2\big((0, T); \big[H^{m-1}(\Omega)\big]^2\big)$ *we have that*

$$\sup_{0<t\leq T} |||\mathbf{u}(t) - \mathbf{u}_h(t)||| \lesssim \frac{h^{\mu}}{k^m} \sup_{0<t\leq T} \Big(\|\dot{\mathbf{u}}(t)\|_{m+1} + \|\mathbf{u}(t)\|_{m+1} \Big)$$

$$+ \int_0^T \left(\frac{h^{\mu+1}}{k^m} \big(\|\ddot{\mathbf{u}}(\tau)\|_{m+1} + \|\dot{\mathbf{u}}(\tau)\|_{m+1}\big) + \frac{h^{\mu}}{k^m}\big(\|\ddot{\mathbf{u}}(\tau)\|_{m+1} + \|\dot{\mathbf{u}}(\tau)\|_{m+1}\big) \right) d\tau$$

$$+ \int_0^T h \left\| \big(I - \Pi^0_{k-2}\big)\mathbf{f}(\tau) \right\|_0 d\tau, \tag{10.26}$$

where $\mu = \min(k, m)$. *The hidden constant in* "$\lesssim$" *is independent of h, but may depend on the model parameters and approximation constants, the polynomial degree k, and the final observation time T.*

Finally, we state the convergence result in the L^2 norm, whose proof is again found in [11].

Theorem 10.9 *Let* $\mathbf{u}$ *be the exact solution of problem* (10.10) *under the assumption that domain* Ω *is* H^2-*regular and* $\mathbf{u}_h \in \mathbf{V}^h_k$ *the solution of the virtual element method stated in* (10.21). *If* $\mathbf{u}, \dot{\mathbf{u}}, \ddot{\mathbf{u}} \in L^2\big(0, T; \big[H^{m+1}(\Omega) \cap H^1_0(\Omega)\big]^2\big)$, *with integer* $m \geq 0$, *then the following estimate holds for almost every* $t \in [0, T]$ *by setting* $\mu = \min(m, k)$:

$$\|\mathbf{u}(t) - \mathbf{u}_h(t)\|_0 \lesssim \|\mathbf{u}_h(0) - \mathbf{u}_0\|_0 + \|\dot{\mathbf{u}}_h(0) - \mathbf{u}_1\|_0 + \frac{h^{\mu+1}}{k^{m+1}}\Big(\|\ddot{\mathbf{u}}\|_{L^2(0,T;[H^{m+1}(\Omega)]^2)}$$

$$+ \|\dot{\mathbf{u}}\|_{L^2(0,T;[H^{m+1}(\Omega)]^2)} + \|\mathbf{u}\|_{L^2(0,T;[H^{m+1}(\Omega)]^2)} \Big)$$

$$+ \int_0^T \left\| \big(1 - \Pi^0_{k-2}\big)\mathbf{f}(\tau) \right\|_0^2 d\tau. \tag{10.27}$$

The hidden constant in "$\lesssim$" *is independent of h, but may depend on the model parameters and approximation constants* ϱ, μ^*, *and the polynomial degree k, and the final observation time T.*

10.4.3 Numerical Results

In this section, we report from [11] a set of numerical results assessing the convergence properties of the virtual element discretization by using a manufactured solution on three different mesh families, each one possessing some special feature.

In particular, we let $\Omega = (0, 1)^2$ for $t \in [0, T]$, $T = 1$, and consider initial condition $\mathbf{u}_0$, boundary condition $\mathbf{g}$ and forcing term $\mathbf{f}$ determined from the exact
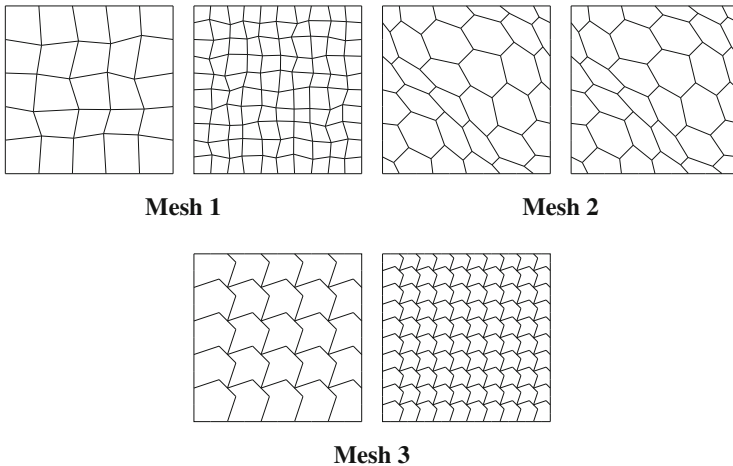
Fig. 10.3 Base meshes (top row) and first refined meshes (bottom row) of the following mesh families from left to right: randomized quadrilateral mesh; mainly hexagonal mesh; nonconvex octagonal mesh

solution:

$$\mathbf{u}(x, y, t) = \cos\left(\frac{2\pi\, t}{T}\right) \begin{pmatrix} \sin^2(\pi x)\sin(2\pi y) \\ \sin(2\pi x)\sin^2(\pi y) \end{pmatrix}. \tag{10.28}$$

To this end, we consider three different mesh partitionings, denoted by:

– *Mesh 1*, randomized quadrilateral mesh;
– *Mesh 2*, mainly hexagonal mesh with continuously distorted cells;
– *Mesh 3*, nonconvex octagonal mesh.

The base mesh and the first refined mesh of each mesh sequence are shown in Fig. 10.3.

The discretization in time is given by applying the leap-frog method with $\Delta t = 10^{-4}$ and carried out for 10^4 time cycles in order to reach time $T = 1$.

For these calculations, we used the VEM approximation based on the conforming space V_k^h with $k = 1, 2, 3, 4$ and the convergence curves for the three mesh sequences above are reported in Figs. 10.4, 10.5, and 10.6. The expected rate of convergence is shown in each panel by the triangle closed to the error curve and indicated by an explicit label. The results are in agreement with the theoretical estimates. To conclude, Fig. 10.7 shows the semilog error curves obtained through a "p"-type refinement calculation for the previous benchmark, i.e. for a fixed 5×5 mesh of type *I* the order of the virtual element space is increased from $k = 1$ to $k = 10$. We employ two different implementations, namely in the first case the space of polynomials of degree k is generated by the standard scaled monomials,
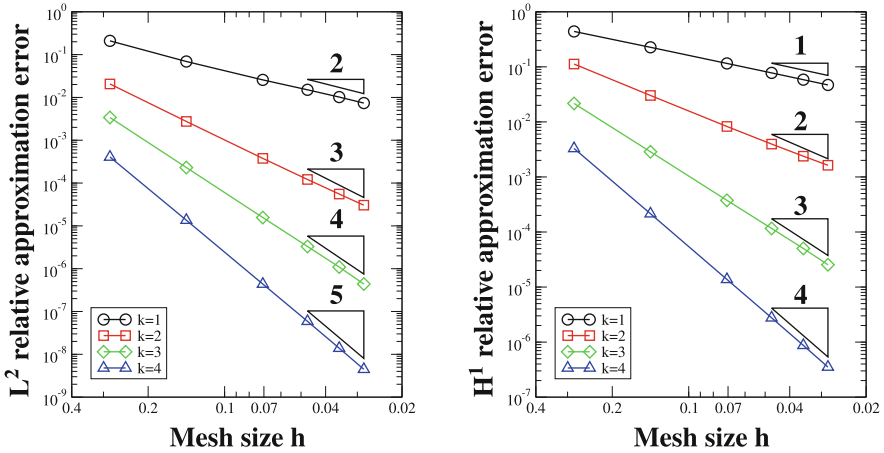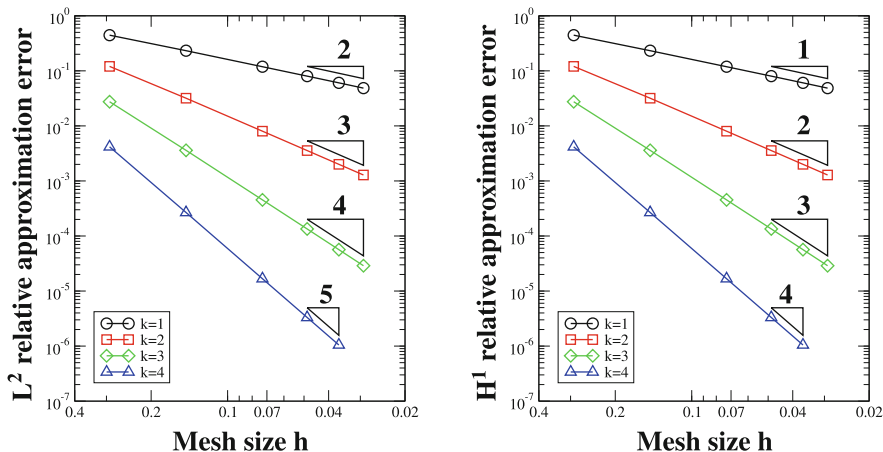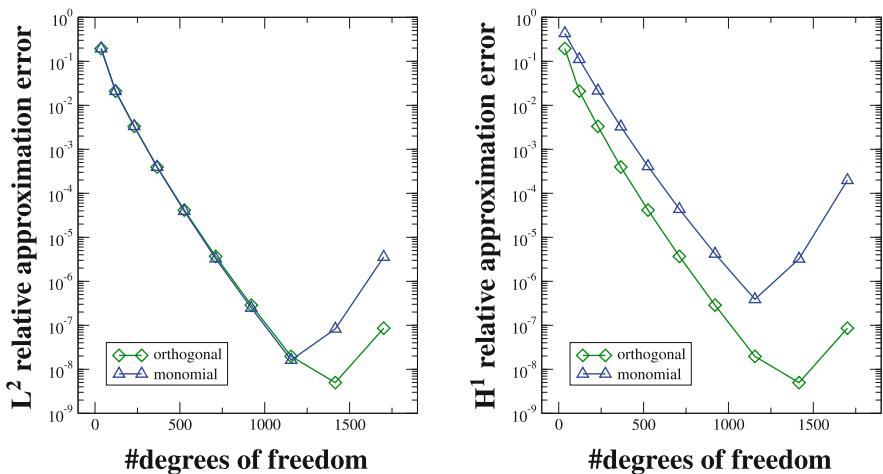
Fig. 10.4 Convergence plots for the virtual element approximation of Problem (10.1)–(10.5) with exact solution (10.28) using family *Mesh 1* of randomized quadrilateral meshes. Error curves are computed using the L^2 norm (left panels) and H^1 norm (right panels) and are plot versus h
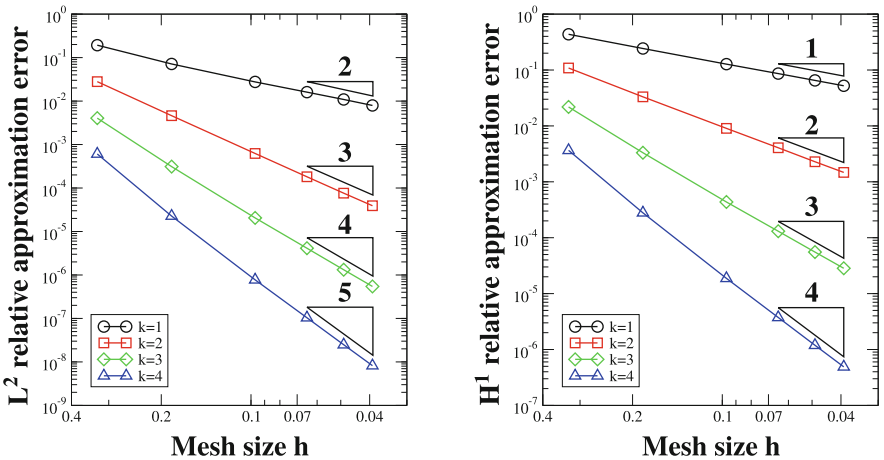
Fig. 10.5 Convergence plots for the virtual element approximation of Problem (10.1)–(10.5) with exact solution (10.28) using family *Mesh 2* of mainly hexagonal meshes. Error curves are computed using the L^2 norm (left panels) and H^1 norm (right panels) and are plotted versus h

while in the second one we consider an orthogonal polynomial basis. The behavior of the VEM when using nonorthogonal and orthogonal polynomial basis shown in Fig. 10.7 is in accordance with the literature, see, e.g., [31, 79].

Fig. 10.6 Convergence plots for the virtual element approximation of Problem (10.1)–(10.5) with exact solution (10.28) using family *Mesh 3* of nonconvex octagonal meshes. Error curves are computed using the L^2 norm (left panels) and H^1 norm (right panels) and are plotted versus h

Fig. 10.7 Convergence plots for the virtual element approximation of Problem (10.1)–(10.5) with exact solution (10.28) using family *Mesh 1* of randomized quadrilateral meshes. Error curves are computed using k-refinement the L^2 norm (left panel) and H^1 norm (right panel) and are plot versus the number of degrees of freedom by performing a refinement of type "p" on a 5×5 mesh. Each plot shows the two convergence curves that are obtained using monomials (circles) and orthogonalized polynomials (squares)

References

1. R.A. Adams, J.J.F. Fournier, in *Sobolev spaces*, 2 edn. Pure and Applied Mathematics (Academic Press, New York, 2003)
2. B. Ahmad, A. Alsaedi, F. Brezzi, L.D. Marini, A. Russo, Equivalent projectors for virtual element methods. Comput. Math. Appl. **66**(3), 376–391 (2013)
3. F. Aldakheel, B. Hudobivnik, A. Hussein, P. Wriggers, Phase-field modeling of brittle fracture using an efficient virtual element scheme. Comput. Methods Appl. Mech. Eng. **341**, 443–466 (2018)
4. P.F. Antonietti, I. Mazzieri, A. Quarteroni, F. Rapetti. Non-conforming high order approximations of the elastodynamics equation. Comput. Methods Appl. Mech. Eng. **209/212**, 212–238 (2012)
5. P.F. Antonietti, B. Ayuso de Dios, I. Mazzieri, A. Quarteroni, Stability analysis of discontinuous Galerkin approximations to the elastodynamics problem. J. Sci. Comput. **68**(1), 143–170 (2016)
6. P.F. Antonietti, L. Beirão da Veiga, S. Scacchi, M. Verani, A C^1 virtual element method for the Cahn-Hilliard equation with polygonal meshes. SIAM J. Numer. Anal. **54**(1), 34–56 (2016)
7. P.F. Antonietti, G. Manzini, M. Verani, The fully nonconforming virtual element method for biharmonic problems. Math. Models Methods Appl. Sci. **28**(2), 387–407 (2018)
8. P.F. Antonietti, I. Mazzieri, High-order discontinuous Galerkin methods for the elastodynamics equation on polygonal and polyhedral meshes. Comput. Methods Appl. Mech. Eng. **342**, 414–437 (2018)
9. P.F. Antonietti, G. Manzini, M. Verani, The conforming virtual element method for polyharmonic problems. Comput. Math. Appl. **79**(7), 2021–2034 (2020)
10. P.F. Antonietti, F. Bonaldi, I. Mazzieri, A high-order discontinuous Galerkin approach to the elasto-acoustic problem. Comput. Methods Appl. Mech. Eng. **358**, 112634, 29 (2020)
11. P.F. Antonietti, G. Manzini, I. Mazzieri, H.M. Mourad, M. Verani, The arbitrary-order virtual element method for linear elastodynamics models. convergence, stability and dispersion-dissipation analysis. Int. J. Numer. Methods Eng. **122**(4), 934–971 (2021)
12. P.F. Antonietti, G. Manzini, S. Scacchi, M. Verani, A review on arbitrarily regular conforming virtual element methods for second- and higher-order elliptic partial differential equations. Math. Models Methods Appl. Sci. **31**(14), 2825–2853 (2021)
13. B. Ayuso de Dios, K. Lipnikov, G. Manzini, The non-conforming virtual element method. ESAIM Math. Model. Numer. **50**(3), 879–904 (2016)
14. J.W. Barrett, S. Langdon, R. Nürnberg, Finite element approximation of a sixth order nonlinear degenerate parabolic equation. Numer. Math. **96**(3), 401–434 (2004)
15. L. Beirão da Veiga, K. Lipnikov, G. Manzini, Arbitrary order nodal mimetic discretizations of elliptic problems on polygonal meshes. SIAM J. Numer. Anal. **49**(5), 1737–1760 (2011)
16. L. Beirão da Veiga, F. Brezzi, A. Cangiani, G. Manzini, L.D. Marini, A. Russo, Basic principles of virtual element methods. Math. Models Methods Appl. Sci. **23**(1), 199–214 (2013)
17. L. Beirão da Veiga, F. Brezzi, L.D. Marini, Virtual elements for linear elasticity problems. SIAM J. Numer. Anal. **51**(2), 794–812 (2013)
18. L. Beirão da Veiga, K. Lipnikov, G. Manzini, in *The Mimetic Finite Difference Method*, ed. MS&A. Modeling, Simulations and Applications, vol. 11, I edn. (Springer, Berlin, 2014)
19. L. Beirão da Veiga, G. Manzini, A virtual element method with arbitrary regularity. IMA J. Numer. Anal. **34**(2), 782–799 (2014).

20. L. Beirão da Veiga, C. Lovadina, D. Mora, A virtual element method for elastic and inelastic problems on polytope meshes. Comput. Methods Appl. Mech. Eng. **295**, 327–346 (2015)
21. L. Beirão da Veiga, G. Manzini, Residual *a posteriori* error estimation for the virtual element method for elliptic problems. ESAIM Math. Model. Numer. Anal. **49**(2), 577–599 (2015)
22. L. Beirão da Veiga, F. Brezzi, L.D. Marini, A. Russo, Mixed virtual element methods for general second order elliptic problems on polygonal meshes. ESAIM. Math. Model. Numer. Anal. **50**(3), 727–747 (2016)
23. L. Beirão da Veiga, F. Brezzi, L.D. Marini, A. Russo, Virtual element methods for general second order elliptic problems on polygonal meshes. Math. Models Methods Appl. Sci. **26**(4), 729–750 (2016)
24. L. Beirão da Veiga, A. Chernov, L. Mascotto, A. Russo, Basic principles of hp virtual elements on quasiuniform meshes. Math. Models Methods Appl. Sci. **26**(8), 1567–1598 (2016)
25. L. Beirão da Veiga, A. Chernov, L. Mascotto, A. Russo, Exponential convergence of the hp virtual element method in presence of corner singularities. Numer. Math. **138**(3), 581–613 (2018)
26. L. Beirão da Veiga, F. Dassi, A. Russo, A C^1 virtual element method on polyhedral meshes. Comput. Math. Appl. **79**(7), 1936–1955 (2020)
27. L. Beirão da Veiga, F. Dassi, G. Manzini, L. Mascotto, Virtual elements for Maxwell's equations. Comput. Math. Appl. **116**, 82–99 (2022)
28. E. Benvenuti, A. Chiozzi, G. Manzini, N. Sukumar, Extended virtual element method for the Laplace problem with singularities and discontinuities. Comput. Methods Appl. Mech. Eng. **356**, 571–597 (2019)
29. C. Bernardi, M. Dauge, Y. Maday, Polynomials in the Sobolev world. Technical report, HAL (2007). hal-00153795
30. S. Berrone, S. Pieraccini, S. Scialò, F. Vicini, A parallel solver for large scale DFN flow simulations. SIAM J. Sci. Comput. **37**(3), C285–C306 (2015)
31. S. Berrone, A. Borio, Orthogonal polynomials in badly shaped polygonal elements for the virtual element method. Finite Elem. Anal. Des. **129**, 14–31 (2017)
32. S. Berrone, A. Borio, G. Manzini, SUPG stabilization for the nonconforming virtual element method for advection–diffusion–reaction equations. Comput. Methods Appl. Mech. Eng. **340**, 500–529 (2018)
33. M.J. Borden, T.J.R. Hughes, C.M. Landis, C.V. Verhoosel, A higher-order phase-field model for brittle fracture: formulation and analysis within the isogeometric analysis framework. Comput. Methods Appl. Mech. Eng. **273**, 100–118 (2014)
34. J.H. Bramble, R.S. Falk, A mixed-Lagrange multiplier finite element method for the polyharmonic equation. RAIRO Modél. Math. Anal. Numér. **19**(4), 519–557 (1985)
35. S.C. Brenner, R. Scott, *The mathematical theory of finite element methods*, vol. 15 (Springer, Berlin, 2008)
36. F. Brezzi, L.D. Marini, Virtual element methods for plate bending problems. Comput. Methods Appl. Mech. Eng. **253**, 455–462 (2013)
37. F. Brezzi, A. Buffa, K. Lipnikov, Mimetic finite differences for elliptic problems. M2AN Math. Model. Numer. Anal. **43**, 277–295 (2009)
38. F. Brezzi, A. Buffa, G. Manzini, Mimetic scalar products for discrete differential forms. J. Comput. Phys. **257**(Part B), 1228–1259 (2014)
39. F. Brezzi, R.S. Falk, L.D. Marini, Basic principles of mixed virtual element methods. ESAIM Math. Model. Numer. Anal. **48**(4), 1227–1240 (2014)
40. J.W. Cahn, On spinodal decomposition. Acta Metall. **9**, 795–801 (1961)
41. J.W. Cahn, J.E. Hilliard, Free energy of a nonuniform system. I. Interfacial free energy. J. Chem. Phys. **28**, 258–267 (1958)
42. J.W. Cahn, J.E. Hilliard, Free energy of a nonuniform system. III. Nucleation in a two-component incompressible fluid. J. Chem. Phys. **31**, 688–699 (1959)
43. A. Cangiani, G. Manzini, A. Russo, N. Sukumar, Hourglass stabilization of the virtual element method. Internat. J. Numer. Methods Eng. **102**(3–4), 404–436 (2015)

44. A. Cangiani, V. Gyrya, G. Manzini, The non-conforming virtual element method for the Stokes equations. SIAM J. Numer. Anal. **54**(6), 3411–3435 (2016)

45. A. Cangiani, E.H. Georgoulis, T. Pryer, O.J. Sutton, A posteriori error estimates for the virtual element method. Numer. Math. **137**, 857–893 (2017)

46. A. Cangiani, V. Gyya, G. Manzini, O. Sutton, Chapter 14: virtual element methods for elliptic problems on polygonal meshes, in K. Hormann, N. Sukumar, eds. *Generalized Barycentric Coordinates in Computer Graphics and Computational Mechanics* (CRC Press, Taylor & Francis Group, Boca Raton, 2017), pp. 1–20

47. A. Cangiani, G. Manzini, O. Sutton, Conforming and nonconforming virtual element methods for elliptic problems. IMA J. Numer. Anal. **37**, 1317–1354 (2017). (online August 2016)

48. O. Certik, F. Gardini, G. Manzini, G. Vacca, The virtual element method for eigenvalue problems with potential terms on polytopic meshes. Appl. Math. **63**(3), 333–365 (2018)

49. O. Certik, F. Gardini, G. Manzini, L. Mascotto, G. Vacca, The p- and hp-versions of the virtual element method for elliptic eigenvalue problems. Comput. Math. Appl. **79**(7), 2035–2056 (2020)

50. F. Chave, D.A. Di Pietro, F. Marche, F. Pigeonneau, A hybrid high-order method for the Cahn-Hilliard problem in mixed form. SIAM J. Numer. Anal. **54**(3), 1873–1898 (2016)

51. F. Chen, J. Shen, Efficient energy stable schemes with spectral discretization in space for anisotropic Cahn-Hilliard systems. Commun. Comput. Phys. **13**(5), 1189–1208 (2013)

52. L. Chen, X. Huang, Nonconforming virtual element method for $2m$th order partial differential equations in $\mathbb{R}^n$. Math. Comp. **89**(324), 1711–1744 (2020)

53. C. Chinosi, L.D. Marini, Virtual element method for fourth order problems: L^2-estimates. Comput. Math. Appl. **72**(8), 1959–1967 (2016)

54. F. Dassi, L. Mascotto, Exploring high-order three dimensional virtual elements: bases and stabilizations. Comput. Math. Appl. **75**(9), 3379–3401 (2018)

55. D.A. Di Pietro, J. Droniou, G. Manzini, Discontinuous skeletal gradient discretisation methods on polytopal meshes. J. Comput. Phys. **355**, 397–425 (2018)

56. C.M. Elliott, S. Larsson, Error estimates with smooth and nonsmooth data for a finite element method for the Cahn-Hilliard equation. Math. Comp. **58**(198), 603–630, S33–S36 (1992)

57. C.M. Elliott, Z. Songmu, On the Cahn-Hilliard equation. Arch. Rational Mech. Anal. **96**(4), 339–357 (1986)

58. C.M. Elliott, D.A. French, Numerical studies of the Cahn-Hilliard equation for phase separation. IMA J. Appl. Math. **38**(2), 97–128 (1987)

59. C.M. Elliott, D.A. French, A nonconforming finite-element method for the two-dimensional Cahn-Hilliard equation. SIAM J. Numer. Anal. **26**(4), 884–903 (1989)

60. C.M. Elliott, D.A. French, F.A. Milner, A second-order splitting method for the Cahn-Hilliard equation. Numer. Math. **54**(5), 575–590 (1989)

61. E. Faccioli, F. Maggio, A. Quarteroni, A. Taghan, Spectral-domain decomposition methods for the solution of acoustic and elastic wave equations. The Leading Edge **61**, 1160–1174 (1996). Faccioli1996

62. D. Gallistl, Stable splitting of polyharmonic operators by generalized Stokes systems. Math. Comp. **86**(308), 2555–2577 (2017)

63. F. Gardini, G. Manzini, G. Vacca, The nonconforming virtual element method for eigenvalue problems. ESAIM Math. Model. Numer. **53**, 749–774 (2019).

64. F. Gazzola, H.-C. Grunau, G. Sweers, in *Polyharmonic Boundary Value Problems*. Lecture Notes in Mathematics, vol. 1991. (Springer, Berlin, 2010). Positivity preserving and nonlinear higher order elliptic equations in bounded domains.

65. H. Gómez, V.M. Calo, Y. Bazilevs, T.J.R. Hughes, Isogeometric analysis of the Cahn-Hilliard phase-field model. Comput. Methods Appl. Mech. Eng. **197**(49–50), 4333–4352 (2008)

66. P. Grisvard, Elliptic problems in nonsmooth domains, in *Monographs and Studies in Mathematics*, vol. 24. (Pitman (Advanced Publishing Program), Boston, 1985)

67. T. Gudi, M. Neilan, An interior penalty method for a sixth-order elliptic equation. IMA J. Numer. Anal. **31**(4), 1734–1753 (2011)

68. D. Kay, V. Styles, E. Süli, Discontinuous Galerkin finite element approximation of the Cahn-Hilliard equation with convection. SIAM J. Numer. Anal. 47(4), 2660–2685 (2009)
69. D. Komatitsch, J. Tromp, Introduction to the spectral element method for three-dimensional seismic wave propagation. Geophys. J. Int. **139**(3), 806–822 (1999)
70. D.J. Korteweg, Sur la forme que prennent les équations du mouvements des fluides si l'on tient compte des forces capilaires causées par des variations de densité considérables mains continues et sur la théorie de la capillarité dans l'hypothése d'une varation continue de la densité. Arch. Néerl Sci. Exactes Nat. Ser. II (1901)
71. L.D. Landau, On the theory of superconductivity, in D. ter Haar, (ed.) *Collected papers of L. D. Landau*, pp. 546–568 (Pergamon, Oxford, 1965)
72. K. Lipnikov, G. Manzini, A high-order mimetic method for unstructured polyhedral meshes. J. Comput. Phys. **272**, 360–385 (2014)
73. K. Lipnikov, G. Manzini, F. Brezzi, A. Buffa, The mimetic finite difference method for 3D magnetostatics fields problems. J. Comp. Phys. **230**(2), 305–328 (2011)
74. K. Lipnikov, G. Manzini, M. Shashkov, Mimetic finite difference method. J. Comput. Phys. **257**, Part B:1163–1227 (2014)
75. X. Liu, Z. Chen, A virtual element method for the Cahn-Hilliard problem in mixed form. Appl. Math. Lett. **87**, 115–124 (2019)
76. C. Lovadina, D. Mora, I. Velásquez, A virtual element method for the von Kármán equations. Technical report, Preprint CI2MA:2019-36 (2019)
77. G. Manzini, A. Russo, N. Sukumar, New perspectives on polygonal and polyhedral finite element methods. Math. Models Methods Appl. Sci. **24**(8), 1621–1663 (2014)
78. G. Manzini, K. Lipnikov, J.D. Moulton, M. Shashkov, Convergence analysis of the mimetic finite difference method for elliptic problems with staggered discretizations of diffusion coefficients. SIAM J. Numer. Anal. **55**(6), 2956–2981 (2017)
79. L. Mascotto, Ill-conditioning in the virtual element method: stabilizations and bases. Numer. Methods Partial Differential Equations **34**(4), 1258–1281 (2018)
80. D. Mora, I. Velásquez, A virtual element method for the transmission eigenvalue problem. Math. Models Methods Appl. Sci. **28**(14), 2803–2831 (2018)
81. D. Mora, I. Velásquez, Virtual element for the buckling problem of Kirchhoff-Love plates. Comput. Methods Appl. Mech. Eng. **360**, 112687, 22 (2020)
82. D. Mora, G. Rivera, R. Rodríguez, A virtual element method for the Steklov eigenvalue problem. Math. Methods Appl. Sci. **25**(08), 1421–1445 (2015)
83. D. Mora, G. Rivera, I. Velásquez, A virtual element method for the vibration problem of Kirchhoff plates. ESAIM Math. Model. Numer. Anal. **52**(4), 1437–1456 (2018)
84. S. Naranjo-Alvarez, V. Bokil, V. Gyrya, G. Manzini, The virtual element method for resistive magnetohydrodynamics. Comput. Methods Appl. Mech. Eng. **381**, 113815 (2021)
85. K. Park, H. Chi, G.H. Paulino, On nonconvex meshes for elastodynamics using virtual element methods with explicit time integration. Comput. Methods Appl. Mech. Eng. **356**, 669–684 (2019)
86. K. Park, H. Chi, G.H. Paulino, Numerical recipes for elastodynamic virtual element methods with explicit time integration. Internat. J. Numer. Methods Eng. **121**(1), 1–31 (2020)
87. G.H. Paulino, A.L. Gain, Bridging art and engineering using Escher-based virtual elements. Struct. Multidisciplinary Optim. **51**(4), 867–883 (2015)
88. I. Perugia, P. Pietra, A. Russo, A plane wave virtual element method for the Helmholtz problem. ESAIM Math. Model. Num. **50**(3), 783–808 (2016)
89. A. Quarteroni, R. Sacco, F. Saleri, Numerical mathematics, in *Texts in Applied Mathematics*, vol. 37 (Springer, Berlin, 2007)
90. P.-A. Raviart, J.-M. Thomas, *Introduction à l'analyse numérique des équations aux dérivées partielles*. Collection Mathématiques Appliquées pour la Maîtrise. [Collection of Applied Mathematics for the Master's Degree] (Masson, Paris, 1983)
91. B. Rivière, M.F. Wheeler, Discontinuous finite element methods for acoustic and elastic wave problems, in *Current trends in scientific computing (Xi'an, 2002)*. Contemporary Mathematical, vol. 329, pp. 271–282 (American Mathematical Society, Providence, RI, 2003)

92. J.S. Rowlinson, Translation of J. D. van der Waals' "The thermodynamic theory of capillarity under the hypothesis of a continuous variation of density". J. Statist. Phys. **20**(2), 197–244 (1979)
93. M. Schedensack, A new discretization for mth-Laplace equations with arbitrary polynomial degrees. SIAM J. Numer. Anal. **54**(4), 2138–2162 (2016)
94. T. Sorgente, S. Biasotti, G. Manzini, M. Spagnuolo, The role of mesh quality and mesh quality indicators in the virtual element method. Adv. Comput. Math. **48**(3), 1–34 (2022)
95. S. Torabi, J. Lowengrub, A. Voigt, S. Wise, A new phase-field model for strongly anisotropic systems. Proc. R. Soc. Lond. Ser. A Math. Phys. Eng. Sci. **465**(2105), 1337–1359 (2009). With supplementary material available online
96. G. Vacca, Virtual element methods for hyperbolic problems on polygonal meshes. Comput. Math. Appl. **74**(5), 882–898 (2017)
97. M. Wang, J. Xu, Minimal finite element spaces for $2m$-th-order partial differential equations in R^n. Math. Comp. **82**(281), 25–43 (2013)
98. G.N. Wells, E. Kuhl, K. Garikipati, A discontinuous Galerkin method for the Cahn-Hilliard equation. J. Comput. Phys. **218**(2), 860–877 (2006)
99. P. Wriggers, W.T. Rust, B.D. Reddy, A virtual element method for contact. Comput. Mech. **58**(6), 1039–1050 (2016)
100. J. Zhao, S. Chen, B. Zhang, The nonconforming virtual element method for plate bending problems. Math. Models Methods Appl. Sci. **26**(9), 1671–1687 (2016)
101. J. Zhao, B. Zhang, S. Chen, S. Mao, The Morley-type virtual element for plate bending problems. J. Sci. Comput. **76**(1), 610–629 (2018)

Chapter 11
The Virtual Element Method in Nonlinear and Fracture Solid Mechanics

Edoardo Artioli, Sonia Marfia, and Elio Sacco

Abstract The chapter presents recently developed two-dimensional Virtual Element Method (VEM) methodologies for problems of nonlinear inelastic material behavior, linear/nonlinear material homogenization and cohesive fracture mechanics. A rational approach ranging from theoretical foundations to implementation and code optimization details is provided, together with a broad gallery of numerical campaigns confirming the efficiency of the new method.

11.1 Introduction

In the last few years, a new finite element methodology has been proposed; in fact, Brezzi, Beirão da Veiga and coworkers developed a new numerical technology for the determination of approximate solution of partial differential equations named virtual element method (VEM) [7, 14–17, 26]. The VEM represents an evolution of modern mimetic finite difference schemes, sharing the same variational background of the finite element method. The main feature of the VEM is to build discrete approximation spaces suitably chosen as the formal solution of a prescribed differential operator leading to an accurate Galerkin scheme with the flexibility to deal with highly general polygonal/polyhedral meshes, including hanging vertices and non-convex shapes. Thus, the VEM results significantly more

E. Artioli
Department of Civil Engineering and Computer Science, University of Rome Tor Vergata, Rome, Italy
e-mail: artioli@ing.uniroma2.it

S. Marfia
Department of Engineering, University of Roma Tre, Roma, Italy
e-mail: sonia.marfia@uniroma3.it

E. Sacco (✉)
Department of Structures for Engineering and Architecture, University of Naples Federico II, Naples, Italy
e-mail: elio.sacco@unina.it

flexible than standard FEM, as it is possible to discretize the domain by polygons characterized by any number of edges, without any major limitation. Moreover, VEM presents several advantages with respect to classical FEM, such as the ability to accurately deal with complex (possibly curved) geometries, flexibility in mesh generation, no need of using a parent element for quadrature purposes, arbitrary high polynomial degree elevation, and very good performances for distorted meshes. For these reasons, VEM has been successfully implemented in a series of applications involving material and geometrical nonlinearity [5, 8, 40], unilateral contact [41] and in micro-mechanical and homogenization problems [2, 9].

In particular, in [8], numerical results remarked the ability of the VEM formulation to get accurate solutions for nonlinear 2D structural problems, including plasticity, viscoelasticity and shape memory alloy constitutive behavior. In fact, the solutions obtained using VEM are accurate when compared to FEM ones and, as a positive byproduct, require in general less iterations than FEM approach when the same tangent (Newton) algorithm is adopted. Thus, the VEM formulation for nonlinear 2D structural problems demonstrated the accuracy of the approach and, also, the simplicity of the implementation into any available FEM code.

An interesting field of application of the VEM approach is the micromechanics and homogenization of nonlinear composite materials. In [9] the VEM has been suitably adopted to solve homogenization problems for composites characterized by nonlinear response of the matrix, which typically represents a quite interesting and hard test for the assessment of the homogenization procedure. A significant reduced computational effort in recovering the overall response of the composite was found, discretizing the internal part of the inclusion by a unique element characterized by many edges. This approach appeared challenging, opening new opportunities in designing smart discretizations.

The features of the VEM appear particularly suitable for the development of a procedure able to follow the crack growth in a solid. Indeed, a standard VEM method, joined by classical zero-thickness interface elements, have been adopted in [18] to simulate crack opening processes in concrete aggregates characterized by complex geometries. The possibility to combine the use of VEM with the minimal remeshing procedures, i.e. to extend and smartly implement the founding idea at the basis of the XFEM through an inter-element approach, appears very interesting and challenging. A nonlinear fracture mechanics procedure within VEM with minimal remeshing technique has been illustrated in [36]. Crack propagation in 2D solids adopting the VEM technique within the context of linear elastic fracture mechanics has been proposed in [33] and, then, in [29] where, as in the present work, a true mesh refinement process guided by crack propagation is actually implemented. In the latter work, the advantages of mesh flexibility proper of VEM are highlighted, while the stress intensity factors are computed by using the interaction domain integral. An X-VEM formulation for Laplace problem has been proposed in [19]. The presented procedure can be considered as a nontrivial translation of the extended FEM technique to VEM, obtained by augmenting the standard virtual element space with an additional contribution that consists of the product of virtual nodal basis (partition-of-unity) functions with enrichment functions.

A novel procedure for reproducing the nucleation and propagation of fracture in 2D cohesive media has been proposed in [11], combining the virtual element technique with a splitting methodology and a minimal remeshing procedure, suitably taking advantage of the specific features of VEM mesh adaptivity. A numerical algorithm has been proposed for reproducing the crack nucleation, the fracture path generation and tracking. The procedure fundamentally consists in two steps, i.e. the nucleation and propagation criteria and the adaptive mesh refinement. Numerical applications have been developed in order to assess the ability of the proposed procedure to satisfactorily reproduce the crack nucleation and growth in solids.

In the present chapter, the VEM formulation is reviewed. Then, the following three developments, in the framework of two-dimensional solid mechanics, are presented:

– VEM for nonlinear (plasticity, viscoelasticity and shape memery alloy) constitutive response;
– VEM for linear and nonlinear homogenization problems;
– VEM for cohesive fracture mechanics.

Several numerical results are reported illustrating the performances and the reliability of the VEM formulation.

11.2   Position of the Problem

A two-dimensional (2D) body Ω subjected to volume forces $\mathbf{b}$, surface forces $\mathbf{p}$ on $\partial_f \Omega$ and prescribed displacements $\hat{\mathbf{u}}$ on $\partial_u \Omega$, such that $\partial_u \Omega \cup \partial_f \Omega = \partial \Omega$ and $\partial_u \Omega \cap \partial_f \Omega = \emptyset$, is considered. The body contains a cohesive crack $\Im$ inside Ω, where a cohesive traction $\mathbf{t}$ is present. In Fig. 11.1, the body Ω with the cohesive crack $\Im$ is schematically illustrated. The structural behavior of the body is herein studied

Fig. 11.1 Schematic of the body with cohesive crack, subjected to volume and surface forces
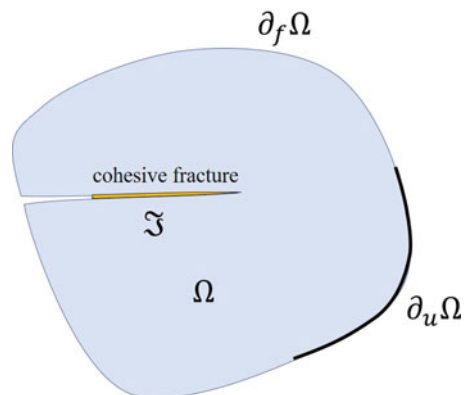
in the framework of small strain and small displacement formulation, adopting a Voigt notation so that second order tensors are organized in vectors and fourth order tensors in matrices. The coordinate system (O, x, y) is introduced in the plane of the body Ω.

Neglecting the inertial effects in the equilibrium condition, the governing equations are:

$$\boldsymbol{\varepsilon} = \mathbf{L}\,\mathbf{u} \tag{11.1}$$

$$\mathbf{L}^T \boldsymbol{\sigma} + \mathbf{b} = \mathbf{0} \qquad\qquad \text{in } \Omega \tag{11.2}$$

$$\boldsymbol{\sigma} = \mathbf{C}\,(\boldsymbol{\varepsilon} - \boldsymbol{\pi}) \tag{11.3}$$

$$\mathbf{N}^T \boldsymbol{\sigma} = \mathbf{p} \qquad\qquad \text{on } \partial_f \Omega \tag{11.4}$$

$$\mathbf{u} = \hat{\mathbf{u}} \qquad\qquad \text{on } \partial_u \Omega \tag{11.5}$$

$$\mathbf{N}^T \boldsymbol{\sigma} = \mathbf{t} \qquad\qquad \text{on } \Im \tag{11.6}$$

where $\mathbf{u} = \{u_x\ u_y\}^T$ is the displacement, $\boldsymbol{\varepsilon} = \{\varepsilon_x\ \varepsilon_y\ \gamma_{xy}\}^T$ is the strain, $\boldsymbol{\pi} = \{\pi_x\ \pi_y\ \pi_{xy}\}^T$ is a possible inelastic strain, $\boldsymbol{\sigma} = \{\sigma_x\ \sigma_y\ \sigma_{xy}\}^T$ is the stress, $\mathbf{C}$ is the 3×3 elasticity matrix, $\mathbf{L}$ is the compatibility operator and $\mathbf{N}$ is the matrix associated with the outward unit normal vector $\mathbf{n}$ to $\partial \Omega$, resulting:

$$\mathbf{L} = \begin{bmatrix} \bullet_{,x} & 0 \\ 0 & \bullet_{,y} \\ \bullet_{,y} & \bullet_{,x} \end{bmatrix}, \qquad\qquad \mathbf{N} = \begin{bmatrix} n_x & 0 \\ 0 & n_y \\ n_y & n_x \end{bmatrix}, \tag{11.7}$$

with $\bullet_{,x}$ and $\bullet_{,y}$ indicating the partial derivative with respect to x and y, respectively.

The traction on $\Im$ is due to the cohesive forces arising because of the crack opening. These stresses are different from zero in the so-called cohesive process zone, close to the crack tip, and are zeros when the real crack is formed. The inelastic strain $\boldsymbol{\pi}$ can be due to different inelastic phenomena, such as plasticity, viscoelasticity and shape memory effects. In the next sections, the equations governing the cohesive response of the fracture and the specific evolution of the inelastic strain will be presented.

The weak form of the equilibrium equation at a given time t takes the form:

$$\int_\Omega [\boldsymbol{\varepsilon}\,(\delta\mathbf{u})]^T\ \mathbf{C}\,(\boldsymbol{\varepsilon}\,(\mathbf{u}) - \boldsymbol{\pi})\,dA = \int_\Omega \delta\mathbf{u}^T\,\mathbf{b}\,dA + \int_{\partial_f \Omega} \delta\mathbf{u}^T\,\mathbf{p}\,dA + \int_\Im \delta\mathbf{s}^T\,\mathbf{t}\,d\xi \tag{11.8}$$

where $\mathbf{s} = \mathbf{u}^+ - \mathbf{u}^-$ is the relative displacement evaluated along the fracture line $\Im$ and ξ is the curvilinear abscissa on it and $\delta\mathbf{u}$ is a compatible variation of the displacement field. The left-hand side of Eq. (11.8) represents the variation of the elastic internal energy of the body Ω, while the right-hand side the virtual work of the external forces and of the tractions along the fracture line.

The weak formulation (11.8) of the strong form Eqs. (11.1)–(11.6), completed with the equations governing the evolution of the inelastic strain $\boldsymbol{\pi}$ and the crack growth, is numerically solved adopting the Virtual Element Method.

11.3 Basis of the VEM in 2D Solid Mechanics

A polygonal discretization of the 2D body Ω is performed, considering non overlapping polygons Ω_E characterized by a number m of edges. The discussion is herein limited to the case of straight edges, even if curved edges can be also considered in the VEM formulation as proposed in [10]. In Fig. 11.2 the typical virtual element is drawn, with the Cartesian coordinate system (x, y). Note that the virtual element (VE) is a polygon characterized by a desired number of straight edges and vertexes, without any limitation.

11.3.1 Kinematics

Within each element, an approximating displacement field, $\mathbf{u}^h$, is considered, whose explicit expression is not given, as it is not required in the development of the VEM formulation.

As no explicit expression is given for the displacement field $\mathbf{u}^h$ within each VE, the strain cannot be computed using the compatibility Eq. (11.1). Thus, a consistent strain field is determined as the projection of the compatible strain on an approximating subspace. In fact, the consistent part of the strain field is explicitly

Fig. 11.2 Typical polygonal virtual element with the Cartesian coordinate system
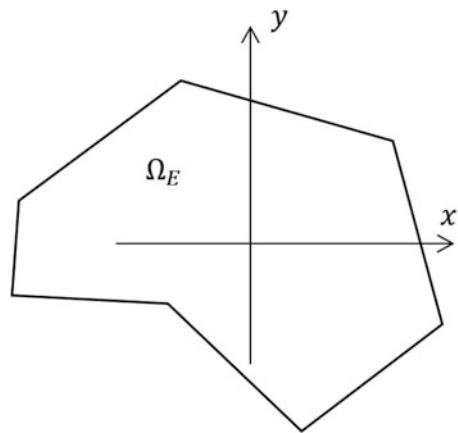
represented element-wise in the form:

$$\boldsymbol{\varepsilon}^c = \mathbf{N}^P \hat{\boldsymbol{\varepsilon}} \tag{11.1}$$

where $\hat{\boldsymbol{\varepsilon}}$ is a vector of $3\,(p+1)$ strain parameters and $\mathbf{N}^P$ is the matrix of the polynomial approximation functions of degree p.

The projection of the compatible strain on the approximating subspace of the consistent strain can be simply performed by minimizing the distance:

$$\min_{\hat{\boldsymbol{\varepsilon}}} \left\| \mathbf{N}^P \hat{\boldsymbol{\varepsilon}} - \mathbf{L}\mathbf{u}^h \right\|^2 \tag{11.2}$$

which leads to:

$$\int_{\Omega_E} \left(\mathbf{N}^P \right)^T \left(\mathbf{N}^P \hat{\boldsymbol{\varepsilon}} \right) dA = \int_{\Omega_E} \left(\mathbf{N}^P \right)^T \left(\mathbf{L}\mathbf{u}^h \right) dA. \tag{11.3}$$

Integrating by parts of the right-hand side of Eq. (11.3), it results:

$$\int_{\Omega_E} \left(\mathbf{N}^P \right)^T \left(\mathbf{N}^P \hat{\boldsymbol{\varepsilon}} \right) dA = \int_{\partial\Omega_E} \left(\mathbf{N}^P \right)^T \mathbf{N}_E \tilde{\mathbf{u}}^h \, dA - \int_{\Omega_E} \left(\mathbf{B}^P \right)^T \mathbf{u}^h \, dA \tag{11.4}$$

with $\partial\Omega_E$ the boundary of Ω_E, $\mathbf{N}_E$ the matrix of the components of the outward normal to Ω_E, analogously to the one reported in Eq. (11.7), $\tilde{\mathbf{u}}^h$ the restriction of the displacement field to $\partial\Omega_E$ and $\mathbf{B}^P = \mathbf{L}^T \mathbf{N}^P$.

An explicit representation form for the displacement components on the boundary of the VE is assumed. In particular, it is introduced a polynomial approximation on each straight edge of the element, characterized by a degree $k = p + 1$, so that $k \geq 1$. Other choices of the approximating displacement on the VE boundary can be assumed, as discussed in [22]. The displacement field on $\partial\Omega_E$ is explicitly written in terms of the displacements of nodes placed on the vertexes and on the edges of the polygonal VE. The number of nodes on VE, n_d, is related to the degree k of the polynomial approximation, resulting $n_d = k\,m$ so that the number of nodal degrees of freedom is $2\,k\,m$. Finally, it is set:

$$\tilde{\mathbf{u}}^h = \mathbf{N}^V \tilde{\mathbf{U}}, \tag{11.5}$$

where $\tilde{\mathbf{U}}$ is a vector of nodal displacement and $\mathbf{N}^V$ is the matrix of the edge-piecewise polynomial approximation functions of degree k. Note that expression given in (11.5) is almost formal as from practical point of view, the approximation of the displacement field on the boundary is explicitly given edge-wise involving the displacement components of the nodes lying on the edge, according to formula:

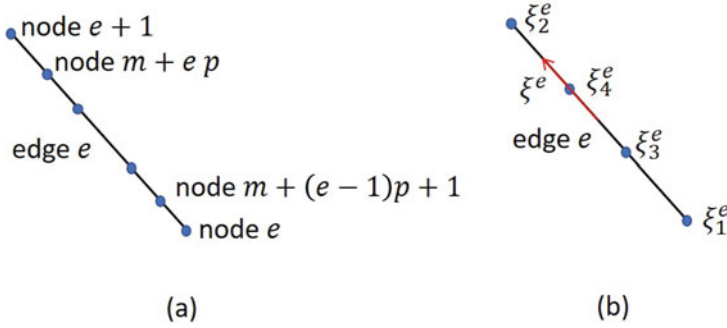$$\tilde{\mathbf{u}}_e^h = \mathbf{N}_e^V \tilde{\mathbf{U}}_e, \tag{11.6}$$

Fig. 11.3 Typical VE edge: (**a**) numbering of the nodes on the edge, (**b**) local abscissa ξ^e for the case $k = 3$

with clear meaning of the symbols. Normally, the nodes are numbered starting from the vertexes and, then, introducing the nodes inside the edges, as schematically illustrated in Fig. 11.3a. The $k - 1 = p$ nodes in the typical edge are placed dividing the edge in k equal parts. On the typical edge e a local abscissa ξ^e is introduced whose origin is situated at the mid-length of the edge, as reported in Fig. 11.3b. The matrix $\mathbf{N}_e^V$ takes the explicit form:

$$\mathbf{N}_e^V = [N_1 \mathbf{I}_2 \ \ldots \ N_{k+1} \mathbf{I}_2] \,, \tag{11.7}$$

with $\mathbf{I}_2$ the 2×2 identity matrix and N_i with $i = 1, .., k + 1$ classical Lagrangian functions:

$$N_i = \frac{(\xi - \xi_1) \ldots (\xi - \xi_{i-1})(\xi - \xi_{i+1}) \ldots (\xi - \xi_{k+1})}{(\xi_i - \xi_1) \ldots (\xi_i - \xi_{i-1})(\xi_i - \xi_{i+1}) \ldots (\xi_i - \xi_{k+1})} \,. \tag{11.8}$$

Taking into account expression (11.5), the first term of the right-hand side Eq. (11.4) becomes:

$$\int_{\partial \Omega_E} \left(\mathbf{N}^P \right)^T \mathbf{N}_E \tilde{\mathbf{u}}^h \, dA = \hat{\mathbf{B}} \, \tilde{\mathbf{U}} \qquad \text{with } \hat{\mathbf{B}} = \int_{\partial \Omega_E} \left(\mathbf{N}^P \right)^T \mathbf{N}_E \mathbf{N}^V \, dA \tag{11.9}$$

The last term of Eq. (11.4) is a vector that can be evaluated as:

$$\int_{\Omega_E} \left(\mathbf{B}^P \right)^T \mathbf{u}^h \, dA = \tilde{\mathbf{B}} \, \mathbf{q} \,, \tag{11.10}$$

where the typical component of the vector $\mathbf{q}$ is:

$$\int_{\Omega_E} x^i y^j u_\alpha^h \, dA \qquad \text{with } 0 \le i + j < p \text{ and } \alpha = 1, 2 \tag{11.11}$$

and $\tilde{\mathbf{B}}$ is a suitable matrix. Of course, if $p = 0$ the $\mathbf{B}^P$ is null and the integral over Ω_E in Eq. (11.4) disappears. Note that the values of the components of the vector $\mathbf{q}$ are not known, representing together to the components of $\tilde{\mathbf{U}}$ further unknowns to be determined. The $k(k-1)$ components of $\mathbf{q}$ can be considered as internal degrees of freedom that are often named as displacement moments or weighted average displacements in the element.

Finally, Eq. (11.4) can be rewritten as:

$$\mathbf{G}\,\hat{\boldsymbol{\varepsilon}} = \mathbf{B}\,\mathbf{U}\,, \tag{11.12}$$

where

$$\mathbf{G} = \int_{\Omega_E} \left(\mathbf{N}^P\right)^T \mathbf{N}^P \, dA \qquad \mathbf{B} = \begin{bmatrix} \hat{\mathbf{B}} & \tilde{\mathbf{B}} \end{bmatrix} \qquad \mathbf{U} = \left\{ \begin{matrix} \tilde{\mathbf{U}} \\ \mathbf{q} \end{matrix} \right\} \tag{11.13}$$

so that, taking into account Eq. (11.3), the consistent strain results:

$$\boldsymbol{\varepsilon}^c = \mathbf{\Pi}\,\mathbf{U} \qquad \text{with } \mathbf{\Pi} = \mathbf{N}^P \mathbf{G}^{-1} \mathbf{B}\,. \tag{11.14}$$

In such a way, the consistent strain is determined as function of the $2mk + k(k-1)$ components of the vector $\mathbf{U}$, i.e. of the displacements at the nodes on the VE boundary, $\tilde{\mathbf{U}}$, and of the internal degrees of freedom $\mathbf{q}$.

As the consistent strain has degree $p = k - 1$, the space of the associated displacement field within the virtual element is of degree k; thus, the consistent displacement field $\mathbf{u}^c$ can be introduced as:

$$\mathbf{u}^c = \mathbf{P}(\mathbf{x})\,\mathbf{d} \tag{11.15}$$

with $\mathbf{P}(\mathbf{x})$ the matrix whose components are the basis of the order k polynomial and $\mathbf{d}$ the vector of the coefficients multiplying the functions of the basis. The consistent displacement at the i−th node of the VE can be computed as $\mathbf{u}_i^c = \mathbf{P}(\mathbf{x}_i)\,\mathbf{d}$ for $i = 1, .., n_d$, being $\mathbf{x}_i = \{x_i \ y_i\}^T$ the coordinate vector of the i−th node of the VE. Moreover, the weighted average displacements associated to $\mathbf{u}^c$, namely $\mathbf{q}^c$, can be evaluated properly integrating the functions in the matrix $\mathbf{P}(\mathbf{x})$.

The vector collecting all the values of the nodal displacements $\mathbf{u}_i^c$ of the VE is:

$$\mathbf{U}^c = \mathbf{D}\mathbf{d} \qquad \text{with } \mathbf{U}^c = \left\{ \begin{matrix} \mathbf{u}_1^c \\ \mathbf{u}_2^c \\ \ldots \\ \ldots \\ \mathbf{u}_{n_d}^c \\ \mathbf{q}^c \end{matrix} \right\} \tag{11.16}$$

with $\mathbf{D}$ obtained simply arranging the matrices $\mathbf{P}(\mathbf{x}_i)$ and the integral definitions (11.11).

The displacement vector $\mathbf{U}^c$ can be considered as the projection of vector $\mathbf{U}$ on the space of the polynomials of degree k, corresponding to the projected strain $\boldsymbol{\varepsilon}^c$ of degree $p = k - 1$. This projection can be, then, determined minimizing the distance between the vectors $\mathbf{U}$ and $\mathbf{U}^c$, leading to:

$$\min_{\mathbf{d}} |\mathbf{U} - \mathbf{Dd}\|^2 \tag{11.17}$$

which gives:

$$\mathbf{d} = \left(\mathbf{D}^T\mathbf{D}\right)^{-1}\mathbf{D}^T\mathbf{U} \quad \rightarrow \quad \mathbf{U}^c = \mathbf{\Pi}^c\mathbf{U} \quad \text{with } \mathbf{\Pi}^c = \mathbf{D}\left(\mathbf{D}^T\mathbf{D}\right)^{-1}\mathbf{D}^T , \tag{11.18}$$

so that the matrix $\mathbf{\Pi}^c$ represents, in some way, the projector of the displacement field corresponding to the operator $\mathbf{\Pi}$ acting on the strain field. Thus, it is possible to recover the counter-projected displacement field as:

$$\mathbf{U}^s = \mathbf{\Pi}^s\mathbf{U} \quad \text{with } \mathbf{\Pi}^s = \mathbf{I} - \mathbf{\Pi}^c . \tag{11.19}$$

It could be remarked that the consistent strain could be not implicitly kinematically compatible, as the quantity

$$r = \varepsilon^c_{x,yy} + \varepsilon^c_{y,xx} + \gamma^c_{xy,xy} \tag{11.20}$$

could not be automatically equal to zero. In fact, taking into account Eq. (11.1), the expression (11.20) leads to:

$$r = \sum_{j=1}^{\frac{3}{2}(p+1)(p+2)} \left(N^P_{1j,yy} + N^P_{2j,xx} - N^P_{3j,xy}\right)\hat{\varepsilon}_j . \tag{11.21}$$

11.3.2 Stiffness Matrix

In the VEM formulation, the stress field is determined from the consistent strain; in other words, the constitutive equation (11.3) is intended in the form:

$$\boldsymbol{\sigma} = \mathbf{C}\left(\boldsymbol{\varepsilon}^c - \boldsymbol{\pi}\right) . \tag{11.22}$$

According to the VEM, the internal force vector $\boldsymbol{\Lambda}$ emerging from the variation of the elastic internal energy for a typical element Ω_E given by the left-hand side of

Eq. (11.8), is evaluated as:

$$\boldsymbol{\Lambda} = \int_{\Omega_E} \boldsymbol{\Pi}^T \, \mathbf{C} \, (\boldsymbol{\Pi} \, \mathbf{U} - \boldsymbol{\pi}) \, dA + \tau \, \boldsymbol{\Pi}^s \, \mathbf{U} \,, \tag{11.23}$$

where the first term directly comes form the consistent strain, while the second term derives from the counter-projection of the displacement field. Thus, the global elastic stiffness matrix of the element is:

$$\mathbf{K} = \mathbf{K}^c + \mathbf{K}^s \,, \tag{11.24}$$

where

$$\mathbf{K}^c = \int_{\Omega_E} \boldsymbol{\Pi}^T \, \mathbf{C} \, \boldsymbol{\Pi} \, dA \qquad\qquad \mathbf{K}^s = \tau \, \boldsymbol{\Pi}^s \tag{11.25}$$

are named the consistent and the stabilization stiffness matrices of the VE, respectively. The factor τ present in the definition of $\mathbf{K}^s$ is generally set as function of the trace of the consistent elastic matrix $\mathbf{K}^c$:

$$\tau = \frac{1}{2}\mathrm{tr}\mathbf{K}^c \,. \tag{11.26}$$

The stabilization term deriving from the counter-projection of the displacement field is very important as accounts for the energy that is neglected by the consistent term, playing the fundamental role to avoid free energy element deformations.

11.3.3   Force Vector

The force vector due to the external distributed load $\mathbf{b}$ is determined consistently with the VEM formulation starting from the right-hand side of Eq. (11.8).

The distributed load $\mathbf{b}$ is approximated by a polynomial form of degree $k-2$, resulting:

$$\mathbf{b} = \mathbf{b}^{(0)} + x \, \mathbf{b}^{(x)} + y \, \mathbf{b}^{(y)} + \ldots + y^{k-2} \, \mathbf{b}^{(y^{k-2})} \,. \tag{11.27}$$

Introducing the representation (11.27) in the first term of right-hand side of Eq. (11.8), written at the single element level, the virtual work of the external force $\mathbf{b}$ is:

$$W_b = \int_{\Omega_E} \delta \mathbf{u}^{h^T} \left(\mathbf{b}^{(0)} + x \, \mathbf{b}^{(x)} + y \, \mathbf{b}^{(y)} + \ldots + y^{k-2} \, \mathbf{b}^{(y^{k-2})} \right) dA \,. \tag{11.28}$$

Recalling the expression (11.11) of the components of the vector $\mathbf{q}$, the virtual work of the mass force can be evaluated as:

$$W_b = \delta q_1\, b_1^{(0)} + \delta q_2\, b_2^{(0)} + \delta q_3\, b_1^{(x)} + \delta q_4\, b_2^{(x)} + \ldots + \delta q_{(k-2)(k-1)}\, b_2^{(y^{k-2})}. \qquad (11.29)$$

Introducing the vector $\mathbf{F}^q = \left\{ b_1^{(0)}\ b_2^{(0)}\ \ldots\ b_2^{(y^{k-2})} \right\}^T$ and recalling the definition of $\mathbf{U}$ in Eq. (11.13), the virtual work becomes:

$$W_b = \delta\mathbf{q}^T\, \mathbf{F}^q = \delta\mathbf{U}^T\, \mathbf{F}, \qquad (11.30)$$

where $\mathbf{F} = \left\{ \mathbf{0}^T\ \mathbf{F}^{q\,T} \right\}^T$ is the vector of the external forces associated with the order k of the VEM formulation.

Note that the polynomial approximation of the mass load $\mathbf{b}$ given in formula (11.27), considering the terms until the degree $k - 2$, is consistent with the internal degrees of freedom arranged in the vector $\mathbf{q}$.

The discussed approach for evaluating the external forces associated with distributed load in the VE is rigorous, but it fails when the interesting case $k = 1$ is considered. In fact, in this case the vector $\mathbf{q}$ disappears. Thus, the force vector is computed evaluating the virtual work as:

$$W_b = \frac{1}{n_d}\mathbf{A}\,\delta\mathbf{U}^T\,\bar{\mathbf{b}}, \qquad (11.31)$$

where the $2 \times 2n_d$ matrix $\mathbf{A}$ and the 2 components vector $\bar{\mathbf{b}}$, representing the resultant force acting on the VE, are defined as:

$$\mathbf{A} = [\mathbf{I}_2\ \mathbf{I}_2\ \ldots\ \mathbf{I}_2] \qquad\qquad \bar{\mathbf{b}} = \int_{\Omega_E} \mathbf{b}\, dA. \qquad (11.32)$$

Finally, the force vector for $k = 1$ is:

$$\mathbf{F} = \frac{1}{n_d}\mathbf{A}^T\,\bar{\mathbf{b}}. \qquad (11.33)$$

11.3.4 The Case $k = 3$

Next, the case $p = 2$, i.e. $k = 3$, is considered and an explicit form of the fundamental matrices and vectors involved in this case is given. Of course, cases with a lower value of the polynomial approximation can be simply determined just suitably deleting redundant terms.

The $\mathbf{N}^P$ matrix takes the explicit form:

$$\mathbf{N}^P = \begin{bmatrix} \mathbf{I}_3 & x\mathbf{I}_3 & y\mathbf{I}_3 & x^2\mathbf{I}_3 & xy\mathbf{I}_3 & y^2\mathbf{I}_3 \end{bmatrix}, \tag{11.34}$$

with $\mathbf{I}_3$ the 3×3 identity matrix; the matrix $\mathbf{N}_e^V$ becomes:

$$\mathbf{N}_e^V = [N_1\mathbf{I}_2 \ N_2\mathbf{I}_2 \ N_3\mathbf{I}_2 \ N_4\mathbf{I}_2], \tag{11.35}$$

with N_i $(i = 1, .., 4)$ the classical Lagrangian functions:

$$N_1 = \frac{(\xi - \xi_2)(\xi - \xi_3)(\xi - \xi_4)}{(\xi_1 - \xi_2)(\xi_1 - \xi_3)(\xi_1 - \xi_4)} \quad N_2 = \frac{(\xi - \xi_1)(\xi - \xi_3)(\xi - \xi_4)}{(\xi_2 - \xi_1)(\xi_2 - \xi_3)(\xi_2 - \xi_4)}$$
$$N_3 = \frac{(\xi - \xi_1)(\xi - \xi_2)(\xi - \xi_4)}{(\xi_3 - \xi_1)(\xi_3 - \xi_2)(\xi_3 - \xi_4)} \quad N_4 = \frac{(\xi - \xi_1)(\xi - \xi_2)(\xi - \xi_3)}{(\xi_4 - \xi_1)(\xi_4 - \xi_2)(\xi_4 - \xi_3)}. \tag{11.36}$$

The $\mathbf{B}^P$ matrix is:

$$\mathbf{B}^P = [\mathbf{O}_{2\times 3} \ \mathbf{J}_1 \ \mathbf{J}_2 \ 2y\mathbf{J}_1 \ y\mathbf{J}_1 + x\mathbf{J}_2 \ 2x\mathbf{J}_2], \tag{11.37}$$

being $\mathbf{O}_{2\times 3}$ the 2×3 zero matrix and

$$\mathbf{J}_1 = \begin{bmatrix} 1 & 0 & 0 \\ 0 & 0 & 1 \end{bmatrix} \qquad \mathbf{J}_2 = \begin{bmatrix} 0 & 0 & 1 \\ 0 & 1 & 0 \end{bmatrix}, \tag{11.38}$$

so that the matrix $\tilde{\mathbf{B}}$ and the vector $\mathbf{q}$ take the form:

$$\tilde{\mathbf{B}} = \begin{bmatrix} \mathbf{O}_{3\times 2} & \mathbf{O}_{3\times 2} & \mathbf{O}_{3\times 2} \\ \mathbf{J}_1^T & \mathbf{O}_{3\times 2} & \mathbf{O}_{3\times 2} \\ \mathbf{J}_2^T & \mathbf{O}_{3\times 2} & \mathbf{O}_{3\times 2} \\ \mathbf{O}_{3\times 2} & 2\mathbf{J}_1^T & \mathbf{O}_{3\times 2} \\ \mathbf{O}_{3\times 2} & \mathbf{J}_1^T & \mathbf{J}_2^T \\ \mathbf{O}_{3\times 2} & \mathbf{O}_{3\times 2} & 2\mathbf{J}_2^T \end{bmatrix} \quad \text{and} \quad \mathbf{q} = \int_{\Omega_E} \begin{Bmatrix} u_x^h \\ u_y^h \\ x\,u_x^h \\ x\,u_y^h \\ y\,u_x^h \\ y\,u_y^h \end{Bmatrix} dA. \tag{11.39}$$

The matrix $\mathbf{P}$ takes the explicit form:

$$\mathbf{P} = \begin{bmatrix} \mathbf{I}_2 & x\mathbf{I}_2 & y\mathbf{I}_2 & x^2\mathbf{I}_2 & xy\mathbf{I}_2 & y^2\mathbf{I}_2 & x^3\mathbf{I}_2 & x^2y\mathbf{I}_2 & xy^2\mathbf{I}_2 & y^3\mathbf{I}_2 \end{bmatrix}, \tag{11.40}$$

Thus, the matrix **D** required for the stabilization term assumes the following block-partitioned form:

$$
\mathbf{D} = \begin{bmatrix}
\mathbf{I}_2 & x_1\mathbf{I}_2 & y_1\mathbf{I}_2 \ldots & y_1^3\mathbf{I}_2 \\
\mathbf{I}_2 & x_2\mathbf{I}_2 & y_2\mathbf{I}_2 \ldots & y_2^3\mathbf{I}_2 \\
\vdots & \vdots & \ldots & \\
& \vdots & \vdots & \\
\mathbf{I}_2 & x_{n_d}\mathbf{I}_2 & y_{n_d}\mathbf{I}_2 \ldots & y_{n_d}^3\mathbf{I}_2 \\
\int_{\Omega_E} dA\,\mathbf{I}_2 & \int_{\Omega_E} x\,dA\,\mathbf{I}_2 & \int_{\Omega_E} y\,dA\,\mathbf{I}_2 \ldots & \int_{\Omega_E} y^3\,dA\mathbf{I}_2
\end{bmatrix}.
\tag{11.41}
$$

11.4   Nonlinear Inelastic Material Response

This section presents a set of representative macroscopic nonlinear constitutive models, adopting the *energetic formulation* (see [31], for example), in a unified manner. The first constitutive model is the von Mises plasticity model with linear isotropic and kinematic strain hardening [37], secondly the generalized Maxwell viscoelastic model is presented [42]. Lastly, the shape memory alloy model proposed in [38] and subsequently modified in [12, 24] is presented. The selected constitutive models aim at giving a broad assessment of the VEM performance in reproducing typical material nonlinear response of structural elements, giving a comparison to standard displacement-based finite element schemes.

11.4.1   Plastic Behavior

The von Mises plasticity model with combined linear isotropic/kinematic hardening is here considered [13].

Infinitesimal strain is additively decomposed into deviatoric **e**, and volumetric (spherical) ϑ, parts as:

$$
\boldsymbol{\varepsilon} = \mathbf{e} + \frac{1}{2}\vartheta\mathbf{1}\,,
\tag{11.1}
$$

where $\mathbf{e} = \text{dev}\boldsymbol{\varepsilon}$, $\vartheta = \text{tr}\boldsymbol{\varepsilon}$ and $\mathbf{1} = \{110\}^T$. Both the deviatoric and spherical strains are decomposed in the elastic and plastic parts:

$$\mathbf{e} = \mathbf{e}^e + \mathbf{e}^p \tag{11.2}$$

$$\vartheta = \vartheta^e \tag{11.3}$$

such that plastic flow is purely isochoric.

For an isotropic material, Helmholtz free energy density has the form:

$$\psi = \psi^e + \psi^{tr}, \tag{11.4}$$

where:

$$\psi^e(\boldsymbol{\varepsilon}^e) = \frac{1}{2}K(\vartheta^e)^2 + G\|\mathbf{e}^e\|^2 \tag{11.5}$$

$$\psi^{tr}(\mathbf{e}^p) = \frac{1}{2}H^{kin}\|\mathbf{e}^p\|^2 \tag{11.6}$$

with K and G the bulk and shear elastic moduli, respectively, and where H^{kin} is the linear kinematic hardening parameter.

Owing to a standard thermodynamic procedure, the constitutive equations are derived as:

$$\boldsymbol{\sigma}' \in \partial_{\mathbf{e}^e}\psi \tag{11.7}$$

$$\mathbf{X} \in -\partial_{\mathbf{e}^p}\psi, \tag{11.8}$$

Here, the symbol ∂ represents the subdifferential operator in the sense of Convex Analysis. In the present case the function ψ is differentiable, and the above inclusions are indeed equalities involving standard partial differentiation. The *relative stress* $\mathbf{X}$ in Eq. (11.8) is conveniently rewritten as:

$$\mathbf{X} = \boldsymbol{\sigma}' - \boldsymbol{\alpha} \tag{11.9}$$

where $\boldsymbol{\sigma}'$ is the *stress deviator*, and $\boldsymbol{\alpha}$ is the *back stress tensor*, which result, respectively:

$$\boldsymbol{\sigma}' = 2G\left(\mathbf{e} - \mathbf{e}^p\right) \tag{11.10}$$

$$\boldsymbol{\alpha} = H^{kin}\mathbf{e}^p. \tag{11.11}$$

The activation of the plastic flow is governed by the von Mises yield function expressed in terms of the relative stress:

$$f\left(\mathbf{X}, \bar{e}^p\right) = \|\mathbf{X}\| - \frac{\sqrt{2}}{2}\sigma_y, \tag{11.12}$$

which defines the *elastic domain* as the set $\mathcal{E} = \{\mathbf{X} \in \text{SymDev} : f(\mathbf{X}) \leq 0\}$, where SymDev denotes the space of symmetric traceless second-order tensors written in Voigt notation. The function $\sigma_{\text{y}} = \sigma_{\text{y}_0} + H^{\text{i}}\bar{e}^{\text{p}}$ represents the uniaxial yield stress, depending on the initial yield stress σ_{y_0}, on the isotropic hardening parameter H^{i}, and on the accumulated plastic strain, defined as:

$$\bar{e}^{\text{p}} = \int_0^t \|\dot{\mathbf{e}}^{\text{p}}\| d\tau. \tag{11.13}$$

Plastic flow is governed by the *associated* law, such that the plastic strain rate and unit normal to yield domain are related as:

$$\dot{\mathbf{e}}^{\text{p}} = \dot{\zeta}\frac{\partial f}{\partial \mathbf{X}} \tag{11.14}$$

from which it results:

$$\dot{\bar{e}}^{\text{p}} = \frac{\sqrt{2}}{2}\dot{\zeta}. \tag{11.15}$$

The inelastic problem is completed by the Kuhn-Tucker optimality conditions:

$$\dot{\zeta} \geq 0 \qquad\qquad f \leq 0 \qquad\qquad \dot{\zeta} f = 0. \tag{11.16}$$

for the plastic rate parameter $\dot{\zeta}$.

Note that the inelastic strain introduced in the previous section is represented by the plastic strain, i.e. $\boldsymbol{\pi} = \mathbf{e}^{\text{p}}$.

11.4.2   Viscoelastic Behavior

The considered viscoelastic constitutive model is represented by a linear elastic element in parallel with M spring-dashpot linear elements, leading to a Helmholtz internal energy density in the form of:

$$\psi^{\text{e}}(\boldsymbol{\varepsilon}, \mathbf{w}^{(m)}) = \frac{1}{2}\boldsymbol{\varepsilon}^{(0)}\mathbf{V}^{(0)}\boldsymbol{\varepsilon}^{(0)} + \frac{1}{2}\sum_{m=1}^{M}\mathbf{w}^{(m)}\mathbf{V}^{(m)}\mathbf{w}^{(m)}. \tag{11.17}$$

The quantities $\boldsymbol{\varepsilon}^{(0)} = \boldsymbol{\varepsilon}$ and $\mathbf{V}^{(0)}$ are the strain and linear elasticity matrix associated with the single elastic element, respectively. The terms $\mathbf{w}^{(m)}$ and $\mathbf{V}^{(m)}$, $m = 1, \ldots M$, are the *partial strains* and associated elasticities in the dissipative spring-dashpots elements [42].

According to standard thermodynamic arguments, the corresponding constitutive equation is [42]:

$$\boldsymbol{\sigma}(t) = \mathbf{V}^{(0)}\boldsymbol{\varepsilon}^{(0)}(t) + \sum_{m=1}^{M} \mathbf{V}^{(m)}\mathbf{w}^{(m)}(t).$$ (11.18)

In the previous evolution law, each partial strain $\mathbf{w}^{(m)}(t)$ evolves according to:

$$\dot{\mathbf{w}}^{(m)} + \frac{1}{\lambda^{(m)}}\mathbf{w}^{(m)} = \dot{\boldsymbol{\varepsilon}},$$ (11.19)

where the terms $\lambda^{(m)}$ are the *coefficients of relaxation*. In an integral form, the stress-strain behavior may be described through a convolutive form as:

$$\boldsymbol{\sigma}(t) = \mathbf{V}(t)\boldsymbol{\varepsilon}(0) + \int_0^t \mathbf{V}(t - \tilde{t})\,\dot{\boldsymbol{\varepsilon}}\,d\tilde{t}$$ (11.20)

where the components of $\mathbf{V}(t)$ are *relaxation moduli* functions.

Assuming isotropic material behavior, and considering a purely deviatoric inelastic response, the above relations simplify to:

$$(\sigma)' = 2G(t)\mathbf{e}$$ (11.21)

with $(\sigma)' = \text{dev}\boldsymbol{\sigma}$, and $\mathbf{e} = \text{dev}\boldsymbol{\varepsilon}$, and with $G(t)$ defined as the *shear modulus relaxation function*.

In integral form, the constitutive behavior is described as:

$$(\sigma)'(t) = \int_{-\infty}^t 2G(t - \tilde{t})\,\dot{\mathbf{e}}\,d\tilde{t}.$$ (11.22)

The integral equation form may be defined as a generalized Maxwell model by assuming the *shear modulus relaxation function* in Prony series form [42]:

$$G(t) = G\left(\mu_0 + \sum_{i=1}^{M}\mu_i\,\exp(-t/\lambda_i)\right).$$ (11.23)

In this constitutive model, the inelastic strain is given by the set of terms $\boldsymbol{\pi} = \{\boldsymbol{\varepsilon}^{in,m}\} = \{\mathbf{w}^{(m)}\}$, $m = 1, \ldots, M$. Note that the model does not need the introduction of history variables. Indeed, in every spring-dashpot element, the total strain is additively decomposed in elastic and viscous parts.

11.4.3 Shape Memory Alloy Behavior

The present section is devoted to presenting a nowadays classical phenomenological constitutive model for shape memory alloy materials which mainly proves efficient for metallic materials [12, 38]. The thermodynamic state variables of this constitutive model are defined as the infinitesimal strain $\boldsymbol{\varepsilon}$, the absolute temperature T, and the *transformation* strain $\mathbf{e}^{\text{tr}}$, assuming the typical strain additive decomposition:

$$\boldsymbol{\varepsilon} = \boldsymbol{\varepsilon}^{\text{e}} + \mathbf{e}^{\text{tr}} \tag{11.24}$$

into elastic strain, $\boldsymbol{\varepsilon}^{\text{e}}$, and transformation strain. The traceless tensor function $\mathbf{e}^{\text{tr}}$ is the inelastic strain associated with the phase transformation which still indicates that phase transition is isochoric for the present constitutive model for shape memory alloy materials [34]. Inelastic evolution enforces transformation strain to be included in the *saturation* domain $\mathscr{S} = \{\mathbf{e}^{\text{tr}} \in \text{SymDev} : c(\mathbf{e}^{\text{tr}}) \leq 0\}$, where $c(\mathbf{e}^{\text{tr}}) = \|\mathbf{e}^{\text{tr}}\|^2 / \boldsymbol{\varepsilon}_{\text{L}}^2 - 1$, and $\boldsymbol{\varepsilon}_{\text{L}}$ is a material parameter related to the maximum transformation strain reached at the end of the forward isothermal transformation during a uniaxial test. From a modeling point of view, $\mathbf{e}^{\text{tr}}$ being the inelastic strain capable of representing the reorientation of the product phase in the saturated condition [12].

The Helmholtz free energy density ψ is assumed like a strictly convex potential depending on the local thermodynamic state of the material:

$$\psi(\boldsymbol{\varepsilon}^{\text{e}}, \mathbf{e}^{\text{tr}}, T) = \psi^{\text{e}}(\boldsymbol{\varepsilon}^{\text{e}}) + \psi^{\text{ch}}(\mathbf{e}^{\text{tr}}, T) + \psi^{\text{tr}}(\mathbf{e}^{\text{tr}}), \tag{11.25}$$

under the constraint $\mathbf{e}^{\text{tr}} \in \mathscr{S}$. Here:

– ψ^{e} is the elastic strain energy, which, assuming linear isotropic elastic behavior, is given by:

$$\psi^{\text{e}}(\boldsymbol{\varepsilon}^{\text{e}}) = \frac{1}{2} K (\text{tr} \boldsymbol{\varepsilon}^{\text{e}})^2 + G \| \text{dev} \, \boldsymbol{\varepsilon}^{\text{e}} \|^2 \tag{11.26}$$

with K the bulk modulus and G the shear modulus;
– ψ^{ch} is the chemical energy, associated with the thermally-induced martensitic transformation:

$$\psi^{\text{ch}}(\mathbf{e}^{\text{tr}}, T) = \beta \Delta T^+ \|\mathbf{e}^{\text{tr}}\| \tag{11.27}$$

with β a material parameter related to the dependence of the critical stress on the temperature, and $\Delta T^+ = \langle T - M_{\text{f}} \rangle$, being M_{f} the temperature corresponding to the end of the forward transformation, and $\langle \bullet \rangle$ the positive part of the argument;

– ψ^{tr} is the transformation strain energy, associated with transformation-induced strain hardening:

$$\psi^{\mathrm{tr}}(\mathbf{e}^{\mathrm{tr}}) = \frac{1}{2}h\|\mathbf{e}^{\mathrm{tr}}\|^2 \tag{11.28}$$

with h a material parameter defining the slope of the linear stress-transformation strain relation in the uniaxial case.

Owing to the principle of maximum inelastic dissipation [28], the thermodynamic equilibrium state is expressed in terms of the functions thermodynamically conjugate to the arguments $(\boldsymbol{\varepsilon}^{\mathrm{e}}, \mathbf{e}^{\mathrm{tr}}, T)$. By definition:

$$\begin{aligned}
\boldsymbol{\sigma} &= \partial_{\boldsymbol{\varepsilon}^{\mathrm{e}}}\psi \\
\mathbf{X} &= -\partial_{\mathbf{e}^{\mathrm{tr}}}\psi - \partial_{\mathbf{e}^{\mathrm{tr}}}\mathcal{I}_{\mathcal{S}} \\
\eta &= -\partial_T\psi
\end{aligned} \tag{11.29}$$

where $\boldsymbol{\sigma}$ is the Cauchy stress, $\mathbf{X}$ is the symmetric traceless thermodynamic stress, and η is the entropy density. Equation $(11.29)_2$ is usually rewritten as:

$$\mathbf{X} = (\sigma)' - \boldsymbol{\alpha}\,, \tag{11.30}$$

where $(\sigma)'$ is the stress deviator, and $\boldsymbol{\alpha}$ is the back stress tensor, given by:

$$\boldsymbol{\alpha} = \beta\Delta T^+ \partial_{\mathbf{e}^{\mathrm{tr}}}\|\mathbf{e}^{\mathrm{tr}}\| + h\,\mathbf{e}^{\mathrm{tr}} + \partial_{\mathbf{e}^{\mathrm{tr}}}\mathcal{I}_{\mathcal{S}}(\mathbf{e}^{\mathrm{tr}})\,. \tag{11.31}$$

Moreover, the indicator function $\mathcal{I}_{\mathcal{S}}(\mathbf{e}^{\mathrm{tr}})$ of the saturation domain is introduced:

$$\begin{cases}
\mathcal{I}_{\mathcal{S}}(\mathbf{e}^{\mathrm{tr}}) = 0 & \text{if } c(\mathbf{e}^{\mathrm{tr}}) \le 0 \\
\mathcal{I}_{\mathcal{S}}(\mathbf{e}^{\mathrm{tr}}) = +\infty & \text{otherwise}
\end{cases} \tag{11.32}$$

whose subdifferential results:

$$\partial_{\mathbf{e}^{\mathrm{tr}}}\mathcal{I}_{\mathcal{S}}(\mathbf{e}^{\mathrm{tr}}) = \begin{cases}
\{\mathbf{0}\} & \text{if } c(\mathbf{e}^{\mathrm{tr}}) < 0 \\
\gamma\,\partial_{\mathbf{e}^{\mathrm{tr}}}c(\mathbf{e}^{\mathrm{tr}}) & \text{if } c(\mathbf{e}^{\mathrm{tr}}) = 0 \\
\emptyset & \text{if } c(\mathbf{e}^{\mathrm{tr}}) > 0
\end{cases} \tag{11.33}$$

being $\gamma \in \mathbb{R}_0^+$ the Kuhn-Tucker parameter associated with the thermodynamic reaction explicated by the saturation constraint.

The phase transformation mechanism is governed by a flow law for the transformation strain, defined through a *transformation function* $f(\mathbf{X})$ which bounds the

set of admissible thermodynamic stresses as the nonempty, closed *elastic domain* in deviatoric stress space:

$$\mathscr{E} = \{\mathbf{X} \in \text{SymDev} : f(\mathbf{X}) \leq 0\} . \tag{11.34}$$

The function $f(\mathbf{X})$ is usually expressed similarly to a plasticity yield function, deviatoric isotropic, and represented in von Mises form in the present context [4]:

$$f(\mathbf{X}) = ||\mathbf{X}|| - \sqrt{\frac{2}{3}}\sigma_{y_0} . \tag{11.35}$$

Accordingly, inelastic flow activation obeys to the following criterion:

$$\begin{cases} \text{if } f(\mathbf{X}) < 0, \ \dot{\mathbf{e}}^{\text{tr}} = \mathbf{0} \\ \text{if } f(\mathbf{X}) = 0, \ \dot{\mathbf{e}}^{\text{tr}} = \mathbf{0}, \text{OR } \dot{\mathbf{e}}^{\text{tr}} \neq \mathbf{0}. \end{cases} \tag{11.36}$$

In particular, the flow law is obtained by postulating the principle of maximum inelastic (or transformation) work rate [27, 28], which entails convexity of the elastic domain, and leads to an associated flow rule in the form:

$$\dot{\mathbf{e}}^{\text{tr}} = \dot{\zeta}\nabla f(\mathbf{X}) \tag{11.37}$$

being $\mathbf{X}$ the admissible thermodynamic stress at equilibrium, with the Kuhn-Tucker conditions for the inelastic rate parameter $\dot{\zeta}$:

$$\dot{\zeta} \geq 0 , \ \ f \leq 0 , \ \ \dot{\zeta}f = 0 . \tag{11.38}$$

Note that the inelastic strain introduced in the previous section is represented by the plastic strain, i.e. $\boldsymbol{\pi} = \mathbf{e}^{\text{tr}}$.

11.4.4 Numerical Applications

In this section a general assessment of the presented VEM formulation in conjunction with inelastic material behaviors previously examined is carried out. The treatment focuses on a set of classical benchmark boundary value problems and on the comparative evaluation in terms of accuracy with respect to standard Lagrangian displacement finite element schemes. Interestingly, the same coding environment is used for both methods, such for instance Newton solver for equilibrium equations is still retained in the present context, highlighting modularity and versatility of a VEM platform.

Fig. 11.4 Geometry,
boundary conditions and
loading for thick-walled
viscoelastic cylinder with
uniform internal pressure.
(From: Artioli, E., Beirao da
Veiga, L., Lovadina, C.,
Sacco, E., Arbitrary order 2D
virtual elements for polygonal
meshes: Part II, inelastic
problem, Computational
Mechanics, 657, 2017.
Springer. Reproduced with
permission)
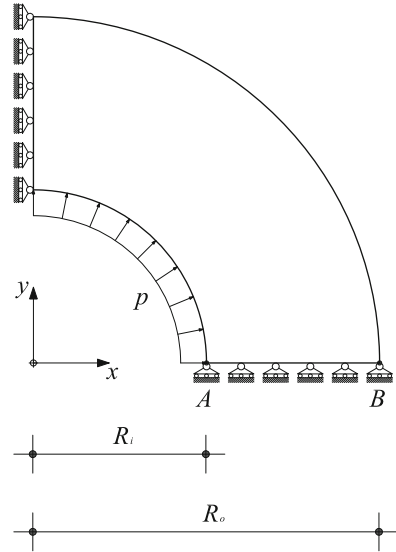
11.4.4.1 Viscoelastic Cylinder Subjected to Internal Pressure

The first benchmark is the classical thick-walled cylinder with a viscoelastic constitutive material behavior. The cylinder, subjected to uniform internal pressure, inner radius $R_i = 2$ and outer radius $R_o = 4$. For symmetry, only a quarter of the cylinder cross section is studied, as reported in Fig. 11.4. Zero normal displacements are enforced along the radial edges. The material is isotropic and modeled by viscoelastic response in deviatoric stress-strain only, in compliance with the constitutive model outlined in Sect. 11.4.2.

The material properties are $M = 1$ and $\lambda_1 \equiv \lambda = 1$ [42]. Young's modulus and Poisson's ratio are $E = 1000$ and $\nu = 0.3$, respectively. Two sets of viscoelastic parameters are adopted in the present analysis (cf. (11.23)), i.e. $(\mu_0, \mu_1)_{\text{ve1}} = (0.01, 0.99)$ and, $(\mu_0, \mu_1)_{\text{ve2}} = (0.3, 0.7)$, respectively. The former case is tailored such as the ratio of the bulk modulus to shear modulus for instantaneous loading is $K/G(0) = 2.167$ and such as, for extended time loading, say at $t = 8$, it results $K/G(8) = 216.7$. This setup is characterized by a nearly incompressible behavior for sustained loading cases (at $t = \infty$ the Poisson ratio results 0.498). The second material set corresponds to a sort of intermediate response at theoretically infinite time after loading application.

The simulation regards the structural response for a suddenly applied internal pressure set equal to 10. The loading history is discretized through 20 equal time integrations as for the constitutive equation which integrated through a set of discrete instants t_j, $j = 1, \ldots, 20$; by using the generalized Maxwell model in Prony series form (cf. Eq. (11.23)), solution is reduced to a recursion formula in
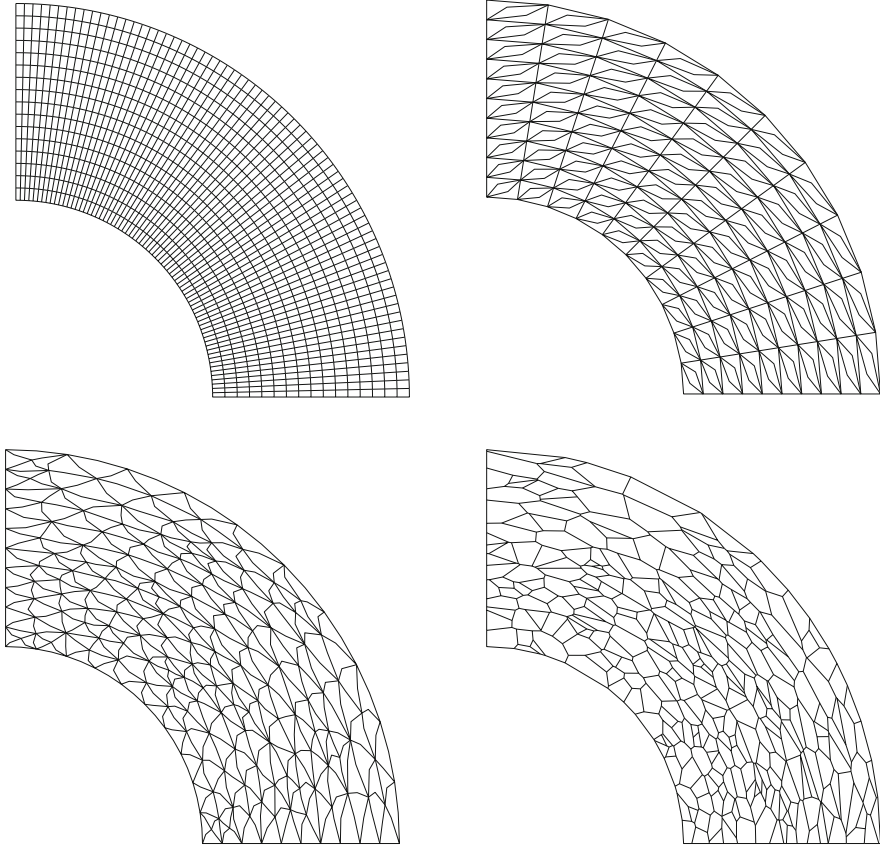
Fig. 11.5 Thick-walled viscoelastic cylinder with uniform internal pressure. (**a**) structured symmetric convex quadrilateral mesh m_1; (**b**) structured skew-symmetric concave quad mesh m_2; (**c**) unstructured concave quad mesh m_3; (**d**) random-based Voronoi tessellation m_4. (From: Artioli, E., Beirao da Veiga, L., Lovadina, C., Sacco, E., Arbitrary order 2D virtual elements for polygonal meshes: Part II, inelastic problem, Computational Mechanics, 657, 2017. Springer. Reproduced with permission)

which each material state is computed by a simple update of the previous one. Details on the coding of this integration algorithm may be found in [43].

In this context, a comparison is made between the proposed VEM formulation, for $k = 1$ and $k = 2$, and quadrilateral displacement-based finite elements with four nodes $Q4$ (linear quadrilateral) and nine nodes $Q9$ (quadratic quadrilateral) [43]. Different mesh types are tested, as portrayed in Fig. 11.5a–d. In particular, the solutions are computed respectively on: a structured convex symmetric quad (a), a structured skew-symmetric convex/concave quad (b), a random-based concave quad (c), and a random-based Voronoi convex poly (d) case. Comparison with FEM solution obviously refers to the case of mesh (a) only. A reference solution
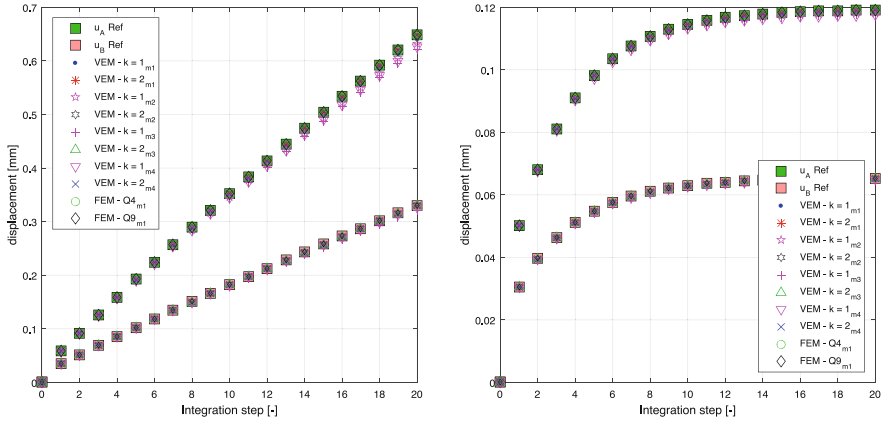
Fig. 11.6 Thick-walled viscoelastic cylinder with uniform internal pressure. Integration step *vs.* radial displacement curves for control points *A* (higher curve), and *B* (lower curve). (**a**) case $(\mu_0, \mu_1)_{ve1} = (0.01, 0.99)$; (**b**) case $(\mu_0, \mu_1)_{ve2} = (0.3, 0.7)$. (From: Artioli, E., Beirao da Veiga, L., Lovadina, C., Sacco, E., Arbitrary order 2D virtual elements for polygonal meshes: Part II, inelastic problem, Computational Mechanics, 657, 2017. Springer. Reproduced with permission)

is computed with mixed quadrilateral finite elements (see [42]) on a very fine space discretization. Response curves for control points A and B (see Fig. 11.4) are portrayed in Fig. 11.6a–b for the different solutions in comparison with the reference one, for the two material parameter sets ve1 and ve2 introduced above. It is observed that the $k = 1, 2$ VEM formulations present accurate response as well as standard displacement finite elements, for a convex quadrilateral spatial discretization. VEM solutions also prove very accurate for non structured convex/concave and highly distorted polygonal discretizations of the domain, showing the effectiveness of the newly introduced formulation.

11.4.4.2 Elastoplastic Plate with Circular Hole

A rectangular plate of base $2L = 200$ mm and height $2H = 360$ mm with a circular hole of $2R = 100$ mm diameter in the center is considered (viz. Fig. 11.7a). The plate obeys to a von Mises constitutive model (see Sect. 11.4.1), and is characterized by $E = 7000$ kg/mm^2, $\nu = 0.3$, $\sigma_{y,0} = 24.3$ kg/mm^2 [42]. Plane strain condition is retailed, hence any (native 3D) integration algorithm for the constitutive model reviewed in Sect. 11.4.1 may be properly used for the purpose of updating material state at the level of a quadrature node in the VEM nonlinear solver framework. In this numerical campaign, for simplicity, a standard backward Euler scheme with return mapping projection is adopted as state update algorithm [37].

Owing to symmetry, only a quarter of the perforated plate is discretized as shown in Fig. 11.7a. Dirichlet boundary conditions are prescribed for normal components

Fig. 11.7 Plastic plate with
circular hole. Geometry,
boundary conditions, applied
displacement on upper edge.
(From: Artioli, E., Beirao da
Veiga, L., Lovadina, C.,
Sacco, E., Arbitrary order 2D
virtual elements for polygonal
meshes: Part II, inelastic
problem, Computational
Mechanics, 657, 2017.
Springer. Reproduced with
permission)
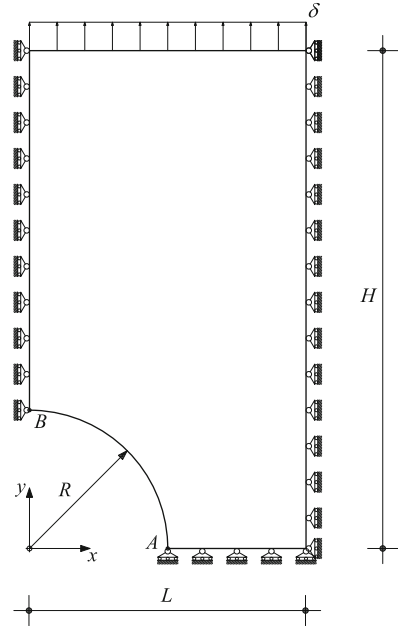
on symmetry boundary edges and on top and lateral boundaries. A uniform normal
displacement $\delta = 2$ mm is incrementally enforced on the upper edge through 200
equal steps, see Fig. 11.7. Different domain discretizations are taken into account
using the code presented in [39], in particular: a quadrilateral structured [resp.
unstructured] (Quad (s) [resp. Quad (u)]) mesh, a triangular (Tri) mesh, and a
centroid based Voronoi tessellation (viz. Fig. 11.8) are generated. The simulation
is carried out considering virtual element spaces of order $k = 1, 2$, on the presented
meshes. For comparative accuracy assessment and validation, also triangular [resp.
quadrilateral] displacement based finite elements $T3$ (linear), and $T6$ (quadratic)
[resp. $Q4$ (linear), and $Q9$ (quadratic)] (see [43]) are tested for the first two
mesh types. A reference solution obtained with an overkilling discretization of
quadrilateral mixed finite elements (see [42]) is computed and used for comparison.
It is noted that VEM elements with $m = 3$, $k = 1$ and triangular Lagrangian finite
elements $T3$ coincide, their results are then reported on a single curve.

The values of horizontal [resp. vertical] displacement of point A [resp. B]
(see Fig. 11.7) at the end of the loading history are reported in Table 11.1 for
accuracy and robustness assessment of the compared different methods, together
with the average number of Newton iterations for an incremental loading step. Good
agreement between linear and quadratic VEM/FEM formulations is observed, with
a slight edge in terms of efficiency in favor of the VEM methodology is found, in
particular when distorted meshes are adopted. The structural response is reported

Table 11.1 Plastic plate with circular hole. Comparison of accuracy and convergence properties in terms of displacement components u_A and v_B at the end of loading history, and average number of iterations per load step

	u_A [mm]	v_B [mm]	Avg. iter/step
	Linear elmts.		Linear elmts.
VEM—Quad (s)	2.538	1.819	4.86
VEM—Quad (u)	2.538	1.818	5.22
VEM—Tri/FEM - T3	2.485	1.823	5.04
VEM—Voronoi	2.540	1.815	4.63
FEM—Q4 (s)	2.692	1.836	5.44
FEM—Q4 (u)	2.689	1.835	6.09
	Quadratic elmts.		Quadratic elmts.
VEM—Quad (s)	2.720	1.851	6.43
VEM—Quad (u)	2.718	1.851	6.75
VEM—Tri	2.719	1.852	6.11
VEM—Voronoi	2.714	1.852	6.21
FEM—Q9 (s)	2.733	1.853	6.70
FEM—Q9 (u)	2.732	1.855	7.24
FEM—T6	2.719	1.853	6.11
Reference solution	2.741	1.859	

in Fig. 11.9, where load-displacement curves for the quadratic methods are reported with favorable agreement.

11.4.4.3 Shape Memory Alloy Device

The present numerical test proves the ability of the VEM methodology of accurately modeling and reproducing complex highly nonlinear material behavior of a simple device made of shape memory alloy material (cf. Sect. 11.4.3).

The device consists of a clamped semicircular arch [6, 24, 25], as shown in Fig. 11.10a subjected to a uniform applied traction on the free edge. Inner [resp. outer] radius is $R_i = 3.5$ mm [resp. $R_O = 4.5$ mm]. Material parameters for the constitutive model are: $E = 53000$ MPa, $\nu = 0.36$, $\varepsilon_L = 0.04$, $M_f = 223$ K, $h = 1000$ MPa, $\beta = 2.1$ MPa/K, $\sigma_{y,0} = 50$ Mpa [24].

In this numerical test, plane stress assumption is invoked. The original 3D form of the constitutive model reviewed in Sect. 11.4.3 is integrated at quadrature point level with the innovative state update algorithm recently proposed in [3, 4]. To comply with plane stress condition, a further nonlinear constraint onto the stress state update procedure is efficiently applied through a reduction algorithm with nested iterations [23, 43]. In the end, the solution procedure can be viewed as an initial boundary problem on a 2D domain with three sources of nonlinearity, i.e. at: state update, plane stress constraint enforcement, overall equilibrium equation solution level, respectively.
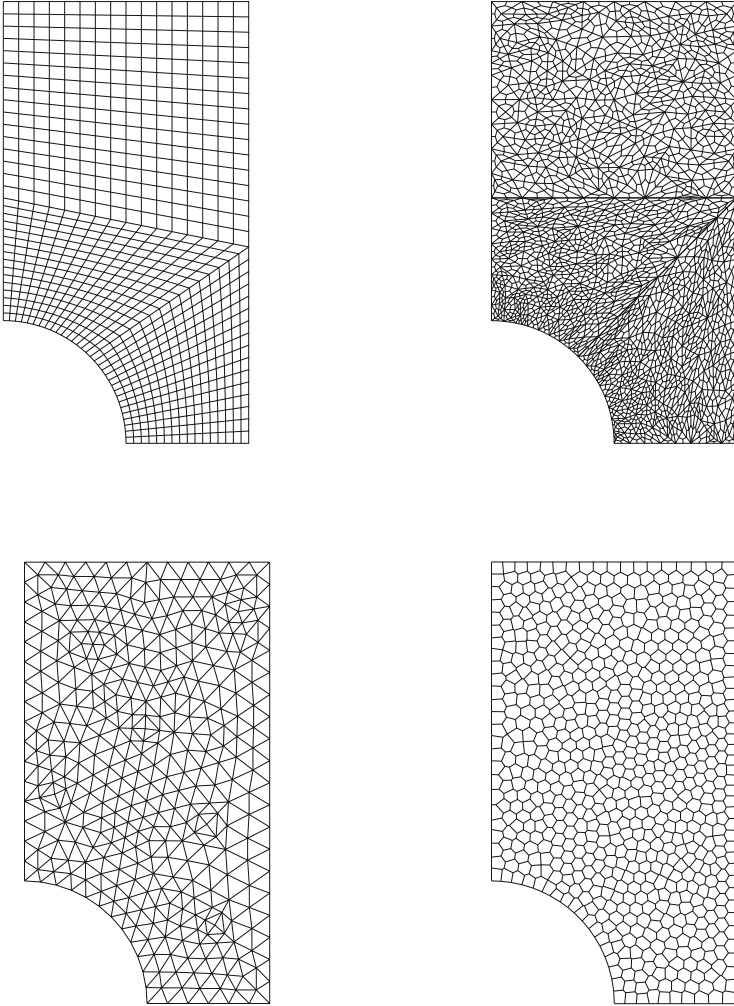
Fig. 11.8 Plastic plate with circular hole. (**a**) Quad (*s*)—structured quadrilateral mesh; (**b**) Quad (*u*)—unstructured quadrilateral mesh; (**c**) Tri—unstructured triangular mesh; (**d**) Voronoi—centroid based tessellation. (From: Artioli, E., Beirao da Veiga, L., Lovadina, C., Sacco, E., Arbitrary order 2D virtual elements for polygonal meshes: Part II, inelastic problem, Computational Mechanics, 657, 2017. Springer. Reproduced with permission)

The structure is subjected to a load-temperature driven loading history which consisting in 5 pseudo-time branches as indicated in Table 11.2. Assuming proportional loading, the incremental solution procedure is carried out with 40 equal increments during the first 4 branches and $N = 10$ equal increments during the final heating branch. Loading parameters are $q_{max} = 60$ N/mm, $T_{room} = 223$ K.
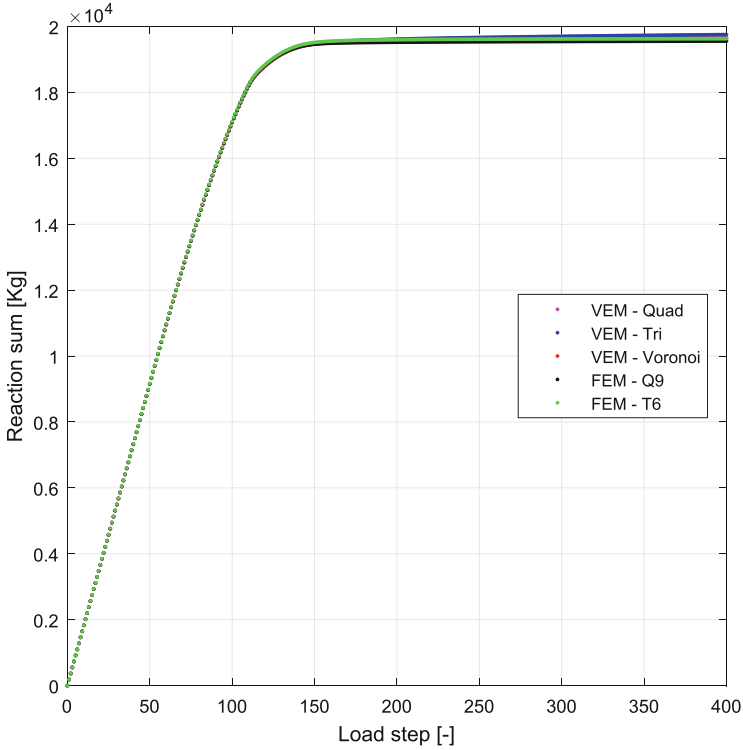
Fig. 11.9 Plastic plate with circular hole. Total vertical reactive force *vs.* vertical displacement of upper edge curves. Comparison between VEM formulation and standard FEM for various meshes. Quadratic VEM ($k = 2$) and quadratic Lagrangian FEM ($T6$, $Q9$) elements. (From: Artioli, E., Beirao da Veiga, L., Lovadina, C., Sacco, E., Arbitrary order 2D virtual elements for polygonal meshes: Part II, inelastic problem, Computational Mechanics, 657, 2017. Springer. Reproduced with permission)
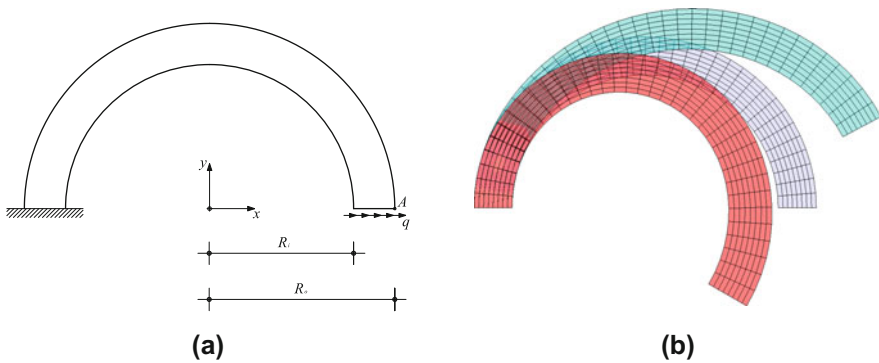
Fig. 11.10 Shape memory alloy arch actuator. (**a**) Geometry, boundary conditions, applied load; (**b**) quadrilateral mesh used in the simulation: reference configuration (grey), deformed configurations at $t = 1$ (cyan) and $t = 3$ (red). (From: Artioli, E., Beirao da Veiga, L., Lovadina, C., Sacco, E., Arbitrary order 2D virtual elements for polygonal meshes: Part II, inelastic problem, Computational Mechanics, 657, 2017. Springer. Reproduced with permission)

Table 11.2 Shape memory alloy arch actuator. Loading history branching for applied load and temperature

Time $[-]$	0	1	2	3	4	5
load q [N/mm]	0	q_{max}	0	$-q_{max}$	0	0
Temperature T [K]	T_{room}	T_{room}	T_{room}	T_{room}	T_{room}	$T_{room} + 80$
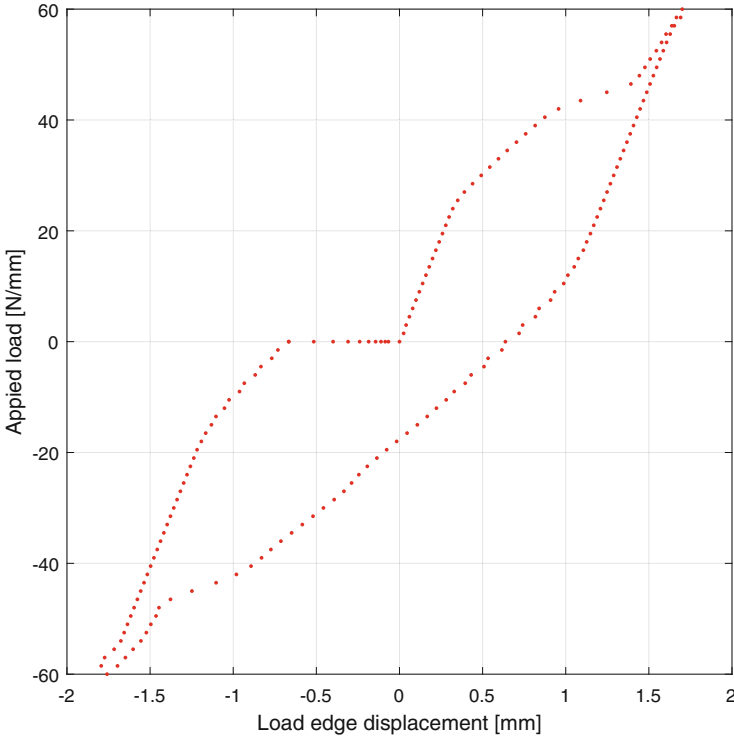
Fig. 11.11 Shape memory alloy arch actuator. Applied load *vs.* point *A* displacement curve. (From: Artioli, E., Beirao da Veiga, L., Lovadina, C., Sacco, E., Arbitrary order 2D virtual elements for polygonal meshes: Part II, inelastic problem, Computational Mechanics, 657, 2017. Springer. Reproduced with permission)

The VEM solution is obtained with the mesh of quad elements shown in Fig. 11.10b (grey). The results presented herein refer to the quadratic case, i.e. $k = 2$.

Deformed configuration snapshots for the adopted mesh at $t = 1$ (cyan) and $t = 3$ (red), respectively, are portrayed in Fig. 11.10b. The functioning curve for the SMA device in terms of applied load *vs.* horizontal displacement of point A shows the classical shape recovery exhibited by the arch device, as can be seen in Fig. 11.11.

The simple benchmarks proposed in this section highlight clearly how implementation of the proposed VEM method into existing structural codes results quite

straightforward and how numerical tools already coded into existing nonlinear finite element codes translate immediately into the new framework without any modification.

11.5 Homogenization of Long Fiber Composites

11.5.1 Problem Formulation

At the micro-scale, the special case of composite material characterized by a regular distribution of inclusions is considered. In particular, a periodic square array of long fiber composite is introduced; of course, other type of periodic arrangements can be considered. In this case, a unit cell (UC) Ω_{UC} with volume V can be introduced for deriving the overall response of the material. Let a local coordinate system be introduced at the micro-scale (x, y, z), with the z axis parallel to the direction of the fiber axis. A 2D rectangular unit cell with dimensions $2\,a_x \times 2\,a_y$ in the plane orthogonal to the fiber and unit thickness in the fiber direction is considered, as illustrated in Fig. 11.12. Note that a unit dimension is considered along the z direction as the material along the $z-$direction is homogeneous.

The displacement and strain fields in this case have to be considered as three-dimensional. Denoting by $\mathbf{E} = \left\{ E_x \ E_y \ E_z \ \Gamma_{xy} \ \Gamma_{yz} \ \Gamma_{xz} \right\}^T$ the overall strain in Ω_{UC}, the displacement field is represented in the form as:

$$u_x = E_x\, x + \frac{1}{2}\Gamma_{xy}\, y + \frac{1}{2}\Gamma_{xz}\, z + u_x^{\star}(\mathbf{x})$$

$$u_y = \frac{1}{2}\Gamma_{xy}\, x + E_y\, y + \frac{1}{2}\Gamma_{yz}\, x_3 + u_y^{\star}(\mathbf{x}) \qquad (11.1)$$

$$u_z = \frac{1}{2}\Gamma_{xz}\, x + \frac{1}{2}\Gamma_{yz}\, y + E_z\, z + u_z^{\star}(\mathbf{x}),$$

where $\mathbf{u}^{\star} = \left\{ u_x^{\star},\ u_y^{\star},\ u_z^{\star} \right\}^T$ is the perturbation displacement, due to the heterogeneity of the UC while $\mathbf{x} = \{x,\ y\}^T$ is the position vector of the typical point of Ω_{UC}.

Fig. 11.12 Schematic of a unit cell for a fiber-reinforced composite material with doubly periodic arrangement of fibers embedded into the matrix
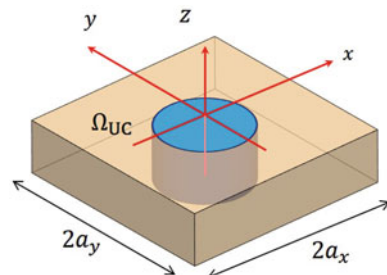
Note that the homogeneity of the material along the $z-$direction ensures that the periodic part of the displacements does not depend on z.

Because of the regular arrangement of the inclusions in the composite material, the perturbation displacement components have to satisfy the periodicity conditions:

$$\begin{aligned}
\mathbf{u}^\star(a_x, y) &= \mathbf{u}^\star(-a_x, y) \quad y \in [-a_y, a_y] \\
\mathbf{u}^\star(x, a_y) &= \mathbf{u}^\star(x, -a_y) \quad x \in [-a_x, a_x]
\end{aligned} . \tag{11.2}$$

From the formula (11.1), the strain at the typical point of Ω_{UC} is:

$$\boldsymbol{\varepsilon}(\mathbf{x}) = \mathbf{E} + \boldsymbol{\varepsilon}^\star(\mathbf{x}) \qquad \text{with } \boldsymbol{\varepsilon}^\star = \mathbf{L}^\star \mathbf{u}^\star , \tag{11.3}$$

where $\boldsymbol{\varepsilon}^\star$ represents the periodic part of the strain, with null average, associated with the displacement $\mathbf{u}^\star$ and $\mathbf{L}^\star$ the 3D compatibility operator, modified with respect to the one introduced in Eq. (11.1), resulting:

$$\mathbf{L}^\star = \begin{bmatrix} \cdot_{,x} & 0 & 0 \\ 0 & \cdot_{,y} & 0 \\ 0 & 0 & 0 \\ \cdot_{,y} & \cdot_{,x} & 0 \\ 0 & 0 & \cdot_{,y} \\ 0 & 0 & \cdot_{,x} \end{bmatrix} , \tag{11.4}$$

as all the derivatives with respect to z are zero, because the displacement components do not depend on z.

The constitutive laws described in the previous sections are adopted for the material constituents. In particular, the inclusion is assumed to have a linear elastic response while the matrix has a nonlinear behavior due to plasticity.

Once the constitutive equation for evaluating the stress in Ω_{UC} is introduced, the micromechanical problem can be solved computing the displacement, strain and stress fields in the UC.

Of course, by averaging the strain field, the overall strain $\mathbf{E}$ is given back; the overall stress $\boldsymbol{\Sigma} = \left\{\Sigma_x \ \Sigma_y \ \Sigma_z \ \Sigma_{xy} \ \Sigma_{yz} \ \Sigma_{xz}\right\}^T$ is obtained as:

$$\boldsymbol{\Sigma} = \frac{1}{V} \int_{\Omega_{UC}} \boldsymbol{\sigma} \, dV \tag{11.5}$$

11.5.2 Computational Homogenization: Smart Use of VEM Meshing Versatility

This section aims at showing one of the main feature of the VEM technology capable of reducing computational cost, in performing multiscale structural analysis. The feature under consideration is the generalized concept of *simple* polygonal mesh as opposed to standard *conforming* mesh required by finite element technology. The former concept, in general, allows to discretize and refine VEM polygonal meshes more easily and more efficiently than FEM meshes, saving on mesh size but retaining the required accuracy features.

The idea underneath the proposed illustrative benchmark is that for a composite with sufficiently high value of the elastic modulus of the inclusion, the displacement field varies slowly among the fiber subdomain. This assumption leads to the possibility of coarsening just locally the discretization, still retaining sufficiently low fineness of mesh size over the rest of the domain. The numerical test setup is hence the following: results pertaining to uniform polygonal mesh with 3553 Voronoi polygons are compared with a mesh comprising a single polygon inside the fiber (so called core region for the fiber), two refined circular *crown-shaped* regions across fiber-matrix interface and a matrix region with reasonably fine size. This particular discretization can be used thanks to the VEM simple meshing asset which allows polygonal elements with arbitrarily edges. In this test, the central element in the fiber subdomain is a polygon with 140 equal edges (hence quite proximal to a circle). Choosing a properly fine mesh at the fiber-matrix interface is highly recommendable as the displacement gradient components may be high across this interface, requiring high resolution. A view of the adopted mesh is given in Fig. 11.13 which, in the following, will be denoted as *crown* mesh. The overall
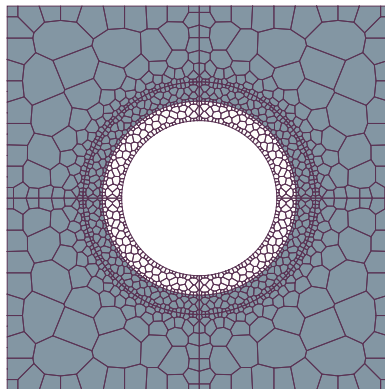

Fig. 11.13 *Crown* unit cell mesh for examined case $v_f = 0.2$. Local mesh refinement across fiber/matrix interface with two circular crown regions with very fine POLY-mesh and a single polygon with 140 edges for the fiber core. (From: Artioli, E., Marfia, S., Sacco, E., High-order virtual element method for the homogenization of long fiber nonlinear composites, Computer Methods in Applied Mechanics and Engineering, 341, 2018. Elsevier. Reproduced with permission)
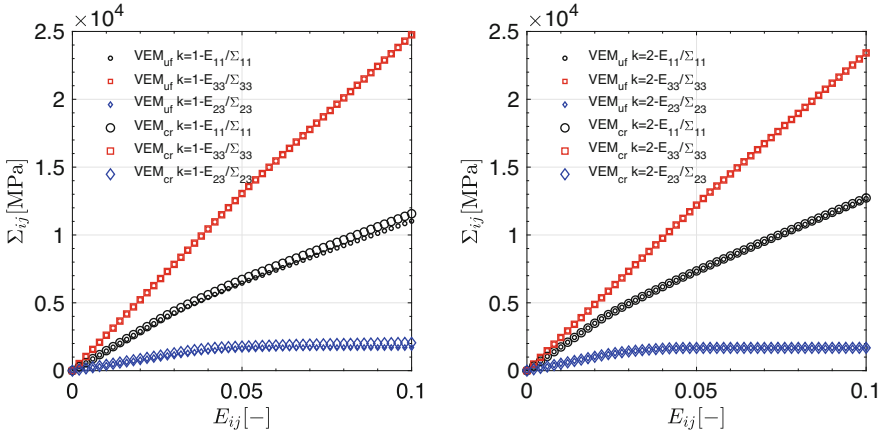
Fig. 11.14 Accuracy for smart VEM discretization. Efficiency of *crown* vs. *uniform* polygonal mesh for elasto-plastic composite. (**a**) $k = 1$, (**b**) $k = 2$, $v_f = 0.2$. (From: Artioli, E., Marfia, S., Sacco, E., High-order virtual element method for the homogenization of long fiber nonlinear composites, Computer Methods in Applied Mechanics and Engineering, 341, 2018. Elsevier. Reproduced with permission)

ratio between uniform and crown mesh number of degrees of freedom is about 4. The scope is numerically proving that crown mesh results are equally accurate than those obtained with a uniform (much finer) mesh, despite its "smart" coarseness.

Performed simulations refer to elasto-plastic composite. In particular, in the former case, material parameters adopted in the previous test are adopted doubling the fiber Young modulus; in the latter, the material parameters are $E^f = 410$ GPa, $v^f = 0.19$, $E^m = 7.5$ GPa, $v^m = 0.33$, $\sigma_y = 0.2$ GPa and $H = 0.02$ GPa. Simulations refer to simple monotonic loading histories and results are determined for $k = 1$ and $k = 2$ order of accuracy.

In Fig. 11.14 the overall stress components Σ_{11}, Σ_{33} and Σ_{23} are plotted versus the corresponding overall strain components for $k = 1$ and $k = 2$, respectively, for the elasto-plastic matrix case. It can be noted that the relative errors between the *crown* and uniform meshes for the VEM solutions in terms of effective response are very reduced, practically less than 5% at maximum strain. On the other hand, it is of interest observing that the computational times for *crown* mesh are roughly 8 times smaller than those needed for the uniform mesh discretization. This impressive result indeed proves the stated point and indicates the efficiency of the proposed methodology in exploiting the relaxed mesh conformity requirements dealing with complex domain shapes.

11.6 Fracture Mechanics

In this section, the aim is to model a cohesive crack growth in an elastic solid. A body Ω subjected to a loading history inducing a fracturing process is studied.

In particular, a cohesive fracturing process is studied, adopting an interface cohesive model, able to account for damage in mode I, in mode II and in mixed mode, the unilateral effect due to the reclosure of the fracture in compression and the frictional effect.

A numerical technique is developed in order to reproduce crack initiation and propagation, exploiting the flexibility of VEM. When the crack arises, a cohesive interface is introduced in the corresponding virtual element directly dividing it in two parts joined by the interface. This process is simplified with respect to the Extended Finite Element approach as the two new generated VEs can have any number of edges and nodes. Furthermore, the proposed approach is able to follow crack propagation in the neighbor virtual elements, performing a remeshing close to the crack tip. The remeshing can be implemented only in narrow area thanks to the VEM flexibility, keeping computational costs low.

Numerical applications are reported in order to assess the ability of the proposed procedure to reproduce the crack growth in a solid. The ability of the proposed procedure to follow a curved crack is investigated. Finally, a comparison with experimental and numerical results, available in literature, is presented.

11.6.1 Interface Model

The cohesive crack $\Im$ inside Ω is modeled introducing an interface. As illustrated in Fig. 11.15, the displacements of the points of the two surfaces defining the interface, are denoted as $\mathbf{u}^+$ and $\mathbf{u}^-$, respectively. Thus, the relative displacement at the interface is:

$$\mathbf{s} = \mathbf{u}^+ - \mathbf{u}^- \tag{11.1}$$

A cohesive interface model, coupling damage and possible friction, is derived performing a simple micromechanical analysis on the basis of the approach proposed in [1, 35].

Fig. 11.15 Fractured body with a cohesive crack
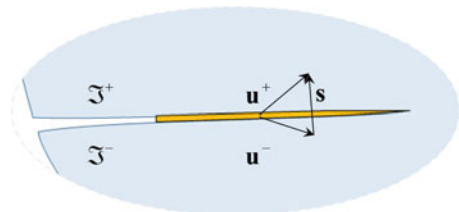
At the typical point of the interface a Representative Interface Area (RIA) is associated. The RIA is simply modeled considering two rigid plates in adhesion; the total area A of the RIA is split in two parts: an undamaged part A_u and a damaged one A_d, so that $A_u + A_d = A$ is the total area of the RIA. The damage parameter D is introduced as the ratio between the damaged part and the total area:

$$D = \frac{A_d}{A} \qquad \text{so that } A_u = (1-D)\,A\,, \ A_d = D\,A \tag{11.2}$$

A linear elastic behavior is considered on A_u, while a constitutive law characterized by unilateral contact and friction is assumed on A_d. Introducing a local coordinate reference system (ξ_t, ξ_n), with ξ_t and ξ_n the axes tangent and normal to $\Im$ respectively, the traction $\mathbf{t}^u = \{t_t^u,\ t_n^u\}^T$ on A_u and $\mathbf{t}^d = \{t_t^d,\ t_n^d\}^T$ on A_d results:

$$\mathbf{t}^u = \mathbf{K}\,\mathbf{s} \tag{11.3}$$

$$\mathbf{t}^d = \mathbf{K}\,\mathbf{H}\left(\mathbf{s} - \mathbf{s}^{di}\right), \tag{11.4}$$

where $\mathbf{K} = \mathrm{diag}[K_t,\ K_n]$ is a diagonal matrix which collects the stiffness values in the normal and tangential directions to the interface, $\mathbf{H} = \mathrm{diag}[1 - h(s_n),\ 1]$, with $h(\bullet)$ being the Heaviside function:

$$h(s_n) = \begin{cases} 1 \text{ if } s_n \geq 0 \\ 0 \text{ if } s_n < 0 \,. \end{cases} \tag{11.5}$$

and $\mathbf{s}^{di}$ the inelastic slip relative displacement.

The total, i.e. overall homogenized, value of traction on the RIA is obtained by weighting the two tractions determined on A_u and A_d by Eqs. (11.3) and (11.4) as:

$$\mathbf{t} = \mathbf{K}\left[(1-D)\mathbf{s} + D\mathbf{H}\left(\mathbf{s} - \mathbf{s}^{di}\right)\right]. \tag{11.6}$$

The evolution of the inelastic slip relative displacement $\mathbf{s}^{di}$, occurring on the damaged part of the RIA, is assumed to be governed by the Coulomb friction with yield function:

$$\varphi(\mathbf{t}^d) = \mu \,\langle t_n^d\rangle_- + |t_t^d|\,, \tag{11.7}$$

where μ is the friction coefficient and the brackets $\langle\bullet\rangle_-$ define the negative part of the argument variable. A purely tangential slip evolution law is considered for the inelastic relative displacement vector $\mathbf{s}^{di}$, as determined by the non-associated flow

rule:

$$\dot{\mathbf{s}}^{di} = \dot{\lambda} \left\{ \begin{array}{c} \dfrac{t_t^d}{|t_t^d|} \\ 0 \end{array} \right\}, \tag{11.8}$$

and is completed by the classical loading-unloading (Kuhn-Tucker) conditions:

$$\dot{\lambda} \geq 0 \qquad \varphi(\mathbf{t}^d) \leq 0 \qquad \dot{\lambda}\, \varphi(\mathbf{t}^d) = 0. \tag{11.9}$$

A model which accounts for the coupling of mode I of mode II of fracture is considered for the damage evolution. Denoting by s_{0n} and s_{0t} the normal and the tangential relative displacement corresponding to the onset damage for pure mode I and pure mode II, respectively, the following ratios are introduced:

$$\chi_n = \frac{s_{0n} t_{0n}}{2 G_{cI}}, \qquad \chi_t = \frac{s_{0t} t_{0t}}{2 G_{cII}}, \tag{11.10}$$

being t_{0n} and t_{0t} the normal and shear peak stresses corresponding to the first cracking relative displacement, and G_{cI} and G_{cII} the specific fracture energies in mode I and mode II, respectively.

The equivalent relative displacement ratio is introduced as:

$$Y = \sqrt{Y_n^2 + Y_t^2} \qquad \text{with } Y_n = \frac{\langle s_n \rangle_+}{s_{0n}} \quad Y_t = \frac{s_t}{s_{0t}} \tag{11.11}$$

being Y_n and Y_t the mode I and mode II relative displacement ratios, respectively, and the brackets $\langle \bullet \rangle_+$ defining the positive part of the number.

The damage evolution is assumed to be governed by the following equation:

$$D = \max_{history} \left\{ 0, \min \left\{ 1, \tilde{D} \right\} \right\} \qquad \text{with } \tilde{D} = \frac{Y - 1}{Y(1 - \chi)} \tag{11.12}$$

whereas χ is defined as:

$$\chi = \frac{1}{\alpha^2} \left[\langle s_n \rangle_+^2 \chi_n + s_t^2 \chi_n \right], \tag{11.13}$$

with $\alpha = \sqrt{\langle s_n \rangle_+^2 + s_t^2}$.

The proposed damage law induces a linear stress-strain softening both in mode I and in mode II. It can be easily proved [35] that the softening branch remains linear even for monotone mixed mode of the damage evolution.

11.6.2   Cracking Process Through VEM Technology

The procedure that governs crack generation and propagation is illustrated in this section. An undamaged structure is considered and a polygonal mesh of virtual elements with $k = 1$ is introduced.

The numerical procedure, able to model the propagation of only one crack during the loading process, accounts for nucleation and propagation criteria and topological adaptive mesh refinement and it is made of the following steps. Each step has a fundamental role into the design of the algorithm for the nonlinear structural solver.

– Initially there are no cracks in the whole structures.
– At the end of each time step the uniform stress state is evaluated in each virtual element considering the projected consistent strain given by Eq. (11.22), taking into account the (11.14) with $\pi = 0$ as the body is assumed to be linear elastic, so that:

$$\boldsymbol{\sigma} = \mathbf{C}\,\boldsymbol{\Pi}\,\tilde{\mathbf{U}} \tag{11.14}$$

– The cracking process starts when the principal tensile stress exceeds the fracturing threshold in a virtual element at the boundary of the body Ω (see Fig. 11.16a).
– This parent element is subdivided in two slave elements defined by a straight cutting line, simulating the fracture, passing through the parent centroid orthogonal to the maximum principal stress. The slave VEM can have any number of edges and nodes.
– Nodes are introduced on the edges of the parent element that are cut by the fracture. The nodes that represents the crack apex are linked (see Fig. 11.16b).
– An interface element, characterized by the cohesive model described in the previous section, is introduced along the newly generated fracture surface shared by the slave elements.
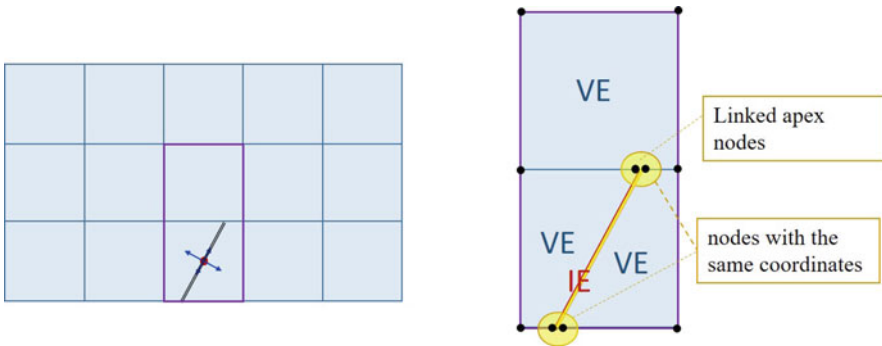
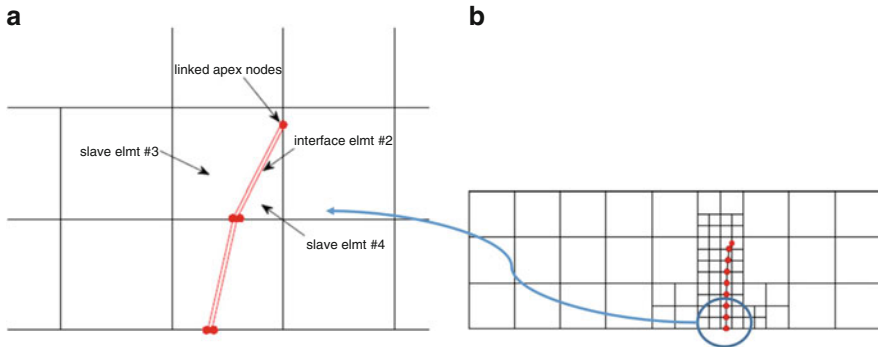

Fig. 11.16 Initial cracking of a boundary element

Fig. 11.17 Cracking propagation: (**a**) splitting of virtual elements; (**b**) mesh refinement. (From: Artioli, E., Marfia, S., Sacco, E., VEM-based tracking algorithm for cohesive/frictional 2D fracture. Computer Methods in Applied Mechanics and Engineering, 365, 2020. Reproduced with permission)

– The value of the normal peak stress of the interface is set equal to the fracturing threshold in the element, i.e. it is $t_{0n} = \sigma_f$.
– The parent and its adjacent elements undergo a mesh refinement, as depicted in Fig. 11.17b.
– The equilibrium solution is revaluated for the same loading considering the new cracked configuration and remeshing.
– A new time step starts and a equilibrium solution is evaluated.
– The next candidate to be cracked is the virtual element that contains the crack tip on one of its edge. When its maximum principal stress results above the tensile threshold the element undergoes a similar cracking process as explained in the previous steps, except that in this case, the fracturing straight line generating the new slave elements is drawn through the apex to insure fracture path continuity.

It can be underlined that the VEM does not require the definition of a map between parent and physical element and, for the specific case $k = 1$ considered in this work, integration is performed only along edges (and, hence, analytically evaluated) and not inside the element. This leads to significantly reduced times of computation.

In the previously outlined procedure, the mesh refinement (see Fig. 11.17b) can be applied upon request, for elements within a certain distance from crack apex. This mesh refinement is possible only adopting VEM characterized by a relaxed mesh conformity concept [14]. This VEM characteristic allows to concentrate the refinement of the mesh along the crack path only, where the nonlinear phenomena are concentrated, saving on computational time. The mesh refinement allows to evaluate the stress state with more accuracy around the crack apex and this is important in order to evaluate accurately the crack path. Thus, the adaptive mesh refinement plays a fundamental role in evaluating crack path detection and

advancement. The user can define the level of mesh refinement at the beginning of the analysis.

It could be underlined that at the typical time step, once an element has been cracked, the nonlinearity of the problem is due only to the behavior of the cohesive interface, simulating the crack and its process zone, introduced in the fractured elements. At each (Gauss or Lobatto) quadrature point of the interface, the nonlinear evolutive problem is solved adopting a predictor-corrector procedure.

The numerical procedure is implemented in Matlab language [30].

11.6.3 Numerical Applications

Some numerical applications are performed to verify the effectiveness and the reliability of the proposed procedure in evaluating the response of fracturing bodies.

An analysis on a realistic domain undergoing curved fracture path is performed to underline the effectiveness of the newly proposed VEM-based methodology. Furthermore, a comparison with the results, achieved by the XFEM method [32], is carried out.

11.6.3.1 Non-Symmetric Three-Point Bending Test with Topological Adaptive Mesh Refinement

The beam with $L = 1$ mm and a vertical notch of length $L/18$ placed at the center of the bottom edge, represented in Fig. 11.18, is considered.
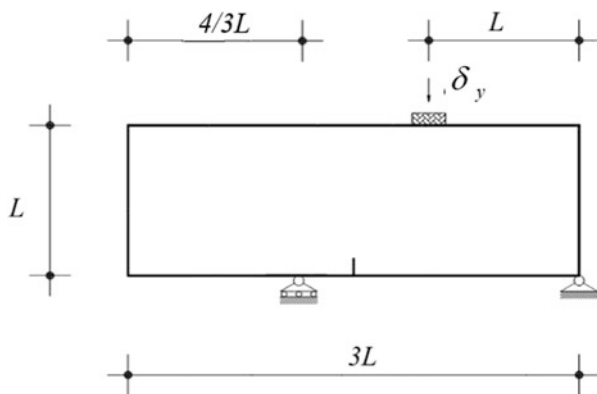

Fig. 11.18 Non-symmetric three-point bending test: geometry, boundary and loading conditions. (From: Artioli, E., Marfia, S., Sacco, E., VEM-based tracking algorithm for cohesive/frictional 2D fracture. Computer Methods in Applied Mechanics and Engineering, 365, 2020. Reproduced with permission)

Table 11.3 Non-symmetric three-point bending test: cohesive interface material properties

k_n [N/mm^3]	k_t [N/mm^3]	t_{0n} [N/mm^2]	t_{0t} [N/mm^2]	G_{cI} [N/mm]	G_{cII} [N/mm^3]	μ
80,000	80,000	0.3	0.3	0.0005	0.01	0.5

The beam is made by a cohesive material whose behavior is linear elastic with Young modulus $E = 10^4$ N/mm^2 and Poisson coefficient $\nu = 0.3$, until a stress threshold is reached, then the crack propagation is modeled by the introduction and propagation of a cohesive interface whose mechanical properties are reported in Table 11.3.

A non-symmetric three-point bending test is performed by applying an incremental eccentric vertical displacement δ_y until a maximum value $9 \cdot 10^{-4}$ mm is reached. The vertical displacement is applied in a region of $L/4$ width at the top edge of the beam, as reported in Fig. 11.18.

An initial discretization made of 27×9 quadrilateral VEM with four nodes is introduced.

The crack starts when the maximum principal stress in the VEM at the notch reaches the tensile threshold. At this point the cohesive interface is introduced in the virtual element following the procedure illustrated in the previous section. Five different levels of adaptive mesh refinement are considered, in particular, around the crack in the process zone, polygons undergo progressive refinement.

In Fig. 11.19, the mechanical response in terms of total vertical reaction R_y versus the prescribed displacement δ_y is reported for the different levels of topological adaptive mesh refinement, denoted by tpl$_\text{ref}$. Increasing tpl$_\text{ref}$ values, convergence is achieved. The mechanical response is initially linear elastic, after the peak it is characterized by a softening branch due to crack initiation and propagation following a curved path.

Progressively higher values for tpl$_\text{ref}$ induce finer discretizations of the process zone, and a higher accuracy in modeling the curved crack path at a reasonable computational cost. The mesh refinement is concentrated around the crack and at the apex and it evolves during the analysis with the crack propagation. The crack path goes from the notch to the extrados of the beam where the displacement is prescribed.

In Fig. 11.20a–e, the beam deformation configuration at the end of the loading phase is represented for the different refinement levels adopted. It can be remarked that the results obtained for the different vales of tpl$_\text{ref}$ are in good agreement both in terms of the mechanical response and of the cracking path, confirming the effectiveness of the proposed adaptive mesh refinement strategy. The five analyses are run on a Intel(R) Core(TM) i7-4800MQ CPU 2.7 GHz machine and the computational time for the five adaptive mesh refinement levels are reported in Table 11.4.
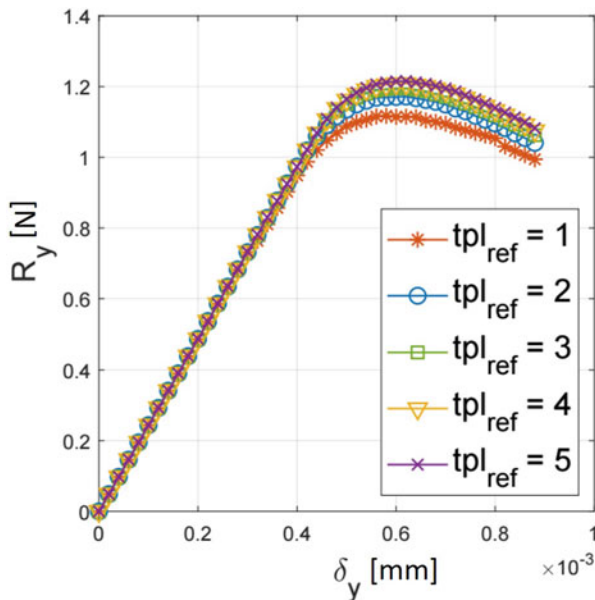
Fig. 11.19 Non-symmetric three-point bending test: Mechanical responses for different topological adaptive mesh refinement levels. (From: Artioli, E., Marfia, S., Sacco, E., VEM-based tracking algorithm for cohesive/frictional 2D fracture. Computer Methods in Applied Mechanics and Engineering, 365, 2020. Reproduced with permission)

11.6.3.2 Symmetric Three-Point Bending Test and Comparison with XFEM

The symmetric three-point bending test of a concrete beam, analyzed with the extended finite element method in [32] and adopting the finite element analysis and the node release technique in [20], is studied with the proposed VEM approach. The geometry of the beam is reported in Fig. 11.21, in particular the specimen is characterized by length $h = 0.15$, height $b = 4h$ and thickness $t = h$. The Young modulus and the Poisson coefficient of the bulk material are $E = 36500$ MPa, $v = 0.1$, respectively, while the tensile stress threshold f_u is equal to 3.19 MPa. The cohesive interface material properties are reported in Table 11.5. In particular, both the normal and tangential stiffness of the interface are set equal to the Young modulus E of the bulk material while the interface normal and shear stress thresholds are set equal to the bulk stress threshold f_u.

As proposed in [32], the analysis is performed under the plane strain assumption, while in [20] a plane stress analysis is carried out. No initial crack is modeled in the beam, as represented in Fig. 11.21, where also the boundary and loading conditions are reported. A structured initial mesh made by 6 × 11 rectangular VEM is considered. In order to be able to reproduce the mechanical response of the beam, characterized by a snap-back branch, the cylindrical arc-length method
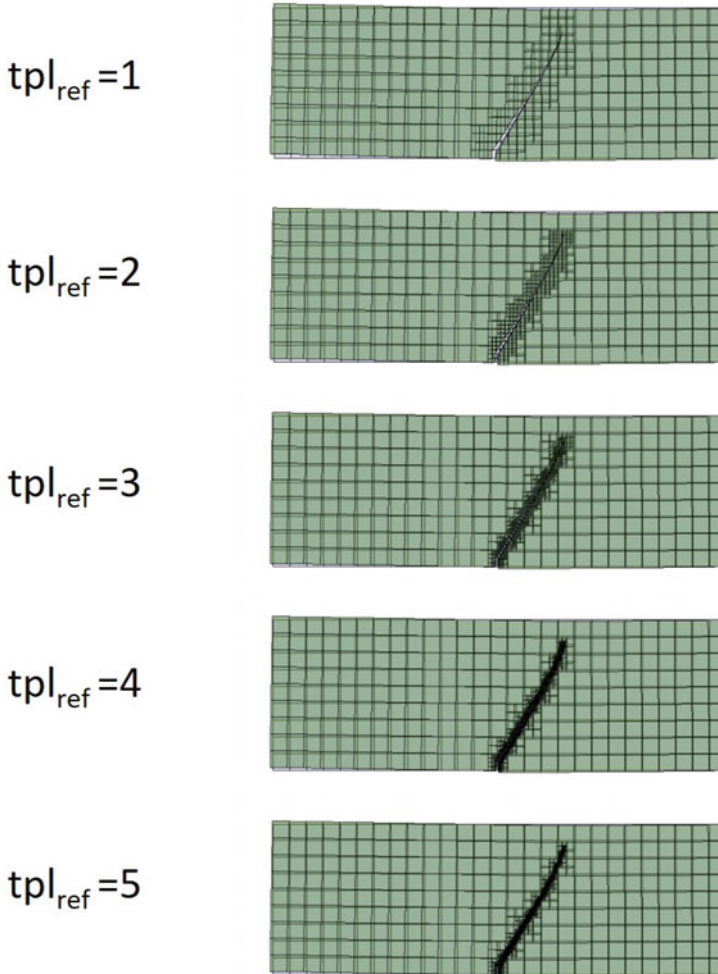
Fig. 11.20 Non-symmetric three-point bending test: Deformed configurations for different topological adaptive mesh refinements. (From: Artioli, E., Marfia, S., Sacco, E., VEM-based tracking algorithm for cohesive/frictional 2D fracture. Computer Methods in Applied Mechanics and Engineering, 365, 2020. Reproduced with permission)

[21] is implemented in the framework of the present approach. This method allows to describe the snap-back branch with high accuracy.

In Fig. 11.22 the mechanical response of the beam in terms of the load versus the deflection in the middle of the span is reported for the proposed methodology in comparison with the results by Moës and Belytschko [32] and by Carpinteri and Colombo [20]. The results carried out with the proposed VEM approach are in

Table 11.4 Computational time of the proposed Matlab implementation of the non-symmetric three-point bending test for different topological adaptive mesh refinements

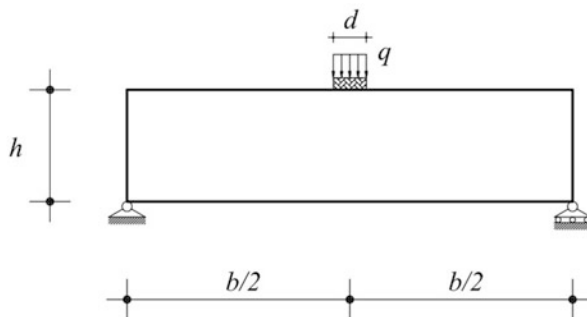| tpl$_{ref}$	1	2	3	4	5
Time	1.1′	2.5′	8.4′	18.1′	39.2′

Fig. 11.21 Three-point bending test: geometry, boundary and loading conditions. (From: Artioli, E., Marfia, S., Sacco, E., VEM-based tracking algorithm for cohesive/frictional 2D fracture. Computer Methods in Applied Mechanics and Engineering, 365, 2020. Reproduced with permission)

Table 11.5 Symmetric three-point bending test: cohesive interface material properties

k_n [N/mm^3]	k_t [N/mm^3]	t_{0n} [N/mm^2]	t_{0t} [N/mm^2]	G_{cI} [N/mm]	G_{cII} [N/mm^3]	μ
36500	36500	3.19	3.19	0.05	0.05	0.5

perfect agreement with the ones presented in [20, 32] in the pre-peak and post-peak branches.

In Fig. 11.23 the final deformed configuration of the beam is represented. The proposed method is able to describe accurately the crack initiation and propagation and it is an alternative tool for describing the mechanical response of cohesive materials respect to standard established procedures.

11.7 Concluding Remarks

The virtual element method appears a very interesting numerical technique for solving complex partial differential equations, even in the presence of nonlinearity. Thus, the VEM formulation for solid mechanics nonlinear plane problems has been presented, illustrating the methodology for the case of elements with linear and higher order approximation of the displacement field, together with implementation details. The stiffness matrix and loading vector have been explicitly derived proving the straightforward implementability of the method into a computer code for structural analysis.
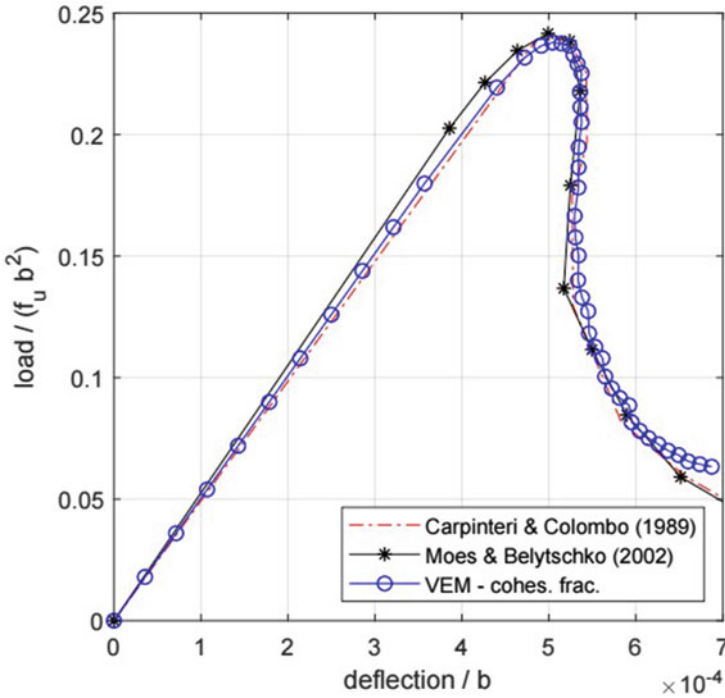
Fig. 11.22 Three-point bending test: mechanical response. (From: Artioli, E., Marfia, S., Sacco, E., VEM-based tracking algorithm for cohesive/frictional 2D fracture. Computer Methods in Applied Mechanics and Engineering, 365, 2020. Reproduced with permission)
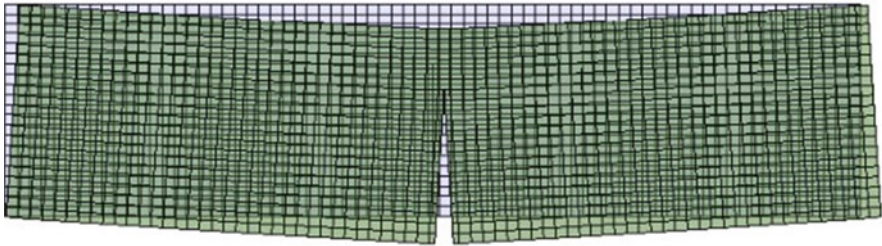

Fig. 11.23 Three-point bending test: deformed configuration. (From: Artioli, E., Marfia, S., Sacco, E., VEM-based tracking algorithm for cohesive/frictional 2D fracture. Computer Methods in Applied Mechanics and Engineering, 365, 2020. Reproduced with permission)

VEM has been successfully implemented and adopted to study the mechanical response of simple structures made of viscoelastic, plastic or shape memory alloy material. Furthermore, the problem of homogenization of long fiber composite and of cohesive body fracturing have been faced adopting VEM tecnology.

Several numerical applications illustrating accuracy and convergence patterns of the method, and its performances in comparison with a classical finite element

approach characterized by the same order of approximation of the unknown fields are presented.

Material nonlinearity laws are implemented in the VEM code substantially in the same way as in standard FEM framework. Thus, the solution algorithm for the typical quadrature point can be developed as for the classical FEM implementation and introduced in VEM code, without substantial changes. Numerical results remark the ability of the VEM formulation to get accurate solutions for nonlinear 2D structural problems considering viscoelasticity, plasticity and shape memory alloy materials. Solutions obtained using VEM are accurate when compared to FEM ones and require in general less iterations than FEM approach when the same tangent (Newton) algorithm is adopted.

VEM has been suitably adopted to solve homogenization problems for periodic composites characterized by nonlinear response of the matrix. The VEM technology has been detailed for the specific kinematic suitable for the modeling of long fiber composites. The homogenization analysis of a composite characterized by a quite stiff elastic inclusion in an elasto-plastic matrix appears very interesting. In fact, due to the high flexibility of the VEM approach in defining suitable discretization of the unit cell, a significant reduced computational effort in recovering the overall response of the composite is found. The idea to discretize the internal part of the inclusion by a unique element characterized by many edges appears challenging opening new opportunities in designing smart discretizations. This point represents an interesting advantage in using the VEM technique compared with other more classical numerical procedures such as FEM. There are other benefits in using the VEM approach. In fact, the possibility of using polygonal meshes with arbitrary number of edges allows easy discretization of complex domains; this leads also to the development of powerful procedures for adaptive remeshing.

An innovative technique for the evaluation of crack evolution in cohesive media has been proposed. The developed procedure is based on the use of the virtual element method, fully taking advantages of the special performances of VEM technique. The possibility to exploit simple elements with as many edges as actually needed in the problem under analysis, opens the possibility to split the initial cracking element in two elements without any limitation and to introduce between the two new elements a cohesive interface. Indeed, this splitting operation is very accurate, simple and fast from a computation point of view. Coupled with the cracking nucleation and evolution algorithm, a fast remeshing technique has been implemented, again taking advantages of the VEM formulation. In fact, the possibility to introduce in the mesh elements characterized by a number of edges as required, without any constraint, allows for a very simple and local refinement of the discretization. The numerical procedure results very fast; in fact, full computations for the presented structural examples take only few minutes, reaching the convergence at each time step with only 2 or 3 iterations.

It can be remarked that although a very simple and straight technique is adopted for the evaluation of stress in the cracking element, without introducing specific enrichment of the displacement field or complex (nonlocal) computation of the

stress at the crack tip, the direction of the crack evolution is satisfactorily determined in all the numerical applications.

Finally, it would be highlighted that the level of complexity of the proposed approach is much reduced with respect to other finite element approaches available in literature for cohesive crack propagation, for what concerns the relevant main bottle necks, namely mesh enrichment, updating and modification, through evolution of the cracking phenomenon. This makes the proposed new methodology globally very competitive with respect the available ones.

All the numerical results demonstrate the accuracy of the approach in all the analyzed field of applications and, also, the simplicity of the implementation into any available FEM code. These features make the VEM very interesting for a wide class of structural applications and highlight the possibility of including VEM elements in available commercial FEM codes element libraries.

References

1. G. Alfano, E. Sacco, Combining interface damage and friction in a cohesive-zone model. Int. J. Numer. Methods Eng. **68**(5), 542–582 (2006)
2. E. Artioli, Asymptotic homogenization of fibre-reinforced composites: a virtual element method approach. Meccanica **53**(6), 1187–1201 (2018)
3. E. Artioli, P. Bisegna, Dissipation-based approach and robust integration algorithm for 3D phenomenological constitutive models for shape memory alloys, in A. Huerta, E.E. Oñate, X. Oliver, eds. *11th World Congress on Computational Mechanics, WCCM 2014, 5th European Conference on Computational Mechanics, ECCM 2014 and 6th European Conference on Computational Fluid Dynamics, ECFD 2014* (2014), pp. 4263–4272
4. E. Artioli, P. Bisegna, An incremental energy minimization state update algorithm for 3D phenomenological internal-variable SMA constitutive models based on isotropic flow potentials. Int. J. Numer. Methods Eng. **105**(3), 197–220 (2016)
5. E. Artioli, R.L. Taylor, VEM for inelastic solids. Comput. Methods Appl. Sci. **46**, 381–394 (2018)
6. E. Artioli, E. Marfia, S. Sacco, R.L. Taylor, A nonlinear plate finite element formulation for shape memory alloy applications. Int. J. Numer. Methods Eng., **89**(10), 1249–1271 (2012)
7. E. Artioli, L. Beirão da Veiga, C. Lovadina, E. Sacco, Arbitrary order 2D virtual elements for polygonal meshes: Part I, elastic problem. Comput. Mech. **60**(3), 355–377 (2017). https://doi.org/10.1007/s00466--017--1404--5
8. E. Artioli, L. Beirão Da Veiga, C. Lovadina, E. Sacco, Arbitrary order 2D virtual elements for polygonal meshes: Part II, inelastic problems. Comput. Mech. (2017). https://doi.org/10.1007/s00466--017--1429--9
9. E. Artioli, S. Marfia, E. Sacco, High-order virtual element method for the homogenization of long fiber nonlinear composites. Comput. Methods Appl. Mech. Eng. **341**, 571–585 (2018)

10. E. Artioli, L. Beirão da Veiga, F. Dassi, Curvilinear virtual elements for 2d solid mechanics applications. Comput. Methods Appl. Mech. Eng. **359**, 112667 (2020)
11. E. Artioli, S. Marfia, E. Sacco, Vem-based tracking algorithm for cohesive/frictional 2d fracture. Comput. Methods Appl. Mech. Eng. **365**, 112956 (2020)
12. F. Auricchio, L. Petrini, Improvements and algorithmical considerations on a recent three-dimensional model describing stress-induced solid phase transformations. Int. J. Numer. Methods Eng. **55**, 1255–1284 (2002)
13. F. Auricchio, R.L. Taylor, A return-map algorithm for general associative isotropic elasto-plastic materials in large deformation regimes. Int. J. Plast. **15**, 1359–1378 (1999)
14. L. Beirão da Veiga, F. Brezzi, A. Cangiani, G. Manzini, L.D. Marini, A. Russo, Basic principles of virtual element methods. Math. Models Methods Appl. Sci. **23**, 119–214 (2013)
15. L. Beirão da Veiga, F. Brezzi, L.D. Marini, Virtual elements for linear elasticity problems. SIAM J. Numer. Anal. **51**(2), 794–812 (2013)
16. L. Beirão da Veiga, F. Brezzi, L.D. Marini, A. Russo, The Hitchhiker's guide to the virtual element method. Math. Models Methods Appl. Sci. **24**(8), 1541–1573 (2014)
17. L. Beirão da Veiga, C. Lovadina, D. Mora, A virtual element method for elastic and inelastic problems on polytope meshes. Comput. Methods Appl. Mech. Eng. **295**, 327–346 (2015)
18. M.F. Benedetto, A. Caggiano, G. Etse, Virtual elements and zero thickness interface-based approach for fracture analysis of heterogeneous materials. Comput. Methods Appl. Mech. Eng. **338**, 41–67 (2018)
19. E. Benvenuti, A. Chiozzi, G. Manzini, N. Sukumar, Extended virtual element method for the Laplace problem with singularities and discontinuities. Comput. Methods Appl. Mech. Eng. **356**, 571–597 (2019)
20. A. Carpinteri, G. Colombo, Numerical analysis of catastrophic softening behavior (snap-back instability). Comput. Struct. **31**, 607–636 (1989)
21. M.A. Crisfield, *Non-Linear Finite Element Analysis of Solids and Structures* (Wiley, London, 1996)
22. A.M. D'Altri, S. de Miranda, L. Patruno, E. Sacco, An enhanced vem formulation for plane elasticity. Comput. Methods Appl. Mech. Eng. **376**, 113663 (2021)
23. E.A. de Souza Neto, D. Peric', D.R.J. Owen, *Computational Methods for Plasticity: Theory and Applications* (Wiley, London, 2008)
24. V. Evangelista, S. Marfia, E. Sacco, Phenomenological 3D and 1D consistent models for shape-memory alloy materials. Comput. Mech. **44**(3), 405–421 (2009)
25. V. Evangelista, S. Marfia, E. Sacco, A 3D SMA constitutive model in the framework of finite strain. Int. J. Numer. Methods Eng. **86**(6), 761–785 (2010)
26. A.L. Gain, C. Talischi, G.H. Paulino, On the virtual element method for three-dimensional linear elasticity problems on arbitrary polyhedral meshes. Comput. Methods Appl. Mech. Eng. **282**, 132–160 (2014)
27. K. Hackl, F.D. Fischer, On the relation between the principle of maximum dissipation and inelastic evolution given by dissipation potentials. Proc. R. Soc. Ser. A **464**, 117–132 (2008)
28. W. Han, B. Daya Reddy, *Plasticity: Mathematical Theory and Numerical Analysis* (Springer, New York, 1999)
29. A. Hussein, F. Aldakheel, B. Hudobivnik, P. Wriggers, P.A. Guidault, O. Allix, A computational framework for brittle crack-propagation based on efficient virtual element method. Finite Elem. Anal. Des. **159**, 15–32 (2019)
30. *MATLAB Release 2018b* (The MathWorks, Inc., Natick, Massachusetts, United States, 2018)
31. A. Mielke, T. Roubíček, *Rate Independent Systems—Theory and Applications* (Springer, Berlin, 2015)
32. N. Moës, T. Belytschko, Extended finite element method for cohesive crack growth. Eng. Fract. Mech. **69**(7), 813–833 (2002)
33. V.M. Nguyen-Thanh, X. Zhuang, H. Nguyen-Xuan, T. Rabczuk, P. Wriggers, A virtual element method for 2d linear elastic fracture analysis. Comput. Methods Appl. Mech. Eng. **340**, 366–395 (2018)

34. L. Orgéas, D. Favier, Non-symmetric tension-compression behavior of NiTi alloy. J. Phys. IV **C8**, 605–610 (1995)
35. E. Sacco, J. Toti, Interface elements for the analysis of masonry structures. Int. J. Comput. Methods Eng. Sci. Mech. **11**(6), 354–373 (2010)
36. E. Sacco, E. Artioli, S. Marfia, Virtual Element Method approach for 2D fracture mechanics problems, in *Proceedings of the 13th World Congress on Computational Mechanics (WCCM XIII) 2nd Pan American Congress on Computational Mechanics (PANACM II) July 22–27, 2018, New York, NY, USA* (2018)
37. J.C. Simo, T.J.R. Hughes, *Computational Inelasticity* (Springer, Berlin, 1998)
38. A.C. Souza, E.N. Mamiya, N. Zouain, Three-dimensional model for solids undergoing stress-induced phase transformations. Eur. J. Mech. A. Solids **17**, 789–806 (1998)
39. C. Talischi, G.H. Paulino, A. Pereira, I.F.M. Menezes, Polymesher: a general-purpose mesh generator for polygonal elements written in matlab. Struct. Multidisc Optimiz. **45**(3), 309–328 (2012)
40. P. Wriggers, B. Hudobivnik, A low order virtual element formulation for finite elasto-plastic deformations. Comput. Methods Appl. Mech. Eng. **327**, 459–477 (2017)
41. P. Wriggers, W.T. Rust, B.D. Reddy, A virtual element method for contact. Comput. Mech. **58**(6), 1039–1050 (2016)
42. O.C. Zienkiewicz, R.L. Taylor, J.Z. Zhu, *The Finite Element Method: its Basis and Fundamentals* (Butterworth Heinemann, Oxford, 2013)
43. O.C. Zienkiewicz, R.L. Taylor, D.D. Fox, *The Finite Element Method for Solid and Structural Mechanics* (Butterworth Heinemann, Oxford, 2014)

Chapter 12
The Virtual Element Method for the Coupled System of Magneto-Hydrodynamics

Sebastian Naranjo Alvarez, Vrushali A. Bokil, Vitaliy Gyrya, and Gianmarco Manzini

Abstract In this chapter, we apply the framework of the Virtual Element Method (VEM) to a model in Magneto-HydroDynamics (MHD), that incorporates a coupling between electromagnetics and fluid flow, to construct novel discretizations for simulating realistic phenomenon in MHD. First, we study two chains of spaces approximating the electromagnetic and fluid flow components of the model. Then, we show that this VEM approximation will yield divergence free discrete magnetic and velocity fields that are important properties in any simulation in MHD. We present a linearization strategy to solve the VEM approximation which respects the divergence free condition on the magnetic field. This linearization will require that, at each non-linear iteration, a linear system be solved. We study these linear systems and show that they represent well-posed saddle point problems. We conclude by presenting numerical experiments exploring the performance of the VEM applied to the subsystem describing the electromagnetics. The first set of experiments provide evidence regarding the speed of convergence of the method as well as the divergence-free condition on the magnetic field. In the second set we present a model for magnetic reconnection in a mesh that includes a series of hanging nodes, which we use to calibrate the resolution of the method. The magnetic reconnection phenomenon happens near the center of the domain where the mesh resolution is finer and high resolution is achieved.

S. Naranjo Alvarez (✉)
Dipartimento di Matematica, Università degli Studi di Milano-Bicocca, Milano, Italia
e-mail: sebastian.naranjo@unimib.it

V. A. Bokil
Department of Mathematics, Oregon State University, Corvallis, OR, USA
e-mail: bokilv@math.oregonstate.edu

V. Gyrya · G. Manzini
Group T-5, Theoretical Division, Los Alamos National Laboratory, Los Alamos, NM, USA
e-mail: vitaliy_gyrya@lanl.gov; gmanzini@lanl.gov

12.1 Introduction

The number of applications involving electrically charged and magnetized fluids, for example plasmas, has "skyrocketed" in the last decades and great efforts have been devoted to the development of predictive mathematical models. One approach that has withstood the test of time and has become "standard" in the area of plasma physics is the area called Magneto-HydroDynamics (MHD), which studies the behavior and the magnetic properties of electrically conducting fluids. The system of equations that describe MHD are a coupling between an electromagnetic submodel and a fluid flow submodel. The electromagnetic submodel in MHD is normally based on Maxwell's equations while the fluid flow submodel relies on conservation principles such as mass and momentum conservation. These two submodels are nonlinearly coupled. Indeed, mass density and momentum distribution in a plasma are determined by the Lorentz force, which, in turn, is generated by the same plasma particles moving in the self-consistent electromagnetic field. The details of the MHD model, its derivation and properties are nowadays well-understood and explained in many textbooks and review papers, e.g., [46, 70].

The topic of this chapter is the review of a novel discretization method for an MHD model, in the framework of the Virtual Element Method (VEM), that has been recently proposed in [72]. In the development of this method we will fix the approximation degree.

VEM was originally proposed as a variational reformulation of the *nodal* mimetic finite difference (MFD) method [14, 34, 35, 60] for solving partial differential equation problems on unstructured polygonal meshes in a finite element setting. A survey of the MFD method can be found in the review paper [61] and the research monograph [15].

Solving partial differential equations (PDEs) on polygonal and polyhedral meshes has become a central and important issue in the last decades. In fact, the generality of the admissible meshes makes the VEM highly versatile and very useful when the mesh must be adapted to the characteristics of the problem. For example, we can mention problems where the domain boundary deforms in time, or there are oddly shaped material interfaces to which the mesh must be conformal, or the mesh needs to be locally refined in those parts of the domain requiring greater accuracy as in adaptive mesh refinement strategies. In all such situations, the mesh refinement process may result in highly skewed meshes or meshes with highly irregular structures and a numerical method must be capable of handling these traits in order to be robust and provide an accurate approximation to the solution of a partial differential equation.

The VEM inherits the great mesh flexibility of the MFD in a setting similar to the finite element method (FEM), so that results and techniques from FEM can be imported over to VEM. Moreover, VEM makes possible to formulate numerical approximations of arbitrary order and arbitrary regularity to PDEs in two and three dimensions on meshes that other methods often consider as pathological. Because of its origins, VEM is intimately connected with other finite element

approaches and the fact that VEM is a FEM implies some important advantages over other discretization methods such as the finite volume methods and the finite difference methods. The connection between VEM and finite elements on polygonal/polyhedral meshes was thoroughly investigated in [38, 48, 66], between VEM and discontinuous skeletal gradient discretizations in [48], and between VEM and BEM-based FEM method in [37].

The main difference between VEM and FEM is that VEM does not require an explicit knowledge of basis functions that generates the finite element approximation space. The formulation of the method and its practical implementations are based on suitable polynomial projections that are always computable from a careful choice of the degrees of freedom. VEM was first proposed for the Poisson equation [6] and, then, extended to convection-reaction-diffusion problems with variable coefficients in [12]. The effectiveness of the virtual element approach is reflected in the many significant applications that have been developed in less than a decade see, for example, [2–5, 12, 13, 19–21, 24–27, 36, 39, 40, 45, 52, 65, 69, 74, 75, 77, 80]. Numerical dispersion can also be greatly reduced on carefully selected polygonal meshes, see [49, 56]. In these works, the Finite Difference Time Domain (FDTD) method is applied to a grid of hexagonal prisms and yields much less numerical dispersion and anisotropy than on using regular hexahedral grids where such method is normally considered.

One of the main advantages of using a VEM for MHD regards the divergence of the velocity field. Unlike classical FEM formulations, the method presented in this chapter yields velocity fields that are exactly divergence free. This is an advantage that has been widely reported in the VEM literature when applied to problems in fluid flow, see [17, 23, 43, 79]. The immediate implication of this fact is that simulations based on the scheme presented will satisfy the law of conservation of mass exactly, thus adding an added layer of accuracy.

Finally, the divergence of the magnetic field is zero in the Maxwell equations thus reflecting the absence of magnetic monopoles. Classical numerical discretizations fail to capture this property when the discrete versions of the divergence and rotational operators do not annihilate each other at the level of the zero machine precision, thus leaving a remainder that can significantly be compounded during a simulation. The consequence of the violation of this divergence-free constraint has thoroughly been investigated in the literature and it was seen that the numerical simulations are prone to significant errors [29, 30, 44, 78], as fictitious forces and an unphysical behavior may appear [44]. Efforts have been devoted to the development of *divergence-free* techniques. For example, in [47] the divergence equation $\nabla \cdot \boldsymbol{B} = 0$ is taken into account through a Lagrange multiplier that is additionally introduced in the set of the unknowns; in [59], the divergence-free condition relies on special flux limiters; in [55] a special energy functional is minimized by a least squares finite element method. Instead, the VEM considered in this chapter provides a numerical approximation of the magnetic field that is intrinsically divergence free as a consequence of a de Rham inequality chain. The VEM described in the papers of References [7, 8, 21, 22] are also pertinent to this issue.

This chapter is structured as follows. In Sect. 12.2, we present the system of equations of the continuous MHD model and introduce its discrete virtual element approximation. In Sect. 12.3, we review the formal definition and properties of the finite dimensional functional spaces of the formulation of VEM. Here, we also discuss the computability of the orthogonal projection operators and the possibility of using oblique projection operators, which are orthogonal with respect to a different inner product. In Sect. 12.4, we present a number of energy estimates that provide evidence of the stability of the method. In Sect. 12.5, we review a possible linearization strategy for solving the nonlinear system that results from virtual element approximation of the MHD model and prove that the approximate magnetic field is divergence free. In Sect. 12.6, we discuss the well-posedness of the linear solver in the setting of saddle-point problems. In Sect. 12.7, we assess the convergence behavior of the method and show an application of the VEM to the numerical modeling of a magnetic reconnection phenomenon. Finally, in Sect. 12.8, we give the full picture about the proposed method we outline.

12.2 Mathematical Formulation

Let the computational domain $\mathscr{D}$ be an open, bounded, polygonal subset of $\mathbb{R}^3$. Further assume that there is a magnetized fluid contained in this domain. We denote by $\overrightarrow{u}$, $\overrightarrow{B}$, $\overrightarrow{E}$ and p the velocity, magnetic and electric fields and the pressure of such a fluid. The evolution of these quantities is governed by the following system of differential equations:

$$\text{Incompressibility of the fluid}: \quad \nabla \cdot \overrightarrow{u} = 0, \tag{12.2.1a}$$

$$\text{Conservation of momentum}: \quad \frac{\partial}{\partial t}\overrightarrow{u} - R_e^{-1}\Delta\overrightarrow{u} - \overrightarrow{J} \times \overrightarrow{B} + \nabla p = \overrightarrow{f}, \tag{12.2.1b}$$

$$\text{Faraday's Law}: \quad \frac{\partial}{\partial t}\overrightarrow{B} + \nabla \times \overrightarrow{E} = \overrightarrow{0}, \tag{12.2.1c}$$

$$\text{Ohm's Law}: \quad \overrightarrow{J} = \overrightarrow{E} + \overrightarrow{u} \times \overrightarrow{B}, \tag{12.2.1d}$$

$$\text{Ampère's Law}: \quad \overrightarrow{J} - R_m^{-1}\nabla \times \overrightarrow{B} = \overrightarrow{0}, \tag{12.2.1e}$$

We denote the two dimensional vector whose components are the x, y components of a three dimensional vector using bold. Thus we denote

$$\overrightarrow{B} = \begin{pmatrix} \boldsymbol{B} \\ B_z \end{pmatrix}, \quad \overrightarrow{E} = \begin{pmatrix} \boldsymbol{E} \\ E_z \end{pmatrix}, \quad \overrightarrow{u} = \begin{pmatrix} \boldsymbol{u} \\ u_z \end{pmatrix}, \quad \overrightarrow{J} = \begin{pmatrix} \boldsymbol{J} \\ J_z \end{pmatrix}, \quad \overrightarrow{f} = \begin{pmatrix} \boldsymbol{f} \\ f_z \end{pmatrix}.$$

In this chapter we will consider that the z-component of the magnetic field is exactly zero. Moreover, we will also consider that the x and y components of the magnetic and electric fields and the z-component of the velocity field do not vary in the z-direction. In summary, we are assuming that

$$B_z = \frac{\partial}{\partial z}\boldsymbol{B} = \frac{\partial}{\partial z}\boldsymbol{E} = \frac{\partial}{\partial z}u_z = 0.$$

The consequence is that the dynamics only occurs in two dimensions effectively reducing the dimensionality of the problem. Our goal will be to attain approximations to the x and y components of the electric and magnetic fields.

Consider an arbitrary, non-empty, cross-section parallel to the x, y-plane of $\mathscr{D}$ denoted by Ω. The domain Ω is embedded in $\mathbb{R}^2$ so each point $p \in \Omega$ has a fixed z-value. Applying the aforementioned set of assumptions allows us to predict the dynamics in Ω as being ruled by:

$$\text{Incompressibility of the fluid}: \quad \text{div }\boldsymbol{u} = 0, \tag{12.2.2a}$$

$$\text{Conservation of momentum}: \quad \frac{\partial}{\partial t}\boldsymbol{u} - R_e^{-1}\Delta\boldsymbol{u} - J \times \boldsymbol{B} + \nabla p = \boldsymbol{f}, \tag{12.2.2b}$$

$$\text{Faraday's Law}: \quad \frac{\partial}{\partial t}\boldsymbol{B} + \text{rot }E = \mathbf{0}, \tag{12.2.2c}$$

$$\text{Ohm's Law}: \quad J = E + \boldsymbol{u} \times \boldsymbol{B}, \tag{12.2.2d}$$

$$\text{Ampère's Law}: \quad J - R_m^{-1}\text{rot }\boldsymbol{B} = \mathbf{0}, \tag{12.2.2e}$$

Consider a scalar function $f : \Omega \to \mathbb{R}$ and vector functions

$$\boldsymbol{g}, \boldsymbol{f} : \Omega \to \mathbb{R}^2, \qquad \text{where} \quad \boldsymbol{f} = \begin{pmatrix} f_x \\ f_y \end{pmatrix}, \quad \boldsymbol{g} = \begin{pmatrix} g_x \\ g_y \end{pmatrix},$$

with the sub-indices denoting components of the vector values functions $\boldsymbol{f}$ and $\boldsymbol{g}$, rather than differentiation. We define two versions of a cross product:

$$f \times \boldsymbol{g} = \begin{pmatrix} -fg_y \\ fg_x \end{pmatrix}, \quad \boldsymbol{f} \times \boldsymbol{g} = f_x g_y - f_y g_x. \tag{12.2.3}$$

The two dimensional curl and divergence operators are defined as:

$$\textbf{rot }E = \begin{pmatrix} \dfrac{\partial}{\partial y}E \\[2mm] -\dfrac{\partial}{\partial x}E \end{pmatrix}, \quad \text{rot }\boldsymbol{B} = \frac{\partial}{\partial x}B_y - \frac{\partial}{\partial y}B_x \quad \text{and} \quad \text{div }\boldsymbol{u} = \frac{\partial}{\partial x}u_x + \frac{\partial}{\partial y}u_y.$$

The initial conditions we prescribe onto the system are:

$$\boldsymbol{u}(0) = \boldsymbol{u}_0 \quad \text{and} \quad \boldsymbol{B}(0) = \boldsymbol{B}_0. \tag{12.2.4}$$

The initial field $\boldsymbol{B}_0$ must be divergence free, as Gauss's Law for the magnetic field requires that $\boldsymbol{B}$ remain divergence free throughout its evolution. Gauss's law, i.e., the divergence free nature of $\boldsymbol{B}$, is not explicitly stated in the system of MHD equations. This is due to the fact that, under the assumption that $\boldsymbol{B}_0$ is divergence free, div $\boldsymbol{B} = 0$ is a consequence of Faraday's Law, implying that $\boldsymbol{B}$ is solenoidal for all time. We have

$$\frac{\partial}{\partial t} (\text{div } \boldsymbol{B}) = \text{div} \left(\frac{\partial}{\partial t} \boldsymbol{B} \right) = \text{div} (-\mathbf{rot}\, E) = 0. \tag{12.2.5}$$

Hence,

$$\text{div } \boldsymbol{B} = \text{div } \boldsymbol{B}_0 = 0. \tag{12.2.6}$$

Such condition is a further evidence of the fact that the magnetic field is divergence free and the violation of this condition will lead to a nonphysical description of a MHD phenomenon. We close the MHD system by adding the boundary conditions

$$\boldsymbol{u} = \boldsymbol{u}_b \quad \text{and} \quad E = E_b \quad \text{on } \partial\Omega. \tag{12.2.7}$$

On using the divergence theorem and the incompressibility condition, we find that

$$\int_{\partial\Omega} \boldsymbol{u} \cdot \boldsymbol{n} \, d\ell = \int_{\Omega} \text{div } \boldsymbol{u} \, dA = 0, \tag{12.2.8}$$

which implies the consistency condition

$$\int_{\partial\Omega} \boldsymbol{u}_b \cdot \boldsymbol{n} \, d\ell = 0 \tag{12.2.9}$$

on the boundary velocity field $\boldsymbol{u}_b$.

12.2.1 Weak Formulation

In this section, we present a weak formulation of problem (12.2.2). Such a formulation requires the definition of the following inner products and norms.

We use standard notation that, for the sake of completeness, we will describe in what follows. For a pair of sufficiently regular real-valued functions $f, g : \Omega \to \mathbb{R}$ or vector valued-functions $\boldsymbol{f}, \boldsymbol{g} : \Omega \to \mathbb{R}^2$ we define

$$(f, g) = \int_\Omega fg \, dx, \quad (\boldsymbol{f}, \boldsymbol{g}) = \int_\Omega \boldsymbol{f} \cdot \boldsymbol{g} \, dx. \tag{12.2.10}$$

We will denote the L^2-norms by

$$\|f\|_{0,\Omega} := \left(\int_\Omega |f|^2 \, dx \right)^{1/2}, \tag{12.2.11a}$$

$$\|\boldsymbol{f}\|_{0,\Omega} := \left(\int_\Omega |\boldsymbol{f}|^2 \, dx \right)^{1/2}. \tag{12.2.11b}$$

The spaces $L^2(\Omega)$ and $[L^2(\Omega)]^2$ will consist of all those scalar and vector functions, respectively, that have finite L^2-norms. Likewise, the H^1-norms and the corresponding spaces $H^1(\Omega)$ and $[H^1(\Omega)]^2$ are defined below. We have

$$\|f\|_{1,\Omega} := \left(\|f\|_{0,\Omega}^2 + \|\nabla f\|_{0,\Omega}^2 \right)^{1/2}, \tag{12.2.12a}$$

$$\|\boldsymbol{f}\|_{1,\Omega} := \left(\|\boldsymbol{f}\|_{0,\Omega}^2 + \|\nabla \boldsymbol{f}\|_{0,\Omega}^2 \right)^{1/2}. \tag{12.2.12b}$$

The setting, in space, will require the following functional spaces:

$$H^1(\Omega) = \left\{ v \in L^2(\Omega) : \nabla v \in [L^2(\Omega)]^2 \right\}, \tag{12.2.13a}$$

$$H(\mathbf{rot}; \Omega) = \left\{ D \in L^2(\Omega) : \mathbf{rot}\, D \in \left[L^2(\Omega) \right]^2 \right\}, \tag{12.2.13b}$$

$$H(\mathrm{div}; \Omega) = \left\{ \boldsymbol{C} \in \left[L^2(\Omega) \right]^2 : \mathrm{div}\, \boldsymbol{C} \in L^2(\Omega) \right\}, \tag{12.2.13c}$$

$$L_0^2(\Omega) = \left\{ q \in L^2(\Omega) : \int_\Omega q \, dA = 0 \right\}, \tag{12.2.13d}$$

$$H_0^1(\Omega) = \left\{ v \in H^1 : v_{|\partial\Omega} = 0 \right\}, \tag{12.2.13e}$$

$$H_0(\mathbf{rot}; \Omega) = \left\{ D \in H(\mathbf{rot}; \Omega) : D_{|\partial\Omega} = 0 \right\}, \tag{12.2.13f}$$

Each of the function spaces in (12.2.13) are endowed with its natural norm. Let us refer to a generic version of the space from (12.2.13) as $S(\Omega)$ and to its natural norm as $\| \cdot \|_S$. We say that a function $f : [0, T] \to S(\Omega)$ is continuous in time if it is

continuous with respect to the natural norm $\| \cdot \|_S$. The space of all time continuous functions $f : [0, T] \to S(\Omega)$ is denoted as $C(0, T; S(\Omega))$. Thus,

$$C^1\left(0, T; \left[H^1(\Omega)\right]^2\right) = \left\{v : [0, T] \to \left[H^1(\Omega)\right]^2 : v \text{ and } \frac{\partial v}{\partial t} \text{ are continuous}\right\},$$

(12.2.14a)

$$C\left(0, T; L_0^2(\Omega)\right) = \left\{q : [0, T] \to L_0^2(\Omega) : q \text{ is continuous}\right\}, \qquad (12.2.14b)$$

$$C(0, T, H(\mathbf{rot}; \Omega)) := \{E : [0, T] \to H(\mathbf{rot}; \Omega) : E \text{ is continuous}\},$$

(12.2.14c)

$$C^1(0, T; H(\mathrm{div}; \Omega)) = \left\{B : [0, T] \to H(\mathrm{div}; \Omega) :\right.$$

$$\left. B \text{ and } \frac{\partial}{\partial t} B \text{ are continuous}\right\}.$$

(12.2.14d)

The weak form of problem (12.2.2a)–(12.2.2e) reads as:
Find

$$u \in C^1\left(0, T; \left[H^1(\Omega)\right]^2\right), \quad B \in C^1(0, T; H(\mathrm{div}; \Omega)),$$
$$E \in C(0, T; H_0(\mathbf{rot}; \Omega)), \quad p \in C\left(0, T; L_0^2(\Omega)\right),$$

such that

$$\left(\frac{\partial}{\partial t}u, v\right) + R_e^{-1}\left(\nabla u, \nabla v\right) - \left(J \times B, v\right) - \left(p, \mathrm{div}\, v\right) = \left(f, v\right), \quad (12.2.15a)$$

$$\left(\mathrm{div}\, u, q\right) = 0, \qquad\qquad\qquad\qquad\qquad\qquad (12.2.15b)$$

$$\left(\frac{\partial}{\partial t}B, C\right) + \left(\mathbf{rot}\, E, C\right) = 0, \qquad\qquad\qquad\qquad (12.2.15c)$$

$$\left(J, D\right) - R_m^{-1}\left(B, \mathbf{rot}\, D\right) = 0, \qquad\qquad\qquad\qquad (12.2.15d)$$

$$J = E + u \times B, \quad u(\cdot, 0) = u_0, \quad B(\cdot, 0) = B_0 \text{ with div } B_0 = 0, \quad (12.2.15e)$$

for any $v \in \left[H_0^1(\Omega)\right]^2$, $C \in H(\mathrm{div}; \Omega)$, $D \in H_0(\mathbf{rot}; \Omega)$, *and* $q \in L_0^2(\Omega)$. In this formulation we are making implicit that

$$u = u_b \quad \text{and} \quad E = E_b \quad \text{along} \quad \partial\Omega. \qquad\qquad (12.2.16)$$

12.3 The Virtual Element Method

In the VEM formulation, that will be presented, we will define conforming finite-dimensional subspaces of the spaces in (12.2.13). To do this we introduce a mesh of the domain Ω with size $h > 0$. Then, we define mesh-dependent finite dimensional virtual element spaces:

$$
\mathscr{P}_h \subset L^2(\Omega), \quad \mathscr{V}_h \subset H(\mathbf{rot}; \Omega), \quad \mathscr{E}_h \subset H(\mathrm{div}; \Omega) \quad \mathscr{T}\mathscr{V}_h \subset \left[H^1(\Omega) \right]^2.
\tag{12.3.1a}
$$

$$
\mathscr{P}_{h,0} \subset L_0^2(\Omega), \quad \mathscr{V}_{h,0} \subset H_0(\mathbf{rot}; \Omega), \quad \mathscr{T}\mathscr{V}_{h,0} \subset \left[H_0^1(\Omega) \right]^2,
\tag{12.3.1b}
$$

with the obvious inclusions

$$
\mathscr{T}\mathscr{V}_{h,0} \subset \mathscr{T}\mathscr{V}_h, \quad \mathscr{V}_{h,0} \subset \mathscr{V}_h, \quad \mathscr{P}_{h,0} \subset \mathscr{P}_h.
\tag{12.3.2}
$$

These spaces will be formally defined in Sects. 12.3.2, 12.3.3, 12.3.4, and 12.3.6, respectively. We endow these finite dimensional spaces with the inner products

$$
\left(\boldsymbol{u}_h, \boldsymbol{v}_h \right)_{\mathscr{T}\mathscr{V}_h} \approx \left(\boldsymbol{u}_h, \boldsymbol{v}_h \right), \quad \left[\boldsymbol{u}_h, \boldsymbol{v}_h \right]_{\mathscr{T}\mathscr{V}_h} \approx \left(\nabla \boldsymbol{u}_h, \nabla \boldsymbol{v}_h \right),
\tag{12.3.3a}
$$

$$
\left(\boldsymbol{B}_h, \boldsymbol{C}_h \right)_{\mathscr{E}_h} \approx \left(\boldsymbol{B}_h, \boldsymbol{C}_h \right), \quad \left(E_h, D_h \right)_{\mathscr{V}_h} \approx \left(E_h, D_h \right),
\tag{12.3.3b}
$$

$$
\left(p_h, q_h \right)_{\mathscr{P}_h} \approx \left(p_h, q_h \right),
\tag{12.3.3c}
$$

which approximate the corresponding inner products in $L^2(\Omega)$ and $H^1(\Omega)$ and their vector variants. In the formulation of the method, we will find it convenient to use a set of local and global interpolation operators embedding the continuous spaces into their discrete versions. We denoted the local operators referring to a specific mesh element P as $\mathscr{I}_{\mathsf{P}}^{\mathscr{E}_h}$, $\mathscr{I}_{\mathsf{P}}^{\mathscr{V}_h}$ and $\mathscr{I}_{\mathsf{P}}^{\mathscr{P}_h}$ and the corresponding global ones $\mathscr{I}^{\mathscr{E}_h}$, $\mathscr{I}^{\mathscr{V}_h}$ and $\mathscr{I}^{\mathscr{P}_h}$. We will also introduce a special projector $\mathfrak{I}^{\mathscr{T}\mathscr{V}_h}$ that we will use in order to attain discrete initial and boundary conditions for the velocity field. Using this projector will ensure that our discrete approximations of the velocity field are exactly divergence free.

Having defined the functional spaces, we now turn our attention to the time variable. To begin we introduce a time-step $\Delta t > 0$ and the time staggering parameter $0 \le \theta \le 1$. The approximate solutions will be considered at time steps given by

$$
t^n = n\Delta t, \quad t^{n+\theta} = (n + \theta)\Delta t.
$$

These approximations are abbreviated by $\boldsymbol{u}_h^n = \boldsymbol{u}_h(\cdot, t^n)$, $p_h^{n+\theta} = p_h(\cdot, t^{n+\theta})$, $\boldsymbol{B}_h^n = \boldsymbol{B}_h(\cdot, t^n)$, and $E_h^{n+\theta} = E_h(\cdot, t^{n+\theta})$ for the time-dependent vector fields $\boldsymbol{u}_h$ and $\boldsymbol{B}_h$ and the scalar fields E_h and p_h, respectively, approximating $\boldsymbol{u}$, $\boldsymbol{B}$, E and p. These vector fields are the solution of the virtual element method, which reads as: *Find* $\{(\boldsymbol{u}_h^n, \boldsymbol{B}_h^n)\}_{n=0}^N \subset \mathscr{T}\mathscr{V}_h \times \mathscr{E}_h$ *and* $\{(E_h^{n+\theta}, p_h^{n+\theta}))\}_{n=0}^{N-1} \subset \mathscr{V}_h \times \mathscr{P}_{h,0}$, *such that*

$$\left(\frac{\boldsymbol{u}_h^{n+1} - \boldsymbol{u}_h^n}{\Delta t}, \boldsymbol{v}_h \right)_{\mathscr{T}\mathscr{V}_h} + R_e^{-1} \Big[\boldsymbol{u}_h^{n+\theta}, \boldsymbol{v}_h \Big]_{\mathscr{T}\mathscr{V}_h} + \underbrace{\left(J_h^{n+\theta}, \mathscr{I}^{\mathscr{V}_h}(\boldsymbol{v}_h \times \Pi^{RT} \boldsymbol{B}_h^{n+\theta}) \right)_{\mathscr{V}_h}}_{(*)}$$

$$- \left(p_h^{n+\theta}, \operatorname{div} \boldsymbol{v}_h \right)_{\mathscr{P}_h} = \left(\boldsymbol{f}_h, \boldsymbol{v}_h \right)_{\mathscr{T}\mathscr{V}_h}, \qquad (12.3.4a)$$

$$\left(\operatorname{div} \boldsymbol{u}_h^{n+\theta}, q_h \right)_{\mathscr{P}_h} = 0, \qquad (12.3.4b)$$

$$\left(\frac{\boldsymbol{B}_h^{n+1} - \boldsymbol{B}_h^n}{\Delta t}, \boldsymbol{C}_h \right)_{\mathscr{E}_h} + \left(\operatorname{\textbf{rot}} E_h^{n+\theta}, \boldsymbol{C}_h \right)_{\mathscr{E}_h} = 0, \qquad (12.3.4c)$$

$$\left(J_h^{n+\theta}, D_h \right)_{\mathscr{V}_h} - R_m^{-1} \left(\boldsymbol{B}_h^{n+\theta}, \operatorname{\textbf{rot}} D_h \right)_{\mathscr{E}_h} = 0, \qquad (12.3.4d)$$

for all $\boldsymbol{v}_h \in \mathscr{T}\mathscr{V}_{h,0}$, $\boldsymbol{C}_h \in \mathscr{E}_h$, $D_h \in \mathscr{V}_{h,0}$ *and* $q_h \in \mathscr{P}_{h,0}$. We define

$$J_h^{n+\theta} := E_h^{n+\theta} + \mathscr{I}^{\mathscr{V}_h}(\boldsymbol{u}_h^{n+\theta} \times \Pi^{RT} \boldsymbol{B}_h^{n+\theta}), \qquad (12.3.5)$$

and the fractional step quantities $\boldsymbol{u}_h^{n+\theta}$, $\boldsymbol{B}_h^{n+\theta}$ are defined through linear (in time) interpolations

$$\boldsymbol{u}_h^{n+\theta} := (1-\theta)\boldsymbol{u}_h^n + \theta \boldsymbol{u}_h^{n+1}, \qquad (12.3.6a)$$

$$\boldsymbol{B}_h^{n+\theta} := (1-\theta)\boldsymbol{B}_h^n + \theta \boldsymbol{B}_h^{n+1}. \qquad (12.3.6b)$$

The initial conditions are given as

$$\boldsymbol{u}_h^0 = \mathfrak{I}^{\mathscr{T}\mathscr{V}_h}(\boldsymbol{u}_0), \quad \boldsymbol{B}_h^0 = \mathscr{I}^{\mathscr{E}_h}(\boldsymbol{B}_0) \quad \text{with} \quad \operatorname{div} \boldsymbol{B}_0 = 0. \qquad (12.3.7)$$

Here, we implicitly assume that for all $t \in [0, T]$:

$$E_h(t) = \mathscr{I}^{\mathscr{V}_h}(E_b(t)) \quad \text{and} \quad \boldsymbol{u}_h(t) = \mathfrak{I}^{\mathscr{T}\mathscr{V}_h}(\boldsymbol{u}_b(t)) \quad \text{along} \quad \partial\Omega.$$

We note that E_b and $\boldsymbol{u}_b$ are only defined along the boundary of Ω and not in the interior. Technically the interpolation operator cannot be applied to boundary functions. Thus, here we use E_b and $\boldsymbol{u}_b$ to the interior of Ω.

The term labeled as (*) in (12.3.4a) is produced by the approximation

$$-\left(J \times B, v\right) = \left(J, v \times B\right) \approx \left(J_h, \mathscr{I}^{\mathscr{V}_h}(v_h \times \Pi^{RT} B_h)\right)_{\mathscr{V}_h}.$$

The reason why we use this discretization will be made clear in Sect. 12.4, where we present the stability estimates in the $L^2(\Omega)$ norm. It is important to note that when $\theta = 0$ the scheme, in time, is a forward Euler step. Whereas if $\theta = 1$ the scheme is a Backward Euler step.

12.3.1   *Mesh Notation and Regularity Assumptions*

In this subsection, we present the main notation and the regularity assumptions that we will make on the mesh.

For ease of exposition, we assume that the computational domain Ω be an open, bounded, connected subset of $\mathbb{R}^2$ with polygonal boundary Γ. We consider the family of domain partitionings $\mathscr{T} = \{\Omega_h\}_{h \in \mathscr{H}}$. Every partition Ω_h, the *mesh*, is a finite collection of polygonal elements P, which are such that $\overline{\Omega} = \cup_{\mathsf{P} \in \Omega_h} \overline{\mathsf{P}}$.

For a polygonal element $\mathsf{P} \in \Omega_h$, we denote the boundary of P by $\partial \mathsf{P}$, the outward unit normal to the boundary by $\mathbf{n}_{\mathsf{P}}$, its diameter by $h_{\mathsf{P}} = \max_{x,y \in \mathsf{P}} |x - y|$, and its area by $|\mathsf{P}|$. Each elemental boundary $\partial \mathsf{P}$ is formed by a sequence of one-dimensional non-intersecting straight edges e with length h_e and midpoint $x_e = (x_e, y_e)^T$.

To enforce mesh regularity we require that there exists $\rho \geq 0$ independent of the mesh size $h > 0$, such that

(M1): every polygonal cell $\mathsf{P} \in \Omega_h$ is star-shaped with respect to every point of some disk of radius ρh_{P};
(M2): every edge $e \in \partial \mathsf{P}$ of cell $\mathsf{P} \in \Omega_h$ satisfies $h_e \geq \rho h_{\mathsf{P}}$.

The regularity assumptions **(M1)–(M2)** allow us to use meshes with cells having quite general geometric shapes. For example, non-convex cells or cells with hanging nodes on their edges are admissible. Nonetheless, these assumptions have some important implications such as: (i) every polygonal element is *simply connected*; (ii) the number of edges of each polygonal cell in the mesh family $\{\Omega_h\}_h$ is uniformly bounded; (iii) a polygonal element cannot have *arbitrarily small* edges with respect to its diameter $h_{\mathsf{P}} \leq h$ for $h \to 0$ and inequality $h_{\mathsf{P}}^2 \leq C(\rho)|\mathsf{P}|h_{\mathsf{P}}^2$ holds, with the obvious dependence of constant $C(\rho)$ on the mesh regularity factor ρ.

Remark 12.1 It is worth mentioning that virtual element methods on polygonal meshes possibly containing "small edges" have been considered in [32] for the numerical approximation of the Poisson problem. The work in [32] extends the results in [16] for the original two-dimensional virtual element method to the version of the virtual element method in [1] that can also be applied to problems

510 S. Naranjo Alvarez et al.

in three dimensions, see [42]. Finally, we note that assumptions **(M1)–(M2)** above also imply that the classical polynomial approximation theory in Sobolev spaces holds [31]. While these assumptions are the minimal necessary to develop theoretical analysis, in practice they can be significantly weakened.

12.3.2 The Nodal Space

Consider the cell P of the polygonal mesh Ω_h. The formal definition of the nodal elemental space is

$$\mathscr{V}_h(\mathsf{P}) := \left\{ D_h \in H(\mathbf{rot}; \mathsf{P}) : D_{h|\partial\mathsf{P}} \in C(\partial\mathsf{P}),\ D_{h|e} \in \mathbb{P}_1(e)\ \forall e \in \partial\mathsf{P}, \right.$$
$$\left. \operatorname{rot}\mathbf{rot}\, D_h = 0\ \text{in } \mathsf{P} \right\}. \qquad (12.3.8)$$

Every function $D_h \in \mathscr{V}_h(\mathsf{P})$ is uniquely determined by the set of degrees of freedom:

(V) the vertex values $D_h(\mathsf{v})$ at the nodes v of cell P.

These are represented by blue disks centered at the nodes, see the sample picture in Fig. 12.1.

As in the classic finite element method, this property is referred to as the *unisolvency* of the degrees of freedom **(V)**, see [68]. Accordingly, every function in $\mathscr{V}_h(\mathsf{P})$ corresponds to one and only one set of degrees of freedom and, conversely, every set of degrees of freedom corresponds to one and only one function in $\mathscr{V}_h(\mathsf{P})$. To formally state this property we define the operators $\mathscr{R}_\mathsf{V} : C^\infty(\Omega) \to \mathbb{R}^N$ such that for any $D \in C^\infty(\Omega)$ the image $\mathscr{R}_\mathsf{V}(D)$ is the array of degrees of freedom of D. This function can be continuously extended to the full space $H(\mathbf{rot}; \mathsf{P})$. The next theorem states the unisolvency of the finite element previously described.

Theorem 12.1 *Define $\mathscr{K}_\mathsf{V} : \mathscr{V}_h(\mathsf{P}) \to \mathbb{R}^N$ as the restriction of $\mathscr{R}_\mathsf{V}$ to $\mathscr{V}_h(\mathsf{P})$. Then, $\mathscr{K}_\mathsf{V}$ is bijective.*

Proof Proof of the above theorem is provided in [11]. □

Fig. 12.1 Representation of the degrees of freedom of functions in $\mathscr{V}_h(\mathsf{P})$
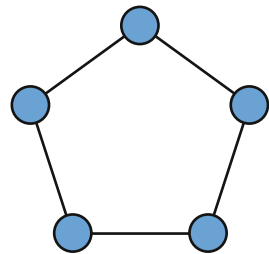
The result of Theorem 12.1 Allows us to define the mapping $\mathscr{I}_{\mathsf{P}}^{\mathscr{V}_h} : H(\mathbf{rot}; \mathsf{P}) \rightarrow \mathscr{V}_h(\mathsf{P})$ given by $\mathscr{I}_{\mathsf{P}}^{\mathscr{V}_h} = \mathscr{K}_{\mathsf{V}}^{-1} \circ \mathscr{R}_{\mathsf{V}}$.

We endow the space $\mathscr{V}_h(\mathsf{P})$ with an L^2-like inner product. The usual strategy for the construction of an inner product in a finite dimensional space relies on the L^2-orthogonal projection onto linear polynomials on P, denoted by $\Pi_{\mathsf{P}}^0 : \mathscr{V}_h(\mathsf{P}) \rightarrow \mathbb{P}_1(\mathsf{P})$. Unfortunately, this projector is not computable in $\mathscr{V}_h(\mathsf{P})$. To have a computable orthogonal projection operator we could change the definition of the space as in the so called "enhancement approach" [1, 10, 11]. This strategy will, effectively, change the definition of the space $\mathscr{V}_h(\mathsf{P})$ calling into question whether or not an important De-Rham complex hold, see Sect. 12.3.5. The reality is that such a diagram holds even in the enhanced scenario, see [8]. However, we were not aware of this enhanced diagram, instead, we follow a different strategy through a special polynomial reconstruction operator $\Pi_{\mathsf{P}} : \mathscr{V}_h(\mathsf{P}) \rightarrow \mathbb{P}_1(\mathsf{P})$ satisfying the following three properties:

(P1) $\Pi_{\mathsf{P}} D_h$ is computable only from the degrees of freedom of $D_h \in \mathscr{V}_h(\mathsf{P})$;
(P2) Π_{P} preserves all linear polynomials, i.e., for any $D_h \in \mathbb{P}_1(\mathsf{P})$, $\Pi_{\mathsf{P}} D_h = D_h$;
(P3) Π_{P} is a bounded operator with respect to L^2 norm with the upper bound constant C_Π independent of the mesh resolution h, i.e., for any $D_h \in \mathscr{V}_h(\mathsf{P})$

$$\|\Pi_{\mathsf{P}} D_h\|_{0,\mathsf{P}} \le C_\Pi \|D_h\|_{0,\mathsf{P}}. \tag{12.3.9}$$

We can use this projector to define an inner product in the space $\mathscr{V}_h$ that will allow us to approximate L^2-inner product as they appear in (12.3.4). In Sect. 12.3.2.1, we discuss three possible implementations of the polynomial reconstruction operator.

We define

$$\left(E_h, D_h\right)_{\mathscr{V}_h(\mathsf{P})} = \left(\Pi_{\mathsf{P}} E_h, \Pi_{\mathsf{P}} D_h\right) + \mathscr{S}^{\mathsf{V}}\left((1 - \Pi_{\mathsf{P}})E_h, (1 - \Pi_{\mathsf{P}})D_h\right), \tag{12.3.10}$$

where $\mathscr{S}^{\mathsf{V}}$ is the stabilization bilinear form. According to the standard VEM construction, $\mathscr{S}^{\mathsf{V}}$ can be *any* bilinear form for which there exist two real constants s_* and s^* independent of h such that

$$s_* \|D_h\|_{0,\mathsf{P}}^2 \le \mathscr{S}^{\mathsf{V}}(D_h, D_h) \le s^* \|D_h\|_{0,\mathsf{P}}^2 \quad \forall D_h \in \ker \Pi \cap \mathscr{V}_h(\mathsf{P}). \tag{12.3.11}$$

In practice, we can design the stabilization as in [45, 67]. This inner product defines the norm in $\mathscr{V}_h(\mathsf{P})$ given by $\||D_h\||_{\mathscr{V}_h(\mathsf{P})}^2 = \left(D_h, D_h\right)_{\mathscr{V}_h(\mathsf{P})}$. When the projection operator Π satisfies properties **(P1)**–**(P3)**, the inner product (12.3.10) satisfies two fundamental properties summarized in the following theorem.

Theorem 12.2 *The inner product* $\left(\,\cdot\,,\,\cdot\, \right)_{\mathscr{V}_h(P)}$ *defined in* (12.3.10) *satisfies*

– *Linear consistency:*

$$\left(p,q \right)_{\mathscr{V}_h(P)} = \left(p,q \right) \quad \forall p,q \in \mathbb{P}_1(P) \subset \mathscr{V}_h(P). \tag{12.3.12}$$

– *Stability: there exists two real constants* α_* *and* $\alpha^* > 0$ *independent of* h *and* P *such that*

$$\alpha_* \|D_h\|_{0,P}^2 \leq \||D_h\||_{\mathscr{V}_h(P)}^2 \leq \alpha^* \|D_h\|_{0,P}^2. \quad \forall D_h \in \mathscr{V}_h(P)^2. \tag{12.3.13}$$

Proof To prove the *linear consistency* (12.3.12), take two polynomial functions $p,q \in \mathbb{P}_1(P)$. Property **(P2)** implies that $\Pi p = p$ and $\Pi q = q$. So, the stabilization term in (12.3.10) is zero, and we find that

$$\left(p,q \right)_{\mathscr{V}_h(P)} = \left(\Pi_P p, \Pi_P q \right)_P = \left(p,q \right)_P.$$

To prove the lower bound of the *stability* condition (12.3.13), we add and subtract $\Pi_P D_h$, apply the triangular inequality, the left-most inequality in (12.3.11) and note that

$$\|D_h\|_{0,P}^2 \leq \left(\|\Pi_P D_h\|_{0,P} + \|(1-\Pi_P)D_h\|_{0,P} \right)^2 \leq 2 \left(\|\Pi_P \boldsymbol{v}_h\|_{0,P}^2 + \|(1-\Pi_P)D_h\|_{0,P}^2 \right)$$

$$\leq 2 \max(1,s^*) \left(\left(\Pi_P D_h, \Pi_P D_h \right)_P + \mathscr{S}^{\mathsf{V}} \left((1-\Pi_P)D_h, (1-\Pi_P)D_h \right) \right)$$

$$= (\alpha_*)^{-1} \left(D_h, D_h \right)_{\mathscr{V}_h(P)} = (\alpha_*)^{-1} \||D_h\||_{\mathscr{V}_h(P)}^2,$$

where the lower bound α_* in (12.3.13) is given by $\alpha_*^{-1} = 2 \max(1,s^*)$.

To obtain the upper bound in (12.3.13), we first note that property **(P3)** implies that:

$$\mathscr{S}^{\mathsf{V}} \left((1-\Pi_P)D_h, (1-\Pi_P)D_h \right) \leq s^* \|(1-\Pi_P)D_h\|_{0,P}^2 \leq s^* \left(\|D_h\|_{0,P} + \|\Pi_P D_h\|_{0,P} \right)^2$$

$$\leq s^* \left(\|D_h\|_{0,P} + C_\Pi \|D_h\|_{0,P} \right)^2 \leq s^* (1+C_\Pi)^2 \|D_h\|_{0,P}^2.$$

To conclude this theorem we use

$$\||D_h\||_{\mathscr{V}_h(P)}^2 = \left(\Pi_P D_h, \Pi_P D_h \right)_P + \mathscr{S}^{\mathsf{V}} \left((1-\Pi_P)D_h, (1-\Pi_P)D_h \right)$$

$$\leq C_\Pi^2 \|D_h\|_{0,P}^2 + s^* (1+C_\Pi)^2 \|D_h\|_{0,P}^2 \leq \alpha^* \|D_h\|_{0,P}^2,$$

where the upper bound α^* in (12.3.13) is given by $\alpha^* = \max(C_\Pi^2, s^*(1+C_\Pi)^2)$.

Note that both lower and upper bounds α_* and α^* depend only on the upper bound C_Π of the projection operator Π and are independent of mesh resolution h.

□

The global space $\mathscr{V}_h$ is the subset of functions in $H(\mathbf{rot}; \Omega)$ whose restriction to any element $\mathsf{P} \in \Omega_h$ belongs to $\mathscr{V}_h(\mathsf{P})$. Formally, we write that

$$\mathscr{V}_h = \left\{ D_h \in H(\mathbf{rot}; \Omega) : \forall \mathsf{P} \in \Omega_h \quad D_{h|\mathsf{P}} \in \mathscr{V}_h(\mathsf{P}) \right\}. \tag{12.3.14}$$

We endow the global space $\mathscr{V}_h$ with the global inner product

$$\left(E_h, D_h \right)_{\mathscr{V}_h} = \sum_{\mathsf{P} \in \Omega_h} \left(E_{h|\mathsf{P}}, D_{h|\mathsf{P}} \right)_{\mathscr{V}_h(\mathsf{P})} \quad \forall E_h, D_h \in \mathscr{V}_h, \tag{12.3.15}$$

and the global norm $\|D_h\|_{\mathscr{V}_h}^2 = \left(D_h, D_h \right)$ The global inner product inherits the properties of accuracy and stability from the elemental inner product that are stated in Theorem 12.2.

Corollary 12.1 *The inner product $\left(\cdot, \cdot \right)_{\mathscr{V}_h}$ defined in (12.3.15) has the two properties:*

– **Linear consistency**:

$$\left(p, q \right)_{\mathscr{V}_h} = \left(p, q \right) \quad \forall p, q \in \mathbb{P}_1(\Omega_h) \subset \mathscr{V}_h(\mathsf{P}). \tag{12.3.16}$$

– **Stability**: *there exists two real constants α_* and $\alpha^* > 0$ independent of h and P such that*

$$\alpha_* \|D_h\|_0^2 \leq \||D_h\||_{\mathscr{V}_h(\mathsf{P})}^2 \leq \alpha^* \|D_h\|_0^2 \quad \forall D_h \in \mathscr{V}_h(\mathsf{P})^2, \tag{12.3.17}$$

where the lower and upper bound constants α_* and $\alpha^* > 0$ are the same constants introduced in Theorem 12.2 and $\mathbb{P}_1(\Omega_h)$ is the space of piecewise linear polynomials built on the mesh Ω_h.

Proof Proof of this Corollary follows immediately from the results of Theorem 12.2. □

Finally, we introduce the *global interpolation operator* $\mathscr{I}^{\mathscr{V}_h} : H(\mathbf{rot}; \Omega) \to \mathscr{V}_h$, whose restriction to any cell coincides with the elemental interpolation operator:

$$\mathscr{I}^{\mathscr{V}_h}(D_h)_{|\mathsf{P}} = \mathscr{I}_{\mathsf{P}}^{\mathscr{V}_h}(D_{h|\mathsf{P}}) \quad \forall D_h \in \mathscr{V}_h \ \mathsf{P} \in \Omega_h. \tag{12.3.18}$$

12.3.2.1 The Polynomial Reconstruction Operators

We discuss here three alternative choices for the oblique projections that can be used to approximate inner products in the space $\mathscr{V}_h(\mathsf{P})$.

(I) Elliptic Projection Operator   We denote this projection operator as

$$\Pi_{\mathsf{P}}^{\mathbf{rot}} : \mathscr{V}_h(\mathsf{P}) \to \mathbb{P}_1(\Omega). \tag{12.3.19}$$

For $D_h \in \mathscr{V}_h(\mathsf{P})$ the elliptic projection operator is the solution to the variational problem

$$\int_{\mathsf{P}} \mathbf{rot}\left(D_h - \Pi_{\mathsf{P}}^{\mathbf{rot}} D_h\right) \cdot \mathbf{rot}\, q \; dA = 0 \quad \forall q \in \mathbb{P}_1(\mathsf{P}), \tag{12.3.20a}$$

$$P_0\left(D_h - \Pi_{\mathsf{P}}^{\mathbf{rot}} D_h\right) = 0, \tag{12.3.20b}$$

where we use the additional projector $P_0(D_h) = \sum_{\mathsf{V} \in \partial \mathsf{P}} D_h(\mathsf{V})$ on $\mathbb{P}_0(\mathsf{P})$ to remove the kernel of operator $\mathbf{rot}$. The linear polynomial $\Pi_{\mathsf{P}}^{\mathbf{rot}} D_h$ is computable because the integral quantities

$$\int_{\mathsf{P}} \mathbf{rot}\, D_h \cdot \mathbf{rot}\, q \; dA \quad \forall q \in \mathbb{P}_1(\mathsf{P}), \tag{12.3.21}$$

are computable from the degrees of freedom **(V)** of D_h. To prove this statement we use the Green's theorem, note that $\mathrm{rot}\,\mathbf{rot}\, q = 0$, since $q \in \mathbb{P}_1(\mathsf{P})$, and split the integral on $\partial\mathsf{P}$ in the summation of edge integrals to obtain

$$\int_{\mathsf{P}} \mathbf{rot}\, D_h \cdot \mathbf{rot}\, q \; dA = \int_{\mathsf{P}} D_h \mathrm{rot}\,\mathbf{rot}\, q \; dA + \int_{\partial\mathsf{P}} D_h \boldsymbol{t} \cdot \mathbf{rot}\, q \; d\ell$$

$$= \sum_{e \in \partial \mathsf{P}} \int_e D_h \boldsymbol{t} \cdot \mathbf{rot}\, q \; d\ell,$$

where $\boldsymbol{t}$ is the unit tangent vector parallel to e. The edge integrals are computable because $\boldsymbol{t} \cdot \mathbf{rot}\, q$ is a known function in $\mathbb{P}_0(e)$ and we can interpolate the trace $D_{h|e} \in \mathbb{P}_1(e)$ using the evaluation of D_h at the vertices of edge e, which are known from the degrees of freedom **(V)**.

(II) Least Squares Polynomial Reconstruction Operator   The second reconstruction operator that we consider is denoted as

$$\Pi_{\mathsf{P}}^{LS} : \mathscr{V}_h(\mathsf{P}) \to \mathbb{P}_1(\Omega). \tag{12.3.22}$$

For a function $D_h \in \mathcal{V}_h(\mathsf{P})$, the linear polynomial $\Pi_{\mathsf{P}}^{LS} D_h$ is the solution of the Least Squares problem

$$\Pi_{\mathsf{P}}^{LS} D_h(\boldsymbol{x}) := \mathrm{argmin}_{q \in \mathbb{P}_1(\mathsf{P})} \sum_{\mathsf{v} \in \partial \mathsf{P}} |D_h(\boldsymbol{x}_{\mathsf{v}}) - q(\boldsymbol{x}_{\mathsf{v}})|^2.$$

The solution to this problem has a closed form that can be easily written as follows. Let $\{m_1, m_2, m_3\}$ be the scaled monomial basis of $\mathbb{P}_1(\mathsf{P})$, which is given by:

$$m_1(x, y) = 1, \quad m_2(x, y) = \frac{x - x_{\mathsf{P}}}{h_{\mathsf{P}}}, \quad \text{and} \quad m_3(x, y) = \frac{y - y_{\mathsf{P}}}{h_{\mathsf{P}}},$$

where $\boldsymbol{x}_{\mathsf{P}} = (x_{\mathsf{P}}, y_{\mathsf{P}})^T$ is the position vector of the barycenter of P. Let

$$\Pi_{\mathsf{P}}^{LS} D_h(x, y) = a m_1(x, y) + b m_2(x, y) + c m_3(x, y).$$

We denote the position vector of the i-th vertex v_i by $\boldsymbol{x}_i$, for $i = 1, \ldots, N$, where N is the number of vertices of P. Then, the coefficient vector $\boldsymbol{\xi} = (a, b, c)^T$ is the solution of the system

$$\mathbb{A}\boldsymbol{\xi} = \boldsymbol{b} \text{ with } \mathbb{A} = \begin{pmatrix} m_1(\boldsymbol{x}_1) & m_2(\boldsymbol{x}_1) & m_3(\boldsymbol{x}_1) \\ m_1(\boldsymbol{x}_2) & m_2(\boldsymbol{x}_2) & m_3(\boldsymbol{x}_2) \\ \vdots & \vdots & \vdots \\ m_1(\boldsymbol{x}_N) & m_2(\boldsymbol{x}_N) & m_3(\boldsymbol{x}_N) \end{pmatrix}, \quad \boldsymbol{b} = \begin{pmatrix} D_h(\boldsymbol{x}_1) \\ D_h(\boldsymbol{x}_2) \\ \vdots \\ D_h(\boldsymbol{x}_N) \end{pmatrix}.$$

$$(12.3.23)$$

Since $\mathbb{A}$ is a maximum rank matrix, the array of the solution coefficients is given by $\boldsymbol{\xi} = (\mathbb{A}^T \mathbb{A})^{-1} \mathbb{A}^T \boldsymbol{b}$.

(III) Galerkin Interpolation Operator The final projector that we consider in this chapter is denoted as Π_{P}^{pw} and is the piecewise linear Galerkin interpolation on a triangular partition of P. If P is a convex polygon, we can easily build such triangular partition by connecting its vertices and the barycenter given by the convex linear combination

$$\boldsymbol{x}_{\mathsf{v}}^* = \sum_{\mathsf{v} \in \partial \mathsf{P}} \alpha_{\mathsf{v}} \boldsymbol{x}_{\mathsf{v}},$$

for some suitable choices of the coefficients α_V that are such that $0 \leq \alpha_V \leq 1$ for every V and $\sum_{V \in \partial P} \alpha_V = 1$. If P is only star-shaped but not necessarily convex, we can still define an inner point V^* by a different choice of the coefficients α_V. For a given function $D_h \in \mathscr{V}_h(P)$, we assume that

$$\Pi_P^{pw} D_h(x_V^*) = \sum_{V \in \partial P} \alpha_V D_h(V) \quad \text{and} \quad \Pi_P^{pw} D_h(x_V) = D_h(x_V) \quad \forall V \in \partial P.$$

Then, in every triangle T with vertices V_1, V_2 and V^*, we define $\Pi_P^{pw} D_h(x)$ as the linear interpolant of the values $D_h(V_1)$, $D_h(V_2)$, and $D_h(V^*)$.

12.3.3   The Edge Space

The next virtual element space that we consider is the finite dimensional counterpart of $H(\text{div}; \Omega)$. This space was introduced in [11]. Like before, we begin by defining a local space over a cell P. The formal definition reads as

$$\mathscr{E}_h(P) := \Big\{ C_h \in H(\text{div}; P) \cap H(\text{rot}; P) : \text{div}\, C_h \in \mathbb{P}_0(P), \quad \text{rot}\, C_h = 0,$$

$$C_{h|e} \cdot \boldsymbol{n} \in \mathbb{P}_0(e)\ \forall e \in \partial P \Big\}.$$
$$(12.3.24)$$

Every virtual element function $C_h \in \mathscr{E}_h(P)$ is characterized by the following set of degrees of freedom

(E) the average of the normal flux on each edge:

$$\forall e \in \partial P : \quad \frac{1}{|e|} \int_e C_h \cdot \boldsymbol{n} \, d\ell.$$

These are represented by red arrows pointing out of the cell P, see the sample picture in Fig. 12.2.

Fig. 12.2 Representation of the degrees of freedom of functions in $\mathscr{E}_h(P)$
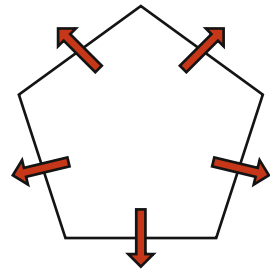
In order to properly state the property of unisolvency we introduce $\mathscr{R}_e$: $H(\text{div}; \mathsf{P}) \to \mathbb{R}^N$ such that for any $\boldsymbol{C} \in H(\text{div}; \mathsf{P})$ the array $\mathscr{R}_e(\boldsymbol{C})$ is the array of degrees of freedom of $\boldsymbol{C}$. This result is stated below

Theorem 12.3 *Let $\mathscr{K}_e : \mathscr{E}_h(\mathsf{P}) \to \mathbb{R}^N$ be the restriction of $\mathscr{R}_e$. Then, $\mathscr{K}_e$ is bijective.*

In view of the unisolvency of $\mathscr{E}_h(\mathsf{P})$, we define the interpolation operator $\mathscr{I}_\mathsf{P}^{\mathscr{E}_h} = \mathscr{K}_e^{-1} \circ \mathscr{R}_e$.

Next, we define an important projector in the space $\mathscr{E}_h(\mathsf{P})$, namely the orthogonal projection $\Pi_\mathsf{P}^0 : \mathscr{E}_h(\mathsf{P}) \to \mathbb{P}_0(\mathsf{P})$ whose image is the solution to the variational problem

$$\left(\boldsymbol{C}_h - \Pi_\mathsf{P}^0 \boldsymbol{C}_h, \boldsymbol{q}\right)_\mathsf{P} = 0 \qquad \text{for all} \quad \boldsymbol{q} \in \left[\mathbb{P}_0(\mathsf{P})\right]^2, \tag{12.3.25}$$

for every $\boldsymbol{C}_h \in \mathscr{E}_h(\mathsf{P})$. This projector is computable using the degrees of freedom **(E)**. Pick $\boldsymbol{q} \in [\mathbb{P}_0(\mathsf{P})]^2$, $p \in \mathbb{P}_1(\mathsf{P})$ where the scalar polynomial p is chosen so that $\boldsymbol{q} = \nabla p$. Then, we apply Green's theorem and find that

$$\int_\mathsf{P} \boldsymbol{C}_h \cdot \boldsymbol{q} \, dA = \int_\mathsf{P} \boldsymbol{C}_h \cdot \nabla p \, dA = -\int_\mathsf{P} (\text{div} \, \boldsymbol{C}_h) p \, dA + \int_{\partial\mathsf{P}} p \boldsymbol{C}_h \cdot \boldsymbol{n} \, d\ell \tag{12.3.26}$$

for all $\boldsymbol{C}_h \in \mathscr{E}_h(\mathsf{P})$. We split the integral on $\partial\mathsf{P}$ in the summation of line integrals

$$\int_{\partial\mathsf{P}} \boldsymbol{C}_h \cdot \boldsymbol{n} p \, d\ell = \sum_{e \in \partial\mathsf{P}} (\boldsymbol{C}_h \cdot \boldsymbol{n})_{|e} \int_e p \, d\ell, \tag{12.3.27}$$

and we note that $\boldsymbol{C}_h \cdot \boldsymbol{n}_{|e}$ is constant on each edge $e \in \partial\mathsf{P}$, cf. space definition (12.3.24), and coincides with the evaluation in **(E)**. In turn, we compute $\text{div} \, \boldsymbol{C}_h \in \mathbb{P}_0(\mathsf{P})$ by applying the divergence theorem:

$$\text{div} \, \boldsymbol{C}_h = \frac{1}{|\mathsf{P}|} \int_{\partial\mathsf{P}} \boldsymbol{C}_h \cdot \boldsymbol{n} \, d\ell = \frac{1}{|\mathsf{P}|} \sum_{e \in \partial\mathsf{P}} |e| \left(\frac{1}{|e|} \int_e \boldsymbol{C}_h \cdot \boldsymbol{n} \, d\ell\right). \tag{12.3.28}$$

Note that the polynomial p is determined by the relation $\nabla p = \boldsymbol{q}$ and is defined up to an additive constant factor. If we choose this constant factor equal to the elemental average of p on P, so that $\int_\mathsf{P} p \, dA = 0$, we can make the area integral vanish since

$$\int_\mathsf{P} (\text{div} \, \boldsymbol{C}_h) p \, dA = (\text{div} \, \boldsymbol{C}_h)_{|\mathsf{P}} \int_\mathsf{P} p \, dA = 0. \tag{12.3.29}$$

In conclusion, the information about a virtual element function $\boldsymbol{C}_h$ in the space $\mathscr{E}_h(\mathsf{P})$ that we need to compute the projection $\Pi_\mathsf{P}^0 \boldsymbol{C}_h$ can be read off the degrees of freedom of $\boldsymbol{C}_h$.

We can use Π^0_{P} to define the inner product:

$$\left(\boldsymbol{B}_h, \boldsymbol{C}_h\right)_{\mathscr{E}_h(\mathsf{P})} = \left(\Pi^0_{\mathsf{P}} \boldsymbol{B}_h, \Pi^0_{\mathsf{P}} \boldsymbol{C}_h\right) + \mathscr{S}^e((\mathscr{I} - \Pi^0_{\mathsf{P}})\boldsymbol{B}_h, (\mathscr{I} - \Pi^0_{\mathsf{P}})\boldsymbol{C}_h)$$
(12.3.30)

for every possible pair of virtual element functions $\boldsymbol{B}_h, \boldsymbol{C}_h \in \mathscr{E}_h(\mathsf{P})$. As before, the stabilization form $\mathscr{S}^e$ can be *any* continuous bilinear form for which there exists two strictly positive constants s_* and s^* independent of h such that

$$s_* \|\boldsymbol{C}_h\|^2_{0,\mathsf{P}} \le \mathscr{S}^e(\boldsymbol{C}_h, \boldsymbol{C}_h) \le s^* \|\boldsymbol{C}_h\|^2_{0,\mathsf{P}} \quad \forall \boldsymbol{C}_h \in \mathscr{E}_h(\mathsf{P}) \cap \ker \Pi^0_{\mathsf{P}} \cap \mathscr{E}_h(\mathsf{P}).$$

Practical implementations of $\mathscr{S}^e$ can be designed according with [45, 67] for more examples. The constants s_* and s^* are different from those in equation (12.3.11). This inner product defines the norm

$$\||\boldsymbol{C}_h\||_{\mathscr{E}_h(\mathsf{P})} = \left(\boldsymbol{C}_h, \boldsymbol{C}_h\right)^{1/2}_{\mathscr{E}_h(\mathsf{P})} \quad \forall \boldsymbol{C}_h \in \mathscr{E}_h(\mathsf{P}),$$
(12.3.31)

and the two fundamental properties of $\mathbb{P}_0$-consistency an stability hold as stated in the following theorem.

Theorem 12.4 *The inner product* $\left(\cdot, \cdot\right)_{\mathscr{E}_h(\mathsf{P})}$ *defined in* (12.3.30) *has the two properties:*

– $\mathbb{P}_0$*-consistency:*

$$\left(\boldsymbol{C}_h, \boldsymbol{q}\right)_{\mathscr{E}_h(\mathsf{P})} = \left(\boldsymbol{C}_h, \boldsymbol{q}\right) \quad \forall \boldsymbol{C}_h \in \mathscr{E}_h(\mathsf{P}), \ \boldsymbol{q} \in [\mathbb{P}_0(\mathsf{P})]^2$$
(12.3.32)

– **Stability:** *there exists two real constants* β_* *and* $\beta^* > 0$ *independent of h and* P *such that*

$$\beta_* \|\boldsymbol{C}_h\|^2_{0,\mathsf{P}} \le \||\boldsymbol{C}_h\||^2_{\mathscr{E}_h(\mathsf{P})} \le \beta^* \|\boldsymbol{C}_h\|^2_{0,\mathsf{P}} \quad \forall \boldsymbol{C}_h \in \mathscr{E}_h(\mathsf{P}).$$
(12.3.33)

Proof We omit the proof of this Theorem since it is essentially the same as the one presented for Theorem 12.2. We just note that here the orthogonality of the projector $\Pi^0_{\mathsf{P}} P$ makes a more general result possible as the consistency condition is verified if at least one and not necessarily both of the entries of $\left(\boldsymbol{C}_h, \boldsymbol{q}\right)_{\mathscr{E}_h(\mathsf{P})}$ is a (vector-valued) polynomial field. In fact, if $\boldsymbol{q} \in \left[\mathbb{P}_2(\mathsf{P})\right]^2$ we have that $\mathscr{S}^e((\mathscr{I} - \Pi^0_{\mathsf{P}})\boldsymbol{C}_h, (\mathscr{I} - \Pi^0_{\mathsf{P}})\boldsymbol{q}) = 0$ because $\Pi^0_{\mathsf{P}}\boldsymbol{q} = \boldsymbol{q}$. Then, the definition of the orthogonal

projection Π_{P}^0, which is also polynomial-preserving, implies that

$$\left(\boldsymbol{B}_h, \boldsymbol{C}_h\right)_{\mathscr{E}_h(\mathsf{P})} = \left(\Pi_{\mathsf{P}}^0 \boldsymbol{C}_h, \Pi_{\mathsf{P}}^0 \boldsymbol{q}\right)_{\mathsf{P}} = \left(\boldsymbol{C}_h, \Pi_{\mathsf{P}}^0 \boldsymbol{q}\right)_{\mathsf{P}} = \left(\boldsymbol{C}_h, \boldsymbol{q}\right)_{\mathsf{P}} \qquad (12.3.34)$$

for all $\boldsymbol{C}_h \in \mathscr{E}_h(\mathsf{P})$ and $\boldsymbol{q} \in \mathbb{P}_0(\mathsf{P})$.   □

We introduce the global virtual element space $\mathscr{E}_h$ built on the mesh Ω_h by pasting together the elemental spaces $\mathscr{E}_h(\mathsf{P})$ built on all cells P:

$$\mathscr{E}_h = \left\{ \boldsymbol{C}_h \in H(\mathrm{div}; \Omega) : \ \boldsymbol{C}_{h|\mathsf{P}} \in \mathscr{E}_h(\mathsf{P}) \ \forall \mathsf{P} \in \Omega_h \right\}.$$

We endow this space with the inner product

$$\left(\boldsymbol{B}_h, \boldsymbol{C}_h\right)_{\mathscr{E}_h} = \sum_{\mathsf{P} \in \Omega_h} \left(\boldsymbol{B}_{h|\mathsf{P}}, \boldsymbol{C}_{h|\mathsf{P}}\right)_{\mathscr{E}_h(\mathsf{P})} \quad \forall \boldsymbol{B}_h, \boldsymbol{C}_h \in \mathscr{E}_h, \qquad (12.3.35)$$

and the induced norm

$$\|\|\boldsymbol{C}_h\|\|_{\mathscr{E}_h}^2 = \left(\boldsymbol{C}_h, \boldsymbol{C}_h\right)_{\mathscr{E}_h} \quad \forall \boldsymbol{C}_h \in \mathscr{E}_h. \qquad (12.3.36)$$

As for the nodal space, this global inner product and associated norm satisfy the fundamental properties of $\mathbb{P}_0$-*consistency* and *stability*, which we state in the next corollary. These properties imply the exactness of the inner product defined in (12.3.35) on the piecewise constant functions and that the norm defined in (12.3.30) is equivalent to the L^2 norm. We omit the proof since these properties are an immediate consequence of Theorem 12.4.

Corollary 12.2 *The inner product* $\left(\,\cdot\,,\,\cdot\,\right)_{\mathscr{E}_h}$ *defined in* (12.3.35) *has the two properties:*

– **Linear consistency**:

$$\left(\boldsymbol{C}_h, \boldsymbol{q}\right)_{\mathscr{E}_h(\mathsf{P})} = \left(\boldsymbol{C}_h, \boldsymbol{q}\right) \quad \forall \boldsymbol{C}_h \in \mathscr{E}_h, \ \boldsymbol{q} \in [\mathbb{P}_0(\Omega_h)]^2. \qquad (12.3.37)$$

– **Stability**: *there exists two real constants* β_* *and* $\beta^* > 0$ *independent of h such that*

$$\beta_* \|\boldsymbol{C}_h\|_{0,P}^2 \leq \|\|\boldsymbol{C}_h\|\|_{\mathscr{E}_h(P)} \leq \beta^* \|\boldsymbol{C}_h\|_{0,P}^2 \quad \forall \boldsymbol{C}_h \in \mathscr{E}_h(P). \qquad (12.3.38)$$

Next, we introduce the *global interpolation operator* $\mathscr{I}_{\mathsf{P}}^{\mathscr{E}_h} : H(\text{div}; \Omega) \to \mathscr{V}_h$. This operator is defined by gluing together its respective elemental definitions, so that

$$\mathscr{I}^{\mathscr{E}_h}(\boldsymbol{C}_h)_{|\mathsf{P}} = \mathscr{I}_{\mathsf{P}}^{\mathscr{E}_h}(\boldsymbol{C}_{h|\mathsf{P}})$$

To end this subsection we will define a second orthogonal projection that we will use to approximate a term unique to MHD. Consider a cell P and define $\Pi_{\mathsf{P}}^{RT} : \mathscr{E}_h(\mathsf{P}) \to \text{RT}_0(\mathsf{P})$. Given $\boldsymbol{C}_h \in \mathscr{E}_h(\mathsf{P})$ the image $\Pi_{\mathsf{P}}^{RT}\boldsymbol{C}_h$ is the solution to the variational formulation

$$\left(\boldsymbol{C}_h - \Pi_{\mathsf{P}}^{RT}\boldsymbol{C}_h, \boldsymbol{q}\right)_{\mathsf{P}} = 0 \qquad \text{for all} \quad \boldsymbol{q} \in \text{RT}_0(\mathsf{P}), \tag{12.3.39}$$

where

$$\text{RT}_0(\mathsf{P}) = \left\{ a \begin{pmatrix} 1 \\ 0 \end{pmatrix} + b \begin{pmatrix} 0 \\ 1 \end{pmatrix} + c \begin{pmatrix} x \\ y \end{pmatrix} : a, b, c \in \mathbb{R} \right\}.$$

This projector is also computable using only the degrees of freedom in $\mathscr{E}_h(\mathsf{P})$. The strategy is the same as the one presented for Π_{P}^0. Consider $\boldsymbol{q} \in \text{RT}_0(\mathsf{P})$ and $p \in \mathbb{P}_2(\mathsf{P})$ with $\int_{\mathsf{P}} p \, dA = 0$ such that $\nabla p = \boldsymbol{q}$. The terms in Green's Theorem (12.3.26) can be computed as before with the only difference being that the quadrature rule used in (12.3.27) needs to be exact for quadratic polynomials.

The *global orthogonal projector* $\Pi^{RT} : \mathscr{E}_h \to \text{RT}_0(\Omega_h)$, where $\text{RT}_0(\Omega_h) = \left\{ \boldsymbol{q} \in H(\text{div}; \Omega) : \boldsymbol{q}_{|\mathsf{P}} \in \text{RT}_0(\mathsf{P}) \right\}$ is defined as

$$(\Pi^{RT}\boldsymbol{C}_h)_{|\mathsf{P}} = \Pi_{\mathsf{P}}^{RT}(\boldsymbol{C}_{h|\mathsf{P}}) \quad \forall \mathsf{P} \in \Omega_h. \tag{12.3.40}$$

We use Π^{RT} to approximate the term "$\boldsymbol{u} \times \boldsymbol{B}$" as can be evidenced in the MHD variational formulation (12.3.4). The main issue with the aforementioned term is that we only have access to the fluxes of the magnetic field across the edges while the inner product in the variational formulation requires nodal evaluations. We amend this inconsistency by projecting the magnetic field onto the space of vector polynomial fields $\text{RT}_0(\mathsf{P})$ and extract the necessary evaluations from this projection. We note that we could use Π_{P}^0 to extract these vertex evaluations. However, more complex MHD models have terms of the form

$$\left((\mathbf{rot}\,\boldsymbol{B}) \times \boldsymbol{B}, D\right). \tag{12.3.41}$$

Such a quantity cannot be estimated using Π_{P}^0 since the codomain of this projector is the space of constants and their curl is zero. In this case using the projector Π^{RT} is ideal for low order approximations.

12.3.4   The Cell Space

The final space that we need to define for the electromagnetic part is the space of piecewise constant functions on Ω_h, i.e., the space of constant polynomials in every element P:

$$\mathscr{P}_h = \left\{ q_h \in L^2(\Omega) : q_{h|P} \in \mathbb{P}_0(P) \; \forall P \in \Omega_h \right\}. \tag{12.3.42}$$

The degrees of freedom of a function $q_h \in \mathscr{P}_h$ are given by

(D) the elemental averages of q_h over every cell $P \in \Omega_h$

$$\frac{1}{|P|} \int_P q_h \, dA. \tag{12.3.43}$$

These are represented by red disks in the interior of the cell P, see the sample picture in Fig. 12.3. It is straightforward to see that such degrees of freedom are unisolvent in $\mathscr{P}_h$. In fact, the constant value given by restricting a function q_h to a cell is precisely the degree of freedom of q_h associated with that cell. We endow the elemental space $\mathscr{P}_h$ with the inner product

$$\left(p_h, q_h \right)_{\mathscr{P}_h} = \sum_{P} |P| p_{h|P} q_{h|P} \quad \forall p_h, q_h \in \mathscr{P}_h,$$

which is the $L^2(\Omega)$ inner product of two piecewise constant functions. This inner product induces the norm

$$\||q_h\||^2_{\mathscr{P}_h} = \left(q_h, q_h \right)_{\mathscr{P}_h}, \quad \forall q_h \in \mathscr{P}_h,$$

which is the $L^2(\Omega)$-norm restricted to the functions of $\mathscr{P}_h$, so that

$$\||q_h\||_{\mathscr{P}_h} = \|q_h\|_{0,\Omega} \quad \forall q_h \in \mathscr{P}_h.$$

Fig. 12.3 Representation of the degrees of freedom of functions in $\mathscr{P}_h(P)$
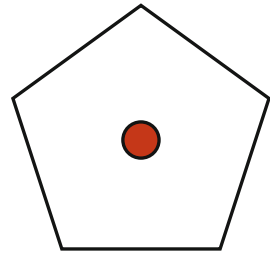
Finally, we define the *global interpolation operator* $\mathscr{I}^{\mathscr{P}_h} : L^2(\Omega) \to \mathscr{P}_h$ such that for every $q \in L^2(\Omega)$ we have:

$$(\mathscr{I}^{\mathscr{P}_h} q)_{|\mathsf{P}} = \frac{1}{|\mathsf{P}|} \int_{\mathsf{P}} q_h \, dA \quad \forall \mathsf{P} \in \Omega_h. \tag{12.3.44}$$

12.3.5   The de Rham Complex

In the previous sections we introduced and discussed the virtual element spaces $\mathscr{V}_h$, $\mathscr{E}_h$ and $\mathscr{P}_h$. It is well-known that the spaces $H(\mathbf{rot}; \Omega)$, $H(\mathrm{div}; \Omega)$ and $L^2(\Omega)$ form the de Rham chain

$$H(\mathbf{rot}; \Omega) \xrightarrow{\ \mathbf{rot}\ } H(\mathrm{div}; \Omega) \xrightarrow{\ \mathrm{div}\ } L^2(\Omega). \tag{12.3.45}$$

If Ω is simply connected, the chain is exact, see [71]. Equivalently, we can say that

$$\mathbf{rot}\, H(\mathrm{rot}; \Omega) = \big\{ \boldsymbol{C} \in H(\mathrm{div}; \Omega) : \mathrm{div}\, \boldsymbol{C} = 0 \big\}.$$

In the spirit of constructing a discrete version of the continuous problem, the spaces $\mathscr{V}_h$, $\mathscr{E}_h$ and $\mathscr{P}_h$ also form a similar exact de Rham chain

$$\mathscr{V}_h \xrightarrow{\ \mathbf{rot}\ } \mathscr{E}_h \xrightarrow{\ \mathrm{div}\ } \mathscr{P}_h. \tag{12.3.46}$$

This chain was first introduced in [9], and explored in more details and generality in [11]. It reveals that the set of degrees of freedom are transformed in accordance with the following diagram:
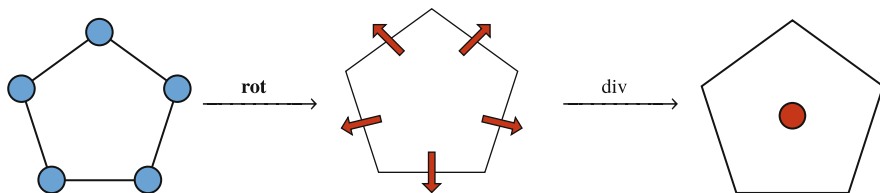
First we want to show that the chain in (12.3.46) is well-defined. This is to say that two important inclusions hold. The first is presented in the following lemma.

Lemma 12.1 *Let $\mathscr{V}_h$ and $\mathscr{E}_h$ be the virtual element spaces defined in* (12.3.8) *and* (12.3.24) *respectively. Then, it holds that*

$$\mathbf{rot}\,\mathscr{V}_h \subset \mathscr{E}_h. \tag{12.3.47}$$

Proof Let P be a mesh cell of Ω_h and take $D_h \in \mathscr{V}_h(\mathsf{P})$. In view of the definition of $\mathscr{V}_h(\mathsf{P})$, we have that rot $\mathbf{rot}\,D_h = 0$ in P and, clearly, div $\mathbf{rot}\,D_h = 0 \in \mathbb{P}_0(\mathsf{P})$. Moreover, for every edge $e \in \partial\mathsf{P}$, we find that $(\mathrm{rot}\,D_h \cdot \boldsymbol{n})_{|e} = (\nabla D_h \cdot \boldsymbol{t})_{|e} \in \mathbb{P}_0(e)$. Consequently, $(\mathbf{rot}\,D_h)_{|\mathsf{P}} \in \mathscr{E}_h(\mathsf{P})$, and, thus, $\mathbf{rot}\,D_h \in \mathscr{E}_h$ for every $D_h \in \mathscr{E}_h$ proving the inclusion relation in (12.3.47). $\qquad\square$

From Lemma 12.1, we know that $\mathbf{rot}\,D_h \in \mathscr{E}_h$ if $D_h \in \mathscr{V}_h$. Moreover, we can compute the degrees of freedom of $\mathbf{rot}\,D_h$ in $\mathscr{E}_h$ from the degrees of freedom of D_h in $\mathscr{V}_h$. In fact, by applying the fundamental theorem of line integrals, we find that

$$\frac{1}{|e|}\int_e \mathbf{rot}\,D_h \cdot \boldsymbol{n}\,d\ell = \frac{1}{|e|}\int_e \nabla D_h \cdot \boldsymbol{t}\,d\ell = \frac{D_h(\mathsf{v}_2) - D_h(\mathsf{v}_1)}{|e|}, \tag{12.3.48}$$

for every edge e of the polygonal boundary $\partial\mathsf{P}$ with endpoints v_1 and v_2 (oriented from v_1 to v_2), where again we used the identity $\boldsymbol{n} \cdot \mathbf{rot}\,(D_h) = \boldsymbol{t} \cdot \nabla(D_h)$. In view of Eq. (12.3.48), we can read the necessary information to identify the image of the rotational of $\mathscr{V}_h$ as a subset of $\mathscr{E}_h$ by using the degrees of freedom defined for $\mathscr{V}_h$.

The second inclusion in the chain (12.3.46) is the conclusion of the following lemma.

Lemma 12.2 *Let $\mathscr{E}_h$ and $\mathscr{P}_h$ be the virtual element spaces defined in* (12.3.24), *and* (12.3.42)*. Then, it holds that*

$$\mathrm{div}\,\mathscr{E}_h \subset \mathscr{P}_h. \tag{12.3.49}$$

Proof To verify this inclusion, we only need to note that any $\boldsymbol{C}_h \in \mathscr{E}_h(\mathsf{P})$ is such that div $\boldsymbol{C}_h \in \mathbb{P}_0(\mathsf{P})$ from the definition of $\mathscr{E}_h(\mathsf{P})$. It follows that div $\boldsymbol{C}_h \in \mathbb{P}_0(\Omega_h) = \mathscr{P}_h$ for every $\boldsymbol{C}_h \in \mathscr{E}_h$, which is the second inclusion relation in (12.3.49). $\qquad\square$

Noting that the divergence of a function in $\mathscr{E}_h$ lies in $\mathscr{P}_h$ will help us identify that its divergence can be entirely characterized by its set of degrees of freedom in $\mathscr{P}_h$. Take $\boldsymbol{C}_h \in \mathscr{E}_h$. From the divergence theorem we have that

$$\frac{1}{|\mathsf{P}|}\int_{\mathsf{P}} \mathrm{div}\,\boldsymbol{C}_h\,dA = \frac{1}{|\mathsf{P}|}\int_{\partial\mathsf{P}} \mathrm{div}\,\boldsymbol{C}_h\,dA = \frac{1}{|\mathsf{P}|}\sum_{e\in\partial\mathsf{P}} |e|\left(\frac{1}{|e|}\int_e \boldsymbol{C}_h \cdot \boldsymbol{n}\,dA\right). \tag{12.3.50}$$

Hence, we can evaluate the divergence of a function $\boldsymbol{C}_h \in \mathscr{E}_h$ using only its degrees of freedom.

The results summarized by Eqs. (12.3.48) and (12.3.50) are essential in order to further study the spaces $\mathscr{V}_h$, $\mathscr{E}_h$ and $\mathscr{P}_h$ and their relationship with the larger spaces $H(\mathbf{rot}; \Omega)$, $H(\mathrm{div}; \Omega)$ and $L^2(\Omega)$. These spaces form the commutative diagram

$$
\begin{array}{ccccc}
H(\mathbf{rot}; \Omega) & \xrightarrow{\ \mathbf{rot}\ } & H(\mathrm{div}; \Omega) & \xrightarrow{\ \mathrm{div}\ } & L^2(\Omega) \\
\downarrow{\scriptstyle \mathscr{I}^{\mathscr{V}_h}} & & \downarrow{\scriptstyle \mathscr{I}^{\mathscr{E}_h}} & & \downarrow{\scriptstyle \mathscr{I}^{\mathscr{P}_h}} \\
\mathscr{V}_h & \xrightarrow{\ \mathbf{rot}\ } & \mathscr{E}_h & \xrightarrow{\ \mathrm{div}\ } & \mathscr{P}_h
\end{array}
\tag{12.3.51}
$$

The proof of this theorem is broken into two lemmas. The first lemma, presented below, involves the spaces $H(\mathbf{rot}; \Omega)$ and $H(\mathrm{div}; \Omega)$, and their discrete counterparts $\mathscr{V}_h$ and $\mathscr{E}_h$.

Lemma 12.3 *The following identity holds*

$$
\forall D \in H(\mathbf{rot}; \Omega): \quad \mathscr{I}^{\mathscr{E}_h} \circ \mathbf{rot}\,(D) = \mathbf{rot} \circ \mathscr{I}^{\mathscr{V}_h}(D),
\tag{12.3.52}
$$

i.e., the interpolation and the rotational operators commute.

Proof Take a scalar function $D \in H(\mathbf{rot}; \Omega)$. By definition, the degrees of freedom of $\mathscr{I}^{\mathscr{E}_h} \circ \mathbf{rot}\,(D)$ in $\mathscr{E}_h$ are the same of $\mathbf{rot}\,D$. So, if e is a mesh edge oriented from endpoint v_1 to v_2, the theorem of line integral yields:

$$
\frac{1}{|e|} \int_e \boldsymbol{n} \cdot \mathbf{rot}\,D\, d\ell = \frac{1}{|e|} \int_e \boldsymbol{t} \cdot \nabla D\, d\ell = \frac{D(\mathsf{v}_2) - D(\mathsf{v}_1)}{|e|}.
\tag{12.3.53}
$$

In turn, the degrees of freedom of $\mathbf{rot} \circ \mathscr{I}^{\mathscr{V}_h}(D)$ are given by

$$
\frac{1}{|e|} \int_e \boldsymbol{n} \cdot \mathbf{rot}\left(\mathscr{I}^{\mathscr{V}_h}(D)\right) d\ell = \frac{1}{|e|} \int_e \boldsymbol{t} \cdot \nabla \mathscr{I}^{\mathscr{V}_h}(D)\, d\ell = \frac{\mathscr{I}^{\mathscr{V}_h} D(\mathsf{v}_2) - \mathscr{I}^{\mathscr{V}_h} D(\mathsf{v}_1)}{|e|},
\tag{12.3.54}
$$

using again the theorem of line integral yields. The definition of operator $\mathscr{I}^{\mathscr{V}_h}$ is such that

$$
\mathscr{I}^{\mathscr{V}_h} D(\mathsf{v}_1) = D(\mathsf{v}_1) \quad \text{and} \quad \mathscr{I}^{\mathscr{V}_h} D_h(\mathsf{v}_2) = D(\mathsf{v}_2).
$$

Thus, Eqs. (12.3.53) and (12.3.54) imply that the functions $\mathscr{I}^{\mathscr{E}_h} \circ \mathbf{rot}\,(D)$ and $\mathbf{rot} \circ \mathscr{I}^{\mathscr{V}_h}(D)$ have the same degrees of freedom in $\mathscr{E}_h$ and relation (12.3.52) follows from the unisolvence. □

The second lemma involves the spaces $H(\mathrm{div}; \Omega)$, $L^2(\Omega)$, $\mathscr{E}_h$ and $\mathscr{P}_h$.

Lemma 12.4 *The following identity holds*

$$\forall C \in H(div; \Omega): \quad \mathscr{I}^{\mathscr{P}_h} \circ div\,(C) = div \circ \mathscr{I}^{\mathscr{E}_h}(C), \tag{12.3.55}$$

i.e., the interpolation and the divergence operators commute.

Proof We prove (12.3.55) by verifying that the two functions in the left and right side share the same degrees of freedom in $\mathscr{P}_h$. Take a vector-valued field $C \in H(\mathrm{div}; \Omega)$. By definition, the degrees of freedom of $\mathscr{I}^{\mathscr{P}_h} \circ div\,(C)$ in $\mathscr{E}_h$ are the same of $div\,(C)$. So, if P is a mesh cell, the divergence theorem yields

$$\frac{1}{|\mathsf{P}|} \int_{\mathsf{P}} \mathrm{div}\, C \, dA = \frac{1}{|\mathsf{P}|} \sum_{e \in \partial \mathsf{P}} \int_e C \cdot n \, d\ell. \tag{12.3.56}$$

In turn, the degrees of freedom of $\mathrm{div} \circ \mathscr{I}^{\mathscr{E}_h}(C)$ are given by

$$\frac{1}{|\mathsf{P}|} \int_{\mathsf{P}} \mathrm{div}\, \mathscr{I}^{\mathscr{E}_h}(C) \, dA = \frac{1}{|\mathsf{P}|} \sum_{e \in \partial \mathsf{P}} \int_e \mathscr{I}^{\mathscr{E}_h}(C) \cdot n \, d\ell. \tag{12.3.57}$$

The definition of operator $\mathscr{I}^{\mathscr{E}_h}$ is such that

$$\forall e \in \partial \mathsf{P}: \quad \int_e \mathscr{I}^{\mathscr{E}_h} C \cdot n \, d\ell = \int_e C \cdot n \, d\ell.$$

Thus, Eqs. (12.3.56) and (12.3.57) imply that the two functions $\mathscr{I}^{\mathscr{P}_h} \circ div\,(C)$ and $\mathrm{div} \circ \mathscr{I}^{\mathscr{E}_h}(C)$ have the same degrees of freedom in $\mathscr{P}_h$ and relation (12.3.55) follows from the unisolvence. $\square$

We summarize our findings in the following theorem

Theorem 12.5 *The chain in (12.3.46) is well-defined and exact, and diagram (12.3.51) is commutative.*

Proof Lemmas 12.1 and 12.2 prove that (12.3.46) is well-defined. Lemmas 12.3 and 12.4 prove that diagram (12.3.51) is commutative. Hence, we are only left to prove that the de Rham chain (12.3.46) is exact, or, equivalently that

$$\mathbf{rot}\, \mathscr{V}_h = \ker\big(\mathrm{div}\, \mathscr{E}_h\big) = \big\{C_h \in \mathscr{E}_h : \mathrm{div}\, C_h = 0\big\}. \tag{12.3.58}$$

Take $D_h \in \mathscr{V}_h$. Lemma 12.1 implies that $\mathbf{rot}\, D_h \in \mathscr{E}_h$, and, obviously, $\mathrm{div}\, \mathbf{rot}\, D_h = 0$, so that $\mathbf{rot}\, D_h \in \ker\big(\mathrm{div}\, \mathscr{E}_h\big)$ as defined in (12.3.58), which implies that $\mathbf{rot}\, \mathscr{V}_h \subseteq \ker\big(\mathrm{div}\, \mathscr{E}_h\big)$. Next, consider $C_h \in \mathscr{E}_h$ with $\mathrm{div}\, C_h = 0$. Since $\mathscr{E}_h \subset H(\mathrm{div}; \Omega)$, then $C_h \in H(\mathrm{div}; \Omega)$ and the exactness of chain (12.3.45) implies the existence of a

scalar function $D \in H(\mathbf{rot};)$ such that $\boldsymbol{C}_h = \mathbf{rot}\, D$. Moreover, $\mathscr{I}^{\mathscr{V}_h} D \in \mathscr{V}_h$ must verify

$$\mathbf{rot} \circ \mathscr{I}^{\mathscr{V}_h} D = \mathscr{I}^{\mathscr{E}_h} \circ \mathbf{rot}\, D = \mathscr{I}^{\mathscr{E}_h} \boldsymbol{C}_h = \boldsymbol{C}_h, \qquad (12.3.59)$$

which implies that $\boldsymbol{C}_h$ is the rotational of a function of $\mathscr{V}_h$ and, thus, $\ker(\mathrm{div}\,\mathscr{E}_h) \subset \mathbf{rot}\,\mathscr{V}_h$. □

12.3.6 Fluid Flow

In this section, we briefly review the virtual element spaces for the discretization of the fluid-flow equations in the MHD model. These spaces were originally proposed in [17, 18, 79].

The first virtual element space is used to discretize the pressure. We consider a subspace of $\mathscr{P}_h$ as defined in Sect. 12.3.4. This subspace is given by

$$\mathscr{P}_{h,0} = \left\{ q_h \in \mathscr{P}_h : \int_\Omega q_h \, dA = 0 \right\}. \qquad (12.3.60)$$

The degrees of freedom of a function $q_h \in \mathscr{P}_{h,0}$ are given by

(P') $\qquad \int_{\mathsf{P}} q_h \, dA \quad$ for every $\mathsf{P} \in \Omega_h$.

These degrees of freedom are the same of $\mathscr{P}_h$ up to a multiplicative scale factor equal to $1/|\mathsf{P}|$. For $\mathscr{P}_{h,0}$ we prefer this definition because the integral over $\mathscr{P}_{h,0}$ of a function $q_h \in \mathscr{P}_{h,0}$ is given by summing the degrees of freedom of q_h:

$$\int_\Omega q_h \, dA = \sum_{i=0}^N \mathrm{dof}_i(q_h).$$

If we enumerate the cells in the mesh Ω_h as $\{P_i : 1 \le i \le N\}$ then the functions $\mathrm{dof}_i : \mathscr{P}_{h,0} \to \mathbb{R}$ map each function in $\mathscr{P}_{h,0}$ to the degree of freedom associated with P_i.

The virtual element space for the velocity approximation reads as

$$\mathbf{V}_h(\mathsf{P}) = \left\{ \boldsymbol{v}_h \in \left[H^1(\mathsf{P}) \right]^2 : \boldsymbol{v}_{h|\partial\mathsf{P}} \in \left[\mathbb{B}\,(\partial\mathsf{P}) \right]^2, \ \mathrm{div}\,\boldsymbol{v}_h \in \mathbb{P}_0(\mathsf{P}), \right.$$

$$\left. -\Delta\boldsymbol{v}_h - \nabla s = \boldsymbol{0} \text{ for some } s \in L_0^2(\mathsf{P}) \right\},$$

$$(12.3.61a)$$

Fig. 12.4 Representation of
the degrees of freedom of
functions in $\mathbf{V}_h(\mathsf{P})$
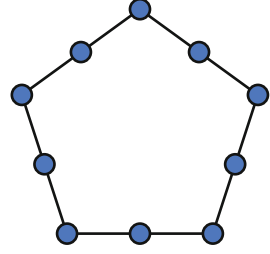
where

$$\mathbb{B}\,(\partial\mathsf{P}) = \left\{ v \in C^0(\partial\mathsf{P}) : v_{|e} \in \mathbb{P}_2(e)\ \forall e \in \partial\mathsf{P} \right\}. \tag{12.3.61b}$$

A function $\boldsymbol{v}_h \in \mathbf{V}_h(\mathsf{P})$ is uniquely characterized by the following degrees of freedom:

($\boldsymbol{D}1$) pointwise evaluations of $\boldsymbol{v}_h$ at the vertices of P;
($\boldsymbol{D}2$) pointwise evaluations at $\boldsymbol{v}_h$ at the midpoint of the edges of $\partial\mathsf{P}$.

These are represented by blue disks centered at the nodes and the mid-point of edges of the cell P, see the sample picture in Fig. 12.4.

Theorem 12.6 *Define the map* $\mathscr{K}_{\mathbf{V}_h} : \mathbf{V}_h(\mathsf{P}) \to \mathbb{R}^N$ *such that for any* $\boldsymbol{v}_h \in \mathbf{V}_h(\mathsf{P})$ *the array* $\mathscr{K}_{\mathbf{V}_h}\boldsymbol{v}_h$ *is given by the degrees of freedom pf* $\boldsymbol{v}_h$. *Then,* $\mathscr{K}_{\mathbf{V}_h}$ *is bijective.*

Proof The proof is omitted and can be found in [17].   □

The largest polynomial space that is contained in $\mathbf{V}_h(\mathsf{P})$ is the space of divergence-free, quadratic polynomial vectors, which is formally written as:

$$\mathbf{P}(\mathsf{P}) = \left\{ \boldsymbol{q} \in \left[\mathbb{P}_2(\mathsf{P})\right]^2 : \mathrm{div}\,\boldsymbol{q} \in \mathbb{P}_0(\mathsf{P}) \right\}.$$

Let $\mathscr{E}_{\P}$ denote the set of vertices and midpoints of the edges forming the polygonal boundary $\partial\mathsf{P}$, and consider the projector $\Pi_{\mathsf{P}}^{\nabla} : \mathbf{V}_h(\mathsf{P}) \to \mathbf{P}(\mathsf{P})$ such that the vector polynomial $\Pi_{\mathsf{P}}^{\nabla}\boldsymbol{v}_h$ for $\boldsymbol{v}_h \in \mathbf{V}_h(\mathsf{P})$ is the solution to the following variational problem

$$\int_{\mathsf{P}} \nabla\Pi_{\mathsf{P}}^{\nabla}\boldsymbol{v}_h : \nabla\boldsymbol{q}\, dA = \int_{\mathsf{P}} \nabla\boldsymbol{v}_h : \nabla\boldsymbol{q}\, dA \quad \forall\boldsymbol{q} \in \mathbf{P}(\mathsf{P}), \tag{12.3.62a}$$

$$P_0\left(\Pi_{\mathsf{P}}^{\nabla}\boldsymbol{v}_h\right) = \mathsf{P}_0(\boldsymbol{v}_h), \tag{12.3.62b}$$

where

$$P_0(\boldsymbol{v}_h) = \sum_{\mathsf{V} \in \mathscr{E}_\P} \boldsymbol{v}_h(\mathsf{V}). \tag{12.3.63}$$

We recall that $\nabla \boldsymbol{v}_h$, $\nabla \Pi_\P^\nabla \boldsymbol{v}_h$ and $\nabla \boldsymbol{q}$ are 2×2-sized tensors and ":" is the usual euclidean scalar product saturating both indices of such tensors, so that

$$\nabla \boldsymbol{v} : \nabla \boldsymbol{w} = \sum_{i,j} (\partial v_i / \partial x_j)(\partial w_i / \partial x_j). \tag{12.3.64}$$

To prove that this projection operator is computable, we need to show that the right-hand side of (12.3.62a) is computable for every vector-valued field $\boldsymbol{v}_h \in \mathbf{V}_h(\P)$ and $\boldsymbol{q} \in \mathbf{P}(\P)$ using only the degrees of freedom of $\boldsymbol{v}_h$. To this end, we first apply the Green theorem to find that

$$\int_\P \nabla \boldsymbol{v}_h : \nabla \boldsymbol{q} \, dA = \int_{\partial \P} \boldsymbol{v}_h \nabla \boldsymbol{q} \cdot \boldsymbol{n} \, d\ell - \int_P \boldsymbol{v}_h \cdot \Delta \boldsymbol{q} \, dA \tag{12.3.65}$$

Then, we note that $\Delta \boldsymbol{q} \in \left[\mathbb{P}_0(\P) \right]^2$ and the scalar polynomial g satisfying that

$$g = \Delta \boldsymbol{q} \cdot (\boldsymbol{x} - \boldsymbol{x}_\P) \quad \text{with} \quad \nabla g = \Delta \boldsymbol{q} \quad \text{and} \quad \int_\P g(\boldsymbol{x}) \, dA = 0. \tag{12.3.66}$$

Using this identity in (12.3.65) we see that

$$\int_\P \nabla \boldsymbol{v}_h : \nabla \boldsymbol{q} \, dA = \int_{\partial \P} \boldsymbol{v}_h \cdot \nabla \boldsymbol{q} \cdot \boldsymbol{n} \, d\ell - \int_P \boldsymbol{v}_h \cdot \Delta \boldsymbol{q} \, dA$$

$$= \int_{\partial \P} \boldsymbol{v}_h \cdot \nabla \boldsymbol{q} \cdot \boldsymbol{n} \, d\ell + \int_\P (\operatorname{div} \boldsymbol{v}_h) g \, dA - \int_{\partial \P} g \boldsymbol{v}_h \cdot \boldsymbol{n} \, d\ell$$

$$= (\mathbf{T1}) + (\mathbf{T2}) + (\mathbf{T3}).$$

The boundary integrals **(T1)** and **(T3)** are computable since the trace of $\boldsymbol{v}_h$ on every edge of $\partial \P$ can be interpolated from its degrees of freedom, while the cell integral **(T2)** is zero because $\operatorname{div} \boldsymbol{v}_h \in \mathbb{P}_0(\P)$ and we have that:

$$(\mathbf{T2}) = \int_\P (\operatorname{div} \boldsymbol{v}_h) g \, dA = (\operatorname{div} \boldsymbol{v}_h)_{|\P} \int_\P g \, dA = 0.$$

Moreover, we can see that div $\boldsymbol{v}_h$ is also computable on using the degrees of freedom of $\boldsymbol{v}_h$ and the divergence theorem:

$$(\text{div}\,\boldsymbol{v}_h)_{|\mathsf{P}}\,|\mathsf{P}| = \int_\mathsf{P} \text{div}\,\boldsymbol{v}_h\,dA = \int_{\partial\mathsf{P}} \boldsymbol{v}_h \cdot \boldsymbol{n}\,d\ell$$

so that

$$(\text{div}\,\boldsymbol{v}_h)_{|\mathsf{P}} = \frac{1}{|\mathsf{P}|} \sum_{e\in\partial\mathsf{P}} \int_e \boldsymbol{v}_h \cdot \boldsymbol{n}\,d\ell.$$

This formula makes it possible to compute the divergence of $\boldsymbol{v}_h$ using only the boundary information that can be extracted from $(\boldsymbol{D1})$ and $(\boldsymbol{D2})$.

To approximate the terms of the MHD variational formulation that depends on the time derivative of the velocity field, we need the L^2-orthogonal projection of the virtual element vector-valued fields. However, such projection operator is not directly computable in the space $\mathbf{V}_h(\mathsf{P})$, so we change the definition of the space according to the enhancement strategy in [79] that we briefly review below. First, we consider the auxiliary finite dimensional functional spaces

$$\mathscr{G}_2\,(\mathsf{P}) = \nabla\mathbb{P}_3(\mathsf{P}) \tag{12.3.67}$$

and its orthogonal complement in $[\mathbb{P}_2(\mathsf{P})]^2$

$$\mathscr{G}_2^\perp\,(\mathsf{P}) = \left\{ \boldsymbol{g}^\perp \in [\mathbb{P}_2(\mathsf{P})]^2 : (\boldsymbol{g}^\perp, \boldsymbol{g})_\mathsf{P} = 0 \;\forall \boldsymbol{g} \in \mathscr{G}_2\,(\mathsf{P}) \right\}. \tag{12.3.68}$$

Then, we introduce the "extended" virtual element space

$$\mathbf{U}_h(\mathsf{P}) = \left\{ \boldsymbol{v}_h \in \left[H^1(\mathsf{P}) \right]^2 : \boldsymbol{v}_{h|\partial\mathsf{P}} \in \left[\mathbb{B}\,(\partial\mathsf{P}) \right]^2, \;\; \text{div}\,\boldsymbol{v}_h \in \mathbb{P}_0(\mathsf{P}) \right.$$

$$\left. - \Delta\boldsymbol{v}_h - \nabla s = \boldsymbol{g}^\perp \text{ for some } s \in L_0^2(\mathsf{P}), \; \boldsymbol{g}^\perp \in \mathscr{G}_2^\perp\,(\mathsf{P}) \right\}. \tag{12.3.69}$$

The projector Π_P^∇ can also defined in $\mathbf{U}_h(\mathsf{P})$ and is computable using only the information from the degrees of freedom $(\boldsymbol{D1})$–$(\boldsymbol{D2})$. However, the degrees of freedom $(\boldsymbol{D1})$–$(\boldsymbol{D2})$ are *not* unisolvent in $\mathbf{U}_h(\mathsf{P})$. Instead, they are unisolvent in $\mathscr{T}\,\mathscr{V}_h(\mathsf{P})$, the subspace of $\mathbf{U}_h(\mathsf{P})$ that is formally defined as

$$\mathscr{T}\,\mathscr{V}_h(\mathsf{P}) = \left\{ \boldsymbol{v}_h \in \mathbf{U}_h(\mathsf{P}) : \left(\boldsymbol{v}_h - \Pi_\mathsf{P}^\nabla\boldsymbol{v}_h, \boldsymbol{g}^\perp \right)_\mathsf{P} = 0 \;\forall \boldsymbol{g}^\perp \in \mathscr{G}_2^\perp\,(\mathsf{P})\,/\mathbb{R}^2 \right\}. \tag{12.3.70}$$

Since the degrees of freedom (**D1**)–(**D2**) are unsolvent in this space, we can define a special projection operator $\mathfrak{I}_P^{\mathscr{T}\mathscr{V}_h} : \left[H^1(\mathsf{P})\right]^2 \to \mathscr{T}\mathscr{V}_h(\mathsf{P})$ such that for $\boldsymbol{v} \in \left[H^1(\mathsf{P})\right]^2$ its evaluation $\mathfrak{I}_P^{\mathscr{T}\mathscr{V}_h}(\boldsymbol{v}) \in \mathscr{T}\mathscr{V}_h(\mathsf{P})$ has the degrees of freedom determined by the following three criteria on every edge $e \in \partial\mathsf{P}$:

(**U1**) $\mathfrak{I}_P^{\mathscr{T}\mathscr{V}_h}(\boldsymbol{v}) \in \mathbb{P}_2(\mathsf{P})$.
(**U2**) $\mathfrak{I}_P^{\mathscr{T}\mathscr{V}_h}(\boldsymbol{v})$ interpolates $\boldsymbol{v}$ at each node.
(**U3**) $\int_e \mathfrak{I}^{\mathscr{T}\mathscr{V}_h}(\boldsymbol{v}) \cdot \boldsymbol{n}d\ell = \int_e \boldsymbol{v} \cdot \boldsymbol{n}d\ell$.

Note that, criterion (**U1**) guarantees that, over each edge, $\mathfrak{I}_P^{\mathscr{T}\mathscr{V}_h}(\boldsymbol{v})$ is entirely determined by the evaluation at three points. Two of these points are attained by criterion (**U2**) since we have that at the endpoints of each edge the evaluation of $\boldsymbol{u}$ and $\mathfrak{I}_P^{\mathscr{T}\mathscr{V}_h}(\boldsymbol{v})$ agree. The last evaluation given at the midpoint is computed specifically to satisfy (**U3**). Having described a method for computing the degrees of freedom of $\mathfrak{I}_P^{\mathscr{T}\mathscr{V}_h}(\boldsymbol{v})$ the unisolvency of the virtual element will guarantee the uniqueness of its image and thus $\mathfrak{I}_P^{\mathscr{T}\mathscr{V}_h}$ is well-defined.

We define the L^2-orthogonal projection operator $\Pi_{\mathsf{P}}^0 : \mathscr{T}\mathscr{V}_h(\mathsf{P}) \to \mathbf{P}(\mathsf{P})$, so that for every $\boldsymbol{v}_h \in \mathscr{T}\mathscr{V}_h(\mathsf{P})$, the vector polynomial $\Pi_{\mathsf{P}}^0\boldsymbol{v}_h$ is the solution to the variational problem

$$\left(\Pi_{\mathsf{P}}^0\boldsymbol{v}_h - \boldsymbol{v}_h, \boldsymbol{q}\right)_{\mathsf{P}} = 0. \quad \forall \boldsymbol{q} \in \mathbf{P}(\mathsf{P}). \tag{12.3.71}$$

We show that $\Pi_{\mathsf{P}}^0\boldsymbol{v}_h$ is computable using only the degrees of freedom (**D1**)–(**D2**) of $\boldsymbol{v}_h$. Let $\boldsymbol{v}_h \in \mathscr{T}\mathscr{V}_h(\mathsf{P})$ and $\boldsymbol{q} \in \mathbf{P}(\mathsf{P})$. We consider the decomposition $\boldsymbol{q} = \nabla g + \boldsymbol{g}^\perp$ where $g \in \mathbb{P}_3(\mathsf{P})$ and apply the Green theorem to obtain:

$$\int_{\mathsf{P}} \boldsymbol{v}_h \cdot \boldsymbol{q}\, dA = \int_{\mathsf{P}} \boldsymbol{v}_h \cdot \nabla g\, dA + \int_{\mathsf{P}} \boldsymbol{v}_h \cdot \boldsymbol{g}^\perp\, dA. \tag{12.3.72}$$

$$= \int_{\partial\mathsf{P}} \boldsymbol{v}_h \cdot \boldsymbol{n}g\, d\ell - \int_{\mathsf{P}} \operatorname{div}\boldsymbol{v}_h g\, dA + \int_{\mathsf{P}} \boldsymbol{v}_h \cdot \boldsymbol{g}^\perp\, dA. \tag{12.3.73}$$

The boundary integral on the right is computable as the trace of $\boldsymbol{v}_h$ on every edge is a quadratic polynomial that can be interpolated from the degrees of freedom freedom (**D1**)–(**D2**) of $\boldsymbol{v}_h$. The second integral in the right-hand side is zero because $\operatorname{div}\boldsymbol{v}_{h|\mathsf{P}} \in \mathbb{P}_0(\mathsf{P})$ and we can always take a function g with zero elemental average (alternatively, it can be computed by noting that the divergence of $\boldsymbol{v}_h$ is given by the divergence theorem). To compute the second integral in (12.3.73) we first write

$$\boldsymbol{g}^\perp = \boldsymbol{c} + (\boldsymbol{g}^\perp - \boldsymbol{c}), \quad \boldsymbol{c} = \frac{1}{|\mathsf{P}|} \int_{\mathsf{P}} \boldsymbol{g}^\perp\, dA.$$

Since $\mathbf{c} \in \mathbb{P}_0(\mathsf{P})$ we can find $q \in \mathbb{P}_1(\mathsf{P})$ such that $\mathbf{c} = \nabla q$ and see that

$$\int_{\mathsf{P}} \mathbf{v}_h \cdot \mathbf{c} \, dA = \int_{\partial\mathsf{P}} q\mathbf{v}_h \cdot \mathbf{n} \, d\ell - \int_{\mathsf{P}} \mathrm{div}\, \mathbf{v}_h q \, dA.$$

Finally, we note that $\mathbf{g}^{\perp} - \mathbf{c} \in \mathcal{G}_2^{\perp}(\mathsf{P})/\mathbb{R}^2$, and the definition of space $\mathscr{T}\mathscr{V}_h(\mathsf{P})$ implies that

$$\int_{\mathsf{P}} \mathbf{v}_h \cdot (\mathbf{g}^{\perp} - \mathbf{c}) \, dA = \int_{\mathsf{P}} \Pi_{\mathsf{P}}^{\nabla} \mathbf{v}_h \cdot (\mathbf{g}^{\perp} - \mathbf{c}) \, dA.$$

The last integral is computable because $\Pi_{\mathsf{P}}^{\nabla} \mathbf{v}_h$ is computable from the degrees of freedom of $\mathbf{v}_h$ and $\mathbf{g}^{\perp} - \mathbf{c}$ is a known function.

We use the projection operators Π_{P}^0 and $\Pi_{\mathsf{P}}^{\nabla}$ to define the inner product and semi-inner product in $\mathscr{T}\mathscr{V}_h(\mathsf{P})$ as follows

$$\big(\mathbf{u}_h, \mathbf{v}_h\big)_{\mathscr{T}\mathscr{V}_h(\mathsf{P})} = \big(\Pi_{\mathsf{P}}^0 \mathbf{u}_h, \Pi_{\mathsf{P}}^0 \mathbf{v}_h\big)_{\mathsf{P}} + \mathscr{S}_{\mathsf{P}}^{\mathscr{T}\mathscr{V}_h}\big((1 - \Pi_{\mathsf{P}}^0)\mathbf{u}_h, (1 - \Pi_{\mathsf{P}}^0)\mathbf{v}_h\big), \tag{12.3.74}$$

$$\big[\mathbf{u}_h, \mathbf{v}_h\big]_{\mathscr{T}\mathscr{V}_h(\mathsf{P})} = \big(\nabla \Pi_{\mathsf{P}}^{\nabla} \mathbf{u}_h, \nabla \Pi_{\mathsf{P}}^{\nabla} \mathbf{v}_h\big)_{\mathsf{P}} + \mathscr{T}_{\mathsf{P}}^{\mathscr{T}\mathscr{V}_h}\big(\nabla(1 - \Pi_{\mathsf{P}}^{\nabla})\mathbf{u}_h, \nabla(\mathscr{I} - \Pi_{\mathsf{P}}^{\nabla})\mathbf{v}_h\big), \tag{12.3.75}$$

for every $\mathbf{u}_h, \mathbf{v}_h$ in $\mathscr{T}\mathscr{V}_h(\mathsf{P})$. Here, $\mathscr{S}_{\mathsf{P}}^{\mathscr{T}\mathscr{V}_h}$ and $\mathscr{T}_{\mathsf{P}}^{\mathscr{T}\mathscr{V}_h}$ are the stabilizing terms, i.e., any continuous bilinear forms for which there exist two pairs of strictly positive constants (t_*, t^*) and (s_*, s^*), which are independent of h, such that

$$s_* \|\mathbf{v}_h\|_{0,\mathsf{P}}^2 \leq \mathscr{S}_{\mathsf{P}}^{\mathscr{T}\mathscr{V}_h}(\mathbf{v}_h, \mathbf{v}_h) \leq s^* \|\mathbf{v}_h\|_{0,\mathsf{P}}^2 \quad \forall \mathbf{v}_h \in \mathscr{T}\mathscr{V}_h(\mathsf{P}) \cap \ker(\Pi_{\mathsf{P}}^0), \tag{12.3.76}$$

$$t_* \|\nabla \mathbf{v}_h\|_{0,\mathsf{P}}^2 \leq \mathscr{T}_{\mathsf{P}}^{\mathscr{T}\mathscr{V}_h}(\nabla \mathbf{v}_h, \nabla \mathbf{v}_h) \leq t^* \|\nabla \mathbf{v}_h\|_{0,\mathsf{P}}^2 \quad \forall \mathbf{v}_h \in \mathscr{T}\mathscr{V}_h(\mathsf{P}) \cap \ker(\Pi_{\mathsf{P}}^{\nabla}). \tag{12.3.77}$$

In practice, we can design such stabilizations as in [45, 67]. The inner and semi-inner products respectively defined in (12.3.76) and (12.3.77) satisfy two fundamental properties, e.g., **Polynomial Consistency** and **Stability**, which are stated in the following theorem.

Theorem 12.7 *The inner product defined in* (12.3.76) *and semi-inner products defined in* (12.3.77) *have the two properties:*

– **Polynomial Consistency**: *for every vector-valued field* $\boldsymbol{v}_h \in \mathscr{T} \mathscr{V}_h(\mathsf{P})$ *and polynomial* $\boldsymbol{q} \in [\mathbb{P}_2(\mathsf{P})]^2$ *it holds that:*

$$\big(\boldsymbol{v}_h, \boldsymbol{q}\big)_{\mathscr{T} \mathscr{V}_h(\mathsf{P})} = \big(\boldsymbol{v}_h, \boldsymbol{q}\big)_\mathsf{P} \quad and \quad \big[\boldsymbol{v}_h, \boldsymbol{q}\big]_{\mathscr{T} \mathscr{V}_h(\mathsf{P})} = \big(\nabla \boldsymbol{v}_h, \nabla \boldsymbol{q}\big)_\mathsf{P}.$$
(12.3.78)

– **Stability**: *there exists a pairs of strictly positive constants* (t_*, t^*) *independent of h such that*

$$t_* \|\boldsymbol{v}_h\|_{0,\mathsf{P}}^2 \leq \big(\boldsymbol{v}_h, \boldsymbol{v}_h\big)_{\mathscr{T} \mathscr{V}_h(\mathsf{P})} \leq t^* \|\boldsymbol{v}_h\|_{0,\mathsf{P}}^2,$$
(12.3.79)

and

$$t_* \|\nabla \boldsymbol{v}_h\|_{0,\mathsf{P}}^2 \leq \big[\boldsymbol{v}_h, \boldsymbol{v}_h\big]_{\mathscr{T} \mathscr{V}_h(\mathsf{P})} \leq t^* \|\boldsymbol{v}_h\|_{0,\mathsf{P}}^2.$$
(12.3.80)

for any $\boldsymbol{v}_h \in \mathscr{T} \mathscr{V}_h(\mathsf{P})$.

Proof The proof of this theorem uses the same argument of the proof of Theorem 12.2 and is, thus, omitted. □

The global space $\mathscr{T} \mathscr{V}_h$ is given by

$$\mathscr{T} \mathscr{V}_h = \Big\{ \boldsymbol{v}_h \in \Big[H^1(\Omega) \Big]^2 : \forall \mathsf{P} \in \Omega_h \quad \boldsymbol{v}_{h|\mathsf{P}} \in \mathscr{T} \mathscr{V}_h(\mathsf{P}) \Big\}.$$

We will endow this space with an inner product and a semi-inner product beginning with their local definitions.

$$\big(\boldsymbol{u}_h, \boldsymbol{v}_h\big)_{\mathscr{T} \mathscr{V}_h} = \sum_{\mathsf{P} \in \Omega_h} \big(\boldsymbol{u}_h, \boldsymbol{v}_h\big)_{\mathscr{T} \mathscr{V}_h(\mathsf{P})} \quad \forall \boldsymbol{u}_h, \boldsymbol{v}_h \in \mathscr{T} \mathscr{V}_h,$$

$$\big[\boldsymbol{u}_h, \boldsymbol{v}_h\big]_{\mathscr{T} \mathscr{V}_h} = \sum_{\mathsf{P} \in \Omega} \big[\boldsymbol{u}_h, \boldsymbol{v}_h\big]_{\mathscr{T} \mathscr{V}_h(\mathsf{P})} \quad \forall \boldsymbol{u}_h, \boldsymbol{v}_h \in \mathscr{T} \mathscr{V}_h.$$

These inner product and semi-inner product induce the norms and semi-norm

$$\||\boldsymbol{v}_h\||_{\mathscr{T} \mathscr{V}_h} = \big(\boldsymbol{v}_h, \boldsymbol{v}_h\big)_{\mathscr{T} \mathscr{V}_h}^{1/2}, \quad |\boldsymbol{v}_h|_{\mathscr{T} \mathscr{V}_h} = \big[\boldsymbol{v}_h, \boldsymbol{v}_h\big]_{\mathscr{T} \mathscr{V}_h}^{1/2},$$
(12.3.81a)

$$\||\boldsymbol{v}_h\||_{1, \mathscr{T} \mathscr{V}_h} = \Big(\||\boldsymbol{v}_h\||_{\mathscr{T} \mathscr{V}_h}^2 + |\boldsymbol{v}_h|_{\mathscr{T} \mathscr{V}_h}^2 \Big)^{1/2}.$$
(12.3.81b)

The norm in the topological dual space of $\mathscr{T}\mathscr{V}_{h,0}$ denoted by $\mathscr{T}\mathscr{V}_{h,0}'$ is:

$$\||\boldsymbol{f}_h\||_{-1,\mathscr{T}\mathscr{V}_h} = \sup_{\boldsymbol{v}_h \in \mathscr{T}\mathscr{V}_{h,0}\backslash\{0\}} \frac{(\boldsymbol{f}_h, \boldsymbol{v}_h)_{\mathscr{T}\mathscr{V}_h}}{|\boldsymbol{v}_h|_{\mathscr{T}\mathscr{V}_h}}.$$

The global inner product and semi-inner product and their induced norm and semi-norm also satisfy the **consistency** and **stability** properties as stated in the following corollary.

Corollary 12.3 *The norms and semi-norm in* (12.3.81) *are equivalent to the* $[L^2(\Omega)]^2$ *and* $[H^1(\Omega)]^2$ *inner products and semi-inner product respectively. In other words, there exists* $t_*, t^* > 0$ *independent of the mesh characteristics such that for any* $\boldsymbol{v}_h \in \mathscr{T}\mathscr{V}_h$ *it holds that*

$$t_*\|\boldsymbol{v}_h\|_{0,\Omega}^2 \le \||\boldsymbol{v}_h\||_{\mathscr{T}\mathscr{V}_h} \le t^*\|\boldsymbol{v}_h\|_{0,\Omega}^2, \tag{12.3.82a}$$

$$t_*\|\nabla\boldsymbol{v}_h\|_{0,\Omega}^2 \le \||\boldsymbol{v}_h\||_{\mathscr{T}\mathscr{V}_h}^{2,\nabla} \le t^*\|\nabla\boldsymbol{v}_h\|_{0,\Omega}^2, \tag{12.3.82b}$$

$$t_*\|\boldsymbol{v}_h\|_{1,\Omega}^2 \le \||\boldsymbol{v}_h\||_{1,\mathscr{T}\mathscr{V}_h}^2 \le t^*\|\boldsymbol{v}_h\|_{1,\Omega}^2. \tag{12.3.82c}$$

Proof This result is an immediate consequence of Theorem 12.7 and we omit the proof. □

We can define the global projector $\mathfrak{I}^{\mathscr{T}\mathscr{V}_h} : [H^1(\Omega)]^2 \to \mathscr{T}\mathscr{V}_h$ such that $\mathfrak{I}^{\mathscr{T}\mathscr{V}_h}(\boldsymbol{v})_{|\mathsf{P}} = \mathfrak{I}_\mathsf{P}^{\mathscr{T}\mathscr{V}_h}\left(\boldsymbol{v}_{|\mathsf{P}}\right)$ for every $\mathsf{P} \in \Omega_h$ and $\boldsymbol{v} \in [H^1(\Omega)]^2$. We also define the global space $\mathscr{T}\mathscr{V}_{h,0}$ of the functions in $\mathscr{T}\mathscr{V}_h$ with zero trace on the boundary of Ω:

$$\mathscr{T}\mathscr{V}_{h,0} = \left\{\boldsymbol{v}_h \in \mathscr{T}\mathscr{V}_h : \boldsymbol{v}_{h|\partial\Omega} \equiv \boldsymbol{0}\right\}.$$

We note that the spaces $\mathscr{T}\mathscr{V}_h$ and $\mathscr{P}_h$ also form a de Rham complex of the form

$$\begin{array}{ccc} [H^1(\Omega)]^2 & \xrightarrow{\text{div}} & L^2(\Omega) \\ \downarrow{\mathfrak{I}^{\mathscr{T}\mathscr{V}_h}} & & \downarrow{\mathscr{I}^{\mathscr{P}_h}} \\ \mathscr{T}\mathscr{V}_h & \xrightarrow{\text{div}} & \mathscr{P}_h \end{array}$$

Similar to the case in Sect. 12.3.5 this complex is commutative as we prove in the following Theorem:

Theorem 12.8 *For every* $\boldsymbol{v} \in \left[H^1(\Omega)\right]^2$ *we have that*

$$div\, \mathfrak{J}^{\mathscr{T}\,\mathscr{V}_h}(\boldsymbol{v}) = \mathscr{I}^{\mathscr{P}_h}(div\,\boldsymbol{v}). \tag{12.3.83}$$

Proof Consider a cell $\mathsf{P} \in \Omega_h$ then according to the criterion (**U3**) we have that

$$\int_{\partial \mathsf{P}} \mathfrak{J}^{\mathscr{T}\,\mathscr{V}_h}(\boldsymbol{v}) \cdot \boldsymbol{n} d\ell = \sum_{e \in \partial \mathsf{P}} \int_e \mathfrak{J}^{\mathscr{T}\,\mathscr{V}_h}(\boldsymbol{v}) \cdot \boldsymbol{n} d\ell =$$

$$= \sum_{e \in \partial \mathsf{P}} \int_e \mathfrak{J}^{\mathscr{T}\,\mathscr{V}_h}(\boldsymbol{v}) \cdot \boldsymbol{n} d\ell = \int_{\partial \mathsf{P}} \mathfrak{J}^{\mathscr{T}\,\mathscr{V}_h}(\boldsymbol{v}) \cdot \boldsymbol{n} d\ell. \tag{12.3.84}$$

Therefore, since $div\, \mathfrak{J}^{\mathscr{T}\,\mathscr{V}_h}(\boldsymbol{u}) \in \mathbb{P}_0(\mathsf{P})$ we can use the divergence theorem to compute its divegence yielding that

$$div\, \mathfrak{J}^{\mathscr{T}\,\mathscr{V}_h}(\boldsymbol{v}) = \frac{1}{|\mathsf{P}|} \int_{\partial \mathsf{P}} \mathfrak{J}^{\mathscr{T}\,\mathscr{V}_h}(\boldsymbol{v}) \cdot \boldsymbol{n} d\ell = \frac{1}{|\mathsf{P}|} \int_{\partial \mathsf{P}} \boldsymbol{v} \cdot \boldsymbol{n} d\ell =$$

$$= \frac{1}{|\mathsf{P}|} \int_{\mathsf{P}} div\, \boldsymbol{v} dA = \mathscr{I}^{\mathscr{P}_h}(div\,\boldsymbol{v}). \tag{12.3.85}$$

$\square$

Note that the set of degrees of freedom are transformed in accordance to the diagram:
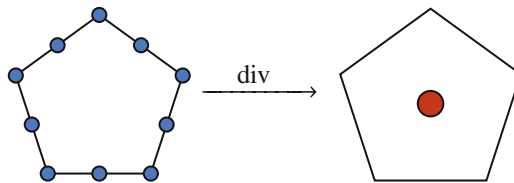
Moreover, we can also guarantee that our scheme yields velocity fields that are exactly divergence free. We prove this fact in the following Theorem:

Theorem 12.9 *Assume that* $\{\boldsymbol{u}_h^n\}_{n=0}^N$ *solve the discrete formulation* (12.3.4) *then*

$$\forall n \in [0, N]: \quad div\, \boldsymbol{u}_h^n = 0. \tag{12.3.86}$$

Proof For the case $n = 0$ we know that div $\boldsymbol{u}_0 = 0$, thus by Theorem 12.8 we have that

$$\text{div } \boldsymbol{u}_h^0 = \text{div } \mathfrak{I}^{\mathscr{T}\mathscr{V}_h}(\boldsymbol{u}_0) = \mathscr{I}^{\mathscr{P}_h}(\text{div } \boldsymbol{u}_0) = \mathscr{I}^{\mathscr{P}_h}(0) = 0. \qquad (12.3.87)$$

Let $0 < n \leq N$ then, we know by definition of $\mathscr{T}\mathscr{V}_h$ that div $\boldsymbol{u}_h^n \in \mathscr{P}_h$. Moreover, since $\mathfrak{I}^{\mathscr{T}\mathscr{V}_h}$ preserves line integrals we can deduce that

$$\int_\Omega \text{div } \boldsymbol{u}_h^n dA = \int_{\partial\Omega} \mathfrak{I}^{\mathscr{T}\mathscr{V}_h}(\boldsymbol{u}_b(n\Delta t)) \cdot \boldsymbol{n} d\ell = \int_{\partial\Omega} uv_b(n\Delta t) \cdot \boldsymbol{n} d\ell = 0. \qquad (12.3.88)$$

Thus, it is the case that div $\boldsymbol{u}_h \in \mathscr{P}_{h,0}$. Finally, by Eq. (12.2.2a) we know that div $\boldsymbol{u}_h^n$ is orthogonal to every function in $\mathscr{P}_{h,0}$ implying that

$$\text{div } \boldsymbol{u}_h^n = 0. \qquad (12.3.89)$$

$\square$

Remark 12.2 Classically in the VEM literature readers will find the more common interpolation operator $\mathscr{I}^{\mathscr{T}\mathscr{V}_h}$ instead of $\mathfrak{I}^{\mathscr{T}\mathscr{V}_h}$. This operator is set in such a way that for $\boldsymbol{v} \in [H^1(\Omega)]^2$ the image $\mathscr{I}^{\mathscr{V}_h}(\boldsymbol{v})$ and preimage $\boldsymbol{v}$ share the exact same degrees of freedom. However, this operator will not yield a commuting De-Rham complex. More importantly, unless the initial and boundary conditions $\boldsymbol{u}_b$ and $\boldsymbol{u}_0$ are piecewise quadratic polynomials over the set of edges of the mesh the value of the line integrals will not agree with the intepolated quantities. This will guarantee that the method will NOT yield divergence free velocity fields since in this case

$$\int_\Omega \text{div } \boldsymbol{u}_h dA = \int_{\partial\Omega} \boldsymbol{u}_h \cdot \boldsymbol{n} d\ell = \int_{\partial\Omega} \mathscr{I}^{\mathscr{T}\mathscr{V}_h}(\boldsymbol{u}_0) \cdot \boldsymbol{n} d\ell \neq 0. \qquad (12.3.90)$$

Rather, the best we can hope for is that the divergence of the velocity field will vanish as the mesh size shrinks. We amend this deficiency by using the special projector $\mathfrak{I}^{\mathscr{T}\mathscr{V}_h}$.

Finally, we present a result regarding the stability of the virtual element approximations using the spaces $\mathscr{T}\mathscr{V}_{h,0}$ and $\mathscr{P}_{h,0}$, which are specifically chosen to satisfy an inf-sup condition.

Theorem 12.10 *The projector* $\mathfrak{I}^{\mathscr{T}\mathscr{V}_h} : [H_0^1(\Omega)]^2 \to \mathscr{T}\mathscr{V}_{h,0}$ *satisfies*

$$\left(\text{div } \mathfrak{I}^{\mathscr{T}\mathscr{V}_h}\boldsymbol{v}, q_h\right)_{\mathscr{P}_h} = \left(\text{div } \boldsymbol{v}, q_h\right)_{\mathscr{P}_h} \quad \text{and} \quad \||\mathfrak{I}^{\mathscr{T}\mathscr{V}_h}\boldsymbol{v}\||_{1,\mathscr{T}\mathscr{V}_h} \leq C_\pi \|\boldsymbol{v}\|_{1,\Omega},$$

for every vector-valued field $v \in \left[H_0^1(\Omega) \right]^2$ *and scalar function* $q_h \in \mathscr{P}_{h,0}$. *Here,* C_π *is a positive, real constant independent of h. As a consequence, the two spaces* $\mathscr{T}\mathscr{V}_{h,0}$ *and* $\mathscr{P}_{h,0}$ *form an inf-sup stable pair and satisfy*

$$\inf_{q_h \in \mathscr{P}_{h,0}} \sup_{v_h \in \mathscr{T}\mathscr{V}_{h,0}} \frac{\left(div\, v_h, q_h \right)_{\mathscr{P}_h}}{|||v_h|||_{1,\mathscr{T}\mathscr{V}_h} |||q_h|||_{\mathscr{P}_h}} > \beta_\pi > 0 \qquad (12.3.91)$$

for some real and strictly positive constant β_π.

This theorem provides a major result since a pair of finite element spaces that do not satisfy such an inf-sup condition will yield unstable simulations of fluid flow phenomena.

12.4 Energy Estimates

The conforming nature of our VEM allows us to mimic many properties of the continuous setting. Among them, one of the more important is the preservation of certain types of estimates in the $L^2(\Omega)$-norm, which are obtained by testing the variational formulation against the exact solution and applying Gronwall's lemma, see [51]. In this section, we present an estimate of this type for the continuous system (12.2.2a)–(12.2.2e) and its discrete counterpart (12.3.4a)–(12.3.5).

We start with the decompositions

$$u = \widehat{u} + u_b \quad \text{and} \quad E = \widehat{E} + E_b, \qquad (12.4.1)$$

where u_b and E_b are extensions of the boundary conditions inside the domain and $\widehat{u} \in \left[H_0^1(\Omega) \right]^2$ and $\widehat{E} \in H_0(\mathbf{rot}; \Omega)$ are functions to be found. The extension to the boundary condition of the velocity field is such that

$$\text{div}\, u_b = 0 \quad \text{in} \quad \Omega \quad \text{and} \quad u_b(x) = \mathbf{0} \quad \text{if} \quad d(x, \partial\Omega) \geq \epsilon$$

for $h > \epsilon > 0$ for a given threshold ϵ, $d(x, \partial\Omega)$ being the distance between x and the boundary $\partial\mathsf{P}$. We can construct such an extension u_b by defining the domain $\Omega_\epsilon = \left\{ x \in \Omega : d(x, \partial\Omega) < \epsilon \right\}$ and taking u_b to be the solution to the problem:

$$-\Delta\widehat{u}_b + \nabla s = \mathbf{0} \qquad \text{in } \Omega_\epsilon, \qquad (12.4.2a)$$

$$\text{div}\,\widehat{u}_b = 0 \qquad \text{in } \Omega_\epsilon, \qquad (12.4.2b)$$

$$\widehat{u}_b = u_b \qquad \text{on } \partial\Omega, \qquad (12.4.2c)$$

$$\widehat{u}_b = \mathbf{0} \qquad \text{on } \partial(\Omega \setminus \Omega_\epsilon). \qquad (12.4.2d)$$

Problem (12.4.2) is well-posed, cf. [28]. We further decompose the current density into its values along the boundary and the interior by:

$$\widehat{J} = \widehat{E} + \widehat{u} \times B \quad \text{and} \quad J_b = E_b + u_b \times B.$$

The following theorem gives the continuous energy estimate. Similar estimates are reported in [54, 62, 63].

Theorem 12.11 *Let* (u, B, E, p) *solve the variational formulation* (12.2.15a)–(12.2.15d) *in the time interval* $[0, T]$. *Then,*

$$\frac{1}{2}\frac{d}{dt}\|\widehat{u}\|_{0,\Omega}^2 + \frac{1}{2R_m}\frac{d}{dt}\|B\|_{0,\Omega}^2 + R_e^{-1}\|\nabla\widehat{u}\|_{0,\Omega}^2 + \|\widehat{J}\|_{0,\Omega}^2$$

$$= \left(f, \widehat{u}\right) - \left(\frac{\partial}{\partial t}u_b, \widehat{u}\right) - R_e^{-1}\left(\nabla u_b, \nabla\widehat{u}\right) - R_m^{-1}\left(\mathbf{rot}\,E_b, B\right) - \left(J_b, \widehat{J}\right),$$

(12.4.3)

and

$$\frac{e^{-T}}{2}\|\widehat{u}(T)\|_{0,\Omega}^2 + \frac{e^{-T}}{2R_m}\|B(T)\|_{0,\Omega}^2 + \int_0^T\left(\frac{e^{-t}}{2R_e}\|\nabla\widehat{u}\|_{0,\Omega}^2 + \frac{e^{-t}}{2}\|\widehat{J}\|_{0,\Omega}^2\right)dt$$

$$\leq \frac{e^{-T}}{2}\|\widehat{u}(0)\|_{0,\Omega}^2 + \frac{e^{-T}}{2R_m}\|B(0)\|_{0,\Omega}^2$$

$$+ \int_0^T\left(e^{-t}R_e\|f\|_{-1,\Omega}^2 + \frac{e^{-t}}{2}\frac{d}{dt}\|u_b\|_{0,\Omega}^2 + R_e^{-1}e^{-t}\|\nabla u_b\|_{0,\Omega}^2\right.$$

$$+ \frac{e^{-t}}{2R_m}\|\mathbf{rot}\,E_b\|_{0,\Omega}^2 + \frac{e^{-t}}{2}\|J_b\|_{0,\Omega}^2\right)dt.$$

(12.4.4)

For the discrete version of the estimates presented in Theorem 12.11, for any $n \in [0, N-1]$, we decompose

$$E_h^{n+\theta} = \widehat{E}_h^{n+\theta} + \mathscr{I}^{\mathscr{V}_h}(E_b^{n+\theta}),$$

(12.4.5)

$$u_h^{n+1} = \widehat{u}_h^{n+1} + \mathfrak{I}^{\mathscr{T}\mathscr{V}_h}(u_b^{n+1}),$$

(12.4.6)

where $(\widehat{E}_h^{n+\theta}, \widehat{u}_h^{n+\theta}) \in \mathscr{V}_{h,0} \times \mathscr{T}\mathscr{V}_{h,0}$ and E_b, u_b are such that their evaluations in $\Omega \setminus \Omega_\epsilon$ are identically zero. The condition on the boundary data is required to guarantee that the degrees of freedom of these boundary fields all lie along the

boundary. Next, for any n, $0 \leq n \leq N-1$, we define

$$\widehat{J}_h^{n+\theta} = \widehat{E}_h^{n+\theta} + \mathscr{I}^{\mathscr{V}_h}(\widehat{\boldsymbol{u}}_h^{n+\theta} \times \Pi^{RT}\boldsymbol{B}_h^{n+\theta}),$$

$$J_{h,b}^{n+\theta} = \mathscr{I}^{\mathscr{V}_h}(E_b^{n+\theta}) + \mathscr{I}^{\mathscr{V}_h}(\boldsymbol{u}_b^{n+\theta} \times \Pi^{RT}\boldsymbol{B}_h^{n+\theta}).$$

The next result is a discrete counterpart of Theorem 12.11.

Theorem 12.12 *Let* $\left\{(\boldsymbol{u}_h^n, \boldsymbol{B}_h^n)\right\}_{n=0}^{N} \subset \mathscr{T}\mathscr{V}_h \times \mathscr{E}_h$ *and* $\left\{(E_h^{n+\theta}, p_h^{n+\theta}))\right\}_{n=0}^{N-1} \subset$ $\mathscr{V}_h \times \mathscr{P}_{h,0}$ *solve the virtual element formulation* (12.3.4a)–(12.3.5)*. Then, it holds that*

$$(\mathbf{L1}) + (\mathbf{L2}) = (\mathbf{R}), \tag{12.4.7}$$

where

$$(\mathbf{L1}) = \Delta t\left(\theta - 1/2\right)\left(\frac{\|\|\widehat{\boldsymbol{u}}_h^{n+1} - \widehat{\boldsymbol{u}}_h^{n}\|\|_{\mathscr{T}\mathscr{V}_h}^2}{\Delta t^2} + \frac{\|\|\boldsymbol{B}_h^{n+1} - \boldsymbol{B}_h^{n}\|\|_{\mathscr{E}_h}^2}{\Delta t^2 R_m}\right)$$

$$+ \left(\frac{\|\|\widehat{\boldsymbol{u}}_h^{n+1}\|\|_{\mathscr{T}\mathscr{V}_h}^2 - \|\|\widehat{\boldsymbol{u}}_h^{n}\|\|_{\mathscr{T}\mathscr{V}_h}^2}{2\Delta t} + \frac{\|\|\boldsymbol{B}_h^{n+1}\|\|_{\mathscr{E}_h}^2 - \|\|\boldsymbol{B}_h^{n}\|\|_{\mathscr{E}_h}^2}{2\Delta t R_m}\right), \tag{12.4.8a}$$

$$(\mathbf{L2}) = R_e^{-1}\left|\widehat{\boldsymbol{u}}_h^{n+\theta}\right|_{\mathscr{T}\mathscr{V}_h}^2 + \|\|\widehat{J}_h^{n+\theta}\|\|_{\mathscr{V}_h}^2 + \tag{12.4.8b}$$

$$(\mathbf{R}) = \left(\boldsymbol{f}_h, \widehat{\boldsymbol{u}}_h^{n+\theta}\right)_{\mathscr{T}\mathscr{V}_h} - \left(\frac{\mathfrak{I}^{\mathscr{T}\mathscr{V}_h}\boldsymbol{u}_b^{n+1} - \mathfrak{I}^{\mathscr{T}\mathscr{V}_h}\boldsymbol{u}_b^{n}}{\Delta t}, \widehat{\boldsymbol{u}}_h^{n+\theta}\right)_{\mathscr{T}\mathscr{V}_h}$$

$$- R_e^{-1}\left[\mathfrak{I}^{\mathscr{T}\mathscr{V}_h}\boldsymbol{u}_b^{n+\theta}, \widehat{\boldsymbol{u}}_h^{n+\theta}\right]_{\mathscr{T}\mathscr{V}_h} - \left(J_{h,b}^{n+\theta}, \widehat{J}_h^{n+\theta}\right)_{\mathscr{V}_h}$$

$$- R_m^{-1}\left(\mathbf{rot}\,\mathscr{I}^{\mathscr{V}_h}E_b^{n+\theta}, \boldsymbol{B}_h^{n+\theta}\right)_{\mathscr{E}_h}. \tag{12.4.8c}$$

If $\theta \in [1/2, 1]$,

$$\alpha^N\left(\|\|\widehat{\boldsymbol{u}}_h^{N}\|\|_{\mathscr{T}\mathscr{V}_h}^2 + R_m^{-1}\|\|\boldsymbol{B}_h^{N}\|\|_{\mathscr{E}_h}^2\right)$$

$$+ \sum_{n=0}^{N}\gamma\alpha^n\left(R_e^{-1}\left|\widehat{\boldsymbol{u}}_h^{n+\theta}\right|_{\mathscr{T}\mathscr{V}_h}^2 + \|\|\widehat{J}_h^{n+\theta}\|\|_{\mathscr{V}_h}^2\right)\Delta t$$

$$\leq \left(|||\mathfrak{I}^{\mathscr{T}\,\mathscr{V}_h}(\boldsymbol{u}_0)|||^2_{\mathscr{T}\,\mathscr{V}_h} + R_m^{-1} |||\mathscr{I}^{\,\mathscr{E}_h}(\boldsymbol{B}_0)|||^2_{\mathscr{E}_h} \right)$$

$$+ \sum_{n=0}^{N} \gamma \alpha^n \big(R_e |||\boldsymbol{f}_h|||^2_{-1,\,\mathscr{T}\,\mathscr{V}_h} + \Delta t^{-1} |||\mathfrak{I}^{\mathscr{T}\,\mathscr{V}_h}(\boldsymbol{u}_b^{n+1} - \boldsymbol{u}_b^n)|||^2_{\mathscr{T}\,\mathscr{V}_h}$$

$$+ R_e^{-1} \big| \mathscr{I}^{\mathscr{V}_h} \boldsymbol{u}_b^{n+\theta} \big|^2_{\mathscr{T}\,\mathscr{V}_h}$$

$$+ R_m^{-1} |||\mathbf{rot}\,\mathscr{I}^{\mathscr{V}_h} E_b^{n+\theta}|||^2_{\mathscr{E}_h} + |||J_{h,b}^{n+\theta}|||^2_{\mathscr{V}_h} \big) \Delta t, \qquad (12.4.9)$$

12.5 Linearization

In this section, we are mainly concerned with the development of a solver for the discrete problem (12.3.4a)–(12.3.5) at a given time instant. For this reason, we keep θ and n fixed, and we omit them from our notation when not strictly necessary. This section is based on the reference [41].

In practice, we manipulate arrays of degrees of freedom of virtual element scalar and vector functions, which we represent as row vectors and denote with the superscript I, e.g., $\boldsymbol{u}_h^I$ is the row vector of degrees of freedom of $\boldsymbol{u}_h$. We introduce the finite dimensional linear space of *column* vectors

$$\mathscr{X}_{h,0} = \left\{ (\boldsymbol{v}_h^I, \boldsymbol{C}_h^I, D_h^I, q_h^I)^T \, : \, (\boldsymbol{v}_h, \boldsymbol{C}_h, D_h, q_h) \in \mathscr{T}\,\mathscr{V}_{h,0} \times \mathscr{E}_h \times \mathscr{V}_{h,0} \times \mathscr{P}_{h,0} \right\},$$

equipped with the Euclidean (ℓ^2) inner product.

We pose the discrete formulation (12.3.4a)–(12.3.5) in the space $\mathscr{X}_h$. In order to exploit symmetry in the Jacobian matrix we replace the discrete form of Faraday's Law (12.3.4c) given by

$$\left(\frac{\boldsymbol{B}_h - \boldsymbol{B}_h^n}{\Delta t}, \boldsymbol{C}_h \right)_{\mathscr{E}_h} + \big(\mathbf{rot}\, E_h, \boldsymbol{C}_h \big)_{\mathscr{E}_h} = 0, \qquad (12.5.1)$$

with the equivalent expression

$$\theta R_m^{-1} \left(\frac{\boldsymbol{B}_h - \boldsymbol{B}_h^n}{\Delta t}, \boldsymbol{C}_h \right)_{\mathscr{E}_h} + \theta R_m^{-1} \big(\mathbf{rot}\, E_h, \boldsymbol{C}_h \big)_{\mathscr{E}_h} = 0, \qquad (12.5.2)$$

and add it to (12.3.4a), (12.3.4b) and (12.3.4d). Then, we define a function $G(\cdot)$ in such a way that $G(\boldsymbol{x}_h) \cdot \boldsymbol{y}_h$ is the left hand side of the resulting expression, where we assume that $\boldsymbol{x}_h$ and $\boldsymbol{y}_h$ are the column vector given by

$$
\boldsymbol{x}_h = \left(\widehat{\boldsymbol{u}}_h^{n+1,I}, \boldsymbol{B}_h^{n+1,I}, \widehat{E}_h^{n+\theta,I}, p_h^{n+\theta,I}\right)^T \quad \text{and} \quad \boldsymbol{y}_h = \left(\boldsymbol{v}_h^I, \boldsymbol{C}_h^I, D_h^I, q_h^I\right)^T.
$$

With these positions, the variational formulation (12.3.4a)–(12.3.5) is equivalent to the problem:
Find $\boldsymbol{x}_h \in \mathscr{X}_h$ such that

$$
G(\boldsymbol{x}_h) = \boldsymbol{0}. \tag{12.5.3}
$$

Indeed, on testing (12.5.3) against $\boldsymbol{y}_h = (\boldsymbol{v}_h, \boldsymbol{0}, 0, 0)$ we retrieve (12.3.4a), and the other three equations can be attained similarly. This is the set up to apply a Jacobian-free Newton–Krylov method. This method is highly parallelizable and has optimal speed of convergence.

The Newton method at every iteration will produce an updated estimate for the zeroes of G according to

$$
\boldsymbol{x}_h^0 = \left(\widehat{\boldsymbol{u}}_h^{n,I}, \boldsymbol{B}_h^{n,I}, \widehat{E}_h^{n-1+\theta,I}, p_h^{n-1+\theta,I}\right)^T, \tag{12.5.4}
$$

$$
\boldsymbol{x}_h^{(m+1)} = \boldsymbol{x}_h^{(m)} + \delta \boldsymbol{x}_h^{(m)}, \qquad \text{where} \quad \partial G(\boldsymbol{x}_h^{(m)}) \delta \boldsymbol{x}_h^{(m)} = -G(\boldsymbol{x}_h^m), \tag{12.5.5}
$$

where $\partial G : \mathscr{X}_{h,0} \to \mathscr{L}(\mathscr{X}_{h,0})$ is the Jacobian of G, the space $\mathscr{L}(\mathscr{X}_{h,0})$ being the collection of bounded linear operators from $\mathscr{X}_{h,0}$ to its dual space $\mathscr{X}'_{h,0}$. The reason we substitute (12.3.4c) with (12.5.2) is to attain some symmetry in the Jacobian matrix (which is useful in the well-posedness analysis). The practical implementation of this method requires to compute and store the Jacobian matrix, which may take a lot of computational power and memory. Instead we propose a Jacobian-Free Krylov method.

At each time step we perform a series on Newton iterations where on each iteration we solve a linear system of the form

$$
\partial G(\boldsymbol{x}) \delta \boldsymbol{x} = -G(\boldsymbol{x}) \tag{12.5.6}
$$

We approximate $\delta \boldsymbol{x}$ using a GMRES iteration. One of the major benefits using GMRES is that we need not know the entries in the Jacobian matrix ∂G. We need only be able to compute the matrix-vector product $\partial G(\boldsymbol{x}) \delta \boldsymbol{y}$ for any $\delta \boldsymbol{y} \in \mathscr{X}_{h,0}$ We can approximate the action of the Jacobian matrix using the operator $DG(\boldsymbol{x}) : \mathscr{X}_{h,0} \to \mathscr{X}_{h,0}$ defined using the finite difference approximation:

$$
DG(\boldsymbol{x}_h) \delta \boldsymbol{x}_h = \frac{G(\boldsymbol{x}_h + \epsilon \delta \boldsymbol{x}_h) - G(\boldsymbol{x}_h)}{\epsilon}, \tag{12.5.7}
$$

with $\epsilon = 10^{-7}$ (see [57, Page 80]). We emphasize that $DG(\boldsymbol{x}_h)$ itself is not computed, only its action $DG(\boldsymbol{x}_h)\delta\boldsymbol{x}_h$ is. Thus, the algorithm updates $\boldsymbol{x}_h^{(m+1)}$ from $\boldsymbol{x}_h^{(m)}$, with $0 \le m \le M - 1$, as follows:

$$\boldsymbol{x}_h^{(m+1)} = \boldsymbol{x}_h^{(m)} + \delta\boldsymbol{x}_h^{(m)}, \qquad \text{where} \quad DG(\boldsymbol{x}_h^{(m)})\delta\boldsymbol{x}^{(m)} = -G(\boldsymbol{x}_h^{(m)}),$$

(12.5.8a)

with the initial guess $\quad \boldsymbol{x}_h^{(0)} = \begin{cases} \left(\widehat{\boldsymbol{u}}_h^{n,I}, \boldsymbol{B}_h^{n,I}, \widehat{E}_h^{n-1+\theta,I}, p_h^{n-1+\theta,I}\right)^T & n > 0, \\ \left(\widehat{\boldsymbol{u}}_h^{0,I}, \boldsymbol{B}_h^{0,I}, 0, 0\right)^T & n = 0. \end{cases}$

(12.5.8b)

We define intermediate approximations at iteration m and the final values through the degrees of freedom of $\boldsymbol{x}_h^{(m)}$ and $\boldsymbol{x}_h^{(m)}$, respectively:

$$\left(\widehat{\boldsymbol{u}}_h^{n+1,(m),I}, \boldsymbol{B}_h^{n+1,(m),I}, \widehat{E}_h^{n+\theta,(m),I}, p_h^{n+\theta,(m),I}\right)^T = \boldsymbol{x}_h^{(m)},$$

$$\left(\widehat{\boldsymbol{u}}_h^{n+1}, \boldsymbol{B}_h^{n+1}, \widehat{E}_h^{n+\theta}, p_h^{n+\theta}\right) = \boldsymbol{x}_h^{(M)}.$$

This Krylov method requires a user-defined input tolerance η_m that we fix as follows:

$$\|DG(\boldsymbol{x}_h^{(m)})\delta\boldsymbol{x}^{(m)} + G(\boldsymbol{x}_h^{(m)})\|_2 \le \eta_m \|G(\boldsymbol{x}_h^{(m)})\|_2,$$

(12.5.9a)

$$\eta_m = \min\left\{\eta_{\max}, \max\left(\eta_m^B, \gamma \frac{\epsilon_t}{\|G(\boldsymbol{x}_h^{(m)})\|_2}\right)\right\},$$

(12.5.9b)

$$\eta_m^B = \min\left\{\eta_{\max}, \max\left(\eta_m^A, \gamma\eta_{m-1}^\alpha\right)\right\}, \quad \eta_m^A = \gamma\left(\frac{\|G(\boldsymbol{x}_h^{(m)})\|_2}{\|G(\boldsymbol{x}_h^{(m-1)})\|_2}\right)^\alpha.$$

(12.5.9c)

with $\alpha = 1.5$, $\gamma = 0.9$, $\eta_{\max} = 0.8$. The value of ϵ_t is chosen to guarantee that the non-linear convergence has been achieved.

$$\|G(\boldsymbol{x}_h^{(m)})\|_2 < \epsilon_a + \epsilon_r\|G(\boldsymbol{x}_h^{(0)})\|_2 = \epsilon_t,$$

(12.5.10)

$$\epsilon_a = \sqrt{\#\text{dof}} \times 10^{-15}, \quad \epsilon_r = 10^{-4}.$$

(12.5.11)

Where #dof is the sum of the number of degrees of freedom in each of our modeling spaces. The value of these parameters is chosen in accordance with [9]. However, this strategy is much more general [50]. The guiding philosophy being a desire

to guarantee super-linear convergence while simultaneously not over-solving with unnecessary GMRES iterations.

The non-linear nature of the inexact Newton steps may shed doubt as to whether or not this solver preserves the divergence free nature of the magnetic and velocity fields. The following result is a consequence of the Faraday law and the conservation of mass law. Note that the finite difference approximation to their Jacobian is exact since both of these laws are linear.

Theorem 12.13 *Suppose that δx_h solves the problem*

$$DG(x_h)\delta x_h = -G(x_h). \tag{12.5.12}$$

Then the velocity component δu_h of δx_h satisfies that

$$div\,\delta u_h = 0. \tag{12.5.13}$$

Moreover, we must have that

$$div\,u_h^{n,(m)} = 0 \quad \forall n \in [0, N], m \in [0, M]. \tag{12.5.14}$$

Proof Firstly, note that $\mathrm{div}\,\delta u_h \in \mathscr{P}_{h,0}$ since by definition of $\mathscr{T}\mathscr{V}_h$, $\mathrm{div}\,\delta u_h \in \mathscr{P}_h$ and

$$\int_\Omega \mathrm{div}\,\delta u_h\,dA = \int_{\partial\Omega} \mathfrak{J}^{\mathscr{T}\mathscr{V}_h}(\delta u_h) \cdot n\,d\ell = \int_{\partial\Omega} \delta u_h \cdot n\,d\ell = 0. \tag{12.5.15}$$

Next we test (12.5.12) against $y_h = (0, 0, 0, q_h^I)$ yields that

$$\forall q_h \in \mathscr{P}_{h,0}: \quad \left(\mathrm{div}\,\partial u_h, q_h\right)_{\mathscr{P}_h} = 0. \tag{12.5.16}$$

Meaning that $\mathrm{div}\,\partial u_h$ is orthogonal to every function in $\mathscr{P}_{h,0}$ obtaining (12.5.13). To obtain (12.5.14) we begin by assuming that $\mathrm{div}\,u_h^{n,(m)}$, thus by the previous result we have that

$$\mathrm{div}\,u_h^{n,(m+1)} = \mathrm{div}\,u_h^{n,(m)} + \mathrm{div}\,\delta u_h = 0. \tag{12.5.17}$$

$\square$

Theorem 12.14 *Suppose δx_h is a solution of the linear problem*

$$DG(x_h)\delta x_h = -G(x_h). \tag{12.5.18}$$

Then we have the following relation for the δB_h, δu_h components of δx_h

$$div\,\delta B_h = div\,(B_h^n - B_h). \tag{12.5.19}$$

Proof Testing (12.5.18) against $\boldsymbol{y}_h = (0, \boldsymbol{C}_h^I, 0, 0)$ yields

$$\Delta t^{-1} \left(\delta \boldsymbol{B}_h, \boldsymbol{C}_h \right)_{\mathscr{E}_h} + \left(\mathbf{rot}\, \delta \widehat{E}_h, \boldsymbol{C}_h \right)_{\mathscr{E}_h} - \left(\frac{\boldsymbol{B}_h - \boldsymbol{B}_h^n}{\Delta t}, \boldsymbol{C}_h \right)_{\mathscr{E}_h} - \left(\mathbf{rot}\, \widehat{E}_h, \boldsymbol{C}_h \right)_{\mathscr{E}_h} = 0.$$

Since $\boldsymbol{C}_h$ can be selected arbitrarily, the relation above is equivalent to

$$\Delta t^{-1} \left[\delta \boldsymbol{B}_h + \boldsymbol{B}_h - \boldsymbol{B}_h^n \right] = -\mathbf{rot} \left(\delta \widehat{E}_h + \widehat{E}_h \right). \tag{12.5.20}$$

The assertion of the theorem follows by taking the divergence of both sides. □

Corollary 12.4 *If the initial conditions on the magnetic field* $\boldsymbol{B}_0$ *satisfy that* $div\, \boldsymbol{B}_0 = 0$ *then updates defined by* (12.5.8) *will satisfy that*

$$div\, \delta \boldsymbol{B}_h^{n,(m)} = 0 \quad \forall n \in [0, N], m \in [0, M].$$

implying that

$$div\, \boldsymbol{B}_h^n = 0 \quad \forall n \in [0, N].$$

Proof The divergence of the initial estimate can be computed using the commuting property of the diagram in Theorem 12.5. Indeed,

$$\mathrm{div}\, \boldsymbol{B}_h^0 = \mathrm{div}\, \mathscr{I}^{\,\mathscr{E}_h}(\boldsymbol{B}_0) = \mathscr{I}^{\,\mathscr{P}_h}(\mathrm{div}\, \boldsymbol{B}_0) = 0.$$

Next, suppose that $\mathrm{div}_h \boldsymbol{B}_h^n = 0$. Then, by definition we have that $\mathrm{div}\, \boldsymbol{B}_h^{n+1,0} = 0$. For the inductive step we can further assume that $\mathrm{div}\, \boldsymbol{B}_h^{n+1,m} = 0$, so that from Theorem 12.14 we find that

$$\mathrm{div}\, \boldsymbol{B}_h^{n+1,(m+1)} = \mathrm{div}\, \boldsymbol{B}_h^{n+1,(m)} + \mathrm{div}\, \delta \boldsymbol{B}_h^{n+1,(m)} = \mathrm{div}\, (2\boldsymbol{B}_h^{n+1,(m)} - \boldsymbol{B}_h^n) = 0,$$

which implies that assertion of the corollary. □

12.6 Well-Posedness and Stability of the Linear Solver

The linearization strategy laid out in Sect. 12.5 can be summarized as follows. We are given a set of initial conditions. Then, at each time step we perform a series of Newton iterations, each one of these requiring the solution $\delta \boldsymbol{x}_h \in \mathscr{X}_{h,0}$ of a linear system like:

$$\partial G(\boldsymbol{x}_h) \delta \boldsymbol{x}_h = -G(\boldsymbol{x}_h). \tag{12.6.1}$$

for any given $\boldsymbol{x}_h \in \mathscr{X}_{h,0}$. To compute the Jacobian $\partial G(\boldsymbol{x}_h)$ we use the definition:

$$\left[\partial G(\boldsymbol{x}_h)\delta\boldsymbol{x}_h\right] \cdot \boldsymbol{y}_h = \lim_{\epsilon \to 0} \frac{G(\boldsymbol{x}_h + \epsilon\delta\boldsymbol{x}_h) \cdot \boldsymbol{y}_h - G(\boldsymbol{x}_h) \cdot \boldsymbol{y}_h}{\epsilon}. \tag{12.6.2}$$

The limit above yields

$$[\partial G(\boldsymbol{x}_h)\delta\boldsymbol{x}_h] \cdot \boldsymbol{y}_h = \ell_1(\boldsymbol{y}_h) + \ell_2(\boldsymbol{y}_h) + \ell_3(\boldsymbol{y}_h) + \ell_4(\boldsymbol{y}_h), \tag{12.6.3}$$

where $\boldsymbol{x}_h = (\widehat{\boldsymbol{u}}_h^I, \boldsymbol{B}_h^I, \widehat{E}_h^I, p_h^I)^T$, $\delta\boldsymbol{x}_h = (\delta\widehat{\boldsymbol{u}}_h^I, \delta\boldsymbol{B}_h^I, \delta\widehat{E}_h^I, \delta p_h^I)^T$, $\boldsymbol{y}_h = (\boldsymbol{v}_h^I, \boldsymbol{C}_h^I, D_h^I, q_h^I)^T$, and

$$\ell_1(\boldsymbol{y}_h) = \Delta t^{-1}\left(\delta\widehat{\boldsymbol{u}}_h, \boldsymbol{v}_h\right)_{\mathscr{T}\mathscr{V}_h} + \vartheta R_e^{-1}\left[\delta\widehat{\boldsymbol{u}}_h, \boldsymbol{v}_h\right]_{\mathscr{T}\mathscr{V}_h}$$

$$+ \vartheta\left(\widehat{E}_h, \mathscr{I}^{\mathscr{V}_h}(\boldsymbol{v}_h \times \Pi^{RT}\delta\boldsymbol{B}_h)\right)_{\mathscr{V}_h}$$

$$+ \vartheta\left(\delta\widehat{E}_h, \mathscr{I}^{\mathscr{V}_h}(\boldsymbol{v}_h \times \Pi^{RT}\boldsymbol{B}_h)\right)_{\mathscr{V}_h} - \left(\operatorname{div}\boldsymbol{v}_h, p_h\right)_{\mathscr{P}_h},$$

$$\ell_2(\boldsymbol{y}_h) = \vartheta\left(\operatorname{div}\delta\widehat{\boldsymbol{u}}_h, q_h\right)_{\mathscr{P}_h},$$

$$\ell_3(\boldsymbol{y}_h) = \Delta t^{-1}\left(\delta\boldsymbol{B}_h, \boldsymbol{C}_h\right)_{\mathscr{E}_h} + \left(\operatorname{rot}\delta E_h, \boldsymbol{C}_h\right)_{\mathscr{E}_h},$$

$$\ell_4(\boldsymbol{y}_h) = \left(\delta\widehat{E}_h + \vartheta\mathscr{I}^{\mathscr{V}_h}(\widehat{\boldsymbol{u}}_h \times \Pi^{RT}\delta\boldsymbol{B}_h + \delta\widehat{\boldsymbol{u}}_h \times \Pi^{RT}\boldsymbol{B}_h), D_h\right)_{\mathscr{V}_h}$$

$$+ R_m^{-1}\vartheta\left(\delta\boldsymbol{B}_h, \operatorname{rot}_h D_h\right)_{\mathscr{E}_h}.$$

These linear systems are in the form of a saddle-point problem satisfying the hypothesis of the following theorem, which can be used to prove the well posedness.

Theorem 12.15 *Let U and P be Hilbert spaces respectively endowed with the norms $\|\cdot\|_U$ and $\|\cdot\|_P$. Let $a : U \times U \to \mathbb{R}$, $b : U \times P \to \mathbb{R}$ be two bounded bilinear forms satisfying the inf-sup conditions*

$$\inf_{u \in U_0} \sup_{v \in U_0} \frac{a(u, v)}{\|u\|_U \|v\|_U} > 0, \quad \inf_{p \in P} \sup_{u \in U} \frac{b(u, p)}{\|u\|_U \|p\|_P} > 0, \tag{12.6.4}$$

where

$$U_0 = \left\{u \in U : \forall p \in P \quad b(u, p) = 0\right\}. \tag{12.6.5}$$

Then, for every pair of bounded linear functionals $f \in U'$ and $g \in P'$ there exists unique $u \in U$ and $p \in P$ such that for any $v \in U$ and $q \in P$ it is the case that

$$a(u, v) - b(v, p) = f(v) \qquad \forall v \in U,$$
$$b(u, q) = g(q) \qquad \forall q \in P.$$

Moreover there exists a constant $C > 0$ independent of f and g such that

$$\|u\|_U + \|p\|_P \le C \left(\|f\|_{U'} + \|g\|_{P'} \right), \tag{12.6.6}$$

with the (standard) definition of the norms in the dual spaces:

$$\|f\|_{U'} = \sup_{u \in U \setminus \{0\}} \frac{|f(u)|}{\|u\|_U}, \quad \|g\|_{P'} = \sup_{p \in P \setminus \{0\}} \frac{|g(p)|}{\|p\|_P}. \tag{12.6.7}$$

Proof A proof of this theorem can be found in [28, 33].   □

Consider the space:

$$\mathfrak{X}_h = \mathcal{T} \mathcal{V}_{h,0} \times \mathcal{E}_h \times \mathcal{V}_{h,0}, \tag{12.6.8}$$

and the bilinear form $a_h : \mathfrak{X}_h \times \mathfrak{X}_h \to \mathbb{R}$, whose evaluation at $\delta \boldsymbol{\xi}_h = (\delta \widehat{\boldsymbol{u}}_h, \delta \boldsymbol{B}_h, \delta \widehat{E}_h)$, $\boldsymbol{\eta}_h = (\boldsymbol{v}_h, \boldsymbol{C}_h, D_h)$ is given by $a_h(\delta \boldsymbol{\xi}_h, \boldsymbol{\eta}_h) = \ell_1(\boldsymbol{v}_h) + \ell_2(\boldsymbol{C}_h) + \ell_3(D_h)$, cf. Eq. (12.6.3). Here, and for the remainder of the section, we fix the value $\boldsymbol{x}_h = (\widehat{\boldsymbol{u}}_h, \boldsymbol{B}_h, \widehat{E}_h)$. We can reformulate problem (12.6.1) as:
Find $(\delta \boldsymbol{\xi}_h, \delta p_h) \in \mathfrak{X}_h \times \mathscr{P}_{h,0}$ such that for all $(\boldsymbol{\eta}_h, q_h) \in \mathfrak{X}_h \times \mathscr{P}_{h,0}$ it holds that

$$a_h(\delta \boldsymbol{\xi}_h, \boldsymbol{\eta}_h) - b_h(\boldsymbol{v}_h, \delta p_h) = f(\boldsymbol{\eta}_h), \tag{12.6.9a}$$
$$b_h(\delta \widehat{\boldsymbol{u}}_h, q_h) = g(q_h), \tag{12.6.9b}$$

Where $f \in \mathfrak{X}_h'$ and $g \in \mathscr{P}_{h,0}'$ are some appropriate bounded linear functionals and

$$b_h(\boldsymbol{v}_h, q_h) = \left(\operatorname{div} \boldsymbol{v}_h, q_h \right)_{\mathscr{P}_h}. \tag{12.6.10}$$

The strategy we follow to prove the well-posedness of the virtual element approximation proceeds in three steps:

(i) we introduce an auxiliary problem;
(ii) we show that the auxiliary problem and problem (12.6.9) are equivalent;
(iii) we show that the auxiliary problem is well posed.

In the rest of this section we briefly sketch the various steps of this argument, see Chapter 5 in [73] for details.

The auxiliary problem is given by: *Find* $(\delta\boldsymbol{\xi}_h, \delta p_h) \in \mathfrak{X}_h \times \mathscr{P}_{h,0}$ *such that for all* $(\boldsymbol{\eta}_h, q_h) \in \mathfrak{X}_h \times \mathscr{P}_{h,0}$ *it holds that*

$$a_{h,0}(\delta\boldsymbol{\xi}_h, \boldsymbol{\eta}_h) - b_h(\boldsymbol{v}_h, \delta p_h) = f_h(\boldsymbol{\eta}_h), \tag{12.6.11a}$$

$$b_h(\delta\widehat{\boldsymbol{u}}_h, q_h) = g_h(q_h). \tag{12.6.11b}$$

Note that

$$a_{h,0}(\delta\boldsymbol{\xi}_h, \boldsymbol{\eta}_h) = a_h(\delta\boldsymbol{\xi}_h, \boldsymbol{\eta}_h) + \theta R_m^{-1}\Big(\operatorname{div}\delta\boldsymbol{B}_h, \operatorname{div}\boldsymbol{C}_h\Big)_{\mathscr{P}_h}. \tag{12.6.12}$$

Then, to establish the equivalence between (12.6.9) and (12.6.11), we need to ensure that approximations using the auxiliary problem (12.6.11) will have divergence free magnetic fields. This is settled in the following Theorem:

Theorem 12.16 *Let* $\delta\boldsymbol{\xi}_h = (\delta\widehat{\boldsymbol{u}}_h, \delta\boldsymbol{B}_h, \delta\widehat{E}_h) \in \mathfrak{X}_h$ *and* $p_h \in \mathscr{P}_{h,0}$ *solve* (12.6.11). *If the initial conditions on the magnetic field are divergence free, then it holds that* $\operatorname{div}\delta\boldsymbol{B}_h = 0$.

We can leverage the result of this theorem to show that both problems (12.6.9) and (12.6.11) are equivalent as stated by the following lemma.

Lemma 12.5 *The problems* (12.6.9) *and* (12.6.11) *are equivalent.*

Finally, we present the well-posedness of (12.6.11). Following the framework laid out in [54], we introduce the norm on $\mathfrak{X}_{h,0}$ such that for any $\boldsymbol{\xi}_h = (\boldsymbol{u}_h, \boldsymbol{B}_h, E_h) \in \mathfrak{X}_{h,0}$ we have

$$|||\boldsymbol{\xi}_h|||^2_{\mathfrak{X}_{h,0}} := |||\boldsymbol{v}_h|||^2_{\Delta t, \nabla} + |||E_h|||^2_{\Delta t, \mathbf{rot}} + |||\boldsymbol{B}_h|||^2_{\Delta t, \operatorname{div}}, \tag{12.6.13a}$$

$$|||\boldsymbol{u}_h|||^2_{\Delta t, \nabla} := \Delta t^{-1}|||\boldsymbol{u}_h|||^2_{\mathscr{T}\mathscr{V}_h} + |\boldsymbol{u}_h|^2_{\mathscr{T}\mathscr{V}_h} + \Delta t^{-1}|||\operatorname{div}\boldsymbol{u}_h|||^2_{\mathscr{P}_h}, \tag{12.6.13b}$$

$$|||\boldsymbol{B}_h|||^2_{\Delta t, \operatorname{div}} := \Delta t^{-1}|||\boldsymbol{B}_h|||^2_{\mathscr{E}_h} + |||\operatorname{div}\boldsymbol{B}_h|||^2_{\mathscr{P}_h}, \tag{12.6.13c}$$

$$|||E_h|||^2_{\Delta t, \mathbf{rot}} := |||E_h|||^2_{\mathscr{V}_h} + \Delta t|||\mathbf{rot}\,E_h|||^2_{\mathscr{E}_h}. \tag{12.6.13d}$$

Well-posedness relies on Theorem 12.15. The first hypothesis established that the bilinear forms in the formulation of (12.6.11) are continuous

Lemma 12.6 *Suppose that* $\Delta t^{1/2}\widehat{\boldsymbol{u}}_h, \widehat{\boldsymbol{u}}_h, \boldsymbol{B}_h \in [L^\infty(\Omega)]^2$ *and* $\widehat{E}_h \in L^\infty(\Omega)$. *Then, the bilinear form* $a_{h,0}$ *is continuous in the norms defined in* (12.6.13a).

The next lemma guarantees that the bilinear form $a_{h,0}$ satisfies the inf-sup condition.

Lemma 12.7 *Let $\theta > 0$, and $\widehat{\boldsymbol{u}}_h$, $\boldsymbol{B}_h \in [L^\infty(\Omega)]^2$ and $\widehat{E}_h \in L^\infty(\Omega)$. For a Δt small enough, we have that*

$$\inf_{\delta\boldsymbol{\xi}_h\in\mathfrak{X}_{h,0}} \sup_{\boldsymbol{\eta}_h\in\mathfrak{X}_{h,0}} \frac{a_{h,0}(\delta\boldsymbol{\xi}_h, \boldsymbol{\eta}_h)}{|||\delta\boldsymbol{\xi}_h|||_{\mathfrak{X}_h} \, |||\boldsymbol{\eta}_h|||_{\mathfrak{X}_h}} \geq C > 0,$$

where $\mathfrak{X}_{h,0} = \big\{(\boldsymbol{v}_h, \boldsymbol{B}_h, E_h) : div\, \boldsymbol{v}_h = 0\big\}$ and C is a strictly positive, real constant independent of h and Δt.

12.7   Numerical Experiments

In this section, we show some numerical results for the approximation of the subsystem of (12.2.2a)–(12.2.2e) that describes the electromagnetic part of the MHD model.

$$\frac{\partial}{\partial t}\boldsymbol{B} + \mathbf{rot}\, E = \boldsymbol{0} \quad \text{in} \quad \Omega, \tag{12.7.1a}$$

$$E + \boldsymbol{u} \times \boldsymbol{B} - R_m^{-1}\text{rot}\,\boldsymbol{B} = 0 \quad \text{in} \quad \Omega, \tag{12.7.1b}$$

$$\boldsymbol{B}(0) = \boldsymbol{B}_0 \quad \text{in} \quad \Omega \tag{12.7.1c}$$

$$E \equiv E_b \quad \text{along} \quad \partial\Omega. \tag{12.7.1d}$$

We present an experimental study of the convergence properties of the VEM and show the performance when we apply the VEM to the numerical modeling of a magnetic reconnection model.

12.7.1   Experimental Study of Convergence

The first test that we perform regards the convergence rate of the VEM. We consider the computational domain $\Omega = [-1, 1] \times [-1, 1]$ partitioned by three different mesh families, a triangular mesh, a perturbed quadrilateral mesh and a Voronoi Tessellation. We assume that an external velocity field $\boldsymbol{u} = (u_x, u_y)^T$ is imposed, whose components are

$$u_x(x, y) = -\frac{(x^2 + y^2 - 1)(\sin(xy) + \cos(xy)) - 120e^x + 100e^y}{2(50e^x - y\sin(xy) + y\cos(xy))}, \tag{12.7.2}$$

$$u_y(x, y) = \frac{(x^2 + y^2 - 1)(\sin(xy) + \cos(xy)) - 120e^x + 100e^y}{2(50e^y + x\sin(xy) - x\cos(xy))}. \tag{12.7.3}$$

The initial and the boundary conditions are set in accordance with the electric and magnetic fields, which we assume as the exact solutions.

$$\boldsymbol{B}(x, y, t) = \begin{pmatrix} 50e^y + x\sin(xy) - x\cos(xy) \\ 50e^x - y\sin(xy) + y\cos(xy) \end{pmatrix} e^{-t}, \tag{12.7.4}$$

$$E(x, y, t) = -\big(50(e^x - e^y) + \cos(xy) + \sin(xy)\big)e^{-t}. \tag{12.7.5}$$

The simulation uses the time discretization given by $\theta = 1/2$ and time step $\Delta_t = 0.05h^2$, and we integrate from $t = 0$ to $t = T$, the final time being $T = 0.25$. We measure the relative errors of E and $\boldsymbol{B}$ through the mesh dependent norms of the difference between the exact and numerical solutions divided by the norm of the exact solution. The results are shown in Fig. 12.5. In each plot, we show three different convergence curves. These curves refer to the three different possibilities that we presented in Sect. 12.3.2.1 for the construction of the inner product in the space $\mathscr{V}_h$. These plots provide evidence that the convergence rate for the electric field is quadratic while the convergence rate for the magnetic field is linear. In the case of Voronoi tessellations the convergence plots associated with the inner product defined by the Galerkin interpolator (GI) show some irregular behavior. These types of meshes may have arbitrarily small edges conflicting with the criteria normally used in the VEM. Another possible explanation may have to do with the G.I, note that this irregular behavior does not happen with the other two sample inner products.

An important feature of the VEM is that the divergence of the magnetic field should remain zero throughout the simulation. In Fig. 12.6 we show plots of the evolution of the L^2-norm of the divergence of the magnetic field. These show that this quantity remains very close, in norm, to the machine epsilon.

12.7.2 Magnetic Reconnection

The next numerical experiment involves a characteristic feature of resistive MHD – the phenomenon of magnetic reconnection. At very large scales, usually in space physics, the behavior of plasmas can be well-approximated using ideal MHD. In this case, according to the Alfven's Theorem, the magnetic field lines will advect with the fluid, see Section 4.3 in [46] for a full discussion. This feature is often referred to as the "frozen-in" condition on the magnetic field. In certain regions of the Earth's magnetosphere, namely the magnetopause and magnetotail, the magnetic reconnection will lead to very thin current sheets that separate regions across which the magnetic field changes substantially.
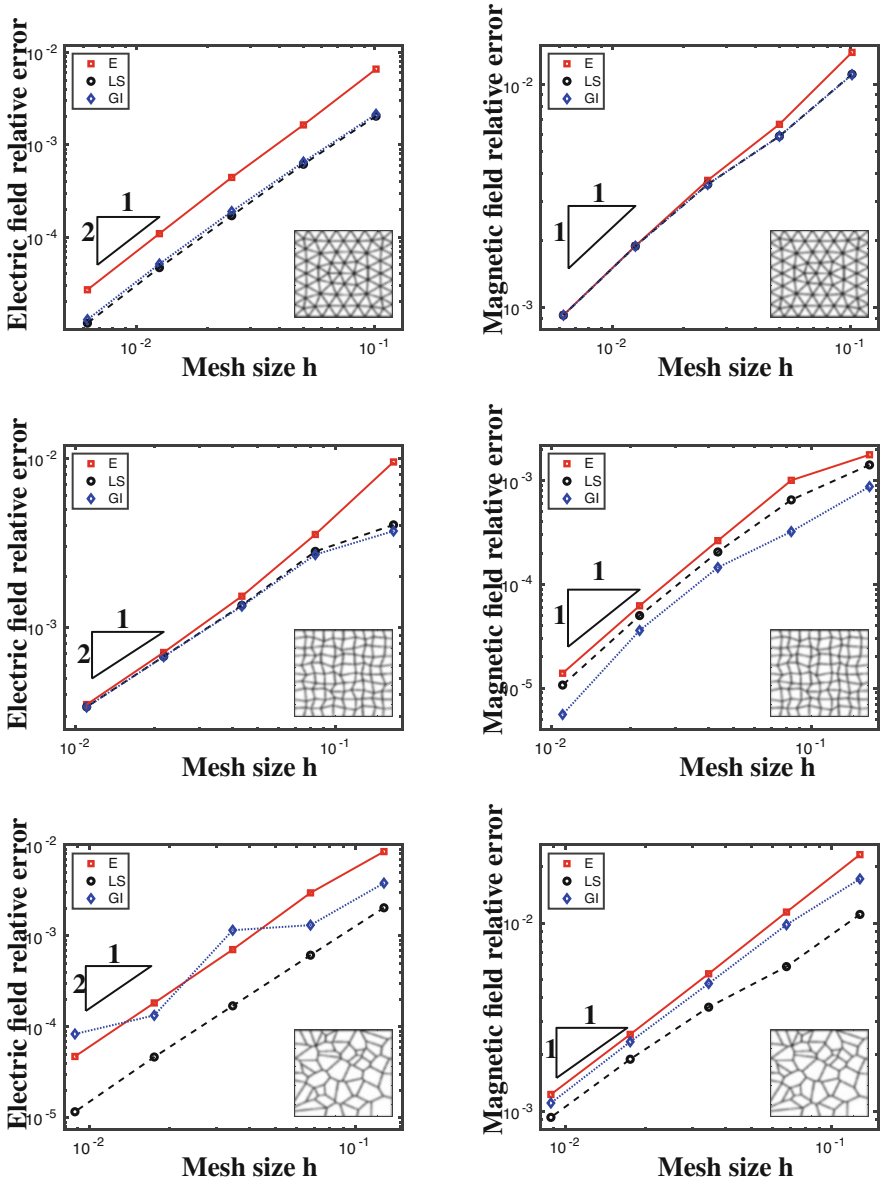
Fig. 12.5 Convergence plots of the VEM developed for the system (12.7.1). The type of mesh used in the simulation is portrayed in the lower right corner of each plot. The three convergence curves shown in each plot show the different performance between the three possibilities of the inner product in the space $\mathcal{V}_h$, see Sect. 12.3.2.1. Each of these inner products is associated with a projector, they are the elliptic projector (E), the least squares projector (LS) and the Galerkin interpolator (GI)
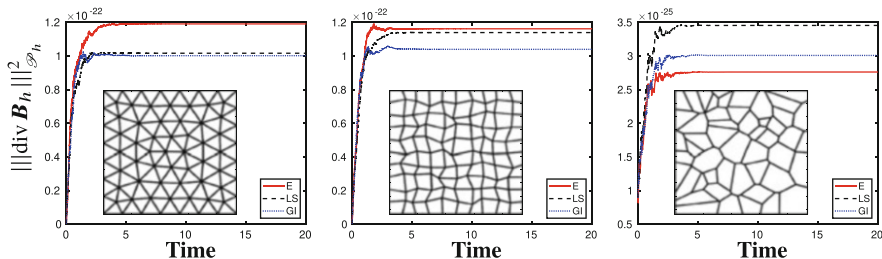
Fig. 12.6 Plots of the time evolution of the square of the L^2 norm of the divergence of the numerical magnetic field. We present three different types of meshes, these are displayed in the lower right hand corner of each plot

In this numerical experiment, we consider one Harris sheet constrained to the computational domain $\Omega = [-1, 1]^2$ and given by the following profile of the magnetic field, first introduced in [53],

$$\boldsymbol{B}_0(x, y) = (\tanh y, 0). \tag{12.7.6}$$

The simplicity of this condition has made it a popular choice in modeling magnetic reconnection. We will use the expression (12.7.6) as the initial condition for the magnetic field. We will further assume that the particles in this sheet are subjected by some external agent to a flow described by

$$\boldsymbol{u}(x, y, t) = (-x, y). \tag{12.7.7}$$

This flow will force the magnetic field lines to come together at a single point making the current density grow. The system becomes highly unstable and the magnetic field lines begin to tear apart, this phenomenon is called a tearing instability and magnetic reconnection happens as a response. This process is described in detail in [58, 76]. We close this model by imposing the boundary conditions

$$\forall t > 0: \quad E_b(t) \in \mathbb{P}_0(\partial\Omega), \quad \text{and} \quad \int_{\partial\Omega} \boldsymbol{B}_b(t) \cdot \boldsymbol{n} d\ell = 0 \tag{12.7.8}$$

The mesh we are using is refined near the center of the domain Ω, to guarantee higher resolution in the region of space where the phenomenon of magnetic reconnection occurs. The downside of using such a mesh is that a series of hanging nodes are introduced. This numerical experiment demonstrates the versatility of the VEM, and the advantage of this method over more classical methods like the FEM or FDM.

In Fig. 12.7 we display the mesh used along with a set of frames displaying the evolution in time of the magnetic field. The phenomenon of magnetic reconnection begins at $T = 0$ and by $T = 0.450$ a steady state is achieved.
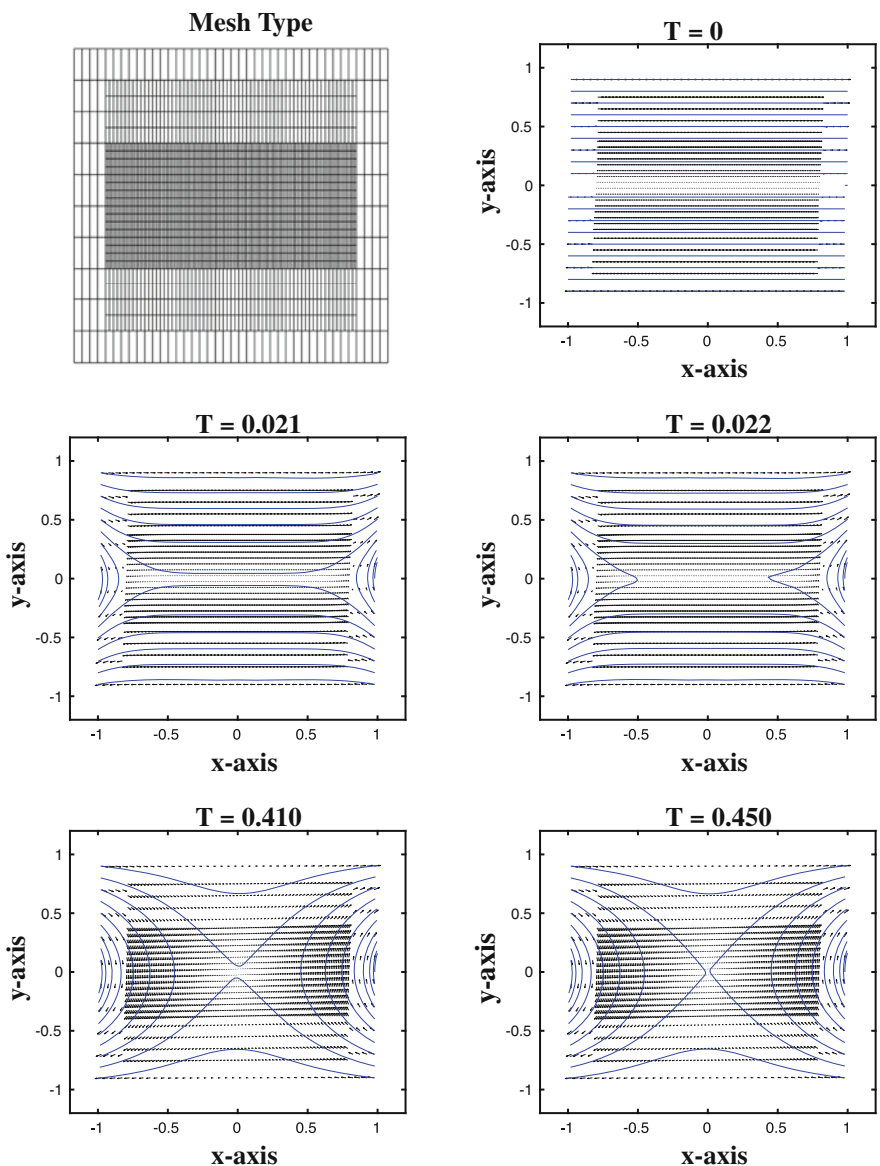
Fig. 12.7 Frames displaying the evolution, in time, of the magnetic field. The phenomenon of magnetic reconnection begins right away and by $T = 0.450$ a steady state is achieved

12.8 Conclusions

In this chapter, we developed a VEM for the PDE system of resistive MHD. In developing this chapter we have introduced two chains of spaces, see Sects. 12.3.5 and the final results in Sect. 12.3.6. One chain of spaces is aimed at approximating the electromagnetics submodel, while the other applies to the submodel for fluid flow. There are terms in the MHD equations that couple the two submodels that require information about both the phenomena of electromagnetics and fluid flow. Special care needs to be taken in discretizing these terms so that the fully discretized MHD system satisfies discrete (stability) energy estimates. These estimate are the main result of Sect. 12.4. They guarantee the stability of the method.

The VEM, when applied to MHD, yields a large system of non-linear equations. In order to arrive at approximate solutions a linearization strategy has to be developed. In Sect. 12.5 we developed a Newton iteration to address this issue. We were able to prove that this linearization strategy will preserve the divergence of the magnetic and velocity fields such that if the initial conditions are divergence free then these non-linear iterations will preserve this divergence free property in the discrete mesh. The analysis of Sect. 12.6 shows that the set of linear systems that need to be solved are, in fact, well-posed saddle point problems. This well-posedness result serves as a first step into developing robust preconditioners following the framework presented in [64].

In Sect. 12.7 we also presented a series of numerical experiments exploring the subsystem that describes the electromagnetics. These experiments show that the (lowest-order) VEM is convergent, the speed of convergence is quadratic for the electric field and linear for the magnetic field. Further experimentation shows that the divergence of the magnetic field remains well below machine epsilon. We also present a model for a phenomenon characteristic of resistive MHD, that of magnetic reconnection. This model accurately describes the behavior of plasmas in tokamaks as well as many electromagnetic interactions in the magnetosphere of a planet. Our compatible discretization closely mimics the behavior of the exact solution to our model. This model was discretized on a mesh that was refined near the center of the computational domain where reconnection will happen. Using this mesh will provide higher resolution in the parts of the domain where such resolution is required and aids in saving computational resources. Other numerical methods struggle with this type of mesh because it introduces a series of hanging nodes. However, the VEM performs just as well in this type of mesh.

References

1. B. Ahmad, A. Alsaedi, F. Brezzi, L.D. Marini, A. Russo, Equivalent projectors for virtual element methods. Comput. Math. Appl. **66**(3), 376–391 (2013)
2. P.F. Antonietti, L. Beirão da Veiga, S. Scacchi, M. Verani, A C^1 virtual element method for the Cahn-Hilliard equation with polygonal meshes. SIAM J. Numer. Anal. **54**(1), 34–56 (2016)
3. P.F. Antonietti, G. Manzini, I. Mazzieri, H.M. Mourad, M. Verani, The arbitrary-order virtual element method for linear elastodynamics models. convergence, stability and dispersion-dissipation analysis. Int. J. Numer. Methods Eng. **122**(4), 934–971 (2021)
4. P.F. Antonietti, G. Manzini, S. Scacchi, M. Verani, A review on arbitrarily regular conforming virtual element methods for second- and higher-order elliptic partial differential equations. Math. Models Methods Appl. Sci. **31**(14), 2825–2853 (2021)
5. P.F. Antonietti, G. Manzini, M. Verani, The conforming virtual element method for polyharmonic problems. Comput. Math. Appl. **79**(7), 2021–2034 (2020)
6. L. Beirão da Veiga, F. Brezzi, A. Cangiani, G. Manzini, L.D. Marini, A. Russo, Basic principles of virtual element methods. Math. Models Methods Appl. Sci. **23**(1), 199–214 (2013)
7. L. Beirão da Veiga, F. Brezzi, F. Dassi, L.D. Marini, A. Russo, Virtual element approximation of 2D magnetostatic problems. Comput. Methods Appl. Mech. Eng. **327**, 173–195 (2017)
8. L. Beirão da Veiga, F. Brezzi, F. Dassi, L.D. Marini, A. Russo, Lowest order virtual element approximation of magnetostatic problems. Comput. Methods Appl. Mech. Eng. **332**, 343–362 (2018)
9. L. Beirão da Veiga, F. Brezzi, D. Marini, A. Russo, Mixed virtual element methods for general second order elliptic problems on polygonal meshes. ESAIM: Math. Model. Numer. Anal. **50**(3), 727–747 (2016)
10. L. Beirão da Veiga, F. Brezzi, L.D. Marini, A. Russo, The hitchhiker's guide to the virtual element method. Math. Models Methods Appl. Sci. **24**(8), 1541–1573 (2014)
11. L. Beirão da Veiga, F. Brezzi, L.D. Marini, A. Russo, H(div) and H(curl)-conforming VEM. Numer. Math. **133**(2), 303–332 (2016)
12. L. Beirão da Veiga, F. Brezzi, L.D. Marini, A. Russo, Virtual element methods for general second order elliptic problems on polygonal meshes. Math. Models Methods Appl. Sci. **26**(4), 729–750 (2016)
13. L. Beirão da Veiga, A. Chernov, L. Mascotto, A. Russo, Basic principles of *hp* virtual elements on quasiuniform meshes. Math. Models Methods Appl. Sci. **26**(8), 1567–1598 (2016)
14. L. Beirão da Veiga, K. Lipnikov, G. Manzini, Arbitrary order nodal mimetic discretizations of elliptic problems on polygonal meshes. SIAM J. Numer. Anal. **49**(5), 1737–1760 (2011)
15. L. Beirão da Veiga, K. Lipnikov, G. Manzini, *The Mimetic Finite Difference Method*, vol. 11 of MS&A. Modeling, Simulations and Applications, 1st edn. (Springer, Berlin, 2014)
16. L. Beirão da Veiga, C. Lovadina, A. Russo, Stability analysis for the virtual element method. Math. Models Methods Appl. Sci. **27**(13), 2557–2594 (2017)

17. L. Beirão da Veiga, C. Lovadina, G. Vacca, Divergence free virtual elements for the Stokes problem on polygonal meshes. ESAIM: Math. Model. Numer. Anal. **51**(2), 509–535 (2017)
18. L. Beirão da Veiga, C. Lovadina, G. Vacca, Virtual elements for the Navier–Stokes problem on polygonal meshes. SIAM J. Numer. Anal. **56**(3), 1210–1242 (2018)
19. L. Beirão da Veiga, G. Manzini, Residual *a posteriori* error estimation for the virtual element method for elliptic problems. ESAIM Math. Model. Numer. Anal. **49**(2), 577–599 (2015)
20. L. Beirão da Veiga, G. Manzini, L. Mascotto, A posteriori error estimation and adaptivity in hp virtual elements. Numer. Math. **143**, 139–175 (2019)
21. Beirão da Veiga, L., F. Dassi, G. Manzini, L. Mascotto, Virtual elements for Maxwell's equations. Comput. Math. Appl. **116**, 82–99 (2022)
22. L. Beirão da Veiga, F. Brezzi, F. Dassi, L.D. Marini, A. Russo, A family of three-dimensional virtual elements with applications to magnetostatics. SIAM J. Numer. Anal. **56**(5), 2940–2962 (2018)
23. L. Beirão da Veiga, F. Dassi, G. Vacca, The Stokes complex for virtual elements in three dimensions. Math. Models Methods Appl. Sci. **30**(3), 477–512 (2020)
24. E. Benvenuti, A. Chiozzi, G. Manzini, N. Sukumar, Extended virtual element method for two-dimensional linear elastic fracture. Comput. Methods Appl. Mech. Eng. **390**, 114352 (2022)
25. E. Benvenuti, A. Chiozzi, G. Manzini, N. Sukumar, Extended virtual element method for the Laplace problem with singularities and discontinuities. Comput. Methods Appl. Mech. Eng. **356**, 571–597 (2019)
26. S. Berrone, A. Borio, Manzini, SUPG stabilization for the nonconforming virtual element method for advection–diffusion–reaction equations. Comput. Methods Appl. Mech. Eng. **340**, 500–529 (2018)
27. S. Berrone, S. Pieraccini, S. Scialò, F. Vicini, A parallel solver for large scale DFN flow simulations. SIAM J. Sci. Comput. **37**(3), C285–C306 (2015)
28. D. Boffi, F. Brezzi, M. Fortin, *Mixed Finite Element Methods and Applications*, vol. 44 (Springer, Berlin, 2013)
29. J. Brackbill, Fluid modeling of magnetized plasmas. Space Sci. Rev. **42**(1–2), 153–167 (1985)
30. J.U. Brackbill, D.C. Barnes, The effect of nonzero Div B on the numerical solution of the magnetohydrodynamic equations. J. Comput. Phys. **35**(3), 426–430 (1980)
31. S.C. Brenner, R. Scott, *The Mathematical Theory of Finite Element Methods*, vol. 15 (Springer, Berlin, 2008)
32. S.C. Brenner, L.-Y. Sung, Virtual element methods on meshes with small edges or faces. Math. Models Methods Appl. Sci. **28**(7), 1291–1336 (2018)
33. F. Brezzi, On the existence, uniqueness and approximation of saddle-point problems arising from Lagrangian multipliers. Rev. Française Automat. Inform. Recherche Opérationnelle Sér. Rouge **8**(R-2), 129–151 (1974)
34. F. Brezzi, A. Buffa, K. Lipnikov, Mimetic finite differences for elliptic problems. M2AN Math. Model. Numer. Anal. **43**, 277–295 (2009)
35. F. Brezzi, A. Buffa, G. Manzini, Mimetic scalar products for discrete differential forms. J. Comput. Phys., **257**(Part B), 1228–1259 (2014)
36. A. Cangiani, E.H. Georgoulis, T. Pryer, O.J. Sutton, A posteriori error estimates for the virtual element method. Numer. Math. **137**, 857–893 (2017)
37. A. Cangiani, V. Gyya, G. Manzini, Sutton. O, Chapter 14: Virtual element methods for elliptic problems on polygonal meshes, in *Generalized Barycentric Coordinates in Computer Graphics and Computational Mechanics*, ed. by K. Hormann, N. Sukumar (CRC Press, Taylor & Francis Group, 2017), pp. 1–20
38. A. Cangiani, G. Manzini, A. Russo, N. Sukumar, Hourglass stabilization of the virtual element method. Int. J. Numer. Methods Eng. **102**(3–4), 404–436 (2015)
39. O. Certik, F. Gardini, G. Manzini, L. Mascotto, G. Vacca, The p- and hp-versions of the virtual element method for elliptic eigenvalue problems. Comput. Math. Appl. **79**(7), 2035–2056 (2020)
40. O. Certik, F. Gardini, G. Manzini, G. Vacca, The virtual element method for eigenvalue problems with potential terms on polytopic meshes. Appl. Math. **63**(3), 333–365 (2018)

41. L. Chacón, An optimal, parallel, fully implicit Newton–Krylov solver for three-dimensional viscoresistive magnetohydrodynamics. Phys. Plasmas **15**(5), 056103 (2008)
42. L. Beirão Da Veiga, F. Dassi, A. Russo, High-order virtual element method on polyhedral meshes. Comput. Math. Appl. **74**(5), 1110–1122 (2017)
43. L. Beirao da Veiga, C. Lovadina, G. Vacca, Virtual elements for the Navier–Stokes problem on polygonal meshes. SIAM J. Numer. Anal. **56**(3), 1210–1242 (2018)
44. W. Dai, P.R. Woodward, On the divergence-free condition and conservation laws in numerical simulations for supersonic magnetohydrodynamical flows. Astrophys. J. **494**(1), 317 (1998)
45. F. Dassi, L. Mascotto, Exploring high-order three dimensional virtual elements: bases and stabilizations. Comput. Math. Appl. **75**(9), 3379–3401 (2018)
46. P.A. Davidson, *An introduction to magnetohydrodynamics* (Cambridge University Press, Cambridge, 2010)
47. A. Dedner, F. Kemm, D. Kröner, C.D. Munz, T. Schnitzer, M. Wesenberg, Hyperbolic divergence cleaning for the MHD equations. J. Comput. Phys. **175**(2), 645–673 (2002)
48. D.A. Di Pietro, J. Droniou, G. Manzini, Discontinuous skeletal gradient discretisation methods on polytopal meshes. J. Comput. Phys. **355**, 397–425 (2018)
49. J. Ding, Y. Yang, Low-dispersive FDTD on hexagon revisited. Electron. Lett. **53**(13), 834–835 (2017)
50. S.C. Eisenstat, H.F. Walker, Choosing the forcing terms in an inexact Newton method. SIAM J. Sci. Comput. **17**(1), 16–32 (1996)
51. E. Emmrich, *Discrete Versions of Gronwall's Lemma and Their Application to the Numerical Analysis of Parabolic Problems* (Techn. Univ., 1999)
52. F. Gardini, G. Manzini, G. Vacca, The nonconforming virtual element method for eigenvalue problems. ESAIM: Math. Model. Numer. Anal. **53**, 749–774 (2019). Accepted for publication: 29 November 2018. https://doi.org/10.1051/m2an/2018074
53. E.G. Harris, On a plasma sheath separating regions of oppositely directed magnetic field. Il Nuovo Cimento (1955–1965) **23**(1), 115–121 (1962)
54. K. Hu, Y. Ma, J. Xu, Stable finite element methods preserving $div B = 0$ exactly for MHD models. Numer. Math. **135**(2), 371–396 (2017)
55. B. Jiang, *The Least-Squares Finite Element Method: Theory and Applications in Computational Fluid Dynamics and Electromagnetics* (Springer, Berlin, 1998)
56. M. Joaquim, S. Scheer, Finite-difference time-domain method for three-dimensional grid of hexagonal prisms. Wave Motion **63**, 32–54 (2016)
57. C.T. Kelley, *Iterative Methods for Linear and Nonlinear Equations*, vol. 16. (SIAM, 1995)
58. M.G. Kivelson, C.T. Russell, *Introduction to Space Physics* (Cambridge University Press, Cambridge, 1995)
59. D. Kuzmin, N. Klyushnev, Limiting and divergence cleaning for continuous finite element discretizations of the MHD equations. J. Comput. Phys. **407**, 109230 (2020)
60. K. Lipnikov, G. Manzini, F. Brezzi, A. Buffa, The mimetic finite difference method for 3D magnetostatics fields problems. J. Comp. Phys. **230**(2), 305–328 (2011)
61. K. Lipnikov, G. Manzini, M. Shashkov, Mimetic finite difference method. J. Comput. Phys. **257**(Part B), 1163–1227 (2014). Review paper.
62. J.G. Liu, W.C. Wang, An energy-preserving MAC–Yee scheme for the incompressible MHD equation. J. Comput. Phys. **174**(1), 12–37 (2001)
63. J.G. Liu, W.C. Wang, Energy and helicity preserving schemes for hydro-and magnetohydrodynamics flows with symmetry. J. Comput. Phys. **200**(1), 8–33 (2004)
64. D. Loghin, A.J. Wathen, Analysis of preconditioners for saddle-point problems. SIAM J. Sci. Comput. **25**(6), 2029–2049 (2004)
65. G. Manzini, K. Lipnikov, J.D. Moulton, M. Shashkov, Convergence analysis of the mimetic finite difference method for elliptic problems with staggered discretizations of diffusion coefficients. SIAM J. Numer. Anal. **55**(6), 2956–2981 (2017)
66. G. Manzini, A. Russo, N. Sukumar, New perspectives on polygonal and polyhedral finite element methods. Math. Models Methods Appl. Sci. **24**(8), 1621–1663 (2014)

67. L. Mascotto, Ill-conditioning in the virtual element method: stabilizations and bases. Numer. Methods Partial Differ. Equ. **34**(4), 1258–1281 (2018)
68. P. Monk et al., *Finite Element Methods for Maxwell's Equations* (Oxford University Press, Oxford, 2003)
69. D. Mora, G. Rivera, R. Rodríguez, A virtual element method for the Steklov eigenvalue problem. Math. Methods Appl. Sci. **25**(8), 1421–1445 (2015)
70. R.J. Moreau, *Magnetohydrodynamics*, vol. 3 (Springer, Berlin, 2013)
71. J.R. Munkres, *Analysis on Manifolds* (CRC Press, Boca Raton, 2018)
72. S. Naranjo-Alvarez, V. Bokil, V. Gyrya, G. Manzini, The virtual element method for resistive magnetohydrodynamics. Comput. Methods Appl. Mech. Eng. **381**, 113815 (2021)
73. S. Naranjo Álvarez, *Virtual Element Methods for Magnetohydrodynamics on General Polygonal and Polyhedral Meshes*. Ph.D. Thesis, Oregon State University, 2021
74. G.H. Paulino, A.L. Gain, Bridging art and engineering using Escher-based virtual elements. Struct. and Multidiscip. Optim. **51**(4), 867–883 (2015)
75. I. Perugia, P. Pietra, A. Russo, A plane wave virtual element method for the Helmholtz problem. ESAIM Math. Model. Num. **50**(3), 783–808 (2016)
76. K. Schindler, *Physics of Space Plasma Activity* (Cambridge University Press, Cambridge, 2006)
77. T. Sorgente, S. Biasotti, G. Manzini, M. Spagnuolo, The role of mesh quality and mesh quality indicators in the virtual element method. Adv. Comput. Math. **48**, 3 (2022)
78. G. Tóth, The $divB = 0$ constraint in shock-capturing magnetohydrodynamics codes. J. Comput. Phys. **161**(2), 605–652 (2000)
79. G. Vacca, An H^1-conforming virtual element for Darcy and Brinkman equations. Math. Models Methods Appl. Sci. **28**(1), 159–194 (2018)
80. P. Wriggers, W.T. Rust, B.D. Reddy, A virtual element method for contact. Comput. Mech. **58**(6), 1039–1050 (2016)

Chapter 13
Virtual Element Methods for Engineering Applications

Peter Wriggers, Fadi Aldakheel, and Blaž Hudobivnik

Abstract Discretization schemes that base on the virtual element method (VEM) have gained over the last decade interest in the engineering community. VEM was applied to different problems in elasticity, elasto-plasticity, fracture and damage mechanics using different theoretical formulations like phase field approaches. For predictive simulations of such problems as well linear as nonlinear weak formulations have to be considered. This contribution is concerned with extensions of the virtual element method to problems of nonlinear nature where VEM has advantages, like in micromechanics, fracture and contact mechanics. Low-order formulations for problems in two dimensions, with elements being arbitrary polygons, are considered.

13.1 Generic Formulation of a Nonlinear Boundary Value Problem

Generally a nonlinear problem in solid mechanics can be written in a strong or weak form. Here we state a generic weak form that will be specified in later sections for the problems at hand. Generally we can write

$$a(\boldsymbol{u}\,,\boldsymbol{v}) = b(\boldsymbol{v}) \tag{13.1.1}$$

where $a(\boldsymbol{u}\,,\boldsymbol{v})$ is a nonlinear operator, being nonlinear in the primal variable $\boldsymbol{u}$ and $\boldsymbol{v}$ is the test function, also known in the engineering literature as virtual displacement. The term $b(\boldsymbol{v})$ on the right hand side of (13.1.1) denotes the loading terms. One

P. Wriggers (✉) · F. Aldakheel · B. Hudobivnik
Institute of Continuum Mechanics, Department of Mechanical Engineering, Leibniz University Hannover, An der Universität 1, Garbsen, Germany
e-mail: wriggers@ikm.uni-hannover.de; aldakheel@ikm.uni-hannover.de; hudobivnik@ikm.uni-hannover.de

possible form for $a(\boldsymbol{u}, \boldsymbol{v})$ for a solid occupying the area/volume Ω under pure mechanical loading is

$$a(\boldsymbol{u}, \boldsymbol{v}) = \int_{\Omega} \boldsymbol{P}(\boldsymbol{u}) \cdot \nabla \boldsymbol{v} \, \mathrm{d}\Omega \qquad (13.1.2)$$

where $\boldsymbol{P}(\boldsymbol{u})$ is the first Piola–Kirchhoff stress tensor which is in general a nonlinear function of $\boldsymbol{u}$. Additionally, the right hand side is given by

$$b(\boldsymbol{v}) = \int_{\Omega} \bar{\boldsymbol{b}} \cdot \boldsymbol{v} \, \mathrm{d}\Omega + \int_{\partial\Omega} \bar{\boldsymbol{t}} \cdot \boldsymbol{v} \, \mathrm{d}\Gamma \qquad (13.1.3)$$

where $\bar{\boldsymbol{b}}$ are volume loads and $\bar{\boldsymbol{t}}$ describe tractions at the surface.

For an approximate solution of (13.1.1) we have to select an ansatz for the primal variable $\boldsymbol{u}$ which we will denote here in a generic way by $\boldsymbol{u}_h$. Hence the weak form yields

$$a(\boldsymbol{u}_h, \boldsymbol{v}) = b(\boldsymbol{v}) \qquad (13.1.4)$$

where $\boldsymbol{u}_h$ is a function with discrete unknown variables at some specific points within Ω.

Additionally it is possible to construct a potential U that can be applied equivalently to the weak form

$$U(\boldsymbol{u}) \longrightarrow EXTREMUM \qquad (13.1.5)$$

Classically the variation of a potential is computed using the directional or Gateaux derivative

$$a(\boldsymbol{u}, \boldsymbol{v}) - b(\boldsymbol{v}) = \left. \frac{d}{d\varepsilon} U(\boldsymbol{u} + \varepsilon \boldsymbol{v}) \right|_{\varepsilon=0} = 0 \qquad (13.1.6)$$

which yields the weak form (13.1.1).

When generating virtual elements using automatic differentiation tools it can be advantageous for numerical efficiency to start from a potential, see e.g. [51]. This is restricted to formulations where a potential can be constructed like in elasticity. However it is possible to use potential forms also in more general applications where no real potential exists. In such cases a pseudo potential U_p can be formulated, see [51] for the general case and e.g. [81] for elasto-plasticity. The idea is to fix during the computation of the directional derivative some quantities. These are in e.g. plasticity the history variables $\boldsymbol{h}$ which depend implicitly on $\boldsymbol{u}$. Then the directional derivative

$$\left. \frac{d}{d\varepsilon} U_p(\{\boldsymbol{u}, \boldsymbol{h}\} + \varepsilon \boldsymbol{v}) \right|_{\varepsilon=0, \boldsymbol{h}=const.} = a(\boldsymbol{u}, \boldsymbol{v}) - b(\boldsymbol{v}) = 0 \qquad (13.1.7)$$

yields the correct weak form. This methodology can also be applied for the discretized form (13.1.4) leading to

$$\frac{d}{d\varepsilon} U_p(\{\boldsymbol{u}_h\,,\boldsymbol{h}\} + \varepsilon\,\boldsymbol{v}) \bigg|_{\varepsilon=0\,,\boldsymbol{h}=const.} = a(\boldsymbol{u}_h\,,\boldsymbol{v}) - b(\boldsymbol{v}) = 0 \qquad (13.1.8)$$

The potentials U and U_p will be specified in the application sections.

13.2   Formulation of the Virtual Element Method

The virtual element method (VEM) is a generalization of the finite element method, which has, inspired from modern *mimetic finite difference schemes*, its roots in the pioneering work by Brezzi et al. [21]. It has proven to be a competitive discretization scheme for meshes with irregularly shaped elements that can even become non-convex.

First work related to the linear Poisson problem and linear elasticity can be found in [6, 10, 12, 36] and [23]. In [15] and [13] the virtual element method was further developed for problems including curved element boundaries. So far applications of virtual elements have been devoted to contact problems in [1, 85], discrete fracture network simulations in [19, 44, 62], isotropic damage in [27] and phase field modeling of fracture in [2] as well as for plasticity problems in [7, 43, 81] and homogenization approaches in [8, 56].

In this section we will define the ansatz function $\boldsymbol{u}_h$ which has to be inserted in the weak form (13.1.4) or the potential forms (13.1.6) and (13.1.8).

Following the work of [21], the main idea of the virtual element method is a Galerkin projection of the unknowns onto a specific ansatz space. The domain Ω is partitioned into non-overlapping polygonal elements which need not to be convex and can have any arbitrary shape with different node numbers, as plotted in Fig. 13.1 representing a *bird-like* element with vertices $\boldsymbol{x}_I$. Here a low-order approach is adopted, see [84] and [81], using linear ansatz functions where nodes are placed only at the vertices of the polygonal elements. Furthermore, the shape functions at the element boundaries are linear functions.

In this paper we will restrict ourselves to linear ansatz spaces for the virtual element method since the resulting elements are extremely robust in nonlinear applications which can be non-smooth, like plasticity, contact or fracture. Generally a linear ansatz for a virtual element Ω_e has the following properties:

1. The values of the ansatz space u_h are known at the vertices.
2. The ansatz u_h is linear and only defined along the edges $\partial\Omega_e$ of the virtual element.
3. The ansatz u_h has the property $\Delta u_h = 0$ in Ω_e.

Due to this definition the space for the virtual element has linear variation at the edges of Ω_e and contains harmonic functions that are implicitly known inside Ω_e.
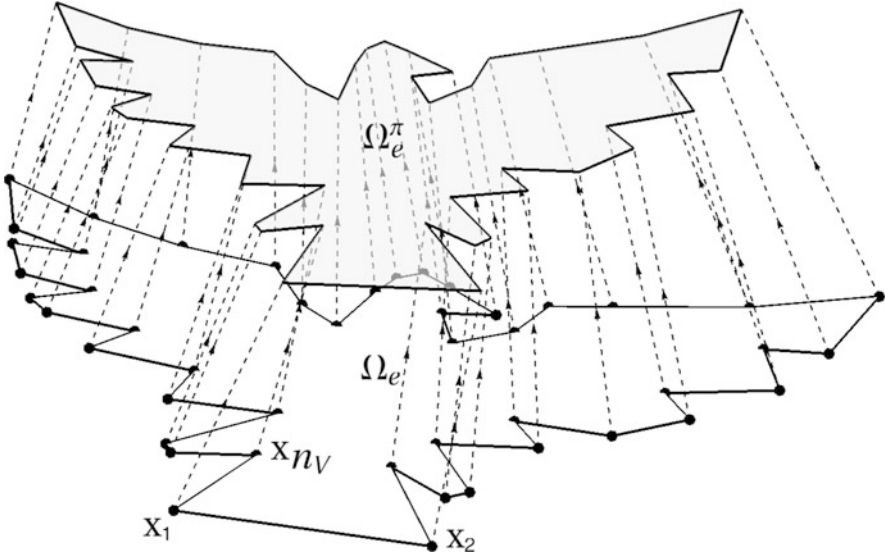
Fig. 13.1 Polynomial basis function for the virtual element ansatz with vertices x_I. (From: F. Aldakheel, B. Hudobivnik, A. Hussein, P. Wriggers, Phase-field modeling of brittle fracture using an efficient virtual element scheme, Computer Methods in Applied Mechanics and Engineering 341, 443–466, 2018. Elsevier. Reproduced with permission)

13.2.1   Ansatz Functions for VEM in Two Dimensions

Classically an ansatz space of a of a problem has to be defined for all primal variables $\mathfrak{U}_h = \{\boldsymbol{u}_h, q_h\}$, like displacements $\boldsymbol{u}_h$ and other variables q_h which could be the temperature θ_h or the phase field d_h in a coupled problem. The virtual element method relies now on the split of the ansatz into a part $\mathfrak{U}_\Pi$ representing the projected fields and a remainder $(\mathfrak{U}_h - \mathfrak{U}_\Pi)$. As an example this split is written here for the phase field methodology which constitutes a multi-field approach

$$\mathfrak{U}_h = \mathfrak{U}_\Pi + (\mathfrak{U}_h - \mathfrak{U}_\Pi) \quad \text{with} \quad \mathfrak{U}_\Pi := \{\boldsymbol{u}_\Pi, q_\Pi\}. \tag{13.2.1}$$

The projection $\mathfrak{U}_\Pi$ is defined at element level by a linear ansatz function $\mathbf{N}_\Pi$ as

$$\mathfrak{U}_\Pi = \begin{bmatrix} u_{\Pi x} \\ u_{\Pi y} \\ q_\Pi \end{bmatrix} = \mathbf{A}\,\mathbf{N}_\Pi = \begin{bmatrix} a_1 & a_4 & a_7 \\ a_2 & a_5 & a_8 \\ a_3 & a_6 & a_9 \end{bmatrix} \begin{bmatrix} 1 \\ x \\ y \end{bmatrix}, \tag{13.2.2}$$

with the unknowns $\mathbf{A}$. The projection $\mathfrak{U}_\Pi$ can now be computed by the Galerkin projection

$$\int_{\Omega_e} \nabla \mathbf{N}_\Pi \cdot \nabla \mathfrak{U}_\Pi \, dV \stackrel{!}{=} \int_{\Omega_e} \nabla \mathbf{N}_\Pi \cdot \text{Grad}\,\mathfrak{U}_h \, dV, \tag{13.2.3}$$

as a function of the nodal unknowns of $\mathfrak{U}_h$ which is shown below.

Noting that $\nabla \mathbf{N}_\Pi$ and $\nabla \mathfrak{U}_\Pi$ are constant due to the linear ansatz in (13.2.2) equation (13.2.3) can be rewritten as

$$\nabla \mathfrak{U}_\Pi|_e \stackrel{!}{=} \frac{1}{\Omega_e} \int_{\Omega_e} \text{Grad}\, \mathfrak{U}_h \, dV = \frac{1}{\Omega_e} \int_{\partial\Omega_e} \mathfrak{U}_h \otimes \mathbf{N} \, dA. \qquad (13.2.4)$$

The vector $\mathbf{N}$ represents the normal at the boundary $\partial\Omega_e$ of the domain Ω_e of a virtual element Ω_e, see Fig. 13.2. The label $\square|_e$ denotes element quantities that have constant value within an element e.

Now the boundary integral in (13.2.4) has to be evaluated. To this end, a linear ansatz for the primary fields along the element edges is introduced as

$$(\mathfrak{U}_h)_k = \sum_{j=1}^{2} M_{k\,j}\, \mathfrak{U}_j = (1 - \xi_k)\, \mathfrak{U}_1 + \xi_k\, \mathfrak{U}_2 \quad \text{with } \xi_k = \frac{x_k}{L_k}, \qquad (13.2.5)$$

for a boundary segment k of the virtual element. The local nodes: 1–2 are chosen in counter-clockwise order and can be found in Fig. 13.2. In (13.2.5) $M_{k\,1} = 1 - \xi_k$ is the ansatz function along a segment k, related to node 1, $\xi_k \in \{0, 1\}$ is the local dimensionless coordinate and $\mathfrak{U}_1$ represents the nodal values at that node. The ansatz function $M_{k\,2} = \xi_k$ is defined in the same way. From (13.2.4)–(13.2.5), the unknowns a_4–a_9 can be computed as

$$\nabla \mathfrak{U}_\Pi|_e = \begin{bmatrix} a_4 & a_7 \\ a_5 & a_8 \\ a_6 & a_9 \end{bmatrix} = \frac{1}{\Omega_e} \int_{\partial\Omega_e} \mathfrak{U}_h \otimes \mathbf{N} \, dA = \frac{1}{\Omega_e} \sum_{k=1}^{n_V} \int_{\partial\Omega_k} \begin{bmatrix} u_x(\mathbf{x})N_x & u_x(\mathbf{x})N_y \\ u_y(\mathbf{x})N_x & u_y(\mathbf{x})N_y \\ q(\mathbf{x})N_x & q(\mathbf{x})N_y \end{bmatrix} dA,$$

$$(13.2.6)$$
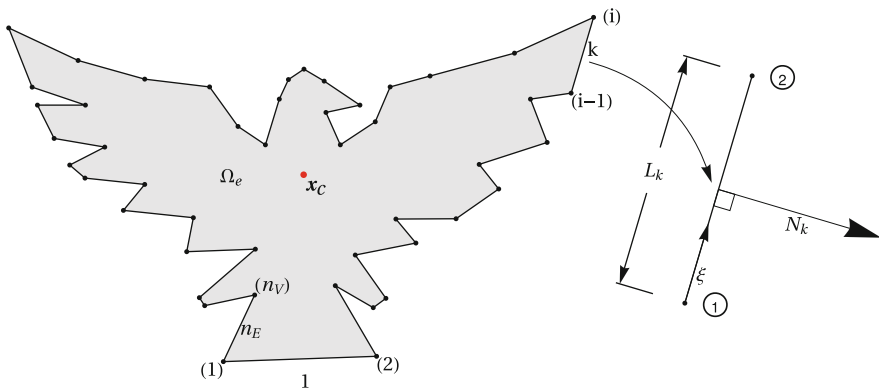
Fig. 13.2 Virtual element with n_V nodes and local boundary segment of the bird-like polygonal element. (From: F. Aldakheel, B. Hudobivnik, A. Hussein, P. Wriggers, Phase-field modeling of brittle fracture using an efficient virtual element scheme, Computer Methods in Applied Mechanics and Engineering 341, 443–466, 2018. Elsevier. Reproduced with permission)

where we have used $N = \{N_x, N_y\}^T$ and $\mathfrak{U}_h = \{u_x, u_y, d\}^T$. The number of element vertices, n_V, coincides with the number of segments (edges) of the element, for first order VEM. Note that the normal vector N changes from segment to segment. In the two-dimensional case it can be computed for a segment k as

$$N_k = \left\{ \begin{matrix} N_x \\ N_y \end{matrix} \right\}_k = \frac{1}{L_k} \left\{ \begin{matrix} y_1 - y_2 \\ x_2 - x_1 \end{matrix} \right\}_k, \tag{13.2.7}$$

with $x = \{x_i, y_i\}_{i=1,2}$ being the local coordinates of the two vertices of the segment k. The integral in (13.2.6) can be evaluated for the ansatz functions (13.2.5) exactly by using the trapezoidal or Gauss–Lobatto rule. By selecting the vertices as the Gauss–Lobatto points it is sufficient to know only the nodal values

$$\mathfrak{U}_e = \{\mathfrak{U}_1, \mathfrak{U}_2, \ldots, \mathfrak{U}_{n_V}\}, \tag{13.2.8}$$

at the n_V vertices V in Fig. 13.2. Since the ansatz function in (13.2.5) fulfills the property $M_I(x_J) = \delta_{IJ}$ the actual form of the function M does not enter the evaluation of the boundary integrals which makes the evaluation extremely simple. The unknowns a_4 to a_9 follow from (13.2.6) by inspection and can be written in terms of the nodal unknowns $\mathfrak{U}_e$, for further details see e.g. [84].

The projection in (13.2.4) does not determine the ansatz $\mathfrak{U}_\Pi$ in (13.2.2) completely and has to be supplemented by a further condition to obtain the constants a_1, a_2 and a_3. For this purpose we adopt the condition that the sum of the nodal values of $\mathfrak{U}_h$ and of its projection $\mathfrak{U}_\Pi$ are equal. This yields for each element Ω_e

$$\sum_{I=1}^{n_V} \mathfrak{U}_\Pi(x_I) = \sum_{I=1}^{n_V} \mathfrak{U}_h(x_I), \tag{13.2.9}$$

where x_I are the coordinates of the nodal point I and the sum includes all boundary nodes. Substituting (13.2.2) and (13.2.5) in (13.2.9), results with the three unknowns a_1, a_2 and a_3 as

$$\begin{bmatrix} a_1 \\ a_2 \\ a_3 \end{bmatrix} = \frac{1}{n_V} \sum_{I=1}^{n_V} \left[\mathfrak{U}_I - \nabla \mathfrak{U}_{\Pi I} \cdot x_I \right] = \frac{1}{n_V} \sum_{I=1}^{n_V} \begin{bmatrix} u_{xI} - u_{x,x}\, x_I - u_{x,y}\, y_I \\ u_{yI} - u_{y,x}\, x_I - u_{y,y}\, y_I \\ q_I - q_{,x}\, x_I - q_{,y}\, y_I \end{bmatrix}. \tag{13.2.10}$$

Thus, the ansatz function $\mathfrak{U}_\Pi$ of the virtual element is completely defined.

13.2.2 Ansatz Functions for VEM in Three Dimensions

In the same way as in the previous section the ansatz function can be defined for a virtual element in a three-dimensional setting. The projection $\mathfrak{U}_\Pi$ in (13.2.1) is now defined at element level by a linear ansatz function $\mathbf{N}_\Pi$ as

$$
\mathfrak{U}_\Pi = \begin{bmatrix} u_{\Pi x} \\ u_{\Pi y} \\ u_{\Pi z} \\ q_\Pi \end{bmatrix} = \mathbf{A}\,\mathbf{N}_\Pi = \begin{bmatrix} a_1 & a_5 & a_9 & a_{13} \\ a_2 & a_6 & a_{10} & a_{14} \\ a_3 & a_7 & a_{11} & a_{15} \\ a_4 & a_8 & a_{12} & a_{16} \end{bmatrix} \begin{bmatrix} 1 \\ x \\ y \\ z \end{bmatrix}, \qquad (13.2.11)
$$

with the unknowns $\mathbf{A}$. As in the two-dimensional case one can use Eqs. (13.2.4) and (13.2.9) to determine the parameters a_1 to a_{16}. The only difference is that now in (13.2.4) the integration on the right hand side has to be carried out over the faces of the polyhydral element. For details, see e.g. [43]

13.2.3 Residual and Tangent Matrix of the Virtual Elements

A virtual element that based only on the projection $\mathfrak{U}_\Pi$ of the displacement and fracture phase-field would lead to a rank deficient element once the number of vertices is greater than 3 in two-dimensional and 4 in three-dimensional applications. Thus the formulation has to be stabilized like the classical one-point integrated elements developed by [16, 33, 50, 61, 68, 69] and [52]. The generic potential functional defined in (13.1.5) can be rewritten by exploiting the split in (13.2.1). Thus we have, by summing up all element contributions for the n_e virtual elements

$$
U(\mathfrak{U}) = \bigwedge_{e=1}^{n_e} U(\mathfrak{U}_e) \text{ with } U(\mathfrak{U}_e) = \big[\, U_c(\mathfrak{U}_\Pi)|_e + U_{stab}(\mathfrak{U}_h - \mathfrak{U}_\Pi)|_e \,\big],
$$

$$(13.2.12)$$

based on a consistency part U_c that is constant and an associated stabilization term U_{stab}. The consistency term in (13.2.12) can be computed as

$$
U_c(\mathfrak{U}_\Pi)|_e = \int_{\Omega_e} W(\mathfrak{C}_\Pi)\,dV \;-\; \int_{\Omega_e} \overline{\boldsymbol{f}} \cdot \mathfrak{U}_\Pi\,dV - \int_{\partial\Omega_t} \bar{\boldsymbol{t}} \cdot \mathfrak{U}_\Pi\,dA \qquad (13.2.13)
$$

where the last two terms describe e.g. mechanical, chemical, thermal actions within the solid, denoted by $\overline{\boldsymbol{f}}$, or at its boundary, given by $\bar{\boldsymbol{t}}$. The projected constitutive state variables are given as $\mathfrak{C}_\Pi = \{\boldsymbol{C}_\Pi, \nabla q_\Pi, \mathscr{H}\}$ where $\mathscr{H}$ is a variable that depends implicitly on the primal variables and thus has to be kept constant in the first variation of U_c.

The projected strain tensor can be computed from the projected displacement as

$$C_\Pi = F_\Pi^T \, F_\Pi = [1 + \nabla u_\Pi]^T \, [1 + \nabla u_\Pi] \, . \tag{13.2.14}$$

where the deformation gradient , F_Π depends linearly on the gradient of the projected displacement u_Π.

The primary fields $\mathfrak{U}_\Pi$ are linear functions and their gradient $\nabla \mathfrak{U}_\Pi$ is constant over the area of the virtual element Ω_e, as a consequence, the potential W is integrated by evaluating the function at the element centroid x_c as shown in Fig. 13.2 and multiplying it with domain size Ω_e analogous to the standard Gauss integration scheme in FEM

$$\int_{\Omega_e} W(\mathfrak{C}_\Pi) \, dV = W(\mathfrak{C}_\Pi)|_c \, \Omega_e \tag{13.2.15}$$

with the label $\square|_c$ refers to quantities evaluated at the element centroid x_c.[1]

13.2.4 Stabilization of the Method

Next, the stabilization potential has to be derived for the coupled problem based on the potential (13.2.12). There exist different approaches that can be followed for stabilization. Form the mathematical point of view a stabilization of the type

$$U_{stab}(\mathfrak{U}_h - \mathfrak{U}_\Pi) = \frac{\gamma}{2} \sum_{I=1}^{n_V} [\mathfrak{U}_I - \mathfrak{U}_\Pi(X_I)]^2 \tag{13.2.16}$$

was introduced in many papers starting with [10] based on the weak form. Here γ is a stabilization parameter that depends on the dimension of the problem, the constitutive matrix and the mesh size.

Following the work of [84], we introduce a non-linear stabilization procedure, that takes the form

$$U_{stab}(\mathfrak{U}_h - \mathfrak{U}_\Pi)|_e = \widehat{U}(\mathfrak{U}_h)\Big|_e - \widehat{U}(\mathfrak{U}_\Pi)\Big|_e \tag{13.2.17}$$

which has a advantage for linear ansatz functions. In such case it allows the enhancement of the bending behaviour of solid elements by choosing $\widehat{U}$ in an adequate way. For the stabilization density function $\widehat{W}$, we propose a similar function to the original density function (13.2.13), however scaled by a constant

---

[1] The above approach can also be used for higher order formulations, see e.g. [26, 82]. However in these cases the integral in (13.2.15) has to be evaluated based on a sub triangular mesh involving more computational effort.

value β as: $\widehat{W} = \beta\ W$. In (13.2.17), the stabilization with respect to the projected primary fields $\widehat{U}(\mathfrak{U}_\Pi)\big|_e$ can be then calculated as in (13.2.15), yielding

$$\widehat{U}(\mathfrak{U}_\Pi)\big|_e = \beta\ W(\mathfrak{C}_\Pi)\big|_c\ \Omega_e \tag{13.2.18}$$

The potential $\widehat{U}(\mathfrak{U}_h)\big|_e$ is computed by applying a standard FEM procedure, i.e. by first discretizing the virtual element domain Ω_e into internal triangle element mesh consisting of $n_T = n_E - 2$ triangles as plotted in Fig. 13.3 for the *bird-like* polygonal element. Note however that this stabilization does not introduce new variables since only the vertices of the virtual element are used. With that the integral over Ω_e is transformed into the sum of integrals over triangles. By using a linear ansatz for the primary fields $\mathfrak{U}$, an approximation can be computed for the constitutive variables $\mathfrak{C}$ within each triangle Ω_m^i of the inscribed mesh, see [84]. This gives

$$\widehat{U}(\mathfrak{U}_h)\big|_e = \int_{\Omega_e} \widehat{W}(\mathfrak{C}_h)\, dV = \beta \int_{\Omega_e} W(\mathfrak{C}_h)\, dV = \beta \sum_{i=1}^{n_T} \Omega_e^i\ W(\mathfrak{C}_h)\big|_c \tag{13.2.19}$$

where $W(\mathfrak{C}_h)\big|_c$ is the potential density function evaluated at the triangle centroid $\boldsymbol{x}_c^i$ and Ω_e^i is the area of the ith triangle in the element e, as plotted in Fig. 13.3.

To compute the stabilization parameter β, a connection to the bending problem was imposed regarding to the bulk energy as outlined in [84]. For $\Omega_e \to 0$ the difference between the potentials will also go to zero: $\widehat{U}(\mathfrak{U}_h) - \widehat{U}(\mathfrak{U}_\Pi) \to 0$, thus the stabilization will not influence a converged solution. The choice of the factor β will be discussed later in the application sections. Generally, the parameter β has to lie in the interval: $0 < \beta \leq 1$. A good choice that works in many cases is provided
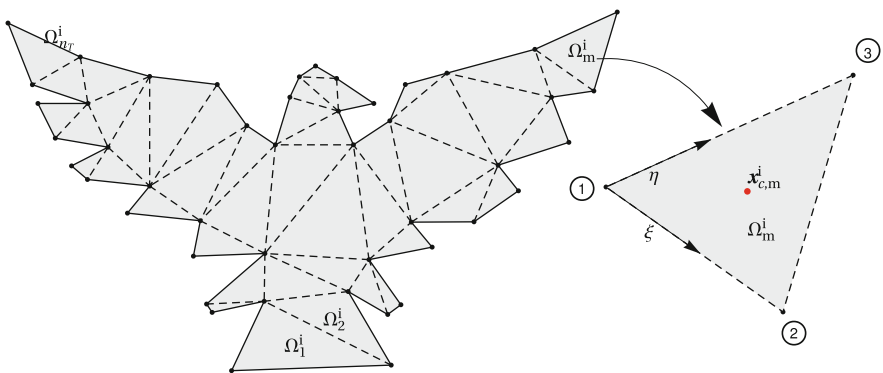
Fig. 13.3 Internal triangular mesh of the bird-like polygonal element. (From: F. Aldakheel, B. Hudobivnik, A. Hussein, P. Wriggers, Phase-field modeling of brittle fracture using an efficient virtual element scheme, Computer Methods in Applied Mechanics and Engineering 341, 443–466, 2018. Elsevier. Reproduced with permission)

by $\beta = 0.3$. Note that for β approaching zero, the potential $U(\mathfrak{U}_h)$ in (13.2.12) will depend only on the projection part $U_c(\mathfrak{U}_\Pi)$, leading to rank deficiency. However, for $\beta = 1$, a pure FEM solution based on macro-elements with the internal mesh as shown in Fig. 13.3 will be reproduced.

All further derivations leading to the residual vector $\mathbf{R}_e$ and the tangent matrix $\mathbf{K}_e$ of the virtual element e were performed with the symbolic tool ACEGEN. This yields for (13.2.12) along with the potentials (13.2.13) and (13.2.17)–(13.2.19) the following:

$$\mathbf{R}_e = \left. \frac{\partial U(\mathfrak{U}_e)}{\partial \mathfrak{U}_e} \right|_{\mathscr{C}=\text{const.}} \quad \text{and} \quad \mathbf{K}_e = \frac{\partial \mathbf{R}_e}{\partial \mathfrak{U}_e} \tag{13.2.20}$$

where $\mathscr{C}$ refers to fields that have to be constant during differentiation, like history variables in plasticity, the driving force in phase field methods, the slip in frictional contact problems, etc.

With these expressions at hand, we adopt a global Newton–Raphson solution procedure for the coupled problem, resulting in the following algorithm

$$\begin{aligned} &\text{do } n = 1, \ldots, \text{convergence} \\ \mathbf{K}(\mathfrak{U}_n) \, \Delta \mathfrak{U}_{n+1} &= -\mathbf{R}(\mathfrak{U}_n) \\ \mathfrak{U}_{n+1} &= \mathfrak{U}_n + \Delta \mathfrak{U}_{n+1} \\ &\text{until } \|\mathbf{R}(\mathfrak{U}_{n+1})\| < TOL \end{aligned} \tag{13.2.21}$$

with

$$\mathbf{R} = \overset{n_e}{\underset{e=1}{\mathbf{A}}} \mathbf{R}_e, \quad \mathbf{K} = \overset{n_e}{\underset{e=1}{\mathbf{A}}} \mathbf{K}_e \quad \text{and} \quad \mathfrak{U} = \overset{n_e}{\underset{e=1}{\mathbf{A}}} \mathfrak{U}_e \tag{13.2.22}$$

that determines at given global primary fields $\mathfrak{U}$ their linear increment $\Delta \mathfrak{U}$ in a typical Newton-type iterative solution step. This system of nonlinear equations has to be solved in a nested algorithm, where the displacement and the crack phase-field are the global unknown variables.

13.3 VEM for Fracturing Solids

In this section, we examine the efficiency of the VEM for predicting the failure mechanisms in solids due to crack initiation and propagation. The fracture of solids can be numerically modeled by using discontinuous approaches, where the displacement field is allowed to have a jump across the crack surface. In this regard, several methods can be applied, such as (i) the meshless method [18, 34], (ii) the boundary element method [46, 66] and (iii) the extended finite

element method (XFEM) [17, 73]. Modeling fracture by using these methods is based on the calculating of the Stress Intensity Factors (SIF), which is one of the fundamental quantities in fracture mechanics to measure the strength of the stress singularity in the vicinity of a crack tip. In the literature, several methods have been proposed to calculate stress intensity factors. Among these are the displacement extrapolation method [24], the crack opening displacement (COD) [65], the virtual crack extension [40], the J-integral [32, 71] and the interaction integral method [91]. In [9, 41]. A hybrid crack element was introduced in [49, 75], which leads to a direct and accurate computation of the SIFs as well as the coefficients of the higher order terms in the elastic asymptotic crack tip field.

The above mentioned approaches consider the fracture of solids as a discontinuous interface. The modeling of crack formation can also be achieved using damage mechanics or a continuum phase-field approaches, which are based on the regularization of sharp crack discontinuities. Phase-field modeling of fracture has attracted considerable attention in recent years due to its capability of capturing complex crack patterns in various problems in solid mechanics. Many efforts have been focused on the regularized modeling of Griffith-type brittle fracture in elastic solids. In this regard, [59] proposed a phase-field approach to fracture with a local irreversibility constraint on the crack phase-field. Work on brittle fracture has been devoted to the dynamic case, cohesive fracture, multiplicative decomposition of the deformation gradient into compressive-tensile parts, hydraulic fracturing and fatigue effects for brittle materials, see e.g. [3, 4, 20, 30, 39, 42, 53, 72, 77].

Here we will discuss the merits of virtual elements when applied to fracturing processes.

13.3.1 Basic Equations of Elastic Solids

Consider an elastic body $\Omega \subset \mathbb{R}^2$ bounded by $\partial\Omega$. As shown in Fig. 13.4, the boundary $\partial\Omega$ is subdivided into Neumann boundary conditions on $\partial\Omega_t$, Dirichlet boundary conditions on $\partial\Omega_u$ and a discontinuity interface on Γ_c (crack line in 2-D and crack surface in 3-D) such that $\partial\Omega = \partial\Omega_t \cup \partial\Omega_u \cup \Gamma_c$. The discontinuity Γ_c is composed of the upper Γ_c^+ and the lower Γ_c^- crack faces.

The crack face Γ_c is assumed to be traction-free, thus

$$\boldsymbol{\sigma} \cdot \boldsymbol{N}_c^+ = \boldsymbol{0} \quad \text{on } \Gamma_c^+, \qquad \text{and} \qquad \boldsymbol{\sigma} \cdot \boldsymbol{N}_c^- = \boldsymbol{0} \quad \text{on } \Gamma_c^-, \qquad (13.3.1)$$

where $\boldsymbol{N}_c^+$ and $\boldsymbol{N}_c^-$ are the outward unit normal vectors defined on Γ_c^+ and Γ_c^-, respectively. The Neumann $\partial\Omega_t$ and Dirichlet $\partial\Omega_u$ boundary conditions are given by

$$\boldsymbol{\sigma} \cdot \boldsymbol{N} = \bar{\boldsymbol{t}} \quad \text{on } \partial\Omega_t, \qquad \text{and} \qquad \boldsymbol{u} = \bar{\boldsymbol{u}} \quad \text{on } \partial\Omega_u, \qquad (13.3.2)$$

Fig. 13.4 Definition of solid with a crack and boundary conditions. (From: A. Hussein, F. Aldakheel, B. Hudobivnik, P. Wriggers, P.A. Guidault, O. Allix Finite Elements in Analysis and Design 159, 15–32, 2019. Elsevier. Reproduced with permission)
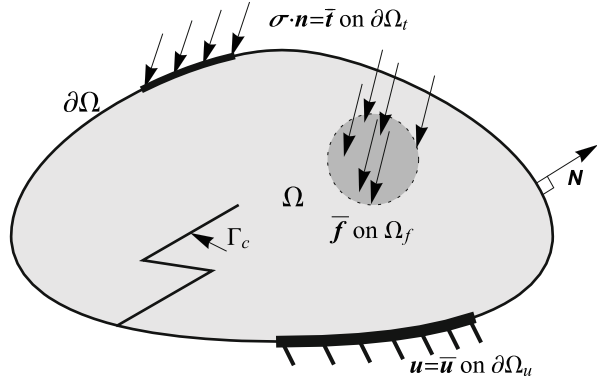
where N is the outward unit normal vector of the boundary, u the displacement vector, $\bar{u}$ the prescribed displacement on $\partial\Omega_u$ and $\bar{t}$ the surface traction on $\partial\Omega_t$. We consider that the body undergoes small deformation, therefore we describe the strain ε by

$$\varepsilon = \frac{1}{2}(\nabla u + \nabla^T u). \tag{13.3.3}$$

For a homogeneous isotropic linear elastic material the strain energy density function W can be expressed as

$$W(\{\varepsilon\}) = \frac{\lambda}{2}\mathrm{tr}^2(\varepsilon) + \mu\,\mathrm{tr}(\varepsilon^2), \tag{13.3.4}$$

where λ and μ are the Lamé constants. The Cauchy stress tensor σ is obtained from the strain energy W in (13.3.4) by

$$\sigma = \frac{\partial W}{\partial \varepsilon} = \lambda\,\mathrm{tr}(\varepsilon)I + 2\mu\varepsilon, \tag{13.3.5}$$

where I is the second order unit tensor. The variational formulation of the equilibrium can be obtained by using the principle of a stationary elastic potential. The potential can be defined in terms of the strain energy density function W and the external load U_{ex} as

$$U(u) = \int_\Omega W(\varepsilon(u))\,\mathrm{d}\Omega \underbrace{- \int_{\Omega_f} \overline{f} \cdot u\,dV - \int_{\partial\Omega_t} \bar{t} \cdot u\,dA}_{U_{ex}}. \tag{13.3.6}$$

13.3.2   Crack Propagation Based on Stress Intensity Factors

In this work, the interaction integral (*I*-integral) is used to determine the stress intensity factors in case of a mixed-mode loading [91]. This integral is based on the classical *J*-Integral. For a homogeneous isotropic linear elastic material the *J*-integral

$$J = \int_{\Gamma} \left(W \, \delta_{1j} - \sigma_{ij} \frac{\partial u_i}{\partial x_1} \right) N_j \, \mathrm{d}\Gamma, \tag{13.3.7}$$

is path independent where W is the strain energy density given by (13.3.4) and u_i is the displacement field, N_j the outward normal vector to the contour integral Γ, δ_{1j} the Kronecker delta and σ_{ij} are the components of the stress and strain tensor which are used for the sake of simplification in this section.

For a linear elastic material, [70] has demonstrated that the *J*-integral of a contour around the crack tip matches the energy release rate g_c. The relationship between these quantities (J, g_c) and the stress intensity factors can be written as

$$J = g_c = \frac{K_{\mathrm{I}}^2 + K_{\mathrm{II}}^2}{E'}, \tag{13.3.8}$$

where E' is given in terms of the Young's modulus E and the Poisson's ratio ν as

$$E' = \begin{cases} E, & \text{plane stress} \\ E/(1 - \nu^2), & \text{plane strain}. \end{cases} \tag{13.3.9}$$

In a mixed-mode fracture problem, it is difficult to use the classical form of the *J*-integral to calculate the individual stress intensity factor for each fracture mode *separately*. To overcome this difficulty, an interaction integral (*I*-integral) based on two independent equilibrium states of a cracked body, was introduced in [90]. The first state represents the actual fields ($\boldsymbol{u}, \boldsymbol{\varepsilon}, \boldsymbol{\sigma}$) and the second state defines the auxiliary fields ($u_i^{(aux)} = K_{\mathrm{I}}^{(aux)} g_i^I + K_{\mathrm{II}}^{(aux)} g_i^{II}, \sigma_{ij}^{(aux)} = K_{\mathrm{I}}^{(aux)} f_i^{\,I} + K_{\mathrm{II}}^{(aux)} f_i^{\,II}$) in terms of Williams' functions ($g_i^{I,II}, f_i^{\,I,II}$), see [78]. By superimposing these states, the *I*-integral of the new equilibrium state can be defined as

$$I = \int_{\Gamma} \left(W^{(aux)} \delta_{1j} - \sigma_{ij} \frac{\partial u_i^{(aux)}}{\partial x_1} - \sigma_{ij}^{(aux)} \frac{\partial u_i}{\partial x_1} \right) N_j \, \mathrm{d}\Gamma, \tag{13.3.10}$$

with the interaction strain energy density $W^{(aux)} = \boldsymbol{\sigma} \cdot \boldsymbol{\varepsilon}^{(aux)} = \boldsymbol{\sigma}^{(aux)} \cdot \boldsymbol{\varepsilon}$. Following [60], the interaction integral for the actual and auxiliary states can be expressed in terms of the stress intensity factors

$$I = \frac{2}{E'} (K_{\mathrm{I}} K_{\mathrm{I}}^{(aux)} + K_{\mathrm{II}} K_{\mathrm{II}}^{(aux)}). \tag{13.3.11}$$

By setting $K_{\mathrm{I}}^{(aux)} = 1$ and $K_{\mathrm{II}}^{(aux)} = 0$ in (13.3.11) the stress intensity factor K_{I} for mode I can be determined as

$$K_{\mathrm{I}} = \frac{E'}{2} I \quad \text{with} \quad u_i^{(aux)} = K_{\mathrm{I}}^{(aux)} g_i^I \quad \text{and} \quad \sigma_{ij}^{(aux)} = K_{\mathrm{I}}^{(aux)} f_i^{\ I}. \quad (13.3.12)$$

Similarly, the same approach can be applied to compute the stress intensity factor K_{II} for mode II

$$K_{\mathrm{II}} = \frac{E'}{2} I \quad \text{with} \quad u_i^{(aux)} = K_{\mathrm{II}}^{(aux)} g_i^{II} \quad \text{and} \quad \sigma_{ij}^{(aux)} = K_{\mathrm{II}}^{(aux)} f_i^{\ II}. \quad (13.3.13)$$

For mixed-mode loading, an equivalent stress intensity factor $K_{\mathrm{aq}}(K_{\mathrm{I}}, K_{\mathrm{II}})$ was introduced to monitor the crack initiation, see [63]. When K_{aq} exceeds a critical fracture toughness K_{Ic}

$$K_{\mathrm{aq}}(K_{\mathrm{I}}, K_{\mathrm{II}}) \geq K_{\mathrm{Ic}} , \quad (13.3.14)$$

the crack begins to propagate. Once a crack has been initiated, the direction of growth can be predicted using different propagation criteria. In this paper, the maximum circumferential stress criterion is considered. The circumferential stress $\sigma_{\theta\theta}$ and the shear stress $\tau_{r\theta}$ in the neighbourhood of the crack tip can be analytically derived as

$$\sigma_{\theta\theta} = \frac{1}{\sqrt{2\pi r}} \left[\frac{K_{\mathrm{I}}}{4} \left(3\cos\frac{\theta}{3} + \cos\frac{3\theta}{2} \right) + \frac{K_{\mathrm{II}}}{4} \left(-3\sin\frac{\theta}{2} - 3\sin\frac{3\theta}{2} \right) \right], \quad (13.3.15)$$

$$\tau_{r\theta} = \frac{1}{2\sqrt{2\pi r}} \cos\frac{\theta}{2} [K_{\mathrm{I}} \sin\theta + K_{\mathrm{II}}(3\cos\theta - 1)]. \quad (13.3.16)$$

Generally, it is assumed that the crack propagates from the crack tip in the direction of the maximum circumferential stress. For this stress state the shear stress in (13.3.16) is zero which yields the propagation angle $\theta_{c,l}$ as a function of the stress intensity factors

$$\theta_{c,l} = -2\arctan \left[\frac{2K_{\mathrm{II}}}{K_{\mathrm{I}} \left(1 + \sqrt{1 + 8\,(K_{\mathrm{II}}/K_{\mathrm{I}})^2} \right)} \right]. \quad (13.3.17)$$

13.3.3 Construction of the Crack Path Using SIF

In this section, the crack path construction procedure during the propagation will be discussed briefly. More details on this can be found in [44]. The main
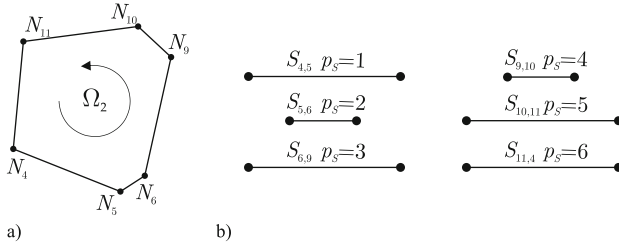
Fig. 13.5 (**a**) A virtual element Ω_2 composed of 6 nodes and (**b**) 6 element segments $\{S_{4,5}, \cdots, S_{11,4}\}_{\Omega_2}$ along with theirs position $p_S = 1, \cdots, 6$. (From: A. Hussein, F. Aldakheel, B. Hudobivnik, P. Wriggers, P.A. Guidault, O. Allix Finite Elements in Analysis and Design 159, 15–32, 2019. Elsevier. Reproduced with permission)
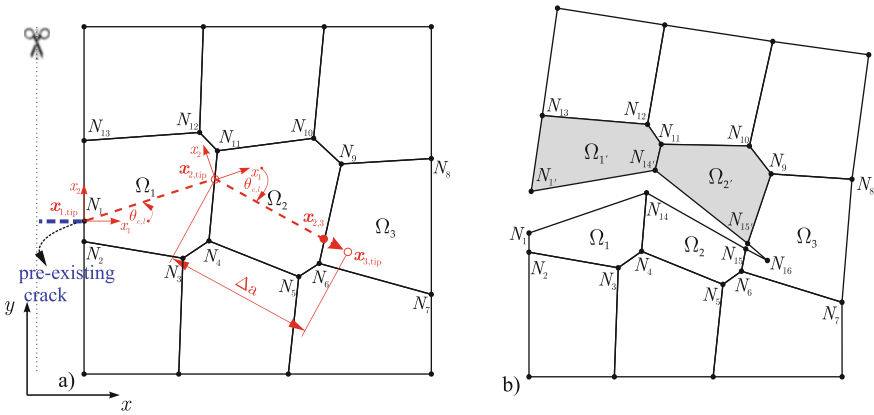

Fig. 13.6 A prescribed crack evolution using the introduced cutting technique procedure. (From: A. Hussein, F. Aldakheel, B. Hudobivnik, P. Wriggers, P.A. Guidault, O. Allix Finite Elements in Analysis and Design 159, 15–32, 2019. Elsevier. Reproduced with permission)

idea of this approach is the splitting of virtual elements in the direction of growth. In this procedure arbitrary elements with arbitrary number of nodes will be produced. This can be easily accomplished by VEM which can deal with arbitrary element shapes. For the visual representation of the splitting algorithm, we will explain the procedure using Figs. 13.5 and 13.6 for a single virtual element Ω_2. As shown in Fig. 13.5, the element Ω_2 consists of counter-clockwise ordered nodes $\{N_4, N_5, N_6, N_9, N_{10}, N_{11}\}_{\Omega_2}$ and segments $\{S_{4,5}, S_{5,6}, S_{6,9}, S_{9,10}, S_{10,11}, S_{11,4}\}_{\Omega_2}$. Hence, the segment $S_{5,6}$ is composed of the second and the third local node $\{N_5, N_6\}_{\Omega_2}$.

Now we consider the whole domain depicted in Fig. 13.6. Here, the solid blue line indicates a pre-existing crack and the dashed red line represents a predicted crack path, which has to be modeled. This path is defined by (i) the coordinates $\{x_{1,tip}, x_{2,tip}, x_{3,tip}\}$, (ii) the constant crack length Δa and (iii) the measured angle between the crack extension and the local coordinate system x_1.

At the beginning of the simulation, we know only the coordinates of the previous crack tip $x_{1,tip}$ (node N_1) and the increment length Δa. The first task is to determine the coordinates of the new crack tip $x_{2,tip}$. For that, we compute the stress intensity factors K_{I}, K_{II} and obtain from (13.3.17) the propagation angle $\theta_{c,l}$. Note that the angle $\theta_{c,l}$ is related to the local coordinate system x_1, x_2. Thus, a transformation to the global system x, y is needed. Next the following expression is used to compute the coordinates of the new crack tip $x_{2,tip}$

$$x_{2,tip} = x_{1,tip} + \left[\Delta a \cos\theta_{c,g} \ \Delta a \sin\theta_{c,g}\right]^T , \qquad (13.3.18)$$

with the global propagation angle $\theta_{c,g}$ generated from the previous crack angle $\theta_{prev.,g}$ by

$$\theta_{c,g} = \theta_{c,l} + \theta_{prev.,g}. \qquad (13.3.19)$$

After determining the second crack tip $x_{2,tip}$, a new node N_{14} will be inserted at the position of $x_{2,tip}$. Simultaneously, node N_1 of $x_{1,tip}$ is duplicated to $N_{1'}$. To let the crack within element Ω_1 propagate, we have to spread the information of this element (nodes and segments) in two groups. While the first group will be assigned to a newly introduced element $\Omega_{1'}$, the second one will belong to the existing element Ω_1. To propagate within element Ω_2, the intersection point $x_{2,3}$ between the crack line $r = x_{3,tip} - x_{2,tip}$ and the segment $S_{6,9}$ has to be obtained. Then, we add a new node N_{15} at the position of $x_{2,3}$ and duplicate node N_{14} to $N_{14'}$. Thus, a new element $\Omega_{2'}$ will be introduced. Finally, the crack propagation ends within element Ω_3, where only the elements connectivity is modified and updated accordingly.

Note that, the outlined procedure can be applied also on the concave (non-convex) elements, by preforming the cutting procedure multiple times, for each cut segment, as illustrated in Fig. 13.7. Moreover the crack path depicted in Fig. 13.6 has

a)   b)   c)
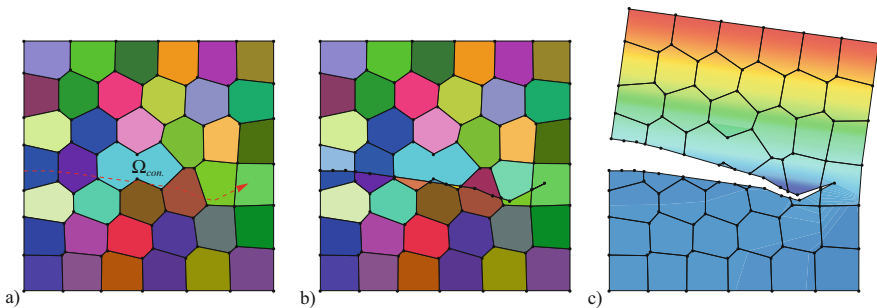
Fig. 13.7 A prescribed crack evolution during a tensile load condition. (**a**–**b**) A crack path on VEM mesh with a non-convex element $\Omega_{con.}$. (**c**) Contour plot of the displacement field $\bar{u}_y$, where red and blue represent the maximum and minimum displacement, respectively. (From: A. Hussein, F. Aldakheel, B. Hudobivnik, P. Wriggers, P.A. Guidault, O. Allix Finite Elements in Analysis and Design 159, 15–32, 2019. Elsevier. Reproduced with permission)

the possibility to change its direction within a virtual element. Due to that, a kinked crack can be modeled using the virtual element formulation without any restriction, see Fig. 13.7 as an example of such crack trajectories.

13.3.4   Phase-Field Approach for Brittle Crack Propagation

Now we consider the situation, where the response of fracturing solid at material points $x \in \Omega$ and time t is described by the displacement field $u(x, t)$ and the crack phase-field $d(x, t)$, with $d(x, t) = 0$ and $d(x, t) = 1$ for the unbroken and the fully broken state of the material, respectively, see Fig. 13.8. Thus the sharp crack topology $\Gamma_c \rightarrow \Gamma_l$ is regularized by the crack surface functional as outlined in [59]

$$\Gamma_l(d) = \int_\Omega \gamma_l(d, \nabla d) \, dV \quad \text{with} \quad \gamma_l(d, \nabla d) = \frac{1}{2l}d^2 + \frac{l}{2}|\nabla d|^2 . \qquad (13.3.20)$$

It is based on the crack surface density function γ_l and the fracture length scale l that governs the width of the diffuse crack, as plotted in Fig. 13.8. The regularized crack phase-field d is obtained by a minimization principle for the diffusive crack

$$d = \text{Arg}\{\inf_d \Gamma_l(d)\} \quad \text{with} \quad d = 1 \text{ on } \Gamma_c \subset \Omega, \qquad (13.3.21)$$

yielding the Euler equation $d - l^2 \Delta d = 0$ on Ω along with the Neumann boundary condition $\nabla d \cdot N = 0$ on $\partial\Omega$. Additionally a monotonous growth $\dot{d} \geq 0$ of the fracture phase-field has to be assured [59].
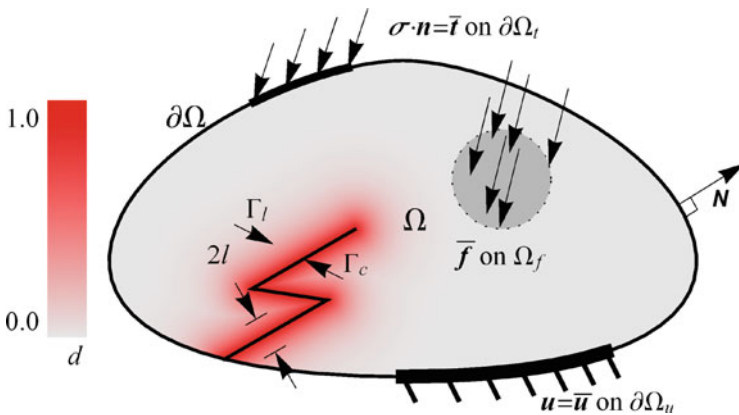
Fig. 13.8 Solid with a regularized crack and boundary conditions

The total specific potential of the phase field problem can be written as sum of the elastic and fracture specific potential

$$W(\boldsymbol{\varepsilon}, d, \nabla d,) = W_{elas}(\boldsymbol{\varepsilon}, d) + W_{frac}(d, \nabla d). \qquad (13.3.22)$$

Here, the specific fracture energy can be defined as a product of the surface density function γ_l (13.3.20) and the Griffith's critical energy release rate g_c

$$W_{frac}(d, \nabla d) = g_c \gamma_l(d, \nabla d). \qquad (13.3.23)$$

The original phase-field formulation, proposed by Francfort and Marigo [35], splits W_{elas} in a multiplicative way in the strain energy W and a degradation function $g(d)$

$$W_{elas}(\boldsymbol{\varepsilon}, d) = g(d) \, W(\boldsymbol{\varepsilon}), \qquad (13.3.24)$$

where $g(d) = (1 - d)^2$ models the degradation of the stored elastic energy of the solid due to fracture. It interpolates between the unbroken response for $d = 0$ and the fully broken state at $d = 1$ by satisfying the constraints $g(0) = 1$, $g(1) = 0$, $g'(d) \leq 0$ and $g'(1) = 0$.

In order to enforce a crack evolution only in tension, the stored elastic energy of the solid is additively decomposed into a positive part W^+ due to tension and a negative part W^- due to compression, outlined in [59]

$$W_{elas}(\boldsymbol{\varepsilon}, d) = g(d)W^+ + W^- \quad \text{with} \quad W^\pm = \frac{\lambda}{2} \langle \mathrm{tr}[\boldsymbol{\varepsilon}] \rangle_\pm^2 + \mu \, \mathrm{tr}[(\boldsymbol{\varepsilon}_\pm)^2], \qquad (13.3.25)$$

in terms of the Macauly bracket $\langle \cdot \rangle_\pm = (\cdot \pm | \cdot |)/2$, the positive $\boldsymbol{\varepsilon}_+ = \sum_{a=1}^3 \langle \varepsilon_a \rangle_+ \, \boldsymbol{N}_a \otimes \boldsymbol{N}_a$ and the negative strain tensors $\boldsymbol{\varepsilon}_- = \boldsymbol{\varepsilon} - \boldsymbol{\varepsilon}_+$, which depend on the principal strains $\{\varepsilon_a\}_{a=1..3}$ and the principal strain directions $\{\boldsymbol{N}_a\}_{a=1..3}$.

The variation of the potential yields

$$\delta W = \frac{\partial (W_{elas} + W_{frac})}{\partial d} \delta d + \frac{\partial W_{frac}}{\partial \nabla d} \cdot \nabla \delta d + \frac{\partial W_{elas}}{\partial \boldsymbol{\varepsilon}} \cdot \delta \boldsymbol{\varepsilon}, \qquad (13.3.26)$$

where the derivative of $\frac{\partial W_{elas}}{\partial d}$ can be defined as a crack driving force $\mathscr{H} = \frac{\partial W_{elas}}{\partial d}$. To ensure crack irreversibility in the sense that cracks can only grow (i.e. $\dot{d} \geq 0$), $\mathscr{H}$ has to be redefined in as:

$$\mathscr{H} = \max_{s \in [0,t]} \frac{\partial W_{elas}}{\partial d} \geq 0, \text{ where from (13.3.24)} \frac{\partial W_{elas}}{\partial d} = W^+, \qquad (13.3.27)$$

Alternatively, to enforce the crack evolution only in tension, the elastic energy can be additively decomposed in positive ψ_{vol}^+ and negative ψ_{vol}^- volumetric parts

in terms of the bulk modulus $\kappa = \lambda + \frac{2}{3}\mu$ and a deviatoric part ψ_{iso}. As outlined in the work of [5] the elastic energy can then be written in the form

$$W_{elas}(\boldsymbol{\varepsilon}, d) = g(d)(\psi_{vol}^+ + \psi_{iso}) + \psi_{vol}^- \qquad (13.3.28)$$

with $\psi_{vol}^\pm = \frac{\kappa}{2}\langle \mathrm{tr}[\boldsymbol{\varepsilon}]\rangle_\pm^2$ and $\psi_{iso} = \mu\, \mathrm{tr}[\boldsymbol{\varepsilon} - \mathrm{tr}[\boldsymbol{\varepsilon}]\,\mathbf{1})^2]$.

Following the recent work of [58] the fracture energy can be redefined in an incremental way as:

$$W_{frac}(d, \nabla d, \mathcal{H}) = g_c \gamma_l(d, \nabla d) + \frac{\eta}{2\Delta t}(d - d_n)^2 + g(d)\mathcal{H} \qquad (13.3.29)$$

where $\Delta t := t - t_n > 0$ denotes the time step and $\eta \geq 0$ is a material parameter that characterizes the viscosity of the crack propagation.

The above introduced variables will characterize the brittle failure response of a solid, based on the two *global primary fields*

$$\text{Global Primary Fields: } \mathfrak{U} := \{\boldsymbol{u}, d\}, \qquad (13.3.30)$$

the displacement field $\boldsymbol{u}$ and the crack phase-field d. The subsequent constitutive approach to the phase-field modelling of brittle fracture focuses on the set

$$\text{Constitutive State Variables: } \mathfrak{C} := \{\boldsymbol{\varepsilon}, d, \nabla d, \mathcal{H}\}, \qquad (13.3.31)$$

reflecting a combination of elasticity with a first-order gradient damage modelling.

The development of the *virtual element* that handle phase-field brittle fracture in elastic solids can start from a pseudo potential density functional instead of using the weak form. This has advantages when the code is automatically generated using the software tool ACEGEN, see [51]. The pseudo potential density functional depends on the elastic and the fracture parts and keeps the crack driving force constant during the first variation. The specific pseudo potential density functional can then be written as

$$W(\mathfrak{C}) = g(d)W^+ + W^- + g_c \gamma_l(d, \nabla d) + \frac{\eta}{2\Delta t}(d - d_n)^2 + (1 - d)^2 \mathcal{H} \qquad (13.3.32)$$

this leads to the total pseudo potential, see (13.2.15),

$$U(\mathfrak{U}) = \int_\Omega W(\mathfrak{C})\, dV \; - \; U_{ext}(\boldsymbol{u}) \qquad (13.3.33)$$

with the external load $U_{ext}(\boldsymbol{u})$ defined in (13.3.6). The $\mathcal{H}$ and $g(d)$ have to be kept constant during the derivation procedure of residual to obtain the correct weak form of the problem.

13.3.5 Numerical Examples

In this section, the accuracy of the proposed virtual element formulation will be investigated for brittle crack propagation at small deformations by means of numerical examples. For comparison purposes, results of the standard finite element method (FEM) are also demonstrated.

13.3.5.1 Crack Propagation using Phase-Field Approach: Bi-Material Plate

We model the fracture phenomena of a bi-material specimen under tensile loading as reported in the recent work of [72]. The aim here is to demonstrate crack phase-field initiation and branching. The geometrical setup and the loading conditions of the specimen are depicted in Fig. 13.9a. The size of the specimen is chosen to be: $L = 50$ mm and the diameter of notch is $D = 10$ mm. We fixed the right edge of the plate in x-direction and applied vertical displacement to the top and bottom edges until final failure. The material parameters used in the simulation are the same as in the reference work of [72]. *B-material* is stiffer than *A-material* and represents purely elastic material behavior without fracturing. Young's modulus is chosen for A-material as $E^A = 100$ kN/mm^2 and for B-material as $E^B = 200$ kN/mm^2, Poisson's ratio is set to $\nu = 0.2$, the viscosity of the crack propagation $\eta^A = 10^{-6}$ kNs/mm^2, the critical energy release rate for A-zone as $g_c^A = 10^{-4}$ kN/mm and the stabilization parameter as $\beta = 0.4$. Different element formulations are studied to illustrate the robustness of the proposed VEM. A mesh refinement in the expected fracture zone is applied, see Fig. 13.9b–c.
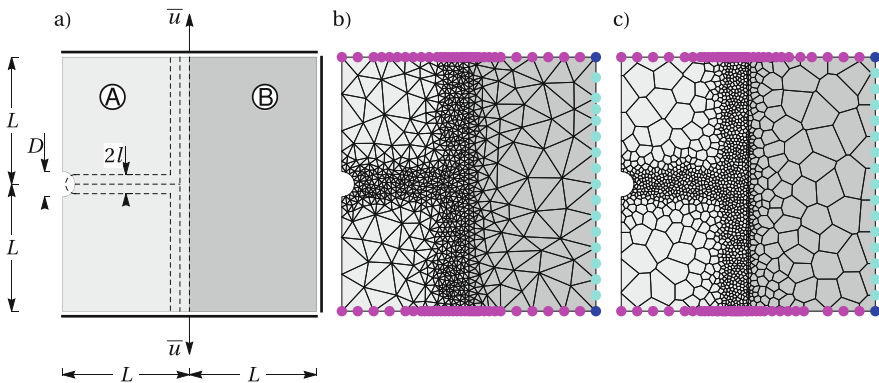
Fig. 13.9 Bi-material specimen. (**a**) Geometry and boundary conditions, (**b**) triangular finite element mesh and (**c**) VEM with Voronoi mesh. (From: F. Aldakheel, B. Hudobivnik, A. Hussein, P. Wriggers, Phase-field modeling of brittle fracture using an efficient virtual element scheme, Computer Methods in Applied Mechanics and Engineering 341, 443–466, 2018. Elsevier. Reproduced with permission)
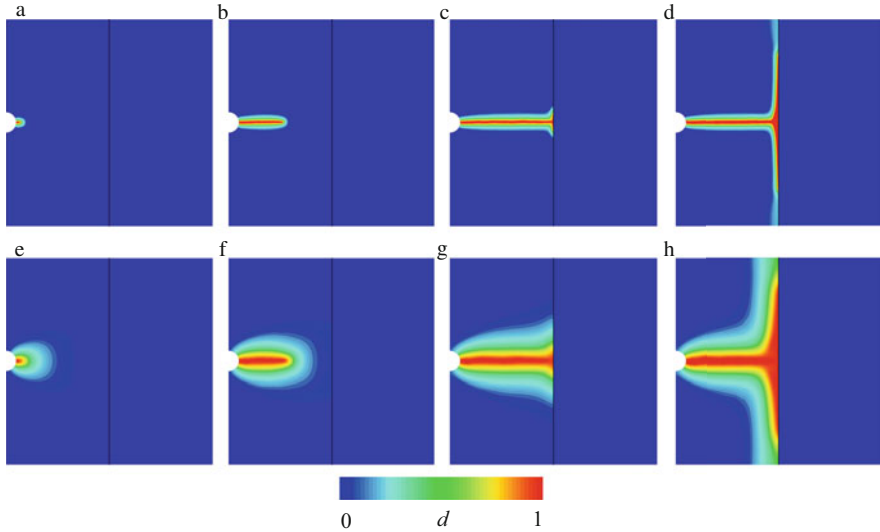
Fig. 13.10 Bi-material specimen. Contour plots of the fracture phase-field d for two fracture length scales l and four different deformation states up to final rupture. (**a–d**) $l_1 = 1.25$ mm and (**e–h**) $l_2 = 5.0$ mm. (From: F. Aldakheel, B. Hudobivnik, A. Hussein, P. Wriggers, Phase-field modeling of brittle fracture using an efficient virtual element scheme, Computer Methods in Applied Mechanics and Engineering 341, 443–466, 2018. Elsevier. Reproduced with permission)

Figure 13.10 shows the contour plot of the fracture phase-field d simulated using the virtual element formulations with a Voronoi mesh, for two different length scales $l_1 = 1.25$ mm and $l_2 = 5.0$ mm with same length/mesh ratio $r = 8$. The crack phase-field initiates at the notch-tip and propagates horizontally up to the interface between A- and B-zones. Thereafter it branches along the interfaces vertically till final failure, as documented in the work of [72]. A sharp crack pattern is obtained for the smaller length scale parameter l, as demonstrated in Fig. 13.10d.

Load-displacement curves for different length scales and elements formulations of FEM and VEM are displayed in Fig. 13.11a. All simulations show similar behavior before crack initiation. Thereafter, the force drops sharply at cracking to a lower level, which represents the residual forces of the undamaged B-zone of the specimen.

13.3.5.2   Crack Propagation Using Stress Intensity Factors

A. Single-Edge Notched Shear Test

In this benchmark test we consider a square plate with a horizontal notch. The geometrical setup and the loading conditions of the specimen are the same as in the reference work of [57] and depicted in Fig. 13.12a. We fixed the bottom and top edges of the plate in y-direction. Furthermore the bottom is also fixed in x-
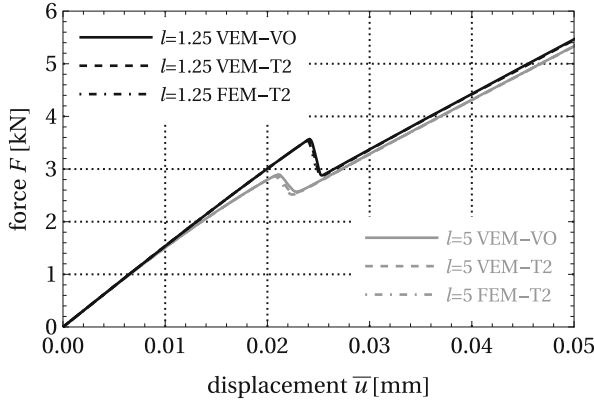
Fig. 13.11 Load–displacement responses for the Bi-material test with two different fracture length scales. A comparison between different VEM and FEM discretization. (From: F. Aldakheel, B. Hudobivnik, A. Hussein, P. Wriggers, Phase-field modeling of brittle fracture using an efficient virtual element scheme, Computer Methods in Applied Mechanics and Engineering 341, 443–466, 2018. Elsevier. Reproduced with permission)
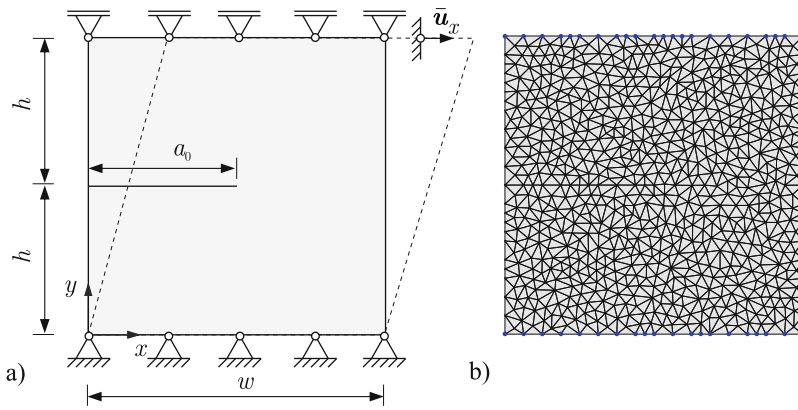
$w = 1$ mm $a_0 = 0.5$ mm $h = 0.5$ mm $E = 2.1 \cdot 10^5$ MPa $\bar{\boldsymbol{u}}_x = 0.01$ mm $\nu = 0.3$

Fig. 13.12 Single-edge notched shear test. Geometry and boundary conditions in (**a**) and VEM-mesh in (**b**). (From: A. Hussein, F. Aldakheel, B. Hudobivnik, P. Wriggers, P.A. Guidault, O. Allix Finite Elements in Analysis and Design 159, 15–32, 2019. Elsevier. Reproduced with permission)

direction and a pure shear loading at the top edge is applied. The specimen is discretized by using 1396 virtual elements under plane strain conditions, as sketched in Fig. 13.12b.

The evolution of the crack-trajectories are depicted in Fig. 13.13 along with the stress σ_{xx} distribution for three different deformation stages up to final failure. The crack propagates at an angle of 70.45° with respect to the initial notch, as shown in the reference works [31, 57]. By using the proposed cutting techniques outlined in
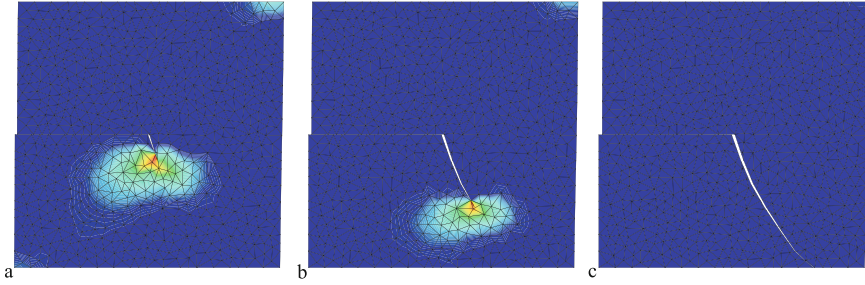
Fig. 13.13 Single-edge notched shear test. Contour plots of the stress σ_{xx} during the crack evolution using constant crack increment of $\Delta a = 0.1$ mm, mesh size $h_e \approx 0.027$ mm and VEM-mesh with 1396 elements at the beginning. (**a**) Crack path with 1400 elements, (**b**) crack path with 1412 elements and (**c**) final crack with 1423 elements. Red and blue contour-plots represent the maximum and minimum stresses, respectively. (From: A. Hussein, F. Aldakheel, B. Hudobivnik, P. Wriggers, P.A. Guidault, O. Allix Finite Elements in Analysis and Design 159, 15–32, 2019. Elsevier. Reproduced with permission)
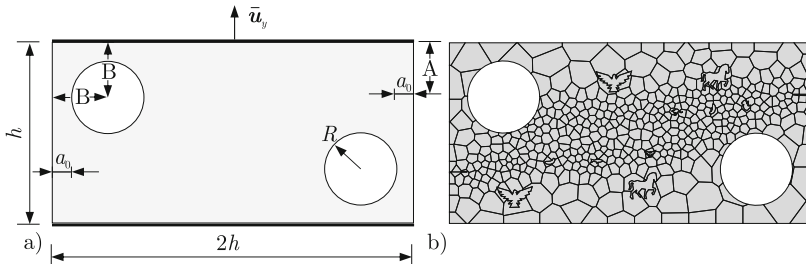
$h{=}10$ mm $R{=}2$ mm $a_0{=}1$ mm   A=2.85 mm   B=3 mm $E{=}2{\cdot}10^5$ MPa $\bar{u}_y{=}0.1$ mm $\nu{=}0.3$

Fig. 13.14 Tensile test with two notches and holes. Geometry and boundary conditions in (**a**) and VEM with Voronoi mesh in (**b**). (From: A. Hussein, F. Aldakheel, B. Hudobivnik, P. Wriggers, P.A. Guidault, O. Allix Finite Elements in Analysis and Design 159, 15–32, 2019. Elsevier. Reproduced with permission)

Sect. 13.3.3, less elements (about 31 elements) are required to track the crack path accurately during the simulation.

B. Tensile Test with Two Notches and Holes

To illustrate the capability and the flexible choice of the number of nodes in an element for VEM, various animals-shaped Voronoi cells (bird, fish, kangaroo, . . .) are employed in the expected fracture zones (i.e. an area of interest) for the virtual element formulation. For this purpose, we consider a tensile test with two notches and holes to demonstrate their effect on the crack-initiation and curved-crack-propagation. The geometrical setup and the mesh are depicted in Fig. 13.14. Herein,
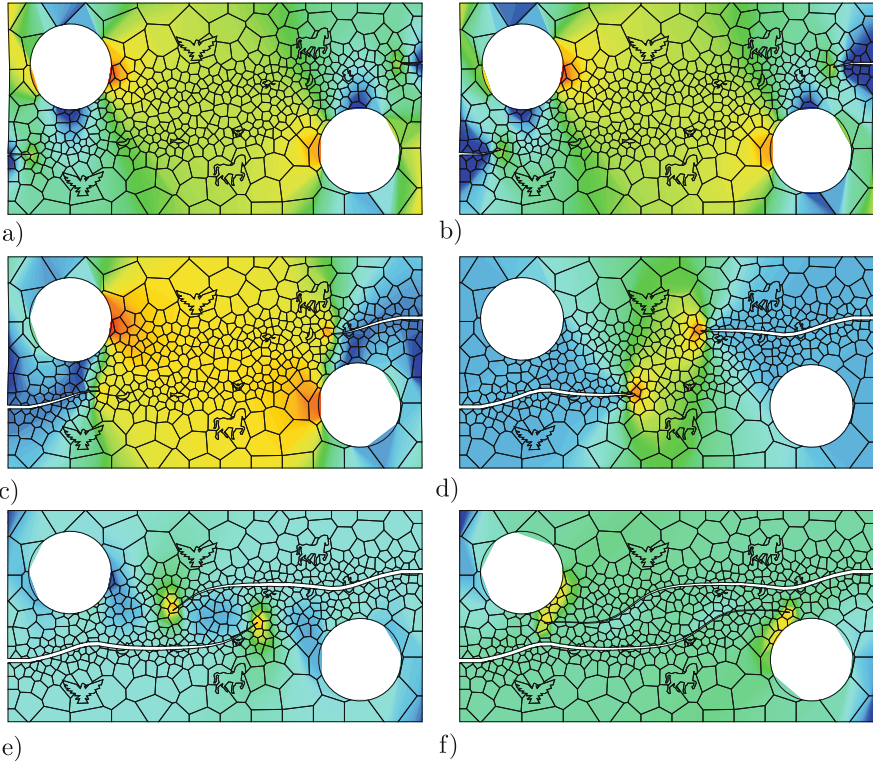
Fig. 13.15 Tensile test of the notched specimen with two holes. Normal stress σ_{yy} during the crack evolution (**a–f**) using VEM-Voronoi mesh with 509 elements at the beginning in (**a**) Crack path with 515 elements in (**b**), crack path with 533 elements in (**c**), crack path with 558 elements in (**d**), crack path with 584 elements in (**e**) and final crack with 605 elements in (**f**). Red and blue corresponds to the maximum and the minimum tensile stresses, respectively. (From: A. Hussein, F. Aldakheel, B. Hudobivnik, P. Wriggers, P.A. Guidault, O. Allix Finite Elements in Analysis and Design 159, 15–32, 2019. Elsevier. Reproduced with permission)

the virtual element formulation with various shaped Voronoi cells is employed around the fractured zones. The material parameters used in the simulation are the same as in the reference works [2, 57].

Figure 13.15 depicts the crack path evolution along with the stress σ_{yy} distribution for different deformation stages. The cracks initiate at the two notches-tip. Thereafter, the left and the right cracks tends to propagate towards the holes as shown in Fig. 13.15b. Once the cracks passed the holes, see Fig. 13.15c, they continue to propagates horizontally till final failure in Fig. 13.15f, resulting with a mixed-mode fracture.

13.4 VEM for Contact

Contact constraints have to be considered in many engineering applications which include parts acting on each other. In many cases the behaviour of the contact has an influence on the performance of machines, looking for example at friction and wear. In the field of finite element methods different approaches and discretization techniques where developed over the last 50 years by many scientists. An overview can be found in the textbooks of [54] and [80].

Generally contact falls in the category of unilateral problems meaning that no penetration can take place and the deformation is restricted. These problems have to be treated as constraint optimization problems since the contact area is a priori unknown. Within this methodology one has to enforce contact constraints. This means that the surfaces in contact have to be coupled and contact tractions need to be transmitted at the interface. This can be achieved by the method of Lagrange multipliers, the penalty method or other techniques like the augmented Lagrangian formulation or barrier techniques.

Within a numerical simulation method another essential topic is the discretization of the contact area. Classical works started from establishing contact pointwise by evaluating contact along contacting nodes or segments, see for example [37, 87] and [38]. To increase the robustness of solution schemes the interpolation was enhanced in [64] or [83] to reach C^1-continuity which leads to a continuous and smooth field of the normal vector. With the method of isogeometric formulation the surface quality was increased further, this approach is discussed by several authors (for example [74] and [29]). In order to have a continuous discretization the so called mortar methods were introduced in recent years. [55] provides a good overview. Here, by integrating on a virtual mortar domain the contact discretisation represents both non-matching sides exactly. However the additional discretisation of non-matching surface patches adds to the complexity of the problem. Another approach to cope with non-matching interfaces was the use of adaptive meshing. By simply moving the underlying mesh to match both meshes at the interface, as shown for contact in [88], leads to a poor mesh quality. This in turn requires additional effort on mesh smoothing.

Within the virtual element formulation the number of nodes can be arbitrary large permitting aligned nodes along edges or non-convex elements. This section is based on the extension of the contact algorithms described in [85] for straight and [1] for curved virtual elements to finite deformation contact problems including friction, see [86]. The methodology is based on adjusting non-matching meshes by simply inserting nodes where a nodal pair along the contact interface is needed. In this way polygonal elements with new nodes are created along the contact surface. Since the elements are only changed locally the rest of the mesh is not affected. A special variant that updates nodal position and nodes within a non-linear solution procedure allows an application to problems with large deformations and large tangential sliding. The possibility to adaptively change the inserted nodes provides the necessary flexibility for large relative tangential displacements along the interface

13.4.1 Governing Equations for Finite Elasticity and Contact

The problem description starts from two elastic bodies with the domains Ω_i ($i = 1, 2$) $\subset \mathbb{R}$. Every material point has an initial position X and is mapped to the position x in the current configuration at time t by

$$x = \varphi(X, t) = X + u(X, t), \qquad (13.4.1)$$

where $u(X, t)$ denotes the displacement field. Once the deformation is defined the deformation gradient F follows from

$$F = \mathrm{Grad}(\varphi) = 1 + \mathrm{Grad}(u(X, t)), \qquad (13.4.2)$$

where the gradient is computed with respect to the initial configuration X. Here the right Cauchy-Green tensor $C = F^T F$ will be used as a strain measure and considered in the internal strain energy W.

In order to set-up a boundary value problem boundary conditions, balance and constitutive equations have to be formulated. Each of the bodies in Fig. 13.16 has a boundary Γ_i that can be split into the parts Γ_{iD}, Γ_{iN} and Γ_{iC}. On the Dirichlet boundaries Γ_{iD} the displacements are prescribed: $u = \overline{u}$ on Γ_{iD}. The Neumann boundaries are related to surface tractions t that can be boldsymbol formulated with respect to the initial configuration as: $P N = \overline{t}$ where N the surface normal vector, P the first Piola–Kirchhoff stress tensor and $\overline{t}$ are the prescribed surface tractions.

The boundary Γ_C is related to the contact part is an a priori unknown area where the two bodies come in contact ($\Gamma_{1C} = \Gamma_{2C}$), see Fig. 13.16. The contact area can be defined using the gap between the two surfaces

$$g_n = (x_2 - x_1) \cdot n_1 \qquad (13.4.3)$$

where x_i is the deformed position of a point on the surface of Ω_i and n_1 the normal in the current configuration of the body Ω_1.[2] The contact normal pressure

Fig. 13.16 Two continuum bodies Ω_1 and Ω_2 in contact. Additional to the Neumann and Dirichlet boundaries there also is a contact partition Γ_C of the boundary

---
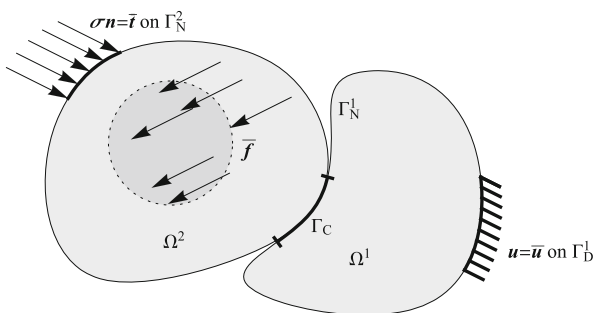
[2] This choice is arbitrary, also n_2 could have been chosen.

$\sigma_n = (\boldsymbol{\sigma}\,\boldsymbol{n}) \cdot \boldsymbol{n}$ is related to the Cauchy stress $\boldsymbol{\sigma} = J^{-1}\,\boldsymbol{P}\,\boldsymbol{F}^T$ in finite deformations. With the normal pressure the so called Kuhn–Tucker–Karush conditions can be formulated

$$g_n \geq 0, \quad \sigma_n \leq 0 \quad \text{and} \quad g_n\,\sigma_n = 0\,. \tag{13.4.4}$$

These conditions state that the bodies do not interpenetrate each other, the contact pressure is always negative.

We apply the potential energy $U(\boldsymbol{u})$ that yields as Euler equations the equilibrium conditions. For the hyperelastic case the potential energy function is given by

$$U(\boldsymbol{u}) = \int_{\Omega} [W(\boldsymbol{u}) - \bar{\boldsymbol{f}} \cdot \boldsymbol{u}]\,\mathrm{d}\Omega - \int_{\Gamma_N} \bar{\boldsymbol{t}} \cdot \boldsymbol{u}\,\mathrm{d}\Gamma + U_c\,. \tag{13.4.5}$$

Here homogeneous compressible isotropic hyperelastic material behaviour is assumed and a neo-Hookean strain energy function introduced as

$$W(\boldsymbol{u}) = \frac{\Lambda}{4}[J(\boldsymbol{u})^2 - 1 - 2\,ln(J(\boldsymbol{u}))] + \frac{\mu}{2}[tr(\boldsymbol{C}(\boldsymbol{u})) - 2 - 2\,ln(J(\boldsymbol{u}))], \tag{13.4.6}$$

where Λ and μ are the Lamé constants and the Jacobian $J = \det \boldsymbol{F}$ represents the change in volume. The stresses in Ω_1 and Ω_2 follow from the strain energy function $W(\boldsymbol{u})$ and the deformation gradient

$$\boldsymbol{P}(\boldsymbol{u}) = \frac{\partial W(\boldsymbol{u})}{\partial \boldsymbol{F}}\,. \tag{13.4.7}$$

The energy contribution for the contact is only present for segments actually in contact. For a penalty contact formulation the energy U_c contributing to (13.4.5) is

$$U_c^P(\boldsymbol{u}) = \frac{1}{2} \int_{\Gamma_C} \left[\epsilon_n (g_n)^2 + \epsilon_t (g_t)^2 \right]\,\mathrm{d}\Gamma \tag{13.4.8}$$

with the contact penalty parameters ϵ_n for the normal and ϵ_t for the tangential direction. A Lagrangian multiplier approach yields the contribution

$$U_c^{LM}(\boldsymbol{u}\,, \lambda_n\,, \lambda_t) = \int_{\Gamma_C} [\,\lambda_n\,g_n + \lambda_t\,g_t\,]\,\mathrm{d}\Gamma \tag{13.4.9}$$

with Lagrange multipliers λ_n and λ_t for the normal and tangential direction. The normal gap g_n was already defined in (13.4.3). The tangential gap g_t will be defined later. It is here formulated for the stick case which is associated with $g_t = 0$ and

thus does not allow sliding at the contact interface. Note that the Lagrange multiplier formulation introduces with λ_n and λ_t additional unknowns.

13.4.2 Virtual Element Method for Contact

The general description of the virtual element method was provided in Sect. 13.2. This yields for finite elastic deformations the consistency part, see (13.2.13),

$$U_c(\boldsymbol{u}_\Pi)|_e = \int_{\Omega_e} W(\boldsymbol{C}_\Pi)\, \mathrm{d}\Omega \, - \int_{\Omega_e} \overline{\boldsymbol{f}} \cdot \boldsymbol{u}_\Pi\, \mathrm{d}\Omega - \int_{\partial\Omega_t} \bar{\boldsymbol{t}} \cdot \boldsymbol{u}_\Pi\, \mathrm{d}\Gamma \qquad (13.4.10)$$

which has the simple constant form for the first part on the right hand side

$$\int_{\Omega_e} W(\boldsymbol{C}_\Pi)\, dV = \, W(\boldsymbol{C}_\Pi)|_c\, \Omega_e \qquad (13.4.11)$$

for a linear ansatz. The projected constant right Cauchy-Green tensor is given by $\boldsymbol{C}_\Pi = [\mathbf{1} + \nabla\boldsymbol{u}_\Pi]^T\,[\mathbf{1} + \nabla\boldsymbol{u}_\Pi]$, see also (13.2.14).

A stabilisation is needed for the virtual element where the projection $\{\boldsymbol{u}_\Pi$ only covers the basic modes. Different stabilization techniques can be employed. Here we discuss three different approaches to formulate the stabilisation part U_{stab} in (13.2.12).

13.4.2.1   Standard Stabilisation

The approach which is described in [10] introduces a pointwise error measure between the projection and the displacement values $\mathbf{u}_I$

$$d_u(\mathbf{X}_I) = [\mathbf{u}_I - \boldsymbol{u}_\Pi(\mathbf{X}_I)] \qquad (13.4.12)$$

where $\mathbf{u}_I$ are just the nodal values at the vertices of the virtual element. When summed up over all element vertices n_V this leads to a stabilisation term

$$U_{stab} = \frac{\gamma}{2} \sum_{I=1}^{n_V} [d_u(\mathbf{X}_I)]^T [d_u(\mathbf{X}_I)] \quad \text{with } \gamma = \gamma_0 \frac{h_D^2\, tr(\mathbb{D})}{tr(\mathbf{H}^T(\mathbf{X}_I)\mathbf{H}(\mathbf{X}_I))}\,.$$
$$(13.4.13)$$

The stabilisation parameter γ includes the element diameter h_D as well as the trace of the constitutive tensor $\mathbb{D} = \frac{\partial^2 W}{\partial \mathbf{C}\, \partial \mathbf{C}}$, evaluated at the current deformation. The matrix $\mathbf{H}$ contains the linear ansatz functions and is evaluated at $\mathbf{X}_I$. The free parameter γ_0 is usually set to 1.
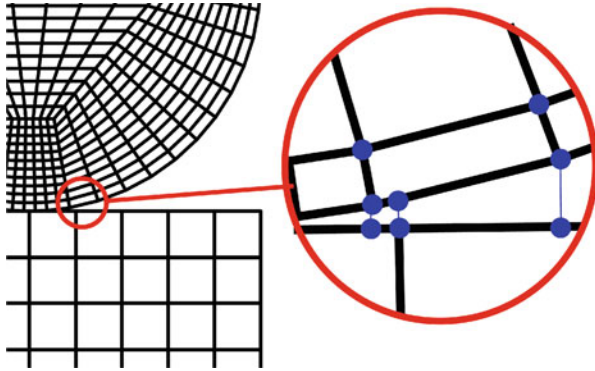
Fig. 13.17 Small edges and collapsing nodes in adaptive mesh methods or arbitrary mesh geometries are creating stability problems

Unfortunately, independently of the factor γ, this element stabilisation leads to large errors in the vicinity of nodes, where vertices are only apart by a small distance. Especially in adaptive schemes and at contact surfaces, as shown in Fig. 13.17, this situation appears frequently, leading to erroneous results. A demonstration of these errors including a comparison with other stabilisations can be found in Sect. 13.4.2.4.

13.4.2.2   Edge Stabilisation

Another type of stabilization is taylored to discretizations with collapsing nodes. Here again the nodal-wise error from (13.4.12) is computed, see left part of Fig. 13.18, but then the difference in errors of two neighbouring nodes I and $I+1$ is introduced as a weighting term. This formulation takes into account the length of the segment $l = |\mathbf{X}_{I+1} - \mathbf{X}_I|$, see right part of Fig. 13.18. In the term

$$U_{stab} = \gamma \sum_{I=1}^{n_V} \frac{1}{|\mathbf{X}_{I+1} - \mathbf{X}_I|} \left[d_u(\mathbf{X}_{I+1}) - d_u(\mathbf{X}_I) \right]^T \left[d_u(\mathbf{X}_{I+1}) - d_u(\mathbf{X}_I) \right]$$

$$(13.4.14)$$
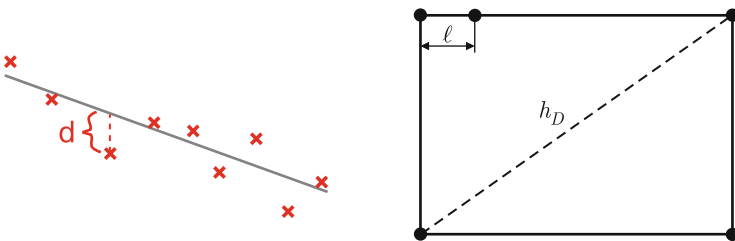
Fig. 13.18 Sketch of the terms for the linear stabilisation approach which includes the distance d_u and an edge stabilisation that considers the distance of nodes l

small edges have a larger impact on the stabilisation. Again the stabilisation factor γ_0 from (13.4.13) needs to be determined. A problem dependent parameter optimisation is discussed in [85] for small deformation contact comparing the normal pressure and tangential gap. In summary it was observed that with an increasing factor γ_0 oscillations in the tangential gap are suppressed and the contact pressure is represented more accurately. However by exceeding an optimal value for γ_0 the results show a stiffening behaviour. Thus parameters γ that yield optimal results lie in a small interval which is in practice not sufficient, in particular when working with unknown problems. Hence γ appears to be problem dependent and needs further investigation. Even though the results are better than for the stabilization in Sect. 13.4.2.1 they are not robust, especially for finite deformation problems.

In non-linear problems the stiffness terms depend on the deformation. Thus the stabilization has to consider such dependencies and hence, different approaches for non-linear problems were developed taking into account the behaviour of the constitutive tensor. Associated formulations can be found in [11] and [25].

13.4.2.3   Energy Stabilisation

To create a stabilisation that will lead to a consistent linearisation for non-linear problems a third approach was developed, see [84]. It is described in Sect. 13.2.4 and can be easily adopted for large deformations. This technique can be employed for contact problems with no additional formulations.

13.4.2.4   Patch Test and Stabilization Test

A classical test that has to be fulfilled by a discretization scheme is the so called patch test. In case of contact this test can be simply employed by using a mesh of two blocks with irregular element spacing in the contact interface. Figure 13.19
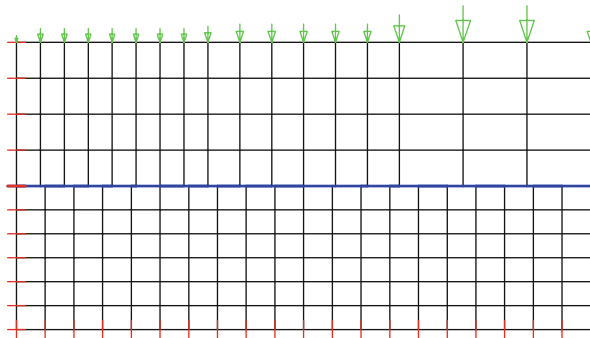

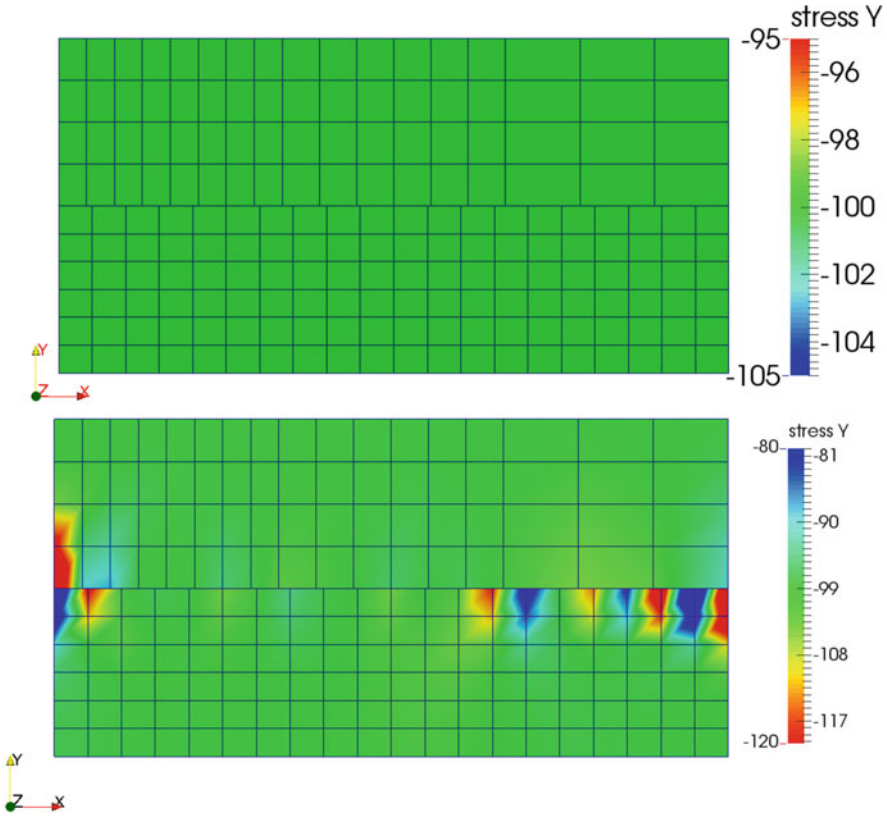**Fig. 13.19**   Patch for contact discretizations

Fig. 13.20 Results of the patch test for node-to-node VEM discretization (top) and node-to-surface FEM discretization (bottom)

depicts the meshes of the two blocks. The lower block has an evenly spaced mesh while the upper block has an increasing element size from left to right. The upper block is loaded by a constant pressure load p while the lower block is fixed at the bottom. For both blocks the same material is assumed and boundary conditions as well as loading are such that a constant stress state is in both blocks.

The solution with the new node-to-node contact using virtual elements is shown in the top of Fig. 13.20. It demonstrated that this formulation results in a constant stress state. Contrary a classical node-to-segment formulation, using a finite element scheme results in the stress distribution depicted in bottom of Fig. 13.20 where stress peaks are visible at non-matching nodes within the contact interface.

For the qualitative assessment of different stabilisation methods [14] developed a similar test. A regular mesh is connected to a Voronoi mesh and loaded by two pressure. For this type of problem it could be shown in [86] that the edge stabilisation as well as the energy stabilization will lead to smooth solutions

for linear and quadratic elements while the standard VEM stabilization yields oscillations in the stress response.

13.4.3   Contact for Large Deformations Including Friction

The virtual element discretization allows a very simple contact formulation, even in the case of large strain. The basic idea is to define additional nodes within an element at the contact interface when contact is detected. Since virtual elements can have an unlimited number of nodes the addition of nodes does not change the general discretization. It is only local. This idea which was presented first in [85] for geometrically linear problems and adopted for contact problems undergoing finite deformations in [86].

13.4.4   Node Insertion Algorithm

In the general case of finite deformation contact there will be always node to segment contact. This is now adapted in VEM by the insertion of nodes to be generated to formulate the contact. For this task a node insertion algorithm has to be defined. Here the scheme described in [85] is used. The starting point for the contact search are two contacting surfaces, Γ^1 and Γ^2, each divided into contact segments which lie between the nodes defining the possible contact interface. Each point $\mathbf{x}(\xi)_i$ on the segment c can be described in a parametrised configuration with respect to the current coordinates

$$\boldsymbol{x}^1(\xi)_i = (1 - \xi)\,\mathbf{x}^1_{i-1} + \xi\,\mathbf{x}^1_{i+1}\,. \tag{13.4.15}$$

Following a similar approach as in the node-to-surface description, an orthogonal projection of each surface node onto the opposite surface provides the correct contact position. For the projection of a node $\mathbf{x}^2_0$ onto a segment c defined by node $\mathbf{x}^1_{i-1}$ to node $\mathbf{x}^1_{i+1}$, as shown in Fig. 13.21, this leads to

$$\xi \;=\; \frac{1}{\ell_c^2}\,(\mathbf{x}^1_{i+1} - \mathbf{x}^1_{i-1}) \cdot (\mathbf{x}^2_0 - \mathbf{x}^1_{i-1}) \tag{13.4.16}$$

with $\ell_c = \|\mathbf{x}^1_{i+1} - \mathbf{x}^1_{i-1}\|$ being the length of segment c. This can be used to define the normalised tangential vector

$$\mathbf{a}_c = \frac{1}{\ell_c}\,(\mathbf{x}^1_{i+1} - \mathbf{x}^1_{i-1})\,. \tag{13.4.17}$$

Note that the reference for the normal and tangential vector during the projection is related to surface c.

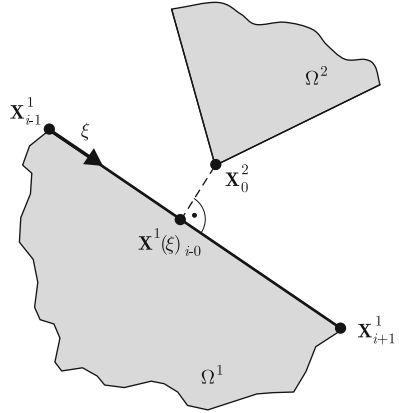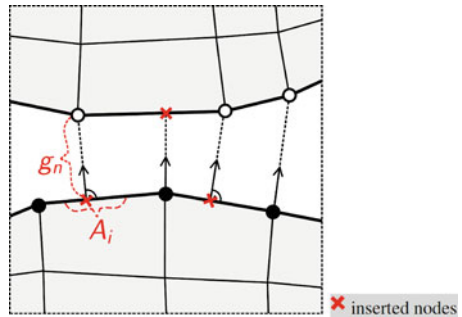**Fig. 13.21** Projection of a node $\mathbf{x}_0^2$ contacting a segment

Fig. 13.22 With the nodal projection and insertion algorithm nodes are projected and inserted symmetrically onto both contact surfaces

Since the changes only affect one element a node can be inserted in the mesh at the found position. This creates what is generally known as *hanging nodes* in standard FEM, but here only the polygonal mesh is extended by an additional node. Differing from the standard contact, the projection is carried out for both surfaces, see Fig. 13.22, leading to a symmetric treatment of contact. This projection creates contact elements along each side of the current contact interface which can be described by an adequate interpolation.

The node insertion algorithm is executed for the complete contact surface within an iteration step of the global Newton–Raphson method before the actual detection step for active/in-active contact is carried out.

13.4.4.1   Contact Discretization: Frictionless

An approach that enforces the contact constraints $g_n = 0$ without introducing new variable is the penalty method. It penalizes the constraint equation using the potential (13.4.8)

$$U_{cn} = \int_{\Gamma_c} \frac{\epsilon_n}{2}\, g_n^2\, d\Gamma \qquad (13.4.18)$$

with the penalty factor ϵ_n. The normal contact traction can be obtained as

$$t_n = \epsilon_n \, g_n \, . \tag{13.4.19}$$

For the case of active contact the segments from both sides coincide and therefore the interpolation is the same. The nodal gap can therefore be written in short by

$$g_{ncA} = \left[\mathbf{x}_A^2 - \mathbf{x}_A^1 \right] \cdot \mathbf{n}_c^1 \, . \tag{13.4.20}$$

The gap function in a contact segment can be interpolated by choosing ansatz functions for the current surface coordinates. For a segment c between two nodes the functions $N_1(\xi_c) = 1 - \xi_c$ and $N_2(\xi_c) = \xi_c$ interpolate the current coordinates at the surface Γ^1 as

$$\mathbf{x}^1(\xi_c) = \sum_{A=1}^{2} N_A(\xi_c) \, \mathbf{x}_A^1 \tag{13.4.21}$$

which is consistent with the linear ansatz for the virtual element. For the surface Γ^2 the similar functions $N_A(\eta_c)$ using η_c as surface coordinate leads to the interpolation within the segment c

$$\mathbf{x}^2(\eta_c) = \sum_{A=1}^{2} N_A(\eta_c) \, \mathbf{x}_A^2 \, . \tag{13.4.22}$$

Since the normal vector $\mathbf{n}_c^1$ is constant within a segment c the gap function can be written as

$$g_n = \left[\mathbf{x}^2(\eta_c) - \mathbf{x}^1(\xi_c) \right] \cdot \mathbf{n}_c^1 \tag{13.4.23}$$

Due to the node projection in each step the coordinates ξ_c and η_c coincide along a segment c the gap function can be written as

$$g_n(\xi_c) = \left[\sum_{A=1}^{2} N_A(\xi_c) \, \mathbf{x}_A^2 - \sum_{A=1}^{2} N_A(\xi_c) \, \mathbf{x}_A^1 \right] \cdot \mathbf{n}_c^1 \tag{13.4.24}$$

Note that the current coordinates can be expressed in terms of the displacements as $\mathbf{x}_A^\alpha = \mathbf{X}_A^\alpha + \mathbf{u}_A^\alpha$ for $\alpha \in 1, 2$. Furthermore the surface coordinate ξ depends on the deformation and with that on the nodal displacements, see (13.4.16). This is also true for the normal vector $\mathbf{n}_c^1 = \mathbf{e}_3 \times \mathbf{a}_c = \mathbf{e}_3 \times 1/\ell_c \, (\mathbf{x}_{i+1}^1 - \mathbf{x}_{i-1}^1)$ which is related to the current configuration. Here $\mathbf{e}_3$ is the unit vector in the third direction. All these dependencies have to be considered when the residual and tangent matrix of the contact potential (13.4.8) are computed.

Again AceGen is used to compute the residual and tangent matrix

$$\mathbf{R}_c = \frac{\partial U_c}{\partial \mathbf{u}_c} \quad \text{and} \quad \mathbf{K}_c = \frac{\partial \mathbf{R}_c}{\partial \mathbf{u}_c} \qquad (13.4.25)$$

where differentiation is performed with respect to the nodal displacements $\mathbf{u}_c = \{\mathbf{u}_1^2, \mathbf{u}_2^2, \mathbf{u}_1^1, \mathbf{u}_2^1\}$ that are related to a segment.

13.4.4.2 Contact Discretization: Friction

At the contact interface the sliding in tangential direction can be split into a stick and a sliding phase. This is related to friction which affects tangential movements and introduces further complexity in the solution of contact problems. No tangential relative movement at the contact interface is associated with stick and leads to a constraint as in normal contact. Thus to include frictional stick it is necessary to constrain the relative tangential movement. In this contribution it is achieved by using the penalty method, see the second term in (13.4.8) where g_t denotes the tangential relative displacement. The relative tangential displacement can be computed as

$$g_t(\xi) = [\mathbf{x}^2(\xi_c) - \mathbf{x}^1(\xi_c)] \cdot \mathbf{a}_c \qquad (13.4.26)$$

where $\mathbf{a}_c$ is the tangent vector at the interface c, see (13.4.17). This discretization leads to a contribution to the potential energy

$$U_{ct} = \sum_{c=1}^{n_c} \int_0^1 \frac{\epsilon_t}{2} \, g_t^2(\xi_c) \, l_c d\xi \qquad (13.4.27)$$

where the stick constraint $g_t = 0$ is enforced by a penalty factor ϵ_t.

A Coulomb friction law provides a relation between the normal and tangential tractions depending on the friction coefficient $\bar{\mu}$. The classical algorithm for frictional problems is based on an operator split technique which leads to a return mapping scheme, like in elasto-plasticity, first introduced in [79], see also [54] and [80]. Here first a 'trial' step, assuming stick is computed. After this trial step the contact state is checked by inserting the computed contact tractions in normal and tangential direction, see (13.4.19) and $t_t = \epsilon_t g_{t,trial}$, into the slip function

$$f_s^{tr} = |\epsilon_t g_{t,trial}| - |\bar{\mu} \, \epsilon_n g_n| \leq 0 \,. \qquad (13.4.28)$$

If the slip function f_s^{tr} is ≤ 0, then the contact state is related to stick in segment c and the computed variables can be used in the next iteration step. Once the slip function is violated the contact segment c is in slip state. By assuming that relative gap function g_t can be split into a stick (elastic) and sliding (plastic) part

$$g_t = g_{t,stick} + g_{t,slip} \qquad (13.4.29)$$

it is possible to compute within the return mapping algorithm the relative tangential sliding $g_{t,slip}$. This yields, see e.g. [80],

$$g_{t,slip} = \frac{f_s^{tr}}{\epsilon_t} = \frac{|\epsilon_t \, g_{t,trial}| - |\bar{\mu} \, \epsilon_n \, g_n|}{\epsilon_t} \;, \forall f_s > 0 \,. \qquad (13.4.30)$$

With the updated tangential gap the contact is recomputed until convergence.

Due to the relative tangential slip the projected nodes do not coincide anymore. This error can be neglected for small changes during one load step. However, after each converged load step the nodes in contact are newly projected onto the surface to keep the error low. Thus the next load step is based on a geometry in which again node-to-node contact is realized. After reprojecting the nodes, the history variable due to friction (the slip amount $g_{t,slip}$) is reset to zero. This is permitted since the Coulomb friction law does not directly depend on the slip amount $g_{t,slip}$.

Let us note, that for a sufficiently small step size (which may be necessary anyway to determine the correct physical behaviour of a frictional problem), good results can be achieved by fixing the normal and tangential vectors within each load step which simplifies the linearization.

Again the additions to the stiffness matrix and residuum directly follow by using (13.4.25), see Sect. 13.4.4.1. Since sliding has no potential formulation it is necessary to compute the residual by keeping the relative tangential slip constant during the derivation

$$\mathbf{R}_c = \left. \frac{\partial U_c}{\partial \mathbf{u}_c} \right|_{g_{t,slip}=const.} \quad \text{and} \quad \mathbf{K}_c = \frac{\partial \mathbf{R}_c}{\partial \mathbf{u}_c} \,. \qquad (13.4.31)$$

This yields a non-symmetric tangent matrix in case of slip.

13.4.5 Numerical Examples

In this section, the virtual element formulation for large deformation contact problems is verified by means of several examples. These are the classical geometrically linear Hertz and Mindlin problems, a finite deformaton ironing problem and a wall mountain of a bolt which provides a mixture of contact and fracture mechanics.

13.4.5.1 Hertzian Contact Problem for Small Deformations

Frictionless Contact The Hertzian contact problem is widely used to verify contact discretization, as an analytical solution exists for the small deformational case. In a two-dimensional setting the Hertz problem describes the contact of an elastic cylinder with an elastic half spaces. Both bodies are considered to have an infinite extension in longitudinal direction and so a plane strain condition is

assumed. The feature of this test is, that the two surfaces are geometrically non-conforming which makes the contact area considerably smaller than the total surface.

The analytical solution can be found in e.g. [47]. For the two bodies it considers a relative curvature $R_* = [1 / R_1 + 1 / R_2]^{-1}$ from the two surface radii R_1 and R_2 and a relative Young's modulus $E_* = [(1 - v_1^2 / E_1) + (1 - v_2^2) / E_2]^{-1}$. With these definitions the width a of the contact area can be computed as a function of the load F by

$$a^2 = \frac{4 R_* F}{\pi E_*}.$$

(13.4.32)

Furthermore the distribution of the surface stress follows as

$$p(x) = \frac{2 F}{\pi a^2} \sqrt{a^2 - x^2}.$$

(13.4.33)

The original setup in 2D is depicted in Fig. 13.23 where a circular cross-section is loaded with a single point load.

Since the problem is symmetric only half of the original geometry is taken into account for the discretization where only one quarter of the circle is sufficient when the single point load is approximated by a distributed load. Figure 13.23 demonstrates the geometry, the boundary conditions and the loading. Both bodies are additionally fixed in tangential direction along the symmetry axis. The top body of radius $R_1 = 10$ is loaded by a distributed load $p_n = 25$ which leads back to a total original force of $F = 2Rp_n = 500$ for the full circle. For the foundation a Young's modulus of $E_2 = 7 \cdot 10^3$ is chosen and a Poisson's ratio of $v = 0.3$. The indenter is stiffer with a Young's modulus of $E_1 = 7 \cdot 10^4$ and a Poisson's ratio of

Fig. 13.23 Hertz contact of a two-dimensional cylindrical body and an elastic halfspace
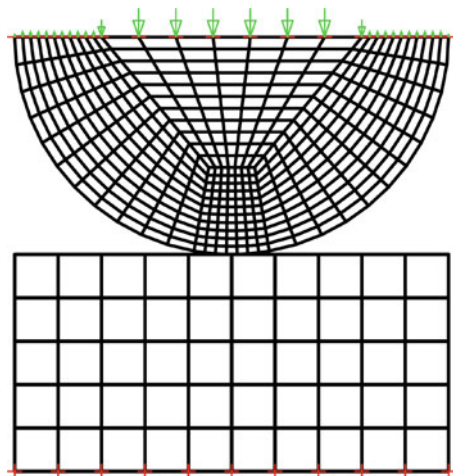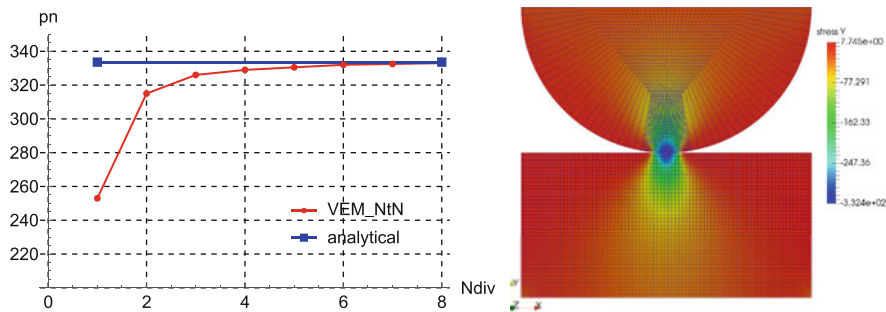
Fig. 13.24 Convergence to the maximum contact pressure $p_{n,max}$ for an increasing number of element divisions and stress distribution σ_{yy} for a fine mesh

$\nu = 0.3$. The given constitutive and geometrical parameters lead with Eq. (13.4.33) to an analytical value of the maximum contact pressure: $p_{n,max} = 333$.

This test is used to check the accuracy of the node insertion algorithm in the virtual element method. Hence the geometry is discretized using 4 noded virtual elements which will at the contact interface to element with more nodes related to the node insertion. Starting from the mesh in Fig. 13.23 with N_e elements for each body, the mesh is refined by homogeneously dividing the elements in N parts along each direction. The maximum pressure, $p_{n,max}$, can now be compared with the maximum pressure resulting from the mesh sequence, see Fig. 13.24. After 5 homogeneous refinements convergence is achieved.

Frictional Contact The node insertion algorithm using virtual elements is verified by the same example with the converged mesh of the frictionless case. Frictional response is triggered by an additional tangential loading Q at the top surface. For the Coulomb friction a friction coefficient of $\bar{\mu} = 0.2$ is chosen.

The analytical solution distinguishes between three cases: full sticking, full sliding and a mixed stick/slip state. In this example the tangential tractions are chosen to cause a mixed state where the outer part of the surface reaches a sliding state but the centre still sticks with the effect that the bodies do not move relative to each other. The analytical solution, see [48], includes the sticking area $-c \le x \le c$ as a part of the full contact area a, see (13.4.32),

$$c = a\sqrt{\left(1 - \frac{Q}{\bar{\mu} F}\right)}. \tag{13.4.34}$$

The resulting tangential traction t_t within the sticking area is then given by

$$t_t(x) = \bar{\mu}\frac{2F}{\pi a^2}\left(\sqrt{a^2 - x^2} - \sqrt{c^2 - x^2}\right), \forall -c \le x \le c \tag{13.4.35}$$
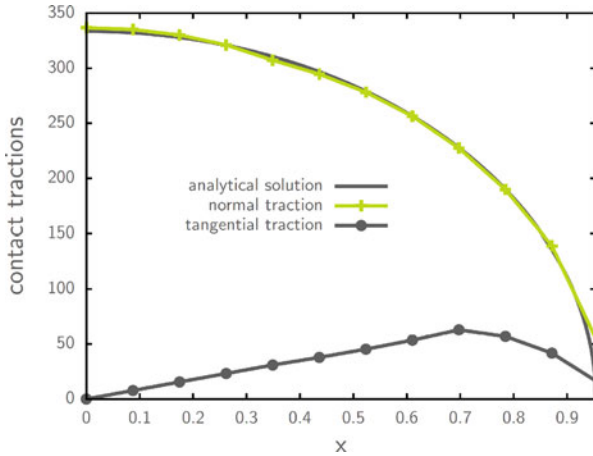
Fig. 13.25 Comparison of normal and tangential contact tractions with the analytical solution for the frictional Hertzian contact problem

while the traction outside the sticking area simply reduces to $t_t(x) = \bar{\mu}\, p(x)$. This implies that the tangential traction has no influence on the normal contact pressure. This is only true for examples where the material properties of both bodies are equal, see [22]. To be able to compare to the analytical solution the Young's moduli are chosen equal $E_1 = E_2 = 7 \times 10^3$. In the graph in Fig. 13.25 the resulting tractions are compared with analytically computed tractions.

Overall the values are in good agreement. In the transition zone from the sticking area to the sliding part of the surface the analytical solution depicts a kink while the numerical result is smooth. This is related to the fact that is that no contact node lies exactly at the stick-slip border and discretization with linear ansatz functions cannot produce a kink within a contact segment.

13.4.5.2 Large Deformational Contact: Ironing Problem

The ironing problem demonstrates the ability of the derived methodology to solve contact problems at finite deformations including large sliding.

This so called ironing problem is similar to those in [89] and [76] which were discretized with finite elements using a mortar contact formulation. The idea is to press a deformable indenter into a deformable block and then slide it over the entire upper surface.

The Neo-Hooke material in (13.4.6) is used to model the material response of the system. The block has the Lamé constants $\Lambda_2 = \mu_2 = 2, 692 \cdot 10^3$ while the indenter is 10 times stiffer with the Lamé constants $\Lambda_1 = \mu_1 = 2, 692 \cdot 10^4$.

Fig. 13.26 Ironing problem
of a stiff indenter and a larger
and softer base. By pushing
the indenter downwards and
dragging it across the surface
the possibility for large
sliding with friction is shown
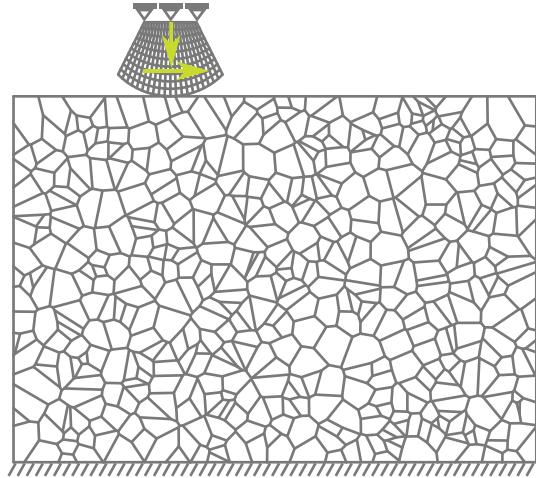
Contact is established using the penalty formulation with re-projection as described
in Sect. 13.4.4.2. The penalty parameters are chosen as $\epsilon_n = 7 \cdot 10^9$ and $\epsilon_t = 7 \cdot 10^4$.
For the Coulomb friction law a coefficient $\bar{\mu} = 0.3$ is selected.

The computations are performed for frictional contact. The frictional case is
computed for an unstructured Voronoi mesh using the virtual element method. The
size of the block's cross-section is 10×7. The indenter has a top surface of length
1 and a radius of $r = \sqrt{2}$. Figure 13.26 depicts the setup of the problem with the
block being meshed by Voronoi cells.

First the indenter is pushed down into the softer block at surface position $x = 3$
by means of a prescribed displacement $u_y = -1$ at the top surface which is applied
in 20 load steps, see Fig. 13.27 (top left) for the associated σ_{yy} stress field. The
vertical prescribed displacement is then fixed and the indentor is dragged along the
surface by applying at the top surface the horizontal $u_x = 8$ in 1000 load steps.

The contour plots on the left of Fig. 13.27 depict the deformed configuration for
a displacement $u_x = 2.25$ at different states of the simulation while the graps on the
right-hand side shows the normal and tangential reaction forces recorded at the top
surface of the indenter for the entire load history.

An increase of the normal reaction during the indentation can be observed. Due to
friction a considerable increase in the tangential force can be noted up to the point
where the contact changes its status from sticking to sliding.

A detailed study of the reaction plot shows a smooth normal reaction and very small
oscillations in the tangential direction. These oscillations where also noted in [67]
and [28] where this issue was resolved with a segment-to-segment mortar approach
or a smooth NURBS discretisation. Compared to the results stated in these papers
the results obtained in this work using the re-projection node-to-node contact are of
comparable accuracy and thus the new approach can be applied for finite tangential
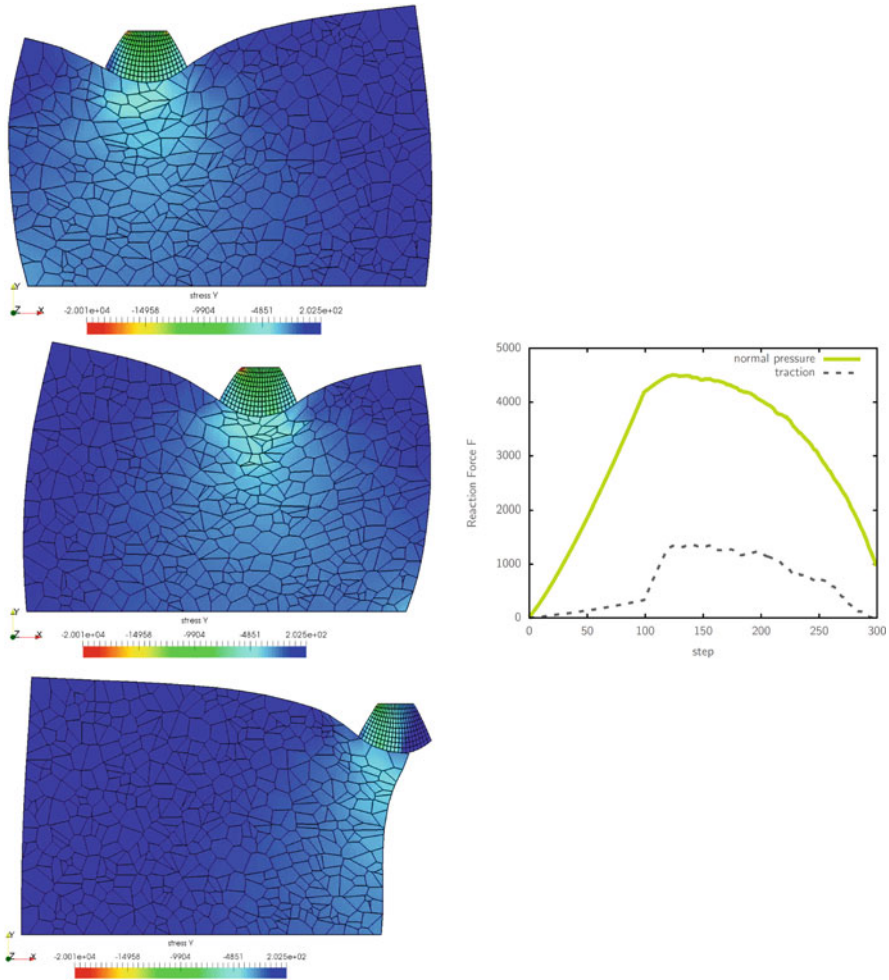sliding problems.

Fig. 13.27 Stress contours (left) and contact traction (right) for the ironing problem with friction for a Voronoi discretization. (top left) initial indentation; (middle left) friction state; (bottom left) final state, sliding from the block. (middle left) reaction forces in normal and tangential direction

As can be seen, the reactions computed with the Voronoi mesh show slight oscillations for the normal reaction and oscillations for the frictional response, see the graph on the right of Fig. 13.27. This can be explained with the coarser mesh and changing local stiffness due to the Voronoi discretization with elements of different size. Even for cases with size differences in the two contacting meshes the new re-projection contact algorithm is robust and stable.
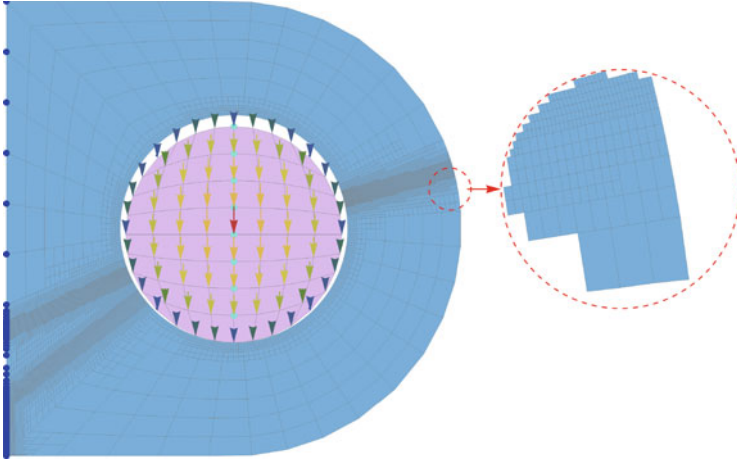
Fig. 13.28 Wall mounting of a bolt, loading, boundary conditions and virtual element mesh and a zoom-in of the mesh

13.4.5.3　Wall Mounting of a Bolt

In this example of a wall mounting for a bolt fracture modeling, using the phase field approach discussed in Sect. 13.3.4, is combined with contact.

A bolt of radius $r_b = 9.5$ [cm] is attached to a mount that is fixed on its left side to a wall, see Fig. 13.28. On this side all nodes are fixed in vertical direction and the middle node is fixed in normal direction. The mount has an external radius of $r_a = 20$ [cm] and an inner radius of $r_i = 10$ [cm]. The distance of the middle of the bolt from the wall is $x_b = 20$[cm] . The material for the bolt is assumed to be elastic with a Young's modulus of $E_b = 70000$ [kN/cm^2] and a Poisson ratio of $\nu_b = 0.3$. The mount has a Young's modulus of $E_m = 7000$ [kN/cm^2] and a Poisson ratio of $\nu_m = 0.3$. The material of the mount is brittle thus the phase field approach for brittle fracture can be applied. The associated critical energy release rate, see (13.3.23), is $g_c^m = 0.1$ [kN/cm] and the viscosity of the crack propagation is $\eta^m = 10^{-5}$ [kNs/cm^2] for the mount. The fracture length scale l in (13.3.20) is chosen as $l = 0.015$ [cm].

The bolt just touches the inner radius of the mount in the beginning of the simulation. The focus of this simulations is the failure mechanism of the mount due to loading. Hence the contact analysis plays a minor role which led to the use of a simple node-to-segment contact discretization using the penalty formulation with a penalty parameter of $\epsilon_n = 20000$ [kN/cm]. Since no tangent movement is expected friction can be neglected at the contact interface. The load is applied as body force in the bolt. The energy stabilization is used for the virtual element discretization with $\beta = 0.4$.
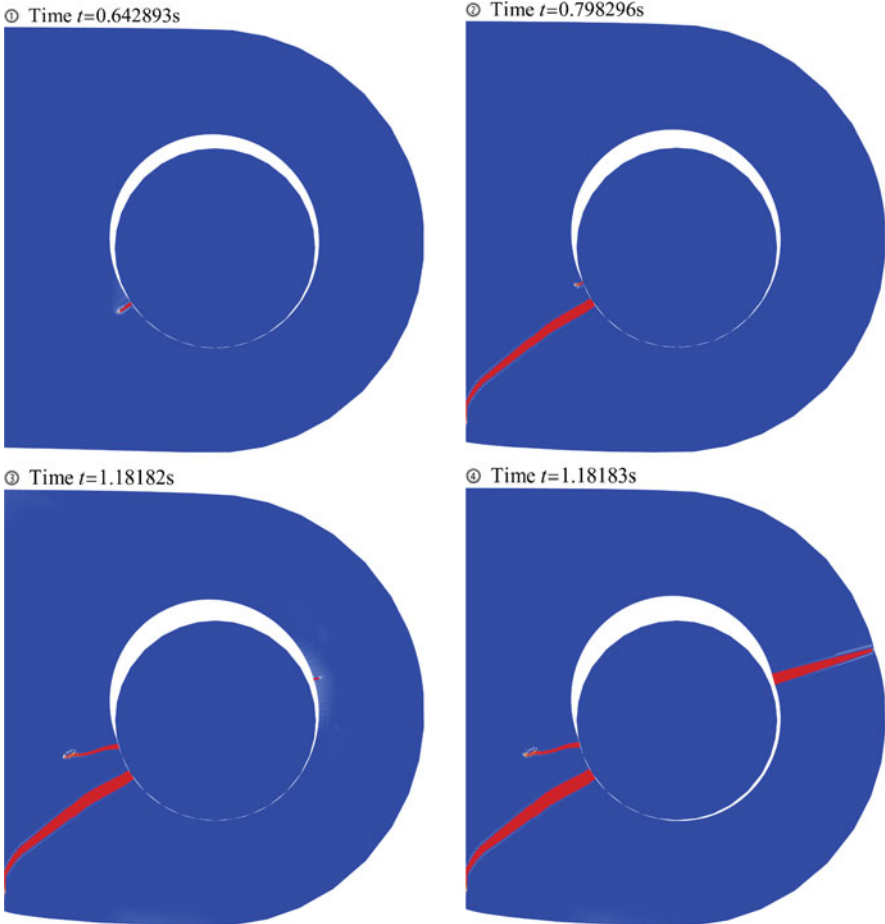
Fig. 13.29 Wall mounting of a bolt, fracture process

Mesh refinement in the expected fracture zone is applied in a adaptive manner. First a fine mesh around the bolt is used to find the location where the crack starts. After that the mesh is refined in this area. Here another advantage of the virtual element scheme pops up which is related to the inserting of arbitrary number of nodes on each edge of an element in a consistent way. This yields a C^0 continuous mesh, see right side of Fig. 13.28 and thus no hanging nodes occur, as would be in a finite element discretization.

When increasing the load a crack develops which is demonstrated in Fig. 13.29 for four different load stages showing the deformed configuration of the system. The crack starts, as is shown in the upper left plot in Fig. 13.29 and then increases to the wall with a new crack developing, see upper right plot in Fig. 13.29. The the second
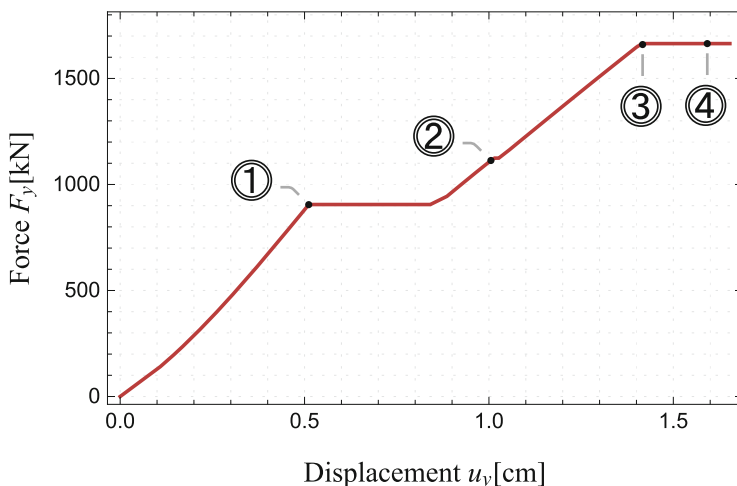
Fig. 13.30 Wall mounting of a bolt, load-delection curve of the fracture process

crack develops further, see lower left plot in Fig. 13.29 until the mount finally fails with a third crack developing as depicted in the lower right plot in Fig. 13.29.

The associated load displacement curve is depicted in Fig. 13.30 where the total load is plotted versus the mid displacement of the bolt. One can observe that first this curve increases almost linearly up to point ①. Here, at a load of around 900 kN the first crack starts to develop, see left upper plot of Fig. 13.29 leading to a damaged structure. However the system still has some residual stiffness and the load be increased further while the second crack develops. In this slope points ② and ③ are associated with the plots in the upper right and lower left part of Fig. 13.29. Note that the slope of the load deflection curve has a lower gradient. At around 1650 kN, point ③ the final failure of the mount is observed, see lower right side of Fig. 13.29 which is related to point ④ in Fig. 13.30 .

By combining the phase field method with the element cutting technology in Sect. 13.3.3, see also [45], we are able to predict the cracked deformed configuration, as shown in Fig. 13.31 (left). In this deformation stage the structure exhibits two main cracks that lead to total failure of the mount. Additionally the von Mises stress is plotted in Fig. 13.31 (right) just before failure which shows the maximum stresses around the first crack on the left and the maximum stress at the tip of the crack on the right.
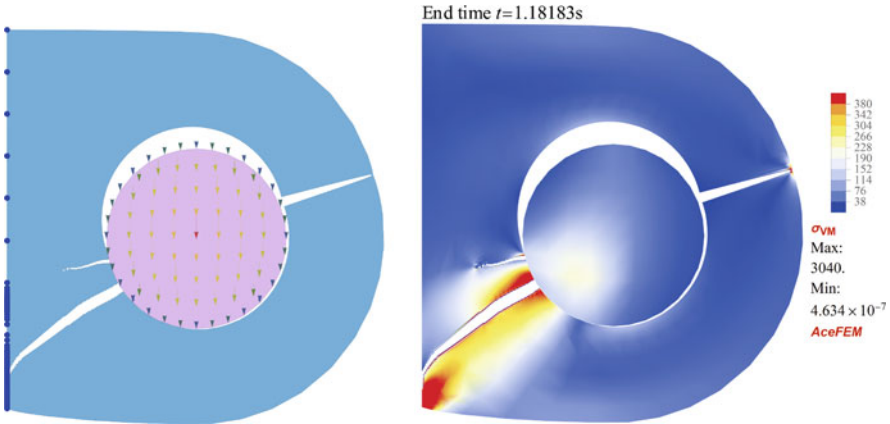
Fig. 13.31 Wall mounting of a bolt, fractured structure at failure load

13.5   Conclusion

In this contribution a relatively new discretization technique, the Virtual Element Method, was presented that introduces some new features to the numerical solution of problems in engineering. In particular, two directions were considered.

In Part I, a computational framework for crack propagation in isotropic brittle materials using an efficient virtual element scheme was outlined. One of the key novel features is the introduction of a robust cutting technique within elements for brittle crack propagation in 2D problems. Hereby the virtual element method confirms its effectiveness, robustness and flexibility in dealing with complex element shapes and arbitrary number of nodes in an element which can be changed due to the cutting process during the simulation. Additionally, crack formation was computed in an efficient way by continuum phase-field approaches to fracture. It is based on the regularization of sharp crack discontinuities. To this end, we proposed a rigorous variational-based framework for the fracture phase-field approach undergoing small strains. We examined the performance of the formulation by means of some numerical examples. It was shown that, the virtual element method offers a high degree of flexibility in terms of the element shape, so that cracks can be modeled with few elements and reduced computational cost.

Part II, explores the application of the virtual element method for large deformations to contact problems. By using a node insertion algorithm it was possible to create a stable node-to-node contact for frictionless and frictional cases. By adjusting the mesh adaptively, using re-projection, large tangential movements are allowed. This was only possible due to the advantage of VEM regarding geometrical flexibility in shape and number of vertices. The results were verified first with an analytical solution in the small deformation regime. Then the application to a finite deformation contact problem was shown. It was observed that for large

tangential sliding the node-to-node contact leads to smooth traction results and due to its simplicity is advantageous compared to classical segment based contact enforcements. Finally an example of a mount system combined contact with failure analysis using the phase field approach.

References

1. F. Aldakheel, B. Hudobivnik, E. Artioli, L. Beirão da Veiga, P. Wriggers, Curvilinear virtual elements for contact mechanics. Comput. Methods Appl. Mech. Eng. **372**, 113394 (2020)
2. F. Aldakheel, B. Hudobivnik, A. Hussein, P. Wriggers, Phase-field modeling of brittle fracture using an efficient virtual element scheme. Comput. Methods Appl. Mech. Eng. **341**, 443–466 (2018)
3. R. Alessi, S. Vidoli, L. De Lorenzis, A phenomenological approach to fatigue with a variational phase-field model: the one-dimensional case. Eng. Fract. Mech. (2017). https://doi.org/10.1016/j.engfracmech.2017.11.036
4. M. Ambati, T. Gerasimov, L. De Lorenzis, A review on phase-field models of brittle fracture and a new fast hybrid formulation. Comput. Mech. **55**(2), 383–405 (2015)
5. H. Amor, J.-J. Marigo, C. Maurini, Regularized formulation of the variational brittle fracture with unilateral contact: Numerical experiments. J. Mech. Phys. Solids **57**(8), 1209–1229 (2009)
6. E. Artioli, L. Beirão da Veiga, C. Lovadina, E. Sacco, Arbitrary order 2d virtual elements for polygonal meshes: part I, elastic problem. Comput. Mech. **60**, 355–377 (2017)
7. E. Artioli, L. Beirão da Veiga, C. Lovadina, E. Sacco, Arbitrary order 2d virtual elements for polygonal meshes: part II, inelastic problem. Comput. Mech. **60**, 643–657 (2017)
8. E. Artioli, Asymptotic homogenization of fibre-reinforced composites: a virtual element method approach. Meccanica **53**(6), 1187–1201 (2018)
9. R.S. Barsoum, Application of quadratic isoparametric finite elements in linear fracture mechanics. Int. J. Fract. **10**(4), 603–605 (1974)
10. L. Beirão da Veiga, F. Brezzi, L.D. Marini, Virtual elements for linear elasticity problems. SIAM J. Numer. Anal. **51**, 794–812 (2013)
11. L. Beirão da Veiga, C. Lovadina, D. Mora. A virtual element method for elastic and inelastic problems on polytope meshes. Comput. Methods Appl. Mech. Eng. **295**, 327–346 (2015)
12. L. Beirão da Veiga, F. Brezzi, L.D. Marini, A. Russo, The hitchhiker's guide to the virtual element method. Math. Models Methods Appl. Sci. **24**(8), 1541–1573 (2014)
13. L. Beirão da Veiga, F. Brezzi, L.D. Marini, A Russo, Polynomial preserving virtual elements with curved edges. Math. Models Methods Appl. Sci. **30**(8), 1555–1590 (2020)
14. L. Beirão da Veiga, F. Dassi, A. Russo, High-order virtual element method on polyhedral meshes. Comput. Math. Appl. **74**(5), 1110–1122 (2017)
15. L. Beirão da Veiga, A. Russo, G. Vacca, The virtual element method with curved edges. ESAIM: Math. Model. Numer. Anal. **53**(2), 375–404 (2019)
16. T. Belytschko, L.P. Bindeman, Assumed strain stabilization of the 4-node quadrilateral with 1-point quadrature for nonlinear problems. Comput. Methods Appl. Mech. Eng. **88**(3), 311–340 (1991)
17. T. Belytschko, T. Black, Elastic crack growth in finite elements with minimal remeshing. Int. J. Numer. Methods Eng. **45**(5), 601–620 (1999)
18. T. Belytschko, Y.Y. Lu, L. Gu, Element-free galerkin methods. Int. J. Numer. Methods Eng. **37**(2), 229–256 (1994)
19. M.F. Benedetto, S. Berrone, S. Scialó, A globally conforming method for solving flow in discrete fracture networks using the virtual element method. Finite Ele. Anal. Design **109**, 23–36 (2016)

20. M.J. Borden, C.V. Verhoosel, M.A. Scott, T.J.R. Hughes, C.M. Landis, A phase-field description of dynamic brittle fracture. Comput. Methods Appl. Mech. Eng. **217–220**, 77–95 (2012)
21. F. Brezzi, A. Buffa, K. Lipnikov, Mimetic finite differences for elliptic problems. ESAIM: Math. Model. Numer. Anal. **43**(2), 277–295 (2009)
22. H. Bufler, Zur Theorie der rollenden Reibung. Ingenieur-Archiv **27**(3), 137–152 (1959)
23. A. Cangiani, G. Manzini, A. Russo, N. Sukumar, Hourglass stabilization and the virtual element method. Int. J. Numer. Methods Eng. **102**(3–4), 404–436 (2015)
24. S.K. Chan, I.S. Tuba, W.K. Wilson, On the finite element method in linear fracture mechanics. Eng. Fract. Mech. **2**(1), 1–17 (1970)
25. H. Chi, L. Beirão da Veiga, G.H. Paulino, Some basic formulations of the virtual element method (VEM) for finite deformations. Comput. Methods Appl. Mech. Eng. **318**, 148–192 (2017)
26. M.L. De Bellis, P. Wriggers, B. Hudobivnik, Serendipity virtual element formulation for nonlinear elasticity. Comput. Struct. **223**, 106094 (2019)
27. M.L. De Bellis, P. Wriggers, B. Hudobivnik, G. Zavarise, Virtual element formulation for isotropic damage. Finite Ele. Anal. Design **144**, 38–48 (2018)
28. L. de Lorenzis, I. Temizer, P. Wriggers, G. Zavarise, A large deformation frictional contact formulation using NURBS-based isogeometric analysis. Int. J. Numer. Methods Eng. **87**, 1278–1300 (2011)
29. L. de Lorenzis, P. Wriggers, G. Zavarise, Isogeometric analysis of 3d large deformation contact problems with the augmented lagrangian formulation. Comput. Mech. **49**, 1–20 (2012)
30. W. Ehlers, C. Luo, A phase-field approach embedded in the theory of porous media for the description of dynamic hydraulic fracturing. Comput. Methods Appl. Mech. Eng. **315**, 348–368 (2017)
31. F. Erdogan, G.C. Sih, On the crack extension in plates under plane loading and transverse shear. J. Basic Eng. **85**(4), 519–525 (1963)
32. J.D. Eshelby, The calculation of energy release rates. Prospects Fract. Mech. 69–84 (1974)
33. D. Flanagan, T. Belytschko, A uniform strain hexahedron and quadrilateral with orthogonal hour-glass control. Int. J. Numer. Methods Eng. **17**, 679–706 (1981)
34. M. Fleming, Y.A. Chu, B. Moran, T. Belytschko, Enriched element-free Galerkin methods for crack tip fields. Int. J. Numer. Methods Eng. **40**(8), 1483–1504 (1998)
35. G.A. Francfort, J.-J. Marigo, Revisiting brittle fracture as an energy minimization problem. J. Mech. Phys. Solids **46**(8), 1319–1342 (1998)
36. A.L. Gain, C. Talischi, G.H. Paulino, On the virtual element method for three-dimensional linear elasticity problems on arbitrary polyhedral meshes. Comput. Methods Appl. Mech. Eng. **282**, 132–160 (2014)
37. J.O. Hallquist, Nike2d: An implicit, finite-deformation, finite element code for analysing the static and dynamic response of two-dimensional solids. Technical Report UCRL–52678, University of California, Lawrence Livermore National Laboratory, 1979
38. J.O. Hallquist, G.L. Goudreau, D.J. Benson, Sliding interfaces with contact-impact in large-scale lagrange computations. Comput. Methods Appl. Mech. Eng. **51**, 107–137 (1985)
39. Y. Heider, B. Markert, A phase-field modeling approach of hydraulic fracture in saturated porous media. Mech. Rese. Commun. **80**, 38–46 (2017)
40. T.K. Hellen, On the method of virtual crack extensions. Int. J. Numer. Methods Eng. **9**(1), 187–207 (1975)
41. R.D. Henshell, K.G. Shaw, Crack tip finite elements are unnecessary. Int. J. Numer. Methods Eng. **9**(3), 495–507 (1975)
42. C. Hesch, K. Weinberg, Thermodynamically consistent algorithms for a finite-deformation phase-field approach to fracture. Int. J. Numer. Methods Eng. **99**, 906–924 (2014)
43. B. Hudobivnik, F. Aldakheel, P. Wriggers, Low order 3d virtual element formulation for finite elasto-plastic deformations. Comput. Mech. **63**, 253–269 (2018)
44. A. Hussein, F. Aldakheel, B. Hudobivnik, P. Wriggers, P.-A. Guidault, O. Allix, A computational framework for brittle crack propagation based on an efficient virtual element method. Finite Ele. Anal. Design **159**, 15–32 (2019)

45. A. Hussein, B. Hudobivnik, P. Wriggers, A combined adaptive phase field and discrete cutting method for the prediction of crack paths. Comput. Methods Appl. Mech. Eng. **372**, 113329 (2020)
46. A.R. Ingraffea, G.E. Blandford, J.A. Liggett, Automatic modelling of mixed-mode fatigue and quasi-static crack propagation using the boundary element method, in *Fracture Mechanics: Fourteenth Symposium—Volume I: Theory and Analysis* (ASTM International, 1983)
47. C. Johnson, *Numerical Solution of Partial Differential Equations by the Finite Element Method* (Cambridge University Press, Cambridge, 1987)
48. K.L. Johnson, *Contact Mechanics* (Cambridge University Press, Cambridge, 1985)
49. B.L. Karihaloo, Q.Z. Xiao, Accurate determination of the coefficients of elastic crack tip asymptotic field by a hybrid crack element with p-adaptivity. Eng. Fract. Mech. **68**(15), 1609–1630 (2001)
50. J. Korelc, U Solinc, P. Wriggers, An improved EAS brick element for finite deformation. Comput. Mech. **46**, 641–659 (2010)
51. J. Korelc, P. Wriggers, *Automation of Finite Element Methods* (Springer, Berlin, 2016)
52. P. Krysl, Mean-strain eight-node hexahedron with stabilization by energy sampling. Int. J. Numer. Methods Eng. **103**, 437–449 (2015)
53. C. Kuhn, A. Schlüter, R. Müller, On degradation functions in phase field fracture models. Comput. Mater. Sci. **108**, 374–384 (2015)
54. T.A. Laursen, *Computational Contact and Impact Mechanics* (Springer, Berlin, New York, Heidelberg, 2002)
55. T.A. Laursen, M.A. Puso, J. Sanders, Mortar contact formulations for deformable–deformable contact: past contributions and new extensions for enriched and embedded interface formulations. Comput. Methods Appl. Mech. Eng. **205**, 3–15 (2012)
56. M. Marino, B. Hudobivnik, P. Wriggers, Computational homogenization of polycrystalline materials with the virtual element method. Comput. Methods Appl. Mech. Eng. **355**, 349–372 (2019)
57. C. Miehe, E. Gürses, M. Birkle, A computational framework of configurational-force-driven brittle fracture based on incremental energy minimization. Int. J. Fract. **145**(4), 245–259 (2007)
58. C. Miehe, M. Hofacker, L.-M. Schänzel, F. Aldakheel, Phase field modeling of fracture in multi-physics problems. Part II. brittle-to-ductile failure mode transition and crack propagation in thermo-elastic-plastic solids. Comput. Methods Appl. Mech. Eng. **294**, 486–522 (2015)
59. C. Miehe, F. Welschinger, M. Hofacker, Thermodynamically consistent phase-field models of fracture: variational principles and multi-field FE implementations. Int. J. Numer. Methods Eng. **83**, 1273–1311 (2010)
60. N. Moës, J. Dolbow, T. Belytschko, A finite element method for crack growth without remeshing. Int. J. Numer. Methods Eng. **46**(1), 131–150 (1999)
61. D.S. Mueller-Hoeppe, S. Loehnert, P. Wriggers, A finite deformation brick element with inhomogeneous mode enhancement. Int. J. Numer. Methods Eng. **78**, 1164–1187 (2009)
62. V.M. Nguyen-Thanh, X. Zhuang, H. Nguyen-Xuan, T. Rabczuk, P. Wriggers, A virtual element method for 2d linear elastic fracture analysis. Comput. Methods Appl. Mech. Eng. **340**, 366–395 (2018)
63. R.J. Nuismer, An energy release rate criterion for mixed mode fracture. Int. J. Fract. **11**(2), 245–250 (1975)
64. V. Padmanabhan, T.A. Laursen, A framework for development of surface smoothing procedures in large deformation frictional contact analysis. Finite Ele. Anal. Design **37**, 173–198 (2001)
65. P.C. Paris, G.C. Sih, Stress analysis of cracks, in *Fracture Toughness Testing and Its Applications* (ASTM International, 1965)
66. A. Portela, M.H. Aliabadi, D.P. Rooke, The dual boundary element method: effective implementation for crack problems. Int. J. Numer. Methods Eng. **33**(6), 1269–1287 (1992)
67. M.A. Puso, A 3D mortar method for solid mechanics. Int. J. Numer. Methods Eng. **59**(3), 315–336 (2004)

68. S. Reese, M. Kuessner, B.D. Reddy, A new stabilization technique to avoid hourglassing in finite elasticity. Int. J. Numer. Methods Eng. **44**, 1617–1652 (1999)
69. S. Reese, P. Wriggers, A new stabilization concept for finite elements in large deformation problems. Int. J. Numer. Methods Eng. **48**, 79–110 (2000)
70. J.R. Rice, A path independent integral and the approximate analysis of strain concentration by notches and cracks. J. Appl. Mech. **35**(2), 379–386 (1968)
71. J.R. Rice, G.F. Rosengren, Plane strain deformation near a crack tip in a power-law hardening material. J. Mech. Phys. Solids **16**(1), 1–12 (1968)
72. J.M. Sargado, E. Keilegavlen, I. Berre, J.M. Nordbotten, High-accuracy phase-field models for brittle fracture based on a new family of degradation functions. J. Mech. Phys. Solids **111**, 458–489 (2018)
73. N. Sukumar, J.H. Prévost, Modeling quasi-static crack growth with the extended finite element method part I: computer implementation. Int. J. Solids Struct. **40**(26), 7513–7537 (2003)
74. I. Temizer, P. Wriggers, T.J.R. Hughes, Contact treatment in isogeometric analysis with NURBS. Comput. Methods Appl. Mech. Eng. **200**, 1100–1112 (2011)
75. P. Tong, T.H.H. Pian, S.J. Lasry, A hybrid-element approach to crack problems in plane elasticity. Int. J. Numer. Methods Eng. **7**(3), 297–308 (1973)
76. M. Tur, F.J. Fuenmayor, P. Wriggers, A mortar-based frictional contact formulation for large deformations using lagrange multipliers. Comput. Methods Appl. Mech. Eng. **198**, 2860–2873 (2009)
77. C.V. Verhoosel, R. de Borst, A phase-field model for cohesive fracture. Int. J. Numer. Methods Eng. **96**, 43–62 (2013)
78. M.L. Williams, On the stress distribution at the base of a stationary crack. J. Appl. Mech. **24**, 109–114 (1956)
79. P. Wriggers, On consistent tangent matrices for frictional contact problems, in *Proceedings of NUMETA 87*, ed. by G.N. Pande, J. Middleton (M. Nijhoff Publishers, Dordrecht, 1987)
80. P. Wriggers, *Computational Contact Mechanics*, 2nd edn. (Springer, Berlin, Heidelberg, New York, 2006)
81. P. Wriggers, B. Hudobivnik, A low order virtual element formulation for finite elasto-plastic deformations. Comput. Methods Appl. Mech. Eng. **327**, 459–477 (2017)
82. P. Wriggers, B. Hudobivnik, F. Aldakheel, NURBS-based geometries: a mapping approach for virtual serendipity elements. Comput. Methods Appl. Mech. Eng. **378**, 113732 (2021)
83. P. Wriggers, L. Krstulovic-Opara, J. Korelc, Smooth C^1- interpolations for two-dimensional frictional contact problems. Int. J. Numer. Methods Eng. **51**, 1469–1495 (2001)
84. P. Wriggers, B.D. Reddy, W. Rust, B. Hudobivnik, Efficient virtual element formulations for compressible and incompressible finite deformations. Comput. Mech. **60**, 253–268 (2017)
85. P. Wriggers, W. Rust, B.D. Reddy, A virtual element method for contact. Comput. Mech. **58**, 1039–1050 (2016)
86. P. Wriggers, W.T. Rust, A virtual element method for frictional contact including large deformations. Eng. Comput. **36**, 2133–2161 (2019)
87. P. Wriggers, J.C. Simo, A note on tangent stiffnesses for fully nonlinear contact problems. Commun. Appl. Numer. Methods **1**, 199–203 (1985)
88. D. Xu, K.D. Hjelmstad, A new node-node to-node approach to contact/impact problems for two-dimensional elastic solids subject to finite deformation. Technical report, Newmark Structural Engineering Laboratory. University of Illinois at Urbana-Champaign, 2008
89. B. Yang, T.A. Laursen, X. Meng, Two dimensional mortar contact methods for large deformation frictional sliding. Int. J. Numer. Methods Eng. **62**(9), 1183–1225 (2005)
90. J.F. Yau, S.S. Wang, H.T. Corten, A mixed-mode crack analysis of isotropic solids using conservation laws of elasticity. J. Appl. Mech. **47**(2), 335 (1980)
91. J.F. Yau, S.S. Wang, H.T. Corten, A mixed-mode crack analysis of isotropic solids using conservation laws of elasticity. J. Appl. Mech. **47**(2), 335–341 (1980)